



# Handbook on the Physics and Chemistry of Rare Earths, volume 17

## Lanthanides/Actinides: Physics I

Elsevier, 1993

Edited by: Karl A. Gschneidner, Jr., LeRoy Eyring G.H. Lander and G.R. Choppin  
ISBN: 978-0-444-81502-6

## PREFACE

Karl A. GSCHNEIDNER, Jr., LeRoy EYRING, Gerry H. LANDER, and  
Gregory R. CHOPPIN

---

*These elements perplex us in our rearches [sic], baffle us in our speculations, and haunt us in our very dreams. They stretch like an unknown sea before us – mocking, mystifying, and murmuring strange revelations and possibilities.*

Sir William Crookes (February 16, 1887)

---

This volume of the Handbook is the first of a three-volume set of reviews devoted to the interrelationships, similarities, differences and contrasts of the lanthanide and actinide series of elements. The idea of these volumes grew out of a conversation between one of the editors, KAG, and a member of the editorial board, Stefan Hufner, in early June 1986. This idea was enthusiastically received by the other editor (LE) and editorial board members, and also the publishers. Numerous topics and authors were suggested and soon it was apparent that this special subject was too large to be covered in one or possibly two volumes, and that the editors (KAG and LE) of this series would need help from two leading scientists who had considerable experience and knowledge of both series of elements. Thus, Gerry H. Lander and Gregory R. Choppin were invited to be guest editors for this special set of volumes on the lanthanides/actinides. After they accepted, the four editors carefully and critically chose the various topics, and top experts in the various areas were invited to write reviews keeping in mind that the emphasis was to be on the interrelationships of the lanthanides and actinides. Now, more than seven years after Stefan Hufner's initial suggestion, the first volume, which is devoted to the physical aspects, is in print. Soon to follow are volumes emphasizing chemical comparisons and another dealing with additional physical topics.

The observations and comments of Sir William Crookes (as noted above) over 106 years ago about the lanthanides is even more appropriate to these lanthanide/actinide tomes. This is especially noteworthy because only two of the actinide series of elements were then known (Th and U), and the concept of such a series was not to develop for about 50 years. But we hope that the material presented in these three lanthanide/actinide volumes will shed light on some of the mysteries of yesterday, but as surely as we begin to understand them, new ones will arise to continue to haunt us as we move forward and ever onward.

In this volume we have eight chapters concerned with some of the physical aspects of the lanthanide and actinide series. The first three chapters are theoretical in nature and the last five are more heavily oriented toward experimental studies.

In chapter 110, M.R. Norman and D.D. Koelling have critically examined the validity of standard electronic band structure calculations based on the local density approximation (LDA) as applied to f-electron systems, especially in those systems in which the low-temperature ground state is thought to be a Fermi liquid. They note that the LDA method works well for itinerant f-electron systems and even strongly enhanced ones (whether Ce-base or U-base compounds), but there are some problems especially with regard to the large mass enhancements, magnetic moments and localization.

In the next review (chapter 111), S.H. Liu examines phenomenological approaches to heavy-fermion and mixed-valence materials. He notes that there are two basic approaches to understanding these phenomena: the Fermi-liquid models, which are applicable at low temperatures, and the spin fluctuation models, which work well for describing high-temperature properties and behaviors. At the present time Liu concludes that "the field is still wide open" before we come to even a reasonable understanding of anomalous f-electron behaviors.

In the third theoretical paper (chapter 112), B. Johansson and M.S.S. Brooks describe the use of first principles calculations to obtain the cohesive properties of lanthanide and actinide materials. As the authors note, in the past 20 years theorists have been able to calculate the lattice parameters of the material, evaluate the correct crystal structure, and accurately calculate its cohesive energy.

The first of the five chapters, which, more or less, deal with experimental aspects of the lanthanide/actinide materials, is concerned with the structural behavior of these materials at high pressures (chapter 113 by U. Benedict and W.B. Holzapfel). The authors show that the spatial extent of the f-wave functions around the nucleus plays an important role in governing the formation of various crystal structure as a function of both pressure and atomic number in the elemental metals. Because of the lack of knowledge of the high-pressure behaviors in their compounds, the systematic study and understanding in f-element compounds is much less advanced than for the metals.

In chapter 114, O. Vogt and K. Mattenberger examine the magnetic behaviors of the lanthanide and actinide B1, NaCl-type structures. The magnetic properties of a sample depend upon: the spectroscopic state of the f-element and the possibility of *J*-mixing, the electric crystalline field, the exchange interactions and hybridization. The competition between these various factors can make the materials complicated or simple with respect to their magnetic behaviors.

In the next chapter (115), J.M. Fournier and E. Gratz have reviewed the transport properties of lanthanide/actinide compounds. These include: the electrical resistivity, thermal conductivity, thermoelectric power, magnetoresistance and the Hall effect. As expected, most of this review deals with the electrical resistivity because of the preponderance of data on this property, relative to the other four. Throughout this chapter the authors attempt to use the available information on the transport properties to help improve our understanding of the differences and similarities of

lanthanide and actinide intermetallic compounds, even though an exact theoretical interpretation of the experimental observations is difficult.

The importance of Mössbauer spectroscopy in probing electronic structures of intermetallic compounds, especially those reflected in the magnetic properties, is discussed by W. Potzel, G.M. Kalvius and J. Gal (chapter 116). The authors have focused their discussions on selected samples where the differences between lanthanides and actinides can be best contrasted. As the authors note, the two most interesting elements, at least with respect to anomalous f-electron behaviors, Ce and U, cannot be studied by Mössbauer spectroscopy because of the lack of a suitable isotope in the case of Ce, and just the experimental difficulty in getting Mössbauer spectra for U.

The final chapter (117) by G.H. Lander reviews the elastic neutron scattering behavior, which yields information on the spatial extent of the unpaired electrons that contribute to the spin and orbital moments, the magnetic structure, and correlation effects between magnetic moments that occurs when the material is close to its magnetic ordering temperature. Much of the information obtained by neutron scattering is difficult, if not impossible, to get from other experimental techniques. Some of the more significant results are: the elucidation of the charge-density wave in U; magnetic form factors (i.e. the spatial extent of magnetization densities); the elucidation of magnetic structures, many of which are quite complex; and magnetic critical scattering.

*Dedicated to*

**GLENN T. SEABORG**

Among the many noteworthy scientific achievements of the 20th century, there are only a very few that can match the discovery of the actinide elements in its impact on science and society. The addition of an entire new family of largely man-made elements to the Periodic Table, and the formulation of the actinide concept have had a profound influence on the way physicists and chemists think about the electronic structures of the elements. The new insights arising from studies on the chemistry and physics of the heaviest elements has had an especially important influence on the way we think about the more familiar elements of the Periodic Table, in particular, the rare earths. In the saga of the actinide elements, Glenn Seaborg has been the pivotal figure. The dedication to Glenn Seaborg of these volumes of *the Handbook on the Physics and Chemistry of Rare Earths*, which deal with the relationships of the lanthanide and actinide elements, is thus a fitting recognition of the exceptionally important contribution that his actinide element studies have made to many branches of science.

Glenn Seaborg's scientific career began in the 1930's as a research associate of G.N. Lewis at the University of California. He early became convinced that the science of nuclear chemistry, then in its infancy, provided challenging opportunities for scientific discovery. In the Lawrence Radiation Laboratory, in the course of a few years, he validated his intuition by the discovery of a host of isotopes, many of which have become important in research and medicine. Among these are cobalt-60, iodine-131, technetium-99m, cesium-137, and, of course, the plutonium isotopes. In 1944, he formulated the actinide concept of heavy-element electronic structure that accurately predicted the existence of a family of rare earth-like elements at the end of the Periodic Table as it was generally presented at that time. The actinide concept was the guide to the discovery of the remaining members of the actinide elements. In addition to the fissile plutonium isotopes, he and his co-workers over the years discovered no less than nine additional members of the new rare earth-like family of elements. These discoveries have been of great relevance not only to purely scientific matters but also to such global problems as nuclear energy and the control of nuclear weapons.

In addition to his life as an active scientist, Glenn Seaborg has had a distinguished career in academic and public life. He served at various times as Chancellor of the University of California at Berkeley, Chairman of the Atomic Energy Commission for a period of ten years, and Chairman of the Lawrence Hall of Science, to name only a few of his extra-scientific activities. He was the recipient of a Nobel Prize (1951) for his discoveries in the chemistry of the transuranium elements, and has received encomiums from most of the scientific societies of the world.

In spite of worldly distractions, Glenn Seaborg has never wavered in his life-long commitment to science. He continues his research into the chemistry and nuclear systematics of the actinide elements. Recently, he has focused his attention on the possible existence of still another family of superheavy elements at the end of the Periodic Table, and the development of new methods for the synthesis of superheavy elements. The dedication of these volumes to Glenn Seaborg is not only a testimonial to his scientific achievements; it is also an appreciation of the example that he continues to set.

## CONTENTS

Preface v

Dedication ix

Contents xi

Contents of Volumes 1–16 xiii

110. M.R. Norman and D.D. Koelling  
*Electronic structure, Fermi surfaces, and superconductivity in f electron metals* 1
111. S.H. Liu  
*Phenomenological approach to heavy-fermion systems* 87
112. B. Johansson and M.S.S. Brooks  
*Theory of cohesion in rare earths and actinides* 149
113. U. Benedict and W.B. Holzapfel  
*High-pressure studies – Structural aspects* 245
114. O. Vogt and K. Mattenberger  
*Magnetic measurements on rare earth and actinide mononictides and monochalcogenides* 301
115. J.M. Fournier and E. Gratz  
*Transport properties of rare earth and actinide intermetallics* 409
116. W. Potzel, G.M. Kalvius and J. Gal  
*Mössbauer studies on electronic structure of intermetallic compounds* 539
117. G.H. Lander  
*Neutron elastic scattering from actinides and anomalous lanthanides* 635
- Author index* 711
- Subject index* 753

# CONTENTS OF VOLUMES 1–16

## VOLUME 1: Metals

1978, 1st repr. 1982, 2nd repr. 1991; ISBN 0-444-85020-1

1. Z.B. Goldschmidt, *Atomic properties (free atom)* 1
  2. B.J. Beaudry and K.A. Gschneidner Jr, *Preparation and basic properties of the rare earth metals* 173
  3. S.H. Liu, *Electronic structure of rare earth metals* 233
  4. D.C. Koskenmaki and K.A. Gschneidner Jr, *Cerium* 337
  5. L.J. Sundström, *Low temperature heat capacity of the rare earth metals* 379
  6. K.A. McEwen, *Magnetic and transport properties of the rare earths* 411
  7. S.K. Sinha, *Magnetic structures and inelastic neutron scattering: metals, alloys and compounds* 489
  8. T.E. Scott, *Elastic and mechanical properties* 591
  9. A. Jayaraman, *High pressure studies: metals, alloys and compounds* 707
  10. C. Probst and J. Wittig, *Superconductivity: metals, alloys and compounds* 749
  11. M.B. Maple, L.E. DeLong and B.C. Sales, *Kondo effect: alloys and compounds* 797
  12. M.P. Dariel, *Diffusion in rare earth metals* 847
- Subject index 877

## VOLUME 2: Alloys and intermetallics

1979, 1st repr. 1982, 2nd repr. 1991; ISBN 0-444-85021-X

13. A. Iandelli and A. Palenzona, *Crystal chemistry of intermetallic compounds* 1
  14. H.R. Kirchmayr and C.A. Poldy, *Magnetic properties of intermetallic compounds of rare earth metals* 55
  15. A.E. Clark, *Magnetostrictive RFe<sub>2</sub> intermetallic compounds* 231
  16. J.J. Rhyne, *Amorphous magnetic rare earth alloys* 259
  17. P. Fulde, *Crystal fields* 295
  18. R.G. Barnes, *NMR, EPR and Mössbauer effect: metals, alloys and compounds* 387
  19. P. Wachter, *Europium chalcogenides: EuO, EuS, EuSe and EuTe* 507
  20. A. Jayaraman, *Valence changes in compounds* 575
- Subject Index 613

## VOLUME 3: Non-metallic compounds – I

1979, 1st repr. 1984; ISBN 0-444-85215-8

21. L.A. Haskin and T.P. Paster, *Geochemistry and mineralogy of the rare earths* 1
  22. J.E. Powell, *Separation chemistry* 81
  23. C.K. Jørgensen, *Theoretical chemistry of rare earths* 111
  24. W.T. Carnall, *The absorption and fluorescence spectra of rare earth ions in solution* 171
  25. L.C. Thompson, *Complexes* 209
  26. G.G. Libowitz and A.J. Maeland, *Hydrides* 299
  27. L. Eyring, *The binary rare earth oxides* 337
  28. D.J.M. Bevan and E. Summerville, *Mixed rare earth oxides* 401
  29. C.P. Khattak and F.F.Y. Wang, *Perovskites and garnets* 525
  30. L.H. Brixner, J.R. Barkley and W. Jeitschko, *Rare earth molybdates (VI)* 609
- Subject index 655



**VOLUME 4: Non-metallic compounds – II**

1979, 1st repr. 1984; ISBN 0-444-85216-6

31. J. Flahaut, *Sulfides, selenides and tellurides* 1
32. J.M. Haschke, *Halides* 89
33. F. Hulliger, *Rare earth pnictides* 153
34. G. Blasse, *Chemistry and physics of R-activated phosphors* 237
35. M.J. Weber, *Rare earth lasers* 275
36. F.K. Fong, *Nonradiative processes of rare-earth ions in crystals* 317
- 37A. J.W. O'Laughlin, *Chemical spectrophotometric and polarographic methods* 341
- 37B. S.R. Taylor, *Trace element analysis of rare earth elements by spark source mass spectroscopy* 359
- 37C. R.J. Conzemius, *Analysis of rare earth matrices by spark source mass spectrometry* 377
- 37D. E.L. DeKalb and V.A. Fassel, *Optical atomic emission and absorption methods* 405
- 37E. A.P. D'Silva and V.A. Fassel, *X-ray excited optical luminescence of the rare earths* 441
- 37F. F.W.V. Boynton, *Neutron activation analysis* 457
- 37G. S. Schuhmann and J.A. Philpotts, *Mass-spectrometric stable-isotope dilution analysis for lanthanides in geochemical materials* 471
38. J. Reuben and G.A. Elgavish, *Shift reagents and NMR of paramagnetic lanthanide complexes* 483
39. J. Reuben, *Bioinorganic chemistry: lanthanides as probes in systems of biological interest* 515
40. T.J. Haley, *Toxicity* 553
- Subject index 587

**VOLUME 5**

1982, 1st repr. 1984; ISBN 0-444-86375-3

41. M. Gasgnier, *Rare earth alloys and compounds as thin films* 1
42. E. Gratz and M.J. Zuckermann, *Transport properties (electrical resistivity, thermoelectric power and thermal conductivity) of rare earth intermetallic compounds* 117
43. F.P. Netzer and E. Bertel, *Adsorption and catalysis on rare earth surfaces* 217
44. C. Boulesteix, *Defects and phase transformation near room temperature in rare earth sesquioxides* 321
45. O. Greis and J.M. Haschke, *Rare earth fluorides* 387
46. C.A. Morrison and R.P. Leavitt, *Spectroscopic properties of triply ionized lanthanides in transparent host crystals* 461
- Subject index 693

**VOLUME 6**

1984; ISBN 0-444-86592-6

47. K.H.J. Buschow, *Hydrogen absorption in intermetallic compounds* 1
48. E. Parthé and B. Chabot, *Crystal structures and crystal chemistry of ternary rare earth–transition metal borides, silicides and homologues* 113
49. P. Rogl, *Phase equilibria in ternary and higher order systems with rare earth elements and boron* 335
50. H.B. Kagan and J.L. Namy, *Preparation of divalent ytterbium and samarium derivatives and their use in organic chemistry* 525
- Subject index 567

**VOLUME 7**

1984; ISBN 0-444-86851-8

51. P. Rogl, *Phase equilibria in ternary and higher order systems with rare earth elements and silicon* 1
52. K.H.J. Buschow, *Amorphous alloys* 265
53. H. Schumann and W. Genthé, *Organometallic compounds of the rare earths* 446
- Subject index 573

**VOLUME 8**

1986; ISBN 0-444-86971-9

54. K.A. Gschneidner Jr and F.W. Calderwood, *Intra rare earth binary alloys: phase relationships, lattice parameters and systematics* 1
55. X. Gao, *Polarographic analysis of the rare earths* 163
56. M. Leskelä and L. Niinistö, *Inorganic complex compounds I* 203
57. J.R. Long, *Implications in organic synthesis* 335
- Errata 375
- Subject index 379

**VOLUME 9**

1987; ISBN 0-444-87045-8

58. R. Reisfeld and C.K. Jørgensen, *Excited state phenomena in vitreous materials* 1
59. L. Niinistö and M. Leskelä, *Inorganic complex compounds II* 91
60. J.-C.G. Bünzli, *Complexes with synthetic ionophores* 321
61. Zhiquan Shen and Jun Ouyang, *Rare earth coordination catalysis in stereospecific polymerization* 395
- Errata 429
- Subject index 431

**VOLUME 10: High energy spectroscopy**

1988; ISBN 0-444-87063-6

62. Y. Baer and W.-D. Schneider, *High-energy spectroscopy of lanthanide materials – An overview* 1
63. M. Campagna and F.U. Hillebrecht, *f-electron hybridization and dynamical screening of core holes in intermetallic compounds* 75
64. O. Gunnarsson and K. Schönhammer, *Many-body formulation of spectra of mixed valence systems* 103
65. A.J. Freeman, B.I. Min and M.R. Norman, *Local density supercell theory of photoemission and inverse photoemission spectra* 165
66. D.W. Lynch and J.H. Weaver, *Photoemission of Ce and its compounds* 231
67. S. Hüfner, *Photoemission in chalcogenides* 301
68. J.F. Herbst and J.W. Wilkins, *Calculation of 4f excitation energies in the metals and relevance to mixed valence systems* 321
69. B. Johansson and N. Mårtensson, *Thermodynamic aspects of 4f levels in metals and compounds* 361
70. F.U. Hillebrecht and M. Campagna, *Bremsstrahlung isochromat spectroscopy of alloys and mixed valent compounds* 425
71. J. Röhrler, *X-ray absorption and emission spectra* 453
72. F.P. Netzer and J.A.D. Matthew, *Inelastic electron scattering measurements* 547
- Subject index 601

**VOLUME 11: Two-hundred-year impact of rare earths on science**

1988; ISBN 0-444-87080-6

- H.J. Svec, *Prologue* 1
73. F. Szabadváry, *The history of the discovery and separation of the rare earths* 33
74. B.R. Judd, *Atomic theory and optical spectroscopy* 81
75. C.K. Jørgensen, *Influence of rare earths on chemical understanding and classification* 197
76. J.J. Rhyne, *Highlights from the exotic phenomena of lanthanide magnetism* 293
77. B. Bleaney, *Magnetic resonance spectroscopy and hyperfine interactions* 323
78. K.A. Gschneidner Jr and A.H. Daane, *Physical metallurgy* 409
79. S.R. Taylor and S.M. McLennan, *The significance of the rare earths in geochemistry and cosmochemistry* 485
- Errata 579
- Subject index 581

**VOLUME 12**

1989; ISBN 0-444-87105-5

80. J.S. Abell, *Preparation and crystal growth of rare earth elements and intermetallic compounds* 1
  81. Z. Fisk and J.P. Remeika, *Growth of single crystals from molten metal fluxes* 53
  82. E. Burzo and H.R. Kirchmayr, *Physical properties of  $R_2Fe_{14}B$ -based alloys* 71
  83. A. Szytuła and J. Leciejewicz, *Magnetic properties of ternary intermetallic compounds of the  $RT_2X_2$  type* 133
  84. H. Maletta and W. Zinn, *Spin glasses* 213
  85. J. van Zytveld, *Liquid metals and alloys* 357
  86. M.S. Chandrasekharaiah and K.A. Gingerich, *Thermodynamic properties of gaseous species* 409
  87. W.M. Yen, *Laser spectroscopy* 433
- Subject index 479

**VOLUME 13**

1990; ISBN 0-444-88547-1

88. E.I. Gladyshevsky, O.I. Bodak and V.K. Pecharsky, *Phase equilibria and crystal chemistry in ternary rare earth systems with metallic elements* 1
  89. A.A. Eliseev and G.M. Kuzmichyeva, *Phase equilibrium and crystal chemistry in ternary rare earth systems with chalcogenide elements* 191
  90. N. Kimizuka, E. Takayama-Muromachi and K. Siratori, *The systems  $R_2O_3$ – $M_2O_3$ – $M'O$*  283
  91. R.S. Houk, *Elemental analysis by atomic emission and mass spectrometry with inductively coupled plasmas* 385
  92. P.H. Brown, A.H. Rathjen, R.D. Graham and D.E. Tribe, *Rare earth elements in biological systems* 423
- Errata 453  
Subject index 455

**VOLUME 14**

1991; ISBN 0-444-88743-1

93. R. Osborn, S.W. Lovesey, A.D. Taylor and E. Balcar, *Intermultiplet transitions using neutron spectroscopy* 1
  94. E. Dormann, *NMR in intermetallic compounds* 63
  95. E. Zirngiebl and G. Güntherodt, *Light scattering in intermetallic compounds* 163
  96. P. Thalmeier and B. Lüthi, *The electron–phonon interaction in intermetallic compounds* 225
  97. N. Grewe and F. Steglich, *Heavy fermions* 343
- Subject index 475

**VOLUME 15**

1991; ISBN 0-444-88966-3

98. J.G. Sereni, *Low-temperature behaviour of cerium compounds* 1
  99. G.-y. Adachi, N. Imanaka and Zhang Fuzhong, *Rare earth carbides* 61
  100. A. Simon, HJ. Mattausch, G.J. Miller, W. Bauhofer and R.K. Kremer, *Metal-rich halides* 191
  101. R.M. Almeida, *Fluoride glasses* 287
  102. K.L. Nash and J.C. Sullivan, *Kinetics of complexation and redox reactions of the lanthanides in aqueous solutions* 347
  103. E.N. Rizkalla and G.R. Choppin, *Hydration and hydrolysis of lanthanides* 393
  104. L.M. Vallarino, *Macrocyclic complexes of the lanthanide(III) yttrium(III) and dioxouranium(VI) ions from metal-templated syntheses* 443
- Errata 513  
Subject index 515

**MASTER INDEX, Vols. 1–15**

1993; ISBN 0-444-89965-0

**VOLUME 16**

1993; ISBN 0-444-89782-8

105. M. Loewenhaupt and K.H. Fischer, *Valence-fluctuation and heavy-fermion 4f systems* 1  
106. I.A. Smirnov and V.S. Oskotski, *Thermal conductivity of rare earth compounds* 107  
107. M.A. Subramanian and A.W. Sleight, *Rare earths pyrochlores* 225  
108. R. Miyawaki and I. Nakai, *Crystal structures of rare earth minerals* 249  
109. D.R. Chopra, *Appearance potential spectroscopy of lanthanides and their intermetallics* 519  
Author index 547  
Subject index 579

## Chapter 110

# ELECTRONIC STRUCTURE, FERMI SURFACES, AND SUPERCONDUCTIVITY IN f ELECTRON METALS\*

M.R. NORMAN and D.D. KOELLING

Materials Science Division, Argonne National Laboratory, Argonne, IL 60439, USA

---

### Contents

Symbols	1	3.4.3. TmSe, TmTe, SmS	46
1. Introduction	2	3.5. LaNi, CeNi	47
2. Formalism	3	3.6. C15 cubic Laves phases	48
3. Lanthanide and actinide materials	10	3.7. UCu <sub>5</sub>	52
3.1. L1 <sub>2</sub> structured materials	10	3.8. RB <sub>6</sub> materials	55
3.1.1. CeRh <sub>3</sub> -CePd <sub>3</sub> -URu <sub>3</sub> - URh <sub>3</sub> -UIr <sub>3</sub>	12	3.9. RCu <sub>6</sub> materials	58
3.1.2. The group III and group IV materials	17	3.10. UB <sub>12</sub> , UBe <sub>13</sub>	61
3.1.2.1. UGe <sub>3</sub>	18	3.11. R-AT <sub>2,3</sub> M <sub>2</sub> materials	61
3.1.2.2. CeSn <sub>3</sub> -USn <sub>3</sub> - NpSn <sub>3</sub> -PuSn <sub>3</sub>	22	3.11.1. CeRu <sub>2</sub> Si <sub>2</sub>	63
3.1.2.3. CeIn <sub>3</sub> and UIn <sub>3</sub>	26	3.11.2. URu <sub>2</sub> Si <sub>2</sub>	66
3.2. UPt <sub>3</sub> -UPd <sub>3</sub> -Pr	28	4. Superconductivity in heavy-fermion metals	67
3.3. Gd	38	4.1. Phonons	67
3.4. NaCl structured materials	41	4.2. Charge fluctuations	68
3.4.1. Ce pnictides: especially CeSb	41	4.3. Spin fluctuations	69
3.4.2. ThC and UC	45	5. Conclusions	74
		References	77

---

### Symbols

ASW	augmented spherical wave	$k$	wave vector of electron
dHvA	de Haas-van Alphen effect	$l$	orbital vector of electron
DOS	density of states	$L$	total orbital angular momentum
$e_F, E_F$	Fermi energy	LAPW	linearized augmented plane wave
$g$	$g$ factor	LDA	local density approximation
$I$	spin-spin response function	LMTO	linearized muffin-tin orbital
$j$	angular momentum (spin plus orbital) of electron	LSDA	local spin density approximation
$J$	exchange energy	$m^*$	quasiparticle mass
		$m_b$	band mass

\* This work was supported by the U.S. Department of Energy, Office of Basic Energy Sciences, under Contract No. W-31-109-ENG-38.

$M_S$	$z$ component of total spin angular momentum	$\Gamma$	neutron scattering linewidth
$N$	degeneracy of $f$ level	$\delta_l$	scattering phase shift in the $l$ th channel
$n_f$	number of $f$ electrons	$\Delta$	superconducting order parameter
$q$	momentum transfer	$\varepsilon$	electron energy
$Q$	ordering wave vector	$\Theta_D$	Debye temperature
$s$	spin vector of electron	$\lambda$	superconducting coupling constant
$S$	total spin angular momentum	$\mu$	$z$ component of angular momentum (spin plus orbital) of electron
$T^*$	renormalized energy scale	$\mu^*$	Coulomb pseudopotential
$T_c$	superconducting transition temperature	$\mu_B$	Bohr magneton
$T_K$	Kondo temperature	$\Sigma$	self-energy
$T_N$	Néel transition temperature	$\chi$	magnetic susceptibility
$U$	Coulomb energy	$\chi_0$	non-interacting susceptibility
$V$	superconducting pair potential	$\chi_b$	band susceptibility
$\gamma$	electronic specific heat coefficient	$\omega$	frequency

---

## 1. Introduction

This volume focusses on a comparison and contrasting of rare earth and actinide materials. The obvious point of contact is the nature and behaviour of their  $f$  states. Examining the parallels between these two sets of materials has proven quite instructive, especially in regard to so-called heavy-fermion behavior. Heavy-fermion metals are a remarkable collection of lanthanide and actinide compounds which at high temperatures exhibit local moment behavior, but at low temperatures exhibit a Fermi liquid ground state with a very large electronic specific heat coefficient (100–2000 mJ/mol K<sup>2</sup>) and corresponding large Pauli-like susceptibility. The observed value of  $\gamma$  is of the order of 5–100 times that given by a standard electronic band structure calculation, implying that the quasiparticles are strongly renormalized objects. The actual low-temperature ground states observed have been (1) paramagnetic, (2) antiferromagnetic (with a moment significantly less than the free ion value) and (3) superconducting (Stewart 1984). There is strong evidence that the superconducting ground state, at least in the uranium alloys, is of an anisotropic variety, analogous to the superfluid ground state observed in <sup>3</sup>He. There is also evidence that the superconductivity is also associated with some form of very weak moment magnetism ( $10^{-2}$  to  $10^{-1}\mu_B$ ), the nature of which is not very well understood at this time. Both the superconductivity and the weak moment magnetism are quite sensitive to doping. For instance, doping UPt<sub>3</sub> with a few percent Pd leads to a destruction of the superconducting ground state, and an increase of the magnetic moment from a value of  $0.02\mu_B$  (Aeppli et al. 1988) to about  $0.6\mu_B$  (Frings et al. 1987). Further doping with Pd leads to localization of the  $f$  electrons (De Visser et al. 1987b). Thus, as also seen in the case of <sup>3</sup>He, the superconducting ground state is close to both a magnetic instability and a localization instability.

The strong renormalizations seen in heavy-fermion metals have induced considerable doubt concerning the validity of standard electronic band structure calculations based on the local density approximation (Lee et al. 1986). One of our goals

is to analyze this question in detail by seeing what electronic structure calculations say about the nature of the f electrons in these and related systems. Our scope here will be limited to the low-temperature ground state, which is assumed to be a Fermi liquid.

In section 2, we briefly outline density functional theory and the various approximations employed including the local density approximation (LDA), and discuss generalizations of LDA to incorporate spin (LSDA), orbital, and relativistic effects. We also discuss phenomenological “renormalized band” schemes based on the slave-boson or Kondo phase-shift methods.

In section 3 – the main section – we discuss results for many f electron materials, examining where possible comparisons to LDA calculations which treat the f electrons as either band-like (itinerant f) or core-like (local f), and to renormalized band calculations. Although there is some discussion of bonding properties, we concentrate on the general electronic structure, the Fermi-surface related properties, and magnetism (a detailed discussion of bonding properties is given by Johansson and Brooks in this volume).

In section 4, we discuss various theories for heavy electron superconductors, including possible pairing via phonons, charge fluctuations, and spin fluctuations, and emphasize the importance that the normal state electronic structure will play in determining the correct theory of this most unusual phenomenon.

## 2. Formalism

Most calculations of the electronic structure of solids, including those performed for f electron metals, are based on density functional theory within the Kohn–Sham ansatz to which, in turn, a local density (LDA) or local spin density (LSDA) approximation is applied. Each part of this characterization has its own implications and it is important to understand which is relevant when judging the validity of results.

Density functional theory, as generally applied, is a theory for the ground state (Hohenberg and Kohn 1964) although it can be generalized to a statistical ensemble (Mermin 1965). As a ground state theory, one would expect density functional theory to properly describe the Fermi surface but not the quasiparticle masses (the difference being due largely to the energy dependence of the self-energy). A critical simplification of the theory is achieved by making the Kohn–Sham ansatz (Kohn and Sham 1965) which asserts there is a mapping between the actual system of interacting electrons and a fictitious system of non-interacting electrons which has the same charge density. This assertion is analogous to the assumption made in the Landau theory of Fermi liquids that the low-energy excitations have a one-to-one correspondence to free particle excitations. Of course, these mappings can fail should a singularity be encountered when turning on the electron–electron interaction. When it does apply, and it does in most cases, the advantage of the Kohn–Sham ansatz is that it reduces the problem to a set of single-particle-like equations where the kinetic energy and the direct Coulomb interaction are readily evaluated. The remaining non-direct Coulomb effects (including exchange) constitute an unknown functional called the

exchange–correlation functional. Fortunately, these effects are relatively small, so one might hope to approximate this unknown functional, as will be discussed further below when describing the LDA.

The Kohn–Sham ansatz greatly facilitates Fermi surface studies. One solves for a set of single-particle-like Bloch states and occupies them assuming Fermi–Dirac statistics. Although the resulting Kohn–Sham Fermi surface is not equivalent to the quasiparticle one (Mearns 1988), it is expected to be a good approximation to it. In fact, within the LDA, the Kohn–Sham Fermi surface exactly matches the Fermi surface as determined from the response functions (Mearns and Kohn 1989). For the  $f$  electron case, though, we must consider how the Kohn–Sham ansatz is to be implemented due to their strong atomic localization. For most  $f$  electron materials, the  $f$  states can be successfully described by the standard rare earth model where the  $f$  electrons form an incomplete atomic core shell accomodating an integral number of electrons. For such materials, one can utilize a modified Kohn–Sham mapping which explicitly includes the  $f$  states as core states by not permitting them to hybridize with the other electrons. This scheme works well for rare earth systems (note the discussion of Pr and Gd in section 3). Most of the materials to be considered here are the ones where it does not. Of course, the correct density functional theory would incorporate both the Bloch and localized limits in a unified manner, but it is not clear whether this can be achieved within a single Kohn–Sham ansatz.

Even greater care in interpretation is required when considering low-lying excitations, such as measured by the quasiparticle mass. The single-particle-like solutions of the Kohn–Sham equations, including their energies, are merely auxiliary quantities to be used in constructing the charge density and total energy of the system: strictly speaking, they have no formal meaning. They often do prove to be good approximations to quasiparticle excitations, but only when the excitations are weak perturbations of the ground state. Real quasiparticle excitations can be strongly renormalized due to self-energy effects which are not included in these auxiliary functions. Consequently, the large mass enhancements seen in the heavy-fermion materials do not imply a failure of the Kohn–Sham calculation to describe the ground state.

At this point, we are ready to discuss the evaluation of the exchange–correlation functional. This functional is known to be fairly local, at least for metals, and is thus approximated as a delta function in  $r - r'$ , with the kernel evaluated using results for a homogeneous electron gas with the same density. This is known as the local density approximation (LDA). This approximation is so dominant in the literature that it is often confused with other approximations such as the Kohn–Sham ansatz itself as well as commonly used shape approximations to the effective potential [see Harris (1984) for the colorful history of the water molecule]. Surprisingly, this crude approximation works quite well – even for strongly inhomogeneous systems. A perhaps greater surprise is that meaningful results are obtained for  $f$  electron metals, where one would expect an electron gas functional to be totally inappropriate: one reason for this is that the direct Coulomb interaction is so large that it dominates the physics so that the exchange–correlation functional plays a comparatively minor role.



There are a number of known limitations of the LDA [for a review, see Jones and Gunnarsson (1989)]. We will only note that there appears to be a systematic error arising from the LDA in that it tends to place higher angular momentum states too low in energy relative to the lower angular momentum states (Koelling 1984). These are of order 10 mRy (0.1 eV) although they can be larger as in the case of the 20 mRy d-p shift found in Nb (Crabtree et al. 1987). For f electron systems, this error can be of the order of 40–50 mRy (Norman and Freeman 1989). Making simple phenomenological corrections for this results in improvements in the Fermi surface and other bulk properties. Another limitation of the LDA is that, by design, it totally ignores the non-locality of the true exchange–correlation functional. Much work has gone into constructing tractable approximations such as gradient corrections to ameliorate this problem, but such functionals make little difference for f electron systems (again, due to the dominance of the direct Coulomb interaction). One aspect deserves special attention: the largest effect, as well as the most non-local, in the exchange–correlation functional is the elimination of the self-Coulomb interaction. The LDA self-exchange term does not cancel the self-Coulomb term as in Hartree–Fock theory, since the exchange term has a different functional form than the Coulomb term. Current approaches attempting to correct this limitation lead to an orbital-dependent theory which is basis-function dependent (Perdew and Zunger 1981). No satisfactory theory yet exists for metallic systems (and may never exist in the LDA context), although some recent progress has been made for transition metal oxides (Svane and Gunnarsson 1990). One advantage of such a self-interaction correction formalism is that it tends to force the system to exhibit integral on-site occupations and, thus, offers some possibility to explain both itinerant and localized behavior in f electron materials.

A similar local density formalism can be constructed for spin-polarized systems (von Barth and Hedin 1972), where it is assumed that the density matrix is diagonal in spin indices (and thus that the spin is maximal along the specified quantization axis). This local spin density (LSD) theory works fairly well for 3d transition metals such as Fe, Co, and Ni. LSD theory has less success in f electron systems, where orbital degrees of freedom and multiplet structure play a much more important role. There are basically two classes of problems to consider in the case of LSD theory: (1) the approximations used are less valid since the spin-dependent part of the exchange–correlation functional is more non-local (Ng 1989) and less well characterized [see the analysis by Vosko et al. (1980)], and (2) there is fundamental physics missing when the electrons are spatially localized. For instance, it is well known that LSD does not properly reproduce multiplet structure (von Barth 1979), due both to the assumed diagonality of the spin density matrix and the single-determinant approximation. A related problem occurs for systems with orbital moments which includes many f electron materials. Any orbital moment in LSD must be due to an indirect effect where the spin–orbit interaction induces an orbital moment in a spin-polarized system. But, in reality, most orbital moments in f electron systems arise because of Hund’s second rule. Such effects are present in open-shell Hartree–Fock theory, but not in LSD. Recently, there have been efforts to incorporate these effects into band theory (Eriksson et al. 1990a, Norman 1991c). This is based

on the observation that the Coulomb interaction vertex for two  $f$  electrons can be approximately written in the form  $a + bs_1 \cdot s_2 + cI_1 \cdot I_2$  where  $a, b$  and  $c$  are Racah parameters (linear combinations of Slater integrals). This leads to terms of the form  $S(S + 1)$  and  $L(L + 1)$  in the energy functional. Assuming diagonality of this correction in some single-particle basis, one can differentiate to get an eigenvalue correction which is trivially included in a band code. (LSD does not have the  $L$  term, but has a similar  $S$  term if  $S$  is replaced by  $M_S$ . This approximation is fine for  $f^1$  systems, but questionable for  $f^2$  systems where one often has an  $M_S = 0$  ground state.) It is our belief that a band theory which properly includes Hund's rule effects (both for spin and orbital degrees of freedom) will significantly improve the description of  $f$  electron systems. A more fundamental approach would require starting from the current density functional formalism (Rajagopal and Callaway 1973, Richter and Eschrig 1989, Vignale and Rasolt 1988) that can accommodate orbital interactions and develop the necessary functionals.

The LSD theory can be used to calculate the interacting susceptibility in the paramagnetic state (Vosko and Perdew 1975). The results can be expressed as a Stoner-like theory with  $\chi(\mathbf{q}) = \chi_0(\mathbf{q}) / (1 - I(\mathbf{q})\chi_0(\mathbf{q}))$  where  $\chi_0(\mathbf{q})$  is the non-interacting band susceptibility, and  $I(\mathbf{q})$  is the spin-spin response function, found by differentiating the exchange-correlation energy functional twice with respect to the spin density (it should be noted that for a lattice,  $\chi$  is actually a matrix in reciprocal vector space). In practice, only  $I(0)$  is easy to evaluate and for general  $\mathbf{q}$ , one often has to resort to doing frozen spin-wave calculations on large unit cells (Jarlborg 1986).

For lanthanide and actinide atoms, relativistic effects are significant. One way to deal with this fact is to employ a full relativistic formalism, where one actually solves the Dirac equations. An alternate, less demanding approach is to initially only include a scalar-relativistic component which takes into account the relativistic kinematic effects such as mass-velocity and Darwin terms (Koelling and Harmon 1977), and then add the spin-orbit terms as a second step (MacDonald et al. 1980). This involves a minor approximation that only breaks down for  $p$  orbitals of the very heaviest atoms. The choice between these two becomes more significant when magnetic polarizations are involved. One of the original motivations for the two-step approach was to be able to include spin-polarization and spin-orbit effects on an equal footing. Including spin-polarization effects in the Dirac approach is also done, but it is rather messy to implement and more computationally demanding. The system where this has been most thoroughly explored is ferromagnetic gadolinium which will be discussed in section 3.

The application of the above to a solid requires the numerical exercise of performing a self-consistent band calculation. The technology to perform that task is now reasonably established although there is still room for improvement. Most commonly employed are the so-called linearized methods. These are based on dividing space into spheres centered at each atomic site, known as atomic spheres if they are allowed to overlap or muffin-tin spheres if they do not. Labelling a method as linearized means that one only solves the radial Schroedinger equation at a single energy for each  $\ell$  channel (Andersen 1975). The requisite energy variation of the radial function is incorporated by also including its energy derivative as part of the basis functions.

Such a linearized form is usually adequate, even for f electron systems. The two most common basis sets either use site-centered orbitals such as muffin-tin orbitals (LMTO) and augmented spherical waves (ASW – our discussion is not quite accurate for this method) or else plane waves (LAPW). The prefix L is used to denote a linearized method. Some LMTO and ASW calculations do not correct for the overlap (the atomic sphere approximation or ASA) while others do so approximately (CC, for combined corrections). Most LMTO and ASW calculations involve some approximation in the treatment of the overlap and of the small remaining interstitial region although later versions have significantly improved in this area. The interstitial region is explicitly treated in the APW methods which use non-overlapping spheres. The lowest-order approximation is to use a constant potential in this region (muffin-tin approximation) although it is not difficult to use a general potential (warped muffin-tin approximation). There still remains the incorporation of the non-spherical terms inside the spheres, and the so-called “full” (FLMTO and FLAPW) methods include these terms. In most cases, these different shape approximations give errors roughly comparable to the limitations of the LDA and LSDA but with greater  $k$ -space variation. For close-packed systems, all these methods give comparable results, but for more open systems, the LMTO method becomes deficient. This can often be compensated by adding “empty” spheres (i.e. spheres not centered at an atomic site) to improve the description of the interstitial region. For instance, it must be done when applying the LMTO method to NaCl-type lattices.

While our brief comments on density functional theory and LDA band calculations have emphasized improvements one might desire, it must be remembered that its applications have a remarkable history of success. Even though such calculations are designed only to obtain ground-state properties, there has been a lot of success in most cases of equating the Kohn–Sham eigenvalues (which are merely auxiliary quantities) to quasiparticle energies. But, of course, the most interesting feature of f electron systems is that this approximation does break down. In fact, what will be emphasized in the section on the  $\text{Li}_2$  structured materials is that if the f states are reasonably itinerant, that approach works for them as well. Then, as one moves into the less itinerant materials, large mass renormalizations come into play. This can be handled by constructing an appropriate self-energy correction to the band eigenvalues. This is more tractable than it might appear at first because the momentum variation of the self-energy correction is generally negligible (i.e.  $\partial \Sigma / \partial \mathbf{k} \sim 0$ ) as has been shown in detail for Pd (Joss and Crabtree 1984, Joss et al. 1984). Consequently, one need only deal with the energy dependence of the self-energy correction for which a single-site approximation usually suffices. A self-energy correction based on spin fluctuations gives a good account of the specific heat enhancement for a number of strongly enhanced materials and even gives a good account of the temperature dependence of the electronic specific heat coefficient in  $\text{UPt}_3$  (Norman 1988).

Alternative approaches where one modifies the treatment of the f states to determine a set of quasiparticle bands are also possible. Fulde and co-workers (Fulde 1988, Fulde et al. 1988, Zwicky 1988) have successfully applied a phenomenological model that does build on the strengths of the density functional theory results. The minimal modification of density functional theory is that all the enhancement effects

can be accounted for in the energy dependence of the  $f$  phase shift. Similar techniques, based on phase shift parameterizations (Ketterson et al. 1975) have been used very successfully to fit transition metal de Haas–van Alphen masses. The phase shifts represent the Fermi surface topology and their energy derivatives renormalize the quasiparticle masses. The defining prescription of the renormalized band picture is as follows:

- (a) Determine all phase shifts  $\delta_l(\epsilon)$  except for the  $l=3$  phase shift of the rare-earth/actinide atom using standard band theory methodology but modified by incorporating the  $f$  orbitals as core-like states.
- (b) Determine the bare Fermi energy  $e_F^{(0)}$  by counting all the non- $f$  electrons.
- (c) Holding  $e_F^{(0)}$  fixed, incorporate the  $f$  orbitals using a phase shift of the form

$$\delta = \delta(e_F) + (e - e_F)/T^* + \text{interaction terms.}$$

For Ce, one starts with  $\delta = \frac{1}{2}\pi$  representing a single electron in a Friedel sum rule. The  $T^*$  serves as a phenomenological scaling factor which incorporates the mass enhancements. The final term represents crystal field and spin–orbit splittings as well as quasiparticle interactions, which is generally ignored (see below).

- (d) Using the resulting bands, redetermine the Fermi energy  $e_F$  but this time counting the  $f$  states.
- (e) Readjust the phase shift used in the underlying DFT-like calculation using a Friedel sum rule

$$\delta^0(e_F) = \frac{1}{2}\pi n_f - \delta(e_F)$$

and iterate from step (a) putting only  $(\frac{1}{2}\pi n_f - \delta)$   $f$  electrons in the core.

This is repeated until the DFT-like Fermi energy matches the quasiparticle Fermi energy – a new additional self-consistency requirement. The result is to significantly narrow the  $f$  band to a width of order  $T^*$  and bring it to order  $T^*$  of the Fermi energy. If the crystal field splittings are known to be larger than  $T^*$ , one can project all the other  $f$  states but the ground-state one out since they play no role in the low-energy physics. Virtually all renormalized band calculations performed on real  $f$  electron systems have followed this scheme or a related one (Sticht et al. 1986). (The idea of projecting out all the  $f$  electron configurations except the one known to occur in the ground state is a general phenomenological scheme which is easily implemented in any band code. Kasuya and co-workers have applied this with success to CeSb which will be discussed in section 3.) Other renormalized band schemes will be discussed in the chapter by Liu (ch. 111).

The above formalism or close variants have been applied to  $\text{CeCu}_2\text{Si}_2$ ,  $\text{CeAl}_3$ ,  $\text{CeRu}_2\text{Si}_2$ ,  $\text{CeSn}_3$ , and  $\text{UPt}_3$ . But how reasonable is the prescription and what may we infer from its successes? In general, these models yield the same Fermi surface topology as LDA if the crystal field splitting is less than  $T^*$ . For  $\text{UPt}_3$  and  $\text{CeRu}_2\text{Si}_2$ , it turns out that renormalized band theory and LDA agree, but for systems such as  $\text{CeAl}_3$ , significant deviations are expected. One might also expect disagreement for  $\text{CeSn}_3$ , since LDA has a ground state which is  $\ell$ -like in character (as opposed to a

*j*-like ground state one would expect to obtain in the renormalized schemes), but a self-consistent renormalized calculation has yet to be done on CeSn<sub>3</sub> to test this.

Yet another option to be explored is to incorporate a slave-boson approach into the standard band formulation. In the slave-boson method, one usually starts with a Coqblin–Schrieffer Hamiltonian which is a Kondo limit of the large-*U* Anderson model (Read and Newns 1983). The single-particle energies of the conduction electrons are taken from DFT, an effective exchange interaction is introduced between the conduction electrons and the localized *f* electrons, and the number of *f* electrons is constrained to be equal to some integer multiple of the number of lattice sites. The problem is then cast into a functional integral formalism by introducing two Bose fields: one a Lagrange multiplier associated with the constraint and the other a result of eliminating the two-body exchange interaction via a Hubbard–Stratanovich transformation. The renormalized band theory corresponds to the saddle point of the functional integral. At the saddle point, the Bose fields essentially define the effective *f* level energy and the renormalized hybridization. While not yet having been fully implemented for a real material, the advantage of this approach is that one can go beyond mean field theory by treating fluctuations about this saddlepoint. The most common way to do this is to expand in powers of  $1/N$  (where *N* is the degeneracy of the *f* levels). The first-order term in  $1/N$  is equivalent to Gaussian fluctuations (and thus identical to an RPA approach). One potential problem is that the expansion in powers of  $1/N$  may not be controlled, since if crystal-field splittings are larger than the effective Kondo temperature, then *N* can be as low as 2 (or as low as 1 for magnetic systems). Other schemes involving constraining the *f* count have also been proposed. The most promising starts with a Hubbard model and uses a Gutzwiller saddlepoint (Kotliar and Ruckenstein 1986). Unfortunately, this method has not yet been applied to heavy fermions, although it has been applied to <sup>3</sup>He with some success (Rasul and Li 1988, Rasul et al. 1989) as will be discussed in the section on superconductivity. We should also remark that other renormalized band theories are discussed in the chapter by Liu (this volume).

Finally, we should like to note that the strong correlations that are present in these materials and the higher magnetic fields needed to see their Fermi surfaces may require greater care in the interpretation of experiments. The dHvA effect is generally interpreted in terms of the semiclassical Lifshitz–Kosevich formalism (Lifshitz and Kosevich 1956) as discussed in an earlier volume of this series (Arko et al. 1985). This is generally a very adequate approach (Gold 1968, Shoenberg 1984). The data analysis extracts external cross sectional areas of the Fermi surface from the frequency of the dHvA oscillations in  $1/B$ ; the effective mass from the temperature dependence of the amplitude; the scattering amplitude as a constant additive effective (Dingle) temperature; and a *g* factor from the spin-splitting zeroes. The Lifshitz–Kosevich form has been justified using a quasiparticle formalism valid for low fields (Luttinger 1960, 1961). Corrections for higher fields, incorporation of electron–phonon interactions and impurity scattering, and other extensions of the Lifshitz–Kosevich treatment have been discussed in the literature (Fowler and Prange 1965, Brailsford 1966, Engelsberg and Simpson 1970, Engelsberg 1978, Mann 1971, Wasserman and Bharatiya 1979). Issues as to the modifications by the applied magnetic field other

than the formation of Landau levels are generally discounted. The fact that this approach leaves a set of no-longer-valid quantum numbers in the form of the  $k$  vectors perpendicular to the magnetic field is dealt with by suitable orbital averages over the Fermi surface (Lowndes et al. 1970). A property of at least several f electron systems is that the applied magnetic field does make significant modifications of the system. Stamp (1987) has applied a statistical quasiparticle theory of interacting fermions to get an expression for the oscillatory magnetization. His result reduces to a form similar to the Lifshitz–Kosevich expression but with magnetic-field-dependent parameters plus an additional term. Whether these complex effects really need to be considered in understanding the dHvA data on heavy-fermion metals is still an open question. This issue has recently come up in CeCu<sub>6</sub>, where a number of unusual features exist in the dHvA data (Chapman et al. 1990).

### 3. Lanthanide and actinide materials

The crystal structure of a material dictates much of its electronic behavior so this section has been organized to cluster materials of the same crystal structure and, where possible, to juxtapose those with closely related structures. Comparable lanthanide and actinide materials are discussed together such that the many similarities and occasional significant differences can be considered. These are the only considerations consistently applied in determining the order in which the materials are discussed.

#### 3.1. $Ll_2$ structured materials

Materials with the  $Ll_2$  (Cu<sub>3</sub>Au) structure have had a long and productive history in the study of hybridization of f electrons. The  $Ll_2$  structure is a conceptually simple structure derived from a face-centered cubic structure by occupying the face-centered sites with different atoms from the cube corner sites. Within this relatively simple structure, one finds all possible properties ranging from the very itinerant behavior of superconducting URu<sub>3</sub> ( $T_c = 0.15$  K) (Chen et al. 1985), the Pauli paramagnetism of UGe<sub>3</sub>, URh<sub>3</sub> and UIr<sub>3</sub>, the spin fluctuation behavior of CeSn<sub>3</sub> and USn<sub>3</sub>, and the magnetic behavior of CeIn<sub>3</sub>, UIn<sub>3</sub>, CePb<sub>3</sub> and UPb<sub>3</sub>. All this occurs at sufficient f electron element separations to preclude any direct f–f interaction. This makes the  $Ll_2$  structures a particularly favorable arena in which to study systematic variations in degree of f electron hybridization (Koelling et al. 1985, Crabtree et al. 1985). In the case of the Ce materials, this was earlier viewed as a search for valence change (Harris et al. 1972, Mihalisin et al. 1981, Rambabu et al. 1982) and more recently, for the U materials, it has been viewed in terms of systematically varying the hybridization (Lin et al. 1987b, c).

Using the Hill-type criterion that superconductivity reveals itineracy, however, can be misleading. Perusing tabulations of superconductivity, one notes from its relative infrequent appearance that the  $Ll_2$  structure is not a particularly favorable structure for superconductivity. Of course, it does have some very intriguing examples. One

famous example is  $\text{LaSn}_3$  because of its re-entrant behavior observed with dilute additions of Ce (DeLong et al. 1978). Interestingly, more itinerant behavior does occur for this structure when there is site disordering between the two sublattices.  $\text{UPd}_3$  made Pd-rich becomes cubic and loses its magnetic properties.  $\text{U}(\text{Al-Si})_3$  or  $\text{U}(\text{Ge-Ga})_3$  alloys exhibit superconductivity but only when they are at least partially site disordered (Ott et al. 1985a).

The  $\text{Ll}_2$  structured materials have been extensively explored using alloy studies. The natural assumption is that one can form pseudobinaries where the face-centered sublattices are made a random alloy leaving the f electron containing cubic sublattice intact. This has worked well in many cases. The approach has been especially useful to explore heavy-fermion behavior in the U compounds – by weakening the hybridization of the f orbital in the critical region (Koelling et al. 1985) – and to explore valence fluctuations/changes in the Ce compounds (see the discussion of  $\text{CePd}_3$ ). Alternatively, insightful alloy studies can be performed utilizing the empty site at the center of the cube which very nicely accepts metalloids such as boron and carbon, leaving the rest of the lattice intact. (When that site is completely filled, one arrives at the cubic Perovskite structure.) Examples are  $\text{CePd}_3\text{B}_x$ ,  $\text{URu}_3\text{B}_x$  and  $\text{URh}_3\text{B}_x$  or the nitrogen equivalent (i.e.  $\text{B} \rightarrow \text{N}$ ).

Finally, before considering the individual materials, it is interesting to consider the question as to whether the Ce materials or the U materials exhibit the more local f character. Looking at photoemission (i.e. high-energy data), one would strongly suspect that the Ce materials are the more local: the two-f-peak structure is very clearly seen and quite ubiquitous in the Ce materials while, for the U materials, it is only very weakly seen through careful examination of the systematic variations (Arko et al. 1987). Yet comparable materials involving either of these two elements do show similar behavior as regards localization of the f character – they are not as dissimilar as might be assumed from the photoemission. Actually, one can make a mildly credible case that the f orbitals are slightly more itinerant in the Ce materials than in the U materials. The argument should not be carried too far but it does give some insight by countering the common assumption that the Ce materials have far more localized f character than the U materials. (A comparable argument that the Ce compounds actually display the more itinerant f behavior could be made in other structures as well.) The argument proceeds by comparing related systems.  $\text{UPd}_3$  is a local moment system whereas one must dope with B or N to drive  $\text{CePd}_3$  to display local moment behavior.  $\text{USn}_{3-x}\text{Pb}_x$  becomes antiferromagnetic with only 5% Pb whereas  $\text{CeSn}_{3-x}\text{Pb}_x$  not only requires more lead but also transforms more slowly. Although  $\text{UPb}_3$  and  $\text{CePb}_3$  are both antiferromagnetic systems,  $\text{CePb}_3$  is a weakly antiferromagnetic heavy-fermion system (Lin et al. 1985a) whereas  $\text{UPb}_3$  is more local moment-like.  $\text{CePb}_3$  displays very interesting behavior under an applied magnetic field where the resistivity is dramatically reduced.  $\text{CeIn}_3$  and  $\text{UIn}_3$  are also both antiferromagnetic but with the Ce material exhibiting the very large electronic specific heat (Nasu et al. 1971) that implies strongly enhanced f character in the conduction bands. Further, under pressure,  $\text{CeIn}_3$  becomes steadily more itinerant in nature. Another very weak argument for the relative localization of the f orbitals has to do with the hexagonal phase modifications observed for the uranium compounds such as  $\text{UPd}_3$ . In contrast,

CePd<sub>3</sub> remains in the cubic phase – which could imply greater *f* orbital delocalization. Hexagonal phases occur for uranium–transition-metal materials as one moves into the far right side of the “box” between URh<sub>3</sub>–UIr<sub>3</sub> and UPd<sub>3</sub>–UPt<sub>3</sub>. One finds the hexagonal modifications to have a narrow range of stability both around UPd<sub>3</sub> and around UPt<sub>3</sub>. UPd<sub>3</sub> forms in a structure which can be obtained from the Ll<sub>2</sub> structure in the same manner as one converts an fcc structure to a hexagonal close-packed structure through slipping planes perpendicular to the (111) direction. Similarly, the UPt<sub>3</sub> structure is obtained by using the transformation that would yield a double hexagonal close packed structure from the fcc. This transformation to a hexagonal phase is due to one of three possible causes: (1) the more local behavior of the *f* orbitals which is asserted to be the actual cause. For a number of compound sequences, one frequently observes a conversion from a cubic to a related hexagonal phase on moving to the right in the periodic table. This is most easily related to a reduced bonding. (Matthias exploited this fact when looking for superconductors by carefully examining the alloys just to the cubic side of these transformations); (2) increased *d* character [as pointed out by Duthie and Pettifor (1977) for the rare earth series – see also Min et al. (1986)]. Countering this possible explanation, band calculations show the *U d* character to instead be decreasing as one incorporates transition metals further to the right (Oguchi and Freeman 1986); or (3) greater charge transfer to the Pd/Pt sublattice (Harris et al. 1972). The band calculations again indicate that, beyond the increased atomic charge, the flow of the charge onto the transition metal is very weak. Thus one can take the occurrence of the hexagonal phases to be another indication that the *U* compounds are the more weakly hybridized. One other interesting “anomaly” that is worth mentioning appears in this area of alloy space: The 50–50 pseudobinary alloy of UPd<sub>3</sub> with UPt<sub>3</sub> is very special. Within a very narrow composition range, one finds the only uranium material where the two-*f*-peak photoemission structure can be clearly distinguished (Arko et al. 1989).

Because the Ll<sub>2</sub> structure appears for two sets of materials: those in which the non rare earth/actinide atom is a group VIII transition element and those where it is a group IIIA or group IVA element, we consider them as separate sets.

### 3.1.1. *CeRh<sub>3</sub>–CePd<sub>3</sub>–URu<sub>3</sub>–URh<sub>3</sub>–UIr<sub>3</sub>*

These materials are the cubic Ll<sub>2</sub> materials for *U*, *Ce* exhibiting itinerant *f* character through coupling with the nearly complete 4*d* and 5*d* shell transition metals of group VIII. (CeIr<sub>3</sub> and CePt<sub>3</sub> apparently form as defected Laves phases rather than in the Ll<sub>2</sub> structure.) UPd<sub>3</sub> and UPt<sub>3</sub> form in hexagonal phases although the cubic phase does extend almost all the way to full Pd or Pt in the alloy phase diagram.

Of these five materials, de Haas–van Alphen measurements exist only for URh<sub>3</sub> and UIr<sub>3</sub> and are the earliest made for any *f* electron system (Arko et al. 1975, Arko 1977). The detailed comparison of the measured Fermi surface to the band calculation (utilizing only exchange and no additional correlation terms in the density functional) was made by Arko et al. (1985). The main piece of Fermi surface in both URh<sub>3</sub> and UIr<sub>3</sub> arises from an electron pocket of predominantly *d* character centered about the *M* point. That Fermi surface piece is also a major part of the total CeRh<sub>3</sub> Fermi surface, although there are a significantly larger number of other Fermi surface pieces



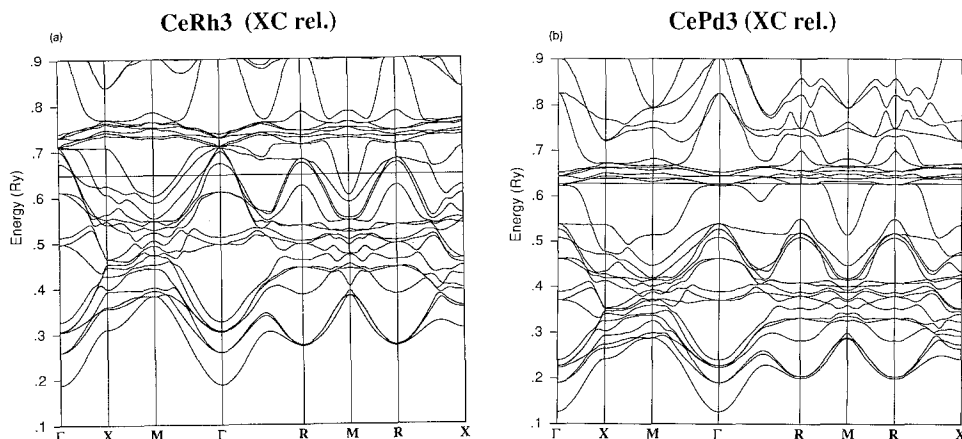


Fig. 1. Band structures of (a)  $\text{CeRh}_3$  and (b)  $\text{CePd}_3$  calculated using a fully relativistic LAPW method. Note how the narrow f bands in  $\text{CeRh}_3$  (about 0.05 Ry above the Fermi energy) pull down to touch the Fermi energy in  $\text{CePd}_3$  which would be consistent with a tetravalent-mixed valent picture of alloys between these materials. However, it should be noted that  $\text{CeRh}_3$  has very nearly a full f electron occupied through hybridization.

as well. In  $\text{URu}_3$ , the M-centered piece has shrunk to a very small pocket and, in  $\text{CePd}_3$ , the band filling has gone beyond having any remnant of this Fermi surface piece.

To aid the discussion, we show in figs. 1 and 2 the band structures for these materials calculated using the full Dirac kinetic energy term (i.e. "full relativistic") and including correlation as well as exchange in the LDA functionals used (Koelling, unpublished). The resulting Fermi surfaces are shown in figs. 3 and 4. In  $\text{URh}_3$  and  $\text{UIr}_3$  the important first step towards rationalizing the de Haas-van Alphen data was to figure out the presence of the necks on the large M-centered surface, the orbits they would preclude, and the various orbits that become possible because of the presence of the necks.  $\text{UIr}_3$  has an additional set of necks besides the ones observed in  $\text{URh}_3$ . These were not present in the early non-self-consistent overlapping-charge-density model calculations but were inferred from the de Haas-van Alphen data. They were later found to be present when the self-consistent calculations were performed. Additional necking to the structure centered at  $\Gamma$  in  $\text{UIr}_3$  is due to a slight downward shift of the band there producing an electron ring around a hole pocket. This appears to be due to a greater interaction with the f states in the case of  $\text{UIr}_3$ . The M-centered piece being of predominantly d character, it is the neck structure that incorporates the greater f admixture. The remaining pieces at  $\Gamma$  and R exhibit the greatest f admixture of all and are also the most poorly described by the calculations. This probably arises from minor deficiencies in the relative placement of the d and f bands by the LDA. The greater relative error is also due to the simple fact that they are small volume pieces. Small volume pieces are more dramatically influenced by any limitations in the calculation because, although the volume change will be of the same general magnitude on the large and small surfaces (charge

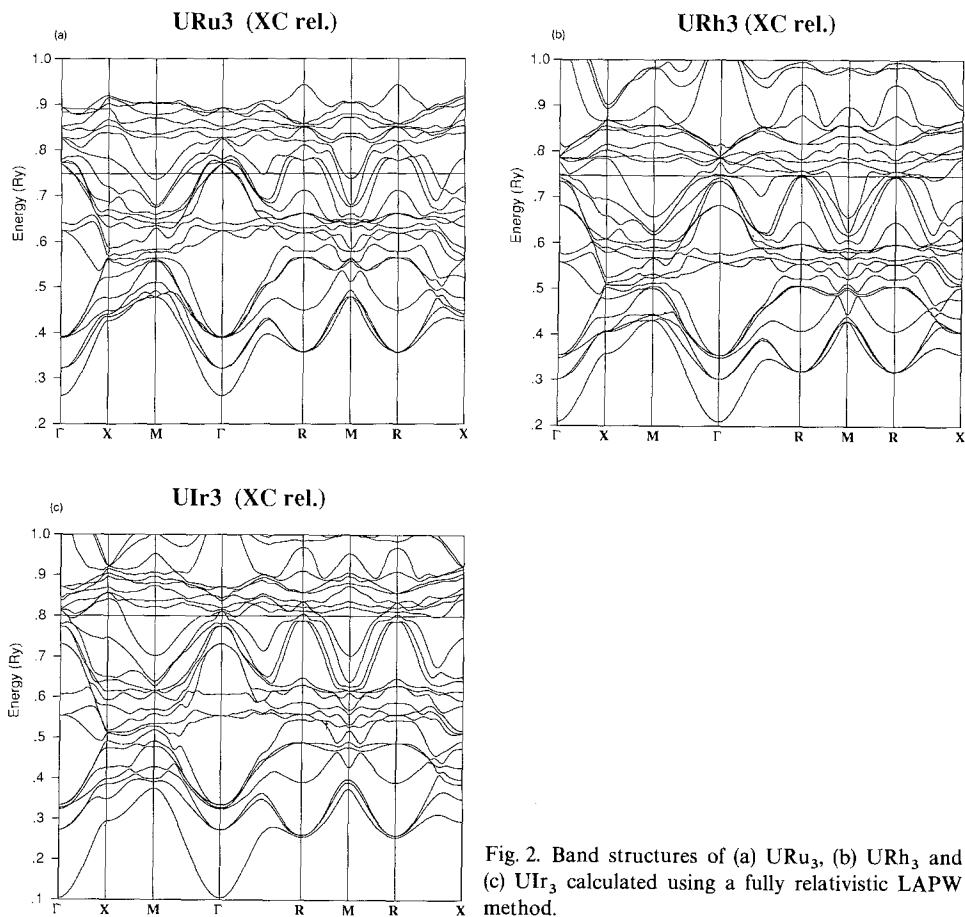


Fig. 2. Band structures of (a) URu<sub>3</sub>, (b) URh<sub>3</sub> and (c) UIr<sub>3</sub> calculated using a fully relativistic LAPW method.

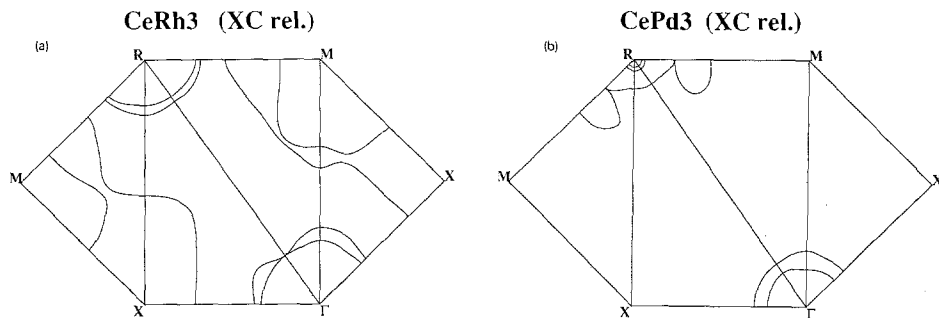


Fig. 3. Fermi surface of (a) CeRh<sub>3</sub> and (b) CePd<sub>3</sub> for the band structures of fig. 1. Shown is the intersection of the Fermi surface with the planes bounding the irreducible wedge of the Brillouin zone.

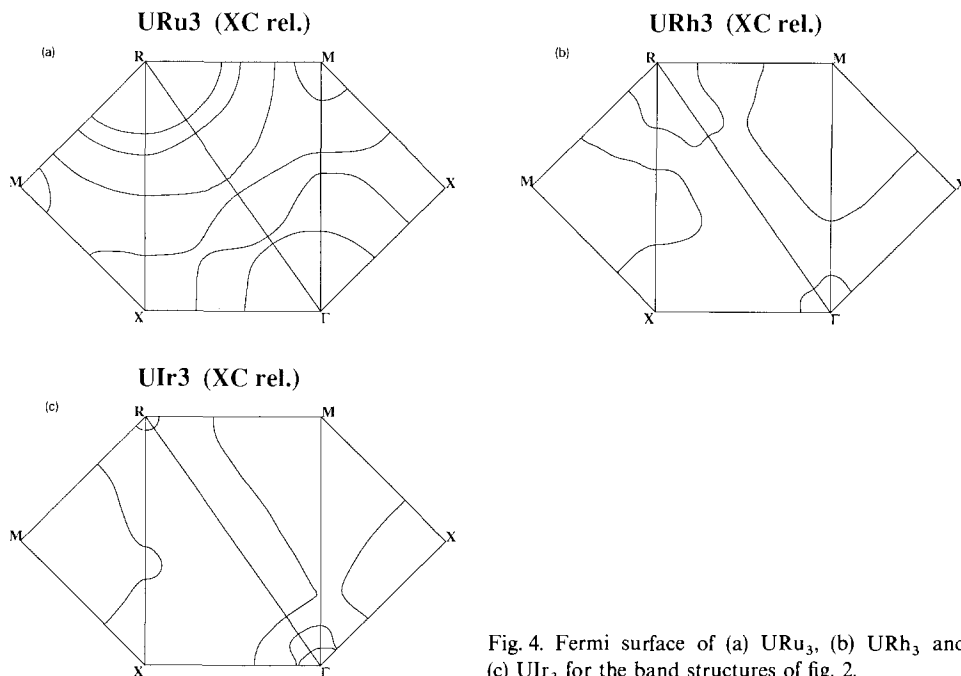


Fig. 4. Fermi surface of (a)  $URu_3$ , (b)  $URh_3$  and (c)  $UIr_3$  for the band structures of fig. 2.

conservation), the relative change is then much larger for the small volume pieces. Arko et al. (1985) puzzled about why the exchange-only calculations worked so well for  $URh_3$ ,  $UIr_3$ ,  $UGe_3$  and  $CeSn_3$ . While it is true that one can give arguments for use of an exchange-only functional, the resolution of that puzzle appears now to be that  $CeSn_3$  is so dominated by the Coulomb repulsion of the f electrons that the choice of exchange correlation potential has very little effect. While  $URh_3$  and  $UIr_3$  are also not very sensitive to the choice of functional, the incorporation of correlation does actually improve matters.

Detailed experimental data in the form of de Haas–van Alphen measurements do not exist for the other three compounds. This is unfortunate as these materials are important parts of the overall picture and such experiments should be feasible.  $URu_3$  is a superconductor and is the material where the Fermi energy lies deeper in the d bands of the transition metal. There are many more Fermi surface pieces and all but one of them are topologically quite simple. Several of these “pockets” contain significant admixtures of f character at the Fermi surface. Thus a careful study of mass enhancements would be revealing.  $CeRh_3$  is also an interesting opportunity. It is the classic “tetravalent” material which band calculations indicate to contain an occupied f electron. Thus,  $CeRh_3$  is the material with the most pronounced itinerant f character. That, together with the interest in comparing to  $URh_3$  and understanding the base system for many of the alloy studies, suggests this material should not be overlooked.

$CePd_3$  has been established as a mixed valent system with  $n_f \sim 0.55$  (Gardner et al. 1972, Holland-Moritz et al. 1977). Interestingly, resonant photoemission (Allen et al. 1981) shows the main f peak extending to the Fermi energy. The calculated

band structures (Hasegawa and Yanase 1987, Koenig 1988, Koenig and Khan 1988; see fig. 1) show the Fermi energy to be above the Pd d bands and on a tail of f character pulled down off a narrow set of f bands. Koenig (1988) has demonstrated that the Ce 4f–Pd 4d hybridization is a major factor determining the nature of the electronic structure. The resulting Fermi surface (fig. 3) is extremely simple topologically, consisting of small hole pockets along the line T from M to R (near R) and electron pockets at  $\Gamma$  and R. If the de Haas–van Alphen data could be obtained for this material, this simplicity would enable a very detailed and incisive analysis. Hasegawa and Yanase (1987) have made a pioneering effort to address the alloy residual resistivity data based on the band structure with very promising, but not quantitative, results.

CePd<sub>3</sub> has been a favored material as the basis for studying valence change with alloying. In the CeRh<sub>3-x</sub>Pd<sub>x</sub> pseudobinary, the lattice constant increases linearly with  $x$  in two regions with one slope in the range  $0 \leq x \leq 2.36$  and a larger slope above  $x = 2.36$ . The room-temperature magnetic susceptibilities slowly drop in the lower Rh-rich region and then dramatically rise in the Pd-rich region (Harris et al. 1972). Replacing Pd by Pt in CePd<sub>3</sub>Pt<sub>x</sub> produces an unchanging lattice constant up to  $x \sim 1$  consistent with Pd and Pt being isoelectronic atoms of roughly comparable size. Above  $x \sim 1$ , the defect Laves phase structure appears – which one may postulate to be caused by the relative shift from d to increased sp character that occurs between Pd and Pt. The alloy systems CePd<sub>3-x</sub>Ag<sub>x</sub> (Mihalisin et al. 1981) and CePd<sub>3</sub>B<sub>x</sub> (Dhar et al. 1981; Kuentzler et al. 1984, Kappler et al. 1985) continue the process of dehybridizing the Ce f states. The substitution of Ag continues the rapid rise in specific heat coefficient  $\gamma$  that started in the Rh–Pd alloy series and is interpreted as driving the system into the Kondo regime. The incorporation of B induces dramatic changes that include a rise in specific heat  $\gamma$  to about 75 mJ/K<sup>2</sup> mol at  $x \sim 0.25$  before making a transition to a magnetic state system at  $x \sim 0.3$ . The rapid rise in lattice constant ceases at about  $x \sim 0.4$ . The addition of boron in the RPd<sub>3</sub>B series also washes out the dip at Ce in the plot of lattice constant versus lanthanide that is typically attributed to mixed valence. Nonetheless, it is difficult to believe an interpretation in terms of valence in light of the fact that GdPd<sub>3</sub>B<sub>x</sub> has almost the identical lattice constant variation except reduced by a factor of two. On the other hand, simple band filling arguments should then try to explain the fact that LaPd<sub>3</sub>B<sub>x</sub> has a lattice constant independent of  $x$ .

While the experimental data has with some success been interpreted in terms of valence changes, band structure results suggest other possibilities. The discussion to follow will proceed from the fact that the Fermi energy in CePd<sub>3</sub> falls *above* the nominal Pd d bands and that this filling occurs between Rh and Pd. Thus, one must consider the details of filling out the d bands in addition to the normal atomic size effects – such a hypothesis is also the basis for the interpretation of URh<sub>3</sub>B<sub>x</sub> and URu<sub>3</sub>B<sub>x</sub> (Dunlap et al. 1989, Zolnieriek et al. 1986). The d states being filled are antibonding within the Pd sublattice and bonding with the 5d's on the Ce sites. As the transition metal d's are filled, the Ce or actinide f orbital plays an unusual role. Because of the quadratic occupation number dependence associated with the large intra-atomic Coulomb energy (i.e.  $Un_f^2$ ), the f electron count will not change

dramatically. Looked at in a band picture, the f bands “float” just above the Fermi energy with an f density tail pulled down, extending below the Fermi energy. On the CeRh<sub>3</sub> side, the f partial density is spread down through the Rh d bands because the Cef orbital is strongly admixed into the d wavefunction. Consequently, d spectral density is also transferred up into the f bands (for the alloys, this can be translated to resonance) and into an anti-bonding (with Ce d states) band higher up. Thus, at the point of filling the nominal d bands, the atomic d character on the Pd sites is still far from being filled out – much like the p bands in the rock-salt structured pnictides and chalcogenides. One expects some form of transition as this filling is completed (Lifshitz 1960) which can be non-analytically enhanced by the changes in the phonon structure (Dagens 1978). Once the d bands have been filled, a different process begins whereby the wavefunction admixture begins to be reduced so that the occupied d bands become more pure and thereby the atomic d character increased. This is occurring as the d and f mean energies are being further separated due to the d states being drawn towards the core (as they are in the case of silver or gold). As a consequence, the main peak in the f partial density of states will be moved closer to the Fermi energy until the Fermi energy no longer falls in a tail pulled off but actually *in* the leading edge of the peak. At this stage, one is dealing with much more weakly hybridized f orbitals. It is in this regime that one has possibility of the Mott transition focussed upon in studying the URh<sub>3-x</sub>Pd<sub>x</sub> alloys (Johansson et al. 1986, Dunlap et al. 1987, Eriksson et al. 1988a) – which is another case where the U compound would appear to be acting as a more local f material than the comparable Ce compound.

### 3.1.2. *The group III and group IV materials*

When the other element in the Ll<sub>2</sub> structure is a group III or group IV element, one can make a credible story based on a competition between p–p bonding amongst the face centered atoms and f–p bonding broadening out the f states. There must be some competition between these two effects due to simple geometrical restrictions on the directions in which p-based bonds can point. Such an observation serves as the basis for an argument explaining the weaker f hybridization with the heavier p orbital elements and with the group III elements. It is this competition which is why one sees increased localization with increased lattice constant, not decreased f–p overlap since the p orbital scales with the size of the group III–IV atom determining the lattice constant. (The pσ matrix element decreases only very slightly down the series. The dfπ matrix element does drop sharply at Sn.)

Certainly, the very extensive alloy work is consistent with weakened f–p hybridization on moving from group IV to group III and in moving down toward the heavier elements. Either of these modifications shows basically the same behavior as the hybridization is diminished: increased density of states with only modest mass enhancement up to a point where the enhancements begin to rise rapidly and then finally the alloy transforms to antiferromagnetic behavior of one form or another. (CeIn<sub>x</sub>Sn<sub>3-x</sub>: Lawrence 1979, Elenbaas et al. 1980) (CeSn<sub>x</sub>Pb<sub>3-x</sub>: Teter et al. 1982, Lin et al. 1987b) (CeIn<sub>x</sub>Pb<sub>3-x</sub>: Lin et al. 1985a) (UIIn<sub>3-x</sub>Sn<sub>x</sub>: Zhou et al. 1986, Lin et al. 1987c) (USn<sub>3-x</sub>Pb<sub>x</sub>: Lin et al. 1985b) In moving from group IV to group III, it

is possible to correlate variations in the Ce system (Lawrence 1979) to a p band density of states taken from what we shall call the W-shaped curve, where a maximum is observed at the mid-point and at both ends of the series with deep minima in between. Initially observed for La compounds when alloying between groups III and IV (Grobman 1972, Toxen et al. 1973), this ubiquitous behavior appears in a large number of properties such as superconducting transition temperature, susceptibility, Knight shift, conductivity, etc. This also implies that one should be able to correlate at least some of this behavior to calculated structure in the p bands.

The  $\text{CeSn}_3$ – $\text{CeIn}_3$ – $\text{CePb}_3$  alloy system can be usefully discussed in this light.  $\text{CePb}_3$  is an incommensurate antiferromagnetic (Vettier et al. 1986) below  $T_N = 1.1$  K and is a heavy-fermion system with  $\gamma \sim 200$  mJ/K<sup>2</sup> mol above  $T_N$ . When Sn is substituted for Pb, the Néel temperature quickly drops to zero. When In is substituted, the Néel temperature first rises to a maximum of 4 K at 40% In and then quickly drops off. Then, near the pure In boundary, a more local moment type II antiferromagnetism appears. [Apparently  $\text{CeTi}_3$  is an even more local antiferromagnetic as discussed by Rahman et al. (1990).] This is remarkably similar to the behavior of the Sn–In alloys.  $\gamma$  goes through a variation very similar to the W-shaped curve (Lin et al. 1987a). In the  $\text{Ce}(\text{Pb}_{1-x}\text{Sn}_x)_3$  alloy system, the residual resistivity is quite large on the Pb-rich side suggesting spin disorder scattering (at  $T > T_N$ ) and is quite comparable to that of the similar La material on the Sn-rich side (Teter et al. 1982). The relation to spin fluctuation enhancements is intriguing since a large mass enhancement is already present in  $\text{CeSn}_3$ .

The U materials  $\text{USi}_3$ ,  $\text{UGe}_3$ ,  $\text{USn}_3$  and  $\text{UPb}_3$  all exist, as do the group III element systems  $\text{UAl}_3$ ,  $\text{UGa}_3$  and  $\text{UIn}_3$ , in the  $\text{Ll}_2$  structure such that systematic behavior can be studied. Of the possible Ce materials, only the heavier element systems  $\text{CeIn}_3$ ,  $\text{CeSn}_3$  and  $\text{CePb}_3$  exist in the  $\text{Ll}_2$  structure. Heavy-fermion  $\text{CeAl}_3$  with  $\gamma = 1.62$  J/K<sup>2</sup> mol (Andres et al. 1975) occurs in the  $\text{Ni}_3\text{Sn}(\text{UPt}_3)$  structure.  $\text{CeSi}_x$  is also an interesting system – but unfortunately not as an  $\text{Ll}_2$  material. Going down the series  $\text{USi}_3$  to  $\text{UPb}_3$ , one finds modest specific heats exhibiting very little mass enhancement for  $\text{USi}_3$  and  $\text{UGe}_3$ ; a strong mass enhancement for  $\text{USn}_3$  with a large specific heat; and antiferromagnetism for  $\text{UPb}_3$ :  $\gamma$  is 14.0 for  $\text{USi}_3$ ; 20.4 for  $\text{UGe}_3$ ; and 170 mJ/K<sup>2</sup> mol for  $\text{USn}_3$  (van Maaren et al. 1974, Hasegawa 1985). This is the same general structure as observed in greater detail in alloy studies. Ce behaves similarly:  $\text{CeSn}_3$  exhibits a strong mass enhancement while  $\text{CePb}_3$  is an antiferromagnetic heavy-fermion system. In fig. 5 we show the unpolarized relativistic band structures and in fig. 6 the Fermi surfaces for this series. Unfortunately, detailed Fermi surface data is incomplete for the series due to materials problems. Data are currently only available for  $\text{CeSn}_3$ ,  $\text{CeIn}_3$  and  $\text{UGe}_3$ . Some additional data are available for  $\text{PrIn}_3$  (Kletowski et al. 1987),  $\text{YbIn}_3$  (Meijer et al. 1973) and  $\text{YbSn}_3$  (Klaasse et al. 1980). Data also exists for the “control systems”  $\text{LaSn}_3$  (Johansson et al. 1981a, b, Umehara et al. 1991b) and  $\text{LaIn}_3$  (Kletowski et al. 1987).

3.1.2.1.  $\text{UGe}_3$ . Progressing down the series from  $\text{USi}_3$  to  $\text{UPd}_3$ , the Si and Ge compounds are viewed as fairly standard metals and  $\text{USn}_3$  as the strongly enhanced material. However, something may already have begun to occur at  $\text{UGe}_3$ : it has been

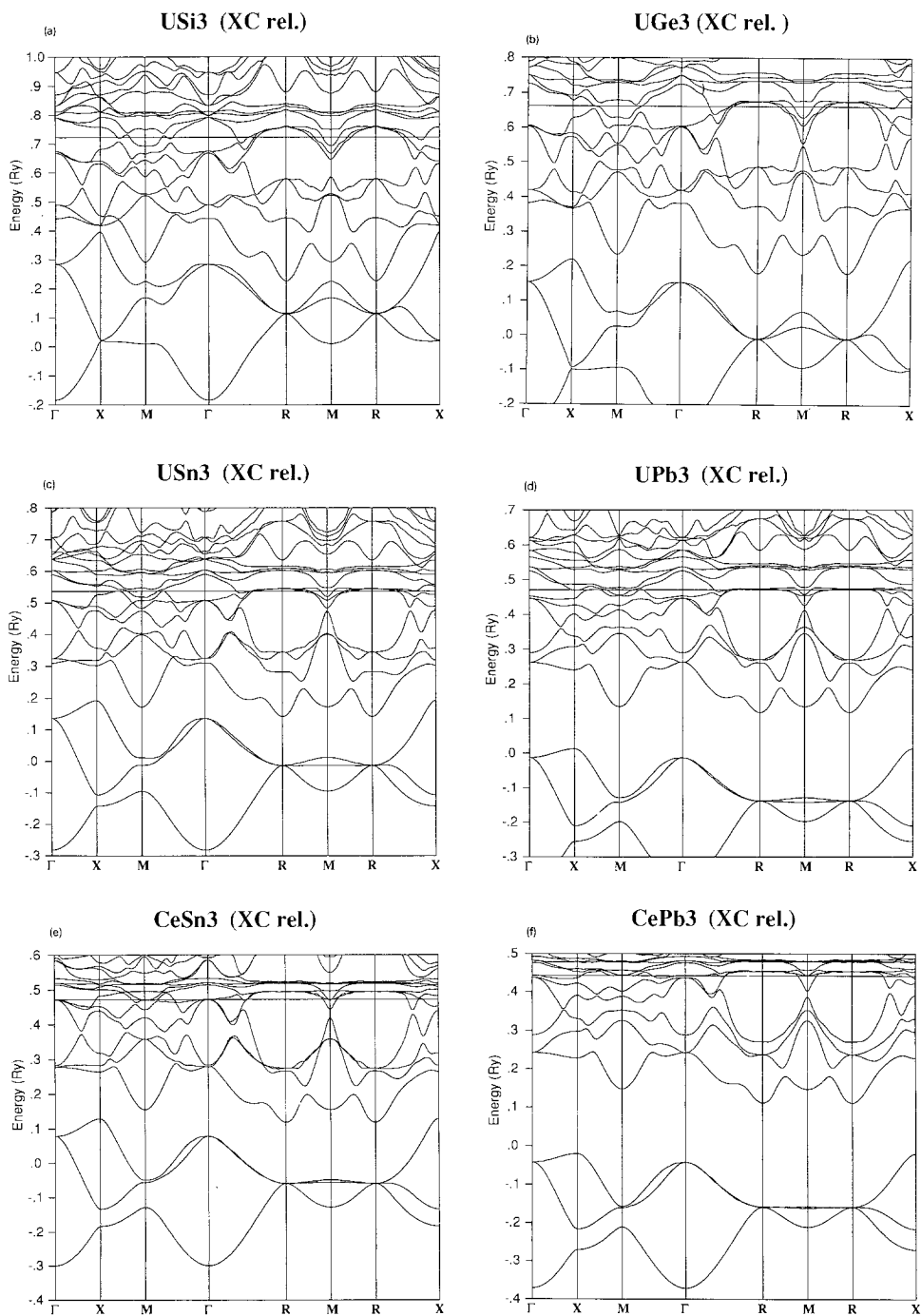


Fig. 5. Band structures of (a) USi<sub>3</sub>, (b) UGe<sub>3</sub>, (c) USn<sub>3</sub>, (d) UPb<sub>3</sub> (paramagnetic), (e) CeSn<sub>3</sub> and (f) CePb<sub>3</sub> (paramagnetic).

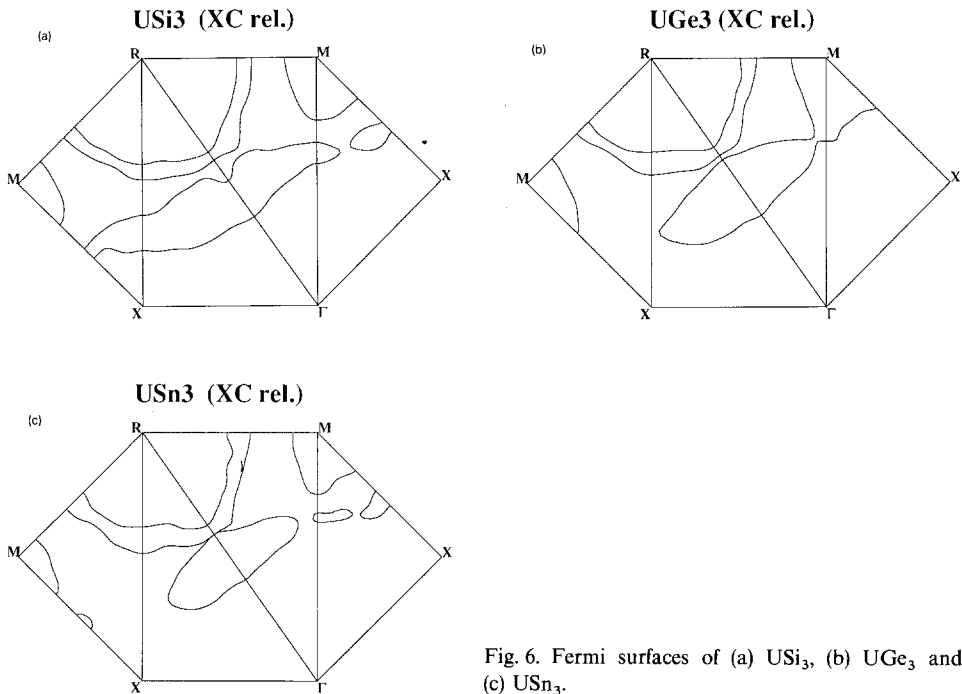


Fig. 6. Fermi surfaces of (a)  $\text{USi}_3$ , (b)  $\text{UGe}_3$  and (c)  $\text{USn}_3$ .

characterized as a spin fluctuation material on the basis of the low-temperature  $T^2$  dependence of its resistivity which is assumed to be due to spin fluctuation scattering (Buschow and van Daal 1971). De Haas–van Alphen measurements have been performed for  $\text{UGe}_3$  (Arko and Koelling 1978) and found to compare reasonably well with the pseudo-self-consistent application of the overlapping charge density model by the authors. The results of that model agree amazingly well when compared to the self-consistent calculation of Hasegawa (1984). Both calculations find two hole surfaces centered on the R point (at the corner of the Brillouin zone) and more complex electron surfaces arising from band 10 consisting of a lens-like piece centered at M (center of the cube edge) and a more complex structure straddling the  $\langle 111 \rangle$  directions. Band masses reported by Hasegawa for the eighth-band R-centered hole sheet are fairly anisotropic – ranging between 3 and 5 electron masses. They are more isotropic on the ninth-band R-centered hole sheet, ranging between 3.5 and 4.5. The two band masses calculated for the band 10 M-centered electron lens are 1.36 and 0.54. Comparing these results where possible to the few experimentally observed masses reflects only a modest enhancement and, in some cases, the observed masses are actually smaller than the calculated masses (thereby revealing a small inaccuracy in the calculation). The density of states reported by Hasegawa – 98 states/Ry per cell – is also very close to the measured value of 118 (van Maaren et al. 1974). Clearly, if the enhancement factor is that small, the presence of spin fluctuations must be called into question unless they are very specific to some small set of as yet unmeasured orbits.



Another very interesting aspect of  $UGe_3$  appears in the induced magnetic form factor (Lander et al. 1980). Besides the moderately standard uranium f orbital form factor appearing at the U site, a small patch of magnetization appears at the Ge site very close to the center of the ion: at a radius of approximately  $0.5 \text{ \AA}$ . This requires very careful consideration and is indicative of the strong effects of the f orbitals. The usual way to model the induced spin density, consistent with the idea of Pauli paramagnetism, is to calculate the charge density of the states at the Fermi energy and use it as the induced spin density. Such an approach clearly cannot be applicable in this instance because it is the outermost *node* of the Ge p orbital that appears where the magnetization is observed. (The principal maximum occurs significantly further out.) A major clue to the origin of this strange patch of magnetization is that, during the last stages of the self-consistency cycles, the difference between cycles is maximal precisely at the radius of the observed magnetization. This then is traced to the maximum for the energy derivative of the Ge p orbital being located there. It is the average orbital energy that is changing from cycle to cycle rather than the orbital occupations. The following scenario is thus suggested. When the magnetic field is applied, the f states are the most affected. But, being hybridized with the Ge p orbitals, and significantly influencing the effective potential seen, they pull the p orbitals along in energy. It is then the change in shape of the orbitals that is the major effect rather than the occupation number change. It would be extremely useful to have more than one instance of such an effect. Unfortunately, adequate samples of  $USi_3$  – where it would be expected to occur – do not exist, and in  $USn_3$ , the effect is not seen as expected (G. Lander, private communication). One might wonder what could be observed through (Ge–Sn) alloy studies.

The nature of the hybridization was explored in  $UGe_3$  both by Arko and Koelling and by Hasegawa. Hasegawa performed the model calculation where the Ge atoms were removed and a calculation done for simple cubic uranium at the  $UGe_3$  lattice constant. He found a small broadening of the f bands due to inter-site hybridization with the 6d orbitals. Arko and Koelling had looked for this interaction in  $UGe_3$  by defining special weighted densities of states and found it not to be present. The implication is that the p–f interaction overwhelms it. As an interesting aside, the pseudo-self-consistent calculation not only gave strong evidence of charge being moved from the uranium to the germanium but that this occurred to the extent that the resulting ions were roughly of the same size.

$UGe_3$  – with further study – could be an excellent material to serve as a basis for a critical experiment in our understanding of f electron materials. Note the dilemma posed by the current view of the de Haas–van Alphen measurements and the induced magnetic form factor measurements. These measurements are performed in comparable magnetic fields yet, in the former, one is interpreting the measurements using unmodified ground-state calculations while, in the latter, it is assumed that the field is modifying the electronic structure. By significantly improving the tolerances on the calculations for the Fermi surface properties, expanding the available experimental measurements of orbits and (especially) masses, and actually performing a calculation for the material in an applied magnetic field, critical information can be obtained with implications about our interpretation of magnetic field probes applied to f-orbital-containing materials.

3.1.2.2.  $CeSn_3$ – $USn_3$ – $NpSn_3$ – $PuSn_3$ . Mixed-valent  $CeSn_3$  was the first cerium alloy to have its Fermi surface determined by the dHvA effect (Johanson et al. 1981a, b, 1983). Recently, the data have been confirmed by another group (Umehara et al. 1990).  $CeSn_3$  is of interest because of its large electronic specific heat coefficient,  $\gamma$ , of 73 mJ/mol K<sup>2</sup> and the strong influence of spin fluctuations on its properties. These spin fluctuations manifest themselves at low temperatures via (1) a  $T^2$  behavior in the resistivity (Stalinski et al. 1973), (2) a  $T^3 \ln T$  contribution in the specific heat, and (3) a quenching of the specific heat coefficient in a field (Ikeda and Gschneidner 1982). Moreover, the results of magnetic form factor measurements (Stassis et al. 1979) indicate that below 40 K, strong mixing occurs between the f and d states.

The basic result of the dHvA experiments is that the Fermi surface of  $CeSn_3$  is different from that of  $LaSn_3$ . Most of the details of the  $CeSn_3$  surface could be explained by an LDA calculation which treated the f electrons as band states (Koelling 1982). Despite this, some differences were seen between theory and experiment which led to some questioning about how good the agreement was (Lee et al. 1986). Several years ago, we undertook a series of well-converged warped muffin-tin LAPW band calculations on  $CeSn_3$  which (1) treated relativistic effects using various approximations, (2) used a variety of exchange–correlation potentials, and (3) used a large  $k$ -point grid supplemented by a spline-fitting technique for an improved representation of the Fermi surface. The result is a Fermi surface in closer agreement with experiment than the original prediction. Equivalent results have recently been obtained (Hasegawa et al. 1990). We concentrate here on the large orbits (areas of 10 MG and larger) since there is a large number of small area orbits, which makes their identification complicated. The Fermi surface, shown in fig. 7, is composed of a large hole sheet around the R point, a large electron sheet around the  $\Gamma$  point, and a smaller piece at M. All calculations have similar Fermi surfaces, since the Coulomb interaction of the f electrons is so large that it “locks” the Fermi surface in place so as to maintain the proper occupied f count of about one, and thus the effect of the exchange–correlation potential is weak. Treatment of spin–orbit effects via a perturbative correction is sufficient for  $CeSn_3$ , since the occupied f states exhibit a pure  $\ell$  character (as opposed to a  $j = \frac{5}{2}$  character) (Koelling 1982).

Comparison of our theoretical results (using a Ceperley–Alder exchange–correlation potential) with experiment is shown in fig. 8. The agreement is excellent. The large orbit which exists for all angles is that from the R piece, the rest come

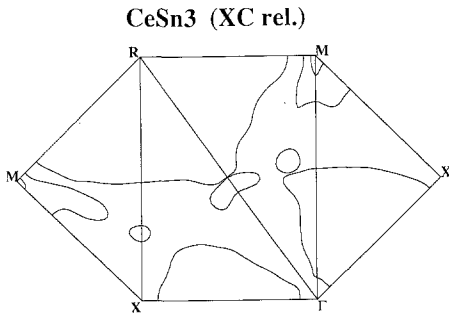


Fig. 7. Fermi surface of  $CeSn_3$  resulting from the band structure of fig. 5.

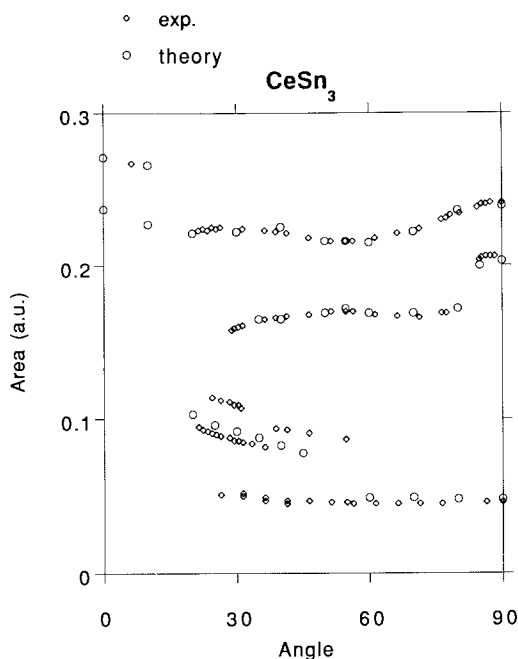


Fig. 8. Comparison of calculated (circle) and experimental (diamond) dHvA areas for CeSn<sub>3</sub> [data taken from Johanson et al. (1981a)].

from the  $\Gamma$  piece. The lowest area orbit shown in the figure cuts off at  $60^\circ$  in our calculation, but in that of Hasegawa et al. extends all the way to  $30^\circ$  as seen experimentally. Not shown are two orbits from the M sheet, which have an area of about 0.04 a.u. and are predicted to exist for all angles. All calculations find this M piece (which comes from the same band as the  $\Gamma$  piece). Its lack of experimental observation is still a mystery.

We turn now to a discussion of mass renormalizations. Comparing the dHvA masses of Umehara et al. (1990) with our band masses, we find that the ratio of  $m^*/m_b$  is about 4 for the R piece, and about 3 for the  $\Gamma$  piece. The ratio of the experimental specific heat coefficient at 10 T (Ikeda and Gschneidner 1982) to our calculated density of states is 3.8, consistent with the dHvA result, which indicates that the quasiparticle contribution fully accounts for the electronic specific heat. The mass renormalization has been simulated by Strange and Newns (1986), who performed a band calculation utilizing a mean field (slave boson) treatment of the Anderson model, where the parameters were adjusted to obtain the correct specific heat coefficient. The result is that the Fermi surface changes little under renormalization. In fact, what changes were seen are likely attributed to the fact that the calculation was not self-consistent (the f count changed by 0.4 electrons; this change would be much smaller in a self-consistent calculation). These observations are consistent with the fact that the self-energy function for heavy fermions is dominated by the frequency dependence and rides with the chemical potential (Varma 1985), thus the quasiparticle Fermi surface is identical to that obtained from a ground-state calculation. A related observation can also be drawn from the work of Zwicky (1988), who showed that

Kondo renormalizations left the Fermi surface unchanged if (1) the LDA  $f$  band width is small compared to the spin-orbit coupling, and (2) the energy scale of crystal field splittings is less than the Kondo temperature. The second condition is more than sufficiently satisfied in  $\text{CeSn}_3$  due to (1) strong hybridization of the  $f$  states, as revealed by neutron scattering form factors (Stassis et al. 1979), and (2) high energy scale as revealed both by neutron scattering (Murani 1983) and by the modesty of the mass renormalizations. The first condition, though, is clearly violated, since LDA predicts an  $\ell$ -like (as opposed to a  $j$ -like) character of the occupied  $f$  states. We have performed calculations where the  $j = \frac{7}{2}$  character is projected out (forcing a  $j = \frac{5}{2}$  character), and find a degraded Fermi surface relative to experiment.

We have also performed LAPW calculations on the related metals  $\text{USn}_3$  and  $\text{NpSn}_3$  (Norman and Koelling 1985, 1986a). Both are predicted to be magnetic, as opposed to  $\text{CeSn}_3$  which is predicted to be paramagnetic. In reality,  $\text{USn}_3$  is paramagnetic, but close to a magnetic instability. The same problem is also observed for  $\text{UPt}_3$  and  $\text{URu}_2\text{Si}_2$  (Norman et al. 1988c), indicating an overtendency to spin polarization in local spin density theory. The most likely explanation for this problem is an improper inclusion of Hund's rule effects for  $f^2$  systems. A correction incorporating Hund's second rule (maximal  $L$ ) has been derived from open-shell Hartree-Fock theory for systems with maximal moment along the quantization axis by Eriksson et al. (1990a) and Norman (1991c), but such ground states are rarely realized for  $f^2$  systems, so a comprehensive theory is lacking at the current time.

Returning to the paramagnetic calculation in  $\text{USn}_3$ , the density of states is about  $23 \text{ mJ/mol K}^2$ , significantly larger than the  $13 \text{ mJ/mol K}^2$  in  $\text{CeSn}_3$ . This is due to the fact that the flat bands around the R point get closer to the Fermi energy as the  $f$  bands are filled. Comparisons to specific heat data give a mass ratio of 7.5. A detailed analysis indicates that the specific heat coefficient falls quite rapidly with temperature and approaches the band result by about 30 K (Norman et al. 1986). This rapid fall with temperature, also seen for related heavy-fermion metals, is consistent with a strong frequency dependence of the self-energy. The fact that the coefficient approaches the value obtained with the  $f$  electrons treated as itinerant would indicate that the  $f$  charge degrees of freedom remain in the Fermi surface as the temperature increases. This is in contrast to common wisdom which would indicate that the  $f$  electrons decouple from the Fermi surface as the temperature is raised. This controversy might be resolved by doing a similar analysis of the temperature dependence of the specific heat on related heavy-fermion metals, or by trying to determine the temperature dependence of the Fermi surface by positron-annihilation experiments.

The proximity of  $\text{USn}_3$  to magnetic behavior is revealed by  $\text{USn}_{3-x}\text{Pb}_x$  alloy studies (Lin et al. 1985c). Antiferromagnetic behavior is observed with as little as 5% Pb. With further substitution of Pb,  $T_N$  rises to 38.2 K with 30% Sn remaining before dropping to the value of 31 K observed for pure  $\text{UPb}_3$ . A possible explanation of this peak in  $T_N$  is the competition between decreasing  $f$  hybridization (which would increase  $T_N$ ) and decreasing interatomic exchange due to the increased U separation (which would decrease  $T_N$ ) as the Pb content is increased. This would be consistent with the rise in spin fluctuation temperature  $T_{\text{SF}}$  induced by pressure. However, it

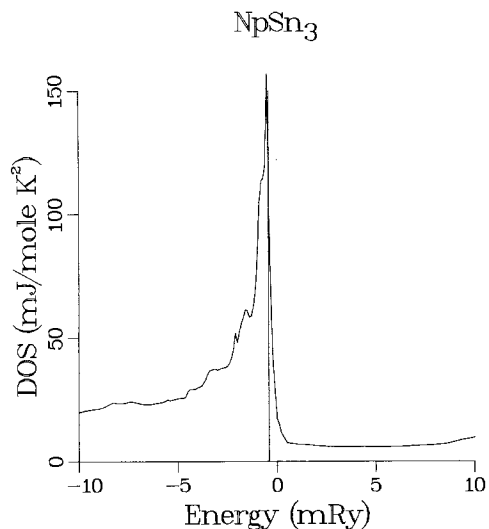


Fig. 9.  $\text{NpSn}_3$  density of states for the paramagnetic phase in the immediate vicinity of the Fermi energy (vertical line).

should be noted that there may be other factors involved since there is also a  $T_N$  peak in  $\text{CePb}_{3-x}\text{In}_x$  which does not fulfill the conditions of this explanation.

The calculated paramagnetic density of states for  $\text{NpSn}_3$  (fig. 9) is an enormous  $102 \text{ mJ/mol K}^2$ , due to the fact that the flat bands around the R point are degenerate with the Fermi energy. Needless to say, a strong magnetic instability is predicted, and, experimentally,  $\text{NpSn}_3$  is an antiferromagnet exhibiting a BCS-like transition in the specific heat (Trainor et al. 1976), indicating an itinerant nature of the magnetism. Comparisons to the specific heat data give a surprisingly low mass renormalization factor of 2.4. An antiferromagnetic ground state is preferred, since the lowering in symmetry can split the narrow peak at the Fermi energy, thus relieving the unfavorable high density of states at the Fermi energy. To test this, we performed polarized calculations including spin-orbit effects. The result was a 61% reduction in the density of states at the Fermi energy (fig. 10), which is consistent with observed 64% reduction in the specific heat coefficient when going through the magnetic phase transition. We also found a total moment of  $0.2\mu_B$  (0.4 orbital,  $-0.2$  spin), consistent with the Mössbauer data of Trainor et al. (1976). Thus,  $\text{NpSn}_3$  is surprisingly well described by local spin density theory, indicating that the magnetism is indeed of an itinerant nature. The itinerant character has been questioned recently by Kalvius et al. (1990). However, because the calculated moment arises purely from the f orbital contributions without admixture, it would be quite consistent with a localized interpretation.

As for  $\text{PuSn}_3$ , one would expect the density of states to drop dramatically, since the flat bands near the R point will be pulled through the Fermi energy in that case. This is consistent with experiment, which finds that  $\text{PuSn}_3$  has a Pauli-like susceptibility (Brodsky 1978). This has been verified by Eriksson et al. (1989a) who calculate a low density of states,  $5 \text{ mJ/mol K}^2$ , for  $\text{PuSn}_3$  when properly including spin-orbit effects.

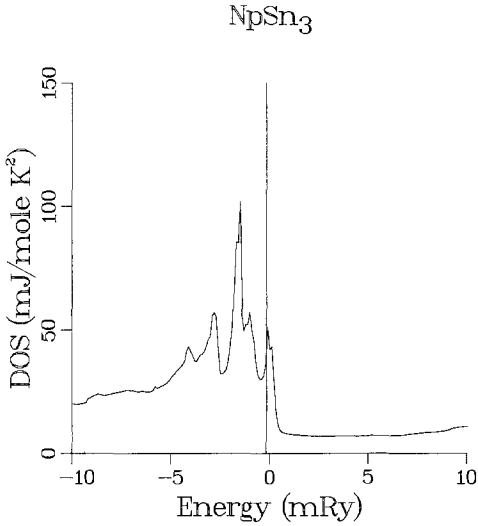


Fig. 10.  $\text{NpSn}_3$  density of states for the antiferromagnetic phase for the same range of energy about the Fermi energy (vertical line) as in fig. 9.

3.1.2.3. *CeIn<sub>3</sub> and UIn<sub>3</sub>*.  $\text{CeIn}_3$  is antiferromagnetic below 10 K with an ordered moment of  $0.65\mu_{\text{B}}$ /Ce atom. Nonetheless, it exhibits an electronic specific heat of  $130 \text{ mJ/K}^2 \text{ mol}$  and behaves as a far more itinerant system under a pressure of 200 kbar (Mignot and Wittig 1982). A magnetoresistance and de Haas–van Alphen effect study has been carried out using fields up to 150 kOe and a temperature down to 0.45 K (Kurosawa et al. 1990, Umehara et al. 1991a). Magnetoresistance indicates open orbits along the  $\langle 110 \rangle$  and  $\langle 112 \rangle$  directions. The de Haas–van Alphen data shows a single frequency in the range of 30 MOe which is not present at all angles. This would be consistent with the  $\langle 111 \rangle$  arms observed through saturation in the magnetoresistance. Unlike  $\text{CeAl}_2$ , these measurements are for the antiferromagnetic phase because the magnetic phase transition is not reached for this material in these fields. The observed orbits have been interpreted (Kitazawa et al. 1985) using a Fermi surface obtained for  $\text{LaIn}_3$  which consists of  $\Gamma$ - and R-centered pieces connected along the  $\langle 111 \rangle$  directions. This piece of surface thereby appears common to the series  $\text{LaIn}_3$ ,  $\text{CeIn}_3$  and  $\text{PrIn}_3$ .  $\text{LaIn}_3$  and  $\text{PrIn}_3$  exhibit the other orbits expected from the calculated surface but  $\text{CeIn}_3$  does not. Possibly the antiferromagnetic interactions have eliminated these parts of the Fermi surface but that would leave the problem that not enough high-mass orbits are observed to account for the large specific heat. Even though the masses are high (2–2.5) for the one observed piece, the large specific heat implies that either more Fermi surface piece(s) with strongly enhanced masses are present, or the remaining orbits of this one piece have much stronger enhancements (consistent with their not being seen).

The recent Fermi surface study for  $\text{LaIn}_3$  presents a slightly different picture (Umehara et al. 1991a) of the Fermi surface. That study concludes from their magnetoresistance measurements that there is no saturation with the implication that the open orbits arising from bridging of the hole surface from  $\Gamma$  to R (and also X) are not present in  $\text{LaIn}_3$ . This is not consistent with the band calculations

(Hasegawa 1982). The angular range of the “d” orbit observed in the de Haas–van Alphen measurements is nonetheless still comparable in  $\text{LaIn}_3$  and  $\text{CeIn}_3$ . The implication is that either the cutoff of the range of observation is due to some other effect or that the necks are there but sufficiently out of line as to not support open orbits. Another worrisome point is that some of the calculated masses are slightly larger than those measured. Were this situation not to be reversed by improved calculations possibly incorporating warped muffin-tin effects and better incorporation of the  $5p$  states, one would need to consider ad hoc upward shifts of the  $f$  orbitals such as has been used for the pnictides (Kasuya et al. 1987, Sakai et al. 1987) and for  $\text{LaB}_6$  (Harima et al. 1988) or, to accomplish roughly the same thing, utilizing a weaker exchange–correlation functional such as achieved with the exchange-only functional. Another possibility in this direction is the use of gradient corrections which often give shifts in the same direction as going from an exchange–correlation functional to an exchange-only functional. However, these are considerations for  $\text{LaIn}_3$  that are not as relevant in  $\text{CeIn}_3$  because the  $f$  electron Coulomb correlations will play the more dominant role as in  $\text{CeSn}_3$ .

Both  $\text{CeIn}_3$  and  $\text{UIn}_3$  are antiferromagnetic. The similarity is more striking when examining the alloy behavior with tin as shown in fig. 11. Substituting tin for the indium destroys the antiferromagnetism in both materials, although more quickly for the Ce compound consistent with it being the weaker antiferromagnet. From the other side, the substitution of In into the Sn compounds causes the specific heat coefficient  $\gamma$ , which is already quite large as a consequence of the large mass enhancements, to rise even more dramatically to a peak near an  $\text{InSn}_2$  composition. The large specific heat coefficient in the  $\text{Sn}_3$  materials being primarily due to spin fluctuation enhancements as discussed above, one naturally suspects that this rise is

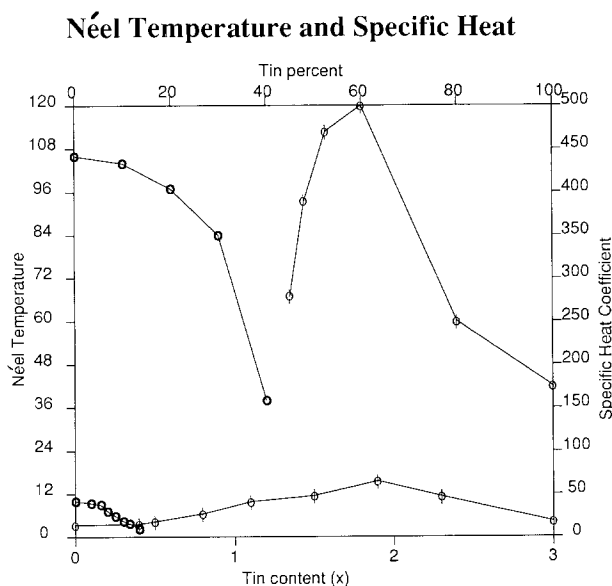


Fig. 11. Néel temperature (heavy circles) and specific heat coefficient  $\gamma$  (light circles with a stroke) for  $\text{CeIn}_{1-x}\text{Sn}_x$  [lower curves, data taken from Elenbaas et al. (1980)] and  $\text{UIn}_{1-x}\text{Sn}_x$  [upper curves, data taken from Lin et al. (1986)].

also due to enhancements rather than a rigid band probing of a peak in the density of states. However, Lawrence (1979) demonstrated that the behavior of the materials does relate to structure in the underlying p orbital partial density of states. In fact, we have found (Norman, unpublished) that the calculated band density of states for an ordered  $\text{UInSn}_2$  alloy is approximately twice that of  $\text{USn}_3$ .

Note the unusual form of the model thus implied. The f count is not changing dramatically as one traverses the phase diagram so the f bands must be floating just above the Fermi energy due to the large Coulomb  $U$  term. The underlying p bands are behaving more like a rigid band system prior to hybridization so that, where there is a minimum in the p band partial density of states, there is a minimum in the hybridization and a maximum in the enhancements. Further examination of this relation could prove very instructive in probing the details of this mechanism.

The behavior shown in fig. 11 is characteristic of the other ordered group III–group IV pseudobinary systems so the behavior is quite general.

### 3.2. $\text{UPt}_3\text{--UPd}_3\text{--Pr}$

$\text{UPt}_3$  is the best studied of the few metals which exhibit the unusual phenomenon of heavy-fermion superconductivity. It has a large electronic specific heat coefficient of  $420 \text{ mJ/mol K}^2$ . It shows clear Fermi-liquid-like behavior at low temperatures, including a  $T^2$  contribution to the resistivity, and a  $T^3 \ln T$  component to the specific heat (Stewart 1984, De Visser et al. 1987b). At around 0.5 K, the metal becomes superconducting. A large body of evidence has accumulated that indicates that the superconducting gap function comes from a non-trivial group representation (Taillefer et al. 1991). This, in turn, supports the conjecture that heavy-fermion superconductors have an “exotic” pairing mechanism. We defer to the section on superconductivity for a more detailed discussion of these points.  $\text{UPt}_3$  is also noteworthy in that its Fermi surface has been mapped out by detailed dHvA experiments (Taillefer et al. 1987, Taillefer and Lonzarich 1988).

A large number of band calculations have been performed on  $\text{UPt}_3$  by various groups, including several spin-polarized calculations (Oguchi and Freeman 1985, Wang et al. 1985, 1986, Albers et al. 1986, Sticht and Kübler 1985b, Norman et al. 1988c). For a detailed discussion of the electronic structure, the reader is referred to the paper by Albers et al. (1986). The calculated density of states in  $\text{UPt}_3$ , which is around  $25 \text{ mJ/mol K}^2$ , is large enough that a magnetic instability is predicted. We have performed a number of polarized calculations on  $\text{UPt}_3$  including spin–orbit effects (Norman et al. 1988c). Both a simple antiferromagnetic  $\mathbf{q} = (0, 0, 1)$  and the observed orthorhombic  $\mathbf{q} = (0.5, 0, 0)$  structures were treated with various moment orientations. The largest moment was found for a  $\mathbf{q} = (0.5, 0, 0)$  arrangement with the moment in the basal plane, consistent with experiment (the complexity of the calculations prevented an accurate total energy comparison). The calculated total moment is  $0.8\mu_B$  (2.0 orbital,  $-1.2$  spin) to be compared to an experimental moment of  $0.02\mu_B$  (Aeppli et al. 1988). Doping with a few percent Th or Pd, though, leads to an experimental moment of  $0.65\mu_B$  (Goldman et al. 1986, Frings et al. 1987) with the same Néel temperature of 5 K, consistent with the calculated moment. First, it should



be remarked that there is still some question about the intrinsic nature of the weak moment seen in  $\text{UPt}_3$ . The correlation length is finite (about 300 a.u.), leading to the suspicion that it is a “dirt” effect. Second, given the Néel temperature of 5 K, one would estimate from standard spin fluctuation theory (see the section on  $\text{UCu}_5$ ) a value of the moment comparable to what is seen in the doped metal, as opposed to the 0.02 value in pure  $\text{UPt}_3$ . This might imply that the primary order parameter is something else (quadrupolar?) with the weak moment being an induced byproduct, or that some effect is acting to suppress the magnetic moment in the stoichiometric material [a Kondo suppression has been recently advocated by Coleman and Gan (1991)]. A related proposal is that the small moment is due to nesting of the Fermi surface (Ozaki and Machida 1989, Miyake and Kuramoto 1991). Despite these claims, our (non-interacting)  $\chi_0(\mathbf{q}, \omega)$  calculations (Norman et al. 1988c), which include relativistic matrix elements, indicate nothing special at  $\mathbf{q} = (0.5, 0, 0)$ . This also occurs for a calculation which treats the f electrons as core states (Norman, unpublished). This confirms the fact that the magnetism in the moment-polarized calculations is being driven by the  $q$ -dependence of the spin–spin response function, as opposed to nesting effects in  $\chi_0(\mathbf{q})$ . This is consistent with the commensurability of the  $q$  vector with the lattice, and is also consistent with the analysis of neutron scattering data (Aeppli et al. 1987, 1991).

This brings up the question of how to interpret the neutron scattering data for  $\text{UPt}_3$ . The localized nature of the fluctuating moments seen in neutron scattering is consistent with the moment-polarized calculations, since in both cases it is the moment–moment response function which is playing the important role: the difference is that experimentally, the moment is fluctuating, whereas in the calculation, it is ordered. It has often been stated that the observed data are inconsistent with Fermi-liquid theory since the neutron scattering linewidth,  $\Gamma$ , remains finite as  $q \rightarrow 0$ . This statement is only partly true: by inclusion of spin–orbit effects, one gets a large interband contribution to the susceptibility, even at  $q = 0$ . In fact, we find in our  $\chi_0(\mathbf{q})$  calculations that 80–85% of the susceptibility is in the interband (Van Vleck) part.

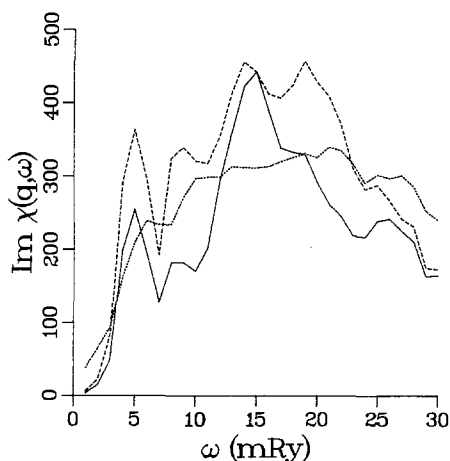


Fig. 12. LDA (unrenormalized) dynamic susceptibility for  $\text{UPt}_3$  including spin–orbit effects. The solid curve is for  $\mathbf{q} = (0, 0, 0)$ , the dashed curve for  $\mathbf{q} = (0, 0, 1)$ , and the dotted curve for  $\mathbf{q} = (0.5, 0, 1)$  with  $\mathbf{q}$  in reciprocal lattice units.

In fig. 12, we show our own calculations of the (non-interacting)  $\text{Im } \chi_0(\mathbf{q})$ , which shows a broad spectrum with a relatively weak  $q$  dependence. This looks similar to the experimental data, if one scales  $\chi$  up and  $\omega$  down by the observed mass renormalization factor. (It should be remembered though, as discussed in the previous paragraph, that inclusion of Stoner renormalizations leads to an unphysical divergent susceptibility, indicating a strong suppression of the LSD spin-spin response function). Of course, there must be an intraband contribution to  $\text{Im } \chi$  at small  $q$  which behaves the same way as in Fermi-liquid theory (i.e.  $\Gamma \rightarrow 0$  as  $q \rightarrow 0$ ), given the observation of the Fermi surface by the dHvA effect. It is a challenge to the neutron scattering community to find this piece to the spectrum. Until these issues are resolved, it will be difficult to understand exactly what is going wrong in the polarized calculations for  $\text{UPt}_3$ . As discussed above for  $\text{USn}_3$ , LSD calculations for  $f^2$  systems are somewhat suspect if Hund's rule effects are important, since one assumes in LSD that the spin moment has maximal projection along the quantization axis, whereas in most hexagonal metals with a localized  $f^2$  state, the ground state is a magnetic singlet (Pr, PrNi<sub>5</sub>, UPd<sub>3</sub>). Thus, whether the "suppression" of the LSD spin-spin response function in  $\text{UPt}_3$  is due to a Kondo effect, or due to Hund's rule effects, remains to be seen.

We return now to a description of the paramagnetic band calculations, where five of the six  $j = \frac{5}{2} f$  bands cross the Fermi energy. In fig. 13, we show the calculated Fermi surface from the LMTO-CC calculation of Norman et al. (1988a). Bands 1 and 2 form disks around the A point [LMTO-ASA gives rings; LMTO-CC and FLAPW give disks, as discussed by Wang et al. (1987)]. The band 2 disks are interconnected by arms. Bands 3, 4, and 5 form closed sheets at  $\Gamma$ . In addition, band 3 has a piece around K, which can be interconnected to the piece at  $\Gamma$  by a small adjustment of the Fermi energy.

In fig. 14, we show the calculated dHvA areas from the work of Norman et al. (1988a), which can be compared to the experimental data of Taillefer and Lonzarich

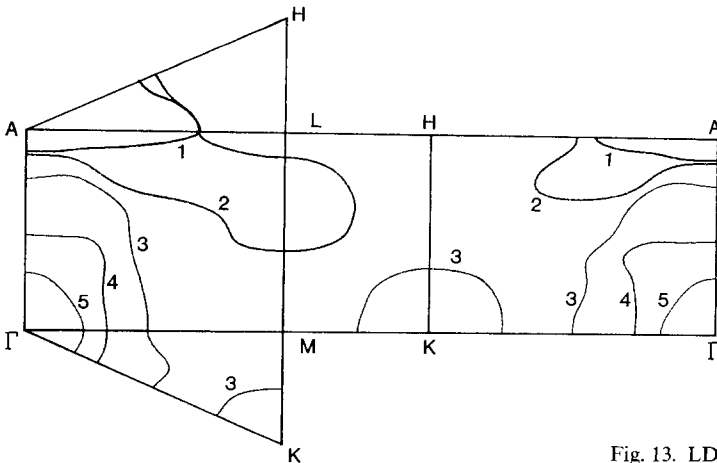


Fig. 13. LDA Fermi surface for  $\text{UPt}_3$ .

(1988) shown in fig. 15. Quite good agreement can be seen, the agreement being comparable to what is observed in transition metals (Christensen et al. 1988). The orbit  $\alpha$  is around the arm jutting from the band 2 disk; the orbit  $\beta$  is an L-centered orbit exterior to the band 2 arms; the orbit  $\lambda$  is around the band 2 disk; the orbit  $\delta$  is around the band 1 disk; the orbit  $\varepsilon$  is around the band 4 surface; the orbit  $\omega$  is around the band 3  $\Gamma$ -centered piece; and the orbit  $\gamma$  is around the band 5 piece. Because bands 1 and 2 touch along the A-L direction, the orbit  $\theta$ ,  $\phi$  and  $\psi$  represent magnetic breakdown orbits between these bands. One thing complicating the analysis, and thus making some of the orbit assignments tentative, is the short angle range over which some of the experimental orbits exist (shorter in many cases than predicted by theory). Some of this could be due to subtle topological changes to the Fermi surface. For instance, the disappearance of the  $\omega$  orbit may be due to formation of a neck between the  $\Gamma$ - and K-centered pieces as discussed in the previous paragraph. A most unusual result is the complete lack of any dHvA signals near the  $c$  axis, which is not understood at the present time. This may be due to a directional dependence of the mass renormalization (see below for Pr).

In table 1, we compare results from the work of Norman et al. (1988a) to experiment (Taillefer and Lonzarich 1988) for a number of orbits. What can be seen is that only small shifts in the bands of order 1 mRy are necessary to obtain areas in agreement with experiment. Also shown are the mass renormalizations, which are large and have a factor of two variation over the Fermi surface. The average mass renormalization is about 15 or so, comparable to a value of 17 extracted when comparing specific heat data to the band structure density of states, so it would appear that the quasiparticle contribution saturates the electronic specific heat. Several years ago, one of us attempted to calculate this mass renormalization using spin fluctua-

TABLE 1  
Comparison of dHvA masses (Taillefer and Lonzarich 1988) to band masses (Norman et al. 1988a) for  $\text{UPt}_3$ . The first column identifies the orbit, the next two are the dHvA areas and masses, the next two the calculated areas and masses, and the final column the mass renormalization. The numbers in parentheses are the shifts of  $E_F$  in mRy necessary to get the listed values.

Orbit	Exp.		Theory		$m^*/m_b$
	Area	Mass	Area	Mass	
<b><math>H \parallel a</math></b>					
$\alpha$ : ML2	5.4	25	5.3 (-2.0)	1.6	16
$\gamma$ : $\Gamma$ 5	7.3	40	7.1 (+0.5)	1.8	22
$\delta$ : A1	14.0	50	14.2 (+2.5)	1.7	29
$\varepsilon$ : $\Gamma$ 4	21.0	60	21.3 (+0.5)	4.8	13
$\omega$ : $\Gamma$ 3	58.5	90	59.0 (-1.0)	5.3	17
<b><math>H \parallel b</math></b>					
$\alpha$ : ML2	4.1	15	3.9 (-2.5)	1.3	12
$\delta$ : A1	12.3	30	12.0 (+3.0)	1.3	23
$\lambda$ : A2	25.1	50	26.2 (+0.0)	4.2	12

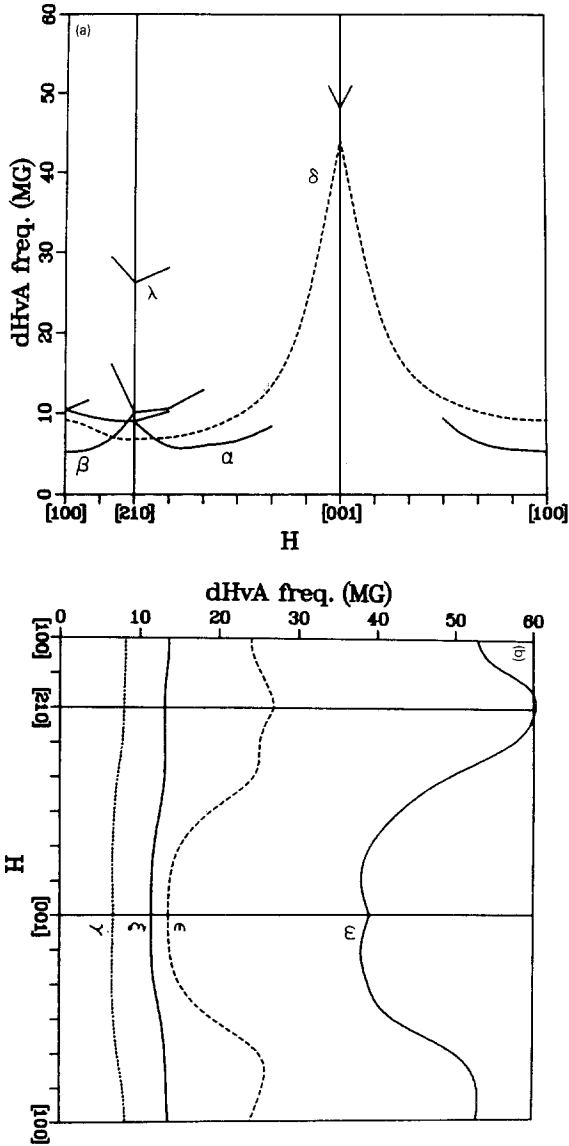


Fig. 14. Calculated dHvA areas for the  $\text{UPt}_3$  Fermi surface of fig. 13. (a) Arising from bands 1 and 2, and (b) arising from bands 3, 4, and 5.

tion theory with the dynamic susceptibility taken from neutron scattering data (Norman 1987, 1988). First, the size of the renormalization is consistent with such a theory, since for localized spin fluctuations, the mass renormalization and the susceptibility enhancement scale together, a behavior commonly seen in heavy fermions (Stewart 1984). This is in contrast with the free electron case where  $m^*/m_b$  scales as the logarithm of  $\chi/\chi_b$  ( $m_b$  is the band mass,  $\chi_b$  the non-interacting band susceptibility). Second, the strong frequency dependence of the dynamic susceptibility leads to a sharp decrease in  $m^*/m_b$  as the temperature increases, which is in quantitative

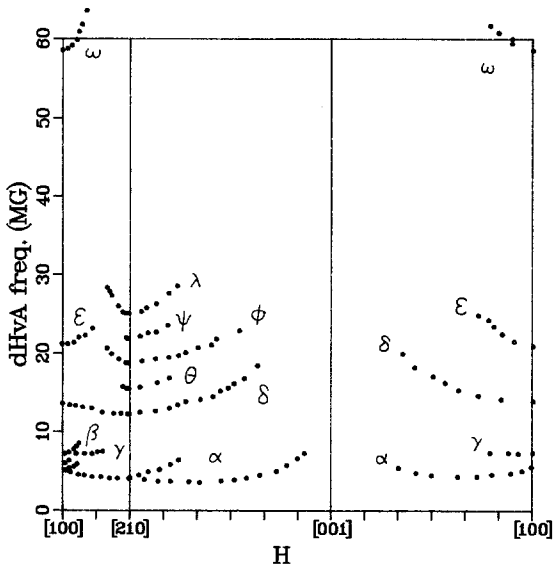


Fig. 15. Experimental dHvA areas for  $UPt_3$  [data taken from Taillefer and Lonzarich (1988)].

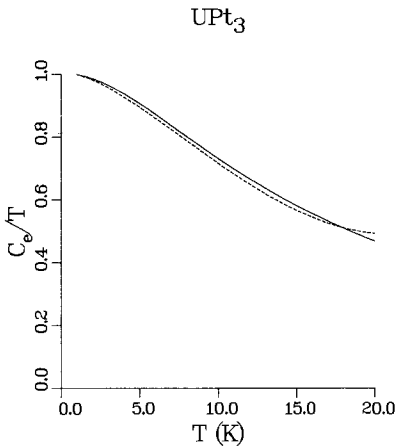


Fig. 16. Temperature dependence of the electron specific heat coefficient for  $UPt_3$ . The solid line is calculated from spin fluctuation theory, the dashed line is the phonon-subtracted experimental data of Renker et al. (1986).

agreement with the specific heat data in  $UPt_3$ , as shown in fig. 16. This was also studied by Konno and Moriya (1987) who showed that a  $T^3 \ln T$  term in the specific heat could be obtained from localized spin fluctuations. This success is gratifying, since a related itinerant spin fluctuation theory is successful in describing similar phenomena in transition metals such as  $MnSi$  and  $Ni_3Al$  (Lonzarich 1986).

Experimentally, Dingle temperatures have been reported for two orbits (Taillefer et al. 1987) with values of 30 and 70 mK. These small values are due to the fact that they are extracted using the quasiparticle masses, when in actuality it is the band mass which enters the Dingle expression (Shoenberg 1984). Taking this into account, we extract Dingle temperatures of 0.5 and 1.0 K, which are quite reasonable. The

important point here is that it is often stated that band theory “fails” to give the correct mass. The band mass, though, is a fundamental quantity, quite distinct from the quasiparticle mass. It is the band mass which enters into response functions which determine magnetic or structural instabilities. In dHvA, it is the band mass which enters both in the Dingle factor and in the spin-splitting factor. This occurs in the Dingle factor because of a cancellation of renormalization factors, related to the fact that the self-energy “rides” with the chemical potential (Varma 1985). In fact, if the  $g$  factor was known and spin-splitting zeros could be seen, the band mass could be extracted from the dHvA experiments, as has been done recently for organics (Wosnitzer et al. 1991).

It has often been suggested that the good agreement of band theory with dHvA data are somehow connected to treating the crystal lattice symmetry properly, and thus the band results are devoid of any intrinsic meaning. To test this, we have run similar calculations for  $\text{UPt}_3$  where the  $f$  electrons were treated as core states (Norman et al. 1988a). The resulting Fermi surface topology was in complete disagreement with experiment. We might also remark that the Fermi surface of  $\text{UPt}_3$  is composed of five  $f$  bands, so the chances of obtaining coincidental agreement is quite low. A more convincing explanation has been offered by Zwicky (1988). She and her collaborators have performed Kondo renormalized band calculations on  $\text{UPt}_3$  and find the same Fermi surface as predicted by LDA. This is presumably due to the fact that crystal field splittings are smaller than the Kondo temperature, and thus all  $f$  bands get renormalized the same way.

Finally, we should mention that LDA calculations have had some success in explaining bulk property data in  $\text{UPt}_3$ . One of the first calculations done were by Sticht and Kübler (1985b) which obtained a lattice constant within 0.4% of experiment, as well as a reasonable estimate of the bulk modulus. This indicates that  $f$  bonding must be playing a role. Later work by Albers et al. (1986) showed that reasonable results were obtained for bulk properties if an exchange-only functional was used (it is widely known that the free-electron correlation functionals used in LDA are inadequate for  $f$  electron systems, and better results are usually obtained if they are not included). Moreover, they showed that Vegard’s law is not obeyed, implying strong U–Pt interactions and  $f$  bonding. The reason that  $\text{UPt}_3$  exhibits weak  $f$  hybridization (and thus is a heavy-fermion system) is that the U  $f$  bands fall in an energy gap between a filled Pt 5d manifold and an empty U 6d manifold.

We now turn to a related system,  $\text{UPd}_3$ , which is the dhcp analogue of hcp  $\text{UPt}_3$ .  $\text{UPd}_3$  is the only known uranium alloy where well-defined crystal field levels have been seen with neutrons, consistent with a localized  $f^2$  configuration (Buyers and Holden 1985). Photoemission experiments (Baer et al. 1980) clearly reveal that the  $f$  electron spectral weight is removed from the vicinity of the Fermi energy by 1 eV. This is consistent with the specific heat data of Andres et al. (1978), which indicate an electronic specific heat coefficient of only 5 mJ/mol K<sup>2</sup>. Two anomalies occur both in the specific heat (Andres et al. 1978) and in the thermal expansion (Ott et al. 1980) at 7 and 5 K which have been interpreted as quadrupolar ordering. Recent high-resolution X-ray scattering work by Singh et al. (1990), though, reveal no evidence for structural distortion. Since satellites at  $q = (0.5, 0, 0)$  are seen in neutron scat-

tering (Buyers and Holden 1985), Singh et al. have raised the possibility of weak moment magnetism, such as observed in  $\text{UPt}_3$  ( $\text{UPt}_3$  orders at the same  $q$  vector). Of course, as discussed by Ott et al. (1980), it is possible that quadrupole ordering occurs without a structural distortion. In that case, as related above for  $\text{UPt}_3$ , the weak moment could be a byproduct of such a transition.

Eriksson et al. (1989b) have given a clear explanation about why the  $f$  electrons are localized in  $\text{UPd}_3$ . For this alloy, the  $5f$  levels fall in between the bonding and antibonding Pd  $4d$  bands, resulting in weak hybridization and sharp  $f$  levels. Spin-polarized calculations give a fully saturated spin moment of  $2\mu_B$ , which is the usual signature of  $f$  localization in band calculations.

dHvA data were obtained on  $\text{UPd}_3$  by Ubachs et al. (1986). One large orbit and two small ones were observed, with masses in the range of 0.5 to 2. At the same time, we performed LMTO calculations for  $\text{UPd}_3$  in the correct dhcp structure for comparison purposes (Norman et al. 1987a). In this calculation, the  $f$  electrons were treated as core states. The resulting Fermi surface is quite complicated and is shown in fig. 17. Band 1 forms a small hole pocket at  $\Gamma$ ; band 2 a large hole pocket at  $\Gamma$  and a small one at A, which are interconnected by a small neck; band 3 a large hole pocket at  $\Gamma$  which is interconnected in the  $k_z = \pi/c$  plane; and bands 4 and 5 form complicated networks along the edge of the zone. There is a clear match with the dHvA data, as can be seen by comparing the experimental data of fig. 18 with the theoretical predictions of fig. 19. Band 1 corresponds to one of the small orbits, and band 2 with the large one. The other small orbit may be related to the band 5 piece (an energy shift of the band turns this surface into small pockets around the H point), although since the experimental amplitude for this orbit is very small, no mass data are available to confirm such an assignment. One might ask why the rest of the surface is not seen. Since  $\text{UPd}_3$  is a compensated metal and only one large orbit is seen, this means that much of the Fermi surface has been unobserved in the dHvA experiments, consistent with our own calculations. It is expected, then, that dHvA experiments on better samples will yield more information. A comparison of the dHvA masses to the band masses indicate a renormalization factor of about four to five. This is similar to what is observed in Pr metal, and has been interpreted as due to interaction of the conduction electrons with virtual  $f$  crystal field excitations (Fulde and Jensen 1983), essentially a spin fluctuation mass enhancement.

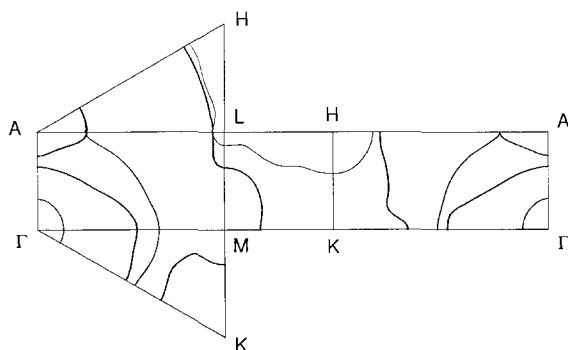


Fig. 17. LDA Fermi surface for  $\text{UPd}_3$  ( $f$  core).

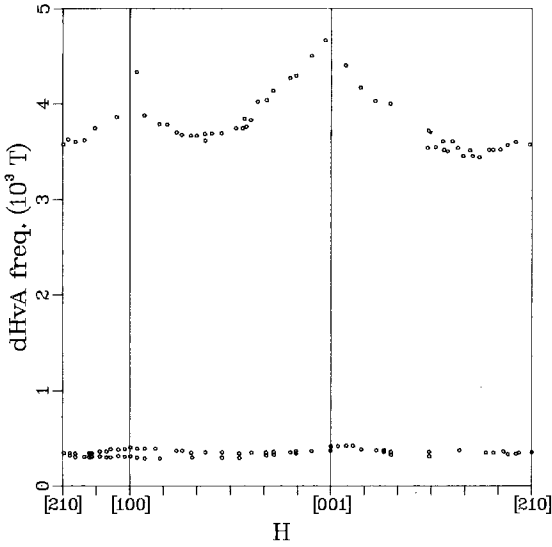


Fig. 18. Experimental dHvA areas for  $\text{UPd}_3$  [data taken from Ubachs et al. (1986)].

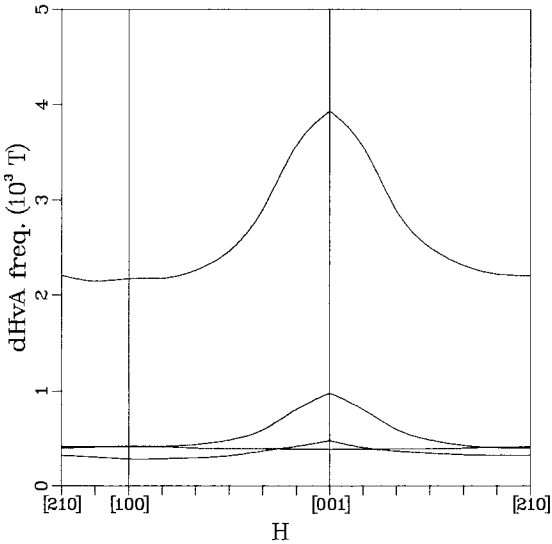


Fig. 19. dHvA areas for the  $\text{UPd}_3$  Fermi surface of fig. 17 arising from bands 1, 2 and 5 (small energy shifts of the bands were done to optimize the comparison to dHvA data).

An interesting issue to raise at this time is the connection between  $\text{UPt}_3$  and  $\text{UPd}_3$ . Both metals are hexagonal, as opposed to the other  $\text{UX}_3$  metals which are cubic. Both have similar U-U separations (in fact, the separation in  $\text{UPd}_3$  is the smaller of the two). Yet,  $\text{UPt}_3$  has  $f$  bands participating in the Fermi surface, and  $\text{UPd}_3$  does not, indicating that Mott localization occurs in between the two. Given the subtle differences between these two metals, it seems to us that what is occurring here is an interplay between hybridization effects (which lowers the kinetic energy) and Hund's rule effects (which lowers the potential energy). In  $\text{UPt}_3$ , the hybridization wins out,



but in UPd<sub>3</sub>, Hund's rules win out. So far, no first-principles theory gives a proper description of this crossover, but the above-mentioned results of Eriksson et al. (1989b) on the bonding properties of UPd<sub>3</sub> lead to some hope that this might be realized. In fact, Eriksson et al. (1990a) have shown that a better description of the  $\alpha$ - $\gamma$  phase transition in cerium is obtained when Hund's second rule (maximal  $L$ ) effects are incorporated in an LSD calculation. In particular, these effects must be included to obtain a proper description of the orbital component of the moment. This theory is based on open-shell Hartree-Fock theory, and assumes a maximal projection of the moment along the quantization axis. This condition is often violated for  $f^2$  systems, where the ground state is usually a singlet. Thus there is a need to develop a similar theory for  $f^2$  systems, which hopefully will give some insight into this crossover effect. Perhaps the most interesting point, though, is that despite this huge difference (localized  $f$  versus itinerant  $f$ ), there are intriguing similarities between these two metals. As emphasized by Wulff et al. (1988), similar spin fluctuation theories describe the mass renormalizations observed in both metals. Second, it is quite surprising that the low-temperature "magnetic" anomalies are similar: they occur at the same  $q$  vector, they happen at the same temperature, they appear both to involve weak moments. They differ only in that there are huge signatures of the transition in thermodynamic properties for UPd<sub>3</sub>, but only small ones for UPt<sub>3</sub>. This could be connected to the fact that in UPd<sub>3</sub> there are sharp crystal field levels, thus any kind of low-temperature collective transition which causes small changes in the energy levels will lead to large changes in the thermodynamics (Ott et al. 1980). In contrast, for UPt<sub>3</sub>, the crystal field levels are smeared out into dispersive energy bands, which acts to quench the anomalies in the thermodynamics. In conclusion, the authors believe that understanding the similarities and differences between UPt<sub>3</sub> and UPd<sub>3</sub> will go a long way in unraveling the mysteries of the heavy-fermion phenomenon. Although many experiments have been conducted in UPt<sub>3</sub>, much fewer exist for UPd<sub>3</sub>, so we encourage experimentalist to devote more attention to this fascinating metal.

A metal related to UPd<sub>3</sub> is dhcp Pr, where neutron scattering data again reveal the presence of sharp crystal fields levels with many similarities to UPd<sub>3</sub> (Houmann et al. 1979). Extensive dHvA data are available (Irvine et al. 1978, Wulff et al. 1988), with the data in good agreement with band calculations which treat the  $f$  electrons as core states. The mass renormalization factor is about 6 at zero field, and is strongly quenched for fields in the basal plane, with a value of 3 at 8 T. Fields along the  $c$  axis have no effect on the mass. These results can be qualitatively explained by the theory of Fulde and Jensen (1983). The origin of the mass renormalization is the interaction of the conduction electron states with virtual  $f$  crystal field excitations, as mentioned above for UPd<sub>3</sub>. The anisotropy of the mass is related to the fact that the fluctuating moments in Pr are confined to the basal plane.

We have performed paramagnetic band calculations on Pr in the observed dhcp structure which treats the  $f$  electrons as band states, and predict a strong magnetic instability, consistent with  $f$  electron localization (this calculation was extremely difficult to converge because of the narrowness of the  $f$  bands). Magnetic band calculations by Eriksson et al. (1990a) including Hund's second rule effects give a saturated spin and orbital moment, consistent with localization. Since Pr has a singlet

ground state, it will be necessary to develop the Hund's rule corrections in a crystal field basis to obtain a proper description of the localized ground state observed in this metal.

### 3.3. *Gd*

Gadolinium is not only one of the few elemental ferromagnets but is one of the conceptually simplest in that it has a half-filled *f* shell and thus a spherical *f* manifold minimizing orbital effects. De Haas–van Alphen measurements were initially made by Young et al. (1973) and later extended by Schirber et al. (1976), Young et al. (1976), Mattocks and Young (1977) and Sondhelm and Young (1985). Correlating with magnetoresistance measurements verified the multiply connected Fermi surface of the minority carriers in the basal plane. Positron annihilation measurements (Hoffmann et al. 1982, Waspe and West 1982) reinforced the picture of the Fermi surface. The initial interpretation obtained for the Fermi surface was effected by applying a phenomenological spin-splitting to non-self-consistent unpolarized relativistic bands. It was found that the applied spin splitting needed to vary by about 15% across the Brillouin zone for this scheme to be brought into line with the experimental data. Nonetheless, it provided an adequate basis to identify the origin of the orbits observed. These were:

- (1) Band 3 majority carrier holes with masses  $\sim 1.2$  in a tube-like Fermi surface along the *c* axis at the zone center. This surface around  $\Gamma$  bulges out to be almost spherical in shape with large necks going up the *c* axis.
- (2) Band 4 majority carrier holes with higher masses (2–3) in a larger tube-like structure along the *c* axis at the zone center. This surface has a waist at  $k_z = 0$  and necks down more sharply at the top and bottom zone face.
- (3) Band 3 minority carriers forming a ring-like structure made up of balls centered at the center of the faces (M points) which intersect at the edges (K points). The one mass determined on this sheet was 2.3.

This model can explain all the larger observed orbits. However, there are numerous smaller orbits observed none of which represent closed surfaces. These are not present in the simple model and are the touchstone for further insight. Using this adjusted paramagnetic model, it was estimated (Sondhelm and Young 1985) that the mass enhancement was of the order of 1.7–2.0, consistent with an electron–phonon enhancement of 0.14 plus the calculated electron–magnon enhancement of 0.75 (Fulde and Jensen 1983).

The standard picture of the rare earths is that the 4*f* manifold forms a strongly correlated atomic like shell that weakly interacts with the transition-metal-like conduction electrons. For *Gd*, this model is clearly a reasonable starting point in light of the success achieved using it to interpret the experimental data. The underlying transition-metal-like band structures initially determined non-self-consistently using the overlapping charge density model (Dimmock and Freeman 1964, Keeton and Loucks 1966, Harmon and Freeman 1974) have proven very robust. For the majority

carriers, the f bands occur 4–5 eV below the Fermi energy when the f states are treated as bands so the difference between the standard rare earth model and the incorporation of the f states as f bands has little effect at the Fermi surface for them. Thus, most calculations agree on the nature of the majority carrier bands and what differences are observed for them are quite small.

The situation is quite the opposite as regards the minority carriers. The minority f orbitals, which should be unoccupied, lie just above the Fermi energy. The large band 3 sheet is roughly right but the situation is not yet in order for the small minority carrier orbits. There are a number of effects which are all significant here:

- (1) The applicability of the local spin density exchange–correlation functional. This is of very great concern for localized f orbitals. Harmon (1979) noted that the calculated minority f character in Gd was falling too low in energy and it does appear that there is too much minority f occupation in all subsequent calculations.
- (2) The proper treatment of spin polarization effects in conjunction with spin–orbit coupling. As the heaviest simple ferromagnet, Gd has become a prime testing ground for this (Ackerman et al. 1984, Sticht and Kübler 1985a, Krutzen and Springelkamp 1989, Temmerman and Sterne 1990).
- (3) The coupling to the 5p orbitals modifies the behavior of the 4f's. These high-lying p orbitals are often referred to as semi-core since they are not quite atomic-like in character having bandwidths of several eV. The coupling is especially severe for the rare earths as the principal maxima of the 4f and 5p very nearly correspond (similarly for the actinides). Unfortunately, the frozen core approximation is a frequent approximation. Temmerman and Sterne found that relaxing the 5p states reduced the calculated lattice constant by 7% and brought the minority f levels 0.1 eV *closer* to the Fermi level – the wrong direction.
- (4) Shape approximations limit the precision of the calculations whether they be the muffin-tin or the atomic-sphere approximations. The minority f character induced at the Fermi energy is not spherically symmetric and will be influenced by these shape approximations, as discussed by Harmon and Freeman (1974). The non-spherical potential terms, not incorporated by Temmerman and Sterne, could significantly modify the interaction of the 5p and 4f orbitals.

The telling issue for the first item is that all calculations yield a density of states larger than the effective density of states of  $21.35(\text{Ry at.})^{-1}$  derived from the specific heat coefficient  $\gamma$ . There is no room in the results for any mass enhancement ( $\lambda = 1 + \lambda_{\text{ep}} + \lambda_{\text{em}} \sim 1.7\text{--}2$ ) as discussed by Sondhelm and Young (1985). Any appeal to many-body effects should require the band density of states to be smaller: it would be extremely difficult to contrive that the many-body effects decrease the effective density of states. The phenomenological application of the standard rare earth model does get this feature correctly (although it does have other deficiencies) because it precludes minority f involvement at the Fermi surface. Despite this, the standard rare earth model would appear to imply a strongly varying mass enhancement within each of the Fermi surface sheets. A general trend observed in transition metal studies is that there should be a milder variation of enhancement within a given sheet with

the major variation being instead from sheet to sheet. Thus while not demanded by theory and perhaps not a valid detraction, the implied mass variation does go against the trend, which might indicate that the underlying band masses are not correct.

Based on the observation that the calculated magnetisation ( $7.55\text{--}7.57\mu_B$ ) would correspond to roughly  $\frac{2}{3}$  the requisite energy splittings necessary to describe the Fermi surface (Schirber et al. 1976), considerable interest has been paid to the  $g$  factor. Sticht and Kübler (1985a) argued on the basis of their  $g$  factor results that one must use an itinerant representation for the  $f$  states (the  $g$  factor from their local  $f$  calculation being too high). But Richter and Eschrig (1989) showed the large polarization of the valence electrons found in the local  $f$  calculation of Sticht and Kübler to be an artifact. They then argued that the local  $f$  picture should not be so easily abandoned because their local  $f$  calculation did in fact give a lower value for the  $g$  factor. Finally, Krutzen and Springelkamp (1989) showed that the spin-orbit interactions lowered the  $g$  value for the itinerant  $f$  model to a value very close to that of the local  $f$  model. At this stage, one has to conclude that on the basis of the  $g$  factor the two models are indistinguishable within the current experimental error.

The recent calculation by Singh (1991b) significantly improves the situation. The calculation is based on a full potential technique so the shape approximation limitations are removed. Techniques thoroughly tested on La (Singh 1991a) were used to incorporate the  $5p$  states as band states such that they could relax, distort, and interact with the  $4f$  states as might be appropriate. The calculations were performed using a scalar relativistic formulation with the spin-orbit coupling included in a second variational step throughout the SCF procedure, i.e. the solutions of the scalar relativistic approximation were used to form the basis states for a variational solution of the Hamiltonian incorporating spin-orbit coupling. This approach should be sufficiently accurate for Gd if an adequate number of bands were included in the second variation. The resulting band structure still suffered from having too great a density of states at the Fermi energy [ $27.1 (\text{Ry at.})^{-1}$ ] but did clearly demonstrate the necessity of having  $f$  character in the bands to get the small (minority) Fermi surface orbits. Two important conclusions can thus be drawn: (1) for this heavy rare earth, it is important to include coupling to the minority  $f$  character – perhaps even via incorporation as  $f$  bands, and (2) the exchange-correlation functional is permitting undue occupation of minority  $f$  states.

Two things would greatly enhance our understanding of Gd. The measurement of masses for more orbits would position us to probe the nature of the enhancements – which will eventually be the exciting problem in Gd. On the other hand, further band studies are still needed. It would appear that Singh has brought the computational uncertainty down to where one must consider what modifications are required to the basic functionals employed. One can understand the situation by noting that a forced upward shift of the  $f$  states, as used for a number of La compounds, would improve the calculated result. That same effect would be accomplished by simply weakening the exchange-correlation functional or increasing the strength of the spin splitting; both of which would be interpreted as *decreased* correlation. These, however, are very ad hoc approaches. Several more fundamentally grounded approaches would all have the same effect of pulling the minority  $f$  states up from

the Fermi surface: self-interaction corrections; nonlocal or gradient corrections; and orbital (Hund's rule) interactions.

### 3.4. *NaCl structured materials*

Rock-salt structured materials are viewed as the classic ionic materials. Indeed, rare earths and actinides as the cation generally form rock-salt materials with carbon, a pnictide, or a chalcogenide as the anion. Combining a formally trivalent rare earth ion with a pnictide, then the nominal anion p bands will lie below the Fermi level with the cation d bands just above. With such a formal charge balance, the Fermi level will lie in a gap, producing a semiconductor unless the cation d bands and anion p bands overlap – which they often do at the X point (the 100 zone face). There is at most minimal overlap for nitrogen yielding a semiconductor for GdN but increasing overlap for the progressively heavier anions (Hasegawa 1980, Hasegawa and Yanase 1977, Hulliger 1979). Replacing the pnictide by a chalcogenide or the trivalent rare earth by a more ionic element, the Fermi level moves up into the cation d bands. While it gives a reasonable picture, it should be recognized that the formal ionic picture is not the whole story. Because the rock-salt structure consists of two interpenetrating fcc lattices displaced by a half lattice constant along the cube edge, the ionic separation is actually quite close in these materials and there is significant covalency such that the nominal p bands below the Fermi level are not “pure” and much less than three electrons are transferred between the ions.

The f states are to be placed into this basic background. Because they reside on the cation, the local positive ionic character causes the f orbital to be contracted. Thus, the f states are far more likely to exhibit magnetic behavior in these materials and those properties have been extensively studied by neutron scattering. Indeed, the magnetic structure has been of considerable interest for the pnictides, the chalcogenides, and their pseudobinaries of both the lanthanides and the actinides (see the article by G. Lander in this volume). The f electron coupling with the conduction bands is weak. However, it should be noted that the anion ligands are located out along the (100) directions which is the directional sense of the  $T_{1u}(\Gamma_{15})$  orbitals and this f orbital subset can have a larger coupling with the p orbitals – which are also (100) directed. Wavefunction mixing (orthogonalization and hybridization) effects appear to be strongest with the lighter anions and grow weaker as one moves down the periodic table to the heavier anions. The rare earth or actinide separation is sufficiently large that f–f overlap can be ignored.

A serious experimental complication for the light-anion materials is that they are rarely stoichiometric: a sample is almost always anion deficient. Thus it is difficult to obtain good studies of Fermi-surface-related properties because of sample limitations. It is for this reason that CeN and UN are not discussed here in spite of the fact that they are fascinating mixed-valent (CeN) or reduced-moment (UN) materials.

#### 3.4.1. *Ce pnictides: especially CeSb*

The Ce pnictides have been extensively studied for their magnetic properties and for the systematic variations in the two f peaks observed in photoemission. Because one

would like to follow the effects of progressively weaker  $f$  orbital interactions for the heavier pnictides, it would be very desirable to have Fermi surface data for the series as well. Alas, dHvA data exists only for the heaviest pnictides CeSb and CeBi (Kitazawa et al. 1988, 1984, Aoki et al. 1985a, b). The data, however, is quite complete and has generated much theoretical interest. Focussing on CeSb, the material has a rich magnetic phase diagram (as does CeBi). The zero-field magnetic structure consists of ferromagnetically ordered (100) sheets stacked antiferromagnetically in a complex repeat pattern. With increased field, the repeat pattern becomes simpler before flipping to a complete ferromagnetic ordering. dHvA data is available for several upper field phases but thus far only discussed theoretically for the ferromagnetic phase. A most noteworthy aspect of the experimental data is the marked deviation from cubic symmetry which can be understood very simply in terms of the lowered symmetry of the magnetic system. Neutron scattering data reveals that the occupied  $f$  orbital is in a  $j = \frac{5}{2}$ ,  $\mu = \frac{5}{2}$  state and strongly pinned along a (100) direction by the anisotropy. Thus, its interaction with the conduction bands lowers their symmetry to tetragonal. Because the moment flops to the (100) crystal direction nearest the field direction, it is not possible to observe the entire Fermi surface with dHvA.

The interesting issue is the nature of the  $f$  orbital conduction electron interaction. Two models have been proposed. Kasuya and co-workers (Takahashi and Kasuya 1985, Sakai et al. 1985) have focussed on the interaction of the  $f$  orbital with the Sb  $p$  states in a  $p$ - $f$  mixing model. Norman and Koelling (1986b) have suggested a standard rare earth ( $f$  core) model where the interaction with the conduction electrons is instead through Coulomb and exchange effects. Of course, both effects are present but one is interested in which is the dominant.

The standard rare earth model is simpler so we consider it first. Several factors suggest that a standard rare earth picture neglecting  $p$ - $f$  mixing could be a reasonable one. (1) Because one is dealing with the heavier pnictide, the  $p$ - $f$  mixing has decreased considerably over that of the lighter pnictides. (2) The observation that the  $f$  orbital is a  $j = \frac{5}{2}$ ,  $\mu = \frac{5}{2}$  state indicates weak hybridization; hybridization normally mixes  $j = \frac{5}{2}$  and  $j = \frac{7}{2}$  orbitals as well as different  $\mu$  states.

The standard rare earth model can be implemented within a modified density functional theory where the  $f$  orbital is treated as atomic-like with a particular  $j, \mu$  state integrally occupied. One then considers the effects of the aspherical charge and spin density arising from this oriented  $f$  orbital coupling on the conduction electrons through the direct Coulomb and exchange (evaluated within LSD) interactions. The calculation actually performed was somewhat crude compared to current standards, but clearly indicated that the symmetry lowering due to the oriented  $f$  moment could explain the dHvA data available at the time. Quantitative agreement was not expected because the effect of the asphericity on the conduction states was not treated self-consistently, no attempt was made to correct for the known deficiencies of the LDA for the lanthanum pnictides, and no attempt was made to improve on the LSD exchange coupling which is suspect in this case. Now first consider the LaSb Fermi surface (Hasegawa 1980, 1985, Norman and Koelling 1986b). The La  $d$  band dips below the top of the Sb  $p$  band around the X point giving a pocket of  $d$  character there (by symmetry, there are three inequivalent surfaces). This must be compensated

for through the deoccupation of p character around  $\Gamma$ . Because the top of the p bands at  $\Gamma$  is a doubly degenerate  $\Gamma_8$  (not counting spin doubling), there are actually two hole surfaces there. The electron ellipses at X are found to be too elongated in the calculation. This can be repaired by artificially shifting the La d character up relative to the Sb p character (this might be compensating for either an error in LDA that places d states too low relative to sp states, or one due to the ionic character of the material). This shift helps to properly reduce the size of the electron, and thereby the compensating hole, surfaces. Returning to CeSb, its Fermi surface is similar to that of LaSb, except that the f core calculations predict three hole surfaces around  $\Gamma$  instead of just two found for LaSb (see fig. 20a). These three hole surfaces plus the electron ellipses at X have a one-to-one correspondence with the (then available) experimental dHvA data. The coupling to the oriented f orbital acts to shrink the size of the electron ellipse at the X point along the moment (field) direction relative to the two ellipses at the perpendicular X points, which is what is seen experimentally. The model also implies that the exchange splitting of all surfaces must be quite small.

The issue of how much the f orbitals do actually couple to the conduction electrons through direct orbital mixing still remains. The p-f mixing model introduced by Kasuya and co-workers (Takahashi and Kasuya 1985, Kasuya et al. 1987, 1988, Sakai et al. 1984) focuses on the effect of hybridization between the oriented f orbital and the p bands. They have explored the effect of this interaction using a Slater-Koster LCAO parameterization adjusted to a combination of band calculation results and experiment. Wills and Cooper (1987) have explored the same model by attempting

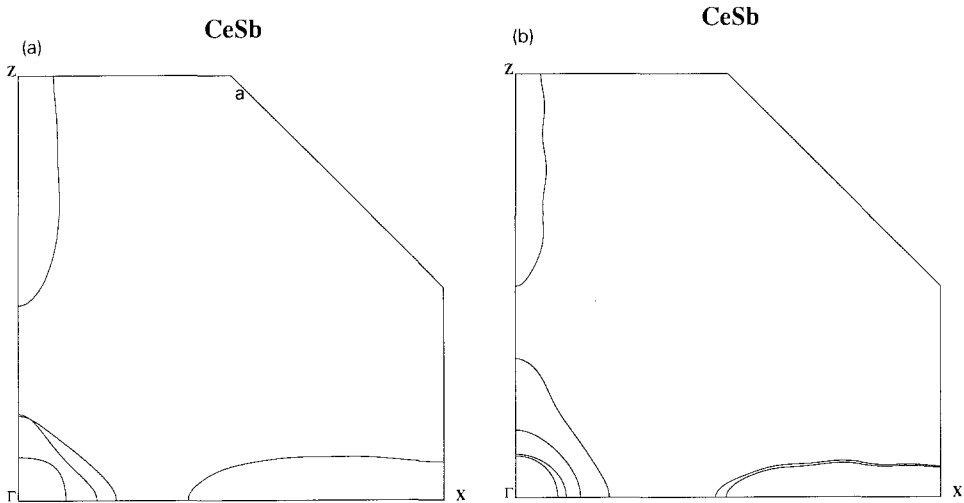


Fig. 20. Fermi surface of CeSb from (a) the f core model of Norman and Koelling (1986b) (only one set of the spin-split surfaces is shown) and (b) an f band model where the  $j = 5/2, \mu = 5/2$  f state was shifted down 2 eV and the other f states shifted up 4 eV (similar to the model of Kasuya and co-workers described in the text). In (b) energy shifts of the bands were done to match dHvA data. The resulting Fermi surface satisfies electron-hole compensation, which is strong support for this model.

to directly calculate the requisite parameters; it is worth noting that they find the model to properly determine the anomalous crystal fields splitting for all the Ce pnictides but that the dominant effect is hybridization with the d bands (Wills et al. 1985). Since both groups utilize an orthogonalized basis, their model deals strictly with hybridization effects and not orthogonalization. On considering the Fermi surface properties, it should be noted that a d-f exchange is also introduced into the Kasuya et al. p-f mixing model and that it does have a major effect on the Fermi surface (Sakai et al. 1985) – actually being the mechanism in the model responsible for the cubic-symmetry-breaking anisotropy of the X-centered ellipses discussed above.

The  $\Gamma$ -centered Fermi surfaces predicted by the p-f mixing model can be understood by taking the four bands considered above in the rare earth model, splitting them due to exchange effects, and then allowing them to hybridize with a  $j = \frac{5}{2}$ ,  $\mu = \frac{5}{2}$  f state (see fig. 20b). Of the six surfaces at  $\Gamma$ , two get pushed below the Fermi energy, three form the same surfaces as predicted in the rare earth model, and the last one forms a large surface which is extended along the moment direction. Of the now two electron ellipsoids at each of the X points, one of the two at the X point along the moment direction gets pushed above the Fermi energy with the other one shrinking in size (as seen in the dHvA data), whereas the other two ellipses at the perpendicular X points remain nearly degenerate (there is some experimental evidence for a weak spin splitting of the X ellipsoids). To obtain this Fermi surface, the unhybridized energy of the f orbital must be below the uppermost Sb p band. The LCAO parametrized from (Kasuya et al. 1988, Sakai et al. 1984) achieves this by shifting the energy of the single occupied f orbital down to the position about 2 eV below the Fermi energy as appropriate for an Anderson Hamiltonian treatment. This energy is approximately the bare f energy for the deeper photoemission f peak (Sakai et al. 1985). DFT-LDA on the other hand must place the f level at or above the Fermi energy and so cannot represent this effect on the Fermi surface. [However, this excitation energy can be obtained in DFT by performing a transition state calculation (Wills and Cooper 1987, Norman et al. 1985).] The p-f mixing model then places the remaining unoccupied f levels at an energy higher by the Coulomb energy of  $U = 6$  eV.

Both the placement and the symmetry of this single occupied f level are significant. The symmetry – which is taken from the neutron scattering data – dictates that only a single Sb p band along the direction of the moment will hybridize strongly with the f orbital. The bare f energy being placed below the upper Sb p bands enables the repulsion of the mixing to push that one band which admixes further up in energy. This results in the large distorted Fermi surface piece at  $\Gamma$  as opposed to a smaller, more spherical surface found in the rare earth model. This large Fermi surface will have significant f admixture and thus can be expected to have a significantly increased mass. The critical experiment is the observation of this predicted high-mass surface along the moment direction, a difficult experimental task since there are many harmonics in that frequency regime. Thus the first report of dHvA frequencies of that orbit (Kitazawa et al. 1988) near (001) were questioned as possible harmonics. However, a re-examination of their original data by Aoki et al. (1991) revealed a large area orbit consistent with the predictions of the p-f hybridization model. If that



interpretation stands and the masses are determined to be high for that frequency branch, then not only is a significant p–f interaction established – which in itself is not so surprising – but also the necessity of a bare f energy level below the top of the p bands and the unoccupied f energy levels well above. While that bare f position is consistent within an Anderson Hamiltonian framework, it is a strong indication of a failure of an LDA treatment for CeSb. Of course, the p–f model is easily incorporated in a band structure calculation by artificially adjusting the positions of the (assumed) occupied f energy and the unoccupied f energies in the secular matrix. This still does not tell us why a particular f orbital is occupied. A Hund’s second rule correction modified by strong spin–orbit effects would tend to give an occupied state of maximal  $\mu$ , as observed in CeSb, and a self-interaction correction would provide the splitting of the occupied and unoccupied states. Such a theory is currently being worked on by the authors, and it is hoped that its implementation in a band calculation will yield similar results to those of the phenomenological p–f mixing model.

### 3.4.2. *ThC and UC*

From a formal valence analysis, one would expect a  $\text{Th}^{4+}\text{C}^{4-}$  such that one comes to the same semi-metal situation discussed in the introduction for this crystal structure. This would appear to be the case although there is a large Th d and C p band overlap at the X point (Hasegawa and Yamagami 1990). The resultant Fermi surface consists of a C p-derived hole sheet centered at X corresponding to 0.062 holes and a compensating electron piece just over half way out along  $\Delta$  derived from strongly admixed Th d–C p character. (The individual hole surfaces at X must be twice the volume the electron surfaces at  $\Delta$  in order to compensate for the fact there are half as many inequivalent surfaces.) The density of states at the Fermi energy is found to be 15 states/(Ryd. cell) corresponding to  $\gamma = 2.6 \text{ mJ/mol K}^2$  which falls between the measured values (see review by Fournier and Troč 1985). Assuming the larger experimental value (2.9) to be correct, one sees that the mass enhancements must be small. If the smaller experimental value were instead to be correct, then one must look to improvements in the calculation but it would still be indicative of a small mass enhancement.

It is most astonishing that a de Haas–van Alphen quality sample of UC has been made although its resistivity ratio is only 38. The resistivity exhibits an excellent  $T^2$  behavior up to about 160 K where it begins to vary more slowly. dHvA measurements have been performed (Onuki et al. 1990c,d). They find an X-centered hole pocket similar to that of ThC but now with an electron surface tentatively identified with the W-centered electron pockets of Hasegawa and Yamagami (1990). The predominantly C p-derived X-centered hole pocket is well established: it is extremely robust in the calculations and enough of it is seen experimentally to be certain of its symmetry position. The W-centered piece is much less clearly seen experimentally and, while certain to be present in the calculated results, is strongly influenced by the possible presence of another hole pocket at L. Hasegawa and Yamagami note this possibility and Koelling (unpublished) has found this additional L-centered hole piece to be present. The W-centered piece is strongly Uf in character weakly

hybridizing with the Cp states. The  $\Delta$ -centered electron surface of ThC has been eliminated by a combination of the greater Ud–Cp band overlap and the presence of the occupied Uf band. The calculated density of states yields a  $\gamma$  of 4.8 mJ/mol K<sup>2</sup> representing a mass enhancement factor of four.

Because the crystal structure is so simple and thus amenable to analysis, further experimental advances will be seized as a great opportunity by the theorists. The occupied band structure does indeed appear to be a modified version of the ThC band structure with an additional Uf band present. The occupied band gives an f count of slightly less than two electrons and the W electron pockets are negligible in this counting being about 0.068 electrons. The total f count in UC is about 2.25 so the remaining f character is through admixture into the occupied Ud and mostly Cp bands. This should be noted in light of the interest in the p–f mixing and its effects.

### 3.4.3. *TmSe, TmTe, SmS*

TmSe is a classic mixed-valent metal. It has a large  $\gamma$  value of 350 mJ/mol K<sup>2</sup> in its paramagnetic phase (Berton et al. 1981). Below 3.2 K, it orders in a type-I antiferromagnetic structure with a moment of 1.7 $\mu_B$  (Moller et al. 1977). In the AF phase, an upper bound to the specific heat coefficient of 50 mJ/mol K<sup>2</sup> has been estimated (Berton et al. 1981). There are strong indications from resistivity measurements that stoichiometric AF TmSe is insulating (Haen et al. 1979), although the largest observed increase in resistivity is about a factor of ten. Doping with Te leads first to a miscibility gap, then to an insulator (Boppart 1985). TmTe is a type-II AF with a moment of 2.3 $\mu_B$ , consistent with a localized  $\Gamma_8$  ground state (Lassailly et al. 1983), with an estimated energy gap of 300 meV (Boppart 1985).

Band structure calculations in the paramagnetic phase using a full potential LAPW method on TmSe have been reported by Jansen et al. (1985). LDA gives the correct lattice constant for TmSe – somewhat surprising since for lanthanides, treating the f electrons as itinerant leads to an overestimation of f bonding, with the lattice constants typically being underestimated by 5% [for reviews, see Norman and Koelling (1987), Freeman et al. (1987), Norman and Freeman (1989) and Johansson and Brooks in this volume]. The LDA bulk modulus is a factor of two too large, although much better agreement is found at higher pressures (Jansen et al. 1986). The LDA bulk modulus can be significantly improved by shifting the f levels 40 mRy downwards. Such shifts are expected since the LDA is known to put the energies of higher angular momentum states incorrectly relative to lower angular momentum ones [in Nb, shifts of the d levels of the order of 20 mRy are needed (Koelling 1984)]. The band calculations also give a good picture of the integer-valent to mixed-valent transition as due to a closing of a gap between the f band and conduction d band, with the Se p bands playing an important role.

Paramagnetic and magnetic band calculations in the observed type-I AF phase including spin–orbit coupling have been performed by Norman and Jansen (1988). In the paramagnetic phase, a large  $\gamma$  value of 76 mJ/mol K<sup>2</sup> is found, giving a mass renormalization factor of 4.6, comparable to that of CeSn<sub>3</sub>. In the AF phase, a pseudo-gap is formed with an 86% reduction of the DOS at the Fermi energy. This is the same reduction found experimentally if the upper bound of 50 mJ/mol K<sup>2</sup> in

the AF phase is used, although it is likely that stoichiometric TmSe is insulating. The magnetic moment found is  $4.1\mu_B$  (3.0 orbital, 1.1 spin). This is consistent with one local f hole. Since the experimental moment of  $1.7\mu_B$  is comparable to that of TmTe, which is in a  $\Gamma_8$  ground state (one local f hole), the conclusion is that crystal field effects are quenching the orbital moment. This could be invoked in the band structure calculations by incorporating Hund's second rule effects in a polarized crystal field basis, analogous to what has been done for FeO and CoO (Norman 1991b).

For TmTe, a large  $\gamma$  value is found if the f electrons are treated as itinerant states (Norman and Jansen 1988) and the predicted lattice constant is 4% too small (Monnier et al. 1985). Conversely, treating the f electrons as core states produces an insulating gap of 450 meV, consistent with experiment.

Another classic mixed-valent material is SmS. At zero pressure, the compound is insulating (not associated with a magnetic transition as in TmSe), but for pressures above 6.5 kbar, mixed-valent phase occurs with a 5% decrease in lattice constant (Jayaraman et al. 1970, Keller et al. 1979). In the mixed-valent phase, a  $\gamma$  value of 145 mJ/mol K<sup>2</sup> has been determined (Bader et al. 1973). Relativistic band structure calculations have been reported by Strange (1984) and by Lu et al. (1988). Strange finds an insulating gap both at volumes above the experimental (insulating) volume and at volumes reduced to 0.85 or less while metallic behavior occurs for volume ratios 0.9–1.0. This could be a potential explanation of the transition (the predicted volumes would be too large by at least 5%), but would imply another insulating phase at higher pressure. Lu et al., though, find metallic behavior at 0.78 and 1.0 times the experimental volume, although the DOS at 0.78 is quite small ( $\sim 0.8$  mJ/mol K<sup>2</sup>). Moreover, their total-energy calculations give an equilibrium lattice constant which is 8% less than the insulating phase (3% less than the zero pressure projected value of the mixed-valent phase). In spite of this observed sensitivity, the most likely conclusion is that LDA does a poor job for the electronic structure of SmS.

The incorporation of Hund's second rule effects (using either a crystal field or polarized crystal field basis) probably will yield significant improvements over the LDA results for both TmSe and SmS. A large improvement was found in the description of the  $\alpha$ - $\gamma$  phase transition in Ce metal when such effects were incorporated (Eriksson et al. 1990a). Calculations in progress on SmS by Eriksson et al. (unpublished) show a change in f count near the experimental insulating volume, which would be indicative of a mixed valent to insulating phase transition.

### 3.5. *LaNi*, *CeNi*

CeNi (orthorhombic CrB structure) has an electronic specific heat coefficient of 85 mJ/mol K<sup>2</sup> (Isikawa et al. 1987), about 20% larger than that of CeSn<sub>3</sub>. dHvA and magnetoresistance data on both LaNi (Maezawa et al. 1989) and CeNi (Onuki et al. 1989b) have recently been taken, with band structure calculations being done by Yamagami and Hasegawa (1991b) for comparison's sake (f band for CeNi). Both LaNi and CeNi are predicted to have a complicated two-sheet Fermi surface, but the

sheets are quite different between the two cases. The resulting topologies in both cases are consistent with both the dHvA and magnetoresistance data, thus making CeNi analogous to CeSn<sub>3</sub>. The comparison is not complete for CeNi, since most of the observed data are confined to fields in the vicinity of the *b* axis. An average mass renormalization factor of 3.1 can be extracted by comparing band masses to dHvA masses (for a field along the *b* axis). This should be contrasted with the factor of six inferred from the specific heat data. The simplest explanation for this discrepancy is that the mass is field dependent. A directional dependence to the field variation of the mass (as seen for orthorhombic CeCu<sub>6</sub>) may also be responsible for the lack of many signals for fields away from the *b* axis. This, of course, can only be confirmed by field-dependent specific-heat measurements.

### 3.6. C15 cubic Laves phases

In the AB<sub>2</sub> Laves phase materials, it is possible to sort out the effects of the two sublattices. In this structure, the B atoms form interconnecting chains of tetrahedra with a quite close near-neighbor distance. The A atoms are arranged on an interpenetrating diamond lattice which have only B atoms as nearest neighbors. For a sphere radius ratio of  $R_A/R_B = 1.225$ , spheres on the A sites will just touch those on the B sites. The B sublattice thus serves as a caging backbone for the A atoms and the A atoms accommodate to the B sublattice. Rare earth and actinides occupy these materials as A atoms. When the B atom sublattice is constructed from a transition metal, the choice of transition metal B atom will determine whether the A atom must be compressed or expanded to fit onto the lattice. In the extensively studied case of the dialuminides, the rare earth or actinide is in an oversized hole. The magnetic behavior of those materials exhibiting moments has been extensively studied (see the article by Johansson and Brooks in this volume). Such calculations require careful consideration of all the effects that usually can be neglected in the lighter magnetic systems: relativistic effects, spin-orbit induced orbital effects, and orbital polarization all must be considered to sort out the magnetic behavior.

There are no direct Fermi surface studies of the transition metal Laves phases – which is unfortunate in light of the part they have played, and continue to play, in our understanding of *f* electron behavior. The Np Laves phases have played a special role because they appear to span the critical separation between localized and itinerant behavior (Aldred et al. 1974). The U and Ce-transition metal Laves phases occur on the itinerant side of the Hill (1970) plots, but some do approach, and just cross, the critical separation. The transition to magnetic behavior can be very closely approached by considering NpRu<sub>x</sub>Os<sub>2-x</sub> alloys (Aldred et al. 1975). Because their properties are consistent with the Hill correlation, it would initially appear that one has a nice simple picture based on a direct *f*-*f* overlap analysis. Certainly, a Hill plot analysis was part of the motivation for the extensive studies of the Np materials. However, it appears that these materials heavily involve interaction with the ligands.

The first aspect eroding the direct *f*-*f* interaction picture is that the transition metal *d* orbitals are found to hybridize strongly with the *f* orbitals. Eriksson et al. (1989c,

1990b) have effectively demonstrated this for the actinides using an LMTO formalism. And it quite clearly also holds for the Ce compounds (Eriksson et al. 1988b, Koelling 1986). In fact, to probe precisely that property, CeRu<sub>2</sub> has been calculated with a fictitious f repulsion of 25 Ry which only reduced the f count on the Ce by half. Similarly, in the thorium compounds, where one would expect very little f orbital contribution, ThRu<sub>2</sub> exhibits an induced f character of half an electron within a muffin-tin sphere (Koelling, unpublished) and ThIr<sub>2</sub> has 0.8 f electron within a (larger) atomic sphere (Eriksson et al. 1989c).

The magneto-strictive properties of the rare earth Fe<sub>2</sub> materials – which are driven by the Fe – have caused them to receive a great deal of attention. The actinide-Fe<sub>2</sub> materials have been analysed theoretically and found to also involve significant f-d hybridization (Eriksson et al. 1990b). The magnetism reflects profoundly the significance of this f-d hybridization. In both the lanthanide CeFe<sub>2</sub> (Eriksson et al. 1988b) and actinides UFe<sub>2</sub> and PuFe<sub>2</sub>, the f spin moment is found to be antiparallel to the Fe moment. This can be understood by noting the significance of the extensive work on Rh-Pt pseudobinaries: Pt offers a very nearly filled d shell which will suppress f-d orbital hybridization (in addition to a larger lattice spacing). So the addition of Pt will drive localized f behavior. The Rh-Pt alloy studies of Laves phases do indeed clearly exhibit a transition from mixed-valent to localized behavior for both Ce (Barberia et al. 1982) and Eu (Bauminger et al. 1974) Laves pseudobinaries. In the case of the Fe materials, the majority Fe d band is essentially filled and thus not available for hybridization while the minority d band is not filled and hybridizes effectively with the f states. Since this hybridization provides the major operative mechanism for the f orbital occupation, the f orbital spin will be aligned with the minority carriers. The confirming evidence for this observation is to be found in the partial densities of states. While the heavy lanthanides also have their f orbital spin moment aligned with the minority carriers, that occurs through a more indirect effect involving the lanthanide 5d states (Brooks et al. 1988).

That the situation is even more complex can be deduced from the fact that CeRu<sub>2</sub> and CeRh<sub>2</sub> have very nearly identical lattice constants: CeRu<sub>2</sub> is a famous 6.1 K superconductor [the basis of many alloy studies examining coexistence of superconductivity and magnetism which would appear to be of a spin-glass type (Roy and Coles 1990)]. CeRh<sub>2</sub> undergoes neither a superconducting nor a magnetic transition. Since they are both itinerant in nature, they are therefore not in conflict with the simple Hill analysis. But, because Rh has one more electron than Ru, simple ideas of d bonding or d-f bonding being modified through band filling cannot easily explain the equal lattice constant. They might be consistent with the superconducting properties if one claims the Rh d bands have been filled. Further, there is a hexagonal modification of the Laves phase (the C14 structure) which would appear to somewhat favor itineracy (Maple 1976, Raubschwalbe et al. 1984). Specifically, the rare earth Os<sub>2</sub> systems exist in either the cubic C15 or the hexagonal C14 structures. CeOs<sub>2</sub> is a 1.1 K superconductor in the C14 structure but does not undergo a superconducting transition in the C15 structure (Torikachvili et al. 1985).

The standard Hill-type analysis is further eroded by the detailed analysis of NpOs<sub>2</sub>, the material that might be interpreted as just-localized. NpOs<sub>2</sub> is instead found to

be an itinerant ferromagnet with a significant direct f–f interaction (Eriksson et al. 1990c). So the direct f–f interaction should not be casually disregarded even for this system on the “localized” side of a Hill plot. On the other hand, one can presume direct f–f interactions to be minimal in the Ce materials, in spite of the fact they occur far more into the itinerant side of the Hill plots, since the  $A_{2u}$  orbital – the requisite  $\langle 111 \rangle$  directed f orbital to achieve a sigma bond in the diamond sublattice – is found not to be occupied.

It is the dialuminides for which there is the most direct Fermi surface data amongst the Laves phase materials: dHvA measurements exist for  $CeAl_2$  (Lonzarich 1988, Springford and Reinders 1988, Reinders and Springford 1989). The primary reason for interest in the dialuminides is that one may expect that there will be no direct f–f interaction and that the hybridization interactions will also be very weak: lattice separations are well beyond the critical separation of the Hill plots and Al has no d orbitals to hybridize with the lanthanide or actinide f states. Consequently, heavy-lanthanide dialuminides have been studied as classic systems of crystal-field-split f states interacting through RKKY interactions.

The light lanthanides and light actinides, however, do exhibit weak hybridization effects.  $LaAl_2$  is a superconductor which, when very lightly doped with Ce, exhibits re-entrant behavior. In the process of studying this fascinating phenomena, it was shown that the system did not follow the classical Abrikosov–Gorkov theory for pair breaking by a local moment: the host had modified the Ce atomic moment.  $CeAl_2$  exists as a not-quite-commensurate antiferromagnet (Barbara et al. 1979) and is interpreted as exhibiting single ion Kondo behavior (Bredl et al. 1978). Band calculations (Jarlborg et al. 1986) have demonstrated the ferromagnetic state to be unstable and the antiferromagnetic state (for the commensurate  $q$  vector) to be stable with a spin-only moment  $0.88\mu_B$  quite comparable to the maximum moment ( $0.89\mu_B$ ) found in neutron measurements. The electronic specific heat coefficient of  $CeAl_2$  is quite large ( $45\text{ mJ/g at. K}^2$ ), a factor of nine larger than the band specific heat, which included the f states as band states. This is quite interesting since the Fermi surface topology in the metamagnetic state probed by the dHvA appears at first glance best represented by treating the f states as local (Reinders and Springford 1989). The question naturally arises then as to whether  $CeAl_2$  is a case similar to Pr but for a single f electron ion.

To consider the  $CeAl_2$  Fermi surface within a local-f model, one starts from the Fermi surface of  $LaAl_2$ . The Fermi surfaces of  $YAl_2$  and  $LaAl_2$  have been successfully studied (Hasegawa and Yanase 1980a, b, Jarlborg et al. 1986, Seitz 1978, Seitz et al. 1979). There being two formula units per unit cell, the Fermi energy should represent nine filled bands but a better first cut is to consider bands 9 and 10 each near half-filling – band 9 more so and band 10 less so. Band 10 produces a spherical-like electron surface centered about the zone center  $\Gamma$  but puckered out in the (100) directions toward X [the 3D drawings of Hasegawa and Yanase (1980a, b) are useful for visualization]. It is this closed surface which in  $CeAl_2$  appears as two large moment-split surfaces. Obtaining the existence of this surface by extrapolating from  $LaAl_2$  or from a paramagnetic  $CeAl_2$  band calculation (Guo 1990) is quite natural but the determination of the spin splitting is not. The masses on this surface are of

the order of 15 and so must involve significant interaction effects. The corresponding masses in  $\text{LaAl}_2$  are about 1.5 – ten times smaller. As for band 9, it might have been a comparable electron surface about  $\Gamma$  but, having greater occupation, expands out and contacts the Brillouin zone surface and so is better viewed as a multi-connected hole surface. One high frequency orbit in the vicinity of (111) remains of the electron surface character but the remaining orbits are all smaller neck-like frequencies.  $\text{CeAl}_2$  masses on this surface are of order 1.5 but are still enhanced, since the comparable  $\text{LaAl}_2$  masses are of order 0.2. The expected moment splitting is not as easy to pick out for this surface. One other feature is worthy of note. Along the (100) directions, the Fermi energy in  $\text{LaAl}_2$  cuts through an anti-crossing arising from the La d bands coming down to intersect the underlying Al bands.  $\text{YAl}_2$  is useful to consider at this point because its d states lie higher in energy so that the cross-over occurs above the Fermi energy and it is in the (100) directions that the two Fermi surfaces differ the most markedly being otherwise quite similar. It is this effect that gives rise to the puckering in the band 10 surface, to the magnetic breakdown effects (Lonzarich, unpublished), and to a sensitivity that well could prove the touchstone of this system.

The evidence is quite strong that the local-f model with band masses enhanced by coupling to virtual f crystal field excitations holds great promise for  $\text{CeAl}_2$ . But should one abandon the itinerant model? Dialuminides present an interesting situation when looked at as an aluminum backbone into which one places a transition metal (where there are numerous examples), a rare earth, or an actinide on an intertwined diamond lattice. The aluminum presents a set of standard bands onto which the remaining electronic structure is superimposed. As discussed above, the first effect is the presence of the new atom's d bands. Given this much, the gross features of the Fermi surface are fixed and this can be taken from band calculations. However, the magnetic interactions have not been properly modeled for the Fermi surface studies. Because there are two Ce atoms per unit cell, it would be possible to have one f band completely filled below the Fermi energy (although not easily in LDA). The remaining f bands would then be above the Fermi energy but hybridizing into the underlying band structure. Such a result would be quite helpful towards understanding the strong variations of the masses. Clearly, practical considerations involving our very limited knowledge of the magnetic interactions will make utilization of the local f model prudent but an itinerant f model for  $\text{CeAl}_2$  should not quite be buried yet.

Turning attention to the actinides, the sequence  $\text{UAl}_2$ – $\text{NpAl}_2$ – $\text{PuAl}_2$  is unusual in that  $\text{UAl}_2$  is a spin fluctuation system,  $\text{NpAl}_2$  is a ferromagnetic system, and  $\text{PuAl}_2$  is an antiferromagnetic spin fluctuating system: rather unusual behavior when compared to expectations based on actinide contraction. Band calculations (Boring et al. 1985) indicate significant actinide d–f hybridization, decreasing actinide d occupation across the series, and occupied f states of predominantly  $t_{2u}$  symmetry – not the  $A_{2u}$  symmetry one would expect for a direct f–f interaction. Eriksson et al. (1990d), analyzing  $\text{NpAl}_2$ , find a dominant orbital contribution ( $-4.5\mu_B$ ) to the moment opposing a large f orbital spin polarization ( $3.5\mu_B$ ). Their calculations are able to resolve the anomalous neutron form factor and differences between the magnetization-determined moment ( $1.2\mu_B$ ) and the neutron diffraction and Mössbauer moment ( $1.5\mu_B$ ) due to the conduction electron polarization (Aldred

et al. 1976) as they find a total Np moment of  $-1.3\mu_B$  with a conduction electron polarization of  $+0.3\mu_B$ . They conclude from their analysis of the calculations and the comparison with lattice constant and neutron form factor data that, although the f states primarily behave as localized, there however is still significant f orbital admixture into the band states. The dialuminides are truly unusual materials.

### 3.7. $UCu_5$

There are a number of f electron metals which exhibit the phenomenon of heavy-fermion magnetism. These metals are characterized by a large magnetic moment of the order of  $\mu_B$  and a large electronic specific heat coefficient (200–1000 mJ/mol K<sup>2</sup>). Despite the large value of the moment, this value is still significantly less than the free ion one. The most studied heavy electron magnets are  $U_2Zn_{17}$ ,  $UCd_{11}$  and  $UCu_5$ . The first two have extremely complicated crystal structures, and no band structure calculations exist at present.  $UCu_5$ , though, is in the simpler zincblende Laves phase, making magnetic calculations feasible.

$UCu_5$  antiferromagnetically orders with a  $q$  of  $\pi/a(1, 1, 1)$  at 15 K, with zero temperature moments reported of 0.9, 1.3 and  $1.55\mu_B$  (Murasik et al. 1974, Chakravarthy et al. 1985, Schenck et al. 1990). The sensitivity of the moment value is most likely due to the extreme dependence of physical properties of  $UCu_5$  on sample quality. The hump in the temperature dependence of the resistivity seen near the Néel transition is reminiscent of that seen in Cr (Ott et al. 1985b). The  $\gamma$  value is 560 mJ/mol K<sup>2</sup> in the paramagnetic phase and is reduced by 60% in the antiferromagnetic phase (Ott et al. 1985b). At a temperature of 1 K,  $UCu_5$  undergoes another (hysteretic) phase transition which reduces  $\gamma$  to 86 mJ/mol K<sup>2</sup>. This transition leads to a factor of seven increase in the resistivity. The 1 K transition is extremely sample dependent, and the transition temperature increases with field (Bruls et al. 1987, Onuki et al. 1988), similar to what is observed for the antiferroquadrupolar transition in  $CeB_6$ . At the transition, the susceptibility increases by 6% (Onuki et al. 1988), implying some change in the magnetic structure. The increase in the Hall coefficient by a factor of 50 below the transition (Onuki et al. 1988) indicates a substantial reduction of carriers. Recent NMR measurements by Nakamura et al. (1991) are consistent with an energy gap opening up ( $1/T_1$  decreases by a factor of 100 below the transition). Moreover, the NMR data are consistent with a change in the AF structure, possibly from a 4q to a 1q structure. An alternate interpretation based on  $\mu$ SR data is that an additional weak moment magnetic state, analogous to  $UPt_3$  and  $URu_2Si_2$ , is being induced (Schenck et al. 1990).

Band structure calculations both in the paramagnetic and AF structures have been done by our group including spin-orbit coupling (Norman et al. 1988b). In the paramagnetic phase, a large  $\gamma$  of 100 mJ/mol K<sup>2</sup> is found, surprising since the Fermi energy is in a minimum in the density of states (fig. 21a). Compared to specific heat, this indicates a mass renormalization factor of 5.6, comparable to that of  $CeSn_3$ . The moment-polarized calculations give a 70% reduction of the density of states (fig. 21b) due to symmetry lowering in the AF state smearing out the sharp DOS structure near  $E_F$ . This is consistent with reductions of 60% and 68% seen in specific heat data



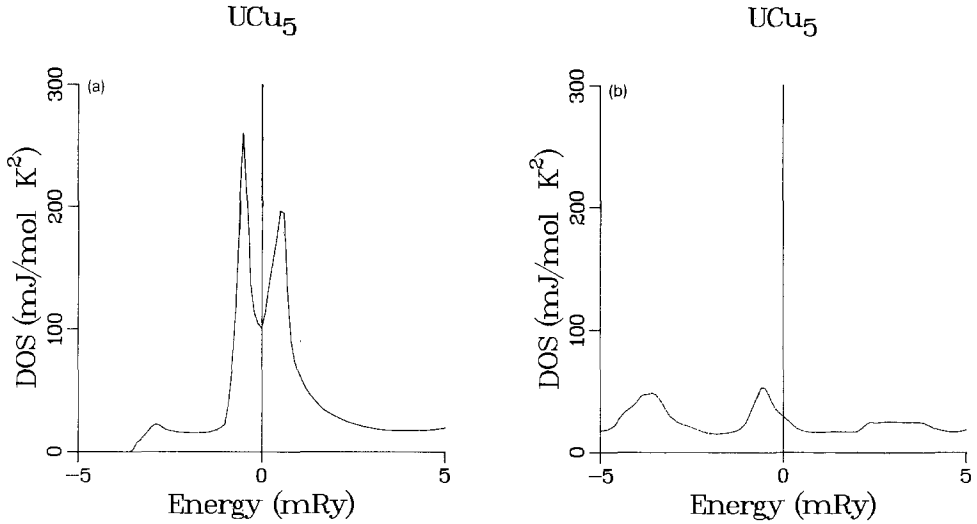


Fig. 21. LDA density of states for  $\text{UCu}_5$  in the immediate vicinity of the Fermi energy (set to zero) in (a) the paramagnetic state, and (b) the antiferromagnetic state. Note in (a) the presence of a gap just below the Fermi energy. In (b) the exchange splitting caused by the large moment has filled in the gap and even pushed much of the density of states out of this narrow energy window.

(Ott et al. 1985b, Welp 1989). The moment value calculated is  $1.0\mu_B$  (2.8 orbital,  $-1.8$  spin). This is somewhat less than the values of  $1.3$  and  $1.55\mu_B$  seen experimentally, although we know that inclusion of orbital polarization effects will lead to an increased orbital moment. We have also calculated the non-interacting  $\chi_0(\mathbf{q})$  including relativistic matrix elements and find that the  $q$  dependence is temperature sensitive, which may be related to the magnetic phase transition seen at  $1\text{ K}$ .  $\chi_0(\mathbf{q})$  was larger for the moment along the  $\langle 111 \rangle$  direction than along  $\langle 001 \rangle$ , consistent with neutron scattering data. As in  $\text{UPt}_3$ ,  $\chi$  is dominated by the Van Vleck term due to spin-orbit effects, and in fact, a strong peak is seen in  $\text{Im } \chi$  due to the sharp peaks in the density of states seen in fig. 21a. In fig. 22, we plot  $\text{Im } \chi_0(\omega)$  for  $\mathbf{q} = \pi/a(1, 1, 1)$  and compare it

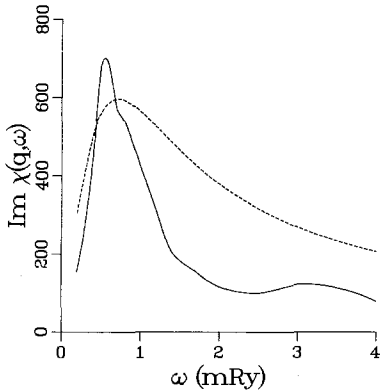


Fig. 22. LDA dynamic susceptibility (including spin-orbit effects) for  $\text{UCu}_5$  at  $\mathbf{q} = \pi/a(1, 1, 1)$  with a renormalized spin-spin response integral,  $I_{\text{ex}}$ , of  $0.97\text{ mRy}$  (7% of the LSD value). The dashed curve is the quasi-elastic part of the neutron scattering data at  $10\text{ K}$  of Walter et al. (1987).

to the neutron scattering data of Walter et al. (1987). Our  $\chi_0(\mathbf{q})$  was renormalized by a factor  $[1 - I\chi_0(\mathbf{q})]^{-1}$ , with  $I$ , the moment–moment response function, adjusted to reproduce the bulk susceptibility (we note that the adjusted  $I$  is about 7% of the LSD  $I$ , indicating strong spin fluctuation renormalizations). The agreement is somewhat surprising, and may be fortuitous, since the neutron data are consistent with a standard relaxational response, with the line width,  $\Gamma$ , being a measure of the hybridization strength of the f electrons with the conduction electrons, as seen in many mixed-valent and heavy-fermion metals. The point here is that the observed broad (non-Fermi-liquid-like) frequency response is also seen in the band calculations when including relativistic effects.

We now turn to a discussion of the Néel temperature. Our estimated Stoner temperature for  $\text{UCu}_5$  is 1000 K. Given the experimental value of 15 K, this implies that  $T_N$  is totally controlled by spin fluctuation effects, as observed for a number of transition metal magnets. This prompted us to calculate  $T_N$  using spin fluctuation theory (Lonzarich 1986, Moriya 1987). For antiferromagnets, this formalism has been derived by Nakayama and Moriya (1987). The only change we make is to replace the assumed form of the susceptibility of Nakayama and Moriya by the Lorentzian form observed in neutron scattering,

$$\text{Im } \chi(\mathbf{q}, \omega) = \chi_0 \Gamma \omega / \{ \Gamma^2 [1 - \chi_0 I(\mathbf{q})]^2 + \omega^2 \}, \quad (1)$$

where  $\chi_0$  is the bare ion susceptibility,  $\Gamma$  the neutron scattering linewidth, and  $I(\mathbf{q})$  the momentum-dependent spin–spin response function. At  $T_N$ ,  $\chi_0 I(\mathbf{Q}) = 1$  where  $\mathbf{Q}$  is the ordering vector, and we assume  $\chi_0 I(\mathbf{q}) = 1 - A|\mathbf{q} - \mathbf{Q}|^2$ . The mean-square local amplitude of the spin fluctuations is

$$S_i^2 = \frac{2}{\pi} \int d\omega / e^{\omega/T} - 1 \sum \text{Im } \chi_i(\mathbf{q}, \omega), \quad (2)$$

where  $i$  is  $x, y, z$ . From the free-energy expansion, one can derive the following relation (Nakayama and Moriya 1987)

$$1/\chi_t = F \left[ \frac{5}{3} \sum S_i^2 - M^2 \right], \quad (3)$$

where  $F$  is the coefficient of the  $M^4$  terms in the free energy, and  $2M$  is the staggered magnetic moment.

Above  $T_N$ ,  $S_i$  should be isotropic ( $\text{UCu}_5$  is cubic), so from eq. (3),  $T_N$  ( $1/\chi_t = 0$ ) is given by

$$S_i^2 = \frac{1}{5} M^2 \quad (4)$$

Using eqs. (1) and (4) in eq. (2), we find

$$T_N = 0.7137 [A^{3/2} \Gamma^{1/2} (2M^2) / (\chi_0 \Omega_0)]^{2/3} \quad (5)$$

where  $\Omega_0$  is the volume per formula unit, and  $\chi_0$  is in units of  $4\mu_B^2$ . We assume that  $I(\mathbf{q})$  doubles from the zone center to  $\mathbf{Q}$  (such a doubling is found from neutron scattering in  $\text{UPt}_3$ , no such data exists for  $\text{UCu}_5$ ). This implies that  $\chi_0$  is half the bulk susceptibility. The  $T_N$  formula is not very sensitive to this assumption since a change in  $A$  is compensated by one in  $\chi_0$ . Since  $\mathbf{Q}$  is  $0.409 \text{ a.u.}^{-1}$ ,  $A$  is  $2.99 \text{ a.u.}^2$  from

eq. (1). With an  $\Omega_0$  of  $588.1 \text{ a.u.}^3$ , a  $2M$  of  $1.55\mu_B$  (Schenck et al. 1990), a  $\Gamma$  of 114 K (Walter et al. 1987), and a  $\chi_0$  of 0.0023 states/K [in  $4\mu_B^2$  units, gotten by using the bulk susceptibility value of 0.0069 emu/mol of Brodsky and Bridger (1974) in eq. (1)], we obtain a Néel temperature of 15 K. Of course, the exact agreement with experiment is somewhat fortuitous, but the point is that the value of the Néel temperature is consistent with spin fluctuation theory. This same  $T_N$  formula would imply that the Néel temperatures observed for  $\text{UPt}_3$  and  $\text{URu}_2\text{Si}_2$  are much too high given the small moments involved, indicating that the primary order parameter in those cases is not magnetic but possibly quadrupolar.

### 3.8. $\text{RB}_6$ materials

The rare earth hexaborides are some of the best studied of the rare earth alloys.  $\text{CeB}_6$ , in particular, has attracted much attention. This metal undergoes a transition at 3.2 K into what is thought to be an antiferroquadrupolar phase (Effantin et al. 1985). At 2.4 K, antiferromagnetic order develops. A large electronic specific heat coefficient of  $260 \text{ mJ/mol K}^2$  has been estimated which is strongly quenched in a field (Peysson et al. 1986, Bredl 1987). The resistivity shows Kondo-like behavior (Jaccard and Flouquet 1985). Both neutron scattering and specific heat data in  $\text{CeB}_6$  are consistent with a  $\Gamma_8$  crystal field ground state.

The Fermi surface of  $\text{CeB}_6$  has been seen with the dHvA effect (van Deursen et al. 1985, Joss et al. 1987, 1988, Onuki et al. 1989a, 1990a, Springford 1991). At this field value,  $\text{CeB}_6$  is in an induced ferromagnetic state. In fig. 23, we show the data of Onuki et al. (1989a). The experimental Fermi surface looks identical to that in  $\text{LaB}_6$ ,

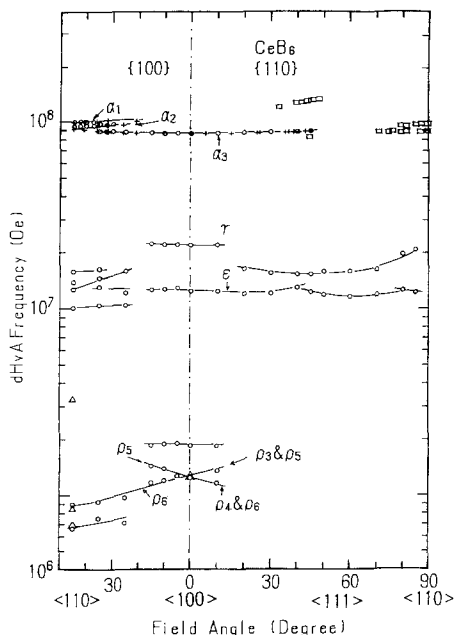


Fig. 23. Experimental dHvA data for  $\text{CeB}_6$  (from Onuki et al. 1989a).

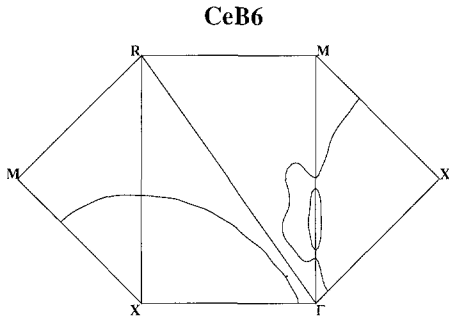


Fig. 24. LDA Fermi surface for  $\text{CeB}_6$  (f core).

which is composed of large (interconnected) ellipsoids centered at the X points, along with small pockets centered along the  $\Gamma$ -M directions. In fig. 24, we show plots of the Fermi surface from our f core calculation (Norman and Min, unpublished). From this figure, we can interpret the experimental orbits as follows: the orbits  $\alpha$  are around the belly of the ellipsoids, the orbit  $\gamma$  around the M point, the orbit  $\epsilon$  around the  $\Gamma$  point, and the  $\rho$  orbits are around the  $\Gamma$ -M pockets inside the necks connecting the ellipsoids. One puzzling thing, though, is that the extremal orbits around the X ellipsoids are about 10% larger than in  $\text{LaB}_6$ . To investigate this question, we (Norman and Min, unpublished) calculated the Fermi surface by treating the f electrons in various ways: as band or core states with and without spin polarization. The paramagnetic f band calculation has no relation to experiment. The polarized f band calculation has one spin surface which is similar to  $\text{LaB}_6$ , but the X ellipsoids are too small to explain the data. Similar polarized f band calculations by Langford et al. (1990) give even smaller ellipsoids. The paramagnetic f core calculation, as discussed above, gives the most satisfactory explanation of the data, but the 10% increase in the area size over  $\text{LaB}_6$  is not explained, indicating that the anisotropy of the ellipsoids are not described quite correctly (we believe that this problem is largely a shape problem, as opposed to the actual occupied volume of the surface being 10% larger). The polarized f core calculation gives one spin surface which is slightly smaller than experiment, and one much smaller. This leads to the question of why only one of the two spin-split surfaces is seen (spin-split surfaces are seen in  $\text{CeAl}_2$ ). The above suggests to the authors that a proper calculation of the Fermi surface of  $\text{CeB}_6$  has yet to be done. Incorporating Hund's second rule effects in an f band calculation may be one way to proceed. This would require a generalization of the current formalism from a spherical harmonic basis to a crystal field basis for the f electrons, similar to what has been done for d electrons in transition metal oxides (Norman 1991b). Another possibility is to properly include the spatial anisotropy of the f electron in an f core calculation. Finally, given the Kondo-like properties of this metal, the most satisfying calculation would be a Kondo renormalized band calculation similar to those discussed by Zwicky (1988).

The most unusual thing about  $\text{CeB}_6$ , though, is the large mass renormalization inferred from experiment. In fig. 25, we plot results from specific heat and dHvA data versus field, normalized to the band mass and band density of states from the paramagnetic f core calculation. The dashed line is a fit to the dHvA data using the

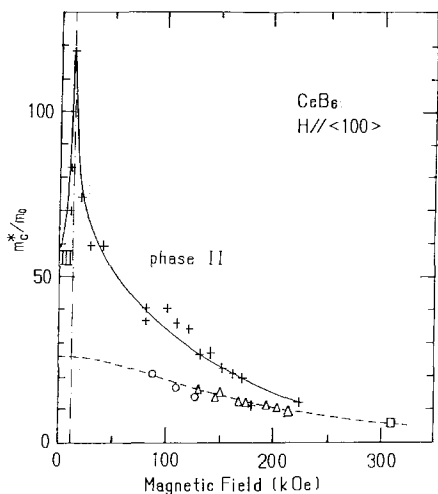


Fig. 25. Field dependence of the  $\alpha_3$  dHvA mass for  $\text{CeB}_6$ . The circles, squares and triangles represent different data sets. The dashed line is a Kondo resonance model fit to the data (Norman and Min, unpublished). The solid line and crosses are from specific heat data (from Onuki et al. 1990a).

simple Kondo resonance model of Schotte and Schotte (1975). This fit goes as  $A\Delta^2/[\Delta^2 + (gH)^2]$  where  $A$  is the zero field value,  $\Delta$  the resonance width (9.3 K in our case),  $g$  the  $g$  factor ( $\frac{6}{7}$ ), and  $H$  the field, with an extrapolated zero field value for  $m^*/m_b$  of 47. We note that this simple resonance model gives a remarkably good fit to the data over a large field range. The large value of  $m^*/m_b$  is difficult to reconcile with the Fulde–Jensen model for conduction electron mass enhancement due to virtual  $f$  crystal field excitations (Thalmeier, personal communication). This is another indication of the possible inadequacy of an  $f$  core model for the Fermi surface. Another interesting point is that the specific heat mass is considerably higher than the dHvA mass, although it appears that they will be equal at high fields. This indicates that there is an incoherent contribution to the specific heat, presumably related to the magnetic phase transition (the singularity in  $C/T$  at 2 T marks the transition from the antiferromagnetic phase). An alternative explanation offered by Onuki et al. (1989a) is that this mass discrepancy is due to only seeing one spin surface. This explanation is doubtful for two reasons: (1) the two sets of data appear to be converging at high fields, and (2) the polarized  $f$  band calculations discussed above do a poor job of describing the Fermi surface. Finally, we note that an alternative description of the mass renormalization in terms of an Anderson lattice model has been given by Wassermann et al. (1989). Their fit deviates from the one we describe at low field values, so it will be of interest to obtain dHvA mass data at even lower fields to differentiate between these two models.

dHvA data also exists for antiferromagnetic  $\text{PrB}_6$  and  $\text{NdB}_6$  (Onuki et al. 1985, 1989c). The data in  $\text{PrB}_6$  is again similar to  $\text{LaB}_6$ , but with additional features which can be explained by the fact that antiferromagnetism acts to fold the bands back into a smaller magnetic Brillouin zone (also see Min and Jang 1991). The mass renormalization in  $\text{PrB}_6$  is about three times larger than in  $\text{LaB}_6$ . Such a value is comparable to what is seen in Pr, indicating that a Fulde and Jensen (1983) interpretation of the mass renormalization should apply here as well.

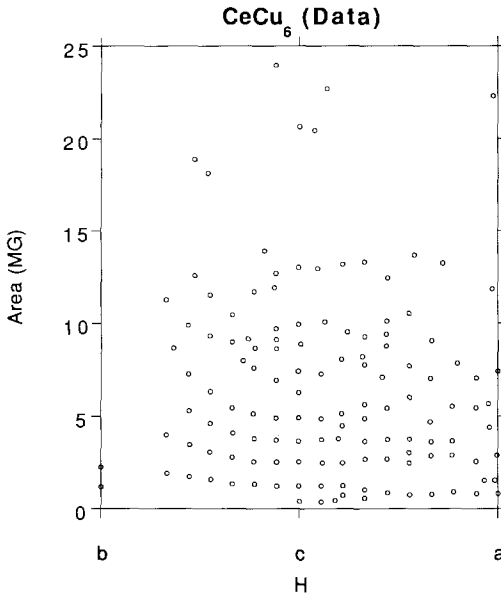


Fig. 26. Experimental dHvA data for  $\text{CeCu}_6$  [data taken from Chapman et al. (1990)].

### 3.9. $\text{RCu}_6$ materials

$\text{CeCu}_6$  has one of the largest known electronic specific heat coefficients,  $1670 \text{ mJ/mol K}^2$  (Amato et al. 1987). Despite this, the metal does not undergo any known instability down to very low temperatures. Measurements on dilute  $(\text{Ce, La})\text{Cu}_6$  indicate a Kondo temperature of 4 K. Measurements of low-temperature properties in  $\text{CeCu}_6$  indicate a coherence temperature of the order of 300 mK below which the metal shows characteristic Fermi liquid behavior, such as a  $T^2$  behavior in the resistivity (Amato et al. 1987).  $\text{CeCu}_6$ , which has a weak monoclinic distortion from an orthorhombic structure (four formula units per cell), also has highly anisotropic magnetization properties, with the orthorhombic  $c$  axis being the easy axis for field-induced magnetization and the  $b$  axis being the hardest (we will use orthorhombic notation throughout). The  $g$  value is strongly reduced for fields along the easy axis (Sato et al. 1985, Amato et al. 1987).

$\text{CeCu}_6$  was one of the first heavy-fermion metals where the dHvA effect was observed (Reinders et al. 1986, Chapman et al. 1990), with masses up to 80 times the free-electron mass. Related dHvA data exists for  $\text{LaCu}_6$ ,  $\text{PrCu}_6$ ,  $\text{NdCu}_6$ , and  $\text{SmCu}_6$  (Onuki et al. 1986, 1987a, 1991). Fermi surface analysis from band structure calculations have been provided for  $\text{CeCu}_6$  (Chapman et al. 1990, Harima personal communication) and for  $\text{LaCu}_6$  (Harima et al. 1990). Given the complexity of these systems, we discuss the data of non-f  $\text{LaCu}_6$ .

In the paper by Harima et al. (1990) nice 3D plots of the Fermi surface are made, from which the extremal orbits were determined. Our own  $f$  core calculation on  $\text{CeCu}_6$  gives a very similar Fermi surface topology (Chapman et al. 1990). The Fermi surface consists of four sheets, each with a highly complicated topology. The one common

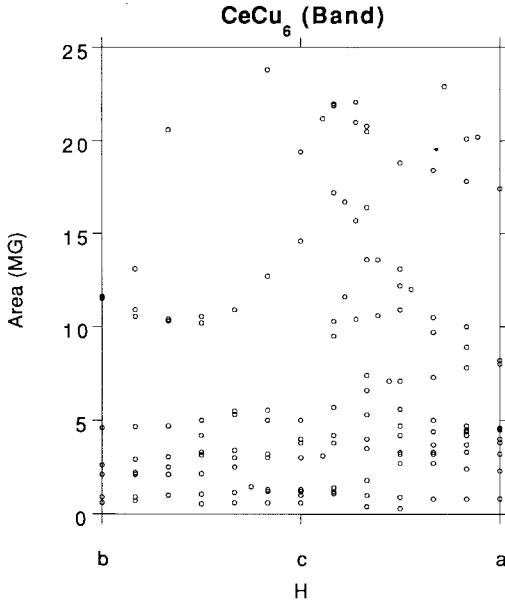


Fig. 27. LDA dHvA areas for CeCu<sub>6</sub> (f band).

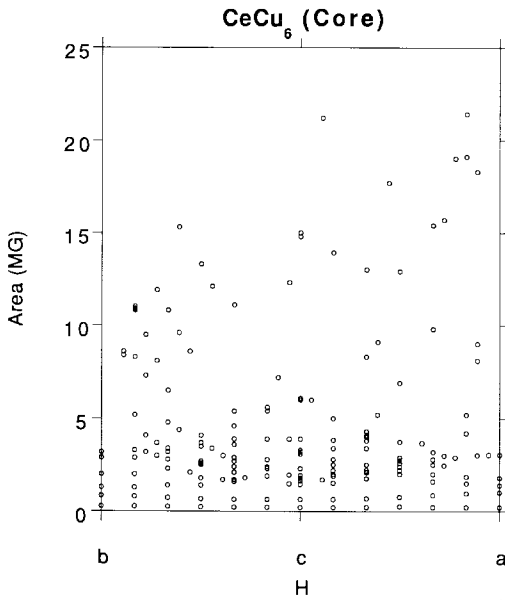


Fig. 28. LDA dHvA areas for CeCu<sub>6</sub> (f core).

thing is that all sheets have tubes running along the *c* axis. Such a topology is consistent with experiment (Onuki et al. 1986). Comparing the dHvA orbits of Onuki et al. with those calculated by Harima et al., one finds that although many orbit identifications are possible, many are not, so a completely satisfactory explanation of the data still remains to be found. At this point, we should say that because of the complexity of the unit cell (28 atoms per cell), a detailed analysis of the sensitivity

of the band structure to computational details has not been done. The calculation of Harima et al. used a muffin-tin approximation (LAPW), but included spin-orbit effects. They did test for plane-wave convergence, but, of course, do not include warping terms either inside or outside the spheres. Our own LMTO calculations (Norman) included combined correction terms but did not include spin-orbit (except on cruder  $k$ -point grids, from which it was determined that spin-orbit effects did not appear to affect the Fermi surface much), nor was any analysis done concerning the utility of including empty spheres or including non-spherical potential terms inside the spheres. Much work, therefore, is left to be done, although the comparison to experiment so far looks promising.

A similar optimistic outlook, though, does not occur for  $\text{CeCu}_6$ . In fig. 26, we show the experimental data of Springford's group, and compare it to our own calculated orbits in fig. 27 (f band) and fig. 28 (f core). No clear identification can be seen. Our f core surface is similar to that of Harima et al. (1990), and our f band surface is similar to unpublished results of Harima. At this point, some remarks should be made about the experimental data. Despite the large number of observed orbits, most of them can be seen to be harmonics of fundamental orbits. Therefore, the actual number of fundamental orbits seen is quite small. Moreover, very few data points exist for areas larger than 14 MG. Thus, only a small part of the Fermi surface has been seen. Also, there is an unusual disappearance of signals near the  $b$  axis. Thus, given the sensitivity of the extremal orbits to details of the band calculations, as well as the incompleteness of the experimental data, it is difficult to reach a conclusion. On the other hand, given the strong differences between the data for  $\text{LaCu}_6$  and  $\text{CeCu}_6$ , an f core treatment appears to be ruled out. Since the band calculations did yield a topology consistent with the  $\text{LaCu}_6$  data, and given that no clear topological matches exist for  $\text{CeCu}_6$ , one is led to conclude that the LDA f band calculations are deficient. This may be the first indication of the situation discussed by Zwicky (1988) concerning the failure of LDA when the Kondo temperature is smaller than the crystal field splitting. In that case, only the ground state f level would be renormalized, thus effectively projecting out all f states but that one in the vicinity of the Fermi energy. The resulting Fermi surface would be quite different from the LDA one. Thus, there is a need to do a renormalized band calculation on  $\text{CeCu}_6$  to see whether the above discrepancies can indeed be explained.

Also, we should note that the mass renormalizations seen for fields along the  $c$  axis have a field dependence consistent with that determined from specific heat (Chapman et al. 1990). For a field of 12 T, the mass is about 25% of the zero field value. It was this comparison that led to the conclusion that only 30% of the Fermi surface was being observed in the dHvA experiments. On the other hand, the specific heat is hardly reduced for fields along the  $b$  axis (Satoh et al. 1985), indicating high dHvA masses for that field direction. This may be the source of the dHvA signal loss for fields near the  $b$  axis.

Finally, we mention the cases of  $\text{PrCu}_6$  and  $\text{NdCu}_6$ . The dHvA data are similar to that of  $\text{LaCu}_6$  (Onuki et al. 1991), with differences seen in  $\text{NdCu}_6$  being attributed to the band folding back into the antiferromagnetic zone. The mass in  $\text{PrCu}_6$  is about twice that of  $\text{LaCu}_6$ , whereas that in  $\text{NdCu}_6$  is about the same as in  $\text{LaCu}_6$ .



### 3.10. $UB_{12}$ , $UBe_{13}$

$UB_{12}$  and  $UBe_{13}$  are cubic metals composed of U atoms separated by B or Be cages. The U–U separation is large, 5.28 Å for  $UB_{12}$  and 5.25 Å for  $UBe_{13}$ . Despite these similarities,  $UB_{12}$  has a low  $\gamma$  of 20 mJ/mol K<sup>2</sup>, whereas  $UBe_{13}$  is a heavy-fermion superconductor with a  $\gamma$  of 1100 mJ/mol K<sup>2</sup>. The Fermi surface of  $UB_{12}$  has been determined by the dHvA effect by Onuki et al. (1990b), with band structure calculations done by Yamagami and Hasegawa (1991a). The data are consistent with an f band Fermi surface (one electron and one hole sheet), and a comparison of band density of states to specific heat data yields a tiny mass renormalization factor of 1.1, hardly enough to account for even an electron–phonon interaction.

This can be contrasted to  $UBe_{13}$ . At present, no dHvA data exists, but given the observation of such signals in  $CeCu_6$  and  $UPt_3$ , success in the near future is anticipated. Of course, numerous band structure calculations have been done on this important metal. As in  $UPt_3$ , a magnetic instability is predicted (barely, since the paramagnetic DOS is about half that of  $UPt_3$ ), with spin-polarized calculations yielding a moment of  $0.8\mu_B$  (Pickett et al. 1985). Comparisons of the paramagnetic density of states to specific heat give an enormous mass renormalization factor of 90. Since the band masses range from 1 to 4.1, the predicted quasiparticle masses would range from 100 to 400, making dHvA experiments very difficult. Fortunately, the predicted Fermi surface is quite simple (Norman et al. 1987b), with a nested surface at  $\Gamma$  and pillboxes at the X points. Of course, given many of the unusual properties of  $UBe_{13}$ , such as strong indications from specific heat of crystalline field effects (Felten et al. 1986) and Kondo-like behavior, it is highly questionable [in the sense of Zwicky (1988)] that the LDA Fermi surface will yield the correct topology. We conclude by emphasizing that subtle differences in structure can lead to huge changes in electronic properties.  $UB_{12}$  has a larger U–U spacing than  $UBe_{13}$ , yet has a  $\gamma$  value lower than  $UBe_{13}$  by a factor of 55. This is analogous to the subtle differences between  $UPt_3$  and  $UPd_3$  discussed above. Again, we anticipate that it is a competition between Hund's rule effects and hybridization which determine whether the f electrons in the metal are itinerant, heavy fermion, or localized in nature. This is consistent with the interpretation of Zwicky (1988).

### 3.11. $R-AT_{2,3}M_2$ materials

An extensive class of materials exist of the form  $RT_nM_2$  with  $n = 2, 3$ ; R–A, a rare earth or actinide; T, generally Rh or Ru although most transition elements are also used; and M, one of the non-transition elements B, Al, Si, or Ge. The primary interest is the magnetic behavior and the influence of the Rf to Rf and Td interactions. The additional non-transition metal provides an interesting mechanism for parameter adjustment in that it affects crystal structure, lattice spacings, and charge balance without a major contribution to states at the Fermi energy. Thus these materials offer the opportunity to study the transition from moment behavior through Kondo behavior to Pauli paramagnetism (Palstra et al. 1986) with the transition metal d electron count the primary parameter modulated by the choice of the non-transition

element. Most of the systems of interest here occur in the  $\text{ThCr}_2\text{Si}_2$  crystal structure which is body-centered tetragonal. It can be visualized as a tetragonal distortion of a Heusler phase where the transition elements form the (formerly simple cubic) backbone with the R and  $\text{M}_2$  dimer sitting in the alternating body-centered sites. In addition to the unit cell volume and  $c/a$  ratio, the dimer separation adds another important geometric variable influencing the properties of the system. The systematic trend with the filling of the transition element d states from itinerant behavior – except Mn where the 3d moment drives the magnetism – to antiferromagnetic and eventually even to ferromagnetic behavior (Dirkmaat et al. 1992, Szytuła et al. 1988). A minimum of the unit cell volume occurs at Co/Rh/Ir that does not closely correlate with the onset of antiferromagnetism. Nor is there any clear correlation between any of the other geometrical factors and the magnetic behavior. The trends are unlikely to be tied to simple bond-strength as a function of separation type arguments. Most of these materials exhibit large specific heat coefficients above the magnetic transition temperature. As observed in other systems, one finds strong mass enhancements for the materials in the cross-over region – which is precisely where  $\text{CeRu}_2\text{Si}_2$  and  $\text{URu}_2\text{Si}_2$  fall.

In the Ce-(3d)-Si series, behavior is shifted towards the itinerant side, perhaps in this case tied to the much smaller basal plane lattice constant. The transition only begins to occur at the end of the series giving rise to that most famous example,  $\text{CeCu}_2\text{Si}_2$ , which not only exhibits antiferromagnetic fluctuations, but was the first discovered heavy-fermion superconductor [see the discussion by Rauschwalbe (1987)]. De Haas-van Alphen data exist for  $\text{CeCu}_2\text{Si}_2$  (Hunt et al. 1990). The first calculation of the Fermi surface for both  $\text{CeCu}_2\text{Si}_2$  and  $\text{LaCu}_2\text{Si}_2$  was by Jarlborg et al. (1983). In retrospect, the most noteworthy feature to be found in those calculations is the presence in both materials of one complicated surface. Harima and Yanase (1991, 1992) also find a complex jungle gym structure for both  $\text{CeCu}_2\text{Si}_2$  and  $\text{LaCu}_2\text{Si}_2$  (which is used as a model for the local-f case) which they relate to the set of frequencies observed by Hunt et al. (1990). Given the fact that only a small part of the Fermi surface has been seen with dHvA, it is too early to tell yet whether a local f model, a band f model, or a renormalized band model based on a particular f crystal field ground state, is the appropriate one for this material. Sticht et al. (1986) have performed a renormalized band calculation for  $\text{CeCu}_2\text{Si}_2$  that utilizes an itinerant f LDA band calculation as the basis – as opposed to an fcore calculation. They find that to properly place the Fermi energy between the two peaks in the quasi-particle density of states, they must correct the original crystal field parameters (Horn et al. 1981) as had been previously suggested (Bredl et al. 1985). Unfortunately, they did not determine the Fermi surface topology.

Before turning the focus to  $\text{CeRu}_2\text{Si}_2$  and  $\text{URu}_2\text{Si}_2$ , we should acknowledge that many of the materials that do exhibit moments are also still interesting. Their magnetic behavior is not straightforward and must involve Fermi surface effects. Although not of the  $\text{ThCr}_2\text{Si}_2$  structure,  $\text{CeRh}_3\text{B}_2$  nonetheless is a good example because it is well studied and also it typifies some of the unusual behavior. The effective moment deduced from the high temperature Curie-Weiss dependence is about  $\mu_B$  – already significantly reduced from the free-ion value. Low-temperature magnetization mea-

measurements give an even smaller moment of  $0.38\mu_B$ . This lower value is consistent with that obtained from hyperfine measurements ( $0.4\mu_B$ ) which also indicate the moment to be on the Ce. Single-crystal measurements, however, yield a moment of  $0.56\mu_B$  oriented along the  $c$  axis. The magnetic entropy observed is too small for a  $j = \frac{5}{2}$  ion. Particularly interesting is that the transition temperature is unusually high. Alloying Co onto the Rh site reduces the moment and alloying Ru or Os onto that site quickly destroys it. Initial band calculations (Misemer et al. 1984) found significant Cef interactions both with the nearby Cef states in the  $c$  axis directed chains of Ce and with the neighboring Rh d, all producing large anisotropy at the Ce site. It was then found that only when the spin-orbit coupling was incorporated into the self-consistent process a magnetic state was obtained (Eriksson et al. 1989d). Otherwise, no moment was obtained no matter what one did for the treatment of exchange-correlation effects. It was also found that there was a strong charge coupling to the Rh with little spin build-up; the spin is built up between Ce atoms in the Ce chains. It was further found that the moment was critically sensitive to the lattice spacing. So the lattice expansion compensates for the thermal degradation of the moment as the temperature is raised and this is the mechanism that raises the transition temperature.

$CeRu_2Si_2$  and  $URu_2Si_2$  both behave as weak magnetic systems.  $CeRu_2Si_2$  is metamagnetic (Mignot et al. 1988) above 80 kG with the easy axis of magnetization along the  $c$  axis. It also orders when alloyed with La, Rh, or Ge (Besnus et al. 1987, Godart et al. 1986, Lloret et al. 1987, Quezel et al. 1988) on the appropriate site.  $URu_2Si_2$  becomes antiferromagnetic at 17.5 K through the formation of a spin wave with an 11 meV gap (Broholm et al. 1987, Maple et al. 1986). Like  $UPt_3$ ,  $URu_2Si_2$  then becomes a superconductor below 1.2 K. The small moments ( $0.03\mu_B$ ) couple into ferromagnetic sheets perpendicular to the  $c$  axis with alternating spin on the body-centered sites. Alloying Rh onto the Ru sites quickly reduces both  $T_N$  and  $T_C$ . The large ( $180 \text{ mJ/mol K}^2$ ) specific heat coefficient is not significantly altered until about a 3% replacement (where the antiferromagnetic transition is just suppressed) whereupon there is a dramatic jump up to roughly twice this value. Alloying Re onto the Rh site (Torikachvili et al. 1990, Dalichaouch et al. 1989) produces ferromagnetic order and a moment about half that found in spin-polarized band calculations (Norman et al. 1988c). Yet, the specific heat coefficient remains high.  $URu_2Si_2$  is also metamagnetic but at a much higher field (35–40 T) where the moment jumps by  $\mu_B$  to a value close to that found by the band calculations (De Visser et al. 1987a).

### 3.11.1. $CeRu_2Si_2$

$CeRu_2Si_2$  has a low-temperature specific-heat coefficient  $\gamma = 385 \text{ mJ/mol K}^2$  (Thompson et al. 1985) making it at least a pudgy, if not a heavy-fermion material. It does not superconduct like  $CeCu_2Si_2$  but exhibits short-range magnetic fluctuations (Regnault et al. 1988) peaked at  $\mathbf{k}_1 = (0.3, 0, 0)$  and  $\mathbf{k}_2 = (0.3, 0.3, 0)$ . The moment fluctuates along the  $c$  axis with the correlation length in the  $a$ - $b$  plane saturating at about 15 a.u. at low temperatures. Alloying La onto the Ce sites extends the range of the correlations such that long-range magnetic order occurs at low temperatures (Regnault et al. 1990). There is a positive magnetoresistance which increases with the

field up to the metamagnetic transition at 8 T where it then begins to decrease. This anomalous scattering decreases with temperature and vanishes roughly at the same temperature as does the inelastic neutron line (Haen et al. 1987). That this metamagnetic transition occurs at an experimentally accessible field as well as being associated with the fluctuation induced anomalies makes this material extremely interesting. But further, the fluctuations can be suppressed by pressure. A pressure of 4 kbar decreases the zero-temperature susceptibility  $\chi_0$  by over a factor of two while virtually eliminating the low-temperature maximum. The pressure dependence of the susceptibility can be interpreted in terms of an increase of a Fermi-liquid characteristic energy  $\partial E^*/\partial P = 171 \text{ Mbar}^{-1}$  or  $\partial E^*/\partial V = 180$  (Mignot et al. 1988).

$\text{CeRu}_2\text{Si}_2$  can be prepared as a single crystal of excellent quality, so that dHvA measurements have been made both above and below the metamagnetic transition (Lonzarich 1988). Cyclotron masses vary over a wide range (1–20) indicating a mixture of enhanced and unenhanced carriers. The light-mass orbits are found to be not significantly modified by the transition whereas the heaviest-mass orbits are found to vanish above the metamagnetic transition. Six frequencies are observed in the high-field region (note that all orbits in the basal plane are below the metamagnetic transition – which occurs at  $80/\cos \Theta$  kOe for field direction  $\Theta$  relative to the  $c$  axis). That all frequencies are single suggests both that all closed surface orbits are centered either at  $\Gamma$  or at  $Z$  (the center of the zone face perpendicular to the  $c$  axis) and that spin splittings are either quite small or very huge. The individual frequencies are:

$\alpha$ : an orbit of uniform size ( $\sim 4.5 \text{ MG}$ ) for the field oriented in the basal  $a$ - $b$  plane. The orbit is only reported for a range of  $30^\circ$  as the field is tipped towards the  $c$  axis. The frequency increases steadily across that short range. Such a pattern would only be consistent with a closed surface were the amplitude factor to destroy the signal as the field is tipped up. An alternate explanation would be a uniform ring-like surface centered about  $\Gamma$ . This would also be consistent with the  $\delta$  and  $\epsilon$  orbits to be discussed below. The possibility is mentioned because the band calculations yield a ring-like structure in the basal plane with arms extending up the  $c$  direction at the (110) face ( $f$  band only). We will call this the “ $\alpha$ ” surface and it is shown in fig. 29.

$\beta$ : a closed surface orbit of roughly unit mass. It is nearly constant in size over the entire range when the field is in the basal  $a$ - $b$  plane ( $\sim 9.5 \text{ MG}$ ) and drops to  $6 \text{ MG}$  as the field is oriented to the  $c$  axis. This surface should be a cylinder of revolution elongated along the  $c$  axis (cigar shape). The band calculations find such a surface centered at  $Z$ .

$\gamma$ : a closed surface orbit of roughly unit mass. This orbit occurs in the range about  $15 \text{ MG}$ . It has a slight variation in the basal plane indicating a weak protrusion in the (110) directions. It drops to about  $10 \text{ MG}$  as the field is oriented to the  $c$  axis. The band calculations also find such a surface centered at  $Z$ .

$\delta$ : a neck-like orbit observed along the  $c$  axis ( $\sim 11 \text{ MG}$ ) that rises to about  $18 \text{ MG}$  before vanishing at  $45^\circ$ . This is consistent with the “ $\alpha$ ” surface.

$\epsilon$ : a neck-like structure pointed along the (100) or  $a$  axis where it is  $25 \text{ MG}$  in size and then increases until vanishing. This is a large mass orbit of approximately 20 electron masses. This is consistent with the “ $\alpha$ ” surface.

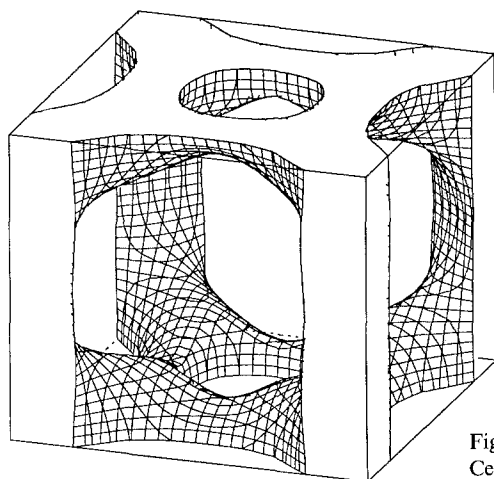


Fig. 29. The “ $\alpha$ ” surface from an  $f$  band calculation for  $\text{CeRu}_2\text{Si}_2$  (plot provided by Greg McMullen).

$\eta$ : an orbit observed along the  $c$  axis ( $\sim 31$  MG) that rises about another MG before vanishing at  $30^\circ$ . This could be due to either the third surface around  $Z$  (so, one would then have to explain why the orbit terminates as this surface is closed) or another predicted neck orbit on the “ $\alpha$ ” surface.

LDA-based band calculations (Zwicknagl et al. 1990, Christensen et al., unpublished) are at least qualitatively consistent with this Fermi surface although they predict a few more orbits than are seen experimentally and also seem to be sensitive to the details of the spin-orbit coupling. In particular, an  $f$  band calculation gives a better description of the data than an  $f$  core one, especially with regards to the  $\alpha$ ,  $\delta$  and  $\epsilon$  orbits. Additional care is needed because one must properly set three geometrical factors, as mentioned above, instead of a single lattice constant and the results will be sensitive to that choice. Zwicknagl et al. also reported a model renormalized-band calculation where they assumed a crystal field level scheme since that information was not available. The resulting orbit sizes were little changed over the LDA results. For some orbits, no mass enhancement was seen, but for others, a large value was found, in rough agreement with experiment.

Of particular importance is a large high-mass surface centered at  $Z$  seen in the LDA and renormalized-band calculations but not yet observed experimentally. Only if this surface is present can the specific heat be accounted for in terms of quasiparticle excitations. Unfortunately, the large size and heavy mass of that surface also mean that it will be extremely difficult to observe. Evidence that it should be present can be inferred from a rather complete study existing for the isoelectronic, but ferromagnetic, compound  $\text{CeRu}_2\text{Ge}_2$  (King and Lonzarich 1991). In  $\text{CeRu}_2\text{Ge}_2$ , a comparison to an adjusted band calculation was able to account for all surfaces and to make a very plausible case that all the electronic specific heat coefficient could be accounted for through quasiparticle excitations. The mass enhancements for this material average about 3.5 implying that fluctuation phenomena are still present but

not dominant. Significantly, the large Z-centered surface was observed in  $\text{CeRu}_2\text{Ge}_2$  making the existence of a similar surface in  $\text{CeRu}_2\text{Si}_2$  quite credible.

### 3.11.2. $\text{URu}_2\text{Si}_2$

$\text{URu}_2\text{Si}_2$  has proven of interest not only because of its modestly heavy electronic specific-heat coefficient [ $180 \text{ mJ/mol K}^2$  just above  $T_N$  (Palstra et al. 1985); below  $T_N$ : 75 (Schlabitz et al. 1986), 65.5 (Maple et al. 1986), 42 (Maple et al. 1991)] but also because of the coexistence of small moment magnetism and superconductivity (Broholm et al. 1987). The magnetism has been interpreted as a spin wave (Maple et al. 1986) that destroys a significant part of the Fermi surface (Onuki et al. 1987b) or as being due to local f moment behavior involving two singlet crystal field levels by about 75 K as seen in neutron scattering (Broholm et al. 1991, Walter et al. 1986, Nieuwenhuys 1987, Radwanski 1992). This latter view is supported by the presence of a ‘‘Schottky’’ peak at 32 K which would be consistent with two levels separated by 75 K. However, it should be pointed out that  $\text{UPt}_3$  also has a ‘‘Schottky’’ peak at an even lower 23 K and yet can be described in a band picture by incorporating mass enhancements due to spin fluctuation (Norman 1988). A similar approach has been applied to  $\text{URu}_2\text{Si}_2$  by Mason and Buyers (1991) which gives a good qualitative fit to the data and implies that the Fermi surface is not gapped below  $T_N$ , rather that the mass renormalization changes through  $T_N$ . However, none of these models can explain why the moment is so small. The singlet–singlet model (Nieuwenhuys 1987) gives a magnetic moment even larger than the  $1.2\mu_B$  calculated in band theory (Norman et al. 1988c). One possible explanation is that the primary order parameter is not magnetic in origin but rather quadrupolar with a Kondo suppression of the magnetic moment. Recent experimental evidence supporting this has been given by Ramirez et al. (unpublished), which would also explain why the size of the band structure moment is restored in a large magnetic field.

De Haas–van Alphen area and mass data would be extremely useful in sorting out some of these issues, including the question of itinerancy of the f electrons. There is currently no published dHvA data for  $\text{URu}_2\text{Si}_2$  although experiments are in progress. However, positron annihilation data has been recently used to address this problem (Roizing et al. 1991a, b). Unfortunately for a Fermi surface determination, the positron is highly anisotropic within the unit cell. (As a compensation, that anisotropy favors the examination of the f–ligand interaction.) Comparison with two band structures performed assuming itinerant f states (Norman et al. 1988c, Roizing et al. 1991a) offers at best only limited agreement. The hole surfaces centered at Z should be very clearly seen and they are indeed seen. The electron surfaces predicted at the zone center should also not be obscured by matrix-element effects, but are very clearly not present in the data. Yet, while there are differences between the two band calculations, both do give electron sheets centered at  $\Gamma$ . So unless the mass renormalization factor has strongly reduced the momentum discontinuity at the Fermi surface for those sheets, one must conclude there is a discrepancy between the LDA itinerant f model and the positron annihilation data. As a check, it would be desirable to make a localized  $f^2$  calculation. This has not yet been done but is in progress. An interesting aside is that the positron data is unchanged between 6 and 72 K, which

would indicate no gapping of the Fermi surface when going through  $T_N$ , in agreement with the model of Mason and Buyers.

#### 4. Superconductivity in heavy-fermion metals

The observation of superconductivity in heavy-fermion metals was quite surprising at the time, given the nearly magnetic nature of the f electrons in such metals. This discovery has led to a tremendous amount of work, and to date seven heavy-fermion superconductors are known ( $CeCu_2Si_2$ ,  $UBe_{13}$ ,  $UPt_3$ ,  $U_2PtC_2$ ,  $URu_2Si_2$ ,  $UNi_2Al_3$  and  $UPd_2Al_3$ ). Reviewing even the theoretical developments in this field are far beyond the scope of this paper. We recommend the following theoretical reviews: Lee et al. (1986), Fulde et al. (1988), Pickett (1987), Rainer (1988) and Sigrist and Ueda (1991), although we should remark that a current, comprehensive review of the entire field is still lacking.

In this section, we will mention some of the work done assuming the following pairing mechanisms: phonons, charge fluctuations and spin fluctuations.

##### 4.1. Phonons

There have been two thrust areas assuming pairing via the electron-phonon interaction: first, standard theory as applied to normal superconductors, and second, a Kondo lattice theory.

A side-product of band structure calculations is an estimate of the electron-phonon coupling parameter using the rigid muffin-tin approximation (RMFTA) formulated by Gaspari and Gyorffy (1972). This has been done for  $CeCu_2Si_2$  by Jarlborg et al. (1983), for  $UPt_3$  by Oguchi and Freeman (1985), Oguchi et al. (1986), Wang et al. (1986) and Norman et al. (1988c), for  $UBe_{13}$  by Pickett et al. (1986), for  $URu_2Si_2$  by Norman et al. (1988c), and for  $U_2PtC_2$  by Norman (unpublished). We tabulate these results in table 2. It has been assumed that the average phonon frequency squared,

TABLE 2  
Electron-phonon coupling constants  $\lambda$  as calculated within the rigid muffin-tin approximation for heavy-fermion superconductors. The appropriate references, as well as the assumed Debye temperatures, are listed in the text. Also tabulated are the mass renormalization factors, which are the ratio of the specific heat  $\gamma$  to the band density of states.

	$\lambda$	$m^*/m_b$
$UPt_3$	0.290	16
$UBe_{13}$	0.035	90
$URu_2Si_2$	0.072	11
$U_2PtC_2$	0.084	15
$CeCu_2Si_2$	0.070	70

$\langle \omega^2 \rangle$ , is approximately  $0.5 \Theta_D^2$ , where  $\Theta_D$  (in K) was taken to be 210 for  $\text{UPt}_3$ , 150 (U) and 790 (Be) for  $\text{UBe}_{13}$ , 312 for  $\text{URu}_2\text{Si}_2$ , 273 for  $\text{U}_2\text{PtC}_2$ , and 310 for  $\text{CeCu}_2\text{Si}_2$ . Also tabulated are the estimated mass renormalization factors. The first thing to note from this table is that all  $\lambda$ 's are quite small, smaller than any reasonable Coulomb pseudopotential ( $\mu^*$ ), implying a net repulsive interaction. The possible exception is  $\text{UPt}_3$ , where a  $\lambda$  of 0.3 is found. As first noted by Wang et al. (1986),  $\lambda$  in a strong-coupling expression for  $T_c$  will be reduced by the mass renormalization factor, which for  $\text{UPt}_3$  is huge ( $\sim 20$ ). Even taking into account the fact that this mass renormalization has a frequency scale much smaller than the phonons, a  $T_c$  of the order of  $10^{-23}$  K is found for parameters appropriate to  $\text{UPt}_3$  (Fenton 1986, 1987, Norman 1988). The only way to get around this result is if  $\lambda$  was approximately three times larger than that calculated in the RMTA (assuming an optimistically small value of  $\mu^*$ ). These findings that a standard electron-phonon model does not account for superconductivity in the heavy-fermion metals are not surprising. The observed superconducting states are highly anisotropic, with nodes in the gap function, and thus not explainable by an s-wave theory. Also, no evidence for phonon softening has been seen in these metals, whereas in  $\text{U}_6\text{Fe}$  (a superconductor with a moderate effective mass), strong phonon softening has been seen (Renker et al. 1987a, b).

Another approach has been to note that the effective Kondo temperatures in these metals have a strong volume dependence (large electronic Grüneisen parameter). This occurs because the f electrons are highly localized, with the hybridization (and thus the energy scale,  $T_K$ ) being determined by a small "tail" which extends towards the ligand sites, this tail being very sensitive to volume. This has led Razafimandimby et al. (1984) to show that this large Grüneisen parameter could lead to a sizeable electron-phonon coupling in a Kondo lattice, with a reasonable estimate for  $T_c$  given for  $\text{CeCu}_2\text{Si}_2$ . Recent calculations within a slave-boson scheme (Keller et al. 1990), though, lead to the conclusion that the net interaction is repulsive for on-site pairing, a consequence of the large on-site Coulomb repulsion. Related calculations by Miyake et al. (1984), Ohkawa (1984) and by Ohkawa and Fukuyama (1984) indicate that such a scheme can lead to pairing for electrons on near-neighbor sites. The advantage of this is that non-s-wave states are obtained since the on-site pairing was repulsive in their models. A modern treatment of near-neighbor pairing, analogous to that of Keller et al. (1990), has yet to be performed. Thus, at this stage, it is unclear whether this electron-phonon model is sufficient to explain superconductivity in these metals.

#### 4.2. Charge fluctuations

Pairing due to charge fluctuations has been tackled from two angles: (1) pairing via f density fluctuations in a slave-boson scheme (Auerbach and Levin 1986, Lavagna et al. 1987, Zhang and Lee 1987, Newns 1987, Kotliar and Liu 1988), and (2) pairing induced via a quadrupolar Kondo effect (Cox, unpublished).

In the first method, the Landau scattering amplitudes are calculated up to order  $1/N$  in a slave-boson scheme. The  $1/N$  terms represent hybridization (charge) fluctuations. From this, it was found for the Anderson lattice by Lavagna et al. (1987) that a weak instability occurred in the  $l = 2$  (d wave) channel. Soon after, though, Zhang



and Lee (1987) showed that by including the anisotropy of the Coulomb repulsion, the net interaction in the even parity channels was repulsive. Newns (1987) proposed a more generalized model that included more degrees of freedom ( $f^0$ ,  $f^1$  and  $f^2$  charge fluctuations), and estimated a reasonable transition in the s-wave channel for  $\text{CeCu}_2\text{Si}_2$ . An alternative approach has been to use a Hubbard model instead of an Anderson model. From this, Kotliar and Liu (1988) found either p-wave or d-wave instabilities depending on the band filling for a cubic lattice.

At this stage, it should be remarked that, as to be discussed in the spin-fluctuation section, inclusion of  $1/N^2$  terms in the Anderson lattice theories leads to a qualitatively different picture. Moreover, Millis (1987) has shown that the normal state  $T^3 \ln T$  correction to the specific heat in these theories are two orders of magnitude too small to explain the experimental data in  $\text{UPt}_3$ . In the Hubbard model approach, Rasul (1991) has shown that order  $1/N^2$  corrections actually lead to a repulsive interaction, so conclusions at the  $1/N$  level must be regarded with some suspicion.

Another possible pairing mechanism involves shape fluctuations of the charge. Quadrupolar interactions are known to be important in many f electron systems, but the investigation of these effects in heavy-fermion metals is still at an early stage. One possible scenario is an exchange of quadrupolar fluctuations, but such a theory has not been developed to the authors' knowledge. Cox (1987) has suggested that some of the unusual properties of metals such as  $\text{UPe}_{13}$  may be understandable in terms of a quadrupolar Kondo effect. Recently, he has suggested that this interaction can induce local on-site pairing (Cox, unpublished). Symmetries of gap functions for various heavy-fermion superconductors were determined, although these assignments depend crucially on the assumed partial waves of the conduction electrons and the assumed crystal field (doublet) ground state of the U ion. Although this theory shows great promise, it is still at too early a stage of development for us to judge its ultimate success.

### 4.3. Spin fluctuations

Since the discovery of the uranium-based heavy-fermion superconductors, it has been suspected that spin fluctuations are the pairing mechanism (Anderson 1984). Over the years, this belief has been re-enforced by the observations that followed in  $\text{UPt}_3$ ,  $\text{UPe}_{13}$ ,  $\text{URu}_2\text{Si}_2$  and  $\text{CeCu}_2\text{Si}_2$ , and more recently in  $\text{UNi}_2\text{Al}_3$  and  $\text{UPd}_2\text{Al}_3$ : (1) nearness to a strong magnetic instability, which can be induced by doping, (2) coexistence of small moment magnetism and superconductivity, and (3) anisotropic superconductivity (nodes in the gap function), along with strong evidence that the order parameter is coming from a non-trivial group representation ( $\text{UPt}_3$  and  $\text{UPe}_{13}$ ). All these properties bear a strong resemblance to  $^3\text{He}$ , which can be described with a spin fluctuation pairing model (Levin and Valls 1983).

The first approach taken was to describe heavy fermions in an analogous way to  $^3\text{He}$ , that is by estimating Landau scattering amplitudes and using this to estimate  $T_c$ , calculate the pressure dependence of normal and superconducting state properties, etc. Early models, based as they were on  $^3\text{He}$  methods, naturally led to p-wave pairing (Valls and Tesanovic 1984, Bedell and Quadar 1985, Fay and Appel 1985, Pethick

et al. 1986). In particular, Pethick et al. (1986) were able to demonstrate that their calculated  $T_c$  decreased with pressure for  $\text{UPt}_3$ , just as seen experimentally, even though their effective Fermi energy increases with pressure (which it must since  $\gamma$  decreases with pressure). Despite this nice success, basic problems exist with these theories: they are effective one band models which (1) ignore the multi-sheeted nature of the Fermi surface, (2) ignore the degeneracy and spatial anisotropy of the  $f$  levels, and (3) do not include spin-orbit coupling. The problem is quite important, since neutron scattering up to now has not seen the quasiparticle (intra-band) contribution to the susceptibility, which for  $^3\text{He}$  saturates the susceptibility. What is seen is a Van Vleck part which is outside the bounds of these theories. Moreover, in  $^3\text{He}$ ,  $\gamma$  scales with the logarithm of  $\chi$ , whereas in heavy fermions,  $\gamma$  scales with  $\chi$ . As discussed previously for  $\text{UPt}_3$ , such a difference can be accounted for by taking into account the Van Vleck nature of the susceptibility (Konno and Moriya 1987, Norman 1988). A very lucid discussion of the qualitative differences between  $^3\text{He}$  and heavy fermions can be found in Varma (1985).

An alternate Fermi liquid approach is to treat the problem in the slave-boson scheme. Spin fluctuation can be recovered either (1) by going to order  $1/N^2$  (Houghton et al. 1988, Kaga and Yoshida 1988, 1989) in an Anderson lattice model, or (2) by expanding around a saddle point which reproduces the Gutzwiller mean field solution (Kotliar and Ruckenstein 1986) in the Hubbard model. In the first method, the spin fluctuations show up as an RKKY interaction [related approaches are discussed by Zhang et al. (1987), Ohkawa and Yamamoto (1987), Evans and Gehring (1989) and Coleman and Andrei (1989)]. In the second method, the spin and charge fluctuations both appear at order  $1/N$ . This model does well for both normal-state properties (Rasul and Li 1988) and superconducting-state properties (Rasul et al. 1989) of  $^3\text{He}$ , so an application to heavy-fermion systems would be highly desirable. The basic conclusion from both methods is that (1) the spin fluctuation part dominates over the charge fluctuation part for pairing, and (2) either p-wave or d-wave pairing is possible depending on parameters. The basic problem with these theories is that they have not been applied to a realistic model of a heavy-fermion superconductor, so their ultimate success remains to be determined.

The final approach used for spin fluctuations is a semi-phenomenological theory which takes the observed dynamic susceptibility, uses this as a model to construct a pair potential, and then tries to solve for  $T_c$  for real systems. This approach was first advocated by Miyake et al. (1986), who observed that the spin fluctuations in heavy fermions were of an antiferromagnetic nature, as opposed to the ferromagnetic nature seen in  $^3\text{He}$ . This leads to d-wave pairing for a simple lattice [see Scalapino et al. (1986, 1987) and Béal-Monod et al. (1986) for related approaches]. A nice review of the physics behind these models can be found in Pethick and Pines (1987), which is highly recommended reading.

The linearized gap equation in this model is

$$\Delta(\mathbf{k}) = \sum V(\mathbf{k} - \mathbf{k}') \Delta(\mathbf{k}') / \varepsilon_{\mathbf{k}'} \tanh(\varepsilon_{\mathbf{k}'}/2T_c),$$

where  $\Delta$  is the gap function,  $\varepsilon$  the quasiparticle energies, and  $V$  the pair potential (assumed to be proportional to  $\chi$ ). The approach was then generalized to include the

frequency dependence of the pair interaction by Norman (1987, 1988) and by Millis et al. (1988), which is necessary to set the temperature scale for  $T_c$  (Millis et al. also discuss the importance of pair-breaking effects in anisotropic superconductors). Using a simplified model of the susceptibility and the Fermi surface, order parameters were calculated for both  $\text{UPt}_3$  and  $\text{UPt}_3$  by Norman. The actual observed momentum dependence of the dynamic susceptibility for  $\text{UPt}_3$  (Aeppli et al. 1987, Goldman et al. 1987, Frings et al. 1988) was fit by Putikka and Joynt (1988, 1989) and then used to determine an  $E_{1g}$  (d-wave) gap function for hcp  $\text{UPt}_3$  (this susceptibility has an energy scale of 5 meV and is due to antiferromagnetic correlations between near-neighbor atoms in neighboring planes). Such a gap function has both a nodal structure (line and point nodes) and a group representation (two-dimensional) consistent with a large body of experimental data for  $\text{UPt}_3$  in the superconducting state.

Unfortunately, at this point, the actual complexities of  $\text{UPt}_3$  became apparent.  $\text{UPt}_3$  is a non-symmorphic lattice (two atoms per unit cell, separated by a non-primitive translation vector). Because of this, the observed dynamic susceptibility is not invariant under reciprocal lattice translations (ignoring form factors, it has a periodicity of two reciprocal lattice vectors in the  $c$  direction and three in the basal direction, due to the non-primitive translation vector). Using this susceptibility in a gap equation, then, gives gap functions which are not properly lattice periodic. Thus both the solutions of Norman and of Putikka and Joynt are invalid.

Several ways have been proposed to get around this problem, none of them completely satisfactory. The susceptibility of Putikka and Joynt was of the form  $U + J \text{Re}(\phi)$  where  $\phi(\mathbf{q})$  is equal to  $\sum e^{i\mathbf{q}\cdot\mathbf{r}}$  with  $\mathbf{r}$  being vectors connecting near-neighbor atoms to the first U site in the unit cell. Only the real part enters since  $\phi^*$  is obtained when summing relative to the second site, and thus the total sum in the cell is  $\phi + \phi^* = 2 \text{Re}(\phi)$ . Since  $\text{Re}(\phi)$  is not invariant under a reciprocal lattice translation, the first proposal was to generalize the gap equations to include the umklapp processes (Norman 1989, Monien and Pethick, unpublished)

$$\Delta(\mathbf{k}) = -\ln(1.13\Gamma/T_c) \sum V(\mathbf{k} - \mathbf{k}' - \mathbf{Q}) \Delta(\mathbf{k}')$$

where  $\mathbf{k}$  and  $\mathbf{k}'$  are restricted to the first zone,  $\mathbf{Q}$  are reciprocal lattice vectors, and  $\Gamma$  is the neutron scattering linewidth (energy scale). The cut-off in the  $\mathbf{Q}$  sum is achieved by including the form factor of the f electron in the susceptibility. The calculated gap function is of the  $A_{1u}$  (p-wave) representation (line nodes), with the second highest  $T_c$  solution being in the  $E_{1u}$  (p-wave) representation (point nodes), where it was assumed that the order parameter  $d$  vector ( $\mathbf{d}\cdot\mathbf{S} = 0$ ,  $\mathbf{S}$  being the spin vector of the Cooper pairs) was orientated along the  $c$  axis. An odd parity state is obtained since the effective pair potential peaks at  $q=0$  ( $\chi$  peaks at a reciprocal lattice vector, which is an umklapp scattering from  $q=0$ ). In fact, the susceptibility in such a formalism should be a matrix in reciprocal lattice space, so the above equation has several implicit assumptions in it, whose validity have yet to be established.

A second approach is to treat the susceptibility as a  $2 \times 2$  matrix, with the indices referring to the two uranium sites in the unit cell (Broholm 1988, Norman 1990). In such a model,  $\chi_{11} = \chi_{22} = U$ , and  $\chi_{12} = \chi_{21}^* = J\phi$ . Summing all four terms would

recover the Putikka and Joynt form. Diagonalizing this matrix would lead to two eigenvalues,  $U \pm J|\phi|$ , both of which are lattice periodic. The proposal, then, was to use either eigenvalue as a pair potential (in the actual theory, it is the moment–moment response function,  $I$ , which takes this form, and an RPA series is summed to get either  $\chi$  or  $V$ , as in  $^3\text{He}$  theory). The decision to use each pair potential separately, of course, is an assumption. In the model of Monien and Pethick, it is the sum that is used [thus for the simple Putikka and Joynt model, the AF correlations between planes drops out of the pair potential, i.e.  $(U + J|\phi|) + (U - J|\phi|) = 2U$ ]. In the model proposed by Konno and Ueda (1989), the combination of the two pair potentials depends on the relative phase between the two atoms in the unit cell for each particular energy band and  $k$  point involved. Thus, the only way to apply such a model is to take into account the radial/angular character of the quasiparticle wavefunctions over the Fermi surface into account. If one is going to do this, one might as well include them from the beginning when Fourier-transforming the pair interaction from real space. This is a complicated procedure, and so no full solution to this problem exists at present.

If, though, one uses these two pair potentials independently, one finds the same  $T_c$  ordering of solutions as with the umklapp method. This occurs because the two pair potentials (corresponding to an acoustic and optic branch) are essentially a foldback of the susceptibility into the first zone. Thus, the peak in  $\chi$  at the reciprocal lattice vector  $\mathbf{Q} = (0, 0, 1)$  corresponds to a peak in the optic branch at  $q = 0$ , and so one obtains again odd parity solutions with  $A_{1u}$  the highest and  $E_{1u}$  the next highest. An additional feature of these calculations occurs if one takes into account the anisotropy of the susceptibility (i.e. the  $^3\text{He}$  form of the pair potential,  $V_s \cdot s$ , is replaced by  $V_{ij} s_i s_j$  where  $s$  are Pauli matrices, and  $i, j$  are cartesian indices). Since the AF correlations are only present in the  $\chi_{xx}$  and  $\chi_{yy}$  components of the susceptibility, it turns out that the order parameter  $d$  vector is locked to the  $c$  axis since  $V_{xx} = V_{yy}$  and  $V_{zz}$  drops out of the gap equation since it is a constant. This is equivalent to saying that the spin vector of the Cooper pairs is confined to the basal plane, just as observed for the normal-state spin fluctuations (note, since the pair potential allows only one component of the vector order parameter, line node solutions are possible). In  $^3\text{He}$ , these effects are only picked up when including higher-order (strong coupling) corrections, but here they are obtained at the weak coupling level because the susceptibility is already anisotropic in the normal state. One can also get more sophisticated by including the intrinsic ferromagnetic correlations between next-neighbor atoms in the plane (Goldman et al. 1987). Including this effect leads to  $E_{1u}$  being the highest  $T_c$  solution (Norman 1991a). This solution has two desirable properties: (1) it is a two-dimensional group representation, and thus can explain the highly complicated phase diagram in the  $H$ – $T$  plane of superconducting  $\text{UPt}_3$ , and (2) it is an odd parity solution with the order parameter vector locked to the  $c$  axis. The latter property can be used to explain the observed anisotropy in the  $H_{c2}$  phase line (Choi and Sauls 1991). Unfortunately, the solution has point nodes, whereas thermodynamic data indicate line nodes. The  $E_{2u}$  solution, which has all three desirable properties, has a very low  $T_c$  in this formalism relative to  $E_{1u}$ .

These problems led us to consider pairing via low-frequency fluctuations (Norman

1990), which peak at  $\mathbf{Q}=(0.5, 0, n)$ , with an elastic component connected to the observed weak magnetic ordering (Aeppli et al. 1988, Frings et al. 1988). These fluctuations correspond to AF correlations in the plane, and F correlations between planes, as opposed to the high frequency fluctuations, which are F in the plane and AF between planes. The disadvantages of these fluctuations over the high-frequency ones are (1) a smaller spectral weight (Aeppli et al. 1991), and (2) a lower energy scale [ $\Gamma(\mathbf{Q}) \sim 0.3$  meV]. An advantage is that their peak value at the above  $q$  vector is quite strong, being about five times the bulk susceptibility (Broholm 1988), as opposed to a much smaller peak value for the high-frequency ones. To obtain peaks in  $\chi$  at  $(0.5, 0, n)$  wavevectors requires including substantial basal plane anisotropy, taking into account the fact that the moments lie along certain directions in the basal plane (thus  $\chi_{xx}$  is not equal to  $\chi_{yy}$ , and a  $\chi_{xy}$  term must be included). The isotropic part of the interaction ( $V_{xx} + V_{yy}$ ) enters into the expression for singlet and  $M_S = 0$  triplet ( $d$  vector along  $c$ ) solutions, whereas the anisotropic term ( $V_{xx} - V_{yy}$ ,  $V_{xy}$ ) determines a new odd-parity solution with the  $d$  vector in the basal plane (note, the odd-parity solutions with  $d$  along  $c$  and  $d$  in the basal plane do not mix unless there is a  $V_{xz}$  or  $V_{yz}$  term). The isotropic term gives an even parity solution for the same reason as Miyake et al. (1986), that is the susceptibility peaks at the zone boundary. This solution is of  $A_{1g}$  form, which may be surprising since one would expect to get a “d-wave” solution.  $A_{1g}$  turns out to be preferred since it has no symmetry requirements on nodes, and thus the nodes of the gap function (which must be there because of the strong  $U$  term) are able to lie in the most favorable location so as to minimize the free energy (note, our gap functions are numerical and not restricted by assumed basis function forms as in earlier models). This is a general feature we have found, that is all models of pair potentials we have used for UPt<sub>3</sub> always gives an  $A_{1g}$  solution as the highest of even-parity solutions. It turns out, though, that the anisotropic term ( $V_{xx} - V_{yy}$ ) is so large that an odd-parity  $A_{1u}$  solution with the  $d$  vector in the basal plane has the highest  $T_c$ . This solution (transforming like  $k_x x + k_y y$ ) has neither the group representation, nodal structure, or  $d$  vector orientation to explain experimental data. As for the magnitude of  $T_c$ , it is comparable to that from pairing via the high-frequency spin fluctuations, since it is the bare line-width,  $\Gamma$ , which enters as an energy cut-off in the  $T_c$  expression, and not  $\Gamma(\mathbf{Q})$ .  $\Gamma$  turns out to be 5 meV, the same as for the high-frequency case, even though  $\Gamma(\mathbf{Q})$  at the AF  $\mathbf{Q}$  vector is quite small.

In conclusion, the spin fluctuation models have gone a long way beyond their <sup>3</sup>He counterparts. On the other hand, the theories do not give a gap function with which one is totally happy (see table 3), and the theories are still probably too simplistic for real heavy-fermion metals. First, they replace the complicated quasiparticle matrix elements, of the form  $\langle \mathbf{k}, -\mathbf{k} | V(\mathbf{r}, \mathbf{r}') | \mathbf{k}', -\mathbf{k}' \rangle$ , by a simplistic  $V(\mathbf{k} - \mathbf{k}')$  as used above (in fact, the ambiguities discussed above about the momentum dependence of the pair potential are all due to this simple replacement). Second, the vertex is treated as a product of Pauli (spin) matrices, as in <sup>3</sup>He, and completely ignores any orbital or spin-orbital contributions (in fact, the only thing included at this stage is the directional anisotropy terms in  $\chi$ ). Finally, the frequency dependences of the pair interaction, the quasiparticle dispersions, and the gap function have been treated in

TABLE 3

Calculated symmetry of the gap function for  $U\text{Pt}_3$  from the semi-phenomenological spin fluctuation theory assuming pairing by either high-frequency spin fluctuations ( $\Gamma \sim 5 \text{ meV}$ ) or low-frequency spin fluctuations [ $\Gamma(Q) \sim 0.3 \text{ meV}$ ]. Tabulated is the group representation, the functional form that the order parameter transforms under group operations (the actual order parameter is determined numerically), and the nodal structure. Note that two possible solutions are found for high- $\omega$  pairing depending on the ratio of near-neighbor to next-near-neighbor interactions. Also listed are the two most likely order parameters from phenomenological fits to experimental data.

	Rep.	Form	Nodes
Theory (high $\omega$ )	$A_{1u}$	$k_z z$	line
	$E_{1u}$	$(k_x \pm ik_y)z$	point
Theory (low $\omega$ )	$A_{1u}$	$k_x x + k_y y$	point
	$E_{1g}$	$k_z(k_x \pm ik_y)$	line, point
Experiment (?)	$E_{1g}$	$k_z(k_x \pm ik_y)$	line, point
	$E_{2u}$	$k_z(k_x \pm ik_y)^2 z$	line, point

a highly simplistic fashion. Any of these effects could lead to a qualitative change in the solutions found. For instance, the fact that odd-parity solutions are found for AF correlations between planes may be a total artifact of the assumptions made on the matrix elements mentioned above. The problem, of course, is that a simple theory ( $U$  on-site,  $J$  between sites) may no longer be sufficient once one decides to include matrix element effects, and one is thus forced to work with a truly microscopic model, as opposed to the semi-phenomenological assumptions of the current models.

Thus, the problem of heavy-fermion superconductors is far from being solved, although we feel at this stage that a spin fluctuation approach has the correct physics for constructing the “ultimate” theory. A likely scenario is one that uses the semi-phenomenological developments as a guide to construct a more realistic Kondo lattice theory. We might note that the dynamic susceptibility calculated from a slave-boson approach has many things in common with the experimentally observed neutron scattering data (Auerbach et al. 1988), although as emphasized repeatedly by Varma, an intrinsic multi-site approach is probably necessary to get an adequate description of the moment–moment response function (Varma 1991). Given an adequate microscopic theory for the dynamic susceptibility, a pairing self-energy can be constructed and a proper strong-coupling gap equation solved. The resulting solution will then give us some guidance about the validity of a spin fluctuation treatment, and whether it should be pursued or abandoned in favor of a more promising theory, possibly based on quadrupolar or inter-site phonon exchange.

## 5. Conclusions

Density functional formalism, including using the LDA, works quite well for the very itinerant f electron metals such as  $UGe_3$ ,  $URh_3$  and  $UIr_3$ . One expects it to work equally well for  $CeRh_3$  and  $URu_3$  since they also have very itinerant f electrons.

Even the strongly enhanced metals  $\text{CeSn}_3$  and  $\text{UPt}_3$  are well described – with regard to Fermi surface topology. But there is room for improvement in numerous cases. There are three basic concerns: large mass enhancements, magnetic moments and localization.

*Enhancements:* In the strongly enhanced materials, approximating the quasi-particle masses by the density functional band masses fails dramatically. One of the interesting aspects of the  $L1_2$  structured materials is that they offer sufficient examples to be able to see the mass enhancements grow (i.e. this approximation breaks down) as the f states become more localized and then diminish with the advent of antiferromagnetism. Magnetic fluctuation derived enhancements have been successfully calculated for a number of strongly enhanced materials. In seeking to develop a band structure reflecting the quasiparticle spectrum, the renormalized band structures start from DF-LDA results and phenomenologically incorporate the enhancements. The successes of the renormalized band structures are a clear indication of the accuracy of the DF-LDA charge densities even for these strongly enhanced materials. Thus, the observation of large enhancement factors alone should not be interpreted as a failure of DF-LDA but merely the indication that self-energy (excited state) effects are important.

*Moments:* For magnetically polarized metals, although the LSDA appears to work well for some materials ( $\text{Gd}$ ,  $\text{UCu}_5$ ,  $\text{NpSn}_3$ ), it predicts sizable moments for  $\text{USn}_3$  and  $\text{UBe}_{13}$  where none exist. It also predicts large moments for  $\text{UPt}_3$  and  $\text{URu}_2\text{Si}_2$  which actually have very small moments. There are several concerns that make the calculation of moments less secure. (1) The basic functionals to be used for the spin dependence are less well known (the overtendency to magnetism may be due to the fact that Kondo-like correlations are not included in the LSD functional). (2) The local approximation is even less valid for the spin dependence than for the charge dependence. (3) The only orbital contributions incorporated within the LSDA are those induced by spin-orbit coupling (note the discussion of  $\text{Gd}$ ). Consequently, the moments of lanthanide materials which have sizable orbital moment contributions ( $\gamma\text{-Ce}$ ,  $\text{TmSe}$ ) are poorly determined. This failure is largely a result of improper treatment of Hund's rule effects by LSDA. It can be remedied either by going to an open-shell Hartree-Fock formalism, or by using the Hartree-Fock formalism as a guide to construct a correction to the LSDA. There have now been enough successful applications of this approach to give it considerable credibility.

*Localization:* The pervasive question for f electron materials is: "Under what circumstances do the f electrons behave as itinerant or as localized in the ground state?" Localization occurs when the energy gain from Coulomb  $U$  and Hund's rule effects exceeds the kinetic energy gain achieved through hybridization. Unfortunately, it is not clear how well current ab initio methods treat these localizing effects for realistic solids. Thus, we are forced to resort to ad hoc schemes to properly describe localized systems. As examples, for  $\text{Pr}$  or for  $\text{UPd}_3$ , one artificially localizes the f electrons in the core (i.e. manually suppresses the hybridization) to obtain a good representation of the Fermi surface. But such an approach is not always appropriate.  $\text{Gd}$  should fit the requirements of the f core model, yet continuing to incorporate the f states in the band structure is necessary to understand the minority carrier

Fermi surface. And for  $\text{CeB}_6$ , while the topology of the Fermi surface is generally consistent with an  $f$  core model, (1) the observed extremal areas are larger than allowed by an  $f$  core model, and (2) one finds a mass enhancement of 50 implying  $f$  orbital involvement in the conduction bands. Similarly, for  $\text{CeAl}_2$   $f$  core modelling is approximately correct but not correct in detail. In a related way, neither an  $f$  core nor an  $f$  band treatment appears to work for  $\text{CeCu}_6$ . This metal may satisfy the conditions discussed by Zwicknagl where all the  $f$  states but the ground state one are effectively projected out if the crystal field splitting of the ground state multiplet is larger than the effective Kondo temperature. A related projector method was used by Kasuya's group to get a good representation of the Fermi surface of  $\text{CeSb}$  suggesting that projection onto the suspected crystal field ground state may also work for  $\text{CeB}_6$ ,  $\text{CeAl}_2$  and  $\text{CeCu}_6$ . (It should be remembered that the occupied and unoccupied  $f$  levels in  $\text{CeSb}$  were shifted to lie where they would be in an Anderson model – i.e. several eV away from the Fermi energy.) Incorporation of Hund's rule effects might provide the basis for this effective projection.

Several improvements to density functional formalism would help clarify the situation for localized materials although very possibly not resolve it. (1) Improvements discussed for the moments apply as well for localization. After all, the question of localization and moment formation is highly intertwined in these metals. (2) Self-interaction corrections (a way of including  $U$  effects in LDA) act to further localize the more local orbitals. SIC would also reduce the tendency of the LDA to overbond the higher  $\ell$  orbitals. SIC also acts to provide an energy separation between occupied and unoccupied states that are often incorporated in phenomenological descriptions. With all these desirable features, it is unfortunate that there are serious unsolved conceptual issues when applying it to solids [there has been a recent application of this method, though, to Pr metal: Szotek et al. (1991)]. (3) Further correlations due to the strong intra-atomic Coulomb interactions could be significant. Anderson model results indicate that the closer restriction to  $f$  orbital integral occupation would significantly reduce the  $f$  level broadening due to hybridization.

Each of the improvements which could probably be incorporated into a density functional formalism would act to permit greater localization with reduced hybridization. But would it be enough? Localized states are particularly difficult to describe in an *ab initio* formalism, not being possible even at the level of Hartree–Fock, for example. The issue of how far one can get with the evolutionary improvements discussed above and when one must seek a new approach (such as a slave-boson treatment of the Anderson model using realistic parameters determined by DF-LDA) is a very real one. Despite some progress, there is yet no definitive way from any *ab initio* calculation to determine whether the  $f$  states will behave as an  $f$  band metal or as an  $f$  core one. Until this can be done, we will not have truly understood the  $f$  electron problem.

Finally, we would also like to say that after more than a decade's worth of work, the origin of superconductivity of heavy-fermion metals is still a mystery. It will probably remain a mystery until we get a truly rigorous understanding of the normal ground state of these metals.



## References

- Ackermann, X., R. Feder and E. Tamura, 1984, *J. Phys. F* **14**, L173.
- Aeppli, G., A. Goldman, G. Shirane, E. Bucher and M.-Ch. Lux-Steiner, 1987, *Phys. Rev. Lett.* **58**, 808.
- Aeppli, G., E. Bucher, C. Broholm, J.K. Kjems, J. Baumann and J. Hufnagl, 1988, *Phys. Rev. Lett.* **60**, 615.
- Aeppli, G., C. Broholm, E. Bucher and D.J. Bishop, 1991, *Physica B* **171**, 278.
- Albers, R.C., A.M. Boring and N.E. Christensen, 1986, *Phys. Rev. B* **33**, 8116.
- Aldred, A.T., B.D. Dunlap, D.J. Lam and I. Nowik, 1974, *Phys. Rev. B* **10**, 1011.
- Aldred, A.T., D.J. Lam, A.R. Harvey and B.D. Dunlap, 1975, *Phys. Rev. B* **11**, 1169.
- Aldred, A.T., B.D. Dunlap and G.H. Lander, 1976, *Phys. Rev. B* **14**, 1276.
- Allen, J.W., S.-J. Oh, I. Lindau, J.M. Lawrence, L.I. Johansson and S.B. Hagström, 1981, *Phys. Rev. Lett.* **46**, 1100.
- Amato, A., D. Jaccard, J. Flouquet, F. Lapierre, J.L. Tholence, R.A. Fisher, S.E. Lacy, J.A. Olsen and N.E. Phillips, 1987, *J. Low Temp. Phys.* **68**, 371.
- Andersen, O.K., 1975, *Phys. Rev. B* **12**, 3060.
- Anderson, P.W., 1984, *Phys. Rev. B* **30**, 1549.
- Andres, K., J.E. Graebner and H.R. Ott, 1975, *Phys. Rev. Lett.* **35**, 1779.
- Andres, K., D. Davidov, P. Dernier, F. Hsu, W.A. Reed and G.J. Nieuwenhuys, 1978, *Solid State Commun.* **28**, 405.
- Aoki, H., G.W. Crabtree, W. Joss and F. Hulliger, 1985a, *J. Appl. Phys.* **57**, 3033.
- Aoki, H., G.W. Crabtree, W. Joss and F. Hulliger, 1985b, *J. Magn. & Magn. Mater.* **52**, 389.
- Aoki, H., G.W. Crabtree, W. Joss and F. Hulliger, 1991, *J. Magn. & Magn. Mater.* **97**, 169.
- Arko, A.J., 1977, in: *Proc. Int. Conf. on the Electronic Structure of the Actinides*, eds J. Mulak, W. Suski and R. Troc (Ossolineum, Wroclaw, Poland) p. 309.
- Arko, A.J., and D.D. Koelling, 1978, *Phys. Rev. B* **17**, 3104.
- Arko, A.J., M.B. Brodsky, G.W. Crabtree, D.P. Karim, D.D. Koelling and L.R. Windmiller, 1975, *Phys. Rev. B* **12**, 4102.
- Arko, A.J., D.D. Koelling and J.E. Schirber, 1985, in: *Handbook of the Physics and Chemistry of the Actinides*, Vol. 2, eds A.J. Freeman and G.H. Lander (North-Holland, Amsterdam) p. 175.
- Arko, A.J., B.W. Yates, B.D. Dunlap, D.D. Koelling, A.W. Mitchell, D.J. Lam, C.G. Olson, M. del Giudice, Z. Fisk and J.L. Smith, 1987, in: *Theoretical and Experimental Aspects of Valence Fluctuations and Heavy Fermions*, eds L.C. Gupta and S.K. Malik (Plenum, New York) p. 39.
- Arko, A.J., D.D. Koelling, B.D. Dunlap, C. Capasso and M. Del Giudice, 1989, *J. Less-Common Met.* **48**, 133.
- Auerbach, A., and K. Levin, 1986, *Phys. Rev. Lett.* **57**, 877.
- Auerbach, A., J.H. Kim, K. Levin and M.R. Norman, 1988, *Phys. Rev. Lett.* **60**, 623.
- Bader, S.D., N.E. Phillips and D.B. McWhan, 1973, *Phys. Rev. B* **7**, 4686.
- Baer, Y., H.R. Ott and K. Andres, 1980, *Solid State Commun.* **36**, 387.
- Barbara, B., M.F. Rossignol, J.X. Boucherle, J. Schweizer and J.L. Buevoz, 1979, *J. Appl. Phys.* **50**, 2300.
- Barberia, G.E., B. Roden, P. Weidner, L.C. Gupta, D. Davidov and I. Felner, 1982, *Solid State Commun.* **42**, 659.
- Bauminger, E.R., I. Felner, D. Froindlich, D. Levron, I. Nowik, S. Ofer and Y. Yanovsky, 1974, *J. Phys. Paris Colloq.* **C6**, 61.
- Béal-Monod, M.T., C. Bourbonnais and V.J. Emery, 1986, *Phys. Rev. B* **34**, 7716.
- Bedell, K.S., and K.F. Quadar, 1985, *Phys. Rev. B* **32**, 3296.
- Berton, A., J. Chaussy, B. Cornut, J. Flouquet, J. Odin, J. Peyrard and F. Holtzberg, 1981, *Phys. Rev. B* **23**, 3504.
- Besnus, M.J., P. Lehmann and A. Meyer, 1987, *J. Magn. & Magn. Mater.* **63-64**, 323.
- Boppart, H., 1985, *J. Magn. & Magn. Mater.* **47-48**, 436.
- Boring, A.M., R.C. Albers, G.R. Stewart and D.D. Koelling, 1985, *Phys. Rev. B* **31**, 3251.
- Brailsford, A.D., 1966, *Phys. Rev.* **149**, 456.
- Bredl, C.D., 1987, *J. Magn. & Magn. Mater.* **63-64**, 355.
- Bredl, C.D., F. Steglich and K.D. Schotte, 1978, *Z. Phys. B* **29**, 327.
- Bredl, C.D., W. Lieke, R. Schefzyk, M. Lang, U. Rauchschwalbe, F. Steglich, J.C.P. Klaasse, J. Aarts and F.R. de Boer, 1985, *J. Magn. & Magn. Mater.* **47-48**, 30.
- Brodsky, M.B., 1978, *Rep. Prog. Phys.* **41**, 1547.
- Brodsky, M.B., and N.J. Bridger, 1974, in: *Magnetism and Magnetic Materials - 1973*, eds C.D. Graham Jr and J.J. Rhyne (AIP, New York) p. 357.

- Broholm, C., 1988, Thesis (Risø National Laboratory).
- Broholm, C., J.K. Kjems, W.J.L. Buyers, P. Matthews, T.T.M. Palstra, A.A. Menovsky and J.A. Mydosh, 1987, *Phys. Rev. Lett.* **58**, 1467.
- Broholm, C., H. Lin, P.T. Matthews, T.E. Mason, W.J.L. Buyers, M.F. Collins, A.A. Menovsky, J.A. Mydosh and J.K. Kjems, 1991, *Phys. Rev. B* **43**, 12809.
- Brooks, M.S.S., O. Eriksson, B. Johansson, J.J.M. Franse and P.H. Frings, 1988, *J. Phys. F* **18**, L33.
- Bruls, G., W. Joss, U. Welp, H.R. Ott, Z. Fisk, G. Cors and M. Karkut, 1987, *J. Magn. & Magn. Mater.* **63-64**, 181.
- Buschow, K.H.J., and H.J. van Daal, 1971, *AIP Conf. Proc.* **5**, 1464.
- Buyers, W.J.L., and T.M. Holden, 1985, in: *Handbook on the Physics and Chemistry of the Actinides*, Vol. 2, eds A.J. Freeman and G.H. Lander (North-Holland, Amsterdam) p. 239.
- Chakravarthy, R., S.K. Paranjpe, M.R.L.N. Murthy, L.M. Rao and N.S.S. Murthy, 1985, *Phys. Status Solidi A* **88**, K155.
- Chapman, S., M. Hunt, P. Meeson, P.H.P. Reinders, M. Springford and M.R. Norman, 1990, *J. Phys.: Condens. Matter* **2**, 8123.
- Chen, J.W., R.R. Hake, S.E. Lambert, M.B. Maple, C. Rossel, M.S. Torikachvili and K.N. Yang, 1985, *J. Appl. Phys.* **57**, 3090.
- Choi, C.H., and J.A. Sauls, 1991, *Phys. Rev. Lett.* **66**, 484.
- Christensen, N.E., O.K. Andersen, O. Gunnarsson and O. Jepsen, 1988, *J. Magn. & Magn. Mater.* **76-77**, 23.
- Coleman, P., and N. Andrei, 1989, *J. Phys.: Condens. Matter* **1**, 4057.
- Coleman, P., and J. Gan, 1991, *Physica B* **171**, 3.
- Cox, D.L., 1987, *Phys. Rev. Lett.* **59**, 1240.
- Crabtree, G.W., B.D. Dunlap and D.D. Koelling, 1985, *Physica B* **135**, 38.
- Crabtree, G.W., D.H. Dye, D.P. Karim, S.A. Campbell and J.B. Ketterson, 1987, *Phys. Rev. B* **35**, 1728.
- Dagens, L., 1978, *J. Phys. F* **8**, 2093.
- Dalichaouch, Y., M.B. Maple, M.S. Torikachvili and A.L. Giorgi, 1989, *Phys. Rev. B* **39**, 2423.
- De Visser, A., F.R. de Boer, A.A. Menovsky and J.J.M. Franse, 1987a, *Solid State Commun.* **64**, 527.
- De Visser, A., A. Menovsky and J.J.M. Franse, 1987b, *Physica B* **147**, 81.
- DeLong, L.E., M.B. Maple and M. Tovar, 1978, *Solid State Commun.* **26**, 469.
- Dhar, S.K., S.K. Malik and R. Vijayaraghavan, 1981, *Phys. Rev. B* **24**, 6182.
- Dimmock, J.O., and A.J. Freeman, 1964, *Phys. Rev. Lett.* **13**, 750.
- Dirkmaat, A.J., T. Endstra, E.A. Knetsch, A.A. Menovsky, G.J. Nieuwenhuys and J.A. Mydosh, 1992, *J. Magn. & Magn. Mater.*, to be published (I.C.M. 91).
- Dunlap, B.D., F.J. Litterst, S.K. Malik, H.A. Kierstead, G.W. Crabtree, W.K. Kwok, D.J. Lam and A.W. Mitchell, 1987, in: *Theoretical and Experimental Aspects of Valence Fluctuations and Heavy Fermions*, eds L.C. Gupta and S.K. Malik (Plenum, New York) p. 365.
- Dunlap, B.D., G.W. Crabtree, J.D. Jorgensen, H.A. Kierstead, D.D. Koelling, W.K. Kwok, D.J. Lam, S.K. Malik, A.W. Mitchell and S.C. Strite, 1989, *Phys. Rev. B* **39**, 5640.
- Duthie, J.C., and D.G. Pettifor, 1977, *Phys. Rev. Lett.* **38**, 564.
- Effantin, J.M., J. Rossat-Mignod, P. Burlet, H. Bartholin, S. Kunii and T. Kasuya, 1985, *J. Magn. & Magn. Mater.* **47-48**, 145.
- Elenbaas, R.A., C.J. Schinkel and C.J.M. van Deudekom, 1980, *J. Magn. & Magn. Mater.* **15-18**, 979.
- Engelsberg, S., 1978, *Phys. Rev. B* **18**, 966.
- Engelsberg, S., and G. Simpson, 1970, *Phys. Rev. B* **2**, 1657.
- Eriksson, O., B. Johansson, M.S.S. Brooks and H.L. Skriver, 1988a, *Phys. Rev. B* **38**, 12858.
- Eriksson, O., L. Nordström, M.S.S. Brooks and B. Johansson, 1988b, *Phys. Rev. Lett.* **60**, 2523.
- Eriksson, O., M.S.S. Brooks and B. Johansson, 1989a, *Phys. Rev. B* **39**, 13115.
- Eriksson, O., B. Johansson and M.S.S. Brooks, 1989b, *Phys. Rev. B* **40**, 9508.
- Eriksson, O., B. Johansson, M.S.S. Brooks and H.L. Skriver, 1989c, *Phys. Rev. B* **40**, 5647.
- Eriksson, O., B. Johansson, H.L. Skriver, J. Sjöström and M.S.S. Brooks, 1989d, *Phys. Rev. B* **40**, 5270.
- Eriksson, O., B. Johansson and M.S.S. Brooks, 1990a, *Phys. Rev. B* **41**, 7311.
- Eriksson, O., B. Johansson and M.S.S. Brooks, 1990b, *Phys. Rev. B* **41**, 9087, and references therein.
- Eriksson, O., B. Johansson and M.S.S. Brooks, 1990c, *Phys. Rev. B* **41**, 9095.
- Eriksson, O., B. Johansson and M.S.S. Brooks, 1990d, *J. Phys.: Condens. Matter* **2**, 1529.

- Evans, S.M.M., and G.A. Gehring, 1989, *J. Phys.: Condens. Matter* **1**, 10487.
- Fay, D., and J. Appel, 1985, *Phys. Rev. B* **32**, 6071.
- Felten, R., F. Steglich, G. Weber, H. Rietschel, F. Gompf, B. Renker and J. Beuers, 1986, *Europhys. Lett.* **2**, 323.
- Fenton, E.W., 1986, *Solid State Commun.* **60**, 351.
- Fenton, E.W., 1987, *Solid State Commun.* **64**, 897.
- Fournier, J.M., and R. Troć, 1985, in: *Handbook on the Physics and Chemistry of the Actinides*, Vol. 2, eds A.J. Freeman and G.H. Lander (North-Holland, Amsterdam) ch. 2.
- Fowler, M., and R.E. Prange, 1965, *Physics* **1**, 315.
- Freeman, A.J., B.I. Min and M.R. Norman, 1987, in: *Handbook on the Physics and Chemistry of Rare Earths*, Vol. 10, eds K.A. Gschneidner Jr, L. Eyring and S. Hufner (North-Holland, Amsterdam) p. 165.
- Frings, P., B. Renker and C. Vettier, 1987, *J. Magn. & Magn. Mater.* **63-64**, 202.
- Frings, P., B. Renker and C. Vettier, 1988, *Physica B* **151**, 499.
- Fulde, P., 1988, *J. Phys. F* **18**, 601.
- Fulde, P., and J. Jensen, 1983, *Phys. Rev. B* **27**, 4085.
- Fulde, P., J. Keller and G. Zwignagl, 1988, *Solid State Phys.* Vol. 41, eds H. Ehrenreich and D. Turnbull (Academic, New York) p. 1.
- Gardner, W.E., J. Penfold, T.F. Smith and I.R. Harris, 1972, *J. Phys. F* **2**, 133.
- Gaspari, G.D., and B.L. Gyorffy, 1972, *Phys. Rev. Lett.* **28**, 801.
- Godart, C., A.M. Umarji, L.C. Gupta and R. Vajayaraghavan, 1986, *Phys. Rev. B* **34**, 7733.
- Gold, A.V., 1968, in: *Solid State Physics*, Vol. I: *Electrons in Metals*, eds J.F. Cochran and R.F. Haering (Gordon & Breach, New York) p. 39.
- Goldman, A.I., G. Shirane, G. Aeppli, B. Batlogg and E. Bucher, 1986, *Phys. Rev. B* **34**, 6564.
- Goldman, A.I., G. Shirane, G. Aeppli, E. Bucher and J. Hufnagl, 1987, *Phys. Rev. B* **36**, 8523.
- Grobman, W.D., 1972, *Phys. Rev. B* **5**, 2924 and references therein.
- Guo, G.Y., 1990, *Physica B* **165-166**, 335.
- Haen, P., F. Lapierre, J.M. Mignot, R. Tournier and F. Holtzberg, 1979, *Phys. Rev. Lett.* **43**, 304.
- Haen, P., J. Flouquet, F. Lapierre, P. Lejay and G. Remenyi, 1987, *J. Low Temp. Phys.* **67**, 391.
- Harima, H., and A. Yanase, 1991, *J. Phys. Soc. Jpn.* **60**, 21.
- Harima, H., and A. Yanase, 1992, *J. Magn. & Magn. Mater.* (I.C.M. 91).
- Harima, H., O. Sakai, T. Kasuya and A. Yanase, 1988, *Solid State Commun.* **66**, 603.
- Harima, H., A. Yanase and A. Hasegawa, 1990, *J. Phys. Soc. Jpn.* **59**, 4054.
- Harmon, B.N., 1979, *J. Phys. Colloq. (Paris)* **40**, C5-65.
- Harmon, B.N., and A.J. Freeman, 1974, *Phys. Rev. B* **10**, 1979.
- Harris, I.R., M.R. Norman and W.E. Gardner, 1972, *J. Less-Common Met.* **29**, 299.
- Harris, J., 1984, in: *The Electronic Structure of Complex Systems*, eds P. Phariseau and W.M. Temmerman (Plenum, New York) p. 141.
- Hasegawa, A., 1980, *J. Phys. C* **13**, 6147.
- Hasegawa, A., 1982, in: *Crystalline Electric Field Effects in f-electron Magnetism*, eds R.P. Guertin, W. Suski and Z. Zolnierok (Plenum, New York) p. 201.
- Hasegawa, A., 1984, *J. Phys. Soc. Jpn.* **53**, 3929.
- Hasegawa, A., 1985, *J. Magn. & Magn. Mater.* **52**, 425.
- Hasegawa, A., and H. Yamagami, 1990, *J. Phys. Soc. Jpn.* **59**, 218.
- Hasegawa, A., and A. Yanase, 1977, *J. Phys. Soc. Jpn.* **42**, 492.
- Hasegawa, A., and A. Yanase, 1980a, *J. Phys. F* **10**, 847.
- Hasegawa, A., and A. Yanase, 1980b, *J. Phys. F* **10**, 2207.
- Hasegawa, A., and A. Yanase, 1987, *J. Phys. Soc. Jpn.* **56**, 3990.
- Hasegawa, A., H. Yamagami and H. Johbettoh, 1990, *J. Phys. Soc. Jpn.* **59**, 2457.
- Hill, H.H., 1970, in: *Proc. Plutonium 1970 and Other Actinides*, Santa Fe, NM, Nuclear Metallurgy Series, Vol. 17, ed. W.M. Miner (AIME, New York) p. 2.
- Hoffmann, K.R., S. Berko and B.J. Beaudry, 1982, in: *Positron Annihilation*, eds P.G. Coleman, S.C. Sharma and L.M. Diana (North-Holland, Amsterdam) p.325.
- Hohenberg, P., and W. Kohn, 1964, *Phys. Rev.* **136**, B864.
- Holland-Moritz, E., M. Loewenhaupt, W. Schmatz and D. Wohlleben, 1977, *Phys. Rev. Lett.* **38**, 983.
- Horn, S., E. Holland-Moritz, M. Loewenhaupt, F. Steglich, H. Scherer, A. Benoit and J. Flouquet, 1981, *Phys. Rev. B* **23**, 3171.
- Houghton, A., N. Read and H. Won, 1988, *Phys. Rev. B* **37**, 3782.
- Houmann, J.G., B.D. Rainford, J. Jensen and A.R. Mackintosh, 1979, *Phys. Rev. B* **20**, 1105.

- Hulliger, F., 1979, in: Handbook on the Physics and Chemistry of the Rare Earths, Vol. 4, eds K.A. Gschneidner Jr and L. Eyring (North-Holland, Amsterdam) p. 153.
- Hunt, M., P. Meeson, P.-A. Probst, P.H.P. Reinders, M. Springford, W. Assmus and W. Sun, 1990, *J. Phys.: Condens. Matter* **2**, 6859.
- Ikeda, K., and K.A. Gschneidner Jr, 1982, *Phys. Rev. B* **25**, 4623.
- Irvine, S.J.C., R.C. Young, D. Fort and D.W. Jones, 1978, *J. Phys. F* **8**, L269.
- Isikawa, Y., K. Mori, T. Mizushima, A. Fujii, H. Takeda and K. Sato, 1987, *J. Magn. & Magn. Mater.* **70**, 385.
- Jaccard, D., and J. Flouquet, 1985, *J. Magn. & Magn. Mater.* **47-48**, 45.
- Jansen, H.J.F., A.J. Freeman and R. Monnier, 1985, *Phys. Rev. B* **31**, 4092.
- Jansen, H.J.F., A.J. Freeman and R. Monnier, 1986, *Phys. Rev. B* **33**, 6785.
- Jarlborg, T., 1986, *Solid State Commun.* **57**, 683.
- Jarlborg, T., H.F. Braun and M. Peter, 1983, *Z. Phys. B* **52**, 295.
- Jarlborg, T., A.J. Freeman and D.D. Koelling, 1986, *J. Magn. & Magn. Mater.* **60**, 291.
- Jayaraman, A., V. Narayanamurti, E. Bucher and R.G. Maines, 1970, *Phys. Rev. Lett.* **25**, 1430.
- Johanson, W.R., G.W. Crabtree, A.S. Edelstein and O.D. McMasters, 1981a, *Phys. Rev. Lett.* **46**, 504.
- Johanson, W.R., G.W. Crabtree, D.D. Koelling, A.S. Edelstein and O.D. McMasters, 1981b, *J. Appl. Phys.* **52**, 2134.
- Johanson, W.R., G.W. Crabtree, A.S. Edelstein and O.D. McMasters, 1983, *J. Magn. & Magn. Mater.* **31-34**, 377.
- Johansson, B., O. Eriksson, M.S.S. Brooks and H.L. Skriver, 1986, *Phys. Scr. T* **13**, 65.
- Jones, R.O., and O. Gunnarsson, 1989, *Rev. Mod. Phys.* **61**, 689.
- Joss, W., and G.W. Crabtree, 1984, *Phys. Rev. B* **30**, 5646.
- Joss, W., L.N. Hall and G.W. Crabtree, 1984, *Phys. Rev. B* **30**, 5637.
- Joss, W., J.M. van Ruitenbeek, G.W. Crabtree, J.L. Tholence, A.P.J. van Deursen and Z. Fisk, 1987, *Phys. Rev. Lett.* **59**, 1609.
- Joss, W., J.M. van Ruitenbeek, G.W. Crabtree, J.L. Tholence, A.P.J. van Deursen and Z. Fisk, 1988, *J. Phys. Colloq. (Paris)* C8-747.
- Kaga, H., and T. Yoshida, 1988, *Phys. Rev. B* **38**, 12047.
- Kaga, H., and T. Yoshida, 1989, *Physica C* **159**, 727.
- Kalvius, G.M., S. Zwirner, U. Potzel, J. Moser, W. Potzel, F.J. Litterst, J. Gal and J.C. Spirlet, 1990, *Physica B* **163**, 487.
- Kappler, J.P., M.J. Besnus, E. Beaurepaire, A. Meyer, J. Sereni and G. Nieva, 1985, *J. Magn. & Magn. Mater.* **47-48**, 111.
- Kasuya, T., O. Sakai, J. Tanaka, H. Kitazawa and T. Suzuki, 1987, *J. Magn. & Magn. Mater.* **63-64**, 9.
- Kasuya, T., O. Sakai, H. Harima and M. Ikeda, 1988, *J. Magn. & Magn. Mater.* **76-77**, 46.
- Keeton, S.C., and T.L. Loucks, 1966, *Phys. Rev.* **146**, 429.
- Keller, J., R. Bulla and Th. Hohn, 1990, *Phys. Rev. B* **41**, 1878.
- Keller, R., G. Güntherodt, W.B. Holzapfel, M. Dietrich and F. Holtzberg, 1979, *Solid State Commun.* **29**, 753.
- Ketterson, J.B., D.D. Koelling, J.C. Shaw and L.R. Windmiller, 1975, *Phys. Rev. B* **11**, 1447 and references therein.
- King, C.A., and G.G. Lonzarich, 1991, *Physica B* **171**, 161.
- Kitazawa, H., T. Suzuki, M. Sera, I. Oguro, A. Yanase, A. Hasegawa and T. Kasuya, 1984, *J. Magn. & Magn. Mater.* **31-34**, 421.
- Kitazawa, H., Q.Z. Gao, H. Ishida, T. Suzuki, A. Hasegawa and T. Kasuya, 1985, *J. Magn. & Magn. Mater.* **52**, 286.
- Kitazawa, H., Y.S. Kwon, A. Oyamada, N. Takeda, H. Suzuki, S. Sakatsume, T. Satoh, T. Suzuki and T. Kasuya, 1988, *J. Magn. & Magn. Mater.* **76-77**, 40.
- Klaasse, J.C.P., R.T.W. Meijer and F.R. de Boer, 1980, *Solid State Commun.* **33**, 1001.
- Kletowski, Z., M. Gliniski and A. Hasegawa, 1987, *J. Phys. F* **17**, 993.
- Koelling, D.D., 1982, *Solid State Commun.* **43**, 247.
- Koelling, D.D., 1984, in: *The Electronic Structure of Complex Systems*, eds P. Phariseau and W.M. Temmerman (Plenum, New York) p. 183.
- Koelling, D.D., 1986, *Int. J. Quant. Chem.* **S20**, 377.
- Koelling, D.D., and B.N. Harmon, 1977, *J. Phys. C* **10**, 3107.
- Koelling, D.D., B.D. Dunlap and G.W. Crabtree, 1985, *Phys. Rev. B* **31**, 1966.
- Koenig, C., 1988, *Solid State Commun.* **68**, 727.
- Koenig, C., and M.A. Khan, 1988, *Phys. Rev. B* **38**, 5887.
- Kohn, W., and L.J. Sham, 1965, *Phys. Rev.* **140**, A1133.
- Konno, R., and T. Moriya, 1987, *J. Phys. Soc. Jpn.* **56**, 3270.

- Konno, R., and K. Ueda, 1989, *Phys. Rev. B* **40**, 4329.
- Kotliar, G., and J. Liu, 1988, *Phys. Rev. Lett.* **61**, 1784.
- Kotliar, G., and A.E. Ruckenstein, 1986, *Phys. Rev. Lett.* **57**, 1362.
- Krutzen, B.C.H., and F. Springelkamp, 1989, *J. Phys.* **1**, 8369.
- Kuentzler, R., S.K. Dhar, S.K. Malik, R. Vijayaraghavan and B. Coqblin, 1984, *Solid State Commun.* **50**, 145.
- Kurosawa, Y., I. Umehara, M. Kikuchi, N. Nagai, K. Sato and Y. Onuki, 1990, *J. Phys. Soc. Jpn.* **59**, 1545.
- Lander, G.H., J.F. Reddy, A. Delpalme and P.J. Brown, 1980, *Phys. Rev. Lett.* **44**, 603.
- Langford, H.D., W.M. Temmerman and G.A. Gehring, 1990, *J. Phys.* **2**, 559.
- Lassailly, Y., C. Vettier, F. Holtzberg, J. Flouquet, C.M.E. Zeyen and F. Lapierre, 1983, *Phys. Rev. B* **28**, 2880.
- Lavagna, M., A.J. Millis and P.A. Lee, 1987, *Phys. Rev. Lett.* **58**, 266.
- Lawrence, J., 1979, *Phys. Rev. B* **20**, 3770.
- Lee, P.A., T.M. Rice, J.W. Serene, L.J. Sham and J.W. Wilkins, 1986, *Comments on Cond. Matter Phys.* **12**, 99.
- Levin, K., and O.T. Valls, 1983, *Phys. Rep.* **98**, 1.
- Lifshitz, I.M., 1960, *Zh. Eksp. & Teor. Fiz.* **38**, 1569 [*Sov. Phys. JETP* **11**, 1130].
- Lifshitz, I.M., and A.M. Kosevich, 1956, *Sov. Phys. JETP* **2**, 636.
- Lin, C.L., J. Teter, J.E. Crow, T. Mihalisin, J. Brooks, A.I. Abou-Aly and G.R. Stewart, 1985a, *Phys. Rev. Lett.* **54**, 2541.
- Lin, C.L., L.W. Zhou, J.E. Crow and R.P. Guertin, 1985b, *J. Appl. Phys.* **57**, 3146.
- Lin, C.L., L.W. Zhou, C.S. Lee and J.E. Crow, 1985c, *J. Appl. Phys.* **57**, 3146.
- Lin, C.L., L.W. Zhou, J.E. Crow, R.P. Guertin and G.R. Stewart, 1986, *J. Magn. & Magn. Mater.* **54-57**, 391.
- Lin, C.L., J.E. Crow, T. Mihalisin and P. Schlottmann, 1987a, in: *Theoretical and Experimental Aspects of Valence Fluctuations and Heavy Fermions*, eds L.C. Gupta and S.K. Malik (Plenum, New York) p. 159.
- Lin, C.L., J.E. Crow, P. Schlottmann and T. Mihalisin, 1987b, *J. Appl. Phys.* **61**, 4376.
- Lin, C.L., L.W. Zhou, C.S. Lee, A. Wallash and J.E. Crow, 1987c, *J. Less-Common Met.* **133**, 67.
- Loret, B., B. Chevalier, B. Buffat, J. Étourneau, S. Quezel, A. Lamharrar, J. Rossat-Mignod, R. Calemczuk and E. Bonjour, 1987, *J. Magn. & Magn. Mater.* **63-64**, 85.
- Lonzarich, G.G., 1986, *J. Magn. & Magn. Mater.* **54-57**, 612.
- Lonzarich, G.G., 1988, *J. Magn. & Magn. Mater.* **76-77**, 1.
- Lowndes, D.H., K. Miller and M. Springford, 1970, *Phys. Rev. Lett.* **25**, 1111.
- Lu, Z.W., D.J. Singh and H. Krakauer, 1988, *Phys. Rev. B* **37**, 10045.
- Luttinger, J.M., 1960, *Phys. Rev.* **119**, 1153.
- Luttinger, J.M., 1961, *Phys. Rev.* **121**, 1251.
- MacDonald, A.H., W.E. Pickett and D.D. Koelling, 1980, *J. Phys. C* **13**, 2675.
- Maezawa, K., T. Kato, Y. Isikawa, K. Sato, I. Umehara, K. Sato, Y. Kurosawa and Y. Onuki, 1989, *J. Phys. Soc. Jpn.* **58**, 4098.
- Mann, E., 1971, *Phys. Kondens. Materie* **12**, 210.
- Maple, M.B., 1976, *Appl. Phys.* **9**, 179.
- Maple, M.B., J.W. Chen, Y. Dalichaouch, T. Kohara, C. Rossel, M.S. Torikachvili, M.W. Elfresh and J.D. Thompson, 1986, *Phys. Rev. Lett.* **56**, 185.
- Maple, M.B., Y. Dalichaouch, B.W. Lee, C.L. Seaman, P.K. Tsai, P.E. Armstrong, Z. Fisk, C. Rossel and M.S. Torikachvili, 1991, *Physica B* **171**, 219.
- Mason, T.E., and W.J.L. Buyers, 1991, *Phys. Rev. B* **43**, 11471.
- Mattocks, P.G., and R.C. Young, 1977, *J. Phys. F* **7**, 1219.
- Mearns, D., 1988, *Phys. Rev. B* **38**, 5906.
- Mearns, D., and W. Kohn, 1989, *Phys. Rev. B* **39**, 10669.
- Meijer, R.T.W., L.W. Roeland, F.R. de Boer and J.C.P. Klaasse, 1973, *Solid State Commun.* **12**, 93.
- Mermin, N.D., 1965, *Phys. Rev.* **137**, A1441.
- Mignot, J.-M., and J. Wittig, 1982, in: *Valence Instabilities*, eds P. Wachter and H. Boppert (North-Holland, Amsterdam).
- Mignot, J.-M., J. Flouquet, P. Haen, F. Lapierre, L. Puech and J. Voiron, 1988, *J. Magn. & Magn. Mater.* **76-77**, 97.
- Mihalisin, T., P. Scoboria and J.A. Ward, 1981, *Phys. Rev. Lett.* **46**, 862.
- Millis, A.J., 1987, *Phys. Rev. B* **36**, 5420.
- Millis, A.J., S. Sachdev and C.M. Varma, 1988, *Phys. Rev. B* **37**, 4975.
- Min, B.I., and Y.-R. Jang, 1991, *Phys. Rev. B* **44**, 13270.
- Min, B.I., H.J.F. Jansen, T. Oguchi and A.J. Freeman, 1986, *J. Magn. & Magn. Mater.* **61**, 139.
- Misemer, D.K., S. Auluck, S.I. Kobayashi and

- B.N. Harmon, 1984, *Solid State Commun.* **52**, 955.
- Miyake, K., and Y. Kuramoto, 1991, *Physica B* **171**, 20.
- Miyake, K., T. Matsuura, H. Jichu and Y. Nagaoka, 1984, *Prog. Theor. Phys.* **72**, 1063.
- Miyake, K., S. Schmitt-Rink and C.M. Varma, 1986, *Phys. Rev. B* **34**, 6554.
- Moller, H.B., S.M. Shapiro and R.J. Birgeneau, 1977, *Phys. Rev. Lett.* **39**, 1021.
- Monnier, R., H.J.F. Jansen and A.J. Freeman, 1985, *J. Less-Common Met.* **111**, 203.
- Moriya, T., 1987, in: *Metallic Magnetism*, ed. H. Capellmann (Springer, Berlin) p. 15.
- Murani, A.P., 1983, *Phys. Rev. B* **28**, 2308.
- Murasik, A., S. Ligenza and A. Zygmunt, 1974, *Phys. Status Solidi A* **23**, K163.
- Nakamura, H., Y. Kitaoka, K. Asayama and Y. Onuki, 1991, *Physica B* **171**, 329.
- Nakayama, K., and T. Moriya, 1987, *J. Phys. Soc. Jpn.* **56**, 2918.
- Nasu, S., A.M. vanDiepen, H.H. Newmann and R.S. Craig, 1971, *J. Phys. & Chem. Solids* **32**, 2773.
- Newns, D.M., 1987, *Phys. Rev. B* **36**, 2429.
- Ng, T.K., 1989, *Phys. Rev.* **39**, 9947.
- Nieuwenhuys, G.J., 1987, *Phys. Rev. B* **35**, 5260.
- Norman, M.R., 1987, *Phys. Rev. Lett.* **59**, 232.
- Norman, M.R., 1988, *Phys. Rev. B* **37**, 4987.
- Norman, M.R., 1989, *Phys. Rev. B* **39**, 7305.
- Norman, M.R., 1990, *Phys. Rev. B* **41**, 170.
- Norman, M.R., 1991a, *Phys. Rev. B* **43**, 6121.
- Norman, M.R., 1991b, *Phys. Rev. B* **44**, 1364.
- Norman, M.R., 1991c, *Int. J. Quant. Chem. S* **31**, 431.
- Norman, M.R., and A.J. Freeman, 1989, in: *The Challenge of d and f Electrons*, eds D.R. Salahub and M.C. Zerner (Am. Chem. Soc., Washington, DC) p. 273.
- Norman, M.R., and H.J.F. Jansen, 1988, *Phys. Rev. B* **37**, 10050.
- Norman, M.R., and D.D. Koelling, 1985, *Physica B* **135**, 95.
- Norman, M.R., and D.D. Koelling, 1986a, *Phys. Rev. B* **33**, 3803.
- Norman, M.R., and D.D. Koelling, 1986b, *Phys. Rev. B* **33**, 6730.
- Norman, M.R., and D.D. Koelling, 1987, *J. Less-Common Met.* **127**, 357.
- Norman, M.R., D.D. Koelling and A.J. Freeman, 1985, *Phys. Rev. B* **31**, 6251.
- Norman, M.R., S.D. Bader and H.A. Kierstead, 1986, *Phys. Rev. B* **33**, 8035.
- Norman, M.R., T. Oguchi and A.J. Freeman, 1987a, *J. Magn. & Magn. Mater.* **69**, 27.
- Norman, M.R., W.E. Pickett, H. Krakauer and C.S. Wang, 1987b, *Phys. Rev. B* **36**, 4058.
- Norman, M.R., R.C. Albers, A.M. Boring and N.E. Christensen, 1988a, *Solid State Commun.* **68**, 245.
- Norman, M.R., B.I. Min, T. Oguchi and A.J. Freeman, 1988b, *Phys. Rev. B* **38**, 6818.
- Norman, M.R., T. Oguchi and A.J. Freeman, 1988c, *Phys. Rev. B* **38**, 11193.
- Oguchi, T., and A.J. Freeman, 1985, *J. Magn. & Magn. Mater.* **52**, 174.
- Oguchi, T., and A.J. Freeman, 1986, *J. Magn. & Magn. Mater.* **61**, 233.
- Oguchi, T., A.J. Freeman and G.W. Crabtree, 1986, *Phys. Lett. A* **117**, 428.
- Ohkawa, F.J., 1984, *J. Phys. Soc. Jpn.* **53**, 3568.
- Ohkawa, F.J., and H. Fukuyama, 1984, *J. Phys. Soc. Jpn.* **53**, 4344.
- Ohkawa, F.J., and T. Yamamoto, 1987, *Physica B* **148**, 84.
- Onuki, Y., M. Nishihara, M. Sato and T. Komatsubara, 1985, *J. Magn. & Magn. Mater.* **52**, 317.
- Onuki, Y., M. Nishihara, Y. Fujimura and T. Komatsubara, 1986, *J. Phys. Soc. Jpn.* **55**, 21.
- Onuki, Y., M. Nishihara, Y. Fujimura, T. Yamazaki and T. Komatsubara, 1987a, *J. Magn. & Magn. Mater.* **63-64**, 317.
- Onuki, Y., T. Yamazaki, I. Ukon, T. Omi, K. Shibusani, T. Komatsubara, I. Sakamoto, Y. Sugiyama, R. Onodera, K. Yonemitsu, A. Umezawa, W.K. Kwok, G.W. Crabtree and D.G. Hinks, 1987b, *Physica B* **148**, 29.
- Onuki, Y., T. Yamazaki, I. Ukon, T. Komatsubara, H. Sato, Y. Sugiyama, I. Sakamoto and K. Yonemitsu, 1988, *J. Phys. (Paris) C* **8**, 481.
- Onuki, Y., T. Komatsubara, P.H.P. Reinders and M. Springford, 1989a, *J. Phys. Soc. Jpn.* **58**, 3698.
- Onuki, Y., Y. Kurosawa, K. Maezawa, I. Umehara, Y. Isikawa and K. Sato, 1989b, *J. Phys. Soc. Jpn.* **58**, 3705.
- Onuki, Y., A. Umezawa, W.K. Kwok, G.W. Crabtree, M. Nishihara, T. Yamazaki, T. Omi and T. Komatsubara, 1989c, *Phys. Rev. B* **40**, 11195.
- Onuki, Y., T. Komatsubara, P.H.P. Reinders and M. Springford, 1990a, *Physica B* **163**, 100.
- Onuki, Y., I. Umehara, Y. Kurosawa, N. Nagai,

- K. Satoh, M. Kasaya and F. Iga, 1990b, *J. Phys. Soc. Jpn.* **59**, 2320.
- Onuki, Y., I. Umehara, Y. Kurosawa, K. Satoh and H. Matsui, 1990c, *J. Phys. Soc. Jpn.* **59**, 229.
- Onuki, Y., I. Umehara, Y. Kurosawa, K. Satoh, H. Matsui, A. Hasegawa and H. Yamagami, 1990d, *Physica B* **163**, 273.
- Onuki, Y., I. Umehara, N. Nagai, Y. Kurosawa and K. Satoh, 1991, *J. Phys. Soc. Jpn.* **60**, 1022.
- Ott, H.R., K. Andres and P.H. Schmidt, 1980, *Physica B* **102**, 148.
- Ott, H.R., F. Hulliger, H. Rudigier and Z. Fisk, 1985a, *Phys. Rev. B* **31**, 1329.
- Ott, H.R., H. Rudigier, E. Felder, Z. Fisk and B. Batlogg, 1985b, *Phys. Rev. Lett.* **55**, 1595.
- Ozaki, M., and K. Machida, 1989, *Phys. Rev. B* **39**, 4145.
- Palstra, T.T.M., A.A. Menovsky, J. van der Berg, A.J. Dirkmaat, P.H. Kes, G.J. Nieuwenhuys and J.A. Mydosh, 1985, *Phys. Rev. Lett.* **55**, 2727.
- Palstra, T.T.M., A.A. Menovsky, G.J. Nieuwenhuys and J.A. Mydosh, 1986, *J. Magn. & Magn. Mater.* **54-57**, 435.
- Perdew, J.P., and A. Zunger, 1981, *Phys. Rev. B* **23**, 5048.
- Pethick, C.J., and D. Pines, 1987, in: *Novel Superconductivity*, eds S.A. Wolf and V.Z. Kresin (Plenum, New York) p. 201.
- Pethick, C.J., D. Pines, K.F. Quadar, K.S. Bedell and G.E. Brown, 1986, *Phys. Rev. Lett.* **57**, 1955.
- Peysson, Y., C. Ayache, J. Rossat-Mignod, S. Kunii and T. Kasuya, 1986, *J. Phys. (Paris)* **47**, 113.
- Pickett, W.E., 1987, in: *Novel Superconductivity*, eds S.A. Wolf and V.Z. Kresin (Plenum, New York) p. 233.
- Pickett, W.E., H. Krakauer and C.S. Wang, 1985, *Physica B* **135**, 31.
- Pickett, W.E., H. Krakauer and C.S. Wang, 1986, *Phys. Rev. B* **34**, 6546.
- Putikka, W., and R. Joynt, 1988, *Phys. Rev. B* **37**, 2372.
- Putikka, W., and R. Joynt, 1989, *Phys. Rev. B* **39**, 701.
- Quezel, S., P. Burllet, J.L. Jacoud, L.P. Regnault, J. Rossat-Mignod, C. Vettier, P. Lejay and J. Flouquet, 1988, *J. Magn. & Magn. Mater.* **76-77**, 403.
- Radwanski, R.J., 1992, *J. Magn. & Magn. Mater.* **103**, L1.
- Rahman, S., J. Timlin, J.E. Crow, T. Mihalisin and P. Schlottmann, 1990, *Physica B* **163**, 649.
- Rainer, D., 1988, *Phys. Scr. T* **23**, 106.
- Rajagopal, A.K., and J. Callaway, 1973, *Phys. Rev. B* **7**, 1912.
- Rambabu, D., S.K. Dhar, S.K. Malik and R. Vijayaraghavan, 1982, *Phys. Lett. A* **87**, 294.
- Rasul, J.W., 1991, *Physica B* **171**, 10.
- Rasul, J.W., and T. Li, 1988, *J. Phys. C* **21**, 5119.
- Rasul, J.W., T. Li and H. Beck, 1989, *Phys. Rev. B* **39**, 4191.
- Rauchschwalbe, U., 1987, *Physica B* **147**, 1.
- Rauchschwalbe, U., W. Lieke, F. Steglich, C. Godart, L.C. Gupta and R.D. Parks, 1984, *Phys. Rev. B* **30**, 444.
- Razafimandimby, H., P. Fulde and J. Keller, 1984, *Z. Phys. B* **54**, 111.
- Read, N., and D.M. Newns, 1983, *J. Phys. C* **16**, 3273.
- Regnault, L.P., W.A.C. Erkelens, J. Rossat-Mignod, P. Lejay and J. Flouquet, 1988, *Phys. Rev. B* **38**, 4481.
- Regnault, L.P., J.L. Jacoud, J.M. Mignot, J. Rossat-Mignod, C. Vettier, P. Lejay and J. Flouquet, 1990, *Physica B* **163**, 606.
- Reinders, P.H.P., and M. Springford, 1989, *J. Magn. & Magn. Mater.* **79**, 295.
- Reinders, P.H.P., M. Springford, P.T. Coleridge, R. Boulet and D. Ravot, 1986, *Phys. Rev. Lett.* **57**, 1631.
- Renker, B., F. Gompf, J.B. Suck, H. Rietschel and P. Frings, 1986, *Physica B* **136**, 376.
- Renker, B., F. Gompf, E. Gering, P. Frings, H. Rietschel, R. Felten, F. Steglich and G. Weber, 1987a, *Physica B* **148**, 41.
- Renker, B., F. Gompf, E. Gering and H. Rietschel, 1987b, *Physica B* **148**, 70.
- Richter, M., and H. Eschrig, 1989, *Solid State Commun.* **72**, 263.
- Roy, S.B., and B.R. Coles, 1990, *Physica B* **163**, 424.
- Rozing, G.J., P.E. Mijnarends and D.D. Koelling, 1991a, *Phys. Rev. B* **43**, 9515.
- Rozing, G.J., P.E. Mijnarends, A.A. Menovsky and P.F. de Châtel, 1991b, *Phys. Rev. B* **43**, 9523.
- Sakai, O., H. Takahashi, M. Takeshige and T. Kasuya, 1984, *Solid State Commun.* **52**, 997.
- Sakai, O., M. Takeshige, H. Harima, K. Otaki and T. Kasuya, 1985, *J. Magn. & Magn. Mater.* **52**, 18.
- Sakai, O., Y. Kaneta and T. Kasuya, 1987, *Jpn. J. Appl. Phys. S* **26-3**, 477.

- Satoh, K., T. Fujita, Y. Maeno, Y. Onuki, T. Komatsubara and T. Ohtsuka, 1985, *Solid State Commun.* **56**, 327.
- Scalapino, D.J., E. Loh Jr and J.E. Hirsch, 1986, *Phys. Rev. B* **35**, 6694.
- Scalapino, D.J., E. Loh Jr and J.E. Hirsch, 1987, *Phys. Rev. B* **34**, 8190.
- Schenck, A., P. Birrer, F.N. Gygax, B. Hitti, E. Lippelt, M. Weber, P. Boni, P. Fischer, H.R. Ott and Z. Fisk, 1990, *Phys. Rev. Lett.* **65**, 2454.
- Schirber, J.E., F.A. Schmidt, B.N. Harmon and D.D. Koelling, 1976, *Phys. Rev. Lett.* **36**, 448.
- Schlabitz, W., J. Baumann, B. Pollit, U. Rauchschalbe, H.M. Mayer, U. Ahlheim and C.D. Bredl, 1986, *Z. Phys. B* **62**, 171.
- Schotte, K.D., and U. Schotte, 1975, *Phys. Lett. A* **5**, 38.
- Seitz, E., 1978, *J. Phys. F* **8**, L189.
- Seitz, E., B. Lengeler, G. Kamm and J. Kopp, 1979, *J. Phys. C* **5**, 76.
- Shoenberg, D., 1984, *Magnetic Oscillations in Metals* (Cambridge University Press, Cambridge).
- Sigrist, M., and K. Ueda, 1991, *Rev. Mod. Phys.* **63**, 239.
- Singh, D.J., 1991a, *Phys. Rev. B* **43**, 6388.
- Singh, D.J., 1991b, *Phys. Rev. B* **44**, 7451.
- Singh, M.A., S.L. Smith, S.E. Nagler and W.J.L. Buyers, 1990, *Solid State Commun.* **74**, 439.
- Sondhelm, S.A., and R.C. Young, 1985, *J. Phys. F* **15**, L261.
- Springford, M., 1991, *Physica B* **171**, 151.
- Springford, M., and P.H.P. Reinders, 1988, *J. Magn. & Magn. Mater.* **76-77**, 11.
- Stalinski, B., Z. Kletowski and Z. Henkie, 1973, *Phys. Status Solidi A* **19**, K165.
- Stamp, P.C.E., 1987, *Europhys. Lett.* **4**, 453.
- Stassis, C., C.-K. Loong, B.N. Harmon, S.H. Liu and R.M. Moon, 1979, *J. Appl. Phys.* **50**, 7567.
- Stewart, G.R., 1984, *Rev. Mod. Phys.* **56**, 755.
- Sticht, J., and J. Kübler, 1985a, *Solid State Commun.* **53**, 529.
- Sticht, J., and J. Kübler, 1985b, *Solid State Commun.* **54**, 389.
- Sticht, J., N. d'Ambrumenil and J. Kübler, 1986, *Z. Phys. B* **65**, 149.
- Strange, P., 1984, *J. Phys. C* **17**, 4273.
- Strange, P., and D.M. Newns, 1986, *J. Phys. F* **16**, 335.
- Swane, A., and O. Gunnarsson, 1990, *Phys. Rev. Lett.* **65**, 1148.
- Szotek, Z., W.M. Temmerman and H. Winter, 1991, *Physica B* **172**, 19.
- Szytuła, A., S. Siek, J. Leciejewicz, A. Zygmunt and Z. Ban, 1988, *J. Phys. & Chem. Solids* **49**, 1113.
- Taillefer, L., and G.G. Lonzarich, 1988, *Phys. Rev. Lett.* **60**, 1570.
- Taillefer, L., R. Newbury, G.G. Lonzarich, Z. Fisk and J.L. Smith, 1987, *J. Magn. & Magn. Mater.* **63-64**, 372.
- Taillefer, L., J. Flouquet and G.G. Lonzarich, 1991, *Physica B* **169**, 257.
- Takahashi, H., and T. Kasuya, 1985, *J. Phys. C* **18**, 2697, 2709, 2721, 2731, 2745, 2755.
- Temmerman, W.M., and P.A. Sterne, 1990, *J. Phys* **2**, 5529.
- Teter, J., R. Freitag, J.E. Crow and T. Mihalisin, 1982, *J. Appl. Phys.* **53**, 7910.
- Thompson, J.D., J.O. Willis, C. Godart, D.E. MacLaughlin and L.C. Gupta, 1985, *Solid State Commun.* **56**, 169.
- Torikachvili, M.S., K.N. Yang, M.B. Maple and G.P. Meisner, 1985, *J. Appl. Phys.* **57**, 3137.
- Torikachvili, M.S., L. Rebersky, K. Motoya, S.M. Shapiro, Y. Dalichaouch and M.B. Maple, 1990, *Physica B* **163**, 117.
- Toxen, A.M., R.J. Gambino and L.B. Welsh, 1973, *Phys. Rev. B* **8**, 90 and references therein.
- Trainor, R.J., M.B. Brodsky, B.D. Dunlap and G.K. Shenoy, 1976, *Phys. Rev. Lett.* **37**, 1511.
- Ubachs, W., A.P.J. van Deursen, A.R. de Vroomen and A.J. Arko, 1986, *Solid State Commun.* **60**, 7.
- Umehara, I., Y. Kurosawa, N. Nagai, M. Kikuchi, K. Satoh and Y. Onuki, 1990, *J. Phys. Soc. Jpn.* **59**, 2848.
- Umehara, I., N. Nagai and Y. Onuki, 1991a, *J. Phys. Soc. Jpn.* **60**, 591.
- Umehara, I., N. Nagai and Y. Onuki, 1991b, *J. Phys. Soc. Jpn.* **60**, 1294.
- Valls, O.T., and Z. Tesanovic, 1984, *Phys. Rev. Lett.* **53**, 1497.
- van Deursen, A.P.J., R.E. Pols, A.R. de Vroomen and Z. Fisk, 1985, *J. Less-Common Met.* **111**, 331.
- van Maaren, M.H., H.J. van Daal and K.H.J. Buschow, 1974, *Solid State Commun.* **14**, 145.
- Varma, C.M., 1985, *Phys. Rev. Lett.* **55**, 2723.
- Varma, C.M., 1991, *Physica B* **171**, 142.
- Vettier, C., P. Morin and J. Flouquet, 1986, *Phys. Rev. Lett.* **56**, 1980.
- Vignale, G., and M. Rasolt, 1988, *Phys. Rev. B* **37**, 10685.



- von Barth, U., 1979, *Phys. Rev. A* **20**, 1963.
- von Barth, U., and L. Hedin, 1972, *J. Phys. C* **5**, 1629.
- Vosko, S.H., and J.P. Perdew, 1975, *Can. J. Phys.* **53**, 1385.
- Vosko, S.H., L. Wilk and N. Nusair, 1980, *Can. J. Phys.* **58**, 1200.
- Walter, U., C.-K. Loong, M. Loewenhaupt and W. Schlabitz, 1986, *Phys. Rev. B* **33**, 7875.
- Walter, U., M. Loewenhaupt, E. Holland-Moritz and W. Schlabitz, 1987, *Phys. Rev. B* **36**, 1981.
- Wang, C.S., H. Krakauer and W.E. Pickett, 1985, *Physica B* **135**, 34.
- Wang, C.S., H. Krakauer and W.E. Pickett, 1986, *J. Phys. F* **16**, L287.
- Wang, C.S., M.R. Norman, R.C. Albers, A.M. Boring, W.E. Pickett, H. Krakauer and N.E. Christensen, 1987, *Phys. Rev. B* **35**, 7260.
- Waspe, R.L., and R.N. West, 1982, in: *Positron Annihilation*, eds P.G. Coleman, S.C. Sharma and L.M. Diana (North-Holland, Amsterdam) p.328.
- Wasserman, A., and N. Bharatiya, 1979, *Phys. Rev. B* **20**, 2303.
- Wasserman, A., M. Springford and A.C. Hewson, 1989, *J. Phys.* **1**, 2669.
- Welp, U., 1989, Thesis, University of Konstanz.
- Wills, J.M., and B.R. Cooper, 1987, *Phys. Rev. B* **36**, 3809.
- Wills, J.M., B.R. Cooper and P. Thayamballi, 1985, *J. Appl. Phys.* **57**, 3185.
- Wosnitza, J., G.W. Crabtree, H.H. Wang, K.D. Carlson, M.D. Vashon and J.M. Williams, 1991, *Phys. Rev. Lett.* **67**, 263.
- Wulff, M., G.G. Lonzarich, D. Fort and H.L. Skriver, 1988, *Europhys. Lett.* **7**, 629.
- Yamagami, H., and A. Hasegawa, 1991a, *J. Phys. Soc. Jpn.* **60**, 987.
- Yamagami, H., and A. Hasegawa, 1991b, *J. Phys. Soc. Jpn.* **60**, 1011.
- Young, R.C., R.G. Jordan and D.W. Jones, 1973, *Phys. Rev. Lett.* **31**, 1473.
- Young, R.C., R.G. Jordan and D.W. Jones, 1976, *J. Phys. F* **6**, L37.
- Zhang, F., and T.K. Lee, 1987, *Phys. Rev. B* **35**, 3651.
- Zhang, F., T.K. Lee and Z.B. Su, 1987, *Phys. Rev. B* **35**, 4728.
- Zhou, L.W., C.L. Lin, J.E. Crow, S. Bloom, R.P. Guertin and S. Foner, 1986, *Phys. Rev. B* **34**, 483.
- Zolnierrek, Z., A.J. Arko and D.D. Koelling, 1986, *J. Less-Common Met.* **122**, 89.
- Zwicknagl, G., 1988, *J. Magn. & Magn. Mater.* **76-77**, 16.
- Zwicknagl, G., E. Runge and N.E. Christensen, 1990, *Physica B* **163**, 97.

## Chapter 111

# PHENOMENOLOGICAL APPROACH TO HEAVY-FERMION SYSTEMS\*

S.H. LIU

*Solid State Division, Oak Ridge National Laboratory, Oak Ridge,  
 TN 37831–6032, USA*

### Contents

Symbols	87	3.2. The Kondo lattice	114
1. Introduction	89	3.3. The spin fluctuation resonance model	119
2. Review of key normal state properties	90	3.3.1. Single-site spin fluctuation resonance	119
2.1. Specific heat	91	3.3.2. Toward a coherent lattice	125
2.2. Magnetic susceptibility	93	3.4. The electronic polaron model	127
2.3. Resistivity and magnetoresistance	95	3.4.1. The f hole screening problem	129
2.4. Neutron paramagnetic form factor	99	3.4.2. The f band problem	131
2.5. De Haas–van Alphen effect	103	3.4.3. Results of model calculation	133
3. Theoretical approaches	104	3.4.4. Inelastic neutron scattering	140
3.1. The Fermi liquid models	105	4. Summary and conclusion	145
3.1.1. The one-band Fermi liquid model	105	References	146
3.1.2. The two-band model	110		
3.1.3. Local-density-functional band calculations	113		

### Symbols

$a_{k\sigma}$	wave-function coefficient	$f(x)$	a function related to the Fermi distribution function
$A$	constant or normalization factor	$f_{\sigma\uparrow}, f_{\uparrow}, f_{\downarrow}$	local f electron annihilation operator
$B$	constant	$f_{\sigma\uparrow}^\dagger, f_{\uparrow}^\dagger, f_{\downarrow}^\dagger$	local f electron creation operator
$c_{k\sigma}$	band electron annihilation operator	$f_{k\sigma}$	f electron annihilation operator
$c_{k\sigma}^\dagger$	band electron creation operator	$f_{k\sigma}^\dagger$	f electron creation operator
$\text{csc}(\pi\alpha)$	cosecant function with argument $\pi\alpha$	$\tilde{f}_\sigma^\dagger$	creation operator of electron in spin fluctuation resonance level
$C$	specific heat	$F_m, F_M(\theta)$	neutron magnetic scattering amplitude
$C(T)$	specific heat as a function of temperature	$F_N$	neutron nuclear scattering amplitude
$e$	absolute value of electron charge		
$E_0, E'_0$	ground state energy		

\* This work is supported by the Division of Materials Sciences, U.S. Department of Energy under Contract No. DE-AC05-85OR21400 with Martin Marietta Energy Systems, Inc.

$\mathbf{G}$	reciprocal lattice vector	$\mathbf{S}$	local electron spin operator
$G_f(\omega)$	f electron propagator	$t$	time
$\hbar$	Planck's constant divided by $2\pi$	$T$	temperature
h.c.	hermitian conjugate	$T_0$	characteristic temperature or Kondo temperature
$H$	magnetic field or Hamiltonian	$T_c$	critical temperature
$H_1$	Hamiltonian of $f^0$ state	$T_D$	Dingle temperature
$H_{\text{eff}}$	effective Hamiltonian	$T_F$	Fermi temperature
$i$	$\sqrt{-1}$	$T_K$	Kondo temperature defined as $T_0$ times a band-structure-dependent factor
$J$	exchange interaction	$U_{df}$	Coulomb interaction between band and f electrons
$\mathbf{k}$	wave vector or crystal momentum of band electrons	$U_{ff}$	Coulomb interaction between f electrons
$k$	amplitude of $\mathbf{k}$	$V$	hybridization potential or matrix element
$k_F$	Fermi wave vector	$V_0, V_1$	potential parameters
$k_B$	Boltzmann constant	$V(\mathbf{r})$	crystal potential
$l$	index for atom position	$V_{xc}(\mathbf{r}), V_{xc}$	exchange-correlation potential
$m$	magnetization	$V_H(\mathbf{r}), V_H$	electrostatic potential
$m_0$	bare electron mass	$V_N(\mathbf{r}), V_N$	nuclear potential
$m^*$	effective mass of electrons	$W$	width of model electron band
$m(\mathbf{r})$	nonuniform induced magnetic moment	$x$	impurity concentration
$m(\mathbf{G})$	Fourier component of $m(\mathbf{r})$ at reciprocal lattice $\mathbf{G}$	$Z_l$	charge of atom at position $l$
$n$	energy band index	$\alpha$	Mahan-Nozières-de Dominicis exponent
$n_f$	occupation of local f level	$\beta$	$1/k_B T$
$n_{\mathbf{k}}, n_{\mathbf{k}}^{(a)}, n_{\mathbf{k}}^{(a)}$	Fermi distribution function or occupation number	$\gamma$	electronic specific heat coefficient
$n_{\mathbf{k}}^{(b)}, n_{\mathbf{k}}^{(b)}$		$\Gamma$	width of f level
$n_{\mathbf{k}}^{(c)}, n_{\mathbf{k}}^{(c)}$		$\Gamma(1 - \alpha)$	gamma function with argument $1 - \alpha$
$N$	number of atoms or number of electrons	$\delta$	positive infinitesimal or Dirac delta function
$N_f$	f level degeneracy	$\Delta$	one-half of hybridization gap
$ N\rangle$	filled Fermi sea with $N$ electrons	$\Delta E$	range of energy transfer
$N(0)$	uniform density of electron states of simple band model	$\Theta$	paramagnetic Curie temperature
$N(\varepsilon)$	density of electron states	$\varepsilon$	electron energy
$N(\mu)$	density of electron states at the Fermi level	$\varepsilon_0$	spin fluctuation resonance level
$N_{\pm}(\varepsilon), N_{\pm}(\omega)$	density of states of hybridized electron bands	$\varepsilon_f$	f electron energy level
$N_{+}(\mu)$	density of states of the upper hand at the Fermi level	$\varepsilon_{\mathbf{k}}, \varepsilon_{\mathbf{k}}^{(a)}, \varepsilon_{\mathbf{k}}^{(b)}, \varepsilon_{n\mathbf{k}}$	band energy
$N_e$	total occupation of an electron band	$\varepsilon_{\mathbf{k}}^{\pm}$	energy of hybridized bands
$p$	electron momentum operator	$\eta$	basic energy scale in electronic polaron model
$\mathbf{q}$	momentum transfer or wave vector of band electron	$\sigma, \sigma'$	electron spin index
$\mathbf{Q}$	momentum transfer or zone boundary wave vector	$\rho$	electrical resistivity
$\mathbf{r}, \mathbf{r}'$	position vector of electron	$\rho_{e-e}$	electrical resistivity due to electron-electron scattering
$\mathbf{R}_l$	position vector of atom	$\rho_{e-ph}$	electrical resistivity due to electron-phonon scattering
$s$	band electron spin operator	$\rho_{\text{imp}}$	electrical resistivity due to impurity scattering
$S$	total angular momentum of local electron	$\rho_{\text{mag}}$	electrical resistivity due to magnetic scattering
$S(T)$	thermopower as function of temperature		
$S(T, H)$	thermopower as functions of magnetic field and temperature		

$\rho(T)$	electrical resistivity as a function of temperature	$\chi(\mathbf{G} = \mathbf{0})$	extrapolated value of neutron magnetic form factor to $\mathbf{G} = \mathbf{0}$
$\rho(T, 0)$	magnetoresistance at zero field, same as $\rho(T)$	$\chi^{(0)}(\mathbf{q}, 0)$	unenhanced dynamical susceptibility at zero frequency
$\rho(T, H)$	magnetoresistance	$\chi^{(0)}(\mathbf{q}, \omega)$	unenhanced dynamical susceptibility
$\rho(\mathbf{r})$	electron density	$\chi_{ab}^{(0)}(\mathbf{q}, \omega)$	
$\rho_f(\omega)$	f electron spectrum	$\chi_{++}^{(0)}(\mathbf{q}, \omega)$	intra-band contribution to unenhanced dynamical susceptibility
$\mu$	Fermi energy	$\chi_{-+}^{(0)}(\mathbf{q}, \omega)$	inter-band contribution to unenhanced dynamical susceptibility
$\mu_B$	Bohr magneton	$\chi(\mathbf{q}, \omega)$	enhanced dynamical susceptibility
$\mu_{\text{eff}}$	effective magnetic moment	$ \Psi\rangle,  \Psi'\rangle$	many-electron wave function
$\mu_i$	total magnetic moment of impurity atom	$\psi_{nk}(\mathbf{r})$	band electron wave function
$\mu(0)$	Fermi energy at zero temperature	$\omega$	frequency or energy
$\chi$	magnetic susceptibility	$\omega_k, \omega_k^\pm$	energy of f-like band in electronic polaron model
$\chi(0)$	susceptibility at zero temperature	$\omega_q$	phonon frequency
$\chi(T)$	susceptibility as a function of temperature	$\omega_{\text{peak}}$	frequency at the peak of phonon line
$\chi(\mathbf{G})$	neutron magnetic form factor		

---

## 1. Introduction

Heavy-fermion materials exhibit unusual physical properties which prove to be fascinating to explore but frustrating to explain. Most of these materials are inter-metallic compounds containing Ce or U, whose atoms have incomplete f shells. A few contain the lanthanide Yb or the actinide Np or Pu as the essential ingredient. It is now well established that the f electrons on the lanthanide or actinide atoms are responsible for all of the unusual properties, but there is no agreement among the investigators on the mechanism or mechanisms by which f shell electrons can produce the observed effects. Stated briefly, it seems that the low-temperature properties of these materials can be consistently interpreted as due to a band of very heavy mobile fermions, but the high-temperature properties point to the existence of unpaired f shell electrons localized on the rare-earth or actinide sites. The main issue of theoretical controversy concerns the exact role played by the f electrons. Two opposite points of view have sharpened in recent years. One school of thought argues that the heavy electrons are f electrons in Bloch states. While many low-temperature properties can be explained on this basis, the simple band model fails to account for the high-temperature properties. The opposite camp maintains that the f electrons remain localized at all temperatures, but their moments are quenched at low temperatures and a narrow band is induced concurrently. Theoretical as well as experimental publications supporting either point of view proliferate in the mean time, and there seems to be little room for compromise.

The main thrust of this review is to bring out fully all the points of contention. It begins with a review of the experimental results to illustrate that a person can always choose a subset of experimental findings to support either point of view, but is quickly driven schizophrenic when he tries to look at the total problem. A review of the theoretical approaches will follow, with emphasis on summarizing the successes and

failures of all models. As the title of this chapter implies, the theoretical discussion will be on the phenomenological level. No effort will be made to discuss the increasingly sophisticated mathematical techniques developed in recent years for solving the various model Hamiltonians, because, as will be emphasized later, the models fail for physical reasons, not for the lack of exact solutions. In the literature there exist comprehensive reviews of the more promising theories (Bickers 1987, Newns and Read 1987, Fulde et al. 1988, Schlottmann 1989), and interested readers may consult them for mathematical details.

A few side issues lurk behind the main controversy. For instance, there is another group of intermetallic compounds of Ce and other lanthanides called mixed-valence materials. Like heavy-fermion materials, they have anomalous magnetic susceptibility and transport properties, but have only moderately heavy charge carriers at low temperatures. Do they belong to the same class of materials as heavy-fermion solids? This question will come up repeatedly throughout this review. Also, there are certain similarities between heavy-fermion materials and strongly correlated d band materials, such as the normal state of high- $T_c$  copper-oxide superconductors. Many investigators believe that a firm understanding of one system will shed light on the other. This question will not be covered in this review, but it does make this chapter more relevant and timely.

## 2. Review of key normal state properties

In metallic solids, heavy-fermion materials included, one routinely classifies the electrons in the constituent atoms into two groups, those whose orbits are confined to the immediate vicinity of the atomic nuclei are called core or localized electrons, and those whose orbits extend throughout the entire solid are called itinerant electrons. This classification is important in practice, for instance, the itinerant electrons provide the binding forces that hold the atoms together into a solid, and the core electrons provide the repulsive forces which prevent the solid from collapsing. The delicate balance between the two forces determines the atomic arrangement and the inter-atomic spacings of the solid. As a result, the modern theory of metallic substances begins, implicitly or explicitly, with an account of which electrons belong to which group.

The classification scheme also provides a first understanding to a number of physical properties. The itinerant electrons determine the metallic properties of the solid, such as the low-temperature specific heat, the magnetic susceptibility, the electrical and thermal conductivities, and other transport coefficients. The electronic contribution to the specific heat is proportional to the temperature. The magnetic response of the itinerant electrons is rather simple, namely, a temperature-insensitive Pauli paramagnetic susceptibility. Those core electrons in closed atomic shells contribute to a weak diamagnetic response, while those in partially filled shells, however, give rise to a rich repertoire of magnetic properties, such as Curie or Curie–Weiss susceptibility, ferromagnetism, antiferromagnetism, and other exotic magnetically ordered states. Magnetic ordering also contribute to a  $\lambda$ -type anomaly in the specific heat and similar

anomalies in transport properties. Thus, thermodynamic, magnetic and transport measurements form the standard set of basic tools for probing both itinerant electrons and core electrons in unfilled shells. For instance, we have learned through this set of experiments that in heavy lanthanide metals the 6s, 5p and 5d electrons are itinerant and all others are localized. In particular, most members are magnetic due to their partially filled 4f shells.

The above-mentioned set of experimental tools are less than perfect. The dichotomy encountered its first serious challenge in the 3d electrons of iron-group transition metals. The ferromagnetic ordering of Fe, Co and Ni would indicate that electrons in the 3d states are localized, but the nonintegral magnetic moment per atom would argue for the itinerant nature of these same electrons. The problem was finally resolved when the sophisticated de Haas-van Alphen measurement detected the 3d parts of the spin-polarized Fermi surfaces in Fe and Ni, thus confirming unequivocally the itinerant nature of the 3d electrons. This development put the itinerant theory of magnetism on a sound experimental footing. History is repeating itself in heavy-fermion materials. This time the troublesome electrons are the 4f electrons in Ce and Yb and the 5f electrons in U, Np and Pu. In this section we will examine closely the available evidence from basic as well as advanced measurements on heavy-fermion materials to show the difficulties in trying to classify the f electrons as either localized or itinerant. Much of the experimental results under discussion have been reviewed in more detail in this volume and elsewhere (Stewart 1984, Fisk et al. 1986, P.A. Lee et al. 1986). As a result, we will choose a few systems as typical examples to illustrate the challenges presented to us by this class of materials.

### 2.1. Specific heat

The specific heat  $C(T)$  per unit volume of a band of noninteracting itinerant electrons has a linear dependence on the temperature  $T$  given by (Blatt 1968):

$$C(T) = \gamma T, \quad (1)$$

where

$$\gamma = \frac{2}{3} \pi^2 N(\mu) k_B^2. \quad (2)$$

In the above relation  $k_B$  is the Boltzmann constant and  $N(\mu)$  is the density of electron states per spin per unit volume at the Fermi level  $\mu$ . In the free electron approximation the density of states is related to the effective mass  $m^*$  and Fermi wavevector  $k_F$ :

$$N(\mu) = m^* k_F / 2\pi^2 \hbar^3, \quad (3)$$

where  $\mu = \hbar^2 k_F^2 / 2m^*$ ,  $\hbar$  is Planck's constant divided by  $2\pi$ . In real metallic solids there are usually many bands crossing the Fermi level, so  $\gamma$  is a measure of the average mass of the band electrons weighted by the Fermi wavevectors of the individual bands. Since  $k_F$  is confined by the size of the Brillouin zone and does not vary much from material to material, a large  $\gamma$  would indicate the presence of heavy carriers, electrons or holes, at the Fermi level. In table 1 we list the specific heat  $\gamma$  of a number of metallic substances to illustrate that there is practically a continuous spectrum of

TABLE 1  
The specific heat  $\gamma$  of some metals and intermetallic compounds.

Material	$\gamma$ [mJ/(mol K <sup>2</sup> )]	Remark
Cu	0.7	s, p band metal
K	2.2	s, p band metal
Sr	3.6	s, p band metal
Fe	4.5	d band metal
Y	8.5	d band metal
Pd	10	d band metal
$\alpha$ -Ce	13	mixed valence
CeSn <sub>3</sub>	53	mixed valence
CeBe <sub>13</sub>	115	mixed valence
UPt <sub>3</sub>	450	heavy fermion
UBe <sub>13</sub>	1100	heavy fermion
CeAl <sub>3</sub>	1600	heavy fermion

$\gamma$  values, from approximately 1 mJ/(mol K<sup>2</sup>) for simple metals to over 1 J/(mol K<sup>2</sup>) for heavy-fermion materials. This list points to the most striking anomaly of heavy-fermion substances, namely that whatever electrons are responsible for the specific heat, they have masses well over 1000 times the rest mass of the electrons. To be more precise, this mass only refers to the mass which enters the orbital motion of the electrons when they move in extended orbits throughout the solid. By this definition the core electrons, which remain in orbits around the nuclei, have infinite effective mass. In the tight-binding picture, heavy mass implies a band of tightly bound, almost atomic-like, and yet weakly mobile electrons.

The large value of  $\gamma$  is not the only anomaly seen in the specific heat. Figure 1 is a plot of  $C/T$  versus  $T^2$  of CeAl<sub>3</sub> (Benoit et al. 1981). This curve has a peak around 0.3 K, which indicates a peak in  $C(T)$  at a slightly higher temperature. Beyond the peak the specific heat declines according to the  $T^{-2}$  law. Similar behavior has been seen in other materials as well (Stewart 1984). The total entropy as calculated from integrating the  $C/T$  curve is close to  $k_B \ln 2$  per Ce site. One therefore faces the task of explaining the entire anomaly, not just the large mass. For mixed-valence materials, such as CeSn<sub>3</sub>, the  $\gamma$  value is 53 mJ/(mol K<sup>2</sup>) (Liu et al. 1981), roughly 30 times lower than that for CeAl<sub>3</sub>, while the peak in  $C(T)$  occurs at a temperature

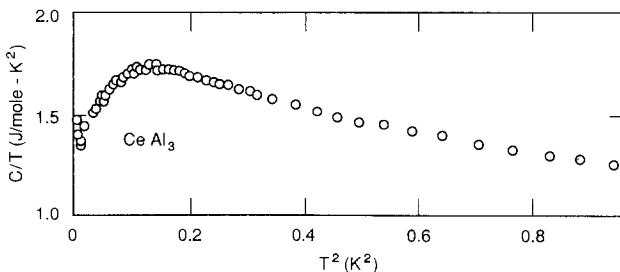


Fig. 1. The  $C(T)/T$  versus  $T^2$  plot for CeAl<sub>3</sub> (Benoit et al. 1981). The asymptotic value at  $T=0$  is the electronic specific heat  $\gamma$ .

around 3 K, about 10 times that for  $\text{CeAl}_3$ . The  $C(T)$  curves of these two materials look qualitatively the same, aside from a change of scale.

## 2.2. Magnetic susceptibility

The low-temperature part of the magnetic susceptibility,  $\chi(T)$ , of  $\text{CeAl}_3$  is shown in fig. 2 (Andres et al. 1975). Below 0.1 K it is clear that the susceptibility approaches a constant value,  $\chi(0) \simeq 36 \times 10^{-3} \text{ emu}/(\text{mol G})$ , which is indicative of itinerant electron behavior, but its value is roughly 1000 times that of simple metals. The temperature-insensitive susceptibility, called the Pauli susceptibility, has the following expression for noninteracting band electrons (Blatt 1968):

$$\chi(0) = 2N(\mu)\mu_B^2, \quad (4)$$

where  $\mu_B$  is the Bohr magneton. Thus the large value of  $\chi(0)$  is also indicative of large effective mass and is entirely consistent with the large value of specific heat constant  $\gamma$ . With increasing temperature the function  $\chi(T)$  increases slightly and reaches a maximum at about 0.6 K. Subsequently, it decreases with increasing temperature until for  $T \gg 1$  K it has the empirical expression

$$\chi(T) = N\mu_{\text{eff}}^2/(T + \Theta), \quad (5)$$

where  $N$  is Avogadro's number,  $\Theta \simeq 30$  K is the paramagnetic Curie temperature, and  $\mu_{\text{eff}} \simeq 2.6\mu_B$  is the effective magnetic moment per Ce atom. This temperature dependence indicates local magnetic moments on Ce sites generated by one electron in the f orbital, which gives a theoretical value for  $\mu_{\text{eff}} = 2.54\mu_B$  (Stewart 1984). The positive value for  $\Theta$  would indicate antiferromagnetic ordering around 30 K, but there is no experimental evidence of that. All Ce-based materials have  $\mu_{\text{eff}}$  around

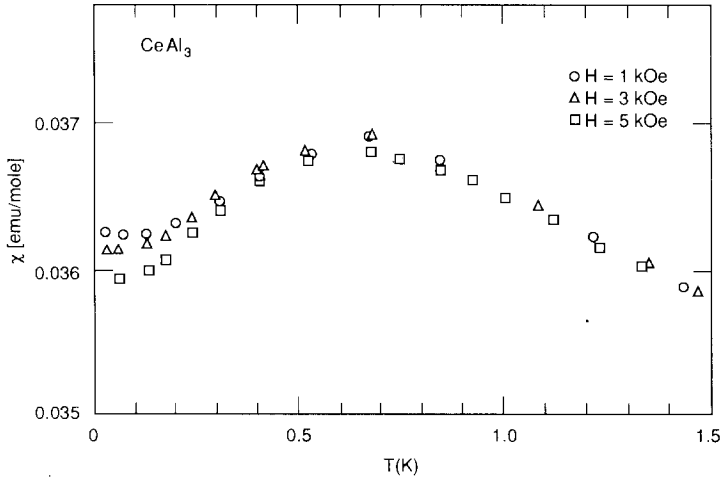


Fig. 2. The low-temperature part of the magnetic susceptibility of  $\text{CeAl}_3$  (Andres et al. 1975). The three sets of data were measured under different magnetic fields.



$2.6\mu_B$ , while U-based materials tend to cluster around  $3.0\mu_B$ . The theoretical value for  $\mu_{\text{eff}}$  of  $U^{3+}$  in the  $5f^3$  configuration is  $3.62\mu_B$ . Most well studied systems have  $\Theta$  ranging from 20 to 200 K. Some heavy-fermion materials, such as  $CeAl_2$  (Barbara et al. 1979) and  $U_2Zn_{17}$  (Ott et al. 1984a) do develop antiferromagnetic order with Néel temperatures much below  $\Theta$  while  $CeCu_2Si_2$  (Steglich et al. 1979),  $UBe_{13}$  (Ott et al. 1983) and  $UPt_3$  (Stewart et al. 1984) become superconducting with critical temperatures of approximately 1 K, also significantly below their individual  $\Theta$ .

We now encounter the first serious challenge to the rules of separating core from itinerant electrons mentioned earlier. The high-temperature susceptibility data would lead us unequivocally into classifying the 4f electrons on the Ce atoms as localized, but if so, why is the susceptibility suppressed at low temperatures without antiferromagnetic ordering? How are the heavy itinerant electrons, which generate the Pauli susceptibility, related to the localized f electrons, which generate the Curie–Weiss susceptibility? To complicate the matter further, we will discuss in detail later that recent neutron magnetic form factor measurements give evidence that the heavy fermions are f electrons themselves. In those materials which become superconducting at low temperatures, the superconducting electrons also have the spatial distribution of f electrons. This and other puzzling results, such as de Haas–van Alphen measurements, will be the topics of later subsections.

The graph in fig. 3 is a plot of the specific heat  $\gamma$  versus the low-temperature susceptibility  $\chi(0)$  for a number of mixed-valence and heavy-fermion materials (Jones 1985). For noninteracting fermions, we see from eqs. (2) and (4) that the ratio of these two quantities contains only fundamental constants, and this is indicated by the solid line in the graph. Many-body interactions will modify the specific heat and the susceptibility, but in different ways. In particular, exchange interaction between pairs of fermions enhances  $\chi(0)$  but not  $\gamma$ , and this would put the actual points to the right of the solid line. The deviation from the solid line, then, is a measure of

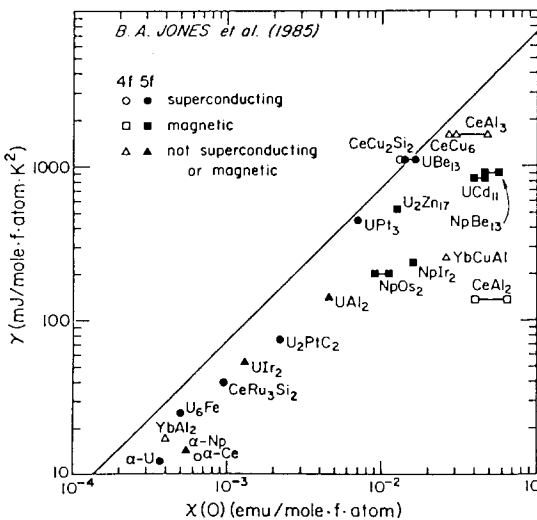


Fig. 3. A plot of the specific heat  $\gamma$  versus the low-temperature susceptibility  $\chi(0)$  for a number of mixed-valence and heavy-fermion materials (Jones 1985).

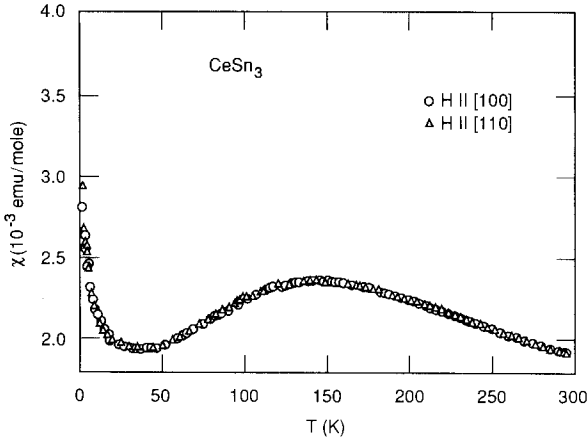


Fig. 4. The magnetic susceptibility of  $\text{CeSn}_3$  as a function of  $T$  (Tsang et al. 1984).

exchange enhancement (see Lee et al. 1986). The graph shows that exchange enhancement exists, but not large enough so that the large susceptibility could be attributable to incipient ferromagnetic instability.

The magnetic susceptibility of  $\text{CeSn}_3$  is shown in fig. 4 (Tsang et al. 1984). If we ignore the sharp rise below 50 K, the curve looks like that for  $\text{CeAl}_3$  (fig. 2) except for changes of horizontal as well as vertical scales. The peak occurs at around 150 K, and the maximum value is around  $2 \times 10^3$  emu/mol. The similarity in shape of the  $\chi(T)$  curves of these two materials suggests a scaling behavior (Lawrence and Béal-Monod 1981), which means that the same mechanism determines the susceptibility curves of both mixed-valence and heavy-fermion materials. On the other hand, the low-temperature tail in  $\text{CeSn}_3$ , also seen in  $\alpha\text{-Ce}$  (Koskimaki and Gschneidner 1975) and  $\text{CePd}_3$  (Gardner et al. 1972) but not in heavy-fermion systems, seems to suggest a fundamental difference between these two classes of materials. This point will be developed further in later sections.

### 2.3. Resistivity and magnetoresistance

In normal metals we find three major components to the electrical resistivity  $\rho(T)$  (Blatt 1968):

$$\rho(T) = \rho_{\text{imp}} + \rho_{e-e} + \rho_{e-ph}, \quad (6)$$

where  $\rho_{\text{imp}}$  is the temperature independent contribution due to scattering of charge carriers by impurities and other lattice imperfections,  $\rho_{e-e}$  comes from mutual scattering of charge carriers and has a  $T^2$  temperature dependence, and  $\rho_{e-ph}$  arises from scattering by phonons and has a  $T^5$  temperature dependence at low temperatures and a linear  $T$  dependence at high temperatures. For metals which contain small amounts of magnetic impurities, such as Fe, Co, Ce or U, the impurity part, which is denoted by  $\rho_{\text{mag}}$ , has the approximate temperature dependence in the form

$$\rho_{\text{mag}} = A + B \ln(T/T_0), \quad (7)$$

where  $A$  and  $B$  are two constants, for  $T \geq T_0$ , where  $T_0$  is a characteristic temperature, and a constant value for  $T \ll T_0$ . The physical meaning of this result is that, under suitable conditions, the scattering of mobile electrons from local magnetic moments undergoes a resonance at the Fermi level. The low-temperature resistivity samples the maximum scattering cross-section (Kondo 1969). With increasing temperature, more electrons are scattered off resonance. The resonance itself is produced collectively by the mobile electrons, and it broadens as the temperature increases. These two effects cause the resistivity to decrease with increasing temperature. The characteristic temperature  $T_0$ , called the Kondo temperature, is a measure of the width of the resonance. In dense magnetic systems, such as Fe or Gd,  $\rho_{\text{mag}}$  has a  $\lambda$ -type cusp at the magnetic ordering temperatures and decreases with increasing magnetic ordering at lower temperatures (Blatt 1968). The Kondo effect is usually unobservable in these systems.

With this background we now look at the electrical resistivity curve of  $\text{CeAl}_3$ , shown in fig. 5 (Ott et al. 1984b). Above 200 K the resistivity, about  $180 \mu\Omega \text{cm}$ , is roughly one order of magnitude higher than the typical phonon contribution in simple and transition metals (Blatt 1968). This would indicate that there is a set of strong and incoherent scatterers in the material, similar to magnetic rare earth metals above their ordering temperatures (McEwen 1978). This picture is entirely consistent with the high-temperature susceptibility data, that the  $f$  electrons in Ce are localized and their magnetic moments are randomly oriented. Between 35 and 200 K the resistivity decreases with increasing temperature, and the temperature dependence resembles what one finds in metallic systems containing Ce impurities, with a Kondo temperature  $T_0 \simeq 100$  K. This reinforces the notion that there are localized magnetic moments on Ce sites. Below 35 K, however,  $\rho$  decreases dramatically, indicating that the random magnetic scatterers are either disappearing or becoming aligned. The temperature of resistivity maximum is consistent with the Curie temperature  $\Theta$ , but

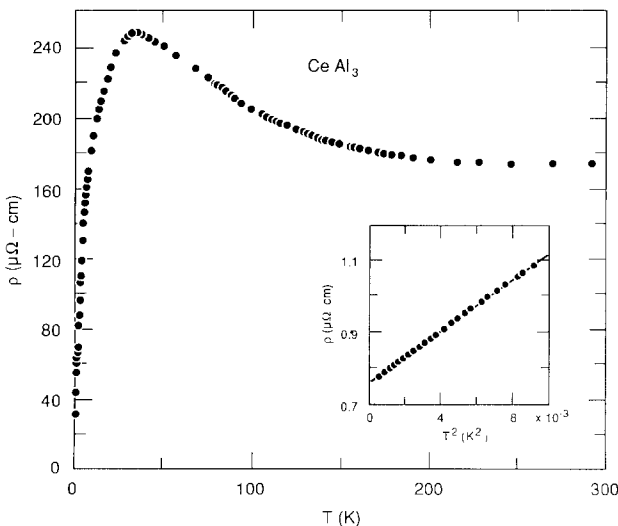


Fig. 5. The electrical resistivity of  $\text{CeAl}_3$  as a function of  $T$  (Ott et al. 1984b). The inset shows the  $T^2$  dependence of the low-temperature resistivity.

the rounded resistivity maximum shows that no magnetic ordering takes place in this temperature range. At temperatures much below the maximum, i.e.  $T \leq 1$  K, the resistivity has a  $T^2$  dependence (Remenyi et al. 1983, Andres et al. 1975), which is consistent with the picture that the charge carriers are mobile fermions which interact with each other, as deduced from low-temperature specific heat and magnetic susceptibility. On the other hand, the temperature of maximum resistivity is more than an order of magnitude higher than the temperatures for specific heat and susceptibility maxima. What is happening to the Ce moments between 1 and 35 K? Other heavy-fermion materials may have somewhat different resistivity behavior at high temperatures (Stewart 1984). As shown in fig. 6, the Kondo anomaly is not at all apparent in  $\text{UPt}_3$ , while the compounds  $\text{CeCu}_2\text{Si}_2$  and  $\text{UBe}_{13}$  have a resistivity peak followed by a plateau at a higher temperature. Unlike the susceptibility curves, there is no semblance of scaling behavior among the resistivity curves.

In fig. 7 we show a set of resistivity curves of  $\text{Ce}_x\text{La}_{1-x}\text{Pb}_3$ , for four different values of  $x$  to illustrate the effect of doping (Lin et al. 1987). The pure compound,  $x = 1$ , has a  $\rho(T)$  curve very similar to  $\text{CeAl}_3$ . Replacing some Ce by the nonmagnetic La results in much higher zero-temperature resistivity and a much lower temperature for the resistivity maximum. Larger amounts of doping (smaller  $x$  values) tend to remove the resistivity maximum altogether. The high-temperature part of the resistivity, when normalized to the Ce content, changes very little with doping. These data demonstrate further that at high temperatures the Ce sites scatter conduction electrons individually, but at low temperatures they act coherently such that any disruption of the Ce lattice causes a large increase in the resistivity.

In the case of magnetic metals or metals containing magnetic impurities, the resistivity is suppressed by an externally applied magnetic field, because the localized magnetic moments are better aligned and therefore more coherent (Van Peski-Tinbergen and Dekker 1963). As a result, a decrease of resistivity in a magnetic field is a reliable diagnostic tool for magnetic scattering. In particular, at temperatures where the moments are randomly oriented, the magnetoresistance depends on the

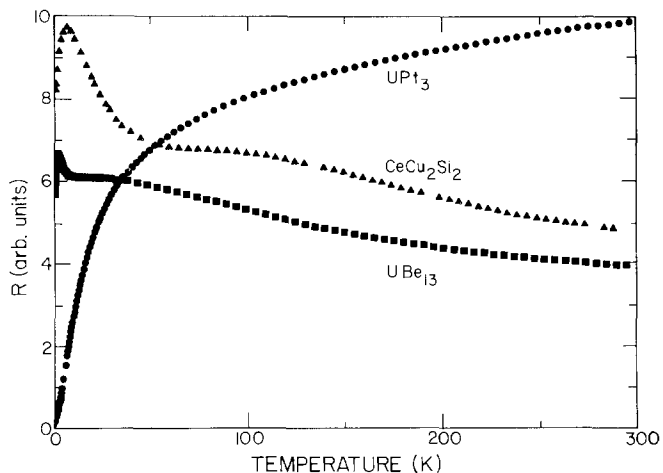


Fig. 6. The resistivity curves for  $\text{UPt}_3$ ,  $\text{CeCu}_2\text{Si}_2$  and  $\text{UBe}_{13}$  (Stewart 1984).

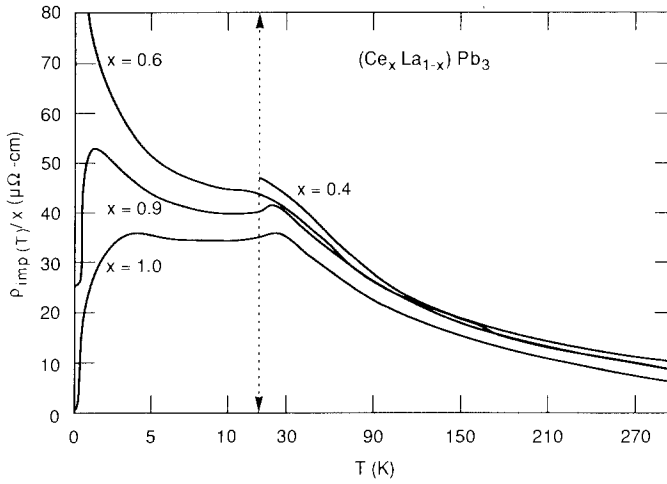


Fig. 7. The resistivity curves of  $Ce_xLa_{1-x}Pb_3$  for four different values of  $x$  to illustrate the effects of doping (Lee et al. 1986). The curves are normalized by the Ce concentration  $x$ . The temperature scale is expanded below 12 K, marked by the vertical dashed line, to show details of the low-temperature behavior.

field  $H$  according to:

$$\rho(T, H) - \rho(T, 0) \propto -H^2. \tag{8}$$

In fig. 8 we show the resistivity of  $UBe_{13}$  at several temperatures plotted as functions of the magnetic field (Remenyi et al. 1986). This substance has an estimated  $\gamma$  value around  $1100 \text{ mJ}/(\text{mol K}^2)$ , a specific heat maximum around 2 K. Its electrical

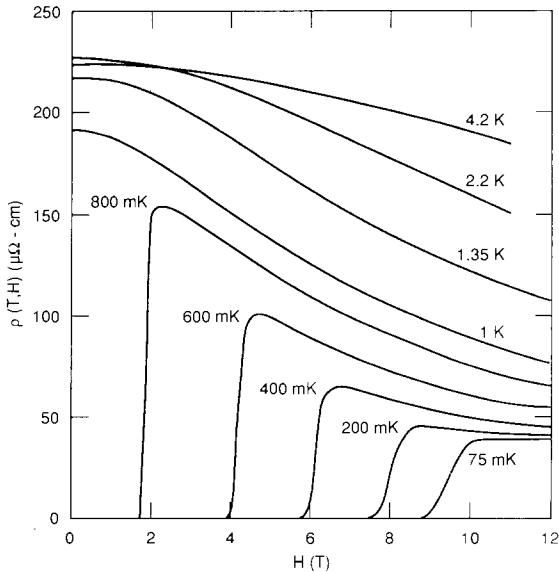


Fig. 8. The magnetoresistance of  $UBe_{13}$  for a number of temperatures above and below the resistivity maximum. This is an abbreviated version of the results reported by Remenyi et al. (1986). The rapid drop of  $\rho(T, H)$  below 1 K at low fields is due to superconductivity.

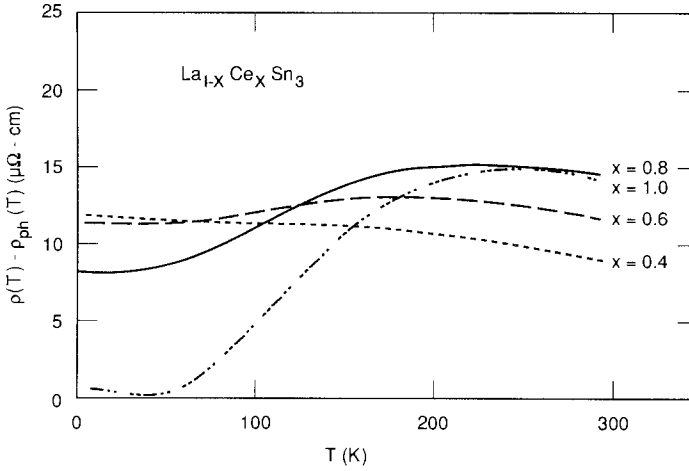


Fig. 9. The electrical resistivity curves of  $\text{La}_{1-x}\text{Ce}_x\text{Sn}_3$  (Maury et al. 1979). These curves are not normalized by the Ce concentration.

resistivity, shown in fig. 6, peaks at 2.35 K, and its Curie temperature is  $\Theta = 70$  K, which is close to the temperature of resistivity plateau. Above the resistivity peak, e.g. at 4.2 K, the magnetoresistance is well described by eq. (8). Below the peak temperature, however, the field dependence is considerably more complex, and in the high field limit the resistivity seems to approach zero. Below 1 K the substance becomes superconducting, and the resistivity drops abruptly to zero at the upper critical field. These results demonstrate that the high-temperature resistivity is indeed due to magnetic scattering, but below the resistance maximum the cross section is very effectively quenched by the field.

The electrical resistivity of the mixed-valence system  $\text{La}_{1-x}\text{Ce}_x\text{Sn}_3$  for four values of  $x$  are shown in fig. 9 (Maury et al. 1979). The resistivity of the pure  $\text{CeSn}_3$  peaks at about 250 K, which indicates that the Kondo temperature is higher than this value. This temperature is of the same order of magnitude as that of the susceptibility maximum, roughly 150 K. The low-temperature part has the expected  $T^2$  dependence (Stalinski et al. 1973). Thus, aside from a large difference in the temperature scale, the electrical resistivity of  $\text{CeSn}_3$  behaves in a way similar to  $\text{CeAl}_3$ . Also shown in fig. 9 is that the effects of replacing Ce with La in  $\text{CeSn}_3$  affects the resistivity in the same way as in  $\text{CePb}_3$ .

#### 2.4. Neutron paramagnetic form factor

Under a uniform magnetic field  $H$  a paramagnetic material develops a macroscopic magnetization given by  $m = \chi H$ . The magnetization is not uniform on the microscopic scale, because it reflects the spatial distribution of the electrons which are polarized by the field. In a crystalline material the magnetic moment distribution  $m(\mathbf{r})$  is a periodic function of the lattice, and the neutron paramagnetic form factor measures its Fourier transform  $m(\mathbf{G})$ , where  $\mathbf{G}$  is a reciprocal lattice vector (Moon 1986, Stassis

1979, 1986). The data are collected over a discrete set of points in the reciprocal space. One defines  $\chi(\mathbf{G})$  by

$$m(\mathbf{G}) = \chi(\mathbf{G})H, \quad (9)$$

whose  $\mathbf{G}=0$  component is the static susceptibility  $\chi$ . The shape of  $\chi(\mathbf{G})$  gives information about the orbital states of the electrons which respond to the magnetic field. For example, d and f electrons have distinct form factors, because the latter has a spatially much tighter wavefunction and a correspondingly broader form factor. The s and p electrons in metals have orbital wavefunctions that spread almost uniformly throughout the solid, so their form factors are  $\delta$ -functions in  $\mathbf{G}$ . Since only the  $\mathbf{G} \neq 0$  components are actually measured by neutron scattering, one can only infer the s and p contributions to the susceptibility by the discrepancy between the static susceptibility and the value of  $\chi(\mathbf{G}=0)$  extrapolated from the data for nonzero  $\mathbf{G}$ . In magnetically ordered materials where a distribution  $m(\mathbf{r})$  exists spontaneously, one can measure the form factor without the need for an external field. It has been determined in this way that in the 3d metals Fe and Ni the ferromagnetic moments are mainly due to the d electrons, with small s and p contributions pointing in the opposite direction from the d moments (Moon 1986).

Stassis and co-workers (Stassis et al. 1985, 1986) have measured the neutron paramagnetic form factors of three superconducting heavy-fermion systems,  $\text{CeCu}_2\text{Si}_2$ ,  $\text{UPt}_3$  and  $\text{UBe}_{13}$ , both above and below their critical temperatures. The material  $\text{CeCu}_2\text{Si}_2$  has  $T_c \approx 1$  K. The form factor  $\chi(\mathbf{G})$  at 4.2 K is well fitted by the theoretical atomic form factor for  $\text{Ce}^{3+}$  state, i.e. one electron in the 4f shell, as shown in fig. 10. The form factor remains the same at 300 K where the susceptibility is Curie-Weiss, and at 0.1 K where the material is superconducting. This indicates that the same set of electrons are polarized by the magnetic field at all three temperatures. The resistivity maximum of this material appears at about 20 K and the Curie temperature is

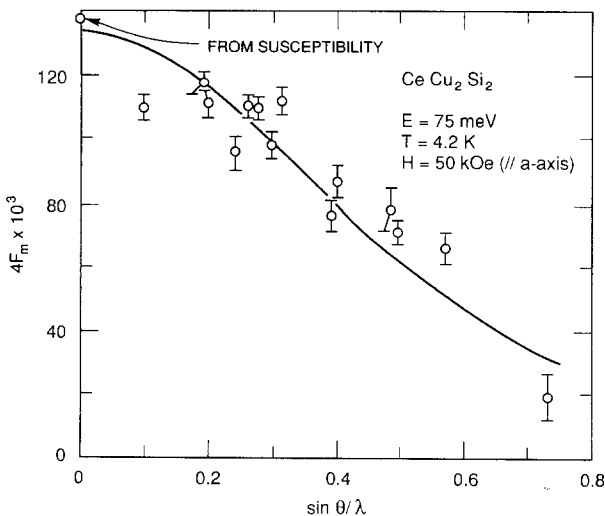


Fig. 10. The neutron paramagnetic form factor of  $\text{CeCu}_2\text{Si}_2$  (Stassis et al. 1985). The magnetic scattering amplitude  $F_m$  is proportional to the form factor  $\chi(\mathbf{G})$ . The solid curve is the theoretical form factor for  $\text{Ce}^{3+}$  state, which is the Fourier transform of the magnetic moment distribution for one 4f electron.

$\Theta = 170$  K, thus we can conclude from the data that the heavy mobile electrons at 4.2 K are the same 4f electrons which act like independent local moments at 300 K. Furthermore, they are also the electrons that become superconducting. The conclusion holds for the two U-based materials except that the form factors, shown in figs. 11 and 12, are best fitted by that of the  $U^{3+}$  ion. These experimental results drive home the dual nature of the f electrons in heavy-fermion materials – localized at high temperatures and itinerant at low temperatures.

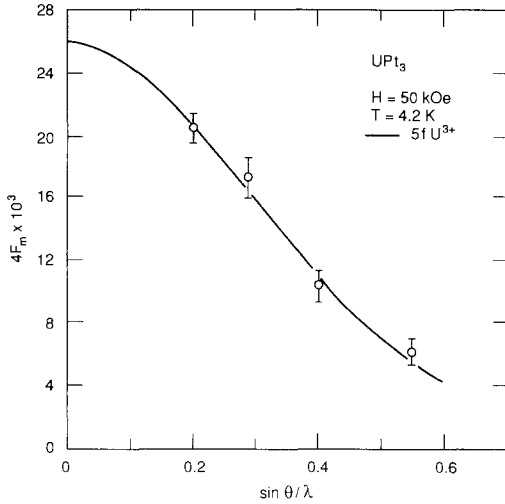


Fig. 11. The neutron paramagnetic form factor of UPt<sub>3</sub> (Stassis et al. 1986). The solid curve is the theoretical form factor for  $U^{3+}$ , which is the Fourier transform of the magnetic moment distribution of three 5f electrons in Hund's rule coupled ground state.

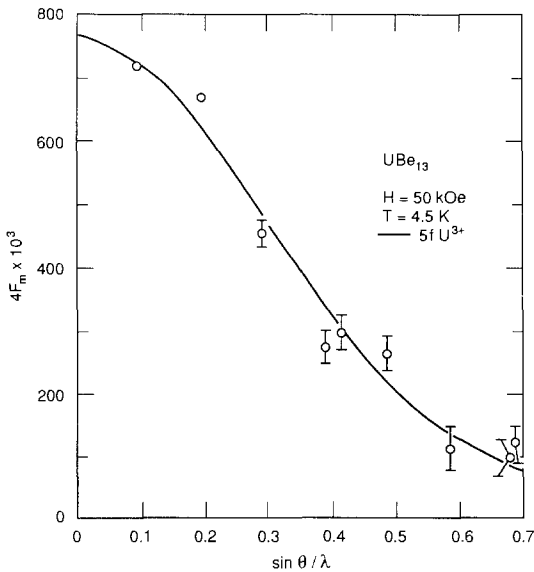


Fig. 12. The neutron paramagnetic form factor of UBe<sub>13</sub> (Stassis et al. 1986). The solid curve is the theoretical form factor for  $U^{3+}$ .



The form factors of all three materials remain unchanged in amplitude above and below the superconducting critical temperature, and the authors regarded this as a strong indication that the Cooper pairs are in the triplet spin configuration.

The same experiments have been performed on mixed-valence materials  $CeSn_3$  (Stassis et al. 1979a, b) and  $CePd_3$  (Stassis et al. 1982). The data for  $CeSn_3$  from 300 K down to 40 K are shown in fig. 13, and those at 4.2 K are shown in fig. 14. For a

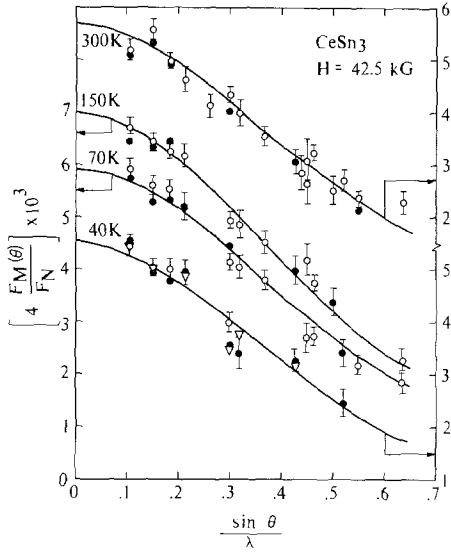


Fig. 13. The neutron paramagnetic form factor of  $CeSn_3$  between 40 and 300 K (Stassis et al. 1979a). The ratio between the magnetic scattering amplitude  $F_M(\theta)$  and the nuclear scattering amplitude  $F_N$  is a measure of the form factor  $\chi(\mathbf{G})$ . The open and solid circles denote data points obtained for a 4 mm and a 2 mm thick crystal, respectively, with the magnetic field parallel to the [110] direction. The triangles are data obtained with the 2 mm thick crystal at 40 K with the field parallel to the [100] direction. The solid curves are the theoretical form factor for  $Ce^{3+}$ , which has one electron in the 4f orbital.

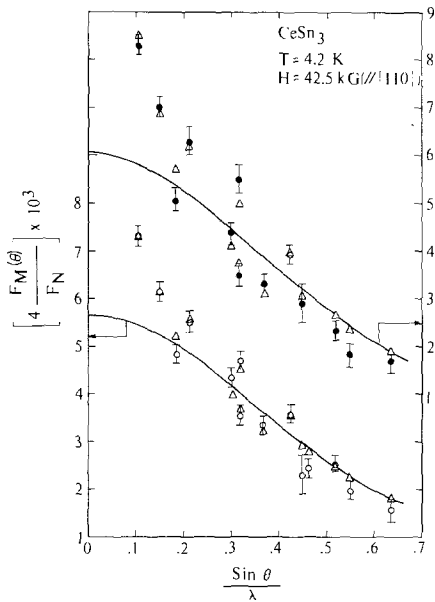


Fig. 14. The neutron paramagnetic form factor of  $CeSn_3$  at 4.2 K, obtained for a 4 mm (open circles) and a 2 mm (solid circles) thick crystal with the field parallel to the [110] direction (Stassis et al. 1979a). The triangles are calculated values assuming that the induced moment consists of a 4f and a Ce 5d component of  $e_g$  symmetry. The solid lines represent the theoretical 4f form factor.

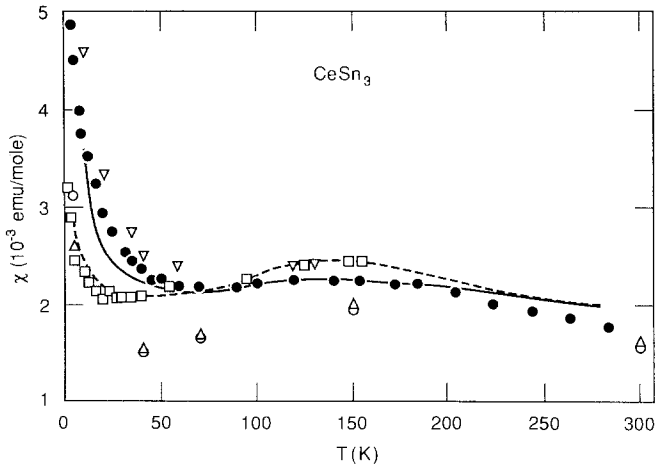


Fig. 15. Comparison of the magnetic susceptibility of  $\text{CeSn}_3$  reported by different workers by magnetization and neutron scattering measurements. The inverted triangles and squares represent data taken by Toxen (1979); the full circles were taken by Legvold (1979); the solid line was reported by Tsuchida and Wallace (1965); the dashed line reported by Malik et al. (1975), and the triangles and open circles are deduced from elastic neutron scattering measurements (Stassis et al. 1979b). The emergence of the 5d form factor coincides with the susceptibility tail.

wide temperature range, both above and well below the resistivity and susceptibility peaks, the material has the simple 4f form factor. The 4.2 K data show a significant anomaly, namely that a narrower component is added to the 4f form factor, and this component fits well with the spin form factor of a Ce 5d electron in the  $e_g$  orbital. As this added component grows rapidly with decreasing temperature, it causes the extrapolated  $\chi(\mathbf{G}=\mathbf{0})$  to follow the susceptibility tail at low temperatures, as shown in fig. 15. The data for  $\text{CePd}_3$  is similar, although the d part seems to be an even mixture of  $e_g$  and  $t_{2g}$  orbitals. In both cases the d contribution has the same periodicity as the Ce sublattice, so it seems that the low-temperature susceptibility tail, which was widely believed to be an impurity effect, is actually intrinsic (Gschneidner 1985). We will discuss the possible origin of this effect in section 3.

### 2.5. De Haas–van Alphen effect

In a strong magnetic field the motion of the itinerant electrons in a metal is modified from Bloch waves into quantized Landau orbits. With the field varying in time, various Landau orbits move in or out of the Fermi surface, causing the diamagnetic susceptibility to undergo periodic variations. The periodicity, measured in units of the magnetic field, determines directly the extremal cross-sectional area of the Fermi surface in the plane perpendicular to the field. If the Fermi surface is nonspherical, one can tilt the field relative to the crystalline axes to map out the cross sections in many directions, and thereby reconstruct the shape of the surface. In case the Fermi surface of a material has many pieces, one needs to Fourier-analyze the signal and

determine all detectable extremal areas from the frequency spectrum. The effective masses of the various pieces can be determined from the temperature dependence of the amplitudes of the corresponding frequency components. Since the amplitudes diminish with increasing temperature and impurity scattering, especially when the effective mass is high, successful measurements on heavy-fermion materials require high magnetic fields, low temperatures and high-quality samples.

Unlike the neutron paramagnetic form factor, the de Haas–van Alphen effect does not give direct information on the wave function of the electrons. A model of the Fermi surface, such as that obtained from a band calculation, is needed to sort out the various pieces. On the other hand, the experiment usually provides such a large amount of specific information that only a highly realistic model can have any chance to fit the observed frequencies and their dependences on the field direction.

Taillefer and co-workers (Taillefer et al. 1987, Taillefer and Lonzarich 1988) have reported successful observation of de Haas–van Alphen oscillations in  $\text{UPt}_3$ . To interpret their results, they compared the measured frequencies and masses with those calculated from the energy bands of Wang et al. (1987). There is generally good agreement between theory and experiment on the frequencies, and the agreement can be made exact by a small rigid shift of the calculated Fermi level. The measured masses, however, differ from calculated ones by factors around 20. The present-day band calculations employ the local-density functional approximation, which reduces the interacting many-electron problem into a one-electron problem in an effective potential. The calculation for  $\text{UPt}_3$  treats the  $f$  electrons on U as itinerant, so its impressive success in predicting the orbital frequencies has strong implications, that the  $f$  electrons are indeed itinerant in the temperature range where the experiments are performed. The failure of the calculation to account for the orbital masses is also significant, because it implies that there is a strong mass enhancement not properly handled by the one-electron approximation. We will return to these questions in section 3. A complete review of band calculations of heavy-fermion systems is the subject of chapter 110 of this volume. Similar experiments and calculations on mixed-valence systems tell the same story, with the exception that the mass enhancement is smaller (Johanson et al. 1981, Koelling 1982). These results point to the picture that both types of materials are  $f$  band metals. If so, what physical effect would cause the  $f$  electrons to acquire local magnetic moments at high temperatures? To what extent we can answer the numerous questions raised in this section will be the subject of the next section.

### 3. Theoretical approaches

The goal of this section is to summarize the present status of our understanding of the heavy-fermion problem. In many ways this is an impossible task, because there is no consensus among the community of theorists on the definition of the problem, let alone the proper approach to its solution. At the same time, the number of theoretical publications has grown so large that a mere list of the titles would reach the length of an average scientific article. To make it possible to write a meaningful

review without being bogged down by details, the author must exercise some choice in what to discuss and what to omit. The reader is forewarned that the choice reflects the author's personal bias, which may or may not stand the test of time. To those investigators whose contributions are not covered, we plead ignorance either of their publications or the future impact of their work.

We begin by reiterating our provisional definition of the heavy-fermion problem as outlined in the last section, that is, how to describe the behavior of the  $f$  electrons in various temperature regimes, and how to understand the continuous evolution from the apparent itinerant properties at low temperatures to the localized properties at high temperatures. We will discuss in separate subsections four classes of theories. The many variations of the Fermi liquid theory, which are based on the quasi-particle picture, are useful at low temperatures but not at high temperatures. The Kondo lattice model, which assumes localized  $f$  electrons from the start, works well at high temperatures, but fails to shed light on the low-temperature properties. The spin fluctuation resonance model is the modern version of the Kondo lattice model. It has provided some hope in understanding the narrow band at low temperatures, but we will demonstrate that this band, although fascinating, is most likely not the band of heavy fermions seen in the de Haas-van Alphen measurements. Finally, the electronic polaron model depicts the  $f$  electrons as itinerant from the start, but shows that the Coulomb interaction between the  $f$  and the conduction electrons causes the former to localize at high temperatures. The shortcoming of this theory is that it does not reproduce the spin fluctuation phenomenology observed at high temperatures. When theories are in conflict, we will appeal to experiments as the arbiter. Since physics thrives on controversy, it is the author's hope that any controversy this chapter may stir up will result in more careful analyses of the data and more refinements of the ideas.

### 3.1. *The Fermi liquid models*

There are three broad versions of Fermi liquid models in the literature, each is applicable for specific problems. The one-band model has provided the first understanding of the low-temperature thermodynamic and transport properties. The interpretation of inelastic neutron scattering data requires a two-band hybridization model. The band model based on the local-density functional approximation is by far the most elaborate noninteracting Fermi fluid model. We will discuss only the basic principle of this approach because the details appear elsewhere in this volume.

#### 3.1.1. *The one-band Fermi liquid model*

For the benefit of beginners, we will start the discussion from the most primitive level. This will also serve the purpose of defining a set of basic quantities which will be useful later. Let us consider a band of noninteracting fermions with mass  $m^*$ . The kinetic energy  $\varepsilon_k$  is related to the wave vector  $\mathbf{k}$  by

$$\varepsilon_k = k^2/2m^*. \quad (10)$$

It is customary to measure the wave vector in momentum units, so the quantity  $\hbar$

will be set equal to unity. There are  $N$  fermions per unit volume in two spin states, so the Fermi level  $\mu$ , which is a function of the temperature  $T$ , is determined by the implicit relation

$$N = \int \frac{2N(\varepsilon) d\varepsilon}{\exp[\beta(\varepsilon - \mu)] + 1}, \quad (11)$$

where  $\beta = 1/k_B T$ ,  $k_B$  is the Boltzmann constant, and  $N(\varepsilon)$  is the density of states per spin per unit volume defined by

$$N(\varepsilon) = \frac{(2m^*)^{3/2} \varepsilon^{1/2}}{4\pi^2}. \quad (12)$$

At  $T=0$  the Fermi energy has the expression

$$\mu(0) = k_F^2/2m^*, \quad (13)$$

where  $k_F = (3\pi^2 N)^{2/3}$  is the Fermi wavevector introduced in section 2. We define a Fermi temperature by  $T_F = \mu(0)/k_B$ , then at temperatures much less than  $T_F$ , the Fermi level depends weakly on temperature and the density of states at the Fermi level  $N(\mu)$ , defined in eq. (3), determines the specific heat and the magnetic susceptibility. For temperatures much greater than  $T_F$ , the fermion gas is no longer degenerate so that the specific heat reaches the classical limit determined by equipartition of energy:

$$C(T) = \frac{3}{2} N k_B. \quad (14)$$

Since this is not what is observed in heavy-fermion systems, we conclude that a band of free heavy fermions is not a viable model for high-temperature properties.

One can do a little better by postulating a band of finite width. It can be verified that, for rather general forms of the density-of-states curve  $N(\varepsilon)$ , the high-temperature specific heat satisfies the  $T^{-2}$  law and the high-temperature susceptibility goes like  $T^{-1}$ . On the other hand, it seems quite difficult to design an  $N(\varepsilon)$  curve which will yield both the total entropy and the Curie constant in the susceptibility. Besides, the  $T^2$  dependence of the low-temperature resistivity argues strongly that the pair interaction between the fermions cannot be ignored if one intends to understand the total problem.

A simple interacting fermion system may be represented by the following Hamiltonian:

$$H = \sum_{k\sigma} \varepsilon_k c_{k\sigma}^\dagger c_{k\sigma} + \frac{1}{2} \sum_{kk'q} \sum_{\sigma\sigma'} (V_0 - V_1 s \cdot s') c_{k\sigma}^\dagger c_{k'\sigma'}^\dagger c_{k'-q,\sigma'} c_{k+q,\sigma}. \quad (15)$$

In the above Hamiltonian the quantities  $c_{k\sigma}$  and  $c_{k\sigma}^\dagger$  are fermion operators in the momentum state  $\mathbf{k}$  and spin state  $\sigma$ . The electron spin operators are denoted by  $s$  and  $s'$ . The direct interaction term  $V_0$  is independent of the spin, while the exchange term is explicitly spin dependent. The sign of  $V_1$  is chosen so that parallel spins are favored. In principle, the potentials are functions of the momenta  $\mathbf{k}$ ,  $\mathbf{k}'$  and  $\mathbf{q}$ , but for the purposes of illustrating the physics, it is sufficient to restrict ourselves to the

momentum-independent s-wave scattering and omit all higher partial wave components.

As discussed in textbooks (Blatt 1968), the interaction term in eq. (15) does not give rise to any resistivity unless the fermion gas is imbedded in a lattice so that umklapp scattering can occur. Furthermore, since at  $T \ll T_F$  only those electrons within an energy shell of width  $k_B T$  around the Fermi level can conduct electric current, the pair of electrons affected by the interaction must be within this energy shell both before and after scattering. Thus, the phase space argument shows that the resistivity must be scaled by  $(T/T_F)^2$ , as observed experimentally. Unfortunately, the theory contains too many parameters to allow a reliable determination of the interaction potential from the resistivity data of real materials.

The exchange interaction modifies the magnetic susceptibility formula so that at zero temperature

$$\chi(0) = \frac{2N(\mu)\mu_B^2}{1 - V_1 N(\mu)}. \quad (16)$$

The denominator, which is less than unity, causes an enhancement of the susceptibility. This is the reason that on the  $\gamma$  versus  $\chi(0)$  plot in fig. 3 the points for some materials appear on the right of the straight line. In case the denominator is less than zero, the paramagnetic state is unstable against the spontaneous splitting of the spin degeneracy. This results in a ferromagnetic state for which the moment per magnetic atom is nonintegral. So far only a few heavy-fermion ferromagnets have been found. One example is the series of compound  $\text{CePt}_x\text{Si}$  for  $x < 0.97$ . In particular, the material with  $x = 0.7$  becomes ferromagnetic below 5.5 K with the saturation moment of  $0.18\mu_B$  per Ce atom (Lee et al. 1988). Metallic ferromagnets with nonintegral moments are said to be itinerant. The reader may consult the review by Herring (1966) for further details of the theory of itinerant ferromagnetism.

Even in nonmagnetic materials the exchange enhancement effect produces spin fluctuations which can influence the thermodynamic properties of the material. One defines the dynamical susceptibility function  $\chi^{(0)}(\mathbf{q}, \omega)$  for the noninteracting Fermi gas by

$$\chi^{(0)}(\mathbf{q}, \omega) = \sum_{\mathbf{k}} \frac{n_{\mathbf{k}} - n_{\mathbf{k}+\mathbf{q}}}{\varepsilon_{\mathbf{k}+\mathbf{q}} - \varepsilon_{\mathbf{k}} - (\omega + i\delta)}, \quad (17)$$

where  $n_{\mathbf{k}} = \{\exp[\beta(\varepsilon_{\mathbf{k}} - \mu)] + 1\}^{-1}$  is the Fermi distribution function,  $\delta = 0^+$ , and the frequency  $\omega$  is measured in energy units. It is easy to verify that  $2\mu_B^2 \chi^{(0)}(0, 0)$  is the static susceptibility of the noninteracting Fermi gas in eq. (4). For the interacting gas the dynamical susceptibility function is enhanced into

$$\chi(\mathbf{q}, \omega) = \frac{\chi^{(0)}(\mathbf{q}, \omega)}{1 - V_1 \chi^{(0)}(\mathbf{q}, \omega)}. \quad (18)$$

Again, aside from a factor  $2\mu_B^2$  the quantity  $\chi(0, 0)$  reduces to the enhanced static susceptibility in eq. (16). The dynamical susceptibility is the linear response function

of the interacting gas to an external magnetic field which has the sinusoidal spatial and temporal dependence given by  $\exp(i\mathbf{q}\cdot\mathbf{r} - i\omega t)$ .

The unenhanced dynamical susceptibility for zero frequency has the expression:

$$\chi^{(0)}(q, 0) = N(\mu) \frac{1}{2} \left[ 1 + \frac{1}{2} \left( \frac{2k_F}{q} - \frac{q}{2k_F} \right) \ln \left| \frac{2k_F + q}{2k_F - q} \right| \right]. \tag{19}$$

This function is largest at  $q = 0$ , as shown in fig. 16, so the uniform susceptibility receives the highest enhancement. In fig. 17 we show qualitatively the real and imaginary parts of  $\chi^{(0)}(\mathbf{q}, \omega)$  for nonzero  $\omega$ , and in fig. 18 the imaginary part of the enhanced susceptibility for  $1 - V_1 N(\mu) = 0.5$  for three different values of the momentum. One can think of  $\chi(\mathbf{q}, \omega)$  as the propagator or Green's function of a spin fluctuation mode, then the imaginary part is the spectral density of the mode. This

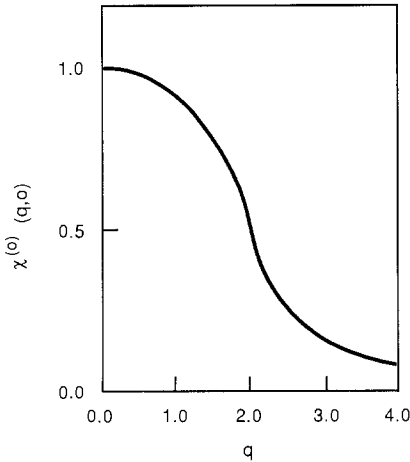


Fig. 16. The wave-vector-dependent susceptibility  $\chi^{(0)}(\mathbf{q}, 0)$  for the free-electron gas. The wave vector  $q$  is measured in units of the Fermi momentum  $k_F$ , and the susceptibility is normalized by the density of states at the Fermi level.

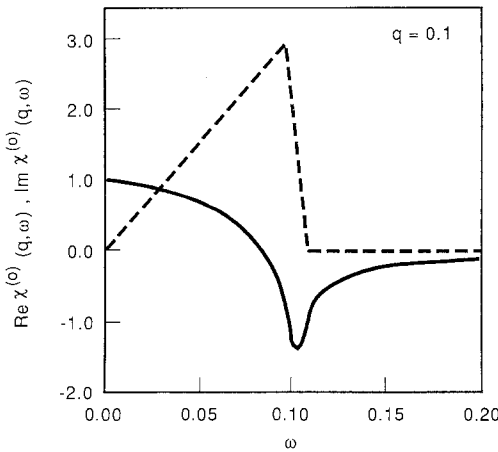


Fig. 17. The real (solid curve) and imaginary part (dashed curve) of the dynamical susceptibility  $\chi^{(0)}(\mathbf{q}, \omega)$  for the free-electron gas. The energy  $\omega$  is measured in units of Fermi energy  $\mu$ , and the susceptibility components are normalized by the density of states at the Fermi level.

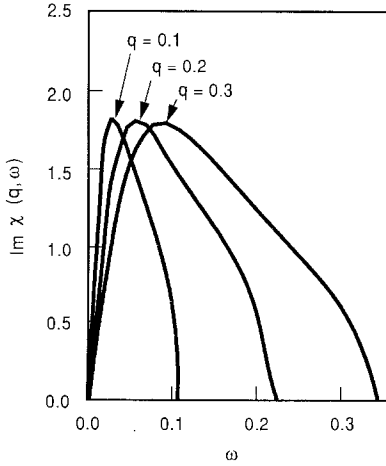


Fig. 18. The imaginary part of the enhanced dynamical susceptibility  $\chi(\mathbf{q}, \omega)$  for an interacting electron gas. The wave vector is measured in units of  $k_F$ , the energy is measured in units of  $\mu$ , and the susceptibility is normalized by the density of states at the Fermi level.

mode is over-damped, because the linewidth is substantial compared with the energy at the maximum of the spectral density. The peak position shifts linearly with the momentum, giving the mode a linear dispersion relation. In the ferromagnetic system, i.e.  $1 - V_1 N(\mu) < 0$ , a permanent moment develops spontaneously and the quantity  $\text{Im } \chi(\mathbf{q}, \omega)$  evolves into a  $\delta$ -function, which is the spectral function of the spin-wave or magnon mode. As a result, the spin fluctuation modes in the paramagnetic system are also called paramagnons.

Just like other boson modes in solids, paramagnons also contribute to the specific heat of the material (Doniach and Engelsberg 1966). A propagating mode with a linear dispersion relation gives a  $T^3$  contribution to the specific heat, but the natural width of the paramagnon mode modifies this contribution so that the entire electronic contribution to the specific heat is

$$C(T) = \gamma T + BT^3 \ln T. \quad (20)$$

The coefficient  $B$  in the above expression contains a number of material-dependent parameters. The spin fluctuation contribution to the specific heat is clearly seen in many heavy-fermion compounds such as  $\text{UPt}_3$  (Stewart et al. 1984) and mixed-valence compounds such as  $\text{CeSn}_3$  (Tsang et al. 1984).

It is also possible to excite these modes by neutron scattering, because the magnetic moment of the neutron interacts with the electron spin to produce the spatial and temporal dependent magnetic field. The wavevector  $\mathbf{q}$  and the frequency  $\omega$  are, respectively, the momentum and energy transfer of the scattering process. The theory predicts a broad inelastic peak near the center of the Brillouin zone. Actual experiments carried out on  $\text{CeCu}_6$  (Aeppli et al. 1986),  $\text{UPt}_3$  (Aeppli et al. 1987) and  $\text{UBe}_{13}$  (Mook 1987) reveal such a broad peak near the Brillouin zone boundary. This is evidence that the one-band model is less than adequate for the real material. We will show next that a two-hybridized-band model is needed to understand these results.



### 3.1.2. The two-band model

Two different two-band models have been proposed by Liu (1988) and Auerbach et al. (1988) to explain the inelastic neutron scattering data in heavy-fermion systems. The two models differ in how the bands are formed, and both mechanisms will be discussed in detail in later sections. We will show here that the main result, that the inelastic neutron scattering peak may appear at the zone boundary, can be understood on the basis of a generic two-band model. The two bands arise from the hybridization of a broad conduction band and a dispersionless f band. The phenomenological Hamiltonian of such a system is

$$H = \sum_{k\sigma} \varepsilon_k c_{k\sigma}^\dagger c_{k\sigma} + \varepsilon_f \sum_{k\sigma} f_{k\sigma}^\dagger f_{k\sigma} + V \sum_{k\sigma} (c_{k\sigma}^\dagger f_{k\sigma} + \text{h.c.}), \quad (21)$$

where  $f_{k\sigma}$  is the f electron annihilation operator,  $\varepsilon_f$  is the energy of the f level, and  $V$  is the hybridization matrix element between the conduction and f electrons. The parameters are not necessarily those estimated from atomic or band-structure calculations, because renormalizations due to many-body correlations are expected.

It is straightforward to obtain the energies of the hybridized bands:

$$\varepsilon_k^{(\pm)} = \frac{1}{2} \{ \varepsilon_k + \varepsilon_f \pm [(\varepsilon_k - \varepsilon_f)^2 + 4V^2]^{1/2} \}. \quad (22)$$

The two bands are shown schematically in fig. 19, in which the original unhybridized bands are shown in dotted lines. The bands become flat on both sides of  $\varepsilon_f$ , so electrons in these parts of the bands have heavy masses provided that  $V$  is sufficiently weak. Assuming that the broad conduction band spans an energy range from 0 at the center of the Brillouin zone to  $W$  at the zone boundary and the f level is at the middle of the band,  $\varepsilon_f = W/2$ , then for the physically interesting case  $V \ll \varepsilon_f$ , we find that the top of the lower band occurs at the zone boundary with energy  $\varepsilon_f - \Delta$ , where  $\Delta = V^2/\varepsilon_f$ , and the bottom of the upper band occurs at the zone center with energy  $\varepsilon_f + \Delta$ . An energy gap of the size  $2\Delta$  opens up around  $\varepsilon_f$ . Let  $N(\varepsilon)$  be the density of

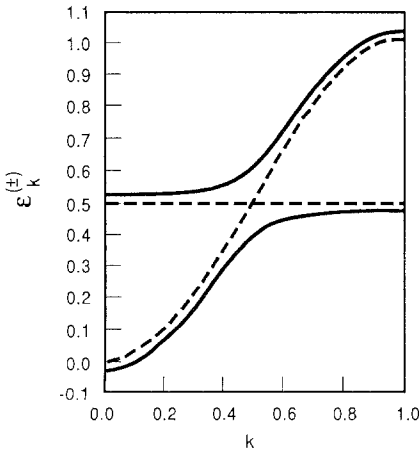


Fig. 19. Schematic representation of the two hybridized bands (solid curves) for the simple two-band model. The unperturbed broad band is represented by the dashed curve and the f level by the dashed line. The wave vector  $k$  is measured in units of the zone boundary vector, and the energy is in units of the total bandwidth.

states of the unhybridized broad band, then  $N_{\pm}(\varepsilon)$  for the hybridized bands are

$$N_{\pm}(\varepsilon) = N \left( \varepsilon - \frac{V^2}{\varepsilon - \varepsilon_f} \right) \left[ 1 + \frac{V^2}{(\varepsilon - \varepsilon_f)^2} \right]. \quad (23)$$

These functions are shown schematically in fig. 20 for the case of small  $V$ . Both peak sharply at or near the edges of the gap, which indicates that the band mass is vastly enhanced over the mass of the broad band, by an amount measured by  $\varepsilon_f/\Delta$ .

In the two publications mentioned earlier the authors proposed different mechanisms for the formation of the two bands, and they put the Fermi level within different bands. In our phenomenological discussion we can use either model and obtain the same result, as guaranteed by the symmetry between particles and holes. Thus, for the sake of argument, we will put  $\mu$  slightly above the bottom of the upper band so that this band is slightly occupied while the lower band is full. The dynamical susceptibility function now has two components, the intraband component  $\chi_{++}^{(0)}$  and the interband component  $\chi_{-+}^{(0)}$  defined by

$$\chi_{ab}^{(0)}(\mathbf{q}, \omega) = \sum_{\mathbf{k}} \frac{n_{\mathbf{k}}^{(a)} - n_{\mathbf{k}+\mathbf{q}}^{(b)}}{\varepsilon_{\mathbf{k}+\mathbf{q}}^{(b)} - \varepsilon_{\mathbf{k}}^{(a)} - (\omega + i\delta)}, \quad (24)$$

where a, b are band indices and  $n_{\mathbf{k}}^{(a)}, n_{\mathbf{k}}^{(b)}$  are the occupation numbers of the bands. In particular,  $\chi_{++}^{(0)}(0, 0) = N_+(\mu)$  as found previously, where  $N_+(\mu)$  can be found from eq. (23). The interband component at zero energy transfer is large for  $\mathbf{Q}$  between the center and the boundary of the Brillouin zone because the energy denominator is small. We can estimate that

$$\chi_{-+}^{(0)}(\mathbf{Q}, 0) \simeq \frac{1 - N_e}{2\Delta}, \quad (25)$$

where  $N_e \ll 1$  is the total occupation of the partially filled upper band. To obtain some feeling for the relative sizes of the two contributions, we consider a very simple band model for which the density of states  $N(\varepsilon)$  is a constant, which we denote by  $N(0)$ . The band can accommodate one conduction electron per spin such that  $N(0)W = 1$ . We find, after some simple algebra that

$$\frac{\chi_{-+}^{(0)}(\mathbf{Q}, 0)}{\chi_{++}^{(0)}(0, 0)} \simeq \frac{1 - N_e}{(1 - 2N_e)^2}. \quad (26)$$

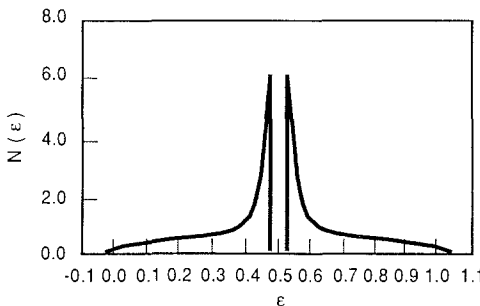


Fig. 20. The density-of-states curve of the two-band model in fig. 19.

The ratio is greater than unity for any finite but small  $N_e$ , which means that the total susceptibility  $\chi^{(0)}(\mathbf{q}, 0) = \chi_{++}^{(0)}(\mathbf{q}, 0) + \chi_{-+}^{(0)}(\mathbf{q}, 0)$  has a peak at or near  $\mathbf{Q}$ . For an interacting gas the susceptibility at the peak will receive the highest amount of enhancement. In case  $\chi^{(0)}(\mathbf{q}, 0)$  peaks at  $\mathbf{Q}$  and  $V_1\chi^{(0)}(\mathbf{Q}, 0) > 1$ , the system will be magnetically ordered at sufficiently low temperatures with a simple antiferromagnetic structure, as seen in most heavy-fermion antiferromagnets.

If the stable state is paramagnetic, i.e.  $V_1\chi^{(0)}(\mathbf{Q}, 0) < 1$ , the neutrons can excite paramagnon type of modes with momenta near the zone boundary point  $\mathbf{Q}$ . The scattering cross-section is given by the imaginary part of the enhanced susceptibility given by eq. (19). The qualitative nature of the line shape can be seen from the unenhanced susceptibility

$$\text{Im } \chi_{-+}^{(0)}(\mathbf{Q}, \omega) = \sum_{\mathbf{k}} (n_{\mathbf{k}+\mathbf{Q}}^{(-)} - n_{\mathbf{k}}^{(+)}) \delta(\varepsilon_{\mathbf{k}}^{(+)} - \varepsilon_{\mathbf{k}+\mathbf{Q}}^{(-)} - \omega). \quad (27)$$

If we measure the Fermi level  $\mu$  from the bottom of the lower flat band, the quantity in eq. (27) can be put in the closed form

$$\text{Im } \chi_{-+}^{(0)}(\mathbf{Q}, \omega) = \frac{\Delta}{\omega^2} [f(-\Delta - \mu - \omega/2) - f(-\Delta - \mu + \omega/2)], \quad (28)$$

with  $f(x) = 1/(e^{\beta x} + 1)$ ,  $\beta = 1/k_B T$ . A typical line shape is shown in fig. 21. Both Liu and Auerbach et al. showed that the observed neutron scattering line shape can be well fitted by this theory.

The new paramagnon mode determined by the enhanced susceptibility at the zone boundary point  $\mathbf{Q}$  has little dispersion, so it is not responsible for the  $T^3 \ln T$  contribution to the specific heat. If the broad band has a more complex density of states curve  $N(\varepsilon)$ , it is perhaps not unthinkable that for certain values of  $N_e$  or  $\mu$  the enhanced system may prefer the ferromagnetic state rather than the antiferromagnetic state, as has been found in some heavy-fermion materials. This would suggest that suitable adjustment of the Fermi level by doping can cause a material to have different magnetic states. This possibility deserves further investigation.

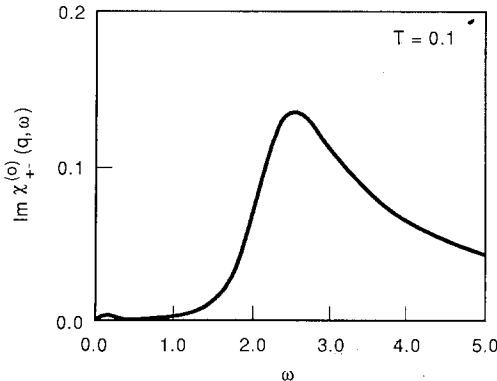


Fig. 21. The theoretical neutron scattering cross section under constant- $q$  scan as predicted by the two-band model. The momentum transfer  $\mathbf{q}$  is at the boundary of the Brillouin zone. The temperature is measured in units of  $\Delta$ , one-half of the hybridization gap.

### 3.1.3. Local-density-functional band calculations

The band calculations with potentials generated from local density functional approximations give the most detailed one electron band structures. As was discussed in section 2, one obtains Fermi surface dimensions in good agreement with experiments. We will mention briefly the basic principle of the calculation in order to illustrate that the calculation is surprisingly unsophisticated in terms of many-body correlation effects to be discussed later.

The band calculation is based on the one-electron approximation to the many-electron problem for metallic solids. The one-electron wave functions  $\psi_{nk}(\mathbf{r})$  and energies  $\varepsilon_{nk}$  are eigenstates and eigenvalues of the Schrödinger equation:

$$\left[ \frac{p^2}{2m_0} + V(\mathbf{r}) \right] \psi_{nk}(\mathbf{r}) = \varepsilon_{nk} \psi_{nk}(\mathbf{r}), \quad (29)$$

where  $m_0$  is the bare electron mass, the index  $n$  labels the bands, and the vector  $\mathbf{k}$  represents the wave vector or crystal momentum. The potential  $V(\mathbf{r})$  is the sum of three terms,

$$V(\mathbf{r}) = V_N(\mathbf{r}) + V_H(\mathbf{r}) + V_{xc}(\mathbf{r}). \quad (30)$$

The nuclear potential  $V_N$  is the electrostatic potential due to the nuclear charges. It is given by the expression

$$V_N(\mathbf{r}) = - \sum_l \frac{Z_l e^2}{|\mathbf{r} - \mathbf{R}_l|}, \quad (31)$$

where  $e$  is the absolute value of the electron charge and  $Z_l e$  is the nuclear charge of the atom at the lattice site  $\mathbf{R}_l$ . The lattice sum on  $l$  runs over all atomic species that comprise the material. The Hartree potential  $V_H$  is the electrostatic potential of the charge distribution of all electrons, and is calculated from the total electron density  $\rho(\mathbf{r})$  by

$$V_H(\mathbf{r}) = e^2 \int \frac{\rho(\mathbf{r}')}{|\mathbf{r} - \mathbf{r}'|} d^3 r'. \quad (32)$$

The electron density is calculated from the wave functions of the occupied Bloch states:

$$\rho(\mathbf{r}) = \sum_{\text{occ}} |\psi_{nk}(\mathbf{r})|^2. \quad (33)$$

The exchange–correlation potential  $V_{xc}$  represents all many-body effects due to electron–electron interaction that are not included in the Hartree potential. The correlation problem in metals remains largely unsolved, and in heavy-fermion materials the many-body correlation is thought to be the cause of all the observed anomalous properties. On the other hand, it has been found empirically that one can perform extremely good band calculations for simple as well as transition metals by using the local-density-functional approximation (LDA) for  $V_{xc}$  (Kohn and Sham 1965):

$$V_{xc}(\mathbf{r}) = - 2e^2 \left( \frac{3\pi}{8} \right)^{1/3} [\rho(\mathbf{r})]^{1/3}. \quad (34)$$

Now the band calculation is reduced to a self-consistent calculation, that the potential is determined by the charge density, which in turn is determined by the potential. An iterative procedure is used to perform this massive calculation. In practice, only the itinerant electrons need to be treated self-consistently, because the core electrons are not affected by the formation of the solid.

Early band calculations for lanthanide metals and their intermetallic compounds assigned the f electrons to the core because the f levels of most these materials are situated far below the Fermi energy. In recent calculations for mixed-valence and heavy-fermion materials, however, it has been found necessary to include the f electrons as itinerant in order to obtain the correct lattice constants, binding energy and bulk modulus of the solids. The band calculation for UPt<sub>3</sub> cited earlier by Wang et al. (1987) was done in this manner, and the calculation yielded an excellent description of the Fermi surface geometry as measured by the de Haas–van Alphen effect. The electrons near the Fermi level are predominantly of the f character, in agreement with neutron paramagnetic form factor measurements. At the same time, the electron mass came out too small by a factor of 20 to 30. Thus, the band calculation only gives a partial answer to the heavy-fermion problem. The complete answer must account for the effective mass and the temperature induced transformation from itinerant to local properties of the f electrons.

### 3.2. *The Kondo lattice*

The Kondo lattice model occupies a special position in the theory of mixed-valence and heavy-fermion systems. It was found more than two decades ago that dilute alloys of Ce exhibited the so-called Kondo effect, i.e. the impurity contribution to the electrical resistivity has a strong dependence on the temperature (Maple et al. 1978). Historically the Kondo effect was associated with magnetic 3d transition metal impurities in simple or nonmagnetic transition metals. The understanding of the phenomenon, along the line first proposed by Kondo (1964, 1969), has been one of the most actively pursued goals among condensed matter theorists. When it was discovered that ordered intermetallic compounds of Ce, U and some other lanthanide and actinide elements also had the Kondo-type resistivity behavior at high temperatures, they were given the name dense Kondo system. The name is still in use today, although it is now widely accepted that the spin fluctuation resonance model is more basic and should be the starting point of a complete theory for dense systems. We have chosen to discuss the Kondo model separately because it is the first to give a spin-induced, temperature-sensitive scattering resonance at the Fermi level, and this resonance is central to the phenomenology of many observed anomalies. The discussion will be merely a compact summary of the results, because there exist excellent reviews by leading contributors of this field (Andrei et al. 1983, Bickers 1987, Newns and Read 1987, Schlottmann 1989).

Consider first one Ce impurity atom imbedded in a nonmagnetic metal. The Hamiltonian of such a system can be written as

$$H = \sum_{\mathbf{k}\sigma} \varepsilon_{\mathbf{k}} c_{\mathbf{k}\sigma}^{\dagger} c_{\mathbf{k}\sigma} + \sum_{\sigma} \varepsilon_f f_{\sigma}^{\dagger} f_{\sigma} + V \sum_{\mathbf{k}\sigma} (c_{\mathbf{k}\sigma}^{\dagger} f_{\sigma} + f_{\sigma}^{\dagger} c_{\mathbf{k}\sigma}) + U_{ff} f_{\uparrow}^{\dagger} f_{\uparrow} f_{\downarrow}^{\dagger} f_{\downarrow}. \quad (35)$$

In the above equation  $f_\sigma^\dagger$  and  $f_\sigma$  are the f electron operators in the spin state  $\sigma$  for the impurity atom situated at the origin, and  $U_{ff}$  is the Coulomb repulsion between two f electron if they occupy the same site. All other symbols have been defined under eq. (21). The energy level scheme of the impurity atom is such that the energy is zero when the atom is empty of f electrons,  $\varepsilon_f$  when one f electron is present, and  $2\varepsilon_f + U_{ff}$  if two f electrons are on the atom simultaneously. The parameters are chosen so that  $\varepsilon_f < \mu$ , where  $\mu$  is the Fermi level of the conduction electron system, and  $\varepsilon_f + U_{ff} > \mu$ . Accordingly, the f level is singly occupied in the ground state. The Hamiltonian only includes the spin degeneracy of the f level, not its orbital degeneracy. It is applicable to the case where the crystal field removes the orbital degeneracy in such a way that the ground state consists of two degenerate levels, the Kramers doublet. This is the case in many mixed-valence and heavy-fermion materials at temperatures much below the crystal field splitting.

With single occupation of the f level, the atom automatically acquires a magnetic moment. The hybridization interaction  $V$  gives rise to a spin-dependent interaction between the conduction electrons and the f electron. The effective Hamiltonian of this interaction is (Schrieffer and Wolfe 1966):

$$H_{\text{eff}} = \sum_{k\sigma} c_{k\sigma}^\dagger c_{k\sigma} - 2J \mathbf{S} \cdot \mathbf{s}, \quad (36)$$

where  $\mathbf{S}$  is the spin operator of the f electron,  $\mathbf{s}$  is that of the conduction electron, and

$$J = V^2 \left[ \frac{1}{\varepsilon_f - \mu} - \frac{1}{\varepsilon_f + U_{ff} - \mu} \right]. \quad (37)$$

The interaction term is a scattering process of a conduction band electron by the localized f electron. Assuming that the band electron is scattered from the initial state  $k\sigma$  to the final state  $k'\sigma'$ . The following process can take place:

$$(k\sigma, f\sigma') \rightarrow (k\sigma, k'\sigma') \rightarrow (f\sigma, k'\sigma'),$$

and

$$(k\sigma, f\sigma') \rightarrow (f\sigma, f\sigma') \rightarrow (f\sigma, k'\sigma').$$

The first process has an intermediate state in which the f level is empty. The matrix element of this process is the first in the square brackets in eq. (37), after we approximate both initial and final electron energies by  $\mu$ . The process is spin dependent because the term with  $\sigma \neq \sigma'$  allows an exchange of spin between the band and f electrons. The second process involves a doubly occupied f level in the intermediate state provided that  $\sigma \neq \sigma'$ . It is also spin dependent and its matrix element appears in the second term in the expression for  $J$  in eq. (37). Usually  $U_{ff}$  is much larger than all other energies involved, so the second process can be ignored. This is the infinite- $U$  limit one finds in literature. Notice that the overall sign of  $J$  is negative, indicating antiferromagnetic interaction between the local magnetic spin and the conduction electron spin. Coqblin and Schrieffer (1969) have extended this result to include the orbital degeneracy of the f electron. The result has the same form as eq. (37) except that the total angular momentum operator of the f electron

appears in the interaction term. For simplicity we will use  $S$  to represent the total angular momentum of the impurity atom: the pure spin model has  $S = \frac{1}{2}$ , while Ce impurity has  $S = \frac{5}{2}$ .

The scattering between band and  $f$  electrons described in eq. (36) undergoes a resonance at the Fermi level. The width of the resonance is measured by  $k_B T_0$ , where  $T_0$ , called the Kondo temperature, is the only temperature or energy scale in the problem. If we simplify the structure of the conduction band by assuming a constant density of states  $N(0)$  and the occupied part of the band spans between the energies  $0 < \varepsilon_k < \mu$ , we can write (Kondo 1969):

$$k_B T_0 = \mu \exp[-1/2N(0)|J|], \quad (38)$$

for  $N(0)|J| \ll 1$ . At elevated temperatures the resonance broadens steadily while the effects of the resonance diminish. We will discuss the resonance in its modern context in section 3.3. For the moment we will merely summarize some analytical results (Rajan 1983) and give an overall assessment of the model.

The specific heat  $C(T)$  has a linear temperature dependence for  $T \ll T_0$ , peaks near  $T_0$ , and declines steadily at higher temperatures, as shown in fig. 22. The magnetic susceptibility  $\chi(T)$  is independent of  $T$  for  $T \ll T_0$ . The susceptibility has a peak around  $T_0$  for impurity spin  $S > \frac{1}{2}$ . At  $T \gg T_0$  the quantity  $\chi(T)$  has a  $1/T$  dependence as shown in fig. 23. Both results are in good accord with experimental data provided that one regards the material as a lattice of Ce or U impurities and scales up the thermodynamic quantities by the density of impurity atoms. In fig. 24 we show the magnetic field dependence of the specific heat and compare the results with the data on Ce ( $S = \frac{5}{2}$ ) impurity in  $\text{LaAl}_2$  (Bader et al. 1975). The predicted magnetization behavior for the same system is compared with the data at various fields and temperatures in fig. 25. The success of these and other comparisons to be discussed later are widely accepted as convincing evidence that the Kondo effect embodies the most important physics in mixed-valence and heavy-fermion systems.

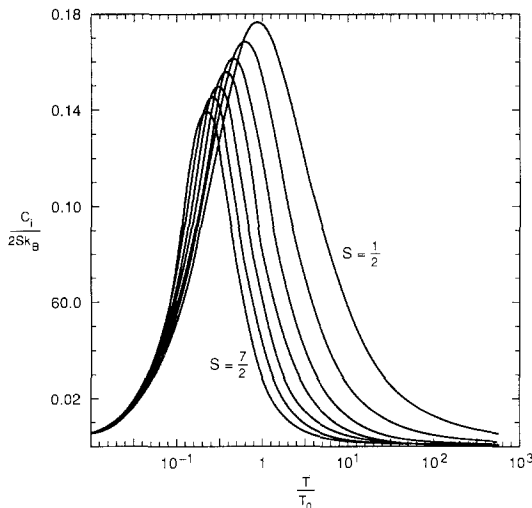


Fig. 22. The specific-heat curve  $C(T)$  of the Kondo model for a range of integral and half-odd integral spin values  $S$  from  $\frac{1}{2}$  to  $\frac{7}{2}$  (Rajan 1983).

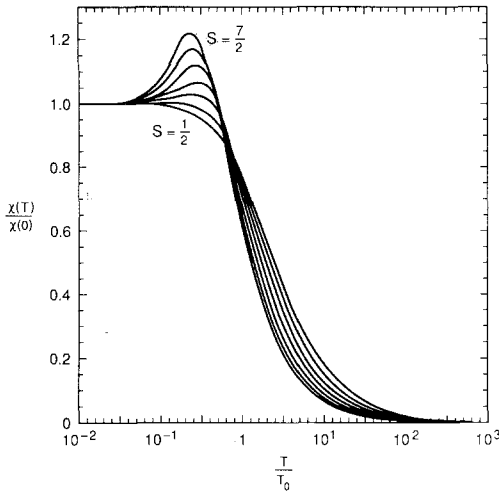


Fig. 23. The susceptibility curve  $\chi(T)$  of the Kondo model for a range of spin values  $S$  (Rajan 1983).

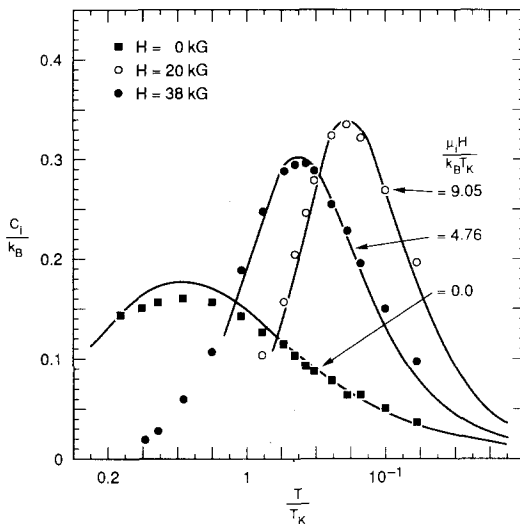


Fig. 24. The magnetic field dependence of the specific heat curve for dilute alloys of Ce in  $\text{LaAl}_2$  (Rajan et al. 1982) compared with experimental results (Bader et al. 1975). The magnetic moment per Ce impurity is denoted by  $\mu_i$ . The temperature scale  $T_K$  is related to the Kondo temperature  $T_0$  by a simple factor which depends on the band model (Andrei and Lowenstein 1981).

One calculates transport properties by correlating the resistivity with the total scattering cross-section. The electrical resistivity is found to be temperature insensitive at low temperatures, has the  $\ln(T/T_0)$  dependence near  $T_0$ , and decreases steadily for  $T > T_0$ . The shape of the resistivity curve will be discussed in section 3.3. Clearly the low-temperature resistivity is in disagreement with experiments, which indicate the  $T^2$  type Fermi liquid behavior. The discrepancy comes from the implicit assumption that the impurity atoms scatter the conduction electrons incoherently. How the system achieves coherence at low temperatures is now studied in terms of the spin fluctuation resonance model, but the analysis has not yet reached the level of sophistication of the single-impurity problem.



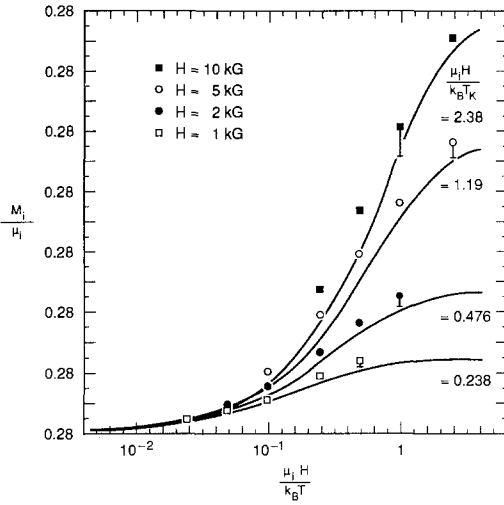


Fig. 25. The magnetization curves of dilute alloys of Ce in LaAl<sub>2</sub> (Rajan et al. 1982) compared with experimental results (Bader et al. 1975). The magnetic moment per Ce impurity is denoted by  $\mu_i$ .

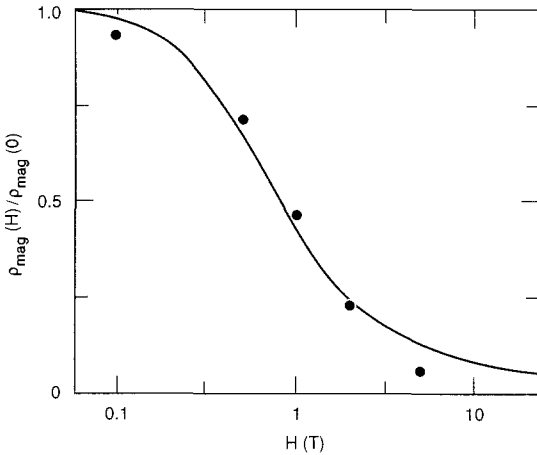


Fig. 26. The zero temperature magnetoresistance for the Kondo model (solid curve) in comparison with data for a dilute alloy of Ce (Schlottmann 1989).

The magnetoresistance has been calculated at zero temperature by Andrei (1982). The result is compared with experimental data for a dilute alloy of Ce in fig. 26 (Schlottmann 1989).

The important concept of scaling has resulted from the study of the Kondo problem. The model Hamiltonian in eq. (35) contains a host of parameters, but only one combination of the parameters, the Kondo temperature  $T_0$ , appear in all of the final results. This implies that the temperature or magnetic field dependence of a physical property measured for all different materials can be collapsed into one universal curve by a suitable change of scale. We have already mentioned this effect in connection with the susceptibility data, and will discuss further generalizations of this concept to other properties later.

### 3.3. The spin fluctuation resonance model

In deriving the Kondo Hamiltonian, we have considered only one  $f$  site and allowed the  $f$  electron to make virtual transitions to the Fermi level and back to the same site. This assumption holds in a dilute alloy in which the individual Ce or U sites are far apart. Consequently, although the Kondo model has been found highly successful in fitting the specific heat and susceptibility data of dense systems (Schlottmann 1989), one should regard the agreement with a healthy dose of skepticism. In a dense system the  $f$  sites may communicate with each other via intersite transitions, and this process is considered to be crucial to the development of the coherent state at low temperatures. Attempts to analyze this effect have all been carried out in the context of the spin fluctuation resonance model, which is the modern version of the Kondo model. It has been shown that for the one-site problem the model completely reproduces the Kondo model results. We will now discuss the essential physics of the model without going into the methods of solution. The reader is urged to consult the reviews by Bickers (1987), Newns and Read (1987) and Schlottmann (1989) for mathematical details.

#### 3.3.1. Single-site spin fluctuation resonance

We begin the discussion by giving a variational derivation of the ground state of the single-site problem whose Hamiltonian is given in eq. (35). We temporarily regard the hybridization term as a weak perturbation on the band plus  $f$  electron system. For clarity we will study the infinite- $U$  model so that the  $f$  level can at most be singly occupied. The unperturbed state consists of one  $f$  electron in spin state  $\sigma$  and  $N$  conduction electrons in the filled Fermi sea. We denote this state by

$$|\Psi'_\sigma\rangle = f_\sigma^\dagger |N\rangle. \quad (39)$$

The energy of the system is

$$E'_0 = \epsilon_f + \sum_{\mathbf{k}, \text{occ}}^N \epsilon_{\mathbf{k}}, \quad (40)$$

where the sum of  $\mathbf{k}$  is over all occupied states up to the Fermi level  $\mu$  of the  $N$  electron band. The first interaction term excites the  $f$  electron to an unoccupied level. For minimum energy gain the electron is excited to  $\mu$ . Subsequently the second term removes an electron from the occupied portion of the band and refills the  $f$  level in spin  $\sigma'$ , which may or may not be the same as  $\sigma$ . The net result is that a hole is created in the band with the possibility of a spin-flip of the  $f$  electron. Therefore, a variational ground state should contain the ground state of the  $N + 1$  band electron with zero  $f$  occupation and all possible states with one  $f$  electron and one hole in the band. Thus, we write (Varma and Yafet 1976)

$$|\Psi\rangle = |N + 1\rangle + \sum_{\mathbf{k}, \sigma} a_{\mathbf{k}\sigma} f_\sigma^\dagger c_{\mathbf{k}\sigma} |N + 1\rangle, \quad (41)$$

where  $a_{\mathbf{k}\sigma}$  is the variational parameter. Putting  $|\Psi\rangle$  into the Schrödinger equation

$H|\Psi\rangle = E_0|\Psi\rangle$ , and equating coefficients of like terms, we obtain

$$a_{k\sigma} = V/(-\varepsilon_0 - \mu + \varepsilon_k), \quad (42)$$

where

$$-\varepsilon_0 = E_0 - E'_0 = \mu - \varepsilon_f + V \sum_{k\sigma} a_{k\sigma}. \quad (43)$$

Assuming a band with a constant density of states  $N(0)$  and occupied from 0 up to  $\mu$ , we can carry out the sum on  $k$  in eq. (43) to obtain

$$-\varepsilon_0 = \mu - \varepsilon_f + 2N(0)V^2 \ln \left[ \frac{\varepsilon_0}{\mu + \varepsilon_0} \right]. \quad (44)$$

An iterative solution valid for weak hybridization is

$$\varepsilon_0 = \mu \exp[-(\mu - \varepsilon_f)/2N(0)V^2] = \mu \exp[-1/2N(0)|J|] = k_B T_0, \quad (45)$$

where  $J$  is the infinite- $U$  limit of eq. (37) and  $T_0$  is the Kondo temperature defined in eq. (38). This derivation illustrates that the system can gain energy by forming a correlated state which consists of an f electron and a hole in the band. Furthermore, both spin states of the f electron enter the ground state with equal weight. A trial wave function with spin can be constructed by eliminating the sum on  $\sigma$  in eq. (40), but the energy of this state  $E'_0 - \mu \exp[-1/N(0)|J|]$ , which is higher than  $E_0$ . Therefore, the correlated state with no net spin is the most stable.

The f level occupation in the spinless ground state is

$$n_f = \frac{\langle \Psi | \sum_{\sigma} f_{\sigma}^{\dagger} f_{\sigma} | \Psi \rangle}{\langle \Psi | \Psi \rangle} = \left[ 1 + \frac{\varepsilon_0}{2N(0)V^2} \right]^{-1}. \quad (46)$$

The two spin states share the occupation equally. In the weak coupling limit  $n_f$  is slightly less than unity. The number of holes in the conduction band is equal to  $n_f$ , also with one-half of the amount in each spin state. Since a hole with spin up leaves an unpaired electron with spin down and vice versa, the ground state may be looked upon as a singlet state formed by the f electron and a local wave packet formed by band electrons.

Another consequence of the f electron and band hole correlation is that the energy of the f level is spread out all over the width of the band. The level spreading is best represented by the f electron spectrum:

$$\rho_f(\omega) = \frac{1}{\pi} \text{Im} G_f(\omega), \quad (47)$$

where  $G_f(\omega)$  is the f electron propagator, which when calculated under the same approximation as the ground state, has the expression

$$G_f(\omega) = \left[ \omega + \mu - \varepsilon_f - 2N(0)V^2 \ln \left( \frac{\omega + \mu}{\omega} \right) \right]^{-1}. \quad (48)$$

The spectrum is shown qualitatively in fig. 27. In the negative  $\omega$  side, which is the

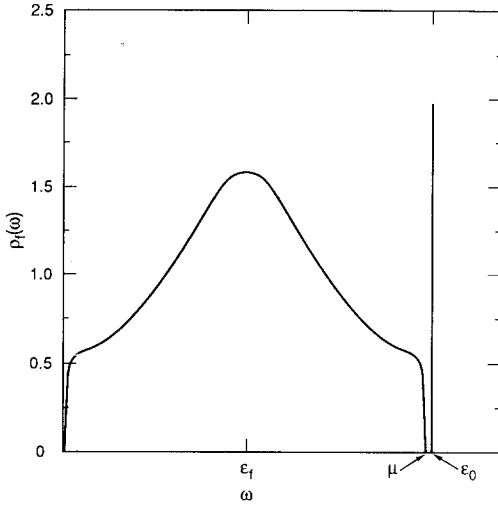


Fig. 27. The approximate f electron spectrum in the infinite- $U$  limit. The sharp line at  $\epsilon_0$  marks the spin fluctuation resonance level. Higher-order correction terms broaden the resonance and closes the gap, leaving the continuum part unaffected.

occupied part, the spectrum has the Lorentzian shape with a half-width at half-maximum equal to  $2\Gamma$  where

$$\Gamma = \pi N(0)V^2. \quad (49)$$

The area under this part of the spectrum is  $n_f$ . In addition,  $G_f(\omega)$  has a pole in the positive part of the spectrum at  $\omega = \epsilon_0$ . The strength of the pole is found to be  $1 - n_f$ , so that the total area under the spectrum is unity. The sharp spectral line acquires a width of the order  $k_B T_0$  when the hybridization effect is calculated to higher orders. At the same time the apparent gap between the pole and the continuum disappears. The resonance line, now centered slightly above the Fermi level, is the modern version of the Kondo resonance.

It is interesting to note that in the extreme Kondo limit, i.e.  $n_f \rightarrow 1$ , the pole of the resonance level disappears from the f level spectrum. The existence of a pole in the unoccupied part of the spectrum gives hint to an excited state of the system. A suitable trial wave function for the excited state is  $|\Psi'_\sigma\rangle$  defined in eq. (49), because it has the correct variational energy. In this state, which is doubly degenerate, the singlet correlation between f and band electrons is broken. One can think of the resonance level as a single-particle state (Liu 1989a), and the operator which puts an electron in this state is

$$\tilde{f}_\sigma^\dagger = A(f_\sigma^\dagger + \sum_{\mathbf{k}} a_{\mathbf{k}\sigma} c_{\mathbf{k}\sigma}^\dagger), \quad (50)$$

where  $A$  is a normalization factor equal to  $A = [2(1 - n_f)/(2 - n_f)]^{1/2}$ . The energy required to promote an electron from the Fermi level to the resonance level is  $\epsilon_0$ . The f content of the operator in eq. (50) is  $|A|^2$ , which is very small in the practical case of  $n_f \simeq 1$ . In the extreme Kondo limit the resonance level persists but its f content is vanishingly small.

For Ce atoms the 4f level has the total angular momentum  $S = \frac{5}{2}$  and a total number of rotational levels  $N_f = 2S + 1 = 6$ . The crystal field usually splits the degeneracy, but if the level splitting is sufficiently small, all  $N_f$  substates can participate in spin fluctuation. The theory of the resonance level remains qualitatively the same, but the large  $N_f$  value allows the so-called  $1/N$  approximation, which helps to simplify the calculation of the level width (Bickers et al. 1985, 1987). At zero temperature the resonance is found to have an asymmetric lineshape with a level width measured by  $k_B T_0$ . When the temperature is increased the line drops in height and shifts in energy as shown in fig. 28. Although the theory introduces a new parameters  $n_f$  in addition

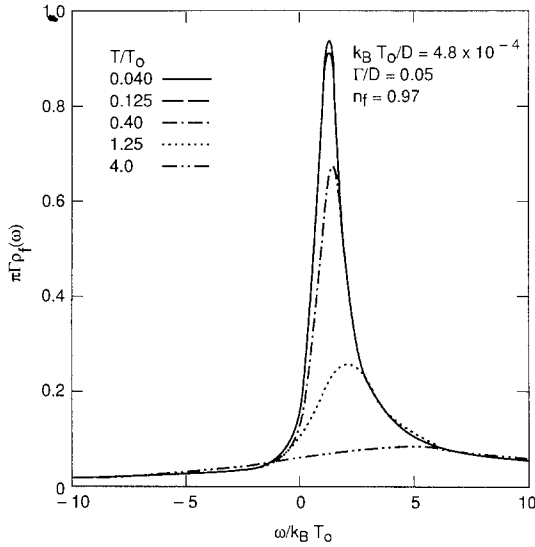


Fig. 28. The shape and temperature dependence of the spin fluctuation resonance for  $N_f = 6$ , which represents Ce impurity (Bickers et al. 1987).

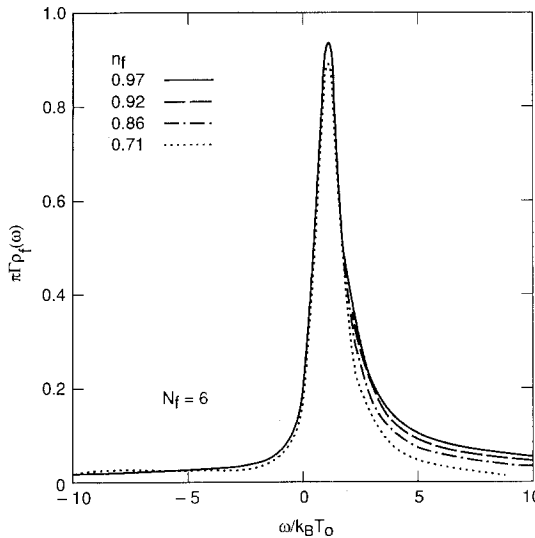


Fig. 29. The shapes of zero-temperature Kondo resonance for four values of  $n_f$ , showing that the resonance is insensitive to  $n_f$  (Bickers et al. 1987).

to the Kondo temperature  $T_0$ , the line shape is insensitive to  $n_f$  as shown in fig. 29. Consequently the Kondo scaling remains valid in practice.

We summarize the results of some  $1/N$  calculations in a set of figures. In figs. 30 and 31 we compare the susceptibility and specific heat results of the  $1/N$  calculation with those of the Kondo model. The two sets of results, for  $N_f = 6$  and 4 respectively, show that the spin fluctuation model virtually reproduces the predictions of the Kondo model. In fig. 32 the specific heat of a dilute alloy of Ce in  $\text{LaB}_6$  is compared

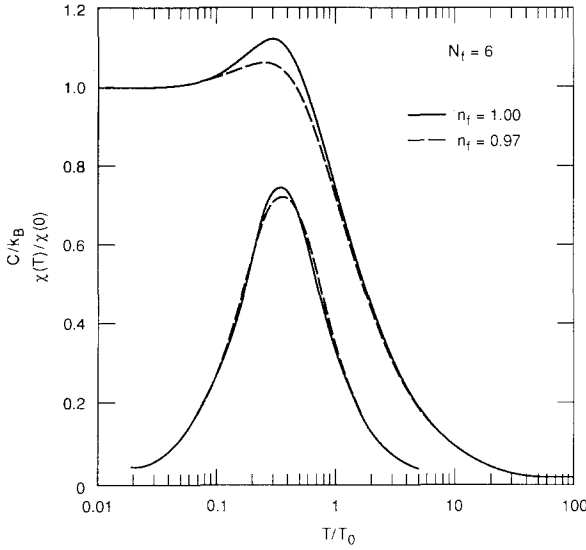


Fig. 30. The magnetic susceptibility (upper curves) and specific heat (lower curves) for the single Ce impurity as predicted by the spin fluctuation resonance model for  $N_f = 6$  and  $n_f = 0.97$ . The  $n_f = 1$  curves are the prediction of the Kondo model (Bickers et al. 1987).

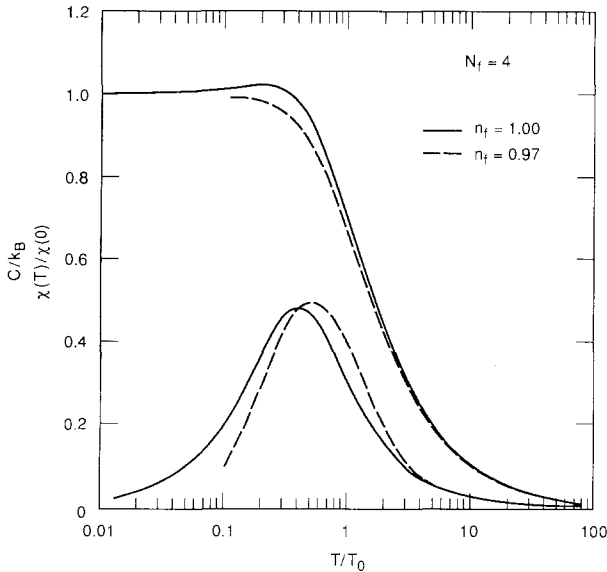


Fig. 31. The magnetic susceptibility (upper curves) and specific heat (lower curves) for the single Ce impurity as predicted by the spin fluctuation model for  $N_f = 4$  and  $n_f = 0.97$ . The  $n_f = 1$  curves are the prediction of the Kondo model (Bickers et al. 1987).

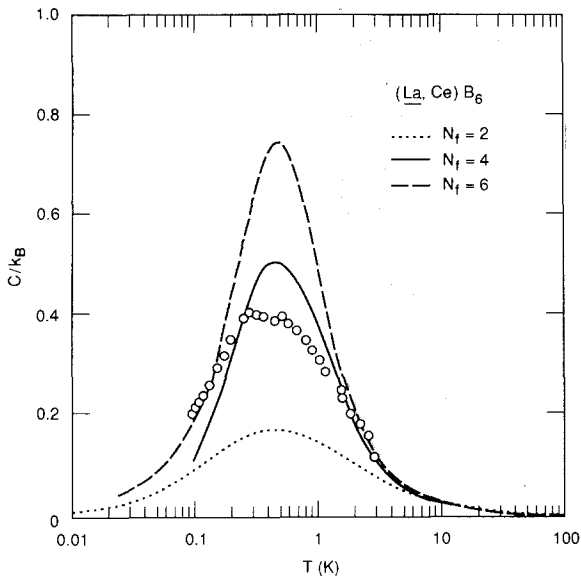


Fig. 32. Comparison between theoretical and experimental specific heat results for a dilute alloy of Ce in  $\text{LaB}_6$  (Bickers et al. 1987). The  $N_f = 4$  curve gives the best overall fit to the data (Ernst et al. 1984).

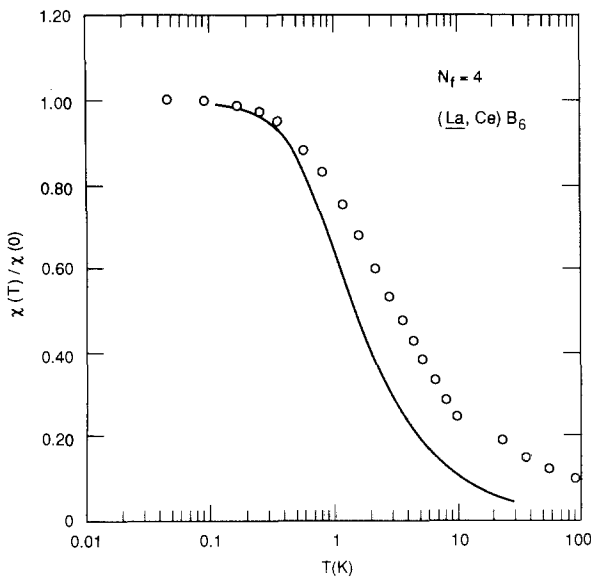


Fig. 33. Comparison between theoretical and experimental susceptibility results for a dilute alloy of Ce in  $\text{LaB}_6$  (Bickers et al. 1987). The measurement was reported by Felsch (1978).

with calculated results assuming  $N_f = 2, 4$  and 6. The  $N_f = 4$  curve gives the best overall fit to the data, suggesting the ground state quartet are the active levels. The susceptibility, resistivity and thermal power of the same alloy are compared with theory in figs. 33–35. All calculations are done for  $N_f = 4$ . More comparisons can be found in the reviews by Bickers (1987), News and Read (1987) and Schlottmann (1989). It is safe to conclude that the single-impurity problem is now completely understood.

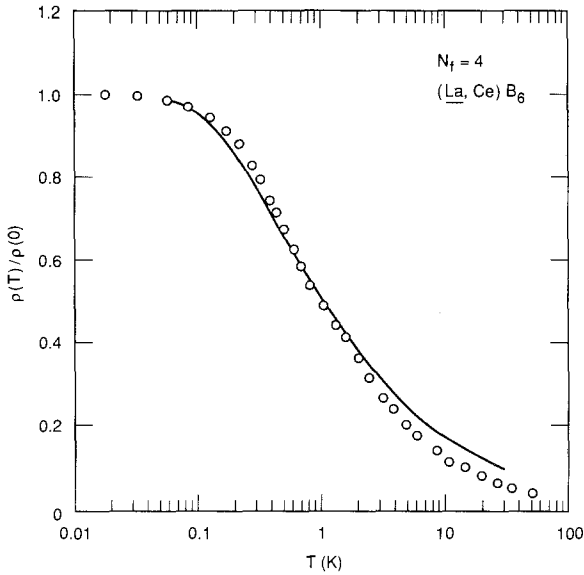


Fig. 34. Comparison between theoretical and experimental resistivity results for a dilute alloy of Ce in  $\text{LaB}_6$  (Bickers et al. 1987). The measurement was reported by Winzer (1975).

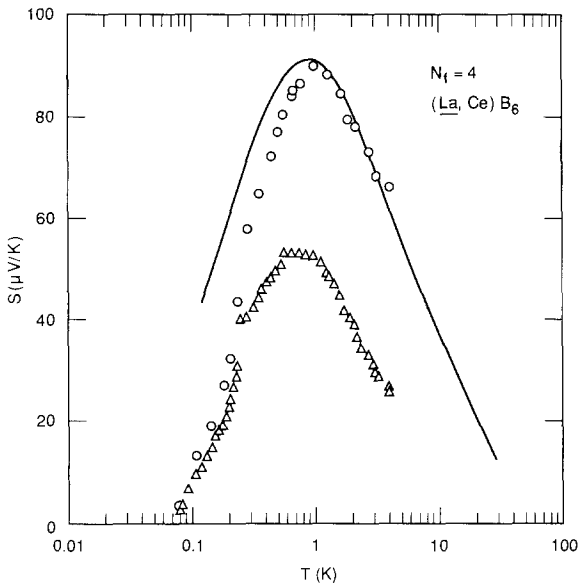


Fig. 35. Comparison between theoretical and experimental thermopower results for a dilute alloy of Ce in  $\text{LaB}_6$  (Bickers et al. 1987). The measurement was reported by Ernst et al. (1984). The raw data for a sample with 0.25% Ce impurities are denoted by triangles, and the magnetic contribution is denoted by open circles.

### 3.3.2. Toward a coherent lattice

It has been pointed out previously that a heavy-fermion compound is more than a collection of independent Kondo scatterers, because this physical picture completely misses the low-temperature coherent state. We will now discuss recent attempts to describe the coherent state and compare their predictions with various experiments which probe the ground state electronic structure. A lattice of  $f$  sites in a normal



metal is described by the Anderson Hamiltonian:

$$\begin{aligned}
 H = & \sum_{\mathbf{k}\sigma} \varepsilon_{\mathbf{k}} c_{\mathbf{k}\sigma}^\dagger c_{\mathbf{k}\sigma} + \sum_{j\sigma} \varepsilon_f f_{j\sigma}^\dagger f_{j\sigma} + V \sum_{j\mathbf{k}\sigma} (c_{\mathbf{k}\sigma}^\dagger f_{j\sigma} e^{-i\mathbf{k}\cdot\mathbf{R}_j} + \text{h.c.}) \\
 & + U_{\text{ff}} \sum_j f_{j\uparrow}^\dagger f_{j\uparrow} f_{j\downarrow}^\dagger f_{j\downarrow},
 \end{aligned} \tag{51}$$

where the sum on  $j$  is over all  $f$  sites at  $\mathbf{R}_j$ . All other quantities have been defined in eq. (35). Now all  $f$  sites undergo spin fluctuations. Once an electron moves out of the  $f$  level and fills a band hole, it can move freely to a different site and fills its  $f$  level provided that site is temporarily empty. This kind of intersite spin fluctuation leads to a coherent ground state. At the same time, the translational symmetry of the ground state ensures that elementary excitations are Bloch waves, which are thought to form the narrow band or bands detected by the de Haas–van Alphen effect.

The band problem is tractable in the same level of approximation as the variational ground state in eq. (41) (Millis and Lee 1987, Auerbach et al. 1988). The energy  $\omega$  of an elementary excitation with momentum  $\mathbf{k}$  is solved from the following equation:

$$\omega - \varepsilon_{\mathbf{k}} - V^2 G_f(\omega) = 0, \tag{52}$$

where  $G_f(\omega)$  is the  $f$  electron propagator defined in eq. (48). This equation determines the pole of the band electron propagator, which by definition is the energy of the elementary excitation. We can also regard this equation as the result of a Brillouin–Wigner perturbation calculation, with the fully renormalized  $f$  state as the intermediate state. The  $f$  electron propagator has a pole at  $\varepsilon_0$ , so we expand  $G_f(\omega)$  around the pole and reduce the above equation to

$$\omega - \varepsilon_{\mathbf{k}} - \frac{V^2(1 - n_f)}{\omega - \varepsilon_0} = 0. \tag{53}$$

The solutions of this equation are the two bands in eq. (22), section 3.1.2, with  $\varepsilon_0$  as the renormalized  $f$  level energy and  $V(1 - n_f)^{1/2}$  as the renormalized hybridization matrix element. The latter renormalization owes its origin to the reduced  $f$  content of the spin fluctuation resonance level. As a result of the renormalization of  $V$ , which determines the bandwidth, the bands are expected to be very narrow in the limit  $n_f \simeq 1$ .

It is tempting to identify these bands with the  $f$  bands measured by the de Haas–van Alphen effect in heavy-fermion materials for the following reasons: (1) the band masses calculated by LDA are too low in comparison with the measured values, and the renormalization of the hybridization potential  $V$  provides a natural way to explain the discrepancy; (2) the two-band model explains well the inelastic neutron scattering line shape; and (3) the band structure is derived in a manner consistent with the single-site theory, so that one theory suffices for both dilute and dense Kondo systems. On the other hand, the following arguments tend to dampen our enthusiasm. As pointed out in section 3.1.3, the local-density functional calculation is based on a mean-field theory which cannot compare with the spin fluctuation theory in sophistication. It is not possible to construct a local, one-body potential that embodies the physics of spin fluctuation. Consequently, there is no reason to expect that the two divergent theories can produce the same complex sets of bands. Although there

is a one-to-one correspondence between the local levels  $\varepsilon_f$  and  $\varepsilon_0$ , there is no proof that the correspondence can be extended to the band problem. Finally, the resonance level has very little  $f$  content, so that when the narrow band is polarized by a magnetic field, the induced moment should have the spatial distribution determined by the broad band electrons, which to a large extent have the Ce or U  $d$  electron wave function. The neutron magnetic form factors of heavy-fermion materials indicate that the induced moments in the Fermi liquid state have the  $f$  electron distribution. The  $d$  and  $f$  distributions are so different that there is no possibility of misinterpreting the experimental results. Thus, the case for associating the narrow band of spin fluctuation resonance with the band of heavy fermions is less than convincing.

It was reviewed in section 2.4 that, at sufficient low temperatures, the neutron magnetic form factors of a number of Ce-based mixed-valence materials do exhibit an additional feature which has the spatial distribution of Ce  $5d$  electrons. This part follows the temperature dependence of the so-called susceptibility tail, and becomes vanishingly small when the temperature is raised to 40 K, which is much below the temperature of maximum susceptibility, about 150 K for  $\text{CeSn}_3$ . There has been one suggestion (Liu 1989a) that this unusual feature is the contribution of the spin fluctuation resonance band because it has the expected wave function characteristic. If this interpretation is correct, then one must find a different reason for the characteristic temperature for susceptibility and resistivity peaks. Also, it is not understood why such a feature has not been seen in heavy-fermion systems.

There are other theoretical questions concerning this picture of the coherent state. The theory does not touch upon the important question of why the coherence is lost at high temperatures. The  $f$  electron propagator in eq. (48) is not calculated to a sufficiently high order that is consistent with the Kondo behavior of a single impurity. It has been argued that a higher-order calculation is necessary for determining the entire resistivity curve (Yoshimori and Kasai 1983, Coleman 1987). How would the higher-order correction affect the bands remains unclear.

The band picture preserves the scaling properties, that there is still only one energy scale in the theory. Auerbach and Levin (1986) have discussed many experimental properties of  $\text{UPt}_3$  in this context. A necessary consequence of scaling is that the specific heat peak, the susceptibility peak or shoulder, and the resistivity peak must all fall at roughly the same temperature (Coleman 1987). This is true for  $\text{UPt}_3$  but not for  $\text{UPt}_3$ , because the resistivity curve of the latter has no apparent peak. The compound  $\text{CeAl}_3$  has a susceptibility peak around 0.6 K but a resistivity peak at 35 K. The two characteristic temperatures differ by more than one order of magnitude. This brief survey seems to indicate that the resistivity behavior is influenced by some other factor or factors. One such factor, which should play an important role in dense systems but not in dilute systems will be discussed next.

### 3.4. *The electronic polaron model*

The electronic polaron model is based on the assumption that the band calculation using the local-density functional approximation gives the correct ground state of the system. The agreement between the calculated Fermi surface geometry and the

observed de Haas–van Alphen frequencies lends credence to this view. It is also a known fact that LDA does not predict the excited state spectrum correctly, for example, Coulomb renormalization is needed to obtain the correct band gap in insulators (Hybertsen and Louie 1985). An extension of this consideration to the  $f$  band problem leads to the electronic polaron model.

The fundamental premise of the electronic polaron model is diagonally opposite to that of the spin fluctuation resonance model. The former starts from the band state at low temperatures and studies how the  $f$  electrons can become localized at high temperatures, and in contrast, the latter starts from the high-temperature state where the  $f$  electrons are localized and attempts to reach a Fermi liquid state at low temperatures. The distinction between the two is best illustrated by the schematic diagrams in fig. 36. Figure 36a captures the essence of the spin fluctuation resonance model. The parabola represents the broad conduction band which is filled up to the Fermi level  $\mu$ . The  $f$  level, labelled by  $\varepsilon_f$ , is deeply buried in the broad band. The hybridization interaction between the two groups of electrons produces the resonance level  $\varepsilon_0$  above  $\mu$ , and it hybridizes with the broad band to produce the two narrow bands. The lower band is partially filled. The explanation of physical properties of heavy-fermion materials lies in the energy and temperature dependence of the resonance. Figure 36b shows the gist of the electronic polaron model. The  $f$  level is assumed to be close to the Fermi level, and it hybridizes directly with the broad band electrons. The upper band is partially filled. The motion of the  $f$  hole is always accompanied by a massive and local redistribution of the conduction electrons, and the dynamical nature of the screening process gives clue to the observed phenomena. The picture in fig. 36b is often called the mixed-valence regime in the literature. The electronic polaron model, however, does not make the distinction between mixed-valence and heavy-fermion systems because both are thought to be the results of the same set of interactions. The fact that there is no obvious break in the  $\gamma$  versus  $\chi(0)$  plot in fig. 3 between mixed-valence and heavy-fermion materials supports this hypothesis.

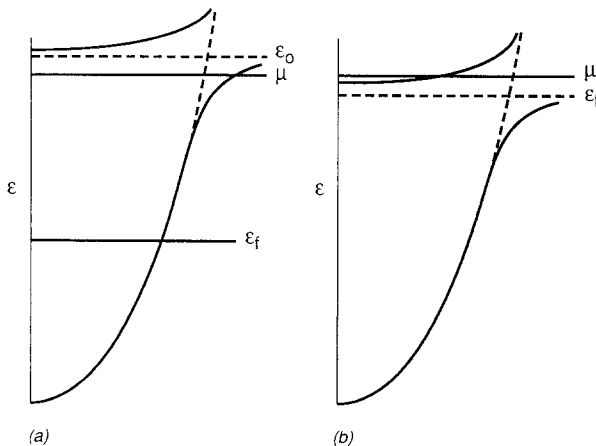


Fig. 36. Schematic diagrams showing the distinction between the mechanisms for energy band formation of (a) the spin fluctuation resonance model, and (b) the electronic polaron model.

This review begins with a nontechnical discussion of the dynamical screening process of an  $f$  hole by the band electrons, showing that it creates an asymmetrical resonance similar to the spin fluctuation resonance. The formation of a narrow hybridized band due to  $f$  hole hopping follows. The temperature dependence of the resonance causes the  $f$  electron motion to evolve from Bloch waves at low temperatures to diffusion and eventually to localization at high temperatures. This subsection will close with comparisons between the predictions of this model and experimental results for dense systems.

### 3.4.1. The $f$ hole screening problem

Unlike semiconductors and insulators, the renormalization program for  $f$  electrons in the context of the LDA band calculation is beyond the present capability of computational technology. This necessitates the use of the following simple band Hamiltonian for the discussion:

$$H = \sum_{k\sigma} \varepsilon_k c_{k\sigma}^\dagger c_{k\sigma} + \sum_{j\sigma} \varepsilon_f f_{j\sigma}^\dagger f_{j\sigma} - U_{df} \sum_{j,\sigma\sigma'} \sum_{k,k'} f_{j\sigma} f_{j\sigma'}^\dagger c_{k\sigma}^\dagger c_{k'\sigma'} e^{i(k-k')\cdot R_j} + V \sum_{jk\sigma} (c_{k\sigma}^\dagger f_{j\sigma} e^{-ik\cdot R_j} + \text{h.c.}). \quad (54)$$

The  $U_{df}$  term, first invoked by Falicov and Kimball (1969) to study the  $\alpha$ -to- $\gamma$  phase transition of Ce, represents the Coulomb attraction between an  $f$  hole and the band electron. The  $f$  orbital is more tightly bound than the  $6s$  and  $5d$  electrons which form the conduction band, and the presence or absence of an  $f$  electron at a lanthanide or actinide site produces a major perturbation to the local potential of that site. Since LDA calculations for Ce includes nearly one electron in the crystal potential, so it is consistent to regard the absence of the  $f$  electron as the perturbation, as written in the above effective Hamiltonian. The  $U_{ff}$  term is left out of the Hamiltonian, but its main effect of restricting of  $f$  occupation to unity will be built into the eigenstates. The hybridization term will be treated later by perturbation, which is justified because  $U_{df} \gg V$ .

The ground state consists of the filled Fermi sea up to  $\mu$  plus one  $f$  electron at every site. The energy of the system is

$$E_0 = 2 \sum_{k,\text{occ}} \varepsilon_k + \sum_i \varepsilon_f. \quad (55)$$

Consider the excited state which has the  $f$  electron at one site removed. The effective Hamiltonian of the conduction electrons is

$$H_1 = \sum_{k\sigma} \varepsilon_k c_{k\sigma}^\dagger c_{k\sigma} + \sum_i \varepsilon_f - \varepsilon_f - U_{df} \sum_{kk',\sigma} c_{k\sigma}^\dagger c_{k'\sigma}, \quad (56)$$

where the  $f^0$  site is chosen as the origin. The Coulomb term excites electron-hole pairs from the filled Fermi sea. If we compare the energy of the one-hole state with that of the ground state, the difference is the binding energy of the  $f$  electron plus the energy of the excited electron-hole pairs. As a result, the  $f$  electron spectrum is no longer a  $\delta$ -function at  $\varepsilon_f$  but spreads out over the side of higher binding energy.

The spectrum was shown to have a power law singularity at  $\varepsilon_f$  (Mahan 1967, Nozières and de Dominicis 1969):

$$\rho_f(\omega) = A|\omega|^{-\alpha}, \quad \omega < 0, \quad (57a)$$

and

$$\rho_f(\omega) = 0, \quad \omega > 0. \quad (57b)$$

In this and later equations we will follow the convention of this field and measure all energy levels relative to  $\varepsilon_f$ , because this substantially simplifies the notation. The exponent  $\alpha = 1 - (\delta/\pi)^2$ , where  $\delta$  is the phase shift of the band electron at the Fermi level when scattered by  $U_{df}$ . The coefficient  $A$  contains band parameters. For an idealized band with a flat density of states extending from  $-W/2$  to  $W/2$ , it has the expression  $A = (0.9W)^{\alpha-1}/\Gamma(1-\alpha)$ . The exponent  $\alpha$ , being bounded by unity for  $U_{df} = 0$  and 0.75 for  $U_{df} \gg W$ , has a small range of variation. All theoretical calculations reported later are done for  $\alpha = 0.8$ .

The singularity in the spectrum originates from the sharp cutoff of the electron population at zero temperature. At finite temperatures the singularity is rounded off in such a way that the spectrum spreads out over both sides of  $\varepsilon_f$  and spans an increasingly wider range of energy for higher temperatures, as shown in fig. 37 (Liu and Ho 1983). It is clear by comparing figs. 37 and 27 that the Mahan–Nozières–de Dominicis singularity has nearly the same shape and temperature dependence as the spin-fluctuation resonance. It will not come as a surprise that the theory based on this singularity produces the same phenomenology as discussed earlier in section 3.3.

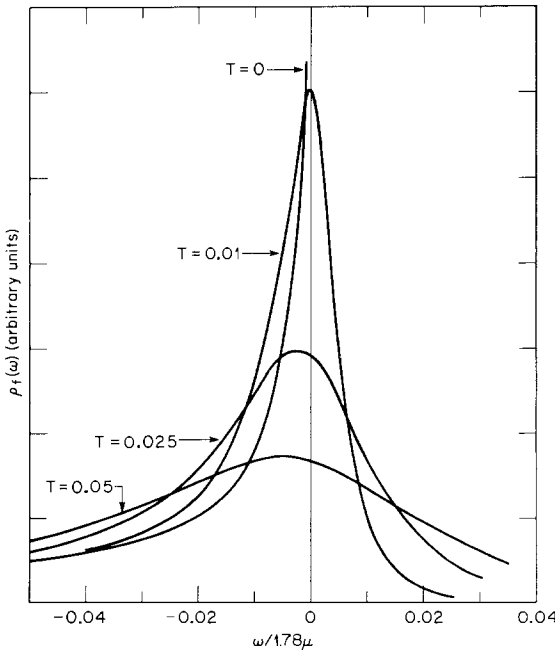


Fig. 37. The spectral density of the  $f$  hole as a function of temperature (Liu and Ho 1983). The temperature causes a broadening of the line and a shift of the peak. The unit of temperature is unimportant, because all curves are similar under a suitable change of energy scale.

The power-law singularity causes major difficulties when one attempts an ab initio calculation of the spectrum. The spectrum is the Fourier transform of the dynamical response of the conduction electrons to the creation of an f hole. In real time the response is entirely in the transient regime, and thus cannot be analyzed by the steady state methods developed so far in connection with LDA band calculations.

The use of the simple model in eq. (54) can cause problems when we attempt to compare the theoretical predictions with experimental findings. For instance, the model is incapable of dealing with the complex of f bands caused by the crystal field effect. As a result, the predicted properties at temperatures higher than the crystal field splitting are inherently unreliable.

### 3.4.2. The f band problem

The motion of a heavy particle when accompanied by a screening cloud of band electrons was first studied by Kondo (1984) and later by Kagan and Prokofev (1986) as a model for muon diffusion in metals. Liu (1987) and Kagan and Prokofev (1987) independently proposed that the same mechanism applies in heavy-fermion systems. The idea is that the f band is formed by the hopping of an f hole whose motion is accompanied by the screening cloud. Just like the band problem in the spin fluctuation resonance model, the hopping is the result of the hybridization interaction. Consequently, the dispersion of the f band is again solved from eq. (52) where  $G_f(\omega)$  is now calculated from the f hole spectrum in eq. (57) (Liu 1987, 1988):

$$G_f(\omega) = \int \frac{\rho_f(\omega') d\omega'}{\omega - \omega'}. \quad (58)$$

The integration can be carried out analytically so that eq. (52) reduces to

$$\omega - \varepsilon_k = \pi V^2 A \csc(\pi\alpha) \omega^{-\alpha}. \quad (59)$$

The potential  $V$  that enters the above band equation is expected to be reduced from the LDA result by the correlation effect of  $U_{ff}$ . Based on a mean-field argument Varma and Yafet (1976) proposed that  $V^2$  is scaled down by the factor  $1 - n_f$  in the limit of very large  $U_{ff}$ . The results of a computer simulation by Blankenbecler et al. (1987) shows that large  $U_{ff}$  tends to increase the f electron localization and cuts down the hybridization matrix element, in qualitative agreement with the mean-field theory.

The solution of the band equation eq. (59) can be divided into two parts: the conduction band part for which the right-hand side is negligible, and the f band part for which the term  $\omega$  in the left-hand side is negligible. The f band consists of an upper band with real energies

$$\omega_k^{(+)} = \eta(-W/2\varepsilon_k)^{1/\alpha}, \quad \varepsilon_k < 0, \quad (60)$$

and a lower band with complex energies

$$\omega_k^{(-)} = \eta(W/2\varepsilon_k)^{1/\alpha} e^{i\pi/\alpha}, \quad \varepsilon_k > 0, \quad (61)$$

where  $\eta = [2\pi V^2 A \csc(\pi\alpha)/W]^{1-\alpha}$  is the bottom of the upper band measured from the f level. Both bands are degenerate with respect to the spin. The band structure

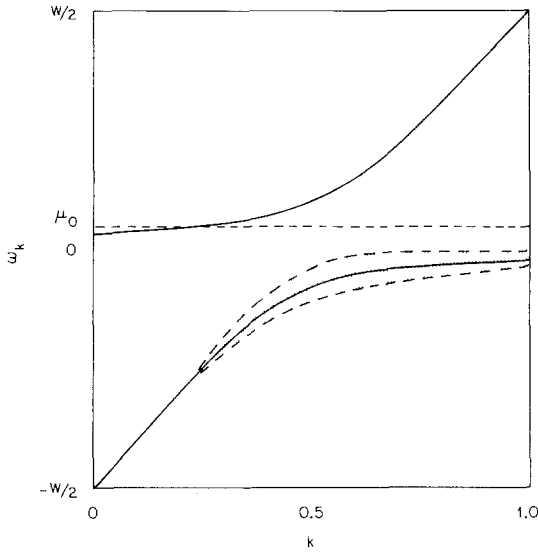


Fig. 38. Schematic representation of the band structure obtained from the electronic polaron model (Liu 1987, 1988).

is schematically represented in fig. 38. The dotted curves around the lower band mark the width of the band energy level at half maximum. The large width of the lower band implies that it is actually a localized level. At finite temperatures the single-site  $f$  spectrum is broadened, and this gives a finite width to the energies of the upper band but has little effect on the lower band. The  $f$  contribution to the density of states  $N_{\pm}(\omega)$  for a sequence of temperatures is shown in fig. 39. The temperatures are measured in units of  $\eta/k_B$ . The upper band also becomes broad when  $T \gg \eta/k_B$ , indicating that the  $f$  state evolves from a propagating state into a localized state as

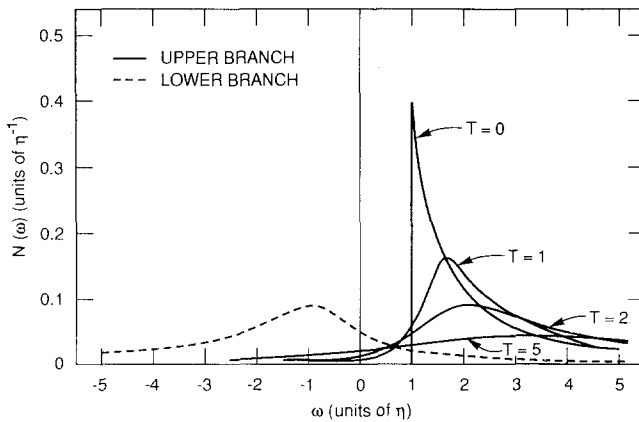


Fig. 39. The density of states of the  $f$ -like band plotted for a sequence of temperatures. Solid curves represent  $N_{+}(\omega)$  for the upper band, and the dotted curve represents  $N_{-}(\omega)$  for the lower band (Liu 1987, 1988). The temperature is expressed in units of  $\eta/k_B$ .

the temperature is raised. The damping of the upper band comes from scattering of the band electron by excited electron-hole pairs in the conduction band. The scattering effect is turned on exponentially slowly at low temperatures and becomes significant when  $T \simeq \eta/k_B$ . Therefore, the model predicts that the system behaves like a Fermi liquid for  $T \ll \eta/k_B$  and a collection of local moments for  $T \gg \eta/k_B$ .

Real materials have  $n_f \simeq 1$ , which puts the Fermi level  $\mu$  of the model system within the upper band. When the temperature is increased the Fermi level tends to sink because we must preserve the occupation of the  $f$  bands. Eventually when  $T \gg \eta/k_B$  the Fermi level falls into the lower band, causing the  $f$  electrons to be totally localized.

The upper band is qualitatively the same as the simple two-band model discussed in section 3.1.2, but the band mass at zero temperature is enhanced by roughly a factor of 5 for  $\mu(0) = 1.3\eta$ , where  $\mu(0)$  is the Fermi level as temperature  $T=0$  (Liu 1987, 1988). This factor plus the correlation effect due to  $U_{ff}$  could put the mass enhancement factor to within the measured range of 20–30. When there are many  $f$  levels and many broad bands as in a real LDA calculation, there should be a one-to-one correspondence between the model bands and the LDA bands at the Fermi level. On the other hand, until the  $f$  hole screening dynamics can be calculated from realistic band eigenvalues and eigenstates, the present theory should only be considered qualitative or at most semi-quantitative. The quantity  $\mu(0)$  cannot be determined with certainty, and we will treat it as a parameter in the model calculation.

### 3.4.3. Results of model calculation

Once the energy bands are determined, the calculation of thermodynamic quantities is a simple exercise. The only complication is that the bands are temperature dependent and the Fermi energy  $\mu(T)$  must be determined as a function of temperature. In contrast to the spin fluctuation resonance model, the present model has two energy parameters, namely  $\eta$  and  $\mu(0)$ . The interplay of these two parameters causes a breakdown of the simple scaling idea. For instance, it will be demonstrated that the thermodynamic properties are more sensitive to the quantity  $\mu(0) - \eta \ll \eta$  but the transport properties are more sensitive to  $\eta$ . The exponent  $\alpha$  also affects the result somewhat, but since  $\alpha$  has a narrow range of variation, its influence on the results is weak.

The specific heat is calculated by numerically differentiating the internal energy. A typical result for  $C(T)$  per lanthanide or actinide atom versus  $T$  calculated for  $\mu(0) = 1.3\eta$  is shown in fig. 40. It rises linearly at low temperatures, has a peak near  $0.2\eta/k_B$  and declines slowly at higher temperatures. The peak value is  $0.18k_B$  per atom, which is close to that predicted by the Kondo model for  $S = \frac{1}{2}$ . In practical units the maximum specific heat is 1.5 J/(mol K), which agrees in order of magnitude with the available experimental values, 1.5 for polycrystalline  $UBe_{13}$  (Andres et al. 1975), 1.5 for polycrystalline, and 2.0 for single crystal  $CeCu_2Si_2$  (Ott et al. 1984c). The position of the specific heat peak fixes the energy scale  $\eta$ , which is found to be 10 K for both  $UBe_{13}$  and  $CeCu_2Si_2$ . The value of  $\eta$  determines the density of states at the Fermi level and the specific heat  $\gamma$ , which is found to be 1.5 J/(mol K<sup>2</sup>). This compares well with the experimental values estimated from the low-temperature specific heat data, 1.1 for  $UBe_{13}$  and  $CeCu_2Si_2$  and 1.55 for  $CeAl_3$  (Stewart et al. 1983). The curve for



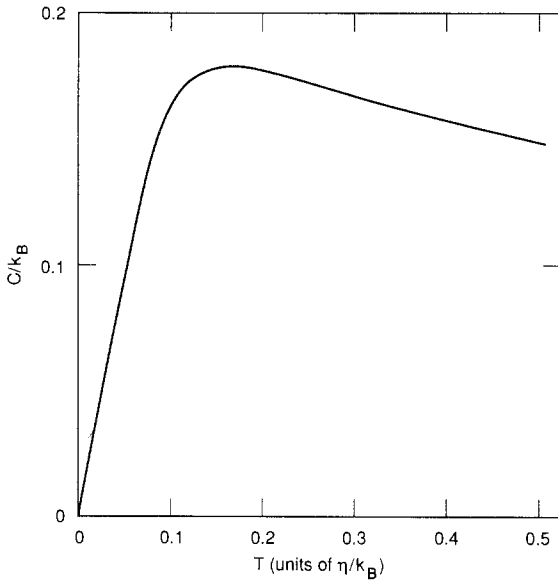


Fig. 40. The specific heat per lanthanide or actinide atom as a function of temperature, as predicted by the electronic polaron model (Liu 1987, 1988).

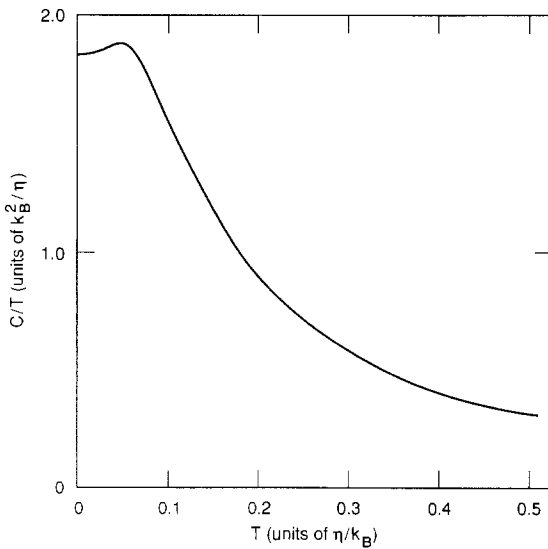


Fig. 41. The  $C(T)/T$  versus  $T$  curve predicted by the electronic polaron model (Liu 1988). The area under the curve is the entropy per  $f$  site, which is found to be approximately  $k_B \ln 2$ .

$C(T)/T$  versus  $T$  is shown in fig. 41. The curve has a slight rise at low temperatures, which comes from the positive curvature of the density-of-states curve for the upper band. The high-temperature part is proportional to  $T^{-3}$ , and the area under the curve is estimated to be  $k_B \ln 2$ . One can vary  $\mu(0)$  within a small range and obtain slightly different  $C(T)$  curves. The specific heat peak appears at higher temperatures for larger values of  $\mu(0) - \eta$ .

The magnetic susceptibility  $\chi(T)$  is calculated from

$$\chi(T) = 2\mu_{\text{eff}}^2 \int \frac{N_+(\omega)e^{\beta(\omega-\mu)} d\omega}{[e^{\beta(\omega-\mu)} + 1]^2}, \quad (62)$$

where  $\beta = (k_B T)^{-1}$ ,  $N_+(\omega)$  is the density of states of the upper band, and  $\mu_{\text{eff}}$  is the effective magnetic moment which includes the orbital and crystal field effects (Liu 1988). The contribution of the lower band is negligible. The calculated  $\chi(T)$  curve is shown in fig. 42. The slight rise at low temperatures is a result of the positive curvature of the density-of-states curve. After the peak the temperature dependence follows  $T^{-1}$ . The value of  $\eta$  estimated from the specific heat also yields a fairly good estimate of the low-temperature susceptibility. The high-temperature susceptibility is not reliable because the theory fails to include the f level degeneracy in a realistic manner. A possible manifestation of this failure is seen in the inverse susceptibility curve. The curve extrapolates to zero at a negative Curie-Weiss temperature  $\Theta = 0.2\eta/k_B$ , which is about 2 K for the estimated value of  $\eta = 10$  K. This is much lower than the experimental values, for instance, 35 K for CeAl<sub>3</sub>.

The electrical resistivity is determined by the inverse lifetime of the quasi-particles averaged over the Fermi distribution. The calculated  $\rho(T)$  curve, shown in fig. 43, starts from zero at  $T = 0$ , rises exponentially until a peak is reached around  $T = \eta/k_B$ , and drops smoothly to zero at higher temperatures. Again, variations of  $\mu(0)$  produces only slightly different results. The low-temperature part is in disagreement with experiments, because the calculation fails to include the mutual scattering effect of quasi-particles. The resistivity peak reflects the breakdown of the band structure, which takes place when the temperature reaches  $\eta/k_B$ . The model does not shed light on the variety of resistivity behaviors shown in fig. 6.

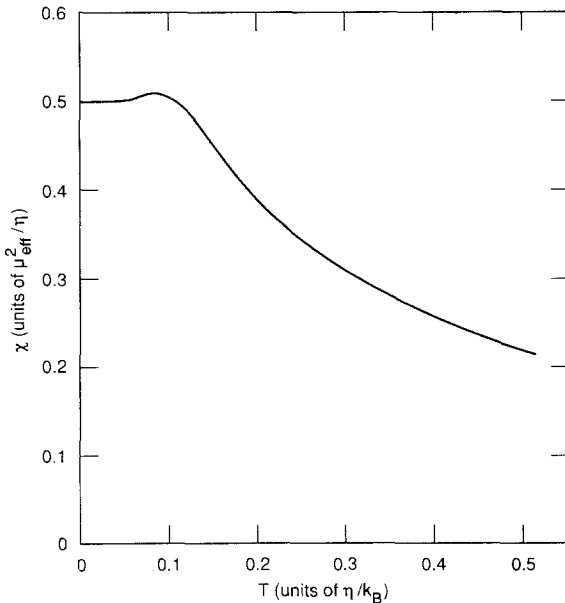


Fig. 42. The magnetic susceptibility per lanthanide or actinide atom as a function of temperature, as predicted by the electronic polaron model. The susceptibility is in units of  $\mu_{\text{eff}}^2/\eta$ , where the effective moment  $\mu_{\text{eff}}$  includes the orbital contribution, as discussed in Liu (1988).

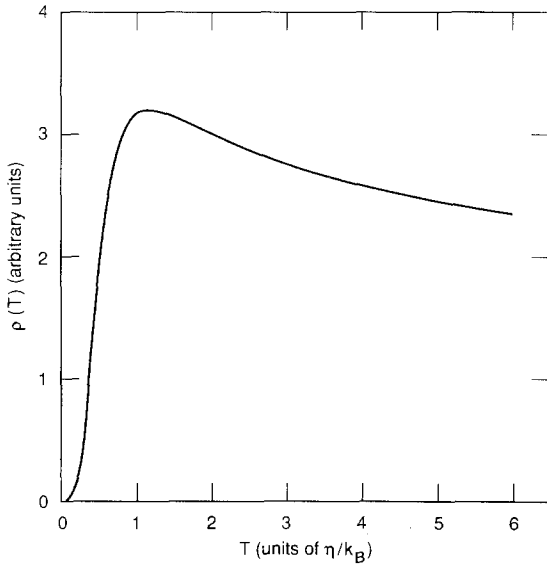


Fig. 43. The electrical resistivity versus temperature as predicted by the electronic polaron model (Liu 1988).

In the presence of impurities the Mahan–Nozières–de Dominicis singularity is broadened due to scattering of band electrons, as shown by Doniach and Sunjic (1970). This effect gives rise to additional quasi-particle damping and resistivity. One simple way to incorporate the impurity effect in the band calculation is to replace the temperature  $T$  by  $T + T_D$ , where  $T_D$  is the Dingle temperature which measures impurity scattering. The calculated resistivity curves for various values of  $T_D$  are shown in fig. 44. These curves compare well with the data for  $\text{Ce}_x\text{La}_{1-x}\text{Pb}_3$  in fig. 7 and for  $\text{La}_{1-x}\text{Ce}_x\text{Sn}_3$  in fig. 9.

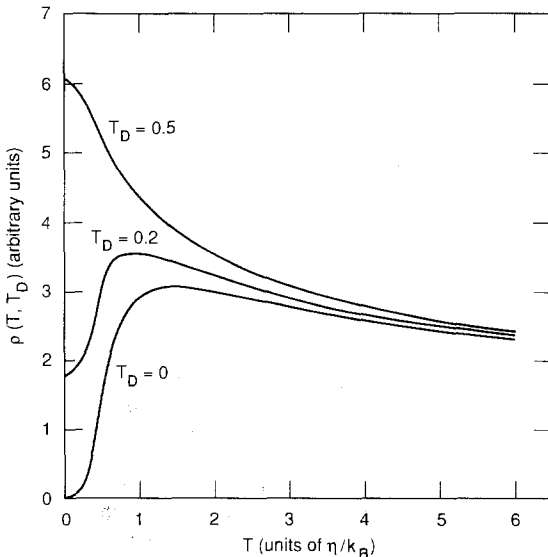


Fig. 44. The calculated resistivity curves for impure systems. The amount of impurity is represented by the Dingle temperature  $T_D$ , which is measured in units of  $\eta/k_B$  (Liu 1988). The theoretical results are to be compared with the experimental data in figs. 7 and 9.

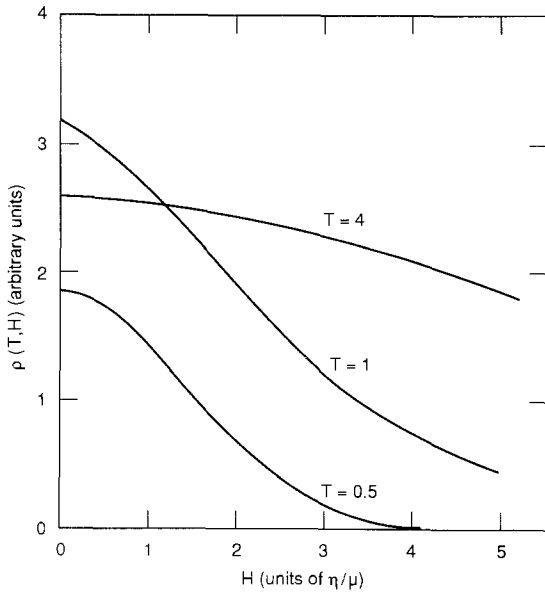


Fig. 45. The calculated magnetoresistance for three temperatures above and below the resistivity peak (Liu 1988). The temperature is measured in units of  $\eta/k_B$ .

An applied magnetic field splits the doubly degenerate bands by energy shifts  $\pm \mu_{\text{eff}}H$ . The resistivity of both bands can be calculated and the contributions are added in parallel to obtain the magnetoresistance  $\rho(T, H)$ . The results, shown in fig. 45, are in qualitative agreement with the data for  $\text{UBe}_{13}$  except for the sharp drop at the superconducting critical temperature. The unit of  $H$  in the theoretical curves equals roughly 4 T for this material. The low-temperature curve,  $T = 0.5\eta/k_B$  is also similar to the prediction of the Kondo model in fig. 26. Above the resistivity maximum the curve is parabolic, indicating local moment behavior.

The thermopower  $S(T)$  is related to the resistivity through the simple relationship

$$S(T) = \frac{\pi^2 k_B^2 T}{3e} \frac{\partial \ln \rho}{\partial \mu}, \quad (63)$$

where the partial derivative is evaluated at the Fermi level  $\mu(T)$ , and  $e$  is the absolute value of the electron charge. The result of the numerical calculation is shown in fig. 46. In the Fermi-liquid regime  $S(T)$  is large and negative. Since the theory leaves out the interparticle scattering effects, which is predominant at low temperatures, this part of the result is unreliable. A careful calculation should change this part of the curve to the dotted curve in the figure. The thermopower changes sign near  $T = \eta/k_B$ , which can be traced to the fact that the Fermi level sinks below the upper band at elevated temperatures. Such a change of sign has been observed in many dense systems, for instance,  $\text{CeAl}_3$  (Van Aken et al. 1974),  $\text{CeAl}_2$  (Bauer et al. 1982) and  $\text{CeCu}_2\text{Si}_2$  (Schneider et al. 1983, Steglich et al. 1985). Negative thermopower just above the superconducting critical temperature of  $\text{UBe}_{13}$  has been reported by Jaccard et al. (1985). On the other hand, in real materials  $S(T)$  does not necessarily change sign at a temperature near the resistivity maximum. For instance, the thermopower

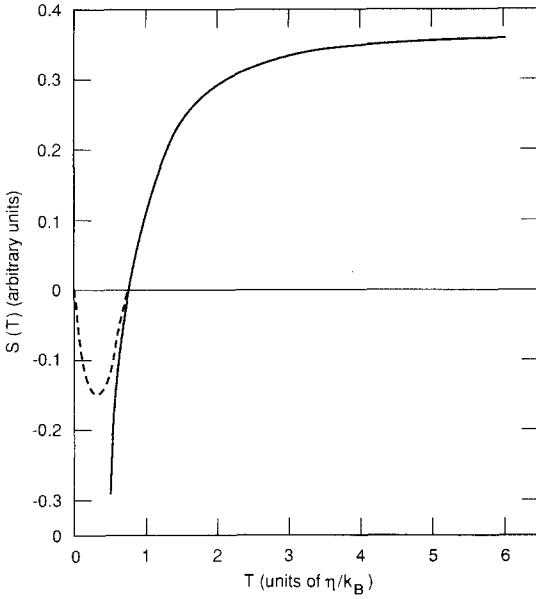


Fig. 46. The calculated thermopower as a function of temperature (Liu 1988). The dotted curve indicates the expected result if interparticle scattering is properly included.

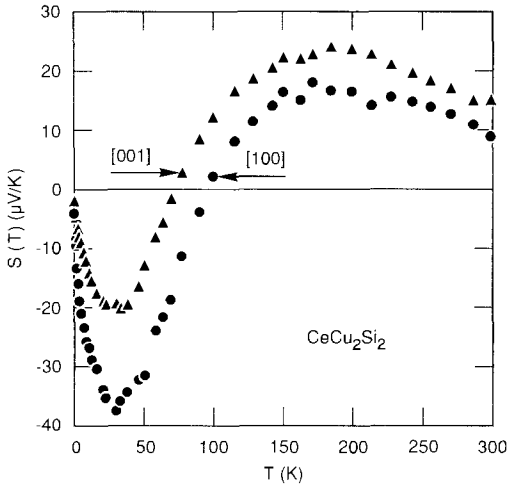


Fig. 47. The thermopower for a single crystal of  $CeCu_2Si_2$  along two crystal axes (Schneider et al. 1983). Both curves cross the horizontal axes at temperatures close to the resistance plateau around 100 K.

of  $CeCu_2Si_2$ , shown in fig. 47, changes sign at about 70 K in the [001] direction and 100 K in the [100] directions. Both are close to the temperature where the resistivity has a plateau. The resistivity maximum occurs at a much lower temperature, about 20 K. This discrepancy may reflect a failure of the oversimplified Hamiltonian which leaves out many effects, notably the crystal field splitting of the f levels.

The effect of magnetic field on the thermopower has been calculated by differentiating the magnetoresistance. The result, shown in fig. 48, shows positive  $H^2$  dependence in both positive and negative regions of  $S(T)$ . The only data available for comparison

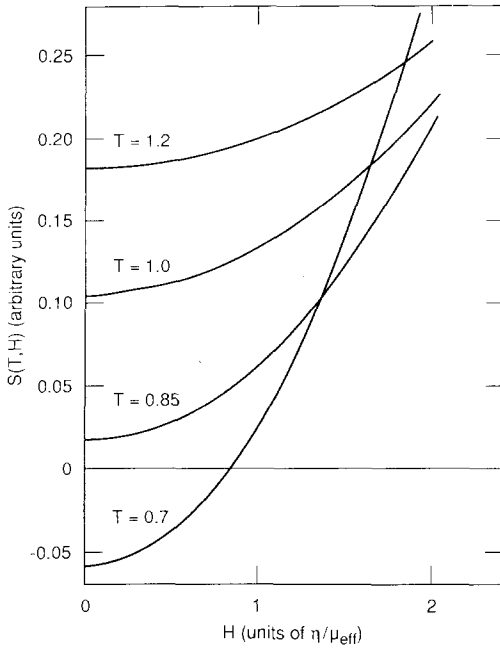


Fig. 48. The calculated effect of applied magnetic field on the thermopower (Liu 1988). Each unit of the magnetic field corresponds to about 4 T.

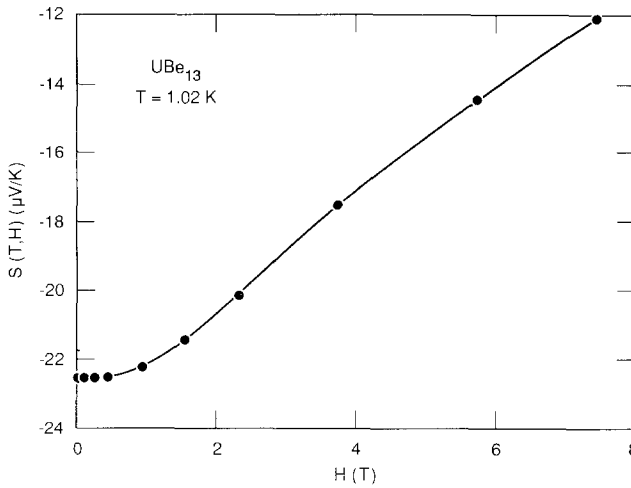


Fig. 49. The magnetic field dependence of the low-temperature thermopower of  $\text{UBe}_{13}$  (Jaccard et al. 1985).

are for  $\text{UBe}_{13}$  (Jaccard et al. 1985), showing in fig. 49. Each unit of field in the theoretical curve corresponds to roughly 4 T.

To conclude, the model gives a good qualitative to semi-quantitative account of many thermodynamic and transport properties of heavy-fermion and mixed-valence materials. It elucidates the cross-over from Fermi liquid behavior at low temperatures to local moment behavior at high temperatures, although it is not capable of treating the problem fully in either extreme region. It can, however, provide insight into the

findings of those experiments that probe specifically the electronic structure in the cross-over regime, such as inelastic neutron scattering to be discussed next.

3.4.4. *Inelastic neutron scattering*

It has been discussed in section 3.1.2 that the inelastic neutron scattering line shape can be interpreted in terms of a two-band model. The electronic polaron model results in two bands but with an additional twist, namely the lower band has an intrinsic width even at zero temperature. This effect broadens the theoretical neutron scattering line shown in fig. 21, and the result compares quite favorably with the data for  $UBe_{13}$  (Mook 1987), as shown in fig. 50 (Liu 1988). In addition to the vertical scale, the only fitting parameter is  $\eta$ , which was determined to be 10 K from the specific heat peak. The data were taken in a constant- $q$  scan near the Brillouin zone boundary at a temperature much lower than  $\eta/k_B$ . Shown in fig. 51 is the integrated neutron scattering intensity within an energy window between 0 and 7 meV for a range of momentum transfer. The intensity has peaks at the zone boundary and a valley at the zone center, or in this case a reciprocal lattice away from the zone center. The solid curve is the theoretical result calculated using the same  $\eta$  value. As the temperatures varies, the model gives a complete prescription of how the two bands

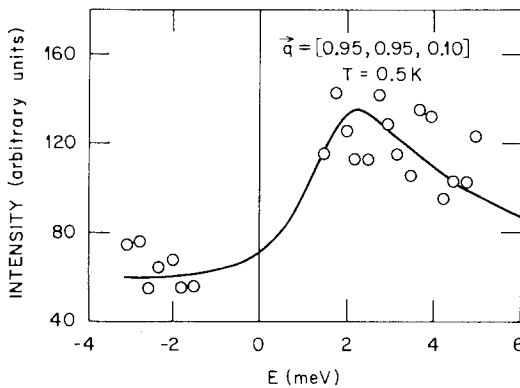


Fig. 50. The calculated (solid curve) versus measured line shapes for a constant- $q$  scan where the fixed  $q$  is near the Brillouin zone boundary (Liu 1988). The material is  $UBe_{13}$  which has  $\eta/k_B = 10$  K.

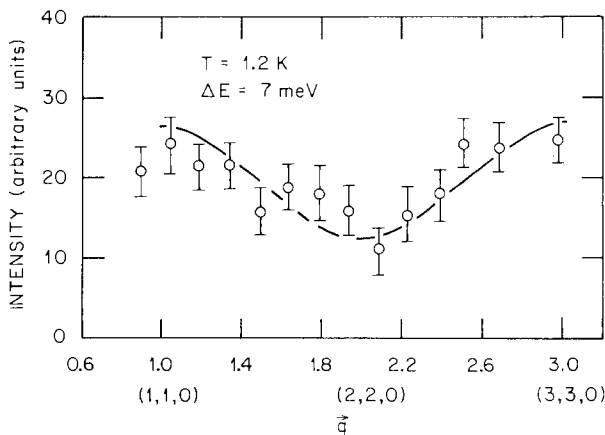


Fig. 51. The calculated (solid curve) versus measured results of integrated intensity for  $UBe_{13}$  in the energy range  $0 \leq \Delta E \leq 7$  meV (Liu 1988).

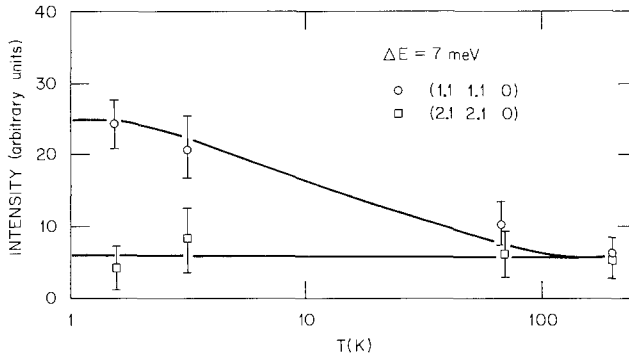


Fig. 52. The difference in intensity between the zone-boundary point  $(1,1,0)$  and the zone center  $(2,2,0)$  plotted versus temperature (Liu 1988). The measured points were obtained for  $UBe_{13}$  by Mook (1987). The lower solid curve represents a constant background, and the upper solid curve is the prediction of the electronic polaron theory.

broaden gradually, and this determines how the neutron scattering line shape varies with temperature. In the extreme local limit where the bands break down, the difference in intensity between the peaks and the valley in fig. 51 should disappear. This evolution of line shape is shown in fig. 52 in terms of the temperature dependence of the maximum and minimum cross sections. The lower solid line represents a constant background, and the upper solid curve is the theoretical result. Again, no new parameters are needed for this comparison between theory and experiment.

Stassis et al. (1979c) have observed a neutron scattering line shape similar to fig. 50 at the zone boundary point  $[111]$  of the mixed valence material  $\gamma$ -Ce.

It has been known for a long time that hydrostatic pressure induces dramatic changes in the properties of Ce (Koskenmaki and Gschneidner 1978). Similar effects have been observed in mixed-valence compounds of Ce, Sm and Yb. These observations have stimulated a considerable amount of theoretical and experimental effort to elucidate the interaction between the longitudinal acoustic (LA) phonon, which is a pressure wave, and the electron gas in mixed-valence systems. In a series of publications Mook and co-workers (Mook et al. 1979, Mook and Nicklow 1979, Mook and Holtzberg 1981, Mook et al. 1982) reported a softening of the LA phonons in the  $Sm_{0.25}Y_{0.75}S$  and  $TmS$  systems. A more subtle phonon softening near the zone boundary in the  $[111]$  direction has been reported by Stassis et al. (1980). Explanations of the phonon softening in the  $Sm$ - $Y$ - $S$  system all invoke the  $d$  to  $f$  transition induced by the lattice vibration suggested by Bilz et al. (1979). The idea is that the phonons are strongly coupled to the  $f$  electron spectrum, which has a large density of states at the Fermi energy. Calculations reported by various investigators differ in detail but with similar results, namely a softening of the LA frequency and a corresponding broadening of line width (Entel et al. 1979, Bennemann and Avignon 1979, Matsuura et al. 1980, Wakabayashi 1980, Entel and Sietz 1981). The effect is especially pronounced in the  $[111]$  direction, as shown in fig. 53 (Wakabayashi 1980). In fitting the data the author included a phenomenological relaxation term in the electronic contribution to the restoring force. This term has the effect of imparting some local character to the  $f$  electron, and the similarity of



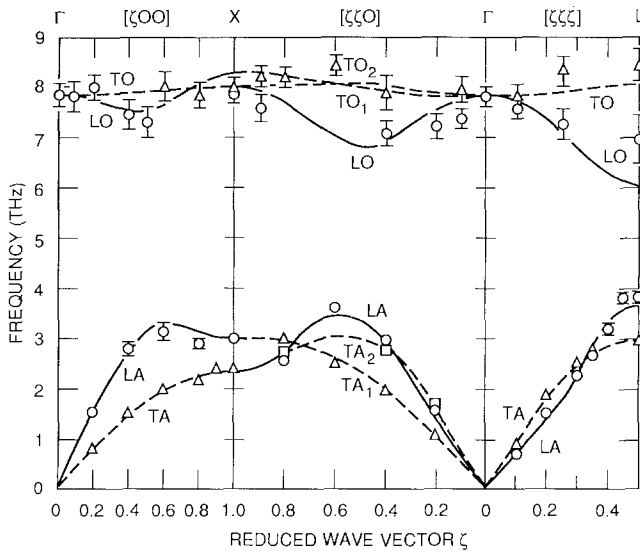


Fig. 53. Experimental and calculated phonon frequencies for  $\text{Sm}_{0.75}\text{Y}_{0.25}\text{S}$ . The data were reported by Mook et al. (1979). The solid and dashed curves are the calculated longitudinal and transverse mode frequencies, respectively (Wakabayashi 1980).

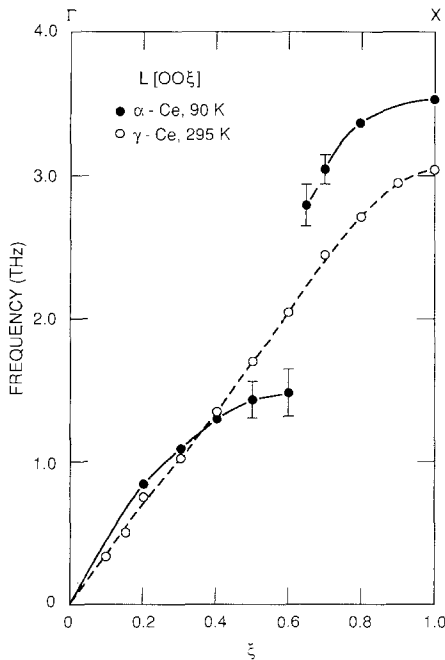


Fig. 54. The longitudinal acoustic phonon dispersion relations along the  $[100]$  axis of  $\alpha$ - and  $\gamma$ -Ce (Stassis 1988). The splitting of the dispersion curve for  $\alpha$ -Ce is the result of mode mixing.

the predictions by various theories indicates that it makes very little difference whether the  $f$  electrons are treated in the band or local limit.

Recently a new and puzzling phenomenon has been observed by two experimental groups in two different materials. In a preliminary study of  $\alpha$ -Ce Stassis and co-workers (Stassis 1988) have found that the LA phonon mode in the  $[100]$  direction splits in the middle of the Brillouin zone as if it were mixed with an invisible mode at a frequency of 2 THz or an energy of 8.3 meV. The phonon dispersion relation along this direction is shown in fig. 54, together with the result for  $\gamma$ -Ce for comparison. The data have not been published pending further measurements. Severing et al. (1988) independently reported a similar finding in  $\text{CePd}_3$ . The results, shown in fig. 55, shows normal phonon peaks at temperatures below 140 K, but split modes above 200 K. The energy of the invisible mode is approximately 10 meV, which is 120 K in the temperature scale. The static susceptibility of this material has a peak around 140 K. The closeness of these two temperatures suggests that the electronic polaron model may offer an explanation to this phenomenon (Liu 1989b).

A fundamental energy scale in this model is  $\eta$ , which measures the distance of the  $f$  level from the Fermi level. At  $T \ll \eta/k_B$  the  $f$  electrons are in band states, and they

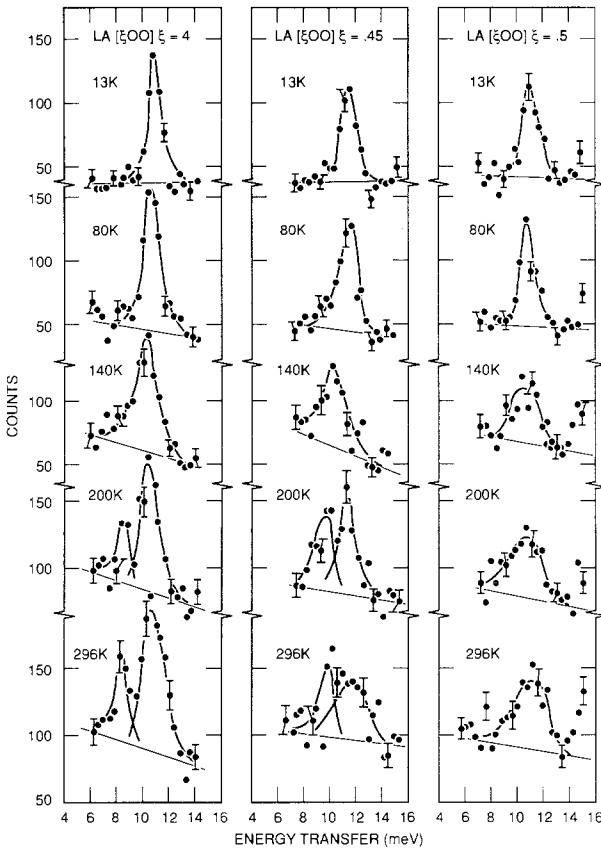


Fig. 55. The phonon line shapes along the  $[100]$  axis of  $\text{CePd}_3$ , showing the split peak structure above 200 K (Severing et al. 1988).

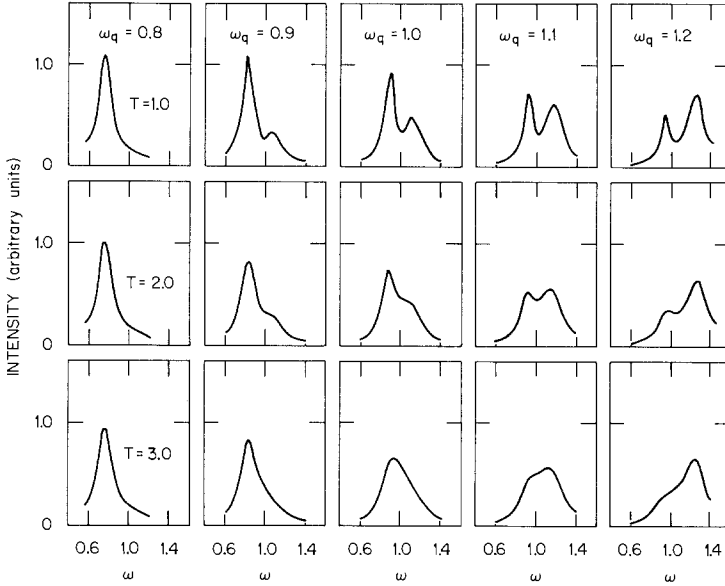


Fig. 56. The calculated phonon line shapes in the mode mixing region at three temperatures. The phonon energy is measured in units of the electron-hole excitation energy  $\eta$ , and the temperature is in units of  $\eta/k_B$  (Liu 1989b).

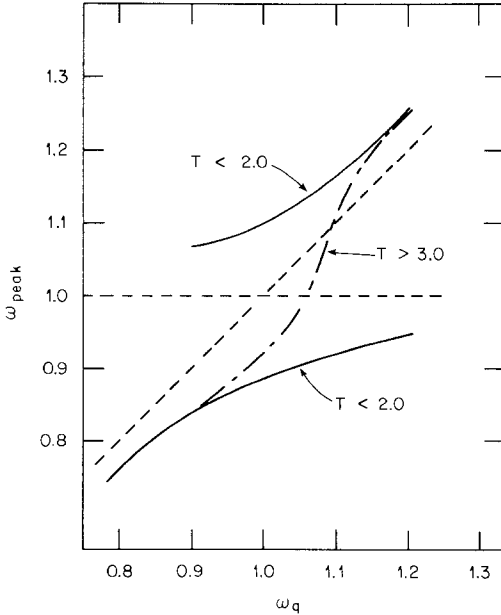


Fig. 57. The evolution of LA phonon peak position as a function of the temperature and the unnormalized phonon energy (Liu 1989b). It gives qualitatively the shape of the LA phonon dispersion curve near the mode splitting frequency. All frequencies are in units of  $\eta$ .

affect the LA phonon as described by the theories mentioned above. For  $T \simeq \eta/k_B$ , the f electrons are localized and provide rapidly fluctuating local moments. The excitation of an f electron into the d-like conduction band leaves a hole which must be screened by the band electrons. Again, the screening dynamics enters the picture, and the problem should be treated on a local basis. The invisible mode corresponds to the energy of a locally correlated f hole and d electron pair, just like excitons in insulators. In metallic systems the exciton is highly damped, and the damping increases with increasing temperature. The results of the calculation are summarized in figs. 56 and 57. The phonon line shapes in the mode mixing region are shown in fig. 56. It shows that the splitting is expected to disappear at temperatures much higher than the characteristic temperature, as is seen in  $\gamma$ -Ce shown in fig. 54. In fig. 57 the position of the phonon peak is plotted versus the unrenormalized phonon energy, showing the split modes for  $T < 2$  and the slightly softened mode for  $T > 3$ , where the temperature is measured in units of  $\eta/k_B$ . Although not a plot of dispersion relations, we may compare this graph qualitatively with the dispersion relations in fig. 54.

Aside from the work of Auerbach et al. (1988), there has been no further analysis of the neutron scattering data by the spin fluctuation resonance model.

#### 4. Summary and conclusion

This paper consists of a highly condensed review of the experimental and theoretical studies of heavy-fermion and mixed-valence materials. It points out the applicability and limitations of the various theoretical models. The Fermi liquid models are applicable at low temperatures, and whether one chooses to use the one-band, two-band or the LDA model depends on the amount of detail demanded by the experimental situation. The spin fluctuation model is the model of choice for single impurities as well as dense systems at high temperatures. The electronic polaron model is principally a model for the cross-over regime between Fermi liquid and local moment limits. Whether there is any hope of uniting all theories remains to be resolved. The situation is comparable to the theory of ferromagnetism in local moment systems. At very low temperatures one can understand the experimental results in terms of the spin wave theory. Near the Curie temperature all measurements on the critical phenomena are united by the scaling theory. Between these two well-understood limits the average properties of the system is best handled by the mean-field theory, which is a rather crude approximation. An exact solution of the Heisenberg Hamiltonian continues to elude us.

As mentioned in the introduction, there is a tendency in literature to classify mixed-valence and heavy-fermion systems as two distinct classes of materials. It is our view that the distinction is artificial, because as fig. 3 clearly shows, there is no gap in the mass spectrum from mixed-valence systems at the lower left corner to heavy-fermion systems at the upper right corner. Other experimental results also demonstrate a lack of clear demarcation between systems in the low-mass end and those in the high-mass end. One can only see a steady decrease in the characteristic energy or temperature

as one traverses up the graph. It is also clear that lanthanide and actinide compounds are evenly distributed in fig. 3, indicating that members of both series can make mixed-valence as well as heavy-fermion compounds provided that the environment is right. There are differences in detail, however, between lanthanide and actinide compounds. The lanthanides Ce and Yb have one 4f electron or hole, making it easier to analyze the cross-over from local to itinerant behavior. The actinide systems, on the other hand, have many 5f electrons per atom, and the role of the Hund's rule coupling among the many f electrons has not been studied in a systematic manner. It is hoped that this review will provide impetus for further investigations.

Since the main subject of this review is controversial, we hasten to emphasize that the views presented here are less than objective. The reader has the perfect right to weigh the evidence differently or invoke evidence unknown to this reviewer and reach a radically different point of view. After all, Nature has no respect for human intelligence. It should not surprise us if different interactions may play the dominant role in different, albeit very similar substances. What is also likely is that some new mechanism may be found some day that explains everything or produces more confusion. The only safe conclusion one can draw at this point is that the field is still wide open.

## References

- Aeppli, G., H. Yoshizawa, Y. Endoh, E. Bucher, J. Hufnagl, Y. Onuki and T. Komatsubara, 1986, *Phys. Rev. Lett.* **57**, 122.
- Aeppli, G., A.I. Goldman, G. Shirane, E. Bucher and M.-Ch. Lux-Steiner, 1987, *Phys. Rev. Lett.* **58**, 808.
- Andrei, N., 1982, *Phys. Lett. A* **87**, 299.
- Andrei, N., and J.H. Lowenstein, 1981, *Phys. Rev. Lett.* **46**, 356.
- Andrei, N., K. Fukuya and J.H. Lowenstein, 1983, *Rev. Mod. Phys.* **55**, 331.
- Andres, K., J.E. Graebner and H.R. Ott, 1975, *Phys. Rev. Lett.* **35**, 1979.
- Auerbach, A., and K. Levin, 1986, *Phys. Rev. B* **34**, 3524.
- Auerbach, A., J.K. Kim, K. Levin and M.R. Norman, 1988, *Phys. Rev. Lett.* **60**, 623.
- Bader, S.D., N.E. Phillips, M.B. Maple and C.A. Luengo, 1975, *Solid State Commun.* **16**, 1263.
- Barbara, B., M.F. Rossignol, J.X. Boucherle, J. Schweizer and J.L. Buevoz, 1979, *J. Appl. Phys.* **50**, 2300.
- Bauer, E., E. Gratz, W. Mikovits, H. Sassik and H. Kirchmayr, 1982, *J. Magn. & Magn. Mater.* **29**, 192.
- Bennemann, K.H., and M. Avignon, 1979, *Solid State Commun.* **31**, 645.
- Benoit, A., A. Berton, J. Chaussy, J. Flouquet, J.C. Lasjaunias, J. Odin, J. Palleau, J. Peyrard and M. Ribault, 1981, in: *Valence Fluctuations in Solids*, eds L.M. Falicov, W. Hanke and M.P. Maple (North-Holland, Amsterdam) p. 283.
- Bickers, N.E., 1987, *Rev. Mod. Phys.* **59**, 845.
- Bickers, N.E., D.L. Cox and J.W. Wilkins, 1985, *Phys. Rev. Lett.* **54**, 230.
- Bickers, N.E., D.L. Cox and J.W. Wilkins, 1987, *Phys. Rev. B* **36**, 2036.
- Bilz, H., G. Güntherodt, W. Kleppmann and W. Kress, 1979, *Phys. Rev. Lett.* **43**, 1998.
- Blankenbecler, R., J.R. Fulco, W. Gill and D.J. Scalapino, 1987, *Phys. Rev. Lett.* **58**, 411.
- Blatt, F.J., 1968, *Physics of Electronic Conduction in Solids* (McGraw-Hill, New York).
- Coleman, P., 1987, *J. Magn. & Magn. Mater.* **63-64**, 245.
- Coqblin, B., and J.R. Schrieffer, 1969, *Phys. Rev.* **185**, 847.
- Doniach, S., and S. Engelsberg, 1966, *Phys. Rev. Lett.* **17**, 433.
- Doniach, S., and M. Sunjic, 1970, *J. Phys. C* **3**, 285.
- Entel, P., and M. Sietz, 1981, *Solid State Commun.* **39**, 249.
- Entel, P., N. Grewe, M. Sietz and K. Kowalski, 1979, *Phys. Rev. Lett.* **43**, 2002.
- Ernst, H.J., H. Grühl, T. Krug and K. Winzer, 1984, in: *Proc. of the 17th Int. Conf. on*

- Low Temperature Physics, eds U. Eckern, A. Schmid, W. Weber and H. Wühl (North-Holland, Amsterdam) p. 137.
- Falicov, L.M., and J.C. Kimball, 1969, *Phys. Rev. Lett.* **22**, 997.
- Felsch, W., 1978, *Z. Phys. B* **29**, 211.
- Fisk, Z., H.R. Ott, T.M. Rice and J.L. Smith, 1986, *Nature* **320**, 124.
- Fulde, P., J. Keller and G. Zwicknagl, 1988, in: *Solid State Physics*, Vol. 41, eds H. Ehrenreich and D. Turnbull (Academic Press, Orlando) pp. 2-150.
- Gardner, W.E., J. Penfold, T.F. Smith and I.R. Harris, 1972, *J. Phys. F* **2**, 133.
- Gschneidner Jr, K.A., 1985, *J. Magn. & Magn. Mater.* **47-48**, 57.
- Herring, C., 1966, in: *Magnetism*, Vol. IV, eds G.T. Rado and H. Suhl (Academic Press, New York).
- Hybertsen, M.S., and S.G. Louie, 1985, *Phys. Rev. Lett.* **55**, 1418.
- Jaccard, D., J. Flouquet, Z. Fisk, J.L. Smith and H.R. Ott, 1985, *J. Phys. (Paris) Lett.* **46**, L811.
- Johanson, W.R., G.W. Crabtree, A.S. Edelstein and O.D. McMasters, 1981, *Phys. Rev. Lett.* **46**, 504.
- Jones, B., 1985, as cited in Lee et al. (1986).
- Kagan, Y., and N.V. Prokofev, 1986, *Zh. Eksp. & Teor. Fiz* **90**, 2176 [*Sov. Phys.-JETP* **63**, 1276].
- Kagan, Y., and N.V. Prokofev, 1987, *Zh. Eksp. & Teor. Fiz* **93**, 366 [*Sov. Phys.-JETP* **66**, 211].
- Koelling, D.D., 1982, *Solid State Commun.* **43**, 247.
- Kohn, W., and L.J. Sham, 1965, *Phys. Rev.* **140**, A1133.
- Kondo, J., 1964, *Prog. Theo. Phys. (Kyoto)* **32**, 37.
- Kondo, J., 1969, in: *Solid State Physics*, Vol. 23, eds F. Seitz, D. Turnbull and H. Ehrenreich (Academic Press, New York) pp. 183-281.
- Kondo, J., 1984, *Physica B+C* **126**, 377.
- Koskenmaki, D.C., and K.A. Gschneidner Jr, 1975, *Phys. Rev. B* **11**, 4463.
- Koskenmaki, D.C., and K.A. Gschneidner Jr, 1978, in: *Handbook on the Physics and Chemistry of Rare Earths*, eds K.A. Gschneidner Jr and L. Eyring (North-Holland, Amsterdam) ch. 4.
- Lawrence, J., and M.T. Béal-Monod, 1981, in: *Valence Fluctuations in Solids*, eds L.M. Falicov, W. Hanke and M.P. Maple (North-Holland, Amsterdam) p. 53.
- Lee, P.A., T.M. Rice, J.W. Serene, L.J. Sham and J.W. Wilkins, 1986, *Comm. Condens. Mater. Phys.* **12**, 99.
- Lee, W.H., H.C. Ku and R.N. Shelton, 1988, *Phys. Rev. B* **38**, 11562.
- Legvold, S., 1979, as cited in Stassis et al. (1979b).
- Lin, C.L., A. Wallash, J.E. Crow, T. Mihalisin and P. Schlottmann, 1987, *Phys. Rev. Lett.* **58**, 1232; and as cited in Lee et al. (1986).
- Liu, S.H., 1987, *Phys. Rev. Lett.* **58**, 2706.
- Liu, S.H., 1988, *Phys. Rev. B* **37**, 3542.
- Liu, S.H., 1989a, *Phys. Rev. B* **39**, 7381.
- Liu, S.H., 1989b, *Phys. Rev. B* **39**, 1403.
- Liu, S.H., and K.-M. Ho, 1983, *Phys. Rev. B* **30**, 3039.
- Liu, S.H., C. Stassis and K.A. Gschneidner Jr, 1981, in: *Valence Fluctuations in Solids*, eds L.M. Falicov, W. Hanke and M.P. Maple (North-Holland, Amsterdam) p. 99.
- Mahan, G.D., 1967, *Phys. Rev.* **163**, 612.
- Malik, S.K., R. Vijayaraghavan, S.K. Garg and R.J. Ripmeester, 1975, *Phys. Status Solidi B* **68**, 399.
- Maple, M.B., L.E. DeLong and B.C. Sales, 1978, in: *Handbook on the Physics and Chemistry of Rare Earths*, eds K.A. Gschneidner Jr and L. Eyring (North-Holland, Amsterdam) ch. 11.
- Matsuura, T., R. Kittler and K.H. Bennemann, 1980, *Phys. Rev. B* **21**, 3467.
- Maury, A., P. Scoboria, J.E. Crow and T. Mihalisin, 1979, *J. Appl. Phys.* **50**, 7572.
- McEwen, K.A., 1978, in: *Handbook on the Physics and Chemistry of Rare Earths*, eds K.A. Gschneidner Jr and L. Eyring (North-Holland, Amsterdam) ch. 6.
- Millis, A.J., and P.A. Lee, 1987, *Phys. Rev. B* **35**, 3394.
- Mook, H.A., 1987, private communication.
- Mook, H.A., and F. Holtzberg, 1981, in: *Valence Fluctuations in Solids*, eds L.M. Falicov, W. Hanke and M.B. Maple (North-Holland, Amsterdam) p. 113.
- Mook, H.A., and R.M. Nicklow, 1979, *Phys. Rev. B* **20**, 1656.
- Mook, H.A., R.M. Nicklow, T. Penney, F. Holtzberg and M.W. Shafer, 1979, *Phys. Rev. B* **18**, 2925.
- Mook, H.A., D.B. McWhan and F. Holtzberg, 1982, *Phys. Rev. B* **25**, 4321.
- Moon, R.M., 1986, *Physica B* **137**, 19.
- Newns, D.M., and N. Read, 1987, *Adv. in Physics* **36**, 799.
- Nozières, P., and C.T. de Dominicis, 1969, *Phys. Rev.* **178**, 1097.
- Ott, H.R., H. Rudigier, Z. Fisk and J.L. Smith, 1983, *Phys. Rev. Lett.* **50**, 1595.
- Ott, H.R., H. Rudigier, P. Delsing and Z. Fisk,

- 1984a, *Phys. Rev. Lett.* **52**, 1551.
- Ott, H.R., H. Rudigier, Z. Fisk and J.L. Smith, 1984b, *Physica B* **127**, 359.
- Ott, H.R., H. Rudigier, Z. Fisk and J.L. Smith, 1984c, in: *Moment Formation in Solids*, ed. W.J.L. Buyers (Plenum, New York) p. 305.
- Rajan, V.T., 1983, *Phys. Rev. Lett.* **51**, 308.
- Rajan, V.T., J.H. Lowenstein and N. Andrei, 1982, *Phys. Rev. Lett.* **49**, 497.
- Remenyi, G., A. Briggs, J. Flouquet, O. Laborde and F. Lapiere, 1983, *J. Magn. & Magn. Mater.* **31-34**, 407.
- Remenyi, G., D. Jaccard, J. Flouquet, A. Briggs, Z. Fisk, J.L. Smith and H.R. Ott, 1986, *J. Phys. (Paris)* **47**, 367.
- Schlottmann, P., 1989, *Phys. Rep.* **181**, 2.
- Schneider, H., Z. Kletowski, F. Oster and D. Wohlleben, 1983, *Solid State Commun.* **48**, 1093.
- Schrieffer, J.R., and P.A. Wolfe, 1966, *Phys. Rev.* **149**, 491.
- Severing, A., W. Reichardt, E. Holland-Moritz, D. Wohlleben and W. Assmus, 1988, *Phys. Rev. B* **38**, 1773.
- Stalinski, B., Z. Kletowski and Z. Henkie, 1973, *Phys. Status Solidi A* **19**, K165.
- Stassis, C., 1979, *Nukleonika* **24**, 765.
- Stassis, C., 1986, *Physica B* **137**, 61.
- Stassis, C., 1988, as cited in Liu (1989).
- Stassis, C., C.-K. Loong, O.D. McMasters and R.M. Moon, 1979a, *J. Appl. Phys.* **50**, 2091.
- Stassis, C., C.-K. Loong, B.N. Harmon, S.H. Liu and R.M. Moon, 1979b, *J. Appl. Phys.* **50**, 7567.
- Stassis, C., T. Gould, O.D. McMasters, K.A. Gschneidner Jr and R.M. Nicklow, 1979c, *Phys. Rev. B* **19**, 5746.
- Stassis, C., C.-K. Loong, J. Zarestky, O.D. McMasters and R.M. Nicklow, 1980, *Solid State Commun.* **36**, 677.
- Stassis, C., C.-K. Loong, J. Zarestky, O.D. McMasters, R.M. Moon and J.R. Thompson, 1982, *J. Appl. Phys.* **53**, 7890.
- Stassis, C., J.D. Axe, C.F. Majkrzak, B. Batlogg and J. Remeika, 1985, *J. Appl. Phys.* **57**, 3087.
- Stassis, C., J. Arthur, C.F. Majkrzak, J.D. Axe, B. Batlogg, J. Remeika, Z. Fisk, J.L. Smith and A.S. Edelstein, 1986, *Phys. Rev. B* **34**, 4382.
- Steglich, F., J. Aarts, C.D. Bredl, W. Lieke, D. Meschede, W. Franz and J. Schäfer, 1979, *Phys. Rev. Lett.* **43**, 1892.
- Steglich, F., U. Ahlheim, J.J.M. Franse, N. Grewe, D. Rainer and U. Rauchschwalbe, 1985, *J. Magn. & Magn. Mater.* **52**, 54.
- Stewart, G.R., 1984, *Rev. Mod. Phys.* **56**, 755.
- Stewart, G.R., Z. Fisk and J.O. Willis, 1983, *Phys. Rev.* **28**, 172.
- Stewart, G.R., Z. Fisk, J.O. Willis and J.L. Smith, 1984, *Phys. Rev. Lett.* **52**, 679.
- Taillefer, L., and G.G. Lonzarich, 1988, *Phys. Rev. Lett.* **60**, 1570.
- Taillefer, L., R. Newbury, G.G. Lonzarich, Z. Fisk and J.L. Smith, 1987, *J. Magn. & Magn. Mater.* **63-64**, 372.
- Toxen, A.M., 1979, as cited in Stassis et al. (1979b).
- Tsang, T.-W.E., K.A. Gschneidner Jr, O.D. McMasters, R.J. Stierman and S.K. Dhar, 1984, *Phys. Rev. B* **29**, 4185.
- Tsuchida, T., and W.E. Wallace, 1965, *J. Chem. Phys.* **43**, 3811.
- Van Aken, P.B., H.J. van Daal and K.H.J. Buschow, 1974, *Phys. Lett. A* **49**, 201.
- Van Peski-Tinbergen, T., and A.J. Dekker, 1963, *Physica* **29**, 917.
- Varma, C.M., and Y. Yafet, 1976, *Phys. Rev. B* **13**, 2950.
- Wakabayashi, N., 1980, *Phys. Rev. B* **22**, 5833.
- Wang, C.S., M.R. Norman, R.C. Albers, A.M. Boring, W.E. Pickett, H. Krakauer and N.E. Christensen, 1987, *Phys. Rev. B* **35**, 7260.
- Winzer, K., 1975, *Solid State Commun.* **16**, 521.
- Yoshimori, A., and H. Kasai, 1983, *J. Magn. & Magn. Mater.* **31-34**, 475.

## Chapter 112

# THEORY OF COHESION IN RARE EARTHS AND ACTINIDES

**BÖRJE JOHANSSON**

*Condensed Matter Theory Group, Institute of Physics, University of Uppsala,  
BOX 530, S-75121 Uppsala, Sweden*

**M.S.S. BROOKS**

*Commission of the European Communities, Joint Research Centre, European  
Institute for Transuranium Elements, Postfach 2340, W-7500 Karlsruhe, Germany*

---

### Contents

1. Introduction	149	4.3. Atomic volume	185
2. Chemical bonding in metals	151	4.4. Bulk modulus	192
2.1. Assignment of valence	151	4.5. Crystal structure	193
2.2. Cohesive energy	157	4.6. Cohesive energy	198
2.3. Crystal structure	160	4.7. Elastic constants	203
3. Physical theory of bonding in metals	163	4.8. Cerium	204
3.1. Density functional theory	165	4.9. Surfaces	208
3.2. The LMTO method	166	5. Rare earth compounds	209
3.3. Rare earths and actinides	168	5.1. Electronic structure	209
3.4. The force theorem and the electronic pressure	170	5.1.1. Model considerations	209
3.5. The magneto-volume effect	174	5.1.2. Calculated electronic structure	212
3.6. The relativistic volume effect	175	5.2. Magneto-volume effects	217
3.7. Spin polarization and the cohesive energy	177	5.3. Cerium compounds	218
4. The elemental metals	180	6. Actinide compounds	221
4.1. Electronic structure of the lanthanide metals	180	6.1. 5f-ligand hybridization, electronic structure and volume	221
4.2. Electronic structure of the actinide metals	183	6.2. Vegard's law, magneto-volume and relativistic volume effects	228
		References	237

---

### 1. Introduction

This chapter concerns first-principles calculations of the cohesive properties of rare earths and actinides. This is only a small, but very important, part of the contri-



bution of the theory of electronic structure to an understanding of the properties of these elements. Other articles in these volumes deal with other aspects of electronic-structure theory. For example, Norman and Koelling (ch. 110) review Fermi surface studies and superconductivity and Liu (ch. 111) reviews the problem of electron correlation that manifests itself in heavy-fermion systems.

By electronic structure we mean the spatial and energy distribution of electrons in solids. When the electronic structure is known, it is, in principle, possible to calculate all the ground-state properties of the solid. Early electronic-structure calculations for rare earths and actinides were made under far more difficult circumstances than we enjoy today. When Dimmock and Freeman (1964) calculated the energy band structure of Gd there were very few electronic computers and no workstations. The calculations did not yield fundamental quantities, such as electron occupation numbers or magnetic moments. They did, however, reveal that the conduction band structure of rare earths was dominated by d states and was not free-electron like – a considerable advance in itself. It also became possible, at least semi-quantitatively, to explain the various magnetic structures of the rare earth metals in terms of the wave vector dependent susceptibility (e.g. Liu 1978), although obtaining accuracy for response functions remains difficult. Similarly, early energy band structure calculations for the actinides (Keeton and Loucks 1968, Freeman and Koelling 1974) revealed that the conduction band structure was dominated by f states.

The electronic-structure calculations from which cohesive properties are evaluated are now self-consistent, the only input to the calculations being the atomic numbers and, sometimes, the crystal structure. The theoretical framework of self-consistent electronic-structure calculations is provided by *density functional theory* (Hohenberg and Kohn 1964, Kohn and Sham 1965), which is independent of the particular elements composing the solid. The structure of density functional theory is outlined very briefly in sect. 3, but there are many articles and books which treat the topic in great detail (e.g. Kohn and Sham 1965, Gunnarsson and Lundqvist 1976, Moruzzi et al. 1978, Mackintosh and Andersen 1979, Koelling 1981, Kohn and Vashista 1983, Williams and von Barth 1983, Callaway and March 1984, Hedin and Lundqvist 1971, von Barth and Hedin 1972). It suffices here to note that the most-used approximation to the density functional – the *local density approximation* (LDA) (Kohn and Sham 1965) – provides us with the potential in which the electrons move, if the electron density is known. A knowledge of the potential and some quantum mechanics are then sufficient to calculate the density. The calculations are therefore started with a guess at the density and are iterated until the output and input densities are the same. The iteration procedure is one reason that electronic-structure calculations require so much computer time. The second reason is that solving the equations for an electron moving in a periodic potential – the band-structure calculation – increases in complexity with the complexity of the systems being studied. Actinide-transition metal intermetallics with many atoms per unit cell and f states in the band structure are complex systems. The numerical techniques used to solve the band-structure problem have been improved dramatically by the introduction of *linear methods* (Andersen 1975), which can produce solutions up to two orders of magnitude faster than older methods. Most of the work referred to in this chapter will have used linear

methods, which turn the problem of solving for scattering states into an eigenvalue problem susceptible to efficient solution.

Evaluation of cohesive properties often requires calculation of the total energies, for which there are now excellent algorithms. The application of total-energy calculations to find cohesive properties of transition metals and rare earths has been reviewed by Moruzzi et al. (1978) and Freeman et al. (1987), respectively. It is also possible to use the *force theorem* (Mackintosh and Andersen 1979) to calculate the energy difference between different structures, or to use the *electronic pressure formula* (Pettifor 1976) to calculate the electronic equation of state and to separate it into its different angular momentum components – something that cannot be done with the total energy. These techniques have been exploited by Pettifor (1977, 1978), Andersen et al. (1985), Skriver (1983a, b, 1985), Brooks et al. (1984), Christensen and Heine (1985), Eriksson et al. (1988a–d, 1989a–d, 1990a–d) and Nordström et al. (1990) and their basis is explained in more detail in sect. 3.

The bonding in rare earths, actinides and their compounds has also been examined in some detail by Harrison and co-workers (Harrison 1980, Wills and Harrison 1983, Harrison 1984, Harrison and Straub 1987) using a model theory of bonding. In this type of approach, the description of chemical bonding is expressed in terms of the minimum number of *potential parameters* possible, and parameters involving the structure. It is then frequently possible to calculate many properties by hand, and the method has the advantage of being physical and transparent. We will not dwell upon this work in this chapter, because it normally requires the experience obtained from self-consistent calculations to provide input parameters. Nevertheless, it is useful to explain the results of self-consistent calculations by using such models of bonding, and with increasing experience such models may be expected to improve in predictive capacity. In this chapter we have not hesitated to simplify results where possible and to use models to explain them.

In 1975, at the symposium *Actinides 1975*, an eminent chemist accused theorists of producing complicated theories for the energy band structure without being able to calculate even a lattice constant. It is in fact not that easy to calculate a lattice constant from first principles, but in the meantime many workers have been doing not only that, but they have also evaluated the correct crystal structures and are even able to calculate cohesive energies accurately.

## 2. Chemical bonding in metals

### 2.1. Assignment of valence

Since the 4f electrons are localized, or non-bonding, most lanthanides have three valence electrons and there is a smooth (approximately linear) change in volume between lanthanum and lutetium, both of which are trivalent. The exceptions are the anomalously large volumes of europium and ytterbium, which are divalent. The small volume decrease between lanthanum and lutetium is, of course, the consequence of the incomplete screening of the additional nuclear charge by the 4f electrons.

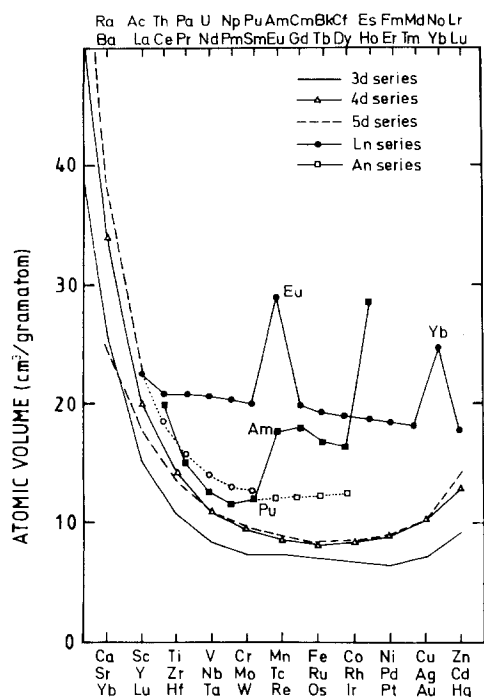


Fig. 1. The experimental equilibrium atomic volumes of the 3d, 4d and 5d transition metals, the lanthanides and the actinides.

The parabolic decrease in volume of the earlier elements in each d transition metal series with increasing atomic number (fig. 1) is closely connected to the number of valence electrons. A parabolic trend in volume means that the *relative* contraction, the ratio of the volume of the  $Z + 1$  atom to that of the  $Z$  atom, decreases approximately linearly with the number of valence electrons. Furthermore, the relative volume decrease is similar for the different series, see fig. 2.

The number of bonding electrons at the beginning of the 5d series may be inferred from comparing the measured atomic volumes of rare earths and transition metals. On the right in fig. 1, Yb is clearly a divalent lanthanide and, therefore, has two valence electrons. Similarly, lutetium is a trivalent lanthanide and has three valence electrons. On the left in the same figure, these two elements are seen to be also the first two members of the 5d transition series and the third, hafnium, will have four valence electrons.

In contrast, the assignment of valencies to the actinides, in order to derive the number of (6d7s) valence electrons (Zachariasen 1952, 1961, 1964, 1973, Cunningham and Wallmann 1964, Sarkisov 1966, Weigel and Trinkl 1968, Smith et al. 1969, Fahey et al. 1972), should be treated with caution. It was assumed, implicitly or explicitly, that the 5f electrons are, like the 4f's in the lanthanides, localized. Although such methods are useful for the heavy actinide elements, and probably also for light actinides, in connection with bonding in certain molecules and ionic compounds (i.e. in those cases for which the f electrons are non-bonding), they are less appropriate for the light actinide metals.

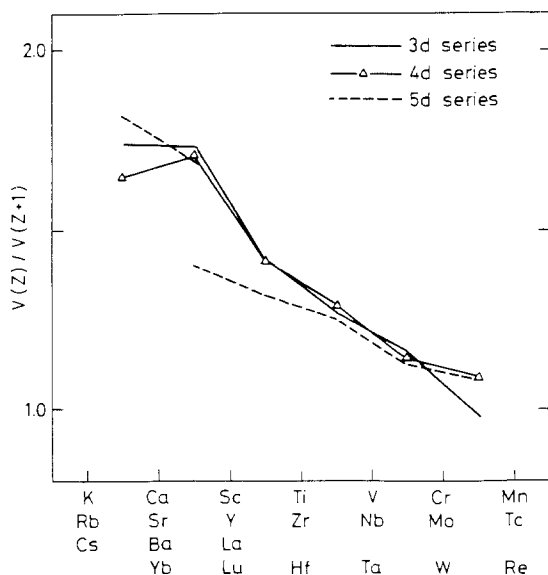


Fig. 2. Ratio of the equilibrium atomic volumes of the  $Z$  and  $Z + 1$  elements for the lighter 3d, 4d and 5d transition series.

Another type of analysis directs attention not to the atomic volume, but to the energetics of the valence electrons in the metallic state. Originating from the work of Engel (1949) and Brewer (1963), it is assumed that there are two components in bonding. The first is a bonding energy, the second a promotion energy, required to bring the free atom to the configuration of the atom in the solid. Irregularities in cohesive energies are usually due to the promotion-energy component, and if this can be isolated and removed, the remainder – the bonding energy – should be a smooth function, which may be interpolated across a series. This type of analysis may be used to investigate some basic properties of the lanthanides and heavy-actinide metals in which the  $f$  electrons do not participate in bonding. It is especially useful for the heavier actinides (e.g. Brewer 1971, Nugent et al. 1973, Johansson and Rosengren 1975b), where the relative stability of the divalent and trivalent metallic phases may be expressed in terms of the free-atom promotion energy,  $f^{n+1} \rightarrow f^n$ , which is measured independently (Johansson and Rosengren 1975a, b, Johansson 1977a).

The cohesive energies (Brewer 1975) of the (non- $f$ ) elements in the left part of the periodic table show representative trends, being consistently close to 40 kcal/mol for divalent metals (such as barium and strontium), about 100 kcal/mol for trivalent metals (such as lanthanum and yttrium) and about 145 kcal/mol for tetravalent metals (such as hafnium and zirconium).

The cohesive energies of the trivalent lanthanides should therefore be about 100 kcal/mol relative to the *trivalent* atomic state ( $f^n ds^2$ ). However, the cohesive energy of gadolinium is slightly less – 95 kcal/mol – although the configuration of the free gadolinium atom is  $f^7 5d 6s^2$ . The difference is due to the multiplet coupling between the open  $4f$  and  $5d$  shells in the gadolinium free atom – which is, of course, absent in 3d, 4d and 5d transition metals. This coupling may easily be estimated in the local

spin density approximation (LSDA) (sect. 3.7). In this approximation the multiplet coupling energy is  $-\frac{1}{2}J_{4f5d}\mu_{4f}^s\mu_{5d}^s$  in terms of the 4f5d exchange interaction and the spin components of the 4f and 5d moments. We calculate  $J_{4f5d}$  to be 105 meV (or 2.4 kcal) for a free Gd atom (sect. 3.7). Therefore, with a 4f spin moment of seven and a 5d spin moment of one, the magnitude of the multiplet coupling energy is estimated to be about 8.4 kcal/mol in LSDA. Thus the corrected (i.e. with the multiplet coupling energy subtracted) cohesive energy for Gd becomes about 103 kcal/mol, to be compared with observed values of 103 kcal/mol for La and 102 kcal/mol for Lu. The corrected cohesive energy is a smooth function across the series. Actually not all of the multiplet coupling energy is lost in the solid, since a small 5d moment remains. Furthermore, the exchange integrals are slightly different in the free atom and the solid. A more exact estimate of the change in coupling energy is given in sect. 3.7.

The same atomic coupling is also present, with about the same magnitude, in other trivalent free lanthanide atoms (Johansson and Munck 1984). The cohesive energy, relative to the trivalent free atoms, should therefore be about 95 kcal/mol, rather than 100 kcal/mol, for metals with no f shell – a net reduction of about 5 kcal/mol. Similarly, the measured cohesive energy of the trivalent actinide element curium is about 90 kcal/mol (Ward et al. 1975), which may be taken to be representative of the cohesive energy of the trivalent actinide metals – again relative to the corresponding trivalent ( $5f^76d7s^2$ ) free-atom configuration.

Therefore, relative to the trivalent free atoms, the cohesive energy is about 50 and 55 kcal/mol greater for the trivalent metals than for the divalent metals, for lanthanides and actinides, respectively. The corresponding difference between the cohesive energies of tetravalent and trivalent metals is also about 45 kcal/mol. However, a promotion energy is required to take the free atom from the divalent to the trivalent state in preparation for a trivalent solid, but not for a divalent solid. Therefore, only if this promotion energy is less than the difference between the divalent and trivalent cohesive energies will the solid be trivalent. The free-atom promotion energies are known experimentally for most of the lanthanides (Martin et al. 1978), but only for some of the actinides. However, the missing promotion energies have been estimated (Brewer 1971, Vander Sluis and Nugent 1972). The measured promotion energies (or estimates where necessary) are plotted in fig. 3, with the critical values (55 and 50 kcal/mol for actinides and rare earths, respectively) at which the metallic state changes from trivalent to divalent.

It is clear from fig. 3 that europium and ytterbium are correctly stated to be the only divalent rare earth metals. Americium, the actinide analogue of europium, should be trivalent. Physically, this is because the free-atom promotion energy in americium is less than the extra energy gained by forming a trivalent solid, and again this agrees with experiment. The promotion energies of the actinides do show that the half-filled shell is especially stable, but for the earlier part of the series the absolute values are lower than those of the corresponding lanthanides, making the divalent condensed phase of americium – in contrast to europium – unstable. Curium and berkelium should be trivalent metals. The elements Am–Bk crystallize in the typical lanthanide dhcp structure (Lee and Waldron 1972), which is completely consistent with a trivalent metallic ground state (see sect. 4.5).

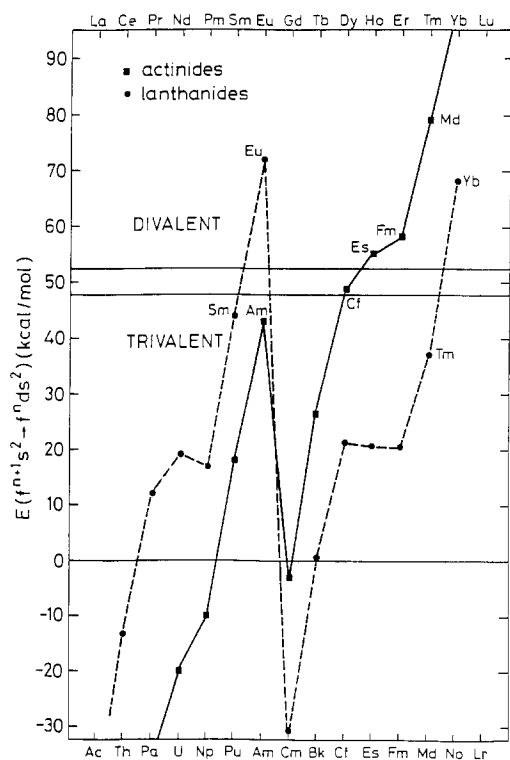


Fig. 3. Energy comparison between the atomic excitation energy,  $f^{n+1}s^2 \rightarrow f^n ds^2$ , and the critical value separating the divalent and trivalent metallic states.

Figure 3 also shows that, of the heavy actinides, not only the ytterbium analogue, nobelium, but also mendelevium and probably fermium and einsteinium should be divalent metals. Unfortunately, the limited availability of these elements has so far prevented any experimental studies of No, Md and Fm in their elemental metallic states. Californium is an interesting case, where the metallic ground state, according to fig. 3, is on the borderline between the divalent and trivalent condensed phases. Heat of vaporization measurements on large samples of californium (Ward et al. 1979) show that californium is a trivalent metal. Now, samarium metal, which is trivalent in the bulk, has been found to have a divalent surface (Wertheim and Creselius 1978, Allen et al. 1978, Johansson 1979, Rosengren and Johansson 1982). Results of experiments on microgram quantities of californium by Haire and Asprey (1976) and Noé and Peterson (1976) were extremely dependent upon the preparation conditions, and various forms of californium metal showing divalent, intermediate and trivalent behaviour, were obtained – encouraging the hypothesis that the surface of californium is, like that of samarium, divalent. Microfilm techniques have been used to prepare thin films of einsteinium (Haire and Baybarz 1979). Electron diffraction studies showed that the crystal structure was fcc (as in ytterbium) and that the lattice constant was typical of a divalent metal. Finally, it is quite possible that *bulk* einsteinium is also divalent.

X-ray diffraction measurements on californium under high pressure have been performed (Burns and Peterson 1978, Peterson et al. 1983), and the data clearly shows that Cf is trivalent at zero pressure. If either bulk einsteinium or fermium turns out to be divalent under ambient conditions, it follows from fig. 3 that modest compression would be sufficient to induce a valence transformation to the trivalent state of either of these two elements. But considerably higher pressures would be required to induce a valence change in mendelevium or, more so, in nobelium.

One of the main differences, therefore, between actinides and rare earths is the steeper change of the  $f-d$  energy difference along the actinide series (fig. 3). This first of all makes americium trivalent, but also implies that a *series* of elements at the end of the actinide series will be divalent. Indeed, the divalent state of nobelium is so relatively stable that, of the possible halide compounds, the only trivalent compound it will be able to form is the trifluoride (Johansson 1977a).

The energy difference between the trivalent and tetravalent metallic states can be investigated in exactly the same way (fig. 4) as between the di- and trivalent states. It is obvious that no lanthanide can be a tetravalent metal – not even cerium (Johansson 1974). The trivalent state is also more stable for the actinides americium, curium and berkelium. But, in the valence picture, both plutonium and neptunium have lower energies as trivalent than tetravalent metals. Hence, tetravalent ground states for Np and Pu may be eliminated. In fact, by comparing figs. 3 and 4 it is easy

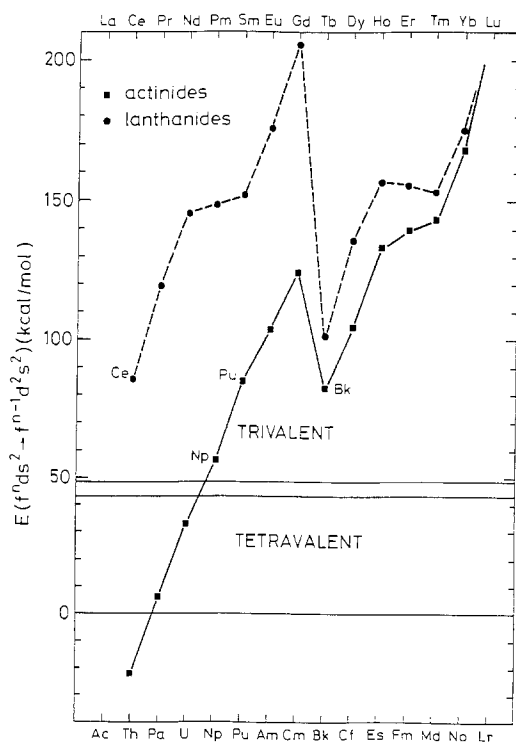


Fig. 4. Energy comparison between the atomic excitation energy  $f^n d s^2 \rightarrow f^{n-1} d^2 s^2$ , and the critical value separating the trivalent and tetravalent metallic states.

to see that in the valence picture both these metals must be trivalent. But it was evident from the trend in the atomic volume for the entire actinide series (fig. 1) that neither Np nor Pu can be trivalent metals. It follows that the 5f electrons must be playing a fundamental role in the cohesion of Np and Pu.

## 2.2. Cohesive energy

The cohesive energies are not smooth functions across the series, and to be able to interpolate a smoothly varying quantity across the series it is again necessary to remove the promotion energy contribution. The room-temperature analogue of the cohesive energy is the heat of sublimation,  $\Delta H_s$ , which has been studied by Nugent et al. (1973) and Brewer (1971). Johansson and Rosengren (1975b) studied the cohesive energy, but since there is only a minor difference between these two quantities we will not distinguish between them.

Nugent et al. (1973a, b) based their treatment on the assumption that, relative to the lowest lying trivalent  $f^n ds^2$  atomic level, the heat of sublimation is a smooth function along the lanthanide series. Therefore, they interpolated the function  $\Delta H_s + \Delta E(f \rightarrow d)$ , where  $\Delta E$  is the promotion energy of one f electron into the d shell, between La and Gd and between Gd and Lu. Then, by using experimental (and, in some cases, estimated) data for the promotion energy  $\Delta E(f \rightarrow d)$ , they calculated the heats of sublimation with, on the whole, quite good agreement with experiment. This method was later improved by Johansson and Munck (1984), who, by eliminating energies specific to the atoms, arrived at very smoothly varying valence bond energies.

Johansson and Rosengren (1975b) studied the binding energy,  $E_B$ , the energy gained by bringing free trivalent  $f^n$  ions and three electrons per atom together to form the metal. This quantity is obtained by adding the sum of the first three ionization potentials to the cohesive energy. The reason that the binding energy was chosen as the quantity to interpolate by Johansson and Rosengren is that, with the 6s and 5d shells empty in the triply ionized ion, the multiplet coupling between the open f and d shells in the trivalent atom is removed. The binding energy is, therefore, a smooth function across the series, resulting in a more accurate interpolation scheme. The measured values of the binding energy for Ce, Gd and Lu were used to interpolate the binding energy for the rest of the lanthanides, then the first three ionization potentials were subtracted from the interpolated values to obtain the interpolated value for the cohesive energy. Johansson and Rosengren (1975b) found that, by following this procedure, they obtained better agreement with the experimental cohesive energies than Nugent et al. (1973). The main limitation to using the binding energy for interpolation is that the second and third ionization potentials have not been determined as accurately as the first ionization potential, which is, however, known to extremely high accuracy. The sum of the first three ionization potentials has, in general, an experimental uncertainty of about 0.1–0.2 eV for the lanthanides.

Both Nugent et al. (1973) and Johansson and Rosengren (1975b) applied their respective interpolation schemes to the actinides. Unfortunately, since the availability of the required optical spectroscopic data is much more limited for the actinide atoms,



the accuracy of the results has suffered. This is especially so when the binding energy is interpolated, since, although the method is in principle better, it is dependent upon sound experimental data for the ionization potentials. The lack of data compelled Johansson and Rosengren to invoke a quite complicated scheme when they applied their interpolation to the actinide metals. Despite the difficulties, Nugent et al. (1973) and Johansson and Rosengren (1975b) were at least able to identify a substantial 5f contribution to the bonding in the earlier actinides.

Another smoothly varying function across the series is based upon the standard enthalpy of formation,  $\Delta H_f^0[\text{M}(X), \text{aq}]$ , of the metal aqueous ion (ionization stage =  $X$ ) in aqueous solution at room temperature (Morss 1976), which is shown in fig. 5a for  $X = \text{III}$ . The quantity  $\Delta H_f^0[\text{M}(\text{III}), \text{aq}]$  changes slowly and regularly – with the exception of europium and ytterbium – across the series, with a dip, due to the nephelauxetic effect (Nugent 1970, Peppard et al. 1969, Fidelis and Siekierski 1966), in the middle of the series. The regular behaviour occurs for those elements which are trivalent in the metallic phase. If the part of  $\Delta H_f^0[\text{M}(\text{III}), \text{aq}]$  which behaves regularly is denoted by  $\Delta H_f^0[\text{M}^\times(\text{III}), \text{aq}]$ , then their difference is the energy difference between the true metallic and trivalent metallic states,  $\Delta H_{\text{m,III}}$ . This energy difference for europium metal is 20 kcal/mol – the energy difference between the divalent and trivalent metallic states.

The corresponding experimental data for the actinides (Fuger 1982) in fig. 5 is very different from that of the lanthanides. It is unfortunate that there are no accurate data available for actinium, but, by comparing with the lanthanides, we estimate that the value indicated by the open square in the figure should be appropriate. We now take the values for Ac, Am and Cm to be typical for trivalent actinide metals and simply interpolate between them to produce the dashed line for  $\Delta H_f^0[\text{M}^\times(\text{III}), \text{aq}]$  in fig. 5. This represents the case in which the metallic state is truly trivalent (in the sense of non-bonding  $f^n$  configurations). The differences between the interpolated values and the experimental data are therefore the stabilization energies of the real metals relative to the hypothetical trivalent metals. The stabilization energies are due to bonding 5f electrons, and estimated to be about 10 kcal/mol in plutonium, 25 kcal/mol in neptunium and 35 kcal/mol in uranium. Extrapolation of the data to Am yields a *negative* value, which means that the trivalent state of Am is stable – in agreement with experiment. The experimental data for  $\Delta H_f^0[\text{M}(\text{IV}), \text{aq}]$  (Fuger 1982) is plotted in fig. 5b. The value for thorium can be taken as typical for a tetravalent 6d transition metal. Unfortunately there are no other tetravalent actinide metals, preventing an estimate of how much  $\Delta H_f^0[\text{M}^\times(\text{IV}), \text{aq}]$  should change across the series. The trend is indicated by the dashed line in fig. 5, which, although reasonable, is very inaccurate. But the experimental data in the figure are so different from the estimated, dashed, tetravalent line for the lighter actinides that one can be sure that the true metallic state is not tetravalent.

The experimental data for Am, Cm and Bk are not very accurate. Nevertheless, there are very obvious deviations from tetravalent behaviour, which are directly related to the energy difference between the actual trivalent metallic state and the hypothetical tetravalent state (compare with the divalent–trivalent energy separation

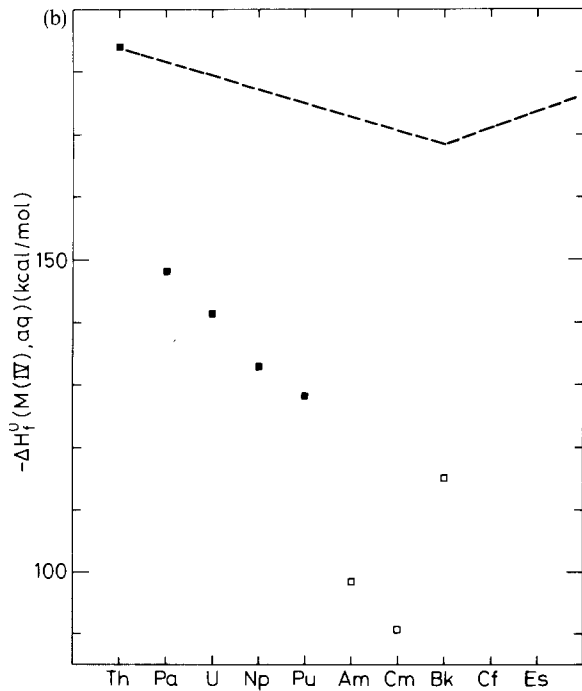
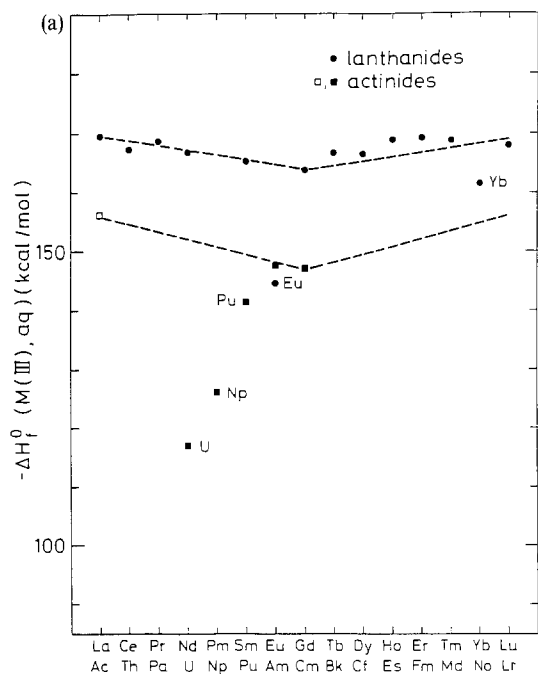


Fig. 5. Standard enthalpy of formation: (a)  $\Delta H_f^0[M(III), aq]$  for the lanthanides and actinides and (b)  $\Delta H_f^0[M(IV), aq]$  for the actinides.

for Eu and Yb in fig. 5). Thus, fig. 5 demonstrates that the energy of the tetravalent state is well above the energy of the metallic ground state for these metals.

The kind of analysis outlined above can yield accurate assessments of the extent to which f electrons participate in the chemical bonding in the lighter actinides, but they are dependent upon accurate experimental data for actinium and the transplutonium elements. Both thermochemical and optical spectroscopic data are also useful for analysis of the factors determining the oxidation states of the actinide atom in compounds (Johansson 1977a, Brooks et al. 1984). For example, the stability of 450 different halides and oxides of the lanthanides were investigated, and the existence or non-existence of di-, tri- and tetravalent compounds was accounted for very well (Johansson 1977a).

### 2.3. *Crystal structure*

At room temperature lanthanum has the double hexagonal close packed, dhcp, structure with a stacking arrangement of hexagonal layers of the type ABAC, ABAC, . . . . Slightly above room temperature the fcc (ABC, ABC, . . .) structure becomes stable, and just before melting there is a bcc phase. Praseodymium and neodymium have the same structures, the main difference being that the temperature range in which the fcc structure is stable is smaller. At moderate and high temperatures cerium has the same structure sequence. The crystal structure of samarium is called the Sm-type, with a stacking sequence ABABCBCAC, ABABCBCAC, . . . . Finally, gadolinium and the heavy lanthanides have the hcp (i.e. AB, AB, . . .) structure. For all the lanthanides except the most heavy ones, there is a bcc phase before melting. Hence, across the series, with decreasing atomic number, the low-temperature crystal structures change in the sequence: hcp → Sm-type → dhcp → fcc (Beaudry and Gschneidner 1978). The same crystal structure sequence is observed for the intra-rare earth alloys as a function of alloying (Harris et al. 1966, Gschneidner and Valetta 1968), and for an individual element under pressure. Thus, as far as the crystallographic properties are concerned, a heavier lanthanide under pressure becomes similar to a lighter lanthanide at ambient pressure. Hence, Jayaraman and Sherwood (1964) were led to propose that the crystal structures of the lanthanides under pressure always evolve in the sequence hcp → Sm-type → dhcp → fcc. Subsequent high-pressure work has confirmed the validity of this conjecture (Liu 1975), and the close connection between the individual phase diagrams was used (Johansson and Rosengren 1975a) to construct a generalized phase diagram for the trivalent lanthanides. Grosshans et al. (1982a, b) have detected the existence of an additional crystal structure in the lanthanide sequence, namely a distorted fcc structure (ABCA'B'C' . . .). This structure was observed at high pressures in lanthanum, praseodymium and yttrium, and might also have been observed in gadolinium (Akella 1980). The more complete crystal structure sequence is therefore hcp → Sm-type → dhcp → fcc → fcc', and we would speculate that, under even higher pressures, additional new phases will be discovered.

Various models have been proposed to explain this fascinating structure sequence. Correlation between the hexagonal  $c/a$  ratio and the crystal structure was noted by Harris and Raynor (1969), while Hodges (1967) considered the interaction energy

between the hexagonal planes and McWhan (1961, 1971) correlated the crystal structures with compression. McWhan and Stevens (1965) and Gschneidner and Valletta (1968) invoked a bonding contribution from the 4f electrons. Johansson and Rosengren (1975a) dismissed the f-bonding picture since the lanthanide structure sequence is independent of the number of f electrons. Thus, the rare earth structure sequence is found for alloys of different lanthanides and for both lanthanum–lutetium and lanthanum–yttrium alloys as a function of concentration. High-pressure experiments on yttrium (Vohra et al. 1981) reveal the complete crystal structure sequence hcp → Sm-type → dhcp → fcc, although (Johansson 1978a) there can be no 4f-electron influence upon the crystal structure of a 4d metal. Instead, Johansson and Rosengren (1975a) correlated the crystal structure with the ratio,  $f$ , of the Wigner–Seitz radius to the ionic radius – as a function of the individual elements, of alloying and of pressure. The motivation for using this ratio was that it is related to the concept of a pseudopotential (Johansson 1978a).

Duthie and Pettifor (1977), in a microscopic treatment, interpreted the correlation parameter,  $f$ , in terms of the d occupancy. They showed that, when hybridization is neglected, the d-band contribution to the bonding is responsible for the lanthanide structure sequence. In particular, they found that for  $N_d < 1.7$  the hcp structure, for  $1.7 < N_d < 2.3$  the Sm-type structure, for  $2.3 < N_d < 2.6$  the dhcp structure and, finally, for  $N_d > 2.6$  the fcc structure is energetically the most stable. Since lanthanum has a higher d-band occupation number than lutetium and since the number of d electrons increases with pressure, it follows that the observed structure sequence is reproduced. However, the critical values of the d occupation numbers are probably not exact, since fully hybridized energy band calculations (Skriver 1983b) yield  $N_d = 2.0$  for lanthanum and  $N_d = 1.45$  for lutetium – values which do not quite fit the critical ranges calculated by Duthie and Pettifor (1977). Skriver (1983b) suggested that if critical values for  $N_d$  are assigned empirically, the observed transition pressures for an individual element can still be rationalized. The evaluation of the differences in the energies of the various crystal structures (Skriver 1985, Freeman et al. 1987, Wills and Eriksson 1992) is discussed in sect. 4.

The crystal structures of actinium and thorium are fcc. However, the following actinide elements have most unusual crystal structures at low temperatures – although, at high temperatures, just before melting, there is a bcc phase, and in plutonium there is also an fcc phase in a temperature range well above room temperature. It is only for americium and beyond that the simple crystal structures of elemental metals in other parts of the periodic table are encountered. Hence there is believed to be a correlation between the presence of metallic f electrons and distorted and unusual crystal structures. An understanding of the underlying mechanisms through which metallic f electrons influence the structure is beginning to emerge (Wills and Eriksson 1992a) and is discussed in sect. 3. Here we restrict our discussion to the crystal structures of the heavier 5f elements and how they fit into the pattern of crystal structures set by the rare earth metals.

Since we believe that the trans-plutonium elements have localized 5f electrons, we are led to attempt to establish a relationship between their crystallographic properties and those of the rare earths. That is, we want to compare trivalent 6d transition

metals with 5d transition metals. The structure sequence of the 4d transition metal yttrium is the same as the structure sequence of the lanthanides and one would expect something similar for the 6d trivalent 5f series. The fact that americium, curium, berkelium and californium all have the dhcp structure is already evidence for the existence of such a relationship. Of all the other metallic elements in the periodic table, only the lanthanides have a dhcp structure. By means of the correlation parameter  $f$ , Johansson and Rosengren (1975a) placed americium in a position equivalent to praseodymium, which is consistent with their common crystal structure. If, crystallographically, the two metals corresponded completely, americium would have fcc and bcc phases at elevated temperatures. The fcc phase has been observed (McWhan 1961), but whether or not there is a bcc phase before melting is not yet settled. However, high-pressure experiments have established that americium undergoes a crystallographic change from dhcp to fcc. Early measurements yielded a transition pressure of  $50 \pm 10$  kbar (Akella et al. 1979, 1980, Smith et al. 1981), whereas, later, Benedict et al. (1985) measured the transition pressure to be 95 kbar. The corresponding critical pressure in praseodymium is 40 kbar (Donohue 1974), suggesting that there is indeed a close resemblance between the two metals. At still higher pressures the 5f electrons in americium can behave quite differently to the 5f electrons in a trivalent system, and the analogy with the trivalent rare earths should not be continued.

By analogy with the rare earths one would expect berkelium, or at least californium, to have appeared in the Sm-type structure. Although not yet observed, this might, nevertheless, be the case, since the Sm-type structure could be stable in a lower temperature range than to date investigated – or, since the dhcp  $\rightarrow$  Sm-type transition is rather sluggish, it could be an experimental artifact that the Sm-type structure has not been observed. But it may be that the change in  $N_d$  from one element to another is smaller in the actinides than in the rare earths, delaying the appearance of the Sm-type structure in the actinide series. However, the calculated d occupation numbers across the series are very similar (sect. 4.2). It has been observed that under pressure Cm, Bk and Cf (as above for Am) undergo a phase transformation to the fcc structure (Benedict et al. 1984, Haire et al. 1984), which gives confirmation that the lanthanide structure series also applies to the heavy actinides. Even the fcc' structure seems to have been observed for Am and Cf (Benedict et al. 1985).

Experiments (Haire and Baybarz 1979) suggest that einsteinium has an fcc structure, but with an atomic volume corresponding to a divalent ion configuration. This crystal structure should therefore be compared with those of europium (bcc) and ytterbium (fcc). One can also discern a crystal structure sequence for divalent metals (Johansson and Rosengren 1974, 1975a), which may also be correlated with the d occupation number (Skriver 1982). When viewed in this light, einsteinium is more similar to ytterbium than to europium. Radium, on the other hand, has a bcc phase, which should be compared with barium (bcc) and europium (bcc). Slightly compressed radium is predicted to be a superconductor (Skriver 1982).

Perhaps the most interesting discovery during the last decade, as regards the elemental actinides, is the observation of an orthorhombic high-pressure phase for each of the elements Am, Cm, Bk and Cf. For Am (Roof et al. 1980) and Cf (Benedict

et al. 1985) this phase has been indexed as the  $\alpha$ -uranium structure. In addition, for Cm (Benedict et al. 1985), Bk and Cf (Benedict et al. 1984) the associated volume change has the character of a volume collapse, with a relative volume change in the region of 12–22% – in accordance with the hypothetical low equilibrium volumes shown in fig. 1. The observed volumes and structures correspond very well with those expected for metallic f bonding. Thus, these experimental observations support the view, expressed in fig. 1 through the hypothetical volumes, that the actinides form an f transition metal series, where the f states play a role similar to the d states in the 3d–5d transition metal series.

At zero pressure there is a crossover from bonding 5f electrons to standard lanthanide behaviour in the middle of the series, between Pu and Am. If we consider, instead, the actinide metals at 500 kbar, the crossover takes place further along the series, between Cf and Fm. In contrast, the lanthanides have localized  $f^n$  configurations – with the exception of the  $\alpha$ -phase of Ce. It is significant that Ce at 50 kbar transforms to an orthorhombic structure, as do Pr – at 200 kbar – and Nd – at 390 kbar (sect. 4.5). In both Ce and Pr this is the  $\alpha$ -U structure, and in both cases this is a collapsed volume phase. As for the actinides, there is apparently a crossover from bonding to non-bonding 4f electrons – but it takes place very early in the series. We have, again, in fig. 1 indicated the expected volumes of the hypothetical zero-pressure bonding state for the early lanthanides. Thus, there is a close relationship between the lanthanides and actinides, which is, however, obscured by the different position of the crossover region in the two series. This difference may be understood in terms of the greater radial extent of the 5f orbitals relative to the 4f orbitals. High-pressure experimental work has been extremely useful in revealing this fundamental correspondence between these two series of elements.

An unresolved problem that should be mentioned is that, when the high-pressure phase of Am is indexed as the  $\alpha$ -U structure, the volume difference between the low- and high-pressure phases is much smaller than the volume difference to be expected between f-bonding and non-bonding states. This problem has been investigated in some detail by Eriksson and Wills (1992), who were led to question the correctness of the crystal structure assignment for Am. Further experimental and theoretical work will be required to settle this question.

### 3. Physical theory of bonding in metals

The physical theory of bonding in metals always involves, in one way or another, finding approximations to the eigenvalues and eigenfunctions of the Hamiltonian

$$\mathcal{H} = -\frac{\hbar^2}{2} \sum_i \frac{\nabla_i^2}{2M_i} + \frac{1}{2} \sum_i \sum_j \frac{Z^2 e^2}{|\mathbf{R}_i - \mathbf{R}_j|} - \frac{\hbar^2}{2m} \sum_k \nabla_k^2 + \frac{1}{2} \sum_l \sum_k \frac{e^2}{|\mathbf{r}_k - \mathbf{r}_l|} - \sum_k \sum_i \frac{Ze^2}{|\mathbf{r}_k - \mathbf{R}_i|}, \quad (1)$$

where  $\{\mathbf{R}_i\}$  are the nuclear and  $\{\mathbf{r}_i\}$  the electronic coordinates and  $\{M_i\}$  and  $m$  are

the corresponding masses. The solid is a strongly coupled system with two species, electrons and nuclei, with Coulomb interaction both between themselves and each other. The rare earths and actinides differ only in their nuclear charge,  $Z$ , and their number of electrons, even though they often have very different solid-state properties. All attempts to solve eq. (1) involve a fair number of approximations. The first of these is the Born–Oppenheimer approximation, which isolates the electronic structure. The nuclei are far more massive than the electrons and their velocities relatively low. To a very good approximation the nuclei may be taken to be stationary. In practice, the ion cores are also taken to be stationary, along with the nuclei, which isolates the electronic structure of the conduction electrons. There remains the much simpler (but still very difficult to solve) Hamiltonian for the electrons (or sometimes just the conduction electrons)

$$\mathcal{H} = -\frac{\hbar^2}{2m} \sum_k \nabla_k^2 + \frac{1}{2} \sum_l \sum_k \frac{e^2}{|\mathbf{r}_k - \mathbf{r}_l|} - \sum_k \sum_i \frac{Ze^2}{|\mathbf{r}_k - \mathbf{R}_i|}. \quad (2)$$

The last term, the interaction with the nuclei, is regarded in electronic-structure theory as an external potential acting upon the electrons. Evidently the wave functions are not products of single-particle wave functions, since eq. (2) is not separable, but methods have been developed where this appears to be approximately so.

The simplest way to reduce eq. (2) to a soluble problem is by the Hartree approximation. In eq. (2) the potential felt by one electron depends upon the positions of the other electrons, but if this potential is approximated by an average single-particle potential,

$$V_k(\mathbf{r}_k) = \sum_{l \neq k} \int n_l \frac{e^2 |\Psi_l(\mathbf{r}_l)|^2}{|\mathbf{r}_k - \mathbf{r}_l|} d\mathbf{r}_l, \quad (3)$$

where  $n_l$  are the occupation numbers and  $\{\Psi_l(\mathbf{r}_l)\}$  are the single-particle wave functions that arise if this approximation is made, i.e. they are the solutions to

$$\left[ -\frac{\hbar^2}{2m} \nabla_l^2 - \sum_i \frac{Ze^2}{|\mathbf{r}_l - \mathbf{R}_i|} + V_l(\mathbf{r}_l) \right] \Psi_l(\mathbf{r}_l) = \varepsilon_l \Psi_l(\mathbf{r}_l), \quad (4)$$

then the equations become separable, as we have assumed them to be. The above is an entirely intuitive approximation, and great effort has been expended in trying to formalize it. The equations are actually non-linear, since  $V_l(\mathbf{r}_l)$  depends upon  $\{|\Psi_l(\mathbf{r}_l)|^2\}$ . They must therefore be solved self-consistently by iteration – the operator on the left-hand side of eq. (4) depends upon the solution of the equation itself. In practice, a guess at  $V_l(\mathbf{r}_l)$  is made and eq. (4) is solved for each  $l$ , a choice is then made (usually via the lowest eigenvalues) with regard to the occupation of the single-electron states and eq. (3) is used to reconstruct the potential. The new potential is mixed with the old potential (use of the entire new potential can lead to numerical instability) to form a new input to eq. (4). The procedure is repeated until the input and output potentials, or charge densities, are practically identical.

Each of the eqs. (4) has a complete set of solutions. The Pauli principle is taken partially into account by not allowing more than one particle in any given state.

Hartree theory embodies the self-consistent nature of the type of theories that one deals with in modern electron theory, but the many-electron wave functions of Hartree theory,

$$\Psi(\mathbf{r}_1, \mathbf{r}_2, \dots, \mathbf{r}_N) = \prod_l \Psi_l(\mathbf{r}_l), \quad (5)$$

are not antisymmetric under interchange of electron coordinates. This defect is rectified by Hartree–Fock theory. Further, the derivation of the Hartree–Fock equations is based upon the variational principle for the energy, rather than upon the intuitive derivation of the Hartree equations given above.

### 3.1. Density functional theory

The principal weakness of the Hartree and Hartree–Fock approximation is that the ground-state wave functions belong to a very restricted set and dynamic screening of the Coulomb interaction, or electron correlation, is neglected. Their strength is that, because the theories are self-consistent, static screening is included. The whole point of self-consistent field theory is that the system cannot distinguish the difference between externally and internally produced fields, since it has been allowed to relax. The density functional technique of Kohn and co-workers (Hohenberg and Kohn 1964, Kohn and Sham 1965) uses similar ideas to express the ground-state properties of a system in terms of the electron density, which is considered to be the variable in a variational calculation.

The Hamiltonian, eq. (2), has the general form

$$\mathcal{H} = \mathcal{H}_0 + \mathcal{H}_{\text{interac}} + \phi_{\text{ext}}(\mathbf{r}), \quad (6)$$

where  $\phi_{\text{ext}}(\mathbf{r})$  is the potential due to the nuclei, which we now consider to be the variable external potential; then for a given number of electrons,  $N$ ,

$$\mathcal{H}_{\phi_{\text{ext}}} |N, \phi\rangle = E_{\phi_{\text{ext}}} |N, \phi\rangle \quad (7)$$

gives the ground state for a given  $\phi_{\text{ext}}$ , and changing  $\phi_{\text{ext}}$  will change the ground state. The density,  $n(\mathbf{r})$ , is then a functional of the external potential. Put in another way: the electron density is fixed by the external potential. Associated with the foregoing is a variational principle for the energy,

$$E[n] = F[n] + \int \phi_{\text{ext}}(\mathbf{r})n(\mathbf{r})d\mathbf{r}, \quad (8)$$

where  $F[n]$  is a universal functional of the density.

Kohn and Sham (1965) then broke up the functional  $F[n]$  by first separating off the classical Coulomb interaction and then a special kinetic energy,  $T_s$ , the kinetic energy of a non-interacting electron gas with the same density as the real interacting system. This procedure transfers the problem of finding the kinetic energy of the real interacting system into a different part of the functional. Thus,

$$F[n] = \frac{1}{2} \int \frac{n(\mathbf{r})n(\mathbf{r}')}{|\mathbf{r} - \mathbf{r}'|} d\mathbf{r} d\mathbf{r}' + T_s[n] + E_{\text{xc}}[n], \quad (9)$$



and the new functional  $E_{xc}[n]$  – called the *exchange and correlation energy* – actually contains a kinetic-energy contribution. Equation (9) is very convenient, since all the results of many-body theory are contained in  $E_{xc}$ .

If the density is now varied, the change in total energy,  $\delta E$ , becomes

$$\delta E = \int \delta n(r) \left[ \phi_{\text{ext}}(r) + \phi_{\text{interac}}(r) + \frac{\delta T_s[n]}{\delta n(r)} + \frac{\delta E_{xc}[n]}{\delta n(r)} \right] dr, \quad (10)$$

which is just the Euler equation for a non-interacting electron system in a potential

$$V(r) = \phi_{\text{ext}}(r) + \phi_{\text{interac}}(r) + \mu_{xc}(r), \quad (11)$$

where the *exchange–correlation potential* is

$$\mu_{xc}(r) = \frac{\delta E_{xc}[n]}{\delta n(r)}. \quad (12)$$

Thus, the many-body problem is reduced to a set of effective one-electron equations of the form of eq. (4), with an orbital-independent potential if the exchange–correlation potential is known. Approximate expressions for  $E_{xc}$  and  $\mu_{xc}$  have been derived by many authors (see e.g. Kohn and Sham 1965, Gunnarsson and Lundqvist 1976, Moruzzi et al. 1978, Mackintosh and Andersen 1979, Koelling 1981, Kohn and Vashista 1983, Hedin and Lundqvist 1971, von Barth and Hedin 1972). In particular, the local density approximation (LDA) uses for  $E[n]$  the exchange and correlation energy of a uniform electron gas at the same local density. The exchange and correlation potential is then local.

### 3.2. The LMTO method

In energy-band theory, not only the external potential, but also the single-electron potential, have all the symmetry, translational included, of the crystal lattice. The eigenfunctions of eq. (4), therefore, obey Bloch's theorem and are functions of the wave vector,  $\mathbf{k}$ , in reciprocal space. They may be constructed from the energy-dependent solutions of the wave equation inside the atomic spheres,

$$\Psi_{lm}(r, E) = i^l R_l(r, E) Y_{l,m}(r). \quad (13)$$

In the muffin-tin orbital (MTO) method (Andersen 1975, Andersen and Jepsen 1977, Andersen et al. 1985, Skriver 1983a) the partial waves are augmented by solutions to Laplace's equation

$$\begin{aligned} \chi_{lm}(r, E) &= i^l Y_{lm}(r) = R_l(r, E) + \frac{1}{2(2l+1)} P_l(E) \left( \frac{r}{S} \right)^l, & r < S, \\ &= \left( \frac{S}{r} \right)^{l+1}, & r > S, \end{aligned} \quad (14)$$

where the potential functions,  $P_l$ , are

$$P_l(E) = 2(2l+1) \frac{D_l(E) + l + 1}{D_l(E) - l}, \quad (15)$$

in terms of the logarithmic derivatives at the Wigner–Seitz radius,  $S$ ,

$$D_l(E) = S \frac{R_l'(S, E)}{R_l(S, E)}. \quad (16)$$

If the  $\chi_{lm}(\mathbf{r}, E)$  are used as basis orbitals, a Bloch function is constructed as in the LCAO method,

$$\chi_j^k(\mathbf{r}, E) = \sum_{lm} a_{j,lm}^k \sum_{\mathbf{R}} \chi_{lm}(\mathbf{r} - \mathbf{R}, E). \quad (17)$$

The condition that eq. (17) should be a solution to the wave equation gives

$$\sum_{lm} [P_l(E) \delta_{l,l'} \delta_{m,m'} - S_{l'm',lm}^k] a_{j,lm}^k = 0. \quad (18)$$

The structure constants,  $S_{l'm',lm}^k$ , contain, as in the KKR method, all the structural information. They arise from the expansion of the tails of the orbitals about other sites in the crystal. In contrast to the KKR structure constants, which they approach in the zero-energy limit, they are independent of the scale of the lattice. The potential functions,  $P_l(E)$ , contain all the potential information.

Equation (18) becomes particularly interesting when hybridization, which is entirely contained in the structure constants, between different values of the angular momentum is neglected. Then the solutions to eq. (18) are obtained by diagonalizing the submatrices  $S_{lm',lm}^k$  for each  $l$ , and

$$P_l(E_\alpha) = S_{l\alpha}^k, \quad (19)$$

where  $\alpha$  labels the eigenvalues of  $S_{lm',lm}^k$ . Equation (19) is an implicit equation for the unhybridized eigenvalues,  $E_{l\alpha}^k$ . The unhybridized band centre,  $C_l$ , is conveniently defined in terms of the zeros of the potential function

$$D_l(C_l) = -l - 1. \quad (20)$$

And the poles of the potential function define the different branches of the unhybridized energy bands

$$D_l(V_l) = l. \quad (21)$$

Then, in terms of these *potential parameters*, the unhybridized eigenvalues are

$$E_{l\alpha} = C_l + \frac{1}{\mu_l S^2} \frac{S_{l\alpha}^k}{1 - \gamma_l S_{l\alpha}^k}, \quad (22)$$

where the band mass,  $\mu_l$ , is defined as

$$\mu_l = \frac{2}{S^3 R_l^2(S, C_l)} \quad (23)$$

and the potential parameter  $\gamma_l$  is defined as

$$\gamma_l = \frac{1}{S^2 \mu_l (C_l - V_l)}. \quad (24)$$

The unhybridization energy bands are therefore obtained by placing them on the energy scale with  $C_l$  and scaling the structure constants, in which the  $k$ -dependence is contained, with the band mass,  $\mu_b$ , and distorting them with  $\gamma_l$ .

### 3.3. Rare earths and actinides

Viewed in terms of their conduction electrons the lanthanide metals are early 5d transition metals since the 5d shell is much less than half-filled and the 4f shell chemically inert. The actinides are more complex. The light actinides are 5f transition metals with bonding 5f electrons, while the heavy actinides, which have an essentially chemically inert 5f shell, are early 6d transition metals.

The characteristic properties of transition metals are due to the centrifugal potential in the radial Schrödinger equation,

$$\left[ -\frac{d^2}{dr^2} + V(r) + \frac{l(l+1)}{r^2} \right] u_l(r, E) = E u_l(r, E), \quad (25)$$

where  $V(r)$  is the spherically averaged effective potential due to the nucleus and other electrons and  $u_l(r, E) = rR_l(r, E)$  is the radius times the radial solution for the angular momentum,  $l$ . The centrifugal potential,  $l(l+1)/r^2$ , is large near the nucleus and vanishes at large distances. For sufficiently smaller  $r$ , it is much larger than  $V(r) - E$  and  $u_l \approx r^{l+1}$ . Orbitals with a large value of the angular momentum are therefore pushed away from the nucleus.

The centrifugal potential raises the energy of the state with angular momentum  $l$  by  $4\pi \int u_l^2 l(l+1) dr$  compared with the energy of the state with  $l = 0$ . Therefore states with large  $l$  and a given principal quantum number lie higher in energy than those with smaller  $l$  and become occupied later. Hence, 3d states, e.g., fill when the 4s and 4p states are already partially occupied, whereas, if it were not for the centrifugal term, they would be core electrons before the 4s and 4p states became occupied.

The 3d and 4f state are the first d and f states in the periodic table, and have no nodes to orthogonalize them to lower states. Their kinetic energies are therefore relatively small, and their wave functions and densities relatively contracted. Since the size of an atom is determined mostly by the 4s and 4p states – whose density lies further out as they have more nodes in the wave function – the 3d density lies mostly within the atom. But, because of the centrifugal potential, the 3d density is also pushed away from the nucleus. The spherical average of the 3d densities is therefore a shell at intermediate distance from the nucleus and the 3d density is small at the boundary of the atom. The effect of the centrifugal potential is therefore to raise the energy of what would be core states to somewhere close to zero energy, so that the electrons can tunnel through to the free-electron states outside the atom. Such states are called resonances.

The actual potential in which the d or f electrons move is the same as that in which any other electrons move. But the d or f states – being more localized – sample the potential closer to the nucleus than s and p states. They shield the s and p states from the nucleus, which pushes the s and p states further out. The s and p states, in turn, do not shield the d and f states so well, which pushes them further in. The final total potential is all part of a self-consistent process.

Much insight in the transition metal band structure is provided by the LMTO method (Andersen 1975, Andersen and Jepsen 1977, Andersen et al. 1985, Skriver 1983a), which gives a very useful approximate description of narrow transition-metal bands when they hybridize little with s and p bands. The unhybridized energy band eigenvalues given by eq. (22) become particularly simple when  $\gamma_l$  is small. Then

$$E_{ii}^k = C_l + \Delta_l S_{il}^k \tag{26}$$

where  $C_l$  – the band centre – and  $\Delta_l$  – the bandwidth parameter – depend upon potential, but  $S_{il}^k$  – the structure constants – depend only upon the structure and are independent of the scale of the lattice. The bandwidth parameter is

$$\Delta_l = \frac{1}{2} S R_l^2 (S, C_l) = \frac{1}{\mu_l S^2}, \tag{27}$$

where  $R_l(S, C_l)$  is the wave function evaluated at the atomic-sphere boundary at the energy  $C_l$ . The band mass parameter is  $\mu_b$ , which is unity for free electrons, but may become very large for narrow resonances. The bandwidth parameter,  $\Delta_b$ , depends only upon the size of the atomic sphere and the value of the wave function at the sphere boundary. It is therefore an *atomic property* and measures the probability of the electron reaching the boundary of the atom. The bandwidth is obtained from the second moment of the energy bands,  $\langle E^2 \rangle_{ii} = \int (E - C_l)^2 N_l(E) dE$ , and may be written

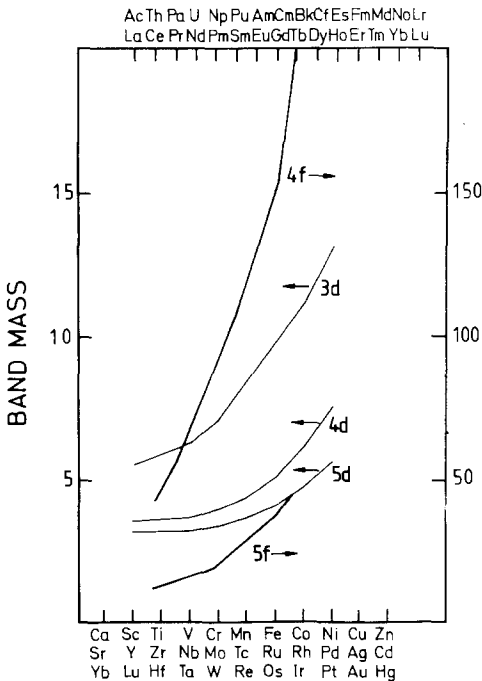


Fig. 6. The calculated band masses of transition metals, lanthanides and actinides (after Andersen and Jepsen 1977 and Brooks 1979).

as

$$W_l = \Delta_l \langle E^2 \rangle_{ll}, \quad (28)$$

where  $\langle E^2 \rangle_{ll}$  is the second moment of the  $l$ -diagonal structure constants, which is 28 for all fcc d-bands and 45 for all fcc f-bands. The calculated band mass parameters for the transition metals, rare earths and actinides are plotted in fig. 6. The bandwidths are obtained by scaling by  $\langle E^2 \rangle_{ll}/S^2$ . The band masses increase across any series due to contraction of the orbitals, since the extra, added electron is incompletely shielded by the other electrons in the same shell. They also decrease down a column of the periodic table, since additional orthogonality nodes push the wave functions outwards.

### 3.4. *The force theorem and the electronic pressure*

The modern theory of crystal structure and lattice constants (or atomic volume) owes so much to the force theorem that it is worth describing briefly how it is derived. The Hellmann–Feynman theorem (Hellmann 1937, Feynman 1939) is due to the fact that the wave function is a stationary state satisfying the variational principle for the energy. By this is meant the following. Suppose that  $\Psi$  is the wave function for energy  $E$ . Then for any *small* change in  $\Psi$  the change in energy is zero ( $O(\Psi^2)$ ). The change in the kinetic and potential energies due to any small change in the wave function cancel, leaving the total energy as a minimum with respect to variations in  $\Psi$ . When the Hamiltonian is changed (by changing some parameter in  $\mathcal{H}$  by a small amount) the energy and wave function also change, but, as above, the change in energy due to the change in wave function is zero, leaving a total energy change arising from the change in the Hamiltonian alone.

The Hohenberg–Kohn theorem (Hohenberg and Kohn 1964) is a variational principle for the energy of a many-electron system in terms of the electron density. Consequently, for small changes in the electron density, the changes in kinetic and potential energies also cancel. The force theorem (Mackintosh and Andersen 1979, Pettifor 1976, Christensen and Heine 1985), although a little more difficult to derive than the Hellmann–Feynman theorem, is based upon the same principle of cancellation as the Hellmann–Feynman theorem, and states that any distortion of the system changes the total energy to first order by

$$\delta E = \delta \int EN(E) dE, \quad (29)$$

where  $N(E)$  is the electron density of states function. That is, the first-order energy change is the change in the sum of the single-electron energy eigenvalues – in a frozen potential. Equation (29) is particularly useful in the theory of crystal structure. It is perfectly possible, and sometimes done, to calculate the total energy for two different structures to find which structure is stable, but eq. (29) isolates a smaller quantity, which is particularly easy to calculate accurately. Moreover, a formula for the electronic pressure may be derived from eq. (29).

The electronic pressure is obtained from the change in the total energy when the volume, or Wigner–Seitz radius, is increased slightly,

$$\delta E = -4\pi PS^2 \delta S = -3PV \delta \ln S, \quad (30)$$

hence

$$3PV = -\frac{\delta}{\delta \ln S} \int_{-\infty}^{E_F} EN(E) dE. \quad (31)$$

This integral is transformed to a more useful form by partial integration,

$$3PV = \int_{-\infty}^{E_F} \frac{\delta n(E)}{\delta \ln S} dE. \quad (32)$$

The reason for transforming to an integral in terms of the number of states function,  $n(E)$ , is that the latter is a canonical function of the vector of logarithmic derivatives

$$\mathbf{D} = (D_0, D_1, D_2, \dots),$$

since the functional dependence of the number of states function upon  $\mathbf{D}$  is given entirely by the structure constants. Therefore, the partial density of states may be written

$$N_l(E) = \frac{dn_l(E)}{dE} = \frac{\partial n_l(E)}{\partial D_l} \dot{D}_l. \quad (33)$$

Furthermore, the energy derivative of  $D_l$  in terms of the partial-wave amplitude at the ASA sphere boundary is known,

$$N_l(E) = \frac{\partial n_l(\mathbf{D})}{\partial D_l} \dot{D}_l = \frac{\partial n_l}{\partial D_l} \left( -\frac{1}{S\phi_l^2(E, S)} \right), \quad (34)$$

and the electronic pressure may be written as

$$3PV = \sum_l \int_{-\infty}^{E_F} N_l(E) S\phi_l^2(E, S) \left( -\frac{\delta D_l(E)}{\delta \ln S} \right) dE. \quad (35)$$

The radial Schrödinger equation may be recast as an equation for the logarithmic derivatives and their derivatives, hence, at the sphere boundary,

$$-\frac{\delta D_l}{\delta \ln S} = [D_l(E) + l + 1][D_l(E) - l] + S^2[E - \varepsilon_{xc} + \mu_{xc} - V(S)], \quad (36)$$

and the electronic pressure formula is finally

$$\begin{aligned} 3PV &= 3V \sum_l P_l, \\ 3P_l V &= \int_{-\infty}^{E_F} N_l(E) S\phi_l^2(E, S) \\ &\quad \times \{ [D_l(E) + l + 1][D_l(E) - l] + S^2[E - \varepsilon_{xc} + \mu_{xc} - V(S)] \}. \end{aligned} \quad (37)$$

This formula is actually used in LMTO-ASA calculations to compute the electronic pressure as a function of volume, and from this the lattice constants and bulk moduli. The decomposition of the electronic pressure into partial-wave components is extremely useful since it allows the chemical bond to be analyzed in a new way. It should not, however, be assumed that the total energy may be decomposed in the same way. Here we are concerned with virtual work processes, which may be decomposed, but the work, once part of the internal energy, is no longer decomposable.

It is illuminating to study the bonding in metals in terms of approximations to the electronic pressure formula, eq. (37). The potential functions in ASA are

$$P_l(E) = 2(2l+1) \frac{D_l(E) + l + 1}{D_l(E) - l}, \quad (38)$$

so that the equivalent of the KKR equations is

$$|S_{l,l'} - P_l(E)\delta_{l,l'}| = 0. \quad (39)$$

The number of states function is a canonical functional of the potential functions, and

$$\dot{P}_l(E) = \frac{1}{\frac{1}{2}S\chi_l^2(E, S)}, \quad (40)$$

where  $\chi_l(E, r)$  is the radial part of the muffin-tin orbital. The band centre,  $C_l$ , is the energy at which  $D = l - 1$ . The  $P_l$  may be expanded,

$$P_l(E) = (E - C_l)\dot{P}_l(C_l) = (E - C_l)\mu_l S^2, \quad (41)$$

where  $\mu_l$  is the central band mass, related to the bandwidth. For nearly free electrons eq. (41) is a poor expansion and it is better to use instead of  $C_l$  the square-well pseudopotential energy,  $V_l$ ,

$$P_l(E) = (E - V_l)\dot{P}_l(V_l), \quad (42)$$

where

$$\frac{1}{2}S\chi_l^2(E, S) = \frac{\tau_l S^2 (E - V_l)}{2(2l+1)^2(2l+3)} \quad (43)$$

or

$$P_l(E) = \frac{2(2l+1)^2(2l+3)}{S^2\tau_l} \frac{1}{E - V_l}, \quad (44)$$

where  $\tau_l$  is the band-bottom mass parameter. In terms of these parameters the change in single-particle energies may be written as

$$\delta \int_{-\infty}^{E_F} EN(E) dE = - \sum_l \frac{\partial n}{\partial P_l} \delta P_l dE, \quad (45)$$

and the partial electronic pressures are given by

$$3PV = -n_l \left[ \frac{\delta C_l}{\delta \ln S} + (\langle E \rangle_l - C_l) \frac{\delta \ln W_l}{\delta \ln S} \right]$$

$$= \frac{2n_l}{\mu_l} \{ [C_l - V(S)] + \mu_{xc}(S) - \varepsilon_{xc}(S) \} + n_l \langle E \rangle_l - C_l \left( 2l + 1 + \frac{2}{\mu_l} \right) \quad (46)$$

for a resonant band and

$$\begin{aligned} 3PV &= -n_l \left[ \frac{\delta V_l}{\delta \ln S} + (\langle E \rangle_l - V_l) \frac{\delta \ln \tau_l S_l^2}{\delta \ln S} \right] \\ &= n_l \frac{2l+3}{\tau_l} \{ [V_l - V(S)] + \mu_{xc}(S) - \varepsilon_{xc}(S) \} \\ &\quad + n_l (\langle E \rangle_l - V_l) \left( -(2l+1) + \frac{2l+3}{\tau_l} \right) \end{aligned} \quad (47)$$

for a nearly free electron band.

The physical interpretation of eq. (46) is that the first term – the band-centre term – is positive, due to the exclusion principle, when neighbouring shells overlap and negative when the atoms are well separated, in which case it becomes the van der Waals interaction. The second term is the band-filling term, which is attractive when the bonding orbitals are filling and is zero for empty and filled ideal bands. For metals, with neutral Wigner–Seitz spheres, the Coulomb potential at the sphere boundaries vanishes,  $V(S) = 0$ , and the exchange and correlation contributions in eqs. (46) and (47) may be estimated quite easily. Since the exchange–correlation hole contains a charge of one, it gives rise to a potential at the sphere boundary of  $\mu_{xc}(S) \simeq -(2/S)$  Ry if the hole is centred on the atom, which is about 0.6–0.7 Ry for typical sphere radii of between 3 and 3.5 au. This is not a bad estimate, since calculations yield the actual effective charge to be 1.12 and 1.23 for rare earths and actinides, respectively. Further, for the uniform electron gas  $\varepsilon_{xc} = \frac{3}{4}\mu_{xc}$ .

Equation (46) becomes particularly simple when the real partial  $l$  state density is approximated by a rectangular state density of width  $W_l$ . The partial state density and Fermi energy are then fixed, in terms of the width, by evaluating the zeroth moment,

$$n_l = \int_{-w_l/2}^{E_F} N_l(E) dE,$$

whence  $N_l(E) = 2(2l+1)/W$  and  $E_F = W_l(f_l - \frac{1}{2})$ , where  $W_l$  is the bandwidth and  $f_l$  is the fractional occupation. The first moment of the state density is given by

$$n_l \langle E \rangle_l - C_l = \int_{-w_l/2}^{E_F} EN(E) dE = (2l+1)W_l f_l(1-f_l).$$

Then the band-filling term in eq. (46) yields a contribution to the pressure given by

$$3PV_l^{\text{band}} \simeq n_l (\langle E \rangle_l - C_l) (2l+1) = -(2l+1)^2 W_l f_l (1-f_l), \quad (48)$$

when  $\mu_l \gg 1$ .

We may go back one step, to eq. (37), which is exact, to examine the behaviour of the logarithmic derivatives for the values of  $D_l$  corresponding to  $V_l$  and  $C_l$ , i.e.  $D_l = l$



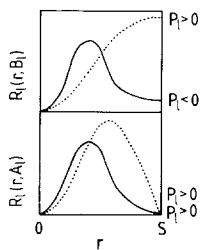


Fig. 7. The radial wave functions at the bottom ( $B$ ) and top ( $A$ ) of an energy band. The dotted lines are for the case where both  $B$  and  $A$  are greater than the total effective potential at the atomic sphere boundary. The corresponding sign of the electronic pressure, from eq. (37), is indicated (after Andersen et al. 1985).

and  $D_l = -l - 1$  or  $B_l$  and  $A_l$ , i.e.  $D_l = 0$  and  $D_l = -\infty$  (corresponding to bond and anti-bond, respectively). Here we note

$$[D_l + l + 1][D_l - l] + (E - V)S^2 = D_l(D_l + 1) + (E - V_l)S^2,$$

with  $V_l = V + [l(l + 1)/S^2]$ . Hence the electronic pressure at the bottom of the band is positive if the electron is allowed to pass classically out of the atomic sphere, but negative if it tunnels. The magnitude of the electronic pressure is proportional to the partial-wave density at the sphere boundary. The contribution to the electronic pressure for  $A$ -states is always repulsive. The wave functions for these different cases are illustrated in fig. 7. At the bonding energy the wave function is a minimum between the atoms if the region is classically forbidden. The slope of the wave function is negative at  $S$ . Thus, the energy of a tunnelling state must be lowered if the solid is compressed, to maintain the bonding condition. The opposite is true for free states. The transition metals and actinides are, therefore, bonded by resonant, or tunnelling, electrons.

The usual chemical picture of bonding corresponds to neglecting the band-centre term – or replacing it with an empirical short-range repulsion – whence all bonding states are taken to bond. However, from the above we see that, if the states do not tunnel, the band-centre term may be large and positive.

### 3.5. The magneto-volume effect

The electronic-pressure formula, eq. (48), may be easily modified (Andersen et al. 1979, Eriksson et al. 1989b, c) to include the effects of moment formation in the  $5f$  states. If the number of spin-up and spin-down electrons are denoted by  $n_i^\pm$  and the fractional occupations by  $f_i^\pm = n_i^\pm/[2(2l + 1)]$ , the total fractional occupation number and moment are given by

$$f_i = \frac{1}{2}(f_i^+ + f_i^-), \quad \mu_i = \frac{1}{2}(f_i^+ - f_i^-).$$

The approximate band-filling pressure term, eq. (48), is then re-written in terms of the spin-up and spin-down contributions, each with  $2l + 1$  states,

$$3PV_i^{\text{band}} \simeq n_i[\langle E \rangle_l - C_l][2l + 1] = -(2l + 1)^2 W_l[f_i(1 - f_i) - \mu_i^2]. \quad (49)$$

The  $5f$  contribution to the band-filling part of the electronic pressure in the ferro-

magnetic state is given in terms of the pressure in the paramagnetic state by

$$3PV_{5f}^{\text{pol}} = 3PV_{5f}^{\text{para}} \left( 1 - \frac{\mu_{5f}^2}{[n_{5f}(14 - n_{5f})]} \right), \quad (50)$$

where  $n_{5f}$  is the number of 5f electrons and  $\mu_{5f}$  the 5f spin moment. When the 5f states polarize, the spin-up electrons occupy more anti-bonding states, reducing the magnitude of the (negative) 5f electronic pressure.

### 3.6. The relativistic volume effect

The standard procedure (Rose 1961), for heavy atoms, is to solve the wave equation in a spherical potential with relativistic kinematics. In open-shell systems the charge density is spherically symmetrized by averaging over all azimuthal quantum numbers. The wave equations to be solved in practice are, therefore, the coupled first-order differential equations for the radial components of the Dirac equation (Rose 1961)

$$g'_\kappa = -\frac{(\kappa + 1)g_\kappa}{r} + cf_\kappa \left( 1 + \frac{(E - V)}{c^2} \right), \quad (51a)$$

$$cf'_\kappa = \frac{(\kappa - 1)cf_\kappa}{r} + (V - E)g_\kappa, \quad (51b)$$

where  $g_\kappa$  and  $f_\kappa$  are the major and minor components of

$$\Phi_{\kappa\mu} = \begin{pmatrix} g_\kappa \chi_{\kappa\mu} \\ -if_\kappa \sigma_r \chi_{\kappa\mu} \end{pmatrix}, \quad (52)$$

where  $\kappa$  is the Dirac quantum number,  $\chi_{\kappa\mu}$  is a two-component Pauli spinor and  $\sigma_r$  is the radial component of the Pauli spin matrices. The properties and solutions of the Dirac equation for spherical symmetry have been reviewed in detail by Rose (1961), Grant (1970) and Desclaux (1973).

In the RLMTO or RKKR methods the solutions corresponding to a given  $l$  are replaced by the two solutions  $j = l \pm \frac{1}{2}$  of the Dirac equation. The potential is specified by a set of parameters twice as large as the LMTO set (Andersen 1975, Godreche 1982, Brooks 1983, 1984a, Christensen 1984a). Thus, the Hamiltonian and overlap matrices have the same form as the LMTO matrices, but, like the structure constants, are doubled in size. It is then convenient to think of the sets of potential parameters as giving rise to pure  $j$ -bands rather than  $l$ -bands. The charge density is reconstructed by taking the spherical average

$$n(r) = \sum_{l,j} \int N_{l,j}(E) [f_{l,j}^2(E, r) + g_{l,j}^2(E, r)] dE, \quad (53)$$

where  $N_{l,j}(E)$  is the partial  $l, j$  resolved state density.

The immediate effect of separate  $j$ -projected state density is that this leads to distinct occupation numbers for the two  $j$ -bands with a given  $l$ . In the limit of vanishing spin-orbit splitting,  $\Delta_{s.o.}$ , of the two  $j$ -bands, the ratio of their populations becomes equal to the ratio of their degeneracies. But in the other limit, when  $\Delta_{s.o.}$  is much

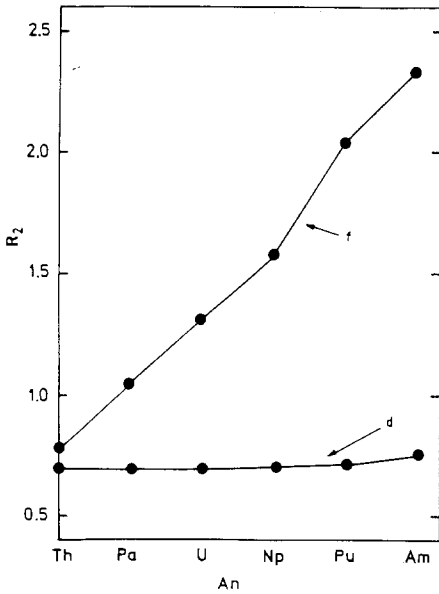


Fig. 8. The ratio of the number of electrons in the  $j=l-\frac{1}{2}$  and  $j=l+\frac{1}{2}$  bands ( $l/(l+1)$ ), for zero spin-orbit splitting, for both d and f electrons in the actinide metals.

greater than the bandwidth,  $W$ , the two  $j$ -bands are split apart and the  $j=l-\frac{1}{2}$  band fills first. The ratio  $R_2 = n_{j=l-\frac{1}{2}}/n_{j=l+\frac{1}{2}}$  changes from  $2l/(2l+2)$  to infinity as the ratio  $R_1 = \Delta_{s.o.}/W_l$  increases, as long as there is a total of less than  $2l$  electrons of type  $l$ . Therefore  $R_2$  is an excellent measure of the importance of spin-orbit interaction in the ground state. It has been evaluated in self-consistent, fully relativistic, band calculations (Brooks 1983) for the light actinide metals, Ac–Am. The ratio for d and f electrons is plotted in fig. 8 as a function of atomic number.  $R_2$  approaches  $\frac{3}{4}$  and  $\frac{2}{3}$  in the limit  $R_1 \rightarrow 0$  for f and d electrons, respectively. It is clear from fig. 8 that there are considerable departures from this ratio for f electrons in the metals Np–Am, but not for d electrons. The reason for this is that the preferential occupation of the  $j=l-\frac{1}{2}$  band is determined not by the spin-orbit splitting alone, but also by the ratio  $R_1$ , which is inversely proportional to the bandwidth. Thus, spin-orbit interaction does not have any major effect upon the bulk ground-state properties, even for heavy metals, unless the corresponding energy bands are narrow. This is exactly what does happen to the f bands with increasing atomic number, since there is both an increase in  $\Delta_{s.o.}$  and a decrease in  $W$ , producing an increase in  $R_1$ .

The effect of preferential occupation of the  $j=\frac{5}{2}$  f band is made explicit by the relativistic form of eq. (47),

$$3PV = \frac{2n_{j,l}}{\mu_{j,l}} \{ [C_{j,l} - V(S)] + \mu_{xc}(S) - \epsilon_{xc}(S) \} + n_{j,l} (\langle E \rangle_{j,l} - C_{j,l}) \left( 2j + 1 + \frac{2}{\mu_{j,l}} \right), \quad (54)$$

where now  $n_{l,j}$  is the number of partial  $l, j$  electrons,  $C_{l,j}$  is the centre of the  $l, j$ -band,  $\mu_{l,j}$  is the effective mass and  $\langle E \rangle_{l,j}$  is the first energy moment.  $\langle E \rangle_{l,j}$  is zero for an empty or filled band and is minimal for a half-filled band. When  $\Delta_{s.o.}/W$  is large, the

first moment vanishes for 0,  $l$  and  $2(2l + 1)$  electrons and has minima at the centre of each partial  $l, j$ -band.

Therefore the trend in atomic volume across a transition metal series, which for a constant compressibility follows the pressure, will tend to increase towards the centre of the series if  $\Delta_{s.o.}/W$  is large.

3.7. Spin polarization and the cohesive energy

In LSDA the spin polarization energy may also be expressed in terms of radial integrals (Gunnarsson 1976, 1977, Janak 1977, Brooks and Johansson 1983)

$$E_{SP}^{LSDA} = -\frac{1}{4} \sum_{l,l'} J_{ll'} m_l m_{l'}, \tag{55}$$

where the LSDA atomic exchange integral matrices are given by

$$J_{ll'} = \frac{2}{3} \int \{r^2 \phi_l^2(r) \phi_{l'}^2(r) A[n(r)]/n(r)\} dr \tag{56}$$

and  $A[n(r)]$  is a well known (von Barth and Hedin 1972) function of the density. The LSDA exchange integrals for the  $f$  and  $d$  states of free lanthanide and actinide atoms are plotted in figs. 9 and 10. In the self-consistent free-atom calculations the  $d^{n-1}s$  configurations for the transition metals and  $f^n ds^2$  configurations for the rare earths and actinides were used. Since for free atoms the eigenstates are bound states, there are only solutions at discrete energy eigenvalues and only one possible exchange interaction for a given value of  $ll'$ . In the solid state, where the conduction-electron bands are scattering states, the radial wave functions are continuous functions of the energy and the exchange integrals are energy dependent.

The reason that the  $f$ - $d$  exchange integrals decrease across each series is the contraction of the  $f$  shell, which decreases the overlap with the  $d$  states. The overlap between

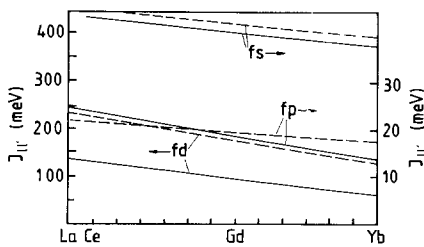


Fig. 9. Calculated exchange integrals across the lanthanide series for free atoms. The full lines are the LSDA exchange integrals, eq. (56), and the dashed lines are the Hartree-Fock exchange integrals.

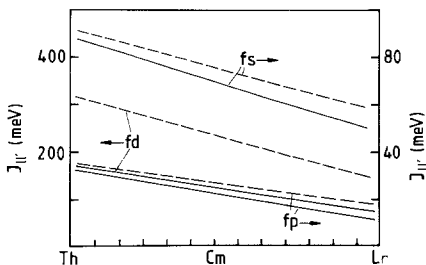


Fig. 10. The same exchange integrals as in fig. 9, but for the actinide series.

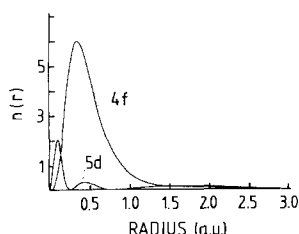


Fig. 11. The calculated 4f and 5d radial densities for a free Gd atom.

4f and 5d densities occurs over a relatively small region of space, corresponding to the outer part of 4f density and the inner part of the 5d density (fig. 11). When the 4f shell contracts, the region of overlap decreases.

As an example of the usefulness of eq. (56) we consider the cohesive energies of the transition metals (Gunnarsson et al. 1974, Friedel and Sayers 1977, Johansson et al. 1980, Brooks and Johansson 1983), shown in fig. 12a, which are not regular across the series. However, the cohesive energy,  $E_c$ , of an elemental metal is defined as the energy difference between the free atom in its ground state and the energy of the metal per atom at zero temperature, and therefore contains a free-atom energy contribution (see sect. 2.2),  $\Delta E_{\text{atom}}$ , which is the preparation energy required to take the atom from its ground state to a state similar to the non-magnetic ground-state configuration of the metal. It is this contribution which behaves irregularly across the series. The cohesive energy may therefore be written as

$$E_c = E_b - \Delta E_{\text{atom}}, \quad (57)$$

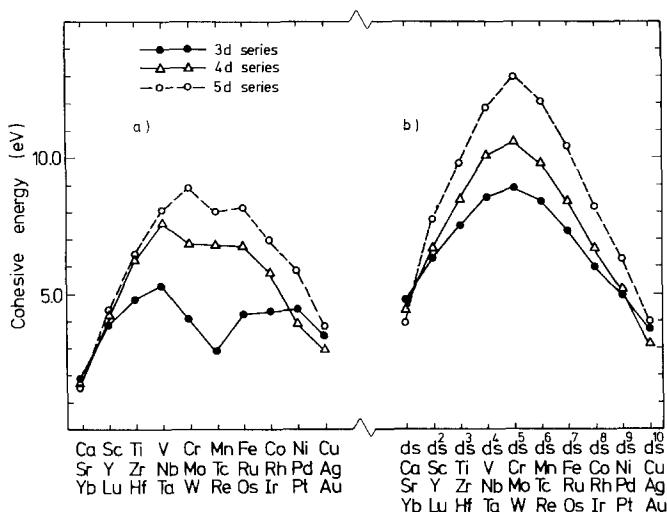


Fig. 12. (a) The measured cohesive energies of the d transition metal series. (b) The calculated valence bond energies by application of eqs. (57) and (58) to the cohesive energies shown in (a).

thus defining the valence bond energy,  $E_b$ , which is expected to vary more smoothly across the series. If the relatively small contributions to the total energy of the atom from Hund's second rule and spin-orbit interaction are neglected,  $\Delta E_{\text{atom}}$  may be separated according to

$$\Delta E_{\text{atom}} = E_p - E_{\text{SP}}^{\text{LSDA}}, \quad (58)$$

where  $E_p$  is the preparation energy required to take the atom from its ground state configuration to the *magnetic* ground-state configuration of the prepared atom, which for d electrons may be taken to be the  $sd^{n+1}$  configuration.  $E_p$  may be obtained from experimental data (Moore 1958). The spin polarization energy is the LSDA equivalent of Hund's first rule energy (Gunnarsson and Lundqvist 1976) and is lost when the free atom is prepared in the *non-magnetic* ground state, and in the form (55) contains the coupling between open shells.

When  $E_p$  and  $-E_{\text{SP}}^{\text{LSDA}}$  are added to the measured cohesive energies shown in fig. 12a, the valence bond energies of the three d transition metal series shown in fig. 12b are obtained. The valence bond energies, relative to the  $d^{n+1}s$  non-magnetic ground states of transition metal atoms, are – in contrast to the cohesive energies – approximately parabolic functions of the d occupation number. Thus, the valence bond energy, defined by eq. (57), is that part of the cohesive energy which is essentially a solid-state property, changes smoothly across a series, and is therefore most useful for interpolation (sect. 2.2).

If contributions to cohesion other than the transition metal “d band” contribution (Friedel 1969) were negligible,  $E_b$  and the “d band” contribution would be equivalent. Then  $E_b$  could be estimated independently by assuming that the number of states function is a straight line and fitting the second moment of the d band by a rectangular density of states function (Friedel 1969, Cyrot and Cyrot-Lackmann 1976). In general, however, the repulsive interactions between atoms, the sp contribution and any additional correlation energies in the solid that also show a parabolic trend, are included in  $E_b$  without being distinguishable in fig. 12b.

The cohesive energies of the trivalent rare earths should, therefore, be about 100 kcal/mol relative to the *trivalent* atomic state ( $f^n ds^2$ ). However, the cohesive energy of gadolinium is slightly less – 95 kcal/mol – although the configuration of the free gadolinium atom is  $f^7 5d 6s^2$ . The difference is due to the multiplet coupling between the open 4f and 5d shells in the free gadolinium atom. This coupling may easily be estimated in the local spin density approximation. In this approximation the multiplet coupling energy is  $-\frac{1}{2} J_{4f5d} \mu_{4f}^s \mu_{5d}^s$  in terms of the 4f–5d exchange interaction and the spin components of the 4f and 5d moments. We calculate  $J_{4f5d}$  to be 0.105 eV (or 2.41 kcal) for a Gd atom. Therefore, with a 4f spin moment of seven and a 5d spin moment of one the coupling energy is 8.4 kcal.

In Gd metal the 4f moment remains saturated but the 5d states are itinerant and have a small moment of  $0.475 \mu_B$  with a splitting of the spin-up and spin-down states at the Fermi energy due to exchange between the 4f and conduction electrons. The reduction of both the 5d moment and the 4f–5d exchange interaction means that much of the exchange energy of multiplet coupling is absent in the solid. The exchange interaction,  $J_{4f5d}$ , is reduced to 0.092 eV (2.11 kcal) in Gd metal, hence the coupling

is 3.5 kcal. The difference between the 4f–5d multiplet coupling in the free atom and the solid is therefore 8.4 minus 3.5 kcal or about 5 kcal. The same coupling is also present with about the same magnitude in other trivalent free rare earth atoms. The cohesive energy – relative to the trivalent free atoms – should therefore be about 95 kcal/mol rather than 100 kcal/mol for metals where there is no f shell. Similarly, the measured cohesive energy of the trivalent actinide element curium is about 90 kcal/mol (Ward et al. 1975), which may be taken to be representative of the cohesive energy of the trivalent actinide metals – again relative to the corresponding trivalent ( $5f^n 6d 7s^2$ ) free-atom configuration.

#### 4. The elemental metals

The electronic structure of the rare earth metals was first studied by Dimmock and co-workers (Dimmock and Freeman 1964, Dimmock et al. 1965) and by Liu (1978). The systematics of the bonding and structure has been very completely described by Pettifor (1970), Duthie and Pettifor (1977) and by Skriver (1983b).

The cohesive properties which we wish to describe are the atomic volume, the structure, the bulk modulus and the cohesive energy. It is necessary to calculate the total energy of both the free atoms and the solid in order to arrive at the cohesive energy, whereas the former three properties may be obtained from the force theorem (sect. 3.1). Although the total energy could be, and sometimes is, used to compute the volume, structure and bulk modulus, no separation into angular momentum contributions is then possible.

##### 4.1. *Electronic structure of the lanthanide metals*

Studies of the magnetism of the lanthanide metals and their compounds using spin polarized energy calculations are now plentiful (for reviews see Liu 1978, Jensen and Mackintosh 1991, Brooks and Johansson 1993), but the first systematic studies of the conduction bands and their influence on cohesion were due to Pettifor (1977), Duthie and Pettifor (1977) and Skriver (1983b). The systematics of cohesive energies have been studied by Eriksson et al. (1990c), who also examined the structures of the heavy actinides. Skriver's (1983b) energy band calculations for the lanthanide metals have not been significantly improved upon, therefore it is to these that we will mostly refer in the following. An overview of the electronic structure of the trivalent rare earths, La–Lu, is shown in fig. 13. The figure shows the bottom, centre and top of the d bands and the bottom of the s and p bands of the entire series, evaluated for an atomic radius of 3.75 au and for the fcc structure (Skriver 1983b). The most prominent, and important, single feature is that the energy of the s and p bands falls more rapidly than the energy of the d bands as the series is traversed. Consequently, the number of 5d electrons decreases and the number of 6s electrons increases across the series.

The bottom of the s and p bands is essentially governed by orthogonality to core states (Pettifor 1977). The 6s states, for example, must be orthogonal to the 5s states.

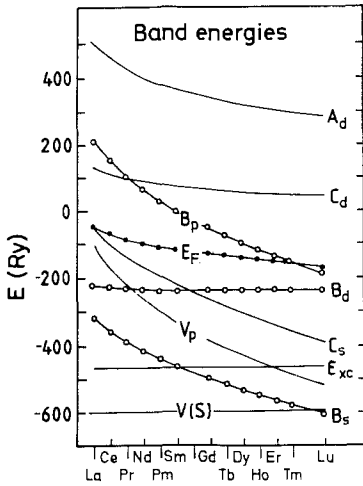


Fig. 13. An overview of the electronic structure of the trivalent lanthanides, evaluated at a common Wigner–Seitz radius of 3.75 au (after Skriver 1983b). The bottom,  $B_b$ , top,  $A_b$ , centre,  $C_b$ , and square-well pseudopotential,  $V_b$ , are plotted, and  $V(S)$  is the potential and  $\epsilon_{xc}$  the exchange–correlation density at the sphere boundary. The Fermi energy is labelled by  $E_F$ .

The 5s and other core states contract with increasing atomic number since the added 4f electron does not shield them from the increased nuclear charge completely. Orthogonalization to the core states increases the kinetic energy of the 6s states and tends to “exclude” them from the core region. Since the core region shrinks with incomplete screening of the increased nuclear charge, the kinetic energy of the 6s states decreases as the series is traversed. The same applies to the 6p states, which also fall rapidly in energy across the series. However, the bottom of the 6p band remains quite high throughout the series, never falling below the Fermi energy, and the partial 6p occupation – which is due entirely to hybridization with states below the Fermi energy – increases less rapidly than the partial 6s occupation. To a lesser extent, the 5d states, which are themselves only partially shielded by the added 4f electron, also contract – the band mass,  $\mu_{5d}$ , increases from two to three as the partial 5d density at the Wigner–Seitz sphere boundary decreases – and fall in energy across the series. The partial 4f and 5d densities in Gd metal are shown in fig. 14. At an energy corresponding to the bottom of the 5d bands the bonding 5d density is very large, whereas

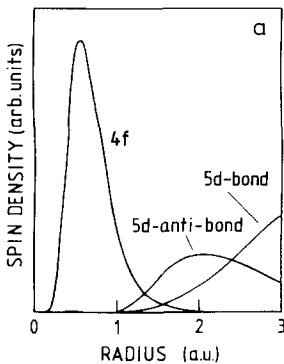


Fig. 14. The calculated 4f and 5d radial densities for Gd metal. The 5d density is shown for the bottom (bond) and top (anti-bond) of the 5d bands.



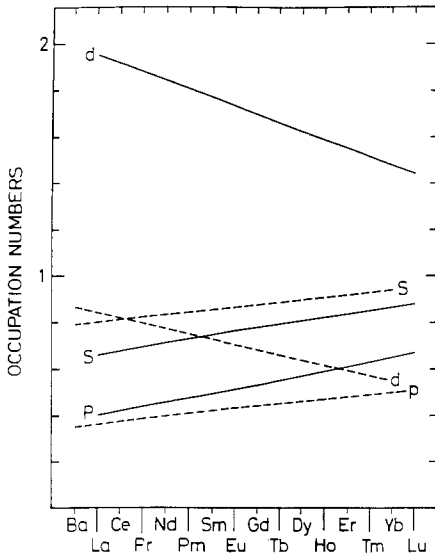


Fig. 15. The calculated s, p and d occupation numbers across the lanthanide series. The dashed lines correspond to divalent metals (Ba, Eu and Yb).

it is relatively small at an energy corresponding to the top of the 5d bands. The states at the bottom of the 5d bands are, therefore, better shielded from the increased nuclear charge and the energy of the bottom of the 5d bands falls less rapidly across the series than does the energy of the top of the bands. Since it is the bottom of the 5d bands that is occupied, the result is a net transfer of 5d to 6s electrons as the series is traversed. The partial s, p and d occupation numbers calculated for the di- and trivalent metals by Eriksson et al. (1990c), are plotted as a function of atomic number in fig. 15. The d occupation numbers decrease along the series for both values of the

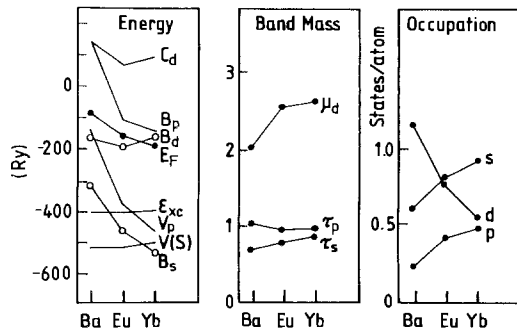


Fig. 16. An overview of the electronic structure of the divalent lanthanides in the left panel, evaluated at a common Wigner-Seitz radius of 4.10 au (after Skriver 1983b). The bottom,  $B_b$ , top,  $A_t$ , centre,  $C_t$ , and square-well pseudopotential,  $V_t$ , are plotted, and  $V(S)$  is the potential and  $\epsilon_{xc}$  the exchange-correlation density at the sphere boundary. The Fermi energy is labelled by  $E_F$ . The centre panel displays the corresponding band masses and the right panel the occupation numbers.

valency, and it is precisely the d occupation number that is correlated with the crystal structure sequence discussed in sects. 2.3 and 4.5.

Although the 4f states are not part of the band structure, it is the 4f electrons that are responsible for the change in electronic structure across the series. Since the Wigner–Seitz radius used in the calculations summarized in fig. 13 was kept constant, the effect of the screening of the increased nuclear charge by the 4f electrons was isolated, and is the only cause of any changes in the conduction electron band structure. When the number of 4f electrons for a given nuclear charge is changed, as in the divalent rare earths, the effect on the conduction electron band structure is much greater. An overview of the electronic structure of the divalent lanthanide and barium is shown in fig. 16. The figure shows the bottom, centre and top of the d bands and the bottom of the s and p bands, evaluated for an atomic radius of 4.1 au and for the fcc structure (Skriver 1983b). Since there is now one extra 4f electron and one less 5d electron, the 5d band becomes almost depleted for Yb. Otherwise the trends in the energy band structure are similar to those of the trivalent rare earths.

#### 4.2. Electronic structure of the actinide metals

An overview of the electronic structure of the actinide metals is shown in fig. 17. The figure shows the bottom, centre and top of the 5f bands and the bottom of the s, p and d bands of the entire series, Fr–Lr, as a function of the Wigner–Seitz radius, as evaluated by Skriver and co-workers (Brooks et al. 1984). For the left of the series, Ra–Th, at the equilibrium radius,  $S_0$ , the bottom of the 7s band always lies below the Fermi energy, the bottom of the 6d band moves through the Fermi energy from above between Fr and Th, and the bottom of the 5f band is above the Fermi energy. Hence the 7s and 6d bands are the only occupied bands and Th is a 6d-band transition metal. However, the unoccupied 5f band is so close to the Fermi energy that it

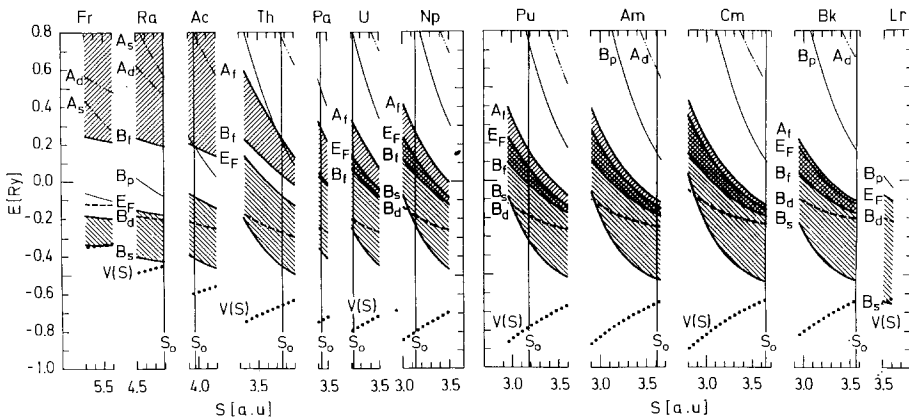


Fig. 17. Energy bands for Fr and the actinides, evaluated as function of the atomic radius,  $S$ . The potential,  $V(S)$ , at the sphere, the bottom,  $B_i$ , and the top,  $A_i$ , of the relevant bands, together with the Fermi energy,  $E_F$ , are plotted.  $S_0$  is the measured equilibrium atomic radius.

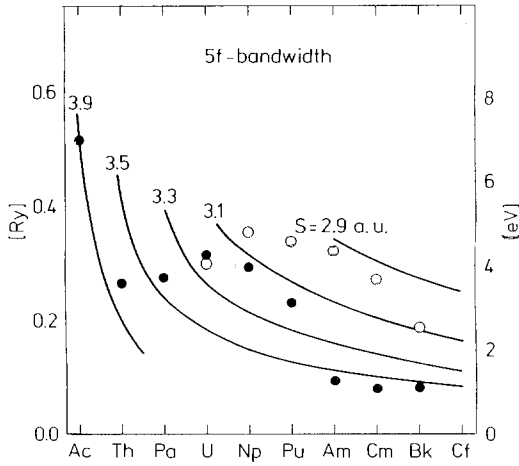


Fig. 18. The  $f$  bandwidth,  $W_f$ , evaluated as a function of atomic volume and atomic radius,  $S$ . The solid circles indicate the  $5f$  bandwidths calculated at the experimental equilibrium atomic radii, while the open circles indicate the bandwidths obtained at the calculated (non-spin-polarized) equilibrium atomic radii.

influences the occupied part of the band structure through hybridization, and this effect has proven to be important for the details of the Fermi surface (Gupta and Loucks 1969, 1971, Koelling and Freeman 1975, Skriver and Jan 1980).

The bands rise in energy under compression, as in the lanthanides, due to increasing kinetic energy, where now the  $7s$  states are required to be orthonormal to the  $6s$  core states. As a function of the atomic number, band filling occurs as follows. The  $7s$  band in Fr takes the first electron, between Ra and Th the  $6d$  band takes most of the next three electrons, the first real occupancy of itinerant  $5f$  states occurs in Pa, and thereafter the  $5f$  band fills up to Lr.

The gradual filling of the  $5f$  bands is analogous to the filling of the  $d$  bands in transition metals, therefore the atomic volumes of the actinides should be parabolic as a function of the atomic number as first the bonding and then the anti-bonding orbitals become filled. Such a parabolic trend is indeed observed for the metals Th–Pu, and the analogy with the  $d$  transition series is correct for the light actinides. However, the  $5f$  electrons are localized in the heavy actinides, where the trend in atomic volume is similar to that for the lanthanides.

The  $5f$  bandwidth is shown in fig. 18, and, for fixed atomic radius, it decreases with increasing atomic number. This occurs because at the beginning of the series the potential due to the added proton contracts the  $5f$  orbitals and lowers the amplitude of the wave function, hence, increases the band mass, at the Wigner–Seitz sphere. The narrowing is most pronounced at the beginning of the series because later the extra electron added to the system enters the  $5f$  shell and partially screens the nuclear charge seen by the other  $5f$  electrons. A similar trend is found for the  $6d$  and  $7s$  states, which are located outside the  $5f$  shell and, therefore, also see the nuclear charge partially screened. For fixed atomic number the bandwidth decreases with increasing atomic radius since the amplitude of the wave function at the Wigner–Seitz sphere decreases. The  $5f$  bandwidths evaluated at the measured atomic volume (solid circles in fig. 18) remain, however, nearly constant between Th and Pu, since the volumes

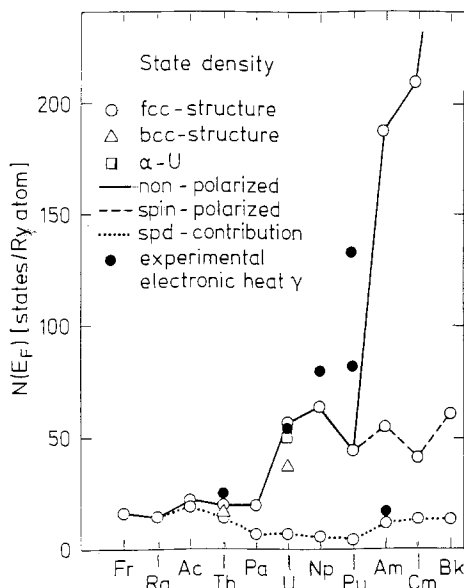


Fig. 19. The state density at the Fermi energy calculated at the experimental equilibrium radius, compared to the experimentally obtained electronic specific heat,  $\gamma$ . The dotted curve represents the spd contribution to the total state density.

decrease. The difference between theory and experiment for Np and Pu is at least partly caused by the relativistic volume effect, and the large jump in volume at Am, due to localization of the 5f states, is a magneto-volume effect.

The calculated state densities at the Fermi energy have been collected and compared to experimentally observed specific heat coefficients in fig. 19. One should bear in mind that most of the calculations assume an fcc structure, and therefore one cannot expect too detailed an agreement between theory and experiment. In the beginning of the series, i.e. for Fr–Th, the 5f contribution is small, and  $N(E_F)$  for Th is typical for a transition metal. In Pa the 5f contribution starts to dominate the state density, which by Am has increased by an order of magnitude. The measured electronic specific heat coefficients show a similar trend up to, and including, Pu. However, in Am it is down by one order of magnitude with respect to the value for Pu, and is in fact close to the spd contribution to the state density. Hence, in this respect Am behaves like a rare earth metal. The interpretation of the above-mentioned observations is that the 5f electrons in Pa–Pu are metallic, hence the high electronic specific heat, in the same sense that the 3d, 4d and 5d electrons in the ordinary transition series are metallic, and that this metallic 5f state turns into a localized one at Am, hence the relatively low electronic specific heat. Am and the later actinides form a second rare earth series.

#### 4.3. Atomic volume

We now consider the partial *l*-resolved contributions to the electronic pressure (sect. 3.4, eq. (37)) as functions of both atomic volume and atomic number. The partial pressures originally calculated by Skriver (1983b) for the trivalent rare earth metals

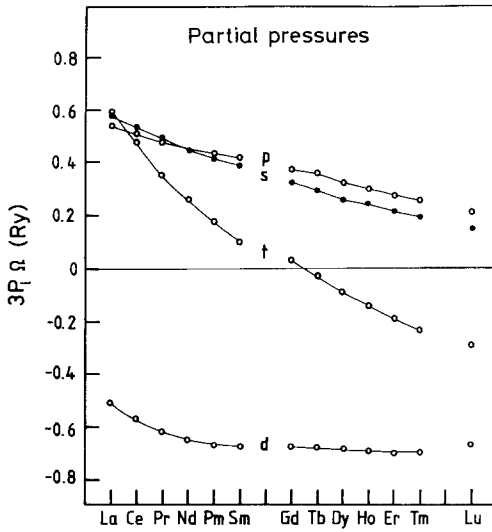


Fig. 20. The partial s, p, d and total electronic pressures of the trivalent lanthanides, evaluated at a common Wigner-Seitz radius of 3.75 au (after Skriver 1983b).

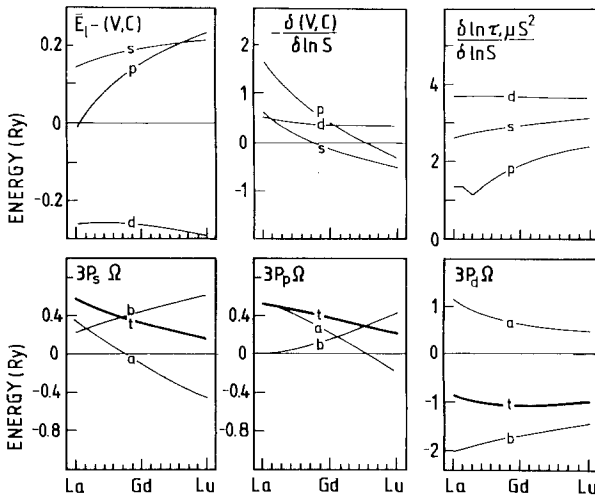


Fig. 21. Decomposition of the partial pressures into bandwidth and band-position terms (lower panel) for the trivalent lanthanides. Approximate pressure expressions, eqs. (46) and (47) (after Skriver 1983b).

at a fixed atomic radius of 3.75 au in the fcc structure are shown in fig. 20. The s and p partial pressures are positive (repulsive) and the d partial pressure is negative (bonding). In terms of eq. (37) and the discussion following eq. (48), only the 5d states are both bonding and resonant states. Alternatively, in terms of eqs. (46) and (47), the partial pressures may be further resolved into band-centre and bandwidth contributions. At the beginning of the series the square-well pseudopotentials of the s and p states are greater than  $\epsilon_{xc}(S)$  (fig. 13) and the corresponding band-position contribution is positive, as shown in fig. 21. As the relative core size shrinks with increasing atomic number, the square-well pseudopotentials of the s and p bands fall below  $\epsilon_{xc}(S)$  and the band-position contributions change sign. The bandwidth contribution

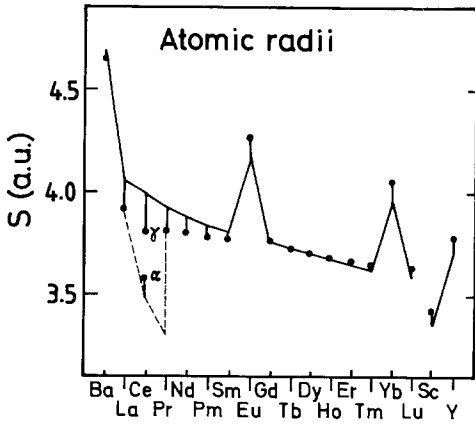


Fig. 22. The Wigner–Seitz radii of the rare earth metals. The points represents measurements and the full line the results of LMTO calculations by Skriver (1983b).

is also influenced by the decrease in the core size across the series, which causes  $\langle E \rangle_l - V_l$  in eq. (47) to increase. The bandwidth contribution therefore increases, and the sum of the position and bandwidth contributions to the partial s and p pressures remains positive throughout the series, providing the repulsive pressure required to balance the *bonding* pressure of the d electrons.

We now consider the band-centre term in eq. (46) for the d states. Since the band mass,  $\mu_l$ , is always positive, the sign of this contribution is determined by the position of the band centre relative to the exchange–correlation energy,  $\epsilon_{xc}(S)$ , at the sphere, see eq. (46). The centre,  $C_l$ , of the d bands lies far above  $\epsilon_{xc}$  (fig. 13) and the position contribution (fig. 21) is positive, i.e. repulsive, throughout the series. It is the bandwidth term in eq. (46) that provides the bonding since  $\langle E \rangle_l - C_l$  is negative, the d bands being less than half-filled. As the number of d electrons decreases across the series so does this contribution, due to the factor  $n_d$  in eq. (46).

The atomic radii calculated by Skriver (1983b) from an evaluation of eq. (37), are shown in fig. 22. The variations in the lattice constant and the total pressure at fixed

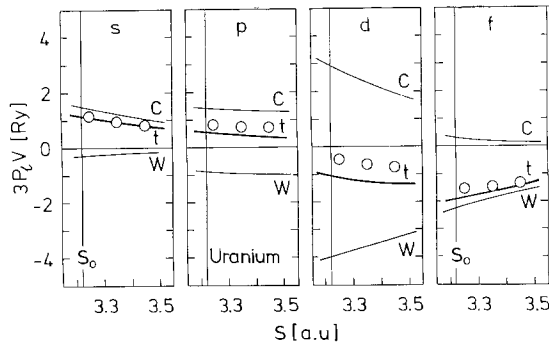


Fig. 23. The partial pressures for uranium decomposed into the band-centre contribution (C) and the bandwidth contribution (W) as functions of the atomic radius, and the partial pressures for U decomposed according to the first-order pressure expression, eq. (46), (full lines). The letter t denotes the total pressure and the open circles are the results of the full calculations.

radius, fig. 20, are similar and, for an approximately constant bulk modulus, the trend in the radius is due to the trend in the electronic pressure. The origin of the rare earth contraction is, therefore, the shrinking core size and resulting fall in the band centres and square-well pseudopotentials (fig. 13).

The rare earths are early transition metals where the number of d electrons changes only slightly. In the actinides the 5f electrons play the premier role in the bonding. In fig. 23 we show the volume dependences of the s, p, d and f pressures for uranium, analyzed according to eqs. (37) and (46).

Since the band mass,  $\mu_l$ , is always positive, the sign of the band-centre contribution is determined by the position of the band centre relative to the exchange–correlation energy,  $\varepsilon_{xc}(S)$ , at the sphere, (eq. (37)), as before. This relative position may be judged from the bands in fig. 23 by noting that  $C_l$  is approximately halfway between  $B_l$  and  $A_l$ , and that  $\varepsilon_{xc}(S) \simeq 0.75V(S)$ . It follows that the centre term is positive, i.e. repulsive, for all values of the angular momentum. The magnitude of the centre term is governed by the occupation number,  $n_l$ , the centre position,  $C_l$ , and the band mass,  $\mu_l$ . The band masses for the 7s and 7p states are nearly equal, while  $C_p - \varepsilon_{xc}$  is approximately three times  $C_s - \varepsilon_{xc}$ . The partial occupation numbers of the actinide metals treated as di- and trivalent metals, as well as with 5f states in the energy bands (Brooks et al. 1984, Eriksson et al. 1990c), are plotted in fig. 24 as a function of atomic number. Since  $n_p$  is between one half and one third of  $n_s$  in uranium metal, the centre terms for all the s and p states have similar magnitudes. For the 6d states  $C_d - \varepsilon_{xc}$  is intermediate

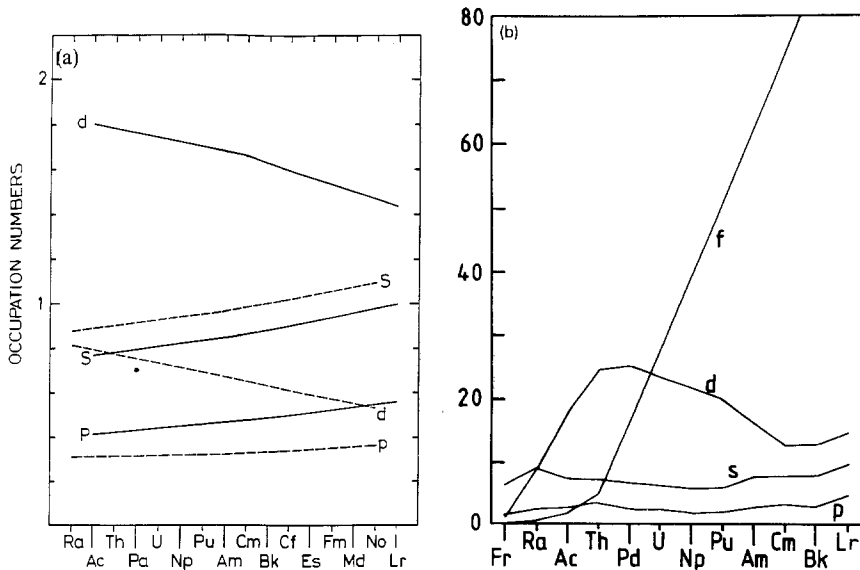


Fig. 24. (a) The calculated s, p and d occupation numbers across the actinide series when the 5f states are part of the core. The full line is for trivalent actinides and the dashed line is for divalent actinides. (b) The calculated s, p, d and f occupation numbers across the actinide series when the 5f states are in the energy bands.

between the centre position for the s and p states, but since the occupation number is much larger and the band mass only twice as large as for the s and p states, the d centre term is the largest of those shown in fig. 23. The 5f centre term is the smallest of the four band-centre terms on account of the very large f band mass. The bands rise and the magnitude of the centre terms increases under compression because the band masses decrease.

The sign of the bandwidth term in eq. (46) is determined by the position of the centre of gravity of the occupied part of the  $l$ -band,  $\langle E_l \rangle$ , relative to the band centre,  $C_l$ . The magnitude of the bandwidth terms for the d and f states increases under compression as a result of the corresponding increase in bandwidth, but for the s and p states – which are losing electrons to the d and f bands – this band-broadening effect is counterbalanced by the drop in occupation number, yielding the volume dependences shown in fig. 23.

In summary, the repulsive s pressure is determined mainly by the centre term, and its volume dependence results from the change in kinetic energy required to maintain orthogonality to the core states with changing volume. The bonding f pressure is determined mainly by the bandwidth term, and its volume dependence is, therefore, that of the bandwidth. In contrast, the p and d pressures arise as a balance between the centre and bandwidth terms, causing their volume dependence to be less transparent.

The variation of the individual s, p, d, and f pressures with atomic number, shown in fig. 25, may now easily be analyzed in terms of eq. (46). The slow decrease in the s pressure with increasing atomic number simply reflects the effect on the band-centre term of the lowering of the s band. This decrease in the band position is caused by

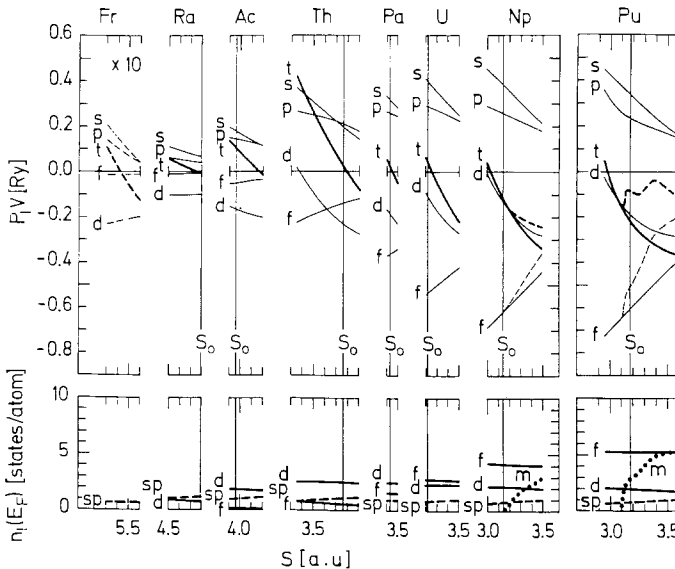


Fig. 25. The total (t) and partial (s, p, d, f) pressures evaluated by means of eq. (37), as functions of atomic number and radius.  $S_0$  is the measured equilibrium radius. The lower panels show the occupation numbers (sp, d, f) and spin polarization (m).



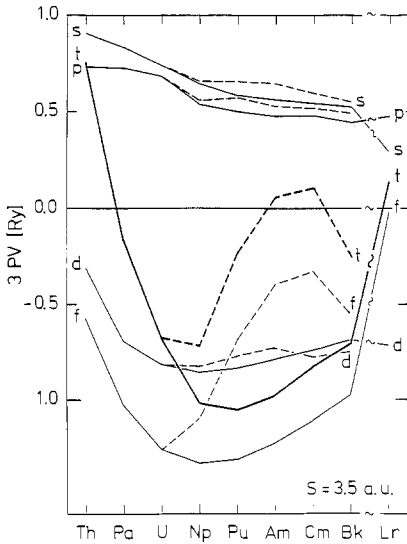


Fig. 26. The total (t) and partial pressures (s,p,d,f) evaluated by means of eq. (37) at the common radius  $S = 3.5$  au across the actinide series. The effect of spin polarization is indicated by the dashed lines.

the incomplete 5f screening of the extra nuclear charge – as in the rare earths. The variation of the p pressure is mainly an occupation-number effect, reflected in the centre term. The initial decrease in the d pressure is caused by the lowering of the d band centre, and when this lowering slows down on account of the partial screening of the nuclear charge, the pressure varies proportional to the occupation number. The variation in the f pressure simply reflects the parabolic dependence on the occupation number in eq. (48) for the bonding bandwidth contribution. The minimum in this parabola occurs for a half-filled band, i.e. at Cm. However, since the bandwidth, which also enters eq. (48), decreases with increasing atomic number, the parabolic behaviour is modified and the maximum magnitude of the (negative) f pressure is already found for Np, where the partial 5f occupation is 4.1.

The total pressure also has a parabolic variation with atomic number, which, according to eq. (48), may be attributed to the increasing filling of the bonding 5f states. If the bulk modulus were independent of atomic number and volume, the atomic volumes (radii) could be obtained directly from the total-pressure curve. Although the bulk modulus does depend upon atomic number and volume, it is still correct to conclude that the parabolic trend observed in the atomic volumes of the light actinides, Th–Pu, is determined mainly by the properties of the 5f electrons.

Figure 26 shows the equations of state, eq. (37), of the actinide metals, calculated by Skriver and co-workers (Skriver et al. 1978, 1980, Brooks et al. 1984), for the fcc structure and fig. 27 shows the calculated atomic radii, evaluated from eq. (37). The agreement between theory and experiment implies that the approximations to density functional theory outlined in sect. 3.1 contain the essential physics. Early in the series, Fr–Th, we observe a decrease in radius, which is caused by an increase in the amount of d character (fig. 24). For Th–Pu the calculated atomic radius continues to decrease, but now the cause can be traced to the increasing occupation of the 5f orbitals, which,

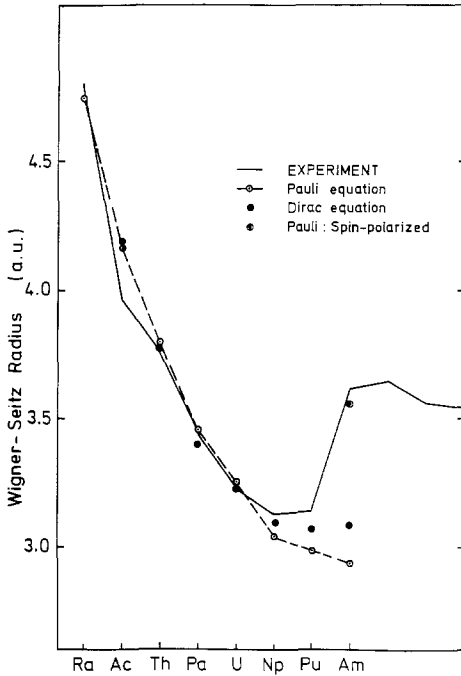


Fig. 27. Calculated (in the fcc structure) and experimental atomic radii for the actinide metals. The value estimated for Ac was obtained from Zachariasen (1973).

in the simplest possible approximation, gives rise to a parabola with its minimum at curium.

It has been suggested by Brooks (1983) that the deviations from theory observed in Np and Pu may in part be explained by the relativistic volume effect (sect. 3.8). If there is a preferential occupation of the  $j = \frac{5}{2}$  band, there is a  $j = \frac{5}{2}$  contribution to the pressure in eq. (54), which, in the limit where the spin-orbit interaction is much larger than the 5f bandwidth, vanishes for  $n_f = 6$ , i.e. between Pu and Am. It turns out that this limit is not realized in any of the metals Np, Pu or Am, but the effect is sufficiently large to cause deviations from Pauli theory. Even with spin-orbit interaction included, the calculated radii of Np and Pu are too low compared with experiments. The remaining deviation may be due to correlation effects not included in our one-electron scheme. Both Np and Pu are known to be nearly magnetic (Brodsky 1978), which indicates strong f correlations. An additional reason for the discrepancies might be found in the crystal structures.

Between Pu and Am, the parabolic trend, which stems from the filling of bonding 5f states, is terminated and the calculated radius of Am is 16% larger than the calculated radius of Pu. This anomaly is caused by 5f localization. In energy-band theory it appears as a large magneto-volume effect (sect. 3.5). The spin-polarized solution to the Pauli equation, which exists only for expanded volumes in Np and Pu, exists at positive pressures in Am – and has the lowest energy. Since the spin-polarization in Am is practically complete,  $m = n$ , and the f occupation is 6.4 (i.e. close to 7), most of the bonding f pressure is lost (eq. (50)), and the 5f electrons have become essentially non-bonding. Hence, the totally polarized solution represents, correctly, the localized non-bonding  $f^6$  state in americium. The radii calculated by means of the spin-polarized

band theory are also found to be in good agreement with experimental observations for Am, Cm and Bk – indicating that the spin-polarized theory gives a suitable description of the localized ground state in these metals.

#### 4.4. Bulk modulus

The bulk modulus may be obtained from the calculated equation of state by differentiation. This quantity is more difficult to calculate accurately than is the equilibrium volume, both because it involves the difference in two calculated numbers and it is sensitive to the volume at which it is calculated. The calculated volumes of the transition metals (Andersen et al. 1985) are usually a little lower than those measured (LDA tends to overbond), and bulk moduli evaluated at the calculated volumes tend to be higher. The bulk moduli of the lanthanide metals calculated by Skriver (1983b) for the fcc structure at the calculated equilibrium radii, are shown in fig. 28. The observed slow increase across the series, broken only by the low values for the divalent metals, is reproduced well, although the calculated bulk moduli are typically 30% too high.

The bulk modulus depends upon the volume at which it is evaluated. For a common volume it would decrease across the series, since the core size decreases and leaves more space to the s and p electrons which are excluded from the core region by orthogonality constraints. However, the calculated equilibrium volume decreases with increasing atomic number enough to reverse this effect, and the bulk modulus increases with increasing atomic number. Actually the bulk modulus of La is anomalously low due to transfer of s electrons into the d bands as the volume is decreased (McMahan et al. 1981), an effect that is far smaller in Lu and partially responsible for the increase in bulk modulus across the series.

The bulk moduli of the actinides, calculated by Skriver and co-workers (Brooks et al. 1984), are shown in fig. 29. The rise from a low value in Fr to the maximum in U is caused initially by the sp and later also the d electrons, which become trapped between the rapidly decreasing atomic volume and their slowly contracting cores. If the atomic volume continued to decrease with atomic number as much as the calculated volume (fig. 27), the bulk modulus would rise to a value of approximately 2 Mbar in

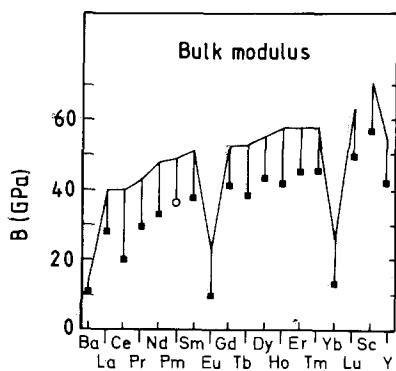


Fig. 28. The bulk moduli of the rare earth metals. The full line indicates the results of calculations (Skriver 1983b). The circles and squares are experimental values.

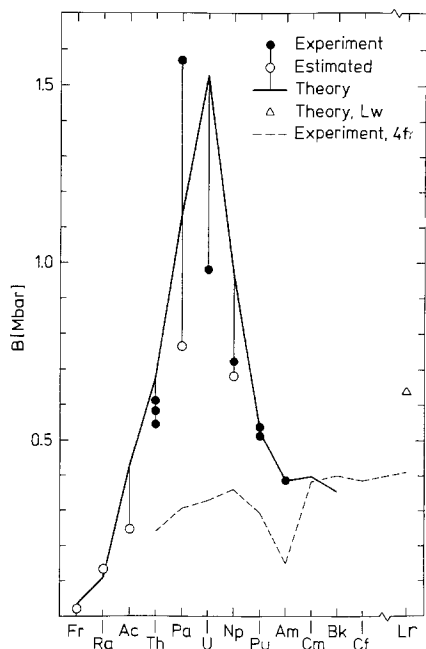


Fig. 29. Calculated and experimental bulk moduli for the actinide metals. The calculated values are obtained from the experimentally observed atomic radii.

Pu. However, the bulk modulus is extremely volume dependent, and if it is evaluated at the experimentally observed equilibrium radius – which deviates from the calculated values for Np and Pu – it drops from U to Pu, as shown in fig. 29. In the heavy actinides, i.e. beyond americium, the atomic volume has increased considerably, due to the localization of the 5f states, and hence the bulk moduli attain low values – typical of those found in the lanthanide series.

The agreement between the calculated and experimental bulk moduli seen in fig. 29, is less satisfactory than the agreement found for the atomic radii. The worst discrepancy occurs in Pa, where static high-pressure measurements (Benedict et al. 1982) suggest that this metal has the highest bulk modulus in the actinide series. In this connection one should note that, although the theory is parameter free, it nevertheless contains a number of approximations. For example, we have frozen the radon core and assumed the fcc structure throughout instead of the quite complicated structures which are found experimentally. Both approximations no doubt influence the calculated bulk modulus. On the other hand, apart from the case of the bulk modulus of Pa, which requires both more experimental and theoretical study, the local spin density functional formalism gives a correct description of the trends observed along the actinide series.

#### 4.5. Crystal structure

That the crystal structures of the elemental metals occur in sequences as a function of *either atomic number or pressure* is both fascinating and a challenge to theorists of electronic structures. The earliest attempts to explain the structure sequences

(Brewer 1967) were qualitative and based upon the Engel (1949) correlation, involving the number of sp electrons. The first physical theories were due to Ducastelle and Cyrot-Lackman (1971) and Dalton and Deegan (1969), here relationships between crystal structure and band structure were sought. A more complete treatment for the transition metals, due to Pettifor (1970, 1972), related the hcp  $\rightarrow$  bcc  $\rightarrow$  hcp  $\rightarrow$  fcc sequence to the change in d occupation number across the transition metal series.

For the lanthanides the structure sequence hcp  $\rightarrow$  Sm-type  $\rightarrow$  dhcp  $\rightarrow$  fcc was shown by Duthie and Pettifor (1977) to depend upon the 5d occupation number, which itself is related to the Johansson–Rosengren *f*-parameter (Johansson and Rosengren 1975a, b, Johansson 1978a), used to rationalize the structure sequence. In fact, the structure sequence for the lanthanides is that of the early 5d transition metals, and it is also found for the 4d transition metal Y and the heavy actinides, which should be regarded as 6d transition metals at pressures where the 5f states remain localized. The *f*-parameter is the ratio of the Wigner–Seitz radius to some effective core radius. The Fröhlich–Bardeen expression for the energy of the bottom of the s band is also related to the effective core radius, which specifies the extent of the core region from which the s states are excluded by orthogonality constraint (Pettifor 1977). Duthie and Pettifor (1977) related the ratio of the Wigner–Seitz to the core radius to the relative s and d occupation numbers. They calculated the structural energy differences of the trivalent rare earths using unhybridized LMTO theory and showed that the partial d occupation numbers increase along the structure sequence, but they were unable to obtain the hcp structure for Lu – probably due to the unhybridized-bands approximation. A major advance in understanding the structure sequence had nevertheless been made.

A subsequent, more complete treatment of the band-structure problem for the lanthanides by Skriver (1983b, 1985) confirmed the essence of the Duthie–Pettifor (Duthie and Pettifor 1977) theory, at the same time adding accuracy to the computed structural energy differences. By using full LMTO calculations Skriver was also able to obtain the correct partial occupation numbers – the same as those subsequently calculated by Eriksson et al. (1990c), and shown in fig. 15. By calculating the partial occupation numbers at the pressures required to induce the structural transitions in La, Sm and Gd, Skriver (1983b) was able to associate  $n_d = 2.0, 1.85$  and  $1.75$  with the dhcp  $\rightarrow$  fcc, Sm-type  $\rightarrow$  dhcp and hcp  $\rightarrow$  Sm-type transition, respectively. Then, calculation of the partial d occupation numbers as function of the pressure, led to fig. 30, which predicts the pressure-induced transitions for the lanthanides.

That electronic-structure theory has been so successful in the computation of the correct ground-state structures is mostly due to the force theorem (sect. 3.4). Once a self-consistent calculation has been done for a given structure, the so obtained *frozen* potential is used for a single iteration for another structure at the same atomic radius, and the energy difference is just the difference in the sum of the single-electron eigenvalues plus a small structure-dependent electrostatic correction. The structural-energy differences of La as a function of volume computed by Skriver (1985) using full LMTO calculations and with the fcc structure as reference, are shown in fig. 31.

Similar calculations have been done by Skriver (1985) for the light actinide metals, where the hcp, bcc and fcc structures were compared (fig. 32). These energy differences

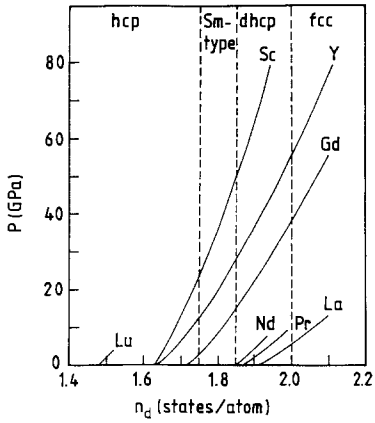


Fig. 30. The calculated electronic pressure as a function of d occupation number for the lanthanides. The vertical lines indicate the d occupation numbers for which structural phase transitions are expected to occur (after Skriver 1983b).

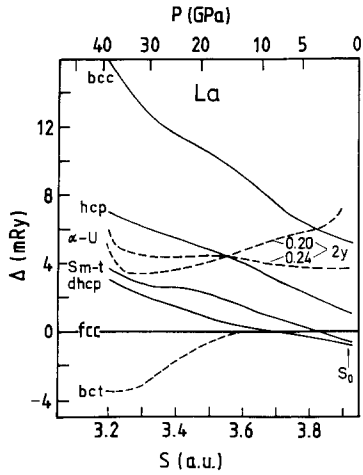


Fig. 31. Structural-energy differences for La as functions of atomic radius. The equilibrium radius is 3.92 au (after Skriver 1985).

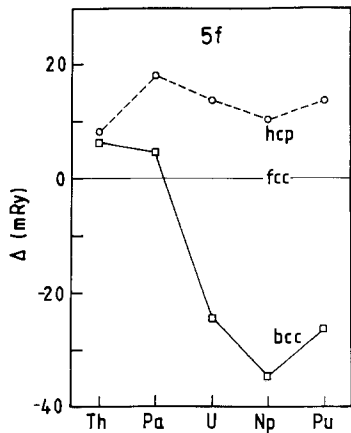


Fig. 32. The calculated structural-energy differences for the actinide metals relative to the fcc structure (after Skriver 1985).

appear to be in agreement with experiment, since the measured low-temperature phase of Th is fcc and Pa may well have a high-temperature fcc phase. Further, U and Np have no high-temperature fcc phases but become bcc prior to melting. Pu has high-temperature fcc and bcc phases, the fcc phase being rather unstable. Nevertheless, the problem of the low-temperature structural stability of the light actinides is a difficult problem, since Pa is bct, U is orthorhombic with 2 atoms/cell, Np is orthorhombic with 8 atoms/cell and Pu is monoclinic with 16 atoms/cell. Wills and Eriksson

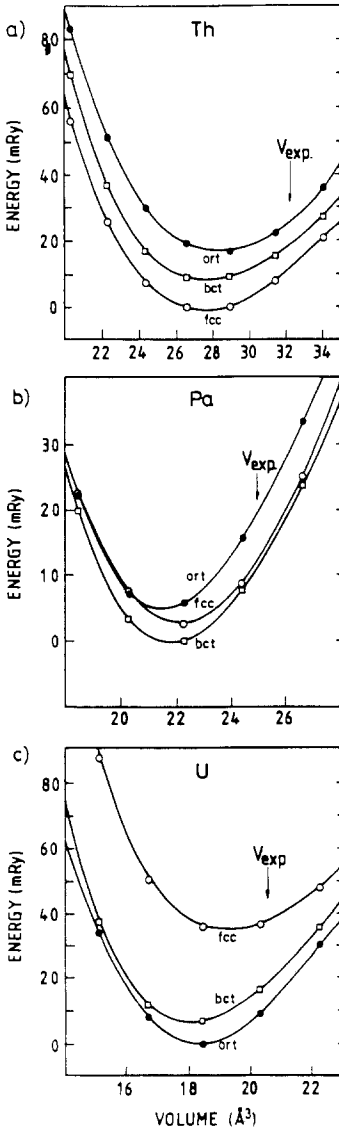


Fig. 33. Calculated total energy of Th, Pa and U in the fcc, bct and ort structure (after Wills and Eriksson 1992).

(1992), in something of a computational tour de force, have done full-potential LMTO calculations for Th, Pa and U. The total energies of the three elements were calculated in three structures: fcc, bct and the orthorhombic  $\alpha$ -U structure. The experimentally observed structures were found to have the lowest energies. The results of the calculations for the three elements are shown in fig. 33. Wills and Eriksson (1992) argue that the preference of materials to form open structures is due to non-sphericity of the charge densities – or covalent bonding. The energy gain from covalent bonding is at the expense of the electrostatic Madelung energy. In many metals the Madelung contribution dominates and high-symmetry structures are formed. When a complex of energy bands, such as the 5f-derived bands in the actinide metals, cross the Fermi energy, the covalent bonding energy gain is particularly large and low-symmetry (or open) structures become stable. Evidently there is an analogy with the formation of Jahn–Teller–Peierls distortions, in the sense that complex systems have at least one contribution to their Hamiltonian that tends to reduce the symmetry of the ground state. That charge density waves have also been observed in actinides which also have low-symmetry structures (Marmeggi et al. 1990, Grübel et al. 1991), is suggestive, and we would suggest that the underlying mechanism is the same.

The heavy actinide metals Am, Cm, Bk and Cf all have dhcp structures at ambient pressure, and the analogy with the rare earth metals is inescapable. The transition to an fcc structure (Akella et al. 1979, 1980, Smith et al. 1981, Benedict et al. 1985, Benedict 1987) has also been observed under pressure. Eriksson et al. (1990c) used

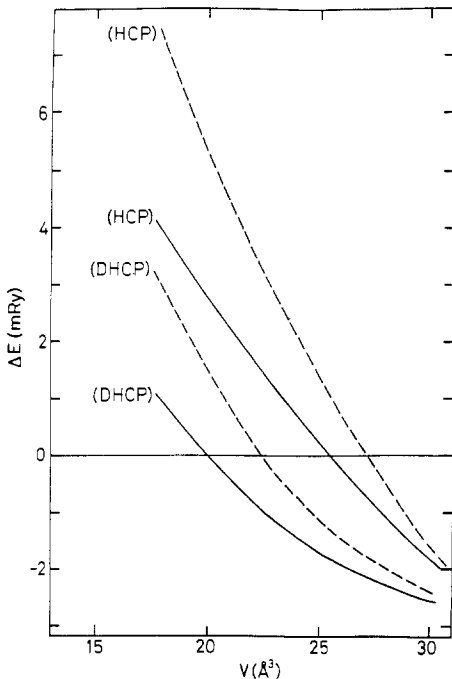


Fig. 34. Calculated energy differences for the fcc, hcp and dhcp crystal structure relative to the energy of the fcc structure (equal to zero in the graph) as a function of volume for Am (full lines) and Cf (dashed lines). (After Eriksson et al. 1990c.)



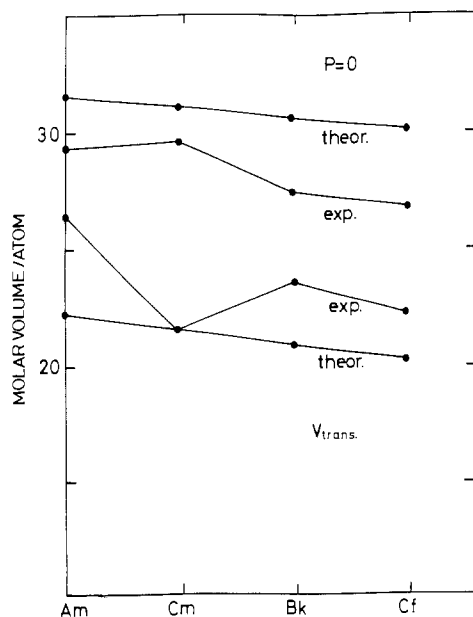


Fig. 35. A comparison between the calculated and measured equilibrium volumes, and the calculated and measured volumes for the dhcp  $\rightarrow$  fcc transformation of Am-Cf (after Eriksson et al. 1990c).

the force theorem to compare the energies of the hcp and dhcp crystal structure with that of the fcc structure for the heavy actinides Am-Cf. These energies are plotted as a function of volume in fig. 34. The dhcp structure has the lowest energy, but at reduced volumes the fcc structure becomes more stable. Since a reduction in volume leads to an increase in the partial d occupation number, the fcc structure is also stable for a larger number of d electrons. Eriksson et al. (1990c) found, however, that the transition to the fcc structure does not occur for exactly the same number of d electrons for the elements Am-Cf. The calculated volumes (Eriksson et al. 1990c) at ambient pressure and the critical volumes for the transition from the dhcp to fcc structure for Am-Cf are shown in fig. 35, where they are compared with measurements (Benedict et al. 1985, Benedict 1987). The best agreement between theory and experiment is obtained for Cm, which, not surprisingly, also has an ( $5f^7, {}^8S_{7/2}$ ) configuration, which is spherically symmetric.

#### 4.6. Cohesive energy

Central to almost every theory of transition metal bonding – from Friedel's (1969) rectangular density of states model, through the renormalized atom theories of Gelatt et al. (1977), to the unhybridized energy band calculations in the atomic sphere approximation employed by Pettifor (1978) – is that there is a d-band contribution to the total energy which is an approximately parabolic function of the d-band occupation number across a transition metal series. Although a parabolic trend in the measured cohesive energies (Gschneidner 1964) may be recognized, the cohesive

energies of elements close to the centre of each series are far smaller than they would be if they contained only the d-band contribution. It has been recognized for some time (e.g. Gunnarsson et al. 1974, Friedel and Sayers 1977, Gelatt et al. 1977, Johansson et al. 1980) that the cohesive energy also contains, apart from the s and p conduction-electron contributions in the solid, a negative contribution from the preparation energy required to take a free atom from its ground state to a state similar to the non-magnetic ground-state configuration of the metal. This free-atom preparation energy tends to increase rapidly towards the middle of a transition metal series, and is thought to be responsible for the corresponding drop in the cohesive energies – as we have described in detail in sect. 3.5.

In sect. 3.7 we also defined the valence bond energy (eq. (57)) – which is expected to vary smoothly across a transition metal series – in terms of the cohesive energy and the free-atom promotion and spin polarization energies (eq. (58)). Finally, fig. 12 illustrates that the valence bond energies are smooth functions of the atomic number. The free-atom preparation energies also featured in sect. 2.1, where they were held responsible for the irregularities in the cohesive energies of the rare earth metals. The reason for the irregularities in the cohesive energies of the lanthanides is that in the condensation process one 4f electron is promoted to the conduction bands. The divalent free atoms become trivalent metals and, since the di- to trivalent promotion energies are not smooth functions of the atomic number, neither are the cohesive energies.

Eriksson et al. (1990c) have calculated the valence bond energies of the lanthanide metals in LSDA, treating the 4f electrons as part of the atomic cores. The total energy of the heavy atoms exceeds  $10^4$  Ry, whereas the cohesive energies of the metals are less than  $\frac{1}{2}$  Ry per atom. If the total energy is computed as a function of volume in the condensed phase, it is difficult to maintain enough accuracy to be able to compute the cohesive energy reliably. However, the *frozen-core approximation* (Gunnarsson et al. 1977, Harris and Jones 1979) separates the total energy into a part depending only upon the core charge density (and is large) and a part depending upon the valence charge density (and is small). The free-atom core charge density is retained in the solid-state calculation, only the valence charge density being allowed to relax self-consistently. The first part of the energy does not change in this approximation and is dropped from the calculations. The remaining part of the total energy is the valence electron energy.

von Barth and Gelatt (1980) have shown that corrections to the frozen-core approximation vanish to first order in the difference between the true charge density and the frozen-core charge density, leading to cancellation of errors and more accurate total-energy differences than might otherwise be expected. It is possible that the errors introduced are larger for the actinides, which have extended outer (particularly 6p) cores. However, the problem is reduced to that of finding the differences between small numbers and yields good estimates of the cohesive energies. The “valence energy” referred to here is not in any sense the energy of the valence electrons, which is not defined as a separate entity since there are always interactions between the core and valence electrons. It is just that part of the total energy that can change when the valence charge density alone is allowed to vary. The valence energy is given

by (Gunnarsson et al. 1977)

$$E_v = \sum_i n_i \varepsilon_i - \frac{1}{2} \int n_v(r) \left\{ \frac{1}{2} \phi_{\text{interac}} + \mu_{xc}[n(r)] - \varepsilon_{xc}[n(r)] \right\} dr$$

$$+ \int n_c(r) \left\{ \varepsilon_{xc}[n(r)] - \varepsilon_{xc}[n_c(r)] \right\} dr, \quad (59)$$

where  $n_i$  and  $\varepsilon_i$  are the occupation numbers and eigenvalues, respectively,  $\varepsilon_{xc}$  and  $\mu_{xc}$  are the exchange–correlation energy and potential,  $n_v$  and  $n_c$  are the valence and core charge densities and  $\phi_{\text{interac}}$  is the Coulomb potential due to the valence electrons (eq. (11)).

Figure 36 shows the calculated valence bond energies for trivalent La, Gd and Lu and for divalent Ba, Eu and Yb – all of which are atoms retaining the same valence in the solid as in the free atom; therefore the valence bond energies are also the cohesive energies in these cases, except for small corrections due to differences in the magnetism of the conduction electrons between free atom and solid (the calculations were not spin-polarized). Also shown are the measured cohesive energies, with an approximate correction made for Gd to allow for the change in the magnetism of the conduction electrons as described in sect. 2.1. Theory and measurement agree within a few percent, which is a success for LDA. The difference between the measured cohesive energies of the divalent and trivalent rare earths is reproduced very well. We recall our discussion in sect. 2.1, where it was reasoned on the basis of measurements that the divalent and trivalent cohesive energies should be about 50 and 100 kcal/mol, respectively. The difference between the cohesive energies of the divalent and trivalent

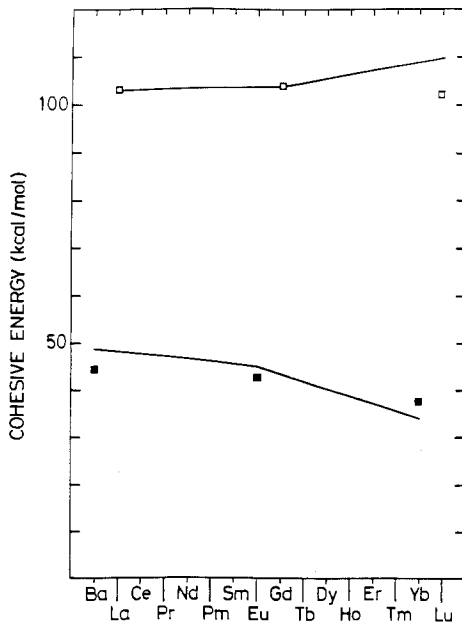


Fig. 36. Calculated cohesive energies of the divalent (lower curve) and trivalent (upper curve) lanthanides. The measured cohesive energies are indicated by squares (after Eriksson et al. 1990c).

elements is due, firstly, to the additional bonding electron in the trivalent elements and, secondly, the d level in the trivalent atom is at a relatively high energy and a larger bonding energy is gained when the lower part of the d band is occupied. The interpolated valence bond energies for the other rare earths in fig. 36 may be used in the theory described in sect. 2.1 to obtain the cohesive energies.

Similar cohesive-energy calculations have been done by Eriksson et al. (1990c) for the heavy actinides. Here the valences of the free-atom ground states frequently differ from those of the lanthanides. For example, the ground-state configuration of Th is  $d^2s^2$ . Furthermore, Am metal, unlike Eu metal, is trivalent. The heavy actinides may be treated in the same way as the lanthanides, however, by doing the calculations for divalent Ra, Am and No, i.e. the configurations  $f^{n+1}s^2$  with  $n = 1, 6, 13$ , and  $n = 0, 7, 14$  for the trivalent metals. The results are shown in fig. 37. Theory is here very much on its own, since the only measured cohesive energy is 92.6 kcal/mol for Cm (Ward 1983), to which an estimated (Johansson and Munck 1984) fd coupling energy (sect. 2.1) has been added. The calculated valence bond energies of both di- and trivalent heavy actinides are similar to those of the rare earths, and in good agreement with the values used in sect. 2.1 to estimate the valence states of the heavy actinides. All the main conclusions of sect. 2.1 therefore remain intact.

It has been suggested (Brewer 1971) that Lr, due to relativistic effects, has an  $s^2p$  configuration in the free atom, which would modify its cohesive energy somewhat. It has also been suggested (Keller 1984) that the same configuration might remain in the metal, making Lr a 3a-type metal. The calculations of Eriksson et al. (1990c) reveal that Lr is a normal d transition metal, and in fig. 24 we have already plotted the partial s, p and d occupation numbers of the heavy actinides against atomic number. For the next element, Rf, Eriksson et al. (1990c) calculated a valence bond energy of 160 kcal/mol, a value typical for a tetravalent transition metal (sect. 2.1).

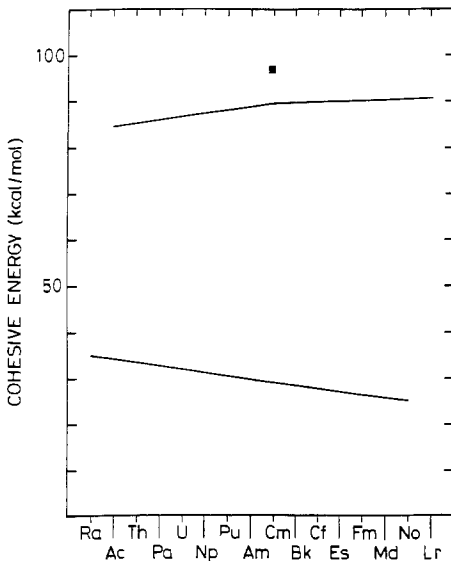


Fig. 37. Calculated cohesive energies of the divalent (lower curve) and trivalent (upper curve) actinides. The measured cohesive energy of Cm is the square (after Eriksson et al. 1990c).

The consistent success of LDA in obtaining agreement with measurements of the cohesive properties of metals across the periodic table gives us confidence that in the case of very heavy elements, where no measurements have been made, the calculated properties are also correct.

The cohesive energies of the light actinides are, as illustrated in sect. 2.1, influenced by 5f bonding. The measured cohesive energies of the light actinide metals, Pa–Am, compiled by Ward (1982, unpublished) are, in eV, for Th 6.2, for Pa 5.93, for U 5.52, for Np 4.83, for Pu 3.57 and for Am 2.95. Bradbury (1981) reports a cohesive energy of 6.7 eV for Pa. The cohesive energy of Ac has to date not been measured. Thus, the cohesive energies of the light actinides appear to decrease regularly – almost linearly – across the series, which is more reminiscent of the trend in the cohesive energies of the lanthanides (Gschneidner 1964) than that in a transition metal series – in apparent conflict with both the measured and calculated trends in the atomic volumes. This apparent conflict is due to the free-atom preparation energies, which obscure the essentially parabolic trend in the 5f-band contribution to the cohesive energy (Johansson et al. 1980, sect. 2.1).

The valence bond energies, relative to the trivalent and paramagnetic free-atom ground state, of the light actinides in the fcc structure have been calculated by Brooks (1984a), and are plotted in fig. 38. The valence bond energies were computed using both LMTO and RLMT0 energy band calculations for the solid to compute  $E_v$ , eq. (59), and the energy difference  $E_{\text{val}} = E_v(\text{atom}) - E_v(\text{solid})$  was calculated. The

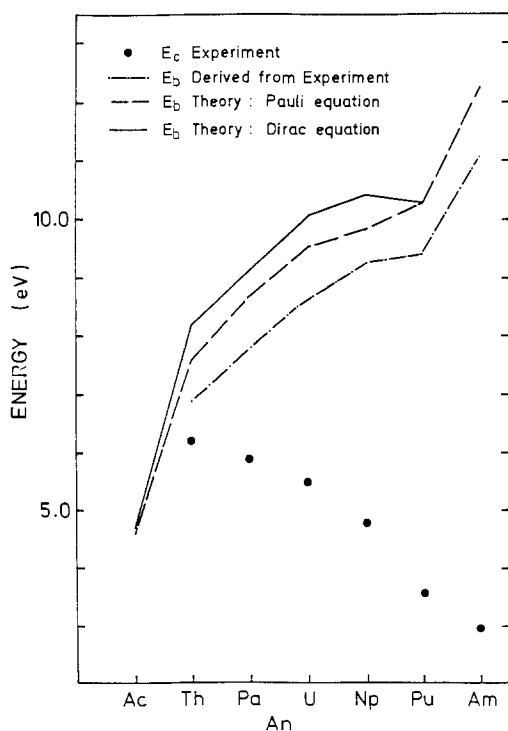


Fig. 38. The calculated band contribution to cohesion (full line) for the light actinide metals, evaluated using self-consistent RLMT0 calculations. The dashed line is the same quantity evaluated using LMTO calculations. The dash-dotted curve is the band contribution to cohesion evaluated from the experimental cohesive energies after analysis of the free atoms (see text).  $E_c$  are the experimental cohesive energies (Ward 1983), which follow a different trend. A value of  $E_c$  for Pa, equal to 7 eV per atom reported by Bradbury (1981), is not plotted.

calculated band contribution to the cohesion is already falling at Pu, partly due to the fact that the  $5f_{5/2}$  band is more than half-filled at this stage, but also because the experimental equilibrium volume – at which the energies were evaluated – is anomalously high (Brooks 1983). The latter effect reduces the calculated band contribution to the cohesion from the LMTO calculation even more since here the difference between the calculated and measured equilibrium volumes is even greater (Skriver et al. 1978).

The promotion energy required to take the atom from the Dirac–Fock ground state to a state with the same configuration as the prepared atom is non-zero for Pu and Am, where the Dirac–Fock ground-state configurations are  $f^{n-2}s^2$  but the prepared-atom configurations are  $f^{n-3}ds^2$ . The optical data quoted by Nugent and Vander Sluis (1971) yields promotion energies of 0.79 and 2.23 eV for Pu and Am, respectively.

In addition, the actinide metals are non-magnetic, whereas the free atoms have a large spin-pairing energy (sect. 3.4). The calculated spin polarization energies of the free neutral atoms in LSDA, which include the coupling between open d and f shells (Johansson et al. 1980), were also added to the free-atom energies, as was the energy of spin–orbit interaction of the 5f and 6d electrons, calculated in the Russell–Saunders limit. Finally, the energy associated with orbital correlations in the free-atom ground state – i.e. the energy associated with Hund’s second rule – was also added. There is no LSDA equivalent of this effect – density functionals are derived for the homogeneous electron gas where there is no centre of symmetry – the values were obtained from experiment (Nugent 1970). When this very complete list of promotion and correlation energies, present in the free atoms but lost in the metal, was added to the measured cohesive energies, the valence bond energies deduced from the measured cohesive energies were found to come close to the calculated valence bond energies (fig. 38). The added energies increase rapidly across the light actinide series. The dominant contribution is the spin-polarization energy, but the others are not negligible, and it is this that is responsible for the measured decrease in the cohesive energy between Pa and Pu. The cohesive energy of actinium has never been measured, but it is calculated to be 4.4 eV or about 100 kcal/mol. When it has been measured, it will also become clear from experiment that the actinide cohesive energies peak early in the series and do not have merely the monotonically decreasing trend suggested by the experiments to date.

#### 4.7. *Elastic constants*

Accurate *ab initio* methods for the calculation of elastic constants have been developed (Christensen 1984b), and a few calculations have been done for some cubic lanthanide and actinide systems (Söderlind et al. 1993, Wills et al. 1992). The tetragonal shear constant,  $C'$ , is calculated as the second derivative of the total energy as a function of small tetragonal distortions. That is, the unit cell is stretched or compressed along the  $z$ -axis, while the cube edges in the  $x$ - and  $y$ -directions are varied equally by the amount necessary to conserve the volume of the unit cell. Both the bcc and fcc structures may be considered to be body centred tetragonal (bct) with

TABLE 1  
Elastic constants ( $C_{44}$ ,  $C'$ ,  $C_{11}$  and  $C_{12}$ ) and bulk modulus ( $B$ ) in kbar for La,  $\alpha$ -Ce and Th. (From Söderlind et al., unpublished.)

	$B$		$C_{44}$		$C'$		$C_{11}$		$C_{12}$	
	theory	exp.	theory	exp.	theory	exp.	theory	exp.	theory	exp.
La	209	231	168	180	64	71	294	345	166	204
Ce	370	240–290	446	–	119	–	529	–	291	–
Th	420	577	459	478	100	132	553	753	353	489

$c/a = 1$  and  $c/a = \sqrt{2}$ , respectively. The total energy as a function of  $c/a$  defines the *Bains path deformation*, which provides a continuous way to proceed from the bcc to the fcc structure. Local stability of the cubic structures requires a positive curvature of the total energy along the Bains path close to  $c/a = 1$  and  $c/a = \sqrt{2}$ , hence a positive value for  $C'$ . Since  $C'$  is related to the elastic constants by

$$C' = \frac{1}{2}(C_{11} - C_{12})$$

and since the bulk modulus  $B$ , for a cubic crystal, obeys the relation

$$B = \frac{1}{3}(C_{11} + 2C_{12}),$$

a calculation of  $C'$  and  $B$  yields  $C_{11}$  and  $C_{12}$ . The third elastic constant,  $C_{44}$ , is calculated from a trigonal distortion of the lattice. In this case the second derivative of the total energy as a function of the distortion yields  $C_{44}$ . This approach has been applied to fcc La, fcc  $\alpha$ -Ce and fcc Th. In table 1 we compare the calculated results with experiment (except for  $\alpha$ -Ce, for which no experimental data exists). Satisfactory agreement with experiment was obtained, and we anticipate that this method will soon be extended to hexagonal structures, making it possible to study theoretically the elastic properties of the entire lanthanide series.

#### 4.8. Cerium

The electronic structure of cerium has been studied intensely for a long time. The  $\gamma$ - $\alpha$  transition, which occurs at room temperature and a pressure of 7 kbar (Lawson and Tang 1949), has been the focus of much of the interest. Here the high-volume ( $\gamma$ ) phase collapses to the low-volume ( $\alpha$ ) phase, the crystal structure remaining fcc on both sides of the transition line. The observed volume collapse of 14% is very large for an elemental metal. The phase change is driven by the electronic states, and is often referred to as an electronic transition from a low-density to a high-density phase. Since the two phases mainly differ by their densities, there is a clear resemblance to the well-known gas-liquid phase transformation. Indeed, the  $\gamma$ - $\alpha$  transition line in the pressure-temperature plane ends in a critical point ( $P \approx 20$  kbar,  $T \approx 600$  K) (Jayaraman 1965), a fact which further accentuates this similarity.

Many review articles have been written about the cerium problem (e.g. Koskenmaki and Gschneidner 1978, Coqblin 1982, Macintosh 1985, McMahan 1989). Here we

will not attempt to give a complete review, but will concentrate on the results of some electronic-structure calculations of significance for an understanding of the  $\gamma$ - $\alpha$  transition.

There is general agreement that the 4f electrons in the  $\gamma$ -phase of cerium are localized and behave essentially the same as the 4f<sup>n</sup> configurations in the other lanthanide metals. This is confirmed experimentally in many types of investigations on cerium, not least by the fact that the different crystal structures observed at low pressures and high temperatures (dhcp, fcc and bcc) are in complete agreement with the general behaviour of all the other lanthanide metals (Johansson and Rosengren 1975a). The main difference in opinion about cerium concerns the electronic structure of the low-temperature and high-pressure  $\alpha$ -phase.

The first suggestion was that cerium in the  $\alpha$ -phase is a tetravalent transition metal, like zirconium or hafnium, with a conduction electron configuration of (spd)<sup>4</sup> and an empty (but still localized) 4f level (Zachariasen 1949, Pauling 1950, Zachariasen 1973). The classical example of such a valence transition is the pressure-induced volume collapse in SmS, which originates from an f<sup>6</sup> to f<sup>5</sup>d electronic transition accompanied by an insulator-metal phase transition (Jayaraman 1978). However, careful consideration of the energetics of the Ce valence change by Johansson (1974, 1977b, 1978b) led to the conclusion that the energy of the tetravalent state was 2 eV *higher* than the energy of the trivalent state. Thus a valence change is ruled out as a feasible explanation for the occurrence of the cerium  $\alpha$ -phase. Johansson (1974) argued that the  $\gamma$ - $\alpha$  transition originates from a radical change in the nature of the 4f state from localized (non-bonding) to itinerant (bonding). This may be looked upon as a transformation from the insulating to the metallic phase *within the 4f configuration* and in this sense is a Mott transition (Mott 1961, Gustafsson et al. 1969). Actually this view of the  $\gamma$ - $\alpha$  transition is analogous to the vapour-liquid condensation transformation of metallic atoms where the insulating atomic gas phase transforms to a metallic liquid state. In this transformation the nature of the valence electrons changes from non-bonding (localized or atomic) to bonding (metallic) and there is a dramatic change in density. The main difference is that in cerium a change in 4f behaviour occurs in the solid, where the atoms are already held together by spd electrons. The metallization of the 4f electrons is delayed relative to that of the spd electrons since the 4f orbitals have considerably less spatial extension than the 5d, 6s and 6p orbitals.

Another, and widely held, view of the electronic structure of  $\alpha$ -cerium is contained in the so-called "Kondo volume collapse model" (Allen and Martin 1982, Lavagna et al. 1982, 1983, Martin and Allen 1985), where the 4f electrons are localized but strongly coupled to the spd conduction electrons. The strong volume dependence of this coupling drives  $\gamma$ -cerium to  $\alpha$ -cerium. A detailed analysis of this model has been performed by Allen and Liu (1992).

At about 50 kbar and at room temperature, fcc  $\alpha$ -cerium undergoes a crystallographic change to an orthorhombic - the  $\alpha$ -uranium - structure (Ellinger and Zachariasen 1974, Zachariasen and Ellinger 1977), with only a very small change in volume. Johansson (1974) interpreted this as strong confirmation of itinerant 4f electrons in the dense phases of cerium, since this phase is also the ground state of



uranium metal, where the 5f electrons are known to be itinerant. Subsequently, cerium was found to transform to a bct structure at about 120 kbar (Endo et al. 1977, Olsen et al. 1985). This bct structure is also found for protactinium, with a different  $c/a$  ratio. Again, since the 5f electrons are itinerant in Pa, the view that the 4f electrons are itinerant in the dense phases of Ce is supported. The fact that such unusual crystal structures are observed only for high-density cerium and the light actinide metals, seems to provide an important clue for the nature of the Ce 4f states.

Electronic structure calculations by Glötzel (1978), where the 4f states were treated as itinerant, yielded a calculated volume for  $\alpha$ -cerium in acceptable agreement with experiment, and later calculations gave similar results (Pickett et al. 1980, Skriver 1985, Min et al. 1986). In these calculations it was found that the paramagnetic state becomes unstable to ferromagnetism at volumes within the volume-collapse region. However, the observed large volume collapse was not reproduced. Subsequently, the same electron correlation that gives rise to Hund's second rule in atoms and which gives rise to orbital polarization, was implemented approximately in solid-state calculations (Eriksson et al. 1990b, d, 1991a). In such calculations the energies of the atomic orbitals, labelled by the magnetic quantum number,  $m_l$ , become dependent upon their occupation numbers. The atomic orbitals acquire an extra energy contribution equal to  $-L^\sigma m_l E^3$ , where  $L^\sigma$  is the orbital moment of the  $\sigma$  spin channel and  $E^3$  is the Racah parameter. For volumes corresponding to  $\gamma$ -cerium it was found that the energy was minimized when Ce had one filled 4f orbital, with the others empty. For volumes corresponding to  $\alpha$ -cerium, in contrast, the paramagnetic state was stable. The calculated volume collapse was found to be close to the experimental one. In another approach, Boring et al. (1992) applied the Kanamori-Hubbard formalism, in conjunction with energy band calculations, to show that a large value of the Coulomb self-energy,  $U$ , of about 6 eV is necessary to localize a 4f electron in  $\alpha$ -cerium, whereas for  $\gamma$ -cerium the required value of  $U$  is somewhat smaller,  $\approx 5$  eV. The estimated values of  $U$  for Ce are about 5 eV (Johansson 1974, Pickett et al. 1980, Johansson and Mårtensson (1981), suggesting that the 4f electrons are localized in  $\gamma$ -cerium and delocalized in  $\alpha$ -cerium.

In his thorough investigation of the crystal-structure stability of the elemental metals Skriver (1985) also considered the cerium problem. He pointed out that itinerant 4f electrons were crucial for determining the high-pressure phase diagram of cerium. Subsequent treatments (Wills et al. 1991, Eriksson et al. 1992) have fully confirmed this view. The full-potential muffin-tin orbital technique (Wills and Cooper 1987, Price and Cooper 1989, Wills unpublished) used by Wills and co-workers is fully relativistic and employs no shape approximation to the charge density. With the f states treated as part of the conduction bands, the total energies of fcc, bct and  $\alpha$ -uranium were calculated as functions of the volume. At zero pressure (fig. 39) they found the fcc structure to be stable with an equilibrium volume of  $28.1 \text{ \AA}^3$  – in good agreement with experiment. At a volume of  $24.2 \text{ \AA}^3$  the fcc curve is intersected by the  $\alpha'$  curve. The associated volume collapse was calculated to be quite small, and the zero-temperature pressure for the  $\alpha$ - $\alpha'$  transition was found to be about 70 kbar. At an even smaller volume of  $20 \text{ \AA}^3$  the  $\alpha'$ -phase was found to transform to the bct phase, the corresponding pressure being 150 kbar. Therefore, if – and only if – the 4f

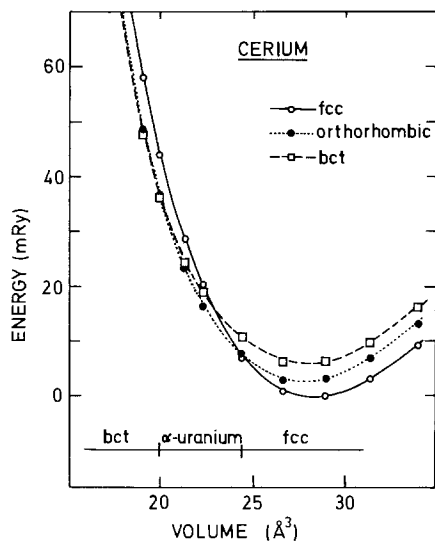


Fig. 39. The calculated total energy of Ce metal as a function of volume for the fcc, bct and orthorhombic structure (after Eriksson et al. 1992).

electrons are included in the conduction bands, all the observed structures are obtained.

Pr has also been observed to undergo a relative volume collapse, of 10% at 200 kbar (Mao et al. 1981, Smith and Akella 1982, Grosshans et al. 1983), in which the crystal structure changes from fcc to orthorhombic. The next lanthanide, neodymium, has been observed to undergo a transformation from fcc to orthorhombic at 390 kbar (Grosshans and Holzapfel 1984), presumably also involving a substantial volume reduction. The connection with the phase diagram of cerium is suggestive, and calculations by Eriksson et al. (1990d) support the picture of a change from a localized  $f^n$  state to an itinerant  $f$  state, in much the same way as for  $\gamma$ - $\alpha$  cerium. The main difference is that for Pr and Nd the electronic phase change is accompanied by a crystallographic transformation. Similar phase changes have been observed for the heavy actinides Am, Cm, Bk and Cf, where the collapsed phase has an orthorhombic crystal structure, at least for Am and Cf (Benedict et al. 1985, Benedict 1987). Calculations by Skriver et al. (1980) for Am and by Johansson et al. (1981) for Cm suggest the same type of  $f$ -delocalization for these elements as for the light lanthanides. All the collapsed phases, whether for light lanthanides or for actinides, attain an orthorhombic structure. The implication is that itinerant  $f$ -states favour distorted structures, whereas  $d$  states do not, and quantitative assessment of this phenomenon has begun (Wills and Eriksson 1992, Eriksson and Wills 1992).

The problem of  $\alpha$ -cerium raises the question of whether or not “ $\alpha$ -like” cerium compounds exist. Studies of  $\text{CeFe}_2$ ,  $\text{CeCo}_2$ ,  $\text{CeNi}_2$  and  $\text{CeCo}_5$  are discussed in sect. 5.4. Similarly, the cerium-nickel compounds  $\text{CeNi}$ ,  $\text{CeNi}_2$  and  $\text{CeNi}_5$  have been studied by Nordström et al. (1992b). Weschke et al. (1991) have done inverse-photoemission experiments with  $\text{CeRh}_3$  and observed a  $4f$  signal at 1.5 eV and a  $5d$  signal at 3.4 eV above the Fermi energy. Both of these features are in good agreement with calculations in which the  $4f$  states are treated as part of the band structure.

#### 4.9. Surfaces

In contrast to the case of bulk properties, very few *ab initio* calculations have been done for lanthanide or actinide surfaces. Although there has been much interest in the valence state at the surface of lanthanides, this has been treated by other means than first-principles electronic-structure calculations (Johansson and Mårtensson 1987). However, Hong et al. (1992) considered the Sm surface and applied the FLAPW method to a five-layer fcc (100) slab in order to investigate theoretically the possibility of a valence change relative to the bulk. Although the results were not conclusive, this demonstrates the type of problems which can now be addressed by means of the present computational techniques.

Wu and Freeman (1991) and Wu et al. (1991) considered the hcp Gd(0001) surface by essentially the same method. They calculated a surface layer *expansion* of 6% coupled antiferromagnetically to the underlying bulk ferromagnet. This is probably the first prediction of a surface-layer expansion on a pure-metal surface. These authors suggest it originates from the fact that Gd has a relatively low bulk modulus combined with a magnetic pressure due to the  $4f^7$  moment. In the calculations they also found a surface resonance state for the majority spin bands, which has been confirmed experimentally by Li et al. (1991).

Eriksson et al. (1991b) treated the fcc (100) surface of  $\alpha$ -Ce in the paramagnetic state and included the 4f states in the conduction bands. The calculation used a film (five-layer slab) linearized muffin tin orbitals method (Fernando et al. 1986, Ma et al. 1986). From the results they concluded a magnetic instability for the surface layer. Based upon earlier experiences of such Ce instabilities, they suggested that the surface layer of  $\alpha$ -Ce should be  $\gamma$ -like. This prediction was subsequently verified by Weschke et al. (1991) by means of photoelectron spectroscopy experiments. This demonstrates that surface properties can be radically different from those of the bulk. The same type of surface effect has also been seen for  $\alpha$ -like cerium compounds, CeIr<sub>2</sub>, CePd<sub>3</sub> and CeRh<sub>3</sub> (Laubschat et al. 1990), where again the Ce surface atoms show  $\gamma$ -like behaviour. This means that some photoelectron spectroscopy data for  $\alpha$ -like Ce systems should be reanalyzed before spectra representing the bulk can be obtained. Calculations by Eriksson et al. (unpublished), where both spin and orbital polarization are allowed for, explicitly show the  $\gamma$ -like property of the surface layer.

In the same spirit, Eriksson et al. (unpublished) considered the possibility of a similar difference between the bulk and surface for Pu as above for  $\alpha$ -Ce. The main limitation in their work was that for calculational reasons they were compelled to represent  $\alpha$ -Pu by an fcc structure. Nevertheless, the results suggested very different surface and bulk behaviour and that the surface of Pu is  $\delta$ -like (the anomalous fcc phase observed at elevated temperatures for bulk Pu). Photoelectron spectroscopy data on  $\alpha$ -Pu taken by Cox (unpublished) show features which may be rationalized by such a physical situation. It seems significant that the five-layer slab calculation by Eriksson and co-workers yields a central layer which is not bulk-like at all. Instead, a large magnetic moment was obtained, which shows that there is a metamagnetic state for bulk fcc Pu, which for the thin film was induced in the central layer of the slab by the presence of the surface. It would, therefore, be interesting to investigate

the magnetic response of bulk  $\alpha$ -Pu at very high magnetic fields. If the energy of the metamagnetic state were not too high, and the magnetic state were induced, there would be the possibility that a field-induced crystallographic change to the fcc phase could occur.

## 5. Rare earth compounds

The relative scarcity of first-principles theory for lanthanide compounds is due to the difficulty of handling the 4f electrons self-consistently within energy-band theory, especially since most of the interest in the intermetallics concerns their magnetism. Consequently, most early studies have been on yttrium ( $4d^{15}s^2$ ) or lutetium ( $5d^16s^2$ ) compounds (Cyrot et al. 1979, Cyrot and Lavagna 1979, Yamada and Shimizu 1985, 1986, Yamada 1988, Mohn and Schwarz 1985, Szpunar and Wallace 1986, Szpunar 1985, Szpunar and Smith 1990, Coehoorn 1991, Jaswal 1990, Sellmyer et al. 1988). Studies on Y and Lu compounds do, in fact, simulate the conduction-electron band structure of many lanthanide compounds well. The effects of the localized 4f magnetism on the conduction band structure (Brooks et al. 1991a, b, 1992, Nordström et al. 1991a, Hummler and Fähnle 1992) have also been studied, although earlier work seems to have suffered from convergence problems (Malik et al. 1977, Gu and Ching 1987).

### 5.1. Electronic structure

#### 5.1.1. Model considerations

A general picture of the valence electronic structure of compounds of rare earths (which are early transition metals) and late 3d transition metals is shown in fig. 40, where the localized 4f states are not included. The lanthanide (R) contributes 5d, 6s and 6p valence states and the 3d transition metal (M) contributes 3d, 4s and 4p states. Since in the solid the s and p projected orbitals will form broad and rather feature-less free-electron bands, these may be neglected as a first approximation, leaving the 5d and 3d states. In the free atom the energy of the M 3d states lies far lower than that of the R 5d states, as shown on the left in fig. 40. The first

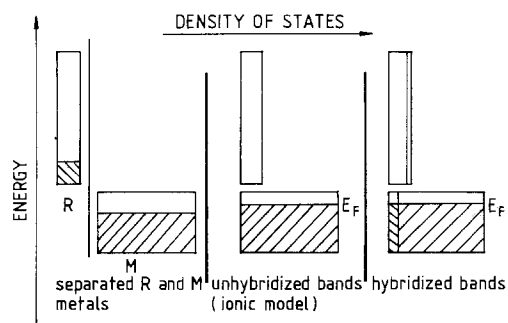


Fig. 40. Model state densities (d bands only), drawn to scale, for early and late transition metals. Occupation is denoted by shading.

approximation for the solid is that electrons flow from the 5d to the 3d states to establish a common Fermi energy, as shown in the middle of fig. 40. The 5d and 3d states then hybridize, yielding the bonding–anti-bonding level scheme illustrated on the right in fig. 40. The bonding bands will obviously be dominated by the 3d states, while the anti-bonding bands will have mainly 5d character. The degree of mixing between the 3d and 5d states depends on the transfer matrix element and on the energy separation between the 3d and 5d levels. Both these quantities may be obtained from energy band calculations. The first depends on the structure constants, eq. (18), and the band-mass potential parameters, eq. (23). The second depends upon the band-position potential parameters, eq. (20). If the energy separation is increased, the mixing will decrease, and the opposite holds when the separation is decreased. Thus one expects two sets of bands, which are conventionally referred to as bonding and anti-bonding bands. There is usually no clear separation in energy between these two parts of the band structure.

It is common practice to discuss electronic structure in terms of the filling of the 3d bands in connection with compounds composed of early and late transition metals. However, as the simple approach above shows, this must be understood as filling of the bonding part of the state density for the compound, and should therefore not necessarily be associated with real transfer of electrons from the 5d states into the 3d states. Actual calculations show that there is hardly any change in the R and M d occupation numbers between the pure elements and the metallic compounds. Charge transfer rapidly modifies the energy distance between the 3d and 5d bands, changing the mixing between them, until self-consistency is achieved. It turns out that the so obtained d occupation numbers differ little from those of the pure elements.

In most of the lanthanide compounds the 4f electrons retain their atomic character in the solid. Therefore the energy location of the 4f states relative to the 5d and 3d state energies is not important. When the 4f electrons remain localized in the compound, they will influence the magnetic properties of the valence electrons through the exchange potential. Since the 4f wave function has limited range, this coupling will take place essentially within the lanthanide atom and mainly with the 5d electrons, which have a larger density and overlap with the 4f states than have the 5p or 5s states (fig. 14). The local exchange interactions are positive and the 4f and 5d spins will align parallel. The strength of the coupling will clearly be dependent upon the number of unpaired 4f spins (eqs. (54) and (55)). Therefore a large 4f spin moment enhances the local 5d spin moments. Since the 5d states in their turn are hybridized with the 3d states, this means that the 4f spin moments couple indirectly to the 3d spin moments.

As a specific example we first consider the case of a non-magnetic 4f configuration, e.g.  $\text{LuFe}_2$ . We assume that the 3d electrons spin-polarize. We also assume, for simplicity, that the magnetization is saturated, i.e. that the high-field susceptibility is vanishing. The energy separation between the bonding and anti-bonding subbands becomes different for the two spin directions, therefore the 3d–5d hybridization is different for majority and minority spins. Hybridization is decreased for the majority bands and there is a decrease of the 5d content. The opposite is true for the minority bands. This has the effect that the spin-up (majority) occupation of the 5d part

becomes less than the spin-down (minority) occupation of the 5d part. Thus, there is a total spin-down 5d moment on the lanthanide atom. The 3d and 5d spin moments are in opposite directions and the system is ferrimagnetic.

For a standard lanthanide system, the localized 4f<sup>n</sup> spin configuration will interact with the surrounding 5d-electron spin cloud by means of local exchange–correlation and this will enhance the total 5d spin-down moment. Therefore the 5d spin-up band will be pushed away further from the majority bonding (3d) band, and the associated hybridization will be further decreased. This means that the local 3d spin-up moment will increase in size. However, since the initial state was assumed to be saturated, the total conduction electron moment is fixed, and only its distribution between the R and M atoms changes. Thus, although the individual 5d and 3d moments both increase in size, there is for this situation an exact cancellation between the two 4f spin induced changes of the local moments.

Thus the presence of the 4f spin moment induces a redistribution of the spin moment between the lanthanide and M sites, while the total conduction electron moment remains constant. This cancellation between the two 4f-induced extra spin moments also occurs to a large extent for non-saturated magnetism, and explains the successful interpretation of experimental magnetic moment data in terms of a constant conduction electron spin moment and an atomic 4f<sup>n</sup> magnetic moment for a series of compounds.

The 4f states are rarely part of the conduction band structure, but in cases where this is so, the model may be extended, in which case it connects to light actinide systems which we shall review in sect. 6. In CeFe<sub>2</sub>, for example, the standard lanthanide model must be abandoned, the 4f states being included in the conduction bands since 4f–3d hybridization is important. The model system, fig. 40, should now include the 4f states at the Fermi energy. The 4f states polarize and the total conduction electron moment for this saturated magnet must decrease by about one  $\mu_B$ , simply as a consequence of the required band filling. In the same way as above for the 5d electrons, due to the difference in 3d–4f hybridization between the spin-up and spin-down states, there will be an induced 4f spin moment in the direction opposite to the 3d moment. In contrast, in the standard model the localized 4f electron would be in a  $j = \frac{5}{2}$  state with a total moment antiparallel to the spin moment. Thus the active participation of the 4f electron in the band formation means that the total magnetic moment will not be in accordance with the standard model value, but will appear anomalous when compared with other homologous lanthanide compounds, even when the relatively small induced orbital moment in the conduction bands is included (Eriksson et al. 1988a). Since the number of M 3d electrons is practically constant, and since it is also clear from fig. 40 that the number of 3d spin-up electrons is reduced due to the 4f–3d hybridization, the M 3d moment is also reduced. This reduction and the reduction of the total conduction-electron spin moment are the most likely reasons why the Curie temperatures of many of the cerium intermetallic ferromagnets are anomalously low relative to the corresponding standard lanthanide systems.

For more complicated lanthanide–transition metal intermetallic systems than the Laves-phase compounds a picture very similar to the one above should apply. Even

for the technologically important class of materials,  $R_2Fe_{14}B$ , the notion of 3d–5d hybridization is an essential ingredient for the understanding of its behaviour. This is again the mechanism which governs the 4f–3d coupling, an important quantity for the total intrinsic magnetic anisotropy of these compounds.

### 5.1.2. Calculated electronic structure

A more realistic overview of the *conduction-band* electronic structure of rare earth transition metals compounds has been obtained from studies of yttrium–transition metal compounds. Yttrium forms Laves-phase compounds with Mn, Fe, Co and Ni. For compounds of yttrium with Mn, Fe, and Co, no local 4f-moments need be considered, and the magnetism of the conduction bands may be studied in isolation. Of these systems  $YCo_2$  (C15) is a strongly exchange-enhanced paramagnet,  $YNi_2$  (C15) is a weak paramagnet with a temperature-independent susceptibility,  $YFe_2$  (C15) orders ferromagnetically and  $YMn_2$  (C15) is antiferromagnetic at low temperatures. A metamagnetic transition with a critical field varying from 90, 100 to 350 T has been predicted (Cyrot et al. 1979, Schwarz and Mohn 1984, Yamada and Shimizu 1985) for  $YCo_2$ . The electronic structure and the magnetic moment of  $YFe_2$  has also been calculated (Yamada et al. 1984, Mohn and Schwarz 1984) and agrees well with measurements (Buschow and van Stapele 1970). Since yttrium compounds with Fe are magnetic whereas with Co they are non-magnetic, the pseudobinary alloys  $Y(Fe_{1-x}Co_x)_2$  offer the possibility of studying the electronic structure, the magnetism and its effect upon volume as a function of concentration.

These alloys have been simulated in calculations (Eriksson et al. 1988b, 1989b) by constructing ordered compounds with the same stoichiometry intermediate between  $Y_2Fe_4$  and  $Y_2Co_4$  – i.e. the ternary compounds  $Y_2(Fe_3Co)$ ,  $Y_2(Fe_2Co_2)$  and  $Y_2(FeCo_3)$ . The band structure for the five ordered compounds is found to be very similar (fig. 41), with a band originating from 3d orbitals lying below the more broad yttrium 4d band. The separation between these two features is very small, and consequently the hybridization between them is very strong. As cobalt is substituted for iron, valence electrons are added and the 3d band fills. However, the overall features of the paramagnetic state densities remain intact, suggesting that a rigid-band model is a good approximation.

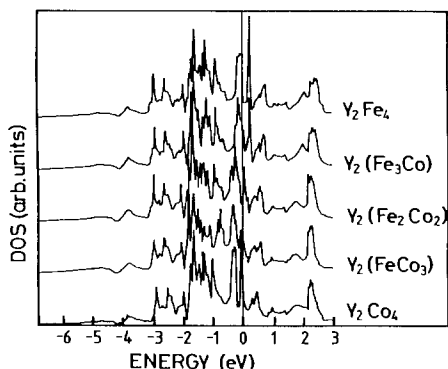


Fig. 41. The calculated state densities of the compounds  $Y_2Fe_4$ ,  $Y_2(Fe_3Co)$ ,  $Y_2(Fe_2Co_2)$ ,  $Y_2(FeCo_3)$  and  $Y_2Co_4$  (see text for details). The zero energy is the Fermi energy (after Eriksson et al. 1989b).

The calculated total moments (Eriksson et al. 1988b, 1989b) of the ordered compounds  $Y(Fe_{1-x}Co_x)_2$  with  $x = 0.0, 0.25, 0.5, 0.75, 1.0$  are compared with the measured moments of the real alloys (Hilscher 1982a, b) in fig. 42. At each end of the concentration range the calculated paramagnetic state for  $YCo_2$  and the ferromagnetic moment of  $YFe_2$  are in agreement with established theory and experiment (Yamada et al. 1984, Mohn and Schwarz 1984, Buschow and van Stapele 1970). The trend of the total magnetic moment, with a maximum at approximately 30% Co substitution, is also reproduced. The calculations reveal that the maximum in the total moment is due to a maximum in the Fe 3d moment, whereas the Y and Co moments remain more or less constant at  $-0.4\mu_B$  and  $1.3\mu_B$ , respectively, as a function of concentration for  $x < 0.8$ . The explanation for antiparallel alignment of the moment at the yttrium site has been given in sect. 5.1.

The origin of the functional dependence of the measured magnetic moment upon  $x$  (fig. 42) may easily be understood from the simple model state density shown in fig. 40. Since there are four transition metal atoms in a primitive cell, each with ten 3d states, the lower square – the 3d-derived state density – holds a total of 40 electrons, of which approximately 3.2 are calculated to be yttrium 4d electrons. There is therefore room for 36.8 3d electrons per primitive cell, or 18.4 3d electrons/f.u. in these bands – i.e. 9.2 3d electrons/f.u. in the spin-up bands. Since incomplete screening of the valence electrons causes the 3d orbitals to contract, the 3d moment increases with  $x$  in  $Y(Fe_{1-x}Co_x)_2$ , until the majority spin band is filled, where a maximum is followed by a decrease in the moment with  $x$ , since now the minority spin band has to be filled – a Slater–Pauling curve. Therefore the maximum in the 3d moments should correspond to 9.2 electrons in the majority spin band/f.u. The 3d occupation number per formula unit was found (Eriksson et al. 1988b, 1989b) to obey the linear relation  $n_{3d} = 2[6.64(1-x) + 7.74x]$  and, by applying a Stoner splitting to the bands, Eriksson et al. found that there are 9.2 electrons in the majority spin band/f.u. for  $x$  about 0.3.

For  $x < 0.8$  the moment on Co is almost saturated with a majority band occupation of 4.5. The Fe moment is not quite one  $\mu_B$  larger than the Co moment and, therefore, not quite saturated at any Co concentration. Therefore, although the Co moments are *induced* by the Fe magnetism ( $YCo_2$  is a paramagnet), the Co moment is more

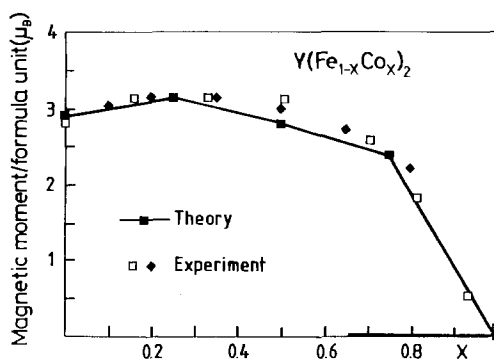


Fig. 42. The total magnetic moment of  $Y(Fe_{1-x}Co_x)_2$ . The thick part of the  $x$ -axis denotes the concentration region where the paramagnetic state is locally stable. The squares and diamonds are the results of experiments by Piercy and Taylor (1968), Steiner and Ortbauer (1974) and Guimares and Bunbury (1973).



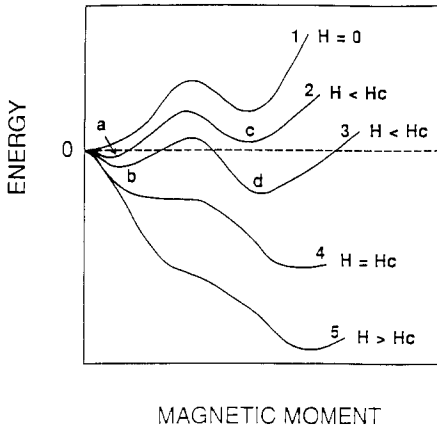


Fig. 43. The total energy of a metamagnetic conduction band system as a function of magnetization, for various values of the applied field.

saturated – which suggests that the induced magnetic state of Co in these alloys is the high-spin metamagnetic state.

The metamagnetism of conduction bands has been the subject of study by Wohlfarth and Rhodes (1962), Shimizu (1964, 1965) and Yamada (1988). The total energy of a metamagnet as a function of magnetic moment is shown schematically in fig. 43 for several values of the applied field. Curve 1 corresponds to  $\text{YCo}_2$  in zero applied field and Schwarz and Mohn (1984) have estimated the critical field (curve 4) above which only the high-moment state is locally stable. Upon removal of the field the high-moment state remains locally stable, although it is not the ground state (curve 1).

The partial M-3d state density for  $\text{YbCo}_2$  (with a trivalent,  $4f^{13}$ , configuration for Yb) for the paramagnetic ground state is shown in fig. 44. It is very similar to the state density of  $\text{YCo}_2$  calculated by Yamada (1988). The Fermi energy lies in a dip of the state density, with a large double peak just below and a somewhat broader peak above it. The criterion for local stability of a metamagnetic state is given in terms of the high-field unenhanced susceptibility,

$$\frac{1}{\chi^0} = \frac{1}{4} \left( \frac{1}{N^+(E_F)} + \frac{1}{N^-(E_F)} \right), \quad (60)$$

by

$$\frac{1}{2} I \chi^0 \geq 1. \quad (61)$$

At a finite splitting of the energy bands in fig. 44, both the spin-up and spin-down state densities become large enough to satisfy this criterion.

The effects of the localized 4f moments on the band structure have been studied in detail for the  $\text{RFe}_2$  (Brooks et al. 1991a, b) and  $\text{RCO}_2$  (Nordström et al. 1991a, b) series by treating the localized 4f states as outer core states. This is done in order to fix the number of 4f electrons to an integer, as in the infinite- $U$  limit of the Hubbard model (Hubbard 1963). Again the number of spin-up and spin-down 4f electrons is an input to the calculation, but, subject to this constraint, the 4f spin densities are calculated self-consistently. The 4f spin densities contribute to the total spin densities,

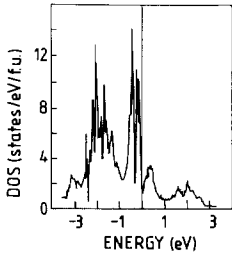


Fig. 44. The partial M-3d state density of  $\text{YbCo}_2$  in the paramagnetic ground state.

and hence to the spin-up and spin-down potentials. In the absence of hybridization between the 4f states and the conduction band states, the interaction between the 4f electrons and the conduction electrons is electrostatic plus local exchange. The problem of how to fix the number of spin-up and spin-down 4f electrons is solved by using the Russel–Saunders coupling scheme for the  $4f^n$  configuration. For the elements Gd–Yb this results in a spin-up occupation of seven and a spin-down occupation which increases by one for each unit increase in the atomic number, starting with zero for Gd.

In fig. 45 we show the calculated total conduction electron spin moment along the series and its decomposition into the 3d and 5d contributions (Brooks et al. 1991a). As expected from model considerations, these two d moments have opposite directions. The individual 5d and 3d moments depend much more strongly upon the

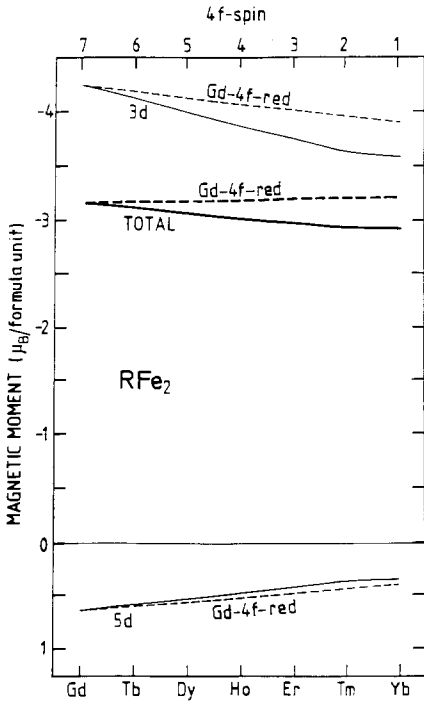


Fig. 45. The calculated conduction-electron spin contributions to the moments of the  $\text{RFe}_2$  series (full lines). A negative spin for the total and M-3d contribution was chosen because they are antiparallel to the R-4f moment and the total moment is therefore positive. The dashed lines marked Gd-4f-red are for  $\text{GdFe}_2$  with the Gd-4f spin moment reduced to that of the corresponding lanthanide – hence the effect of varying volume is removed.

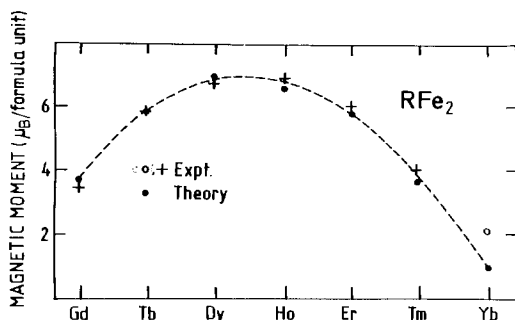


Fig. 46. Comparison between the measured (Clark 1980) and calculated total magnetic moments for the  $RFe_2$  series.

lanthanide than does the total moment. The reason for this is the partial cancellation that occurs between the induced conduction-electron spin moments.

The calculated total moments are compared with experiment in fig. 46. Here we have added the rare earth moment to the calculated conduction-electron moment. Due to the 3d-5d hybridization a significant spin density is produced at the R sites, even when the f moments are zero. This hybridization is believed to be responsible for the important coupling between the 4f and 3d spin directions (Brooks et al. 1991a). The essential point to realize is that in the local spin density approximation the R-4f and R-5d spins are coupled by local exchange interactions to give a parallel spin alignment. The interaction between the R-4f and Fe-3d spins is mediated by the R-5d spin and it aligns the 4f and 3d spins antiparallel.

The metamagnetism of  $YCo_2$  suggests that similar effects should occur in  $RCo_2$  compounds. In  $RCo_2$  compounds the polarizing field at the Co sites arises from polarization of the 5d states by the 4f spin and subsequent hybridization with the 3d states. In calculations by Nordström et al. (1991b) on  $GdCo_2$  and  $TbCo_2$  a high-moment conduction-electron state was obtained (with the moment at the Co site saturated) when the calculations were started with only a 4f moment, corresponding to curve 5 in fig. 43. The large 4f spin polarizes the 5d states enough to, through hybridization with the 3d states, saturate the Co moments, see fig. 47. The calculations were started with only a 4f moment for the compounds  $DyCo_2$ - $YbCo_2$ , the results corresponded to either curve 2 or curve 3 in fig. 43 when a low moment (small unsaturated moment at the Co site) state was obtained, see fig. 47. Thus when the

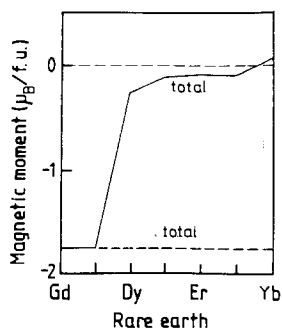


Fig. 47. The total conduction-electron moments of the  $RCo_2$  compounds. When the calculations are started with zero moment on the Co, only a small Co-3d moment is induced for R atoms heavier than Tb (full line). When the calculations are started with a large spin on the Co, the high-moment state remains stable (dashed line).

calculations were started with zero moment on Co, the low-moment state corresponding to a or b in fig. 43 was obtained. Hysteresis in the moment could be obtained by re-starting the calculations with a large moment on the Co, moving to the local minimum at c or d. The calculated moments for these states are also shown in fig. 47. The effective field from the 4f states therefore exceeded the critical field for metamagnetism only for  $\text{GdCo}_2$  and  $\text{TbCo}_2$ .

### 5.2. Magneto-volume effects

The measured lattice constants of the  $\text{Y}(\text{Fe}_{1-x}\text{Co}_x)_2$  system are not linear in the concentration, fig. 48, as they would be according to Vegard's law (Vegard 1921), which states that the volume of a compound or alloy is the sum of the volumes of the constituents with appropriate weighting. For these alloys Vegard's law would be

$$V[\text{Y}(\text{Fe}_{1-x}\text{Co}_x)_2] = (1-x)V[\text{YFe}_2] + xV[\text{YCo}_2]. \quad (62)$$

The lattice constants of paramagnetic  $\text{YFe}_2$  may be estimated accurately from paramagnetic calculations. From the results the lattice constants for the non-magnetic alloys  $\text{Y}(\text{Fe}_{1-x}\text{Co}_x)_2$  according to Vegard's law may be derived and it is these which are plotted in fig. 48. The origin of the deviation from this paramagnetic Vegard's law is the magneto-volume effect (sect. 3.5), and the difference between the measured and Vegard's law volumes in fig. 48 is the magneto-volume expansion. Since there are 20 3d-derived bonding states in these alloys, the change in electronic pressure for the polarized state in terms of the electronic pressure of the paramagnetic state is estimated by modifying eq. (50) to this case

$$3PV_{3d}^{\text{pol}} = 3PV_{3d}^{\text{para}} \left( 1 - \frac{\mu_{3d}^2}{[n_{3d}(20 - n_{3d})]} \right). \quad (63)$$

So, the negative 3d bonding pressure is reduced in magnitude by the 3d moment,  $\mu_{3d}$ . Therefore the volume increases with the moment. The volume increase was calculated to be  $1.75 \text{ \AA}^3$  for  $\text{YFe}_2$  (Eriksson et al. 1988b, 1989b) or a 3.5% relative volume expansion. Eriksson et al. (1988b, 1989b) also calculated both  $dP/dV$  and the change in pressure as a function of moment from eq. (63), and from these the volume change

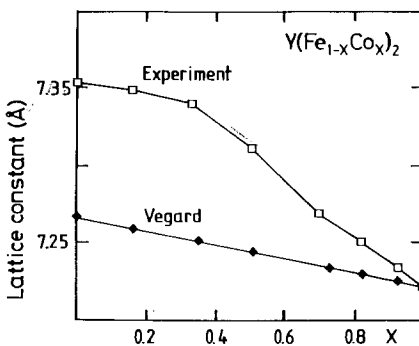


Fig. 48. The measured and estimated (via Vegard's law) lattice constants for  $\text{Y}(\text{Fe}_{1-x}\text{Co}_x)_2$ . The curve labelled Vegard refers to hypothetical paramagnetic compounds.

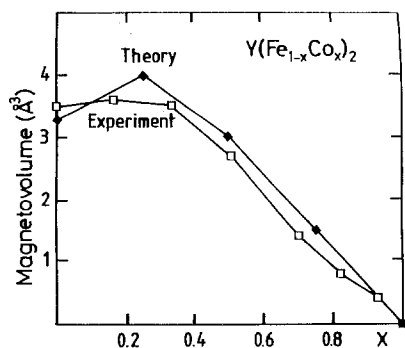


Fig. 49. The calculated magneto-volume effect for  $Y(Fe_{1-x}Co_x)_2$  (marked theory) compared with the same effect estimated from experiments (see text). (After Eriksson et al. 1989b.)

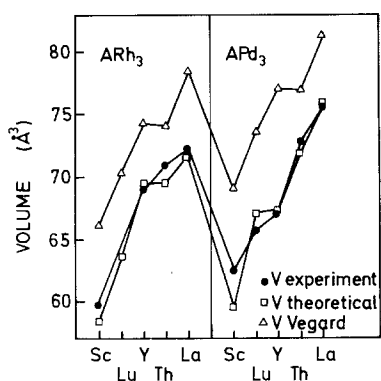


Fig. 50. Experimental and calculated volumes of  $MRh_3$  and  $MPd_3$  ( $M = Sc, Y, Lu, Th$  and  $La$ ). Also shown are the volumes obtained from Vegard's law.

due to the moment. The results are compared with experiment (the difference between the two curves in fig. 48) in fig. 49. The largest magneto-volume effect occurs for the largest moment, as may be seen by comparison with fig. 43. It was also suggested by Eriksson et al. (1988b, 1989b) that deviations from Vegard's law in other yttrium or rare earth alloy systems, e.g.  $Er(Fe_{1-x}Co_x)_2$ , are due to the magneto-volume effect.

The particular stability of compounds of early and late transition metals means that their volumes do not, in general, obey Vegard's law very well. Figure 50 is a plot of the volumes of the  $RRh_3$  and  $RPd_3$  series compared with the volumes according to Vegard's law. Vegard's law always overestimates the volume, because the large cohesive energy gained in compound formation when the bonding states originating from the late transition metal bands are filled, is accompanied by volume contraction. The volumes evaluated from equation of state calculations by Eriksson et al. (1989a) are also shown in the figure and they reproduce the experimental data very well.

### 5.3. Cerium compounds

The cubic  $CeM_2$  Laves-phase intermetallic compounds ( $M = Fe, Co, Ni$ ) have anomalously small lattice constants compared with those of the corresponding compounds of all other rare earths. This is illustrated in fig. 51, where we have plotted the lattice constants of the trivalent rare earth  $RM_2$  compounds taking Gd and Pr

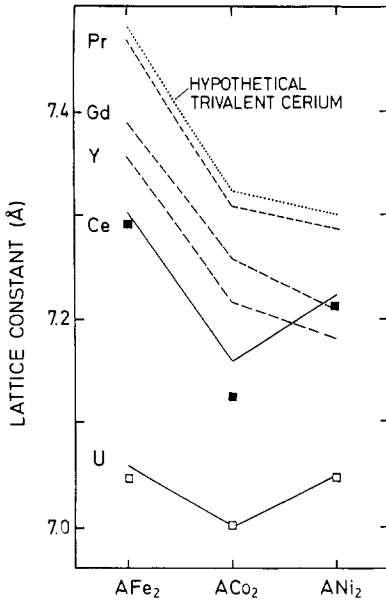


Fig. 51. The full and dashed lines connect experimental lattice-constant data for  $AM_2$  systems ( $A = U, Ce, Y$  and  $Gd$  and  $M = Fe, Co$  and  $Ni$ ). The squares are the calculated lattice constants for  $CeM_2$  and  $UM_2$ .

as examples, and including “trivalent cerium” which was extrapolated from data for the trivalent rare earths. The lattice constants decrease monotonically from  $RFe_2$  to  $RCO_2$  to  $RNi_2$ , and they do for the  $YM_2$  compounds. Also plotted are the lattice constants of the  $CeM_2$  and  $UM_2$  series, both of which are anomalous, with a minimum at  $ACo_2$  (Eriksson et al. 1988a). The lattice constants of the  $CeM_2$  compounds are considerably smaller than would be expected for a standard localized  $4f^1$  configuration. Their Curie temperatures are also low in comparison with the other isostructural lanthanide compounds, such as the corresponding praseodymium compounds. In addition, the magnetic moments deviate from the values one would expect for normal trivalent ( $f^1$ ) ions at the cerium sites.

Self-consistent calculations (Eriksson et al. 1988a) on the  $CeM_2$  ( $M = Fe, Co$  and  $Ni$ ) cubic Laves-phase systems, where the  $4f$  states were treated as part of the conduction-electron complex, have shown that their peculiar lattice-constant trends can be explained. There is a minimum in the lattice constant for  $CeCo_2$  – in contrast to the trivalent  $RM_2$  systems, where the lattice constant decreases monotonically from  $RFe_2$  to  $RNi_2$ . Previously the volume anomaly between  $CeCo_2$  and  $CeNi_2$  was explained in terms of a valence change from 4 to 3.4 (Oliviera and Harris 1983, Scoboria et al. 1984). However,  $L_{III}$ -edge measurements (Weidner et al. 1985) indicate a constant valence of about 3.3 across the  $CeFe_2$ – $CeNi_2$  series. Eriksson et al. (1988a) found a  $4f$  occupation number of about 1.15 for the three compounds, in agreement with the latter observations, and explained the volume anomaly quantitatively in terms of  $3d$ – $4f$  hybridization, which leads to an earlier filling of the bonding bands compared with when the  $4f$  electrons are localized.

The theory suggests that only  $CeFe_2$  should to be a magnet, in agreement with experiment. From a spin-polarized calculation (Eriksson et al. 1988a) for  $CeFe_2$

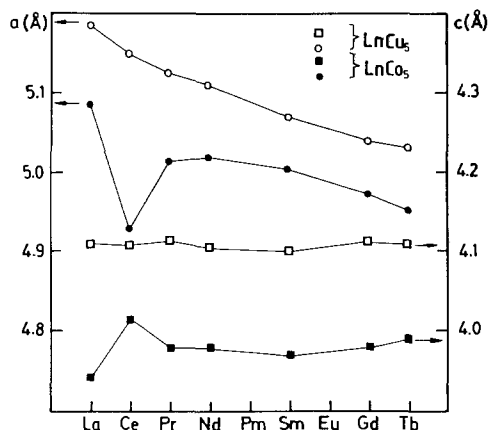


Fig. 52. The measured hexagonal lattice constants,  $a$  (circles) and  $c$  (squares), along the  $\text{RCo}_5$  (filled circles and squares) and  $\text{RCu}_5$  (open circles and squares) series ( $R = \text{La-Tb}$ ). (After Nordström et al. 1990.)

a total spin moment of  $2.16\mu_{\text{B}}/\text{f.u.}$  was obtained. The calculated total conduction-electron moment for  $\text{GdFe}_2$ , was  $3.15\mu_{\text{B}}/\text{f.u.}$  (Brooks et al. 1989). So the *conduction electron spin moment* is  $1\mu_{\text{B}}/\text{f.u.}$  less in  $\text{CeFe}_2$  than in  $\text{GdFe}_2$ , which agrees with our model considerations above. It is not unreasonable to assume that if the 4f states were removed from the conduction electron states in  $\text{CdFe}_2$  and placed in the core, the spd ferromagnetism would be essentially saturated and the conduction electron moment would be about  $3.1\text{--}3.2\mu_{\text{B}}/\text{f.u.}$ , as for  $\text{GeFe}_2$ . When the 4f electrons are itinerant a 4f electron is transferred from the core to the conduction band states. Since the magnet is assumed to be saturated, this extra conduction electron must enter the spin-down states, thus reducing the total moment by  $1\mu_{\text{B}}/\text{f.u.}$  This is what was calculated self-consistently for  $\text{CeFe}_2$ .

Of course, the real situation is not quite as simple as a fully saturated magnetic state would suggest, but the main reason for the decreased spin moment in  $\text{CeFe}_2$  originates from the effect of one additional conduction electron. Notice that this is not a valence transition from a trivalent state (where the 4f electron is in the core) to a tetravalent state in the traditional sense, although it is true that the number of cerium valence electrons is three when the 4f electron is in the core and four when the 4f electron is treated as one of the conduction electrons. The point is that in the first case the 4f state is treated as inert and in the second case as part of the bonding complex built up from hybridizing the s, p, d and f conduction electron states, while in the conventional meaning of a tetravalent state one would have only s, p and d conduction-electron states. Put another way, it is not the 4f *occupation number* that changes, but the *nature* of the 4f state. This change in nature is a Mott transition within the 4f configuration (Johansson 1974).

The trend in the lattice constants of the hexagonal  $\text{RCo}_5$  compounds (fig. 52) with the  $\text{CuCo}_5$  structure is also anomalous for  $\text{CeCo}_5$ . Calculations (Nordström et al. 1990) for the ferromagnet  $\text{CeCo}_5$  yielded results similar to those for  $\text{CeFe}_2$ , namely a 4f spin moment of opposite sign to the cobalt spin moment.  $\text{LaCo}_5$  was used as reference system and it was found that its cobalt moment is larger than in  $\text{CeCo}_5$ . This reduction for  $\text{CeCo}_5$  is caused by the hybridization between the Ce-4f and the Co-3d

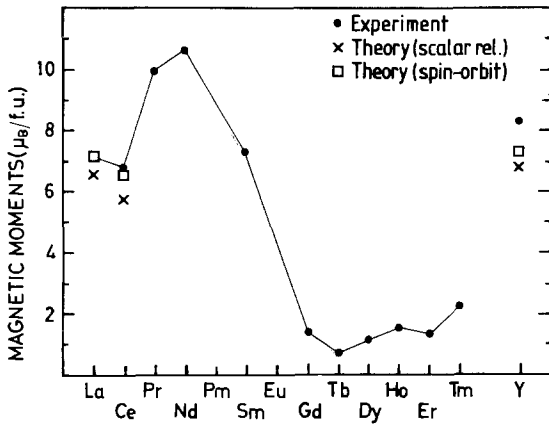


Fig. 53. Experimental (filled circles) and calculated magnetic moments (crosses and squares) per formula unit for the  $\text{RCo}_5$  ( $\text{R} = \text{La-Tm}$ ) series and  $\text{YCo}_5$ .

states, which induces a 4f spin moment antiparallel to the cobalt moment *and* reduces the cobalt moment. Therefore the calculations give a total magnetic spin moment which is less for  $\text{CeCo}_5$  than for  $\text{LaCo}_5$ . Such a moment reduction is actually observed experimentally (Buschow 1977, 1979), and is the opposite of what would be expected for a localized  $4f^1$  cerium configuration in this compound. This is again evidence for a system with itinerant 4f states. It is also interesting to note that the Curie temperature (Buschow 1977, 1979) for  $\text{CeCo}_5$  is anomalous, since it is about 200 K less than would have been expected from a comparison with the other  $\text{RCo}_5$  compounds. If one again assumes, as for the  $\text{RFe}_2$  systems, that the  $\text{RCo}_5$  compounds have an essentially saturated ferromagnetic moment, the extra electron in Ce (compared to La) must enter the spin-down band and the spin moment should decrease by about  $1\mu_{\text{B}}/\text{f.u.}$ , which is nearly the case. In fig. 53 we compare the calculated moments with experiments (Alameda et al. 1981, Velge and Buschow 1968, Gupta et al. 1984) for  $\text{LaCo}_5$ ,  $\text{CeCo}_5$  and  $\text{YCo}_5$ . As can be seen, the calculations reproduce the observed difference in moments between  $\text{LaCo}_5$  and  $\text{CeCo}_5$  well.

## 6. Actinide compounds

### 6.1. 5f-ligand hybridization, electronic structure and volume

The calculated state densities of the three typical uranium NaCl-type compounds UC, UO and UN are shown in fig. 54. Although UO does not exist, it is used for illustrative purposes since oxygen lies in the same row of the periodic table as C and N, and is representative of the chalcogenides. In UO there is a gap between the valence and conduction band of just less than 2 eV, whilst most of the 5f-projected state density lies close to the Fermi energy with an admixture in the valence band, which, although relatively small, is important in any description of the chemical bonding. The same general picture describes any of the uranium monochalcogenides, of which the densities of states may be obtained by scaling the state density of UO



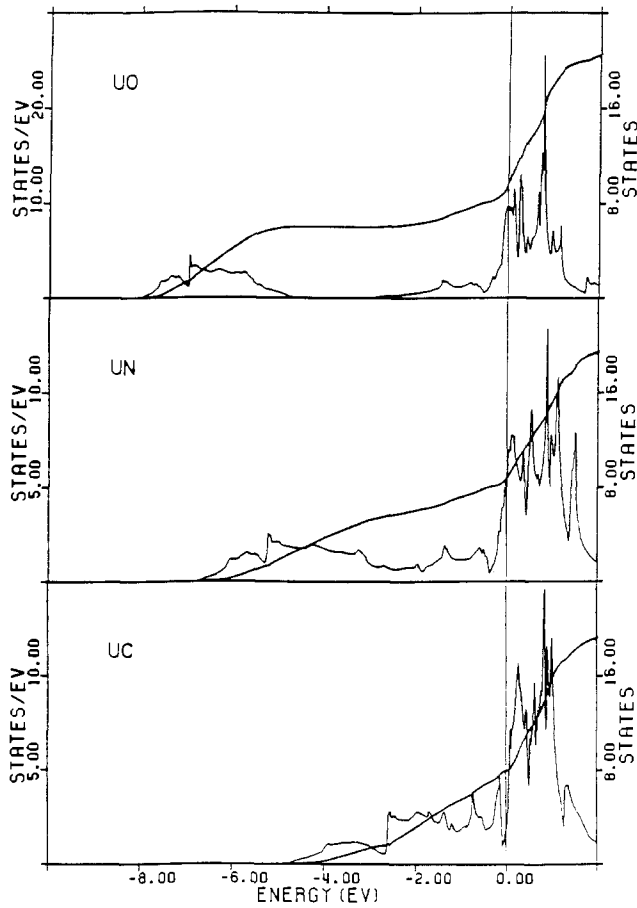


Fig. 54. Total density of states and number of states functions for UC, UN and UO. The number of states function is monotonically increasing. The zero in energy is the Fermi energy.

to allow for the change in lattice constant. In UN there is no gap between the valence and conduction band – and the valence bands of all of the uranium monopnictides lie about 2 eV closer to their Fermi energy than they do in the monochalcogenides. The *f* admixture in the valence band increases as the *f*–*p* bond strengthens.

In UC the *f*–*p* covalent bond is even stronger. There is no gap and the partial 5*f* state density has a long tail extending from the Fermi energy into the valence band. The 2*p* state density has a tail around the Fermi energy. The state density at the Fermi energy decreases from UO to UN and from UN to UC. Therefore, not surprisingly, UC does not order magnetically.

The zero-temperature equations of state, eq. (37), of the three compounds and other NaCl-type uranium compounds have been calculated by Brooks (1984b, c, d) and Brooks et al. (1984), and are shown in fig. 55. The equilibrium lattice constants, evaluated directly from fig. 56, are within 3% of the measured values. UN is correctly calculated to have the smallest lattice constant. The magnitude of the partial 5*f* contribution to the electronic pressure is largest in UN and smallest in UO, but is significant in all three compounds. The electronic partial 5*f* pressure corresponding

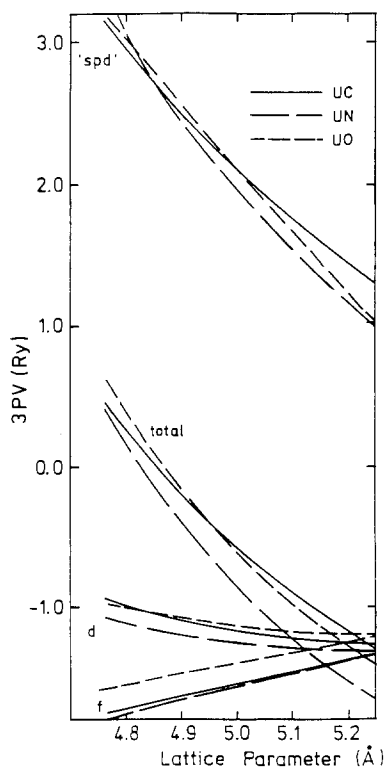


Fig. 55. The equations of state of UN, UC and UO. The curves labelled "total" are the equations of state. The uranium d and f contributions are also shown. The curves labelled "spd" are the contributions from all other electrons (i.e. all s and p contributions plus the contribution of the d electrons on the anion plus Madelung contributions).

to  $3PV = 1.6 \text{ Ry}$  is about 40 GPa, which is very large. In fact, the 5f electronic pressure in these compounds is comparable with that in uranium metal. However, in contrast to the metal, it arises from both cation-cation  $f-f$  and cation-anion  $f-p$  bonds.

UN has a larger bulk modulus than UC since the magnitude of the (negative) 5f pressure is greater, which decreases the equilibrium volume and increases the slope of the equation of state through the "sp" contribution.

The lattice constants of the NaCl-type monochalcogenides and pnictides were evaluated by Brooks (1984b) from calculated equations of state similar to those shown in fig. 55, and the results are compared with experiment in fig. 56. The agreement between theory and experiment is at least good enough (always within 3%) to show that the 5f electrons are involved in the chemical bonding, since removal of the 5f electronic pressure would increase the lattice constants by more than 7%. The bulk moduli were also evaluated by Brooks (1984b, c, d) by numerical differentiation of the calculated equations of state, and are compared with experiment in fig. 57. The calculated bulk moduli did not appear to be in good agreement with the measurements available at the time, but subsequent experiments have tended to converge towards the theory (fig. 57).

The trend in the lattice constant of a given chalcogenide or pnictide across the actinide series differs from the trend for the elemental metals in that the dip in the

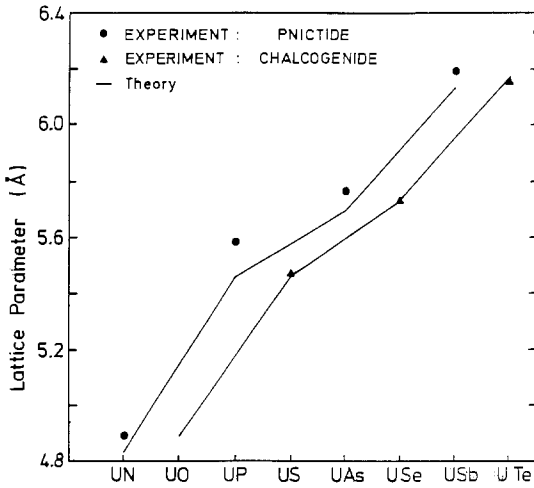


Fig. 56. The measured (filled triangles and circles) and calculated (indicated by full line) lattice constants of the uranium mono-chalcogenides and monpnictides.

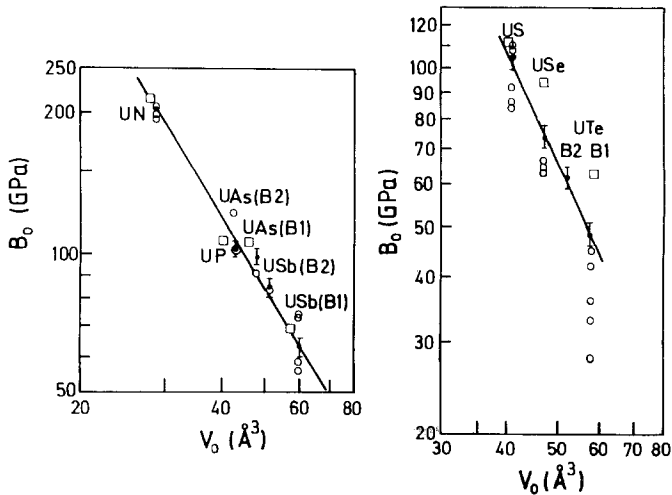


Fig. 57. The calculated bulk moduli (open squares) of the uranium mono-chalcogenides (right) and monpnictides (left) compared with measurements. The open circles indicate data from measurements by Holden et al. (1982), Vedel et al. (1986), Neuenschwander et al. (1984), Buyers et al. (1983), Jackman et al. (1986), Oisen et al. (1984) and DuPlessis et al. (1985) for the chalcogenides and from Guinan and Cline (1972), Padel et al. (1970), Van Doorn and DuPlessis (1977), Fournier et al. (1980), Léger et al. (1986, 1988), Stirling et al. (1983) and Neuenschwander et al. (1986) for the pnictides. More details of the measurements are given by Gerward et al. (1989) and Olsen et al. (1989), from which the filled-circle data points are taken.

lattice constant is moved towards the beginning of the series. This has been attributed to the effect of (cation)  $5f$ -(anion)  $p$  hybridization (Brooks and Glötzel 1980, Brooks et al. 1984), and may be readily explained. The approximate form of the potential function, eq. (41), must be modified for compounds where a particular atom type

does not fill space. Equation (41) becomes

$$P_T(E) = \frac{(E - C_T)}{\Delta_T}, \quad T = t, l, \quad (64)$$

where  $l$  has been replaced by  $T = t, l$ , where  $t$  is the atom type, and eq. (27) has been used with the bandwidth parameter redefined as

$$\Delta_T = \frac{v_t^{(2l+1)/3}}{\mu_T S_t^2}, \quad (65)$$

where  $v_t$  is the fractional volume,  $V_t/V$ , of the unit cell occupied by an atom of type  $t$ . Here  $S_t$  is the Wigner–Seitz (or atomic sphere) radius of a type- $t$  atom,  $\mu_T$  is the band mass of a type  $T$  atomic sphere orbital and  $C_T$  is the centre of the unhybridized  $T$ -band.

With eq. (64) for  $P_T(E)$  eq. (18) reduces to an eigenvalue problem with Hamiltonian matrix

$$\mathcal{H}_{QQ'} = C_T + \Delta_T^{1/2} S_{QQ'} \Delta_T^{1/2}. \quad (66)$$

The bandwidths,  $W_T$ , may easily be estimated from this Hamiltonian once the potential parameters and structure constants are known. For UN, for example, we find the following bandwidths

$$W_f = 70 \text{ mRy}, \quad W_d = 680 \text{ mRy} \quad \text{for U and} \quad W_p = 370 \text{ mRy} \quad \text{for N.}$$

A model, rectangular, unhybridized state density for an NaCl-type pnictide, with the dimensions appropriate to UN and bandwidths converted to eV, is sketched in fig. 58. The bands have been positioned at the band centres. In LDA the rectangular densities of states must be populated by the available valence electrons according to Fermi statistics. Uranium mononictides have nine valence electrons (6 from uranium and 3 from the anion). Therefore, in fig. 58, the anion p band is filled and the three remaining electrons go into the uranium f band. Thus, the neglect of cation–anion valence electron hybridization leads to an ionic model with an  $N^{3-}$  ion, a  $U^{3+}$  ion, an f band at the Fermi energy containing about two electrons, and an almost empty d band. Bonding, in this approximation, arises from a metallic f–f bond and a Madelung contribution. If the f electrons were localized, the metallic f–f bond would also disappear, leaving a magnetic insulator bound solely by the Madelung term.

The diagonal ( $tl$ ) blocks of the structure constants are responsible for the dispersion of the unhybridized bands. Hybridization arises from the off-diagonal blocks of the structure constants,  $T \neq T'$ , in eq. (66). Hybridization leads to repulsion between the bands and to transfer of charge between them. The repulsion between the two bands, in the limit of weak hybridization (Andersen et al. 1979, Brooks et al. 1984), gives rise to a change,  $\delta_T$ , in the average band position of

$$\delta_T = \frac{1}{N_T} \langle E^2 \rangle_{TT'} \frac{\Delta_T \Delta_{T'}}{C_T - C_{T'}}, \quad (67)$$

where  $\langle E^2 \rangle_{TT'}$  is the second moment of the hybridization structure constants. The

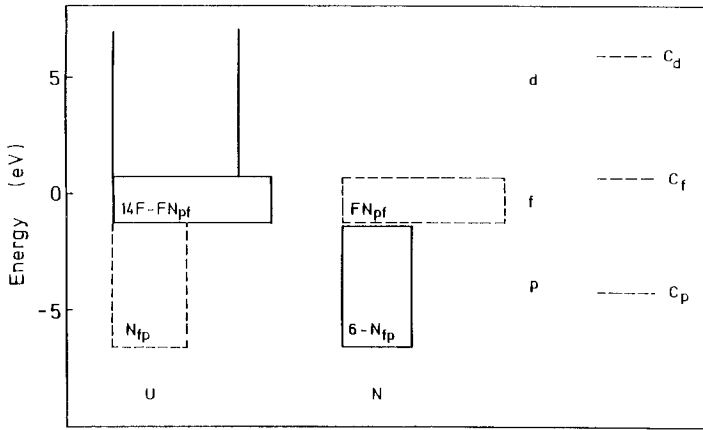


Fig. 58. Unhybridized model densities of states for UN, with uranium on the left and nitrogen on the right. In ascending order: nitrogen valence band; f band tied to the Fermi energy; the d conduction band. The Fermi energy is at zero on the energy scale. The unhybridized band centres,  $C_b$  are shown on the right. This unhybridized model corresponds to the fully ionic model (see text). Also shown are hybridized model densities of states for UN. The full rectangles are the original unhybridized densities of states. The dashed rectangles are the additional projected densities of states due to hybridization. The electron transfer, in terms of the fractional occupancy ( $F$ ) of the unhybridized f-band, is shown.

shift is proportional to the product of the bandwidths and inversely proportional to the separation between the band centres. The number of electrons with local  $T'$  character to be found in what was originally a filled  $T$  band is

$$N_{T'T} = \frac{2\delta_T N_T}{C_T - C_{T'}} \quad (68)$$

The electron transfer from a partially filled band is obtained by multiplying  $N_{T'T}$  by the fractional occupation of the  $T$  band. The purely ionic model is transformed by the latter two equations into a model containing a bonding charge that reproduces the essential features of the electronic structure of NaCl-type compounds when the hybridization is reasonably weak. Whereas the atom and angular-momentum projected densities of states in the unhybridized model arose simply from the  $T$  unhybridized bands, they now contain additional parts due to hybridization with the  $T'$  bands. Dashed lines have been added to complete the hybridized density of states in fig. 58. The number of electrons transferred between the atoms by this interaction is estimated from eq. (68) to be, with UN as example,

$$N_{fp} = 0.97, \quad N_{dp} = 1.99, \quad FN_{pf} = 0.14, \quad FN_{df} = 0.26,$$

where  $xy$  denotes transfer from  $y$  to  $x$  and we have restricted ourselves to the cation d, f and anion p interactions for which the weak hybridization approximation is good. Here  $F$  is the fractional occupation of the unhybridized f band ( $= 2/14$ ). The valence p band now contains about three electrons on the nitrogen, the remaining three having been transferred to the uranium states with local d or f character. At

the top of the valence band, tied to the Fermi energy, is an f band containing about 2.5 f electrons with local cation f character and a small number of electrons with local anion p character. The net charge transfer out of the unhybridized anion p band arises because it was filled and the charge transfer is proportional to the original fractional occupation. Similarly, the entire content of the uranium d band is due to hybridization. If the d band were far above the Fermi energy, the denominator of eq. (68) would be large and  $N_{dp}$  smaller, increasing the ionicity as in large-gap insulators such as  $\text{UO}_2$ . Since the f band contains fourteen states, it is always tied to the Fermi energy by Fermi statistics for the Pa–Pu chalcogenides and pnictides when the f electrons are itinerant.

Hybridization also broadens the bands, and the f bandwidth is increased by more than a factor of two by f–p hybridization in UN, but is changed little by f–d hybridization. The f electrons travel through the crystal as much via the anion p states as by direct f–f overlap, and the increase in bandwidth is a direct result of the kinetic energy changes due to these processes. The origin of the effect is the symmetry of the f and p states on neighbouring atoms in an NaCl-type lattice, since it can be traced back to the potential independent structure constants, which contribute to an abnormally large f–p second hybridization moment,  $\langle E^2 \rangle_{pf}$ .

The approximate electronic-pressure formula, eq. (46), is slightly modified for compounds by inclusion of the Madelung contribution, and becomes

$$3PV = \sum n_T \left[ \frac{2(C_T - \varepsilon_{xc})}{\mu_T} + (E_T - C_T)(2l + 1) \right] + U_M, \quad (69)$$

where  $U_M$  is the Madelung contribution (which is just the Madelung energy),  $n_T$  is the number of type- $T$  electrons after hybridization,  $\varepsilon_{xc}$  is the exchange and correlation energy functional at the Wigner–Seitz sphere boundary ( $-600$  mRy) and  $E_T$  is the centre of gravity of the occupied states of type  $T$ . The electron band mass,  $\mu$ , is about 18 for the uranium f states and about 3 for the anion p states.

Equation (69) divides the pressure into contributions from the volume dependence of the band centres (the first term) and the volume dependence of the bandwidth (the second term). The band contribution vanishes for empty and filled bands. Equation (69) may be transformed into a very instructive form by inserting estimates for  $E_f$  and  $E_p$  and evaluating the cation f and anion p contributions to the pressure. The total number of states, per formula unit, in the p and f bands are 6 and 14, respectively. The p band is pushed downwards by an amount  $\delta_p$  by the f band and contains  $6 - N_{fp}$  electrons with local anion p character and  $N_{fp}$  electrons with local cation f character. The f band is pushed upwards by an amount  $\delta_f$  and contains  $f(14 - N_{pf})$  electrons with local cation f character and  $fN_{pf}$  electrons with local anion p character. The lower and upper parts of the projected densities of states (fig. 58) are the bond and anti-bond parts, respectively, and their centres of gravity may be estimated separately. This has been done by Andersen et al. (1979) for transition metal monoxides and by Brooks et al. (1984) for NaCl-type actinide compounds. When these estimates are inserted, eq. (69) reduces, when  $N_{fp} \ll 14$ , to

$$3PV(\text{ff} - \text{bond} + \text{fp} - \text{bond}) = -49f(1 - f)W_f - 10N_{pf}(C_f - C_p)(1 - f), \quad (70)$$

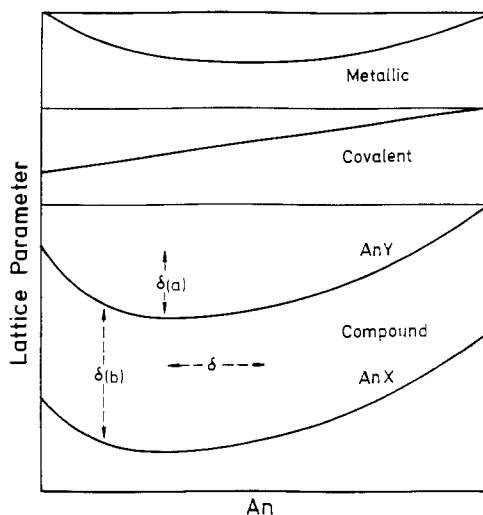


Fig. 59. Schematic theoretical trend in the lattice parameter, to be expected from the simplified  $f$ - $p$  model, in which it was assumed that the  $f$  electrons were not localized. Top: the trend due to the metallic contribution. Middle: the trend due to the covalent ( $f$ - $p$ ) contribution. Bottom: the trend in compounds where both contributions are present. The minimum is shifted away from the centre of the series by  $\delta$ . The depth of the minimum is  $\delta(a)$ , and the difference between the lattice parameters of an  $AnY$  (e.g. USb) compound and an  $AnX$  (e.g. UN) compound is  $\delta(b)$ .

and this is the contribution to the pressure that changes with the cation along an  $AnX$  series. The dependence of the first term upon  $f$  is parabolic with a minimum for a half-filled band, although the parabola becomes skew if the bandwidth narrows as the atomic number increases. This term is the metallic  $f$ -bond contribution and is the same as in the elements, eq. (48). The second term depends linearly upon  $f$ , being zero for a filled band and with maximum magnitude when  $f$  is zero. This is the term due to  $f$ - $p$  hybridization and it is proportional to the number of electrons transferred by  $f$ - $p$  hybridization,  $N_{pf}$ , given by eq. (68). This contribution is actually a maximum when the unhybridized  $5f$  band is *empty*, since the charge transfer is then entirely from  $p$  to  $f$  states. When the  $f$  bands are full, the  $p$  to  $f$  and  $f$  to  $p$  charge transfers are equal and no "covalent" bonding occurs.

The sum of the two contributions is a skew parabola with its minimum moved towards the beginning of the series. Further, the skewness and the distance of the minimum from the centre of the series increase as the strength of  $f$ - $p$  hybridization increases, as shown in fig. 59. A model similar to that summarized in fig. 58 may also be used for actinide transition metal compounds, with  $d$  bands replacing the  $p$  bands of the chalcogenide or pnictide. The resulting state densities are then similar to those in fig. 40, modified to include  $f$  states in the bands, as in sect. 5.3 for cerium compounds.

## 6.2. Vegard's law, magneto-volume and relativistic volume effects

The  $AnRh_3$  ( $An = Th-Cm$ ) series crystallizes in the  $CuAu_3$  structure and the trend in the volume across the series is similar to that of the elements as far as  $URh_3$ , but increases for the  $Np$  and  $Pu$  compounds (fig. 60). There is a volume discontinuity between  $Pu$  and  $Am$  which is only  $4.4 \text{ \AA}^3$ , compared with  $8 \text{ \AA}^3$  for the elements.  $ThRh_3$  and  $URh_3$  are temperature-independent paramagnets,  $NpRh_3$  is highly enhanced, with a specific-heat coefficient of  $95 \text{ mJ/mol K}^2$ , compared with 10 for the  $Th$  and  $U$  compounds, and  $PuRh_3$  is an antiferromagnet (Brodsky 1978).

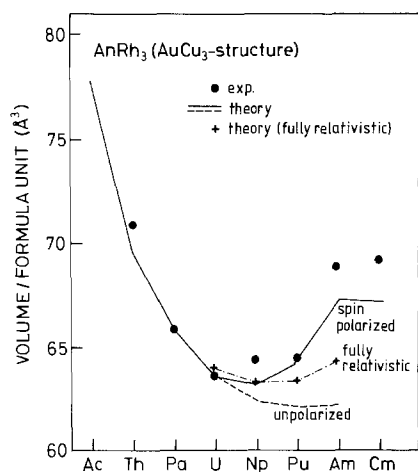


Fig. 60. Measured and calculated molar volumes of the  $AnRh_3$  compounds.

The nature of the 5f-electron states in both  $URh_3$  and  $UPd_3$  has been explored in dHvA experiments (Arko et al. 1985, Ubachs et al. 1986). In  $URh_3$ , a Fermi velocity smaller than the Fermi velocity of Nb indicated significant 5f character of the conduction states. The measured Fermi velocities – only slightly lower in d transition metals – and the agreement between the results of energy band calculations and experiment (Arko et al. 1975, 1985) for the Fermi surface geometries suggest that the 5f electrons are itinerant. Furthermore,  $URh_3$  has a temperature-independent magnetic susceptibility (Nellis et al. 1981), a monotonically decreasing resistance as a function of temperature (Crabtree 1985), with no features indicative of Kondo or crystal field effects, and a photoemission spectrum with 5f state density at the Fermi energy (Arko et al. 1987). In  $UPd_3$ , in contrast, there are two types of orbits (Ubachs et al. 1986) with effective masses of 0.8 and 2.0. These small values of the electron mass, and the low measured value of the linear specific-heat coefficient (Andres et al. 1978), are consistent with a negligible contribution of the 5f state density at the Fermi energy. A crystal-field excitation consistent with an  $f^2$  ground state has been observed in neutron scattering experiments (Buyers and Holden 1985) and the 5f spectral density in photoemission (Baer et al. 1980, Reihl et al. 1982) experiments is centred about 1 eV below the Fermi energy.

Eriksson et al. (1989a) and Johansson et al. (1986) made detailed theoretical studies of both the  $AnRh_3$  ( $An = Th-Cm$ ) and the  $UM_3$  ( $M = Mo-Ag$ ) series, thus changing both the actinide and the ligand. Zero-temperature equation of state (eq. (37)) calculations for the  $AnRh_3$  intermetallic compounds (Eriksson et al. 1989a, Johansson et al. 1986) reproduced the increase in the measured lattice constant for the heavier actinides, Np-Cm. Both the measured and the calculated lattice constants are plotted in fig. 60. The Th-U compounds are paramagnetic, and good results for the lattice constants are obtained from non-polarized calculations. A small moment was obtained for  $NpRh_3$ , although it is an enhanced paramagnet. The magneto-volume expansion for the compounds Pu-Cm, although less than in the elements, is quite pronounced and it improves the calculated lattice constants. The experimental evidence, partic-



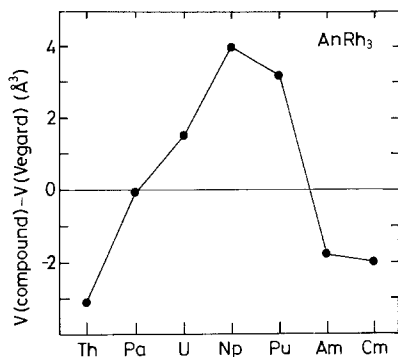


Fig. 61. Deviation from Vegard's law for the AnRh<sub>3</sub> compounds.

ularly the magnetic entropy of PuRh<sub>3</sub>, shows that the 5f electrons in these three compounds are localized. The magneto-volume expansion obtained in spin-polarized calculations reduces the 5f bonding contribution to the equation of state, which occurs when the 5f electrons localize.

One curious feature of the theoretical results was, however, that the volume expansion between PuRh<sub>3</sub> and AmRh<sub>3</sub> was only 4.4 Å<sup>3</sup>/f.u. A possible reason for this may be found by comparing Vegard's law (sect. 5.2) with experiment, as is done in fig. 61, where the difference between the volumes according to Vegard's law and the measured volumes,  $\Delta V$ , is plotted. Figure 61 becomes more enlightening if it is compared with fig. 50. When there is little or no 5f contribution to the bonding, the actinides are early transition metals, and one would expect  $\Delta V$  to be negative, as it is for the rare earth compounds. This is so for Th, Am and Cm – as expected. When the 5f electrons are bonding, both in the elemental metal and the compound an extra factor influences the relative volumes. If the 5f bands are narrower in the compound than in the metal, an amount of metallic 5f bonding, and its concomitant volume contraction, will be lost in the compound. The compounds for which the 5f electrons are bonding in the elemental metal will, therefore, have relatively large volumes, as is observed. This effect is responsible for the fact that  $\Delta V$  is not negative for the compounds PaRh<sub>3</sub> to NpRh<sub>3</sub> and would reduce the volume change between PuRh<sub>3</sub> and AmRh<sub>3</sub>. It would also lead to a reduction in the energy gained in compound formation relative to the elemental metals. However, it is also possible that the 5f electrons in PuRh<sub>3</sub> are localized in a tetravalent 4f<sup>4</sup> configuration.

The effect of changing the ligand in UM<sub>3</sub> compounds on the volumes is shown in fig. 62. Also shown are the calculated volumes for both the paramagnetic and spin-polarized ground states. Both the calculated and measured volumes increase with increasing atomic number of the transition metal since the anti-bonding orbitals become filled (Ru has a more than half-filled d shell). However, the calculated volume of UPd<sub>3</sub> is too small – even for the spin-polarized solution. The calculated state densities for these compounds (Eriksson et al. 1990a) are shown in fig. 63. The 5f states in UPd<sub>3</sub> lie in a gap between the bonding and anti-bonding d states. This reduces the f–d hybridization in UPd<sub>3</sub> (as well as the shielding of f electrons by d

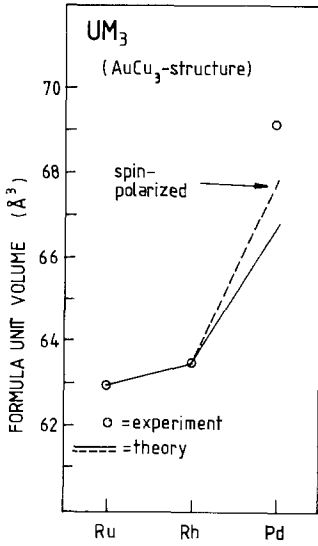


Fig. 62. Calculated and measured volumes of the UM<sub>3</sub> compounds in the AuCu<sub>3</sub> structure.

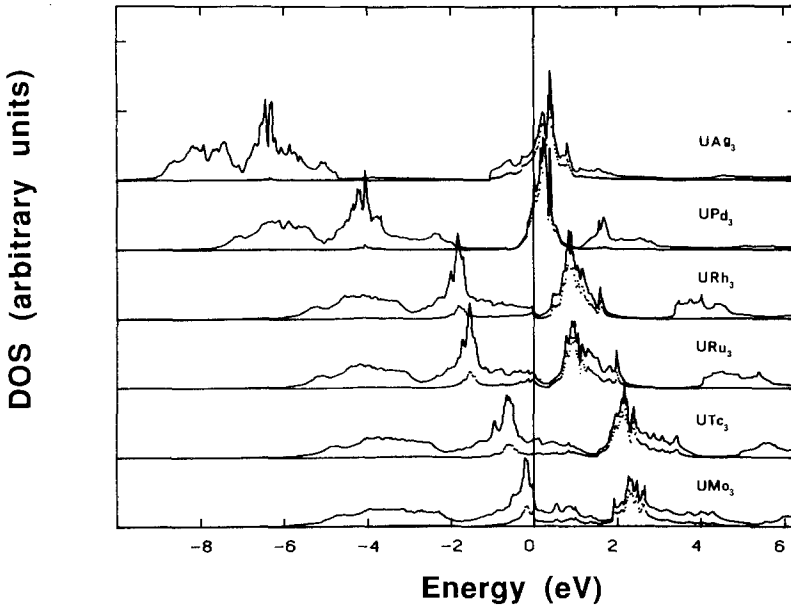


Fig. 63. The state densities of the AnRh<sub>3</sub> compounds. The full lines are the total state densities and the dotted lines are the partial 5f state densities. The Fermi energy is at the zero of energy. (After Eriksson et al. 1990a.)

electrons) and probably leads to 5f localization, for which there is much experimental evidence (Ubachs et al. 1986, Andres et al. 1978, Buyers and Holden 1985, Baer et al. 1980, Reihl et al. 1982).

Since the evidence is that there is a change in the nature of the 5f states between  $\text{URh}_3$  and  $\text{UPd}_3$ , studies of  $\text{U}(\text{Rh}_{1-y}\text{Pd}_y)_3$  alloys should be particularly interesting. Photoemission experiments (Arko et al. 1987) on  $\text{URh}_{2.0}\text{Pd}_{1.0}$  show a 5f peak at the Fermi energy which is narrower but similar to that in the  $\text{URh}_3$  spectra. For  $\text{URh}_{1.0}\text{Pd}_{2.0}$  the experimental partial 5f spectrum is much wider than that in  $\text{URh}_{2.0}\text{Pd}_{1.0}$ . However, by subtracting these two spectra (with appropriate weighting factors) one obtains a spectrum that very much resembles that of  $\text{UPd}_3$ . This suggests that there are two distinct types of 5f response in  $\text{URh}_{1.0}\text{Pd}_{2.0}$ . For increasing values of  $y$  we do, in fact, expect gradual 5f-band narrowing since the 5f-4d hybridization decreases. The linear specific-heat coefficient (Ubachs et al. 1986, Dunlap et al. 1987) increases and, when  $y$  approaches 0.67, reaches the heavy-fermion value of  $200 \text{ mJ/mol K}^2$ . With a further increase of  $y$  the 5f electrons finally become fully localized.

The pseudobinary alloys under study crystallize in the cubic  $\text{Cu}_3\text{Au}$ -structure for  $y$  smaller than 0.9, and in the hexagonal  $\text{TiNi}_3$ -structure when  $y$  is greater than 0.93. Calculations (Eriksson et al. 1988d) were done at the measured molecular volume, but for the  $\text{Cu}_3\text{Au}$  structure.

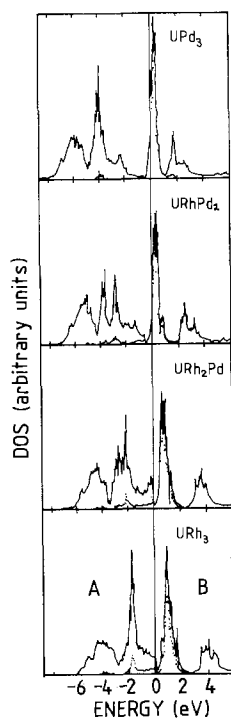


Fig. 64. Calculated state densities for the compounds  $\text{UPd}_3$ ,  $\text{URhPd}_2$ ,  $\text{URh}_2\text{Pd}$  and  $\text{URh}_3$  (see text). The full lines are the total state densities and the dotted lines are the partial 5f state densities. The Fermi energy is at the zero of energy.

Theoretical studies were done on the compounds  $\text{URhPd}_2$  and  $\text{URh}_2\text{Pd}$ , with one Pd and 2 Rh atoms occupying the three Au sites in the  $\text{CuAu}_3$  primitive cell for  $\text{URh}_2\text{Pd}$  and the reverse for  $\text{URhPd}_2$  (Eriksson et al. 1988a). The calculated state densities are plotted in fig. 64. The main features of the density of state for  $\text{URh}_3$  can be described by a “bonding” 4d band (marked by A), separated by approximately 6 eV from an “anti-bonding” 6d band (marked by B). The 5f states are located at the top of the “bonding” 4d states and hybridize strongly with them. This hybridization is crucial for the 5f bandwidth – an estimate of the unhybridized 5f bandwidth in  $\text{URh}_3$  is only 0.3 eV, which is much narrower than the calculated fully hybridized 5f bandwidth of about 3 eV. As the Pd concentration increases, the “bonding” d states move down in energy, decreasing their overlap with the 5f levels. This causes a reduction of 5f–4d hybridization and 5f bandwidth. In  $\text{UPd}_3$  the 5f states are situated in the gap between the “bonding” and the “anti-bonding” d states. Consequently, the 5f bandwidth is far narrower than in  $\text{URh}_3$ , strongly increasing the tendency of the 5f electrons to localize.

Since there is an unusually strong ligand effect on the 5f bandwidth in these systems, and narrowing and movement of the partial 5f relative to 4d state densities, a rigid-band model should not be used over a large concentration range. It is the nearest-neighbour environment of the uranium atom which determines the nature of the 5f states, which is consistent with the fact for all these systems the U–U distances are considerably larger than the Hill limit. The largest contributions to the 5f bandwidths are from the f–d and f–f hybridization, with f–d hybridization dominant for the  $\text{Cu}_3\text{Au}$  structure. Calculations (Eriksson et al. 1988d) show that the contribution from near neighbours accounts for more than 99.5% of the total f–d or f–f hybridization and, therefore, to the 5f bandwidth.

Since the elements that are varied in these alloys (Rh and Pd) are next to each other in the periodic table, their band masses differ by less than 15% across the range of compounds studied. Thus their hopping matrix elements are similar, whereas their band centres differ by as much as 1.3 eV. In a substitutional alloy this corresponds to the case of diagonal disorder, but relatively small off-diagonal disorder.

The calculated Stoner product (Eriksson et al. 1988d) for these compounds predicts  $\text{URh}_3$  and  $\text{URh}_2\text{Pd}$  to be paramagnetic and the contrary for  $\text{URhPd}_2$  and  $\text{UPd}_3$ . Self-consistent spin-polarized calculations yielded saturated U-5f moments for concentrations with  $y \geq \frac{2}{3}$ , which is consistent with localized 5f states, and Eriksson et al. (1988d) argued that  $y = \frac{2}{3}$  might be identified with the critical concentration for localization of the 5f electrons on the uranium atom.

The lattice constants of these alloys as a function of concentration are plotted in fig. 65, where they are compared with the lattice constants of the  $\text{Zr}(\text{Rh}_{1-y}\text{Pd}_y)_3$  alloys. The  $\text{Zr}(\text{Rh}_{1-y}\text{Pd}_y)_3$  alloys obey Vegard’s law, whereas the  $\text{U}(\text{Rh}_{1-y}\text{Pd}_y)_3$  alloys do not. The calculated lattice constants (Eriksson et al. 1988d), with the f states treated as itinerant and paramagnetic, are also shown, and they do obey Vegard’s law. Eriksson et al. (1988d) then removed the 5f contribution to the electronic pressure, eq. (37), in their calculated equation of state, and re-evaluated the lattice constants. The result is the curve labelled “calculated-5f” in fig. 65. This calculated curve agrees with the measured lattice constant of  $\text{UPd}_3$  quite well, whereas the “itinerant” results

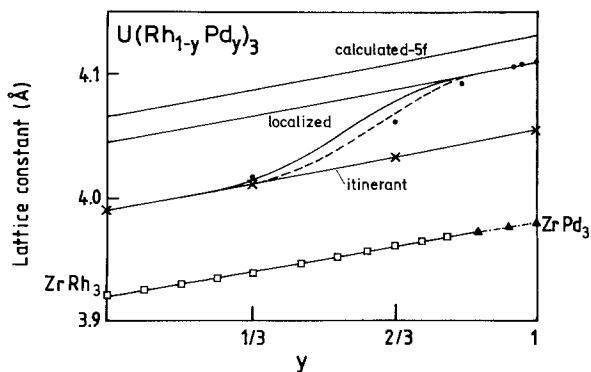


Fig. 65. Experimental (filled circles) and theoretical lattice constants for  $U(Rh_{1-y}Pd_y)_3$  as a function of the concentration,  $y$ . The dashed and solid curves correspond to a localization criterion of 8 and 7 Pd atoms surrounding a U atom, respectively. The calculated lattice constants with bonding 5f electrons are denoted by crosses for the ordered compounds. The curve labelled itinerant is obtained by interpolation between the results for the ordered compounds. The lattice constants obtained by subtracting the 5f contribution to the bonding for the ordered compounds are labelled "calculated-5f". The lattice constants obtained from calculations for a chemically inert  $5f^2$  configuration are labelled "localized". The measured lattice constants for  $Zr(Rh_{1-y}Pd_y)_3$  are also plotted. (After Eriksson et al. 1988d.)

agree with experiment at the other end of the concentration range. If Vegard's law was obeyed for localized 5f states across the concentration range, the lattice constants would lie on the curve labelled "localized" in fig. 65.

Eriksson et al. (1988d) also argued that U-f-M-d hybridization was essentially a local effect, arising almost entirely from the nearest neighbours, as may be seen from an examination of the dependence of the transfer integrals (or structure constants) in eq. (57) upon distance. Each uranium atom has twelve M nearest neighbours in the  $AuCu_3$  structure. Since the critical concentration  $y = \frac{2}{3}$  corresponds to about eight Pd and four Rh nearest neighbours on average, Eriksson et al. argued that uranium atoms with more than eight Pd nearest neighbours have localized electrons. Then, if  $P(n)$  is the probability of finding  $n$  Pd nearest neighbours, the lattice constants of the random alloys should be given by  $a = \sum_m P(n)a(n)$ , where  $a(n)$  is obtained by linearly interpolating along the itinerant curve for  $n < 8$  or along the localized curve for  $n > 8$ . The results are also plotted in fig. 65, and they agree well with the measurements.

The pseudo-binary alloys  $Y(Fe_{1-y}Co_y)_2$  were discussed in detail in sect. 5.1 representing rare earth-transition metal intermetallics. The properties of the  $Y(Fe_{1-y}Ni_y)_2$  alloys have been measured by Andreev et al. (1988). Eriksson et al. (1988b, 1989b) have studied the more complex pseudo-binary alloys  $U(Fe_{1-y}Ni_y)_2$  for  $y = 0, 0.5, 1$  and  $UCo_2$ , again by using ordered compounds with the same composition to simulate the alloy. The properties of these alloys have been studied in some detail (Andreev et al. 1988).  $UCo_2$  is isoelectronic with the alloy with  $y = 0.5$ , and would therefore correspond to the virtual crystal approximation for this compound. The calculated results (Eriksson et al. 1989b) for the volumes are compared with measurements in fig. 66. The calculated volume of  $UFe_2$  is too small, even for the

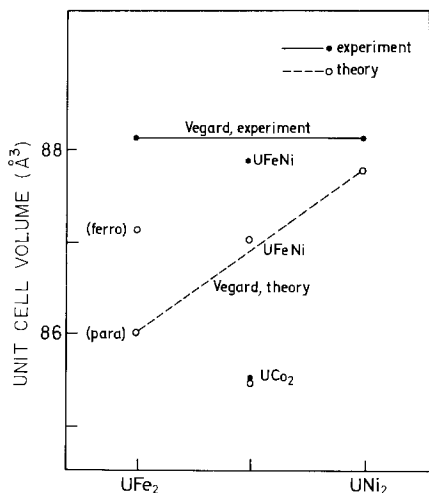


Fig. 66. The volumes of the  $U(Fe_{1-x}Co_x)_2$  alloys. The filled circles are measured volumes. The calculated volumes for the ordered compounds are shown as open circles. The dashed line represents the estimated volumes for *paramagnetic*  $U(Fe_{1-x}Co_x)_2$  alloys from Vegard's law. The full line represents the estimated volumes for  $U(Fe_{1-x}Co_x)_2$  alloys from Vegard's law (see text). After Eriksson et al. (1989b).

spin-polarized solution, as is the same quantity for UFeNi. Also shown in the figure are Vegard's law interpolations for the measurements and the theory. Vegard's law is obeyed quite well in both experiment and theory. What is immediately noticeable is that the volume of  $UCo_2$  is far smaller than that of UFeNi. The virtual crystal approximation (VCA) is therefore, in this case, poor. This remains true even if one takes only the calculated results.

Eriksson et al. (1989b) found that the reason for the failure of VCA lies in the fact that in the alloy the bonding part of the Fe and Ni partial state densities are as schematically shown in fig. 67, the bonding part of the partial state density of Co in  $UCo_2$  is also shown. Nearly all the bonding bands in  $UCo_2$  are filled (the Fermi energy is at zero), whereas in the alloy both the Fe and Ni bands are broader and the partial Ni bonding state density lies below the Fermi energy. The result is that some anti-bonding bands with Ni character are filled and not all of the bonding bands with Fe character are filled. The situation is analogous to that in a spin-polarized metal, with the Ni bands corresponding to spin up and the Fe bands corresponding to spin down. This is not allowed for in VCA, where Ni and Fe in the alloy are approximated by the same potential.

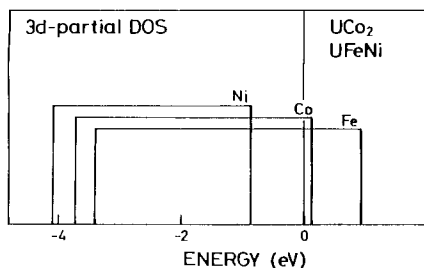


Fig. 67. The bonding part of the model state density for  $UCo_2$  and UFeNi with the Fermi energy at zero. For details see text. After Eriksson et al. (1989b).

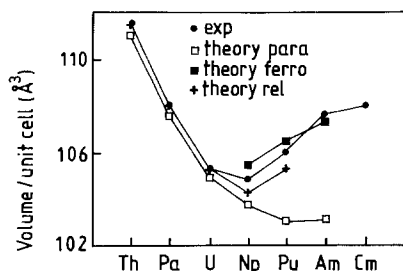


Fig. 68. Calculated and measured volumes of the  $AnIr_2$  compounds. After Eriksson et al. (1989c).

Although both  $UFe_2$  and  $UNi_2$  are magnetic  $U(Fe_{0.5}Ni_{0.5})_2$  is a paramagnet. Eriksson et al. (1989b) found that the magnetism in  $UFe_2$  is driven by the moment on Fe, whereas the magnetism in  $UNi_2$  is driven by the moment on U, there being a negligible moment on Ni. These conclusions have since been confirmed in very detailed calculations by Severin et al. (1991). In  $UFe_2$ , hybridization between the 3d and 5f states reduces the moment on Fe to well below its value in elemental Fe and leads to a small induced moment at the U site. In the alloys, as Ni is substituted for Fe, 3d–5f hybridization is steadily reduced and the induced moment on the U site decreases. The substituted Ni, with its bonding bands filled, is essentially non-magnetic. As more Ni is substituted the state density at the Fermi energy is reduced enough for the alloy to become paramagnetic. The U–5f derived bands narrow due to the decrease in 3d–5f hybridization as the Ni concentration increases and, for large Ni concentrations, they are narrow enough for a small moment to form at the U site.

Figure 60 also provides a good example of a large relativistic volume effect (sect. 3.6). The volumes evaluated from the equation of state calculated using the Dirac equation, display a minimum *before* the middle of the series, which arises from preferential filling of the  $f_{5/2}$  bands and their anti-bonding orbitals. However, the volume increase is too small compared with experiment, as for the elemental metals, and it is quite likely that relativistic effects – correctly treated in the Dirac equation, but in isolation – are suppressed by many-body effects.

The  $AnIr_2$  ( $An = Th-Cm$ ) series is also isostructural in the cubic Laves phase (C15), and  $NpIr_2$  is the first compound to order magnetically, becoming antiferromagnetic at 5.8–7.5 K.  $ThIr_2$  is a superconductor below 6.5 K and  $UIr_2$  is an almost temperature-independent antiferromagnet with a specific-heat coefficient of  $62 \text{ mJ/mol K}^2$ , and is probably a spin-fluctuation compound (Sechovsky and Havela 1988).

The measured and calculated (Eriksson et al. 1989c) lattice constants of the  $AnIr_2$  systems are shown in fig. 68. The approximate electronic pressure, modified to include the effects of the magnetic moment of the 5f states, is given by eq. (50). When the 5f states polarize, the spin-up electrons occupy more anti-bonding states, reducing the magnitude of the (negative) 5f electronic pressure. The computed 5f spin increases from  $2.7\mu_B$  to  $5.8\mu_B$  between  $NpIr_2$  and  $AmIr_2$ . It may be seen from eq. (50) that the 5f electronic pressure vanishes for a half-filled spin-up band, which is almost achieved

for AmIr<sub>2</sub>. For the Np and Pu compounds the electronic pressure reduction is less, but there are still considerable magneto-volume effects.

## References

- Akella, J., 1980, private communication.
- Akella, J., Q. Johnson, W. Thayer and R.N. Shock, 1979, *J. Less-Common Met.* **68**, 95.
- Akella, J., Q. Johnson and R.N. Schock, 1980, *J. Geophys. Res. B* **85**, 7056.
- Alameda, J.M., D. Givord and Q.J. Lu, 1981, *J. Appl. Phys.* **52**, 2079.
- Allen, J.W., and S.H. Liu, 1992, *Phys. Rev. B* **46**, 5047.
- Allen, J.W., and R.M. Martin, 1982, *Phys. Rev. Lett.* **49**, 1106.
- Allen, J.W., L.I. Johansson, R.S. Bauer, S. Lindau and S.B.M. Hagström, 1978, *Phys. Rev. Lett.* **41**, 1499.
- Andersen, O.K., 1975, *Phys. Rev. B* **12**, 3060.
- Andersen, O.K., and O. Jepsen, 1977, *Physica B* **91**, 317.
- Andersen, O.K., H.L. Skriver, H. Nohl and B. Johansson, 1979, *Pure & Appl. Chem.* **52**, 93.
- Andersen, O.K., O. Jepsen and D. Glötzel, 1985, in: *Highlights of Condensed Matter Theory, Proc. Int. School of Physics 'Enrico Fermi'*, eds F. Bassani, F. Fumi and M.P. Tosi (North-Holland, Amsterdam) p. 59.
- Andreev, A.V., L. Havela and V. Sechovsky, 1988, *J. Phys. Colloq. (Paris)* **49**, C 49.
- Andres, K., D. Davidov, P. Dernier, F.S.L. Hsu, W.A. Reed and G.J. Nieuwenhuys, 1978, *Solid State Commun.* **28**, 405.
- Arko, A.J., M.B. Brodsky, G.W. Crabtree, D. Karim, D.D. Koelling, L.R. Windmiller and J.B. Ketterson, 1975, *Phys. Rev. B* **12**, 4102.
- Arko, A.J., D.D. Koelling and J.E. Schirber, 1985, in: *Handbook on the Physics and Chemistry of the Actinides*, Vol. 2, eds A.J. Freeman and G.H. Lander (North-Holland, Amsterdam) p. 175.
- Arko, A.J., B.W. Yates, B.D. Dunlap, D.D. Koelling, A.W. Mitchell, D.J. Lam, C.G. Olson, M. del Giudice, Z. Fisk and J.L. Smith, 1987, in: *Theoretical and Experimental Aspects of Valence Fluctuations and Heavy Fermions*, Bangalore 1987, eds L.C. Gupta and S.K. Malik (Plenum, New York) p. 39.
- Baer, Y., H.R. Ott and K. Andres, 1980, *Solid State Commun.* **36**, 387.
- Beaudry, B.J., and K.A. Gschneidner Jr, 1978, in: *Handbook on the Physics and Chemistry of Rare Earths*, Vol. 1, eds K.A. Gschneidner Jr and L. Eyring (North-Holland, Amsterdam) p. 173.
- Benedict, U., 1987, in: *Handbook on the Physics and Chemistry of the Actinides*, Vol. 4, eds A.J. Freeman and G.H. Lander (North-Holland, Amsterdam) p. 227.
- Benedict, U., J.C. Spirlet, C. Dufour, I. Birkel, W.B. Holzapfel and J.R. Peterson, 1982, *J. Magn. & Magn. Mater.* **29**, 287.
- Benedict, U., J.R. Peterson, R.G. Haire and C. Dufour, 1984, *J. Phys. F* **14**, L43.
- Benedict, U., J.P. Itié, C. Dufour, S. Dabos and J.C. Spirlet, 1985, in: *Americium and Curium Chemistry and Technology*, eds N.M. Edelstein, J.D. Navratil and W.W. Schulz (Eidil, Dordrecht/Boston) p. 213.
- Boring, A.M., R.C. Albers, O. Eriksson and D.D. Koelling, 1992, *Phys. Rev. Lett.* **68**, 2652.
- Bradbury, M.J., 1981, *J. Less-Common Met.* **78**, 207.
- Brewer, L., 1963, *Prediction of High Temperature Metallic Phase Diagrams UC RL10701, UC-25 Metals, Ceramics and Materials.*
- Brewer, L., 1967, in: *Batelle Institute Material Science Colloquia*, eds P.S. Rudman, J. Stringer and R.I. Jaffee (McGraw-Hill, New York) p. 39.
- Brewer, L., 1971, *J. Opt. Soc. Am.* **61**, 1101.
- Brewer, L., 1975, LBL report no. 3720.
- Brodsky, M.B., 1978, *Rep. Prog. Phys.* **41**, 1547.
- Brooks, M.S.S., 1979, *J. Phys. Colloq. (Paris)* **40**, C4-155.
- Brooks, M.S.S., 1983, *J. Phys.* **13**, 103.
- Brooks, M.S.S., 1984a, *J. Phys. F* **14**, 1157.
- Brooks, M.S.S., 1984b, *J. Phys. F* **14**, 639.
- Brooks, M.S.S., 1984c, *J. Phys. F* **14**, 653.
- Brooks, M.S.S., 1984d, *J. Phys. F* **14**, 857.
- Brooks, M.S.S., and D. Glötzel, 1980, *Physica B* **102**, 51.
- Brooks, M.S.S., and B. Johansson, 1983, *J. Phys. F* **13**, L197.
- Brooks, M.S.S., and B. Johansson, 1993, in: *Ferromagnetic Materials*, Vol. 7, ed. K.H.J. Buschow (North-Holland, Amsterdam)
- Brooks, M.S.S., B. Johansson and H.L. Skriver, 1984, in: *Handbook on the Physics and Chemistry of the Actinides*, Vol. 1, eds.



- A.J. Freeman and G.H. Lander (North-Holland, Amsterdam) p. 153.
- Brooks, M.S.S., O. Eriksson and B. Johansson, 1989, *J. Phys.: Condens. Matter* **1**, 5861.
- Brooks, M.S.S., L. Nordström and B. Johansson, 1991a, *J. Phys.: Condens. Matter* **3**, 2357.
- Brooks, M.S.S., T. Gasche, S. Auluck, L. Nordström, L. Severin, J. Trygg and B. Johansson, 1991b, *J. Appl. Phys.* **70**, 5972.
- Brooks, M.S.S., S. Auluck, T. Gasche, L. Trygg, L. Nordström, L. Severin and B. Johansson, 1992, *J. Magn. & Magn. Mater.* **104-107**, 1496.
- Burns, J.H., and J.R. Peterson, 1978, *Inst. Phys. Conf. Ser.* **37**, 52.
- Buschow, K.H.J., 1977, *Rep. Prog. Phys.* **40**, 1179.
- Buschow, K.H.J., 1979, *Rep. Prog. Phys.* **42**, 1373.
- Buschow, K.H.J., and R.P. van Stapele, 1970, *J. Appl. Phys.* **41**, 4066.
- Buyers, W.J.L., and T.M. Holden, 1985, in: *Handbook on the Physics and Chemistry of the Actinides*, Vol. 2, eds A.J. Freeman and G.H. Lander (North-Holland, Amsterdam) p. 239.
- Buyers, W.J.L., T.M. Holden, J.A. Jackman, A.F. Murray, P. de V. DuPlessis and O. Vogt, 1983, *J. Magn. & Magn. Mater.* **31**, 229.
- Callaway, J.C., and N.H. March, 1984, in: *Solid State Physics*, Vol. 38, eds H. Ehrenreich, F. Seitz and D. Turnbull (Academic Press, New York) p. 136.
- Christensen, N.E., 1984a, *Int. J. Quantum Chem.* **25**, 233.
- Christensen, N.E., 1984b, *Phys. Rev.* **29**, 5547.
- Christensen, N.E., and V. Heine, 1985, *Phys. Rev. B* **32**, 6145.
- Clark, A.E., 1980, in: *Ferromagnetic Materials*, Vol. 1, ed. E.P. Wohlfarth (North-Holland, Amsterdam) p. 531.
- Coehoorn, R., 1991, in: *Supermagnets, Hard Magnetic Materials*, Lecture Notes Nato-ASI, eds G.J. Long and F. Grandjean (Kluwer Academic, Dordrecht) p. 133.
- Coqblin, B., 1982, in: *Magnetism of Metals and Alloys*, ed. M. Cyrot (North-Holland, Amsterdam).
- Crabtree, G.W., 1985, *J. Magn. & Magn. Mater.* **52**, 169; *J. Phys. Colloq. (Paris)* **40**, C5-171.
- Cunningham, B.B., and J.C. Wallmann, 1964, *J. Inorg. Nucl. Chem.* **26**, 271.
- Cyrot, M., and F. Cyrot-Lackman, 1976, *J. Phys. F* **6**, 2257.
- Cyrot, M., and M. Lavagna, 1979, *J. Phys. (Paris)* **40**, 763.
- Cyrot, M., D. Gignoux, F. Givord and M. Lavagna, 1979, *J. Phys. Colloq. (Paris)* **40**, C5-171.
- Dalton, N.W., and R.A. Deegan, 1969, *J. Phys. C* **2**, 2369.
- Desclaux, J.P., 1973, in: *Atomic and Nuclear Data Tables*, Vol. 12, ed. K. Way (Academic Press, New York) pp. 311-406.
- Dimmock, J.O., and A.J. Freeman, 1964, *Phys. Rev. Lett.* **13**, 750.
- Dimmock, J.O., A.J. Freeman and R.E. Watson, 1965, *J. Appl. Phys.* **36**, 1132.
- Donohue, J., 1974, *The Structures of the Elements* (Wiley, New York).
- Ducastelle, F., and F. Cyrot-Lackman, 1971, *J. Phys. & Chem. Solids* **32**, 285.
- Dunlap, B.D., F.J. Litterst, S.K. Malik, H.A. Kierstead, G.W. Crabtree, W. Kwok, D.J. Lam and A.W. Mitchell, 1987, in: *Theoretical and Experimental Aspects of Valence Fluctuations and Heavy Fermions*, Bangalore, 1987, eds L.C. Gupta and S.K. Malik (Plenum, New York) p. 365.
- DuPlessis, P. de V., T.M. Holden, W.J.L. Buyers, J.A. Jackman, A.F. Murray and C.F. van Doorn, 1985, *J. Phys. C* **18**, 2809.
- Duthie, J.C., and D.G. Pettifor, 1977, *Phys. Rev. Lett.* **38**, 564.
- Ellinger, F.H., and W.H. Zachariassen, 1974, *Phys. Rev. Lett.* **32**, 773.
- Endo, S., H. Sasaki and T. Mitsui, 1977, *J. Phys. Soc. Jpn.* **42**, 882.
- Engel, N., 1949, *Kem. Maanesblad* **5**, **6**, **8**, **9** and **10**.
- Eriksson, O., and J.M. Wills, 1992, *Phys. Rev. B* **45**, 3198.
- Eriksson, O., L. Nordström, M.S.S. Brooks and B. Johansson, 1988a, *Phys. Rev. Lett.* **60**, 2523.
- Eriksson, O., B. Johansson and M.S.S. Brooks, 1988b, *J. Phys. Paris C* **8**, 295.
- Eriksson, O., B. Johansson and M.S.S. Brooks, 1988c, *Phys. Rev.* **37**, 1706.
- Eriksson, O., B. Johansson, M.S.S. Brooks and H.L. Skriver, 1988d, *Phys. Rev. B* **38**, 12858.
- Eriksson, O., B. Johansson, M.S.S. Brooks and H.L. Skriver, 1989a, *Phys. Rev. B* **40**, 9508.
- Eriksson, O., B. Johansson, M.S.S. Brooks and H.L. Skriver, 1989b, *Phys. Rev. B* **40**, 9519.
- Eriksson, O., B. Johansson, M.S.S. Brooks and H.L. Skriver, 1989c, *Phys. Rev. B* **39**, 5647.
- Eriksson, O., B. Johansson and M.S.S. Brooks, 1989d, *J. Phys.: Condens. Matter* **1**, 4005.
- Eriksson, O., M.S.S. Brooks and B. Johansson, 1990a, *Phys. Rev. B* **41**, 9087.
- Eriksson, O., B. Johansson, R.C. Albers, A.M. Boring and M.S.S. Brooks, 1990b, *Phys.*

- Rev. **42**, 2707.
- Eriksson, O., M.S.S. Brooks and B. Johansson, 1990c, *J. Less-Comm. Met.* **158**, 207.
- Eriksson, O., M.S.S. Brooks and B. Johansson, 1990d, *Phys. Rev. B* **41**, 7311.
- Eriksson, O., M.S.S. Brooks, B. Johansson, R.C. Albers and A.M. Boring, 1991a, *J. Appl. Phys.* **69**, 5897.
- Eriksson, O., R.C. Albers, A.M. Boring, G.W. Fernando, Y.G. Hao and B.R. Cooper, 1991b, *Phys. Rev. B* **B3**, 3137.
- Eriksson, O., J.M. Wills and A.M. Boring, 1992, *Phys. Rev. B* **46**, 12981.
- Fahey, J.A., J.R. Petersen and R.D. Baybarz, 1972, *Inorg. Nucl. Chem. Lett.* **8**, 101.
- Fernando, G.W., B.R. Cooper, M.V. Ramana, H. Krakauer and C.Q. Ma, 1986, *Phys. Rev. Lett.* **56**, 2299.
- Feynman, R.P., 1939, *Phys. Rev.* **56**, 340.
- Fidelis, I., and S. Siekierski, 1966, *J. Inorg. Nucl. Chem.* **28**, 185.
- Fournier, J.M., J. Beille, A. Boeuf, C. Vettier and F.A. Wedgwood, 1980, *Physica B* **102**, 282.
- Freeman, A.J., and D.D. Koelling, 1974, in: *The Actinides: Electronic Structure and Related Properties*, Vol. 1, eds A.J. Freeman and J.B. Darby (Academic Press, New York) p. 51.
- Freeman, A.J., B.I. Min and M.R. Norman, 1987, in: *Handbook on the Physics and Chemistry of Rare Earths*, Vol. 10, eds K.A. Gschneidner Jr, L. Eyring and S. Hüfner (North-Holland, Amsterdam) p. 165.
- Friedel, J., 1969, in: *The Physics of Metals*, ed. J.M. Ziman (Cambridge Univ. Press) p. 341.
- Friedel, J., and C.M. Sayers, 1977, *J. Phys. (Paris)* **38**, 697.
- Fuger, J., 1982, in: *Actinides in Perspective*, ed. N. Edelstein (Pergamon, Oxford) p. 409.
- Gelatt, C.D., H. Ehrenreich and R.E. Watson, 1977, *Phys. Rev.* **15**, 1613.
- Gerward, L., S.J. Olsen, U. Benedict, S. Dabos and O. Vogt, 1989, *High-Pressure Research* **1**, 235.
- Glötzel, D., 1978, *J. Phys. F* **8**, 1163.
- Godreche, C., 1982, *J. Magn. & Magn. Mater.* **29**, 262.
- Grant, I.P., 1970, *Adv. Phys.* **19**, 747.
- Grosshans, W.A., and W.B. Holzapfel, 1984, *J. Phys. Colloq. (Paris)* **45**, C8-573.
- Grosshans, W.A., Y.K. Vohra and W.B. Holzapfel, 1982a, *J. Magn. & Magn. Mater.* **29**, 282.
- Grosshans, W.A., Y.K. Vohra and W.B. Holzapfel, 1982b, *Phys. Rev. Lett.* **49**, 1572.
- Grosshans, W.A., Y.K. Vohra and W.B. Holzapfel, 1983, *J. Phys. F* **15**, L147.
- Grübel, G., J.D. Axe, D. Gibbs, G.H. Lander, J.C. Marmeggi and T. Brückel, 1991, *Phys. Rev. B* **43**, 8803.
- Gschneidner Jr, K.A., 1964, in: *Solid State Physics*, Vol. 16, eds H. Ehrenreich, F. Seitz and D. Turnbull (Academic Press, New York) p. 276.
- Gschneidner Jr, K.A., and R.M. Valetta, 1968, *Acta Metall.* **16**, 477.
- Gu, S.Q., and W.Y. Ching, 1987, *Phys. Rev. B* **36**, 8350.
- Guimares, A.P., and D.St.P. Bunbury, 1973, *J. Phys. F* **3**, 885.
- Guinan, M., and C.F. Cline, 1972, *J. Nucl. Mater.* **43**, 205.
- Gunnarsson, O., 1976, *J. Phys. F* **6**, 587.
- Gunnarsson, O., 1977, *Physica B* **91**, 329.
- Gunnarsson, O., and B.I. Lundqvist, 1976, *Phys. Rev. B* **13**, 4274.
- Gunnarsson, O., B.I. Lundqvist and J.W. Wilkins, 1974, *Phys. Rev. B* **10**, 1319.
- Gunnarsson, O., J. Harris and R.O. Jones, 1977, *Phys. Rev. B* **15**, 3027.
- Gupta, H.O., S.K. Malik and W.E. Wallace, 1984, *J. Magn. & Magn. Mater.* **42**, 239.
- Gupta, R.P., and T.L. Loucks, 1969, *Phys. Rev. Lett.* **22**, 458.
- Gupta, R.P., and T.L. Loucks, 1971, *Phys. Rev. B* **3**, 1834.
- Gustafson, D.R., J.D. McNutt and I.O. Roellig, 1969, *Phys. Rev.* **183**, 435.
- Haire, R.G., and L.B. Asprey, 1976, *Inorg. Nucl. Chem. Lett.* **12**, 73.
- Haire, R.G., and R.D. Baybarz, 1979, *J. Phys. Paris* **40**, C4-101.
- Haire, R.G., J.R. Peterson, U. Benedict and C. Dufour, 1984, *J. Less-Common Met.* **102**, 119.
- Harris, I.R., and G.V. Raynor, 1969, *J. Less-Common Met.* **17**, 336.
- Harris, I.R., C.C. Koch and G.V. Raynor, 1966, *J. Less-Common Met.* **11**, 436.
- Harris, J., and R.O. Jones, 1979, *J. Chem. Phys.* **70**, 830.
- Harrison, W.A., 1980, in: *Electronic Structure and the Properties of Solids* (Freeman, New York).
- Harrison, W.A., 1984, *Phys. Rev. B* **29**, 2917.
- Harrison, W.A., and G. Straub, 1987, *Phys. Rev. B* **36**, 2695.
- Hedin, L., and B.I. Lundqvist, 1971, *J. Phys. C* **4**, 1971.
- Hellmann, H., 1937, *Einführung in die Quantenchemie* (Deuticke, Leipzig).
- Hilscher, G., 1982a, *J. Magn. & Magn. Mater.*

- 25, 229.
- Hilscher, G., 1982b, *J. Magn. & Magn. Mater.* **27**, 1.
- Hodges, C.H., 1967, *Acta Metall.* **15**, 1787.
- Hohenberg, P., and W. Kohn, 1964, *Phys. Rev.* **136**, 864.
- Holden, T.M., W.J.L. Buyers, E.C. Svensson, J.A. Jackman, A.F. Murray, O. Vogt and P. de V. DuPlessis, 1982, *J. Appl. Phys.* **53**, 1967.
- Hong, S.C., J.I. Lee, Y.Y.-R. Yang, B.I. Min and A.J. Freeman, 1992, *J. Magn. & Magn. Mater.* **104-107**, 659.
- Hubbard, J., 1963, *Proc. Roy. Soc. A* **276**, 238.
- Hummeler, K., and M. Fähnle, 1992, *Phys. Rev.* **45**, 3161.
- Jackman, J.A., T.M. Holden, W.J.L. Buyers and P. de V. DuPlessis, 1986, *Phys. Rev. B* **33**, 7144.
- Janak, J.F., 1977, *Phys. Rev. B* **16**, 255.
- Jaswal, S.S., 1990, *Phys. Rev. B* **41**, 9697.
- Jayaraman, A., 1965, *Phys. Rev. A* **137**, 179.
- Jayaraman, A., 1978, in: *Handbook on the Physics and Chemistry of Rare Earths*, Vol. 1, eds K.A. Gschneidner Jr and L. Eyring (North-Holland, Amsterdam) p. 707.
- Jayaraman, A., and R.C. Sherwood, 1964, *Phys. Rev. A* **134**, 691.
- Jensen, J., and A.R. Mackintosh, 1991, *Rare Earth Magnetism* (Clarendon Press, Oxford).
- Johansson, B., 1974, *Philos. Mag.* **30**, 469.
- Johansson, B., 1977a, in: *Proc. 2nd Int. Conf. on Electronic Structure of the Actinides*, eds J. Mulak, W. Suski and R. Troč (Ossolineum, Wroclaw) p. 49.
- Johansson, B., 1977b, *J. Phys. F* **7**, 877.
- Johansson, B., 1978a, in: *Inst. Phys. Conf. Ser.* **37**, eds W.D. Corner and B.K. Tanner (Institute of Physics, London) p. 39.
- Johansson, B., 1978b, *J. Phys. & Chem. Solids* **39**, 467.
- Johansson, B., 1979, *Phys. Rev. B* **19**, 6615.
- Johansson, B., and N. Martensson, 1981, *Phys. Rev. B* **24**, 4484.
- Johansson, B., and N. Mårtensson, 1987, in: *Handbook on the Physics and Chemistry of Rare Earths*, Vol. 10, eds K.A. Gschneidner Jr, L. Eyring and S. Hufner (North-Holland, Amsterdam) p. 361.
- Johansson, B., and P. Munck, 1984, *J. Less-Common Met.* **100**, 49.
- Johansson, B., and A. Rosengren, 1974, *FOA 4 Rapport*, C4594-A2.
- Johansson, B., and A. Rosengren, 1975a, *Phys. Rev. B* **11**, 2836.
- Johansson, B., and A. Rosengren, 1975b, *Phys. Rev. B* **11**, 1367.
- Johansson, B., H.L. Skriver, N. Martensson, O.K. Andersen and D. Glötzel, 1980, *Physica B* **102**, 12.
- Johansson, B., H.L. Skriver and O.K. Andersen, 1981, in: *Physics of Solids Under High Pressure*, eds J. Schilling and R.N. Shelton (North-Holland, Amsterdam, 1981) p. 245.
- Johansson, B., O. Eriksson, M.S.S. Brooks and H.L. Skriver, 1986, *Phys. Scr. T* **13**, 65.
- Keeton, S.C., and T.L. Loucks, 1968, *Phys. Rev.* **168**, 672.
- Keller, D.L., 1984, *Radiochemica Acta* **37**, 169.
- Kennedy, S.J., and B.R. Coles, 1990, *J. Phys.* **2**, 1990.
- Koelling, D.D., 1981, *Rep. Prog. Phys.* **44**, 139.
- Koelling, D.D., and A.J. Freeman, 1975, *Phys. Rev. B* **12**, 5622.
- Kohn, W., and L.J. Sham, 1965, *Phys. Rev. A* **140**, 1133.
- Kohn, W., and P. Vashishta, 1983, in: *Theory of the Inhomogeneous Electron Gas*, eds S. Lundqvist and N.H. March (Plenum Press, New York) p. 79.
- Koskenmaki, D.C., and K.A. Gschneidner Jr, 1978, in: *Handbook on the Physics and Chemistry of Rare Earths*, Vol. 1, eds K.A. Gschneidner Jr and L. Eyring (North-Holland, Amsterdam) p. 337.
- Laubschat, C., E. Weschke, C. Holtz, M. Domke, O. Strebels and G. Kaindl, 1990, *Phys. Rev. Lett.* **65**, 1639.
- Lavagna, M., C. Lacroix and M. Cyrot, 1982, *Phys. Lett. A* **90**, 210.
- Lavagna, M., C. Lacroix and M. Cyrot, 1983, *J. Phys. F* **13**, 1007.
- Lawson, A.W., and T.Y. Tang, 1949, *Phys. Rev.* **76**, 301.
- Lee, J.A., and M.B. Waldron, 1972, *Contemp. Phys.* **13**, 113.
- Léger, J.M., K. Oki, A.M. Redon, I. Vedel, J. Rossat-Mignod and O. Vogt, 1986, *Phys. Rev. B* **33**, 7205.
- Léger, J.M., I. Vedel, A.M. Redon, J. Rossat-Mignod and O. Vogt, 1988, *Solid State Commun.* **66**, 1173.
- Li, D., C.W. Hutchings, P.A. Dowben, C. Hwang, R.T. Wu, M. Onellion, B. Andrews and J.L. Erskine, 1991, *J. Magn. & Magn. Mater.* **99**, 85.
- Liu, L.G., 1975, *J. Phys. & Chem. Solids* **36**, 31.
- Liu, S.H., 1978, in: *Handbook on Physics and Chemistry of the Rare Earths*, Vol. 1, eds

- K.A. Gschneidner Jr and L. Eyring (North-Holland, Amsterdam) p. 233.
- Ma, C.Q., M.V. Ramana, B.R. Cooper and H. Krakauer, 1986, *Phys. Rev. B* **34**, 3854.
- Mackintosh, A.R., 1985, *Physica B* **130**, 112.
- Mackintosh, A.R., and O.K. Andersen, 1979, in: *Electrons at the Fermi Surface*, ed. M. Springford (Cambridge Univ. Press, Cambridge) p. 149.
- Malik, S.K., F.J. Arlinghaus and W.E. Wallace, 1977, *Phys. Rev. B* **16**, 1242.
- Mao, H.K., R.M. Hazen, P.M. Bell and J. Wittig, 1981, *J. Appl. Phys.* **52**, 4572.
- Marmeggi, J.C., G.H. Lander, S. van Smaalen, T. Brückel and C.M.E. Zeyen, 1990, *Phys. Rev. B* **42**, 9365.
- Martin, R.M., and J.W. Allen, 1985, *J. Magn. & Magn. Mater.* **47-48**, 257.
- Martin, W.C., R. Zulabas and L. Hagan, 1978, *Atomic Energy Levels - The Rare Earth Elements* (National Bureau of Standards, US) Spec. Publ. 60.
- McMahan, A.K., 1989, *J. Less-Common Met.* **149**, 1.
- McMahan, A.K., H.L. Skriver and B. Johansson, 1981, *Phys. Rev. B* **23**, 5016.
- McWhan, D.B., 1961, PhD Thesis UCRL-9695 Lawrence Radiation Laboratory, Berkeley, California.
- McWhan, D.B., 1971, *Science* **176**, 751.
- McWhan, D.B., and A.L. Stevens, 1965, *Phys. Rev. A* **139**, 682.
- Min, B.I., H.J.F. Jansen, T. Oguchi and A.J. Freeman, 1986, *Phys. Rev. B* **34**, 369.
- Mohn, P., and K. Schwarz, 1984, *Physica F* **130**, 26.
- Moore, C.E., 1958, *Atomic Energy Levels*, US NBS Circular No 467, Vols. 1-3.
- Morss, L.R., 1976, *Chem. Rev.* **76**, 827.
- Moruzzi, V.L., J.F. Janak and A.R. Williams, 1978, *Calculated Electronic Properties of Metals* (Pergamon, New York).
- Mott, N.F., 1961, *Philos. Mag.* **6**, 287.
- Nellis, W.J., A.R. Harvey and M.B. Brodsky, 1981, in: *Magnetism and Magnetic Materials*, AIP Conf. Proc., Vol. 10, eds C.D. Graham Jr and J.J. Rhyne (AIP, New York) p. 1076.
- Neuenschwander, J., H. Boppert, J. Schoenes, E. Voit, O. Vogt and P. Wachter, 1984, in: *Proc. 14èmes Journées des Actinides*, ed. J. Schoenes (ETH, Zürich) p. 30.
- Neuenschwander, J., O. Vogt, E. Voit and P. Wachter, 1986, *Physica B* **144**, 66.
- Noé, M., and J.R. Peterson, 1976, in: *Transplutonium Elements 1975*, eds W. Müller and R. Lindner (North-Holland, Amsterdam) p. 69.
- Nordström, L., O. Eriksson, M.S.S. Brooks and B. Johansson, 1990, *Phys. Rev. B* **41**, 9111.
- Nordström, L., B. Johansson and M.S.S. Brooks, 1991a, *J. Appl. Phys.* **69**, 5708.
- Nordström, L., M.S.S. Brooks and B. Johansson, 1991b, *J. Appl. Phys.* **70**, 6583.
- Nordström, L., B. Johansson and M.S.S. Brooks, 1992b, to be published.
- Nugent, L.J., 1970, *J. Inorg. Nucl. Chem.* **32**, 3485.
- Nugent, L.J., and K.L. Van der Sluis, 1971, *J. Opt. Soc. Am.* **61**, 1112.
- Nugent, L.J., J.L. Burnett and L.R. Morss, 1973, *J. Chem. Thermodyn.* **5**, 665.
- Oliviera, J.M.C.B., and I.R. Harris, 1983, *J. Mater. Sci.* **18**, 3649.
- Olsen, S.J., S. Steenstrup, L. Gerward, U. Benedict, J.C. Spirlet and G.D. Andreetti, 1984, *J. Less-Common Met.* **98**, 291.
- Olsen, S.J., L. Gerward, U. Benedict and J.P. Itié, 1985, *Physica B* **133**, 129.
- Olsen, S.J., L. Gerward, U. Benedict, S. Dabos, J.P. Itié and O. Vogt, 1989, *High-Pressure Research* **1**, 253.
- Padel, A., A. Groff and C.H. de Novion, 1970, *J. Nucl. Mater.* **36**, 297.
- Pauling, L., 1950, as quoted by A.V. Schuck and J.H. Sturdivant, in: *J. Chem. Phys.* **18**, 145.
- Peppard, D.F., G.W. Mason and S. Lewey, 1969, *J. Inorg. Nucl. Chem.* **31**, 2271.
- Peterson, J.R., U. Benedict, C. Dufour, I. Birkel and R.G. Haire, 1983, *J. Less-Common Met.* **93**, 353.
- Pettifor, D.G., 1970, *J. Phys. C* **3**, 367.
- Pettifor, D.G., 1972, in: *Metallurgical Chemistry*, ed. O. Kubaschewsky (H.M. Stationary Office, London).
- Pettifor, D.G., 1976, *Commun. Phys.* **1**, 141.
- Pettifor, D.G., 1977, *J. Phys. F* **7**, 613.
- Pettifor, D.G., 1978, *J. Phys. F* **8**, 219.
- Pickett, W.E., A.J. Freeman and D.D. Koelling, 1980, *Physica B* **120**, 341.
- Piercy, A.R., and K.N.R. Taylor, 1968, *Proc. R. Soc.* **7**.
- Price, D.L., and B.R. Cooper, 1989, *Phys. Rev. B* **39**, 4945.
- Reihl, B., N. Martensson, D.E. Eastman, A.J. Arko and O. Vogt, 1982, *Phys. Rev. B* **26**, 1842.
- Roof, R.B., R.G. Haire, D. Schiferl, L.A. Schwalbe, E.A. Kmetko and J.L. Smith, 1980, *Science* **207**, 1353.

- Rose, M.E., 1961, *Relativistic Electron Theory* (Wiley, New York).
- Rosengren, A., and B. Johansson, 1982, *Phys. Rev. B* **26**, 3068.
- Sarkisov, E.S., 1966, *Dokl. Akad. Nauk SSSR* **166**, 627 [*Sov. Phys. Dokl. Chem. Sec.* **166**, 135].
- Schwarz, K., and P. Mohn, 1984, *J. Phys. F* **14**, L129.
- Scoboria, P., A. Harrus, B. Andracka, T. Mihalisin, S. Raean and R.D. Parks, 1984, *J. Appl. Phys.* **55**, 1969.
- Sechovsky, V., and L. Havela, 1988, in: *Ferromagnetic Materials*, Vol. 4, eds E.P. Wohlfarth and K.H.J. Buschow (North-Holland, Amsterdam) p. 309.
- Sellmyer, D.J., M.A. Engelhardt, S.S. Jaswal and A.J. Arko, 1988, *Phys. Rev. Lett.* **60**, 2077.
- Severin, L., L. Nordström, M.S.S. Brooks and B. Johansson, 1991, *Phys. Rev. B* **44**, 9392.
- Shimizu, M., 1964, *Proc. Phys. Soc.* **84**, 397.
- Shimizu, M., 1965, *Proc. Phys. Soc.* **86**, 147.
- Skriver, H.L., 1982, *Phys. Rev. Lett.* **49**, 1768.
- Skriver, H.L., 1983a, in: *Muffin Tin Orbitals and Electronic Structure* (Springer, Heidelberg).
- Skriver, H.L., 1983b, in: *Systematics and Properties of the Lanthanides*, ed. S.P. Sinha (Reidel, Dordrecht) p. 213.
- Skriver, H.L., 1985, *Phys. Rev.* **31**, 1909.
- Skriver, H.L., and J.P. Jan, 1980, *Phys. Rev. B* **21**, 1489.
- Skriver, H.L., O.K. Andersen and B. Johansson, 1978, *Phys. Rev. Lett.* **41**, 42.
- Skriver, H.L., O.K. Andersen and B. Johansson, 1980, *Phys. Rev. Lett.* **44**, 1230.
- Smith, G.S., and J. Akella, 1982, *J. Appl. Phys.* **53**, 9212.
- Smith, G.S., J. Akella, R. Reichlin, Q. Johnson, R.N. Schock and M. Schwab, 1981, paper presented at Conf. on Actinides 81, Asilomar, CA, Sept. 1981.
- Smith, P.K., W.H. Hale and M.C. Thompson, 1969, *J. Chem. Phys.* **50**, 5066.
- Söderlind, P., O. Eriksson, J.M. Wills and A.M. Boring, 1993, *Phys. Rev.*, in press.
- Steiner, W., and H. Ortbauer, 1974, *Phys. Status Solidi* **26**, 451.
- Stirling, W.G., G.H. Lander and O. Vogt, 1983, *J. Phys. C* **16**, 4093.
- Szpunar, B., 1985, *Physica B* **130**, 29.
- Szpunar, B., and V.H. Smith Jr, 1990, *J. Solid State Chem.* **88**, 217.
- Szpunar, B., and W.E. Wallace, 1986, *Lanthanide and Actinide Research* **1**, 335.
- Ubachs, W., A.P.J. van Deursen, A.R. de Vroomen and A.J. Arko, 1986, *Solid State Commun.* **60**, 7.
- Van der Sluis, K.L., and L.J. Nugent, 1972, *Phys. Rev. A* **6**, 86.
- van Doorn, C.F., and P. de V. DuPlessis, 1977, *J. Magn. & Magn. Mater.* **5**, 164.
- Vedel, I., A.M. Redon and J.M. Léger, 1986, *Physica B* **144**, 61.
- Vegard, L., 1921, *Z. Phys.* **5**, 17.
- Velga, W.A.J.J., and K.H.J. Buschow, 1968, *J. Appl. Phys.* **39**, 1717.
- Vohra, Y.K., H. Olijnik, W. Grosshans and W.B. Holzapfel, 1981, *Phys. Rev. Lett.* **47**, 1065.
- von Barth, U., and C.D. Gelatt, 1980, *Phys. Rev. B* **21**, 2222.
- von Barth, U., and L. Hedin, 1972, *J. Phys. C* **5**, 1629.
- Vosko, S.H., and J.P. Perdew, 1975, *Can. J. Phys.* **53**, 1385.
- Vosko, S.H., J.P. Perdew and A.H. MacDonald, 1975, *Phys. Rev. Lett.* **35**, 1725.
- Ward, J.W., 1982, unpublished.
- Ward, J.W., 1983, *J. Less-Common Met.* **93**, 279.
- Ward, J.W., R.W. Ohse and R. Reul, 1975, *J. Chem. Phys.* **62**, 2366.
- Ward, J.W., P.D. Kleinschmidt and R.G. Haire, 1979, *J. Phys. Colloq. (Paris)* **40**, C-233.
- Weidner, P., K. Keulerz, R. Löhe, B. Roden, J. Röhler, B. Wittershagen and D. Wohlleben, 1985, *J. Magn. & Magn. Mater.* **47-48**, 75.
- Weigel, F., and A. Trinkl, 1968, *Radiochem. Acta* **10**, 78.
- Wertheim, G.K., and G. Creselius, 1978, *Phys. Rev. Lett.* **40**, 813.
- Weschke, E., C. Laubschat, T. Simmons, M. Domke, O. Strebel and G. Kaindl, 1991, *Phys. Rev. B* **44**, 8304.
- Williams, A.R., and U. von Barth, 1983, in: *Theory of the Inhomogeneous Electron Gas*, eds S. Lundqvist and N.H. March (Plenum Press, New York) p. 189.
- Wills, J.M., and B.R. Cooper, 1987, *Phys. Rev. B* **36**, 3809.
- Wills, J.M., and O. Eriksson, 1992, *Phys. Rev. B* **45**, 13879.
- Wills, J.M., and W.A. Harrison, 1983, *Phys. Rev. B* **28**, 4363.
- Wills, J.M., O. Eriksson and A.M. Boring, 1991, *Phys. Rev. Lett.* **67**, 2215.
- Wills, J.M., O. Eriksson, P. Söderlind and A.M. Boring, 1992, *Phys. Rev. Lett.* **68**, 2802.
- Wohlfarth, E.P., and P. Rhodes, 1962, *Philos. Mag.*

- 7, 1817.
- Wu, R., and A.J. Freeman, 1991, *J. Magn. & Magn. Mater.* **99**, 81.
- Wu, R., C. Li, A.J. Freeman and C.L. Fu, 1991, *Phys. Rev. B* **44**, 9400.
- Yamada, H., 1988, *Physica B* **149**, 390.
- Yamada, H., and M. Shimizu, 1985, *J. Phys. F* **15**, L175.
- Yamada, H., and M. Shimizu, 1986, *J. Phys. F* **16**, 1039.
- Yamada, H., H. Inoue, J. Terao, S. Kanda and M. Shimizu, 1984, *J. Phys. F* **14**, 1943.
- Zachariasen, W.H., 1949, as quoted by A.W. Lawson and T.Y. Tang, 1949, *Phys. Rev.* **76**, 301.
- Zachariasen, W.H., 1952, *Acta Crystallogr.* **5**, 19, 660, 664.
- Zachariasen, W.H., 1961, in: *The Metal Plutonium*, eds A.S. Coffinberry and W.N. Miner (University of Chicago Press) p. 99.
- Zachariasen, W.H., 1964, in: *The Law of Mass Action Centenary Volume* (Norwegian Academy of Science, Oslo) p. 183.
- Zachariasen, W.H., 1973, *J. Inorg. Nucl. Chem.* **35**, 3487.
- Zachariasen, W.H., and F.H. Ellinger, 1977, *Acta Crystallogr. A* **33**, 155.

## Chapter 113

# HIGH-PRESSURE STUDIES – STRUCTURAL ASPECTS

U. BENEDICT

*Commission of the European Communities, Joint Research Centre, Institute for Transuranium Elements, Postfach 2340, D-76125 Karlsruhe, Federal Republic of Germany*

W.B. HOLZAPFEL

*Universität (GH) Paderborn, Fachbereich 6-Physik, Postfach 1621, D-33095 Paderborn, Federal Republic of Germany*

### Contents

List of symbols and acronyms	246	4.2.4. Discussion	280
1. Introduction	246	4.3. Comparison between LnX and AnX compounds	282
2. The elements	249	5. Other compounds	285
2.1. The lanthanides	249	5.1. M <sub>3</sub> X <sub>4</sub> compounds	285
2.2. The actinides	255	5.1.1. Ln <sub>3</sub> X <sub>4</sub> compounds	285
2.3. Yttrium and scandium	263	5.1.2. An <sub>3</sub> X <sub>4</sub> compounds	285
2.4. Scaling rules for regular rare earth elements	265	5.2. M <sub>2</sub> X <sub>3</sub> compounds	286
2.5. Comparison of rare earth and actinide elements	266	5.3. MX <sub>2</sub> and MX <sub>Y</sub> compounds	288
2.6. Interlanthanide and interactinide alloys	268	5.3.1. Lanthanide and actinide dioxides	288
3. Intermetallic compounds	269	5.3.2. Compounds of the Fe <sub>2</sub> As (PbFCl) structure type	290
3.1. Compressibility data	269	5.3.3. Dihalides	291
3.2. Phase transitions	270	5.3.4. Other MX <sub>2</sub> compounds	291
3.3. High-pressure, high-temperature synthesis	271	5.3.5. LnOF and LnSF compounds	292
3.3.1. Laves phases	272	5.3.6. High pressure, high temperature synthesis	292
3.3.2. Other intermetallic compounds	272	5.4. MX <sub>3</sub> compounds	292
4. MX compounds	272	5.4.1. Halides of the AlCl <sub>3</sub> , BiI <sub>3</sub> , UCl <sub>3</sub> , and PuBr <sub>3</sub> type	292
4.1. LnX compounds	273	5.4.2. Other MX <sub>3</sub> compounds	294
4.2. AnX compounds	276	5.5. MX <sub>4</sub> compounds	294
4.2.1. High-pressure phases and volume compression	278	5.6. MX <sub>6</sub> and MX <sub>12</sub> compounds	294
4.2.2. Hysteresis to re-transformation	279	5.7. Ternary and quaternary compounds	294
4.2.3. The bulk moduli	279	6. Summary and outlook	294
		References	296

## List of symbols and acronyms

An	actinide
B1 (type)	NaCl-structure type
B2 (type)	CsCl-structure type
$_{\text{del}}$	referring to the delocalized state
dhcp	double hexagonal close-packed
EOS	equation of state
EXAFS	extended X-ray absorption fine structure
fcc	face-centered cubic
hcp	hexagonal close-packed
HPXRD	high-pressure X-ray diffraction
$K_0$	isothermal bulk modulus at ambient pressure
$K'_0$	pressure derivative of $K$ at ambient pressure
$K''_0$	second pressure derivative of $K$ at ambient pressure
Ln	lanthanide
M	metallic element
$R_{\text{ws}}$	Wigner–Seitz radius
$V_0$	volume at ambient pressure
$V_{\text{odel}}$	volume at ambient pressure for the delocalized state
X	ligand element
XANES	X-ray absorption near-edge structure
$\eta$	normalized stress, see eq. (1)
$\sigma_p$	root mean square deviation in the pressure

---

## 1. Introduction

Lanthanides, from cerium on, successively fill the 4f shell until, at lutetium, the f occupation is 4f<sup>14</sup>. Although in the actinide series there is a delay in 5f filling – thorium has practically no 5f occupancy at ambient pressure – the filling then proceeds similar to the lanthanides, reaching 5f<sup>14</sup> at lawrencium, Lr. At first sight, one would thus expect a very similar evolution of the properties in general, and of the pressure behavior in particular, along the two series.

However, there are important differences. While the spatial extension of the 4f wave functions around the nucleus in the lanthanide metals is relatively small, the 5f wave functions in the actinide metals are more extended (Johansson et al. 1981). This favors direct interactions of 5f electrons with conduction electrons and indirect interactions with 5f electrons of neighboring atoms. Such interactions exist, at ambient pressure, in the lighter actinides, protactinium to plutonium. The 5f electrons of these actinide metals are considered to be “delocalized” or “itinerant” and participate in the metallic bonding. In contrast, the 4f electrons of the lanthanides and the 5f electrons of americium and the heavier actinides are usually considered to be “localized”.

The tighter bonding in the actinide metals Pa to Pu is clearly apparent from their smaller atomic volumes and higher densities (fig. 1). We shall see below that this effect leads to important differences in their behavior under pressure, both for the type of phase transitions observed and for the bulk moduli.

There is another difference which is relevant for pressure studies. The localized f electrons of the lanthanide and the heavier actinide metals allow these metals to



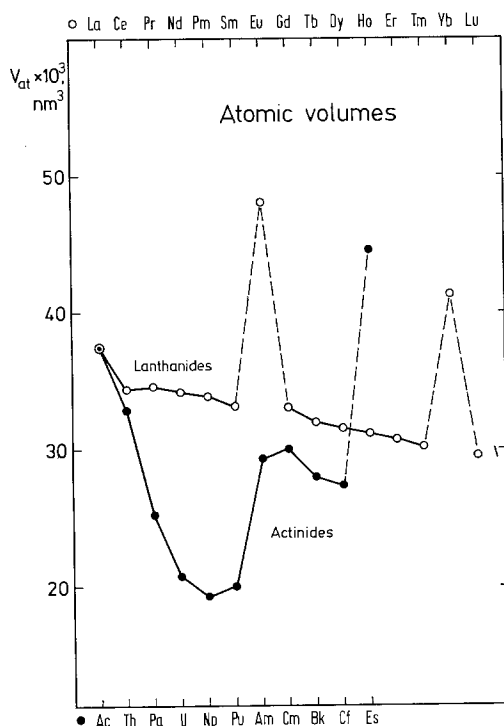


Fig. 1. Atomic volumes of lanthanide and actinide metals. Pa, U, Np and Pu: density increased by 5f-bonding. Eu, Es, Yb: low density due to divalency.

adopt crystal structures with high symmetry. Structures with high symmetry are not compatible with the highly directional hybridized orbitals which 5f orbitals form with the conduction electrons. These orbitals favor low-symmetry structures, as they exist in the actinide metals uranium, neptunium and plutonium at ambient pressure.

Pressure-induced structural transitions in these metals will be reviewed in sect. 2. We will see that detailed studies of these materials under pressure have revealed clear systematic trends and a basic theoretical understanding. Nevertheless, some way remains to be gone before we really can say that the pressure behavior of these two series of metals is completely understood.

For the pressure behavior of the compounds of the f elements, we are still much less advanced in systematic study and understanding than for the f elements themselves. The only group of compounds where systematic trends begin to emerge is that having the B1-type structure. This is the largest group of compounds formed by lanthanides and actinides. Nearly all 1:1 LnX and AnX compounds exhibit the NaCl (B1)-type structure. High-pressure structural studies have only been reported for about 26 of the 121 known B1-type rare earth compounds. The proportion is much higher for the actinides than for the lanthanides: 29 of the reported 67 B1-type actinide borides, carbides, pnictides, and chalcogenides have undergone structural study under high pressure.

The lattice-parameter plots in fig. 2 show a similar dip for the group Pa to Pu as was observed for the volumes of the pure metals in fig. 1. Here the interpretation

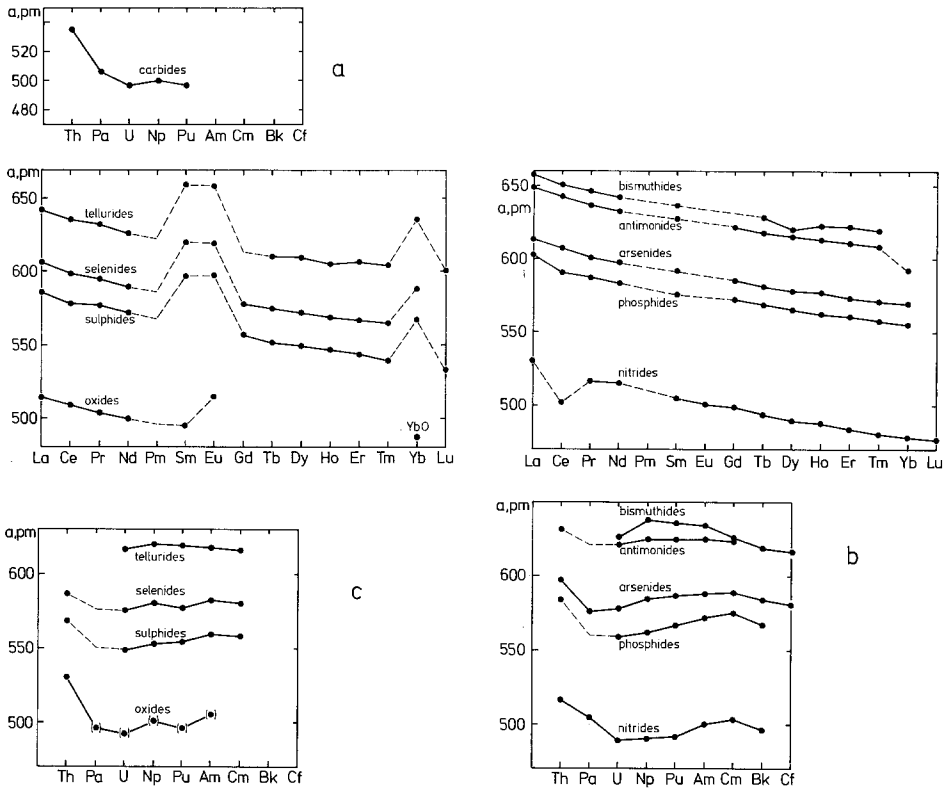


Fig. 2. Lattice parameters of BI-type lanthanide and actinide compounds at ambient conditions. (a) Actinide monocarbides. Monocarbides are not known for the heavier actinides and for the lanthanides. (b) Monopnictides. Note the regular decrease with  $Z$  for lanthanide compounds (exception: CeN). The lattice parameters of actinide compounds, in contrast, go through a minimum in the region Pa to Pu. See also sect. 4. (c) Monochalcogenides. Note the regular decrease with  $Z$  for lanthanide compounds (exception: divalent lanthanides). The lattice parameters of actinide compounds, in contrast, go through a minimum in the region Pa to Pu. See also sect. 4. (●): monoxides of actinides only observed as surface layers or stabilized by impurities.

seems less clear: no low-symmetry structures are observed, but the high density observed for the light actinides may indicate that a certain proportion of 5f bonding also occurs in these compounds. The compounds of lanthanides and heavier actinides show in general a regular decrease of volume with atomic number of the cation, with anomalies for Sm, Eu, and Yb compounds. The only lanthanide compound having a distinctly lower volume than its neighbors, and thus resembling the UN–NpN–PuN group, is CeN.

In the section on the metals, the reader will be referred to previous reviews for details. This is not possible for the sections on compounds (sections 3, 4, and 5), since no recent comprehensive reviews are known. Consequently, the present chapter aims at giving as complete a review as possible on the compounds, including most of the published results.

As recommended by the editors, the terms “lanthanides” (Ln) and “actinides” (An) will be used to include the elements La and Ac, for which no f occupancy is observed under ambient pressure.

## 2. The elements

Both above-mentioned particularities of actinides with itinerant electrons, high density and low-symmetry structures, can be induced in actinides and lanthanides with localized f electrons by the action of pressure. Compression leads to hybridization and overlapping of f electron orbitals and, thus, generates also in these “regular” metals states which are similar to those found in U, Np, and Pu at ambient pressure. Phase transitions under pressure to low-symmetry structures have up to now been reported in Am, Cm, Bk, and Cf for the actinides, and in Ce, Pr, Nd, and Sm for the lanthanides.

### 2.1. The lanthanides

The lanthanide metals represent a group of elements which is well known for its close systematics in structural, elastic, and electronic properties for most of its members, but also with some well-established anomalies for the elements Ce, Eu, and Yb, not only at ambient pressures but also extending over the whole pressure range studied so far (Gschneidner 1985, Krüger et al. 1990, Grosshans and Holzapfel 1992 and references therein, Staun Olsen et al. 1985a, Haire et al. 1990a).

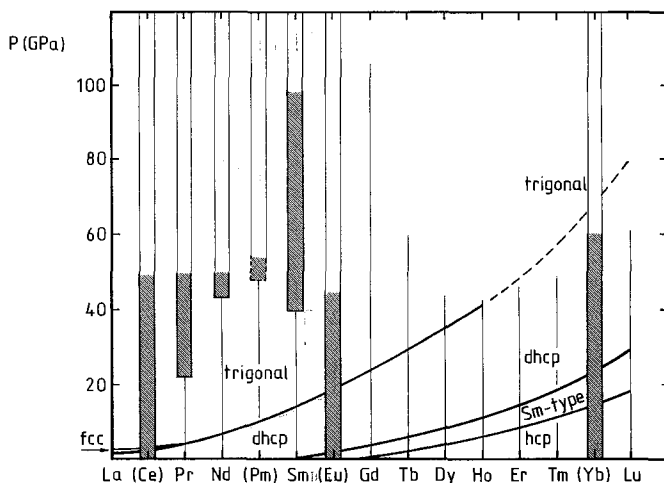


Fig. 3. Generalized phase diagram for the regular lanthanides and regular intra-lanthanide alloys at low temperatures (0K), taken with slight modifications from Krüger et al. (1990). The region covered by experiments on the regular elements is marked by thin vertical lines. The anomalous regions for the elements Ce, Eu, and Yb, as well as Pr, Nd, and Sm, under higher pressures are marked by heavy vertical bars. Dashed lines represent extrapolations.

First of all, the structural systematics for the regular lanthanide metals have been well established over an extended region in pressure and temperature in recent years (Krüger et al. 1990 and references therein), and, based on an idea of Gschneidner (1985) (see also Gschneidner and Calderwood 1986), a generalized alloy phase diagram for the regular lanthanide metals, including more recent data for all these elements at higher pressures, is shown in fig. 3. Here one can notice immediately that the structural sequence  $\text{fcc} \leftrightarrow \text{dhcp} \leftrightarrow \text{Sm-type} \leftrightarrow \text{hcp}$  is observed not only along the series of lanthanide metals with increasing atomic number, going from La to Lu, but also with increasing pressure for constant atomic number, and is seen most completely for the heavier lanthanides, while the lighter elements start already at ambient pressure with the high-pressure structures of the heavier elements. Since detailed illustrations of these typical rare earth structures can be found at many places in the literature (Young 1991 and references therein), it may be sufficient to recall here that all these "regular" rare earth structures can be envisaged as different stackings of close-packed hexagonal layers with periodic repetition of different basic sequences: ABC for fcc, ABAC for dhcp, ABABCBCAC for Sm-type and with just AB for hcp.

It is now supposed that this generalized alloy phase diagram, fig. 3, is also valid for binary alloys of regular elements in the neighborhood of the anomalous elements Ce, Eu, and Yb, in the sense that the alloy  $\text{La}_{0.5}\text{Pr}_{0.5}$  may represent a regular "pseudo-Ce" and  $\text{Sm}_{0.5}\text{Gd}_{0.5}$  or  $\text{Tm}_{0.5}\text{Lu}_{0.5}$  a regular "pseudo-Eu" or "pseudo-Yb", respectively. In fact, the first high-pressure studies on the "pseudo-Ce" alloy  $\text{La}_{0.5}\text{Pr}_{0.5}$  over an extended pressure region indicate that this assumption holds very well (Porsch et al. 1992). So, the irregular behavior of the three elements Ce, Eu, and Yb themselves is indicated in fig. 3 just by the brackets around these elements and by the heavy vertical lines. The thin vertical lines at the places of the other elements denote only the regions in pressure which have been studied experimentally in each case up to fall 1991. For later comparison with theoretical studies, the diagram presents the values for the equilibrium transition pressures extrapolated down to zero temperature from pressure cycles at room temperature and above (Krüger et al. 1990). Therefore, only a marginal region of stability for the fcc phase can be observed near La, while otherwise the trigonal (or distorted fcc) phase must be considered as the stable phase at low temperatures (and high pressures) (Krüger et al. 1990).

Indicated by dashed portions of these phase boundaries, extrapolations to pressures beyond the present experimental range are plotted for some of the heavier lanthanide metals, using critical radius ratios, discussed below in relation with fig. 5, and using in addition best estimates for the equation of state (EOS) data appropriate for this extended pressure range (Grosshans and Holzapfel 1992).

Finally, additional heavy vertical lines for Pr, Nd, and Sm at high pressures mark here also the regions where new low-symmetry structures occur, which are commonly associated with anomalous behavior similar to the case of Ce and, therefore, are attributed to f contributions to the bonding (Benedict et al. 1986b, McMahan 1989).

If one is interested, on the other hand, in an alloy phase diagram including the anomalous metals Ce, Eu, and Yb together with their neighboring elements, and if one takes directly the "forward transition pressures", measured commonly just with increasing pressure (at ambient temperature), one obtains a slightly different diagram, fig. 4, which illustrates more clearly all the possible anomalies.

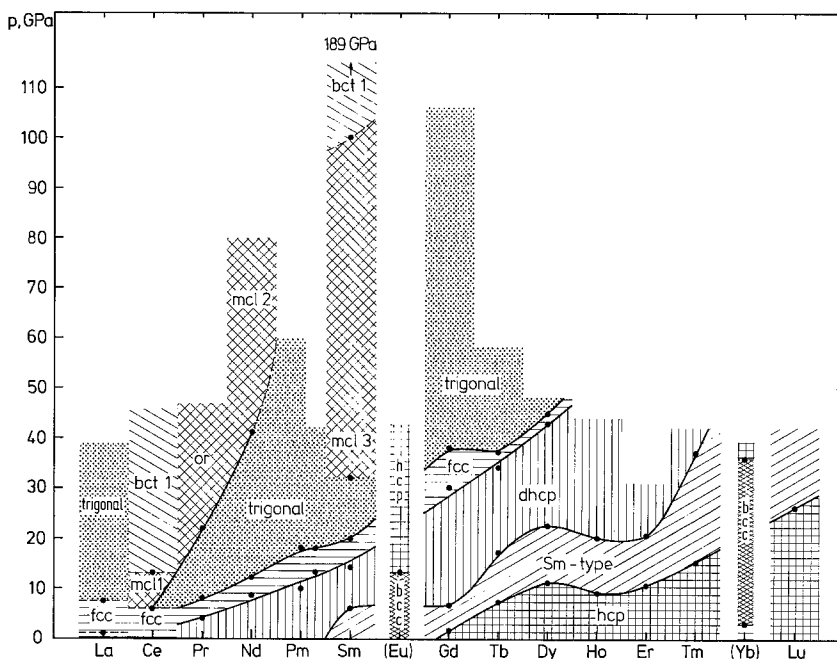


Fig. 4. General diagram of the phase relations of the lanthanide metals under pressure. ●: experimentally observed phase transitions (upstroke transition pressures); or: orthorhombic; mcl 1, 2, 3: three different monoclinic structures; bct 1, 2: two different body-centred tetragonal structures; the other symbols have their usual meaning. The highest pressure reached for Sm is indicated above the arrow. Dashed lines: exact line to be determined by further pressure studies of the alloys. The data are mainly taken from Grosshans (1987), Staun Olsen et al. (1985a, b, 1990), Haire et al. (1990a), Vohra et al. (1991), Akella et al. (1988b), and Akella and Smith (1987).

To gain further insight in these systematics, fig. 5 represents an updated version of a previously shown diagram (Benedict et al. 1986b, Krüger et al. 1990), which uses now all the available EOS data for the extended pressure range (Grosshans and Holzappel 1992) together with the previously compiled transition pressures (Krüger et al. 1990) to plot the critical radius ratios,  $r_r = R_{ws}/R_{5p}$ , for each transition, starting with the ratio at ambient pressure.  $R_{ws}$  stands for the Wigner-Seitz radius and  $R_{5p}$  represents the 5p core radius (Waber and Cromer 1965), which can also be considered as a good measure for the ionic core radius.

In this radius ratio plot, one can also clearly notice that all the “regular” structural transitions (not leading to low-symmetry structures) for the “regular” lanthanide metals (and intralanthanide alloys) are very well characterized, within the given experimental uncertainties, just by one typical value for this radius ratio  $r_r = R_{ws}/R_{5p}$  for each transition. The values are  $r_r = 2.78$  for the hcp ↔ Sm-type, 2.70 for the Sm-type ↔ dhcp and 2.46 for the dhcp ↔ fcc or trigonal transition (at 0 K), keeping in mind that the region of stability for the fcc phase is at first just marginal at low temperatures but reappears for La at  $r_r < 1.9$  (Porsch and Holzappel 1993).

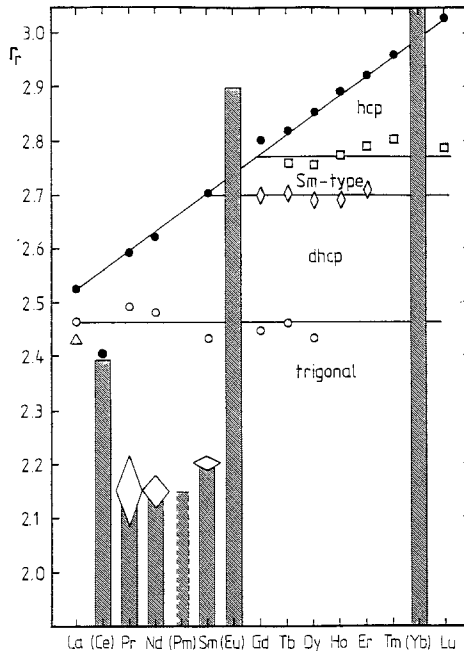


Fig. 5. Critical radius ratios  $r_r = R_{ws}/R_{sp}$  for phase transitions in the regular lanthanides under pressure extrapolated to low temperature (0 K), with the Wigner-Seitz radii,  $R_{ws}$ , from Krüger et al. (1990) and the ionic radii,  $R_{sp}$ , from Waber and Cromer (1965). Open squares mark the hcp $\leftrightarrow$ Sm-type transition, open diamonds locate the Sm-type $\rightarrow$ dhcp transition, open circles present the dhcp $\leftrightarrow$ fcc or trigonal transition, and the open triangle stands for the fcc $\leftrightarrow$ trigonal transition of La, while the closed circles represent the starting values  $r_{r0}$  at ambient pressure. The continuous straight lines are just guides for the eye. The vertical bars mark the locations of the irregular elements Ce, Eu, and Yb, as well as the regions of low-symmetry structures for Pr, Nd, and Sm, with the volume jumps indicated by open diamonds on top of these bars.

In this diagram, fig. 5, the “volume collapse” or the respective jump in the radius ratio can be illustrated as shown by the diamonds on top of the heavy lines, which represent the regions of collapsed or f-bonded structures. As far as we know, intralanthanide alloys (besides the regular “pseudo-Ce”) have not been studied in these anomalous regions. Strong deviations from simple alloy behavior might be expected for these alloys.

On the other hand, systematic behavior is also observed in EOS data for the “regular” lanthanides (Grosshans and Holzapfel 1992), at least for the isothermal parts. In fact, systematics in the thermal contributions have not been studied so far.

These systematics in the ambient-temperature EOS data (Grosshans and Holzapfel 1992) are visualized most directly in graphical form, fig. 6, where a normalized stress or more precisely the quantity

$$\eta = \ln\{p/p_{FG}/[1 - (r_r/r_{r0})]\} \quad (1)$$

is plotted versus the length scale  $r_r$ , which becomes  $r_{r0}$  at ambient pressure and

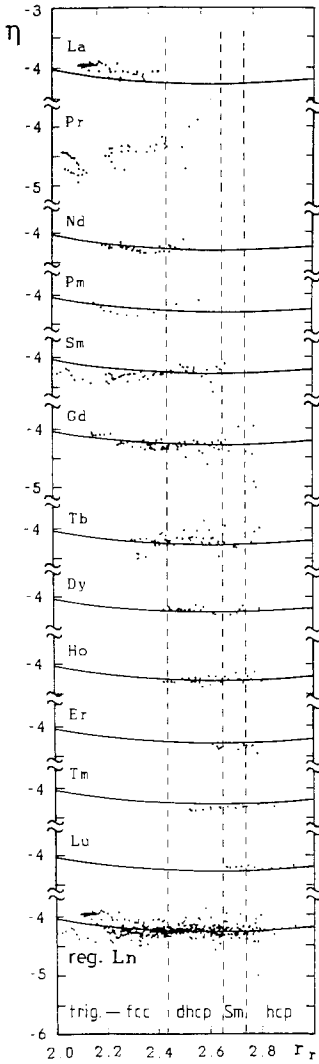


Fig. 6. EOS data for the regular lanthanides, from Grosshans and Holzapel (1992), plotted in the form of normalized stress,  $\eta$ , versus scaled radii,  $r_r$ , to illustrate the common scaling behavior and the special anomalies of Pr. The continuous lines represent the common best fitting curve for the combined data set (excluding Ce, Pr, Eu, and Yb), shown in the lowest section of this diagram.

represents just the radius ratio  $r_r = R_{ws}/R_{sp}$  already used in fig. 5. Due to the scaling with the Fermi gas pressure  $p_{FG}$ , the quantity  $\eta$  approaches 0 at infinite compression and shows a simple linear variation for many simple solids (Holzapfel 1990, 1991), and the Fermi gas pressure  $p_{FG} = a_{FG}(Z/V)^{5/3}$  involves only the universal parameter  $a_{FG} = 2.3369 \text{ TPa } \text{\AA}^5$ , the electron number per atom,  $Z$ , and the atomic volume  $V = (4\pi/3)R_{ws}^3$ .

What is most surprising in such a plot for the regular lanthanides, fig. 6, is the observation (Grosshans and Holzapel 1992) that one common curve represents all the data within the present experimental uncertainties.

However, Pr, which is usually considered to be a regular lanthanide below its phase transition to the  $\alpha$ -U structure at 21 GPa, shows in this plot significant deviations

from this common curve already at much lower pressures, where the trigonal structure would indicate only regular behavior. If one excludes, therefore, not only the data for Ce, Eu, and Yb but also those for the trigonal phase of Pr from the common plot of all the EOS data for regular lanthanides in the lowest section of fig. 6, one finds that the spread of the data around the common curve is not significantly larger than in the individual diagrams for each element in fig. 6, and the parameters  $a_1 = 3.64$  and  $a_2 = 0.775$  are obtained for the best fitting quadratic form  $\eta = -a_1 r_r + a_2 r_r^2$ . In fact, one can notice that all the ambient pressure values  $\eta_0 = -4.20(7)$  and the initial slopes  $\eta'_0 = 0.01(1)$  fit these common values closely (Grosshans and Holzapfel 1992) and determine, therefore, two simple scaling relations for all the corresponding bulk moduli,  $K_0$ , and their pressure derivatives at ambient pressure,  $K'_0$ , as given by the relations (Holzapfel 1990, 1991):  $K_0 = \frac{1}{3} p_{FG0} \exp \eta_0$  and  $K'_0 = 3 - \frac{2}{3} \eta'_0 r_{r,0} = 2.9(1)$ .

These two relations are also represented as best fitting curves in fig. 7, which shows in graphical form all the data for  $K_0$  and  $K'_0$  that have been compiled from different sources in the recent review by Grosshans and Holzapfel (1992). A closer inspection of fig. 7 shows again that only the values for Ce, Eu, and Yb deviate significantly from the common behavior.

At this point, however, the special EOS relations for Ce, Pr, Eu, and Yb, as illustrated by the special  $\eta$ - $r_r$ -curves in fig. 8, deserve some further consideration. Since the low values of  $\eta$  near the volume-collapse transition in Ce (and, less pronounced, in Pr) are directly related to special softening in  $K(p)$ , one wonders why no such anomalies are noticed near the phase transitions of Nd and Sm to their low-symmetry

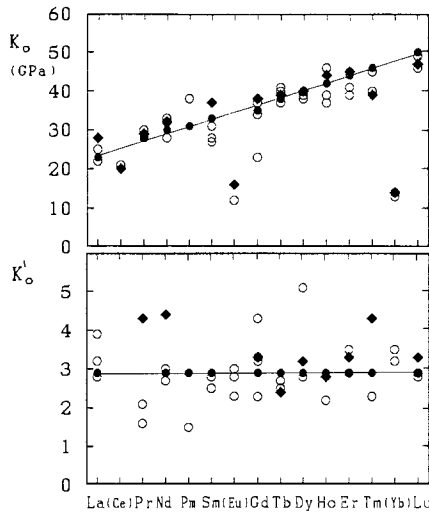


Fig. 7. Comparison of the literature data on  $K_0$  and  $K'_0$  for all the lanthanide metals, illustrating the spread of the data for the regular lanthanides around the best fitting lines. Solid circles represent the estimated best values (Grosshans and Holzapfel 1992), open circles mark isothermal values from static measurements, and solid diamonds stand for isothermal values deduced from ultrasonic measurements. All references are given in the previous review (Grosshans and Holzapfel 1992). Best estimates are not given for the irregular elements Ce, Eu, and Yb, which are marked by parentheses.



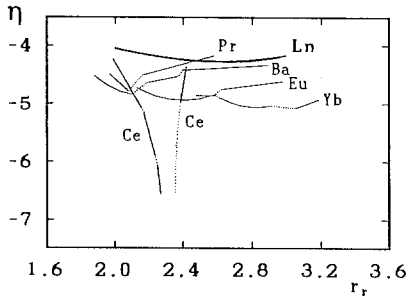


Fig. 8. Comparison of the EOS data on the regular lanthanides, with the data for Ce, Pr, Eu, Yb, and Ba taken from the review of Grosshans and Holzapfel (1992) and plotted in the same form of normalized stress,  $\eta$ , versus scaled radii,  $r_r$ , as in fig. 6.

phases. If one considers, however, that the anomalies  $\Delta K$  are of the same order of magnitude in all these cases, and takes into account that just the regular background values  $K_r = K - \Delta K$  increase quite strongly with increasing pressure, one can expect that the anomalies in  $\eta$  must decrease when they are shifted to the higher pressure regions.

Eu and Yb, however, in comparison, start out with a completely different electronic configuration at ambient pressure, where they are usually considered as divalent elements with similarities to Sr and Ba, respectively. As shown in fig. 8 by the comparison with data for Ba, this similarity is not too close, and at the highest pressure, where Eu and Yb give almost trivalent signatures in XANES measurements (Röhler 1986, Syassen et al. 1982), both of these elements approach the 4f-band behavior presented by Ce and Pr in their collapsed phases. One can speculate, therefore, that all the lanthanide curves in this plot will merge into a common 4f-band behavior at tera-Pascal pressures where the localized moments are also destroyed in the regular heavier lanthanides.

## 2.2. The actinides

The actinide metals clearly represent a group of elements with a wider range of individual behavior, where systematics in the structural, elastic, and electronic properties are much less obvious than for the lanthanides.

Already at ambient pressure the field of thermal phase transitions is very rich (Smith and Kmetko 1983), with the most pronounced anomalies for Pu and its alloys. Furthermore, the ambient-temperature section of the generalized high-pressure phase diagram for intra-actinide alloys, as previously discussed by Benedict (1987, 1989) and shown in an updated version in fig. 9, has at first glance little resemblance with the much simpler behavior of the lanthanides, discussed before (cf. figs. 3 and 4). Nevertheless, when one uses also here the available EOS data together with tabulated (Waber and Cromer 1965) and partly interpolated values for the 6p-shell radii,  $R_{6p}$ , to determine the radius ratios  $r_r = R_{ws}/R_{6p}$  at first for ambient pressure and then also for all the individual phase transitions, one obtains fig. 10, which has been presented previously in almost the same form (Benedict et al. 1986b, McMahan 1989, Benedict 1987), and which discloses more readily the underlying physics than the raw data in fig. 9.

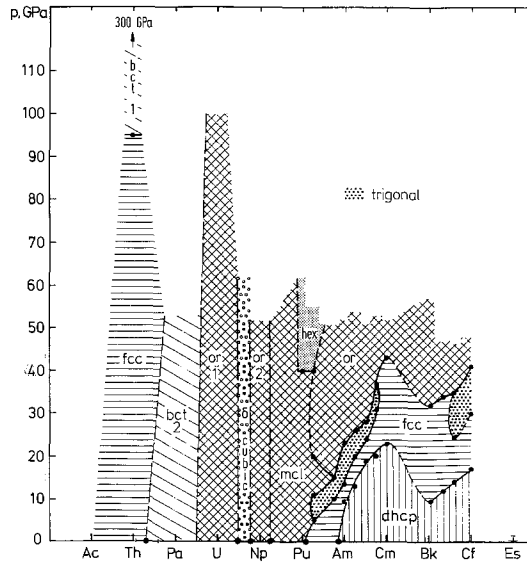


Fig. 9. General diagram of the phase relations of actinide metals under pressure, status of end 1991. ●: experimentally observed phase transitions (upstroke transition pressures for pressure-induced transitions); or, or 1, or or 2: three different orthorhombic structures; mcl: monoclinic; bct 1, 2: two different body-centred tetragonal structures; hex: hexagonal; the other symbols have their usual meaning. The highest pressure reached for Th is indicated above the arrow. Dashed lines: exact line to be determined by further pressure studies of the alloys. Data mainly from Benedict (1987 and references therein), Vohra and Akella (1991) for Th, and, for the alloys, from the work mentioned in sect. 2.6.

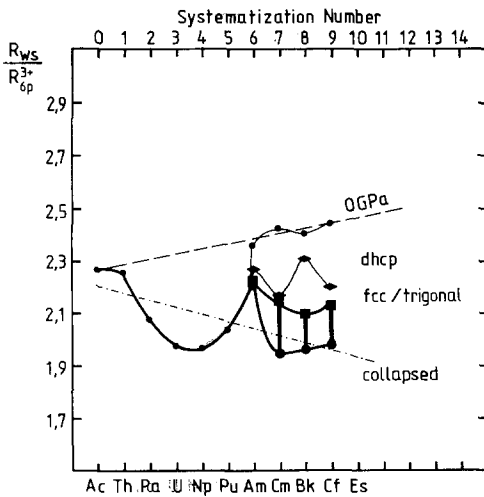


Fig. 10. Radius ratios  $r_r = R_{ws}/R_{6p}$  for the actinides at ambient pressure (solid circles), and critical values for the phase transitions dhcp → fcc or trigonal (solid diamonds) and fcc or trigonal → collapsed (solid squares), with the heavy vertical bars representing the volume collapse transitions (Benedict et al. 1986b).

First of all, one can notice, for the initial values  $r_{r,0}$ , a strongly pronounced minimum between U and Np, which is considered to be a finger print for strong f bonding in these elements already at ambient pressure, and, correspondingly, the jump in  $r_{r,0}$  between Pu and Am is attributed to the localization of the 5f electrons, typical for the heavier actinide metals at ambient pressure. In addition, the appearance of the typical lanthanide structures (dhcp, fcc, trigonal) for these heavier actinides is taken as another hint for localization of the 5f electrons in these structures; however, neither the initial values  $r_{r,0}$  nor the critical values for  $r_r$  at the transitions from dhcp to fcc or trigonal structures show here the same smooth variation typical for the regular lanthanides. Therefore, stronger 5f-hybridization with the conduction electrons (Eriksson et al. 1990) or other factors, like stronger spin-orbit coupling than in the lanthanides (Brooks et al. 1991), must be responsible for these slight irregularities in the structural behavior of the heavier actinides. Ultimately, after the “volume-collapse” transitions (Benedict et al. 1986b, Benedict 1987 and references therein), the low-symmetry structures show also  $r_r$ -values which are typical for the 5f-band metals U and Np already at ambient pressure, and the rather large value of  $r_r$  for Am after the “collapse”, together with the smaller volume change, could possibly be attributed to a significant increase in the 5f electron count, just in this special case approaching the half-filled 5f-band configuration, similar to the anomalous behavior of Eu under high pressures. In any case, fig. 10 illustrates once more that the structural properties of the actinides are very much influenced by details in the electronic structure (which involve a detailed balance in 7sp, 6d and 5f electron counts), and, apparently, in a more complicated fashion than in the case of the lanthanides.

Thus, one also might expect more complicated systematics for the EOS parameters of the actinides, as already noted in the previous review by Benedict (1987 and references therein) with the then available data for  $K_0$  and  $K'_0$  on actinide metals and some of their intra-actinide alloys. However, already at that time, strong anti-correlations were noticed in the values for  $K_0$  and  $K'_0$  given by different authors, and, by now, this problem can be enlightened in much more detail since the present data, for instance on Th, span a much wider range in pressure (Akella et al. 1988a, b, Vohra and Akella 1991).

For this purpose, we reanalyze all the available static EOS data for Th, as shown in table 1, with a set of three different EOS forms, and compare the effect of the different EOS forms with the effects resulting from different data sets. As EOS forms we use the Birch equation (Birch 1978) in second order, BE2, and two recently proposed forms (Holzapfel 1990, 1991) in second-order form, H02 and H12, which are related to the Thomas-Fermi theory and are distinguished by the fact that H12 is bound to approach the Fermi-gas limit at infinite compression. A close inspection of table 1 shows very clearly that most of the data are fitted almost equally well by any of these forms, without any significant difference in the fitted parameters  $K_0$  and  $K'_0$  or in the minimized standard deviation of the pressure,  $\sigma_p$ . In contrast to many other publications, table 1 presents the unrestricted standard deviations of  $K_0$  and  $K'_0$ , which correspond to the extreme values of the error ellipsoids presented in fig. 11, and not just to the width of the error ellipsoids along  $K_0$  and  $K'_0$  at the center points, which are usually given as (restricted) statistical errors. Thus, it becomes obvious that

TABLE 1

Comparison of EOS data of thorium from different sources, showing also the effects of different EOS forms on the least-squares fitted parameters  $K_0$  and  $K'_0$ . Unrestricted standard deviations of the correlated parameters are placed in parentheses and refer to the last decimal places of the parameter values.  $\sigma_p$  denotes the standard deviation of the data from the fitted curves and  $\epsilon$  gives the correlation coefficient for the fitted parameters  $K_0$  and  $K'_0$ . The usual (restricted) errors can be obtained by multiplication of the unrestricted errors with  $(1 - \epsilon^2)^{1/2}$ . Parameters predetermined by the use of a second-order EOS form or by effective first-order fits using BE2, H02, and H12 with  $K_0$  fixed, are placed in obtuse brackets.

Ref. for data	Codes for fig.	$P_{\max}$ (GPa)	$V_0$ ( $\text{\AA}^3$ )	EOS form used	$K_0$ (GPa)	$K'_0$	$-K_0K''_0$	$\sigma_p$ (GPa)	$-\epsilon$
Bridgman (1948)	48Br	10	32.88	BE2	36(32)	15(27)	—	0.20	0.992
				H02	37(25)	12(13)	—	0.18	0.986
				H12	37(25)	13(14)	—	0.18	0.987
Vaidya and Kennedy (1972)	72VK	5	32.88	BE2	54(10)	5.2(72)	—	0.01	0.973
				H02	54(10)	5.2(71)	—	0.01	0.973
				H12	54(10)	5.2(69)	—	0.01	0.972
Kennedy and Keeler (1972)	72KK	100	32.88	BE2	53(3)	3.9(2)	—	0.09	0.981
				H02	53(3)	4.0(2)	—	0.08	0.983
				H12	56(8)	3.4(8)	—	0.21	0.992
Benjamin et al. (1981)	81BZ	68	32.66 (17)	BE2	56(11)	3.5(6)	—	1.4	0.983
				H02	59(15)	3.2(12)	—	1.3	0.990
				H12	64(17)	2.3(15)	—	1.2	0.992
Bellussi et al. (1981)	81BB	29	32.88(2)	BE2	64(20)	3.3(29)	—	0.6	0.950
				H02	63(22)	3.4(40)	—	0.6	0.961
				H12	65(24)	2.9(44)	—	0.6	0.964
Akella et al. (1988a, b)	88AS	98	32.88	BE2	44(14)	4.6(12)	—	2.6	0.991
				H02	43(15)	5.0(14)	—	2.6	0.992
				H12	45(17)	4.6(18)	—	2.6	0.992
88AS with new $V_r$	88ASa	98	32.00	BE2	55(12)	4.2(7)	—	2.8	0.974
				H02	54(15)	4.4(11)	—	2.8	0.984
				H12	57(16)	3.9(14)	—	2.8	0.985
Vohra and Akella (1991)	91VA	300	32.88	BE2	33	5.0	—	—	—
				H02	29	5.8	—	—	—
				H12	31	5.4	—	—	—
all the data $K_0$ free	all data	300	32.88	BE2	54(7)	4.0(3)	<4>	3.3	0.883
				H02	52(11)	4.2(8)	<4>	3.3	0.948
				H12	59(13)	3.3(9)	<0>	3.2	0.964
				H13	59(27)	3.3(38)	-1(10)	3.2	0.967
all the data $K_0$ fixed	—	300	32.88	BE2	59.0	3.8(2)	<4>	3.6	—
				H02	fixed	3.8(2)	<4>	3.6	—
				H12		3.3(3)	<0>	3.2	—
				H13		3.3(10)	0(5)	3.2	0.980
Ultrasonic values for isothermal $K_0$									
Reynolds (1951)					60				
Armstrong et al. (1959)					57.1				
Greiner et al. (1977)					59.0				
Present best values					59.0(9)	3.4(4)	1(6)		

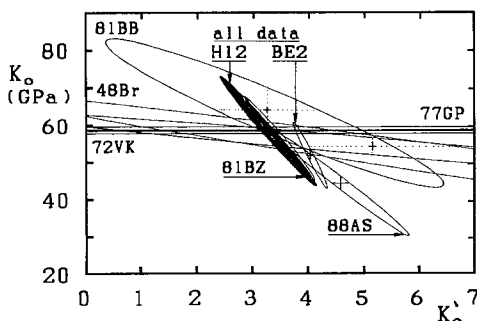


Fig. 11. Illustration of the correlation in the errors of  $K_0$  and  $K'_0$  for Th at ambient conditions according to the different fits presented in table 1. The keys for references are given in table 1. The error ellipsoids mark the level of one standard deviation in the least-squares fitting. The vertical and horizontal bars represent the commonly given “restricted” errors. The heavily drawn ellipsoid represents the result of the best fitting form, H12 in table 1, for all the data together, including the data of Vohra and Akella (1991) with weight ten, but with  $K_0$  free.

most of the fits are in fact compatible with each other from the point of view of the overlap of the corresponding error ellipsoids, and that the large elongation of the ellipsoids or the strong (anti)correlation between  $K_0$  and  $K'_0$  is most pronounced for data sets over limited pressure regions, where first-order forms corresponding to prefixed values of  $K'_0$  ( $\approx 4$ ) would be more reasonable, as seen by arbitrary selections of  $K'_0$  for these cases in fig. 11. A comparison of all these data must finally lead to the conclusion that the isothermal value  $K_{0T}$  derived from the adiabatic value  $K_{0S}$  from ultrasonic measurements at ambient conditions (Reynolds 1951, Armstrong et al. 1959, Greiner et al. 1977), included in table 1 and fig. 11, must be considered as the most accurate determination of  $K_{0T}$  for Th, leading also to rather narrow bounds for the best value of  $K'_0$ . Thus, the final fits of all the static EOS data, given in the last section of table 1, are bound by this fixed value of  $K_{0T} = 59.0(9)$  GPa, which then allows one to distinguish the quality of the fits using the different forms by inspection of the slight differences in  $\sigma_p$ , and it becomes obvious that the use of a third-order form (H13) is not really statistically justified, even when the data of Vohra and Akella (1991), extending to 300 GPa, are included in the fitting. However, further problems can be noticed when one plots the available static EOS data in the form of normalized stress,  $\eta$ , versus scaled radius,  $r_r$ , as shown in fig. 12 for all the data of Th.

Apparently, the data of Akella et al. (1988a, b) deviate from all the other data most strongly at the largest values of  $r_r$ , corresponding to the first few pressure points. Since the calibration of the high-pressure X-ray diffraction apparatus always is a possible source of errors, one may arbitrarily adjust the calibration, or in other words the value of  $V_0$ , used in the presentation of these data, in such a way that the best agreement is observed with all the other data, or just with  $K_0$  from the ultrasonic measurements, which leads to a correction of  $V_0$  by 2.4%, and this change might be considered well within the range of possible uncertainties due to mechanical shifts in the initial calibration. This rescaling of  $V_0$  also improves the agreement for these data, marked 88AS in fig. 11, with respect to all the other data.

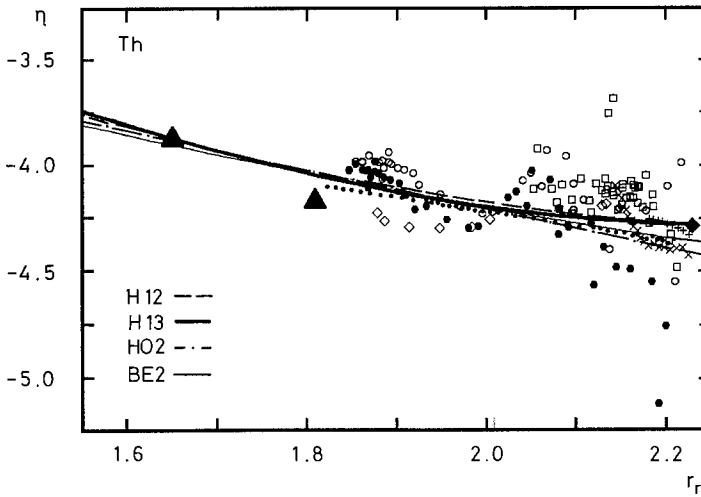


Fig. 12. EOS data for Th at ambient temperature, taken from different sources [stars from Bridgman (1948), crosses from Vaidya and Kennedy (1972), open diamonds from Benjamin et al. (1981), open squares from Bellussi et al. (1981), open circles from Akella et al. (1988a, b), and solid triangles from Vohra and Akella (1991)]. Shock-wave data reduced to isothermal values by Kennedy and Keeler (1972) are represented by the dotted curve. The solid diamond marks the best value of  $K_{0T}$  from ultrasonic measurements by Greiner et al. (1977). Solid circles represent the data from Akella et al. (1988a, b) with rescaled volumes  $V_0 = 32.00 \text{ \AA}^3$ . All the data are plotted in the form of normalized stress,  $\eta$ , versus scaled radius,  $r_r$ , defined in the text. Best fits of different analytical forms to all the experimental data, however, with weight ten for the two data points of Vohra and Akella (1991) and with the rescaled data of Akella et al. (1988a, b) only, are also shown, with the parameter values given in table 1. The best fit with the fixed best value  $K_{0T}$  from ultrasonic measurements, using the third-order form H13, is shown as continuous solid line. But fits using the second-order forms BE2, H02, and H12 are shown by thin dotted, dashed, and dash-dotted lines, respectively. The thin continuous line represents the quadratic best-fitting form for all the 5f-band actinides together.

There is however another effect, which could also be responsible for some of the anomalies in  $\eta$ - $r_r$  plots at moderate pressures, where the precise determination of  $V_0$  affects the initial  $\eta$ -values very much. Different samples of the various actinides may show significant variation in the initial values of  $V_0$ , according to their preparation, and this point may have affected the evaluation of high-pressure X-ray diffraction data.

With these observations in mind, the best fit for Th, using all the data presented in table 1, includes the data of Akella et al. (1988a, b) with the adjusted value of  $V_0 = 32.00 \text{ \AA}^3$  replacing the value for  $V_0$  implicitly used by Akella et al. (1988a, b) instead of the correct value. The two data points of Vohra and Akella (1991) at very high pressures are weighted by a factor ten to compensate somewhat for the dominating weight of the numerous experimental points at moderate pressures, and, finally, we fix in one series of fits the value of  $K_0$  to the most accurate value from ultrasonic measurements to obtain (from our point of view) the best values for  $K'_0$  and for  $-K_0 K''_0$ .

For completeness, also a third-order form, H13, was used in these tests, and the constancy in  $\sigma_p$  indicates that the use of this third-order form finds no statistical justification with respect to the second-order form H12.

When the best value for  $K_0$  from ultrasonic measurements is finally used in these fits as fixed parameter, one finds significant differences in the values for  $K'_0$  and  $\sigma_p$  between BE2 and H02, on the one hand, and H12 and H13, on the other, with the smaller  $\sigma_p$  values in the last two cases.

At the same time, one can notice that the internal constraints lead to the same values of  $-K_0K''_0$  for BE2 and H02, while H12 implies directly the same value as obtained by the two-parameter fit for  $K'_0$  and  $-K_0K''_0$  performed with H13, which then also leads to a more realistic estimate for the uncertainties in these two parameters.

Finally, it can be noticed that the fit of the data from Kennedy and Keeler (1972) by H12 gives a larger value for  $\sigma_p$  than both other fits, while the value for  $K_0$  deduced with H12 comes close to the best value deduced from all the fits and which is also strongly supported by the ultrasonic measurements. However, it must be recalled that Kennedy and Keeler (1972) derived their data from shock-wave results already with a certain smoothing procedure which introduces a special constraint, strongly reduces the values of  $\sigma_p$ , and, finally, also leads to unrealistically small error estimates in both the fits using BE2 and H02 with these data.

After this detailed discussion of the different problems and possible errors in the evaluation of EOS data for a well-behaved solid, the EOS data of less regular solids can be analyzed more critically by inspection of the  $\eta$  versus  $r_r$  plots for all the other actinides, presented in fig. 13. For comparison, the best fit for Th from fig. 12 (corresponding to H12 for all the data with fixed  $K_0$ ) is also included in the  $\eta$  versus  $r_r$  plots for Pa, U, and Np, to illustrate that the quadratic form  $\eta = -a_1r_r + a_2r_r^2$ , with the parameters  $a_1 = 3.54$  and  $a_2 = 0.735$ , represents quite well all these data within the present experimental uncertainties. Thus, one could claim that one common  $\eta(r_r)$  relation fits all the EOS data for the *5f-band* elements and the effect of the *f* bonding is incorporated by the difference in the initial values for  $V_0$ , without any further important contribution to the balance between attractive and repulsive forces.

The special  $\eta(r_r)$  relation for Pu, with some resemblance to the behavior of Ce, see fig. 8, points, on the other hand, to quite anomalous contributions from the *5f* electrons as the delocalization is progressing, while the low-pressure data of the heavier actinides, starting with Am, appear to be compatible with just one other common value  $\eta = -4.8(2)$  for actinides with *localized* *5f* electrons. When the delocalization of the *5f* electrons occurs in these elements, a significant decrease in the  $\eta$  values is observed, as shown in fig. 13 by the data and dashed curves at  $r_r \leq 2.1$ . However, by an adjustment of the values for the zero-pressure volumes,  $V_{0del}$ , for these high-pressure phases, one can shift these data with the dashed curves to the higher values given by the solid curves in this same region. Since these solid curves represent just the common variation of the typical *5f-band* metals Th to U, this procedure allows to determine also for these heavier actinides the hypothetical values  $V_{0del}$ , which represent the most reasonable estimates for the zero-pressure volumes of the phases with delocalized *5f* electrons extrapolated from the high-pressure data down to ambient

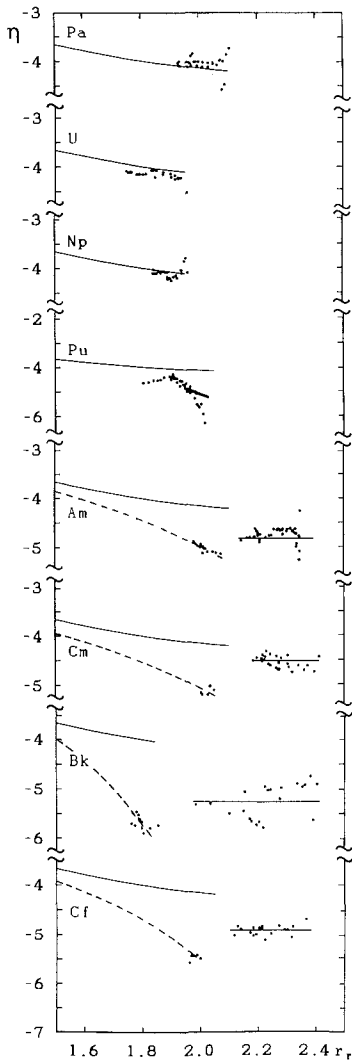


Fig. 13. EOS data for the actinides at ambient temperatures, taken from Benedict (1987 and references therein) and plotted in the form of normalized stress,  $\eta$ , versus scaled radii,  $r_r$ . It can be noted that a common curve fits, within the experimental spread, all the data for Pa, U, and Np. Furthermore, one common value,  $\eta = -4.8(2)$ , seems to be compatible with all the low-pressure data of Am, Cm, Bk, and Cf. Only the deviation for Bk may be significant. The individual curves (dashed lines) for the "collapsed" phases of these elements can be shifted to the common curve (solid lines) by the use of individual values  $V_{0del}$  for the extrapolated ambient-pressure volumes of these phases.

pressure. These extrapolated zero-pressure volumes,  $V_{0del}$ , are shown in fig. 14a as open circles, and one can notice that these estimated values of  $V_{0del}$  are close to the values for the elements Pa to Pu, with an average decrease typical for a regular actinide contraction, however, superimposed with some slight irregularity.

Accordingly, one can use these values  $V_{0del}$  together with the solid curves giving  $\eta_{0del}$  to extrapolate the corresponding values for the bulk moduli,  $K_{0del} = \frac{1}{3}P_{FG0del} \exp \eta_{0del}$  and for the corresponding pressure derivatives,  $K'_{0del} = 3 + \frac{2}{3}(\eta_{0del} + a_2)$ , represented in figs. 14b and c by open circles, respectively. If one compares these data with the literature data of  $K_0$  and  $K'_0$  for the normal pressure phases of all the actinides



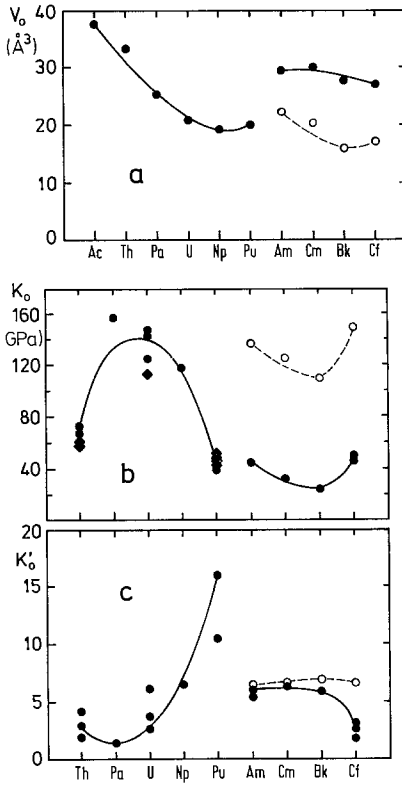


Fig. 14. (a) Comparison of data for  $V_0$  (solid circles) for the actinides at ambient condition, with the data for the "collapsed" phases of the heavier actinides extrapolated to ambient conditions and represented by open circles. (b, c)  $K_0$  (b) and  $K'_0$  (c) values for the actinide metals and some of their alloys, as compiled by Benedict (1987). Solid circles mark isothermal values from static measurements and solid diamonds stand for isothermal values deduced from ultrasonic measurements. Values for the "collapsed" phases extrapolated to ambient conditions are indicated by open circles. The solid lines are guides for the eye, connecting the best present estimates for the stable ambient-pressure structures, and dashed lines connect the extrapolated values for the "collapsed" phases.

previously compiled by Benedict (1987) and represented in figs. 14b and c by solid circles, one can notice, here too, that these extrapolated values for  $K_{0\text{del}}$  are similar to the values of  $K_0$  for the elements Pa to Np and the same holds for the values of  $K'_{0\text{del}}$ . More accurate values for these estimated quantities could be obtained if data over a more extended range of pressure for the elements Am to Cf would become available.

Before we proceed to a detailed comparison of the Ln and An behavior, it appears appropriate to have a short look on the available data for the first two members of the rare earth group.

### 2.3. Yttrium and scandium

X-ray diffraction studies on Y under pressures up to 50 GPa at room temperature (Vohra et al. 1982, Grosshans 1987) gave crucial experimental evidence for the hypothesis that the structural sequence of the regular lanthanides can be attributed purely to the progression of the s to d transfer under pressure, without any (significant) contributions from f electrons. In fact, the typical structural sequence of the regular

lanthanides was observed, with transitions from hcp at 16 GPa to Sm-type, at 34 GPa to dhcp, and around 45 GPa to the trigonal (distorted fcc) structure as the “ultimate” high-pressure phase, for yttrium also.

Since no *f* electrons can contribute to these transitions in Y, earlier suggestions (Wittig 1978) which considered contributions from *f* electrons as essential driving factors for these transitions in the regular lanthanides, are not confirmed. However, more recently, in a comparison of the transition pressures given in the literature (which are “forward” transition pressures) some anomalies were pointed out and interpreted as a possible *f* contribution (Gschneidner 1985). If, on the other hand, best estimates of the equilibrium transition pressures from studies of kinetics and hysteresis (Krüger et al. 1990) are used, no special contributions from *f* electrons seem to be substantiated, since the critical radius ratios  $r_r = R_{ws}/R_{4p}$  at the different phase transitions for Y show the same systematics as the corresponding ratios  $r_r = R_{ws}/R_{5p}$  in the regular lanthanides under pressure, as also illustrated in fig. 15. In fact, by using covalent radii,  $R_c$ , instead of the orbital radii,  $R_{np}$ , almost quantitative agreement is obtained.

Similar studies on Sc under pressure (Vohra et al. 1982, Grosshans et al. 1982, Akella et al. 1986) show quite a different structural behavior, as also illustrated in fig. 15, while theoretical considerations (Skriver 1983) have up to now treated Sc only in analogy to Y, without considering the possible occurrence of a different structural sequence. The experimentally observed transition at 20 to 23 GPa (Vohra et al. 1982, Akella et al. 1986) seems to be best described by a structural change from hcp to the  $\beta$ -Np-type structure (tetragonal, space group P4/nmm) with the four atoms in the unit cell occupying the positions 2a and 2c with  $z = 0.375$ . The proposal of a different tetragonal cell by Akella et al. (1986) was rejected by Grosshans (1987) on the following grounds:

(1) Out of the 12 lines of the  $\beta$ -Np structure in the range  $265.0 > d_{hkl} > 121.2$  pm, 11 lines, with  $\beta$ -Np indexing from (101) to (321), were observed by Vohra et al. (1982),

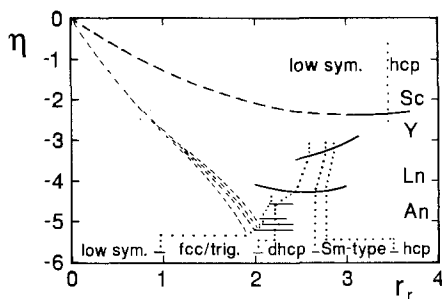


Fig. 15. Comparison of EOS data and structures for Sc and Y with the data for the regular Ln and An elements using the  $\eta$  versus  $r_r$  representation, with data from Grosshans and Holzapel (1992) for the rare earth elements and from Benedict (1987) for the regular An elements including Am, Cm, Bk, and Cf in their spin-polarized (low-pressure) phases (solid lines) and in their “collapsed” phases (dashed lines) with the appropriate values for  $V_{0del}$  from fig 14a.

and only the weak (112) line at 144.7 pm in the upper range of the EDX spectrum was possibly hidden in the background.

(2) Additional lines in the structure proposed by Akella et al. (1986), especially the lines at 294.6, 201.1, 174.2, and 158.2 pm corresponding to the lines (101), (102), (201), and (211) of the primitive tetragonal indexing proposed by Akella et al. (1986), were not observed by Vohra et al. (1982).

(3) The volume collapse of over 10% required by the indexing scheme of Akella et al. (1986) is rather large, while the much smaller volume discontinuity required by the  $\beta$ -Np-type indexing fits perfectly to the available shock-wave data (Carter et al. 1975) for Sc at pressures over 25 GPa.

In any case, it can be noticed that Sc under pressure follows a different structural sequence than Y and the regular lanthanides, which could be explained on the ground that the 3d electrons of Sc in their open 3d shell tend to be localized more strongly than the 4d electrons in Y or the 5d electrons in the regular lanthanides, due to the absence of an inner, closed d-electron shell in Sc, which in the other cases leads to an extra orthogonality condition and, therefore, to extra core repulsion. This difference in the 3d transition metals with respect to the 4d and 5d transition metals also seems to account for the various differences in Ti, Mn, Fe, Co, and Ni with respect to their 4d and 5d counterparts.

#### 2.4. *Scaling rules for regular rare earth elements*

Up to this point, various scaling rules have already been introduced for the structural behavior of the “regular” rare earth elements.

First, the radius ratio  $r_r = R_{ws}/R_{np}$  was introduced as a useful parameter to scale the structural transitions to critical values of this parameter, leading to the observation that all the “regular” lanthanides, and, somewhat less rigorously, also Y and the heavier actinides from Am on, follow the same structural sequence, with respect to this scaling.

Furthermore, within each group “regular” behavior for the EOS data could be defined by the use of the appropriate scaling in the  $\eta$  versus  $r_r$  plots, which then generate simple scaling rules for all the regular lanthanides and, less rigorously, also for the “regular” actinides (with localized 5f electrons) on the one hand, and for the 5f-band actinides on the other hand, scaling the values of  $K_0$  and  $K'_0$  to the two input parameters  $Z$  and  $V_0$  only. In fact, even the values for  $V_0$  of the regular lanthanides follow quite closely the simple scaling rule (related to the Thomas–Fermi scaling)  $V_0 \sim 1/Z$ , as discussed in the recent review of the EOS data on the lanthanides (Grosshans and Holzapfel 1992).

Furthermore, one can notice that not only the radius ratios  $r_{r0}$  for the regular lanthanides at ambient condition show an almost *linear* increase with  $Z$ , but also a *linear* decrease of the effective d-electron number,  $n_d$ , for the conduction bands of these lanthanides was derived from theory (Skriver 1985), and, therefore, one can consider the simple scaling with the radius ratio  $r_r$  just as the purely experimental manifestation of simple scaling rules related to the d-band occupation,  $n_d$ , and to the related  $s \rightarrow d$  transfer induced under pressure.

Further scaling rules with respect to the delocalization of the f electrons can only be derived by comparison of the lanthanide and actinide metals with each other, and are therefore postponed to the next section.

### 2.5. Comparison of rare earth and actinide elements

As we have seen in the last sections, there are many common features in the structural behavior of the rare earth and actinide elements under pressure.

First of all, there is the class of "regular" rare earth elements including Y, the "regular" lanthanides (La, Pr, Nd, Pm, Sm, Gd, Tb, Dy, Ho, Er, Tm, and Lu), and, less rigorously, also the "regular" actinides (Am, Cm, Bk, and Cf). These elements follow, at ambient pressure, the rule of simple correlation between critical values for the radius ratio  $r_r = R_{ws}/R_{np}$  and the regions of stability of the "regular" rare earth structures, hcp  $\leftrightarrow$  Sm-type  $\leftrightarrow$  dhcp  $\leftrightarrow$  trigonal (or fcc at high temperatures). Due to the observation that Y also follows this structural sequence under pressure, it can be considered also a well-established experimental fact that the occurrence of this structural sequence is dominated by the sp  $\rightarrow$  d redistribution in the conduction bands under pressure (or in general with decreasing  $r_r$ ). Slight irregularities in the actual transition pressures for the "regular" actinides point to some minor additional influences from 5f hybridization. The contributions from the magnetic ordering of the localized 4f and 5f moments at low temperatures are neglected here, being only small perturbations of the high-temperature structures, and have been excluded from the previous discussion.

With this background on regular behavior, a classification can be given also for the remaining "irregular" elements. The first element of the rare earth group, Sc, represents one group by itself, due to the stronger binding of the 3d electrons in its conduction band in comparison with the 4d, 5d, and 6d electrons for Y, the lanthanides, and the actinides, respectively, as discussed in sect. 2.3. The elements Eu and Yb, with their anomalies, are usually described as typical divalent rare earth metals, and recent theoretical considerations by Eriksson et al. (1990) make clear that a similar behavior should be expected for the heaviest actinide metals starting from Fm to No, with Es being a borderline case, just marginally divalent, as indicated by its (irregular) fcc structure (Eriksson et al. 1990).

While EXAFS measurements on Eu (Röhler 1986) and Yb (Syassen et al. 1982) under pressure point to a more or less continuous promotion of almost one f electron into the conduction band in the experimentally studied pressure range from 0–20 GPa, it is not clear whether the other f electrons also delocalize in this "mixed valence" state and, therefore, contribute (continuously) to a volume decrease beyond that expected for a regular trivalent lanthanide. The particular softness of Eu and Yb, illustrated in fig. 8, seems to give an indication for such an additional delocalization.

The next class of "irregular" f elements includes at ambient pressure Ce in the  $\alpha$ -Ce phase and all the light actinides from Th to Pu, which are characterized by 4f and 5f bands or bonding f contributions, respectively. In this respect it is not clear whether Ac and Th should also be included in this class; however, from the close similarity of the EOS data for Th in the  $\eta$  versus  $r_r$  plot presented in fig. 12 in comparison with the

data for Pa, U, and Np compiled in fig. 13, we expect a continuous increase in the 5f hybridization to the conduction band of Th under pressure, which would make it a regular member of the 5f-band actinides under pressure (Skriver and Jan 1980). On the other hand, Ce and Pu, which are borderline cases with respect to the f delocalization, are characterized by very special softness at ambient conditions (for Ce in the  $\alpha$ -Ce phase), as illustrated in figs. 8 and 13, respectively, and by this softness as well as by the appearance of many different structures, partly with low symmetries under pressure, they represent the prototype cases for the effects of f-electron delocalization under pressure and temperature. Finally, Am, Cm, Bk, and Cf as well as Pr show also similar anomalies in their EOS, which can be attributed to f delocalization.

This leads to the question whether a critical nearest-neighbor distance typical for each element characterizes these f delocalizations, as originally proposed by Hill (1970). In fact Smith (1980) points out that a critical radius ratio corresponding to  $R_H = R_{ws}/R_{nf} = 3.6$  represents this “Hill limit” for all the lanthanide and actinide metals. Since the scaling here involves the radii for the principal maxima of the 4f and 5f electrons instead of the 5p and 6p electrons used for the radius ratios  $r_r$  in figs. 5 and 10, the Hill limit would be determined in these figures by the relation  $r_H = 3.6R_f/R_{np}$ , which shows a small decrease from U to Pu, but gives, within the limits of this model, the almost constant value  $r_H \approx 2.2$  for the actinides, in rough agreement with data presented in fig. 10. However, the respective lanthanide value  $r_H \approx 1.6$  would be in complete disagreement with the lanthanide data presented in fig. 5. Thus, we conclude that the scaling of the Hill limit,  $R_H$ , by the respective p-radii,  $R_{np}$ , leads to the better approximation  $r_H \approx 2.2$  for both the lanthanides and the actinides, but figs. 5 and 10 seem to point out that only a variation of the Hill limit from element to element describes the actual observations. The Hill limit would thus show maxima of  $r_H \approx 2.4$  near Ce and U and a strong decrease towards the heavier lanthanides and actinides, with the possibility, however, of a local maximum for the special configurations of Eu and Am. Thus, even if the observation of a typical Hill limit for each of the lanthanide and actinide elements appears as a useful fact, the variation of the Hill limit from element to element follows a pattern which is not yet fully understood.

In any case, the experimental facts illustrated in figs. 5 and 10 disprove at least the general trend proposed by Harrison (1984) with its theoretical prediction of a minimum value of  $r_H < 1.7$  for Gd, i.e. in the center of the lanthanide (and actinide) series. In contrast, simple experimental analogies for the structural and electronic behavior of the “regular” lanthanides and actinides rather lead to the speculation that the Hill limits in the radius ratios,  $r_H$ , observed for the elements Am, Cm, Bk, and Cf may also serve as good guesses for the elements Eu, Gd, Tb, and Dy. With the use of the corresponding EOS data one thus arrives at estimates for the “delocalization pressures” of 75 GPa for Eu, 90 GPa for Gd, 123 GPa for Tb, and 130 GPa for Dy, which are well in the range accessible to static X-ray diffraction experiments with synchrotron radiation (Vohra and Akella 1991); however, due to hysteresis effects, significantly higher pressures may be necessary to induce these phase transitions at ambient temperature.

Thus, a comparison of the lanthanide and actinide behavior under pressure can serve in the development of heuristic models and working hypotheses for future experimental studies, and can advance our understanding of changes in the electronic structure under pressure.

There is an interesting difference for one metal of the lanthanide series with respect to the heavy actinide metals. While high density (“volume collapse”) and low structural symmetry simultaneously appear at the same pressure in Cm, Bk, and Cf (Benedict 1987), and only low structural symmetry, with no appreciable volume decrease, is observed in Am, the lanthanide metal Ce is the only one where volume collapse (by 16%, in an isostructural phase transition) and formation of a low-symmetry structure occur successively at two different pressures (Staun Olsen et al. 1985a).

A number of properties have been found to correspond to “shifted homologs” having  $f$  counts differing by four, rather than to identical  $f$  count homologs (Ward 1985). Cerium, for example, with a formal configuration  $4f^1$  corresponds in many properties to those of the actinide Pu, with configuration  $5f^{1+4}$ . A striking example of this kind of homology is that it brings together the two divalent elements Eu and Es, whose  $f$  counts also differ by four.

This shifted homology also holds for certain regions of the general diagrams of the phase relations under pressure for the lanthanides (fig. 4) and for the actinides (fig. 9). If these are superimposed according to equal  $f$  counts, there is only a limited resemblance. However, if the diagram for the lanthanides is shifted to higher  $Z$  by four atomic numbers, there is a closer similarity in the structural sequences with increasing pressure and with increasing  $Z$ .

## 2.6. Interlanthanide and interactinide alloys

Only a few alloy systems of  $4f$  and  $5f$  metals have been studied by HPXRD up to now. For the lanthanides, these are  $\text{La}_{0.5}\text{Pr}_{0.5}$ , which has the same electron count as Ce and has been studied as a “regular pseudo-Ce” (see sect. 2.1), and  $\text{Pm}_{0.7}\text{Sm}_{0.3}$  formed from Pm by  $\beta$ -decay (Heathman et al. 1993a). In the actinide field, structural studies were reported for U–Np (Dabos-Seignon et al. 1990a), Pu–Am (Benedict 1993), Am–Cm (Haire et al. 1990b), and Bk–Cf (Itié et al. 1985). All these results have been included in figs. 4 and 9. The work on Am–Cm and Bk–Cf has been summarized by Benedict (1987, 1989). In the Pm–30%Sm alloy, the same structural sequence with increasing pressure was observed as in pure Pm, with only a slight shift of the dhcp to fcc transition to higher pressure (Heathman et al. 1993a). The two Pu–Am alloys studied, which have a cubic structure at the outset, show a pressure behavior intermediate between the pure Pu and Am metals (fig. 9). Their study has supplied much more detailed information on the complicated transition region between those two metals, where, amongst other things,  $5f$  electrons of the actinides change from an itinerant to a localized state. The area of stability of the trigonal phase in fig. 9 is now quite well established through the study of eight different compositions from pure Pu to pure Cm.

A surprising result was obtained for the U–Np system. The cubic delta phase of composition  $\text{U}_{0.4}\text{Np}_{0.6}$  did not transform up to 62 GPa, the highest pressure reached

in the experiment. Up to this pressure at least, a cubic “island” is formed in the large area of low-symmetry structures in fig. 9 (Dabos–Seignon et al. 1990a).

### 3. Intermetallic compounds

Lanthanides and actinides form a large number of intermetallic compounds of different families. Among the binary ones, a large group are the Laves phases of composition  $\text{MX}_2$ . Most of the Laves phases have the face-centered cubic  $\text{MgCu}_2$  (C15) structure type (space group  $\text{Fd}\bar{3}\text{m}$ , no. 227), some are of the hexagonal  $\text{MgZn}_2$  (C14) type (space group  $\text{P6}_3/\text{mmc}$ , no. 194). Among the ternary compounds, some of the  $\text{ThCr}_2\text{Si}_2$  type have in recent years gained importance as heavy-fermion compounds ( $\text{CeCu}_2\text{Si}_2$ ,  $\text{URu}_2\text{Si}_2$ ). Heavy-fermion properties were also found in the binary compounds  $\text{UPt}_3$  and  $\text{UBe}_{13}$ .

Intermetallic compounds with antimony and bismuth will be considered in sections 4 and 5, because of their close structural similarity to compounds with the non-metals of group Va.

#### 3.1. Compressibility data

Many of the intermetallic lanthanide and actinide compounds studied under pressure did not exhibit any pressure-induced phase transition. The ambient-pressure structure was retained to the highest pressures reached. Table 2 lists the compounds studied, their crystal structures, the maximum pressure reached in each case, the bulk moduli, and the references.

The bulk modulus of  $\text{ThBe}_{13}$  is practically the same as that of the corresponding uranium compound, with only a minor difference in the pressure derivatives. The value of 108 GPa compares to the bulk moduli for beryllium, 126 GPa (Landolt–Börnstein 1967), for uranium, 147 GPa (Benedict 1987), and for thorium, 58 GPa (Bellussi et al. 1981). It is noteworthy that the large difference in bulk modulus between thorium and uranium is not reflected in the bulk moduli of their  $\text{MBe}_{13}$  compounds. This seems to show that the compression of these compounds is to a large extent determined by the skeleton of beryllium atoms, into which a relatively small number of actinide atoms is imbedded.

$\text{UPt}_3$  is considerably less compressible than the  $\text{AnBe}_{13}$  compounds studied. This parallels the situation found in the bulk moduli of the Laves-phase intermetallic compounds of uranium (see table 2). In both cases, the intermetallics with a transition metal (Fe, Co, Mn, Ir for the Laves phases, Pt for the heavy-fermion compounds) are considerably stiffer than those incorporating a metal of one of the main groups of the periodic table (Al for the Laves-type compounds, Be for the heavy-fermion compounds). In interpreting compression data of these types of compounds, one should think of a possible stiffening effect linked to the existence of partly filled shells.

The bulk modulus of  $\text{CeAl}_2$  determined by Bartholin et al. (1980) (table 2), contrasts with the ultrasonic value of 59 GPa, determined by Lüthi and Ligner (1979) at 250 K.

TABLE 2  
 Isothermal bulk modulus  $K_0$  (GPa) and its pressure derivative  $K'_0$  for intermetallic compounds of the lanthanides and actinides, as determined from high-pressure X-ray diffraction study. Errors as indicated in the original publications (n.d.: not determined.)

	$P_{\max}$ (GPa)	$K_0$ (GPa)	$K'_0$	Ref.*
MgZn <sub>2</sub> (C14) type				
UNi <sub>2</sub>	41	189(3)	7(1)	[1]
MgCu <sub>2</sub> (C15) type				
CeAl <sub>2</sub>	5.5	125	n.d.	[2]
PrAl <sub>2</sub>	3.7	102	n.d.	[2]
YbAl <sub>2</sub>	3.5	79	n.d.	[2]
UAl <sub>2</sub>	39	74	n.d.	[3]
UMn <sub>2</sub>	42	320(30)	n.d.	[3]
UFe <sub>2</sub>	48	239	n.d.	[3]
UCo <sub>2</sub>	35	217	n.d.	[3]
UIr <sub>2</sub>	50	290	n.d.	[3]
SnNi <sub>3</sub> type				
CeAl <sub>3</sub>	25	50(9)	4(3)	[4]
MgCd <sub>3</sub> type				
UPt <sub>3</sub>	52	235(7)	5.8(6)	[5]
NaZn <sub>13</sub> type				
CeBe <sub>13</sub>	25	89(4)	5.5(6)	[6]
ThBe <sub>13</sub>	46	108(2)	5(1)	[5]
UBe <sub>13</sub>	43	109(2)	5.5(10)	[5]
ThCr <sub>2</sub> Si <sub>2</sub> type				
YCu <sub>2</sub> Si <sub>2</sub>	?	n.d.	n.d.	[8]
LaCu <sub>2</sub> Si <sub>2</sub>	28	n.d.	n.d.	[8]
LaCu <sub>2</sub> Si <sub>2</sub>	8	≈ 148	n.d.	[7]
CeCu <sub>2</sub> Si <sub>2</sub>	31	n.d.	n.d.	[8]
EuCu <sub>2</sub> Si <sub>2</sub>	8	≈ 104	n.d.	[7]
GdCu <sub>2</sub> Si <sub>2</sub>	8	≈ 160	n.d.	[7]
LuCu <sub>2</sub> Si <sub>2</sub>	8	≈ 167	n.d.	[7]
URu <sub>2</sub> Si <sub>2</sub>	50	247(2)	4(1)	[9]

\*References: [1] Dabos et al. (1988), [2] Bartholin et al. (1980) [3] Itié et al. (1986), [4] Vaidya et al. (1987), [5] Benedict et al. (1987), [6] Léger and Redon (1989), [7] Neumann et al. (1985), [8] Spain et al. (1986), [9] Luo et al. (1988).

### 3.2. Phase transitions

In CeAl<sub>2</sub>, Croft and Jayaraman (1979) and Bartholin et al. (1980) observed an isostructural transition around 7 GPa, accompanied by a volume collapse of about 4%. This observation was interpreted, like in the case of the lanthanide chalcogenides, as a valence change from +3 to +4 of the Ce ion. This interpretation was supported by the fact that the corresponding compound of the non-4f metal La, LaAl<sub>2</sub>, did not show any phase transition up to 3 GPa, the highest pressure reached for both



TABLE 3  
Pressure–temperature-induced structural transitions for rare earth tri-  
aluminides, determined on quenched samples by Cannon and Hall  
(1975).

	Phase transition (structure types)	Pressure (GPa)	Temperature (K)
GdAl <sub>3</sub>	Ni <sub>3</sub> Sn → BaPb <sub>3</sub>	4.5	1240
TbAl <sub>3</sub>	BaPb <sub>3</sub> → HoAl <sub>3</sub>	4.4	850
DyAl <sub>3</sub>	TiNi <sub>3</sub> → HoAl <sub>3</sub>	1.5	1070
DyAl <sub>3</sub>	TiNi <sub>3</sub> → Cu <sub>3</sub> Au	6.4	1510

compounds (Croft and Jayaraman 1979). Later, Vedel et al. (1986c) reported that there is no volume discontinuity near 6.5 GPa, but only an anomalous softening. However, more recent studies on this same question under truly hydrostatic pressure conditions (Ramesh and Holzapfel 1987) confirmed the observation of a small (1%) volume discontinuity at 7.7 GPa on increasing pressure, with the possibility that the slight differences in the pressure values resulted from hysteresis around the equilibrium transition pressure, not really determined in any of these experiments.

In UAl<sub>2</sub> a second-order transition to another, not yet determined, structure was indicated by the appearance of some additional diffraction lines above 10 GPa (Itié et al. 1986).

LaOs<sub>2</sub>, CeOs<sub>2</sub>, and PrOs<sub>2</sub> of the MgCu<sub>2</sub> type transformed to the hexagonal MgZn<sub>2</sub> type at temperatures around 1270 K and pressures ranging from about 1 to about 7 GPa (Cannon et al. 1973).

EuSi<sub>2</sub> and YbSi<sub>2</sub> treated at 4 GPa and 1770 K did not show any sign of a phase transformation in the quenched samples (Evers et al. 1976).

Cannon and Hall (1975) treated rare earth trialuminides and powdered rare earth–aluminium mixtures of the same stoichiometry at high pressure and elevated temperature. The products of these treatments were studied by X-ray diffraction after quenching to room temperature. The observed pressure–temperature-induced phase transitions are listed in table 3. In HoAl<sub>3</sub> at 1040 K, the HoAl<sub>3</sub> structure type was found to be the stable allotrope at 2.2 GPa, and the Cu<sub>3</sub>Au-type structure was stable at 6.4 GPa. LuAl<sub>3</sub> was synthesized at elevated temperature and pressure and found to have the Cu<sub>3</sub>Au-type structure. Up to 6.4 GPa no transformation was observed for the trialuminides of Sc, Y, Sm, Er (Cu<sub>3</sub>Au type), and Tm. All pressures were determined by calibration of the force applied to the tetrahedral anvil device used with the known transition pressures of Bi, Yb, and Ba.

### 3.3. High-pressure, high-temperature synthesis

The following new phases could be obtained by high-pressure, high-temperature synthesis from the elemental constituents.

### 3.3.1. *Laves phases*

*Of the C14(MgZn<sub>2</sub>) type:* NdRu<sub>2</sub>, SmRu<sub>2</sub>, and LaOs<sub>2</sub> (Cannon et al. 1972b); LnFe<sub>2-x</sub> (Ln = Tb, Ho, Er, Tm, Yb, Lu) (Tsvyashchenko and Popova 1985); LnFeCu for Ln = Pr, Nd, and Sm (Tsvyashchenko and Fomicheva 1985); RENiAl for RE = Y, Sm to Lu (Tsvyashchenko and Fomicheva 1987); UCoAl (Tsvyashchenko and Fomicheva 1991).

*Of the C15(MgCu<sub>2</sub>) type:* PrFe<sub>2</sub>, NdFe<sub>2</sub>, and YbFe<sub>2</sub> (Cannon et al. 1972a); LaCo<sub>2</sub> (Robertson et al. 1972); RFeCu for R = Y, Ce, Gd, Tb, Dy, Ho, Er, Tm, Yb, and Lu (Tsvyashchenko and Fomicheva 1985).

### 3.3.2. *Other intermetallic compounds*

YSn<sub>3</sub>, TbSn<sub>3</sub>, DySn<sub>3</sub>, HoSn<sub>3</sub>, ErSn<sub>3</sub>, and LuPb<sub>3</sub> of the AuCu<sub>3</sub> structure type (Miller and Hall 1972, 1973).

## 4. MX compounds

Checking the frequency of occurrence of the B1 (NaCl)-type structure among the 1:1 compounds of the metals (Manes and Benedict 1985) shows that at ambient pressure and temperature practically all LnX and AnX compounds have this structure, while only  $\frac{1}{3}$  of the other MX compounds (M: metal) crystallize in this structure type. This may indicate that either the incomplete f shells or the low d-electron counts favor the formation of the B1-type structure.

This large family of isostructural compounds lends itself particularly well to systematic studies of physical properties as a function of the nature of the anion, the nature of the cation, the pressure, and the temperature. A central question in such studies is whether the observed changes in properties are linked to the f electrons of the lanthanide or actinide element.

In principle, the B1 structure is strongly ionic in character. But in the lanthanide and actinide compounds having this structure, the ionic character is more or less weakened, since their anions are less electronegative than those of the halogens, which are the anions of the typical basic representatives of this structure type.

It was inferred from simple geometrical considerations (the condition for contact between neighboring X anions) that this structure can only be formed if the ratio of the cation radius to the anion radius is between 0.41 and 0.73. If the tabulated ionic radii are used many of the AnX compounds are in the range mentioned, but some of them are outside, e.g. the monocarbides.

The isomorphism of the lanthanide and actinide B1 compounds allows the bond-length variation to be visualized by simply plotting the lattice parameters. This was done in fig. 2 for the monocarbides (a), the mononpnictides (b), and the monochalcogenides (c). As in the case of the pure actinide metals (Manes and Benedict 1985), bond shortening is observed for the actinides Pa to Pu, with respect to the other actinides and to the corresponding lanthanide compounds. This effect is most clearly marked for the compounds with the lighter non-actinide elements (e.g. N, P, S, Se) and becomes weaker with increasing Z of the non-actinide partner. Like in

the case of the metals, this bond shortening can be taken as an indication of enhanced participation of the 5f electrons in the bond.

Although intermetallic compounds have been considered in sect. 3 of this review, compounds with the metallic elements antimony and bismuth will be included in the following sections, because their structural properties are similar to those of compounds with the other Va elements N, P, and As.

#### 4.1. *LnX compounds*

The known LnX compounds crystallize in the B1 structure type. A certain number of them has been studied under high pressure by X-ray diffraction and by other methods.

The lanthanide monochalcogenides are of metallic character, with the exception of those with a divalent metal (Sm, Eu, Yb, and, to some extent, Tm), which are

TABLE 4

Isostructural volume collapses observed under pressure in lanthanide pnictides and chalcogenides LnX. For each compound the table lists, from top to bottom: the pressure (range) of collapse (GPa), the volume decrease on collapse (%), and references. (× means compound unknown, – studied under pressure, but no isostructural transition observed, and + compound exists, but no HPXRD study known.)

X	Ln				
	Ce	Sm	Eu	Tm	Yb
P	10 GPa 8%,   3% (ref. [11,   2])	+	×	+	+
Bi	–	2.6 GPa ≈10% (ref. [3])	×	+	×
O	0–3 GPa ≈8% (ref. [12])	+	30 GPa ≈5% (ref. [1])	×	8–? GPa (ref. [9])
S	12.5 GPa 4.5% (ref. [4])	0.65 GPa ≈11%   13.5% (ref. [5,   13])	–	+	16–20, 11–16 GPa ≈6%   2.5% (ref. [8,   10])
Se	+	≈4 GPa ≈8% (ref. [5])	–	–	15–17 GPa ≈7% (ref. [8])
Te	–	2–8, ≈4 GPa ≈17%   15% (ref. [5,   7])	≈1.5 GPa ≈5% (ref. [6])	1.5–3 GPa ≈9% (ref. [5])	13–18 GPa ≈10% (ref. [5])

References: [1] Jayaraman (1979), [2] Vedel et al. (1987), [3] Jayaraman and Bucher (1979), [4] Croft and Jayaraman (1980), [5] Chatterjee et al. (1972), [6] Rooymans (1965), [7] Rooymans (1966), [8] Jayaraman et al. (1974), [9] Werner et al. (1981a), [10] Syassen (1986), [11] Jayaraman et al. (1976), [12] Vedel et al. (1986b), [13] Keller et al. (1979).

TABLE 5

Pressure-induced structural transitions in lanthanide pnictides and chalcogenides LnX of the B1 structure type. For each compound the table lists, from top to bottom: the structure of the high-pressure phase, the pressure (range) of transition (GPa), the volume decrease on transition (%), and references. (× means compound unknown, – studied under pressure, but no phase transition observed, and + compound exists, but no HPXRD study known.)

X	Ln					
	La	Ce	Pr	Sm	Eu	Tm
P	–	B2 19 GPa 10.5% (ref. [2])	+	+	×	+
As	+	B2 16 GPa 14% (ref. [6])	+	+	– (hexagonal)	+
Sb	tetrag. 11 GPa ≈10% (ref. [9])	tetrag. 11 GPa ≈10% (ref. [9])	+	+	×	+
Bi	–	tetrag. + B2 13 GPa 5.5% (ref. [5])	+	–	×	+
O	+	–	+	+	B2 ≈40 GPa ≈8% (ref. [8])	×
S	+	–	+	–	B2 21.5 GPa ≈12% (ref. [1])	+
Se	+	B2 18 GPa ≈9% (ref. [10])	+	–	B2 14.5 GPa ≈13% (ref. [1])	–
Te	–	B2 8(1) GPa 8.5% (ref. [4])	B2 ≈9(1) GPa ≈11.5% (ref. [7])	B2 ≈11 GPa 9% (ref. [7])	B2 11(1) GPa ≈13% (ref. [7])	hexag. 15 GPa ≈4% (ref. [3])

References: [1] Jayaraman et al. (1974), [2] Vedel et al. (1987), [3] Usha Devi and Singh (1984), [4] Léger et al. (1983), [5] Léger et al. (1985), [6] Werner et al. (1983), [7] Chatterjee et al. (1972), [8] Jayaraman (1979), [9] Léger et al. (1984), [10] Léger and Redon (1989).

TABLE 6

Isothermal bulk moduli,  $K_0$  (GPa), and pressure derivatives  $K'_0$  determined from high-pressure X-ray diffraction, for the lanthanide (Ln) pnictides and chalcogenides of the B1 structure type. For each compound the table lists, from top to bottom: the bulk modulus, in GPa, the pressure derivative, and references. Errors as indicated in the original publications. ( $\times$  means compound unknown,  $-$  studied under pressure, but no compressibility data known,  $+$  compound exists, but no HPXRD study known and constr.: constrained.)

X	Ln							
	La	Ce	Sm	Eu	Gd	Tm	Yb	
N	+	+	+	+	192(35) 4 (constr.) (ref. [14])	+	+	
P	1 data point (ref. [13])	115, (ref. [5, 3])	64(4) 3(1)	+	$\times$	+	+	
As	+	69(1) 2.6(2) (ref. [7])	+	46 (hexag.) (ref. [17])	+	+	+	
Sb	72(3) 2.5(5) (ref. [8])	72(3) 2.5(5) (ref. [8])	+	$\times$	+	+	+	
Bi	55 (ref. [7])	50 2 (ref. [2])	-	$\times$	$\times$	+	$\times$	
O	+	( $\approx$ 30)  (ref. [10])	+	110(5)  (ref. [1])	$\times$	$\times$	130(19) 4 (constr.) (ref. [4])	
S	+	130, (ref. [5,12, 9])	82(3) 2.3(3)	42(3) 4 (constr.) (ref. [15])	61(5)  (ref. [1])	120(5)  (ref. [13])	+	72(5)  (ref. [1])
Se	+	76(4) 4.9(5) (ref. [16])	40(5)  (ref. [1])	52(5)  (ref. [1])	+	38(1) 11(1) (ref. [11])	61(5)  (ref. [1])	
Te		53(4) 14(2) (ref. [6])	40(5)  (ref. [1])	40(5)  (ref. [1])	$\times$	46(5)  (ref. [1])	46(5)  (ref. [1])	

References: [1] Jayaraman et al. (1974), [2] Léger et al. (1985), Vedel et al. (1987), [4] Werner et al. (1981a), [5] Léger et al. (1985), [6] Léger et al. (1983), [7] Werner et al. (1983), [8] Léger et al. (1984), [9] Vedel et al. (1986a), [10] Vedel et al. (1986b), [11] Debray et al. (1982), [12] Bartholin et al. (1980), [13] Jayaraman (1978), [14] McWhan (1966), [15] Keller et al. (1979), [16] Léger and Redon (1989), [17] Werner et al. (1982).

semiconductors. Semiconducting LnX can undergo transition to a metallic state under pressure. That is why divalent Ln chalcogenides have been extensively studied under pressure. Several semiconductor  $\rightarrow$  metal transitions, e.g. in SmS, SmSe, SmTe, EuO, TmTe, YbO, YbS, YbSe, and YbTe, were observed.

Isostructural volume collapses under pressure were observed for monochalcogenides of Ce, Sm, Eu, Tm, and Yb, and for CeP and SmBi. The known "electronic transitions" of this type are tabulated in table 4.

Lawrence et al. (1981) review the effects of different NaCl-type additives, forming solid solutions with SmS, on the isostructural-transition pressure.

Pressure-induced structural transitions were observed for monopnictides of La and Ce, for the monochalcogenides of Eu, and for the monotellurides of Ce, Pr, Sm, Eu, and Tm (table 5). Not all of the remaining Ln monopnictides and monochalcogenides have been studied under pressure up to now. Compressibility data derived from high-pressure X-ray diffraction studies are listed in table 6 and plotted versus atomic number in fig. 18. Figure 16 gives an overview over all pressure-induced electronic and structural transitions observed up to now in LnX compounds.

The monoxides of La, Ce, Pr, Nd and Sm were obtained by high-pressure, high-temperature synthesis from the metals and a higher oxide (Léger et al. 1981).

#### 4.2. AnX compounds

The stable, room temperature, ambient pressure phase of the 1:1 actinide compounds AnX is of the NaCl (B1) type. The only known exceptions are ThTe and

	La	Ce	Pr	Sm	Eu	Tm	Yb
P	-	10 19	+	+	X	+	+
As	+	16	+	+	-	+	+
Sb	11	11	+	+	X	+	+
Bi	-	13	+	3	X	+	X
O	+	3	+	+	30 40	X	8
S	+	4	+	1	22	+	16
Se	+	+	+	4	15	5	16
Te	-	8	9	4 11	2 11	2 15	16
	La	Ce	Pr	Sm	Eu	Tm	Yb


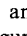
Fig. 16. Overview of the occurrence of pressure-induced electronic  and structural  transitions in LnX compounds. Figures are upstroke transition pressures in GPa. X: compound unknown, +: compound exists, but was not studied under pressure, and -: studied under pressure, but no phase transition observed.

TABLE 7

Pressure-induced structural transitions in actinide carbides, pnictides, and chalcogenides AnX (An = Th, U, Np, Pu). For each compound the table lists, from top to bottom: the structure of the high-pressure phase, the pressure (range) of upstroke transition (GPa), the volume decrease on transition, and references. (ThC, ThN: no transition in pressure range studied, ThBi, ThTe: B2 as ambient pressure phase; no transition, + means compound exists, but no HPXRD study known).

X	An			
	Th	U	Np	Pu
C	(B1 up to 65 GPa) (ref. [1, 17])	orthorhombic ≈ 27 GPa ≈ 6% (ref. [2])	+	+
N	(B1 up to 47 GPa) (ref. [3])	rhombohedral ≈ 29 GPa ≈ 3% (ref. [4])	+	+
P	B2 ≈ 30 GPa ≈ 12% (ref. [6])	rhomboh. orthor. ≈ 10, ≈ 28 GPa 0% (ref. [7])	+	+
As	B2 18–26 GPa ≈ 10% (ref. [8])	B2 17–30 GPa ≈ 11% (ref. [9])	B2 25–40 GPa ≈ 9% (ref. [10])	B2 35–38 GPa ≈ 9% (ref. [11])
Sb	B2 9–12 GPa ≈ 9% (ref. [8])	B2 9–10, 8–11 GPa ≈ 12, ≈ 9% (ref. [9, 19])	tetragonal 10–18 GPa ≈ 12% (ref. [12])	B2, tetragonal ≈ 20, ≈ 40 GPa ≈ 4, ≈ 5% (ref. [12])
Bi	B2 ≤ 0 GPa +	B2 ≈ 5 GPa ≈ 11% (ref. [5])	tetragonal ≈ 8.5 GPa 12% (ref. [13])	+
S	hexagonal 23–33 GPa 0% (ref. [14])	rhombohedral ≈ 12 GPa 0% (ref. [15])	+	+
Se	B2 ≈ 15 GPa ≈ 9% (ref. [16])	B2 20–26 GPa ≈ 8% (ref. [15])	B2 ≈ 23 GPa ≈ 9% (ref. [20])	rhombohedral B2 ≈ 20, ≈ 35 GPa 0, ≈ 11% (ref. [18])
Te	B2 ≤ 0 GPa (ref. [16])	B2 9–20 GPa ≈ 8% (ref. [15])	B2 12–20 GPa ≈ 7% (ref. [12])	B2 15–19 GPa ≈ 9% (ref. [12])

[1] Gerward et al. (1990b), [2] Staun Olsen et al. (1986), [3] Gerward et al. (1985), [4] Staun Olsen et al. (1985b), [5] Gensini et al. (1993a), [6] Staun Olsen et al. (1989b), [7] Staun Olsen et al. (1988b), [8] Gerward et al. (1988), [9] Staun Olsen et al. (1989a), [10] Dabos et al. (1986), [11] Dabos-Seignon et al. (1989), [12] Dabos-Seignon et al. (1990b), [13] Gensini (1992), [14] Benedict et al. (1984), [15] Gerward et al. (1989), [16] Staun Olsen et al. (1988a), [17] Heathman et al. (1993b), [18] Gensini et al. (1990), [19] Vedel et al. (1986d), [20] Gensini et al. (1993b).

ThBi, which are of the CsCl (B2) type, and a few compounds of truly intermetallic character.

The uranium compounds of this class, and also ThS, are metallic in character, with room-temperature resistivities from 30 to 400  $\mu\Omega\text{cm}$ . Some of the Pu compounds have been found to have semimetallic character, with room-temperature resistivities in the range 500–800  $\mu\Omega\text{cm}$ . NpP has a particularly high room-temperature resistivity of about 3740  $\mu\Omega\text{cm}$ . PuS is an intrinsic semiconductor above 425 K.

A large number of B1-type compounds of Th, U, Np and Pu have been investigated by high-pressure X-ray diffraction. Systematic trends in the nature of the high-pressure phases, the transition pressures, the hysteresis to re-transformation on pressure release, and the compressibility were observed for this group of compounds.

#### 4.2.1. High-pressure phases and volume compression

Table 7 gives the phase transitions observed in AnX compounds of the B1 type for An from Th to Pu. In a majority of cases, the B2 (CsCl)-type structure was observed as the high-pressure phase. A number of other, less symmetric high-pressure structures was also found.

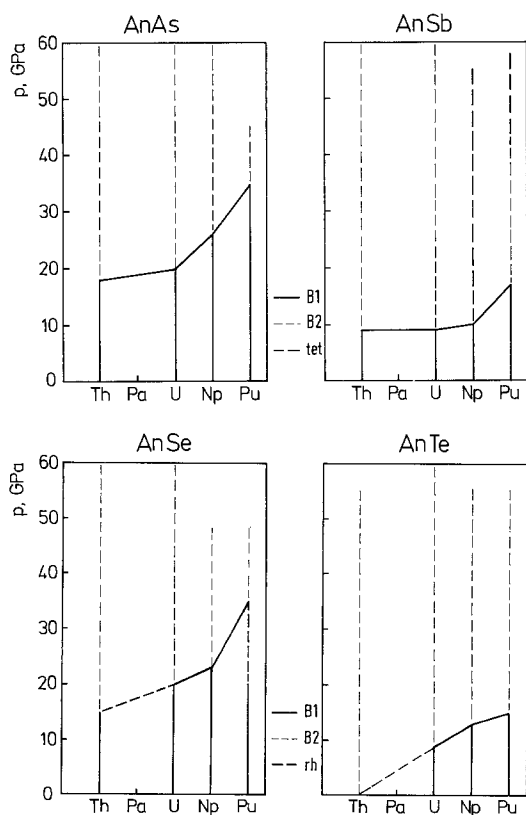


Fig. 17. Stability ranges of the different phases for monoarsenides, monoantimonides, monoselenides, and monotellurides of the actinides Th, U, Np, and Pu (from Gensini et al. 1990).



Table 7 does not include compounds of heavier actinides, for which only a few results (for AmN, CmN, CfN, CmBi, and CfBi) are available up to now. CmBi was studied up to 48 GPa (Gensini et al. 1993a). It undergoes a first-order phase transition to the B2 type around 12 GPa, with a volume decrease of about 11%, and then a second-order transition to a third phase with tetragonal symmetry. The isothermal bulk modulus of B1-type CmBi was determined to be  $K_0 = 53(3)$  GPa, its pressure derivative to be  $K'_0 = 8(2)$ . CfBi transformed to the B2 type at 11–12 GPa, with a volume decrease of about 7% (Haire et al. 1993). A bulk modulus of  $K'_0 \approx 104$  GPa was determined, with a negative pressure derivative  $K'_0$ . AmN, CmN, and CfN keep the face-centered cubic structure up to about 50 GPa (Dabos-Seignon et al. 1993, Haire 1987). AmN shows indication of a rapid volume decrease of the order of 2% at 33 GPa (Dabos-Seignon et al. 1993). If this observation can be confirmed, AmN would be one of the first actinide compounds for which an isostructural electronic transition is found. Such a transition was expected on the basis of theoretical considerations (Brooks 1982). The isothermal bulk modulus of AmN was determined to be  $K_0 = 88(5)$  GPa, its pressure derivative to be  $K'_0 = 11(2)$  (Dabos-Seignon et al. 1993).

Figure 17 shows a comparison of bar diagrams of the stability ranges of the different phases for the monoarsenides, -antimonides, -selenides, and -tellurides. The indicated transition pressures refer to pressure increase. Two general trends are visible in these diagrams:

- (1) The transition pressures increase with increasing atomic number of the actinide.
- (2) The transition pressures decrease with increasing atomic number of the anion in a given column of the periodic table.

#### 4.2.2. *Hysteresis to re-transformation*

In general, the B1-type actinide compounds show a large difference between the transition pressure on pressure increase and the transition pressure on pressure decrease (Dabos-Seignon and Benedict 1990). This hysteresis is probably due to delayed establishment of thermodynamic equilibrium. It has been shown in some lanthanide metals (Krüger et al. 1990) that a slight temperature increase reduces the width of this “hysteresis zone” and that the equilibrium transition pressure has some intermediate value.

In UTe, USb, and UBi, re-transformation to the B1-type phase on pressure release does not occur at room temperature. The B2-type high-pressure phase is maintained in a metastable condition at ambient pressure. This is another example of pressure-induced preparation of a new polytype of material, the best known being high-pressure, high-temperature synthesis of diamond. It should be recalled, too, that ThBi and ThTe have a *stable* B2-type phase at ambient pressure, or otherwise expressed, they have a theoretical B1–B2 transition at negative pressure.

#### 4.2.3. *The bulk moduli*

The bulk moduli (inverse of compressibility) of the B1-type compounds of Th, U, Np, and Pu are listed in table 8 and plotted versus atomic number in fig. 18. There is a tendency of decreasing bulk moduli with increasing atomic number of the actinide.

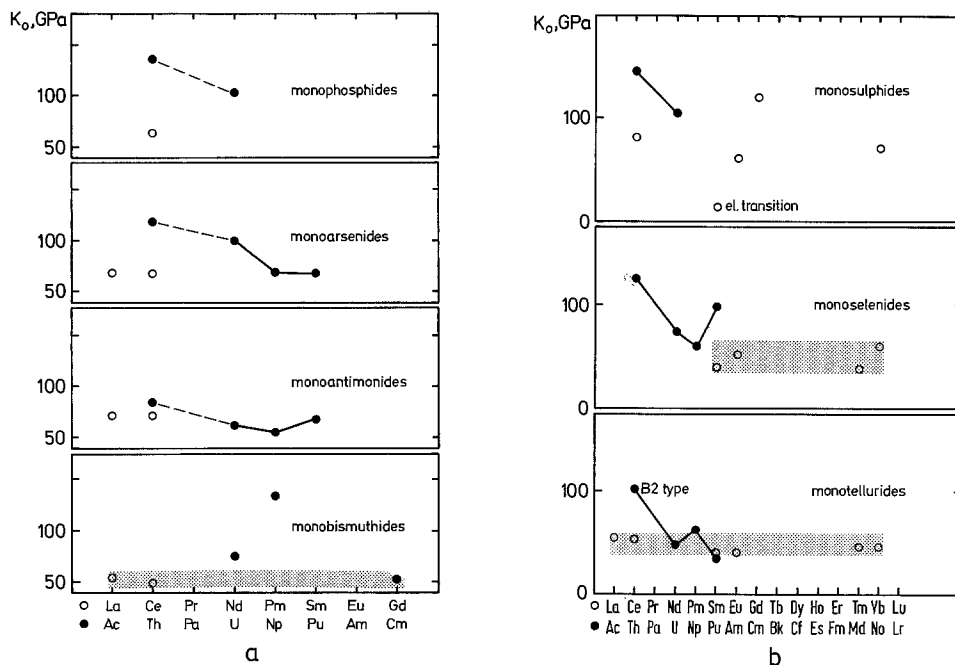


Fig. 18. Isothermal bulk moduli of B1-type compounds of the lanthanides and actinides. (a) Monopnictides with P, As, Sb, and Bi. (b) Monochalcogenides with S, Se, and Te.

#### 4.2.4. Discussion

The B1–B2 phase transition is the prominent feature in the high-pressure structural behavior of these compounds. Although the interactinide distances reach the Hill transition zone (Hill 1970) under pressure in some of these compounds, the 5f electrons do not seem to have any link to this phase transition, since it is also the typical pressure-induced structural transition for the alkali halides. In addition, for a structural phase transition linked to 5f delocalization, one would in general expect that the high-pressure structure has lower symmetry than cubic. This assumption is based on an empirical correlation between itinerant f-states and low-symmetry structures, and is thought to be connected with strong directionality of the hybridized (s, p, d, f) orbitals.

In the AnX compounds, the B1 → B2 transition is accompanied by a volume decrease of the order of 10%. Antimony and bismuth as anions favor tetragonal high-pressure structures. Monocarbides, -nitrides, -phosphides, and -sulfides of thorium and uranium either did not transform in the pressure range studied (ThC, ThN) or transformed to structures of relatively low symmetry (UC, UN, UP, US, ThS), which could possibly point to an f contribution in bonding. In this group of Th and U compounds with light anions, only ThP shows the B1–B2 structural transition.

The hysteresis zones, i.e. the pressure ranges between transitions at increasing and decreasing pressure, have a tendency to widen with increasing atomic number of the actinide. PuAs has the largest hysteresis zone of these compounds, of the order of

TABLE 8

Isothermal bulk moduli  $K_0$  (GPa) and pressure derivatives  $K'_0$  for the actinide carbides, pnictides, and chalcogenides  $AnX$  ( $An = Th, U, Np, Pu$ ). For each compound the table lists, from top to bottom: the bulk modulus, the pressure derivative, and references. Errors as indicated in the original publications. (+ means compound exists, but no HPXRD study known and constr.: constrained.)

X	Ln			
	Th	U	Np	Pu
C	109(4) 4.0(3) (ref. [1])	160(4) 3.6(5) (ref. [2])	+	+
N	175(15) 4.0(4) (ref. [3])	203(6) 6.3(6) (ref. [4])	+	+
P	137(7) 5(1) (ref. [6])	102(4), 102 4(1) (ref. [7, 19])	+	+
As	118(4) 3.4(10) (ref. [8])	100(4) 4.4(4) (ref. 9)	70(1) 6.2(6) (ref. [10])	69(3) 3.3(3) (ref. [11])
Sb	84(8) 5(2) (ref. [8])	62(3), 73 4(1) 2 (ref. [9, 19])	55(2) 8(2) (ref. [12])	68(2) 3.3(5) (ref. [12])
Bi	B2 type! +	75(5) 91(4) -5(3) <0 (ref. [5])	145(30) <0  (ref. [13])	+
S	145(6) 5(1) (ref. [16])	105(8) 5(1) (ref. [15])	+	+
Se	125(10) 4 (constr.) (ref. [16])	74(4) 5(1) (ref. [15])	60(3) 2.5(2) (ref. [5])	98(4) 2.6(5) (ref. [18])
Te	102(4) B2! 3.8(4) (Ref. [16])	48(3), 45 4.9(3), 6 (ref. [15, 19])	62(2) 1.8(4) (ref. [12])	34(3) 12(4) (ref. [12])

References can be found below table 7.

30 GPa. In USb, UBi, and UTe the large hysteresis to re-transformation enables us to obtain metastable B2-type phases at ambient pressure.

There is a trend to decreasing bulk moduli with increasing atomic number of the actinide element. This tendency is most clearly marked for the monoarsenides. There is also a tendency for monoantimonides to be more compressible than monoarsenides of the same actinide.

#### 4.3. Comparison between LnX and AnX compounds

Isostructural volume collapses under pressure were observed for monochalcogenides of Ce, Sm, Eu, Tm, and Yb, and for CeP and SmBi. The known "electronic transitions" of this type were tabulated in table 4 (see also fig. 16).

Pressure-induced structural transitions were observed for the mononictides of La and Ce, for the monochalcogenides of Eu, and for the monotellurides of Ce, Pr, Sm, Eu, and Tm (table 5) (see also fig. 16).

Contrary to the lanthanide compounds, isostructural volume collapses were not detected until recently in the AnX compounds, except for the above-mentioned case of AmN, where, however, the observed slight volume collapse awaits confirmation. This situation may change due to recent HPXRD studies of certain AnX compounds. Recent work on the monobismuthides of uranium, neptunium, and californium (Gensini 1992, Gensini et al. 1993a, Haire et al. 1993) revealed a negative curvature of the  $V(p)$  curves for these compounds. This phenomenon had been taken in lanthanide compounds such as SmS, SmSe as the sign of a commencing 4f participation in the bonding, or, otherwise expressed, of a so-called electronic transition, which was often thought to be linked to an increase of the valence of the cation.

On the basis of these results, one should consider the possibility that an electronic transition also occurs in UBi, NpBi, and CfBi. But it is difficult to give definite proof for this assumption based on the data available up to now, because if an electronic transition occurs in these compounds, it is immediately followed and in part masked by the structural B1 to B2 transition, as shown in fig. 19.

In the case of AmN (Dabos-Seignon et al. 1993) there are indications of a 2–3% isostructural volume collapse around 34 GPa. Whether an  $\approx 1\%$  volume decrease

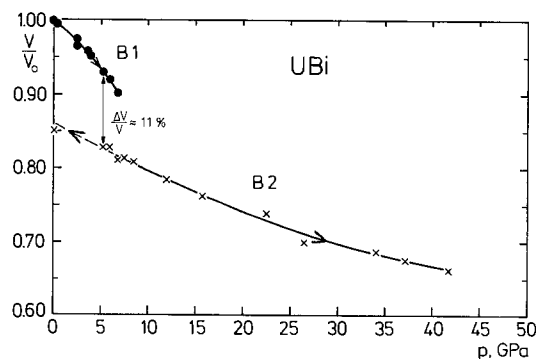


Fig. 19. Relative volume of UBi versus pressure (from Gensini et al. 1993a).

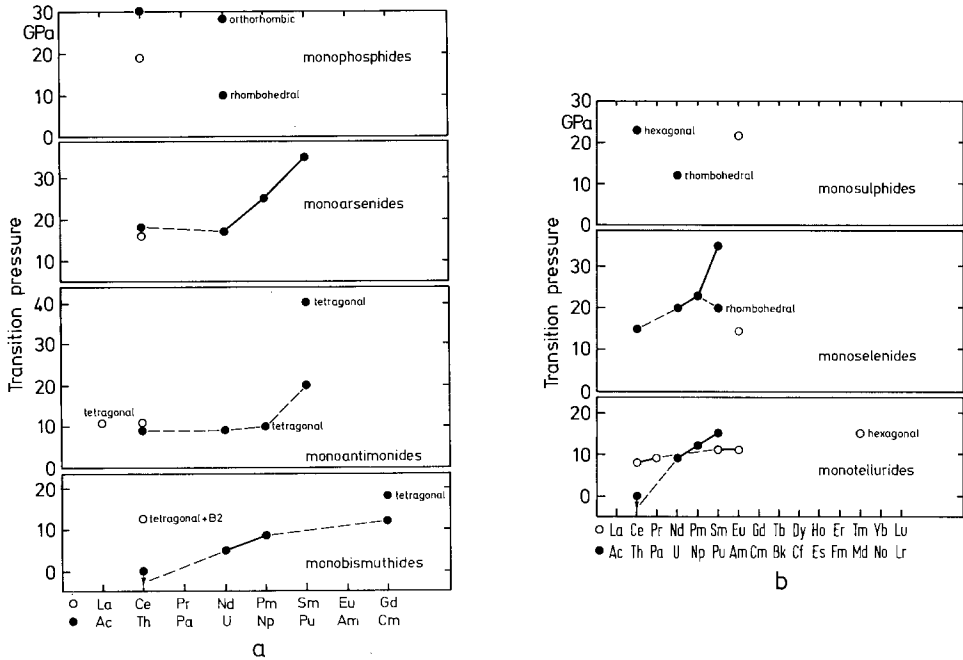


Fig. 20. Pressure of upstroke transition versus  $Z$  for B1-type phases of lanthanide and actinide compounds. (a) Monopnictides. (b) Monochalcogenides. Mononitrides and monoxides are not included because only isolated data are available. Indications of crystal structures in the graphs mark transitions to structures other than B2. Downward arrows for ThBi and ThTe indicate theoretical transition to B2 at negative pressures.

around 20 GPa in ThN (Gerward et al. 1985) can be interpreted in the same way is not clear.

A comparison of the pressure behavior of B1-type compounds of direct homologs is at present not possible because there is practically no case where both the lanthanide and the actinide compound with the same  $f$  count have been studied. But this is maybe not even the best thing to do. From the limited information available up to now, we can at least see one example where the above-mentioned “shifted homologous relationship” holds. For the B1-type compounds, the predominant high-pressure phase is the B2 structure. But there are a number of different high-pressure structures, and in particular there is the case of a tetragonal high-pressure structure observed in LaSb and CeSb. This same high-pressure structure is not observed for the direct homolog of CeSb, ThSb, which exhibits the “standard” transformation to the B2 structure, but it is for the “shifted homologs” NpSb and PuSb. The rather small values of the lattice parameter and volume for CeN mentioned in sect. 1 may also be an expression of the shifted homology of Ce with Pu.

Apart from this, LnX as well as AnX prefer B2 as high-pressure structure, and there is no difference apparent which could be linked to the higher density of the U, Np, and Pu compounds relative to their direct Ln homologs. It has to be noted too

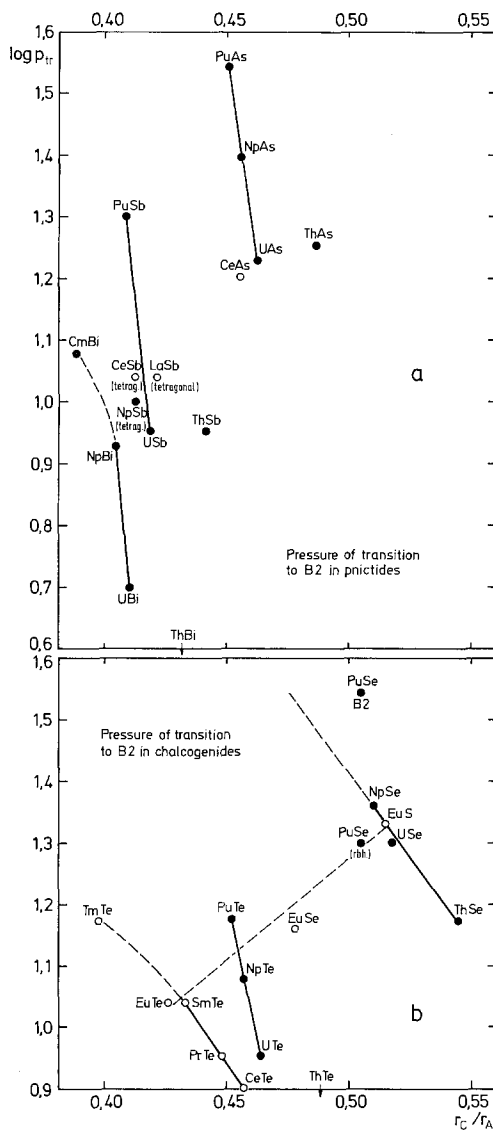


Fig. 21. Logarithm of upstroke-transition pressure versus cation/anion radius ratio for the B1 to B2 transition in lanthanide and actinide compounds. Trivalent ionic radii are used for all cations. Some transitions to other high-pressure structures are included for comparison and have been marked as such in the graphs. (a) Mononictides with As, Sb, and Bi. The isolated data for the phosphides CeP and ThP are not included. No mononitrides have been observed to transform to the B2 type under pressure. (b) Monochalcogenides with S, Se, and Te. The EuO transition is outside the graph.

that if we interpret these high densities as due to the 5f contribution to the bonding, this type of bonding does not lead to low-symmetry structures, as in the elemental metals.

Figures 20 and 21 compare the transition pressures of  $AnX$  compounds and of some  $LnX$  compounds. In particular, fig. 21 gives the dependence of the transition pressures on the cation-anion radius ratio at ambient pressure. This ratio is in general between 0.41 and 0.73 for B1-type compounds. In the actinide mononictides and monochalcogenides, as well as in the lanthanide monotellurides, the transition pressure is seen to increase with decreasing  $r_C/r_A$ . This even includes a few of the

TABLE 9

Data for pressure-induced structural transitions and isothermal bulk moduli of the ambient-pressure phases for lanthanide 4/3 compounds of the anti-Th<sub>3</sub>P<sub>4</sub> structure type (Werner et al. 1981b). The high-pressure phase was assumed to be of a deficient B1-type.

	Transition pressure (GPa) (upstroke)	Volume decrease on transition (%)	$K_0$ (GPa)	$K'_0$
Sm <sub>4</sub> Bi <sub>3</sub>	9.5–≥ 20	≈ 15	52(5)	not determined
Yb <sub>4</sub> Sb <sub>3</sub>	22–≥ 36	≈ 19	43(3)	7
Yb <sub>4</sub> Bi <sub>3</sub>	12–≥ 36	≈ 15	32(3)	7

transitions to structures different from B2. But some of the thorium compounds (ThAs, ThSb) do not follow this rule.

An explanation of this general trend could be given in the following way: the anion is more compressible in these compounds than the cation. The ratio  $r_C/r_A$  thus increases under pressure up to a critical value, which induces the phase transition. Lower initial radius ratios need higher pressures to reach this critical value.

## 5. Other compounds

### 5.1. $M_3X_4$ compounds

The known lanthanide and actinide compounds with this M/X ratio have the Th<sub>3</sub>P<sub>4</sub>-type structure, except Th<sub>3</sub>N<sub>4</sub>. The Va group elements P, As, Sb, and Bi and the VIa group elements (chalcogens) S, Se, and Te can form cubic Th<sub>3</sub>P<sub>4</sub>-type compounds with the lanthanides and actinides. Each lanthanide or actinide atom has eight equidistant nearest X neighbors in these compounds. Figure 22 shows the variation of the lattice parameters in the actinide series for the known compounds of this type.

Some 4/3 compounds of the anti-Th<sub>3</sub>P<sub>4</sub> type (metal and non-metal changing places) are also discussed in this section.

#### 5.1.1. $Ln_3X_4$ compounds

No high-pressure structural studies have been reported for such compounds. But three compounds of the so-called anti-Th<sub>3</sub>P<sub>4</sub> structure type, thus with M/X ratio 4/3, were studied using high-pressure X-ray diffraction (table 9). For Sm<sub>4</sub>Bi<sub>3</sub>, an isostructural first-order transition at 2.7 GPa with a volume collapse of about 9% was observed in addition (Jayaraman et al. 1978). This transition was interpreted as a valence change from Sm<sup>+2</sup> to Sm<sup>+3</sup>. Nakajima et al. (1985) report on a pressure-induced structural transition in Sm<sub>4</sub>Bi<sub>3</sub> below 300 K. This transition occurs around 2 GPa between 35 K and room temperature and is characterized by splitting of the 310 line of the anti-Th<sub>3</sub>P<sub>4</sub>-type Sm<sub>4</sub>Bi<sub>3</sub>.

#### 5.1.2. $An_3X_4$ compounds

Of this class of compounds Gerward et al. (1990a) have studied Th<sub>3</sub>P<sub>4</sub>, U<sub>3</sub>P<sub>4</sub>, U<sub>3</sub>As<sub>4</sub>, and U<sub>3</sub>Sb<sub>4</sub> in the pressure range up to 50 GPa. No structural phase transi-

TABLE 10  
 Isothermal bulk moduli  $K_0$  (GPa) and pressure derivatives  $K'_0$  for actinide compounds of the  $\text{Th}_3\text{P}_4$  structure type (from Gerward et al. 1990a).

	$K_0$ (GPa)	$K'_0$
$\text{Th}_3\text{P}_4$	126(5)	4.0(4)
$\text{U}_3\text{P}_4$	160(15)	4(1)
$\text{U}_3\text{As}_4$	121(10)	4(1)
$\text{U}_3\text{Sb}_4$	93(4)	4(1)

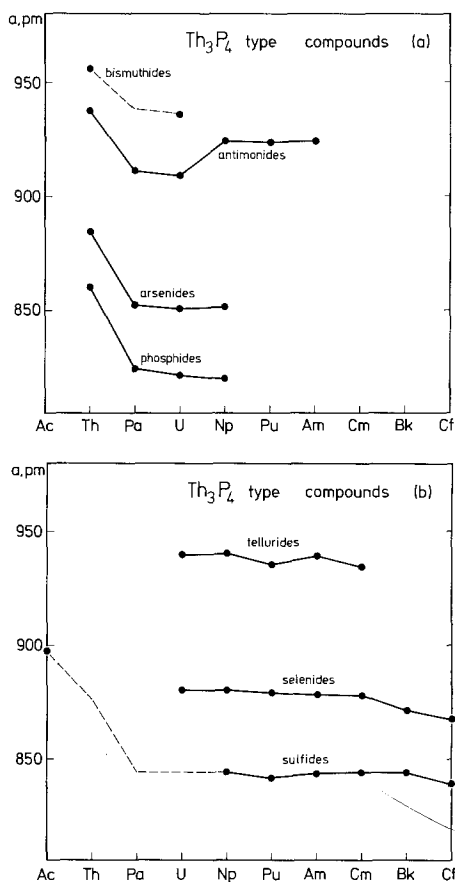


Fig. 22. Lattice parameters of actinide compounds of the  $\text{Th}_3\text{P}_4$  type, (a) pnictides and (b) chalcogenides.

tion was observed up to the highest pressure reached, for each compound. The bulk moduli determined from this work and their pressure derivatives are listed in table 10.

### 5.2. $M_2X_3$ compounds

The cubic C-type allotrope of the sesquioxides of yttrium and of the lanthanides from Sm to Lu, at pressures ranging from 2.5 to 4 GPa and temperatures between



TABLE 11

Pressure–temperature-induced transition to the cubic, deficient  $\text{Th}_3\text{P}_4$ -type structure for rare earth sesquisulfides and sesquiselenides, determined on quenched samples by Eatough et al. (1969) and Eatough and Hall (1970). The selenide phases were prepared from stoichiometric mixtures of the components.

	Initial structure type	Pressure (GPa)	Temperature (K)
$\text{Y}_2\text{S}_3$	monoclinic	$\approx 8$	$\approx 2270$
$\text{Dy}_2\text{S}_3$	monoclinic	$\approx 7$	$\approx 1470$
$\text{Ho}_2\text{S}_3$	monoclinic	$\approx 8$	$\approx 2270$
$\text{Er}_2\text{S}_3$	monoclinic	$\approx 8$	$\approx 2270$
$\text{Tm}_2\text{S}_3$	monoclinic	$\approx 8$	$\approx 2270$
$\text{Tb}_2\text{S}_3$	monoclinic	$\approx 8$	$\approx 2270$
$\text{Yb}_2\text{S}_3$	monoclinic	$\approx 8$	$\approx 2270$
$\text{Lu}_2\text{S}_3$	monoclinic	$\approx 8$	$\approx 2270$
$\text{Y}_2\text{Se}_3$	(stoichiom. mixture)	$\approx 7$	$\approx 2070$
$\text{Ho}_2\text{Se}_3$	(stoichiom. mixture)	$\approx 7$	$\approx 2070$
$\text{Er}_2\text{Se}_3$	(stoichiom. mixture)	$\approx 7$	$\approx 2070$
$\text{Tm}_2\text{Se}_3$	(stoichiom. mixture)	$\approx 7$	$\approx 2070$
$\text{Yb}_2\text{Se}_3$	(stoichiom. mixture)	$\approx 8$	$\approx 2070$
$\text{Lu}_2\text{Se}_3$	(stoichiom. mixture)	$\approx 9$	$\approx 2070$

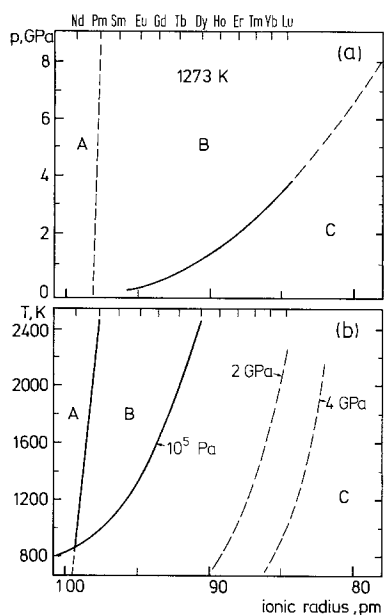


Fig. 23. Effects of pressure on the phase relations of  $\text{Ln}_2\text{O}_3$  (adapted from Hoekstra 1966), (a) 1272 K isotherm and (b) isobars at three different pressures. A: trigonal, B: monoclinic, C: cubic allotope.

1170 and 1300 K, transformed to the monoclinic B-type, which could be quenched to ambient conditions (Hoekstra and Gingerich 1964). C-type  $\text{Sc}_2\text{O}_3$  transforms to B-type at 13 GPa and about 1270 K (Reid and Ringwood 1969). The effects of pressure on the phase relations of  $\text{Ln}_2\text{O}_3$  are summarized in fig. 23 (Hoekstra 1966, Pistorius 1976).

TABLE 12

Pressure-temperature-induced transition to the orthorhombic  $U_2S_3$ -type structure for rare earth sesquisulfides, determined on quenched samples by Range and Leeb (1975).

	Initial structure type	Pressure (GPa)	Temperature (K)	Volume decrease (%)
$Y_2S_3$	monoclinic $Ho_2S_3$	$\approx 2$	$\approx 1120$	$\approx 10$
$Ho_2S_3$	monoclinic $Ho_2S_3$	$\approx 1$	$\approx 1170$	$\approx 9$
$Er_2S_3$	monoclinic $Ho_2S_3$	$\approx 1$	$\approx 1170$	$\approx 9$
$Tm_2S_3$	monoclinic $Ho_2S_3$	$\approx 2$	$\approx 1070$	$\approx 9$
$Yb_2S_3$	rhomboh. corundum	$\approx 2.5$	$\approx 1230$	$\approx 15$
$Lu_2S_3$	rhomboh. corundum	$\approx 3.5$	$\approx 870$	$\approx 15$

$Ho_2Se_3$ ,  $Er_2Se_3$ ,  $Y_2S_3$ , and  $Ln_2S_3$  (Dy–Lu) yield high-pressure phases with defect  $Th_3P_4$ -type structure above about 7 GPa, 1770 K (see table 11) (Eatough et al. 1969).

Range and Leeb (1976) transformed monoclinic  $Tm_2S_3$  I into monoclinic  $Tm_2S_3$  II around 1 GPa, 1270 K, and into orthorhombic  $Tm_2S_3$  III of the  $U_2S_3$  type around 2 GPa, 1270 K. These structures were determined on quenched samples. The  $U_2S_3$ -type structure was also induced by simultaneous action of pressure and temperature on the ambient-pressure allotropes of the sesquisulfides of Y, Ho, Er, Tm, Yb, and Lu (see table 12) (Range and Leeb 1975).

$M_2C_3$  ( $M = Y, Th, La-Er$ ) with the  $Pu_2C_3$  ( $D5_c$ ) type structure (space group I-43d) can be prepared at about 3.5 GPa, 1670 K (Krupka and Bowman 1970).

### 5.3. $MX_2$ and $MXY$ compounds

#### 5.3.1. Lanthanide and actinide dioxides

These compounds have the C1 (fluorite,  $CaF_2$ ) type structure at ambient pressure and temperature. The fluorite structure is predominantly ionic, and contains large cations. The atom packing is such that the main contacts are between atoms of opposite charge and that each atom is surrounded by the maximum number of atoms of opposite charge. The cations in the fluorite structure are surrounded by eight equidistant anions at the corners of a cube. Inversely, each anion has around it four cations at the corners of a tetrahedron. As a rule, this structure is only formed if the ratio of the cation radius to the anion radius is greater than or equal to 0.73.

Of this group of compounds, the high-pressure structural behavior was investigated for  $CeO_2$  (Duclos et al. 1988),  $ThO_2$  (Dancausse et al. 1990),  $UO_2$  (Benjamin et al. 1981, Benedict et al. 1982),  $NpO_2$  (Benedict et al. 1986a),  $PuO_2$  (Dancausse et al. 1990),  $AmO_2$  (Dancausse 1991) and  $CmO_2$  (Dancausse et al. 1992a). In all of these cases, pressure induces a transition to an orthorhombic structure of the  $PbCl_2$  type. For  $UO_2$  and  $NpO_2$ , another possible structure assignment is in space group Cmcn with an atomic arrangement similar to that existing for the  $PbCl_2$ -type structure, whose space group is Pnma.

High-pressure phases, transition pressures, volume decrease on transition, and bulk moduli are listed in tables 13 and 14. Figure 24 shows plots of transition pressures and bulk moduli versus atomic number of the actinide.

TABLE 13  
Pressure-induced structural transitions in  $\text{CeO}_2$  and actinide dioxides  $\text{AnO}_2$ .

	High-pressure structure	Transition pressure (GPa) (upstroke)	Volume decrease on transition (%)	Ref.*
$\text{CeO}_2$	orthorhombic $\text{PbCl}_2$ -like	31.5(10)	7.5(7)	[1]
$\text{ThO}_2$	orthorhombic $\text{PbCl}_2$ (Pnma)	40–50	$\approx 8$	[2]
$\text{UO}_2$	orthorhombic $\text{PbCl}_2$ (Pnma)	between 33 and 40	$\approx 5$	[3]
	orthorhombic $\text{PbCl}_2$ (Pnma) or Cmcm	29–38	$\approx 2.5$ or $\approx 5$	[4]
$\text{NpO}_2$	orthorhombic Cmcm	34–36	$\approx 6$	[5]
$\text{PuO}_2$	orthorhombic $\text{PbCl}_2$ (Pnma)	39–43	$\approx 12$	[2]
$\text{AmO}_2$	orthorhombic $\text{PbCl}_2$ (Pnma)	40–43	$\approx 10$	[6]
$\text{CmO}_2$	orthorhombic $\text{PbCl}_2$ (Pnma)	30–40		[7]

\*References: [1] Duclos et al. (1988), [2] Dancausse et al. (1990), [3] Benjamin et al. (1981), [4] Benedict et al. (1982), [5] Benedict et al. (1986a), [6] Dancausse (1991), [7] Dancausse et al. (1992).

TABLE 14  
Isothermal bulk moduli  $K_0$  (GPa) and their pressure derivatives  $K'_0$  for  $\text{CeO}_2$  and actinide dioxides  $\text{AnO}_2$ .

	$K_0$	$K'_0$	Ref.*
$\text{CeO}_2$	230(10)	4 constrained	[1]
$\text{ThO}_2$	262(4)	6.7(5)	[2]
$\text{UO}_2$	210(10)	7(2)	[3]
	230(8)		[4]
	207(10)	7(2)	[5]
$\text{NpO}_2$	200(2)	3.8(5)	[5]
$\text{PuO}_2$	379(4)	2.4(4)	[2]
$\text{AmO}_2$	280(3)	2.6(6)	[6]
$\text{CmO}_2$	218(5)	7(1)	[7]

\*References: [1] Duclos et al. (1988), [2] Dancausse et al. (1990), [3] Benjamin et al. (1981), [4] Hazen and Finger (1979), [5] Benedict et al. (1986a), [6] Dancausse (1991), [7] Dancausse et al. (1992).

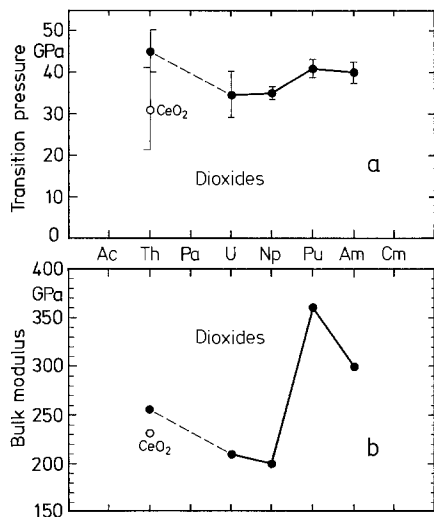


Fig. 24. Upstroke transition pressures (a) and bulk moduli (b) for the actinide dioxides and CeO<sub>2</sub>.

### 5.3.2. Compounds of the Fe<sub>2</sub>As (PbFCl) structure type

Compounds described as Fe<sub>2</sub>As and PbFCl type are discussed together, since any subdivision of this large group of compounds has some arbitrariness. This structure can be thought to be composed of alternating layers of metal and non-metal atoms. It is tetragonal, space group P4/nmm (no. 129); the unit cell contains two formula units. The relative positions of the Ln or An layers and the oxygen layers in oxygen-containing representatives of this structure type are similar to the positions of these layers in the fluorite-type actinide dioxides.

In the Fe<sub>2</sub>As structure the distance between the atoms of the same element is the same as between atoms of different elements. This explains why As and other Va elements can take the places of the iron atoms, and inversely the actinide atoms occupy the arsenic positions. This arrangement is sometimes referred to as the anti-Fe<sub>2</sub>As structure.

Phase transitions under pressure were observed in UP<sub>2</sub>, UAs<sub>2</sub>, and UAsS. These

TABLE 15  
Pressure-induced structural transitions to an orthorhombic structure, probably related to the PbCl<sub>2</sub> type, in actinide compounds of the Fe<sub>2</sub>As-type structure.  
Data from Gerward et al. (1990c).

	Transition pressure, (GPa) (upstroke)	Volume decrease on transition (%)
UP <sub>2</sub>	≈ 22	≈ 7
UAs <sub>2</sub>	≈ 15	≈ 4
UAsS	≈ 45	≈ 7

TABLE 16  
Isothermal bulk modulus  $K_0$  (GPa) and its pressure derivative  $K'_0$  for ambient pressure phases of lanthanide and actinide compounds of the  $\text{Fe}_2\text{As}$  and  $\text{PbFCl}$  structure types.

	$K_0$	$K'_0$	Ref.*
SmFCl	67(10)	5 constrained	[1]
SmFCl	46(1)	7	[2]
EuFCl	58(10)	5(2)	[1]
$\text{UP}_2$	124(15)	9(2)	[3]
$\text{UAs}_2$	101(8)	4.7(7)	[3]
$\text{UAsS}$	105(7)	3.7(5)	[3]
$\text{UAsSe}$	99(6)	3.8(5)	[3]
ThOS	201(3)	3.0(5)	[4]
UOSe	154(2)	1.8(5)	[4]

\*References: [1] Haberkorn (1988), [2] Bolduan et al. (1988), [3] Gerward et al. (1990c), [4] Gensini et al. (1991).

TABLE 17  
Pressure–temperature-induced structural transition to the orthorhombic  $\text{PbCl}_2$  type for lanthanide dihalides, determined on quenched samples by Beck (1979a, b).

	Initial structure type	Pressure (GPa)	Temperature (K)	Volume decrease (%)
$\text{SmI}_2$	Pbca HT?	> 1.5	≈ 550	≈ 7
$\text{EuF}_2$	$\text{CaF}_2$ type	> 10	1120	≈ 10
$\text{EuBr}_2$	$\text{SrBr}_2$ type	7	670	≈ 6
$\text{EuI}_2$	monoclinic	> 1.5	≈ 550	≈ 7

are tabulated in table 15. No phase transition has been found for other compounds of this structure type in the pressure range studied. Data on the bulk moduli for such compounds are given in table 16.

### 5.3.3. Dihalides

Beck (1979a, b) transformed the difluoride, dibromide, and diiodide of europium, as well as  $\text{SmI}_2$ , into quenchable high-pressure phases of the  $\text{PbCl}_2$  structure type by simultaneous action of pressure and temperature (table 17).  $\text{NdI}_2$  of the  $\text{SrBr}_2$  structure type transformed to the tetragonal  $\text{MoSi}_2$  structure type at 4 GPa and 770 K (Beck 1976).

No high-pressure transformations were observed for the  $\text{PbCl}_2$ -type compounds  $\text{EuCl}_2$  and  $\text{SmCl}_2$  (Pistorius 1976). However,  $\text{EuF}_2$  ( $\text{Cl}$  structure type) transforms to the  $\text{PbCl}_2$ -type structure around 11 GPa (Seifert 1968).

### 5.3.4. Other $\text{MX}_2$ compounds

Staub Olsen et al. (1981) have observed a phase transition in  $\text{YbH}_2$  around 14 GPa, where this compound transforms from its orthorhombic structure to a hexagonal phase, accompanied by a volume decrease of about 5%.

Hexagonal  $UB_2$  ( $AlB_2$  type) was studied up to 50 GPa without a phase transition being observed. Its compressibility data are  $K_0 = 225$  GPa;  $K'_0 = 2.6$  (Dancausse et al. 1992b). Tetragonal  $UC_2$  ( $CaC_2$  type) transformed around 18 GPa to a hexagonal high-pressure phase, with a volume decrease of about 3%. Its compressibility data are  $K_0 = 216$  GPa,  $K'_0 = 2.2$  (Dancausse et al. 1993).

### 5.3.5. *LnOF and LnSF compounds*

Beck and Strobel (1985) found that the sulfide fluorides  $ErSF$ ,  $YbSF$ , and  $LuSF$  transform from their usual  $\beta$ -YSF structure to the  $PbFCl$  structure around 1.5, 2, and 3 GPa, respectively, at temperatures  $T \geq 970$  K, and with a volume decrease of the order of 16%. The pressure-induced structures were determined on the quenched samples.

The temperature-induced transition from rhombohedral ( $R-3m$ )  $LaOF$ ,  $SmOF$ ,  $GdOF$ , and  $ErOF$  to the fluorite type shifts to higher temperatures with increasing pressure (studied up to 4 GPa by DTA (Pistorius 1973)). The oxyfluorides  $LnOF$  of La, Pr, Nd, Sm, Eu, and Gd transform to the  $PbCl_2$  type around 1270 K under pressures of 4 to 9 GPa, with a volume decrease of about 6.5% (Gondrand et al. 1970) (quenched samples). Rhombohedral  $YOF$  did not show a phase transformation under these conditions, rhombohedral  $TbOF$  and  $DyOF$  became tetragonal.

### 5.3.6. *High-pressure, high-temperature synthesis*

The following new phases could be obtained by high-pressure, high-temperature synthesis from the elemental constituents:

$LnS_2$  (Y, Gd–Lu) and  $LnSe_2$  (Er, Tm, Yb, Lu) in a tetragonal lattice of space group  $P4/nmm$  (“ $ErSe_2$ ” structure type) (Webb and Hall 1970a, b). These authors give pressure–temperature phase diagrams for some of these disulfides and diselenides.

$RETe_{2-x}$  (RE = Y, Ho, Er, Tm, Lu) in a tetragonal structure of space group  $P4/nmm$  (Cannon and Hall 1970).

$RESb_2$  with RE = Pr, Gd, and Tb in the orthorhombic  $LaSb_2$  structure type and with RE = Y, Gd, Tb, Dy, Ho, Er, Tm, and Yb in another orthorhombic structure (Eatough and Hall 1969, Johnson 1971).

$ScOF$  in a tetragonal structure of space group  $P4/nmm$ ,  $YOF$  and  $LnOF$  (Ln = Tb, Dy, Ho, Er, Lu) in the  $PbCl_2$  structure type (Bendeliani, 1976).

## 5.4. *$MX_3$ compounds*

### 5.4.1. *Halides of the $AlCl_3$ , $BiI_3$ , $UCl_3$ , and $PuBr_3$ type*

These four structure types are arranged in the heading in the order of increasing packing efficiency (Beck and Gladrow 1979). Several compounds transform from one to another of these structure types under the action of temperature or pressure. In particular, pressure favors transformation to structures of denser packing, as has been shown experimentally for  $AmI_3$  (Haire et al. 1985) and  $CfBr_3$  (Peterson et al. 1985).

Beck and Gladrow (1979) could show that lanthanide trihalides of the  $AlCl_3$  or  $BiI_3$  type (coordination 6) transform into the eight-coordinated  $PuBr_3$  type under the combined action of pressure and temperature (quenched samples; see table 18). No phase transition was observed under similar conditions in  $NdBr_3$ ,  $CeI_3$ ,  $NdI_3$ ,  $DyI_3$ , and  $TmI_3$ .

TABLE 18

Pressure–temperature-induced structural transitions to the  $\text{PuBr}_3$  structure type in lanthanide trihalides, determined on quenched samples by Beck and Gladrow (1979).

Initial structure type		Pressure (GPa)	Temperature (K)
$\text{SmI}_3$	$\text{BiI}_3$	not given by authors	
$\text{GdI}_3$	$\text{BiI}_3$	1–4	570–720
$\text{TbBr}_3$	$\text{BiI}_3$	not given by author	
$\text{TbI}_3$	$\text{BiI}_3$	3–4	570–820
$\text{DyCl}_3$	$\text{AlCl}_3$	4	790
$\text{DyBr}_3$	$\text{BiI}_3$	1.3	720
$\text{HoBr}_3$	$\text{BiI}_3$	3	840
$\text{TmCl}_3$	$\text{AlCl}_3$	not given by authors	

$\text{PuBr}_3$ -type  $\text{NdBr}_3$  did not show clear signs of a phase transformation in a diamond anvil cell at room temperature up to 52 GPa. The compound is very compressible; its bulk modulus,  $K_0$ , is of the order of only 17 GPa (Peterson et al. 1993).

Indications for crystallographic phase transitions under pressure in other lanthanide and actinide trihalides were obtained by Raman and optical absorption studies in diamond anvil cells. Monoclinic  $\text{CfBr}_3$  transformed to the  $\text{PuBr}_3$  type between 1.7 and 3.4 GPa (Peterson et al. 1985). Haire et al. (1985) observed that rhombohedral  $\text{AmI}_3$  also showed a pressure-induced transition to that structure type. Wilmarth et al. (1989) concluded that the  $\text{UCl}_3$ -type forms of  $\text{PrCl}_3$  and  $\text{PrBr}_3$  also convert to this structure type under pressure. However, Gregorian et al. (1989) give strong arguments for the possibility that these transitions, as well as similar transitions in  $\text{LaCl}_3$  and  $\text{GdCl}_3$ , lead rather to the  $\text{YF}_3$  structure. Gregorian (1987) determined  $K_0 = 30.1(11)$  GPa and  $K'_0 = 6.0(4)$  for  $\text{LaCl}_3$ .

The structural systematics for  $\text{RX}_3$  compounds and the effects of high pressure on  $\text{LaCl}_3$  are illustrated in fig. 25. From this graph one can speculate that the high-

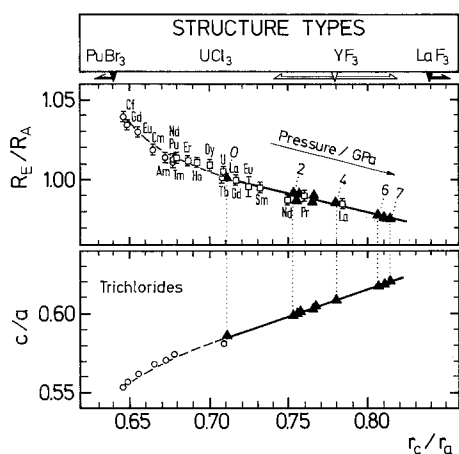


Fig. 25. Correlation of structural systematics for  $\text{RX}_3$  compounds with the effects of high pressure, as discussed by Gregorian et al. (1989) using the variation in  $c/a$ , ionic radius ratios  $r_c/r_a$  and ratios of nearest-neighbor distances for the cations,  $R_E/R_A$ .  $\circ$ : trichlorides, ambient pressure,  $\square$ : trihydroxides, ambient pressure,  $\blacktriangle$ :  $\text{LaCl}_3$ , at pressures up to 7 GPa.

pressure structure of  $\text{LaCl}_3$  and all the other  $\text{LnCl}_3$  compounds should be the  $\text{LaF}_3$  structure type, while the  $\text{LnBr}_3$  compounds which crystallize at ambient pressure in the  $\text{PuBr}_3$  structure type, as, e.g.  $\text{NdBr}_3$ , should transform under pressure into the  $\text{UCl}_3$  structure type. From the value  $r_c/r_a = 0.554$  of  $\text{NdBr}_3$  and the pressure dependence  $d(r_c/r_a)/dp \approx 0.02 \text{ GPa}^{-1}$  for  $\text{LaCl}_3$  one may estimate that  $\text{NdBr}_3$  should transform to the  $\text{UCl}_3$  structure type at a pressure below 10 GPa.

#### 5.4.2. Other $\text{MX}_3$ compounds

Bendeliani (1975) obtained the high-pressure phase  $\text{ScF}_3$  II, of the  $\text{YF}_3$  type, around 10 GPa and 700 K, instead of the ambient-pressure phase  $\text{ScF}_3$  I of a distorted  $\text{ReO}_3$  type. The polymorphic transition from I to II is accompanied by an increase in coordination of Sc from six to nine.  $\text{ScF}_3$  II is more than 1.5 times denser than  $\text{ScF}_3$  I.

Vezzoli (1970) produced an unidentified high-pressure phase ( $\text{LaF}_3$  type?) of  $\text{DyF}_3$  by pressurizing to about 1.2 GPa at about 540 K (quenched sample).  $\text{PrF}_3$  and  $\text{EuF}_3$  showed no sign of a phase transformation up to 4 GPa at the same temperature.

The crystal structure of  $\text{EuAs}_3$  ( $\text{BaAs}_3$  type, space group  $\text{C2/m}$ , no. 12) remained essentially unaltered in a neutron diffraction study up to 2 GPa (Chattopadhyay and Brown 1990).

Orthorhombic  $\text{LuTe}_3$  was synthesized from the constituents by combined action of pressure and temperature by Cannon and Hall (1970).

#### 5.5. $\text{MX}_4$ compounds

Tetragonal  $\text{UB}_4$  ( $\text{ThB}_4$  type) did not exhibit a phase transition up to 53 GPa, the highest pressure reached in the experiment.  $K_0 = 181 \text{ GPa}$ ,  $K'_0 = 5$  (Dancausse et al. 1992b).

Tetragonal  $\text{UCl}_4$  ( $\text{ThBr}_4$  type) undergoes a phase transition around 5 GPa. By high-pressure X-ray diffraction of a  $\text{UCl}_4$  single crystal, the high-pressure phase was identified as monoclinic with  $a = 730.5$ ,  $b = 784.9$ ,  $c = 2761 \text{ pm}$ , and  $\beta = 97.29^\circ$  at 5.4 GPa. Indication for a similar phase transition in the isostructural  $\text{ThCl}_4$  was obtained around 2 GPa. The following compressibility data were determined:  $K_0 = 38 \text{ GPa}$ ,  $K'_0 = 10$  for  $\text{ThCl}_4$ ,  $K_0 = 42 \text{ GPa}$ ,  $K'_0 < 0$  for  $\text{UCl}_4$ , showing that these halides are very soft materials (Dancausse 1991).

#### 5.6. $\text{MX}_6$ and $\text{MX}_{12}$ compounds

Lundström et al. (1982) studied  $\text{LaB}_6$  and  $\text{EuB}_6$  using X-ray diffraction to 0.8 GPa and determined bulk moduli of 172 and 167 GPa, respectively. Léger (1984) determined  $K_0 = 166$  and  $K'_0 = 3$  for  $\text{CeB}_6$ . The fcc structure of  $\text{UB}_{12}$  remained stable upto 54 GPa, the highest pressure reached in the experiment.  $K_0 = 249 \text{ GPa}$ ,  $K'_0 = 3.4$  (Dancausse et al. 1992b).

#### 5.7. Ternary and quaternary compounds

Stubican and Roy (1963a) observed on quenched samples that the orthovanadates and orthoarsenates of scandium and of the lanthanides from Pr to Lu undergo a transformation from the tetragonal xenotime (= zircon) or the monoclinic monazite



type to the tetragonal scheelite type at high pressure. They established univariant pressure–temperature curves and relations between the transition pressures and ionic radii for these phase transformations (Stubican and Roy 1963b).

$\text{LiLnO}_2$  with  $\text{Ln} = \text{Sm to Tb}$ : orthorhombic to monoclinic transformations have been demonstrated, by study of quenched samples, to occur around 4.5 GPa and 970 K (Waintal and Gondrand 1967, Pistorius 1976).

Jayaraman (1978) briefly reviews structural pressure effects on a number of other ternary and quaternary rare earth compounds.

## 6. Summary and outlook

The dualism between localized and delocalized *f* electrons is still a very useful basis for explaining many aspects of the behavior of the *f* metals. In this chapter, the structural phase transitions in lanthanide and heavy-actinide metals have been discussed along these lines. It is of secondary importance, in this context, whether “delocalization” is understood as “itinerancy” of *f* electrons and their hybridization with the conduction band, or as “promotion” of individual electrons into a bonding state with a sharp increase of valency.

In the *f*-metal compounds, *f* delocalization seems to be only a minor aspect of structural phase transitions. Geometrical factors have to be considered as one of the major reasons for inducing phase transitions. Systematics in the compounds is less advanced than in the metals, and this is due in a large part to lack of high-pressure studies on most of the numerous lanthanide compounds with the B1-type structure. Only those which were expected to show electronic transitions have received major attention from experimentalists, and it will be extremely useful to re-start the efforts on high-pressure studies of the remaining B1-type lanthanide compounds.

An interesting observation that needs explanation is the re-transformation, at very high pressure, of the monoclinic metal phases in Ce and Sm to tetragonal phases, i.e. phases of higher symmetry. The hexagonal phase formed around 40 GPa from monoclinic alpha-plutonium may be another example of symmetry increase under pressure in metals assumed to be in an *f*-delocalized state in their monoclinic phase. The simple correlation between *f* delocalization and low structural symmetry, successfully used as a working hypothesis in the *f* metals, will probably need modification or refinement on the basis of these results.

Although identical *f*-occupancy determines similarity in many properties for the two *f*-series, there are other influences that are at the origin of important deviations. One main feature is the larger extension of the 5*f* orbitals relative to the 4*f* ones, which causes delocalization in the light-actinide metals. Other properties are controlled by basic principles that follow the  $Z + 4$  relationship.

For many of the aspects of structural behavior under pressure of the *f* metals and, in particular, of their compounds, we are at present limited to the description of the phenomena, without being able to give a detailed interpretation and explanation. This means that, in addition to more systematic experimental study, theoretical efforts devoted to these phenomena merit to be enhanced.

## Acknowledgement

The help of W. Sievers with bulk modulus calculations and with part of the drawings is gratefully acknowledged.

## References

- Akella, J., and G. Smith, 1987, *Inorg. Chim. Acta* **140**, 117–118.
- Akella, J., J. Xu and G.S. Smith, 1986, *Physica B* **139/140**, 285.
- Akella, J., Q. Johnson, G.S. Smith and L.C. Ming, 1988a, *High Press. Res.* **1**, 91.
- Akella, J., G.S. Smith and A. Jephcoat, 1988b, *J. Phys. & Chem. Solids* **49**, 573–576.
- Armstrong, P.E., O.N. Carlson and J.E. Smith, 1959, *J. Appl. Phys.* **30**, 36.
- Bartholin, H., F. Kervella, A. Waintal, G. Parisot and J.P. Senateur, 1980, *Phys. Status Solidi A* **61**, K87-K90.
- Beck, H.P., 1976, *Z. Naturforschung* **31b**, 1548–1549.
- Beck, H.P., 1979a, *Z. Anorg. Allg. Chemie* **459**, 72–80.
- Beck, H.P., 1979b, *Z. Anorg. Allg. Chemie* **459**, 81–86.
- Beck, H.P., and E. Gladrow, 1979, *Z. Anorg. Allg. Chemie* **453**, 79–92.
- Beck, H.P., and C. Strobel, 1985, *Z. Naturforschung B* **40**, 1644–1650.
- Bellussi, G., U. Benedict and W.B. Holzapfel, 1981, *J. Less-Common Met.* **78**, 147–153.
- Bendeliani, N.A., 1975, *Sov. Phys. Dokl.* **19**, 847.
- Bendeliani, N.A., 1976, *Sov. Phys. Dokl.* **20**, 526–527.
- Benedict, U., 1987, in: *Handbook on the Physics and Chemistry of the Actinides*, Vol. 5, eds A.J. Freeman and G.H. Lander (North-Holland, Amsterdam) pp. 227–269.
- Benedict, U., 1989, *High-Press. Res.* **1**, 139–147.
- Benedict, U., 1993, *J. Alloys & Compounds* **193**, 88–93.
- Benedict, U., G.D. Andreetti, J.M. Fournier and A. Waintal, 1982, *J. Phys. Lett. (Paris)* **43**, L171–L177.
- Benedict, U., J.C. Spirlet, L. Gerward and J. Staun Olsen, 1984, *J. Less-Common Met.* **98**, 301–307.
- Benedict, U., S. Dabos, C. Dufour, J.C. Spirlet and M. Pagès, 1986a, *J. Less-Common Met.* **121**, 461–468.
- Benedict, U., W.A. Grosshans and W.B. Holzapfel, 1986b, *Physica B* **144**, 14–18.
- Benedict, U., S. Dabos, L. Gerward, J. Staun Olsen, J. Beuers, J.C. Spirlet and C. Dufour, 1987, *J. Magn. & Magn. Mater.* **63&64**, 403–405.
- Benjamin, T.M., G. Zou, H.K. Mao and P.M. Bell, 1981, *Carnegie Institution of Washington, Yearbook* **80**, pp. 280–283.
- Birch, F., 1978, *J. Geophys. Res.* **83**, 1257.
- Bolduan, F., H.D. Hochheimer and H.P. Beck, 1988, *Phys. Status Solidi B* **127**, 673–678.
- Bridgman, P.W., 1948, in: *Proc. Am. Acad. Arts and Sci.* **76**, 55; as revised by G.C. Kennedy and R.N. Keeler, 1972, *AIP Handbook*, 3rd Ed. (McGraw Hill, New York) p. 4-45.
- Brooks, M.S.S., 1982, *J. Magn. & Magn. Mater.* **29**, 257–261.
- Brooks, M.S.S., G.H. Lander and B. Johansson, 1991, *Europhys. News* **22**, 87.
- Cannon, J.F., and T. Hall, 1970, *Inorg. Chem.* **9**, 1639–1643.
- Cannon, J.F., and T. Hall, 1975, *J. Less-Common Met.* **40**, 313–328.
- Cannon, J.F., D.L. Robertson and H.T. Hall, 1972a, *Mater. Res. Bull.* **7**, 5–12.
- Cannon, J.F., D.L. Robertson and H.T. Hall, 1972b, *J. Less-Common Met.* **29**, 141–146.
- Cannon, J.F., D.L. Robertson and H.T. Hall, 1973, *J. Less-Common Met.* **31**, 174–176.
- Carter, W.J., J.N. Fritz, S.P. Marsh and R.G. McQueen, 1975, *J. Phys. & Chem. Solids* **36**, 741.
- Chatterjee, A., A.K. Singh and A. Jayaraman, 1972, *Phys. Rev. B* **6**, 2285–2291.
- Chattopadhyay, T., and P.J. Brown, 1990, *Phys. Rev. B* **41**, 4358–4367.
- Croft, M., and A. Jayaraman, 1979, *Solid State Commun.* **29**, 9.
- Croft, M., and A. Jayaraman, 1980, *Solid State Commun.* **35**, 203.
- Dabos, S., C. Dufour, U. Benedict, J.C. Spirlet and M. Pagès, 1986, *Physica B* **144**, 79–83.
- Dabos, S., J. Staun Olsen, L. Gerward, U. Benedict and J.C. Spirlet, 1988, *J. Less-Common Met.* **142**, L19–L21.
- Dabos-Seignon, S., and U. Benedict, 1990, *High-Press. Res.* **4**, 384–386.

- Dabos-Seignon, S., U. Benedict, J.C. Spirlet and M. Pagès, 1989, *J. Less-Common Met.* **153**, 133–141.
- Dabos-Seignon, S., E. Gering, U. Benedict, J.C. Spirlet and M. Pagès, 1990a, *High-Pressure Research* **2**, 255–261.
- Dabos-Seignon, S., U. Benedict, S. Heathman, J.C. Spirlet and M. Pagès, 1990b, *J. Less-Common Met.* **160**, 35–52.
- Dabos-Seignon, S., U. Benedict and J.C. Spirlet, 1993, to be published.
- Dancausse, J.P., 1991, Thèse, Univ. Paris XI, Orsay.
- Dancausse, J.P., E. Gering, S. Heathman and U. Benedict, 1990, *High-Pressure Research* **2**, 381–389.
- Dancausse, J.P., S. Heathman, R.G. Haire and U. Benedict, 1992a, unpublished result; see also: J.P. Dancausse and U. Benedict, paper presented at the 22èmes Journées des Actinides, Méribel, France, April 22–25, 1992.
- Dancausse, J.P., E. Gering, S. Heathman, U. Benedict, L. Gerward, J. Staun Olsen and F. Hulliger, 1992b, *J. Alloys & Compounds* **189**, 205–208.
- Dancausse, J.P., S. Heathman, U. Benedict, L. Gerward, J. Staun Olsen and F. Hulliger, 1993, *J. Alloys & Compounds* **191**, 309–312.
- Debray, D., A. Werner, D.L. Decker, M. Loewenhaupt and E. Holland-Moritz, 1982, *Phys. Rev. B* **25**, 3841–3845.
- Duclos, S.J., Y.K. Vohra, A.L. Ruoff, A. Jayaraman and G.P. Espinosa, 1988, *Phys. Rev. B* **38**, 4250.
- Eatough, N.L., and H.T. Hall, 1969, *Inorg. Chem.* **8**, 1439–1445.
- Eatough, N.L., and H.T. Hall, 1970, *Inorg. Chem.* **9**, 417–418.
- Eatough, N.L., A.W. Webb and H.T. Hall, 1969, *Inorg. Chem.* **8**, 2069.
- Eriksson, O., M.S.S. Brooks and B. Johansson, 1990, *J. Less-Common Met.* **158**, 207.
- Evers, J., G. Oehlinger and A. Weiss, 1976, Conference Report AED-Conf-76-450-004 (Zentralstelle für Atomenergie-Dokumentation, Frankfurt/Main).
- Gensini, M., 1992, Thèse (Univ. Liège, Belgium).
- Gensini, M., E. Gering, S. Heathman, U. Benedict and J.C. Spirlet, 1990, *High-Pressure Research* **2**, 347–359.
- Gensini, M., E. Gering, U. Benedict, L. Gerward, J. Staun Olsen and F. Hulliger, 1991, *J. Less-Common Met.* **171**, L9–L12.
- Gensini, M., R.G. Haire, U. Benedict and F. Hulliger, 1993a, *Physica B*, in press.
- Gensini, M., U. Benedict and J. Rebizant, 1993b, *J. Alloys & Compounds*, submitted.
- Gerward, L., J. Staun Olsen, U. Benedict, J.P. Itié and J.C. Spirlet, 1985, *J. Appl. Cryst.* **18**, 339–341.
- Gerward, L., J. Staun Olsen, U. Benedict, S. Dabos, H. Luo, J.P. Itié and O. Vogt, 1988, *High Temperatures–High Pressures* **20**, 545–552.
- Gerward, L., J. Staun Olsen, U. Benedict, S. Dabos and O. Vogt, 1989, *High-Pressure Research* **1**, 235–251.
- Gerward, L., J. Staun Olsen, U. Benedict, H. Luo and F. Hulliger, 1990a, *High-Pressure Research* **4**, 357–359.
- Gerward, L., J. Staun Olsen, U. Benedict and H. Luo, 1990b, *J. Less-Common Met.* **161**, L11–L14.
- Gerward, L., J. Staun Olsen, U. Benedict, S. Dabos-Seignon and H. Luo, 1990c, *High Temperatures–High Pressures* **22**, 523–532.
- Gondrand, M., J.C. Joubert, J. Chenavas, J.J. Capponi and M. Perroud, 1970, *Mater. Res. Bull.* **5**, 769.
- Gregorian, T., 1987, Diss. Univ. Paderborn (Germany).
- Gregorian, T., H. d'Amour-Sturm and W.B. Holzapfel, 1989, *Phys. Rev. B* **39**, 12497–12519.
- Greiner, J.D., D.T. Peterson and J.F. Smith, 1977, *J. Appl. Phys.* **48**, 3357.
- Grosshans, W., Y.K. Vohra and W.B. Holzapfel, 1982, *J. Magn. & Magn. Mater.* **29**, 28.
- Grosshans, W.A., 1987, Diss. Univ. Paderborn (Germany).
- Grosshans, W.A., and W.B. Holzapfel, 1992, *Phys. Rev. B* **45**, 5171.
- Gschneidner Jr, K.A., 1985, *J. Less-Common Met.* **110**, 1.
- Gschneidner Jr, K.A., and F.W. Calderwood, 1986, in: *Handbook on the Physics and Chemistry of Rare Earths*, Vol. 8, eds K.A. Gschneidner Jr and L. Eyring (North-Holland, Amsterdam) pp. 1–161.
- Haberkorn, R., 1988, Diss. Univ. Erlangen-Nürnberg (Germany).
- Haire, R.G., 1987, in: Report ORNL-6385, Chemistry Division Annual Progress Report for Period Ending March 31, 1987 (Oak Ridge National Laboratory, Oak Ridge, TN) pp. 62–63.
- Haire, R.G., U. Benedict, J.P. Young, J.R. Peterson and G.M. Begun, 1985, *J. Phys. C* **18**, 4595–4601.
- Haire, R.G., S. Heathman and U. Benedict, 1990a, *High-Pressure Research* **2**, 273–288.
- Haire, R.G., S. Dabos, U. Benedict and C. Dufour,

- 1990b, Spring Meeting of the American Chemical Society, Boston, MA, April 23–27, 1990.
- Haire, R.G., M. Gensini, S. Heathman and U. Benedict, 1993, to be published.
- Harrison, W.A., 1984, *Phys. Rev. B* **29**, 2917.
- Hazen, R.M., and L.W. Finger, 1979, Carnegie Institution of Washington, Yearbook 78, p. 633.
- Heathman, S., R.G. Haire and U. Benedict, 1993a, to be published.
- Heathman, S., Y. Kergadallan and P. Link, 1993b, to be published.
- Hill, H.H., 1970, in: *Plutonium 1970 and Other Actinides*, ed. W.N. Miner (Metallurgical Soc. of AIME, New York) p. 2.
- Hoekstra, H.R., 1966, *Inorg. Chem.* **5**, 754.
- Hoekstra, H.R., and K.A. Gingerich, 1964, *Science* **146**, 1163.
- Holzapfel, W.B., 1990, in: *Molecular Solids under Pressure*, eds R. Pucci and G. Piccitto (North-Holland, Amsterdam) p. 61.
- Holzapfel, W.B., 1991, *Europhys. Lett.* **16**, 67.
- Itié, J.P., J.R. Peterson, R.G. Haire, C. Dufour and U. Benedict, 1985, *J. Phys. F* **15**, L213–L219.
- Itié, J.P., J. Staun Olsen, L. Gerward, U. Benedict and J.C. Spirlet, 1986, *Physica B* **139–140**, 330–332.
- Jayaraman, A., 1978, in: *Handbook on the Physics and Chemistry of Rare Earths*, Vol. 1, eds K.A. Gschneidner Jr and L. Eyring (North-Holland, Amsterdam) pp. 707–747.
- Jayaraman, A., 1979, in: *Handbook on the Physics and Chemistry of Rare Earths*, Vol. 2, eds K.A. Gschneidner Jr and L. Eyring (North-Holland, Amsterdam) pp. 575–611.
- Jayaraman, A., and E. Bucher, 1979, *J. Phys. C* **5**, 350–351.
- Jayaraman, A., A.K. Singh, A. Chatterjee and S. Usha Devi, 1974, *Phys. Rev. B* **9**, 2513–2520.
- Jayaraman, A., W. Lowe, L.D. Longinotti and E. Bucher, 1976, *Phys. Rev. Lett.* **36**, 366–369.
- Jayaraman, A., R.G. Maines and E. Bucher, 1978, *Solid State Commun.* **27**, 709–711.
- Johansson, B., H.L. Skriver and O.K. Andersen, 1981, in: *Physics of Solids under High Pressure*, eds J.S. Schilling and J.N. Shelton (North-Holland, Amsterdam) pp. 245–262.
- Johnson, Q., 1971, *Inorg. Chem.* **10**, 2089–2090.
- Keller, R., G. Güntherodt, W.B. Holzapfel, M. Dietrich and F. Holtzberg, 1979, *Solid State Commun.* **29**, 753–758.
- Kennedy, G.C., and R.N. Keeler, 1972, in: *AIP Handbook*, 3rd Ed. (McGraw Hill, New York) p. 4–102.
- Krüger, T., B. Merkau, W.A. Grosshans and W.B. Holzapfel, 1990, *High-Pressure Research* **2**, 193–236.
- Krupka, M.C., and M.G. Bowman, 1970, *Coll. Internat. CNRS* **188**, 409.
- Landolt-Börnstein, 1967, *New Series*, Vol. II/5 (Springer, Heidelberg) p. 236.
- Lawrence, J.M., P.S. Riseborough and R.D. Parks, 1981, *Rep. Progr. Phys.* **44**, 1–84.
- Léger, J.M., 1984, *Rev. Phys. Appl.* **19**, 815–817.
- Léger, J.M., and A.M. Redon, 1989, *J. Less-Common Met.* **156**, 137–143.
- Léger, J.M., N. Yacoubi and J. Lories, 1981, *J. Solid State Chem.* **36**, 261.
- Léger, J.M., R. Épain, J. Lories, D. Ravot and J. Rossat-Mignod, 1983, *Phys. Rev. B* **28**, 7125–7129.
- Léger, J.M., D. Ravot and J. Rossat-Mignod, 1984, *J. Phys. C* **17**, 4935–4943.
- Léger, J.M., K. Oki, D. Ravot, J. Rossat-Mignod and O. Vogt, 1985, *J. Magn. & Magn. Mater.* **47–48**, 277–280.
- Lundström, T., B. Lönnberg, B. Törmä, J. Étourneau and J.M. Tarascon, 1982, *Phys. Scr.* **26**, 414–416.
- Luo, H., S. Dabos, U. Benedict and J.C. Spirlet, 1988, *J. Less-Common Met.* **142**, L23–L25.
- Lüthi, B., and C. Ligner, 1979, *Z. Phys. B* **34**, 157.
- Manes, L., and U. Benedict, 1985, in: *Actinides: Chemistry and Physical Properties*, ed. L. Manes (Springer, Heidelberg) pp. 75–126.
- McMahan, A.K., 1989, *J. Less-Common Met.* **194**, 1.
- McWhan, D.B., 1966, *J. Chem. Phys.* **44**, 3528–3530.
- Miller, K., and H.T. Hall, 1972, *Inorg. Chem.* **11**, 1188–1191.
- Miller, K., and H.T. Hall, 1973, *J. Less-Common Met.* **32**, 275–278.
- Nakajima, T., K. Tsuji, T. Ishidate, H. Takahashi, S. Suzuki, A. Ochiai, T. Suzuki and T. Kasuya, 1985, *J. Magn. & Magn. Mater.* **47–48**, 292–294.
- Neumann, G., J. Langen, H. Zahel, D. Plümacher, Z. Kletowski, W. Schlabit and D. Wohlleben, 1985, *Z. Phys. B* **59**, 133–141.
- Peterson, J.R., J.P. Young, R.G. Haire, G.M. Begun and U. Benedict, 1985, *Inorg. Chem.* **24**, 2466–2468.
- Peterson, J.R., S. Heathman and U. Benedict, 1993, *J. Alloys & Compounds* **193**, 306–308.
- Pistorius, C.W.F.T., 1973, *J. Less-Common Met.* **31**, 119.

- Pistorius, C.W.F.T., 1976, *Progr. Solid State Chem.* **11**, 1–151.
- Porsch, F.P., and W.B. Holzapfel, 1993, *Phys. Rev. Lett.*, in press.  
 Note: The re-entrant behavior for the fcc phase of La published in this paper affects only La, and none of the heavier lanthanides, since the corresponding critical radius ratio of  $r_r \approx 1.9$  implies “low symmetry” f-bonded structures already for all the other lanthanides (see fig. 5).
- Porsch, F.P., P. Sommer and W.B. Holzapfel, 1992, unpublished.
- Ramesh, T.G., and W.B. Holzapfel, 1987, *Pramana – J. Phys.* **29**, 183–185.
- Range, K.J., and R. Leeb, 1975, *Z. Naturforschung b* **30**, 889–895.
- Range, K.J., and R. Leeb, 1976, *Z. Naturforschung b* **31**, 311–314.
- Reid, A.F., and A.E. Ringwood, 1969, *J. Geophys. Res.* **74**, 3238.
- Reynolds, M.B., 1951, Report AECD-3242 (US Atomic Energy Commission, Washington, DC).
- Robertson, D.L., J.F. Cannon and H.T. Hall, 1972, *Mater. Res. Bull.* **7**, 977–982.
- Röhler, J., 1986, *Physica B* **144**, 27.
- Rooymans, C.J.M., 1965, *Solid State Commun.* **3**, 421–424.
- Rooymans, C.J.M., 1966, *Ber. Bunsenges. Phys. Chemie* **70**, 1036.
- Seifert, K., 1968, *Fortschr. Mineralogie* **45**, 214–280.
- Skriver, H.L., 1983, in: *Systematics and the Properties of the Lanthanides*, ed. S.P. Sinha (Reidel, Dordrecht) p. 213.
- Skriver, H.L., 1985, *Phys. Rev. B* **31**, 1909.
- Skriver, H.L., and J.P. Jan, 1980, *Phys. Rev. B* **21**, 1489.
- Smith, J.L., 1980, *Physica B* **102**, 22.
- Smith, J.L., and E.A. Kmetko, 1983, *J. Less-Common Met.* **90**, 83.
- Spain, I.L., F. Steglich, U. Rauchschwalbe and H.D. Hochheimer, 1986, *Physica B* **139&140**, 449–452.
- Staun Olsen, J., B. Buras, L. Gerward, B. Johansson, B. Lebech, H.L. Skriver and S. Steenstrup, 1981, in: *Physics of Solids under High Pressure*, eds J.S. Schilling and R.N. Shelton (North-Holland, Amsterdam) pp. 305–309.
- Staun Olsen, J., L. Gerward, U. Benedict and J.P. Itié, 1985a, *Physica B* **133**, 129–137.
- Staun Olsen, J., L. Gerward and U. Benedict, 1985b, *J. Appl. Crystallogr.* **18**, 37–41.
- Staun Olsen, J., L. Gerward, U. Benedict, J.P. Itié and K. Richter, 1986, *J. Less-Common Met.* **121**, 445–453.
- Staun Olsen, J., L. Gerward, U. Benedict, H. Luo and O. Vogt, 1988a, *High Temperatures–High Pressures* **20**, 553–559.
- Staun Olsen, J., L. Gerward, U. Benedict, S. Dabos and O. Vogt, 1988b, *Phys. Rev. B* **37**, 8713–8718.
- Staun Olsen, J., L. Gerward, U. Benedict, S. Dabos, J.P. Itié and O. Vogt, 1989a, *High-Pressure Research* **1**, 253–266.
- Staun Olsen, J., L. Gerward, U. Benedict, H. Luo and O. Vogt, 1989b, *J. Appl. Crystallogr.* **22**, 61–63.
- Staun Olsen, J., S. Steenstrup, L. Gerward, U. Benedict, J. Akella and G. Smith, 1990, *High-Pressure Research* **4**, 366–368.
- Stubican, V.S., and R. Roy, 1963a, *Z. Krist.* **119**, 90–97.
- Stubican, V.S., and R. Roy, 1963b, *J. Appl. Phys.* **34**, 1888.
- Syassen, K., 1986, *Physica B* **139–140**, 277–283.
- Syassen, K., G. Wortmann, J. Feldhaus, K.K. Frank and G. Kaindl, 1982, *Phys. Rev. B* **26**, 4745.
- Tsuyashchenko, A.V., and L.N. Fomicheva, 1985, *J. Less-Common Met.* **105**, L1–L3.
- Tsuyashchenko, A.V., and L.N. Fomicheva, 1987, *J. Less-Common Met.* **135**, L9–L12.
- Tsuyashchenko, A.V., and L.N. Fomicheva, 1991, *J. Less-Common Met.* **171**, L5–L8.
- Tsuyashchenko, A.V., and S.V. Popova, 1985, *J. Less-Common Met.* **108**, 115–121.
- Usha Devi, S., and A.K. Singh, 1984, *Solid State Commun.* **52**, 303–305.
- Vaidya, S.N., and G.C. Kennedy, 1972, *J. Phys. & Chem. Solids* **33**, 1383.
- Vaidya, S.N., S.K. Sikka and W.B. Holzapfel, 1987, in: *Theoretical and Experimental Aspects of Valence Fluctuations and Heavy Fermions*, eds L.C. Gupta and S.K. Malik (Plenum, New York) pp. 617–620.
- Vedel, I., A.M. Redon, J.M. Léger, J. Rossat-Mignod and O. Vogt, 1986a, *J. Phys. C* **19**, 6297–6302.
- Vedel, I., A.M. Redon and J.M. Léger, 1986b, *J. Phys. C* **19**, 3549–3554.
- Vedel, I., A.M. Redon, J.M. Léger, J.M. Mignot and J. Flouquet, 1986c, *J. Magn. & Magn. Mater.* **54–57**, 361.
- Vedel, I., A.M. Redon and J.M. Léger, 1986d, *Physica B* **144**, 61–65.
- Vedel, I., A.M. Redon, J.M. Léger, J. Rossat-Mignod and O. Vogt, 1987, *J. Phys. C* **20**, 3439–3444.

- Vezzoli, G.C., 1970, *Mater. Res. Bull.* **5**, 213–218.
- Vöhra, Y., J. Akella, S. Weir and G.S. Smith, 1991, *Phys. Lett. A* **158**, 89–92.
- Vohra, Y.K., and J. Akella, 1991, *Phys. Rev. Lett.* **67**, 3563.
- Vohra, Y.K., W. Grosshans and W.B. Holzzapfel, 1982, *Phys. Rev. B* **25**, 6019–6021.
- Waber, J.T., and D.T. Cromer, 1965, *J. Chem. Phys.* **42**, 4116.
- Waintal, A., and M. Gondrand, 1967, *Mater. Res. Bull.* **2**, 889.
- Ward, J.W., 1985, in: *Americium and Curium Chemistry and Technology*, eds N.M. Edelstein, J.D. Navratil and W.W. Schulz (Reidel, Dordrecht) pp. 135–145.
- Webb, A.W., and H.T. Hall, 1970a, *Inorg. Chem.* **9**, 843.
- Webb, A.W., and H.T. Hall, 1970b, *Inorg. Chem.* **9**, 1084.
- Werner, A., H.D. Hochheimer, A. Jayaraman and J.M. Léger, 1981a, *Solid State Commun.* **38**, 325–327.
- Werner, A., H.D. Hochheimer, A. Jayaraman and E. Bucher, 1981b, in: *Physics of Solids under High Pressure*, eds J.S. Schilling and R.N. Shelton (North-Holland, Amsterdam) pp. 295–299.
- Werner, A., H.D. Hochheimer, M. Wittmann, H.G. von Schnering and E. Hinze, 1982, *J. Less-Common Met.* **87**, 327–332.
- Werner, A., H.D. Hochheimer, R.L. Meng and E. Bucher, 1983, *Phys. Lett. A* **97**, 207–209.
- Wilmarth, W.R., G.M. Begun, R.G. Haire, J.P. Young and J.R. Peterson, 1989, *Appl. Spectrosc.* **43**, 1038–1045.
- Wittig, J., 1978, in: *Proc. Conf. on High Pressure and Low Temperature Physics*, Cleveland, 1977, eds C.W. Chu and J.A. Woollam (Plenum, New York).
- Young, D.A., 1991, *Phase Diagrams of the Elements* (University of California Press, Berkeley, CA).

## Chapter 114

# MAGNETIC MEASUREMENTS ON RARE EARTH AND ACTINIDE MONOPNICTIDES AND MONOCHALCOGENIDES

O. VOGT and K. MATTENBERGER

*ETH-Hönggerberg, Laboratorium für Festkörperphysik, CH-8093 Zürich,  
Switzerland*

### Contents

Symbols and abbreviations	302	2.1.5. $H_{CF} \approx H_{ex}$ , singlet ground state	320
1. Introduction	302	2.1.5.1. TbN, TbP, TbAs, TbSb, TbBi	320
2. Stable valencies	304	2.1.5.2. HoN, HoP, HoAs, HoSb, HoBi	324
2.1. Localized f-shells	304	2.1.5.3. DyN, DyP, DyAs, DySb, DyBi	331
2.1.1. $gJ = 0$	304	2.1.5.4. ErN, ErP, ErAs, ErSb, ErBi	336
2.1.1.1. EuN, EuP, EuAs, EuSb	304	2.1.6. $H_{CF} \ll H_{ex}$	338
2.1.1.2. AmN, AmAs, AmBi, AmTe	305	2.1.6.1. (Tb, Dy, Ho, Er)–(S, Se, Te)	338
2.1.2. $gJ$ small	305	2.1.6.2. CfN, CfAs, CfSb	341
2.1.2.1. SmN, SmP, SmAs, SmSb, SmBi	305	2.2. Reshaped f-shells	341
2.1.3. S-state ions, $H_{CF} > H_{ex}$	307	2.2.1. Weak hybridization	341
2.1.3.1. GdN, GdP, GdAs, GdSb, GdBi	308	2.2.1.1. NdN, NdP, NdAs, NdSb, NdBi	341
2.1.3.2. GdS, GdSe, GdTe	310	2.2.1.2. NpN, NpP, NpAs, NpSb, NpBi	344
2.1.3.3. EuO, EuS, EuSe, EuTe	311	2.2.1.3. PuN, PuP, PuAs, PuSb, PuBi	348
2.1.3.4. CmN, CmP, CmAs, CmSb	311	2.2.2. Strong hybridization	354
2.1.3.5. Exchange mechanism in S-state compounds	311	2.2.2.1. UN, UP, UAs, USB, UBi	354
2.1.3.6. Molecular-field approximation	312	2.2.2.2. US, USE, UTe	363
2.1.4. Singlet ground state, $H_{CF} > H_{ex}$	314	2.2.2.3. NpS, NpSe, NpTe	377
2.1.4.1. TmN, TmP, TmAs, TmSb	314	2.2.2.4. NdS, NdSe, NdTe	379
2.1.4.2. PrN, PrP, PrAs, PrSb, PrBi	317	3. Unstable valences	381
2.1.4.3. PrS, PrSe, PrTe	319	3.1. SmS, SmSe, SmTe	381
		3.2. TmS, TmSe, TmTe	382

3.3. YbN, YbP, YbAs, YbSb	384	4.5. CeBi	393
3.4. PuS, PuSe, PuTe	387	4.6. Mixed compounds	395
4. Cerium compounds	388	4.7. CeS, CeSe, CeTe	395
4.1. CeN	389	4.8. Theory	397
4.2. CeP	389	5. Conclusions	397
4.3. CeAs	390	References	398
4.4. CeSb	391		

---

## Symbols and abbreviations

+2(3+)	valencies	multi- <i>k</i>	non-collinear spin structure
CEF	crystal electric field	S, F, H	<sup>n</sup> F <sub>n</sub> (spectroscopic-state symbols)
<i>C<sub>p</sub></i>	molecular field constant	<i>T<sub>C</sub></i>	Curie temperature
<i>g</i>	Landé <i>g</i> -factor	<i>T<sub>N</sub></i>	Néel temperature
<i>H<sub>A</sub></i>	anisotropy field	<i>Θ<sub>p</sub></i>	paramagnetic Curie temperature
<i>H<sub>CF</sub></i>	CEF energy	<i>λ, D</i>	adjusting parameters for <i>H<sub>w</sub></i>
<i>H<sub>ex</sub></i>	exchange energy	<i>μ<sub>B</sub></i>	Bohr magneton
<i>H<sub>w</sub></i>	Weiss field	<i>μ<sub>eff</sub></i>	effective number of magnetons
<i>I<sub>ij</sub></i>	exchange integral	<i>σ</i>	Van Vleck screening factor
<i>J</i>	exchange integral if so defined in text	<i>χ</i>	magnetic susceptibility
<i>J, S, L</i>	total angular momentum, total spin, total orbital momentum, respectively	<i>χ<sub>0</sub></i>	temperature-independent susceptibility

---

## 1. Introduction

Historically, the first and most frequent experiments performed on lanthanides and actinides and their compounds have been measurements of their magnetic properties (magnetochemistry). The magnetic properties of the deep-lying (isolated) 4f and 5f shells were first thought to be easily interpretable. However, as we shall see, many complications are going to be encountered, such as complex structures, mixed valencies and heavy-fermion behaviour.

This chapter will be restricted to materials with 1:1 composition in lanthanides and actinides, although we realize that an enormous number of results on many other types of compounds is available. The 1:1 compounds are mostly of the simple cubic NaCl structure. This is the main reason for us to prefer them to more complicated structures.

Although magnetic measurements can be performed on impure powder samples, we shall demonstrate later on that properties can depend critically on the sample quality. Almost all measurements of magnetic moments depend on the orientation of the applied field (anisotropy of the magnetic properties). Reliable results are thus obtained only by the study of well-defined single crystals of good purity and assured stoichiometry.

It is not an easy task to grow crystals of rare earth and actinide compounds. Their high reactivity is just one, albeit a major, problem. For safety reasons, actinide compounds often have to be treated in glove boxes. A review of sample preparation and crystal growth of actinide compounds is given by Spirlet and Vogt (1984). Those



with 1:1 composition, mostly crystallizing in the NaCl structure are about the easiest to be synthesized as crystals of a useful size (crystal weight above 10 mg). Single crystals of both the lanthanide and the actinide compounds can be grown by mineralization, as described by Spirlet and Vogt (1984), and they form nicely shaped cubes which are easily oriented, even without the aid of X-ray methods. The crystals grow only as stoichiometric compounds. Any deviation in their composition can be detected by micrographic methods.

We shall see that the magnetic properties of a lanthanide or actinide ion in a crystal matrix can be very different from those of the free ion. The crystalline electric field, isotropic and anisotropic exchange forces and hybridization of the *f* electrons with itinerant electrons are the main factors which are determining the observed macroscopic magnetic properties.

The dependence on crystal structure is another reason why we restricted ourselves to the 1:1 pnictides and chalcogenides.

The monopnictides and the monochalcogenides of both the lanthanides and the actinides crystallize, with very few exceptions, in the NaCl-type structure. This simple cubic structure lends itself ideally to experimental and theoretical studies. Pseudobinary mixtures of almost all compounds are possible. This opens up attractive possibilities for changing the electronic environment of a magnetic ion. Furthermore, pseudobinary compounds do exist with the corresponding monochalcogenides and monopnictides of the non-magnetic ions of Y, La, Lu and Th. This allows for magnetic dilution of the primary compounds. The ions of most of these compounds are in the trivalent state (exceptions are the pnictides of Eu and the chalcogenides of Yb, where the Ln ion is divalent). This valency assumption is in agreement with the interatomic distances, as confirmed by X-ray measurements. Most of the ions show Russell–Saunders coupling at elevated (room) temperatures, although this rule may change at low temperatures. The magnetism stems from partially filled 4*f* or 5*f* shells. For actinides, as a general rule, if the interatomic distance is above a certain limit (the so-called Hill limit  $\approx 3.5 \text{ \AA}$ ) we get “localized-moment” behaviour. There are many exceptions to this rule, since it does not include the influence of the chemical environment. However, most of the compounds we are going to discuss are well above the Hill limit and behave accordingly.

There are, of course, earlier reports on the NaCl-type compounds. The first general overview on the actinide compounds is given by Lam and Aldred (1974). Hulliger (1978, 1979) gives a complete collection of data on the rare earth pnictides, together with a very critical discussion of published results. Fournier (1985, 1986) and Fournier and Troč (1985) summarized in their reports on the magnetic properties of actinide solids the results of both the actinide monopnictides and monochalcogenides. An introduction to neutron studies is given by Lander (1987 and ch. 117 in this volume) and a summary of the theory was discussed by Cooper et al. (1985).

To understand the following, the reader will want to become familiar with the idea of multi-*k* structures.

A multi-*k* structure was described as early as 1963 by Kouvel and Kasper (1963). It took 20 years until the second multi-*k* structure was found in an actinide compound by Rossat-Mignod et al. (1979b). Excellent summaries on the properties of multi-*k*

structures are given by Rossat-Mignod et al. (1980b, 1982b, 1984) and Rossat-Mignod (1987).

Nowadays we know that the Fourier components of the magnetization vector not only exist independently of each other, that is to say, ordered antiferro- or ferromagnetically, but that coexistence of ferromagnetic and antiferromagnetic arrangement is also possible. Furthermore, the three components in these non-collinear structures need not have the same magnitude. The concept of multi- $k$  structures led to the understanding of many previously obscure phenomena, and we shall see that very probably they are the key to an understanding of many "mysteries" encountered in Ln compounds about 20 years ago.

In the following we shall classify the compounds according to those parameters which are in fact decisive in defining their magnetic properties:

(1) The spectroscopic data. The two singular cases are S states (spherical symmetry) and  $J = 0$  states (no moment).

(2) The crystal electric field (CEF). The ionic states are split by the interaction (S states excepted) with the CEF. We will name the corresponding energy  $H_{\text{CEF}}$ .

(3) Exchange. We denote with  $H_{\text{ex}}$  the exchange energy. Exchange interaction as a rule has two parts: isotropic exchange, which is of the Heisenberg type, and anisotropic exchange, which stems from hybridization of the f electrons. In favourable cases it is possible to separate the two parts experimentally.

(4) Hybridization, leading to a reshaping of the magnetic ions.

(5) Coupling of 4f or 5f electron shells with delocalized itinerant electrons, which can result in valence instabilities (mixed-valence systems, fluctuating valence systems, heavy-electron systems).

The reader should become familiar with what we generally call interaction between f and outer electrons. We will discuss our compounds according to the classification given in the title. (Since the Ce compounds do not fit into just one scheme, but offer a wide range of interesting phenomena, we shall treat them in a separate section.)

## 2. Stable valencies

### 2.1. Localized f-shells

#### 2.1.1. $gJ = 0$

2.1.1.1. *EuN*, *EuP*, *EuAs*, *EuSb*, *EuBi*. *EuN* and *EuP* are the only two compounds of trivalent Eu, which has a  $^7F_0$  state, which crystallize in the NaCl-type structure. *EuAs* crystallizes in the hexagonal  $\text{Na}_2\text{O}_2$ -type structure and is a semiconductor. *EuSb* and *EuBi* do not exist under normal conditions. There is little information on the magnetic properties of *EuN* and *EuP*, which apparently do not show magnetic order. The crystal electric field splitting of the singlet ground state is known (Hulliger 1978). *EuN* was first thought to be a normal paramagnet ( $\Theta_p = -200$  K, effective moment about  $5\mu_B$ ) (Busch et al. 1964c, Busch 1967). Later it was recognized that the Curie-Weiss law is not obeyed (Busch et al. 1965b), but that paramagnetism as

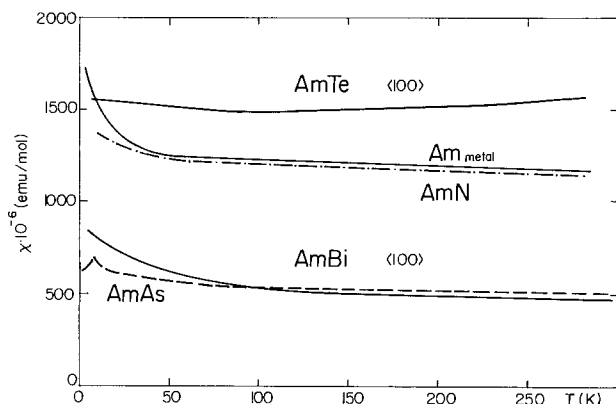


Fig. 1. Susceptibilities versus temperature of americium compounds. The values for Am metal, AmN and AmAs are taken from Kanellakopoulos et al. (1975). The values for AmBi and AmTe are our own measurements.

proposed by Van Vleck (1932) is present. Junod et al. (1969) state that the observed susceptibility of EuN is 25% higher than the calculated values. Jones (1969) found a large sample dependence of the susceptibility of EuN, which was attributed to the presence of  $\text{Eu}^{2+}$  ions. This difference is in fact due to impurities. It was not possible to synthesize clean EuP samples. Impurities are also responsible for disagreement with the theoretical values of the specific heat. No measurements on pure EuP have been published yet (cf. Jones 1969).

2.1.1.2. *AmN*, *AmAs*, *AmBi*, *AmTe*. In fig. 1 we have collected the available data, which are rather scarce, for americium compounds. Those for the nitride and arsenide (as well as the metal) were measured by Kanellakopoulos et al. (1975) – the rest are our own measurements. In all cases we observe an almost temperature-independent paramagnetism. The upturn at low temperature is either intrinsic or due to imperfections (non-stoichiometry, impurities, radiation damage, or presence of Am with a different valency). The observed susceptibilities are rather high. They would have to be interpreted as “enhanced” Pauli susceptibilities. An indication for this explanation is the fact that there is a distinct difference between the pnictides and the chalcogenides (*AmTe*). The extra electron of the chalcogenides might be of crucial importance. Kanellakopoulos et al. (1975) observed a peak in the susceptibility of AmAs at 13 K, which they attribute to an antiferromagnetic transition. We are not convinced that this conclusion is correct. The authors are aware of the questionable sample quality in the case of AmN, which imposes a cautious interpretation of the results on AmAs. Interestingly enough, there does not exist any theoretical approach which would explain the high values of the susceptibilities of these  $J = 0$ , i.e. a priori non-magnetic, substances.

### 2.1.2. $gJ$ small

2.1.2.1. *SmN*, *SmP*, *SmAs*, *SmSb*, *SmBi*. The  $\text{Sm}^{3+}$  ion has a low  $g$ -value ( $g = \frac{2}{7}$ ). Furthermore, the first excited multiplet is rather close to the ground state ( ${}^6\text{H}_{5/2}$  and

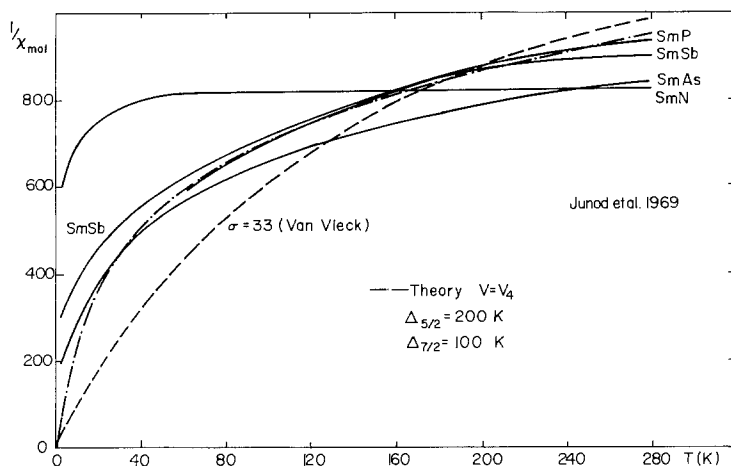


Fig. 2. Comparison of measured and calculated susceptibilities of  $\text{Sm}^{3+}$  compounds, from Junod et al. (1969).

${}^6\text{H}_{7/2}$ ). These two properties, in connection with small exchange forces, lead to a rather complicated behaviour of the magnetic susceptibilities.

Didchenko and Gortsema (1963) report on SmN. They think that their samples were somewhat contaminated by 3–5%  $\text{Sm}^{2+}$  ions. This is one reason why the measured susceptibility is about 20% higher than the values predicted by Van Vleck (1932). Busch et al. (1964c) tried to find a Curie–Weiss law which would yield a paramagnetic Curie temperature of  $-200$  K. This idea was later rejected by Busch et al. (1965b) – they found Van Vleck behaviour and an antiferromagnetic ordering temperature of 15 K. Antiferromagnetism in SmN is suggested in Busch (1967). Stutius (1969b) finds 18.2 K for the ordering of SmN from specific-heat measurements, and confirms antiferromagnetism. Tsuchida and Wallace (1965a) found no Curie–Weiss behaviour in SmBi and no order. The first measurements on all the remaining pnictides stem from Tsuchida and Wallace (1965a). Similar measurements were published by Junod et al. (1969), and are reproduced in fig. 2.

We see in fig. 2 that Van Vleck's (1932) theory gives a general trend for the interpretation of the observed susceptibilities, but the agreement with experiment is not very convincing. A better fit is possible when the crystal-field splitting of the two lowest multiplets ( ${}^6\text{H}_{5/2}$  and  ${}^6\text{H}_{7/2}$ ), which are separated by 1580 K, is taken into account, as can also be seen in fig. 2.

Further progress stems from specific-heat measurements which are delicate enough to determine the crystal-field parameters and ordering temperatures. The crystal-field splitting was measured by Birgeneau et al. (1973) for SmP and SmSb, and by Mullen et al. (1974) for SmSb.

The ordering temperatures as determined from specific-heat measurements are as follows:

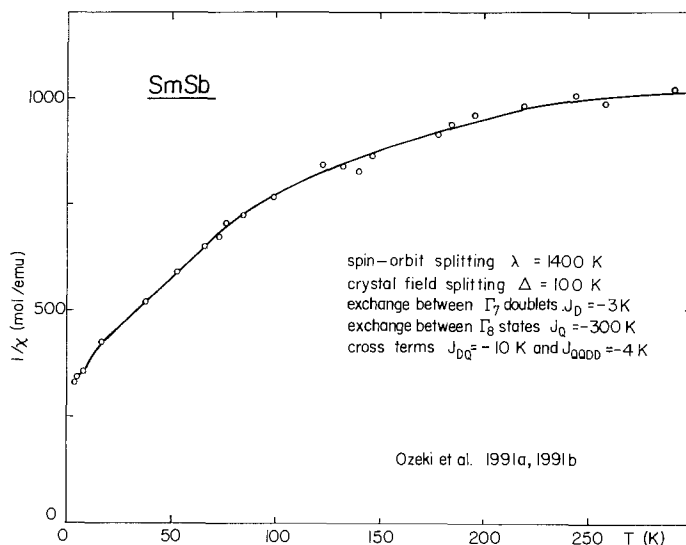


Fig. 3. Magnetic susceptibility of SmSb (open circles). The solid line was calculated with the parameters given in the figure (Ozeki et al. 1991a, b).

- SmN: 18.2 K (Stutius 1969b),
- SmP: 1.65 K (Hulliger 1978, Hulliger et al. 1978b),
- SmAs: 1.8 K (Hulliger 1978, Hulliger et al. 1978b),
- SmSb: 2.11 K (Mullen et al. 1974, Hulliger et al. 1978b),
- SmBi: 8.7 K (Hulliger 1978, Hulliger et al. 1978b).

All the pnictides are reported to be antiferromagnetic, with a yet unknown spin structure.

Recently, a very complete analysis of the susceptibility behaviour of SmSb has been given by Ozeki et al. (1991a, b), which is reproduced in fig. 3. Their analysis is more complete than the one of Junod et al. (1969) (fig. 2). The authors take into account spin-orbit splitting between the  $\Gamma_7$  doublet and the  $\Gamma_8$  quartet (within  ${}^6H_{5/2}$ ), crystal-field splitting, exchange  $J_D$  between  $\Gamma_7$ , exchange  $J_Q$  between  $\Gamma_8$ ,  $J_{DQ}$  exchange interaction between Van Vleck terms induced by the crystal-field split levels and off-diagonal terms between  $\Gamma_8$  and the Van Vleck term.

The calculated curve reproduces the measurements closely, except at very low temperatures. We see that the "temperature dependent moment" magnetism of the Sm pnictides has a very complicated nature and its interpretation is not possible without detailed knowledge of spectroscopic data, which in turn can be obtained from different experiments, mostly specific-heat measurements.

### 2.1.3. *S*-state ions, $H_{CF} > H_{ex}$

If the Ln or An ion is in an S state, the crystal-field splitting can be treated as a weak perturbation in comparison with  $H_{ex}$ . We expect no anisotropy of the magnetic moment, which should reach its maximum value,  $gJ$ , independent of the direction of

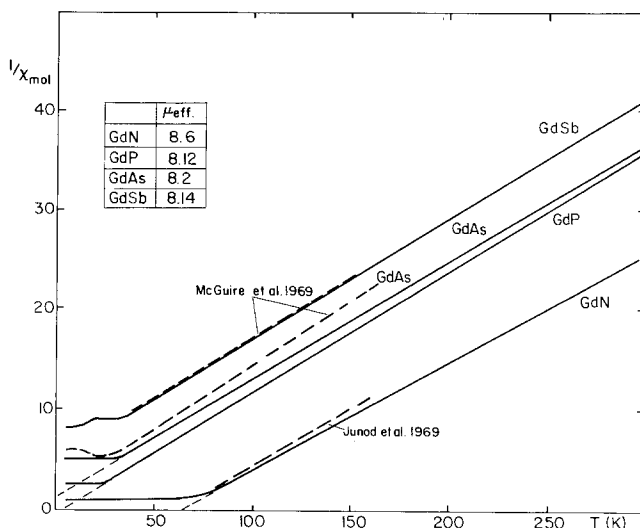


Fig. 4. Reciprocal susceptibility as a function of temperature of the Gd pnictides. The solid lines are our measurements on small crystallites. The dashed lines are from McGuire et al. (1969) and Junod et al. (1969).

the applied field. Thus, for magnetic measurements on compounds with S-state ions powder samples are acceptable. In all other cases the observed magnetization will depend strongly on the direction of the applied field and will have to be measured on oriented single crystals if quantitative conclusions on the magnitude of the observed moment are required.

Let us examine the S-state compounds in detail.

2.1.3.1. *GdN*, *GdP*, *GdAs*, *GdSb*, *GdBi*. In all these compounds Gd is trivalent and in an S state. In fig. 4 we have plotted the inverse susceptibilities of GdAs and GdSb versus temperature, measured on powdered samples or on small crystallites.

At elevated temperatures the Curie-Weiss law is obeyed, GdN behaves as a ferromagnet, and all others are antiferromagnets. If the anisotropy field in an antiferromagnet is lower than a certain threshold field,  $H_t = 2(H_W H_A)^{1/2}$  ( $H_W$  is the Weiss molecular field,  $H_A$  is the anisotropy field), the spins turn perpendicular to an applied field. This turning is called a spin flop (Enz et al. 1962). Above that field, which is of the order of a few hundred Oersted in our case, the magnetization depends strictly linearly on the applied field. The susceptibility is temperature independent as long as the crystal is in the antiferromagnetic state. The shapes of the susceptibility curves in fig. 4 are thus proof that the anisotropy is very weak in Gd pnictides. The slight temperature dependence of the susceptibility below  $T_N$  is due to the sample quality according to all investigators. The effective moments derived from the susceptibility measurements are close to the free-ion value,  $g[J(J+1)]^{1/2} = 7.95$ , for  $\text{Gd}^{3+}$ . The magnetic structures of GdSb and GdBi have been studied using neutron diffraction, and they were found to be antiferromagnets of the second kind (McGuire et al. 1969). The spins are parallel in the (111) planes, and are stacked in a + -

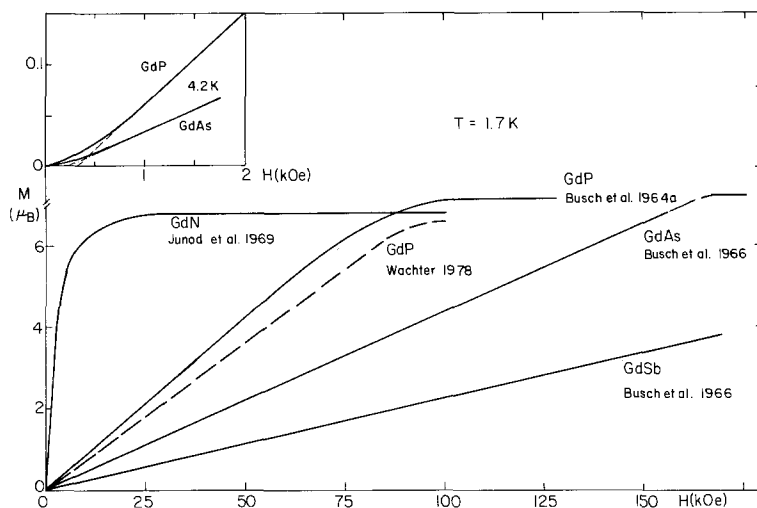


Fig. 5. Magnetization versus applied field for several Gd compounds. The inset shows the spin-flop field of about 300 Oe. (GdN from Junod et al. (1969), GdP from Wachter (1978), GdP, GdAs and GdSb from Busch et al. (1966c).)

sequence along the  $\langle 111 \rangle$  direction. Figure 5 shows the dependence of the magnetization on an applied external field.

The magnetization of GdP and GdAs reaches saturation at a value of about  $7\mu_B$ , which means that all the spins are completely aligned (for  $Gd^{3+}$   $gJ = 7$ ). The inset of fig. 5 shows the spin-flop field of about 300 Oe – indicating that the anisotropy is very small. The available magnetic fields were too low to achieve saturation in GdSb and GdBi.

Although GdN displays the features of a ferromagnet, Wachter and co-workers (Wachter 1978, Wachter and Kaldis 1980) argue that exactly stoichiometric GdN is actually a metamagnet with a critical field of a few kOe, and a Néel temperature of about 40 K. They find a saturation magnetization of  $7.26\mu_B$  and a paramagnetic moment of  $9.05\mu_B$ . Certainly these results are remarkable and should be verified by neutron diffraction experiments. Only such experiments can decide whether we are

TABLE 1  
Magnetic data of gadolinium pnictides.

Order	Type	$\Theta_p$	$\mu_{sat}$	$\mu_{eff}$	$T_{C/N}$
GdN	ferro	69	7.03	8.15	72
GdP	AF	?	0	7.1	20
GdAs	AF	?	-12	7.25	21
GdSb	AF	II	-42	8.1	28
GdBi	AF	II	-65	8.03	32

$$Gd^{3+}: gJ = 7.0, \quad g[J(J+1)]^{1/2} = 7.95.$$

actually dealing with antiferromagnetism or whether we are misled by domain effects. In table 1 we summarize some representative results obtained by various authors. For a complete list of all measurements consult Hulliger (1978), where all available data on Gd monopnictides are compiled. Further insight in the problem of preparing GdN can be found in an article by Cutler and Lawson (1975).

We can see that the paramagnetic moments and saturation moments seem to agree very well with the free-ion values. The observed differences are certainly due to the sample quality. These samples are quite difficult to prepare free from (ferromagnetic) impurities (metallic Gd, for example) and of perfect stoichiometry. All authors are aware of these problems and make the necessary caveats on the validity of their results.

At the end of this section on S-state compounds, we discuss the various exchange mechanisms which have been proposed. On the Gd pnictides Hulliger gives an extensive summary (Hulliger 1978).

2.1.3.2. *GdS*, *GdSe*, *GdTe*. The Gd monochalcogenides have not been investigated to any great extent. This may be because they are rather difficult to prepare as clean stoichiometric crystals. All investigators counsel caution in interpreting results which could be sensitive to the sample quality.

These compounds are all antiferromagnetic. At elevated temperatures the Curie-Weiss law is obeyed. Below the Néel temperature the reciprocal molar susceptibility seems to become more or less temperature independent (McGuire et al. 1969). GdTe, as measured by McGuire et al. (1969), is acknowledged to be somewhat impure. Hulliger's (1979) results confirm the weak temperature dependence of the susceptibility below  $T_N$ . He finds, however, some spin-reorientation transitions below  $T_N$ . In particular, the type II antiferromagnetic spin structure, described by McGuire et al. (1969), for GdS and GdSe remains, but the orientation of the spins within the ferromagnetically ordered (111) planes changes, indicating the existence of anisotropic exchange forces. For more details, especially on the problem of sample quality, the reader may consult Hulliger and Siegrist (1979).

The characteristic values for the magnetic behaviour derived by various authors (on different samples) scatter considerably. In table 2 we list what we find are reasonable values (chosen from McGuire et al. (1969) and Hulliger and Siegrist (1979)). Mössbauer experiments on GdS (Sanchez et al. 1985) confirm the antiferromagnetism and the trivalency of the Gd ion. This is discussed later.

TABLE 2  
Magnetic data of gadolinium chalcogenides.

	Order	Type	$\Theta_p$	$\mu_{\text{eff}}$	$T_C$
GdS	AF	II	-104	8.16	62
GdSe	AF	II	-110	8.23	65
GdTe	AF	?	-90	7.94	70

Gd<sup>3+</sup>:  $gJ = 7.0$ ,  $g[J(J+1)]^{1/2} = 7.96$ .



2.1.3.3. *EuO*, *EuS*, *EuSe*, *EuTe*. The magnetic properties of the Eu chalcogenides have been extensively discussed in a chapter by Wachter (1979) in this Handbook. We can therefore restrict ourselves to mentioning a few publications which have appeared since then. The magnetic phase diagram of *EuSe*, which is indeed unusual for an "isotropic" compound has attracted much attention. De Moura and Callen (1977) studied dipolar interactions, Fukuma et al. (1983) suggest that biquadratic exchange is the stabilizing factor, Fukuma et al. (1985a, b) discuss magnon softening due to cancellation of ferro- and antiferromagnetic exchange in *EuSe*. Eu–Sm mixed chalcogenides were studied by Wachter et al. (1987).

*EuSe*–*YSe* and *EuSe*–*CaS* compounds were investigated for two reasons, the stabilization of the *EuSe* structure at small concentrations and the transition to spin-glass behaviour thereafter. Spin-glass behaviour was observed in  $\text{Eu}_x\text{Sr}_{1-x}\text{S}$  by many authors (Paulsen et al. 1986, Ferré et al. 1986, Löhneysen et al. 1986, Hoogerbeets et al. 1986, Börgermann et al. 1986). Herz and Kronmueller (1980) report on the high-field susceptibility of *EuS*. By applying high magnetic fields on *EuSe* in the paramagnetic phase Yamada and Miura (1985) could study the magnetic conductivity and, therefore, the d–f interactions.

Later we shall discuss the magnetic properties of the Eu chalcogenides, which are considered to be an ideal model for isotropic exchange.

2.1.3.4. *CmN*, *CmP*, *CmAs*, *CmSb*. In order to appreciate the few results obtained on these very rare substances, one should first read about their preparation (Damien et al. 1976, 1979, Haire 1981) and the very elaborate measuring equipment which is needed for investigations (Nave and Huray 1980).

At high temperatures all compounds follow the Curie–Weiss law. Below  $T_C$  they are ferromagnetic. Kanellakopoulos et al. (1975) report on *CmN* ( $T_C = 109$  K,  $\mu_{\text{eff}} = 7.02\mu_B$ ) and *CmAs* ( $T_C = 88$  K,  $\mu_{\text{eff}} = 6.58\mu_B$ ). Nave et al. (1981) reported measurements on *CmP* ( $T_C = 73$  K) and *CmSb* ( $T_C = 162$  K). The magnetization data which are published, confirm a probably isotropic exchange behaviour.

2.1.3.5. *Exchange mechanism in S-state compounds*. Even for the "simple" S-state ions, many theoretical and experimental attempts were made in order to gain more insight in the actual nature of the exchange forces. All authors agree that a Heisenberg-type direct interaction, based on direct overlap of the f electrons, can be excluded. The interactions are thus indirect, either through the p anion-orbitals, or the d cation-orbitals, or via conduction electrons, which in metallic compounds are known as the RKKY interactions.

Less important contributions are the magnetic dipolar and electric quadrupolar interactions. The Anderson type of superexchange (virtual transfer of a 4f electron via p states of the anion from one site to another) has to be ruled out for insulators (Eu chalcogenides), since it is an order of magnitude too small to explain the observed ordering temperatures (Kasuya 1970), and p–d mixing has to be considered.

One way to probe exchange mechanisms is by changing the electron concentration by either going off-stoichiometry or by alloying with isostructural compounds which should either add or subtract one electron from the host. A few examples of such off-

stoichiometric and pseudobinary systems are:  $\text{GdS}_{1-x}$ ,  $\text{GdP-GdS}$  (Wachter 1978),  $\text{GdN}_{1-x}\text{O}_x$  (Wachter and Kaldis 1980),  $\text{GdP}_{1-x}\text{Se}_x$ ,  $\text{GdSb}_{1-x}\text{Te}_x$  (McGuire et al. 1969),  $\text{Gd}_{1-x}\text{S}$ ,  $\text{Gd}_{1-x}\text{Se}$ ,  $\text{GdAs}_{1-x}$  and  $\text{Gd}_{1-x}\text{Te}$  (Hulliger and Siegrist 1979). Corresponding experiments with Eu compounds are described by Wachter (1979) and Köbler and Binder (1980) ( $\text{Eu}_x\text{Sr}_{1-x}\text{S}$ ). The spin glasses  $\text{Eu}_x\text{Sr}_{1-x}\text{S}$  have been mentioned above.

2.1.3.6. *Molecular-field approximation.* The ordering temperatures, plotted versus lattice spacing in fig. 6, seem to lack a characteristic common feature, despite the fact that all samples are S-state compounds.

We can try to split up the exchange forces into two components:  $J_1$  between nearest neighbours and  $J_2$  between next-nearest neighbours. Such a procedure is legitimate in the case of direct Heisenberg-type exchange. Whether or not it makes sense for our problem is a difficult question. If the spin structure of the antiferromagnets is of the second kind, then the following equations hold (for  $S = \frac{7}{2}$ ).

$$J_1 + \frac{1}{2}J_2 = \frac{1}{126}k\Theta_p,$$

$$J_2 = -\frac{1}{63}kT_N,$$

which allow us to separate  $J_1$  and  $J_2$  if the paramagnetic Curie temperature,  $\Theta_p$ ,

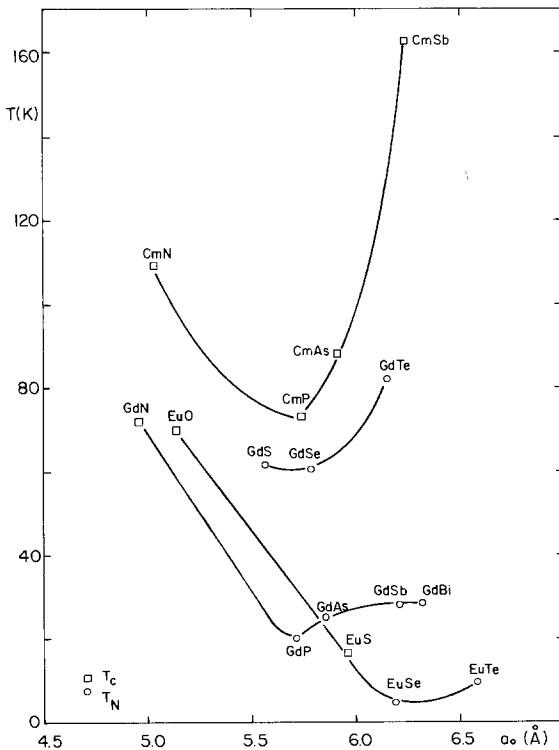


Fig. 6. Ordering temperatures versus lattice spacing of Eu, Gd and Cm compounds.

and  $T_N$  are known. For a ferromagnet all we know is:

$$\frac{1}{126}kT_C = J_1 + \frac{1}{2}J_2,$$

and we have to rely on other experiments, such as neutron diffraction (see Gambino et al. 1970), to separate the exchange parameters.

In fig. 7 we plot the values collected from the literature which we think are the most probable. Unfortunately, we do not have separate values for the Cm compounds. We see that  $J_2$  is decreasing with increasing lattice constant in all cases. On the other hand  $J_1$  is increasing in the case of the Gd chalcogenides. This could mean that the ferromagnetic exchange is caused by different mechanisms in the Eu chalcogenides and Gd pnictides (which are semiconductors and semimetals, respectively), on the one hand, and in the metallic Gd chalcogenides, on the other. A dependence of  $J_1$  and  $J_2$  on the lattice parameters similar to that in the Gd chalcogenides could explain the occurrence of a maximum of the Curie temperature in the case of the Cm pnictides (see fig. 6), which would mean that these compounds are metallic, and the type of exchange is similar to that encountered in Gd monochalcogenides. Unfortunately, no magnetization measurements on Cm monochalcogenides are available.

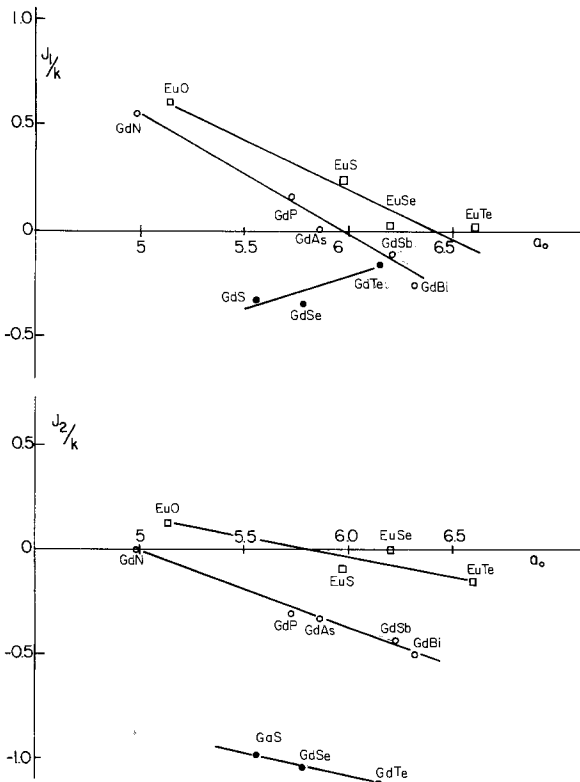


Fig. 7. Exchange parameters versus lattice constants for Gd and Eu compounds.

### 2.1.4. Singlet ground state, $H_{CF} > H_{ex}$

2.1.4.1. *TmN*, *TmP*, *TmAs*, *TmSb*. There is strong experimental evidence that the exchange forces are weak in these substances. Their magnetic behaviour is thus determined mainly by the interaction with the crystal electric field, which lifts the angular-momentum degeneracy of the  $^3H_6$  ground state. The octahedral crystal field potential reduces to  $V_c = B_4V_4 + B_6V_6$ , i.e. to terms of fourth and sixth order.  $B_4$  and  $B_6$  are scaling factors, depending on the detailed nature of the magnetic ion functions. Usually the potential is rewritten according to (Lea et al. 1962)

$$V_c = [xV_4 + (1 - |x|)V_6]W.$$

$W$  is a scaling factor and  $x$  determines the relative importance of the fourth- and sixth-order terms. Using these two quantities as adjustable parameters, we can calculate the magnetic susceptibilities and magnetizations as a function of external fields and fit the results to the findings of the experiment.

Trammell (1963) finds that the lowest crystal-field level is a singlet,  $\Gamma_1$ . Child et al. (1963) report on the absence of magnetic order in *TmN* even at 1.3 K, concluding that the exchange forces are too weak to overcome the crystal-field splitting. In fig. 8 we have summarized the results of susceptibility measurements on Tm pnictides by Busch et al. (1966b). The Curie-Weiss law is followed at elevated temperatures and at low temperatures the inverse susceptibility curve flattens out to a Van Vleck type of temperature-independent paramagnetism. This begins at a temperature that corresponds roughly to the energy difference between the ground state and the first excited state of the ion of which the levels are split. The paramagnetic moments are close to the free-ion moment and the paramagnetic Curie temperatures are about zero, indications that the exchange forces are very small.

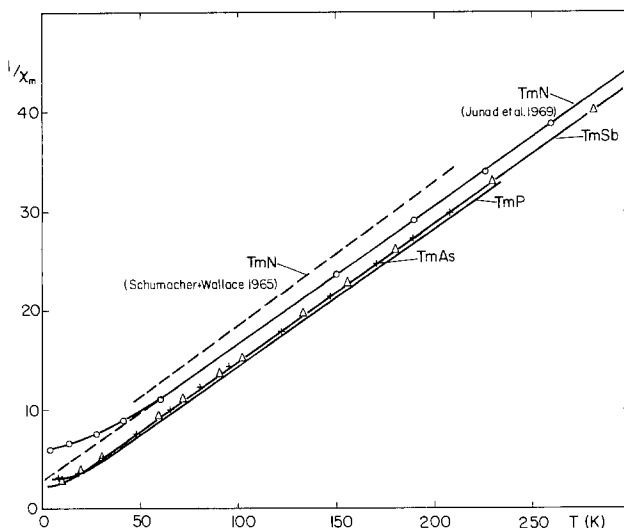


Fig. 8. Reciprocal susceptibilities versus temperature for Tm compounds. The values for *TmN* are from Junod et al. (1969) and Schumacher and Wallace (1965). The values for *TmP* (solid line), *TmAs* (crosses) and *TmSb* (triangles) are our measurements.

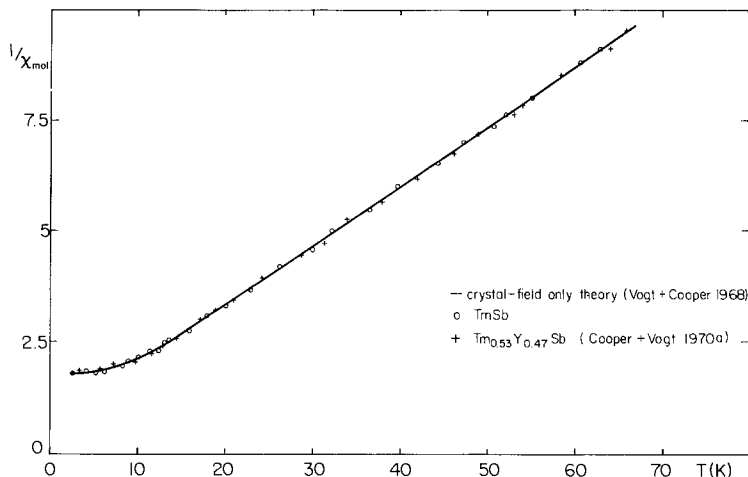
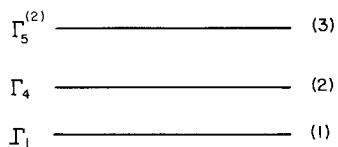
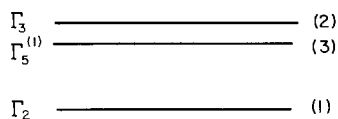


Fig. 9. Inverse susceptibility of TmSb (open circles) and Tm<sub>0.53</sub>Y<sub>0.47</sub>Sb (crosses) versus temperature. The solid line is the calculated crystal-field-only theory. (Vogt and Cooper 1968, Cooper and Vogt 1970a).

Figure 9 shows a comparison between the calculated inverse susceptibility versus temperature and experimental curves. The parameters  $x$  and  $W$  are adjusting parameters ( $x = -1$  means that only fourth-order terms are important). The fact that the curves are almost identical for pure TmSb and TmSb which is diluted with 47% non-magnetic YSb is further proof that the exchange forces are very weak and their contribution can be neglected. The susceptibility is very well described by theory. In fig. 10 we can see, for the case of fourth-order terms only, the crystal-field level scheme of a Tm<sup>3+</sup> ion in an octahedral-symmetry site. A high applied external field can mix these different crystal electric field eigenstates, resulting, in favourable cases, in measurable non-linear anisotropic magnetizations. TmSb is such a favourable



Tm<sup>3+</sup> (J= 6)  $x = -1$ ,  $w = \text{neg.}$  Fig. 10. Crystal-field level scheme for the Tm<sup>3+</sup> ion.

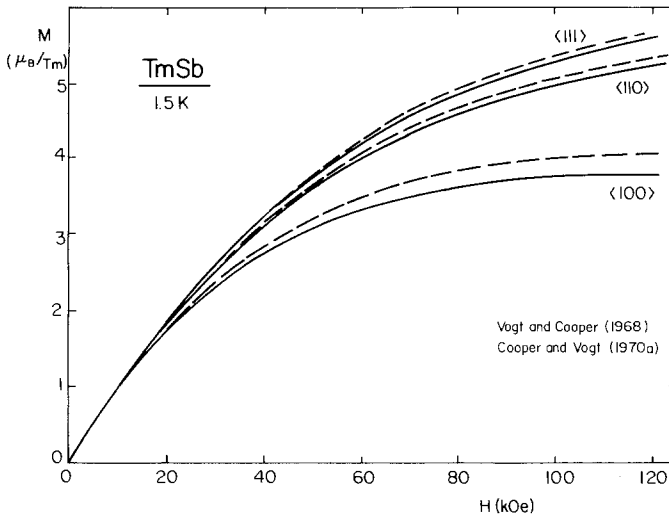


Fig. 11. Magnetization versus applied magnetic field at 1.5 K of TmSb. The solid lines are experimental results, the dashed lines are calculated curves. (See also Cooper (1966, 1968).)

case. Figure 11 shows theoretical (with the same values for  $x$  and  $W$  as used for the interpretation of the susceptibility) and experimental magnetization curves for pure and diluted TmSb. (See also Cooper (1966, 1968) and Busch et al. (1966b).)  $\langle 111 \rangle$  is the easy axis, with almost the full moment,  $gJ = 6$ , whereas a magnetic field applied along  $\langle 100 \rangle$  induces a much lower moment. Only at very high fields the  $\langle 100 \rangle$  magnetization will achieve the full moment in a stepwise fashion.

This kind of behaviour provides the key to the understanding of practically all generally anisotropic magnetic properties which we are going to encounter in the NaCl-type components of lanthanides and actinides. Similar to the case of  $\text{Tm}^{3+}$ , the response to an applied field will be anisotropic under the influence of the crystal electric field. This means every ion will have an "easy" axis. Trammell (1963) discovered the axes by symmetry considerations alone. He clearly states that *only for isotropic* exchange the "crystal-field" axis is necessarily the axis of easy magnetization. If the exchange forces prefer another axis than the crystal field, then the magnetization can be along a different axis and only for weak crystal-field splitting and strong exchange will we find the full moment. If, however, the exchange fields are along the direction of the crystal-field axis, we will observe the full ionic moment.

Another interesting phenomenon was discovered by measuring the magnetization of TmSb in high magnetic fields. Pulsed-field measurements at 1.5 K agree very well with static-field measurements and with the theoretical curve in fig. 11. At 20.4 K, however, only the static-field measurements agree with the (isothermal) crystal-field-only theory; the pulsed-field measurements are closer to an adiabatic theory. Apparently the duration of the pulse (a few milliseconds) is not long enough to allow the excited spin system to reach equilibrium with the lattice. This can be a serious restriction for the application of pulsed fields (Foner et al. 1972). Results are presented in fig. 12.

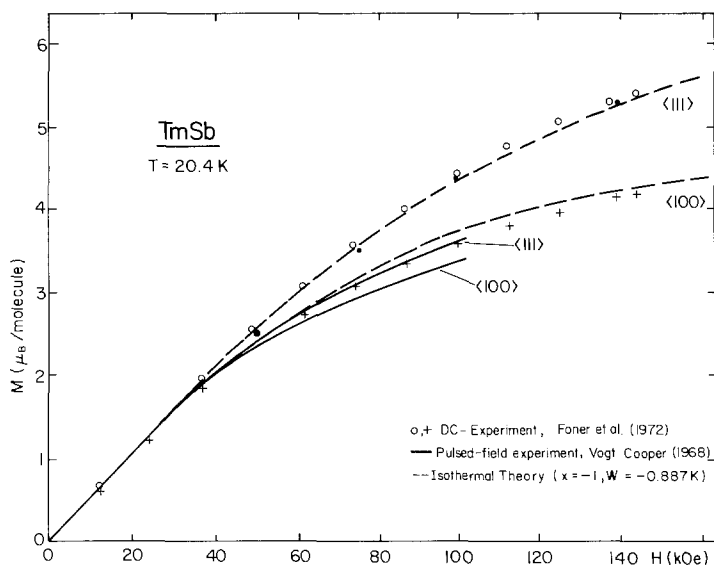


Fig. 12. Magnetization versus applied field at 20.4 K of TmSb. (See also Foner et al. (1972).)

TABLE 3  
Magnetic data of thulium pnictides.

	Order	$\Theta_p$	$\mu_{\text{eff}}$
TmN	no	-18	7.6
TmP	no	-2	7.5
TmAs	no	-2	7.45
TmSb	no	-3	7.4
TmBi	no	12	?

$$\text{Tm}^{3+}: gJ = 7.0, \quad g[J(J+1)]^{1/2} = 7.56.$$

Lander et al. (1973a) have studied the anisotropic magnetization density of the  $\text{Tm}^{3+}$  ion in TmSb using polarized neutrons and found agreement with the magnetization measurements. Guertin et al. (1975) investigated the pressure dependence of the susceptibility of TmAs and TmSb. The susceptibilities increase under pressure, whereas the point-charge model of crystal-field splitting would suggest a decrease.

In table 3 we summarize the data which are presently available for Tm monopnictides.

2.1.4.2. *PrN, PrP, PrAs, PrSb, PrBi.* Magnetic susceptibility measurements show that at high temperatures the Curie-Weiss law is followed, while at low temperatures the susceptibilities become temperature independent, the same behaviour as found in the Tm pnictides. The  $^3\text{H}_4$  ground state of  $\text{Pr}^{3+}$  is split up the same way as the  $\text{Tm}^{3+}$  ground state by the crystal field, giving a singlet ground state.

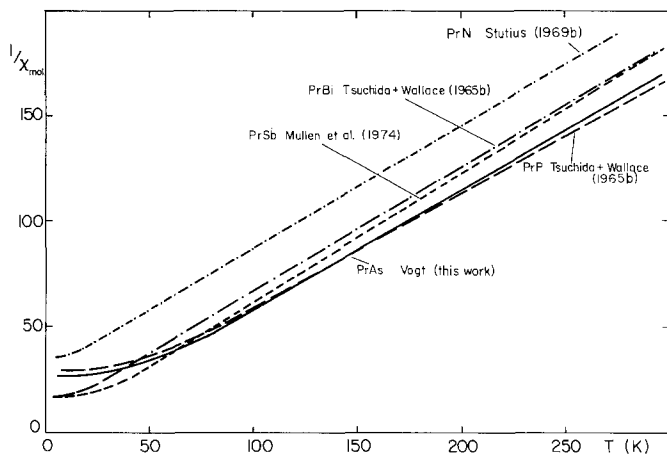


Fig. 13. Inverse molar susceptibilities of Pr compounds versus temperature. References are given in the figure.

An exact analysis of the experimental results is hampered by the often insufficient sample quality. The scatter of the results is very high, as can be seen for the Pr pnictides in the table by Hulliger (1978). We have critically summarized the different results in our figures. As a general remark we might state that in all cases the effective number of magnetons found in the experiment is usually within 10% of the theoretical value  $g[J(J+1)]^{1/2} = 3.68$ . Figure 13 shows the experimentally found inverse molar susceptibilities versus temperature, taken mostly from Tsuchida and Wallace (1965b) (the nitride curve is omitted), and from Stutius (1969b) (PrN) and Schumacher and Wallace (1965). The curve for PrP given in Westerholt and Methfessel (1977), seems

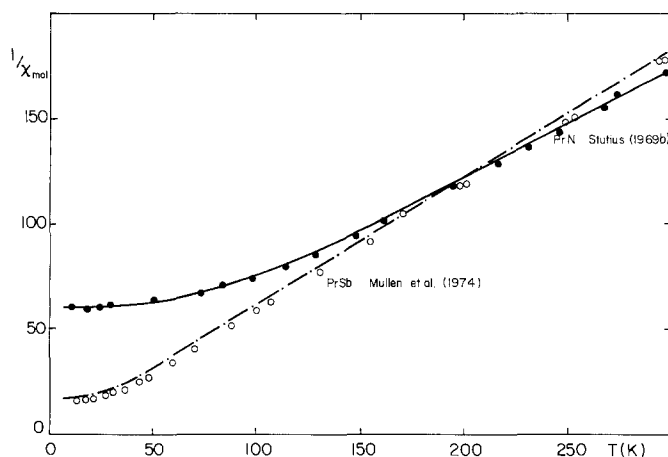


Fig. 14. Inverse molar susceptibilities of PrSb and PrN versus temperature. The solid line and dash-dotted line are calculated results. Points are experimental results from Stutius (1969b) and Mullen et al. (1974).



less reliable. The above curves can be fitted by taking the zero Van Vleck susceptibility as a parameter. This procedure did not seem to work for PrN, as mentioned by Tsuchida and Wallace (1965b).

In fig. 14 we have collected results from Mullen et al. (1974) and Stutius (1969b) for PrSb and PrN. The calculated susceptibilities are based on a neutron-diffraction determination of the overall splitting (Mullen et al. 1974) or values found by specific-heat measurements (Stutius 1969b). In order to fit the PrN curve, moderate exchange forces had to be taken into account. We can see that the crystal-field model describes the experiments very well – apparently the exchange is small for PrSb and not big enough to induce order in PrN. Both the exchange and the crystal-field splitting decrease on going from the nitride to the bismuthide.

The results of Stutius (1969b) for PrN agree quite well with Didchenko and Gortsema (1963), but not with Tsuchida and Wallace (1965b). On the other hand, the results for PrSb obtained by Mullen et al. (1974) agree reasonably well with Tsuchida and Wallace (1965b) and Vogt (1968).

Jones (1969) did Knight shift measurements on PrP and PrAs. In order to fit these results it was necessary to use higher values for  $\Theta_p$  than those obtained from the usual extrapolation of the Curie–Weiss law. Thus, for PrP and PrAs exchange is present and cannot be neglected. Vettier et al. (1977) did neutron inelastic scattering experiments on PrSb single crystals. They show that the exchange, even though it is weak, is highly anisotropic, preferring the  $\langle 001 \rangle$  direction. The energies of the  $\Gamma_1$ – $\Gamma_4$  and  $\Gamma_4$ – $\Gamma_5$  excitons decrease with pressure, rather than increasing as predicted by the point-charge model for the crystal field.

Schoenes et al. (1990) mention that with an applied field of 100 kOe a magnetic moment of  $0.89\mu_B$  was achieved in PrSb. The magnetization curve deviates slightly from linear behaviour, and should thus be anisotropic. Kido et al. (1992) reached, at almost 300 kOe, more than  $2\mu_B$ . The magnetization curves are anisotropic, as expected (unpublished results by Giynu Kido).

The compound PrP exists off-stoichiometry, as found by Franceschi and Olcese (1968), with the NaCl structure. Phosphor-deficient samples show an induced magnetic moment on the Pr sites (Hasanain et al. 1981). Spin-glass behaviour (Westerholt and Methfessel 1977) seems to occur in such compounds.

2.1.4.3. *PrS, PrSe, PrTe*. Only few data are available on these compounds. Figure 15 shows the inverse susceptibilities versus temperature after Smolenskii et al. (1966, 1968). The curve for PrS, showing an antiferromagnetic transition, has been omitted since this transition could not be confirmed later by Bucher et al. (1975), nor was it mentioned by Didchenko and Gortsema (1963). At temperatures well above 400 K Van Vleck paramagnetism of the multiplet is observed.

At low temperatures the chalcogenides are certainly metallic Van Vleck paramagnets with a singlet  $\Gamma_1$  crystal-field ground state. The high-temperature values can nicely be fitted by the Van Vleck formula. The deviation from Curie–Weiss behaviour sets in at about 40 K for PrSe and at a lower temperature for PrTe. Thus, the crystal-field splitting should yield values which are similar to those encountered in the pnictides. It is likely that the exchange forces cannot be ignored. More precise information on

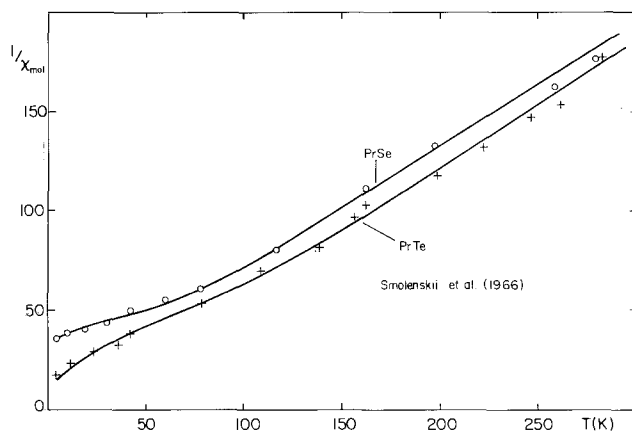


Fig. 15. Inverse molar susceptibilities of PrSe and PrTe, reproduced from Smolenskii et al. (1966).

the Pr monochalcogenides is needed for a thorough understanding of their magnetic properties.

#### 2.1.5. $H_{CF} \approx H_{ex}$ , singlet ground state

2.1.5.1. *TbN, TbP, TbAs, TbSb, TbBi*. In the terbium pnictides Tb is trivalent and the ground state in the cubic crystal field is a singlet (Trammell 1963, Lea et al. 1962). Pioneering results on the magnetic properties were published by Wilkinson et al. (1962) and Child et al. (1963), based on neutron diffraction experiments.

In table 4 we give the results of the above-mentioned authors. The table is completed by including later measurements of different authors and particularly by the addition of the paramagnetic Curie temperatures,  $\Theta_p$ . The additional results stem from Busch et al. (1963) (TbN, TbAs), Busch et al. (1964b) (TbP), Wilkinson et al. (1962) (all pnictides), Busch et al. (1964c) (TbN), Busch et al. (1965a) (TbSb), Busch et al. (1965c) (TbAs), Busch et al. (1965b) (TbN), Tsuchida and Wallace (1965a) (TbBi), Busch (1967) (all pnictides), Stutius (1969b) (TbN), Nereson and Arnold (1971) (TbBi) and Kötztler et al. (1979) (TbP). For the sake of clarity we have included in table 4 "representative numbers" rather than enumerating all measured values.

TABLE 4  
Magnetic data of terbium pnictides.

	Order	$T_C/T_N$	$\Theta_p$	$\mu_{eff}$	$\mu_{order}$	Mag. axis
TbN	ferro	42/34	34	10	6.7/7	$\langle 111 \rangle$
TbP	AF II	9	3	9.2	6.2	$\langle 111 \rangle$
TbAs	AF II	12	-4	9.6	7.7	$\langle 111 \rangle$
TbSb	AF II	14/16.5	-14	9.7	8.2	$\langle 111 \rangle$
TbBi	AF II	18	-33	9.52	7.9	$\langle 111 \rangle$

Tb<sup>3+</sup>:  $gJ = 9.0$ ,  $g[J(J+1)]^{1/2} = 9.72$ .

Complete curves for the inverse susceptibility versus temperature, measured on powders, are published only for TbSb (Busch et al. 1965a) and TbP (Kötzler et al. 1979). The susceptibility drops by a factor of about three below the Néel temperature, a clear indication of anisotropy.

The observed magnetic moments (Child et al. 1963) are lower than the free-ion value,  $gJ$ . With increasing lattice constant – and consequently lowered crystal electric field – the ordered moment approaches the free-ion value. Apparently the exchange is not quite strong enough to overcome the lifting of the angular-momentum degeneracy.

By applying high magnetic fields (100 to 130 kOe) the magnetization can be brought up to almost the free-ion value, this in spite of the fact that many of these measurements were not performed on single crystals. Thus, the easy-axis magnetization is found by only the assumption that the powdered samples (or small crystallites) orient themselves in the direction of maximum magnetization. Some typical values of high-field magnetization are  $8.0\mu_B$  for TbP (Busch et al. 1964b),  $9.3\mu_B$  for TbN (Junod et al. 1969, Busch et al. 1964c),  $7.9\mu_B$  for TbSb (Busch et al. 1965a),  $7.9\mu_B$  for TbAs (Busch et al. 1965c). Single-crystal measurements along the  $\langle 111 \rangle$  easy axis for TbSb (Cooper and Vogt 1970b, Buschbeck et al. 1987) and TbP (Buschbeck et al. 1987) show that even at 145 kOe saturation of the induced magnetization, which would be  $gJ = 9\mu_B$ , is not yet achieved. Neutron diffraction reveals that TbP, TbAs, TbSb and TbBi are antiferromagnets of type II (MnO-type). These results were obtained by Child et al. (1963) and Nereson and Arnold (1971). TbN seems to be “mostly” ferromagnetic – neutron patterns show, however, some peculiarities (Child et al. 1963). We will discuss these features later for the case of HoN; they appear common to all the heavy rare earth nitrides.

The success of the theoretical interpretation of the magnetic properties of TmSb led to the idea of applying the same procedures to TbSb including the exchange forces in the calculations. The main idea was to alloy TbSb with non-magnetic YSb, thereby systematically eliminating exchange forces. The pseudobinary system  $Tb_xY_{1-x}Sb$  was extensively investigated using magnetization measurements (Cooper and Vogt 1970b, Cooper et al. 1971) and by neutron diffraction experiments (Cable

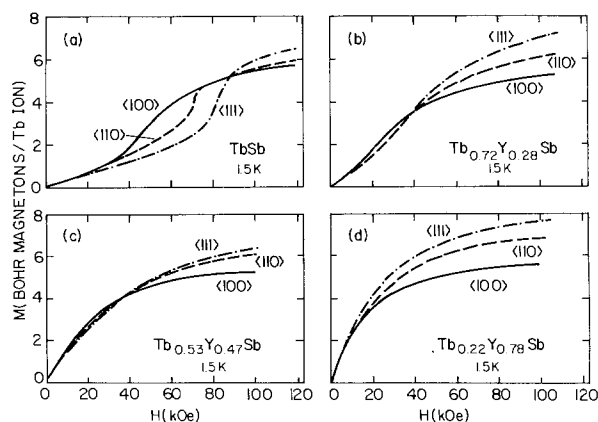


Fig. 16. Magnetization per Tb ion for  $Tb_xY_{1-x}Sb$  at 1.5 K (Cooper and Vogt 1970b).

et al. 1972). Figure 16 shows that the complex anisotropy dependence of the magnetization on the applied field approaches the behaviour found in TmSb.

An explanation for the recorded measurements of the paramagnetic susceptibilities was sought in a simple molecular-field model, by postulating an effective internal magnetic field  $H_{\text{eff}} = H_{\text{ext}} + \lambda M$  and using the results found for TmSb.

Figure 17 shows that the observed susceptibilities are rather well explained for highly diluted TbSb. The same procedure explains equally well the dependence of the Néel temperature on the concentration of YSb.

The magnetization curves could not be fitted satisfactorily using the linear molecular-field model. A somewhat better agreement, but still only for relatively high dilution, was obtained by taking into account fourth-order contributions to the free energy, leading to an effective field (Cooper and Vogt 1970b)

$$H_{\text{eff}} = H_{\text{ext}} + \lambda M + DM^3,$$

where  $D$  depends on the orientation, i.e. the effective field is anisotropic. The temperature dependence of the sublattice magnetization measured by neutron diffraction for Tb-rich samples, on the other hand, is very well explained by the above-mentioned assumption of an effective internal field. Specific-heat measurements by Stutius (1969a) more or less confirmed the results obtained by magnetization measurements. Determination of the crystal-field splitting by neutrons (Birgeneau et al. 1973) show that the assumed values were reasonable. They agree also with the results of a complete study of the magnetic excitations in TbSb (Holden et al. 1974). The above model cannot explain the observed lattice distortions, neither in TbSb (Hulliger and Stucki 1978) nor in  $\text{Tb}_x\text{Y}_{1-x}\text{Sb}$  (Stutius 1969a).

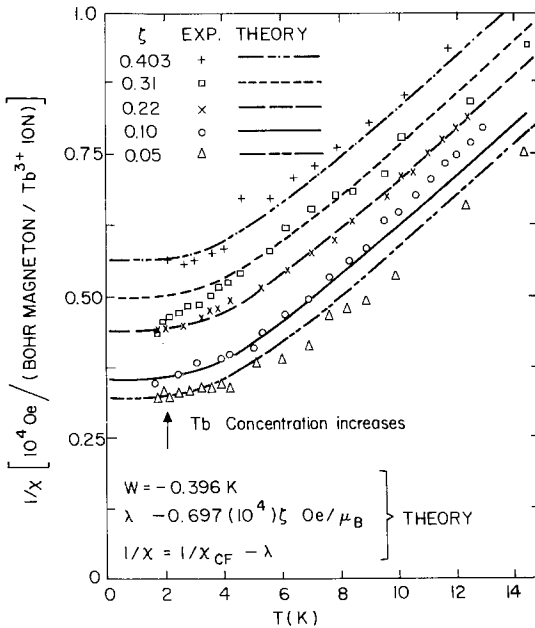


Fig. 17. Inverse susceptibilities versus temperature for a  $\text{Tb}^{3+}$  ion in TbSb diluted with YSb (Cooper and Vogt 1970b).

Further progress arose from some very accurate neutron diffraction and susceptibility measurements on well-defined TbP samples (Kötzler et al. 1979). An analysis of the magnetic properties of all Tb pnictides using the mean-field approximation, was published subsequently (Kötzler and Raffius 1980). Magnetization measurements confirmed a strong quadrupolar coupling between the  $Tb^{3+}$  ions in TbP (Raffius and Kötzler 1983). The most convincing explanation of the magnetic properties of TbP and TbSb is given by Buschbeck et al. (1987). These authors use the usual isotropic bilinear exchange  $H_{ex} = -\sum_{j>i} I_{ij} J_i J_j$ , as well as a biquadratic contribution. Sixth-order terms can be neglected. The corresponding mean-field approximation explains very satisfactorily the temperature dependence of the magnetic moment for TbP and TbSb. Furthermore, and this is a very convincing result, the strange anisotropic behaviour of the magnetization versus applied field in TbSb (see fig. 18) is very well explained.

The general conclusion which we can draw is that exchange forces in Tb pnictides are very anisotropic, in spite of the fact that the observed magnetization axes correspond to the predictions of the crystal-field theory. These predictions are, as is stated clearly by Trammell (1963), valid only for isotropic Heisenberg-type exchange.

In all NaCl-type compounds of the lanthanides and actinides, we should expect (with the exception of S states) anisotropic exchange forces, which are sometimes hidden by the anisotropy which originates from the crystal-field splitting. A more

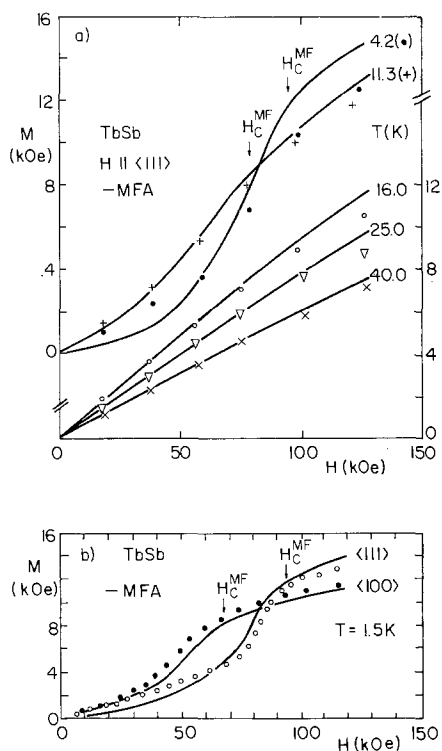


Fig. 18. Magnetization versus applied field of TbSb, reproduced from Buschbeck et al. (1987).

TABLE 5  
Magnetic data of holmium pnictides.

	Order	$T_C/T_N$	$\Theta_p$	$\mu_{\text{eff}}$	$\mu_{\text{order}}$	$\mu_{130 \text{ kOe}}$	Mag. axis
HoN	ferri	13.3	12	10.8	8.9	9.9	$\langle 100 \rangle$
HoP	HoP type	5.5	6	10.2	?	9.2	$\langle 100 \rangle$
HoAs	AF II	4.8	1	10.35	8.8	9.5	$\langle 100 \rangle$
HoSb	AF II	5.5	-2.5	10.8	9.3	9.3	$\langle 100 \rangle$
HoBi	AF II	5.7	?	?	?	8.7	$\langle 100 \rangle$

$\text{Ho}^{3+}$ :  $gJ = 10.0$ ,  $g[J(J+1)]^{1/2} = 10.6$ .

complete analysis is given by Kötzer and Raffius (1980). The mean-field approximation proposed by the authors actually gives a very satisfactory interpretation of the magnetic properties of all Tb pnictides.

2.1.5.2. *HoN, HoP, HoAs, HoSb, HoBi.* Table 5 summarizes the magnetic properties of the Ho pnictides. Most of these results have been known since the fundamental paper of Child et al. (1963) was published. The ferrimagnetic structure of HoN and the HoP structure are discussed in detail below. We conclude from table 5 that all compounds order at relatively low temperatures – the exchange forces are thus rather weak. The effective number of magnetons and the ordered moments (or moments in high applied fields) are close to the values of the free trivalent Ho ion. The magnetic axis is in all cases the  $\langle 100 \rangle$  direction. Trammell (1963) has shown that this direction is to be expected as a result from the interplay between the strong crystalline-field torques and the weaker exchange forces. Actually, Trammell's (1963) calculations start from the assumption that the exchange forces are isotropic. We shall see below that this is by no means the case – but in this case the exchange forces are weak, even though they are highly anisotropic.

From table 5 we can conclude that the exchange forces are predominantly ferromagnetic for the nitride and the phosphide, but on going towards the bismuthide the antiferromagnetic exchange increases. The magnetic properties of the series are thus determined by a delicate balance of the ferro- and antiferromagnetic exchange forces.

*HoN.* Let us now have a more detailed look at the single compounds. Child et al. (1963) and Wilkinson et al. (1962) have examined the spin structure of HoN (fig. 19). Their description is as follows: the individual atomic moments with a value of  $8.9\mu_B$

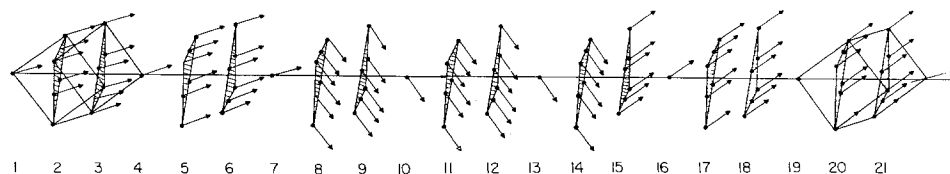


Fig. 19. Possible magnetic spin structure of HoN below 18 K, after Child et al. (1963).

are always along a cube edge. They are arranged in ferromagnetic sheets which are perpendicular to the cube diagonal. For the first seven sheets the spins are pointing along  $+x$ , for the next seven sheets along  $+y$  and finally along  $+z$  for the last seven sheets. We thus observe a cone with a net ferromagnetic moment along  $\langle 111 \rangle$ . The spin structure can be looked upon as a "retarded spiral". For fields higher than 25 kOe the spins are arranged completely ferromagnetically. The authors are very careful to call their interpretation a "possible" spin structure. In any case, it is clear that the anisotropic exchange forces want to impose a periodicity along the  $\langle 111 \rangle$  direction. Nowadays we know about the existence of multi- $k$  structures in the NaCl-structure compounds and of the possible coexistence of antiferromagnetically ordered Fourier components of the magnetic moment with ferromagnetically ordered components. Such structures were observed in Np compounds. The antiferromagnetic structure can be broken up by an applied external field. It might be a very rewarding task to re-examine the spin structures of HoN in the light of these new findings. Most probably, experiments would require single crystals, which are difficult to produce. Magnetization measurements (Busch et al. 1964c, Busch 1967, Junod et al. 1969) on powdered samples confirm that at high fields a complete alignment of the spins can be induced. The observed moments correspond to the free-ion value. No doubt magnetization curves on single crystals would reveal a very pronounced anisotropy.

Results of measurements on powdered samples in high fields are equivalent to values obtained along the easy axis, since the crystallites are oriented in the applied field. However, the absolute values of the magnetization have to be taken with great care. The specific heat of HoN (Stutius 1969b) versus temperature shows at about 9 K a deviation from a smooth curve and, of course, a pronounced peak at the Curie temperature, which is 13.3 K. This might be an indication that the ferrimagnetic structure changes into a ferromagnetic structure above 9 K – a not unusual behaviour.

*HoP.* Child et al. (1963), in their classical paper, found for HoP a peculiar ferrimagnetic spin structure in neutron diffraction experiments. This structure is visualized

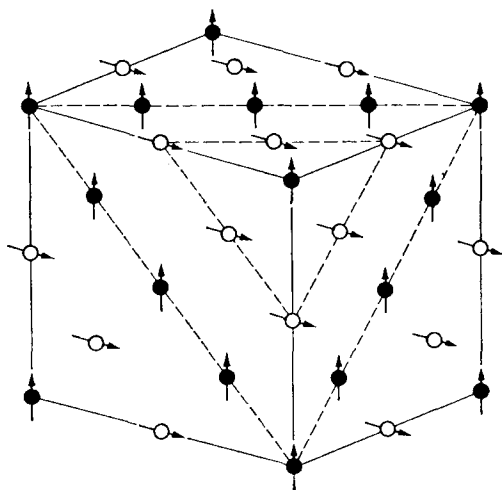


Fig. 20. Magnetic structure of HoP (Child et al. 1963).

in fig. 20. It consists of ferromagnetic sheets normal to the  $\langle 111 \rangle$  axis – but the moments in alternate sheets are perpendicular to each other and parallel to  $\langle 100 \rangle$  and  $\langle 010 \rangle$ , respectively. Magnetization measurements along  $\langle 100 \rangle$ ,  $\langle 110 \rangle$  and  $\langle 111 \rangle$  should therefore lead to  $\frac{1}{2}$ ,  $1/\sqrt{2}$  and  $1/\sqrt{3}$  times the saturation moment, respectively. This is indeed the case, as can be seen in fig. 21. The magnetization measurements are taken from Busch et al. (1964b, 1966a). Earlier measurements (Busch et al. 1963) confirmed the ordering temperature reported by Child et al. (1963) and an effective number of magnetons which is close to the calculated value for the free trivalent Ho ion. If the applied field exceeds a critical value (about 2.1 kOe) a change in the magnetization curve along  $\langle 100 \rangle$  becomes apparent. This must mean that the HoP structure changes into a ferromagnetic spin arrangement. Indeed, the full moment is observed. Due to anisotropy, the spins are strictly confined to the  $\langle 100 \rangle$  axis, even in fields exceeding 100 kOe. Independent of the arrangement of the  $\langle 100 \rangle$  moments (whether ferromagnetic or of the HoP-type), the moments measured along  $\langle 110 \rangle$  and  $\langle 111 \rangle$  will always be  $1/\sqrt{2}$  or  $1/\sqrt{3}$  times the full moment, which is along  $\langle 100 \rangle$ . This explains the fact that the change from the ferrimagnetic HoP-type structure to a ferromagnetic structure cannot be detected by measurements along  $\langle 110 \rangle$  or  $\langle 111 \rangle$  (see fig. 21).

Various other experiments have been performed on HoP, including nuclear magnetic resonance (Jones 1969) and distortion measurements (Levy 1969). The distortion turned out to be very small. The crystal electric field fits in an effective point-charge model (Birgeneau et al. 1973).

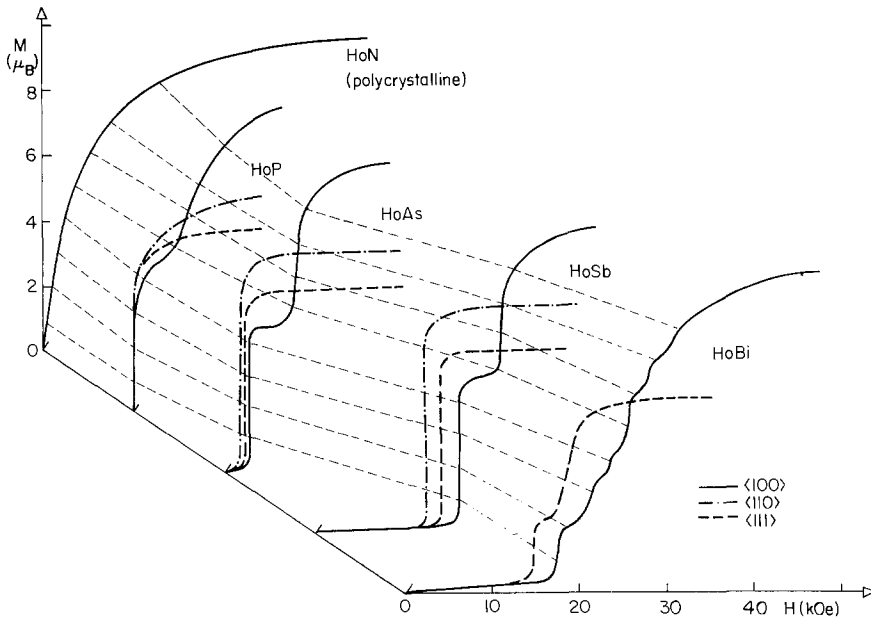


Fig. 21. Magnetic moment versus applied magnetic field for several Ho pnictides. HoN from Junod et al. (1969), HoP, HoAs, HoSb from Busch et al. (1966a), HoBi from Hulliger et al. (1984).



The stability criteria for the unusual HoP structure intrigued theoreticians for a long time. Trammell (1963) argues that dipolar forces are stabilizing the structure. Kim and Levy (1982) have shown, based on neutron diffraction experiments, that bilinear pair interactions do exist in HoP, but that quadrupolar pair interactions are essential in order to explain the stability of the HoP structure. This theory is supported by neutron results obtained by Fischer et al. (1979), who show that with increasing temperature the HoP structure changes into a ferromagnetic structure at 4.7 K, which in turn changes to paramagnetism at 5.6 K. These results were confirmed by Furrer and Kaldis (1980). Looking up old magnetization measurements, we found that these new findings reproduce themselves in  $M(T)$  measurements. Unfortunately, magnetization measurements, which always have to be performed in substantial applied fields, are usually too crude to reveal such details. From all the experimental evidence one is almost able to predict a complete magnetic phase diagram for HoP: for  $H = 0$  on lowering the temperature we go from paramagnetism to ferromagnetism and finally to the HoP “flopside” structure. This structure is destroyed by an applied field of 2.1 kOe at low temperature and possibly at even lower fields near the ordering temperature. The structure is above 2.1 kOe gradually modified into a ferromagnetic spin arrangement, which certainly exists above an applied field of 20 kOe. These are the results as they were known until 1985. Today, one gives a different explanation for the HoP structure – it is regarded as a multi- $k$  structure. Magnetic structures in cubic systems can be non-collinear because the crystalline electric field plays an important role in determining the direction of the moment and because of fourth-order terms in the exchange, which couple Fourier components with two different wave vectors. The HoP structure is described by a perpendicular antiferromagnetic Fourier component  $m_k$  ( $k = (\frac{1}{2}, \frac{1}{2}, \frac{1}{2})$ ) along  $\langle 101 \rangle$  and a ferromagnetic component  $m_0$  along  $\langle 10\bar{1} \rangle$ , resulting in ferromagnetic (111) planes with moments successively along  $\langle 001 \rangle$  and  $\langle 100 \rangle$ . Strong quadrupolar interactions result from this kind of ordering. By applying a magnetic field we destroy the antiferromagnetic component (either gradually or abruptly), and the result is an induced ferromagnetic spin structure. Apparently the antiferromagnetic coupling no longer exists above 4.7 K, whereas the ferromagnetic coupling remains up to the Curie temperature, which is 5.6 K. It is hoped that this kind of interpretation will be verified in neutron diffraction experiments. A first attempt is found in a paper by Fischer et al. (1985b). Such experiments have been performed on NpAs–NpSe mixed crystals, where the coexistence of ferro- and antiferromagnetic coupling of the Fourier components could be nicely demonstrated.

*HoAs.* HoAs is reported to be antiferromagnetic below its Néel temperature in zero magnetic field (Busch et al. 1963, 1965c, Busch 1967). By applying a magnetic field stronger than about 2 kOe a ferrimagnetic spin structure, which is of course of the HoP-type, with half the full saturation moment, is induced (see fig. 21) (Busch et al. 1966a). For fields higher than 8 kOe this structure changes towards ferromagnetism, which is reached fully at an about 15 kOe applied field. The easy axis is the  $\langle 100 \rangle$  direction, to which the spins are strictly confined. The distortion (Levy 1969) in the ordered states is very small. Below 5 K HoAs becomes tetragonal. All these results are very reminiscent of the behaviour of HoP, and the interpretation should be more or less the same.

Neutron diffraction experiments (Schmid et al. 1986) allowed the determination of the complete magnetic phase diagram: for low magnetic fields HoAs is antiferromagnetic type II (presumably a multi- $k$  structure), with the Fourier components along  $\langle 100 \rangle$ , up to the Néel temperature. Above a critical magnetic field (2 kOe at  $T = 0$  and lower near the Néel temperature) the HoP-type spin structure is indeed induced. By further increasing the magnetic field (12 kOe at  $T = 0$ , going towards weak fields near  $T_N$ ) the HoP structure can be gradually turned into a ferromagnetic spin arrangement. For zero applied field the transition from antiferromagnetism to paramagnetism seems to be a direct one – no intermediate ferromagnetism is reported, in contrast with the case of HoP.

*HoSb.* Child et al. (1963) first reported on HoSb. They found it to be antiferromagnetic type II below its Néel temperature. The spins are essentially parallel to  $\langle 100 \rangle$ , even though a better agreement with experiments is obtained if the moments are assumed slightly tilted towards  $\langle 111 \rangle$ . Magnetization measurements (Busch et al. 1965a, Busch 1967) confirmed the existence of antiferromagnetism as well as the effective moments measured by Child et al. (1963) and these are close to the free-ion value. Measurements of the magnetic moment in high fields as a function of the field direction (Busch et al. 1965a), see fig. 21, revealed, similar to the case of HoAs, the existence of an intermediate spin structure (between 20 and 24 kOe applied field), which is most probably of the HoP type. Above 35 kOe the spins are all aligned – the anisotropy is complete, which means the moments are always along  $\langle 100 \rangle$ . At the ordering temperature a pronounced tetragonal distortion sets in (Levy 1969). Very detailed measurements of the magnetization versus temperature and applied field allowed the “construction” of magnetic phase diagrams (Brun et al. 1980). At low fields (15 kOe at  $T = 0$ , going to 0 kOe at  $T_N$ ) HoSb is antiferromagnetic. Above 15 kOe up to 20 kOe (at  $T = 0$ , the upper limit going to 0 kOe at  $T_N$ ) the HoP structure is stable. The authors do not mention “ferromagnetism” at much higher fields – they denote the observed spin arrangement as “paramagnetic”. Taub et al. (1974) and Taub and Parente (1975) observed anomalies in the specific heat, resistivity and neutron scattering behaviour at the Néel point (tricritical behaviour?). Theoretical explanations are discussed by Kim et al. (1975). Neutron studies (Andersen et al. 1980b) did show quite clearly that the magnetization vector is turned out of the  $\langle 100 \rangle$  direction near the Néel temperature. The authors determined the turn-angle (fig. 2 in Andersen et al. (1980b)). Turning the magnetic moment against the crystal-field anisotropy (which favours  $\langle 100 \rangle$ ) reduces the moment. Indeed, an unusually steep decrease of the magnetic moment when approaching the Néel temperature has been observed by Taub and Parente (1975). The turning of the magnetic moment would require a different explanation making the assumption that HoSb, in analogy to HoP, is a multi- $k$  structure and that the ferromagnetic component becomes more predominant near  $T_N$ . Corresponding neutron diffraction experiments would provide a welcome source of further information.

*HoBi.* Fischer et al. (1985a) report on antiferromagnetic type II ordering below  $T_N = 6$  K. The moments are at an angle of  $75^\circ$  out of the (111) planes, which exceeds the value of  $55^\circ$  for the  $\langle 100 \rangle$  direction. The authors consider multi- $k$  ordering, but could not give details with powder measurements. Hulliger et al. (1984) measured a

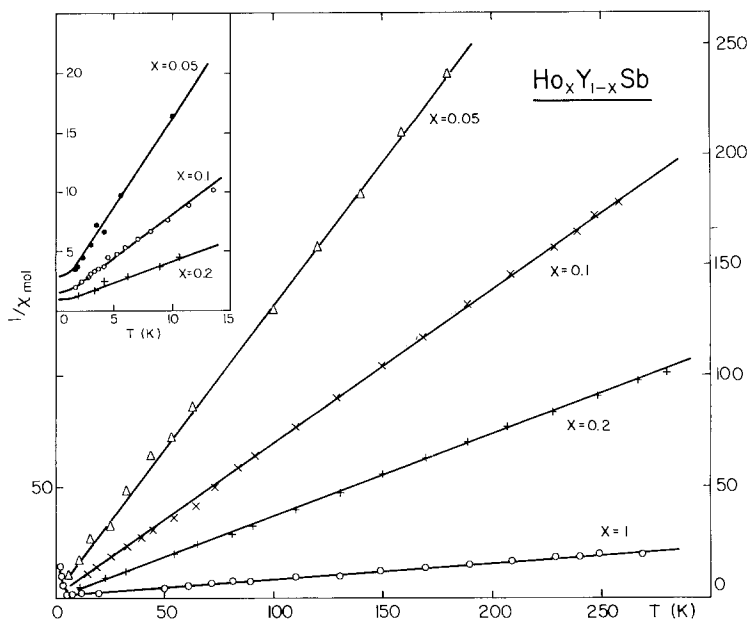


Fig. 22. Inverse molar susceptibilities of  $\text{Ho}_x\text{Y}_{1-x}\text{Sb}$  versus temperature (Jensen et al. 1980).

tetragonal distortion at  $T = 5.72$  K. Thermal-expansion measurements as well as specific-heat measurements indicate a first-order transition. The magnetization curve (Hulliger et al. 1984), partially reproduced in fig. 21, shows a stepwise increase above 15 kOe until the full ferromagnetic moment is reached. The possible intermediate HoP structure is not clearly visible. Thus the assumption that HoBi has actually a multi- $k$  structure and that the antiferromagnetic Fourier components turn from a  $+-$  to some higher-order sequence of  $+$  and  $-$  spins (e.g.  $++-$  or  $+++--$ ) seems plausible – since such ferrimagnetic spin arrangements are often encountered in Ce or actinide compounds. Neutron experiments in external magnetic fields would certainly allow a complete analysis of the interesting magnetization curves.

*Diluted HoSb.* We have seen that the magnetic properties of all the Ho pnictides are based on a delicate balance of isotropic exchange, anisotropic exchange (favouring the  $\langle 111 \rangle$  direction), crystal-field anisotropy (confining the moments to the  $\langle 100 \rangle$  direction) and finally the applied field. Especially near the critical temperature all these four energies are of similar importance and thus render the magnetic behaviour rather complicated. By diluting HoSb with non-magnetic YSb we have a good chance of reducing the exchange forces and get hopefully less complicated results. Figure 22 (partially taken from Jensen et al. (1980)) shows that indeed, for strong dilution, the exchange is weak and no ordering occurs. The full curves are calculated based on crystal-field-only behaviour.

Figure 23 (Vogt 1968) shows that in diluted HoSb the magnetization curve and, especially, anisotropy is only governed by the crystal electric field (cf. results for TmSb, for example). The crystal field forces the moments strictly into the  $\langle 100 \rangle$  direction,

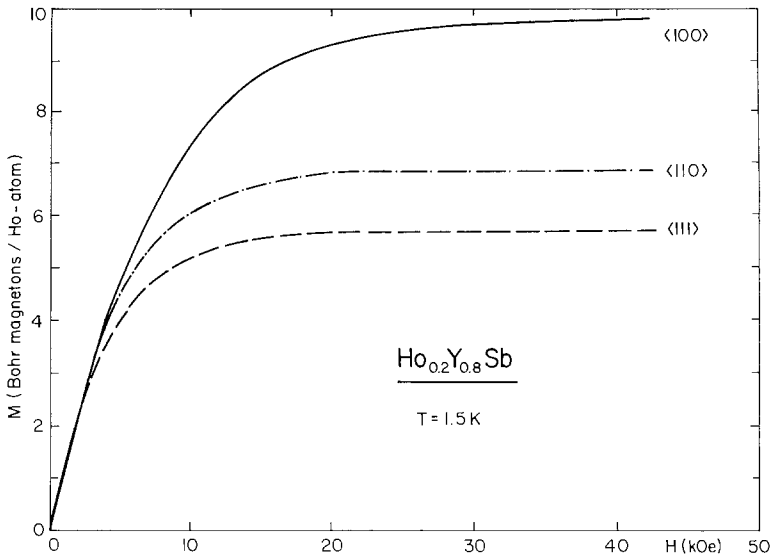


Fig. 23. Magnetic moment of  $\text{Ho}^{3+}$  in diluted HoSb versus applied magnetic field along the three main axes (Vogt 1968).

along any other direction we measure only the projections. This fact is in complete agreement with Trammell's original work (Trammell 1963).

Figure 24 shows magnetization curves for  $\text{Ho}_x\text{Y}_{1-x}\text{Sb}$  for various degrees of dilution. Apparently the intermediate HoP structure is shifted towards lower fields – an indication that the anisotropic part of the exchange energy is vanishing. Jensen

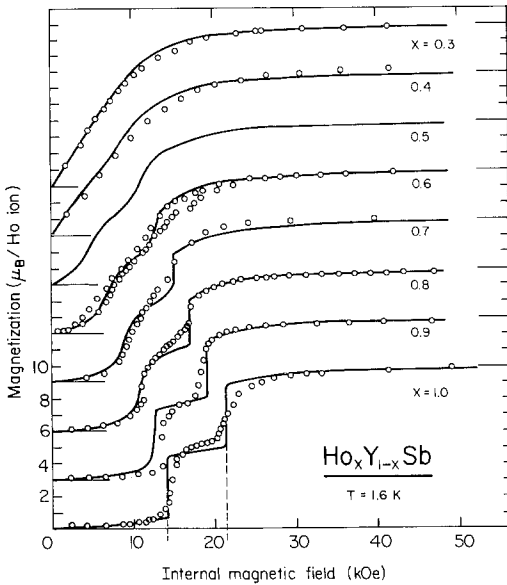


Fig. 24. The bulk magnetization of  $\text{Ho}_x\text{Y}_{1-x}\text{Sb}$  parallel to a field applied along the easy  $\langle 100 \rangle$  axis as obtained at 1.6 K (Jensen et al. 1980).

et al. (1980) give a complete analysis of these magnetization curves – the full lines are theoretical predictions. Taking into account isotropic and anisotropic bilinear pair interactions, quadrupole couplings and the crystal field, the model reproduces the magnetization curves very satisfactorily. Furthermore, it yields two different transitions for pure HoSb, a second-order one at  $T_N = 5.7$  K, followed by a tricritical one at 5.4 K. These results explain the neutron scattering data reported by Taub and Parente (1975) and the specific-heat as well as resistivity measurements (Andersen et al. 1980a). It seems that the model developed by Jensen et al. (1980) is universal for all Ho monopnictides. Some more experiments, especially near the critical points, are necessary to confirm this statement.

2.1.5.3. *DyN, DyP, DyAs, DySb, DyBi.* We have collected the available results on the magnetic properties of the Dy pnictides in table 6. The data stem from Child et al. (1963) (DyN), Busch et al. (1963) (DyN, DyP, DyAs, DySb), Busch et al. (1964c) (DyN), Busch et al. (1964b) (DyP), Tsuchida and Wallace (1965a) (DyBi), Busch et al. (1965c) (DyAs), Busch et al. (1965b) (DyN), Busch et al. (1965a) (DySb), Busch (1967) (all pnictides), Busch and Vogt (1968) (DySb), Junod et al. (1969) (DyN), Stutius (1969b) (DyN), Levy (1969) (all pnictides), Nereson and Arnold (1971) (DyBi), Mullen et al. (1974) (DySb) and Stevens and Pytte (1973) (DyP, DyAs). For the sake of clarity we give only the “most probable” values in table 6. For the determination of the ordering temperatures the methods which do not require an applied magnetic field (specific heat, neutron diffraction, X-ray distortion) generally seem to be more reliable. Measurements on single crystals were preferred to powder measurements. A definite tendency from ferromagnetism towards antiferromagnetism is observed as we go from the nitride to the bismuthide. This is reflected in the behaviour of the paramagnetic Curie temperatures. The data for the Dy pnictides are very similar to those for the Ho pnictides. Since this similarity persists for the magnetization, our discussion will be rather short.

Figure 25 shows the inverse susceptibility versus temperature measurements as reported by several different authors (Tsuchida and Wallace 1965a, Busch et al. 1965a, Junod et al. 1969, some unpublished data). DyN seems to be a ferromagnet. DyP

TABLE 6  
Magnetic data of dysprosium pnictides.

	Order	$T_C/T_N$	$\Theta_p$	$\mu_{\text{eff}}$	$\mu_{\text{order}}$	$\mu_{130 \text{ kOe}}^a$	Mag. axis
DyN	ferro	17.6	20	10.5	7.4	9.3	$\langle 100 \rangle$
DyP	HoP type	8	18	9.9	7.8	6.35(p)	?
DyAs	HoP type	8.5	2	10.1	9.6	5.3(p)	$\langle 100 \rangle$
DySb	AF	9.5	-4	9.75	9.5	9.5	$\langle 100 \rangle$
DyBi	AF II	11.2	-8	10.6	8.7	9.7	$\langle 100 \rangle$

Dy<sup>3+</sup>:  $gJ = 10.0$ ,  $g[J(J+1)]^{1/2} = 10.63$ .

<sup>a</sup>(p): polycrystalline sample.

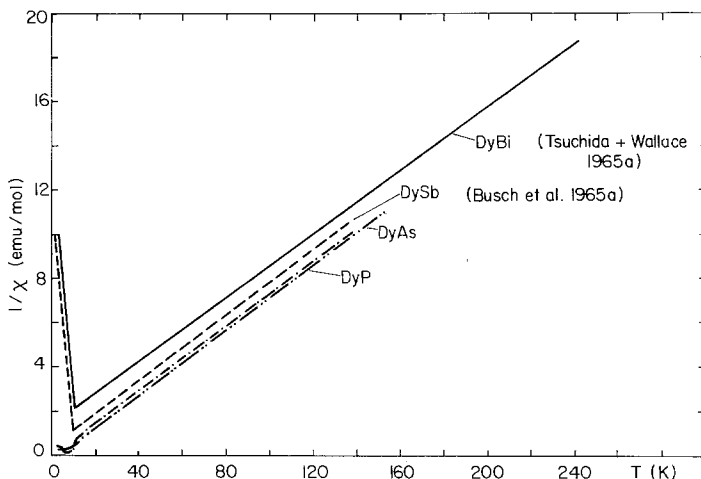


Fig. 25. Inverse molar susceptibilities of Dy compounds versus temperature. Data for DyBi from Tsuchida and Wallace (1965a), for DyP, DyAs and DySb from Busch et al. (1965a).

and DyAs show some peculiar transitions at low temperatures, whereas DySb and DyBi are clearly antiferromagnets. Below the Néel temperature, however, we note an enormous upturn of the inverse susceptibility by more than would be expected in a simple ferromagnet with uniaxial anisotropy. This is a first indication that the transition at the Néel temperature is not conventional. We will discuss this further.

Child et al. (1963) state that at low temperature the ferrimagnetic spin structure of DyN is of the same type as observed in HoN. The moment directions agree with the crystal-field theory (Trammell 1963). There is no indication of a change of this structure with an applied field or at elevated temperatures. In high magnetic fields a value of the magnetization very close to the free-ion value is found (Busch et al. 1964c, Junod et al. 1969) even for powdered samples – the crystallites orient themselves along the easy axis. The anisotropy must be enormous, as is argued by Trammell (1963). DyP and DyAs are apparently ordered in a HoP-type spin arrangement below the ordering temperatures (Busch et al. 1964b, Busch et al. 1965c). By applying a magnetic field in excess of 32 kOe the spins of HoAs can be oriented ferromagnetically (Busch et al. 1965c).

Figure 26 shows magnetization measurements on a DySb single crystal. Looking at the  $\langle 100 \rangle$  magnetization at 1.5 K we note antiferromagnetism up to 24 kOe, followed by the HoP-type structure up to about 42 kOe, which in turn changes to ferromagnetism at even higher fields. Since the HoP structure is of the  $2k$ -type it is induced more easily by applying a field along  $\langle 100 \rangle$ , the direction of the sublattice magnetization. Brun et al. (1975) have performed magnetization measurements on DySb for many different temperatures and constructed a magnetic phase diagram, which is discussed by Kouvel et al. (1977). Figure 27 shows this phase diagram for the  $\langle 100 \rangle$  direction – we do not quite agree with it, since we believe that a boundary paramagnetic–ferromagnetic (dotted line) is missing. (The authors found such a

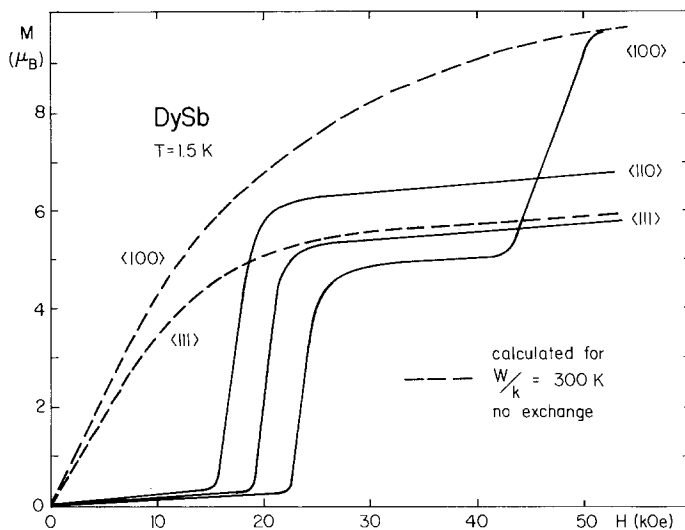


Fig. 26. Magnetic moment versus applied magnetic field of DySb along the three main axes at 1.5 K (Busch and Vogt 1968).

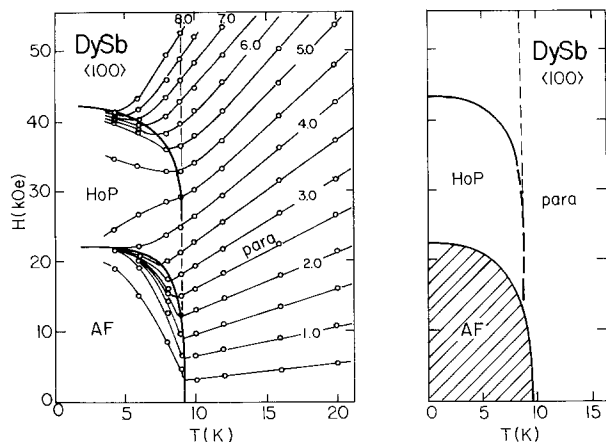


Fig. 27. Magnetic phase diagram of DySb for the  $\langle 100 \rangle$  direction, reproduced from Kouvel et al. (1977) and Brun et al. (1975).

boundary along  $\langle 110 \rangle$  and  $\langle 111 \rangle$ , but they extend the existence of the HoP structure to unlimited high magnetic fields, which is certainly not correct.) The transition from the HoP structure to ferromagnetism is not detectable along  $\langle 110 \rangle$  and  $\langle 111 \rangle$ , since the spins are confined to the  $\langle 100 \rangle$  direction and the resulting net moment along  $\langle 110 \rangle$  or  $\langle 111 \rangle$  will be identical for the HoP structure and ferromagnetism.

On the other hand, the transition from ferromagnetism to paramagnetism is barely detectable in high magnetic fields, since the applied field is higher than the Weiss field. The magnetic structure of DySb was determined using neutron diffraction experiments by Felcher et al. (1973) and Bucher et al. (1972). Gorobchenko et al.

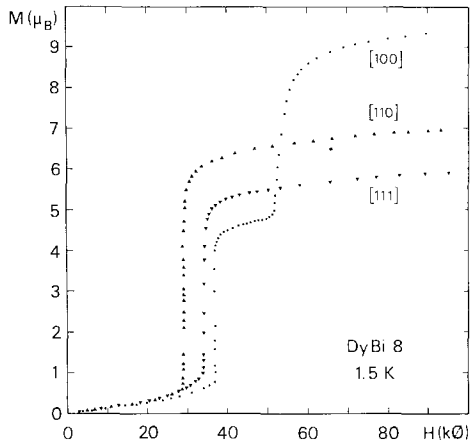


Fig. 28. Dependence of the magnetization upon the effective applied field for DyBi at  $T = 1.5$  K (Hulliger 1980).

(1971) find by Mössbauer measurements that the ordered moments of DyP, DyAs and DySb are almost identical to the free-ion value.

Figure 28 shows magnetization measurements on DyBi (Hulliger 1980). There is a strong resemblance to the results obtained for DySb, and the interpretation of the curves is the same. DyBi was examined by neutron diffraction techniques. It is anti-ferromagnetic of type II with a moment of  $8.7\mu_B$ . The moment direction could not be determined (Nereson and Arnold 1971).

Distortion measurements (Levy and Vogt 1967, Levy 1969) on DyP, DyAs and DySb (fig. 29) show some interesting features. The transition from cubic to tetragonal is very abrupt at the Néel temperature. This means that the internal magnetic field

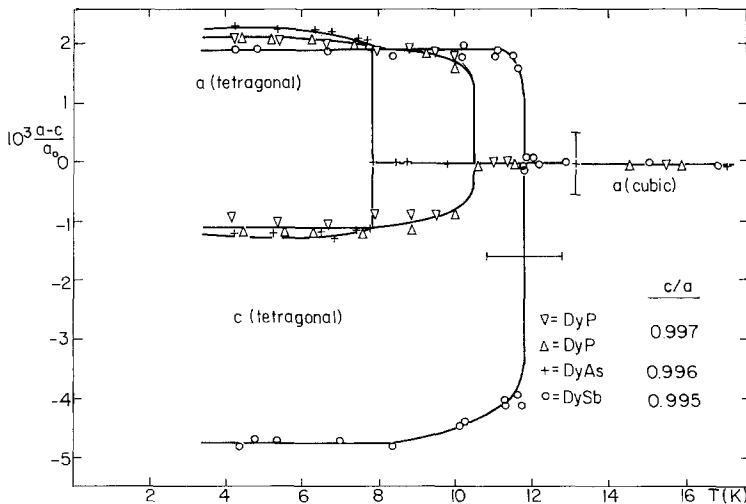


Fig. 29. Tetragonal lattice distortion versus temperature for DyP, DyAs and DySb (Levy 1969).



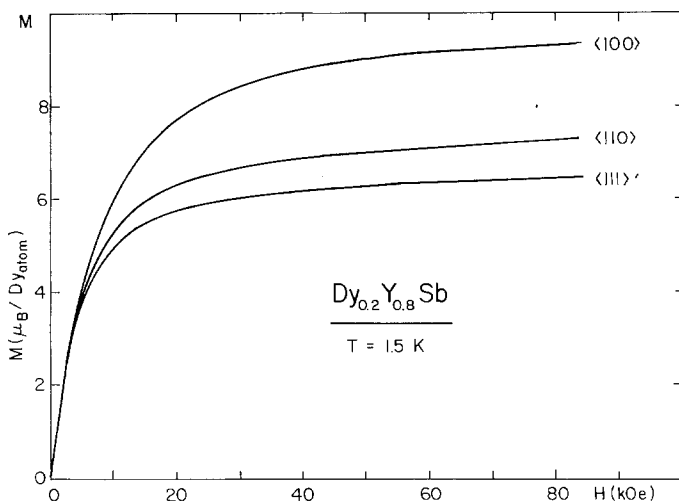


Fig. 30. Magnetic moment versus applied magnetic field for  $\text{Dy}_{0.2}\text{Y}_{0.8}\text{Sb}$  at 1.5 K (Vogt 1968).

varies rapidly – which is confirmed by neutron measurements (Taub and Parente 1975) on DySb. The distortion in DySb is twice as large as in DyP and DyAs, an indication that they have a different spin structure. Since it is not yet known whether or not DySb is a multi- $k$  antiferromagnet more detailed statements would be too speculative. Bucher et al. (1972) find a single first-order transition at  $T_N$  with a marked distortion.

By diluting DySb with non-magnetic YSb, the exchange forces can be eliminated. Figure 30 (Vogt 1968) shows that the free  $\text{Dy}^{3+}$  ion follows the familiar crystal-field-only pattern. Very clearly the crystal field imposes the  $\langle 100 \rangle$  direction to be the easy axis.

The low-temperature behaviour of the Dy pnictides is understood satisfactorily. However, when approaching the ordering temperatures some yet unexplained phenomena appear: the moments of DySb tilt away from the  $\langle 100 \rangle$  direction just below the Néel temperature. The specific-heat measurements cannot be fully explained (Stutius 1969b). Neutron diffraction measurements (Nereson and Arnold 1971) indicate a tricritical transition. Dilatation measurements (Mullen et al. 1974) give the same indication. Critical scattering is enormously large above the Néel temperature (Taub and Parente 1975). The onset of distortions (Levy 1969) does not always coincide with the onset of magnetic ordering.

A very detailed analysis would most probably reveal that, similarly to the case of the Ho compounds, the transition from paramagnetism to the HoP structure or antiferromagnetism is not a direct one. Perhaps there is an intermediate (ferromagnetic?) structure or at least the ordering temperatures observed are of a tricritical nature.

More experiments on well-defined large single crystals are certainly needed to clarify this situation. The numerous results and experiments on the corresponding Ho compounds would be a useful guideline.

TABLE 7  
Magnetic data of erbium pnictides.

	Order	$T_C/T_N$	$\Theta_p$	$\mu_{\text{eff}}$	$\mu_{\text{order}}$	$\mu_{130\text{ kOe}}$	Mag. axis
ErN	ferric	3.39	4	9.4	6	7.5	$\perp \langle 111 \rangle$
ErP	AF II	2.2	1	9.3	5.7	8.5	$\perp \langle 111 \rangle$
ErAs	AF	2.9	-2	9.6	-	8.4	-
ErSb	AF	3.36	-3	9.8	7	7.3	$\perp \langle 111 \rangle$
ErBi	AF	3.53	-6	9.4	-	-	-

$\text{Er}^{3+}$ :  $gJ = 9.0$ ,  $g[J(J+1)]^{1/2} = 9.59$ .

2.1.5.4. *ErN*, *ErP*, *ErAs*, *ErSb*, *ErBi*. Table 7 is a collection of data which were compiled from the work of many authors: Wilkinson et al. (1962) (*ErN*, *ErP*, *ErSb*), Busch et al. (1963) (*ErN*), Child et al. (1963) (*ErN*, *ErP*, *ErSb*), Busch et al. (1964c) (*ErN*), Busch et al. (1964b) (*ErP*), Busch et al. (1965b) (*ErN*), Busch et al. (1965c) (*ErAs*), Tsuchida and Wallace (1965a) (*ErBi*), Busch (1967) (all pnictides), Stutius (1969b) (*ErN*), Hulliger and Natterer (1973) (*ErP*, *ErAs*, *ErSb*, *ErBi*), Hovi et al. (1970) (*ErAs*, *ErSb*) and Landau and Rives (1974) (*ErAs*). We have tried to choose the most probable numbers. A strong sample dependence of these compounds was found by Hulliger and Natterer (1973). Specific-heat measurements are considered to be the most reliable source for the determination of the ordering temperatures. Again we find a tendency towards antiferromagnetism on going from the nitride to the bismuthide. The effective numbers of  $\mu_B$  are close to the free-ion value, which would be  $9\mu_B$ . Since the exchange forces are weak (low ordering temperatures), they are not strong enough to overcome the crystal-field splitting.

*ErN* is reported by Child et al. (1963) and Wilkinson et al. (1962) to be ferrimagnetic with a similar structure as the *Tb*, *Dy* or *Ho* nitrides. The moments are perpendicular to the  $\langle 111 \rangle$  direction. Powder measurements on *ErN* (Busch et al. 1964c) resulted in a value for the magnetization which approaches the free-ion value. A specific-heat measurement (Stutius 1969b) would yield a much too large crystal-field splitting.

*ErP* is reported by Child et al. (1963) to be antiferromagnetic of type II (*MnO*-type). The moments are perpendicular to  $\langle 111 \rangle$ . Trammell (1963) argued that the crystal field would prefer the  $\langle 110 \rangle$  axis. This argument is sustained by Stevens and Pytte (1973). Of course, today we would think that the structure of *ErP* is of the  $2k$  non-collinear type. This would have to be verified. Busch et al. (1964b) have measured the magnetization of *ErP*. Their conclusion that a *HoP*-type structure is induced by fields of only 5.2 kOe is unlikely (see discussion on *ErSb*). The same weak argumentation is used for the interpretation of the magnetization measurements on *ErAs* (Busch et al. 1965c). *ErSb* is up to now the most completely investigated compound.

Figure 31 shows the inverse susceptibilities of *ErSb* for the three main directions as a function of applied field. If we follow the arguments of Trammell (1963) and Stevens and Pytte (1973) and assume that  $\langle 110 \rangle$  is the easy axis ( $2k$  structure), we have a confirmation in the low-field (10 Oe) curves. The  $\langle 110 \rangle$  curve represents the inverse parallel susceptibility, which should go to infinity at 0 K, whereas the  $\langle 100 \rangle$  and  $\langle 111 \rangle$  susceptibilities are close to the perpendicular susceptibility, which is, for isotropic exchange, temperature independent. The flattening of the  $1/\chi$  curve is due

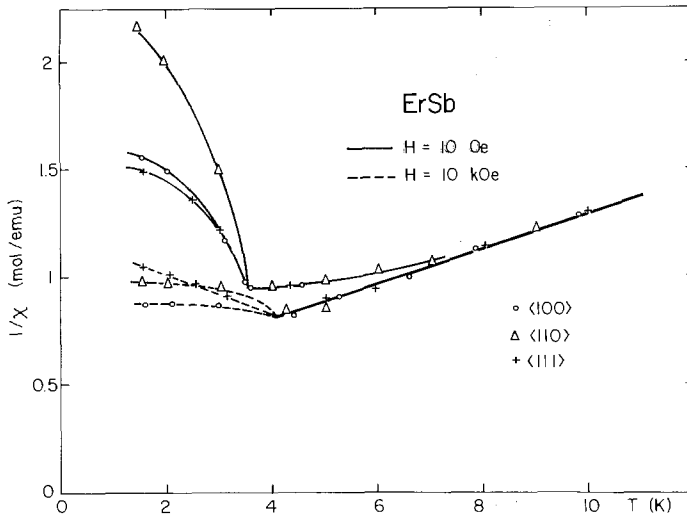


Fig. 31. Inverse molar susceptibilities of ErSb versus temperature (Busch and Vogt 1968).

to the crystal-field interaction. An applied field of 10 kOe suppresses all these effects. The applied field is stronger than the exchange forces and the sample acts as an “isotropic” compound. Mullen et al. (1974) also have found that a magnetic field applied along  $\langle 110 \rangle$  suppresses the anomalies of the elastic modes.

Distortions, which should be trigonal, could unfortunately not be observed (Levy 1969), since the author could not reach low enough temperatures. Shapiro and Bak (1975) state that the distortions should be very small.

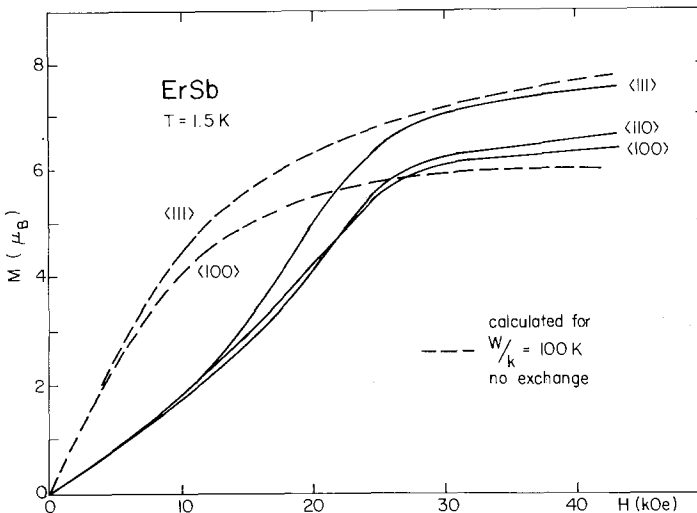


Fig. 32. Magnetization versus applied field along the three main axes of ErSb at 1.5 K (Busch and Vogt 1968).

Figure 32 shows the magnetization of ErSb versus applied field along the three main axes. The calculated crystal-field-only curves (dashed lines) explain the results. In the absence of an applied field the exchange is too weak to induce the full moment (see table 7). When applying an external field we have to consider the exchange and reach, therefore, only gradually the free-ion value. The higher the induced moment, the more effective becomes the molecular field – this is the explanation for the upturn of the magnetization curves.

Neutron diffraction studies on well-defined single crystals would constitute very nice experiments to check the various assumptions mentioned above. Since techniques are currently available to distinguish between collinear and multi- $k$  structures this would be a valuable contribution.

### 2.1.6. $H_{CF} \ll H_{ex}$

2.1.6.1. (*Tb, Dy, Ho, Er*)–(*S, Se, Te*). There is not much information on the magnetic properties of the chalcogenides of the heavy lanthanides. One reason involves problems in sample preparation. It is very difficult to obtain clean and stoichiometric samples of these compounds. Schobinger-Papamantellos et al. (1974) show why this is so. Generally, the ordering temperatures are higher than those of the corresponding pnictides. Since the chalcogenides are coloured compounds (golden, yellow or purple), it is certain that they are metals. The assumption that the stronger exchange forces are due to a greater number of conduction electrons (the pnictides are semimetals) does not seem unreasonable. An overview on some of the chalcogenides is given by Hulliger et al. (1982).

TABLE 8  
Magnetic data of terbium, dysprosium, holmium and erbium chalcogenides.

	Order	$T_C/T_N$	$\Theta_p$	$\mu_{eff}$	$\mu_{order}$	Mag. axis
TbS	AF II	45/49	–88	9.62	8.5	
TbSe	AF II	49/52	–59.5/–73	9.8	7.52	$\langle 111 \rangle$
TbTe	AF II	51/63	–65	9.6	5.6	$\langle 110 \rangle$ or $\langle 221 \rangle$
DyS				10.4		
DySe				10.4		
DyTe				10.5		
HoS	AF II	17.5/21	–15	10.3	7.4	
HoSe				10.6		
HoTe	AF II	20		10.5	7.6	$\langle 111 \rangle$ or $\langle 100 \rangle$
ErS	AF II	7.8/8.5		9.5	5.9	$\langle 111 \rangle$
ErSe	AF II	9.5/10/11	–18	9.44	6.5	$\langle 111 \rangle$
ErTe	AF			9.3	5.5	

Tb<sup>3+</sup>:  $gJ = 9.0$ ,  $g[J(J+1)]^{1/2} = 9.72$ .

Dy<sup>3+</sup>:  $gJ = 10.0$ ,  $g[J(J+1)]^{1/2} = 10.63$ .

Ho<sup>3+</sup>:  $gJ = 10.0$ ,  $g[J(J+1)]^{1/2} = 10.60$ .

Er<sup>3+</sup>:  $gJ = 9.0$ ,  $g[J(J+1)]^{1/2} = 9.59$ .

In table 8 we have collected the relevant available data as contained in the papers of Iandelli (1961), Loginov et al. (1971), Schobinger-Papamantellos et al. (1974), Bucher et al. (1975), Fischer et al. (1977, 1985a), Hulliger and Stucki (1978) and Novikov et al. (1982). We have listed, without evaluation, all available data, since these are rather scarce anyway. Magnetization curves or susceptibility measurements, especially below  $T_N$ , are very rare or incomplete. They are plotted in Novikov et al. (1982) (HoS) and Pokrzywnicki et al. (1985) (ErSe). Most of the information, however, stems from neutron diffraction experiments.

Schobinger-Papamantellos et al. (1974) found antiferromagnetism of type II in TbSe – the moments are along  $\langle 111 \rangle$  and the distortion is rhombohedral, as expected. There is no anisotropy in the form factor. Neutron experiments by Fischer et al. (1977) on TbTe and HoTe yielded type II antiferromagnetism as well. The magnetic moments, however, are tilted away from the  $\langle 111 \rangle$  or  $\langle 221 \rangle$  direction in the case of TbTe and tend towards  $\langle 100 \rangle$  or  $\langle 111 \rangle$  in the case of HoTe. The authors do not offer an interpretation in terms of a multi- $k$  structure, since corresponding experiments could not be done. Hulliger and Stucki (1978) performed very careful distortion measurements on the Tb chalcogenides and found agreement with the neutron results (and with crystal-field theory).

Fischer et al. (1985a) determined the magnetic ordering of HoS, ErS and ErSe, which are all type II antiferromagnets. The magnetic moments of the Er compounds are confined to the  $\langle 111 \rangle$  axis, whereas in the case of HoS they are tilted towards  $\langle 100 \rangle$ . Multi- $k$  structures could not be determined. Pokrzywnicki et al. (1985) find pseudo-tetragonal distortions in DyS, DySe, HoS and HoSe – an indication for multi- $k$  structures. This hypothesis is supported by the fact that high magnetic fields induce the (multi- $k$ ) HoP structure in HoS, HoSe and DyS, which is completely analogous to the corresponding pnictides. Thus, there must be an anisotropic part of the exchange in the monochalcogenides. Pokrzywnicki et al. (1985) give a rather thorough analysis of the magnetic properties of ErSe.

Figure 33 shows the inverse susceptibility of ErSe. There is little upturn of the  $1/\chi$  curve below the Néel temperature – a further indication that the exchange is almost isotropic. As can be seen in the inset, relatively moderate fields (10 kOe) can cause a spin flip, which means that only the perpendicular susceptibility (which is temperature independent and has the same value as encountered at  $T_N$ ) is measured. Tao et al. (1974) found indeed that a large magnetic field can switch the distortion of ErS from tetragonal to trigonal, in agreement with the susceptibility data. The dashed line is a fit using suitable crystal-field parameters. The magnetic moment versus strong applied field (fig. 3 in Pokrzywnicki et al. (1985)) confirms that the exchange is isotropic. The measured curve conforms with the curve for the crystal field alone in fig. 32 if we reduce the applied field by an antiferromagnetic molecular field, which in turn is isotropic. An isotropic exchange suggests that the primary interaction is via the conduction electrons. In such a case the transition temperatures are expected to vary linearly with the de Gennes function,  $(g - 1)^2 J(J + 1)$ . In fig. 34 we see that this indeed is the case for the heavy rare earth selenides. Linearity is also found for the bismuthides (Tsuchida and Wallace 1965a), suggesting that in these the exchange is also caused mainly by the conduction electrons.

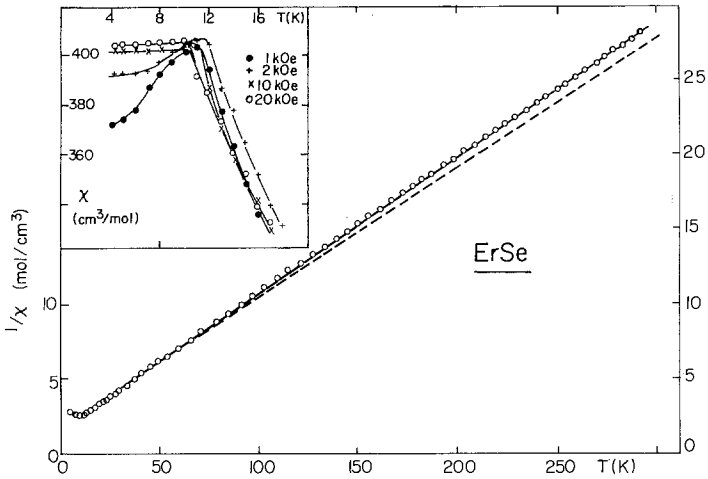


Fig. 33. Inverse susceptibility of ErSe versus temperature. The dashed line is calculated using  $X = 0.75$ ,  $W = 0.44$  K and  $C_p = -1.6$  mol/cm<sup>3</sup> (Pokrzywnicki et al. 1985).

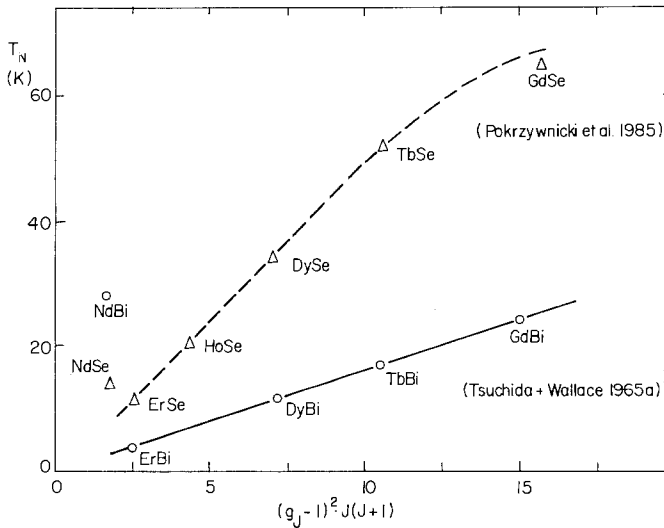


Fig. 34. Néel temperature versus de Gennes function for heavy rare earth selenides and bismuthides (Pokrzywnicki et al. 1985, Tsuchida and Wallace 1965a).

In fig. 34 we have incorporated the corresponding values for the Nd compounds. We note that they do not follow the de Gennes law. The magnetic properties of the heavy lanthanide compounds are well described by the assumption of a quasi-isotropic exchange – but this assumption is invalid for Nd compounds. Their magnetic properties are governed by a completely different mechanism, as we shall discuss later.

2.1.6.2. *CfN, CfAs, CfSb*. Only susceptibility measurements are available (Nave et al. 1986). The preparation and measurements of these compounds require admirable experimental skill. CfN is a ferromagnet ( $T_C = 25$  K), CfAs and CfSb are antiferromagnets with Néel temperatures of 17.5 and 25 K, respectively. The paramagnetic moments are practically identical with the free-ion value, which is  $10.26\mu_B$ . The susceptibility curves show the typical features of isotropic-exchange compounds.

## 2.2. Reshaped *f*-shells

### 2.2.1. Weak hybridization

2.2.1.1. *NdN, NdP, NdAs, NdSb, NdBi*. We have collected in table 9 the characteristic values for the Nd pnictides. As usual, preference was given to those critical temperatures which were evaluated in zero magnetic field from specific-heat or neutron diffraction experiments. The reader will find the detailed results in Didchenko and Gortsema (1963), Busch et al. (1964c, 1965a, b), Veyssie et al. (1964), Tsuchida and Wallace (1965a), Tsuchida et al. (1969), Busch (1967), Junod et al. (1969), Jones (1969), Nereson and Arnold (1971), Furrer et al. (1972) and Schobinger-Papamantellos et al. (1973). Busch et al. (1965b) state that the susceptibility of NdN does not follow exactly the Curie–Weiss law. They attribute this to a temperature-dependent moment of the Van Vleck type. Tsuchida and Wallace (1965a) show in their plot of Néel temperatures versus the de Gennes factor for Ln bismuthides that the Nd compound does not follow the general pattern. Knight shift measurements (Jones 1969) are compatible with the parameters obtained from the Curie–Weiss law. Levy (1969) measured a tetragonal distortion of NdSb in agreement with the  $\langle 100 \rangle$  easy axis as determined by neutron diffraction and magnetization measurements. Nereson and Arnold (1971) performed very careful neutron diffraction studies on NdBi. They find type I antiferromagnetism with moments along  $\langle 100 \rangle$ . The magnetic moment follows the Brillouin functions. The same type of ordering was found by Schobinger-Papamantellos et al. (1973) for NdP, NdAs and NdSb, whereas NdN orders ferromagnetically, again along  $\langle 100 \rangle$ , in agreement with the expectation from crystal-field splitting. The crystal-field parameters determined by neutron spectroscopy (Furrer et al. 1972) are in agreement with the point-charge model. The same conclusions are drawn by Birgeneau et al. (1973) and Wakabayashi and Furrer (1975).

TABLE 9  
Magnetic data of neodymium pnictides.

	Order	$T_C/T_N$	$\Theta_p$	$\mu_{\text{eff}}$	$\mu_{\text{order}}$	$\mu_{130 \text{ kOe}}$	Mag. axis
NdN	ferro	27.6	24	3.65	2.69	3.6	
NdP	AF I	11	11	3.78	1.83	2.2	
NdAs	AF I	10.6	4	3.7	2.18	2.3	$\langle 100 \rangle$
NdSb	AF I	15.5	-3	3.75	2.98	2.7	$\langle 100 \rangle$
NdBi	AF I	25	-1	3.58	3.1		$\langle 100 \rangle$

$\text{Nd}^{3+}$ :  $gJ = 3.27$ ,  $g[J(J+1)]^{1/2} = 3.62$ .

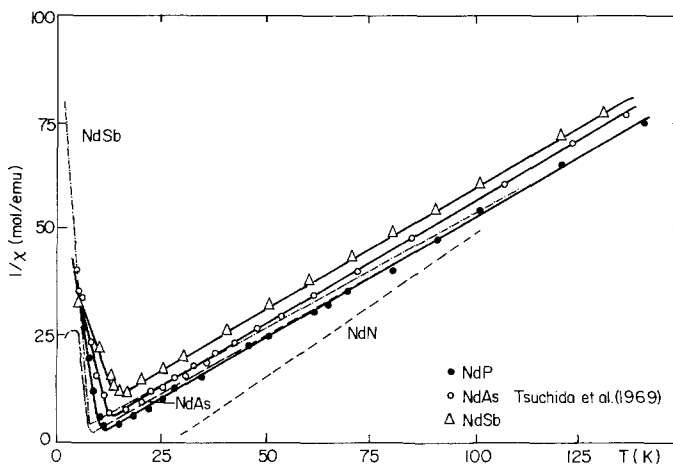


Fig. 35. Inverse molar susceptibilities versus temperature of Nd pnictides. The full lines are taken from Tsuchida et al. (1969), the rest are our own measurements.

The inverse susceptibilities of the Nd pnictides are plotted in fig. 35 (results from Tsuchida et al. (1969) and our own). The enormous upturn below the Néel temperature is, in our opinion, characteristic of a highly anisotropic exchange (see arguments for Ho and Dy compounds). Bak and Lindgard (1973) analyzed magnetization measurements on the basis of the influence of the crystal electric field and biquadratic exchange. The susceptibility curves and distortions are well explained. However, the considerable reduction of the ordered moment (see table 9) remains unexplained – apparently the model is not complete. Cooper et al. (1988) have started to consider “orbitally driven” magnetism and reshaping of the ions, which are both an explanation for anisotropic exchange and reduction of the ordered moment as encountered in Nd compounds. Indeed, Furrer and Tellenbach (1975) found that  $J$ -admixture to the crystal-field Hamiltonian could explain the experimentally observed ordered moments of NdSb and NdS. Neutron diffraction experiments (Furrer et al. 1976, 1977) showed clearly that in NdSb there are three important parameters determining the magnetic properties of NdSb: the cubic crystal electric field, isotropic exchange of the Heisenberg type and a large quadrupolar contribution. Furrer and Heer (1973) include a dynamical exchange interaction term in their Hamiltonian in order to understand the data obtained for NdSb.

Figure 36 shows that the Nd pnictides are “metamagnetic”, which means that large applied fields can induce ferromagnetism (results from Tsuchida et al. (1969) and our own). The magnetization curves are typical of an anisotropic compound, and a further indication that the exchange forces are highly anisotropic. Neutron scattering experiments on NdSb in applied fields were used to study the magnetic phase diagram (Mukamel et al. 1985). We would suggest that “domain switching”, as postulated by the authors, is not the only possibility to explain the observed phenomena. A simpler explanation in terms of multi- $k$  structures ought to be considered.



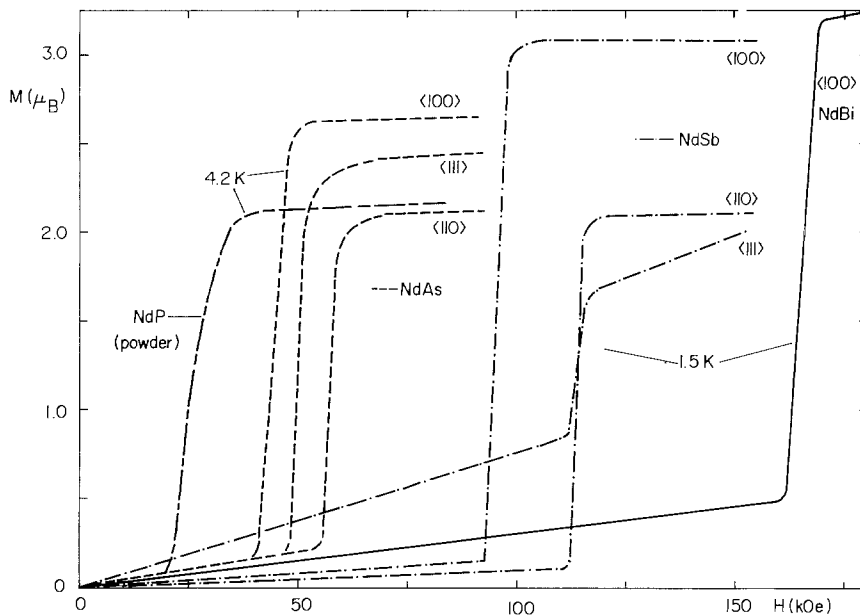


Fig. 36. Magnetic moment versus applied magnetic field for Nd pnictides. The powder measurements on NdP are taken from Tsuchida et al. (1969).

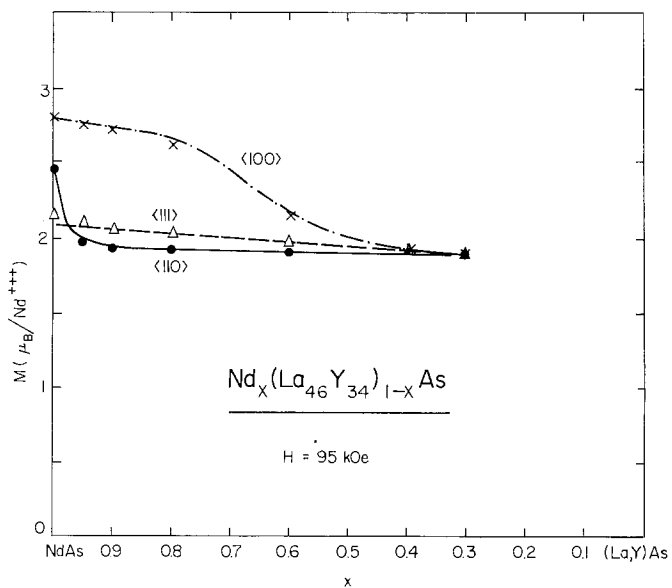


Fig. 37. Ordered moment for  $\text{Nd}^{3+}$  in diluted NdAs at  $H = 95 \text{ kOe}$ .

In order to elucidate the question of anisotropic exchange we have performed dilution experiments on NdAs by mixing it with YAs. The observed ordered moments are plotted in fig. 37. Typically, for a compound with a large anisotropic exchange, only the moments along the “easy” axis are affected at first by dilution. Diluting renders the compound isotropic – this means that the anisotropic exchange vanishes rapidly, whereas the Heisenberg isotropic part of the exchange varies only linearly with the concentration of the dilutant. At the same time the ordered moment is in all cases well below the free-ion value, again due to reshaping of the ion by hybridization.

2.2.1.2. *NpN, NpP, NpAs, NpSb, NpBi*. There are two distinctly marked periods in the research on neptunium pnictides, the pioneering work at Argonne National Laboratories in the years 1970–1974 on powdered samples and the second generation of experiments after 1984, when single crystals became available. The admirable work done at Argonne comprises Mössbauer and neutron studies, susceptibility measurements and, as we will see later, the highly valuable distortion measurements by X-ray diffraction. Aldred et al. (1974) give a complete survey of these efforts – on the whole the results still remain valid. The results as accepted today are summarized in table 10 and will be discussed in the following.

*NpN*. De Novion and Lorenzelli (1968) reported on ferromagnetism in *NpN*, detected by susceptibility measurements. In order to explain their inverse susceptibility curves, they had to rely on a modified Curie–Weiss law, which means they had to add a constant susceptibility,  $\chi_0 = 400 \times 10^6$  emu, to the Curie–Weiss susceptibility. However, measurements reported by Aldred et al. (1974) show a straight linear dependence of the inverse susceptibility on temperature, which means that for a clean sample the simple Curie–Weiss law holds. This should be a warning against overly detailed interpretations of results if the sample quality is not completely assured.

The measured effective moment is slightly lower than the free-ion value. Aldred et al. (1974) report  $2.5\mu_B$  as compared to an expected value of  $2.87\mu_B$ . Lam (1972) measured the magnetic moments versus applied field. Unfortunately the available fields were too low to reach saturation of the sample – the magnetic moment at the

TABLE 10  
Magnetic data of neptunium pnictides.

	Order <sup>a</sup>	$T_C/T_N$	$\Theta_p$	$\mu_{\text{eff}}$	$\mu_{\text{order}}$	$\mu_{130\text{ kOe}}$	Mag. axis
NpN	ferro	87	86	2.52	1.38	0.9	$\langle 111 \rangle$
NpP	AF, LW	120–75	104	2.85	2.2		$\langle 100 \rangle$
	AF 3+3–	74–0					
NpAs	inc. $1k$	172–155	190	2.82	2.5		$\langle 100 \rangle$
	com. $4+4-1k$	154–138					
	AFI $3k$	138–0					
NpSb	AFI $3k$	202	150	2.3	2.56		$\langle 100 \rangle$
NpBi	AFI $3k$	192.5			2.5		$\langle 100 \rangle$

$\text{Np}^{3+}$ :  $gJ = 2.57$ ,  $g[J(J+1)]^{1/2} = 2.87$ .

<sup>a</sup>LW: longitudinal wave, inc: incommensurate, com: commensurate.

maximum field was about  $0.9\mu_B$ . This value is much lower than the results of neutron scattering, which yield an ordered moment of  $1.4\mu_B$ , a value which is definitely below the free-ion value,  $gJ = 2.57$ . There is a considerable moment wash-out due to hybridization (see below).

The distortions measured by Mueller et al. (1973b) below the Curie temperature are rhombohedral, which means that  $\langle 111 \rangle$  is the easy axis. As is argued by Lander and Mueller (1974), the ferromagnetic part of the exchange interaction, which is anisotropic, favours the  $\langle 111 \rangle$  axis.

*NpP*. Neutron and Mössbauer studies by Lander et al. (1972a, 1973b) and Lam et al. (1973) yielded the following results:

Between 120 and 74 K *NpP* is antiferromagnetic and the moments are arranged parallel to the  $\langle 100 \rangle$  direction with a longitudinal sinusoidal modulation. Below 74 K the moments become commensurate with the lattice, with a tendency towards a  $3+3-$  structure. The squaring of the sinusoidal function is still incomplete at 4.2 K, leaving two different Np-moments of 2.4 and  $1.8\mu_B$ .

Mueller et al. (1973a) measured a tetragonal distortion (in accordance with the  $\langle 100 \rangle$  spin direction) below 74 K, but no distortion in the longitudinal wave region (between 120 and 74 K).

*NpAs*. Most studies have concentrated on distortion measurements and on neutron diffraction studies (Mueller et al. 1973b, Lam et al. 1973, Lander and Mueller 1974). *NpAs* orders antiferromagnetically at 175 K. At this temperature a tetragonal distortion sets in, but at about 140 K the structure transforms back to cubic (see fig. 38). Aldred et al. (1974) claim that just below 174 K a commensurate  $4+4-$  spin structure exists in which the moments are oriented along  $\langle 100 \rangle$ , in agreement with the tetragonal distortion. Below 140 K, down to zero temperature, a type I structure is found in, at first sight, disagreement with the absence of distortion (the structure remains cubic). In between these two structure regions, i.e. from  $T = 155$  to 140 K, the two structures coexist. The magnetization measurements as a function of temperature

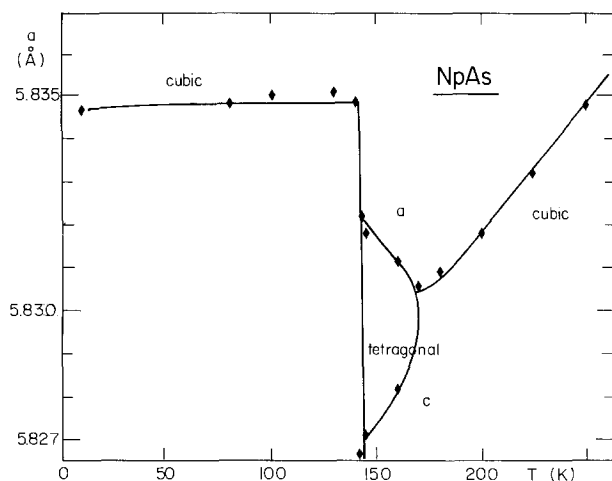


Fig. 38. Lattice distortion versus temperature of *NpAs*, reproduced from Aldred et al. (1974).

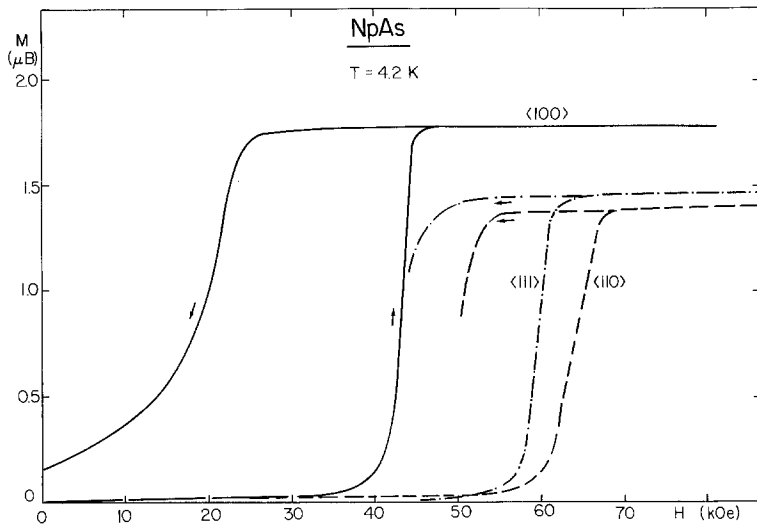


Fig. 39. Magnetic moment versus applied magnetic field of NpAs along the three main axes.

show peaks at the transitions. No magnetic saturation was obtained, since the applied fields were too low.

*NpSb.* Mueller et al. (1973b) and Lam (1972) found antiferromagnetism of type I below 205 K. No distortion was detected by Mueller et al. (1973b). The effective number of magnetons is close to the free-ion value. Samples were difficult to prepare. The authors found no explanation for the absence of distortions.

The influence of the CEF on the magnetic properties of NpP was studied theoretically for all pnictides by Lam and Fradin (1974). The state of the art of powder measurements was summarized by Lander (1978). High-field powder measurements on NpAs were reported by Blaise et al. (1983). Measurements on powder of highly anisotropic compounds do not make sense, although the authors claim that they were able to bring the samples into a ferromagnetic state – a conclusion which turned out to be wrong. The observed reduction of the ordered moment was theoretically explained by Lam and Ellis (1985), based on a hybridization mechanism – a theory which still holds today. Mössbauer spectroscopy on NpSb by Sanchez et al. (1988) could be performed with no restrictions on the powdered samples.

*Results of single crystal measurements.* In 1984 the first single crystals of NpAs became available. Figure 39 shows the magnetizations measured at 4.2 K in high fields by Rebizant et al. (1984). They are highly anisotropic.  $\langle 100 \rangle$  is the easy axis. The full magnetic moment, as derived from neutron diffraction, is even at 90 kOe not obtained. Figure 4 in the paper by Rebizant et al. (1984) provides another proof that the  $\langle 100 \rangle$  moment found at 4.2 K cannot correspond to a ferromagnetic spin arrangement. In fact, some kind of intermediate spin structure must be induced, as is indicated in a tentative magnetic phase diagram by Rebizant et al. (1984), given in fig. 40.

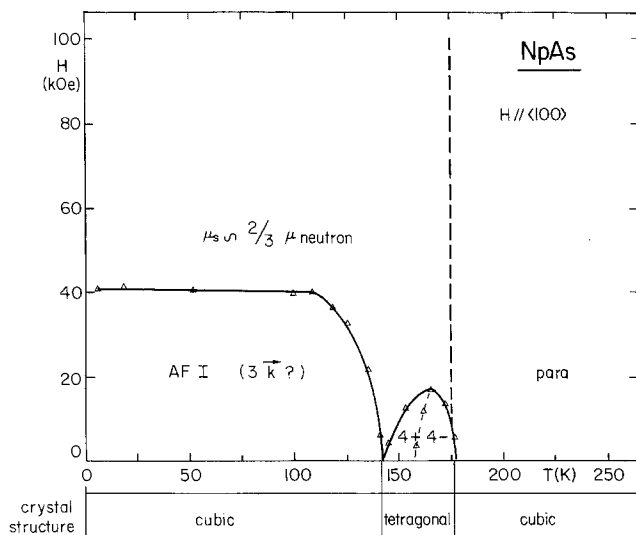


Fig. 40. Tentative magnetic phase diagram of NpAs.

Subsequent neutron diffraction experiments allowed an exact determination of the complete magnetic phase diagram of NpAs, which is reproduced in the contribution by Lander (ch. 117) in this volume. The detailed results were published by Burlet et al. (1986a, 1987a, 1988). In the absence of an external field one finds the following structures:

- 172–155 K: incommensurate single- $k$
- 154–138 K: commensurate  $4+4-$  single- $k$
- 138–0 K: type I  $3k$

Multi- $k$  structures result from competition of anisotropic exchange with single-ion (CEF) anisotropy. The  $3k$  type I structure does not induce a noticeable distortion, as was observed experimentally by Mueller et al. (1973b). At low temperatures the  $3k$  type I structure transforms into a ferrimagnetic phase under the influence of an applied field: one component perpendicular to the field is of type I antiferromagnetism and one component is first aligned ferromagnetically along  $\langle 100 \rangle$  and then rotates towards the  $\langle 110 \rangle$  direction. This explains why the magnetization observed by Rebizant et al. (1984) does not correspond to the full moment. A complete analysis of the magnetic phase diagram for higher temperatures is given by Burlet et al. (1988). Mössbauer studies (Potzel et al. 1987) confirmed the neutron results. Critical scattering experiments are reported by Rossat-Mignod et al. (1990) and Jones et al. (1991).

NpP crystals of suitable size for neutron experiments are not yet available. Magnetization measurements as a function of the field directions could be performed (Mattenberger et al. 1990b), however, and a tentative magnetic phase diagram was produced. As in the case of NpAs, the magnetic moments are highly anisotropic and  $\langle 100 \rangle$  is the easy axis. High applied magnetic fields induce a ferrimagnetic structure.

NpSb was found to be a type I  $3k$  antiferromagnet (Sanchez et al. 1988), which is, of course, the explanation for the absence of distortions. The same structure was found for NpBi (Sanchez et al. 1991). The triple- $k$  structure of NpSb can be broken into a collinear structure just below  $T_N$  with high magnetic fields (Sanchez et al. 1988).

$NpSb_xTe_{1-x}$  and  $NpAs_xSe_{1-x}$ . Mixed crystals of  $NpSb_xTe_{1-x}$  (Sanchez et al. 1990) and  $NpAs_xSe_{1-x}$  (Mattenberger et al. 1990a, 1992) were grown, and their magnetic properties were determined by magnetization measurements as well as by Mössbauer and neutron diffraction experiments. An addition of 10% or more of the chalcogen changes the antiferromagnets into ferromagnets. At the same time the magnetization axis changes from  $\langle 100 \rangle$  to  $\langle 111 \rangle$ , which means, of course, that the anisotropic ferromagnetic exchange is along  $\langle 111 \rangle$  (as found in the nitride) and, therefore, due to hybridization. If we add only 5% of the chalcogen, the system is in a kind of frustrated state. The complete magnetic phase diagram of  $NpAs_{0.95}Se_{0.05}$  is contained in Lander's contribution (ch. 117) in this volume. The sample is antiferromagnetic between 175 and 147 K, and, thereafter, ferromagnetic until 131 K. Below that temperature we find a novel ferrimagnetic spin structure with the easy axis close to  $\langle 110 \rangle$ . This spin structure results from the superposition of the two antiferromagnetically ordered Fourier components (moment  $2.15\mu_B$ ) and the one ferromagnetically ordered component (moment  $0.78\mu_B$ ) along the three cubic main axes. The situation is very similar in the case of  $NpSb_{0.95}Te_{0.05}$ . To our knowledge this is the first time that a multi- $k$  structure with unequal Fourier components was observed. Not only is the exchange anisotropic, but the moments along different directions are of different size.

2.2.1.3. *PuN, PuP, PuAs, PuSb, PuBi*. Table 11 shows the available data on the magnetic properties of Pu pnictides, taken from Lam et al. (1969), Raphael and de Novion (1969a), Lam (1972), Blaise et al. (1973), Lander and Lam (1976), Lander and Reddy (1976), Lander (1981), Cooper et al. (1983a), Boeuf et al. (1984), Burlet et al. (1984, 1987b, 1988) and Mattenberger et al. (1986b). We have taken the usual liberty

TABLE 11  
Magnetic data of plutonium pnictides.

	Order <sup>a</sup>	$T_C/T_N$	$\Theta_p$	$\mu_{\text{eff}}$	$\mu_{\text{order}}$	$\mu_{130\text{ kOe}}$	Mag. axis
PuN	AF (?)	13 (?)	-200 (?)	1.1 (?)	<0.25		?
PuP	ferro	126	126	1.06	0.77	(neutron)	$\langle 100 \rangle$
					0.62	(magn.)	$\langle 100 \rangle$
PuAs	ferro	129	129	1.0	0.67	(neutron)	$\langle 100 \rangle$
					0.58	(magn.)	$\langle 100 \rangle$
PuSb	LW-AF	85-69	85	1.0	0.74	(neutron)	
	ferro	<69			0.75	(Mössb.)	$\langle 100 \rangle$
					0.67	(magn.)	
PuBi	AF $k=3/13$	57	?	0.8	0.5	(neutron)	$\langle 100 \rangle$
					0.61	(magn.)	$\langle 100 \rangle$

$\text{Pu}^{3+}$ :  $gJ = 1.03$ ,  $g[J(J+1)]^{1/2} = 1.22$ .

<sup>a</sup>LW: longitudinal wave.

in just listing the most probable values. There seems to be a tendency towards anti-ferromagnetism on going from the nitride to the bismuthide. The paramagnetic as well as the ordered moments are distinctly below the values for the free trivalent Pu ion. Yet, plutonium is no doubt in the trivalent state for all these compounds. At all temperatures we thus have a moment wash-out due to hybridization. The magnetic axis is the  $\langle 100 \rangle$  direction. The crystal field would favour the  $\langle 111 \rangle$  axis. The anisotropies observed in the plutonium pnictides are caused by anisotropic exchange forces rather than by the interaction of the crystal electric field. In the following sections we discuss the compounds in detail.

*PuN.* Raphael and de Novion (1969a) found that PuN follows a modified Curie–Weiss law, with a rather important  $\chi_0 = 280 \times 10^{-6}$  emu/mol contribution. The paramagnetic Curie temperature is very large,  $\Theta_p = -200$  K. At 13 K the authors find a maximum of the susceptibility, which they associate with a transition to anti-ferromagnetism. This transition was not observed in electrical measurements. Boeuf et al. (1984) could find no order in PuN with neutron diffraction experiments that had a lower limit of  $\approx 0.25\mu_B$ .

It appears that the plutonium moment is heavily quenched by hybridization. This effect was found earlier in PuC samples as a function of the sample quality. In section 2.2.2 we will see that it occurs in many substances. As a matter of fact, PuN shows exactly the same features as NpTe. Finally, the need to analyze the susceptibility curves with an additional parameter,  $\chi_0$ , often indicates a questionable sample quality. In our opinion, the magnetic properties of PuN are not yet convincingly explained. The possibility that PuN shows the same features as the Pu chalcogenides (see below) cannot be excluded. This would give a logical explanation for the high value of  $\chi_0$  (half the actually measured susceptibility value) which is needed to “construct” a Curie–Weiss law in a limited temperature range.

*PuP.* PuP is a well-studied ferromagnet. Again, the susceptibility measurements by Lam et al. (1969) (fig. 41) have to be modified by the addition of a constant susceptibility,  $\chi_0 = 190 \times 10^{-6}$  emu/mol, in order to get a Curie–Weiss law. The authors find a saturation magnetization of  $0.42\mu_B$  for their polycrystalline samples. Since we know today that the magnetization of PuP is highly anisotropic, this value would correspond to about  $0.5\mu_B$  along the easy axis. The authors find that the magnetic moment versus temperature does not follow a Brillouin function. There are two reasons for this: the measurements were not done along the easy axis and the exchange is not isotropic, which is a necessary condition for the validity of the molecular-field approximation. Lander and Lam (1976) performed neutron diffraction experiments and found a moment of  $0.77\mu_B$ . They attribute the large difference between the “magnetic” and the “neutron” moment to conduction-electron polarization, the moments of the conduction electrons being antiparallel to the ionic moments. An admixture of higher states ( $J = \frac{7}{2}$ ) is observed. Polarized-neutron studies (Lander and Reddy 1976) showed unambiguously that Pu is in the trivalent state. A large anisotropy is observed – the moments are confined to the  $\langle 100 \rangle$  axis. This axis corresponds well with the tetragonal distortion observed by Mueller et al. (1979).

Further neutron studies (form factor) by Lander (1980) showed that the amount of  $J$ -mixing had been overestimated. The reduced moment observed for PuP has

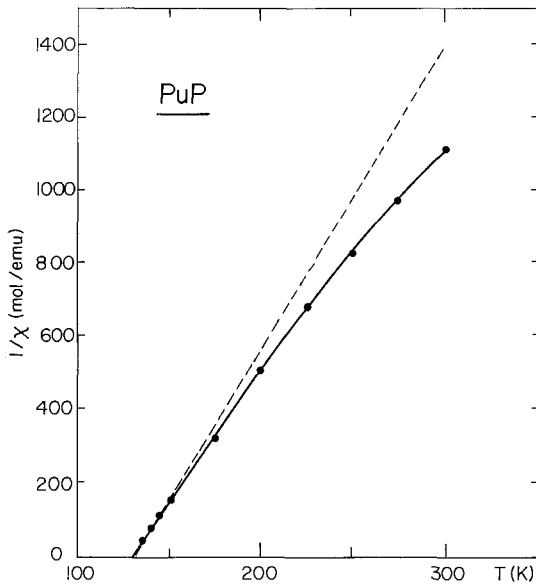


Fig. 41. Inverse molar susceptibility versus temperature of PuP, after Lam et al. (1969). The dashed line is calculated by addition of a constant susceptibility  $\chi_0 = 190 \times 10^{-6}$  emu/mol.

thus to be explained by hybridization. A theoretical approach along these lines was done by Lam and Ellis (1985).

Our own magnetization measurements on a small single crystal of PuP (fig. 42) gave some interesting results:

Along the easy  $\langle 100 \rangle$  axis the magnetic moment is actually  $0.62\mu_B$  per Pu ion. Thus the difference with the neutron value ( $0.77\mu_B$ ) is not appreciable, and the possible contribution of the conduction-electron polarization would be only  $0.15\mu_B$ , a reasonable value. The hysteresis loop is extremely broad. Due to large anisotropy the Bloch

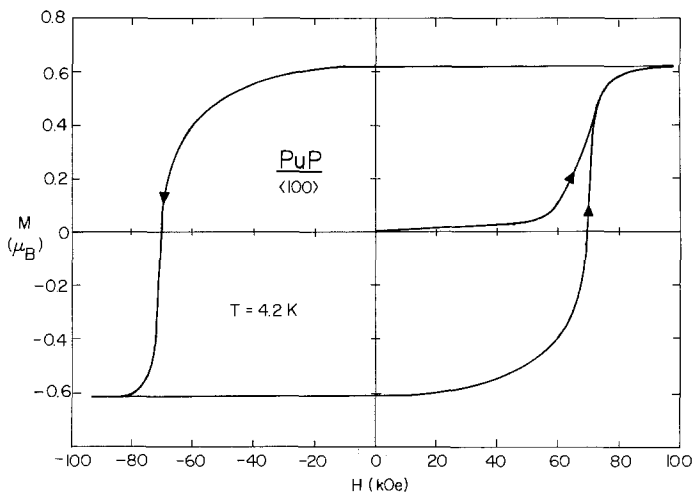


Fig. 42. Hysteresis loop of a small PuP single crystal, measured along the easy  $\langle 100 \rangle$  direction at 4.2 K.



walls are narrow. Experience shows that it is very difficult to get such samples in an unmagnetized state when cooling them down from room temperature. This fact may be one explanation for the observed  $\chi_0$  values, which would actually just reflect some magnetic remanence of strain-induced magnetic moments.

*PuAs.* We again encounter ferromagnetism along  $\langle 100 \rangle$ . Blaise et al. (1973) had to use a modified Curie–Weiss law ( $\chi_0 = 330$  emu/mol) to explain their susceptibility measurements. Our own experiments (Spirlet et al. 1983) on single crystals showed no appreciable temperature-independent susceptibility. Blaise et al. (1973) find that the magnetic moments versus temperature follow the Brillouin function for  $J = \frac{5}{2}$ , a surprising result (see arguments in the section on PuP).

Ferromagnetism along  $\langle 100 \rangle$  was confirmed by neutron diffraction (Burlet et al. 1984). The neutron results yield highly anisotropic exchange forces. The neutron moments reported are  $0.75\mu_B$  (Rossat-Mignod et al. 1985a). Magnetization measurements on single crystals (Mattenberger et al. 1986b) show a Curie–Weiss law with an effective number of magnetons close to one. The magnetic moments are strictly confined to the easy  $\langle 100 \rangle$  direction, while the moments along the other axes are merely the projections of the  $\langle 100 \rangle$  moment (e.g. the moment along  $\langle 111 \rangle$  equals the moment along  $\langle 100 \rangle$  divided by  $\sqrt{3}$ ). The saturation moment is  $0.67\mu_B$ , close to the neutron moment. Thus the influence of conduction-electron polarization, if present, is quite small in PuAs.

*PuSb.* At low temperatures PuSb is ferromagnetic. Earlier susceptibility measurements (Lam 1972) yielded  $\chi_0 = 200 \times 10^{-6}$  emu/mol, but recent measurements on single crystals (Vogt and Mattenberger 1987) show that  $30 \times 10^{-6}$  emu/mol is an upper limit. Again the sample quality seems to be the reason for these differences. The effective number of magnetons equals one, still much below the free-ion value. The magnetic moment measured on powdered samples by Lam (1972) equals  $0.57\mu_B$ , which would correspond to  $0.70\mu_B$  along the easy axis if the crystallites were completely randomly distributed. From magnetization measurements near the transition temperatures (fig. 2 in Cooper et al. (1983a)) we could conclude that below 85 K to about 70 K PuSb is antiferromagnetic, and it becomes ferromagnetic below 70 K. Magnetization measurements on single crystals show that, as for PuP, the  $\langle 100 \rangle$  axis is the moment direction. The anisotropy is complete and the magnetic moments cannot, with experimentally available fields, be rotated out of the  $\langle 100 \rangle$  direction. The saturation value is  $0.67\mu_B$  per Pu ion – distinctly below the free-ion value – (Mattenberger et al. 1986b) due to a hybridization mediated interionic interaction. The delocalization is rather modest.

Neutron diffraction experiments (Burlet et al. 1984, 1988) gave a much more precise insight in the magnetic properties of PuSb. Figure 43 (taken from Burlet et al. (1984)) shows the complete magnetic phase diagram of PuSb. Indeed, just below the Néel temperature there exists an antiferromagnetic region which, however, can be destroyed by modest experimental fields. For more details consult the paper by Burlet et al. (1984). The neutron moment is measured as  $0.74\mu_B$ , again close to the “magnetic” moment but far below the free-ion value.

Experiments by Lander et al. (1984) (magnetization densities) confirm that the anisotropic interactions are overwhelming the natural  $\Gamma_7$  crystalline electric field

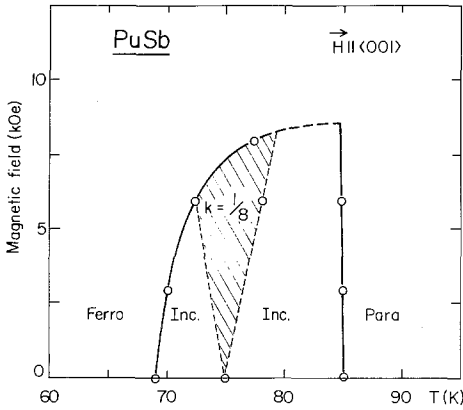


Fig. 43. Magnetic phase diagram of PuSb (Burlet et al. 1988).

ground state. Form factor measurements (Lander et al. 1985) give further evidence for the anisotropic exchange.

Mössbauer measurements yield a magnetic moment of  $0.75\mu_B$ , the same value as obtained from neutron diffraction experiments. Since the “magnetic” value is unambiguously  $0.67\mu_B$ , the contribution of the conduction electrons should be about  $0.08\mu_B$ .

Magnetic excitation studies (Lander et al. 1986) show that the 5f electrons are predominantly localized; however, hybridization and exchange effects cannot be neglected. Neutron elastic scattering experiments (Burlet et al. 1987c) near  $T_N$  reveal magnetic correlations causing planar ordering in the (100) planes with all the moments aligned ferromagnetically – a further indication that the 5f electrons are hybridizing with band electrons.

*PuBi*. Mattenberger et al. (1986b) found PuBi to be metamagnetic below 65 K, i.e. antiferromagnetic in the absence of an external field. Experimentally achievable fields can turn the sample into a ferromagnet. Figure 44 shows how the transition fields depend on temperature.

The easy axis is the <100> direction, the saturation moment at 4.2 K is  $0.61\mu_B$ . The effective number of magnetons is  $0.8\mu_B$  – both values way below the free-ion value. Neutron diffraction studies showed that the antiferromagnetic structure is a quite unusual modification of a  $4+4-$  structure. Actually,  $k = \frac{9}{13}$  fits the experimental findings best (Burlet et al. 1987c) and one finds a single- $k$  commensurate structure with the sequence  $4+, 4-, 5+, 4-, 4+, 5-$ .

Figure 45 shows the magnetic phase diagram as determined by neutron diffraction and magnetization experiments. The transition at  $T_N$  seems to be tricritical, with the coexistence of antiferro-, ferro- and paramagnetism. The ordered moment of PuBi as determined by neutron diffraction is reported to be as low as  $0.5\mu_B$  – a value which does not fit into the general scheme of the Pu pnictides.

*PuSb<sub>x</sub>Te<sub>1-x</sub>*. PuTe shows temperature-independent paramagnetism over a wide range (see below). A study of the pseudobinary series PuSb–PuTe would seem to be of interest.

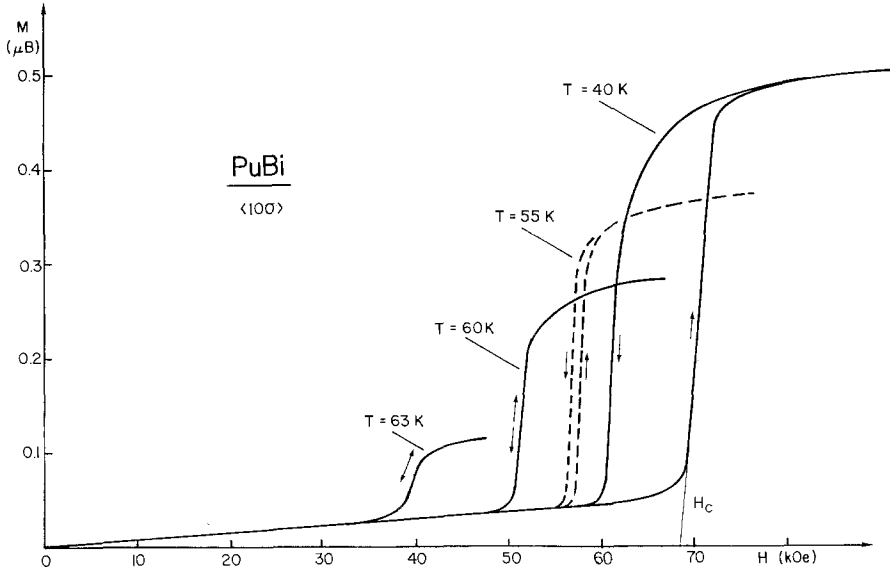


Fig. 44. Magnetic moment versus applied magnetic field of PuBi at several temperatures.

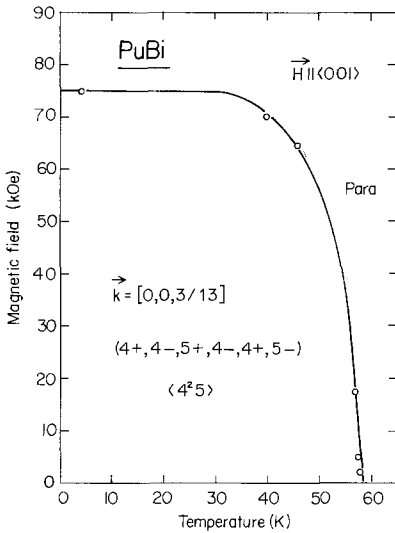


Fig. 45. Magnetic phase diagram of PuBi, after Bulet et al. (1987c).

Figure 46 shows the inverse susceptibility versus temperature for several compositions (Mattenberger et al. 1986a, Vogt and Mattenberger 1987). The Curie–Weiss curve as observed in PuSb, begins to develop a downward curvature. An analysis with a modified Curie–Weiss law yields increasing values for  $\chi_0$ , ending with the extrapolated value  $260 \times 10^{-6}$  emu/mol for PuTe. The Néel temperatures and paramagnetic Curie temperatures decrease systematically. The magnetic phase diagram of PuSb changes drastically with the substitution of 5% Te (Mattenberger et al. 1986a).

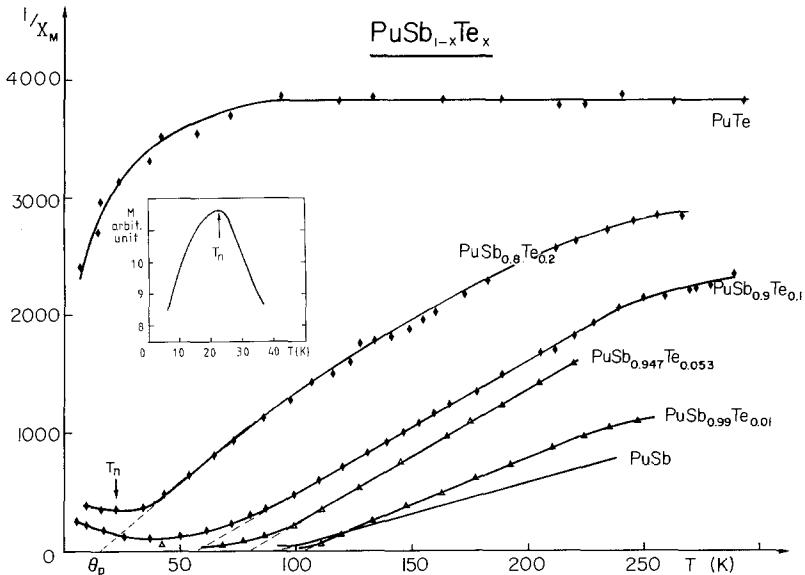


Fig. 46. Inverse molar susceptibility versus temperature for several compositions of  $\text{PuSb}_{1-x}\text{Te}_x$  (Mattenberger et al. 1986a).

Mössbauer experiments (Sanchez et al. 1987) confirm the change of the magnetic structure (from ferro- to antiferromagnetism and absence of order for the Te-rich samples) and a progressive collapse of the Pu moment.

### 2.2.2. Strong hybridization

2.2.2.1. *UN, UP, UAs, USb, UBi*. Since the uranium monopnictides and monochalcogenides are the only actinide compounds of which samples are readily available, and since they can be handled without any special precautions, they have been explored in much detail over the past 40 years. The first summary of the present state of knowledge is a survey up to the year 1970 by Kuznietz (1971). A more extended publication by Lam and Aldred (1974) carefully collects all the results up to 1972. A later summary given by Lander (1978) covers data up to 1977. The following discussion concentrates on the more recent results.

Some papers dealing more generally with uranium pnictides and chalcogenides, should be mentioned beforehand. Rossat-Mignod et al. (1979a) in their effort to understand the neutron and magnetization data on a mixed crystal  $\text{USb}_{0.9}\text{Te}_{0.1}$ , have for the first time used the model of multi- $k$  structures for actinide compounds. This revolutionary concept led thereafter to the understanding of many phenomena in actinide and lanthanide systems, as we have already mentioned in preceding sections. Lander (1980) demonstrates in a very extended survey that neutron diffraction experiments are generally a very powerful tool for research on actinide compounds. Siemann and Cooper (1980a) give theoretical evidence for the general fact that for ferromagnetic compounds the easy axis is always the  $\langle 111 \rangle$  direction.

TABLE 12  
Magnetic data of uranium pnictides and chalcogenides.

	Order	$T_C/T_N$	$\Theta_p$	$\mu_{\text{eff}}$	$\mu_{\text{order}}$	Mag. axis	Structure
UN	AF long range	53.1	-247	2.66	0.75	$\langle 100 \rangle$	AF I $1k$
UP	AF	125/22	35	3.56	1.9	$\langle 100 \rangle$	AF I $1k$
						$\langle 110 \rangle$	AF I $2k$
UAs	AF	127/63	30	3.4	1.9/2.2	$\langle 100 \rangle$	AF I $1k$
						$\langle 110 \rangle$	AF IA $2k$
USb	AF	247	140	3.64	2.85	$\langle 111 \rangle$	AF II $3k$
						( $\langle 100 \rangle$ )	
UBi	AF	28	105	4.1	3	$\langle 111 \rangle$	
US	ferro	180	180	2.35	1.7	$\langle 111 \rangle$	
USe	ferro	160	160	2.4	2.0	$\langle 111 \rangle$	
UTe	ferro	104	105	2.6	2.2	$\langle 111 \rangle$	

$U^{3+}$ :  $gJ = 3.41$ ,  $g[J(J+1)]^{1/2} = 3.77$ .

Table 12 summarizes the magnetic properties of the uranium pnictides and chalcogenides. The antiferromagnetic exchange is becoming stronger with increasing lattice spacings (i.e. on going from the nitride to the bismuthide), the ferromagnetic exchange, on the contrary, is weakened.

The ordered moments of all compounds are distinctly below the free-ion value,  $gJ = 3.41$ . Apparently the 5f electrons are not completely localized and their magnetic moment is "washed out" by hybridization with valence or conduction electrons. This effect gets more pronounced with decreasing interatomic distances. The chalcogenides show a stronger tendency towards hybridization, probably due to their unbound valence electrons.

Let us now discuss the particular compounds in detail.

*UN*. Work done until 1972 is summarized in Lam and Aldred (1974). Very early results stem from Trzebiatowski et al. (1962). Dell and Albutt (1963) report on uranium nitrides, but not on the stoichiometric compound. The most decisive work is reported by Curry (1965). He found the correct Néel temperature of 52 K, a long-range anti-ferromagnetic order with moments along  $\langle 100 \rangle$  and a (greatly reduced) ordered moment of  $0.75\mu_B$ . Susceptibility measurements by Raphael and de Novion (1969a) yield the same Néel temperature. However, the very high value of  $\chi_0 = 500 \times 10^{-6}$  emu/mol they need in order to adjust their results to the modified Curie-Weiss law casts some doubt on their sample quality. NMR measurements (Kuznietz 1969) suggest that uranium is tetravalent in UN. Marples (1970) reports a negative expansion coefficient below  $T_N$ , which would be understandable if the long-range order was temperature dependent. Very reliable measurements of the susceptibility done on a single crystal are reported by DuPlessis and van Doorn (1977). They find a modified Curie-Weiss law, but  $\chi_0$  is as small as  $8 \times 10^{-6}$  emu/mol. The paramagnetic moment is  $2.66\mu_B$ , and the Néel temperature 53.1 K, below which the susceptibility is anisotropic, see fig. 47.

A theoretical analysis of the susceptibility curve and the value of the ordered moment would require a  $5f^2$  configuration in order to give an explanation of the

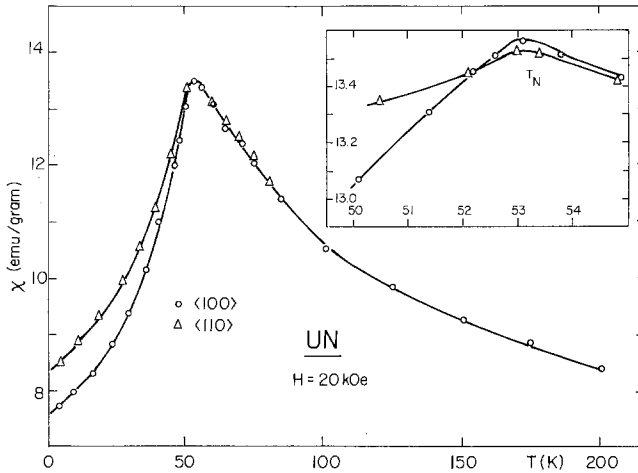


Fig. 47. Susceptibility versus temperature of UN (DuPlessis and van Doorn 1977).

experimental results on the basis of crystal-field splitting (Lemmer and Lowther 1978). The magnetic moment of UN depends linearly on the applied field up to 40 T (Schinkel and Troč 1978). Knott et al. (1980) find no measurable distortion, which is not necessarily compatible with the suggested spin structures – a multi- $k$  structure ought to be considered. Such a structure is possible, since large anisotropies were found in critical scattering experiments (Buyers et al. 1980). Pressure effects were searched for by Fournier et al. (1979).

*UP*. Neutron diffraction (Sidhu et al. 1966) and susceptibility measurements (Albutt et al. 1964, Trzebiatowski and Troč 1963) are relatively old, but still essentially correct. (Néel temperature 130 K, ordered moment  $1.72\mu_B$ , type I ordering.) NMR measurements (Scott et al. 1967) gave slightly different values and show a polarization of the 3s electrons. At about 23 K one observes (by neutrons or NMR) a jump of the magnetic moment without any visible change of the spin structure. This “moment jump” has intrigued many authors: neutron measurements by Sidhu et al. (1966) and Heaton et al. (1969), NMR experiments by Carr et al. (1969), thermal expansion measurements (giving an anomaly at 22 K) by Marples (1970), measurements of the volume change by Steinitz and Grunzweig-Genossar (1979), the lack of a distortion (Knott et al. 1980). A theory was presented by Long and Wang (1971) and Shenoy et al. (1972), which should explain the moment jump. All these efforts found their natural explanation in a transition from single- $k$  to double- $k$  type I antiferromagnetism, as observed and described by Burlet et al. (1985). Nowadays we know that UP is antiferromagnetic of type I between 125 and 22.45 K, with a collinear single- $k$  spin structure. The moment is  $1.7\mu_B$  along  $\langle 100 \rangle$ . Below 22.45 K the spin arrangement changes into a  $2k$  structure – the moments are thus along  $\langle 110 \rangle$ , with a magnitude of  $1.9\mu_B$ . The moment jump stems from the fact that the ionic moment is determined by the crystal-field splitting, which gives rise to an anisotropic response of the f electrons to an exchange field. Figure 48 shows the neutron patterns found in UP around 22.5 K (Burlet et al. 1985).

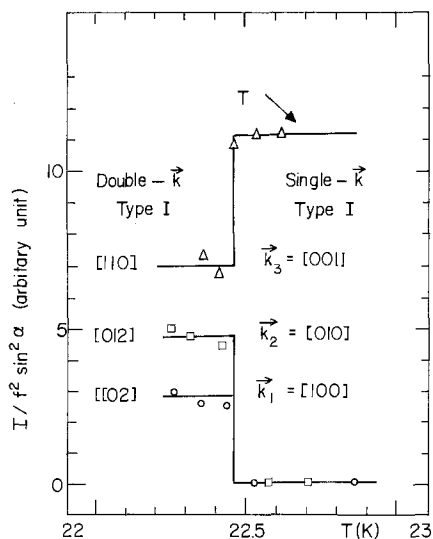


Fig. 48. The magnetic structure factor in UP in a magnetic field  $H = 25$  kOe applied along the  $\langle 100 \rangle$  direction, as a function of temperature (Burlet et al. 1985).

It seems interesting to investigate how the transitions in UP could be detected but not identified in susceptibility measurements. Such measurements are reported by Gulick and Moulton (1971) and Troč and Lam (1974) – the authors of the latter paper needed a temperature-independent additional susceptibility  $\chi_0 = 40 \times 10^{-6}$  emu/mol in order to fit their measurements into a Curie–Weiss law. Busch et al. (1979a) found on single crystals just a straightforward Curie–Weiss law between 130 and 1000 K, but the susceptibilities are anisotropic below the ordering temperature (fig. 49).

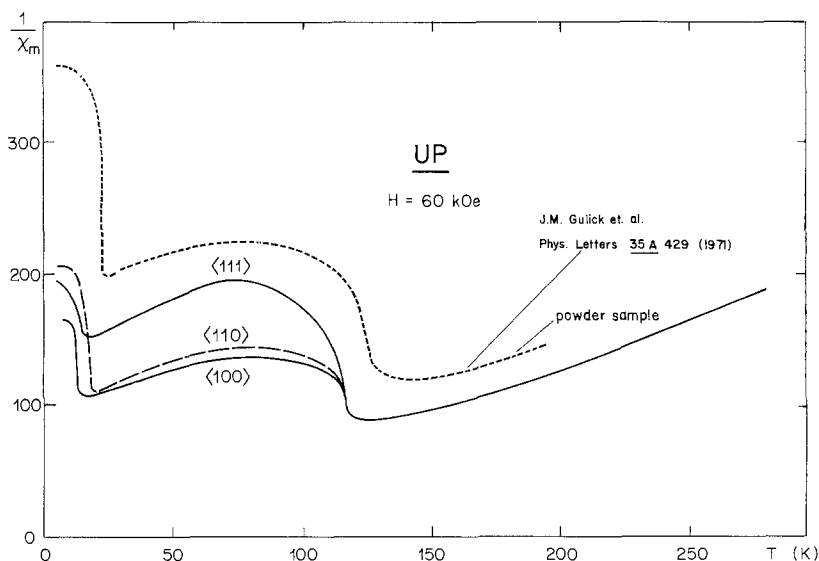


Fig. 49. Inverse magnetic susceptibilities of UP, measured on single crystals and powdered samples.

Precision measurements of the susceptibility by Matsui (1987) reveal some sample dependence. Measurements of the magnetic moment versus high applied fields on powder samples by Schinkel and Troč (1978) and on single crystals by Vogt et al. (1980) and Vogt (1989) show that the magnetization curves are highly anisotropic (fig. 50).

At fields above 100 K a spin structure with a net moment of about  $\frac{1}{3}$  of the full ordered moment is induced. The easy axis is, in accordance with the  $2\vec{k}$  structure, the  $\langle 110 \rangle$  direction. Since neutron measurements in such high fields are up to now not possible, only a tentative magnetic phase (fig. 51) is available.

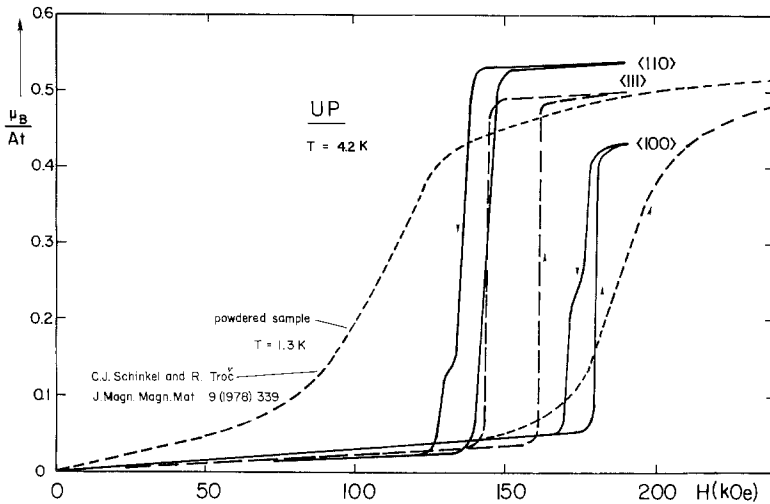


Fig. 50. Magnetic moment versus applied magnetic field of UP for powdered and single crystal samples.

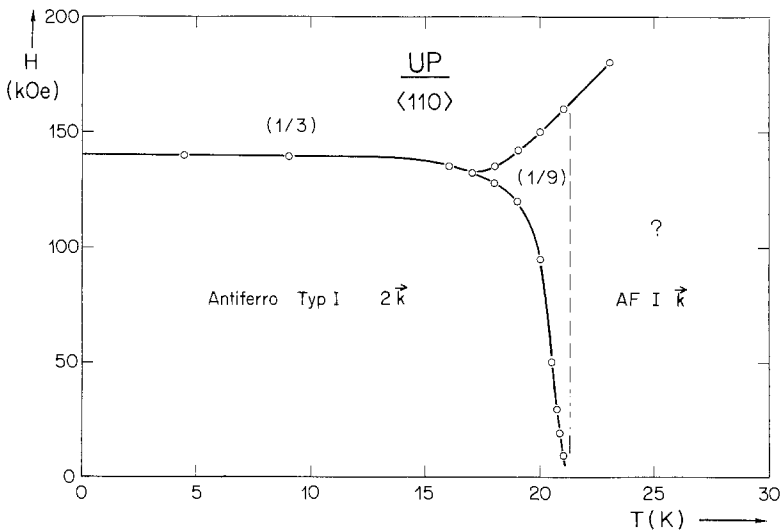


Fig. 51. Magnetic phase diagram of UP for fields applied along the  $\langle 110 \rangle$  axis.



Measurements of the Mössbauer effect (Shenoy et al. 1972), showing no  $J$ -mixing, and high-pressure X-ray experiments (Léger et al. 1986) complete the many investigations done on UP.

*UAs*. From the summary given by Lam and Aldred (1974) (including all references contained in it) we see that thanks to the work done at the Argonne National Laboratory, nearly all magnetic properties of *UAs* that can be explored on powder samples, were known by 1972: below  $T_N = 127$  K there is type I order with spins along the  $\langle 100 \rangle$  direction. At about 66 K the magnetic order changes to type IA and simultaneously a moment jump of the (ordered) magnetic moment is observed – the origin of which remained unexplained. Progress came only when single crystals were available.

Susceptibility measurements on powder samples (Troč and Lam 1974) and on monocrystalline samples (Busch and Vogt 1978) show very distinctly the transition at 66 K (see fig. 52). Up to 1000 K the Curie–Weiss law is strictly obeyed (Busch et al. 1979a). The anisotropy of the magnetic susceptibilities is very well marked. The transition at 66 K was further confirmed by neutron diffraction experiments (Lander et al. 1972b, Marples et al. 1975). There were various attempts to find distortions in *UAs*. Knott et al. (1980) and Lander and Mueller (1974) could not detect measurable distortions. Only recently a tetragonal distortion with  $c/a = 1.0002$  was identified for the type IA structure (McWhan et al. 1990), an indication of strong orbital contributions.

Lander (1978) discusses the problem of assigning a well-determined value to the ionization of the uranium ion. Magnetization measurements in extremely high fields on powdered samples (Schinkel and Troč 1978) could not improve the understanding of the magnetic properties of *UAs*. The magnetization depends critically on the orientation of the applied field (Busch and Vogt 1978), since intermediate spin

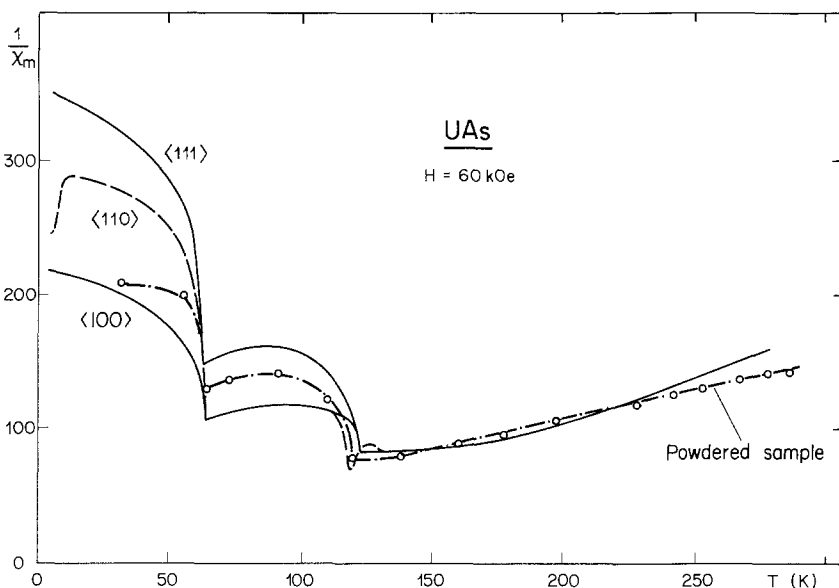


Fig. 52. Inverse magnetic susceptibility of *UAs* versus temperature as a function of crystal orientation, measured on field-cooled samples.

structures are induced. Busch and Vogt (1978) gave a first tentative magnetic phase diagram. Figure 53 demonstrates that the field dependence of the magnetization at various temperatures is very complex (Busch et al. 1979b). The magnetizations are anisotropic, without exceptions. In the induced ferrimagnetic phase,  $\langle 110 \rangle$  is the easy axis.

The tentative phase diagram is shown in fig. 54. By combining neutron diffraction experiments (Rossat-Mignod et al. 1980a, b, Shapiro et al. 1981, Sinha et al. 1980b, 1981) with the many measurements of the anisotropic magnetizations in medium and high fields (Vogt and Bartholin 1980, Rossat-Mignod et al. 1980a) it was possible to construct the complete magnetic phase diagram, as is shown in the contribution of Lander (ch. 117) in this volume. The general pattern in fig. 54 remains unchanged, but the neutron data now allow a detailed description of the spin structures.

The "moment jump" observed at 62 K, finds a simple explanation: above this temperature the moments are along the cube axis, below it they are along  $\langle 110 \rangle$  and since the moments depend on the direction of the field by means of anisotropic exchange forces, they are different for these two directions. The ferrimagnetic structure observed at high field and low temperature is the result of the moment component parallel to the field, which is flipped while the perpendicular components retain the type IA order. Various stacking sequences close to  $++-$  or  $++--++-$  have been found. A progressive flipping of the components could actually be observed by magnetization measurements in high fields (see fig. 55, taken from the paper of Rossat-Mignod et al. (1985a)).

The experimental findings for UAs can be explained by the so-called ANNNI (anisotropic next-nearest-neighbour interaction) model, which considers a strong Ising-like anisotropic planar coupling and weak interplanar couplings  $J_1$  and  $J_2$  between nearest and next-nearest planes. The resulting structures depend on the relative size of these couplings.

The phase transition near a possible Lifshitz point at 66 K was further studied by neutrons (Sinha et al. 1980a, Stirling et al. 1980).

The magnetic properties of UAs seem to be quite well understood today, except for the fact that a quantitative explanation for the reduced ordered moment does not yet exist.

*USb.* There are only a few magnetization measurements available – the earlier ones are summarized by Lam and Aldred (1974) and Lander et al. (1976). The magnetic moment depends linearly on an applied external field of up to 400 kOe (Schinkel and Troč 1978) in the ordered state. Measurements on a single crystal confirmed that the Curie–Weiss law is strictly obeyed between 300 and 1200 K. The effective number of magnetons is 3.64. A clear answer concerning the ionization of uranium is not possible. Further knowledge stems from different experimental techniques. From Mössbauer experiments the ordered moment was determined to be  $2.85\mu_B$  (Shenoy et al. 1972). Neutron diffraction experiments revealed antiferromagnetism of type I with moments along  $\langle 100 \rangle$  – which does not explain the absence of lattice distortions (Kuznietz et al. 1968). Neutron diffraction experiments on single crystals were very fruitful: elastic neutron cross section measurements show that uranium is trivalent with a  $\Gamma_8$  singlet ground state. The spins are oriented along  $\langle 100 \rangle$ , not along  $\langle 111 \rangle$ , which

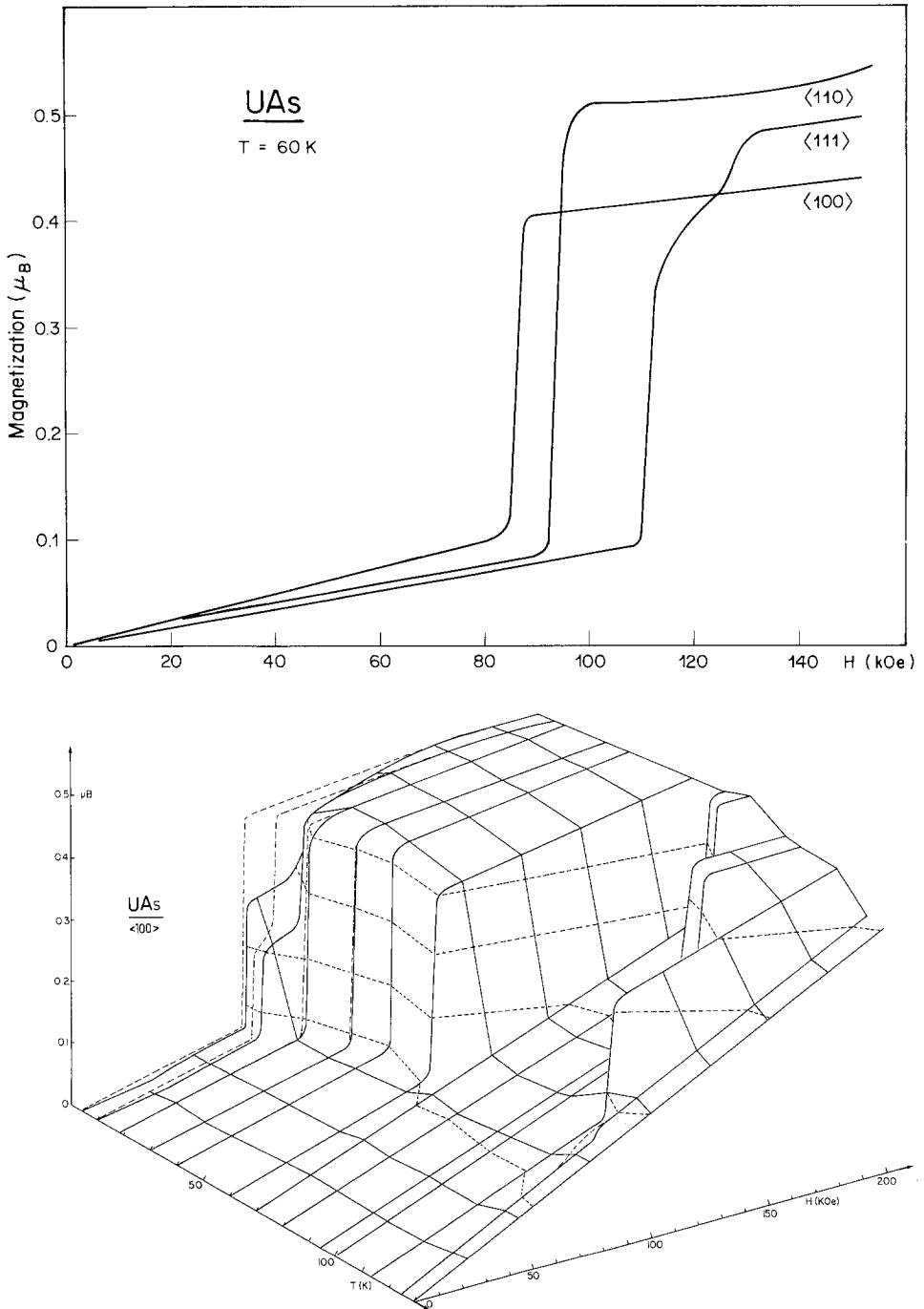


Fig. 53. Magnetic phase diagram of UAs for fields along the  $\langle 100 \rangle$  direction (lower part) and magnetic moments of UAs versus applied magnetic field at  $T = 60$  K (upper part).

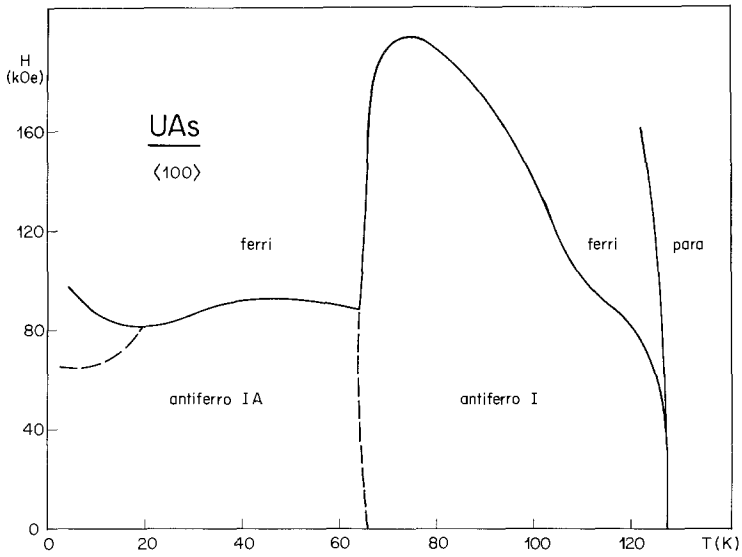


Fig. 54. Magnetic phase diagram of UAs for fields along  $\langle 100 \rangle$ .

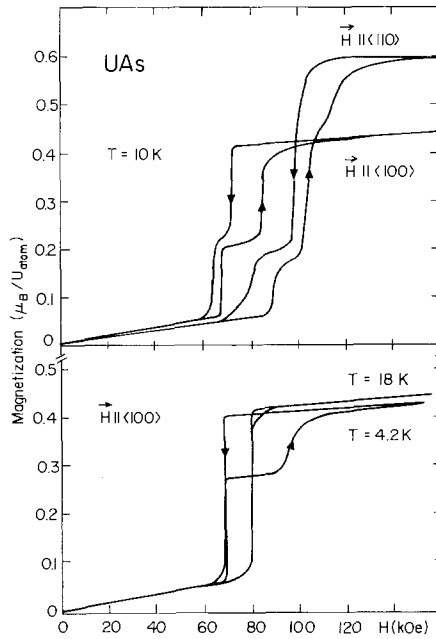


Fig. 55. Magnetization of UAs as function of a magnetic field applied along  $\langle 100 \rangle$  and  $\langle 110 \rangle$  (Rossat-Mignod et al. 1985a).

would be the direction preferred by the crystalline electric field (Lander et al. 1976). Trivalency was further confirmed by Lander (1975) (form factor measurements), Lander et al. (1976), Schinkel and Troč (1978) and Lemmer and Lowther (1978). Well-defined CEF eigenstates were observed.

Measurements of spin correlations (Lander et al. 1978) and collective excitations (Lander et al. 1979a, b, Hälg and Furrer 1984) revealed large anisotropies – the interactions are strong within the (100) planes and weak between the planes, in accordance with the ANNNI model. Optical measurements (Schoenes and Vogt 1978) suggest a non-integer number of 5f electrons and f–d hybridization.

The actual magnetic structure of USb turned out to be a triple-*k* type I structure – this was proven by the fact that the neutron patterns were not modified by an uniaxial stress of 1000 bar (Rossat-Mignod et al. 1980b). The moments in USb are thus along  $\langle 111 \rangle$ , the same direction as the crystal-field-only theory suggests. The crystal structure remains cubic upon ordering, but a volume expansion can be observed (Knott et al. 1980). Based upon this triple-*k* antiferromagnetic structure the magnetic excitations observed in USb (Hälg and Vogt 1985) can be understood.

We should remark that magnetization (or susceptibility) measurements have, in the case of USb, added relatively little to the knowledge of the magnetic properties, which are, however, quite well understood today.

*UBi*. No new results are known since the ones discussed by Lam and Aldred (1974) and Kuznietz et al. (1968). This is probably due to the fact that UBi is very unstable, even if protected from air. Single crystals disintegrate within a short time.

#### 2.2.2.2. *US, USe, UTe*

*US*. Since single crystals of US were already available in 1968, the knowledge of its magnetic properties was almost complete by 1972, and is summarized by Lam and Aldred (1974), where earlier references may be found. Below about 180 K US is undoubtedly a ferromagnet with the magnetic moment oriented along the  $\langle 111 \rangle$  direction (Marple 1970). The neutron moment determined with polarized neutrons, is  $1.7\mu_B$  (Wedgwood 1972), the same as determined in Mössbauer studies (Shenoy et al. 1972).

The moment obtained by magnetization measurements (Shenoy et al. 1972) is only  $1.55\mu_B$  (or  $1.57\mu_B$ , found by Tillwick and De V. du Plessis (1976a)). The difference is explained by antiparallel polarization of the conduction electrons.

Tillwick and DuPlessis (1976a, b) have performed some very careful magnetization measurements on newly grown single crystals.

Figure 56 shows the normal patterns of a ferromagnet. Due to the relatively low available fields, saturation is not complete. The hysteresis loop is not abnormally broad. Figure 57 shows clearly that  $\langle 111 \rangle$  is the easy axis and that the spins are confined rigorously to this axis (cosine law). Neutron diffraction experiments (scattering of thermal neutrons) by Lander et al. (1990b, 1991) allowed the determination of the first-order anisotropy constant, which is among the largest known today.

The magnetic properties of US depend strongly on pressure (Huang et al. 1979) or on fission damage (Matsui et al. 1983). Sample dependence was found by Aldred and Troč (1983) in magnetic studies of the critical behaviour near the Curie temperature.

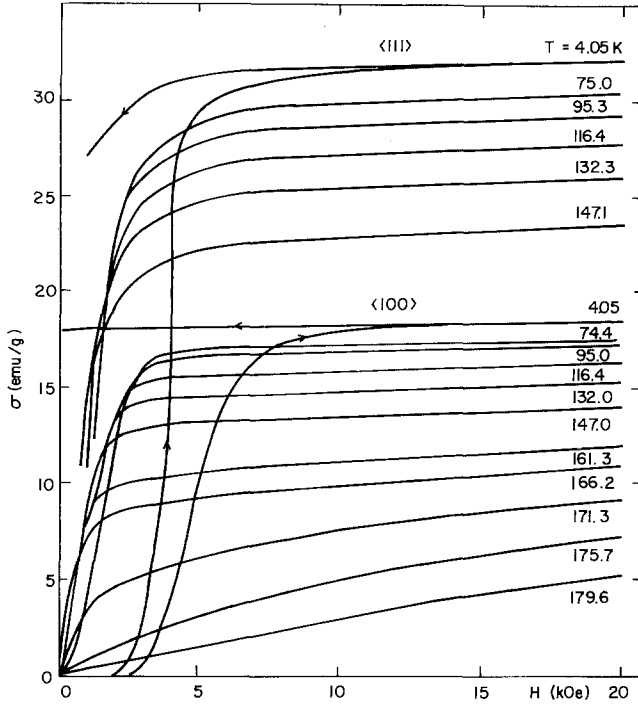


Fig. 56. Magnetization of US versus applied field  $H$  measured along the  $\langle 100 \rangle$  and  $\langle 111 \rangle$  direction at different temperatures (Tillwick and DuPlessis 1976b).

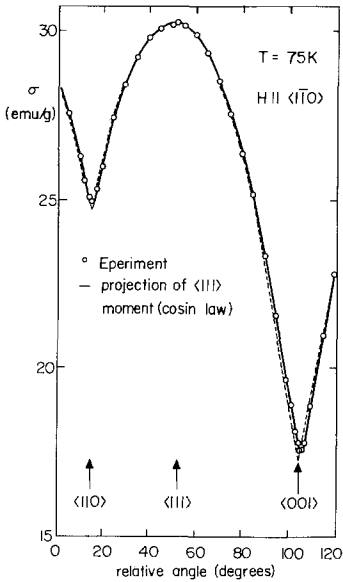


Fig. 57. Magnetization of a US crystal as a function of the relative angle in the  $\langle 110 \rangle$  plane, at 75 K. The open circles denote the experimental points obtained when turning the applied field of 20 kOe in the direction of increasing angle. The dashed "theoretical" line is computed on the assumption that the spins are constrained to the nearest  $\langle 111 \rangle$  direction, so that only the cosine component of the magnetization is measured away from the  $\langle 111 \rangle$  direction (Tillwick and DuPlessis 1976a).

Even though the “macroscopic” magnetization can be understood, we must not overlook the fact that the paramagnetic moment and the ordered moment are far from the values of the trivalent (or tetravalent) uranium ion. Lam and Ellis (1985) stress in a theoretical paper the importance of the hybridization of the 5f electrons with other electrons in the valence or conduction bands. Only if we accept that such an effect actually reduces the still more or less localized actinide moment are we entitled to use the terminology of localized-moment magnetism.

*USe.* The report by Lam and Aldred (1974) states quite clearly that magnetic measurements on well-defined samples were not available until 1972. The many quoted data are very contradictory. Large magnetocrystalline anisotropy was observed, but could not be quantified on powder samples. The maximum moment value obtained on such samples was about  $1.3\mu_B$ . The neutron moment turned out to be  $2.0\mu_B$ . A rhombohedral distortion was observed by Marples (1970).

The availability of single crystals solved many of the mysteries (Busch and Vogt 1978). Figure 58 shows the hysteresis loop for USe along the easy  $\langle 111 \rangle$  axis. Saturation is achieved only at high fields, the initial curve starts outside the hysteresis loop and the magnetization increases stepwise. There must be large anisotropy with narrow domain walls and field-induced distortions, which are initially randomly distributed and thereafter aligned, when the sample is magnetized for the first time below the ordering temperature. Figure 59 reproduces measurements at constant field (30 kOe) versus temperature. The initial rigid anisotropy (the  $\langle 110 \rangle$  and  $\langle 100 \rangle$  moments are merely the projection of the  $\langle 111 \rangle$  moment) persists above the Curie temperature (160 K). The moment dependence cannot be explained by a Brillouin function, which is valid only for isotropic exchange. Susceptibility measurements in reasonable applied fields can therefore not be interpreted in the normal way (Curie-

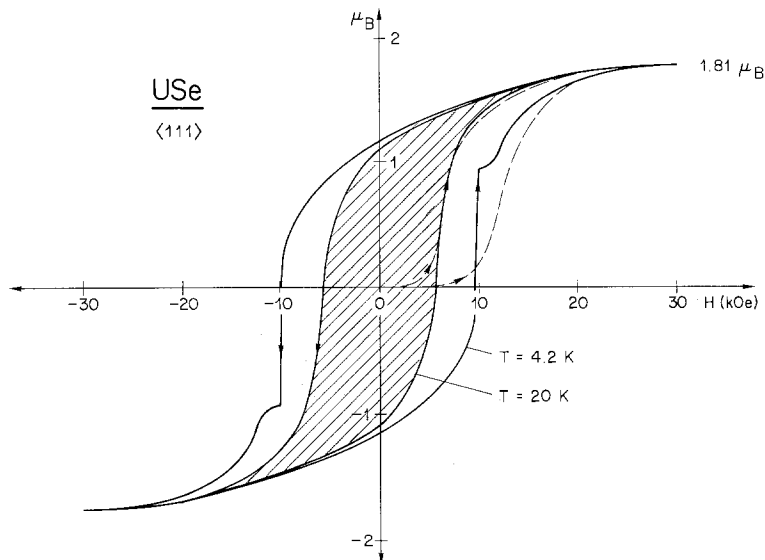


Fig. 58. Hysteresis loop at 4.2 and 20 K of USe along the easy  $\langle 111 \rangle$  axis (Busch and Vogt 1978).

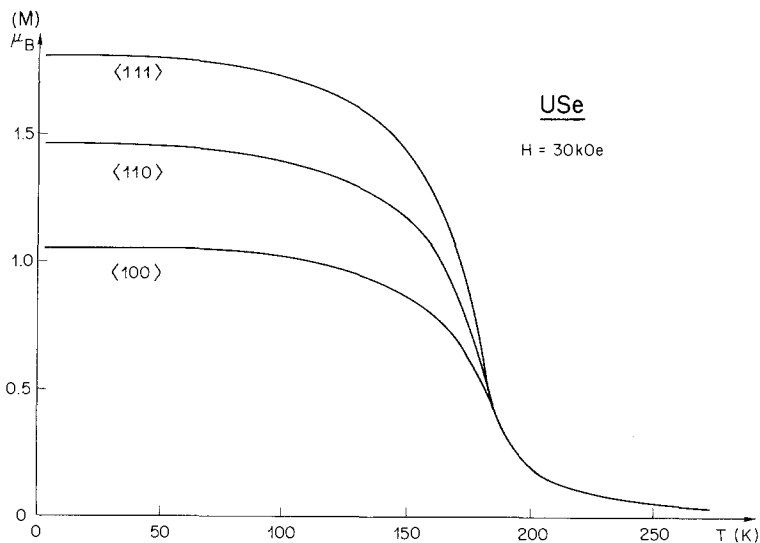


Fig. 59. Magnetization of USe versus temperature at 30 kOe along the three main axes.

Weiss law). Anisotropies, domain effects, internal distortions and large coercive fields are the reasons for the great variation encountered in earlier results. The maximum magnetic moment is  $1.81\mu_B$ , 10% lower than the neutron moment. Again antiparallel polarization of the conduction electrons is assumed to be responsible for this discrepancy. DuPlessis (1986) obtained by careful measurements identical results for the magnetization versus applied field. He performed isofield magnetization measurements at low fields along the three main cubic axes. These curves are very complicated and they give further warning that for such a sample only well-defined single crystal measurements with a well-defined thermal history can be meaningful.

*UTe.* Early results and references are found in Lam and Aldred (1974). Magnetization measurements by Delapalme et al. (1979) on UTe single crystals give similar results as those on USe. The maximum magnetic moment is  $1.91\mu_B$ , again lower than the neutron moment, which is  $2.25\mu_B$ .

The curves have the typical features of a highly anisotropic sample. The magnetic moment at constant field in field-cooled crystals shows that the anisotropy vanishes near the Curie temperature. Still the magnetization curves cannot be fitted with any Brillouin function. The exchange forces must be anisotropic, in addition to the crystal-field anisotropy. An anisotropy gap is observed in the spin wave spectra (Buyers et al. 1980). The crystal-field levels can be observed by neutron scattering (Burllet et al. 1980a). A negative elastic constant  $C_{12}$  is observed, which is typical for mixed-valence compounds (Holden et al. 1982). Excitation measurements (Lander et al. 1990a) point to a strong hybridization of the 5f electrons with conduction electrons. The crystal electric field was determined by neutrons in UTe (Buyers et al. 1981).

*Mixed compounds.* The uranium chalcogenides and pnictides offer almost innumerable possibilities for the formation of pseudobinary mixed crystals. There are three different motivations to study such samples:



(a) By forming mixed crystals with the corresponding Y, La, Th or La compounds, which all are non-magnetic, the compound under investigation is magnetically diluted. Thus, there is some hope to reduce the exchange forces and study the properties of the uncoupled (free) uranium ion in the given electronic environment. The crystal-electric field and its effect on the magnetic ion remains unchanged.

(b) By mixing chalcogenides with the corresponding pnictides (or another pnictide with a compatible lattice spacing), the number of bonding electrons, which in turn influences the exchange interactions, is systematically altered. This provides information on the exchange forces. Since antiferromagnets have their magnetic moments, or at least the components of the magnetic moments, along  $\langle 100 \rangle$  and ferromagnets along  $\langle 111 \rangle$ , it can be foreseen that the resulting spin structures will not be simple. A further problem will be the separation of the isotropic and anisotropic part of the exchange interactions.

(c) A further challenge is the study of mixed crystals containing lanthanides on one side and actinides on the other side. We will discuss the different cases in detail.

#### *Dilution experiments*

*US-ThS*: Lam and Aldred (1974) report on this system. Apparently, the sample qualities were not very convincing. The samples remain ferromagnetic up to 50% ThS. The Curie temperatures decrease, and the effective paramagnetic moments increase towards the free-ion value. Varma (1976) suggests that uranium turns into the tetravalent state. No single crystals have been investigated, so that the anisotropic exchange forces cannot be studied.

*US-YS*: Palewski et al. (1988) found that uranium remains trivalent in this system for all concentrations. These results are questionable.

*USe-ThSe*: Haessler and de Novion (1977) and Palewski (1984) got results which are similar to the ones obtained for the corresponding sulfides. The ferromagnetic interaction up to 50% ThSe and the critical temperatures ( $\Theta_p$  and  $T_C$ ) depend linearly on concentration. The anisotropy is large, but could not be quantified on powder samples.

*UTe-LaTe*: Schoenes et al. (1985) report that the Curie temperature drops very rapidly with increasing LaTe concentration. Order vanishes for a LaTe concentration as low as 30%. The susceptibility is isotropic for all concentrations. The authors propose that the Kondo effect suppresses magnetic order. Uranium is trivalent over the whole concentration range.

*UTe-YTe*: In this system the detailed effect of dilution could be experimentally studied (Mattenberger and Vogt 1992). Figure 60 shows the expected linear decrease of the ordering temperature with the concentration of the diluent. No indication of a possible valence change of the uranium ion is visible – both uranium and yttrium are in the trivalent state. From fig. 61 we can conclude that the anisotropic part of the exchange disappears more rapidly than the isotropic part. As is seen in fig. 62, the susceptibilities of very diluted samples are typical for interference of the crystal-electric field, which becomes stronger than the exchange. The temperature below which the inverse susceptibility curves deviate from linear behaviour and become field dependent is a rough measure for the overall splitting of the ground state by the crystal field. The value of 55 K is quite reasonable. Calculations based on this value explain the observed anisotropies of the magnetization curves.

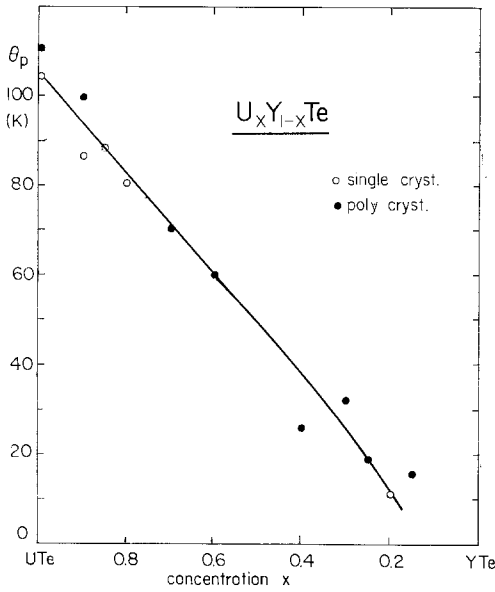


Fig. 60. Paramagnetic Curie temperature of  $U_xY_{1-x}Te$  compounds.

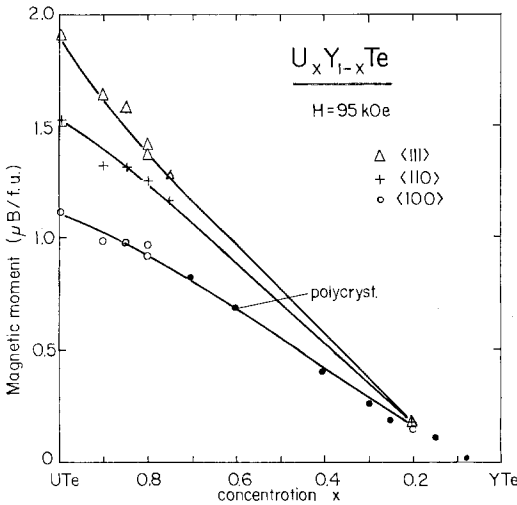


Fig. 61. Anisotropy of the magnetic moments in  $U_xY_{1-x}Te$  compounds.

*UP-ThP*: Lam and Aldred (1974) describe the rather diverse earlier measurements. There is agreement that stable antiferromagnetic order remains for concentrations up to 32% ThP. The Néel temperature and the paramagnetic Curie temperature decrease systematically. No information on anisotropy, spin structures or ordered moments is available.

*UAs-ThAs*: Magnetization measurements by Vogt and Bartholin (1980) and Vogt (1980) revealed that the magnetic phase diagram of UAs is changed drastically by

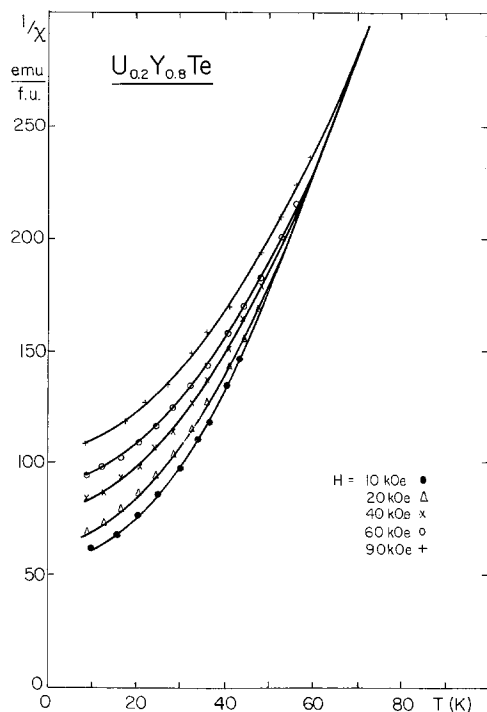


Fig. 62. Inverse molar susceptibility of  $U_{0.2}Y_{0.8}Te$  versus temperature, measured with various applied fields.

minor additions of ThAs – see fig. 63. This phase diagram has been verified by neutron diffraction experiments (fig. 64), which, in addition, allowed the determination of the ordered moment (Fischer et al. 1980). Antiferromagnetism persists up to a concentration of about 30% ThAs. The magnetization curves above that concentration are rather reminiscent of ferromagnetism or induced ferromagnetism (Bartholin et al. 1984). The magnetic properties of UAs are based on a delicate equilibrium of antiferromagnetic and ferromagnetic exchange forces which are certainly not isotropic. Addition of ThAs disturbs this equilibrium significantly, giving rise to very complicated and yet not quantitatively understood properties. The ferromagnetism is enhanced. The fact that thorium in ThAs is tetravalent whereas uranium in UAs is trivalent, may be the main cause for such complications.

*UAs–YAs:* Admixtures of YAs to UAs gradually introduce changes in the magnetic phase diagram of UAs (Cooper et al. 1983b), see fig. 65. The yttrium dilutes the average exchange forces continuously. Thus, this system would be quite appropriate for testing and refining theoretical models for UAs. Since yttrium is definitely trivalent in YAs, we have a further indication that uranium must have the same valency. Small additions of non-magnetic Y-compounds generally seem to favour ferromagnetic exchange (Palewski and Mydlarz 1989).

*UAs–ThSe:* This system, which involves the additional complication of mixing both sites, has been studied by Palewski (1990). The antiferromagnetism of UAs is destroyed by the addition of 25% ThSe. Above that concentration the various compounds are ferromagnetic.

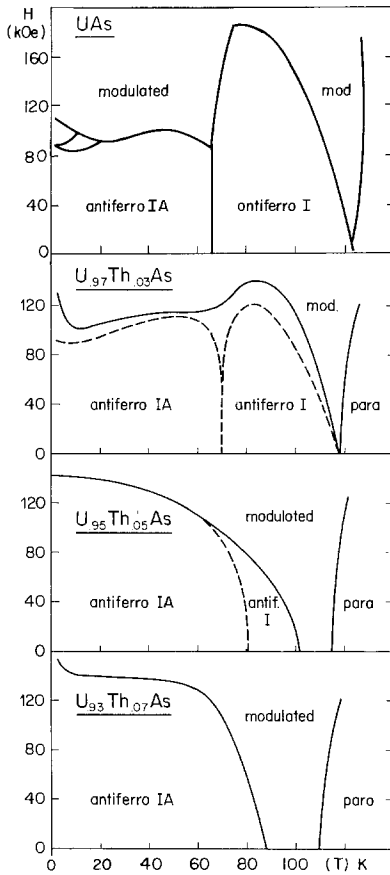


Fig. 63. Magnetic phase diagrams of some  $U_xTh_{1-x}As$  compounds (Vogt and Bartholin 1980).

*USb–ThSb*: In USb the CEF would give a  $\langle 111 \rangle$  easy axis, but the anisotropic exchange aligns the moments along the  $\langle 100 \rangle$  direction. This anisotropy is due to p–f hybridization and thus strongly dependent on the electronic structure. Results of early magnetization measurements (Cooper and Vogt 1979, Vogt 1980) showed that at even low concentrations of ThSb (20%) the antiferromagnetism of USb is destroyed and the samples become ferromagnetic. It was suggested that the valence of the uranium ion was changing to tetravalency (Cooper et al. 1980a). This hypothesis is not supported by photoemission measurements by Reihl et al. (1981). Neutron diffraction experiments (Rossat-Mignod et al. 1982a) and further careful magnetization studies (Tchapoutian et al. 1986) finally allowed the determination of the complete magnetic phase diagram of this system as it is given in fig. 66. In the antiferromagnetic region the magnetic moment remains independent of the Th concentration and its value is  $2.75\mu_B$ , close to the free-ion value. In the ferromagnetic region the ordered moment decreases linearly with the Th concentration. Apparently the value of the uranium moment depends on the number of thorium atoms (adding one extra electron) surrounding the uranium ion. ThSb is not an ideal diluent for USb.

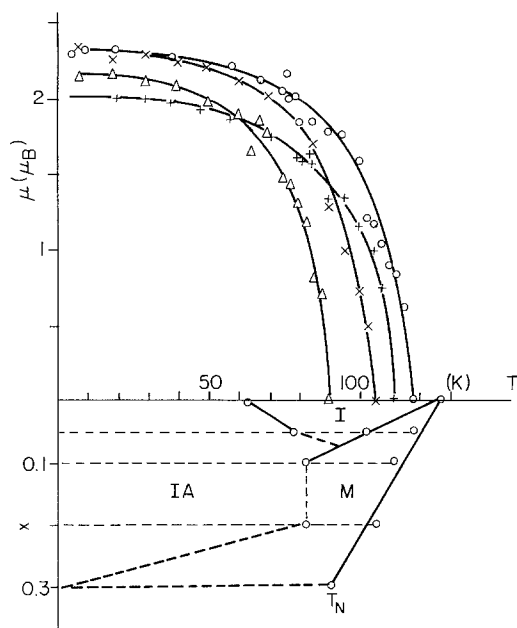


Fig. 64. Temperature dependence of the ordered magnetic moment of U in  $U_{1-x}Th_xAs$  ( $\circ$ :  $x = 0.05$ ;  $+$ :  $x = 0.10$ ;  $\times$ :  $x = 0.20$ ;  $\triangle$ :  $x = 0.30$ ). The lower section of the figure shows the magnetic phase diagram of this system. "M" denotes modulated phases (Fischer et al. 1980).

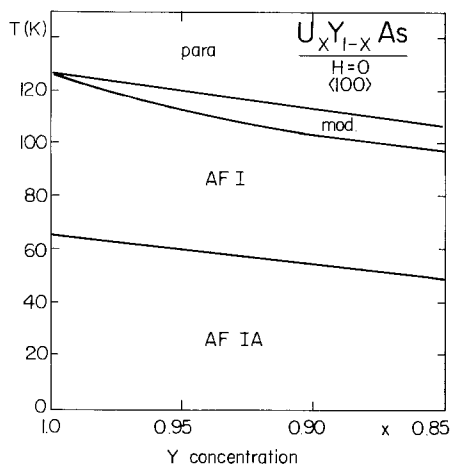


Fig. 65. The magnetic phase diagram (temperature versus composition) of the  $U_xY_{1-x}As$  system in zero applied magnetic field (Cooper et al. 1983b).

*USb–YSb*: Earlier magnetization measurements (Cooper et al. 1980b) showed a transition to ferromagnetism along  $\langle 111 \rangle$  for 50% YSb. No valence change is apparent. The ordered moments decrease rapidly to zero between 50 and 20% YSb concentration. The change from  $\langle 100 \rangle$  antiferromagnetism to  $\langle 111 \rangle$  ferromagnetism is explained by competition of the crystal-field interaction and the anisotropic exchange of the Coqblin–Schrieffer type. Frick et al. (1984) suggest that two different valence states exist for the uranium ion. Combining neutron diffraction data with magnetization measurements, the phase diagram (fig. 67) was obtained by Rossat-

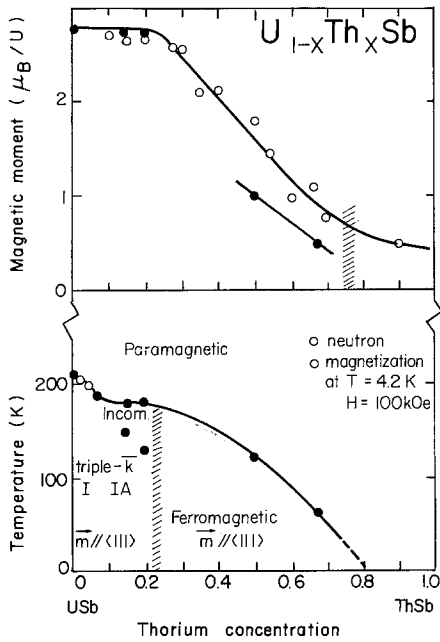


Fig. 66. Magnetic phase diagram of  $U_{1-x}Th_xSb$  compounds and dependence of the U moment versus Th concentration (Rossat-Mignod et al. 1982a).

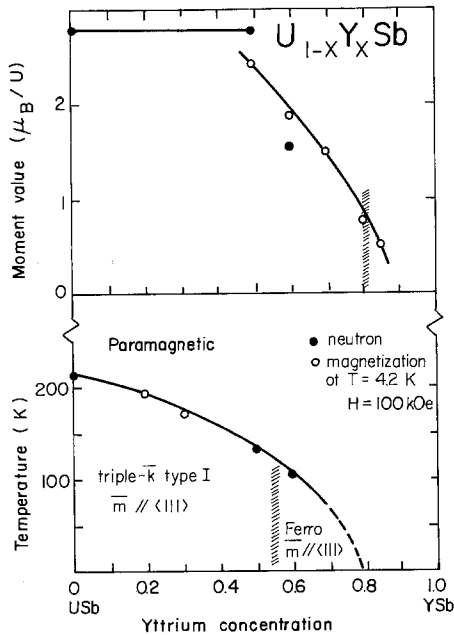


Fig. 67. Magnetic phase diagram of  $U_{1-x}Y_xSb$  compounds and dependence of the U moment versus Y concentration (Rossat-Mignod et al. 1982a).

Mignod et al. (1982a). The magnetic order changes directly from  $\langle 100 \rangle 3k$  antiferromagnetism to ferromagnetism along  $\langle 111 \rangle$ . In the ferromagnetic region the moment decreases. Since yttrium is certainly trivalent, as is uranium, no additional electrons are introduced. The authors claim that a model with  $f$ - $p$  hybridization could explain the moment behaviour, but the problem of the vanishing moments needs further study. However, diluting with YSb gives much simpler results than using ThSb.

#### Mixed pnictogen-chalcogen systems

*UP-US:* The tremendous amount of work on this system (until 1972) is extensively summarized by Lam and Aldred (1974). One of the first neutron diffraction studies on  $UP_{0.75}Se_{0.25}$  by Lander et al. (1969) deserves special attention. The magnetic structures and a moment jump at 20 K (similar to UP) are fully discussed, including a ferrimagnetic structure  $5+4-5+4-$ . The up-to-date version of the complete magnetic phase diagram of  $UP_{1-x}S_x$  is contained in Lander's contribution (ch. 117) to this volume (fig. 23). The influence of the transition from a cubic to a rhombohedrally distorted lattice (Maglic et al. 1974) in the ferromagnetic region could be visualized by magnetization measurements on a  $UP_{0.3}S_{0.7}$  single crystal (Mattenberger and Vogt 1985). The  $\langle 111 \rangle$  axis is favoured by the rhombohedral distortion. Kuznietz et al. (1987b) give for a particular concentration of US the complete magnetic phase diagram (magnetic field versus temperature), see fig. 68. We can see that adding US to UP induces even more complications in the already complex phase diagram of pure UP. All these complicated results confirm that the anisotropic exchange forces, which are responsible for the observed structure, depend critically on the number of unbonded electrons.

*UP-UAs and UP-USe:* Results obtained on these systems are contained in the paper of Lam and Aldred (1974). Crystals of UP-UAs are antiferromagnetic within

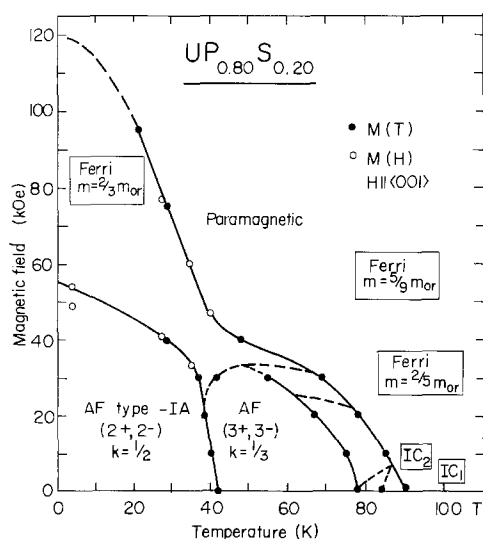


Fig. 68. The magnetic phase diagram (magnetic field versus temperature) of a  $UP_{0.80}S_{0.20}$  single crystal (Kuznietz et al. 1987b).

the whole concentration range, whereas there is a step-like transition to ferromagnetism in the UP–USe system (Burlet et al. 1982, Troč et al. 1980a).

*UAs–US*: Lam and Aldred (1974) summarized the magnetization and neutron diffraction experiments. The Néel temperatures decrease with increasing US concentration, whereas the transition temperature from type I to IA antiferromagnetism increases. At 20% US only the IA structure is stable. Thereafter the moments are no longer commensurate with the lattice in the vicinity of the Néel temperature. For more than 40% US the samples are ferromagnets.

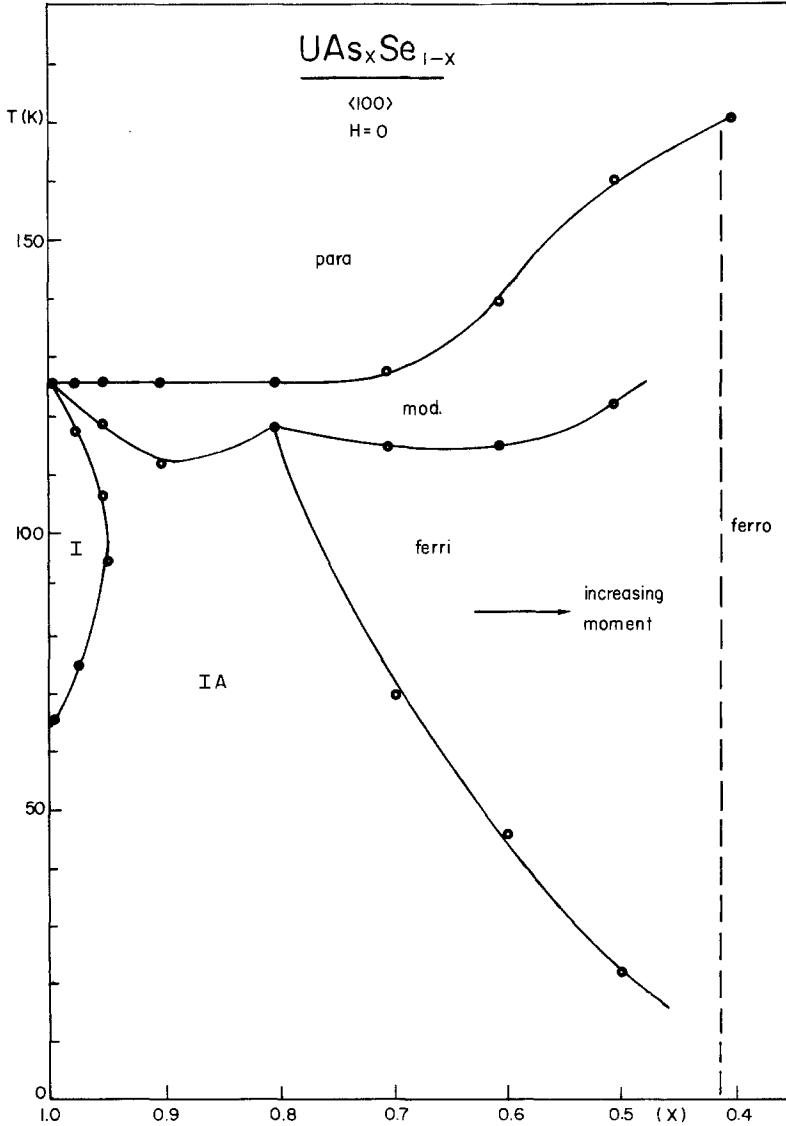


Fig. 69. Suggested phase diagrams of  $UAs_xSe_{1-x}$  for  $H = 0$  versus concentration  $x$ .



*UAs–USe*: There are many new results in addition to the ones reported by Lam and Aldred (1974). The lattice distortions (Palewski et al. 1977) in the ferromagnetic region are rhombohedral, as is expected. Two different approaches contributed to establish the complete phase diagram for the whole system: magnetization measurements by Vogt and Bartholin (1982), Obolenski and Troč (1976), Busch and Vogt (1978) and Bartholin et al. (1984) allowed speculations on the phase diagram (fig. 69), which was investigated by Obolenski and Troč (1976).

The magnetic moment in the ferromagnetic region amounts to almost  $2\mu_B$  along the easy  $\langle 111 \rangle$  axis. Of course, neutron diffraction experiments gave a much more precise phase diagram. Experiments are reported by Kuznietz et al. (1985, 1986a, b, c, 1987a, 1988, 1990), Rossat-Mignod et al. (1990) and Burlet et al. (1986b). Figure 70 reproduces the present version of the rather complicated magnetic phase diagram of *UAs–USe*.

Comparing fig. 70 with fig. 69 we can see that the general pattern of a phase diagram based on magnetization measurements is correct, although detailed descriptions of the spin structures are, of course, missing.

*USb–UTe*: *USb* is an antiferromagnet with a rather high Néel temperature and *UTe* is a ferromagnet along  $\langle 111 \rangle$ . The transition from antiferromagnetism to ferromagnetism on mixing these two components is not a direct one, intermediate structures are formed (Burlet et al. 1979b). The transition temperatures in these structures are not straightforward either – on cooling the crystals an intermediate incommensurate phase is formed. The magnetization curves show a stepwise behaviour, each step corresponding to a distinct spin structure (Vogt and Mattenberger 1987).

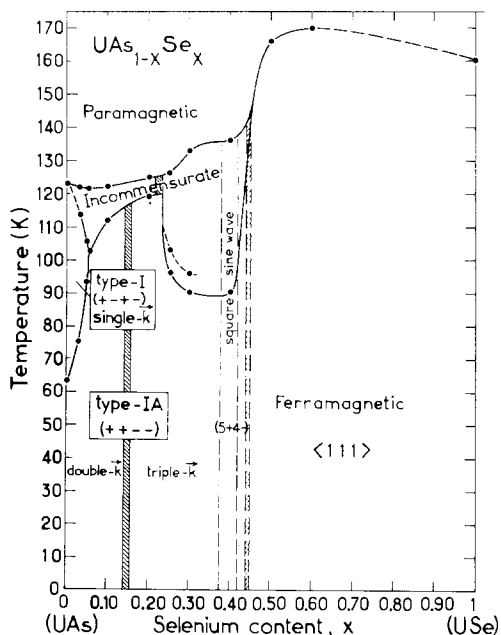


Fig. 70. The magnetic phase diagram (temperature versus composition) of the  $UAs_{1-x}Se_x$  system in zero applied magnetic field (Kuznietz et al. 1986a).

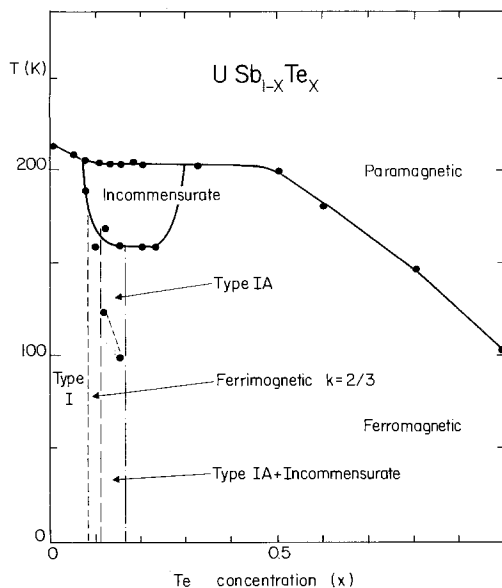


Fig. 71. Magnetic phase diagram of solid solutions  $USb_{1-x}Te_x$  (Rossat-Mignod et al. 1980b).

A sample of  $USb_{0.9}Te_{0.1}$ , studied by Rossat-Mignod et al. (1979a, b), showed for the first time the existence of an incommensurate structure near  $T_N$ . Magnetization measurements at low temperatures yielded a value of only  $\frac{1}{3}$  of the expected full moment. Neutron diffraction data were interpreted using a ferrimagnetic  $++-3k$  structure. The magnetic moment is thus, in accordance with experiment, along  $\langle 111 \rangle$ . This rather complicated multi- $k$  structure was the first of its kind detected in actinide compounds. It casts doubts on the interpretations of earlier results, especially the spin structure of  $USb$ , which was described as a type I ordering with moments along  $\langle 100 \rangle$ .

The sample  $USb_{0.8}Te_{0.2}$  is a  $\langle 111 \rangle$  ferromagnet (Delapalme et al. 1979, Busch et al. 1979c). Its ordered moment ( $2.58\mu_B$ ) is higher than the value  $1.91\mu_B$ , which is found for  $UTe$ . This is a clear indication that in  $UTe$  the magnetic moment is depressed by the electronic environment (hybridization).

Combining magnetization measurements with neutron diffraction results, the complete magnetic phase diagram of the pseudobinary system  $USb_{1-x}Te_x$  was established by Burlet et al. (1980a), Rossat-Mignod et al. (1982a) and Rossat-Mignod et al. (1980b). This phase diagram is reproduced in fig. 71. There is no doubt that all the antiferro- and ferrimagnetic structures (including incommensurate structures) are of the  $3k$  type, as is the ordering in  $USb$  (Burlet et al. 1980a), in agreement with form factor measurements on pure  $USb$  by Lander et al. (1976). The magnetic properties can be understood within the framework of an anisotropic exchange interaction model. The ferromagnetic coupling is strong within (001) planes and there is a weaker coupling  $J_1$  and  $J_2$  between nearest and next-nearest planes. These assumptions are called the ANNNI model (anisotropic next-nearest-neighbour interaction). It is the equilibrium of these weaker couplings which is accomplished by minor additions of

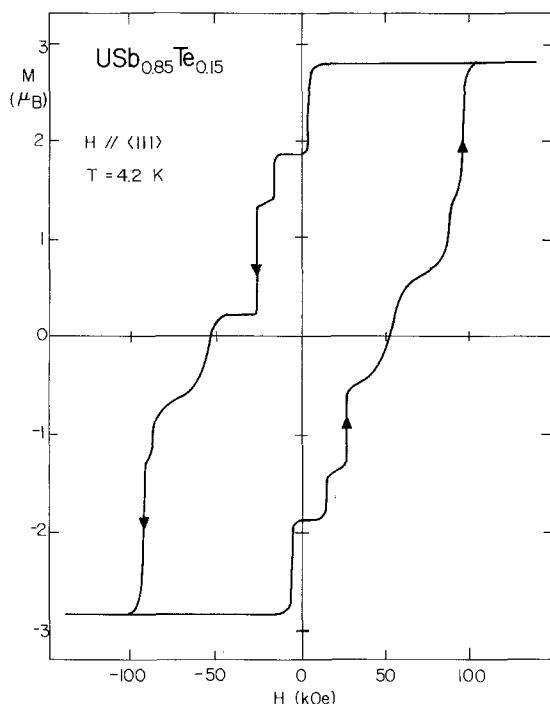


Fig. 72. Hysteresis loop at  $T = 4.2$  K of  $\text{USb}_{0.85}\text{Te}_{0.15}$  (Rossat-Mignod et al. 1982a).

tellurium, by temperature or by an external field – the latter case is nicely demonstrated in fig. 72. The sample  $\text{USb}_{0.85}\text{Te}_{0.15}$  orders in a triple- $k$  IA structure. The single Fourier components are broken up stepwise – every step in the magnetization curve corresponds to a different metastable spin structure (Rossat-Mignod et al. 1982a). At  $T > 20$  K one moment component is ordered ferromagnetically, whereas the other two components retain their  $++--$  sequence. Above 42 K the next component becomes ferromagnetically ordered. In this intermediate phase the ferromagnetic component is oriented along  $\langle 100 \rangle$ , as is confirmed by magnetization measurements. Finally, we may mention that measurements of the initial AC susceptibility (Tchapoutian et al. 1986) allowed a very precise determination of the boundaries in the phase diagram.

*Mixed Ln–An phosphides and sulfides.* The mixed compounds US–PrS, US–NdS, UP–PrP and UP–NdP have also been investigated. A summary of results obtained on these systems is given by Troč (1980) and Troč et al. (1980b), where the corresponding references may be found. The ferromagnetism of US converts into a spin-glass system on addition of the lanthanide. The antiferromagnetism of UP, on the other hand, is not affected. As can be expected, the behaviour of these mixtures is very complicated, and a satisfactory explanation cannot be offered.

2.2.2.3. *NpS, NpSe, NpTe.* Measurements on Np chalcogenides are rather scarce. Table 13 summarizes the few available results (the names of the authors will appear in the text).

TABLE 13  
Magnetic data of neptunium chalcogenides.

Order	$T_C/T_N$	$\Theta_p$	$\mu_{\text{eff}}$	$\mu_{\text{order}}$	Mag. axis
NpS AF II multi- $k$ probable $2k$	20	-150	2.2	0.9	$\langle 100 \rangle, \langle 221 \rangle?$
NpSe AF II multi- $k$	38	-130	2.15	1.35	$m_k \perp k$
NpTe AF II	30	-105	2.47	2.0	Mössbauer?

$\text{Np}^{3+}$ :  $gJ = 2.57$ ,  $g[J(J+1)]^{1/2} = 2.87$ .

Both the paramagnetic and the ordered moment are well below the free trivalent ion values and yet, as Mössbauer measurements show, neptunium is unambiguously in the trivalent state.

Figure 73 shows susceptibility measurements performed on single crystals. The Curie-Weiss law seems to be obeyed and transitions to antiferromagnetism manifest themselves in a minimum of the  $1/\chi$  curves at the corresponding Néel temperatures (Mattenberger and Vogt 1992).

Lam et al. (1974), Lander and Mueller (1974) and Lam and Aldred (1974) were the first to report on the properties of NpS. Their results are still valid. Comments on the unusual properties of NpS, especially the very low moments, are found in the work of Lander (1978) and Lam and Ellis (1985). The latter authors claim that hybridization and crystal-field interactions are responsible for the depression of the ordered moment. Single-crystal neutron diffraction and Mössbauer spectroscopy measurements refined the antiferromagnetic type II structure reported earlier for NpS (Blaise et al. 1992). The structure is of a multi- $k$  type, most probably  $2k$ . NpSe is

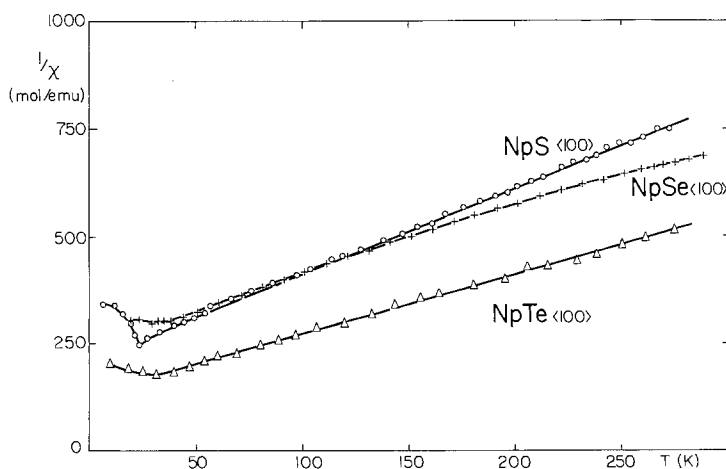


Fig. 73. Inverse molar susceptibilities versus temperature of Np monochalcogenides.

another multi- $k$  antiferromagnet of type I, with the Fourier components perpendicular to the propagation vector (Blaise et al. 1992). NpTe seems to be magnetically ordered at low temperatures, as evidenced by Mössbauer experiments (in addition to the susceptibility results) (Sanchez et al. 1990). A modulated spin structure is suggested, with ordered moments of  $2\mu_B$ . Further confirmation of the onset of order is given by resistivity measurements (Pleska et al. 1988). Neutron diffraction studies by Blaise et al. (1992) confirmed the Mössbauer results on NpS and NpSe, both ordering in a multi- $k$  type II structure, leading to non-equivalent Np sites. Recently, order of type II antiferromagnetism was found in neutron diffraction experiments (P. Burlet, private communication) in NpTe. More information on the properties of NpTe can be found in publications which deal with the pseudobinary system NpSb–NpTe, which was discussed earlier (Sanchez et al. 1990, Mattenberger et al. 1990a). Lander discusses the properties of Np chalcogenides in his contribution (ch. 117) to this volume.

2.2.2.4. *NdS, NdSe, NdTe.* Table 14 gives a synopsis on the available data, taken from publications by Smolenskii et al. (1966, 1968), Starovoitov et al. (1969), Golovsovskii and Plakhty (1973), Tao et al. (1974), Schobinger-Papamantellos et al. (1974) and Hulliger et al. (1975).

The neodymium chalcogenides represent one of the few classes of compounds whose susceptibilities have been measured up to elevated temperatures, by Smolenskii et al. (1966).

Figure 74 shows the results of these measurements. The curvature in the inverse susceptibility versus temperature plot is very satisfactorily explained by the Van Vleck formalism. The screening factor  $\sigma$  is the only adjustable parameter besides those in the spectroscopic data. This explanation is very noteworthy since later many authors had the tendency to explain such measurements with a “modified Curie–Weiss law”, introducing more or less without explanation a temperature independent part  $\chi_0$ . Below 300 K the Van Vleck curve turns steadily into the Curie–Weiss law. The appearance of magnetic order is clearly visible in the inset to fig. 74. The authors are aware that their NdS contained some ferromagnetic impurity, which becomes active at 75 K. McClure (1963) presents a model relating the electrical conductivity to the magnetic susceptibility. Smolenskii et al. (1968) try the molecular-field approach, splitting the exchange up in nearest- and next-nearest-neighbour,  $J_1$  and  $J_2$ , contributions. The stability conditions would allow type II antiferromagnetism in NdS,

TABLE 14  
Magnetic data of neodymium chalcogenides.

	Order	$T_C/T_N$	$\Theta_p$	$\mu_{eff}$	$\mu_{order}$	$\mu_{200\text{ kOe}}$	Mag. axis
NdS	AF non-collinear	8.2	-26.5	3.62	1.9	2.24	24° off $\langle 111 \rangle$
	AF II						
NdSe	AF II	10.6	-9	3.52	1.57	2.34	$\langle 111 \rangle$
NdTe	AF II	10.2	-14	3.54	1.1	2.58	$\langle 111 \rangle$

Nd<sup>3+</sup>:  $gJ = 3.27$ ,  $g[J(J+1)]^{1/2} = 3.62$ .

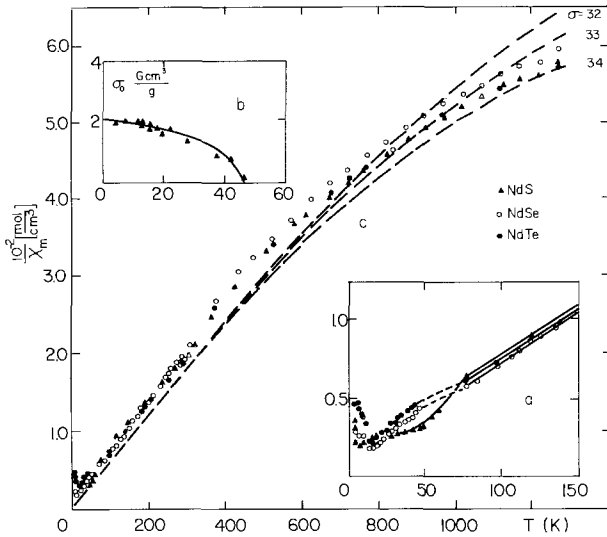


Fig. 74. Inverse molar susceptibilities versus temperature for NdS ( $\blacktriangle$ ), NdSe ( $\circ$ ) and NdTe ( $\bullet$ ); reproduced from Smolenskii et al. (1966).

whereas type I and type II would be allowed in NdSe and NdTe. Starovoitov et al. (1969) found metamagnetic transitions at high pulsed fields for all Nd chalcogenides. The induced moments, measured on polycrystalline samples, are about  $2\mu_B$ .

Early neutron diffraction experiments on NdS yielded the following antiferromagnetic spin structure: collinear spins are arranged antiferromagnetically in the (110) planes, but the direction of the adjacent planes are at a right angle. Tao et al. (1974) find that the anisotropy of the susceptibility of NdS corresponds to a tetragonal distortion.

Careful measurements on single crystals (Schobinger-Papamantellos et al. 1974) revealed that all the Nd chalcogenides show type II antiferromagnetic ordering. The moments of NdSe and NdTe are along  $\langle 111 \rangle$ , but in the case of NdS they are tilted away from  $\langle 111 \rangle$  by an angle of about  $24^\circ$ , coming close to the  $\langle 331 \rangle$  direction. The ordered moments are drastically reduced, as can be seen in table 14. The authors try to explain this reduction by the crystal-field interaction, but they are well aware that the crystal field would choose  $\langle 100 \rangle$  as the magnetic axis.

Hulliger et al. (1975) found tetragonal distortions in all the Nd chalcogenides – incompatible with type II ordering. Figure 75 shows their magnetization curves. At high fields there is a transition to ferromagnetism, with a net moment still below the free-ion value. The magnetic axis is the  $\langle 100 \rangle$  direction, which is, at first sight, surprising for a type II structure. The magnetization curves show some intermediate structure.

With today's knowledge on multi- $k$  structures, speculations on the actual spin arrangements are now possible. NdS could be a  $2k$  type II antiferromagnet (with Fourier components along  $\langle 100 \rangle$ ) and NdSe and NdTe could be  $3k$  type II antiferromagnets. These assumptions are compatible with the observed anisotropic susceptibilities, the tetragonal distortions and the magnetization curves. Of course they ought to be verified. They would offer an easy explanation for the depressed

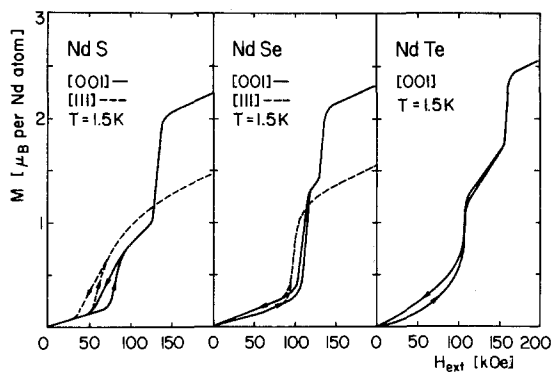


Fig. 75. Magnetizations of NdS, NdSe and NdTe single crystals at 1.5 K in pulsed magnetic fields.

ordered moment: apparently, hybridization-mediated anisotropic exchange prefers the  $\langle 111 \rangle$  direction, but along this direction the full moment cannot be induced since the crystal field allows maximum magnetization only along the  $\langle 100 \rangle$  direction.

### 3. Unstable valences

Valence instability is characterized by a strong coupling between the f shells and delocalized itinerant electrons. Mixed valencies, intermediate valencies, valence fluctuations and heavy-fermion systems are the consequences of such couplings. An overview is given by Flouquet et al. (1982). We shall discuss those groups of compounds in which such phenomena are found.

#### 3.1. *SmS*, *SmSe*, *SmTe*

Very little is known about the actual magnetic properties of these intermediate-valence compounds.

Didchenko and Gortsema (1963) measured the susceptibilities, finding a paramagnetic Curie temperature of  $-195$  K and an effective number of magnetons of 0.94, compared to 0.85 for a free divalent Sm ion.

Later susceptibility measurements by Beeken and Schweitzer (1981) on SmS, SmSe and SmSe–SmAs mixed compounds did not confirm the simple Curie–Weiss behaviour as found by Didchenko and Gortsema (1963). Figure 76 shows the susceptibilities of SmSe and SmAs and some mixed compounds. The authors try to analyze these curves by the superposition of a  $\text{Sm}^{2+}(J=0)$  ion susceptibility taking into account  $J$ -mixing, and a Curie–Weiss contribution of magnetic impurities, which becomes visible at low temperatures. 3% of  $\text{Sm}^{3+}$  ions would explain the results. However, the same explanation is not valid for measurements on SmS.

The more interesting experiments are certainly electrical measurements under pressure (Ohashi et al. 1977), revealing a semiconductor to metal transition at 6.5 kbar. Optical-reflectivity measurements by Batlogg et al. (1977) yield an intermediate valency of 2.85 to 2.9. This is confirmed by a theoretical approach by Aveline and

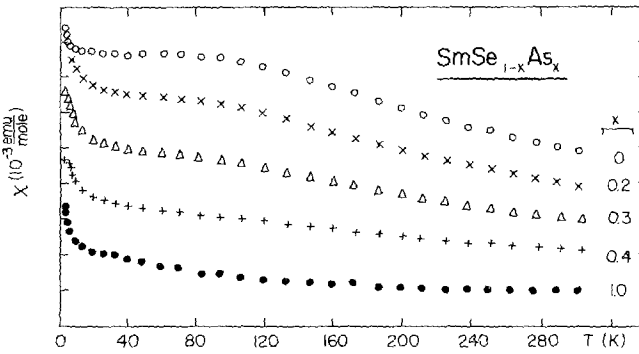


Fig. 76. Magnetic susceptibility as a function of temperature for SmSe, SmAs and several of their solid solutions, reproduced from Beeken and Schweizer (1981).

Iglesias-Sicardi (1980). Hybridization on the f-electrons with 5d conduction electrons (Gronau and Methfessel 1980) is responsible for the results on the electrical resistivities which are reported by Aveline and Iglesias-Sicardi (1981) and Holtzberg and Wittig (1981). Obviously, good magnetic measurements, if possible under pressure, would be very valuable.

3.2. *TmS*, *TmSe*, *TmTe*

These compounds were investigated mostly not by magnetization experiments but by many different physical methods. Table 15 gives the available magnetic data. A review on earlier data was published by Bucher et al. (1975).

*TmS* was found (by neutron diffraction) to order in a complicated structure, close, however, to the  $\langle 111 \rangle$  type II ordering claimed by Koehler et al. (1979). Magnetization measurements by Peyrard et al. (1983) confirmed trivalency of the Tm ion. Peyrard et al. (1983) and Lassailly et al. (1983) found a modulated spin structure by neutron diffraction with a  $k$ -vector close to  $(\frac{1}{2}, \frac{1}{2}, \frac{1}{2})$  and a moment amplitude of  $3.4\mu_B$ . The newest available neutron data (Lassailly et al. 1986) show that in *TmS* at very low temperature we actually encounter a  $4k$  modulated structure with the spins along  $\langle 100 \rangle$ .

TABLE 15  
Magnetic data of thulium chalcogenides.

	Order	$T_C/T_N$	$\Theta_p$	$\mu_{eff}$	$\mu_{order}$	Mag. axis	Valency
<i>TmS</i>	AF type II?					$\langle 111 \rangle?$	
	$4k$ modulated	5.17	-10	7.0	3.4	$\langle 100 \rangle$	3
<i>TmSe</i>	AF I	3.2	-29	6.39	1.7	$\langle 100 \rangle$	2.75
<i>TmTe</i>	AF II	0.21	-5	5.22	~	$\langle 111 \rangle$	2

$Tm^{3+}$ :  $gJ = 7.0$ ,  $g[J(J + 1)]^{1/2} = 7.56$ .



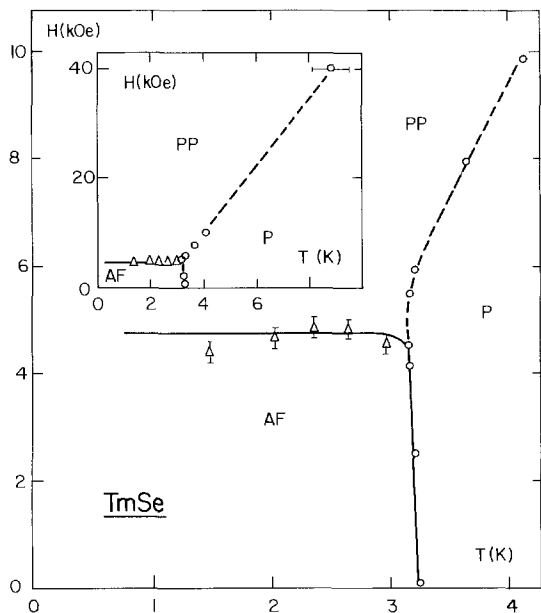


Fig. 77. Magnetic phase diagram of TmSe (Bonnet et al. 1986).

*TmSe* attracted more interest. Bjerrum-Møller et al. (1977) found type I antiferromagnetism. The ordered moment is only  $1.7\mu_B$ , reduced by mixed-valence hybridization. Spin dynamic measurements give a mixture of  $Tm^{2+}$  and  $Tm^{3+}$  ions, 50% of each (Loewenhaupt and Holland-Moritz 1978). Magnetization measurements, yielding the values given in table 15, were performed by Batlogg et al. (1979). Antiferromagnetism in TmSe can easily be destroyed by small external fields. Ott et al. (1975) give a first magnetic phase diagram. Batlogg (1980) found similar results. Bonnet et al. (1986) finally determined, using neutrons, the exact phase diagram (fig. 77). Further experiments on TmSe are: resistivity under pressure (Ribault et al. 1980), neutron diffraction under pressure (Vettier et al. 1980), excitation in applied fields (Loewenhaupt and Bjerrum-Møller 1981) and specific-heat measurements (Berton et al. 1981).

*TmTe* is less well understood. Lassailly et al. (1984) show that Tm is divalent and that TmTe is a semiconductor. The Néel temperature is very low. Ott and Hulliger (1983) stress that samples of TmTe are difficult to get in good stoichiometry. Inverse susceptibility measurements at very low fields (extrapolation to  $H = 0$ ) and low temperatures are needed to visualize the antiferromagnetic transition at 220 mK (fig. 78).

Various experiments were done on the system TmSe–TmTe. Fischer et al. (1982) show that ferromagnetism with a moment of  $1.6\mu_B$  is easily induced. The susceptibilities react immediately to minor additions of tellurium, as is shown in fig. 79 (Batlogg 1981).

The Tm chalcogenides are standard model substances for the study of mixed-valence effects.

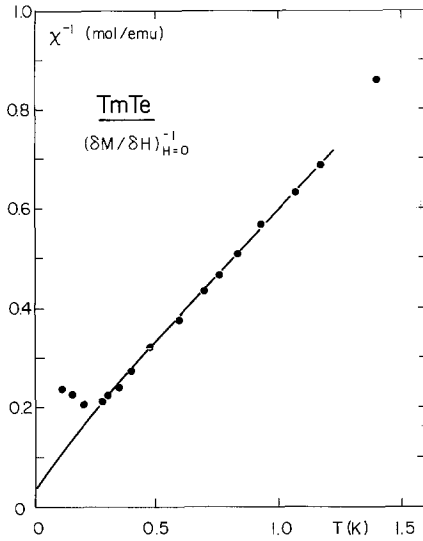


Fig. 78. Inverse magnetic susceptibility of  $\text{Tm}_{0.94}\text{Te}$ , as obtained from the slope of magnetization curves at zero magnetic field, between 0.1 and 1.5 K (Ott and Hulliger 1983).

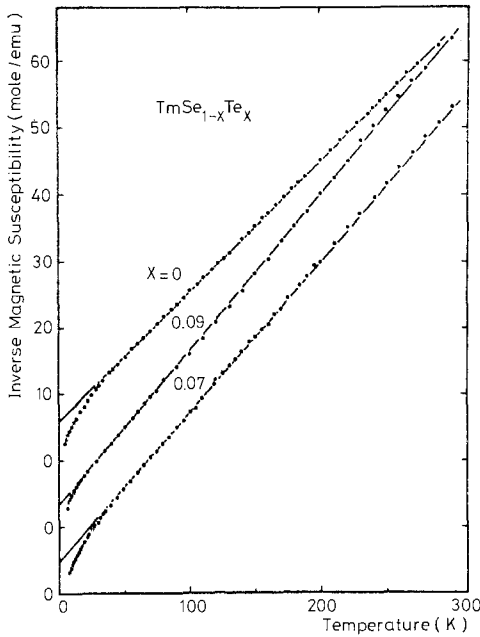


Fig. 79. Inverse magnetic susceptibility as a function of temperature for three metallic and intermediate-valent  $\text{TmSe}_{1-x}\text{Te}_x$  compounds (Batlogg 1981).

### 3.3. $\text{YbN}$ , $\text{YbP}$ , $\text{YbAs}$ , $\text{YbSb}$

Earlier measurements of the magnetic susceptibility of Yb pnictides yielded values for the paramagnetic moment and the paramagnetic Curie temperatures. These measurements are reported by Didchenko and Gortsema (1963), Busch (1967), Bodnar

TABLE 16  
Magnetic data of Yb pnictides.

	Order	$T_N$	$\Theta_p$	$\mu_{\text{eff}}$	$\mu_{\text{order}}$
YbN	AF III	0.73	-11.6	4.8	0.39
YbP	AF II	0.64	-11.5	4.3	0.79 (Mössbauer) 1.03 (neutrons)
YbAs	AF III	0.49	-17	4.25	0.82 (Mössbauer) 0.86 (neutrons)
YbSb	no long- range order	0.32	-20	4.35	0.63

$$\text{Yb}^{3+}: gJ = 4.0, \quad g[J(J+1)]^{1/2} = 4.5, \quad m(\Gamma_6) = 1.33.$$

et al. (1968) and Junod et al. (1969). Order could not be detected. More recent results on all pnictides stem from Ott et al. (1982). Judging from the lattice constants, trivalency for the Yb ion is confirmed. Table 16 summarizes the data which are available today. Of special interest is the type III antiferromagnetism in YbAs found by Dönni et al. (1989, 1990c).

The susceptibility measurements of Ott et al. (1982) are plotted in fig. 80. Ott et al. (1982) were the first authors to realize that at room temperature Yb behaves like a trivalent ion, but at low temperatures order did not set in. They concluded that the Yb pnictides are heavy-fermion materials. a break-through was the detection of order (at very low temperatures) by specific-heat measurements (Ott et al. 1985). Mössbauer experiments by Bonville et al. (1987) confirmed the heavy-fermion behaviour of YbP below 0.41 K. The ordered moment was estimated to be  $0.8\mu_B$ , even lower than the moment of the crystalline electric field  $\Gamma_6$  ground state, which yields a moment of  $1.33\mu_B$ . The moment depression is attributed to hybridization. Order was confirmed by NMR measurements (Takagi et al. 1988).

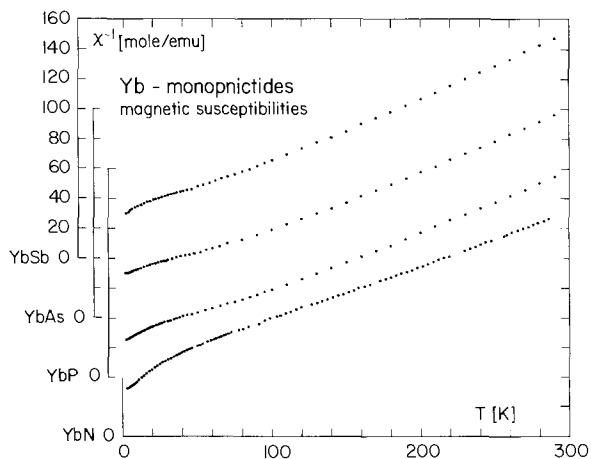


Fig. 80. Temperature dependence of the inverse magnetic susceptibilities,  $1/\chi$ , for YbN, YbP, YbAs and YbSb between 1.5 and 300 K (Ott et al. 1982).

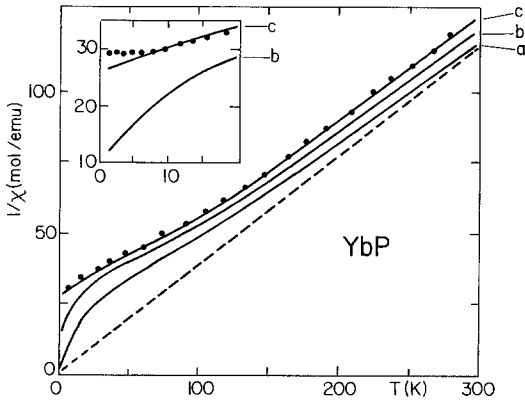


Fig. 81. The temperature dependence of the inverse susceptibility due to the Yb 4f moments. The solid dots represent the experimental data. The curves a, b and c represent the calculated results (after Oyamada et al. 1988).

A careful analysis of the susceptibility curve by Oyamada et al. (1988) (fig. 81) shows that the crystal electric field Kondo effect and exchange interaction have to be taken into account in the interpretation of the low-temperature susceptibility. A Curie-Weiss law is only obeyed above about 200 K.

By extremely high applied magnetic fields (fig. 82) Oyamada et al. (1988) induced magnetic moments which are approaching the full moment of the trivalent  $\text{Yb}^{3+}$  ion.

The low ordering temperatures and low moments are explained by a competition of RKKY exchange with Kondo hybridization (Bonville et al. 1988).

Neutron diffraction experiments gave the spin structures at very low temperatures. Type III antiferromagnetism is found in YbN (Dönni et al. 1990b). YbP orders antiferromagnetically of type II (Dönni et al. 1990a).

YbAs as well shows type III ordering ( $\mathbf{k} = (1, 0, \pm \frac{1}{2})$ ). The moment direction is  $\langle 100 \rangle$ , the saturated ordered moment is only  $0.83\mu_B$ . Transport measurements (Oyamada et al. 1990b) and specific-heat measurements (Oyamada et al. 1990a) confirmed the above-mentioned results.

The crystal-field levels were determined by neutron experiments (Dönni et al. 1991, Kohgi et al. 1990). The crystal-field splitting is one order of magnitude greater than

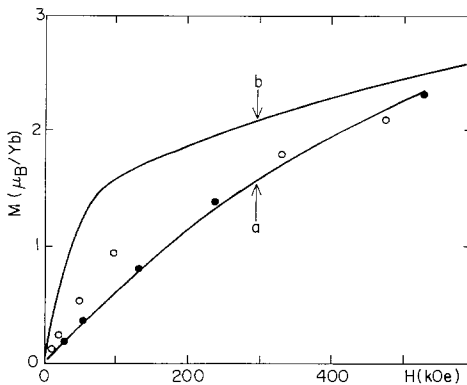


Fig. 82. The magnetization curve,  $M(H)$ , of YbP at 4.3 K. The curves a and b show, respectively, the experimental data and the calculated results obtained by considering only the CEF (after Oyamada et al. 1988).

expected by the point-charge model – still a mystery. Finally, theoretical considerations show that YbAs is not a “classical” heavy-fermion system.

The Yb monochalcogenides are all diamagnetic, since Yb is divalent and thus non-magnetic.

### 3.4. *PuS, PuSe, PuTe*

Since single crystals of good quality became available, reliable measurements on these substances were possible. The measured susceptibilities are plotted in fig. 83. They were first mentioned by Mattenberger and Vogt (1992). The susceptibilities of all the chalcogenides are constant, with a relatively low value, over a wide range of temperatures. Only at low temperatures do we observe an upturn of  $\chi(T)$ . Looking at the lattice constants we can exclude the possibility that Pu is in a divalent (non-magnetic) state. The lattice constant corresponds clearly to trivalent Pu. The absence of the corresponding magnetic moment has for a long time intrigued many researchers: Raphael and de Novion (1969b) found in their early measurements an indication for a Néel transition at 15 K – this was certainly due to impure samples. Their measurements are the only ones which extended to high temperatures (1000 K), and which they attempted to explain by strong crystal-field interaction. What is very important and independent of possible impurities is the fact that even at elevated temperatures there is no sign of a transition towards normal Curie–Weiss behaviour of trivalent  $\text{Pu}^{3+}$ .

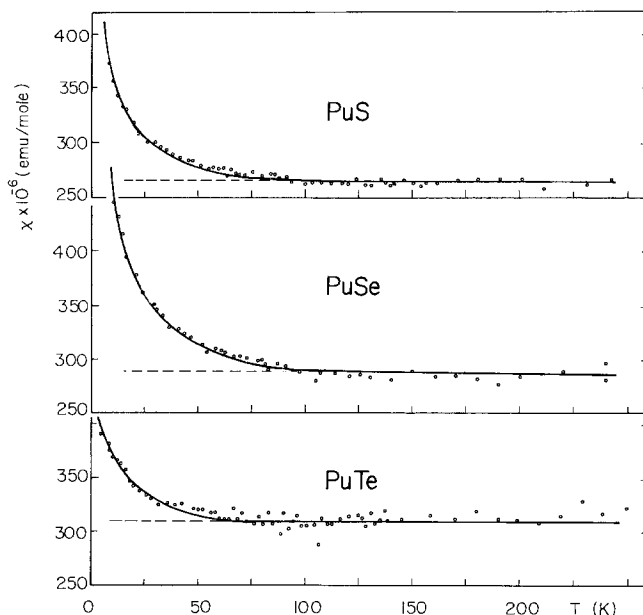


Fig. 83. Molar susceptibilities of Pu chalcogenides versus temperature.

Lam et al. (1974) report temperature-independent paramagnetism for a good-quality sample of PuS. They attribute the low-temperature upturn in the susceptibility to impurities. It is not clear yet whether these compounds are intrinsic semiconductors (Kruger and Moser 1967), small-gap semiconductors of the heavy-fermion type (Fournier et al. 1990) or just metals (Vogt and Mattenberger 1987).

Many theoretical approaches were made to the problem of the plutonium chalcogenides: Lam and Ellis (1985) discuss hybridization of the f-electrons with itinerant electrons. Wachter et al. (1990, 1991) claim that Pu is in an intermediate valence state – the Pu chalcogenides would correspond to the high-pressure collapsed phase of the corresponding Sm chalcogenides. Based on this model a convincing interpretation of the lower part of the susceptibility curve is possible. A band-model calculation of the electronic structure is presently available (Hasegawa and Yamagami 1992). Hybridization of the f-p type is very important.

#### 4. Cerium compounds

We have chosen to treat cerium compounds in a separate section, because it is impossible to integrate them in the frame we set up for all the other lanthanide and actinide systems. The physics of the magnetic properties of the cerium compounds is very diversified, going from intermediate valence (CeN), prevailing CEF (CeP, CeAs), strong anisotropic exchange (CeSb, CeBi) to predominantly hybridization-mediated phenomena (fluctuating valences, heavy electrons) as found in the cerium monochalcogenides. Since cerium compounds are readily available and single crystals are easily grown, they were, and still are, the first choice of materials to study specific phenomena. In addition, since trivalent cerium has only one f-electron, the theory is easiest for this class of lanthanide compounds. These are the reasons why not only experimental, but also theoretical papers are available in a great number today. Table 17 summarizes the data on the magnetic properties. An overview of the properties of Ce pnictides is given by Rossat-Mignod et al. (1983b).

TABLE 17  
Magnetic data of cerium pnictides and chalcogenides.

	Order	$T_N$	$\Theta_p$	$\mu_{eff}$	$\mu_{order}$	Axis
CeN	mixed valent n.o.	–	–	–	–	–
CeP	AF I?	8.5	5	2.56	0.85	$\langle 100 \rangle$
	AF I $3k$ ?					$\langle 111 \rangle$
CeAs	AF I?	7.5	18	2.82	0.85	$\langle 100 \rangle$
	AF I $3k$ ?					$\langle 111 \rangle$
CeSb	AF many phases	16.2	5	2.56	2.08	$\langle 100 \rangle$
CeBi	AF I/AF IA	25.5/12.5	12	2.38	2.1	$\langle 100 \rangle$
CeS	AF II	8.3	–20	2.78	0.57	$\langle 111 \rangle$
CeSe	AF II	5.4	–7	2.58	0.58	$\langle 111 \rangle$
CeTe	AF II	2.2	–4	2.49	0.3	$\langle 111 \rangle$

Ce<sup>3+</sup>:  $gJ = 2.14$ ,  $g[J(J+1)]^{1/2} = 2.54$ .

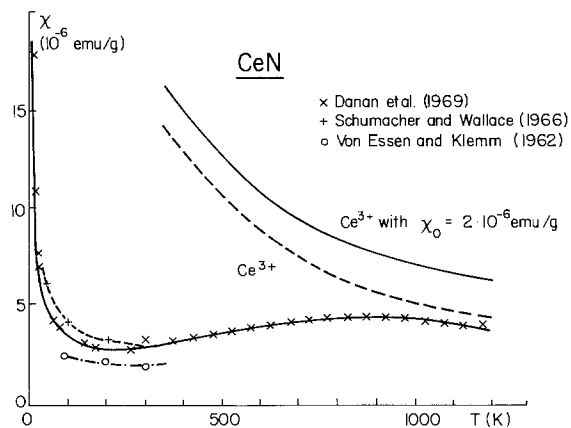


Fig. 84. Susceptibility of CeN versus temperature, after Danan et al. (1969).

#### 4.1. CeN

Various authors (Von Essen and Klemm 1962, Didchenko and Gortsema 1963, Schumacher and Wallace 1966) realized very early that the susceptibility of CeN was quite weak and did not correspond to the expectations for a trivalent cerium ion. By plotting the lattice parameters versus the rare earth radii for the nitrides it can be seen that, indeed, cerium cannot be trivalent, but rather is tetravalent. Danan et al. (1969) calculated a valence of 3.4 based upon the measured lattice constant. The results of their susceptibility measurements are given in fig. 84.

The authors realized that the CEF field cannot be responsible for the observed low susceptibility. They proposed a model of non-bound f-electrons with enhanced Pauli paramagnetism. The sharp upturn at low temperatures could be due to impurities. It would certainly be interesting to reexamine these old results, in view of the progress which has been made in understanding mixed-valence systems. Furthermore, they are among the few available measurements which extended to high temperatures. X-ray photoemission measurements by Baer et al. (1978) confirm the existence of two valence states in CeN. Thus, the explanation of CeN being an intermediate-valence system is sustained.

#### 4.2. CeP

The magnetic susceptibility of CeP has been measured by many authors (Tsuchida and Wallace 1965b, Myers and Narath 1973, Hulliger and Ott 1978, Kwon et al. 1991).

Figure 85 shows the measurements by Hulliger and Ott (1978). At the same time the authors plot calculated values which take into account the crystal-field interaction.

The value of the overall splitting by the CEF was determined by specific-heat measurements by the same authors and by Stevens and Pytte (1973). Their data agree with values obtained by neutron spectroscopy. Kwon et al. (1991) give an even more elaborate calculation of the susceptibility of CeP, taking additionally into account the crystal field splitting exchange interactions within and between the CEF levels.

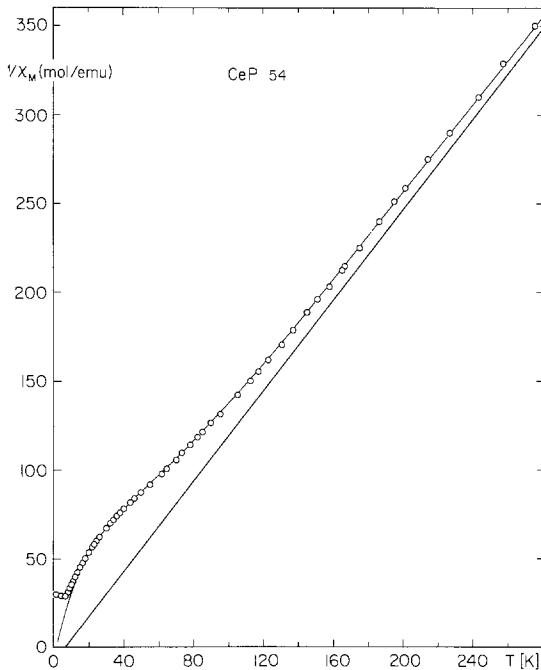


Fig. 85. Inverse magnetic susceptibility of CeP. The curve approximating the measured points (circles) is calculated. The straight line represents the underlying Curie-Weiss law (Hulliger and Ott 1978).

#### 4.3. CeAs

The magnetic susceptibility of CeAs looks almost the same as that of CeP (see Tsuchida and Wallace (1965b) or Hulliger and Ott (1978)). The theoretical explanation is the same. A more elaborate calculation, taking into account various exchange interactions, is given by Suzuki et al. (1990). Neutron diffraction experiments by Rainford et al. (1968) showed type I ordering, a moment of  $0.68\mu_B$  for the lowest  $\Gamma_7$  crystal field level and an overall splitting of 140 K.

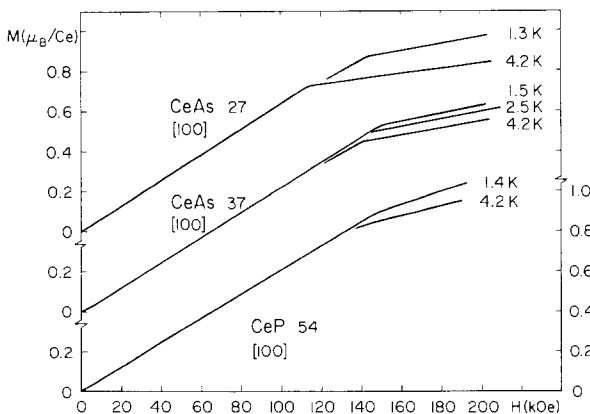


Fig. 86. Magnetization curves for CeP, a sublimed CeAs single crystal (CeAs 27) and a recrystallized CeAs single crystal (CeAs 37), obtained with pulsed fields parallel to the  $\langle 100 \rangle$  axes (Hulliger and Ott 1978).



Hulliger and Ott (1978) performed high-field magnetization measurements on CeAs (fig. 86) and they found indeed some saturation at a level of about  $0.8\mu_B$  – a value which is far below the free-ion value,  $gJ = 2.14$ .

By studying magnetic excitations Hälgl et al. (1983) confirmed that the ground-state  $\Gamma_7$  doublet is well isolated, so that CeAs can be looked upon as an effective  $S = \frac{1}{2}$  antiferromagnet.

There is some controversy on the spin structure of ordered CeAs. Rossat-Mignod et al. (1982b) carried out neutron measurements indicating moments along  $\langle 001 \rangle$ , but the  $\Gamma_7$  ground state leads to a  $\langle 111 \rangle$  easy axis. Experiments in applied magnetic fields make a  $3k$  type I ordering probable – this structure would reconcile the above-mentioned differences in magnetic axes. On the other hand, Hälgl et al. (1983, 1986, 1987a) state that the magnetic ordering in CeAs is unambiguously a collinear single- $k$  type I structure. CeAs is considered to be a Kondo system by Komorita et al. (1992), and a magnetic phase transition was found in high magnetic fields.

#### 4.4. CeSb

Tsuchida and Wallace (1965b) in their pioneering work on cerium pnictides tried to measure the susceptibility of CeSb. They obtained an unusual set of measurements and realized that without the help of neutron diffraction there was no chance to understand the magnetic properties of CeSb. The situation is further complicated by the very strong anisotropy. Figure 87 shows the magnetization measured as a function of the field direction by Busch and Vogt (1967). The magnetic moments are strictly confined to the  $\langle 100 \rangle$  direction – along other directions only the projections of the  $\langle 100 \rangle$  moments are measured. The fields required to induce intermediate or, finally, ferromagnetic structures are only determined by their component along  $\langle 100 \rangle$ . The

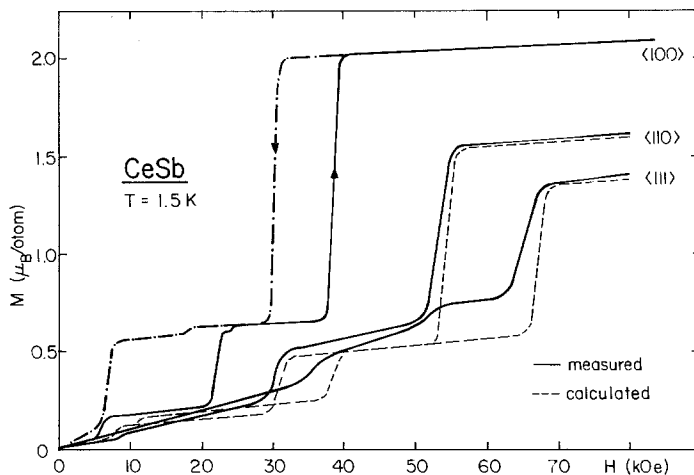


Fig. 87. Magnetic moment of CeSb at 1.5 K, measured in external fields along the  $\langle 110 \rangle$  and  $\langle 111 \rangle$  axis (Busch and Vogt 1967).

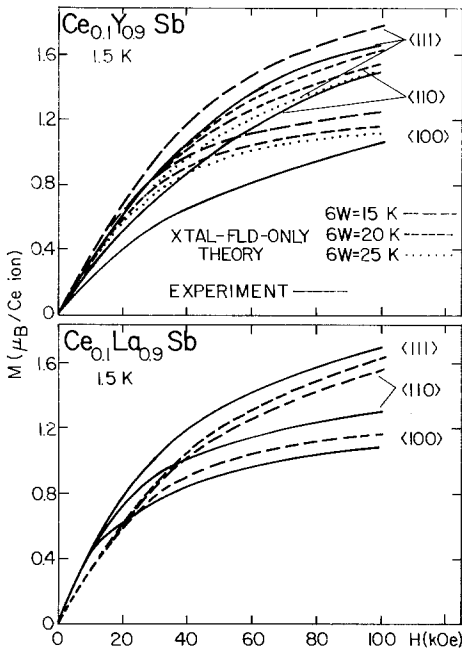


Fig. 88. Comparison of experimental magnetization per Ce ion for  $\text{Ce}_{0.1}\text{Y}_{0.9}\text{Sb}$  and  $\text{Ce}_{0.1}\text{La}_{0.9}\text{Sb}$  at 1.5 K with the crystal-field-only theory for  $6W = 15$ , 20 and 25 K (Cooper et al. 1972).

crystalline electric field splitting was estimated to be about 20 K using neutrons (Rainford et al. 1968), with a  $\Gamma_7$  doublet ground state. This ground state would predict a  $\langle 111 \rangle$  easy axis, in contrast to the measurements shown in fig. 87.

By diluting CeSb with either LaSb or YSb, we can remove the exchange interactions. Such experiments have been performed by Cooper et al. (1972), and they show indeed that the “free” cerium ion has a  $\langle 111 \rangle$  easy axis – the observed magnetizations can be calculated with reasonable parameters for the CEF (see fig. 88). For the first time it was thus possible to demonstrate experimentally that anisotropic exchange can be the decisive factor in choosing the magnetic axis and not, as was usually accepted, the CEF.

Figure 89 shows an overview of the very many magnetization measurements which were performed by Bartholin et al. (1975). These measurements are one basis for establishing the complete, extremely complicated, magnetic phase diagram of CeSb as it is given in Lander’s contribution (ch. 117) to this volume. Very many people have performed neutron diffraction experiments, which resulted in today’s thorough knowledge of this phase diagram. The most important contributions are by Rossat-Mignod et al. (1977a, b, 1985b), Fischer et al. (1978), Meier et al. (1978) and Hälgl et al. (1982a). The phase diagram along  $\langle 111 \rangle$  was investigated by Burlet et al. (1979a). Specific-heat measurements in applied fields (Rossat-Mignod et al. 1980c) gave further confirmation. Fourteen different phases have been observed in CeSb. They are of three main types: phases with ferromagnetic (100) planes with the same moment, phases with antiferromagnetic (100) planes and paramagnetic planes and, finally, phases with ferro- and paramagnetic planes. The reader will be able to identify these

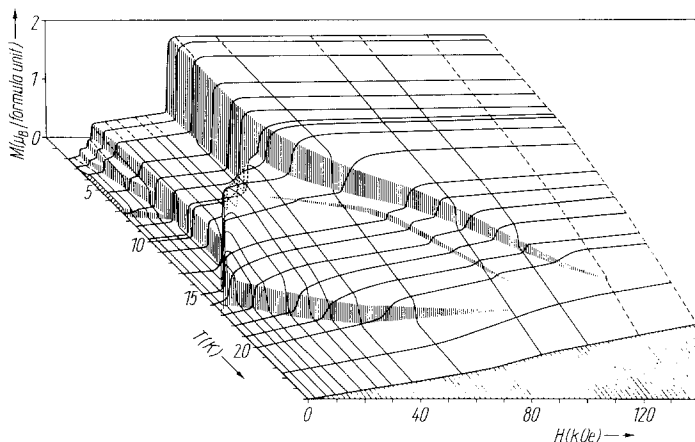


Fig. 89. Magnetization surface of a CeSb single crystal with a field applied along the  $\langle 100 \rangle$  direction, in  $(M, H, T)$  space (Bartholin et al. 1975).

phases in fig. 89. CeSb is an ideal example for the already mentioned ANNNI model (Rossat-Mignod et al. 1980b, 1982b). Additional neutron experiments we would like to mention concern excitations (Furrer et al. 1979a, b, Rossat-Mignod et al. 1985c) and critical scattering (Hälg et al. 1981, Hälg and Furrer 1984). Of special interest are polarized-neutron experiments, from which was proposed that in CeSb the CEF ground state is  $\Gamma_8$ , and not  $\Gamma_7$  as in CeP, CeAs and diluted CeSb (Boucherle et al. 1980). The anisotropy of the exchange is not due to a bilinear interaction. The CEF field is reduced by hybridization (Hälg et al. 1987b), a result which was discussed earlier by Takahashi et al. (1983).

Several high-pressure experiments gave further information on the magnetic phases in CeSb (Bartholin et al. 1977, 1978, Léger et al. 1984, 1987, Mori et al. 1991). Even neutron experiments were performed under pressure, by Chattopadhyay et al. (1986, 1987). The Néel temperature increases drastically, paramagnetic planes do not exist under pressure.

Hälg et al. (1986) performed neutron studies under uniaxial stress.

#### 4.5. CeBi

Tsuchida and Wallace (1965b) found “wild” curves for the magnetization of powdered CeBi. Based on magnetization measurements Tsuchida and Nakamura (1967) already gave a tentative magnetic phase diagram, based on magnetization measurements, which is not far from reality. Cable and Koehler (1972) found the structural transition from type I to type IA at 12.5 K. Magnetization measurements, as complete as possible, were reported by Bartholin et al. (1974), and are plotted in fig. 90.

The magnetic properties of CeBi are very sensitive to applied pressure (Bartholin et al. 1979b). Again by combining magnetization measurements with neutron scattering results a complete magnetic phase diagram was worked out by Rossat-Mignod et al.

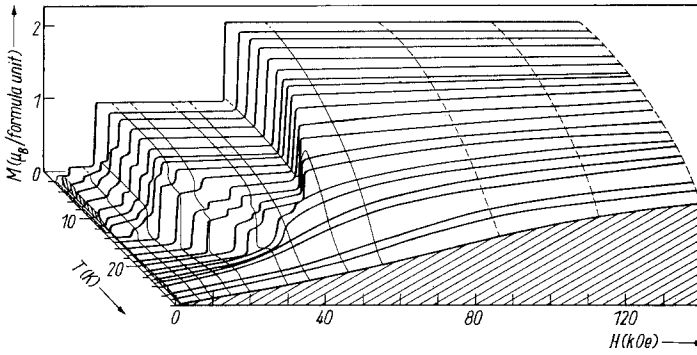


Fig. 90. Magnetization surface of a CeBi single crystal with a field applied along the  $\langle 100 \rangle$  direction, in  $(M, H, T)$  space (Bartholin et al. 1974).

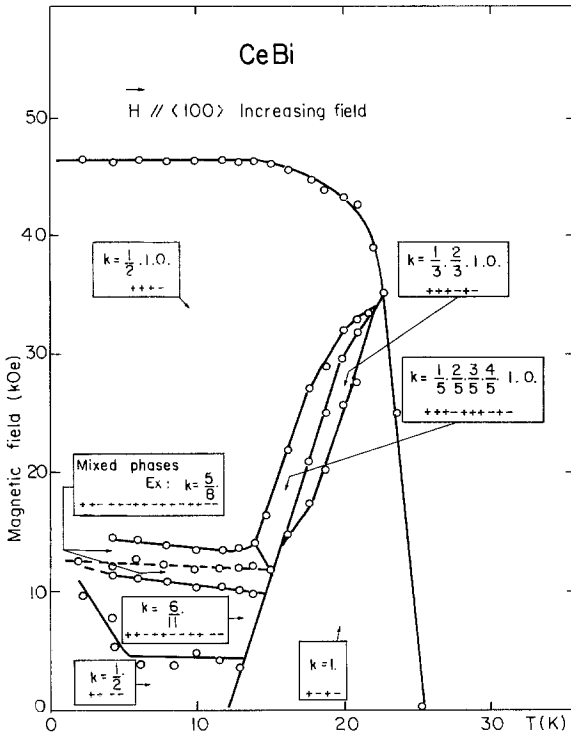


Fig. 91. Magnetic phase diagram of CeBi for a magnetic field applied along the  $\langle 100 \rangle$  direction (Rossat-Mignod et al. 1980b).

(1980b). It is reproduced in fig. 91. A discussion of this diagram can, furthermore, be found in the summary by Rossat-Mignod et al. (1982b), especially of the ANNNI model.

Experiments like neutron diffraction experiments, critical scattering (Hälg et al., 1982b) and excitation (Rossat-Mignod et al. 1983a, 1985c, Léger et al. 1985) have helped to complete our knowledge of CeBi.

## 4.6. Mixed compounds

We have already mentioned dilution experiments with YSb and LaSb by Cooper et al. (1972), Bartholin et al. (1979a) and Halg et al. (1985).

Interesting results were obtained by mixing CeSb with CeBi by Bartholin et al. (1980) and Burlet et al. (1980b) – the most striking result is the fact that in such alloys  $\Gamma_8$  is the CEF ground state.

Further experiments were done on the system CeSb–CeTe by Bartholin et al. (1985), Ravot and Achard (1982), Rossat-Mignod et al. (1982a, b), Escorne et al. (1984) and Ravot et al. (1983). A 5% tellurium addition converts the highly anisotropic exchange observed in CeSb into the simple isotropic Heisenberg-type exchange. Sera et al. (1985) found in the system CeBi–CeTe a transition to spin-glass behaviour.

## 4.7. CeS, CeSe, CeTe

Magnetic data are summarized in table 17. The first available, and very complete, susceptibility measurements are those of Smolenskii et al. (1966, 1968) and Loginov et al. (1970). Most valuable are their high-temperature results, plotted in fig. 92.

At low temperatures the Curie–Weiss law is obeyed. At higher temperatures the Van Vleck formalism ( $J$ -mixing) explains the observed results. Antiferromagnetic transitions are clearly visible. The measurements below 70 K do not seem to be too

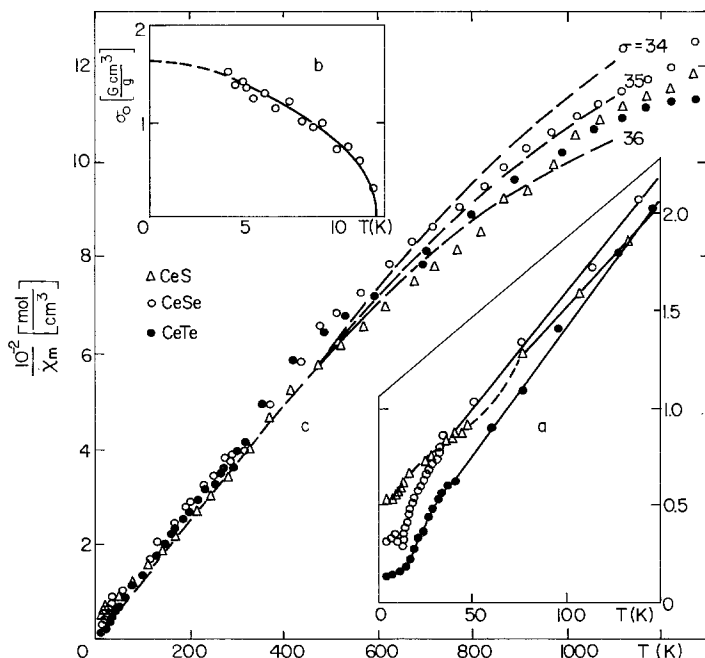


Fig. 92. Inverse molar susceptibilities versus temperature for CeS ( $\Delta$ ), CeSe ( $\circ$ ) and CeTe ( $\bullet$ ), reproduced from Smolenskii et al. (1966).

trustworthy. We believe that the sample quality was not sufficient. Reliable measurements at low temperatures on well-defined single crystals are reported by Hulliger et al. (1978a). The low-temperature susceptibilities of the cerium chalcogenides are very reminiscent of the results obtained for CeP and CeAs. By taking into account the crystal-field interaction the susceptibilities can be calculated. The overall splitting in CeS and CeSe is not affected by the extra electron, but is about the same as in the corresponding pnictides. Thus, there is no screening effect. Schobinger-Papamantellos et al. (1974) found by neutron diffraction that CeS orders in type II antiferromagnetism, with the moments along  $\langle 111 \rangle$ . Similar experiments for CeSe and CeTe are reported by Ott et al. (1979). Hulliger et al. (1978a) performed specific-heat measurements and could determine the crystal-field parameters, all this after very critical evaluation of the sample quality. Since the CEF splitting in CeSe is relatively weak (32 K), a magnetic moment can be induced by an external magnetic field, as is illustrated in fig. 93. The easy axis is the  $\langle 111 \rangle$  direction, as is expected for a  $\Gamma_7$  ground state. Full saturation was not reached with the available field. High-pressure experiments were performed by several authors: Croft and Jayaraman (1980) find a valence instability in CeS. The same results (valence change) are obtained by Vedel et al. (1986) and Léger et al. (1987). At 8 GPa the NaCl structure of CeTe transforms into the CsCl-type. From the abnormal increase of the interatomic distance it is concluded that the valence of cerium changes (Léger et al. 1983).

The apparent magnetic instabilities in CeTe found by Ravot et al. (1980) (in contrast to CeSb, where about the same overall splitting by the CEF is observed), are of great theoretical interest (Kioussis et al. 1990), and the resemblance to the case of UTe is obvious.

The highly anisotropic magnetic interactions in CeSe were studied in neutron scattering experiments (Dönni et al. 1992).

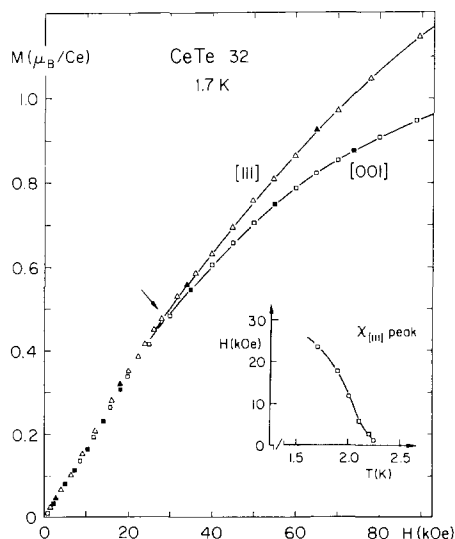


Fig. 93. Magnetization,  $M(H)$ , of CeTe single crystals oriented along the  $\langle 100 \rangle$  and  $\langle 111 \rangle$  direction. The decrease of the  $\chi_{\langle 111 \rangle}$ -peak temperature with increasing external magnetic field is shown in the inset (Hulliger et al. 1978a).

#### 4.8. Theory

No other class of compounds has evoked so much theoretical interest as the cerium pnictides, with their abundance of unusual properties. It is not our task to discuss these theories, we just give the references for the interested reader.

*Planar coupling:* Sieman and Cooper (1980a, b), Ott et al. (1982) and Proetto and Lopez (1982).

*Hybridization (p-f mixing):* Schoenes and Hulliger (1987), Kioussis et al. (1988), Dönni et al. (1990c), Kioussis et al. (1990) and Kasuya et al. (1990).

*Anisotropic exchange:* Thayamballi and Cooper (1984), Cooper et al. (1984) and Thayamballi et al. (1984).

We think that this is a convincing list to show how fruitful research on cerium pnictides turned out to be.

#### 5. Conclusions

Our search of all the magnetization measurements which are presently available, leads us to regret that they are often incomplete. Susceptibility measurements at elevated temperature are rare, yet they would reveal readily whether  $J_0$ - $J_n$  mixing occurs, i.e. whether at high temperature the Van Vleck theory has to be applied. Very often susceptibility values below the Néel temperature are not given or plotted. Yet, they would allow us to draw important conclusions. For isotropic exchange in cubic samples the susceptibility must become temperature independent below  $T_N$ . Any upturn of the inverse susceptibility below  $T_N$  in cubic samples means necessarily that the exchange is anisotropic. Directional dependence of the susceptibilities below  $T_N$  provides some very conclusive information.

Magnetization measurements in the ordered state make sense, in the majority of cases, only on single crystals, since almost all compounds are magnetically anisotropic.

Since many compounds show complicated magnetic phase diagrams, magnetic moments versus temperature should always be measured for many different applied fields. The experimentalists would very much like to compare their results with theory. This has to be done with caution: there are four main factors which determine the magnetic properties of a sample:

(1) The spectroscopic data of the ion determine the ground state and a possible  $J$ -mixing.

(2) *The crystal electric field.* If the exchange is isotropic, and only if the exchange is isotropic, the crystalline electric field splitting determines the magnetic axis. If the values obtained for the crystal electric field are very different from the expectations based on the point-charge model, then application of the CEF theory is doubtful.

(3) *Exchange.* Exchange will always have an isotropic and an anisotropic contribution. Quadropolar, dipolar, bilinear and RKKY exchange has to be considered besides the Heisenberg exchange between ions, which may be shaped by hybridization. In the literature one often finds attempts to divide the exchange into nearest- and next-nearest-neighbour contributions. The corresponding formulae are valid only for

isotropic exchange – in other cases such approximations are invalid. This can be seen from the fact that in cubic systems isotropic exchange would allow only type I, II or III antiferromagnetism or ferromagnetism. On the contrary, a multitude of spin structures is encountered.

(4) *Hybridization*, besides shaping the exchange, determines the moment values – moment wash-out is a frequent phenomenon. In publications one sees often plots of ordering temperatures or ordered moments, either along the lanthanides or actinides for a given anion or along the series for a given cation, versus the lattice constant. These plots, which we have avoided, do not give much information, since there are too many different factors entering into the determination of the critical temperature or the ordered moment. Only if we can separate these factors does it make sense to plot them versus lattice constants. A famous example is the Hill plot, which is successful for many substances but still shows frequent exceptions.

In conclusion, we can say that exactly the same physical interactions are determining the magnetic properties of both the 4f and the 5f systems. The relative importance of these factors makes a system “complicated” or “simple”.

## Acknowledgements

The authors are grateful to Prof. P. Wachter for his great interest in their work and to Dr. F. Hulliger for careful and critical reading of the manuscript.

## References

- Aldred, A.T., and R. Troč, 1983, *J. Magn. & Magn. Mater.* **36**, 217.
- Aldred, A.T., B.D. Dunlap, A.R. Harvey, D.J. Lam, G.H. Lander and M.H. Mueller, 1974, *Phys. Rev. B* **9**, 3766.
- Allbutt, M., A.R. Junkison and R.M. Dell, 1964, in: *Compounds of Interest in Nuclear Reactor Technology in Nuclear Metallurgy*, Vol. 10 (AIME, New York) p. 65.
- Andersen, N.H., J. Jensen and O. Vogt, 1980a, *J. Magn. & Magn. Mater.* **15–18**, 13.
- Andersen, N.H., J.K. Kjems and O. Vogt, 1980b, *J. Phys. C* **13**, 5137.
- Aveline, I., and J.R. Iglesias-Sicardi, 1980, *J. Magn. & Magn. Mater.* **15–18**, 961.
- Aveline, I., and J.R. Iglesias-Sicardi, 1981, *Solid State Commun.* **37**, 749.
- Baer, Y., R. Hauger, Ch. Zürcher, M. Campagna and G.K. Wertheim, 1978, *Phys. Rev. B* **18**, 4433.
- Bak, P., and P.A. Lindgård, 1973, *J. Phys. C* **6**, 3774.
- Bartholin, H., and O. Vogt, 1979, *Phys. Status Solidi A* **52**, 315.
- Bartholin, H., D. Florence, W. Tcheng-Si and O. Vogt, 1974, *Phys. Status Solidi A* **24**, 631.
- Bartholin, H., D. Florence, W. Tcheng-Si and O. Vogt, 1975, *Phys. Status Solidi A* **29**, 275.
- Bartholin, H., D. Florence, G. Parisot, J. Paureau and O. Vogt, 1977, *Phys. Lett. A* **60**, 47.
- Bartholin, H., D. Florence and O. Vogt, 1978, *J. Phys. & Chem. Solids* **39**, 89.
- Bartholin, H., D. Florence and O. Vogt, 1979a, *Phys. Status Solidi A* **52**, 647.
- Bartholin, H., P. Burlet, S. Quezel, J. Rossat-Mignod and O. Vogt, 1979b, *J. Phys. Colloq. (Paris)* **40**, C5-130.
- Bartholin, H., O. Vogt and J.P. Senateur, 1980, *J. Magn. & Magn. Mater.* **15–18**, 1247.
- Bartholin, H., C. Breandon, R. Tchapoutian and O. Vogt, 1984, *J. Phys. (Paris)* **45**, 1183.
- Bartholin, H., J.M. Effantin, P. Burlet, J. Rossat-Mignod, J.C. Achard and D. Ravot, 1985, *J. Magn. & Magn. Mater.* **52**, 381.
- Batlogg, B., 1980, *J. Magn. & Magn. Mater.* **15–18**, 939.
- Batlogg, B., 1981, *Phys. Rev. B* **23**, 650.
- Batlogg, B., A. Schlegel and P. Wachter, 1977,



- Physica B **86-88**, 229.
- Batlogg, B., H.R. Ott, E. Kaldis, W. Thöni and P. Wachter, 1979, Phys. Rev. B **19**, 247.
- Beeken, R.B., and J.W. Schweitzer, 1981, Phys. Rev. B **23**, 3620.
- Berton, A., J. Chaussy, B. Cornut, J. Flouquet, J. Odin, J. Peyrard and F. Holtzberg, 1981, Phys. Rev. B **23**, 3504.
- Birgeneau, R.J., E. Bucher, J.P. Maita, L. Passell and K.C. Turberfield, 1973, Phys. Rev. B **8**, 5345.
- Bjerrum-Møller, H., S.M. Shapiro and R.J. Birgeneau, 1977, Phys. Rev. Lett. **39**, 1021.
- Blaise, A., J.M. Fournier and P. Salmon, 1973, Solid State Commun. **13**, 555.
- Blaise, A., J.M. Fournier, D.A. Damien and A. Wojakowski, 1983, J. Magn. & Magn. Mater. **31-34**, 233.
- Blaise, A., M.N. Bouillet, F. Bourdarot, P. Burlet, J. Rebizant, J. Rossat-Mignod, J.P. Sanchez, J.C. Spirlet and O. Vogt, 1992, J. Magn. & Magn. Mater. **104-107**, 33.
- Bodnar, R.E., H. Steinfink and K.S.V.L. Naresinkan, 1968, J. Appl. Phys. **39**, 1485.
- Boeuf, A., R. Caciuffo, J.M. Fournier, L. Manes, J. Rebizant, E. Roudaut and F. Rustichelli, 1984, Solid State Commun. **52**, 451.
- Bonnet, M., J.X. Boucherle, J. Flouquet, F. Holtzberg, D. Jaccard, J. Schweitzer and A. Stunault, 1986, Physica B **136**, 428.
- Bonville, P., J.A. Hodges, F. Hulliger, P. Imbert and H.R. Ott, 1987, J. Magn. & Magn. Mater. **63-64**, 626.
- Bonville, P., J.A. Hodges, F. Hulliger, P. Imbert, G. Jéhanno, J.B. Marimon da Cunha and H.R. Ott, 1988, J. Magn. & Magn. Mater. **76-77**, 473.
- Börgermann, F.-J., H. Maletta and W. Zinn, 1986, J. Magn. & Magn. Mater. **54-57**, 71.
- Boucherle, J.X., A. Delapalme, C.J. Howard, J. Rossat-Mignod and O. Vogt, 1980, Physica B **102**, 253.
- Brun, T.O., G.H. Lander, F.W. Korty and J.S. Kouvel, 1975, AIP Conf. Proc. **24**, 244.
- Brun, T.O., F.W. Korty and J.S. Kouvel, 1980, J. Magn. & Magn. Mater. **15-18**, 298.
- Bucher, E., R.J. Birgeneau, J.P. Maita, G.P. Felcher and T.O. Brun, 1972, Phys. Rev. Lett. **28**, 746.
- Bucher, E., K. Andres, F.J. di Salvo, J.P. Maita, A.C. Gossard, A.S. Cooper and G.W. Hull, 1975, Phys. Rev. B **11**, 500.
- Burlet, P., J. Rossat-Mignod, H. Bartholin and O. Vogt, 1979a, J. Phys. **40**, 47.
- Burlet, P., S. Quezel, J. Rossat-Mignod, G.H. Lander and O. Vogt, 1979b, J. Magn. & Magn. Mater. **14**, 309.
- Burlet, P., S. Quezel, J. Rossat-Mignod, O. Vogt and G.H. Lander, 1980a, Physica B **102**, 271.
- Burlet, P., S. Quezel, J. Rossat-Mignod, H. Bartholin and O. Vogt, 1980b, Physica B **102**, 353.
- Burlet, P., J. Rossat-Mignod and R. Troč, 1982, Solid State Commun. **43**, 479.
- Burlet, P., S. Quezel, J. Rossat-Mignod, J.C. Spirlet, J. Rebizant, W. Müller and O. Vogt, 1984, Phys. Rev. B **30**, 6660.
- Burlet, P., S. Quezel, J. Rossat-Mignod and R. Horyn, 1985, Solid State Commun. **55**, 1057.
- Burlet, P., S. Quezel, M. Kuznietz, D. Bonnisseau, J. Rossat-Mignod, J.C. Spirlet, J. Rebizant and O. Vogt, 1986a, J. Less-Common Met. **121**, 325.
- Burlet, P., J. Rossat-Mignod, S. Quezel, O. Vogt, J.C. Spirlet and J. Rebizant, 1986b, J. Less-Common Met. **121**, 121.
- Burlet, P., D. Bonnisseau, S. Quezel, J. Rossat-Mignod, J.C. Spirlet, J. Rebizant and O. Vogt, 1987a, J. Magn. & Magn. Mater. **63-64**, 151.
- Burlet, P., J. Rossat-Mignod, G.H. Lander, J.C. Spirlet, J. Rebizant and O. Vogt, 1987b, Phys. Rev. B **36**, 5306.
- Burlet, P., S. Quezel, J. Rossat-Mignod, J.C. Spirlet, J. Rebizant and O. Vogt, 1987c, J. Magn. & Magn. Mater. **63-64**, 145.
- Burlet, P., J.M. Fournier, E. Pleska, S. Quezel, J. Rossat-Mignod, J.C. Spirlet, J. Rebizant and O. Vogt, 1988, J. Phys. Colloq. (Paris) **49**, C8-469.
- Busch, G., 1967, J. Appl. Phys. **38**, 1386.
- Busch, G., and O. Vogt, 1967, Phys. Lett. A **25**, 449.
- Busch, G., and O. Vogt, 1968, J. Appl. Phys. **39**, 1334.
- Busch, G., and O. Vogt, 1978, J. Less-Common Met. **62**, 335.
- Busch, G., P. Junod, O. Vogt and F. Hulliger, 1963, Phys. Lett. **6**, 79.
- Busch, G., P. Junod, P. Schwob, O. Vogt and F. Hulliger, 1964a, Phys. Lett. **9**, 7.
- Busch, G., P. Schwob, O. Vogt and F. Hulliger, 1964b, Phys. Lett. **11**, 100.
- Busch, G., P. Junod, F. Levy and O. Vogt, 1964c, in: Proc. Int. Conf. on Magnetism, Nottingham, ed. A.C. Strickland (Institute of Physics and Physical Society, London) p. 472.
- Busch, G., O. Marincek, A. Menth and O. Vogt, 1965a, Phys. Lett. **14**, 262.

- Busch, G., P. Junod, F. Levy, A. Menth and O. Vogt, 1965b, *Phys. Lett.* **14**, 264.
- Busch, G., O. Vogt and F. Hulliger, 1965c, *Phys. Lett.* **15**, 301.
- Busch, G., P. Schwob and O. Vogt, 1966a, *Phys. Lett.* **23**, 636.
- Busch, G., A. Menth, O. Vogt and F. Hulliger, 1966b, *Phys. Lett.* **19**, 622.
- Busch, G., O. Vogt and P. Schwob, 1966c, in: *Colloq. Int. du Centre National de la Recherche Scientifique*, Nr. 166, ed. R. Pauthenet (Editions CNRS, Paris) p. 401.
- Busch, G., F. Hulliger and O. Vogt, 1979a, *J. Phys. Colloq. (Paris)* **40**, C4-62.
- Busch, G., O. Vogt and H. Bartholin, 1979b, *J. Phys. Colloq. (Paris)* **40**, C4-64.
- Busch, G., O. Vogt, A. Delapalme and G.H. Lander, 1979c, *J. Phys. C* **12**, 1391.
- Buschbeck, A., C.H. Chojnowski, J. Kötzi, R. Sonder and G. Thummes, 1987, *J. Magn. & Magn. Mater.* **69**, 171.
- Buyers, W.J.L., A.F. Murray, T.M. Holden, E.C. Svensson, P. de V. DuPlessis, G.H. Lander and O. Vogt, 1980, *Physica B* **102**, 291.
- Buyers, W.J.L., A.F. Murray, J.A. Jackman, T.M. Holden, P. de V. DuPlessis and O. Vogt, 1981, *J. Appl. Phys.* **52**, 2222.
- Cable, J.W., and W.C. Koehler, 1972, *AIP Conf. Proc.* **5**, 1381.
- Cable, J.W., J.B. Comly, B.R. Cooper, I.S. Jacobs, W.C. Koehler and O. Vogt, 1972, *AIP Conf. Proc.* **10**, 1554.
- Carr, S.L., C. Long, W.G. Moulton and M. Kuznietz, 1969, *Phys. Rev. Lett.* **23**, 786.
- Chattopadhyay, T., P. Burlet, J. Rossat-Mignod, H. Bartholin, C. Vettier and O. Vogt, 1986, *J. Magn. & Magn. Mater.* **54-57**, 503.
- Chattopadhyay, T., P. Burlet, J. Rossat-Mignod, H. Bartholin, C. Vettier and O. Vogt, 1987, *J. Magn. & Magn. Mater.* **63-64**, 52.
- Child, H.R., M.K. Wilkinson, J.W. Cable, W.C. Koehler and E.O. Wollan, 1963, *Phys. Rev.* **131**, 922.
- Cooper, B.R., 1966, *Phys. Lett.* **22**, 244.
- Cooper, B.R., 1968, *Helv. Phys. Acta* **41**, 750.
- Cooper, B.R., and O. Vogt, 1970a, *Phys. Rev. B* **1**, 1211.
- Cooper, B.R., and O. Vogt, 1970b, *Phys. Rev. B* **1**, 1218.
- Cooper, B.R., and O. Vogt, 1979, *J. Phys. Colloq. (Paris)* **40**, C4-66.
- Cooper, B.R., I.S. Jacobs, C.D. Graham and O. Vogt, 1971, *J. Phys. Colloq. (Paris)* **C-1**, 359.
- Cooper, B.R., A. Furrer, W. Bührer and O. Vogt, 1972, *Solid State Commun.* **11**, 21.
- Cooper, B.R., O. Vogt and R. Siemann, 1980a, *J. Magn. & Magn. Mater.* **15-18**, 1249.
- Cooper, B.R., O. Vogt and R. Siemann, 1980b, *Physica B* **102**, 41.
- Cooper, B.R., P. Thayamballi, J.C. Spirlet, W. Müller and O. Vogt, 1983a, *Phys. Rev. Lett.* **51**, 2418.
- Cooper, B.R., P. Thayamballi and O. Vogt, 1983b, *J. Magn. & Magn. Mater.* **31-34**, 235.
- Cooper, B.R., P. Thayamballi and D. Yang, 1984, *J. Appl. Phys.* **55**, 1866.
- Cooper, B.R., R. Siemann, D. Yang, P. Thayamballi and A. Banerjee, 1985, in: *Handbook on the Physics and Chemistry of the Actinides*, Vol. 2, eds A.J. Freeman and G.H. Lander (North-Holland, Amsterdam) p. 435.
- Cooper, B.R., J.M. Wills, N. Kioussis and Q.-G. Sheng, 1988, *J. Phys. Colloq. (Paris)* **49**, C8-463.
- Croft, M., and A. Jayaraman, 1980, *Solid State Commun.* **35**, 203.
- Curry, N.A., 1965, *Proc. Phys. Soc.* **86**, 1193.
- Cutler, R.A., and A.W. Lawson, 1975, *J. Appl. Phys.* **46**, 2739.
- Damien, D.A., A. Wojakowski and W. Müller, 1976, *Inorg. Nucl. Chem. Lett.* **12**, 441.
- Damien, D.A., R.G. Haire and J.R. Peterson, 1979, *J. Phys. Colloq. (Paris)* **40**, C4-95.
- Danan, J., C.H. de Novion and R. Lallement, 1969, *Solid State Commun.* **7**, 1103.
- De Moura, M.A., and H.B. Callen, 1977, *Physica B* **86-88**, 132.
- De Novion, C.H., and R. Lorenzelli, 1968, *J. Phys. & Chem. Solids* **29**, 1901.
- Delapalme, A., G. Busch, O. Vogt and G.H. Lander, 1979, *J. Phys. Colloq. (Paris)* **40**, C4-74.
- Dell, R.M., and M. Allbutt, 1963, *AERE - Report* Nr. 4253.
- Didchenko, R., and F.P. Gortsema, 1963, *J. Phys. & Chem. Solids* **24**, 863.
- Dönni, A., P. Fischer, A. Furrer and F. Hulliger, 1989, *Solid State Commun.* **71**, 365.
- Dönni, A., P. Fischer, A. Furrer, P. Bonville, F. Hulliger and H.R. Ott, 1990a, *Z. Phys. B* **81**, 83.
- Dönni, A., P. Fischer, A. Furrer, W. Bacsa and P. Wachter, 1990b, *Z. Phys. B* **80**, 269.
- Dönni, A., A. Furrer, P. Fischer, F. Hulliger, P. Wachter and H.R. Ott, 1990c, *J. Magn. & Magn. Mater.* **90-91**, 143.
- Dönni, A., A. Furrer, P. Fischer, F. Hulliger and P. Wachter, 1991, *Physica B* **171**, 353.

- Dönni, A., A. Furrer, P. Fischer, F. Hulliger and S.M. Hayden, 1992, *J. Magn. & Magn. Mater.* **104-107**, 1204.
- DuPlessis, P. de V., 1986, *J. Magn. & Magn. Mater.* **54-57**, 537.
- DuPlessis, P. de V., and C.F. Van Doorn, 1977, *Physica B* **86-88**, 993.
- Enz, U., J.F. Fast, S. van Houten and J. Smit, 1962, *Philips Res. Repts.* **17**, 451.
- Escorne, M., A. Mauger, D. Ravot and J.C. Achard, 1984, *J. Appl. Phys.* **55**, 1835.
- Felcher, G.P., T.O. Brun, R.J. Gambino and M. Kuznietz, 1973, *Phys. Rev. B* **8**, 260.
- Ferré, J., M. Ayadi, R.V. Chamberlin, R. Orbach and N. Bontemps, 1986, *J. Magn. & Magn. Mater.* **54-57**, 211.
- Fischer, P., P. Schobinger-Papamantellos, E. Kaldis and A. Ernst, 1977, *J. Phys. C* **10**, 3601.
- Fischer, P., B. Lebech, G. Meier, B.D. Rainford and O. Vogt, 1978, *J. Phys. C* **11**, 345.
- Fischer, P., W. Haelg and E. Kaldis, 1979, *J. Magn. & Magn. Mater.* **14**, 301.
- Fischer, P., J. Schefer and O. Vogt, 1980, *Physica B* **102**, 192.
- Fischer, P., W. Hälgl, P. Schobinger-Papamantellos, H. Boppert, E. Kaldis and P. Wachter, 1982, in: *Valence Instabilities*, eds P. Wachter and H. Boppert (North-Holland, Amsterdam) p. 551.
- Fischer, P., W. Hälgl and F. Hulliger, 1985a, *Physica B* **130**, 551.
- Fischer, P., A. Furrer, E. Kaldis, D.J. Kim, J.K. Kjems and P.M. Levy, 1985b, *Phys. Rev. B* **31**, 456.
- Flouquet, J., P. Haen and C. Vettier, 1982, *J. Magn. & Magn. Mater.* **29**, 159.
- Foner, S., B.R. Cooper and O. Vogt, 1972, *Phys. Rev. B* **6**, 2040.
- Fournier, J.M., 1985, in: *Structure and Bonding* 59/60, eds L. Manes and U. Benedict (Springer, Berlin) p. 127.
- Fournier, J.M., 1986, *J. Less-Common Met.* **121**, 101.
- Fournier, J.M., and R. Troč, 1985, in: *Handbook on the Physics and Chemistry of the Actinides*, Vol. 2, eds A.J. Freeman and G.H. Lander (North-Holland, Amsterdam) p. 29.
- Fournier, J.M., J. Beille and C.H. de Novion, 1979, *J. Phys. Colloq. (Paris)* **40**, C4-32.
- Fournier, J.M., E. Pleska, J. Chiapusio, J. Rossat-Mignod, J. Rebizant, J.C. Spirlet and O. Vogt, 1990, *Physica B* **163**, 493.
- Franceschi, E., and G.L. Olcese, 1968, *J. Phys. & Chem. Solids* **30**, 903.
- Frick, B., J. Schoenes, F. Hulliger and O. Vogt, 1984, *Solid State Commun.* **49**, 1133.
- Fukuma, H., T. Komatsubara, T. Suzuki, S. Kunii, E. Kaldis and T. Kasuya, 1983, *J. Magn. & Magn. Mater.* **31-34**, 431.
- Fukuma, H., T. Suzuki and T. Kasuya, 1985a, *J. Magn. & Magn. Mater.* **52**, 7.
- Fukuma, H., T. Komatsubara, T. Suzuki, E. Kaldis and T. Kasuya, 1985b, *J. Phys. Soc. Jpn.* **54**, 3067.
- Furrer, A., and H. Heer, 1973, *Phys. Rev. Lett.* **31**, 1350.
- Furrer, A., and E. Kaldis, 1980, in: *Crystalline Electric Fields and Structural Effects in f-Electron Systems*, eds J. Crow, R.P. Guertin and T.W. Mihalisin (Plenum, New York) p. 497.
- Furrer, A., and U. Tellenbach, 1975, *Helv. Phys. Acta* **48**, 451.
- Furrer, A., J.K. Kjems and O. Vogt, 1972, *J. Phys. C* **5**, 2246.
- Furrer, A., W.J.L. Buyers, R.M. Nicklow and O. Vogt, 1976, *Phys. Rev. B* **14**, 179.
- Furrer, A., W.J.L. Buyers, R.M. Nicklow and O. Vogt, 1977, *Physica B* **86-88**, 105.
- Furrer, A., W. Hälgl, H. Heer and O. Vogt, 1979a, *J. Phys. Colloq. (Paris)* **40**, C5-122.
- Furrer, A., W. Hälgl, H. Heer and O. Vogt, 1979b, *J. Appl. Phys.* **50**, 2040.
- Gambino, R.J., T.R. McGuire, H.A. Alperin and S.J. Pickart, 1970, *J. Appl. Phys.* **41**, 933.
- Golovsovskii, I.V., and V.P. Plakhty, 1973, *Phys. Status Solidi B* **56**, 61.
- Gorobchenko, V.D., I.I. Lukashevich, V.G. Stankevich, N.I. Filippov, V.I. Chukalin and E.I. Yarembash, 1971, *Sov. Phys. Solid State* **13**, 901.
- Gronau, M., and S. Methfessel, 1980, *J. Magn. & Magn. Mater.* **15-18**, 975.
- Guertin, R.P., J.E. Crow, L.D. Longinotti, E. Bucher, L. Kupferberg and S. Foner, 1975, *Phys. Rev. B* **12**, 1005.
- Gulick, J.M., and W.G. Moulton, 1971, *Phys. Lett. A* **35**, 429.
- Haessler, M., and C.H. de Novion, 1977, *J. Phys. C* **10**, 589.
- Haire, R.G., 1981, in: *Actinides in Perspective*, ed. N.M. Edelstein (Pergamon Press, New York) p. 324.
- Hälgl, B., and A. Furrer, 1984, *J. Appl. Phys.* **55**, 1860.
- Hälgl, B., and O. Vogt, 1985, *J. Magn. & Magn. Mater.* **52**, 410.
- Hälgl, B., A. Furrer, W. Hälgl and O. Vogt, 1981, *J. Phys. C* **14**, L961.
- Hälgl, B., A. Furrer, W. Hälgl and O. Vogt, 1982a,

- J. Appl. Phys. **53**, 1927.
- Hälg, B., A. Furrer, W. Hälg and O. Vogt, 1982b, *J. Magn. & Magn. Mater.* **29**, 151.
- Hälg, B., A. Furrer, J.K. Kjems and O. Vogt, 1983, *Phys. Rev. Lett.* **50**, 1085.
- Hälg, B., A. Furrer and O. Vogt, 1985, *Physica B* **130**, 379.
- Hälg, B., A. Furrer and O. Vogt, 1986, *Phys. Rev. Lett.* **57**, 2745.
- Hälg, B., A. Furrer and J.K. Kjems, 1987a, *Phys. Rev. Lett.* **59**, 1034.
- Hälg, B., A. Furrer and O. Vogt, 1987b, *J. Magn. & Magn. Mater.* **63–64**, 55.
- Hasanain, S.K., R.P. Guertin, K. Westerholt, M. Guyot and S. Foner, 1981, *Phys. Rev. B* **24**, 5165.
- Hasegawa, A., and H. Yamagami, 1992, *J. Magn. & Magn. Mater.* **104–107**, 65.
- Heaton, L., M.H. Mueller, K.D. Anderson and D.D. Zaubers, 1969, *J. Phys. & Chem. Solids* **30**, 453.
- Herz, R., and H. Kronmueller, 1980, *J. Magn. & Magn. Mater.* **15–18**, 1299.
- Holden, T.M., E.C. Svensson, W.J.L. Buyers and O. Vogt, 1974, *Phys. Rev. B* **10**, 3864.
- Holden, T.M., W.J.L. Buyers, E.C. Svensson, J.A. Jackman, A.F. Murray, O. Vogt and P. de V. DuPlessis, 1982, *J. Appl. Phys.* **53**, 1967.
- Holtzberg, F., and J. Wittig, 1981, *Solid State Commun.* **40**, 315.
- Hoogerbeets, R., W.-L. Luo, R. Orbach, N. Bontemps and H. Maletta, 1986, *J. Magn. & Magn. Mater.* **54–57**, 177.
- Hovi, V., M. Lehtinen and R. Vuola, 1970, *Phys. Lett. A* **31**, 451.
- Huang, C.Y., R.J. Laskowski, C.E. Olsen and J.L. Smith, 1979, *J. Phys. Colloq. (Paris)* **40**, C4-26.
- Hulliger, F., 1978, *J. Magn. & Magn. Mater.* **8**, 183.
- Hulliger, F., 1979, in: *Handbook on the Physics and Chemistry of Rare Earths*, Vol. 4, eds K.A. Gschneidner Jr and L. Eyring (North-Holland, Amsterdam) p. 153.
- Hulliger, F., 1980, *J. Magn. & Magn. Mater.* **15–18**, 1243.
- Hulliger, F., and B. Natterer, 1973, *Solid State Commun.* **13**, 221.
- Hulliger, F., and H.R. Ott, 1978, *Z. Phys. B* **29**, 47.
- Hulliger, F., and T. Siegrist, 1979, *Z. Phys. B* **35**, 81.
- Hulliger, F., and F. Stucki, 1978, *Z. Phys. B* **31**, 393.
- Hulliger, F., M. Landolt, R. Schmelzer and I. Zurbach, 1975, *Solid State Commun.* **17**, 751.
- Hulliger, F., B. Natterer and H.R. Ott, 1978a, *J. Magn. & Magn. Mater.* **8**, 87.
- Hulliger, F., B. Natterer and K. Rüegg, 1978b, *Z. Phys. B* **32**, 37.
- Hulliger, F., M. Landolt and R. Schmelzer, 1982, in: *Rare Earths in modern Science and Technology*, eds G.J. McCarthy, H.B. Silber and J.J. Rhyne (Plenum, New York) p. 455.
- Hulliger, F., H.R. Ott and T. Siegrist, 1984, *J. Less-Common Met.* **96**, 263.
- Iandelli, A., 1961, in: *Rare Earth Research*, ed. E.V. Kleber (MacMillan Company, New York) p. 155.
- Jensen, J., N.H. Andersen and O. Vogt, 1980, *J. Phys. C* **13**, 213.
- Jones, D.L., W.G. Stirling, G.H. Lander, J. Rebizant, J.C. Spirlet, M. Alba and O. Vogt, 1991, *J. Phys. C* **3**, 3551.
- Jones, E.D., 1969, *Phys. Rev.* **180**, 455.
- Junod, P., A. Menth and O. Vogt, 1969, *Phys. Kondens. Mater.* **8**, 323.
- Kanellakopoulos, B., J.P. Charvillat, F. Maino and W. Müller, 1975, in: *Transplutonium*, eds W. Müller and R. Lindner (North-Holland, Amsterdam) p. 182.
- Kasuya, T., 1970, *IBM Res. Dev.* **14**, 214.
- Kasuya, T., Y.S. Kwon, T. Suzuki, K. Nakanishi, F. Ishiyama and K. Takegahara, 1990, *J. Magn. & Magn. Mater.* **90–91**, 389.
- Kido, G., K. Komorita, Y. Nakagawa and T. Suzuki, 1992, *J. Magn. & Magn. Mater.* **104–107**, 1239.
- Kim, D.J., and P.M. Lévy, 1982, *J. Magn. & Magn. Mater.* **27**, 257.
- Kim, D.J., P.M. Lévy and L.F. Uffer, 1975, *Phys. Rev. B* **12**, 989.
- Kioussis, N., B.R. Cooper and J.M. Wills, 1988, *J. Appl. Phys.* **63**, 3683.
- Kioussis, N., B.R. Cooper, J.M. Wills and Q.G. Sheng, 1990, *Physica B* **163**, 107.
- Knott, H.W., G.H. Lander, M.H. Mueller and O. Vogt, 1980, *Phys. Rev. B* **21**, 4159.
- Köbler, U., and K. Binder, 1980, *J. Magn. & Magn. Mater.* **15–18**, 313.
- Koehler, W.C., R.M. Moon and F. Holtzberg, 1979, *J. Appl. Phys.* **50**, 1975.
- Kohgi, M., K. Ohoyama, A. Oyamada, T. Suzuki and M. Arai, 1990, *Physica B* **163**, 625.
- Komorita, K., G. Kido, Y. Nakagawa, Y.S. Kwon and T. Suzuki, 1992, *J. Magn. & Magn. Mater.* **104–107**, 1241.
- Kötzler, J., and G. Raffius, 1980, *Z.*

- Phys. B **38**, 139.
- Kötzler, J., G. Raffius, A. Loidl and C.M.E. Zeyen, 1979, *Z. Phys. B* **35**, 125.
- Kouvel, J.S., and J.S. Kasper, 1963, *J. Phys. & Chem. Solids* **24**, 529.
- Kouvel, J.S., T.O. Brun and F.W. Korty, 1977, *Physica B* **86-88**, 1043.
- Kruger, O.L., and J.B. Moser, 1967, *J. Chem. Phys.* **46**, 891.
- Kuznietz, M., 1969, *Phys. Rev.* **180**, 476.
- Kuznietz, M., 1971, *J. Appl. Phys.* **42**, 1470.
- Kuznietz, M., G.H. Lander and F.P. Campos, 1968, *J. Phys. & Chem. Solids* **30**, 1642.
- Kuznietz, M., P. Burllet, J. Rossat-Mignod and O. Vogt, 1985, *Solid State Commun.* **55**, 1063.
- Kuznietz, M., P. Burllet, J. Rossat-Mignod and O. Vogt, 1986a, *J. Less-Common Met.* **121**, 217.
- Kuznietz, M., P. Burllet, J. Rossat-Mignod and O. Vogt, 1986b, *J. Magn. & Magn. Mater.* **54-57**, 553.
- Kuznietz, M., P. Burllet, J. Rossat-Mignod and O. Vogt, 1986c, *J. Magn. & Magn. Mater.* **61**, 246.
- Kuznietz, M., P. Burllet, J. Rossat-Mignod and O. Vogt, 1987a, *J. Magn. & Magn. Mater.* **69**, 12.
- Kuznietz, M., P. Burllet, J. Rossat-Mignod, O. Vogt and K. Mattenberger, 1987b, *Phys. Rev. B* **35**, 7142.
- Kuznietz, M., P. Burllet, J. Rossat-Mignod, O. Vogt, K. Mattenberger and H. Bartholin, 1988, *J. Phys. Colloq. (Paris)* **49**, C8-479.
- Kuznietz, M., P. Burllet, J. Rossat-Mignod, O. Vogt, K. Mattenberger and H. Bartholin, 1990, *J. Magn. & Magn. Mater.* **88**, 109.
- Kwon, Y.S., Y. Haga, O. Nakamura, T. Suzuki and T. Kasuya, 1991, *Physica B* **171**, 324.
- Lam, D.J., 1972, *AIP Conf. Proc.* **5**, 892.
- Lam, D.J., and A.T. Aldred, 1974, in: *The Actinides, Electronic Structure and Related Properties*, eds A.J. Freeman and J.B. Darby (Academic Press, New York) p. 109.
- Lam, D.J., and D.E. Ellis, 1985, *Physica B* **130**, 541.
- Lam, D.J., and F.Y. Fradin, 1974, *Phys. Rev. B* **9**, 238.
- Lam, D.J., F.Y. Fradin and O.L. Kruger, 1969, *Phys. Rev.* **187**, 606.
- Lam, D.J., B.D. Dunlap, A.T. Aldred and I. Nowik, 1973, *AIP Conf. Proc.* **10**, 83.
- Lam, D.J., B.D. Dunlap, A.R. Harvey, M.H. Mueller, A.T. Aldred, I. Nowik and G.H. Lander, 1974, in: *Proc. Int. Conf. on Magnetism, Moscow*, Vol. 6, eds R.P. Ozerov, Yu.A. Izyumov and F.A. Kassan-Ogly (Nauka, Moscow) p. 74.
- Landau, D.P., and J.E. Rives, 1974, *Solid State Commun.* **15**, 665.
- Lander, G.H., 1975, *AIP Conf. Proc.* **29**, 311.
- Lander, G.H., 1978, in: *Rare Earth and Actinides*, *Inst. Phys. Conf. Ser. Nr. 37*, ch. 7, p. 173.
- Lander, G.H., 1980, *J. Magn. & Magn. Mater.* **15-18**, 1208.
- Lander, G.H., 1981, in: *Actinides in Perspective*, ed. N.M. Edelstein (Pergamon Press, New York) p. 107.
- Lander, G.H., 1987, *J. Magn. & Magn. Mater.* **63-64**, 133.
- Lander, G.H., and D.J. Lam, 1976, *Phys. Rev. B* **14**, 4064.
- Lander, G.H., and M.H. Mueller, 1974, *Phys. Rev. B* **10**, 1994.
- Lander, G.H., and J.F. Reddy, 1976, in: *Proc. Conf. on Neutron Scattering*, ed. R.M. Moon (Gatlinburg, USA) p. 623.
- Lander, G.H., M. Kuznietz and D.E. Cox, 1969, *Phys. Rev.* **188**, 963.
- Lander, G.H., B.D. Dunlap, D.J. Lam, A.R. Harvey, I. Nowik, M.H. Mueller and A.T. Aldred, 1972a, *AIP Conf. Proc.* **10**, 88.
- Lander, G.H., M.H. Mueller and J.F. Reddy, 1972b, *Phys. Rev. B* **6**, 1880.
- Lander, G.H., T.O. Brun and O. Vogt, 1973a, *Phys. Rev. B* **7**, 1988.
- Lander, G.H., B.D. Dunlap, M.H. Mueller, I. Nowik and J.F. Reddy, 1973b, *Int. J. Magnetism* **4**, 99.
- Lander, G.H., M.H. Mueller, D.M. Sparlin and O. Vogt, 1976, *Phys. Rev. B* **14**, 5035.
- Lander, G.H., S.K. Sinha, D.M. Sparlin and O. Vogt, 1978, *Phys. Rev. Lett.* **40**, 523.
- Lander, G.H., W.G. Stirling and O. Vogt, 1979a, *Phys. Rev. Lett.* **42**, 260.
- Lander, G.H., W.G. Stirling and O. Vogt, 1979b, *J. Phys. Colloq. (Paris)* **40**, C4-36.
- Lander, G.H., A. Delapalme, P.J. Brown, J.C. Spirlet, J. Rebizant and O. Vogt, 1984, *Phys. Rev. Lett.* **53**, 2262.
- Lander, G.H., A. Delapalme, P.J. Brown, J.C. Spirlet, J. Rebizant and O. Vogt, 1985, *J. Appl. Phys.* **57**, 3748.
- Lander, G.H., W.G. Stirling, J. Rossat-Mignod, J.C. Spirlet, J. Rebizant and O. Vogt, 1986, *Physica B* **136**, 409.
- Lander, G.H., W.G. Stirling, J. Rossat-Mignod, M. Hagen and O. Vogt, 1990a, *Phys. Rev. B* **41**, 6899.
- Lander, G.H., M.S.S. Brooks, B. Lebech,

- P.J. Brown, O. Vogt and K. Mattenberger, 1990b, *Appl. Phys. Lett.* **57**, 989.
- Lander, G.H., M.S.S. Brooks, B. Lebech, P.J. Brown, O. Vogt and K. Mattenberger, 1991, *J. Appl. Phys.* **69**, 4803.
- Lassailly, Y., C. Vettier, F. Holtzberg, J. Flouquet, C.M.E. Zeyen and F. Lapierre, 1983, *Phys. Rev. B* **28**, 2880.
- Lassailly, Y., C. Vettier, F. Holtzberg, A. Benoit and J. Flouquet, 1984, *Solid State Commun.* **52**, 717.
- Lassailly, Y., C. Vettier, F. Holtzberg and P. Burllet, 1986, *Physica B* **136**, 391.
- Lea, K.R., M.J.M. Leask and W.P. Wolf, 1962, *J. Phys. & Chem. Solids* **23**, 1381.
- Léger, J.M., R. Epain, J. Loriers, D. Ravot and J. Rossat-Mignod, 1983, *Phys. Rev. B* **28**, 7125.
- Léger, J.M., D. Ravot and J. Rossat-Mignod, 1984, *J. Phys. C* **17**, 4935.
- Léger, J.M., K. Oki, J. Rossat-Mignod and O. Vogt, 1985, *J. Phys. (Paris)* **46**, 889.
- Léger, J.M., K. Oki, A.M. Redon, I. Vedel, J. Rossat-Mignod and O. Vogt, 1986, *Phys. Rev. B* **33**, 7205.
- Léger, J.M., I. Vedel, A.M. Redon and J. Rossat-Mignod, 1987, *J. Magn. & Magn. Mater.* **63-64**, 49.
- Lemmer, R.H., and J.E. Lowther, 1978, *J. Phys. C* **11**, 1145.
- Levy, F., 1969, *Phys. Kondens. Mater.* **10**, 85.
- Levy, F., and O. Vogt, 1967, *Phys. Lett. A* **24**, 444.
- Loewenhaupt, M., and H. Bjerrum-Møller, 1981, *Physica B* **108**, 1349.
- Loewenhaupt, M., and E. Holland-Moritz, 1978, *J. Magn. & Magn. Mater.* **9**, 50.
- Loginov, G.M., A.T. Starovoitov and A.V. Golubkov, 1970, *Sov. Phys. Solid State* **11**, 3053.
- Loginov, G.M., V.M. Sergeeva and M.F. Bryzhina, 1971, *Sov. Phys. JETP* **32**, 1054.
- Löhneysen, H. v., R. van den Berg, J. Wosnitza, G.V. Lecomte and W. Zinn, 1986, *J. Magn. & Magn. Mater.* **54-57**, 189.
- Long, C., and L.Y. Wang, 1971, *Phys. Rev. B* **3**, 1656.
- Maglic, R.C., G.H. Lander, M.H. Mueller, J. Crangle and G.S. Williams, 1974, *Phys. Rev. B* **10**, 1943.
- Marples, J.A.C., 1970, *J. Phys. & Chem. Solids* **31**, 2431.
- Marples, J.A.C., C.F. Sampson, F.A. Wedgwood and M. Kuznietz, 1975, *J. Phys. C* **8**, 708.
- Matsui, H., 1987, *Phys. Status Solidi A* **104**, 825.
- Matsui, H., M. Tamaki, K. Katori, S. Nakashima and T. Kirihara, 1983, *J. Magn. & Magn. Mater.* **31-34**, 237.
- Mattenberger, K., and O. Vogt, 1985, 15èmes Journées des Actinides, Liège, Belgium, p. I.5.
- Mattenberger, K., and O. Vogt, 1992, *Phys. Scr. T* **45**, 103.
- Mattenberger, K., O. Vogt, J.C. Spirlet and J. Rebizant, 1986a, *J. Less-Common Met.* **121**, 285.
- Mattenberger, K., O. Vogt, J.C. Spirlet and J. Rebizant, 1986b, *J. Magn. & Magn. Mater.* **54-57**, 539.
- Mattenberger, K., O. Vogt, J. Rebizant, J.C. Spirlet, P. Burllet, E. Pleska and J. Rossat-Mignod, 1990a, *Physica B* **163**, 488.
- Mattenberger, K., O. Vogt, J. Rebizant and J.C. Spirlet, 1990b, 20èmes Journées des Actinides, Prague, Czechoslovakia, p. 26.
- Mattenberger, K., O. Vogt, J. Rebizant, J.C. Spirlet, F. Bourdarot, P. Burllet, J. Rossat-Mignod, M.N. Bouillet, A. Blaise and J.P. Sanchez, 1992, *J. Magn. & Magn. Mater.* **104-107**, 43.
- McClure, J.W., 1963, *J. Phys. & Chem. Solids* **24**, 871.
- McGuire, T.R., R.J. Gambino, S.J. Pickart and H.A. Alperin, 1969, *J. Appl. Phys.* **40**, 1009.
- McWhan, D.B., C. Vettier, E.D. Isaacs, G.E. Ice, D.P. Siddons, J.B. Hastings, C. Peters and O. Vogt, 1990, *Phys. Rev. B* **42**, 6007.
- Meier, G., P. Fischer, W. Hälgl, B. Lebech, B.D. Rainford and O. Vogt, 1978, *J. Phys. C* **11**, 1173.
- Mori, N., Y. Okayama, H. Takahashi, Y.S. Kwon and T. Suzuki, 1991, *J. Appl. Phys.* **69**, 4696.
- Mueller, M.H., G.H. Lander, H.W. Knott and J.F. Reddy, 1973a, *Phys. Lett. A* **44**, 249.
- Mueller, M.H., G.H. Lander, H.W. Knott and J.F. Reddy, 1973b, *AIP Conf. Proc.* **10**, 352.
- Mueller, M.H., G.H. Lander, H.A. Hoff, H.W. Knott and J.F. Reddy, 1979, *J. Phys. Colloq. (Paris)* **40**, C4-68.
- Mukamel, D., J.M. Hastings, L.M. Corliss and J. Zhuang, 1985, *Phys. Rev. B* **32**, 7367.
- Mullen, M.E., B. Lüthi, P.S. Wang, E. Bucher, L.D. Longinotti, J.P. Maita and H.R. Ott, 1974, *Phys. Rev. B* **10**, 186.
- Myers, S.M., and A. Narath, 1973, *Solid State Commun.* **12**, 83.
- Nave, S.E., and P.G. Huray, 1980, *Rev. Sci. Instrum.* **51**, 591.
- Nave, S.E., P.G. Huray, J.R. Peterson, D.A. Damien and R.G. Haire, 1981, *Physica B* **107**, 253.
- Nave, S.E., J.R. Moore, R.G. Haire, J.R. Peterson,

- D.A. Damien and P.G. Huray, 1986, *J. Less-Common. Met.* **121**, 319.
- Nereson, N., and G. Arnold, 1971, *J. Appl. Phys.* **42**, 1625.
- Novikov, V.I., A.V. Golubkov and S.A. Kizhaev, 1982, *Sov. Phys. Solid State* **24**, 1268.
- Obolenski, M., and R. Troč, 1976, in: *Proc. 2nd Int. Conf. on Electronic Structure of the Actinides*, Wrocław, eds J. Mulak, W. Suski and R. Troč (Polish Academy of Science, Warsaw) p. 537.
- Ohashi, M., T. Kaneko, H. Yoshida and S. Abe, 1977, *Physica B* **86-88**, 224.
- Ott, H.R., and F. Hulliger, 1983, *Z. Phys.* **49**, 323.
- Ott, H.R., K. Andres and E. Bucher, 1975, *AIP Conf. Proc.* **24**, 40.
- Ott, H.R., J.K. Kjems and F. Hulliger, 1979, *Phys. Rev. Lett.* **42**, 1378.
- Ott, H.R., F. Hulliger and H. Rudigier, 1982, in: *Valence Instabilities*, eds P. Wachter and H. Boppart (North-Holland, Amsterdam) p. 511.
- Ott, H.R., H. Rudigier and F. Hulliger, 1985, *Solid State Commun.* **55**, 113.
- Oyamada, A., S. Takagi, T. Kasuya, K. Sugiyama and M. Date, 1988, *J. Phys. Soc. Jpn.* **57**, 3557.
- Oyamada, A., P. Burlet, L.P. Regnault, A. Bouvet, R. Calemczuk, J. Rossat-Mignod, T. Suzuki and T. Kasuya, 1990a, *J. Magn. & Magn. Mater.* **90-91**, 441.
- Oyamada, A., C. Ayache, T. Suzuki, J. Rossat-Mignod and T. Kasuya, 1990b, *J. Magn. & Magn. Mater.* **90-91**, 443.
- Ozeki, S., Y. Ohe, Y.S. Kwon, Y. Haga, O. Nakamura, T. Suzuki and T. Kasuya, 1991a, *Physica B* **171**, 286.
- Ozeki, S., Y.S. Kwon, Y. Haga, T. Suzuki, G. Kido and T. Kasuya, 1991b, *Physica B* **169**, 499.
- Palewski, T., 1984, *Phys. Status Solidi A* **84**, K47.
- Palewski, T., 1990, *J. Magn. & Magn. Mater.* **92**, 162.
- Palewski, T., and T. Mydlarz, 1989, *Physica B* **155**, 245.
- Palewski, T., S. Węglowski and R. Pajak, 1977, *Physica B* **86-88**, 111.
- Palewski, T., J. Warchulska and W. Wojciechowski, 1988, *J. Less-Common Met.* **141**, 241.
- Paulsen, C.C., S.J. Williamson and H. Maletta, 1986, *J. Magn. & Magn. Mater.* **54-57**, 209.
- Peyrard, J., J. Flouquet, P. Haen, F. Lapierre, Y. Lassailly, F. Holtzberg and C. Vettier, 1983, *J. Magn. & Magn. Mater.* **31-34**, 433.
- Pleska, E., J.M. Fournier, J. Chiapusio, J. Rossat-Mignod, J.C. Spirlet, J. Rebizant and O. Vogt, 1988, *J. Phys. Colloq. (Paris)* **49**, C8-493.
- Pokrzywnicki, S., T. Mydlarz, L. Pawlak and M. Duczmal, 1985, *Acta Phys. Pol. A* **68**, 511.
- Potzel, U., J. Moser, W. Potzel, F.J. Litterst, G.M. Kalvius, M. Bogé, J. Chappert and J.C. Spirlet, 1987, *J. Magn. & Magn. Mater.* **63-64**, 148.
- Proetto, C., and A. Lopez, 1982, *Phys. Rev. B* **25**, 7037.
- Raffius, G., and J. Kötzler, 1983, *Phys. Lett. A* **93**, 423.
- Rainford, B.D., K.C. Turberfield, G. Busch and O. Vogt, 1968, *J. Phys. C* **1**, 679.
- Raphael, G., and C.H. de Novion, 1969a, *Solid State Commun.* **7**, 791.
- Raphael, G., and C.H. de Novion, 1969b, *J. Phys. (Paris)* **30**, 261.
- Ravot, D., and J.C. Achard, 1982, in: *Rare Earths in modern Science and Technology*, eds G.J. McCarthy, H.B. Silber and J.J. Rhyne (Plenum, New York) p. 445.
- Ravot, D., P. Burlet, J. Rossat-Mignod and J.L. Tholence, 1980, *J. Phys. (Paris)* **41**, 1117.
- Ravot, D., A. Mauger, J.C. Achard, H. Bartholin and J. Rossat-Mignod, 1983, *Phys. Rev. B* **28**, 4558.
- Rebizant, J., J.C. Spirlet, K. Mattenberger and O. Vogt, 1984, 14èmes Journées des Actinides, Davos, Switzerland, p. 17.
- Reihl, B., N. Martensson, D.E. Eastman and O. Vogt, 1981, *Phys. Rev. B* **24**, 406.
- Ribault, M., J. Flouquet, P. Haen, F. Lapierre, J.M. Mignot and F. Holtzberg, 1980, *Phys. Rev. Lett.* **45**, 1295.
- Rossat-Mignod, J., 1987, in: *Methods of Experimental Physics*, Vol. 23C, eds K. Sköld and D.L. Price (Academic Press, New York) p. 69.
- Rossat-Mignod, J., P. Burlet, H. Bartholin, J. Villain, D. Florence and O. Vogt, 1977a, *Physica B* **86-88**, 129.
- Rossat-Mignod, J., P. Burlet, J. Villain, H. Bartholin, W. Tchong-Si, D. Florence and O. Vogt, 1977b, *Phys. Rev. B* **16**, 440.
- Rossat-Mignod, J., P. Burlet, O. Vogt and G.H. Lander, 1979a, *J. Phys. C* **12**, 1101.
- Rossat-Mignod, J., P. Burlet, O. Vogt and G.H. Lander, 1979b, *J. Phys. Colloq. (Paris)* **40**, C4-70.
- Rossat-Mignod, J., P. Burlet, H. Bartholin, R. Tchapoutian, O. Vogt, C. Vettier and R. Langnier, 1980a, *Physica B* **102**, 177.
- Rossat-Mignod, J., P. Burlet, S. Quezel and O. Vogt, 1980b, *Physica B* **102**, 237.

- Rossat-Mignod, J., P. Burlet, H. Bartholin, O. Vogt and R. Lagnier, 1980c, *J. Phys. C* **13**, 6381.
- Rossat-Mignod, J., P. Burlet, S. Quezel, O. Vogt and H. Bartholin, 1982a, in: *Crystalline Electric Field and Structural Effects in f-Electron Systems*, eds J.E. Crow, R.P. Guertin and T.W. Mihalisin (Plenum, New York) p. 501.
- Rossat-Mignod, J., P. Burlet, S. Quezel and J.M. Effantin, 1982b, *Ann. Chim. (Paris)* **7**, 471.
- Rossat-Mignod, J., D. Delacôte, J.M. Effantin, C. Vettier and O. Vogt, 1983a, *Physica B* **120**, 163.
- Rossat-Mignod, J., P. Burlet, S. Quezel, J.M. Effantin, D. Delacôte, H. Bartholin, O. Vogt and D. Ravot, 1983b, *J. Magn. & Magn. Mater.* **31-34**, 398.
- Rossat-Mignod, J., G.H. Lander and P. Burlet, 1984, in: *Handbook on the Physics and Chemistry of the Actinides*, Vol. 1, eds A.J. Freeman and G.H. Lander (North-Holland, Amsterdam) p. 415.
- Rossat-Mignod, J., P. Burlet, S. Quezel, O. Vogt, J.C. Spirlet, J. Rebizant and W. Müller, 1985a, *Physica B* **130**, 327.
- Rossat-Mignod, J., J.M. Effantin, P. Burlet, T. Chattopadhyay, L.P. Regnault, H. Bartholin, C. Vettier, O. Vogt, D. Ravot and J.C. Achart, 1985b, *J. Magn. & Magn. Mater.* **52**, 111.
- Rossat-Mignod, J., J.M. Effantin, C. Vettier and O. Vogt, 1985c, *Physica B* **130**, 555.
- Rossat-Mignod, J., P. Burlet, L.P. Regnault and C. Vettier, 1990, *J. Magn. & Magn. Mater.* **90-91**, 5.
- Sanchez, J.P., J.M. Friedt, K. Tomala and F. Holtzberg, 1985, *Phys. Lett. A* **111**, 83.
- Sanchez, J.P., J.C. Spirlet, J. Rebizant and O. Vogt, 1987, *J. Magn. & Magn. Mater.* **63-64**, 139.
- Sanchez, J.P., P. Burlet, S. Quézel, D. Bonnisseau, J. Rossat-Mignod, J.C. Spirlet, J. Rebizant and O. Vogt, 1988, *Solid State Commun.* **67**, 999.
- Sanchez, J.P., K. Tomala, J. Rebizant, J.C. Spirlet and O. Vogt, 1990, *Hyperfine Interactions* **54**, 701.
- Sanchez, J.P., A. Blaise, M.N. Bouillet, F. Bourdarot, P. Burlet, J. Rossat-Mignod, J. Rebizant, J.C. Spirlet and O. Vogt, 1991, *21èmes Journées des Actinides*, Montechoro, Portugal, p. 50.
- Schinkel, C.J., and R. Troč, 1978, *J. Magn. & Magn. Mater.* **9**, 339.
- Schmid, B., P. Fischer and F. Hulliger, 1986, *J. Less-Common Met.* **121**, 192.
- Schobinger-Papamantellos, P., P. Fischer, O. Vogt and E. Kaldis, 1973, *J. Phys. C* **6**, 725.
- Schobinger-Papamantellos, P., P. Fischer, A. Niggli, E. Kaldis and V. Hildebrand, 1974, *J. Phys. C* **7**, 2023.
- Schoenes, J., and F. Hulliger, 1987, *J. Magn. & Magn. Mater.* **63-64**, 43.
- Schoenes, J., and O. Vogt, 1978, *Solid State Commun.* **28**, 261.
- Schoenes, J., B. Frick and O. Vogt, 1985, *J. Appl. Phys.* **57**, 3149.
- Schoenes, J., H. Brändle, A. Weber and F. Hulliger, 1990, *Physica B* **163**, 496.
- Schumacher, D.P., and W.E. Wallace, 1965, *J. Appl. Phys.* **36**, 984.
- Schumacher, D.P., and W.E. Wallace, 1966, *Inorg. Chem.* **2**, 1563.
- Scott, B.A., K.A. Gingerich and R.A. Bernheim, 1967, *Phys. Rev.* **159**, 387.
- Sera, M., T. Kasuya, P. Haen, J.L. Tholence, H. Bartholin, J. Rossat-Mignod and G. Lapertot, 1985, *J. Magn. & Magn. Mater.* **52**, 377.
- Shapiro, S.M., and P. Bak, 1975, *J. Phys. & Chem. Solids* **36**, 579.
- Shapiro, S.M., S.K. Sinha, G.H. Lander and O. Vogt, 1981, *J. Appl. Phys.* **52**, 2220.
- Shenoy, G.K., M. Kuznietz, B.D. Dunlap and G.M. Kalvius, 1972, *Phys. Lett.* **42**, 61.
- Sidhu, S.S., W. Vogelsang and K.D. Anderson, 1966, *J. Phys. & Chem. Solids* **27**, 1197.
- Siemann, R., and B.R. Cooper, 1980a, *Phys. Rev. Lett.* **44**, 1015.
- Siemann, R., and B.R. Cooper, 1980b, *Physica B* **102**, 266.
- Sinha, S.K., G.H. Lander, S.M. Shapiro and O. Vogt, 1980a, *Phys. Rev. Lett.* **45**, 1028.
- Sinha, S.K., G.H. Lander, S.M. Shapiro and O. Vogt, 1980b, *Physica B* **102**, 174.
- Sinha, S.K., G.H. Lander, S.M. Shapiro and O. Vogt, 1981, *Phys. Rev. B* **23**, 4556.
- Smolenskii, G.A., V.P. Zhuze, V.E. Adamyam and G.M. Loginov, 1966, *Phys. Status Solidi* **18**, 873.
- Smolenskii, G.A., V.E. Adamyam and G.M. Loginov, 1968, *J. Appl. Phys.* **39**, 786.
- Spirlet, J.C., and O. Vogt, 1984, in: *Handbook on the Physics and Chemistry of the Actinides*, Vol. 1, eds A.J. Freeman and G.H. Lander (North-Holland, Amsterdam) p. 79.
- Spirlet, J.C., J. Rebizant and O. Vogt, 1983, *13èmes Journées des Actinides*, Elat, Israel, p. B2.
- Starovoitov, A.T., V.I. Ozhogin and G.M. Loginov, 1969, *Phys. Lett. A* **29**, 617.
- Steinitz, M., and J. Grunzweig-Genossar, 1979, *J. Phys. Colloq. (Paris)* **40**, C4-34.



- Stevens, K.W.H., and E. Pytte, 1973, *Solid State Commun.* **13**, 101.
- Stirling, W.G., G.H. Lander and O. Vogt, 1980, *Physica B* **102**, 249.
- Stutius, W., 1969a, *Phys. Kondens. Mater.* **9**, 341.
- Stutius, W., 1969b, *Phys. Kondens. Mater.* **10**, 152.
- Suzuki, T., Y.S. Kwon, S. Ozeki, Y. Haga and T. Kasuya, 1990, *J. Magn. & Magn. Mater.* **90-91**, 493.
- Takagi, S., A. Oyamada and T. Kasuya, 1988, *J. Phys. Soc. Jpn.* **57**, 1456.
- Takahashi, H., K. Takegahara, A. Yanase and T. Kasuya, 1983, *J. Magn. & Magn. Mater.* **31-34**, 405.
- Tao, L.J., J.B. Torrance and F. Holtzberg, 1974, *Solid State Commun.* **15**, 1025.
- Taub, H., and C.B.R. Parente, 1975, *Solid State Commun.* **16**, 857.
- Taub, H., S.J. Williamson, W.A. Reed and F.S.L. Hsu, 1974, *Solid State Commun.* **15**, 185.
- Tchapotian, R., C. Breandon, H. Bartholin and O. Vogt, 1986, *J. Less-Common Met.* **121**, 331.
- Thayamballi, P., and B.R. Cooper, 1984, *Phys. Rev. B* **30**, 2931.
- Thayamballi, P., D. Yang and B.R. Cooper, 1984, *Phys. Rev. B* **29**, 4049.
- Tillwick, D.L., and P. de V. DuPlessis, 1976a, *J. Magn. & Magn. Mater.* **3**, 329.
- Tillwick, D.L., and P. de V. DuPlessis, 1976b, *J. Magn. & Magn. Mater.* **3**, 319.
- Trammell, G.T., 1963, *Phys. Rev.* **131**, 932.
- Troč, R., 1980, *Physica B* **102**, 233.
- Troč, R., and D.J. Lam, 1974, *Phys. Status Solidi B* **65**, 317.
- Troč, R., J. Leciejewicz and G.H. Lander, 1980a, *J. Magn. & Magn. Mater.* **21**, 173.
- Troč, R., R. Niedzielski, J. Leciejewicz and A. Murasik, 1980b, *J. Magn. & Magn. Mater.* **15-18**, 1251.
- Trzebiatowski, W., and R. Troč, 1963, *Bull. Acad. Polon. Sci. Ser. Sci. Chim.* **11**, 661.
- Trzebiatowski, W., R. Troč and J. Leciejewicz, 1962, *Bull. Acad. Polon. Sci. Ser. Chim.* **10**, 395.
- Tsuchida, T., and Y. Nakamura, 1967, *J. Phys. Soc. Jpn.* **22**, 942.
- Tsuchida, T., and W.E. Wallace, 1965a, *J. Chem. Phys.* **43**, 2087.
- Tsuchida, T., and W.E. Wallace, 1965b, *J. Chem. Phys.* **43**, 2885.
- Tsuchida, T., Y. Nakamura and T. Kaneko, 1969, *J. Phys. Soc. Jpn.* **26**, 284.
- Van Vleck, J.H., 1932, *Theory of Electric and Magnetic Susceptibilities* (Oxford University Press).
- Varma, C.M., 1976, *Rev. Mod. Phys.* **48**, 219.
- Vedel, I., A.M. Redon, J.M. Léger, J. Rossat-Mignod and O. Vogt, 1986, *J. Phys. C* **19**, 6297.
- Vettier, C., D.B. McWhan, E.I. Blount and G. Shirane, 1977, *Phys. Rev. Lett.* **39**, 1028.
- Vettier, C., J. Flouquet, J.M. Mignot and F. Holtzberg, 1980, *J. Magn. & Magn. Mater.* **15-18**, 987.
- Veyssie, J.J., J. Chaussy and A. Berton, 1964, *Phys. Lett.* **13**, 29.
- Vogt, O., 1968, *Helv. Phys. Acta* **41**, 1238.
- Vogt, O., 1980, *Physica B* **102**, 206.
- Vogt, O., 1989, *J. Nucl. Mater.* **166**, 36.
- Vogt, O., and H. Bartholin, 1980, *J. Magn. & Magn. Mater.* **15-18**, 531.
- Vogt, O., and H. Bartholin, 1982, *J. Magn. & Magn. Mater.* **29**, 291.
- Vogt, O., and B.R. Cooper, 1968, *J. Appl. Phys.* **39**, 1202.
- Vogt, O., P. Wachter and H. Bartholin, 1980, *Physica B* **102**, 226.
- Vogt, O.R., and K. Mattenberger, 1987, *J. Less-Common Met.* **133**, 53.
- Von Essen, V.U., and W. Klemm, 1962, *Z. Allg. Anorg. Chem.* **317**, 26.
- Wachter, P., 1978, *Phys. Rep.* **44**, 161.
- Wachter, P., 1979, in: *Handbook on the Physics and Chemistry of Rare Earths*, Vol. 2, eds K.A. Gschneidner Jr and L. Eyring (North-Holland, Amsterdam) p. 507.
- Wachter, P., and E. Kaldis, 1980, *J. Magn. & Magn. Mater.* **15-18**, 305.
- Wachter, P., E. Jilek, K. Mattenberger, J. Muller, H.P. Staub and A. Wisard, 1987, *J. Magn. Soc. Jpn.* **11**, 107.
- Wachter, P., F. Marabelli and B. Bucher, 1990, 20èmes Journées des Actinides, Prague, Czechoslovakia, p. 20 (unpublished).
- Wachter, P., F. Marabelli and B. Bucher, 1991, *Phys. Rev. B* **43**, 11136.
- Wakabayashi, N., and A. Furrer, 1975, *Phys. Rev. B* **13**, 4343.
- Wedgwood, F.A., 1972, *J. Phys. C* **3**, 2427.
- Westerholt, K., and S. Methfessel, 1977, *Physica B* **86-88**, 1160.
- Wilkinson, M.K., H.R. Child, W.C. Koehler, J.W. Cable and E.O. Wollan, 1962, *J. Phys. Soc. Jpn.* **17**, 27.
- Yamada, K., and N. Miura, 1985, *J. Magn. & Magn. Mater.* **52**, 440.

## Chapter 115

# TRANSPORT PROPERTIES OF RARE EARTH AND ACTINIDE INTERMETALLICS

JEAN MARC FOURNIER

*Université Joseph Fourier – Grenoble, Domaine Universitaire,  
 BP 53 X, F-38041 Grenoble Cedex, France*

ERNST GRATZ

*Institut für Experimentalphysik, Technische Universität Wien,  
 A-1040 Wien, Austria*

---

### Contents

Symbols	410	2.4.2.3. Paramagnetic case	435
1. Introduction	411	2.4.2.4. Ferromagnetic case	435
2. Theoretical concepts	413	2.4.2.5. Antiferromagnetic case	435
2.1. General remarks on transport theory	413	2.4.2.6. Physical origin of $R_1$ ( $R_S$ )	436
2.2. Boltzmann formalism	414	3. Discussion of experimental results	437
2.2.1. Linearized Boltzmann equation	414	3.1. Rare earth and actinide metals	437
2.2.2. Spectral-function formalism	416	3.2. RPt and AnPt intermetallics	446
2.2.3. Sum rules and their applicability	417	3.2.1. RPt	446
2.3. Transport phenomena without external magnetic field	419	3.2.2. AnPt	448
2.3.1. Interaction mechanism	419	3.3. $RAI_2$ and $AnAl_2$ Laves phases	449
2.3.2. Potential scattering	420	3.3.1. $RAI_2$	449
2.3.3. Phonon scattering	421	3.3.2. $AnAl_2$	459
2.3.4. Spin-dependent scattering mechanisms	421	3.4. $RM_2$ and $AnM_2$ Laves phases ( $M = Mn, Fe, Co, Ni$ )	465
2.3.4.1. Local-moment scattering	421	3.4.1. $RMn_2$	465
2.3.4.2. Spin-fluctuation scattering	424	3.4.2. $UMn_2$	469
2.3.4.3. Kondo scattering	427	3.4.3. $RFe_2$	470
2.4. Transport phenomena with external magnetic field	430	3.4.4. $AnFe_2$	473
2.4.1. Magnetoresistance	430	3.4.5. $RCO_2$	475
2.4.2. Hall effect	434	3.4.6. $UCO_2$	482
2.4.2.1. Normal Hall effect	434	3.4.7. $RNi_2$	483
2.4.2.2. Anomalous Hall effect	435	3.4.8. $UNi_2$	486
		3.5. $RM_3$ and $AnM_3$ intermetallics ( $M = In, Sn$ )	488
		3.5.1. $RIn_3$	489
		3.5.2. $AnIn_3$	493
		3.5.3. $RSn_3$	495
		3.5.4. $AnSn_3$	498

3.6. RCu <sub>5</sub> and UCu <sub>5</sub> intermetallics	500	3.7.2. Actinide monochalcogenides	516
3.6.1. RCu <sub>5</sub>	500	3.7.3. Cerium monopnictides and monochalcogenides	520
3.6.2. UCu <sub>5</sub>	505	4. Summary	529
3.7. An and Ce monopnictides and monochalcogenides	506	References	531
3.7.1. Actinide monopnictides	507		

## Symbols

$A$	coefficient of the resistivity ( $\rho_{\text{mag}} = AT^2$ )	$P_{yy'}$	transition probability per unit time
$\hat{A}$	operator	$p$	number of holes (Hall effect)
$A(\mathbf{q}, \omega)$	spectral density of paramagnons	$Q$	linear collision operator
An	actinides	$Q^{-1}$	inverse linear collision operator
$A, B$	constants	$Q_{nn'}^{-1}$	matrix elements of the inverse collision operator
$B$	magnetic induction (scalar)	$q$	elementary charge
$\mathbf{B}$	magnetic induction vector	$\mathbf{q}$	wave vector of magnons or paramagnons (spin fluctuations)
$B^*$	Hermitian conjugate of operator $B$	R	rare earth (Sc, Y plus lanthanides)
$E$	electric field vector	$R_0$	normal Hall coefficient
$E_y$	electric field in the $y$ -direction (Hall effect)	$R_H$	total Hall coefficient
$F$	Lorentz force	$R_S$	anomalous Hall coefficient
$F_j^v$	component of the field vector $v$	$S$	local spin operator
$f(\gamma, \mathbf{r})$	distorted distribution function	$S$	Stoner factor
$f_0(\epsilon)$	Fermi distribution function	$S$	total thermopower
$f_k, f_{k+q}$	functions related to the Fermi distribution function	$S_e$	electron-diffusion thermopower
$(g-1)^2$	de Gennes factor	$S_{e,i}$	electron-diffusion thermopower of the type $i$
$J(J+1)$		$S_{e,\text{spd}}$	diffusion thermopower due to spin-disorder scattering
$H$	magnetic field or Hamiltonian	$S_{\text{ph}}$	phonon-drag thermopower
$H_0$	Hamiltonian of the band energy of conduction electrons	$S_{\text{mag}}$	magnon-drag thermopower
$H_{\text{int}}$	Hamiltonian of the interaction energy	$S_0$	thermopower due to impurity scattering
$\bar{H}$	normalized magnetic field	s, p, d, f	band index
$i, i'$	initial and final crystal-field states	$T$	temperature
$\mathcal{J}$	exchange constant	$T_C$	Curie temperature
$J$	total quantum number	$T_K$	Kondo temperature
$J_x$	charge density in the $x$ -direction (Hall effect)	$T_N$	Néel temperature
$j^x, j^y$	components of current vector	$T_{\text{sf}}$	spin-fluctuation temperature
$j_i^\mu$	component of the flux density vector $i$	$\nabla T$	temperature gradient (vector)
$\mathbf{j}_e$	charge flux density vector	$t$	time
$\mathbf{j}_d$	heat flux density vector	$U_0$	strength of exchange interaction
$k_B$	Boltzmann constant	$V^2$	matrix elements of the hybridization
$L_{ij}^{\mu\nu}$	transport tensor	$v_y$	conduction-electron velocity
$L_0$	Lorentz number	$W_e$	electronic thermal resistivity
$M$	magnetization	$W_{e,i}$	electronic thermal resistivity of type $i$
$m^*$	effective electron mass	$\alpha^2 F$	spectral function
$m_0$	free electron mass	$\beta_{ij}$	transport coefficients (scalar)
$m_s, m'_s$	spin states of the conduction electrons	$\gamma$	linear term of the electronic specific heat
$N(\epsilon_F)$	density of states at the Fermi energy		
$n$	number of electrons (Hall effect)		

$\gamma, \gamma'$	conduction electron states	$\rho_H$	Hall resistivity
$\Delta$	hybridization strength between f electrons and conduction electrons	$\rho_0$	residual electrical resistivity
$\Delta_{cf}$	overall crystal-field splitting	$\rho_{ph}$	electrical resistivity due to phonon scattering
$\bar{\Delta}\rho$	magneto-resistance	$\rho_i$	electrical resistivity of the type $i$
$\varepsilon, \varepsilon'$	conduction-electron energies	$\rho_{mag}$	resistivity due to spin-dependent scattering
$\varepsilon_F$	Fermi energy	$\rho_{spd}$	spin-disorder resistivity ( $T > T_{ord}$ )
$\varepsilon_{ex}$	excitation energy	$\rho^{xy}$	components of resistivity tensor
$\lambda$	thermal conductivity	$\sigma$	electrical conductivity
$\lambda_e$	electronic thermal conductivity	$\sigma_H$	Hall conductivity tensor
$\lambda_{e,i}$	electronic thermal conductivity of type $i$	$\tau_\gamma$	relaxation time
$\lambda_{e,spd}$	electronic thermal conductivity due to spin-disorder scattering	$\chi_i$	Curie functions
$\lambda_l$	lattice thermal conductivity	$\chi$	magnetic susceptibility
$\lambda_{ph}$	thermal conductivity due to electron-phonon scattering	$\chi_0^p$	unenhanced Pauli susceptibility
$\lambda_0$	residual thermal conductivity	$\chi_{-+}$	transverse magnetic susceptibility
$\mu_0$	Bohr magneton	$\chi_{zz}$	longitudinal magnetic susceptibility
$\mu_n$	mobility of electrons (Hall effect)	$\chi_{+-}(\mathbf{q}, \omega)$	transverse dynamic magnetic susceptibility
$\mu_p$	mobility of holes (Hall effect)	$\chi^*$	effective susceptibility (demagnetization field included)
$\Pi$	Peltier coefficient	$\omega(\mathbf{q})$	magnon or paramagnon dispersion relation
$\rho$	electrical resistivity	$\omega_c$	cyclotron frequency
$\rho(T, 0)$	magneto-resistance at zero field, same as $\rho(T)$	$\omega_q$	energy of paramagnons (spin fluctuations)
$\rho(T, H)$	magneto-resistance		

## 1. Introduction

Within the series of the rare earth (R) and the actinide (An) elements the f shells become progressively filled. What the R elements distinguishes from the An elements is that the 5f wave function of the An elements is more expanded in space and ranges over a larger energy scale. A classification of the 4f and 5f elements can be made by considering the stability of their magnetic moments.

Most of the R elements with partly filled 4f shells are in the 3+ state, with stable magnetic moments. However, there are exceptions among them (e.g. Ce, Sm or Yb). Within the An-element series the filling of the 5f shell is accompanied by an increasing degree of localization of the magnetic moments. Between plutonium and americium, a cross-over from itinerancy to localization is observed.

There exist two additional variables in the R and An intermetallic compounds: namely, the variation of the interatomic distances, depending on the partner elements, and the environment of the R and An atoms inside the lattice. The An-An interatomic distance plays an important role in the stability of the 5f moments in the An compounds.

It is generally observed that the 4f electron states of the R ions are hardly influenced when these elements are alloyed with a non-transition metal. Even in compounds with transition metals, like manganese, iron, cobalt or nickel, the influence on the 4f electron states is weak. The magnetic state of the 5f electrons in the An compounds

is, in general, much more dependent on the partner elements. In fact, a large number of magnetic properties have been found in An intermetallics with non-transition metals.

However, there is also an influence of the 4f and 5f electrons on the state of the partner element. Considering the magnetization of the 3d elements in an f-d compound, it appears that the 3d states of iron are much less influenced than those of manganese, cobalt or nickel. For example, in the R-Ni and An-Ni compounds with 1:2 stoichiometry, the Ni atoms carry no magnetic moments, whereas in 4f-Co or 4f-Mn compounds a large variety of magnetic properties of the 3d elements are observed.

During recent years it has become obvious that the properties of the so-called anomalous rare earth compounds (in particular cerium-based systems) show many similarities to the light-actinide (U, Np, Pu) compounds. The best known property which reflects the similarity is the appearance of heavy-fermion phenomena in many cerium and uranium intermetallics.

It is evident that the magnetic properties belong to the most interesting features observed in the R and An intermetallics. In the present chapter we demonstrate that the transport properties can help to improve our understanding of the differences in the behaviour of R and An intermetallics, although an exact theoretical interpretation of the experimental results is often difficult.

In the following sections the basic concepts of the transport theories within the scope of the Boltzmann formalism are described. In the succeeding discussion the validity and the applicability of the Matthiessen and the Nordheim-Gorter rule are considered. A description of transport phenomena (electrical and thermal resistivity, thermopower) without an external magnetic field is given in sect. 2.3. There, the influence of the various scattering mechanisms on the temperature dependence of the electrical and the thermal resistivity as well as on the thermopower will be briefly discussed.

Section 2.4 deals with transport phenomena under an external magnetic field, concerning mainly the magnetoresistance in magnetic compounds. A theoretical model, developed by Yamada and Takada (1973a, b), for the temperature and field dependence of the magnetoresistance is discussed. This brief description serves to explain qualitatively the magnetoresistance in simple ferromagnetic compounds and to point out that in antiferromagnetically ordered compounds the magnetoresistance can change sign as a function of the applied field. In the discussion of the Hall effect a phenomenological concept will be presented to describe the anomalous Hall effect, dominating in magnetic materials.

At the beginning of sect. 3 a brief overview of the transport phenomena of rare earth and actinide metals is given. This is followed by a comprehensive discussion of transport data of intermetallic compounds with various stoichiometries and crystal structures. The influence of the 3d electrons on the transport phenomena is illustrated by means of the well-known Laves phases.

Subsequent to the discussion of the intermetallic compounds we give a description of the transport properties of cerium monopnictides and monochalcogenides, which are compared with various actinide monopnictide and monochalcogenide systems. In these compounds, which partly show a semimetal-like behaviour, a great and

interesting variety of transport properties has been observed. Large field and pressure dependences of the transport phenomena characterize these compounds.

## 2. Theoretical concepts

### 2.1. General remarks on transport theory

When an external force (e.g. an electric field or a temperature gradient) is applied to a conductor, all the electrons are displaced in  $k$ -space. Random scattering effects tend to restore the electrons to the steady-state distribution. The nature of this distribution is determined by a dynamical balance between the acceleration in the field and the scattering by deviations of perfect symmetry in the lattice (lattice distortion, phonons, disordered local magnetic moments).

In general, we expect a flux as the response of the system to generalized forces. A linear response is expressed by:

$$j_i^\mu = \sum_{j,\nu} L_{ij}^{\mu\nu} F_j^\nu. \quad (1)$$

Here  $j_i^\mu$  denotes a flux of type  $i$ , the superscripts indicate the coordinate components. The coefficients  $L_{ij}^{\mu\nu}$  are usually called the transport coefficients.

If the forces and fluxes are properly selected, they are canonically conjugated in the sense of irreversible thermodynamics ( $L_{ij}^{\mu\nu} = L_{ji}^{\nu\mu}$ ) (Onsager relation). There are two distinctly different kinds of forces which may induce a flux. The first and more familiar is the electrical force. The second kind of forces has its origin in statistics; it is not a "force" in the usual sense, but normally arises from concentration gradients and results in diffusive fluxes. In all our discussions we shall be concerned with an assembly of electrons, i.e. a Fermi system, for which the chemical potential ( $\mu(T)$ ) at  $T = 0$  K is the Fermi energy. Then it is common practice to introduce the electrochemical potential, and to define an effective electric field  $\mathbf{E} = -\nabla(\Phi + \mu/e)$ , which is the field that is normally observed.

If we are dealing with an electric field  $\mathbf{E}$  and a temperature gradient  $\nabla T$ , as external forces, the resulting current densities for the charge ( $\mathbf{j}_e$ ) and the heat ( $\mathbf{j}_q$ ) are expressed as:

$$\mathbf{j}_e = \beta_{00} \mathbf{E} + \beta_{01} \nabla T, \quad (2)$$

$$\mathbf{j}_q = \beta_{10} \mathbf{E} + \beta_{11} \nabla T. \quad (3)$$

For cubic lattice symmetry the values  $\beta_{ij}$  can be considered as scalars. It now remains to relate the coefficients  $\beta_{ij}$  to the experimentally measured quantities, such as electrical resistivity ( $\rho$ ), thermal conductivity ( $\lambda$ ), thermopower ( $S$ ), etc. This can be done by rewriting eqs. (2) and (3) in the following way:

$$\mathbf{E} = \rho \mathbf{j}_e + S \nabla T, \quad (4)$$

$$\mathbf{j}_q = \Pi \mathbf{j}_e - \lambda \nabla T. \quad (5)$$

This representation is preferable because this arrangement shows which physical

quantities are usually controlled in the experiments. These are the electric current and the temperature gradient  $\nabla T$ . If, e.g., the electrical resistivity is measured,  $\nabla T$  is zero, it follows:

$$\begin{aligned} \mathbf{j}_e &= \beta_{00} \mathbf{E} = \sigma \mathbf{E} \quad (\sigma = 1/\rho), \\ \sigma &= \beta_{00}. \end{aligned} \quad (6)$$

The thermal conductivity  $\lambda$  ( $\mathbf{j}_e = 0$ ) is:

$$\lambda = -\beta_{11} + \beta_{10} \beta_{00}^{-1} \beta_{01}. \quad (7)$$

The thermopower measured under open-circuit conditions ( $\mathbf{j}_e = 0$ ) is then given by:

$$S = -(1/\beta_{00})\beta_{01}. \quad (8)$$

The ‘‘Onsager relation’’ gives a simple connection between the thermopower coefficient ( $S$ ) and the Peltier coefficient ( $\Pi$ )

$$\Pi = TS. \quad (9)$$

## 2.2. Boltzmann formalism

### 2.2.1. Linearized Boltzmann equation

The calculation of the coefficients  $\beta_{ij}$  can be carried out in the scope of the Boltzmann formalism. The Boltzmann equation can be written in its general form as:

$$\left( \frac{\partial}{\partial t} + \dot{\mathbf{r}} \cdot \nabla_{\mathbf{r}} + \mathbf{k} \cdot \nabla_{\mathbf{k}} \right) f(\gamma, \mathbf{r}, t) = \left( \frac{\partial f(\gamma, \mathbf{r}, t)}{\partial t} \right)_{\text{coll}} \quad (10)$$

( $\gamma$  is an abbreviation for the wave vector  $\mathbf{k}$ , the band index,  $n$ , and the spin direction,  $\sigma$ , for the conduction electrons). The right-hand side of this equation is the collision term, the left-hand side is usually called the force term. Under steady-state conditions the Boltzmann equation is time independent.

The Boltzmann formalism is based on the assumption that a distribution function,  $f(\gamma, \mathbf{r})$ , can be defined. However, we are dealing with a strongly interacting, quantum-mechanical system, and it is by no means clear, because of the Heisenberg uncertainty principle, that a distribution function in six-dimensional ( $\mathbf{k}, \mathbf{r}$ ) phase space can be correctly defined. However, in many cases one considers the distribution function as a function of  $\mathbf{k}$  only; the Heisenberg uncertainty principle does not preclude the use of this function. When a positional dependence is considered at all, it usually occurs through the dependence of the distribution function on external parameters, such as the dependence of the temperature on  $\mathbf{r}$  in the case when a temperature gradient exists:  $(\partial f_0 / \partial x) = (\partial f_0 / \partial T)(\partial T / \partial x)$ . This expression makes sense if the electron can be localized over macroscopic distances. This can be done by using wave packets which contain only a very small range of wave numbers. In this limited sense one can use a distribution function which is a function of both  $\mathbf{k}$  and  $\mathbf{r}$ .

The linearized Boltzmann equation can be obtained assuming that the unknown distorted distribution function  $f(\gamma, \mathbf{r})$  deviates only slightly from the local Fermi distribution function  $f_0(\varepsilon_\gamma, \mathbf{r})$ , i.e. if we neglect higher-order terms in  $f(\gamma, \mathbf{r}) - f_0(\varepsilon_\gamma, \mathbf{r})$ .

The linearized Boltzmann equation for electrons in a metal under a uniform electric field  $\mathbf{E}$  and a uniform thermal gradient  $\nabla T$  is given by:

$$Q\phi_\gamma = (e\mathbf{E}\cdot\mathbf{v}_\gamma + k_B\beta(\varepsilon_\gamma - \mu)\nabla T\cdot\mathbf{v}_\gamma)\frac{\partial f_0(\varepsilon_\gamma)}{\partial \varepsilon_\gamma}, \quad (11)$$

where  $\mathbf{v}_\gamma$  is the velocity and  $\varepsilon_\gamma$  is the energy of the electrons with quantum number  $\gamma$  ( $\beta = 1/k_B T$ ).  $Q$  denotes the linear collision operator defined by:

$$Q\phi_\gamma = \sum_{\gamma'} \beta f_0(\varepsilon_{\gamma'}) [1 - f_0(\varepsilon_{\gamma'})] P_{\gamma\gamma'} (\Phi_\gamma - \Phi_{\gamma'}), \quad (12)$$

where  $P_{\gamma\gamma'}$  is the equilibrium transition probability per unit time for a transition from state  $\gamma$  to state  $\gamma'$  due to collision processes of the conduction electrons with impurities, phonons or local magnetic moments. The function  $\phi_\gamma$  represents a measure for the deviation of the distorted distribution function  $f(\gamma)$  from thermal equilibrium, which is given by the Fermi distribution  $f_0(\varepsilon_\gamma)$ . The function  $\phi_\gamma$  is defined by the ansatz:

$$f(\gamma) = f_0(\varepsilon_\gamma) - \frac{\partial f_0(\varepsilon_\gamma)}{\partial \varepsilon_\gamma} \Phi_\gamma. \quad (13)$$

Several methods have been developed to solve the linearized Boltzmann equation. The simplest is the relaxation-time approximation. This procedure is based on the assumption that the collision term can be replaced by:

$$\left(\frac{\partial f(\gamma)}{\partial t}\right)_{\text{coll}} = \frac{f(\gamma) - f_0(\varepsilon_\gamma)}{\tau_\gamma}. \quad (14)$$

The relaxation time,  $\tau_\gamma$ , is a measure for the exponential fade-out time of the distorted distribution function  $f(\gamma)$  towards equilibrium, described by the Fermi distribution function  $f_0(\varepsilon_\gamma)$ . It is important to remember that with this method only one relaxation time is considered, irrespectively what external force (electrical field, temperature gradient or magnetic field) gives rise to the distortion of the conduction-electron system. This simplification restricts the applicability of the relaxation-time method. The relaxation time,  $\tau_\gamma$ , depends on the kind of scattering process.

A more sophisticated method to solve the Boltzmann equation is the variational method (for a review see, e.g., Ziman (1960)). If the function  $\Phi_\gamma$  is known (see eq. (11)), the expressions for the electrical current density,  $\mathbf{j}_e$ , and the heat current density,  $\mathbf{j}_h$ , are given (for the determination of  $\Phi_\gamma$  from eq. (11) we use the inverse collision operator  $Q^{-1}$ ) by:

$$\mathbf{j}_e = e \sum_{\gamma} \mathbf{v}_\gamma \frac{\partial f_0}{\partial \varepsilon_\gamma} \Phi_\gamma, \quad (15a)$$

$$\mathbf{j}_h = - \sum_{\gamma} (\varepsilon_\gamma - \mu) \mathbf{v}_\gamma \frac{\partial f_0}{\partial \varepsilon_\gamma} \Phi_\gamma. \quad (15b)$$

Comparing these expressions for the current densities with the macroscopic transport equations, given in eqs. (4) and (5), we obtain the following expressions for the electrical resistivity,  $\rho$ , the thermal conductivity,  $\lambda$ , and the thermopower,  $S$ , in the case of a



cubic or in a polycrystalline material:

$$\rho = \frac{1}{e} \frac{1}{Q_{00}^{-1}}, \quad (16)$$

$$\lambda = \frac{k_B}{\beta} \left[ Q_{11}^{-1} - \frac{Q_{10}^{-1} Q_{01}^{-1}}{Q_{00}^{-1}} \right], \quad (17)$$

$$S = - \frac{k_B}{e} \frac{Q_{01}^{-1}}{Q_{00}^{-1}}, \quad (18)$$

where we have used the short notation:

$$Q_{nn'}^{-1} = \sum_{\gamma} \xi_n(\gamma) Q^{-1} \xi_{n'}(\gamma), \quad (19)$$

with

$$\xi_0(\gamma) = \frac{\partial f_0}{\partial \varepsilon_{\gamma}} v_x(\gamma), \quad (20)$$

$$\xi_1(\gamma) = \beta(\varepsilon_{\gamma} - \mu) \frac{\partial f_0}{\partial \varepsilon_{\gamma}} v_x(\gamma) \quad (21)$$

(the field is in the  $x$ -direction).

In the following we will sketch the calculation of the matrix elements of the inverse collision operator,  $Q^{-1}$  ( $Q$  is given by eq. (12)), within the scope of the variational method for the various scattering mechanisms which can exist in a material. Frequently a set of two trial functions,

$$\chi_0(\gamma) = v_x(\gamma), \quad (22)$$

$$\chi_1(\gamma) = \beta(\varepsilon_{\gamma} - \mu) v_x(\gamma), \quad (23)$$

is used for the calculation of the transport coefficients  $\rho$ ,  $\lambda$  and  $S$  (see eqs. (16)–(18)). We then obtain for the matrix elements of the inverse collision operator:

$$Q_{nn'}^{-1} = \sum_{m,m'} \left[ \sum_{\gamma} \xi_n(\gamma) \chi_m(\gamma) \right] (\hat{Q}^{-1})_{mm'} \left[ \sum_{\gamma'} \chi_{m'}(\gamma') \xi_{n'}(\gamma') \right], \quad (24)$$

where  $\hat{Q}^{-1}$  is the inverse of the matrix

$$\hat{Q}_{mm'} = \sum_{\gamma} \chi_m(\gamma) Q \chi_{m'}(\gamma). \quad (25)$$

It must be emphasized that in the case of the thermopower the variational space has to be at least two-dimensional in order to obtain meaningful results.

### 2.2.2. Spectral-function formalism

If the trial functions  $\chi_m$  are chosen as a product of two functions:

$$\chi_m = X_m(\varepsilon_{\gamma}) Y_m(\gamma) \quad (26)$$

(where the function  $Y$  depends only on the direction of  $\mathbf{k}$  ( $\gamma = k, n, \sigma$ ) in reciprocal space), we can obtain an analogous separation for the  $\hat{Q}$  matrix using the formula:

$$\chi_m(\gamma) - \chi_m(\gamma') = \frac{1}{2} \sum_{\eta'} X_{\eta'm'}(\varepsilon_\gamma, \varepsilon_{\gamma'}) Y_{\eta'm'}(\gamma, \gamma'), \quad (27)$$

with

$$X_{\eta'm'}(\varepsilon_\gamma, \varepsilon_{\gamma'}) = X_m(\varepsilon_\gamma) + \eta' X_m(\varepsilon_{\gamma'}), \quad (28)$$

$$Y_{\eta'm'}(\gamma, \gamma') = Y_m(\gamma) - \eta' Y_m(\gamma'). \quad (29)$$

The matrix elements can then be written as:

$$Q_{mm'} = \frac{2\pi}{\hbar\beta} \int d\omega \left( \frac{\beta\omega/2}{\sin(\beta\omega/2)} \right) \int d\varepsilon d\varepsilon' \delta(\varepsilon - \varepsilon' - \omega) \frac{f(\varepsilon') - f(\varepsilon)}{\varepsilon - \varepsilon'} \\ \times \frac{1}{2} \sum_{\eta' = \pm 1} X_m(\varepsilon) X_{\eta'm'}(\varepsilon, \varepsilon') \alpha_{m,\eta'm'}^2(\varepsilon, \varepsilon') F(\omega), \quad (30)$$

with the spectral function

$$\alpha_{m,\eta'm'}^2(\varepsilon, \varepsilon') F(\omega) = \hbar \frac{1 - e^{-\beta\omega}}{2\pi} \sum_{\gamma, \gamma'} \delta(\varepsilon - \varepsilon_\gamma) \delta(\varepsilon - \varepsilon_{\gamma'}) Y_m(\gamma) P_{\gamma \rightarrow \gamma'} Y_{\eta'm'}(\gamma, \gamma'). \quad (31)$$

The advantage of the spectral-function formalism is that the interaction of the conduction electrons with any kind of distortion enters only into the spectral function  $\alpha^2 F$ . Actually,  $\omega$  denotes an energy difference between excited states of the distortion. Because these excitation energies restrict the important energy range of the  $\varepsilon$  and  $\varepsilon'$  to a small range around the Fermi energy, the dependence of the spectral function on  $\varepsilon$  and  $\varepsilon'$  can be approximated by the first terms of a Taylor series expansion. In this case the integration over  $\varepsilon$  and  $\varepsilon'$  can be done analytically. The temperature dependence of the matrix elements of  $\hat{Q}$ , and consequently that of  $\rho$ ,  $\lambda$  and  $S$ , results mainly from the  $\omega$ -dependence of  $\alpha^2 F$ , which is determined by the actual interaction mechanism (Allen 1978, Gratz et al. 1987a).

### 2.2.3. Sum rules and their applicability

The conduction electrons accelerated by the external fields inside a crystal can suffer a variety of different scattering processes:

(i) Scattering of conduction electrons by vacancies, dislocations, impurities or by grain boundaries. It is assumed that these kinds of interactions are elastic. Normally the electrical and thermal resistivity are dominated in the low-temperature region by these elastic scattering processes.

(ii) Scattering processes of the conduction electrons due to quantized lattice vibrations (phonons) are of growing importance as the temperature rises.

(iii) If magnetic moment carrying atoms exist, as is the case in many of the rare earth and actinide compounds, additional scattering mechanisms must be considered. These spin-dependent scattering processes dominate the transport phenomena at lower temperatures, especially in heavy-fermion, Kondo and spin-fluctuation systems.

(iv) The classical electron-electron interaction, first described by Baber (1937), normally does not have an influence at elevated temperatures (Vucht et al. 1985).

For the analysis of experimental data it is an important question how the different kinds of scattering processes contribute to the transport phenomena, especially since calculations are usually done for one kind of interaction. Therefore, to compare experiment with theory it is necessary to isolate from the experimental data the one contribution for which the calculation has been performed.

Splitting of the transport coefficients into the various contributions is, under certain circumstances, possible using the “sum rules”, although these rules can only be applied in rather limited cases. In the following we will discuss these sum rules, which are: the Matthiessen rule, the Kohler rule and the Nordheim–Gorter rule.

In the scope of the Boltzmann equation, the Matthiessen rule is valid if the total collision operator can be written as a sum of the collision operators for the different scattering mechanisms. This means that the scattering processes can be treated as independent of each other.

The Matthiessen rule for the electrical resistivity is given by:

$$\rho(T) = \sum_{i=1}^n \rho_i \quad (32)$$

and that for the thermal resistivity is:

$$W_e(T) = \sum_{i=1}^n W_{e,i}. \quad (33)$$

(Note that we are neglecting the second term in eq. (17), since we consider the product  $Q_{10}^{-1}Q_{01}^{-1}$  as negligibly small.) The subscript e in eq. (33) expresses that we consider only the heat conduction due the electrons in this formula. The problems in the thermal resistivity, or better the thermal conductivity,  $\lambda$  ( $\lambda = 1/W$ ), are usually more complex, since also the lattice vibrations can lead to a heat current, which can be of the same order of magnitude as the electronic heat transport. The total thermal conductivity,  $\lambda$ , is given by:

$$\lambda = \lambda_e + \lambda_l, \quad (34)$$

where  $\lambda_l$  denotes the lattice thermal conductivity.

The separation of the electronic and the lattice thermal conductivity is difficult in an experiment. The reader is referred to the book of Parrott and Stuckes (1975), where this subject is discussed in detail. As a rule, it can be said that if the electrical resistivity is low, usually  $\lambda_e$  dominates in eq. (34) over  $\lambda_l$ , but there are exceptions.

For the thermopower no such a simple relation as the Matthiessen rule exists. The main reason is that the thermopower (and also the Peltier effect) is a “higher”-order transport phenomenon. This can be seen from eq. (18), where the matrix element  $Q_{01}^{-1}$  is the dominating quantity. However, it can be shown that within the scope of the variational procedure, if the variational space is two dimensional, the so-called “Kohler rule” follows, which is:

$$S_e(T) = \sum_{i=1}^n \frac{\lambda_{e,i}}{\lambda_e} S_{e,i}. \quad (35)$$

$\lambda_e$  and  $\lambda_{e,i}$  denote the total electronic thermal conductivity and the thermal conductivity due to one of the scattering mechanisms ( $i$ ), respectively. The subscript  $e$  in  $S_e$  denotes the electron-diffusion thermopower (see below). Assuming the validity of the Wiedemann–Franz law:

$$\lambda_e = \frac{L_0 T}{\rho} \quad (36)$$

( $L_0 = (\pi^2/3)(k_B/e)^2 = 2.45 \times 10^{-8} \text{ W } \Omega \text{ K}^{-2}$ ), the Nordheim–Gorter rule is derived:

$$S_e(T) = \sum_{i=1}^n \frac{\rho_i}{\rho} S_{e,i}. \quad (37)$$

$\rho$  is the total electrical resistivity,  $\rho_i$  and  $S_{e,i}$  are the contributions to the resistivity and the thermopower due to one of the ( $i$ ) scattering mechanisms, respectively.

Effects other than the diffusion of the conduction electrons can contribute to the total thermopower. These are the different “drag”-effects, so that the total thermopower is:

$$S = S_e + S_{\text{ph}} + S_{\text{mag}}. \quad (38)$$

$S_e$ ,  $S_{\text{ph}}$  and  $S_{\text{mag}}$  are the contributions to the thermopower due to electron diffusion, phonon drag and magnon drag (or paramagnon drag), respectively.

The latter two terms are negligible at higher temperatures, since it can be assumed that the “drag” mechanisms decrease rapidly with increasing temperature. For more details we refer to the books of Blatt (1968), Ziman (1960) and Blatt et al. (1976).

The Kohler rule or the Nordheim–Gorter rule can be used in the same way as the Matthiessen rule to separate the different contributions to the total thermopower  $S_e$ .

The phonon (and magnon) drag are caused by the fact that due to the temperature gradient in the sample the phonon and the magnon systems are in a non-equilibrium state, and the “flowing” phonons, or magnons (paramagnons), will “drag” the electrons with them. However, these mechanisms are limited to the low-temperature region.

At this point it should be mentioned that there are minima in  $S$  versus  $T$  observable at low temperatures in most of the known spin-fluctuation systems (e.g.,  $\text{UAl}_2$ ,  $\text{YCo}_2$ ,  $\text{LuCo}_2$ , etc.). Although there is no theoretical confirmation, it is conceivable that the paramagnon drag is the reason for these experimentally observed minima in  $S$  versus  $T$ .

### 2.3. Transport phenomena without external magnetic field

#### 2.3.1. Interaction mechanism

The previous section concerned the application of the Boltzmann formalism. An exact solution of the linearized Boltzmann equation (eq. (11)) is very difficult. However, there are many examples of calculations which are in good agreement with experiment.

In this section we will first discuss results obtained within the scope of the Boltzmann theory in the absence of an external magnetic field for simple compounds. Secondly, we will concentrate on spin fluctuations and their influence on the transport properties, since it will be shown in sect. 3 that spin fluctuations are of fundamental importance

for the understanding of the transport properties for most of the actinide compounds and also for the R compounds with d elements. Although it is not planned to discuss the transport properties of Kondo and heavy-fermion materials within the family of the R and An compounds, a brief description of the basic ideas will be given at the end of this section.

Above we were speaking of simple compounds. Let us explain this in more detail. In the case of simple compounds we assume that, within the crystal, the conduction electrons are considered as nearly free particles which are responsible for the transport of charge and energy. In compounds containing transition metals or 5f elements, however, the distinction between the valence and the core states is no longer so clear-cut. The d states (or 5f states) cannot simply be bundled into the core region and incorporated into some smoothly varying lattice potential. The wave functions associated with the d or in some cases the f states have significant amplitude outside the atomic core region and play an important role, either by overlapping with those from adjacent atoms forming a narrow band, or via the effect of hybridization with the sp conduction band. As a further consequence, the Fermi surface may be quite irregular and have some parts that are s-like and other that are d-like.

It was initially emphasized by Jones (1956) that impurity, phonon or electron-electron interaction will cause scattering of the s electrons into the s and d states, but since the scattering probability depends upon the density of states into which the electrons are scattered, s-d scattering occurs much more frequently than s-s scattering. Electrons scattered into the d band do not contribute significantly to the transport of charge and energy, because of their increased effective mass, and, therefore, the s-d scattering mechanism could explain the much higher resistivity of transition metals and their alloys. A rapid change in  $N_d(\epsilon)$  with varying energy can thus lead to modification of the temperature dependence of the transport coefficients. For example, Jones (1956) has shown that such an effect would lead to an additional temperature dependence of the resistivity of the form

$$\rho(T) = \rho(\epsilon_F, T) \left( 1 - (\pi^2/6)(k_B T)^2 \{ 3[(1/N) dN/d\epsilon]^2 - (1/N) d^2N/d\epsilon^2 \} \right)_{\epsilon_F}, \quad (39)$$

where  $\rho(\epsilon_F, T)$  denotes the temperature dependence of the resistivity one will obtain if band-structure effects are neglected, i.e. if the conduction electrons are considered as quasi-free particles.

Now some theoretical results for simple compounds, obtained within the scope of the effective-mass conception, will be discussed. The selected examples have been proved to be in agreement with experiment in many measurements.

### 2.3.2. Potential scattering

Since these scattering processes are elastic, no energy transfer from the conduction-electron system to the scatterer takes place. Using the spectral-function formalism it follows that:

$$\alpha^2 F \propto \beta \omega \delta(\omega). \quad (40)$$

The matrix elements  $\hat{Q}_{00}$  and  $\hat{Q}_{11}$  are temperature independent, whereas the matrix elements  $\hat{Q}_{10}$  and  $\hat{Q}_{01}$  are proportional to the temperature. The transport coefficients

for this kind of interactions are then given by:

$$\rho_0 = \text{const.}, \quad (41)$$

$$\lambda_0 \propto T, \quad (42)$$

$$S_0 \propto T. \quad (43)$$

### 2.3.3. Phonon scattering

Within the Debye approximation the spectral functions  $\alpha_+^2 F$  are proportional to  $\omega^4$  in the energy range  $\omega \leq k_B \Theta_D$  ( $\Theta_D$  denotes the Debye temperature). This leads to a temperature dependence of the matrix elements  $\hat{Q}_{00}$  from which the well known Bloch–Grüneisen relation for  $\rho_{\text{ph}}$  follows (see Blatt 1968). For the low- and high-temperature regions the Bloch–Grüneisen law reveals:

$$\begin{aligned} \rho_{\text{ph}}(T) &\propto T^5 \quad \text{for } T \ll \Theta_D, \\ &\propto T \quad \text{for } T \geq \Theta_D. \end{aligned} \quad (44)$$

The matrix elements  $\hat{Q}_{11}$  determine the temperature dependence of the electronic thermal conductivity. Since the spectral function  $\alpha_-^2 F$  is proportional to  $\omega^2$ ,  $\hat{Q}_{11}$  is proportional to  $T^3$  for  $T \ll \Theta_D$  and  $\hat{Q}_{11}$  is proportional to  $T$  for  $T \geq \Theta_D$ . For the low- and high-temperature region the thermal conductivity due to electron–phonon scattering can be written as:

$$\begin{aligned} \lambda_{\text{ph}}(T) &\propto T^{-2} \quad \text{for } T \ll \Theta_D, \\ &= \text{const.} \quad \text{for } T \geq \Theta_D. \end{aligned} \quad (45)$$

For the temperature variation of the thermopower it is practically impossible to present simple relations as for the electrical and thermal resistivity, even for very simple non-magnetic compounds. The sign of  $S(T)$  can be positive or negative and frequently also a change of sign with varying temperature is observable.

The known Mott expression for the diffusion thermopower:

$$S_e(T) = (\pi^2/3)(k_B^2 T/e)(1/\sigma)(d\sigma/d\varepsilon)_{\varepsilon_F} \quad (46)$$

( $\sigma = 1/\rho$ ), is in many cases too simple to describe the measured  $S(T)$  dependence. However, it follows from eq. (46) that the sign of the thermopower is determined by  $N(\varepsilon_F)$  and its derivative  $dN(\varepsilon)/d\varepsilon$  at  $\varepsilon_F$  (for a discussion see the book of Blatt et al. (1976)).

### 2.3.4. Spin-dependent scattering mechanisms

2.3.4.1. *Local-moment scattering.* In the present chapter these kinds of scattering mechanisms are very important, since many of the R and An intermetallics we will discuss in sect. 3 show magnetic order or an enhanced magnetic susceptibility.

Let us first consider the spin-disorder scattering of the conduction electrons by disordered localized spins, typically for R intermetallics. The spectral functions for spin-disorder scattering (in the paramagnetic temperature region) are similar to those for potential scattering, because of the elastic nature of these interactions. We will

neglect for the moment the influence of the crystal field and any kind of short-range correlations.  $\rho$ ,  $\lambda$  and  $S$  due to spin-disorder scattering (for  $T > T_C$ ) are given by:

$$\rho_{\text{spd}} = \text{const.}, \quad (47)$$

$$\lambda_{e,\text{spd}} \propto T, \quad (48)$$

$$S_{e,\text{spd}} \propto T. \quad (49)$$

It is interesting to present these results schematically. In fig. 1 the temperature variation of  $\rho_0$ ,  $\rho_{\text{ph}}$  and  $\rho_{\text{mag}}$  is schematically depicted. Assuming validity of the Matthiessen rule, the total resistivity ( $\rho$ ) is given by the full line in that picture.

Let us make some comments on this figure. The residual resistivity,  $\rho_0$ , is temperature independent. However, if the measurements are performed to very high temperatures,  $\rho_0$  is no longer temperature independent, since atomic diffusion processes, etc. may change  $\rho_0$  and one will observe different residual resistivity values if the experiment is repeated on the same sample.

Concerning  $\rho_{\text{spd}}$ , several authors (Dekker 1965) were able to show that the magnitude of  $\rho_{\text{mag}}(T > T_{\text{ord}}) \equiv \rho_{\text{spd}}$  is given by

$$\rho_{\text{spd}} = \frac{3\pi N m^*}{2\hbar e^2 \varepsilon_F} |\mathcal{J}|^2 (g-1)^2 J(J+1). \quad (50)$$

In the derivation of eq. (50) the conduction electrons are considered as free particles with an effective mass  $m^*$ . Further it was assumed that above  $T_{\text{ord}}$  there are no short-range correlations between the local moments. The factor  $(g-1)^2 J(J+1)$  is the well-known de Gennes factor. For the other symbols in eq. (50) see Dekker (1965). As it will be shown in section 3, the proportionality of  $\rho_{\text{spd}}$  to the de Gennes factor has indeed been observed in R-non-transition metal compounds (e.g.,  $\text{RAl}_2$ ,  $\text{RPt}$ , etc.).

If crystal-field effects are taken into consideration in the calculation, eq. (50) takes the form:

$$\rho_{\text{spd}}(T) = \frac{3\pi N m^*}{\hbar e^2 \varepsilon_F} |\mathcal{J}|^2 (g-1)^2 \sum |\langle m'_s, i' | \mathbf{s} \cdot \mathbf{J} | m_s, i \rangle|^2 \mathbf{p}_i \cdot \mathbf{f}_{ii'}, \quad (51)$$

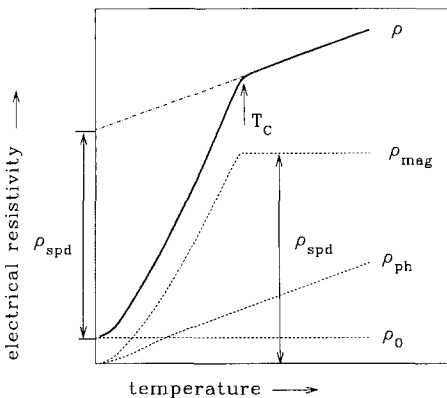


Fig. 1. A schematic representation of the temperature variation of the electrical resistivity,  $\rho$ , for a ferromagnetic compound. The arrow indicates the ferromagnetic transition. Included in the picture is the calculated temperature dependence of  $\rho_{\text{mag}}$  ( $\rho_{\text{spd}} \equiv \rho_{\text{mag}}(T > T_C)$ ),  $\rho_{\text{ph}}$  obtained from the Bloch-Grüneisen relation and the residual electrical resistivity  $\rho_0$ .

where the sum has to be taken over  $m_s, m'_s, i$  and  $i'$  ( $m_s$  and  $m'_s$  denote the spin states of the conduction electrons in their initial and final state,  $i$  and  $i'$  are the initial and the final crystal-field states, due to the scattering process). The consequence of the influence of the crystal field on the resistivity (in the paramagnetic state) is that  $\rho_{spd}$  now becomes temperature dependent because both functions  $p_i$  and  $f_{i'}$  in eq. (51) are temperature dependent (for details see Gratz and Zuckermann 1982a).

In the low-temperature region the conduction electrons interact with spin waves. In magnetically ordered compounds with residual electrical resistivities of a few  $\mu\Omega$  cm the electron–spin-wave scattering dominates the low-temperature resistivity variation. In particular, several authors (Kasuya 1959, Mills and Lederer 1966) derived a  $T^2$ -dependence for the spin-wave resistivity in a ferromagnet (assuming for the spin-wave dispersion relation:  $\omega(q) \propto q^2$ ). The assumption  $\omega(q) \propto q$  for the dispersion relation in antiferromagnets leads to a  $T^4$ -law; however, this is questionable for two reasons: (i) in the dispersion relation of antiferromagnets one usually finds a gap, the magnitude of which depends on the magnetic structure, and (ii) there appears to be, as yet, no experimental verification of any of the calculated temperature dependences in the case of antiferromagnetic order.

In analogy to fig. 1, in fig. 2 we have schematically depicted the  $W_{e,0}, W_{e,ph}$  and  $W_{e,spd}$  contributions to the total electronic thermal resistivity. As for the electrical resistivity, the residual thermal resistivity,  $W_0$ , dominates at low temperatures.  $W_0$  and  $\rho_0$  are related via the Wiedemann–Franz law (eq. (36)). The temperature dependence of  $W_{ph}$  was first calculated in the scope of the Debye approximation by Wilson (see, e.g. Ziman 1960). The dashed line in fig. 2 gives a schematic graph of the temperature variation according to Wilson’s formula. For a non-magnetic compound at low temperatures the electronic thermal conductivity can be approximated as

$$\lambda_e = \frac{T}{A + BT^3}, \tag{52}$$

where  $A$  and  $B$  are constants. The constant  $A$  can be determined from  $\rho_0$  using the Wiedemann–Franz relation (eq. (36)). Non-magnetic materials with small  $\rho_0$  often

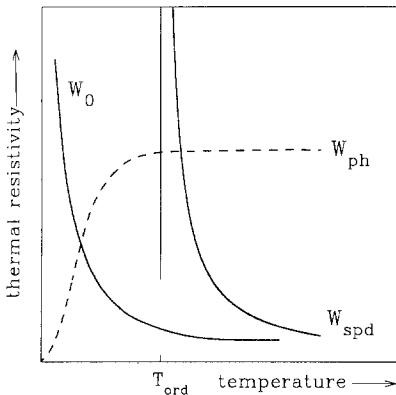


Fig. 2. A representation of the calculated temperature dependences of the thermal resistivity due to magnetic scattering,  $W_{spd}$  ( $W_{spd} \equiv W_{mag}(T > T_{ord})$ ),  $W_{ph}$ , due to electron-phonon scattering and  $W_0$ , the residual thermal resistivity.



exhibit a pronounced maximum in  $\lambda(T)$  at low temperatures (Blatt 1968, Parrott and Stuckes 1975). This follows directly from eq. (52).

Concerning the temperature dependence of  $W_{e,spd}$ , it is easy to show that the constant factor in  $W_{e,spd}(T)$  is proportional to the de Gennes factor. This relation is given by (see Bauer et al. 1986):

$$W_{e,spd}(T) = 1/\lambda_{e,spd} = \frac{9m^*N}{2\pi\hbar k_B^2 \epsilon_F} |\mathcal{J}|^2 (g-1)^2 J(J+1) (1/T). \quad (53)$$

Experimental confirmation of this relation has been found in the analysis of the  $RAI_2$  measurements (see section 3).

There are very few attempts to calculate  $W_{e,mag}$  in the magnetic ordered state, therefore it is difficult to present a general accepted relation between  $W_{e,mag}(T < T_{ord})$  and the temperature.

A linear temperature dependence of  $S_{e,spd}$  (eq. (49)) in the paramagnetic state has been observed in some samples (Gratz 1981, Bauer et al. 1987a). However, the validity of this linear relation seems to be limited to rather small temperature regions above the magnetic ordering temperature.

**2.3.4.2. Spin-fluctuation scattering.** The underlying principle of the spin-fluctuation model can best be illustrated by considering a ferromagnetic system above the Curie temperature,  $T_C$ . As is known, a ferromagnetic spin system retains an appreciable amount of short-range order above  $T_C$ . The spin-spin correlation time,  $\tau$ , as well as the range of spin order increase until both become infinite at  $T = T_C$ , and the system becomes magnetic with all its spins aligned parallel to each other at  $T = 0$ . We expect that a similar behavior is given in nearly magnetic systems at low temperatures, where the spin-spin correlation time,  $\tau$ , and the range of spin order have become considerable. In other words, the spins are aligned parallel to one another over a larger and larger distance in space and for a longer and longer time as magnetic instability is approached. Macroscopically these "long-living" finite-range ordering of spins give rise to fluctuations in space and time of the magnetization of the entire system, and, hence, to the name spin fluctuations (for a review see Schrieffer (1968) or Moriya (1985)). These fluctuations are correlated; the correlation function is related to the imaginary part of the generalized susceptibility function, which measures the linear response of the system to an external disturbance.

In the spin-fluctuation model the tendency towards magnetism is determined by the strength of the effective exchange interaction between electrons in a narrow band. The presence of this exchange interaction leads to an enhanced susceptibility over the Pauli value, predicted for a free-electron gas. At  $T = 0$  K this enhancement factor, known as the Stoner factor, is given by

$$S = \chi/\chi_0^P = [1 - U_0 N(\epsilon_F)]^{-1}, \quad (54)$$

where  $\chi_0^P$  is the unenhanced Pauli susceptibility,  $U_0$  is the strength of the exchange interaction and  $N(\epsilon_F)$  is the density of states at the Fermi energy. The criterion for

the occurrence of ferromagnetism is given by the familiar relation

$$U_0 N(\epsilon_F) = 1. \tag{55}$$

The factor  $S$  was first obtained theoretically by Stoner (1938) in an attempt to rectify the poor agreement between the theoretical prediction of the Pauli susceptibility and the experimental values of the strongly paramagnetic alloys of transition metals. Attempts to clarify the microscopic origin of the enhancement factor came first from Izuyama et al. (1963) and Hubbard (1963). The dynamics of the electrons in the band is now completely described by the Hamiltonian:

$$H = H_0 + H_{\text{int}}. \tag{56}$$

$H_0$  represents the ordinary band energy of the conduction electrons,  $H_{\text{int}}$  their interaction energy. In the interaction term,  $H_{\text{int}}$ , the matrix element of the electron interaction has been replaced by the constant  $U_0$ .

Assuming that  $z$  is the axis of the magnetization, we can calculate two distinct components of the magnetic susceptibility function, namely the transverse function,  $\chi_{-+}$ , and the longitudinal function, denoted by  $\chi_{zz}$ . In a ferromagnetic system the two functions would be different due to the presence of magnetization along the  $z$ -axis, whereas in the paramagnetic phase and in the absence of an external field the three components  $\chi_{xx}$ ,  $\chi_{yy}$  and  $\chi_{zz}$  coincide and are equal to  $\frac{1}{2}\chi_{-+}$  for a cubic system.

Within the random phase approximation (RPA) Izuyama et al. (1963) have shown that the transverse susceptibility can be described by the above Hamiltonian (eq. (56)), which leads to:

$$\chi_{-+}(\mathbf{q}, \omega) = \frac{\Gamma_{-+}(\mathbf{q}, \omega)}{1 - U_0 \Gamma_{-+}(\mathbf{q}, \omega)}. \tag{57}$$

In the paramagnetic phase, where we have an equal number of up- and down-spin electrons, it is only necessary to consider  $\chi_{-+}(\mathbf{q}, \omega)$  in order to gain insight into the nature of the nearly ferromagnetic system at low temperatures. For a paramagnet the function  $\Gamma_{-+}$  is complex and reads according to Izuyama et al. (1963):

$$\begin{aligned} \Gamma_{-+}(\mathbf{q}, \omega) &\equiv \Gamma(\mathbf{q}, \omega) = \text{Re}(\mathbf{q}, \omega) + i \text{Im}(\mathbf{q}, \omega) \\ &= \sum_{\mathbf{k}} \frac{f_{\mathbf{k}} + f_{\mathbf{k}+\mathbf{q}}}{\epsilon(\mathbf{k} + \mathbf{q}) - \epsilon(\mathbf{k}) - \hbar\omega - i\delta}, \end{aligned} \tag{58}$$

where Re and Im are the real and the imaginary parts, given by:

$$\text{Re}(\mathbf{q}, \omega) = \text{P.P.} \sum_{\mathbf{k}} \frac{f_{\mathbf{k}} - f_{\mathbf{k}+\mathbf{q}}}{\epsilon(\mathbf{k} + \mathbf{q}) - \epsilon(\mathbf{k}) - \hbar\omega}, \tag{59}$$

$$\text{Im}(\mathbf{q}, \omega) = \pi \sum_{\mathbf{k}} (f_{\mathbf{k}} - f_{\mathbf{k}+\mathbf{q}}) \delta(\epsilon(\mathbf{k} + \mathbf{q}) - \epsilon(\mathbf{k}) - \hbar\omega) \tag{60}$$

(P.P. means principal part). For low  $q$  and small  $\omega$ , such that  $q \ll k_F$  and  $\omega \ll qv_F$ , where  $k_F$  and  $v_F$  are the Fermi wave vector and the Fermi velocity of the conduction-electron system,  $\text{Re}(\mathbf{q}, \omega)$  and  $\text{Im}(\mathbf{q}, \omega)$  can be expanded to give a polynomial in  $q$  and  $\omega$  (for more details see Izuyama et al. (1963)).

Assuming that  $U_0 N(\varepsilon_F) \simeq 1$ , the generalized susceptibility  $\chi_{-+}(\mathbf{q}, \omega)$  is given by (Doniach and Engelsberg 1966)

$$2 \operatorname{Im} \chi_{-+}(\mathbf{q}, \omega) = \pi N(\varepsilon_F) \frac{\omega}{v_F q} \times \left( \left\{ 1 - U_0 N(\varepsilon_F) \left[ 1 - \frac{1}{12} \left( \frac{q}{k_F} \right)^2 \right] \right\}^2 + \left[ U_0 N(\varepsilon_F) \frac{\omega}{v_F q} \frac{\pi}{2} \right]^2 \right)^{-1}. \quad (61)$$

This function shows a maximum at an energy  $\omega_q$  with

$$\omega_q \cong \frac{1}{4} \varepsilon_F \pi \frac{q}{k_F} \frac{1 - U_0 N(\varepsilon_F)}{U_0 N(\varepsilon_F)}. \quad (62)$$

We see that the spin fluctuations are to some extent phonon-like, with an energy proportional to the wave vector,  $\mathbf{q}$ . Such excitations are often called “paramagnons”. The function  $2 \operatorname{Im} \chi(\mathbf{q}, \omega)$  is referred to as the spectral density of the paramagnons, often denoted by  $A(\mathbf{q}, \omega)$ .

The paramagnons change the physical properties of the system in much the same way as damped phonons do. The scale on which these changes occur is determined by a characteristic temperature, the “spin-fluctuation temperature”, given by

$$T_{sf} \cong [1 - U_0 N(\varepsilon_F)] T_F. \quad (63)$$

At low temperatures ( $T < T_{sf}$ ) the spin-fluctuation effects are dominating, giving rise to the following contributions to the physical properties (see Coqblin et al. 1978):

(i) A term proportional to  $T^2$  in the temperature dependence of the electrical resistivity, of which the prefactor is determined by  $T_{sf}^{-2}$ .

(ii) A term proportional to  $T$  in the thermal resistivity. The prefactor in this case is determined by  $T_{sf}^{-1}$ . The Lorentz factor in the Wiedemann–Franz law is reduced in comparison to its theoretical value (eq. (36)).

(iii) A negative magnetoresistance,  $\Delta\rho/\rho$ , proportional to the square of the applied magnetic field at low temperature (see Moriya 1985).

(iv) An enhanced  $\gamma$ -coefficient of the specific heat (see Doniach and Engelsberg 1966, Coqblin et al. 1978 and Moriya 1985), as well as a  $T^3 \ln T$  term.

Although it is as yet unknown whether paramagnon-drag effects have an influence on the temperature variation of the thermopower, it is at least imaginable that the experimentally observed low-temperature minima in  $S$  versus  $T$  are due to such a drag effect.

Coqblin et al. (1978) and later Moriya (1985) extended the paramagnon model to high temperatures. The main results concerning the transport properties for elevated temperatures can be summarized as:

The electrical resistivity ( $\sigma_{\text{mag}}$ ) shows saturation, somewhat above the spin fluctuation temperature,  $T_{sf}$ . Low  $T_{sf}$ -values are connected with strong curvature of the total resistivity. In some cases the resistivity goes through a maximum above  $T_{sf}$ , followed by a negative gradient in the high-temperature region.

The thermal resistivity ( $W_{\text{mag}}$ ), after its enhanced linear increase, goes through a maximum around  $T_{\text{sf}}$  and shows at high temperatures a  $T^{-1}$  behaviour.

2.3.4.3. *Kondo scattering.* In the following a brief introduction into the physics of instable f-electron systems will be given. A classification of 4f- and 5f-electron compounds can be made considering the stability of their magnetic moments. For example, rare earths with empty, half-filled or full 4f shells (La, Gd, and Lu) are in the 3+ state. The elements beside them show in general also the 3+ state, but there are also deviations from the 3+ configuration, e.g. in Ce, Sm or Yb, which are associated with instability of the magnetic moments.

The instability of the moments is connected with the hybridization of the f electrons with the conduction band. This mechanism may be considered as temporal fluctuations between two neighbouring valence states. For instance, in Ce compounds this transition can take place between the 3+ state, with total angular momentum  $J = \frac{5}{2}$  and the 4+ state with  $J = 0$ .

Figure 3 illustrates schematically the position of the  $4f^n$ ,  $4f^{n-1}$  and  $4f^{n+1}$  state with respect to the Fermi level,  $\epsilon_F$ . The distance between the  $4f^n$  and  $4f^{n+1}$  level is usually of the order of about 5 eV. The excitation energy,  $\epsilon_{\text{ex}}$ , is the energy necessary to bring a 4f electron from the highest occupied state below  $\epsilon_F(4f^n)$  to the Fermi level. In the following discussion we will distinguish the two configurations ( $4f^n$ ) and ( $4f^{n-1} + e$ ).  $\epsilon_{\text{ex}}$  is given by:

$$\epsilon_{\text{ex}} = \epsilon(4f^{n-1} + e) - \epsilon(4f^n). \tag{64}$$

$\epsilon(4f^n)$  and  $\epsilon(4f^{n-1} + e)$  denote the energy of the  $4f^n$  and the ( $4f^{n-1} + e$ ) state, respectively. The hybridization strength,  $\Delta$ , between localized 4f electrons and delocalized conduction electron states is given by

$$\Delta = \pi V^2 N(\epsilon_F), \tag{65}$$

where  $V$  denotes the matrix elements of the hybridization and  $N(\epsilon_F)$  the density of states at the Fermi level.

Concerning stable 4f moments: if the highest occupied 4f level is far below the Fermi level, there is no mixing of the ( $4f^n$ ) and ( $4f^{n-1} + e$ ) states for  $T \rightarrow 0$ . In that

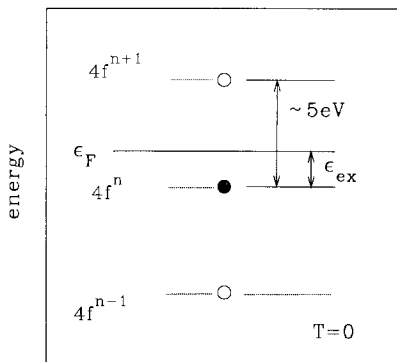


Fig. 3. This picture shows schematically the energy-level position of the empty  $4f^{n+1}$  state and the first occupied state ( $4f^n$ ) relative to the Fermi level,  $\epsilon_F$ .  $\epsilon_{\text{ex}}$  is the energy which is necessary to bring a 4f electron to the Fermi level.

case  $\Delta$  is negligibly small compared to  $\varepsilon_{\text{ex}}$  ( $\Delta \ll \varepsilon_{\text{ex}}$ ). The 4f states, and therefore the magnetic moments, are stable and can be described on the atomic energy scale, eventually modified by the crystal-field influence. The interaction with the conduction band can be treated at finite temperatures as a small perturbation. With increasing interaction of the 4f electrons with the conduction band, the coupling of the 4f electrons on neighbouring lattice sites increases. This kind of interaction, which leads to an indirect long-range magnetic order, is known as RKKY interaction.

Concerning unstable 4f moments: if  $\varepsilon_{\text{ex}}$  is comparable to the value of  $\Delta$ , transitions (fluctuations) between the two states ( $4f^n$ ) and ( $4f^{n-1} + e$ ) can be induced thermally or spontaneously (i.e. even for  $T \rightarrow 0$ ).

The Kondo and heavy-fermion regime are characterized by the condition  $\Delta < \varepsilon_{\text{ex}}$ . Now the hybridization cannot be neglected, thus for  $T \rightarrow 0$  the ground state is a mixture of ( $4f^n$ ) and ( $4f^{n-1} + e$ ). Many of the physical parameters are drastically changed. Because  $\Delta$  is still smaller than  $\varepsilon_{\text{ex}}$  the deviation of the averaged valence from an integer value is very small compared to the intermediate valence state (see below). But this mixture of the 4f configurations gives rise, in second order, to spin fluctuations between the 4f electrons and the conduction band.

Below a certain temperature,  $T^*$ , a cross-over of the static susceptibility from Curie–Weiss behaviour to an enhanced Pauli susceptibility occurs. Furthermore, the  $\gamma$ -value in the linear term of the specific heat increases extremely. Two examples illustrate this situation:  $\chi(\text{CeAl}_3) = 36 \times 10^{-3}$  emu/mol, which is, compared to  $\chi(\text{Pd}) = 0.8 \times 10^{-3}$  emu/mol, strongly enhanced. The same holds for the  $\gamma$ -values ( $\gamma(\text{CeAl}_3) = 1620$  mJ/mol K<sup>2</sup>,  $\gamma(\text{Pd}) = 9.42$  mJ/mol K<sup>2</sup>). For free electrons, both quantities,  $\chi$  and  $\gamma$ , are proportional to  $N(\varepsilon_{\text{F}})$ , and therefore to the effective electron mass,  $m^*$ . The same relation is observable for all the known heavy-fermion systems. Because of this these systems may be described at low temperatures within the scope of the Fermi-liquid theory. (This extremely enhanced effective mass  $m^*$  is the reason why we are speaking of heavy-fermion systems.) The existence of conduction electrons with extremely high  $m^*$  at low temperatures has been verified by de Haas–van Alphen measurements on UPt<sub>3</sub> (Taillefer et al. 1987) and CeCu<sub>6</sub> (Reinders et al. 1987). The so-called concentrated Kondo systems, or Kondo lattices (where the 4f moments are regularly distributed in the lattice), are similar in their behaviour, although the  $m^*$ -values observed in this category are considerably smaller, typical in the range  $m^*/m_0 = 10$  up to 50. The characteristic temperature is usually called the Kondo temperature. Typical examples are CeAl<sub>2</sub>, CeCu<sub>5</sub>, etc. For a review we refer the reader to the articles of Stewart (1984), Varma (1985), Fisk et al. (1986), Brandt and Moshchalkov (1984), Fulde et al. (1988) and Bauer (1991).

In the intermediate valence regime  $\varepsilon_{\text{ex}}$  is smaller than  $\Delta$  ( $\Delta \geq \varepsilon$ ). The ground state is, therefore, a mixture of the ( $4f^n$ ) and the ( $4f^{n-1} + e$ ) configuration. There are quantum-mechanical charge fluctuations which are observable in an experiment. The resulting valence of an R ion strongly deviates from an integer value. These intermediate valence compounds show, like Kondo and heavy-fermion systems, anomalous dependences in many of their physical properties. The bulk susceptibility shows Curie–Weiss behaviour at very high temperatures, after a maximum a constant value follows for  $T \rightarrow 0$ . The coefficient of the specific heat is typically of the order of

50 mJ/mol K<sup>2</sup>. This value is enhanced, but not as much as in the heavy-fermion systems. No long-range magnetic order is observable in these compounds.

The physics of this class of compounds is theoretically accounted for by the Anderson Hamiltonian (see, e.g., Loewenhaupt and Fischer in vol. 16 of this series).

In the limit of small s-f mixing ( $\Delta < \epsilon_{ex}$ ) the hybridization term in the Anderson Hamiltonian can be eliminated. Using the Schrieffer-Wolff transformation an effective s-f coupling constant  $\mathcal{J}$  can be obtained, which is based on a combined spin-exchange and orbit-exchange interaction (Coqblin and Schrieffer 1969). Results within the scope of the Anderson and the Coqblin-Schrieffer model can be obtained by different techniques. Among them there are perturbation calculations, the renormalization-group concept, the Bethe-ansatz diagonalization or the large- $N$  approximation.

These methods allow to calculate the temperature or field dependence of static and dynamic properties, including the temperature dependence of the specific heat, the magnetic susceptibility, the electrical resistivity, the thermal conductivity, the thermopower and the field dependence of the magnetization and the magnetoresistance.

In the following, the behaviour of the transport phenomena of Kondo systems will briefly be discussed.

2.3.4.3.1. *Electrical resistivity.* The best known feature caused by the Kondo interaction (in the presence of crystal-field splitting) is the  $\ln T$  dependence of the resistivity in combination with a maximum in the vicinity of the overall crystal-field splitting. This behaviour has been explained by Cornut and Coqblin (1972) within the scope of their model, applying a perturbation calculation. However, below a certain temperature – the Kondo temperature,  $T_K$  – this calculation fails to describe the observed behaviour, since many-body effects become important. In the case of a Kondo lattice in the low-temperature region the large- $N$  approximation is appropriate to account for the deduced  $T^2$ -dependence of  $\rho(T)$ , as well as the maximum centred roughly around the Kondo temperature.

2.3.4.3.2. *Thermopower.* Thermopower data of Kondo and heavy-fermion compounds are characterized by unusually large minima or maxima in the low-temperature region. Such large values require that the relaxation time,  $\tau_K$ , is asymmetric with respect to the energy around the Fermi level. Neglecting crystal-field effects, a universal behaviour of  $S(T/T_0)$  is obtained, which describes satisfactorily the thermopower data on single-impurity Kondo systems. However, if the crystal-field splitting becomes important, no such universal behaviour can be obtained.

2.3.4.3.3. *Thermal conductivity.* The influence of the Kondo-type interaction on the temperature dependence of the thermal conductivity,  $\lambda$ , in the presence of crystal-field splitting has been studied by Bhattacharjee and Coqblin (1988) and Bauer (1991). If the magnetic contribution to the electronic thermal resistivity,  $W_{mag}$ , is plotted as  $W_{mag}T$  versus  $T$ , similar behaviour as of the electrical resistivity can be observed.  $W_{mag}T$  also goes through a maximum at the temperature of the overall crystal-field splitting,  $\Delta_{cf}$ , and for  $T > \Delta_{cf}$  and  $T < \Delta_{cf}$  a  $\ln T$  behaviour has been deduced by Bauer

et al. (1991). Experimental evidence for the  $\ln T$  dependence of  $W_{\text{mag}}T$  has been observed in several compounds (e.g.  $\text{CeAl}_2$ ,  $\text{CeCu}_2$  and  $\text{CeCu}_5$ ) (see the review of Bauer 1991).

## 2.4. Transport phenomena with external magnetic field

### 2.4.1. Magnetoresistance

If an external magnetic field is additionally taken into consideration in the Boltzmann equation (eq. (11)), to find a solution is extremely difficult. However, many attempts have been made to find solutions of the Boltzmann equation for the magnetoresistance, but they all necessarily include numerous simplifications. Frequently, the relaxation-time approximation has been used to obtain results for the temperature and field dependence of the magnetoresistance. We refer the reader to the books of Blatt (1968), Ziman (1960) and the recently published book by Pippard (1989).

Since the goal of this chapter is to compare the transport properties of R and An intermetallics, we are mainly interested in the magnetoresistance of magnetically ordered materials, i.e. in the question how spin-dependent scattering processes influence the temperature and field variation of the magnetoresistance. However, before going into details, we will briefly discuss the magnetoresistance in normal, non-magnetic materials.

The classical magnetoresistance originates from the influence of the magnetic field on the conduction-electron orbits. In between collision events they are suffering on their way along the electric field gradient.

The magnetoresistance is defined as

$$\frac{\Delta\rho}{\rho} = \frac{\rho(T, H) - \rho(T, 0)}{\rho(T, 0)}. \quad (66)$$

In practice one distinguishes between two limiting cases, known as the “low”- and the “high”-field limit. In the high-field limit one refers to a magnetic field such that the cyclotron frequency of the electrons ( $\omega_c = eB/m$ ) is greater than the collision rate, which may be expressed as an inverse relaxation time ( $1/\tau$ ). Then the condition for the high-field case can be expressed by  $\omega_c\tau > 1$ . Another way of expressing the same condition is to require that in a strong field the electron mean free path is larger than the circumference of its cyclotron orbit. In this case the magnetic field cannot be treated as a “small perturbation” and a quantum-mechanical description, taking full account of the magnetic field, has to be applied.

Although the electron in the low-field limit ( $\omega_c\tau \ll 1$ ) still traverses a circular path in a plane normal to  $\mathbf{B}$ , it completes only a small arc before it suffers a collision and is scattered into another orbital state. In that case the magnetic field is a small perturbation.

It should be pointed out that, if the electric and the magnetic field are collinear, the magnetic field has no influence on a quasi-free-electron gas (with the dispersion relation  $\varepsilon(k) = \hbar^2 k^2 / 2m^*$ ). If a given material shows a longitudinal magnetoresistance, it is almost certain that the conduction band is not of the standard parabolic form. The qualification “almost” relates to the assumption that the relaxation time is

independent of the applied field,  $H$ . In a low field the relaxation time is independent of  $H$  to very good approximation.

However, strong fields ( $\omega_c \tau > 1$ ) can modify the electron wave function, so that  $\tau$  may depend rather sensitively on the magnetic field, and in the high-field limit the use of the Boltzmann equation is questionable, as already pointed out. In this limit quantum-mechanical effects become of importance and cannot be ignored.

In conclusion, even using a multi-band model, but with spherical energy surfaces, the longitudinal magnetoresistance is zero. But, in practice, the longitudinal magnetoresistance is often found to be of the same magnitude as the transverse magnetoresistance. As an example, the transversal and the longitudinal magnetoresistances of the non-magnetic  $YAl_2$  compounds will be presented in sect. 3.

Although it is evident that the theory of the magnetoresistance is complicated, there exists one rule which appears to be obeyed in many cases. This is the Kohler rule:

$$\Delta\rho/\rho_0 = F(H/\rho_0), \tag{67}$$

where  $F$  is a function depending on the nature of the material itself, but independent of the temperature and the impurities (for small impurity concentrations).

It states that the deflection of a carrier is proportional to the product of the magnetic field and the time between collisions. Deviations from Kohler's rule are evidence that different types of scattering mechanisms have different effects on different groups of carriers.

There are several basic works on the magnetoresistance of dilute magnetic alloys (Yosida 1957) and of rare earth metals (Kondo 1962). A rather comprehensive calculation of the magnetoresistance for the paramagnetic, ferromagnetic and antiferromagnetic state has been presented by Yamada and Takada in the early seventies (Yamada and Takada 1973a).

In the following we will present some of the theoretical results they obtained, since their results are in good agreement with many experimental measurements done on magnetic systems with localized magnetic moments.

For the calculation of the resistivity they used the Nakano-Kubo-Mori formalism (Kubo 1959), in which the resistivity for the different directions is given by

$$\rho^{\alpha\gamma} = \langle j^\alpha, j^\gamma \rangle^{-2} \text{Re} \lim_{s \rightarrow +0} \int_0^\infty dt e^{-st} \langle \dot{j}^\alpha(t), \dot{j}^\gamma \rangle \tag{68}$$

( $\alpha, \gamma = x, y, z$ ), using the relation

$$\langle A, B \rangle = \int_0^\beta d\lambda \langle A(-i\lambda), B^* \rangle, \tag{69}$$

and

$$j^\alpha = \frac{e}{V^{1/2}} \sum_{k,\sigma} \frac{\partial \varepsilon_k}{\partial k^\alpha} C_{k\sigma}^* C_{k\sigma} \tag{70}$$

( $\alpha = x, y, z$ ),  $\dot{j}^\alpha$  is the time derivative of  $j^\alpha$ ,  $A(t)$  is the Heisenberg representation of  $A$  and  $\langle \ \ \rangle$  means the grand canonical average of the Hamiltonian.  $B^*$  is the Hermitian conjugate of the operator  $B$  and  $\varepsilon_k$  is the kinetic energy of an electron in the  $k$ -state.



According to the definition in Yamada and Takada (1974), the effect of an external field  $H$  on the resistivity is given by:

$$\tilde{\Delta}\rho(T, H) = [\rho(T, H) - \rho(T, 0)] \frac{1}{\rho(\infty, 0)}, \tag{71}$$

with

$$\rho(\infty, 0) \propto S(S + 1) \tag{72}$$

for the  $S = \frac{1}{2}$  state, and otherwise

$$\rho(\infty, 0) \propto (g - 1)^2 J(J + 1), \tag{73}$$

this is the well-known expression for the spin-disorder resistivity (see eq. (44)).

This calculation performed for the low-field case, gave the following results: for a ferromagnetic spin arrangement  $\tilde{\Delta}\rho$  is negative and proportional to the magnetic field,

$$\tilde{\Delta}\rho = \chi_1 \hat{H}. \tag{74a}$$

In the vicinity of the Curie point,  $\tilde{\Delta}\rho$  depends on the field as

$$\tilde{\Delta}\rho \propto H^{2/3}. \tag{74b}$$

For an antiferromagnetic spin arrangement the corresponding expression in the paper of Yamada and Takada (1974) is:

$$\tilde{\Delta}\rho = \chi_2 \hat{H}^2 \tag{74c}$$

( $\hat{H} = \mu H / T_{\text{ord}}$ ,  $T_{\text{ord}}$  denotes the Curie or Néel point, the constants  $\hbar$  and  $k_B$  are taken to be 1).

The functions  $\chi_1$  and  $\chi_2$  depend in a complex way on the temperature and other sample-specific parameters. It is beyond the scope of this chapter to give details of these calculations; however, it is instructive to reproduce some of the figures in the paper of Yamada and Takada (1974) to illustrate the results they obtained. In fig. 4 a schematic graph of the temperature variation of the negative magnetoresistance for

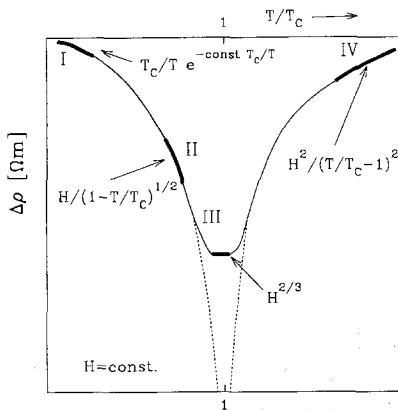


Fig. 4. Schematic graph of the magnetoresistance of a ferromagnet. The regions denoted by I, II, III and IV indicate the following temperature and field ranges: I:  $1 \gg \mu H / T$ ,  $1 \gg T / T_c$ , II:  $1 \gg (1 - T / T_c)^3 \gg (\mu H / T_c)^2$ , III:  $1 \gg (\mu H / T_c)^2 \gg |1 - T / T_c|^2$ , IV:  $T / T_c - 1 \gg \mu H / T_c$  (Yamada and Takada 1974).

a ferromagnet is depicted. The thick lines in the graph indicate the different regions for which analytical expressions are given in the paper of Yamada and Takada (1974). For more details we refer the reader to this paper. The reason why we show this schematic picture is that in several experimental investigations of the magnetoresistance (e.g., in the  $\text{RAI}_2$  compounds) there is good qualitative agreement below and above the ordering temperature (see sect. 3).

For an antiferromagnetic spin structure the function  $\chi_2$  depends not only on the temperature but also on the orientation of the external field,  $H$ , relative to the sublattice magnetization. In fig. 5, the results of these calculations are collected in a  $\rho(T, H)/\rho(T, 0)$  versus  $H$  diagram for some antiferromagnetic spin arrangements and orientations between the sublattice magnetization and the external field direction. From this figure it can be seen that  $\rho(H)/\rho(0) > 1$  and is proportional to  $H^2$  if the magnetic field is parallel to one of the sublattice magnetizations.  $\rho(H)/\rho(0) = 1$  if the magnetic field is perpendicular to the sublattice magnetization. Above the critical field ( $H_{c2}$ ), if ferromagnetism is induced by the field,  $\rho(H)/\rho(0) < 1$ .

It should be mentioned that all these results have been obtained within the molecular-field approximation. In the antiferromagnetic state near the Néel temperature this approximation becomes insufficient, because the effect of spatial spin correlations must be taken into account. In a later published paper Yamada and Takada (1974) applied the RPA for the spin-correlation function. Compared with the results of the molecular-field approximation,  $\rho(H)/\rho(0)$  shows a pronounced increase around the antiferromagnetic to ferromagnetic transition point,  $H_{c2}$ . The results of these calculations are sketched by the dashed line in fig. 5 (Yamada and Takada 1974).

To summarize, the magnetic field has an influence on the effective field in the ferromagnetic case. The change in this effective field suppresses the fluctuations of the localized spins, which leads to a negative magnetoresistance. In the antiferromagnetic state, with a field direction parallel to one of the sublattices, the fluctuations of the spins in one sublattice can be suppressed while these of the other sublattice may increase. Thus, the magnetoresistance is determined by the change in the sum

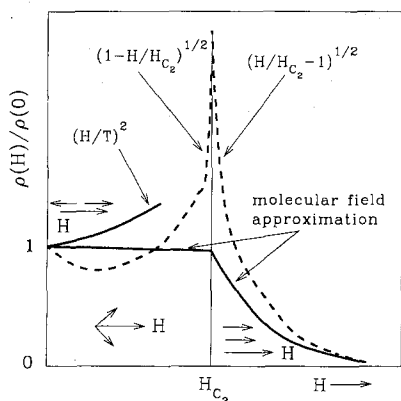


Fig. 5. The field dependence of the reduced resistivity ( $\rho(T, H)/\rho(T, 0)$ ) for an antiferromagnetic spin arrangement and the ferromagnetic alignment, with different orientations of the field and the antiferromagnetic sublattice magnetization (Yamada and Takada 1974). The dashed line represents the theoretical calculation using the random phase approximation (Yamada and Takada 1974).

of the fluctuating spins of both sublattices, which can lead to a positive magnetoresistance. From these results we can expect that, as the magnetic field increases, the magnetoresistance ( $\Delta\rho/\rho$ ) of a polycrystalline antiferromagnetic material changes from positive to zero and, finally, in high enough fields to negative values.

2.4.2. *Hall effect*

With the geometry shown in fig. 6 the following relation is obtained ( $B = \mu_0 H$ ):

$$E_y(B) = \rho_H(B)J_x. \tag{75}$$

$E_y$  and  $\rho_H$  denote the Hall field and the Hall resistivity (or the transverse resistivity), respectively.

2.4.2.1. *Normal Hall effect.* The normal Hall effect, which is observable in all materials, is just the result of the Lorentz force,  $\mathbf{F} = q \cdot (\mathbf{v} \times \mathbf{B})$ . Assuming that there is only one band of free charge carriers, the Hall resistivity is given by:

$$\rho_H = \frac{1}{nq}B, \tag{76}$$

where  $n$  is the volume density of charge carriers and  $q$  is their algebraic charge. The so-called normal Hall coefficient is defined as

$$R_0 = \rho_H/B = 1/nq, \tag{77}$$

thus

$$\rho_H = R_0 B = \mu_0 R_0 H. \tag{78}$$

The analysis of the Hall effect is far more complex than that of the magnetoresistance. In the approximation where  $|E_y| \ll |E_x|$ , which is often fulfilled, one gets in the two-band model:

$$R_0 = \frac{p\mu_p^2 - n\mu_n^2}{q(p\mu_p + n\mu_n)^2}. \tag{79}$$

This expression is especially applicable to semiconductors or semimetals. The symbols  $n$  and  $p$  represent the densities of electrons and holes, respectively;  $\mu_n$  and  $\mu_p$  are the corresponding mobilities of the electrons and the holes. Thus, the Hall effect measurement is a valuable method, especially when associated with resistivity measurements, to determine the sign, the density and the mobility of the charge carriers in materials.

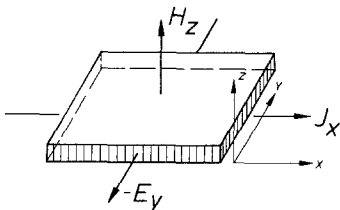


Fig. 6. The orientation of the current density  $J_x$ , the Hall field  $E_y$  and the magnetic field  $H$  with respect to the geometry of the sample.

2.4.2.2. *Anomalous Hall effect.* Very early, as observed by Hall himself, it appeared that metals (like, e.g., iron) have an anomalously high value of the Hall resistivity, which corresponds to no reasonable value of the carrier density and is even not linear in the field. Since in the presence of a magnetization  $B = \mu_0(H + M)$ , a natural extension of the Hall formula is to write the Hall resistivity as:

$$\rho_H = \mu_0(R_0H + R_1M), \quad (80)$$

which gives eq. (78) if  $M = 0$ . The first term in eq. (80) is the response to the external field, the second term is the response to the magnetization. Equation (80) is an empirical formula, which is well followed in many systems. It is simply the approximation that  $\rho_H$  is a linear combination of the responses to  $H$  and  $M$ . It may also be written as:

$$\rho_H = \mu_0[R_0(H + M) + R_S M] = R_0B + \mu_0R_S M, \quad (81)$$

using  $R_1 = R_0 + R_S$ .

$R_S$  is called the anomalous Hall coefficient. In most cases  $R_S$  is at least an order of magnitude larger than  $R_0$ , so that  $R_1 \simeq R_S$ . Before discussing the physical origin of  $R_1$  ( $R_S$ ), let us now discuss under which conditions  $R_0$  and  $R_1$  can be extracted from the experimental data in magnetic compounds. (Note that  $\rho_H/\mu_0H$  is sometimes called the total Hall coefficient,  $R_H$ .)

2.4.2.3. *Paramagnetic case.* In this case,  $M = \chi^*H$  (where  $\chi^*$  is the effective susceptibility including demagnetization-field effects), so that

$$\rho_H = \mu_0(R_0 + R_1\chi^*)H. \quad (82)$$

If one assumes that both  $R_0$  and  $R_1$  are independent of the temperature (which is often the case), then a plot of  $\rho_H(T)$  as a function of  $\chi^*(T)$  easily provides the values of  $R_0$  (as  $\chi^*$  goes to zero) and  $R_1$ . This is particularly easy when the susceptibility follows a Curie-Weiss law, by plotting  $\rho_H$  as a function of  $1/(T - \Theta_p)$ . In fig. 7 the results as obtained for USe (Schoenes et al. 1984) are given as an example.

2.4.2.4. *Ferromagnetic case.* If it is possible to saturate the magnetization and if  $R_1$  and  $R_0$  are independent of the field  $H$ , then the extraction of  $R_0$  is obvious:

$$\rho_H = \mu_0(R_0H + R_1M_S), \quad (83)$$

so that:

$$d\rho_H/dH|_{M_S=0} = \mu_0R_0, \quad (84)$$

which also allows to determine  $R_1$  in the whole temperature range.

2.4.2.5. *Antiferromagnetic case.* This is a very difficult situation, since the magnetization is proportional to  $H$ , as in the paramagnetic case, but  $R_S$  is often strongly temperature dependent, as for ferromagnets. It would be particularly interesting to follow the variations of  $R_0$ , in order to obtain information regarding the changes in the Fermi surface due to the onset of the antiferromagnetic structure. Also the

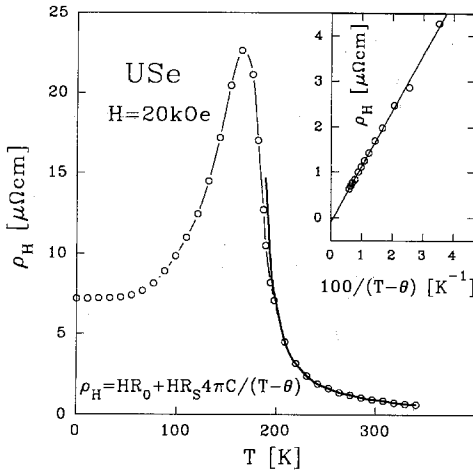


Fig. 7. The Hall resistivity of a USe single crystal as a function of temperature and a fit of the data in the paramagnetic temperature range. The inset shows the separation of the total Hall resistivity of USe in its ordinary and its extraordinary parts for  $T > T_C$  (see the equation in the figure). The fit parameters are  $\Theta = 182$  K,  $HR_0 = -0.12 \mu\Omega \text{ cm}$  and  $HR_s 4\pi C = 123 \mu\Omega \text{ cm K}$  (Schoenes et al. 1984).

variation of  $R_1$  would be interesting, for comparing with theoretical predictions. As a first approximation one may rely on the paramagnetic  $R_0$ -value to check whether it is negligible with respect to the total Hall coefficient,  $R_H$ . If this is the case,  $R_H$  is roughly equal to  $R_1 \chi^*$ , which allows the temperature variation of  $R_1$  to be extracted.

2.4.2.6. *Physical origin of  $R_1$  ( $R_S$ ).* It follows from eq. (83) that if an electric current flows through a single-domain ferromagnetic sample, a transverse voltage results, even in zero field, coming from:

$$\rho_H(H = 0) = \mu_0 R_1 M. \tag{85}$$

Thus  $R_1$  corresponds more to a diffusion than to the usual Hall process. This diffusion is asymmetric with respect to the  $(j, E_H)$ -plane. A review of the theory is given by Hurd (1972). In all the theories, the asymmetry results from the spin-orbit coupling.

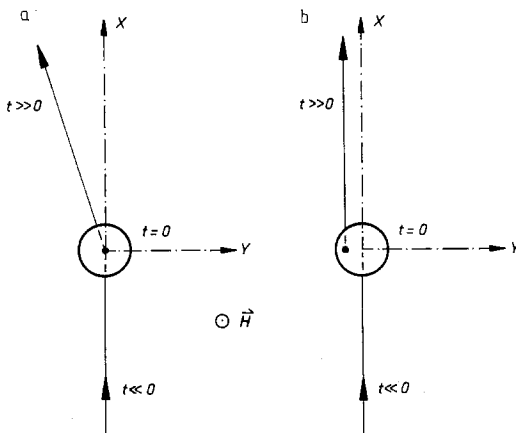


Fig. 8. Skew scattering (a) and side-jump scattering (b) for asymmetric diffusion.

There exist two possible modes of diffusion (Berger and Bergman 1979):

- (i) skew scattering (see fig. 8a),
- (ii) side-jump scattering (see fig. 8b).

Since in most of the theories the conductivity,  $\sigma$ , is calculated, one can write:

$$\mathbf{j} = \boldsymbol{\sigma}\mathbf{E} + \boldsymbol{\sigma}_H\mathbf{E}, \quad (86)$$

where  $\boldsymbol{\sigma}$  is the electrical conductivity tensor and  $\boldsymbol{\sigma}_H$  is the Hall conductivity tensor;  $\boldsymbol{\sigma}$  is diagonal:

$$\boldsymbol{\sigma} = \begin{pmatrix} \sigma_{11} & 0 & 0 \\ 0 & \sigma_{22} & 0 \\ 0 & 0 & \sigma_{33} \end{pmatrix}. \quad (87)$$

In the same way one gets for the resistivity tensor:

$$\mathbf{E} = \boldsymbol{\rho}\mathbf{j} + \boldsymbol{\rho}_H\mathbf{j}. \quad (88)$$

Assuming that  $\rho_{11} = \rho_{22} = \rho_{33}$  (i.e., there is no anisotropy), one obtains by matrix inversion:

$$\rho_H = \rho^2 \sigma_H. \quad (89)$$

In case of skew scattering on magnetic impurities it is found that  $\sigma_H \propto \rho^{-1}$ , so that  $\rho_H$  is proportional to  $\rho$ , whereas in case of side-jump scattering  $\sigma_H$  is constant, so that  $\sigma_H \propto \rho^2$ .

Thus, one expects that the Hall constant reflects essentially the scattering mechanism, as the electrical resistivity does. The calculations have been extended to the case of diffusion by spin waves (Irkhin et al. 1967), to Kondo lattices (Ramakrishnan et al. 1985) and to heavy-fermion systems (Fert and Levy 1987).

### 3. Discussion of experimental results

#### 3.1. Rare earth and actinide metals

Discussing the transport properties of their compounds, it seems to be natural to start with the rare earth and actinide elements, which are all metals. As a matter of fact, pure metals are not always the simplest solid-state systems; this is particularly true in the case of the transition-metal series, where d electrons may act as scattering centres and/or charge carriers.

For experimentalists, measurements of the transport properties of metals are also of great practical interest, since they are very sensitive to the purity of the studied materials. It is known that the residual resistivity ratio  $\rho(300 \text{ K})/\rho(4.2 \text{ K})$  is commonly used as a global purity test. Values as high as 1000 have been obtained for ultra-pure thorium refined by electro-transport (Peterson et al. 1967). Even in the purest lanthanides this ratio is below 300. A value of 50 has been reached for electro-refined plutonium (Arko et al. 1972) and one of 65 for electro-refined neptunium (Fournier and Amanowicz 1992).

At the start of this section on the discussion of the experimental results, we would like to stress that the solid-state physics involved in this volume is closely dependent on material science: much too often data are given for samples of which the purity, stoichiometry and crystallinity are not studied in detail: "X-ray purity" is far from satisfactory if one wants to study the solid-state properties of rare earth and actinide compounds. This is particularly true when the results are critically dependent on the electronic states near the Fermi energy,  $\varepsilon_F$ , which is in fact the case for intermediate-valence systems, heavy fermions, Kondo lattices, structural unstable and metal-insulator transition systems. These problems represent in fact most of our common interest. It has also to be kept in mind that the actinides are radioactive materials. Due to the radiotoxicity, the handling, in particular for transuranium elements, is severely restricted to special laboratories ("hot laboratories"). Another problem comes from the  $\alpha$ -activity, which is mainly absorbed within the samples. This self-irradiation creates defects, and systematic studies of plutonium metal at low temperatures have shown that the transport properties were severely changed (Hall and Purser 1971). This  $\alpha$  absorption is also the source of self-heating. With  $^{239}\text{Pu}$  it reaches 2 mW/g. It is almost impossible to do very-low-temperature measurements with Pu compounds, except if one uses the long-living  $^{242}\text{Pu}$  isotope – it is, however, extremely rare. Therefore, heavy-fermion studies involving plutonium have little hope to be developed.

The electrical resistivity of the rare earth metals has been studied in detail. We refer the reader to review articles by McEwen (1978) and Koskenmaki and Gschneidner (1978) for a more detailed discussion. De Gennes and Friedel (1958) developed their well-known model (see sect. 2.3.4) in order to explain the spin-disorder resistivity in lanthanides for  $T > T_{\text{ord}}$ . As can be seen in fig. 9,  $\rho_{\text{mag}}(T > T_C)$ , as determined from the resistivity in the  $c$ -axis direction for the heavy lanthanide elements, follows the de Gennes factor,  $(g - 1)^2 J(J + 1)$ . Refinements of that model have been made taking

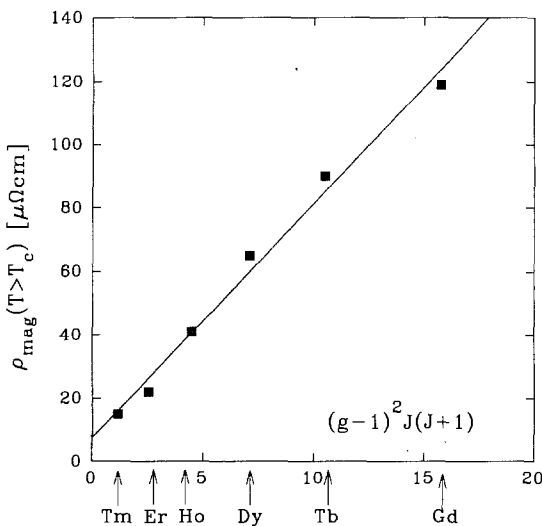


Fig. 9. The magnetic resistivity ( $\rho_{\text{mag}}$ ) versus the de Gennes factor for the heavy lanthanides.

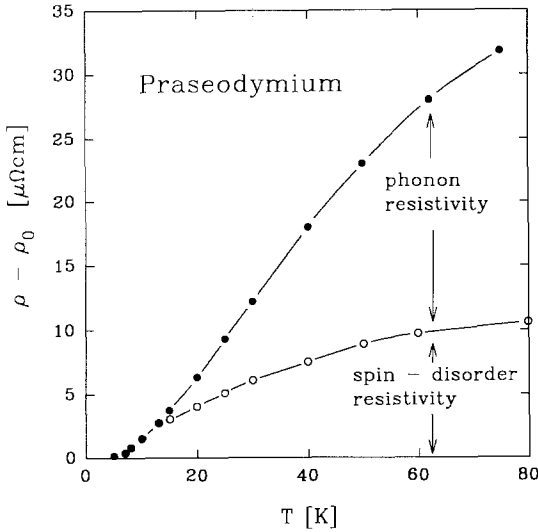


Fig. 10. The electrical resistivity of polycrystalline praseodymium separated into the spin-disorder and the phonon contribution (from McEwen 1978).

into account changes in the population of crystal-field levels with changing temperature (see also eq. (51) in sect. 2.3.4).

As an example we present in fig. 10 the results obtained for praseodymium by McEwen (1978). The curvature in  $\rho_{\text{mag}}$  is due to the increasing population of the crystal-field levels with increasing temperature. In the case of antiferromagnetic lanthanide metals an anomalous behaviour has been observed, since below  $T_N$  gaps are opened in the conduction band as a result of distortions of the Fermi surface, which modify the transport properties of the metals. Figure 11 displays a comparison

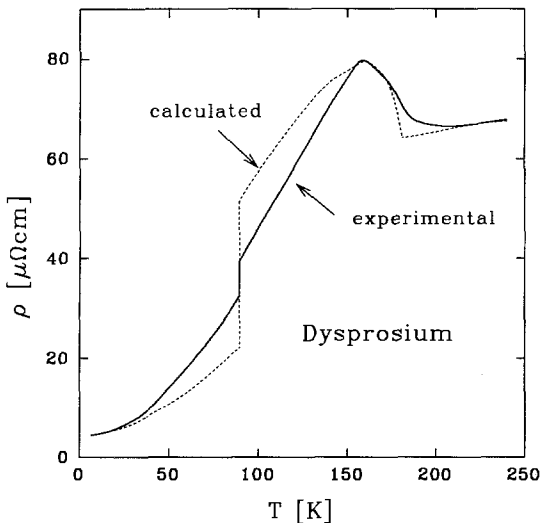


Fig. 11. A comparison of the measured c-axis electrical resistivity for dysprosium (Boys and Legvold 1968) with the calculation of Elliott and Wedgwood (1963) (from McEwen 1978).



of the theoretical results obtained by Elliott and Wedgwood (1963) and the measured electrical resistivity along the *c*-axis for Dy metal (Boys and Legvold 1968).

Spin-wave scattering of the conduction electrons at low temperatures has been studied in particular by Yamada and Takada (1972). Dispersion relations of the type  $\omega \propto q^2$  and  $\omega \propto q$  yield resistivity contributions proportional to  $T^2$  and  $T^4$ , respectively. As is shown in fig. 12, the agreement with the experimental data is fairly good, at least in the case of Gd.

The Hall effect in lanthanide metals exhibits a number of unusual features, which have motivated intensive theoretical work aiming to explain the origin of the

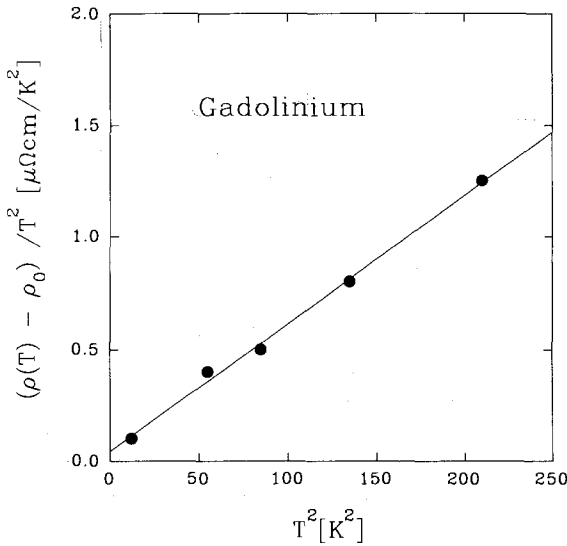


Fig. 12. The *b*-axis resistivity of gadolinium at low temperatures, plotted to give a comparison with the predicted  $T^4$  behaviour (from McEwen 1978).

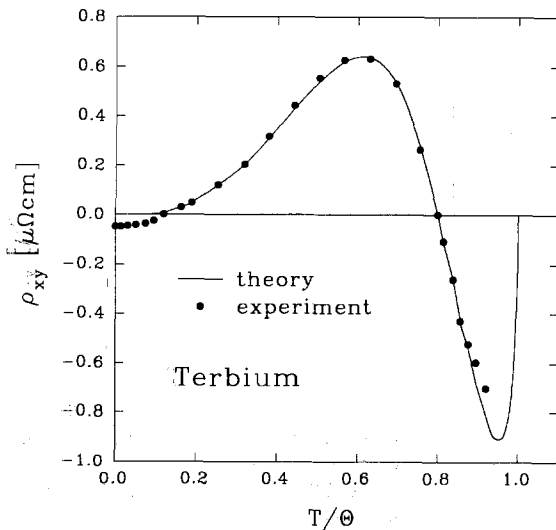


Fig. 13. The extraordinary Hall resistivity of terbium,  $\rho_{xy} = R_1 M$ , as a function of reduced temperature ( $\Theta$  denotes the paramagnetic Curie temperature). The measurements were done with the field in the basal plane (Rhyne 1969). Measurements between  $T_C$  and  $\Theta = T_N$  were done above  $H_C$ , the field needed to create ferromagnetic alignment. The theoretical curve of Fert (1974) includes side-jump and skew scattering contributions (from McEwen 1978).

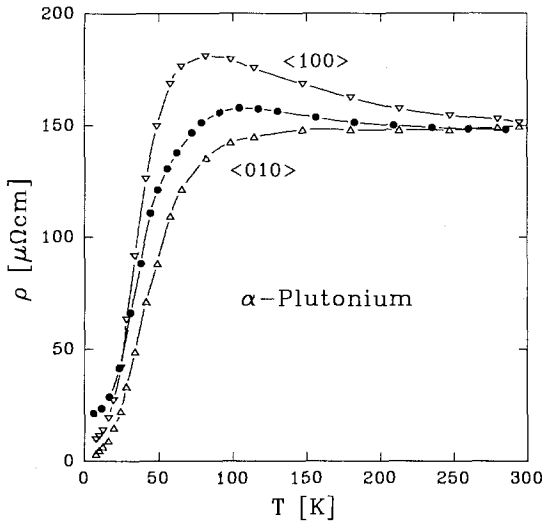


Fig. 14. The electrical resistivity of  $\alpha$ -Pu. The polycrystalline data (filled symbols) are taken from Lee (1971). The single crystal data for the current  $J$  along  $\langle 010 \rangle$  and  $\langle 100 \rangle$  with  $\rho$  normalized to  $150 \mu\Omega \text{ cm}$  at  $300 \text{ K}$  are taken from Arko and Brodsky (1970).

asymmetric diffusion (see section 2.4.2). As an example, fig. 13 demonstrates the excellent agreement between theoretical calculations for the extraordinary Hall resistivity and the experiment in the case of terbium metal (Fert 1974). This presentation illustrates the fundamental importance of the experimental studies of the transport properties of the rare earth metals on the development of an understanding of magnetic scattering.

Let us now consider the behaviour of the actinide metals, together with the anomalous lanthanides. The most famous case is that of plutonium metal, of which the electrical resistivity is displayed in fig. 14 (Arko and Brodsky 1970). There is  $T^2$  dependence at low temperatures, followed by a sharp increase, after which a rounded maximum near  $100 \text{ K}$  appears, with a negative slope up to room temperature. In fig. 14 we have plotted the  $\rho$  versus  $T$  behaviour of a polycrystalline Pu sample, in addition with measurements on a single crystal in two different crystallographic directions. Earlier, this kind of  $\rho$  versus  $T$  curve was referred to the antiferromagnetism of  $\alpha$ -Pu, because of the similarity with  $\alpha$ -Mn. But when the absence of magnetic order in plutonium was confirmed, an explanation for the unusual resistivity behaviour has been given within the scope of the spin-fluctuation theory (Arko et al. 1972, Doniach 1974, Jullien et al. 1974). However, this involves the most complicated interplay between strongly correlated  $5f$ -states hybridized with conduction electrons, which is in fact the central physical problem in the actinide series.

From this point of view, it is of interest to consider the behaviour of the electrical resistivity of the light actinide metals, from thorium to curium (fig. 15). The anomalous behaviour of  $\rho$  versus  $T$ , with increasing atomic number, is associated with the progressive localization of the  $5f$  electrons. The extra scattering of magnetic origin is explained by the development of spin fluctuations, giving rise to a  $T^2$  term at low temperatures (see the  $\rho$  versus  $T$  curves of  $\alpha$ -Pu and Np), while at high temperatures (if there is long-range magnetic order, as in curium metal) a spin-disorder resistivity exists.

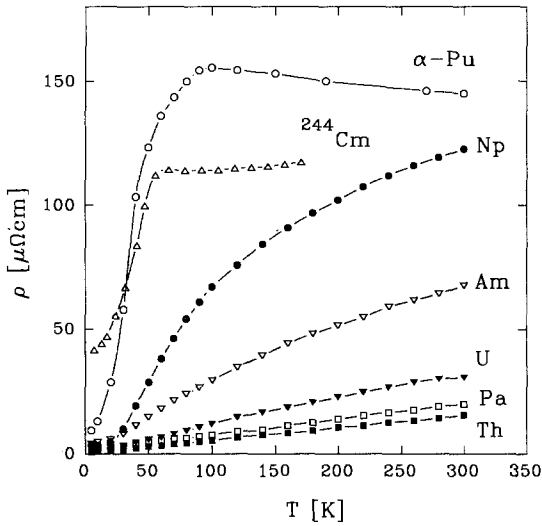


Fig. 15. The electrical resistivity of the light actinide metals from thorium to curium (from Fournier and Troć 1985).

In the case of fcc  $\delta$ -Pu, which is a high-temperature allotropic form of plutonium, Kondo-type behaviour above about 200 K has recently been suggested (Méot-Raymond and Fournier 1992). This behaviour is closely connected with the enhanced localization of the 5f electrons in  $\delta$ -Pu. In fact, the 20% larger atomic volume of  $\delta$ -Pu is even larger than the volume increase between  $\alpha$ -Ce and  $\gamma$ -Ce (both fcc), where a change of only 17% is observed. This suggests a comparison of cerium with plutonium metal (Koskenmaki and Gschneidner 1978). In the case of  $\alpha$ -Ce, no  $T^2$  behaviour was detected at low temperatures and no curvature is observed at higher temperatures (Brodsky and Friddle 1973, Nicolas-Francillon and Jerome 1973). The electrical

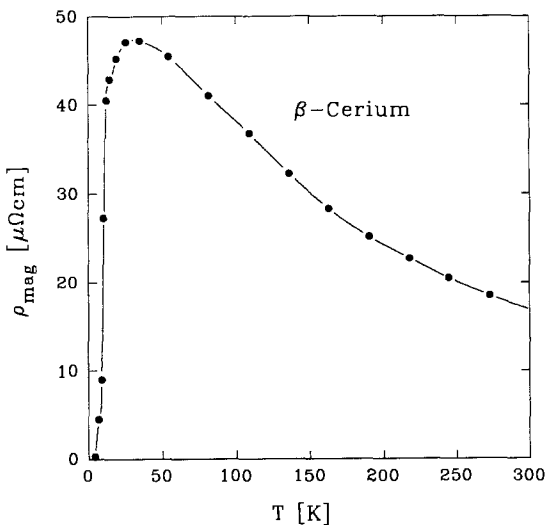


Fig. 16. The anomalous resistivity ( $\rho_{mag}$ ) of  $\beta$ -Ce (obtained by subtracting the phonon and the residual resistivity from the measured  $\rho$ -values) is given by the symbols. The solid line shows the result of the theoretical calculation based on the model of Liu et al. (1976) (from Koskenmaki and Gschneidner 1978).

resistivity of  $\gamma$ -Ce is about 10% smaller than that of  $\beta$ -Ce (dhcp structure), but shows the same temperature dependence above 100 K ( $\gamma$ -Ce transforms into  $\alpha$ -Ce below 100 K). The resistivity of  $\beta$ -Ce (fig. 16) could be fitted with a Kondo-type model by Liu et al. (1976) over a wide temperature range. Anomalous behaviour has also been found in Cm metal, which is antiferromagnetic below  $T_N = 52$  K (Schenkel 1977).

In the case of  $\alpha$ -Ce, which is considered as an exchange-enhanced paramagnet, the absence of a  $T^2$  term in the low-temperature resistivity is surprising. Being presented sometimes as an element having the highest electronic specific-heat coefficient ( $\gamma = 12.8$  mJ/mol K<sup>2</sup>),  $\alpha$ -Ce is, in fact, in this respect comparable with Pd ( $\gamma = 10$  mJ/mol K<sup>2</sup>),  $\alpha$ -U ( $\gamma = 12.2$  mJ/mol K<sup>2</sup> under a pressure of 10 kbar) and even La ( $\gamma = 10$  mJ/mol K<sup>2</sup>), while  $\gamma = 14$  mJ/mol K<sup>2</sup> for  $\alpha$ -Np and  $\gamma = 22$  mJ/mol K<sup>2</sup> for  $\alpha$ -Pu. For  $\delta$ -Pu  $\gamma$  reaches the very large value of 53 mJ/mol K<sup>2</sup>, i.e. four times the value for  $\alpha$ -Ce. Thus, within the f-metal series,  $\alpha$ -Ce is more similar to  $\alpha$ -U or even La than to  $\alpha$ -Pu. In fact, no  $T^2$  term was found in  $\alpha$ -U or La. In the case of Pd a very careful analysis of the resistivity allowed to detect an extremely small coefficient  $A$  ( $A = 0.03$  n $\Omega$  cm/K<sup>2</sup>), which is under the detection limit of the measurements on  $\alpha$ -Ce (Koskenmaki and Gschneidner 1978).

We also emphasize that the behaviour of La is not “normal”, in the sense that it is not comparable with Y or Lu. All the basic physical properties of La show the influence of excited 4f states at  $\epsilon_F$  (high electronic specific-heat coefficient, the curvature of the resistivity and the variation of the superconduction transition temperature under pressure (Ratto et al. 1969)). In fig. 17 we have plotted the electrical resistivity of Y, Lu, La and Am for comparison. Note that Y and Lu have, in fact, a very similar  $\rho(T)$  curve, whereas the hybridization (at least partly) of the f level in the case of La (4f) and Am (5f) causes a deviating behaviour. In table 1 we summarize, for comparison, the electronic specific-heat coefficients,  $\gamma$ , the magnetic susceptibility and the

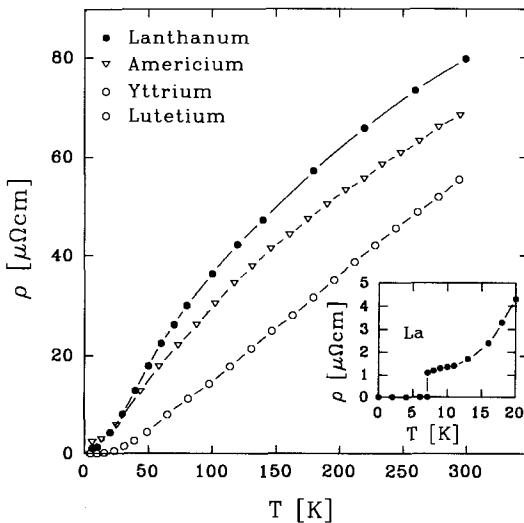


Fig. 17. The electrical resistivity of Y, Lu, La and Am as a function of temperature. The residual resistivity is subtracted using the  $\rho(T)$  curves for Y and Lu (both are practically identical in shape). The inset shows  $\rho$  versus  $T$  for La around the superconduction transition temperature.

TABLE I

The electronic specific heat coefficient,  $\gamma$ , the magnetic susceptibility,  $\chi$ , at 300 K and the coefficient  $A$  in the  $T^2$  term of the resistivity for non-magnetic rare earth and actinide metals as well as for Pd.

	Y	$\alpha$ -La	$\alpha$ -Ce	Th	$\alpha$ -U	$\alpha$ -Np	$\alpha$ -Pu	$\delta$ -Pu	Am	Pd
$\gamma$ (mJ/mol K <sup>2</sup> )	8.2	10 11.5 <sup>a</sup>	12.8	4.3	9.1 12.2 <sup>b</sup>	14	22	53	3±3	10
$\chi$ (10 <sup>-6</sup> emu/mol)	227	111	560	100	400	600	550	550	≈800	561
$A$ (nΩcm/K <sup>2</sup> )	-	-	<1	<1	<1	7	21	-	-	0.03

<sup>a</sup>fcc structure ( $\beta$ -La).

<sup>b</sup>Under pressure.

coefficients of the  $T^2$  term of the resistivity for the non-magnetic rare earth and actinide metals, as well as for Pd.

The Hall effect for the actinide metals has been measured only with Th, U and Pu (Brodsky et al. 1974). In the case of U a very strong temperature dependence, leading even to a change of sign, was observed around 20 K, i.e. near to the temperature where a charge density wave (CDW) is formed in this metal (fig. 18). In fact, such a behaviour has been observed also in transition metal dichalcogenides around the onset of the charge density waves (Huntley and Frindt 1974) and has been linked to a change in the Fermi-surface topology (Bristow et al. 1977, Cornelius and Smith 1980). The application of pressure rapidly suppresses the strong temperature dependence of  $R_H$  (Cornelius and Smith 1981). At the same time it suppresses the CDW (Smith and Lander 1984). So it is most probable that the rapid change in the Hall coefficient around 20 K is due to the onset of the CDW (see fig. 18). Although a detailed

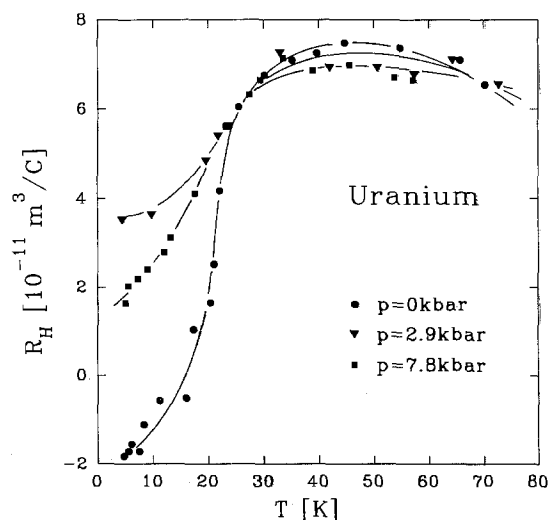


Fig. 18. The Hall coefficient of polycrystalline uranium under external pressure (Cornelius and Smith 1981).

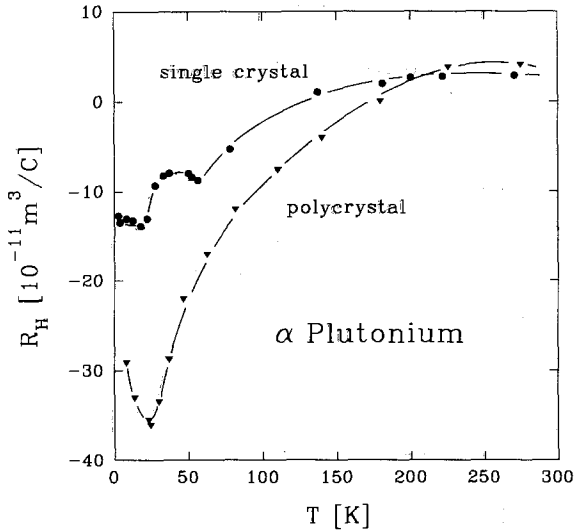


Fig. 19. The Hall coefficient of  $\alpha$ -Pu as a function of temperature. The single crystal data were obtained with  $J$  parallel to  $\langle 010 \rangle$  and  $H$  parallel to  $\langle 001 \rangle$  (Arko and Brodsky 1970).

theoretical calculation may be rather difficult, it has been shown (Fournier 1975) that the onset of the CDW leads to an important decrease of the electron-phonon coupling, and thus to an increase of the electron mobility,  $\mu_n$ .

In a simple two-band model the normal Hall coefficient,  $R_0$ , given by eq. (79), decreases and might even become negative, which is the case for uranium and also for the transition metal dichalcogenides. It is of interest to realize that the Hall resistivity,  $\rho_H$ , of  $\alpha$ -Pu is extremely anomalous, in particular when measured on a single crystal (Brodsky 1965, Arko and Brodsky 1970). Figure 19 shows the temperature dependence of  $R_H$  of a polycrystalline  $\alpha$ -Pu sample and of a single crystal. In the  $R_H(T)$  curve of the single crystal two anomalies, at 20 and 60 K, are observable. It is quite tempting to postulate that the anomaly at 20 K has the same origin as in  $\alpha$ -U. A periodic lattice distortion might be responsible for the 60 K anomaly in  $\alpha$ -Pu. This could also explain anomalies observed around this temperature in other physical properties, in particular in those which are sensitive to the electron-phonon coupling, i.e. the specific heat (Lee et al. 1969), the thermal expansion (Sandenaw 1961) and the ultrasonic attenuation (Rosen et al. 1968). The very complicated and unstable monoclinic structure of  $\alpha$ -Pu makes such an occurrence of a CDW quite possible. It would be extremely interesting to grow a single crystal of  $\alpha$ -Pu metal and to test this hypothesis using neutron diffraction.

However, the overall thermal variation up to room temperature must have another origin since  $\alpha$ -Pu is a spin-fluctuation system, in which magnetic scattering is important. As has been shown by Lapiere et al. (1987), in spin-fluctuation systems asymmetric scattering is certainly present, giving rise to an extraordinary Hall effect (see sect. 2.4.2), and its thermal variation reflects that of the magnetic resistivity. This is even more obvious in the case of  $\beta$ -Pu (see fig. 20), where the Hall resistivity closely follows the thermal variation of the electrical resistivity.

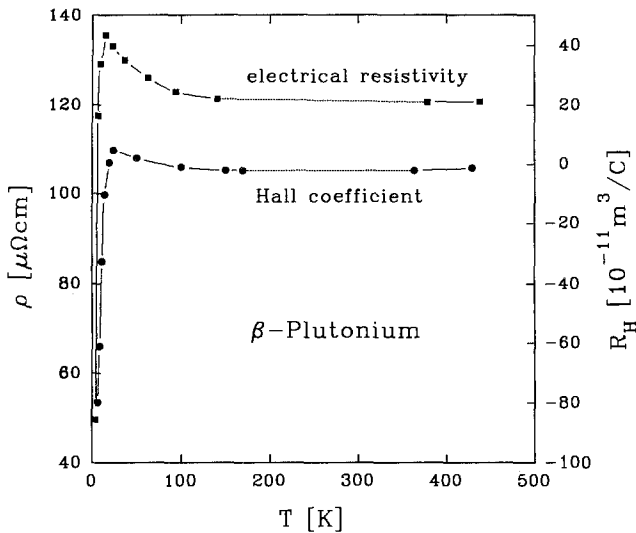


Fig. 20. The electrical resistivity and the Hall coefficient of  $\beta$ -Pu (Brodsky 1965).

No Hall effect measurements on Ce metal are reported after 1963 (Gschneidner and Smoluchowski 1963) and there are no detailed investigations of the pure  $\alpha$ - and  $\gamma$ -Ce phase showing the extraordinary Hall effect. Such studies would be very interesting.

### 3.2. RPt and AnPt intermetallics

#### 3.2.1. RPt

The equiatomic RPt compounds crystallize in two different orthorhombic structures. The heavy RPt compounds ( $R = \text{Gd to Tm}$ ) show the FeB-type structure, whereas the light RPt ( $R = \text{La, Ce, Pr and Nd}$ ) crystallize in the CrB-type structure (Dwight et al. 1965, Le Roy et al. 1978). The RPt compounds are ferromagnets with relatively low ordering temperature (Castets et al. 1980, 1982). The highest Curie temperature has been measured for GdPt ( $T_C = 68 \text{ K}$ ). It can be assumed that the coupling of the 4f moments is caused by an RKKY-type of interaction. Figure 21 shows the temperature dependence of the electrical resistivity of most of the RPt compounds, measured by Gómez-Sal et al. (1986). All these  $\rho$ - $T$  curves (except that for LaPt) exhibit a sharp kink, which indicates the magnetic ordering temperature. The analysis of the resistivity data by Gómez-Sal et al. (1986) is based on the Matthiessen rule (eq. (32)). The phonon contribution to the total resistivity ( $\rho_{\text{ph}}$ ) has been determined from the resistivity of the isostructural non-magnetic LaPt compound. The magnetic contribution ( $\rho_{\text{mag}}$ ) for some of the heavy RPt compounds, obtained by a subtraction of  $\rho_{\text{ph}}$  from the total resistivity, is plotted as a function of the temperature in fig. 22. The steep increase of  $\rho_{\text{mag}}$  with increasing temperature ends at  $T_C$  in a sharp kink. This is only expected in compounds with well-localized magnetic moments and non-magnetic partner elements. The negative curvature in

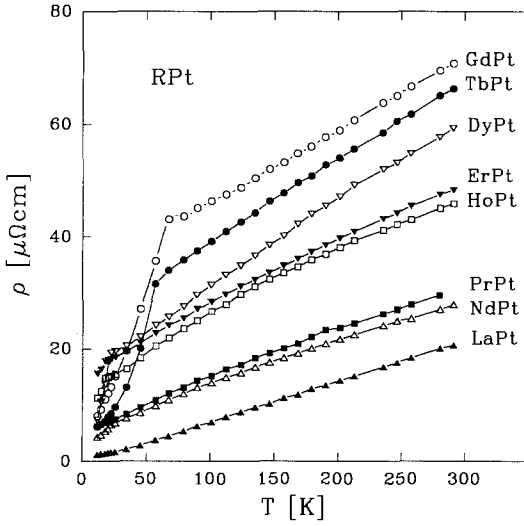


Fig. 21. The thermal variation of the resistivity of the RPt compounds (Gómez-Sal et al. 1986).

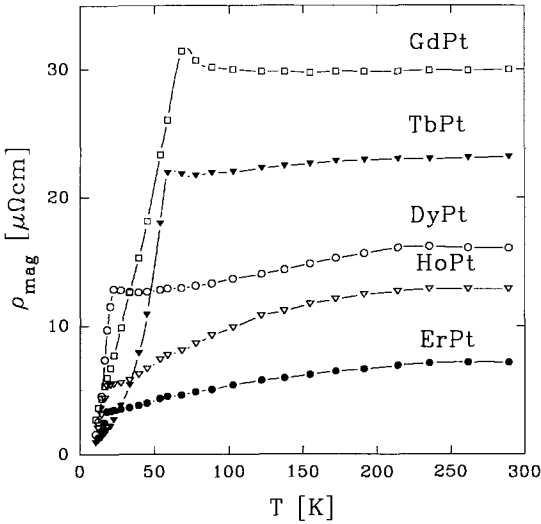


Fig. 22. The temperature dependence of the magnetic contribution,  $\rho_{\text{mag}}$ , to the total resistivity of some RPt compounds.

$\rho_{\text{mag}}(T)$  above  $T_C$ , observed for Tb, Dy, Ho and Er, is due to the influence of the crystal field on  $\rho_{\text{mag}}$ . This can be concluded from a comparison of  $\rho_{\text{mag}}$  of GdPt (where no crystal-field influence exists) with  $\rho_{\text{mag}}$  of the other RPt compounds. Despite the hump at  $T_C$ ,  $\rho_{\text{spd}} (\equiv \rho_{\text{mag}}(T > T_C))$  of GdPt is practically temperature independent, as it is expected for  $\rho_{\text{spd}}$  in a system with well-localized magnetic moments without crystal-field influence (eq. (50)). For other RPt compounds  $\rho_{\text{spd}}$  increases in the paramagnetic region and tends to a constant value at higher temperatures. As is shown by Gómez-Sal et al. (1986), the constant values of  $\rho_{\text{spd}}$  at room temperature show the expected proportionality to the de Gennes factor (eq. (50)).



### 3.2.2. *AnPt*

As the light RPt compounds, the AnPt compounds (An = Th, U, Np and Pu) crystallize in the orthorhombic CrB-type structure (Lam et al. 1974a). Dommann and Hulliger (1988) reported a PdBi-like monoclinically distorted CrB-type structure for UPt.

Already in the early seventies the first indications for magnetic ordering have been obtained for UPt, NpPt and PuPt, from the temperature variation of the electrical resistivity (Lawson 1970, Hill and Elliott 1971). The resistivity of ThPt does not show any sign of a spin-dependent scattering contribution. The very low  $\gamma$ -value (3.5 mJ/mol K<sup>2</sup>) in the electronic specific heat together with the temperature variation of the resistivity are typical for a metallic system in which the f and d states are negligible at the Fermi level. It can be assumed that the Pt 5d band is filled up by the Th valence electrons.

Within the AnPt series UPt is investigated in most detail. This compound shows a ferromagnetic transition at about 27 K. A second transition of magnetic origin has been detected in the temperature dependence of the specific heat at about 20 K by Luengo et al. (1976) and Frings and Franse (1985). Neutron diffraction investigations performed on powdered UPt samples by Lawson et al. (1986) revealed a very complex magnetic structure below 30 K. According to these investigations, the ferromagnetic structure in UPt consists of alternating layers of magnetic and non-magnetic U atoms, on which a non-collinear antiferromagnetic structure, which itself reorders at 20 K, is superimposed. The magnetic moments are aligned along the *b*-direction of the orthorhombic structure. An almost linear  $1/\chi$  versus *T* behaviour above 500 K is followed by a pronounced downward curvature with temperature decreasing below 500 K. From the linear part in  $1/\chi$  versus *T* an effective moment of  $3.6\mu_B$ /f.u. was derived by Frings et al. (1983). The  $\gamma$ -value of UPt (109 mJ/mol K<sup>2</sup>) is considerably high.

Magnetic measurements on NpPt in fields up to 5.5 T reveal antiferromagnetic order below 27 K (Smith and Hill 1974). The temperature dependence of  $1/\chi$  is linear in a limited temperature range above the Néel temperature. An antiferromagnetic phase transition at 44 K has been found for PuPt, which is followed by a first-order phase transition to a ferrimagnetic state at 19 K (Smith and Hill 1974). From the very low saturation magnetization ( $0.22\mu_B$ /Pu-atom) itinerant character of the Pu moments has been concluded. Also a mutual cancellation of the spin and orbital moments, as is known for PuFe<sub>2</sub>, should be considered as a possible reason for the strongly reduced Pu moment.

The temperature dependence of the electrical resistivity of some AnPt compounds, as measured by Hill and Elliott (1971), is shown in fig. 23. The temperature dependence of the resistivity of UPt has also been studied by Lawson (1970), who found that  $\rho(T)$  can be described at low temperatures by the formula  $\rho = \rho_0 + AT^2$  with  $A = 450 \text{ n}\Omega \text{ cm/K}^2$ . Frings and Franse (1985) obtained an *A*-value of  $190 \text{ n}\Omega \text{ cm/K}^2$ . On the assumption of the Matthiessen rule (eq. (32)), the spin-dependent scattering contribution to the total resistivity can be determined by subtracting  $\rho(T)$  of the non-magnetic ThPt. The  $\rho_{\text{mag}}$ -value of UPt is of the order of about  $100 \mu\Omega \text{ cm}$  just

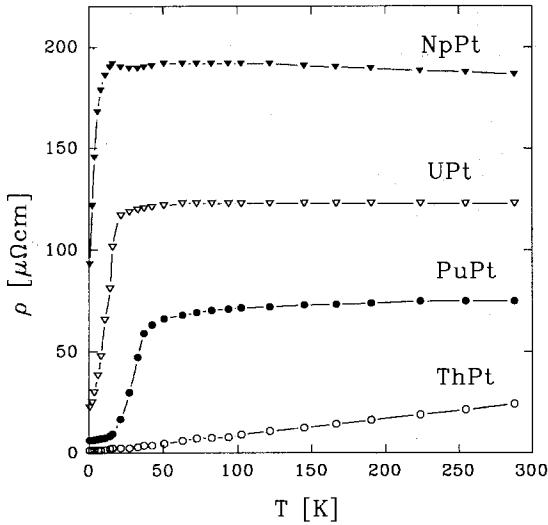


Fig. 23. The temperature dependence of the electrical resistivity for NpPt, UPt, PuPt and ThPt (Hill and Elliott 1971).

above  $T_C$  and shows a slightly falling tendency with increasing temperature. In UPt as well as in NpPt enormously large  $\rho_{\text{mag}}$ -values exist.

### 3.3. $RAI_2$ and $AnAl_2$ Laves phases

#### 3.3.1. $RAI_2$

The most extensively investigated R–non-transition metal compounds showing the cubic Laves-phase structure are those with aluminium. Different reasons can be given for this: the relatively simple crystal structure, the easy accessibility of these compounds, even in form of single crystals, and, finally, their simple ferromagnetic properties. Considering the  $Al^{3+}$  ions as magnetically neutral, we have a magnetic lattice consisting of R ions with two interpenetrating face-centred cubic lattices. We also note that the nearest neighbours are Al atoms which do not change on replacement of one kind of R atoms by another. There are no crystallographic phase transitions observed up to the melting point, which can be traced in the R–Al phase diagrams.

The  $RAI_2$  compounds are of fundamental interest because in most of them the R ion behaves as a well-defined ion in a metallic matrix. For the investigation of many spectroscopic, magnetic and related properties, it is relatively easy to describe the small interaction of the R ions with their non-magnetic surroundings. Therefore, in many aspects,  $RAI_2$  compounds are ideal for the investigation of the physical properties of the R ion in solids. Purwins and Leson (1990) published a review concerning the magnetic properties of  $RAI_2$ . They also discussed the influence of the crystal field on the R ion in these compounds. The intention of that work is to determine the extent to which the crystal-field theory is applicable in explaining the variations in the physical properties of the  $RAI_2$  compounds.

Concerning the transport properties, more than twenty years ago van Daal and Buschow (1969) published the temperature dependence of the electrical resistivity of the  $\text{RAI}_2$  compounds. The results have been analyzed with respect to the spin-disorder scattering contribution to the total resistivity. For the analysis of the resistivity data the authors used eq. (50) for  $\rho_{\text{spd}}$ . This expression has been used to determine the effective mass ( $m^*$ ) and the effective s-f exchange coupling constant ( $\mathcal{J}$ ). The values thus obtained are compared to the values from Knight-shift and susceptibility measurements. The authors noted that  $\text{CeAl}_2$  and  $\text{YbAl}_2$  behave exceptionally. They suspected already, at that time, that the minimum in  $\rho$  versus  $T$  of  $\text{CeAl}_2$  is caused by the Kondo effect. The unusual behaviour of the resistivity in  $\text{YbAl}_2$  was attributed to the intermediate valence state of the Yb ion.

Later, Gratz and Nowotny (1983) repeated the resistivity measurements on the  $\text{RAI}_2$  series. It has been shown that if the phonon contribution is correctly subtracted from the total resistivity, the  $\rho_{\text{spd}}$  values thus determined are proportional to the de Gennes factor for the heavy  $\text{RAI}_2$  compounds. However, the light  $\text{RAI}_2$  compounds do not show such a simple relation. Figure 24 shows  $\rho$  versus  $T$  for some of the heavy  $\text{RAI}_2$  compounds up to room temperature. The measurement on the non-magnetic  $\text{LuAl}_2$  is included for comparison. The arrows indicate the corresponding Curie temperatures as obtained from  $d\rho/dT$  versus  $T$ . In fig. 25,  $\rho_{\text{spd}}$  versus the de Gennes factor for the heavy  $\text{RAI}_2$  compounds is depicted. The temperature dependence of  $\rho_{\text{ph}}$  has been determined from  $\text{LuAl}_2$ . (The results for the  $\text{RPT}$  and  $\text{RNi}_2$  series are also shown in this figure.)

The reason why the light  $\text{RAI}_2$  compounds do not exhibit such a simple relation as the heavy  $\text{RAI}_2$  compounds is connected with the crystal-field properties. Resistivity measurements in the temperature region up to 1000 K on the  $\text{RAI}_2$  compounds have been performed by Burkov et al. (1992). These measurements reveal that the  $\rho$  versus  $T$  curves exhibit curvatures in the region far above room temperature. This is

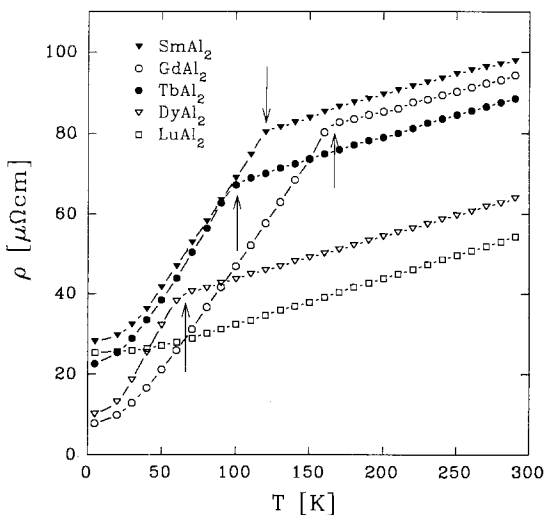


Fig. 24. The temperature dependence of the electrical resistivity of the  $\text{RAI}_2$  ( $\text{R} = \text{Sm, Gd, Tb, Dy}$  and  $\text{Lu}$ ) compounds (Gratz and Nowotny 1983). The arrows indicate the Curie temperatures.

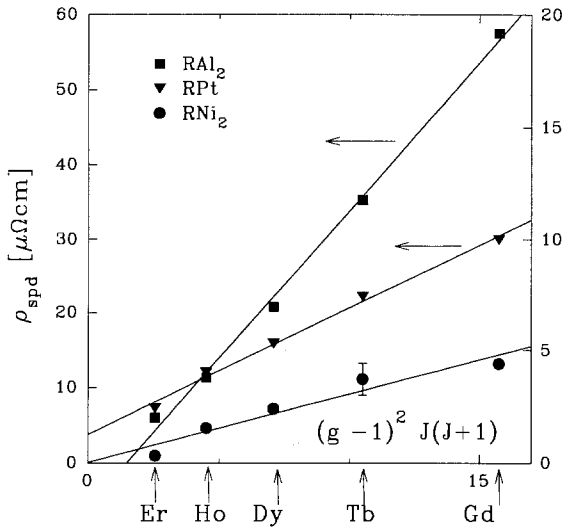


Fig. 25. The experimentally determined  $\rho_{spd}$ -values for the  $RAl_2$ ,  $RPt$  and  $RNi_2$  compounds plotted against the de Gennes factor,  $(g-1)^2 J(J+1)$ .

obviously in contrast with what one would expect from the Bloch–Grüneisen relation, according to which  $\rho$  is a linear function of the temperature above the Debye temperature. It could be shown that the curvature can be explained if the band-structure properties are taken into account in the calculation. Burkov et al. (1992) argued that if the Fermi level is near a local maximum in the density of states, negative curvature in  $\rho$  versus  $T$  follows.

The temperature variation of the resistivity of the non-magnetic  $RA_2$  compounds ( $R = Sc, Y, La$  and  $Lu$ ) has been discussed in several papers (Bauer et al. 1985, Wohlleben and Wittershagen 1985, Burkov et al. 1992). In fig. 26 the  $\rho$  versus  $T$  curves

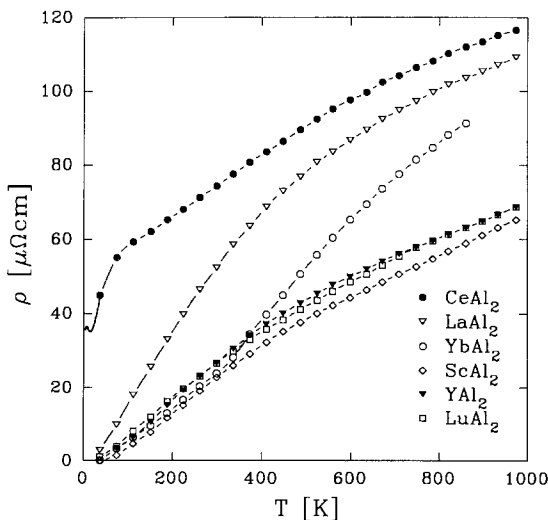


Fig. 26. The temperature dependence of the electrical resistivity for the non-magnetic  $RA_2$  compounds ( $R = Sc, Y, La$  and  $Lu$ ). The data for the Kondo system  $CeAl_2$  are included in the picture for comparison (Slebarski and Wohlleben 1985).

of the non-magnetic  $RAI_2$  compounds are given. The  $\rho(T)$  curve of the Kondo system  $CeAl_2$  is included in this figure. All these experiments show that  $\rho$  versus  $T$  of  $LaAl_2$  is considerably steeper than those of  $YAl_2$ ,  $LuAl_2$  and  $ScAl_2$ . Wohllaben and Wittershagen (1985) argued that the valence of La in  $LaAl_2$  is not three but less (i.e. fractional, with the configuration  $4f^{\nu}5d^{1-\nu}6s^1$ ,  $\nu \ll 1$ ).

In the paper of Bauer et al. (1985) a deviating behaviour of  $LaAl_2$  has been observed also in the temperature dependence of the thermal conductivity and the thermopower. It is shown there that the enhanced electron-phonon coupling and the much higher density of states in  $LaAl_2$  are responsible for the outstanding features of this compound. By Burkov et al. (1992) arguments are given which refer the much steeper increase of  $\rho(T)$  to differences in the band structure of  $LaAl_2$  compared to  $YAl_2$  and  $LuAl_2$ .

The temperature dependence of the thermopower of the light  $RAI_2$  compounds is given in figs. 27 ( $CeAl_2$  and  $LaAl_2$ ) and 28 ( $PrAl_2$  and  $NdAl_2$ ). The measurements for  $SmAl_2$ ,  $GdAl_2$ ,  $TbAl_2$  and  $DyAl_2$  are depicted in fig. 29. The Curie temperatures as obtained from resistivity measurements are indicated by arrows. Since there is a rather complete set of data for the thermopower, it is reasonable to discuss this transport phenomenon in more detail.

Let us first discuss the influence of elastic potential scattering (responsible for the residual resistivity,  $\rho_0$ ) on the thermopower. Gratz and Nowotny (1985) investigated the temperature variation of the thermopower of two  $YAl_2$  samples taken from the same melted batch, in which  $\rho_0$  has been changed by different annealing procedures. Figure 30 shows the  $\rho$  versus  $T$  and the  $S$  versus  $T$  curves of the two differently heat-treated  $YAl_2$  samples (denoted by A and B). The  $\rho$  versus  $T$  curves of these two samples are simply shifted, because of the different  $\rho_0$ -values, whereas the temperature variation of the thermopower differs significantly in its shape. Note that between about 40 up to 100 K  $S$  is positive in the sample with the smaller residual electrical

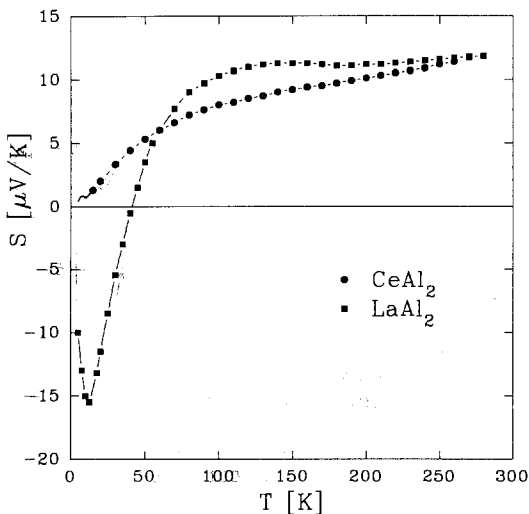


Fig. 27. The temperature dependence of the thermopower of  $LaAl_2$  and  $CeAl_2$  (Bauer et al. 1982).

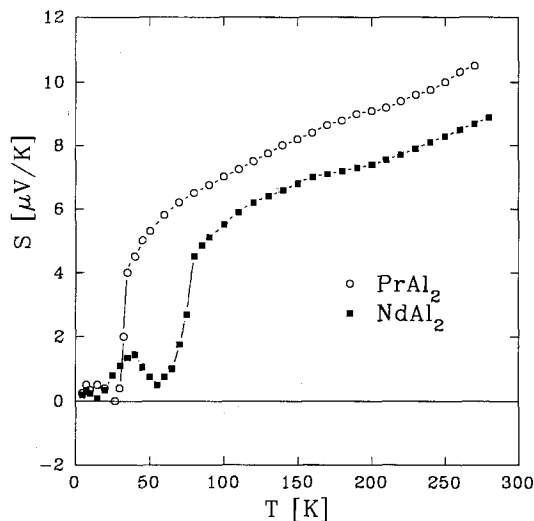


Fig. 28. The temperature dependence of the thermopower of  $\text{PrAl}_2$  and  $\text{NdAl}_2$  (Gratz and Zuckermann 1982b).  $T_C$  occurs at the discontinuity of  $S$  versus  $T$ .

resistivity. This should be discussed in more detail, since a change of sign of the thermopower is sometimes connected with a change in the band structure. However, these experiments show that a change of sign in the thermopower can be of much simpler origin, especially if it appears at low temperatures.

For the analysis of these data Gratz and Nowotny (1985) used the Nordheim-Gorter rule, which is, in the case of a non-magnetic compound like  $\text{YAl}_2$ , given by  $S(T) = (\rho_0/\rho)S_0 + (\rho_{\text{ph}}/\rho)S_{\text{ph}}$ . The temperature variation of  $\rho$  and  $\rho_{\text{ph}}$  and the value of  $\rho_0$  are taken from the resistivity measurements. A calculation of  $S_0$  and  $S_{\text{ph}}$  within the scope of the linearized Boltzmann equation revealed that  $S_0$  is linear in

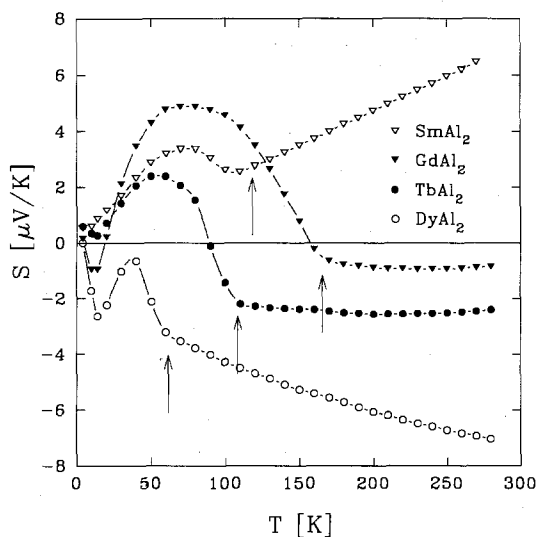


Fig. 29. The temperature dependence of the thermopower of  $\text{SmAl}_2$ ,  $\text{GdAl}_2$ ,  $\text{TbAl}_2$  and  $\text{DyAl}_2$  (Gratz and Zuckerman 1982b). The arrows indicate  $T_C$ .

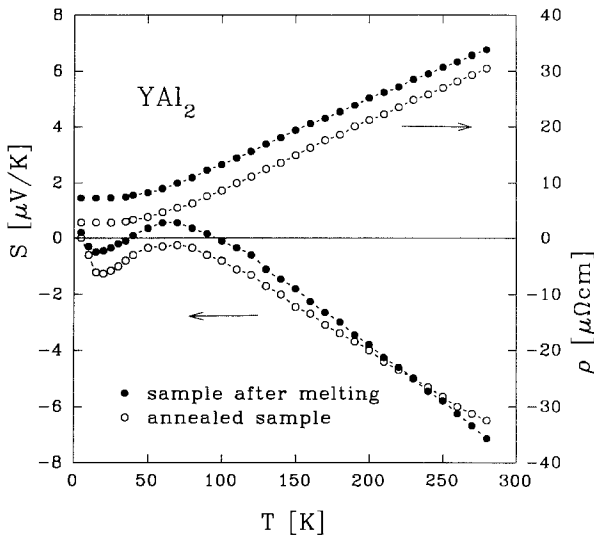


Fig. 30. The temperature dependence of the electrical resistivity,  $\rho$ , and the thermopower,  $S$ , for two  $\text{YAl}_2$  samples: sample A was measured as-cast, sample B was heat treated at  $800^\circ\text{C}$  for 24 h (Gratz and Nowotny 1985).

the temperature, with a negative slope. For the determination of  $S_{\text{ph}}$  the Debye model has been used, with  $\Theta_{\text{D}} = 290$  K. The function  $S_{\text{ph}}(T)$  has a maximum at 60 K and becomes linear in the high-temperature region. According to the calculation in the paper of Gratz and Nowotny (1985) the maximum in  $S$  versus  $T$  around 60 K is due to the electron–phonon interaction. With increasing residual resistivity of the sample  $S(T)$  flattens, and there is no longer a change of sign at elevated temperatures. The minimum in  $S$  versus  $T$  around 20 K has been attributed to phonon drag.

Thermopower measurements up to 1000 K have been performed by Burkov et al. (1992). These measurements revealed a very broad minimum in  $S$  versus  $T$  for  $\text{YAl}_2$ . To explain this non-linear behaviour of the thermopower it is necessary (according to Burkov et al. 1992) to take into account the density of states features around the Fermi level and its shift if the temperature is increased. In fig. 31 the high-temperature measurements for  $\text{YAl}_2$ ,  $\text{LuAl}_2$  and  $\text{LaAl}_2$  are given. Note that  $\text{LaAl}_2$  differs also with respect to the thermopower.

Other high-temperature thermopower data are given in fig. 32. These data show that the minima which appear in magnetic as well as in non-magnetic compounds are obviously not connected with magnetic scattering processes, but have their origin in density of states features (Burkov et al. 1992). For the spin-dependent scattering contribution to the thermopower see figs. 28 and 29. The pronounced change of  $S$  versus  $T$  at the magnetic transition temperature (indicated by the arrows) is clear evidence for the strong influence of this kind of scattering mechanism.

In the Nordheim–Gorter rule (eq. (35)) the spin-dependent scattering processes of the conduction electrons are described by the third term  $((\rho_{\text{mag}}/\rho)S_{\text{mag}})$ . According to the discussion in sect. 2.3 (see eq. (49)),  $S_{\text{mag}}(T > T_{\text{C}}) \equiv S_{\text{spd}}$  is proportional to  $T$  (if the crystal-field influence is neglected). Several attempts have been undertaken to justify this relation experimentally (Gratz 1981). Bauer et al. (1987a) investigated  $S_{\text{spd}}$  in the pseudobinary  $(\text{Gd}_x\text{Y}_{1-x})\text{Al}_2$  series. It has been found in these studies that

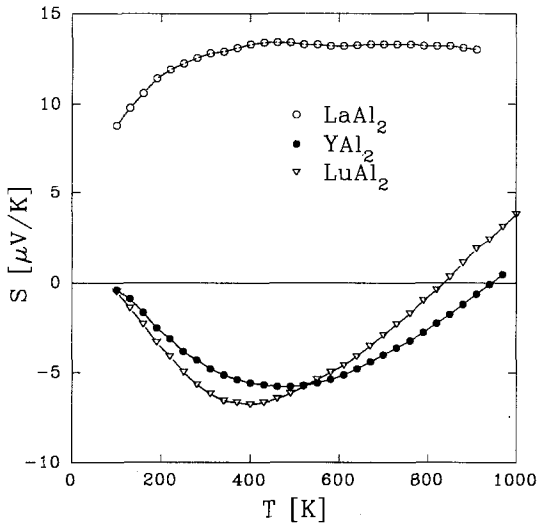


Fig. 31. High-temperature thermopower measurements (77–1000 K) for non-magnetic  $\text{RAl}_2$  compounds (Burkov et al. 1992).

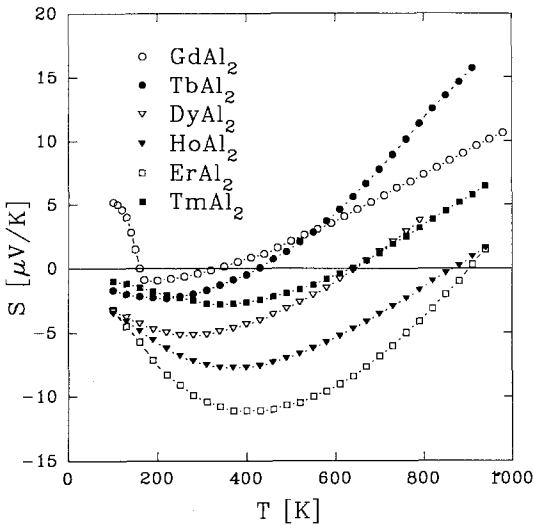


Fig. 32. High-temperature thermopower measurements (77–1000 K) for magnetic heavy  $\text{RAl}_2$  compounds (Burkov et al. 1992).

$S_{\text{mag}}(T)$  is linear in the temperature at least up to room temperature for  $x = 0.6$  to 1.0. As an example of a comprehensive calculation of the thermopower in the magnetically ordered state the paper of Ausloss and Durcewski (1985) should be quoted.

As already has been pointed out in sect. 1, analysis of the thermal conductivity is in general difficult, since various mechanisms can contribute to the heat transport (see eq. (34):  $\lambda = \lambda_e + \lambda_1$ ). Usually  $\lambda_e$  is dominating in metallic systems with low electrical resistivity. However, it may happen that  $\lambda_1$  is not negligible.



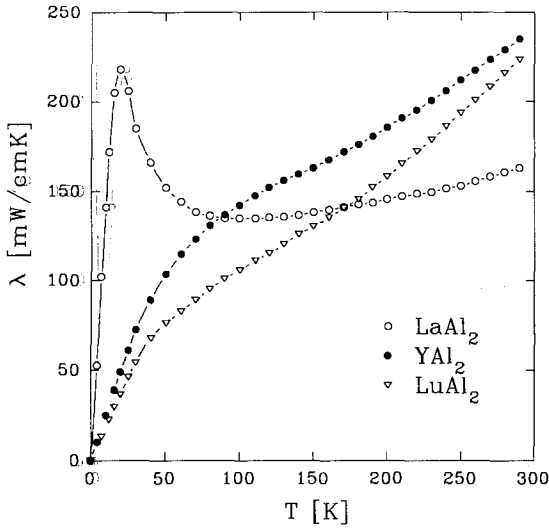


Fig. 33. The temperature dependence of the thermal conductivity for the non-magnetic RAl<sub>2</sub> compounds (R = Y, La and Lu) (Bauer et al. 1986).

Bauer et al. (1986) measured the thermal conductivity of the RAl<sub>2</sub> compounds in the temperature range from 4.2 K up to room temperature. The λ versus T curves of the non-magnetic RAl<sub>2</sub> compounds (R = Y, La and Lu) are given in fig. 33. The pronounced maximum in λ versus T of LaAl<sub>2</sub> is obviously due to the small residual thermal resistivity. Note that, because of the small coefficient A in eq. (50), this function has a maximum at low temperatures. The coefficient A is related to ρ<sub>0</sub> via the Wiedemann–Franz law, eq. (36). The ρ<sub>0</sub> values of these samples were ρ<sub>0</sub> (LaAl<sub>2</sub>) = 3.5, ρ<sub>0</sub> (YAl<sub>2</sub>) = 18 and ρ<sub>0</sub> (LuAl<sub>2</sub>) = 25 μΩ cm. The smaller thermal conductivity at elevated temperatures has the same origin as the higher electrical resistivity (see the discussion above). In the paper of Bauer et al. (1986) an estimation of the lattice contribution to the total thermal conductivity at low temperatures was made. It has been found from the analysis of λ (YAl<sub>2</sub>) that the lattice contribution is only about 5% (an estimation at room temperature gave about 2%). It is emphasized in that paper that the lattice conductivity is practically negligible for all the RAl<sub>2</sub> compounds.

In figs. 34 and 35 the temperature variation of the thermal conductivity of several RAl<sub>2</sub> compounds is given. Bauer et al. (1986) have shown that the contribution due to spin-dependent scattering processes to the thermal resistivity well above the Curie temperature is proportional to T<sup>-1</sup>. This part of the electronic thermal resistivity (denoted by W<sub>e,mag</sub>) is due to scattering processes of the conduction electrons with the disordered localized 4f moments.

The procedure how W<sub>e,mag</sub> can be deduced from the experimental data is outlined below:

Assuming validity of the Matthiessen rule, the electronic thermal resistivity (W<sub>e</sub> = 1/λ<sub>e</sub>) of a non-magnetic (indicated in formulas by the superscript nm) RAl<sub>2</sub> compound can be written as:

$$W_e^{nm} = W_{e,0}^{nm} + W_{e,ph}^{nm} = 1/\lambda_e^{nm} \tag{90}$$

The subscript e indicates the electronic thermal conductivity or resistivity.

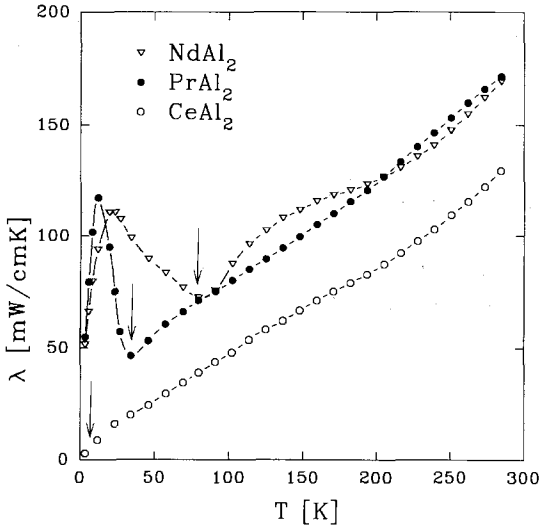


Fig. 34. The temperature dependence of the thermal conductivity of CeAl<sub>2</sub>, PrAl<sub>2</sub> and NdAl<sub>2</sub> (Bauer et al. 1986). The arrows indicate the Curie temperatures.

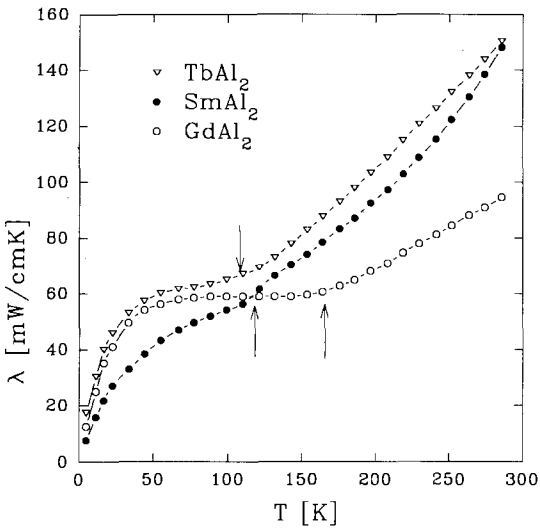


Fig. 35. The temperature dependence of the thermal conductivity of SmAl<sub>2</sub>, GdAl<sub>2</sub> and TbAl<sub>2</sub> (Bauer et al. 1986). The arrows indicate the Curie temperatures.

For a magnetic (m) RAl<sub>2</sub> compound it follows:

$$W_e^m = W_{e,0}^m + W_{e,ph}^m + W_{e,mag} = 1/\lambda_e^m \tag{91}$$

The subscripts e, 0, e, ph and e, mag indicate the terms responsible for the scattering processes of the conduction electrons by static imperfections, phonons and magnetic moments, respectively. To deduce  $W_{e,mag}^m$ , the assumption can be made that  $W_{e,ph}^{nm} = W_{e,ph}^m$ . This gives:

$$\Delta W = (W_{e,0}^m - W_{e,0}^{nm}) + W_{e,mag} \tag{92}$$

As has been shown in the general discussion in sect.2.3.4, both  $W_{e,0}$  and  $W_{e,mag}(T > T_C)$  are proportional to  $T^{-1}$  (eqs. (42) and (48)). We can now rewrite eq. (92):

$$\Delta W = (B^m - B^{nm})T^{-1} + CT^{-1}. \tag{93}$$

The temperature variation of  $\Delta W$  in the paramagnetic temperature region has been determined experimentally from the difference  $1/\lambda^m - 1/\lambda^{nm}$ , where  $\lambda^{nm}$  is the thermal conductivity of  $YAl_2$ . Figure 36 shows  $\Delta W$  versus  $T^{-1}$  for the heavy  $RAI_2$  compounds in the temperature region  $T > T_C$ . In nearly all of these compounds  $\Delta W$  is proportional to the inverse temperature. Since the sample-specific values  $B^m$  and  $B^{nm}$  in eq. (93)

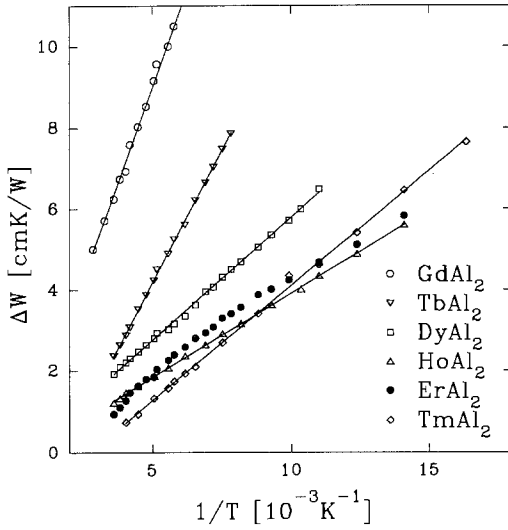


Fig. 36.  $\Delta W = (1/\lambda^m - 1/\lambda^{nm})$  as a function of  $T^{-1}$  for the heavy  $RAI_2$  compounds.  $\lambda^m$  and  $\lambda^{nm}$  are the thermal conductivity of a magnetic  $RAI_2$  compound and of  $YAl_2$ , respectively (Bauer et al. 1986).

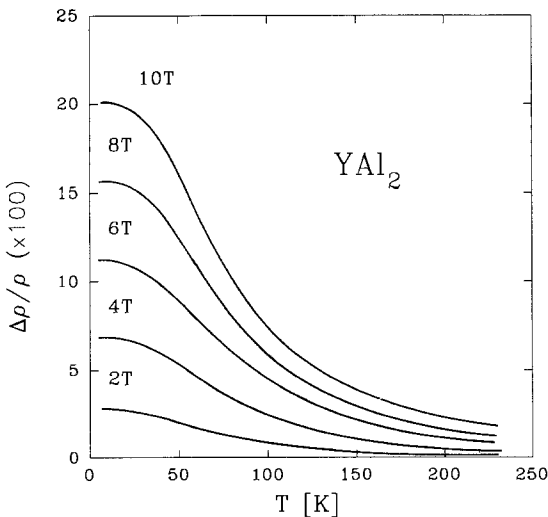


Fig. 37. The temperature dependence of the transverse magnetoresistance of  $YAl_2$  for different magnetic fields (Gratz 1992).

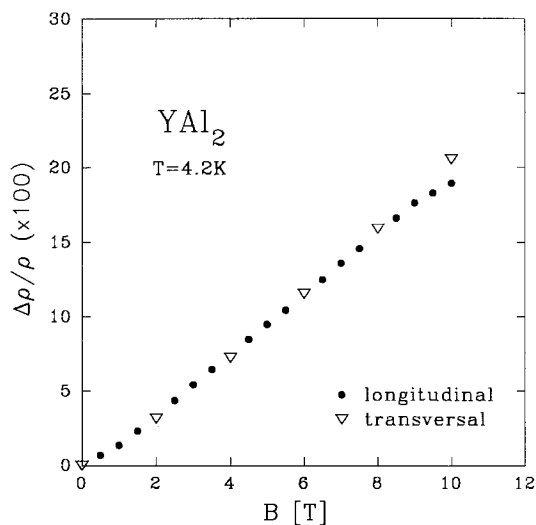


Fig. 38. The transverse and longitudinal magnetoresistance of  $\text{YAl}_2$  at 4.2 K in fields up to 10 T (Gratz 1992).

can be determined from the corresponding  $\rho_0$ -values (using the Wiedemann–Franz law), the coefficients  $C$  can be deduced from the measurements for various  $\text{RAl}_2$  samples. The values of  $C$  are proportional to the de Gennes factor. In the paper of Bauer et al. (1986) this experimental result was justified theoretically within the scope of the relaxation-time approximation of the Boltzmann equation.

The temperature dependence of the transverse magnetoresistance ( $\Delta\rho/\rho$ ) of  $\text{YAl}_2$  at different field strengths is shown in fig. 37. Although  $\text{YAl}_2$  is non-magnetic, at 4.2 K  $\Delta\rho/\rho$  is 0.2 (or 20%) in a field of 10 T. This value is large if it is compared with that for  $\text{YCo}_2$ , where a field of 10 T gives only about 3% for  $\Delta\rho/\rho$ . The field dependence of the transverse and the longitudinal magnetoresistance at 4.2 K is given in fig. 38. As can be seen, there is practically no anisotropy concerning the field direction. The reason why there is no difference between the longitudinal and the transversal magnetoresistance could be the extremely complex shape of the Fermi surface of  $\text{YAl}_2$ . Its shape is shown in the paper of Hasegawa and Yanase (1980).

The temperature variation of the transverse magnetoresistance of  $\text{GdAl}_2$  is given in fig. 39. Apart from the fact that in  $\text{GdAl}_2$  also positive  $\Delta\rho/\rho$  values are observable at low temperatures, the temperature variation of  $\Delta\rho/\rho$  versus  $T$  below and above  $T_C$  is in good qualitative agreement with the calculation of Yamada and Takada (1973a), which has been outlined in sect. 2.4.1 With increasing field  $\Delta\rho/\rho$  becomes more negative and shows a minimum at  $T_C$  of  $\text{GdAl}_2$  ( $T_C = 165$  K). We attribute the positive  $\Delta\rho/\rho$  values below 20 K to the influence of the classical magnetoresistance, which is superimposed on a smaller, negative  $\Delta\rho/\rho$  value caused by the spin-dependent scattering in a ferromagnet.

### 3.3.2. $\text{AnAl}_2$

Within the class of materials that display signatures characteristic for spin fluctuations, i.e. a Curie–Weiss susceptibility at high temperatures, which evolves with

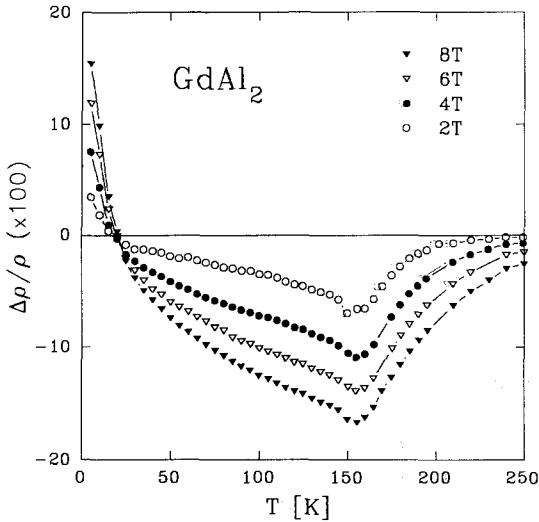


Fig. 39. The temperature dependence of the transverse magnetoresistance of  $\text{GdAl}_2$  for different magnetic fields (Gratz 1992).

decreasing temperature towards enhanced paramagnetism, a resistivity proportional to  $T^2$  at low temperatures and a  $T^3 \ln T$  contribution to the low-temperature specific heat,  $\text{UAl}_2$  is frequently considered as an archetype for a spin-fluctuation system. It is worthwhile to discuss it here in more detail.

$\text{UAl}_2$  is a cubic Laves phase with lattice parameter  $a = 7.776 \text{ \AA}$  (Katz and Jacobs 1962). From this an U–U distance of  $3.375 \text{ \AA}$  follows, which is close to the Hill limit for the appearance of localization of the  $5f$  moments.

Above  $T = 100 \text{ K}$  the susceptibility obeys the Curie–Weiss law with  $\Theta_p = -250 \text{ K}$ , and  $\mu_{\text{eff}} = 3\mu_B$  is close to the free-ion value. There is a plateau around  $50 \text{ K}$ , and below  $40 \text{ K}$  a modified Curie–Weiss law follows ( $\chi_0 = 3.2 \times 10^{-3} \text{ emu/mol}$ ) with  $\Theta_p = -8 \text{ K}$  (Fournier 1985). At low temperatures  $\chi$  saturates, with a  $T^2$  dependence down to  $80 \text{ mK}$  (Fournier 1979). A specific-heat experiment shows the  $T^3 \ln T$  term (Trainor et al. 1975), as predicted by the spin-fluctuation theory for the low-temperature region. The corresponding value of  $T_{\text{sf}}$ , deduced from specific-heat measurements, is  $23 \text{ K}$ . The  $\gamma$ -value is about  $140 \text{ mJ/mol K}^2$ . An applied magnetic field decreases  $\gamma$ , but the  $T^3 \ln T$  term does not disappear in fields up to  $17 \text{ T}$  (Gschneidner and Ikeda 1983).

An investigation of  $\text{UAl}_2$  by inelastic neutron scattering shows that the temperature dependence of the paramagnetic response function consists only of a quasi-elastic component with a line width ( $\Gamma/2$ ), substantially larger than the thermal energy,  $k_B T$ , in the whole range from  $4.2 \text{ K}$  up to room temperature. The half-width of the quasi-elastic line provides a measure for the spin-fluctuation energy. The large width in  $\text{UAl}_2$  therefore indicates that below room temperature the spin-fluctuation energy in this material is much greater than the thermal energy. From these experiments follows that the spin fluctuations do not disappear at least up to room temperature (Loong et al. 1986). However, Franse et al. (1981) could show by magnetoresistance and magnetization measurements at  $4.2 \text{ K}$  that in fields up to  $25 \text{ T}$  the spin fluctuations

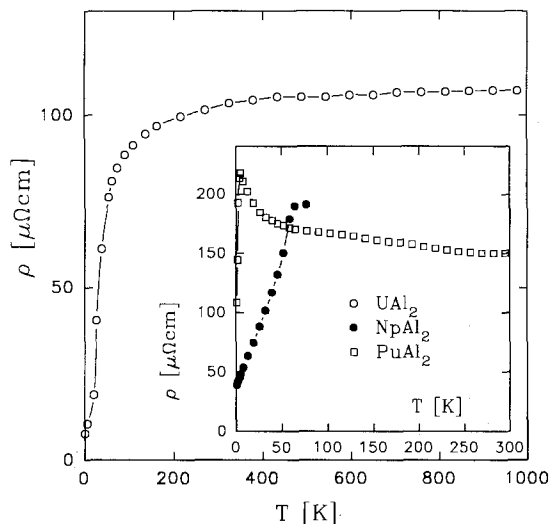


Fig. 40. The temperature dependence of the electrical resistivity of  $\text{UAl}_2$  from 4.2 up to 1000 K (Wire et al. 1984). The inset shows the resistivity of  $\text{PuAl}_2$  up to room temperature (Brodsky 1971) and of  $\text{NpAl}_2$  up to 80 K (Arko et al. 1972).

become nearly suppressed. Magnetization measurements at 77 K show that the spin fluctuations are absent at this temperature, which is in contrast to the above conclusion. A freezing of spin fluctuations in high magnetic fields has also been reported for  $\text{YCo}_2$  (Schinkel 1978) and  $\text{LuCo}_2$  (Schinkel 1978, Ikeda and Gschneidner 1980). Franse et al. (1981) reported that in  $\text{UAl}_2$  a complete suppression of the spin fluctuations could be achieved, in contrast to both above-mentioned Co compounds.

The temperature dependence of the electrical resistivity of  $\text{UAl}_2$  is depicted in fig. 40 (Wire et al. 1984). The  $\rho$  versus  $T$  curve shows an extremely pronounced tendency to be saturated, which is typical for spin-fluctuation systems with a low spin-fluctuation temperature. The low-temperature resistivity behaviour can best be fitted by a  $T^2$ -law ( $\rho = \rho_0 + AT^2$ ) for  $5 < T < 35$  K. The magnitude of  $A$  is estimated as  $53 \text{ n}\Omega\text{cm}/\text{K}^2$ , which is about twenty times higher than the value obtained for a simple ferromagnet such as  $\text{GdAl}_2$ , where the  $T^2$  dependence is caused by ferromagnetic spin waves. From this  $A$ -value a spin-fluctuation temperature  $T_{\text{sf}} = 24$  K can be estimated, while the maximum in  $d\rho/dT$  is at about 25 K, and the specific heat gives 23 K. For temperatures smaller than 3 K a much larger  $A$ -value (about  $250 \text{ n}\Omega\text{cm}/\text{K}^2$ ) was found which seems to scale with  $\gamma^2$ , as has been found for other heavy-fermion compounds (Kadowaki and Woods 1986). Band-structure calculations indicate that in  $\text{UAl}_2$  the 5f electrons form a narrow band at the Fermi energy,  $\varepsilon_{\text{F}}$  (De Groot et al. 1985), a condition favouring spin fluctuations. The strongly enhanced  $\gamma$ -value ( $140 \text{ mJ/mol K}^2$ ) is a measure of either a high density of states at the Fermi level or an enhancement factor due to large interactions.

Decreasing the U-U distances by the application of hydrostatic pressure should increase the 5f wave function hybridization and broaden the band, causing subsequently a decrease in the density of states at the Fermi level. This idea was the motivation for doing pressure experiments at low temperatures. Wire et al. (1984) have shown that the suppression of spin fluctuations with pressure, as deduced from

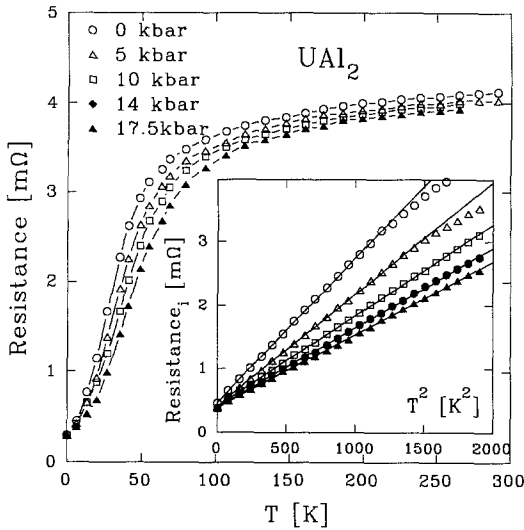


Fig. 41. The pressure dependence of the resistance of  $\text{UAl}_2$ . The inset shows the decrease of the  $T^2$  slope with increasing pressure (Wire et al. 1984).

susceptibility measurements (Fournier and Beille 1979), is reflected directly in the temperature-dependent resistance (see fig. 41). Over an appropriate temperature interval the resistance scales with a pressure-dependent parameter, which may be identified as the spin-fluctuation temperature (see fig. 8 in Wire et al. (1984)). The inset in fig. 41 shows the resistance of the  $\text{UAl}_2$  sample as a function of  $T^2$  at five different pressures at the low-temperature limit. The same tendency must be observed for the electrical resistivity.

Wire et al. (1984) explained the saturation tendency of the resistance of  $\text{UAl}_2$  by applying the "parallel-resistor model", described by the formula:  $1/R = 1/R_i + 1/R_s$ , where  $R_i$  is the ideal and  $R_s$  the shunt resistance. These authors assumed that  $R_i$  reflects the spin-fluctuation contribution to the resistance. They extracted the pressure dependence of  $T_{sf}$  from the slope  $\partial R_i / \partial (T^2) = A$ . Because the sample geometry was not exactly known, they have used the constant  $A$  determined for zero pressure (which corresponds to  $T_{sf} = 26$  K). It follows from that experiment that  $T_{sf}$  increases nearly linear with pressure, by about 40% at a pressure of 17 kbar.

An alternative explanation of the anomalous resistivity, specific heat and susceptibility of  $\text{UAl}_2$  has been suggested by De Groot et al. (1985). Their explanation of the resistivity behaviour is based on band-structure effects. From a band-structure calculation these authors conclude that the structure of the density of states near the Fermi energy can explain the resistivity variation without the necessity of the introduction of spin fluctuations or any other many-body effect.

Fournier (1985) extracted the magnetic contribution to the total resistivity,  $\rho(\text{UAl}_2)$ , by subtracting the resistivity of the isostructural  $\text{LaAl}_2$  ( $\Delta\rho = \rho(\text{UAl}_2) - \rho(\text{LaAl}_2)$ ). The temperature variation of  $\Delta\rho$  thus obtained shows a broad maximum around 100 K, followed by a  $\ln T$  decrease. The picture which emerges is that below 10 K the properties of  $\text{UAl}_2$  are dominated by ferromagnetic spin fluctuations. Up to 50 K

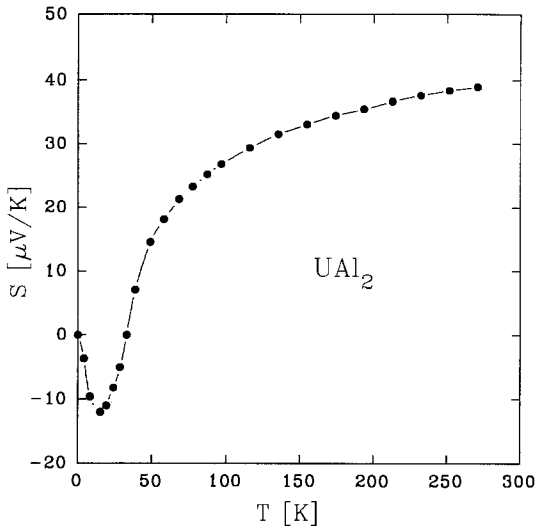


Fig. 42. The temperature dependence of the thermopower of  $\text{UAl}_2$  (Coqblin et al. 1978).

$\text{UAl}_2$  behaves like a Fermi liquid and above 100 K, which may be taken as a Kondo temperature,  $\text{UAl}_2$  behaves like a Fermi gas.

Coqblin et al. (1978) considered  $\text{UAl}_2$  as a good example showing ferromagnetic spin fluctuations. Within the scope of their spin-fluctuation theory they were able to fit the temperature variation of the electrical resistivity, the susceptibility and the nuclear-spin relaxation rate of the Al nucleus of  $\text{UAl}_2$  with the same set of parameters. But all their attempts to describe the temperature dependence of the thermopower (given in fig. 42) failed. In the discussion of their thermopower calculation several reasons have been quoted why the observed temperature variation of the thermopower could not be described within the scope of their theory. The authors came to the conclusion that the behaviour of the thermopower is mainly determined by details in the band structure (which was not known at that time), rather than directly by the temperature variation of the exchange enhancement factor (which plays an important role as a fit parameter in their calculations). We agree with them in that the details of the band structure (which is now available from the calculation of De Groot et al. (1985)) play an important role for the sign and the absolute value of the thermopower.

From figs. 2 and 3 in De Groot's paper it can be seen that the Fermi energy is situated very close to the left-hand side of a sharp local peak in the 5f states. The very large values of  $N(\epsilon_F)$  and  $dN(\epsilon)/d\epsilon$  are mainly responsible for the strong negative curvature of  $S$  versus  $T$  after the sign has changed around 40 K, and also for the large values of  $S$  of nearly  $40 \mu\text{V K}^{-1}$  at room temperature. In this connection it should be pointed out that in our experience it is a rule that in normal intermetallic compounds, which do not show signs of heavy fermions, intermediate valence or spin-fluctuation behaviour, the magnitude of the thermopower normally does not exceed 10 to  $15 \mu\text{V K}^{-1}$  at room temperature.

As far as the minimum in  $S$  versus  $T$  of  $\text{UAl}_2$  (near 25 K) is concerned, Coqblin et al. (1978) assumed that it is probably due to the paramagnon drag. In the literature



several mechanisms have been suggested to explain the minimum at low temperatures in the thermopower. These mechanisms are the phonon drag, the so-called Nielson–Taylor effect and probably also paramagnon drag.

An inspection of the temperature variation of the thermopower in known spin-fluctuation systems reveals that in nearly all of them such a minimum is observable in the low-temperature region. For example, such minima exist at low temperatures in  $\text{YCo}_2$ ,  $\text{LuCo}_2$ ,  $\text{ScCo}_2$  (see sect. 3.4) and in several Pd compounds, which all belong to the class of materials showing spin fluctuations.

Fischer (1974) studied the influence of local spin fluctuations on the thermopower, as well as the electrical and the thermal resistivity. His results for the thermopower seem to be similar to those obtained for Kondo systems. In particular, in his calculation Fischer found the appearance of a giant peak in the spin-dependent part of the absolute thermopower, similar to that in Kondo systems.

In conclusion we may say that the minimum in  $S$  versus  $T$  in the low-temperature region, as well as the  $T^2$  term in the low-temperature resistivity, are signs for the existence of spin fluctuations in  $\text{UAl}_2$ .

Lapierre et al. (1987) performed Hall-effect measurements on  $\text{UPt}_3$ ,  $\text{CeAl}_3$  and  $\text{CeRu}_2\text{Si}_2$ , which are known as heavy-fermion compounds. They also included  $\text{UAl}_2$  in their investigations. From the variation of the Hall constant with the temperature it seems that  $\text{UAl}_2$  fits in its general behaviour to the other compounds, as it can be seen in fig. 43, which shows the Hall constant,  $R_H$ , versus  $\ln T$ . As the temperature increases,  $R_H$  rapidly increases beyond the residual plateau, which is negative for  $\text{UAl}_2$ . A maximum in  $R_H$  appears at a temperature which scales approximately with the temperature of the coherence (according to Lapierre et al. 1987). Such a temperature dependence can be accounted for assuming that the extraordinary Hall contribution is due to skew scattering. The Hall resistivity is then the sum of a weakly temperature-dependent term due to the ordinary Hall effect and the residual skew

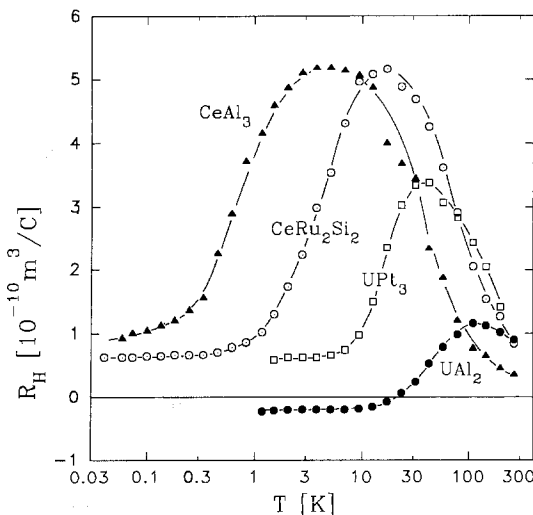


Fig. 43. The temperature dependence of the Hall constant in a  $\ln T$  plot for  $\text{UAl}_2$ , together with the Hall resistivity of the heavy-fermion systems  $\text{CeAl}_3$ ,  $\text{CeRu}_2\text{Si}_2$  and  $\text{UPt}_3$  (Fert and Levy 1987).

scattering, plus another term, which is proportional to  $\chi\rho$  (see fig. 7). Thus, initially  $R_H$  increases sharply with increasing temperature due to the skew scattering, and thereafter the decrease in  $R_H(T)$  is caused by the onset of the Curie–Weiss law in the susceptibility. A theoretical interpretation of this skew scattering has been given by Fert and Levy (1987) (see sect. 2.4).

$\text{PuAl}_2$  crystallizes also in the C15 structure. Its most unusual resistivity behaviour (shown in fig. 40) has been measured already twenty years ago by Arko et al. (1972). A  $T^2$  dependence has been observed in the electrical resistivity, but only below 2 K. The coefficient  $A$  ( $A = 940 \text{ n}\Omega \text{ cm/K}^2$ ) is of the order of that found in heavy-fermion systems. A very sharp maximum is observed at 7 K, but no magnetic ordering is detected by NMR and no anomaly is seen either in the specific heat or in the magnetic susceptibility (Trainor et al. 1976).

Because of its huge  $\gamma$ -value ( $265 \text{ mJ/mol K}^2$ )  $\text{PuAl}_2$  fits into the heavy-fermion sequence in the Kadowaki–Woods plot (Kadowaki and Woods 1986). Trainor et al. (1976) assumed that antiferromagnetic spin fluctuations dominate the low-temperature behaviour of  $\text{PuAl}_2$ ; magnetoresistance experiments would be interesting in this respect. However, the  $^{242}\text{Pu}$  isotope should be used for such low-temperature measurements to avoid self-heating problems.

In contrast to  $\text{UAl}_2$  and  $\text{PuAl}_2$ ,  $\text{NpAl}_2$  orders ferromagnetically at  $T_C = 56 \text{ K}$ . Preliminary resistivity measurements (see fig. 40) have been done below 80 K (Brodsky 1971). The ordering temperature is seen as a maximum in  $d\rho/dT$ . No analysis of the low-temperature resistivity data has been given and no new measurements have been reported.

### 3.4. $\text{RM}_2$ and $\text{AnM}_2$ Laves phases ( $M = \text{Mn, Fe, Co, Ni}$ )

Coming to the intermetallic compounds in which the f and 3d electrons co-exist and to their transport properties, we note that there is no uniform picture concerning the role the itinerant magnetic electrons play in transport phenomena. Indeed, in the intermetallics they can serve as scattering centres as well as charge and heat carriers. Great difficulties arise when trying to separate these mechanisms.

We decided to discuss here the well-known cubic Laves phases (C15) formed by the R and An (mainly uranium) elements with the 3d transition metals Fe, Co, Mn and Ni only. There is a large number of experimental data available for these compounds, which enables us to emphasize some systematics in their transport properties.

#### 3.4.1. $\text{RMn}_2$

Among the  $\text{RMn}_2$  compounds, not all of them which can be prepared in a single phase have the cubic Laves-phase structure. Some crystallize in the hexagonal C14 Laves phase (C15: Y, Gd, Tb and Dy; C14: Sc, Pr, Nd, Er, Tm and Lu).  $\text{HoMn}_2$  as well as  $\text{SmMn}_2$  seem to show both types of structures. It has been found that the magnetic ordering temperatures lie around 100 K for the first half of the  $\text{RMn}_2$  compounds (Pr, Nd, Sm, Gd). Although the ordering temperatures given in the literature vary considerably, the  $T_N$ -values for the heavy  $\text{RMn}_2$  compounds are about two or three times smaller than those of the light  $\text{RMn}_2$  compounds. From magnetiza-

tion (Buschow and Sherwood 1977, Malik and Wallace 1981, Gaydukova et al. 1983, 1985, Makihara et al. 1983) and neutron diffraction studies (Corliss and Hastings 1964, Hardman et al. 1982, Nakamura et al. 1983, Brown et al. 1992) evidence has been obtained for a complex coupling between the R moments and the Mn moments, in those cases where they exist. For example, no Mn moments have been observed in the C14-type compounds  $\text{ErMn}_2$  and  $\text{TmMn}_2$ .

Since for the  $\text{RMn}_2$  compounds very few and incomplete transport data are available, we will restrict our discussion mainly to  $\text{YMn}_2$ , which should then be compared to the isostructural  $\text{UMn}_2$  actinide compound.

$\text{YMn}_2$  is a helimagnet with a complex spin arrangement and a very long period of modulation (Ballou et al. 1987). The magnetic transition is of the first-order type, showing a temperature hysteresis with  $T_N$  about 80 K for cooling and 110 K for heating. The magnetic moment per Mn atom is  $2.7\mu_B$  at 2 K. Polarized neutron scattering studies have been performed in the paramagnetic state up to  $T = 3T_N$  (Deportes et al. 1987). It has been shown that an effective Mn moment persists above  $T_N$ , its magnitude is  $1.6\mu_B$  at 120 K,  $1.7\mu_B$  at 200 K and  $1.9\mu_B$  at 300 K. The conclusion is that the reduction of the magnetic moment, as compared to the ground state, may be the origin of the very large magneto-volume effect observed at  $T_N$ .

The enormously large pressure dependence of the Néel temperature ( $dT_N/dp = -35 \text{ K/kbar}$ ) (Oomi et al. 1987) is evidence for the sensitive role played by the Mn–Mn interatomic distance on the Mn magnetic behaviour. Due to the exceptionally large volume increase at  $T_N$  of about 5% (Gaydukova and Markosyan 1982, Tagawa et al. 1985) caused by the spontaneous volume magnetostriction, a compact sample can hardly be cooled below  $T_N$  without cracking, thus making resistivity measurements very difficult and uncertain.

Figure 44 shows an attempt to measure the resistivity from room temperature down to 4 K (Kamimura et al. 1987). A high-temperature resistivity measurement

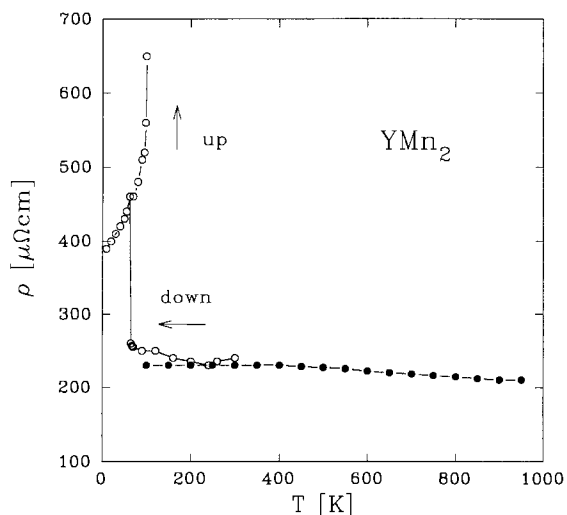


Fig. 44. The temperature dependence of the electrical resistivity of  $\text{YMn}_2$  below and above the Néel temperature. Open symbols are the data of Kamimura et al. (1987), filled symbols are measured by Gratz and Burkov (1992). Arrows show measurements performed during cooling and heating.

from 1000 K down to the Néel temperature (Gratz and Burkoy 1992) is included in fig. 44. In both measurements the sample broke due to cracks after the Néel temperature had been passed. Resistivity measurements on two other  $\text{RMn}_2$  ( $R = \text{Gd}, \text{Tb}$ ) compounds have been published by Makihara et al. (1983). All these measurements below  $T_N$  are not very instructive, since cracks change the sample geometry and thus prevent reproducible results.

Small dilutions of the R atoms can prevent the onset of the Mn magnetism and thus allow to study the non-magnetic behaviour of manganese in the  $\text{RMn}_2$  compounds having large volume anomalies. The  $\gamma$ -value of a 3% Sc-substituted ( $\text{Y}_{0.97}\text{Sc}_{0.03}\text{Mn}_2$ ) paramagnetic compound is  $150 \text{ mJ/mol K}^2$ , it decreases to  $120 \text{ mJ/mol K}^2$  in  $\text{Y}_{0.92}\text{Sc}_{0.08}\text{Mn}_2$  (Wada et al. 1989). If we consider the Sc-substituted compounds as the paramagnetic analogues of  $\text{YMn}_2$ , this result is about 15 times higher than  $\gamma_{\text{calc}}$  ( $9 \text{ mJ/mol K}^2$ ) for the paramagnetic  $\text{YMn}_2$  (Asano and Ishida 1988). This large enhancement is considered as evidence for the enormously large influence of spin fluctuations in the paramagnetic state of  $\text{YMn}_2$  (Wada et al. 1989).

Resistivity measurements under pressure have been performed by Bauer et al. (1992a). A pressure higher than 4 kbar was necessary in order to suppress the transition to the magnetically ordered state. Figure 45 shows the  $\rho$  versus  $T$  curves from 4.2 K up to room temperature at external pressures of 0, 4, 8.5, 12 and 15.5 kbar. Again, destruction of the sample prevents measurements at ambient pressure in the low-temperature range, but for a pressure higher than 4 kbar reproducible results could be obtained. From these pressure experiments it can be concluded that  $\text{YMn}_2$  is a spin-fluctuation system, like  $\text{YCo}_2$ ,  $\text{LuCo}_2$ , etc., because:

(i) There is a  $T^2$  behaviour observable at low temperatures with a coefficient  $A$  of  $80 \text{ n}\Omega \text{ cm/K}^2$ . Note that this value is of the same order of magnitude as for  $\text{UAl}_2$ .

(ii) There is an extremely strong saturation of  $\rho$  versus  $T$  at elevated temperatures.

(iii) A strong decrease of the  $A$ -value with increasing pressure has been found (see the inset of fig. 45) and consequently  $\rho$  versus  $T$  flattens.

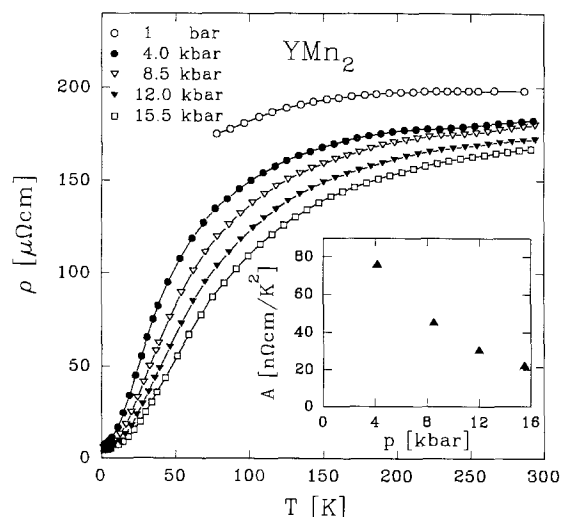


Fig. 45. The temperature dependence of the electrical resistivity of  $\text{YMn}_2$  at external pressures up to 15.5 kbar (Bauer et al. 1992a). The inset shows the value of the coefficient  $A$  as a function of pressure.

There are, besides, some measurements of the resistivity and thermal expansion carried out on “essentially single phase” samples of  $\text{RMn}_2$  in which the cracking caused by the huge positive volume anomaly was prevented (Labroo and Ali 1990, Labroo et al. 1990). Being considered as qualitative, these results provide, however, some useful conclusions on the low-temperature  $\rho(T)$  behaviour of  $\text{RMn}_2$ , i.e. a  $T^2$  dependence of the resistivity for  $\text{R} = \text{Dy-Tm}$  and a large negative jump of  $\rho(T)$  in  $\text{YMn}_2$  at  $T_N$ , indicating the significant role of the d electrons in the transport properties of the manganese Laves phases.

The temperature dependence of the thermopower of  $\text{YMn}_2$  in the region from 4.2 K up to room temperature, as published by Kamimura et al. (1987), is given in fig. 46. As in the case of the resistivity, we have also included in that picture a high-temperature measurement (Gratz and Burkov 1992). The minimum is  $S$  versus  $T$  around 150 K has in our opinion its origin in the band structure, and spin fluctuations play only a minor role. Following the arguments in the paper of Burkov et al. (1992), the minimum in  $S$  versus  $T$  at elevated temperature indicates that the Fermi level is situated in the vicinity of a maximum in the density of states function,  $N(\epsilon)$ . It is also imaginable that spin fluctuations cause a maximum at low temperatures instead of a minimum, since the sign of the thermopower (irrespective of its temperature variation) is according to eq. (46) determined by  $dN(\epsilon)/d\epsilon$  around the Fermi level, which can be positive or negative.

It would be interesting to perform thermopower experiments under external pressure, to check whether also in this spin-fluctuation system a narrow low-temperature minimum appears when the magnetic transition is suppressed by pressure. Indeed, thermopower experiments on  $\text{YMn}_2$  with 3% Sc substituted for Y show a huge maximum around 20 K. In this material the magnetic transition is suppressed by substitution (Kamimura et al. 1987).

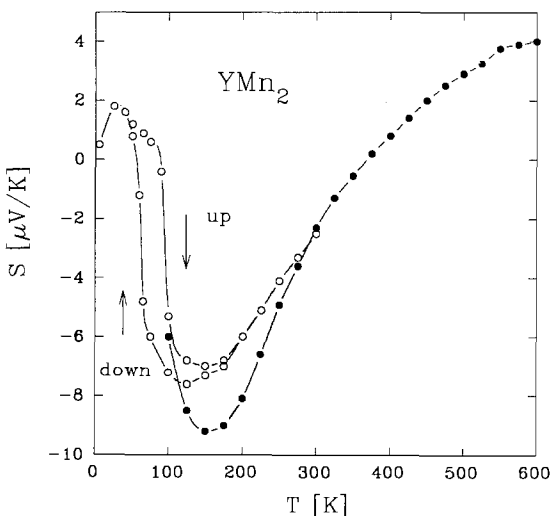


Fig. 46. The temperature dependence of the thermopower of  $\text{YMn}_2$  measured by Kamimura et al. (1987) (open symbols) and by Gratz and Burkov (1992) (filled symbols).

3.4.2.  $UMn_2$ 

The small cusp in  $\chi(T)$  observed for  $UMn_2$  at 230 K was interpreted as due to the onset of antiferromagnetic order below that temperature (Lin and Kaufmann 1957, Lam and Aldred 1975), but no magnetic order could be found in neutron diffraction studies (Marpoe and Lander 1978). Neutron diffraction experiments reveal that the anomaly in  $\chi(T)$  is connected with the appearance of a huge orthorhombic distortion of the cubic C15 unit cell (Lawson et al. 1987). Below about 200 K the susceptibility of  $UMn_2$  is nearly temperature independent. High-temperature susceptibility measurements reveal that  $UMn_2$  obeys a Curie–Weiss behaviour above about 420 K.

The temperature dependence of the electrical resistivity has been investigated by Fournier (1980) and Gratz and Sechovsky (1980). Both results are in very good agreement. The  $\rho(T)$  curve, as shown in fig. 47, is characterized by a low-temperature  $T^2$  dependence with  $A = 8 \text{ n}\Omega \text{ cm/K}^2$ . The inset of fig. 47 shows a  $T^2$  increase of the resistivity ( $\rho - \rho_0$ ) in a log–log plot. A quite pronounced curvature follows between 100 and 200 K. In  $d\rho/dT$  versus  $T$  a cross-over from the negative curved region towards linearity at 230 K can be seen (fig. 47). Many of the observed properties: (i) the  $T^2$  dependence of  $\rho$  versus  $T$  up to 50 K, (ii) the curvature of  $\rho$  versus  $T$  at elevated temperatures, (iii) the enhanced and nearly temperature independent susceptibility below 230 K, (iv) the Curie–Weiss behaviour above 420 K and, finally, (v) the rather high  $\gamma$ -value of  $41 \text{ mJ/mol K}^2$  (Fournier and Troč 1985), are reminiscent of a spin-fluctuation system. An estimation of the spin-fluctuation temperature using the  $A$ -value gives 60 K. A somewhat smaller value (55 K) follows when taking the maximum in  $d\rho/dT$  as a measure for  $T_{sf}$ .

The lower part of fig. 47 shows the temperature dependence of the thermopower. The minimum in  $S$  versus  $T$  near 60 K may be caused by the influence of spin fluctuations, although it is rather broad compared to the much deeper and narrower minima observed for  $YCo_2$  and  $LuCo_2$ , which have comparable  $T_{sf}$  values.

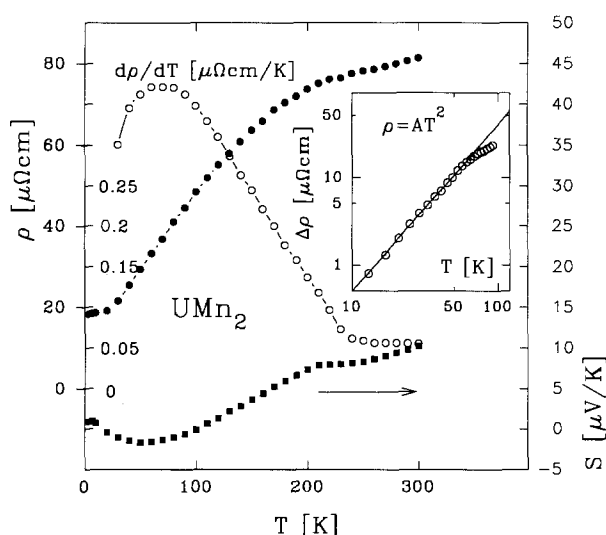


Fig. 47. The temperature dependence of the resistivity and the thermopower of  $UMn_2$ . The dashed line gives  $d\rho/dT$  versus  $T$ . The inset shows the log–log  $T^2$ -dependence of the resistivity ( $\rho - \rho_0$ ) at low temperatures ( $A = 8 \times 10^{-3} \mu\Omega \text{ cm K}^{-2}$ ).

The fact that there is hardly any change in both  $\rho$  versus  $T$  and  $S$  versus  $T$  at 230 K is in agreement with the assumption that the structural transition is phonon induced. Neutron diffraction experiments performed to study the phonon spectra reveal a phonon softening already at room temperature (Fournier and Troč 1985).

### 3.4.3. $RFe_2$

The  $RFe_2$  compounds crystallize in the cubic C15 structure, but under normal pressure do not form for Pr, Nd and Yb; furthermore, no such compound with Eu is known (Meyer et al. 1981). However,  $CeFe_2$  does exist with the C15 structure; its stability is associated with the fact that Ce obviously is not trivalent, like the other R ions (see the discussion for the  $RNi_2$  compounds).

Figure 48 shows the temperature dependence of the resistivity of  $RFe_2$  compounds in the temperature range from 4.2 up to about 1000 K (Gratz et al. 1989). Since there is no substantial difference between the temperature dependences of the resistivities of  $YFe_2$ ,  $LuFe_2$  and the other  $RFe_2$  compounds (where the R ions have magnetic moments), it was argued that the Fe 3d electrons play an essential role in the temperature variation of the resistivity. The magnetic contribution  $\rho_{mag}$  is nearly linear above  $T_C$ , as obtained for the magnetic  $RAI_2$  compounds.

Therefore it can be concluded that the local moments on the Fe sites are well stabilized (this is in contrast to the  $RCO_2$  series, where there is no stable moment without the influence of the magnetic R-moments) and act only as scattering centres.

The magnetic resistivity,  $\rho_{mag}(T > T_C)$ , being dominated by the Fe-moment scattering contribution, does not scale with the de Gennes factor (see fig. 49). Note that, although there are no 4f moments in  $YFe_2$  and  $LuFe_2$ ,  $\rho_{mag}$  is practically of the same magnitude as in  $TmFe_2$ ,  $ErFe_2$ , etc. For comparison, the  $\rho_{mag}(T > T_C)$  values of  $RAI_2$  and of  $RPt$  are plotted also in the figure.

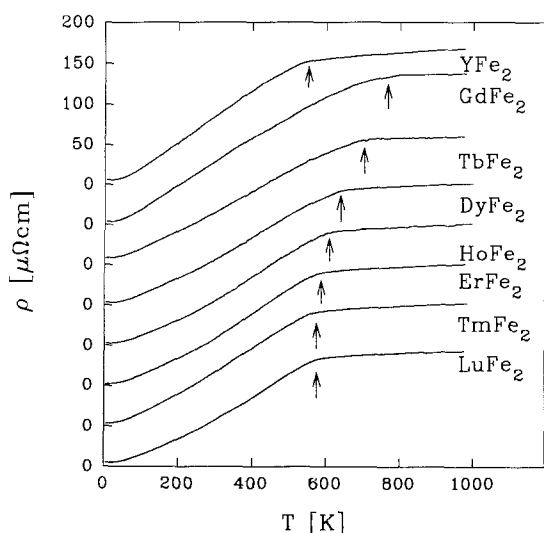


Fig. 48. The temperature dependence of the electrical resistivity of  $RFe_2$  compounds. Arrows indicate the position of  $T_C$  (Gratz et al. 1989).

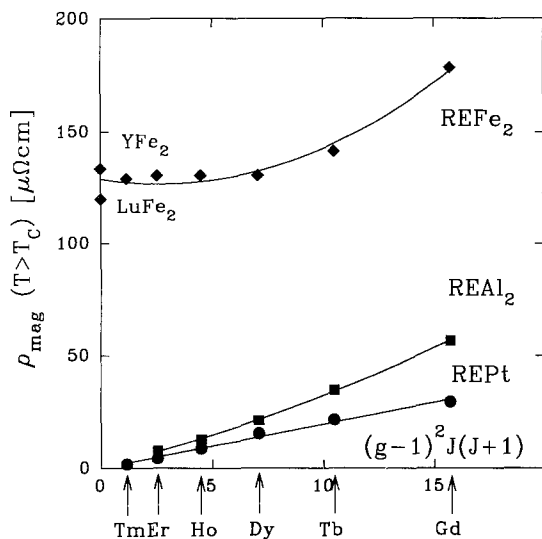


Fig. 49. The magnetic resistivity,  $\rho_{\text{mag}}$ , as a function of the de Gennes factor for  $\text{RFe}_2$ ,  $\text{RAl}_2$  and  $\text{REPt}$  compounds (Gratz et al. 1989).

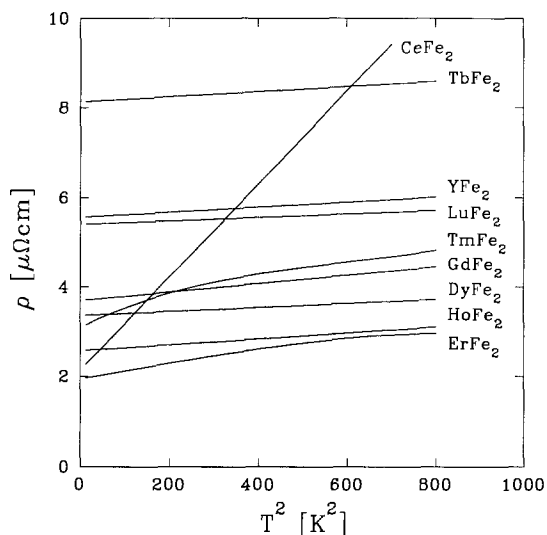


Fig. 50. The low-temperature behaviour of the electrical resistivity of  $\text{RFe}_2$  as a function of  $T^2$  (Gratz et al. 1989).

The low-temperature behaviour of the  $\text{RFe}_2$  compounds is given in fig. 50 in a  $\rho$  versus  $T^2$  plot. Nearly all of them (except  $\text{ErFe}_2$  and  $\text{TmFe}_2$ ) exhibit a  $T^2$  dependence up to about 30 K, with nearly the same gradient. The exceptional status of  $\text{CeFe}_2$  is manifested by the more than ten times larger coefficient of the low-temperature  $T^2$  dependence. The  $T^2$  dependence, as observed for the heavy  $\text{RFe}_2$  compounds, can be attributed to scattering processes of conduction electrons with spin waves in these ferrimagnetic compounds.

Figure 51 shows the temperature dependence of the thermopower of  $\text{RFe}_2$  compounds in the temperature range from 4.2 up to about 800 K. Note that,



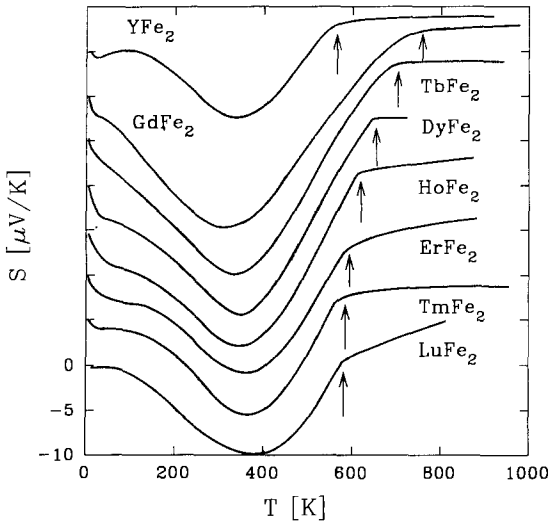


Fig. 51. The temperature dependence of the thermopower of the  $RFe_2$  compounds. Arrows indicate  $T_C$  (Gratz et al. 1988).

irrespective whether the R ion has a magnetic moment or not, the  $S$  versus  $T$  curves are very similar in their shape. Mainly three features characterize these curves: (i) a wide and deep minimum, which is slightly shifted towards lower temperatures when going from Lu to Gd, (ii) a sharp kink near  $T_C$  ( $T_C$  is indicated by an arrow in fig. 51) and (iii) a rather smooth and nearly temperature-independent trend above  $T_C$ .

Following the discussion in sect. 2.3, the thermopower depends sensitively upon the derivative of the density of states around the Fermi energy. Non-spin-polarized band-structure calculations performed for  $YFe_2$  and  $LuFe_2$  reveal a very similar shape of the density of states for both compounds:  $\varepsilon_F$  is situated in a region with negative slope (Gratz et al. 1988, 1989). Such a negative derivative is theoretically connected with a positive sign of the thermopower in the quasi-elastic limit. The quasi-elastic limit is reached for temperatures where the allowed inelastic scattering processes have energies small compared to  $k_B T$ . This condition is fulfilled for the  $RFe_2$  compounds above  $T_C$ .

The shape of the  $S$  versus  $T$  curves below  $T_C$  is also intimately connected with the details of the band structure, but in the low-temperature region it is more difficult to see what the band-structure influence is, since here all the scattering processes (electron-magnon, electron-phonon, etc.) become now inelastic. However, the very similar form of the  $S$  versus  $T$  curves (below and above  $T_C$ ) warrant the conclusion that the density of states across the heavy  $RFe_2$  compounds is at least around  $\varepsilon_F$  similar in shape.

As already pointed out,  $CeFe_2$  has an exceptional position within the family of the  $RFe_2$  compounds. Both the moment per Fe atom and the Curie temperature ( $T_C = 230$  K) are significantly lower compared to the other compounds, whereas the electronic specific-heat coefficient is about four times larger than those of  $YFe_2$ ,  $LuFe_2$  and  $ZrFe_2$  (see, e.g., Eriksson et al. 1988 and Rastogi et al. 1988). Neutron scattering studies reveal strong ferromagnetic correlations above the Curie temperature, which

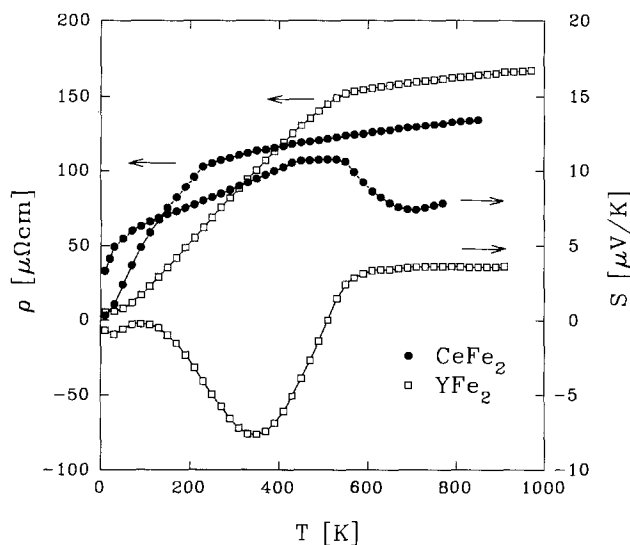


Fig. 52. The electrical resistivity and thermopower of  $\text{CeFe}_2$  as a function of temperature compared to the data for  $\text{YFe}_2$  (Gratz et al. 1989).

persist even up to four times  $T_C$  (Deportes et al. 1981). Recently, the effect of substitution of Al or Co for Fe has been studied by Nishihara et al. (1987).

A dramatic change in the magnetic properties appears, although only a few percent of the iron is replaced. Also, with respect to the transport properties, pronounced differences have been observed in the resistivity and thermopower compared with the general trend in the  $\text{RFe}_2$  compounds. To emphasize the exceptional behaviour of  $\text{CeFe}_2$  within the  $\text{RFe}_2$  series, the  $\rho(T)$  and  $S(T)$  curves are given in a separate figure (fig. 52). For an easier comparison we added the corresponding data of  $\text{YFe}_2$  in the figure.

#### 3.4.4. $\text{AnFe}_2$

Four compounds form in the cubic C15 structure, namely  $\text{UFe}_2$ ,  $\text{NpFe}_2$ ,  $\text{PuFe}_2$  and  $\text{AmFe}_2$ . Their magnetic properties have been studied in some detail (see, e.g., Fournier and Troč 1985 and Sechovsky and Havela 1988), but only the electrical resistivity of  $\text{UFe}_2$  has been measured up to now (Hrebik and Coles 1980). A brief review of the magnetic properties of these compounds is necessary for a better understanding of the transport properties.

The direct 3d–3d exchange interaction dominates the magnetic properties and leads to strong ferromagnetism in  $\text{NpFe}_2$  and  $\text{PuFe}_2$ , whereas ferrimagnetism exists in the case of  $\text{AmFe}_2$ . The iron moments in the ordered state are about  $1.4\mu_B$ . The ordering temperatures of  $\text{NpFe}_2$ ,  $\text{PuFe}_2$  and  $\text{AmFe}_2$  are in the range 500 to 600 K. These values are comparable with the  $T_C$ -values found for the  $\text{RFe}_2$  intermetallics.

Magnetic moments on the An sites of  $1.09\mu_B$ ,  $0.45\mu_B$  and  $0.4\mu_B$  have been found for  $\text{NpFe}_2$ ,  $\text{PuFe}_2$  and  $\text{AmFe}_2$ , respectively ( $\text{Am}^{3+}$  being non-magnetic with a  $J = 0$  ground state).  $\text{UFe}_2$  is an exception, since both  $T_C$  and the iron moment are considerably reduced ( $T_C = 160 \text{ K}$ ,  $\mu_{\text{Fe}} = 0.6\mu_B$ ) and are very sensitive to the

stoichiometry, while  $\mu_U$  is almost, but not quite, equal to zero (Yessik 1969). Moreover, the anisotropic magnetostriction constants measured on a single crystal of  $UFe_2$  are comparatively high (about  $10^{-3}$ ), in spite of the magnetic anisotropy constants  $K_1$  and  $K_2$ , which are small and do not exceed  $10^5$  erg/g (Andreev et al. 1979, Popov et al. 1980). The  $\sigma^2$  versus  $H/\sigma$  plots (Arrott plots) of the magnetization (Aldred 1979) as well as the position of  $UFe_2$  in the Rhodes–Wohlfarth plot and, furthermore, the strong pressure influence on both  $\mu_s$  and  $T_C$  (Franse et al. 1981) point towards itinerant magnetism for Fe. Concerning  $UFe_2$ , recently performed polarized-neutron studies revealed that the spin and orbital moments are large, but almost cancel ( $\mu_s = -0.22\mu_B$  and  $\mu_l = +0.23\mu_B$ ), the total moment being thus only  $0.01\mu_B$  (Wulff et al. 1989). This observation confirms the explanation proposed by Popov et al. (1980) for the anisotropic properties of  $UFe_2$ , and points towards an itinerant character of the 5f states. Structure calculations confirm the itinerancy of the 5f electrons as well as the existence of f–d hybridization (Brooks et al. 1988).

The resistivity of  $UFe_2$  versus temperature is displayed in fig. 53. The ordering temperature is reflected as a weak kink in the  $\rho(T)$  curve. At low temperatures the data can be fitted to  $\rho(T) = \rho_0 + AT^2$ . The inset in fig. 53 shows the  $\rho$  versus  $T^2$  dependences for  $UFe_2$  in comparison to those of  $CeFe_2$  and the paramagnetic spin-fluctuation systems  $YCo_2$  and  $GdFe_2$ , which have stable 3d magnetic moments plus the local 4f moments. As can be seen, the slopes of the curves for  $UFe_2$  and  $CeFe_2$  are the same, nevertheless being higher than for  $GdFe_2$  and smaller than for  $YCo_2$ . This indicates the large spin-fluctuation contribution in the resistivity of  $UFe_2$  as well as  $CeFe_2$  at low temperatures.

The possible reason for the change in the slope of  $\rho$  versus  $T^2$  around 15 K may be the change of the character of the electron–electron correlations, i.e. at low temperatures the spin-wave excitations are dominating.

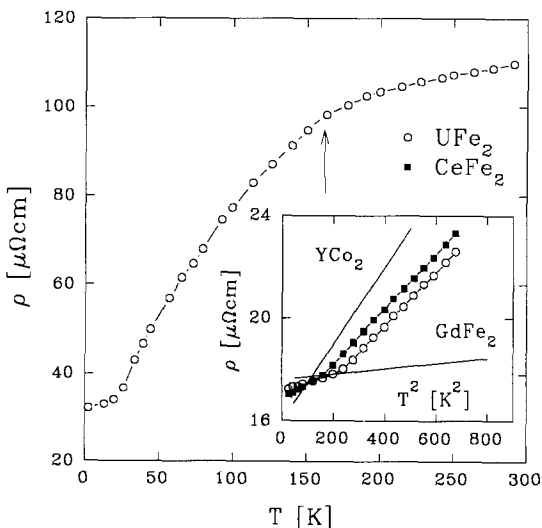


Fig. 53. The temperature dependence of the electrical resistivity of the  $UFe_2$  compound (Hrebik and Coles 1980).  $T_C$  is indicated by an arrow. The  $\rho$  versus  $T^2$  dependences of  $UFe_2$ ,  $CeFe_2$ ,  $GdFe_2$  and  $YCo_2$  are compared in the inset.

3.4.5.  $R\text{Co}_2$ 

In the series of the R-3d Laves phases, the  $R\text{Co}_2$  compounds show unusual varieties of physical properties. In contrast to  $R\text{Fe}_2$ , where the Fe moments are practically independent whether the R ions have a magnetic moment or not, the existence of a Co moment is connected with the existence of a moment on the R ion sites; e.g.  $\text{YCo}_2$ ,  $\text{LuCo}_2$  and  $\text{ScCo}_2$  are non-magnetic (there is no local moment on the Co sites), whereas in all those cases where the R ions possess a magnetic moment, a moment of about  $1\mu_B$  is induced on the Co sites in the magnetic ordered state (Moon et al. 1965). The susceptibility of  $\text{YCo}_2$ ,  $\text{LuCo}_2$  and  $\text{ScCo}_2$  is enhanced, with maxima at 200, 400 and about 600 K, respectively (Gschneidner et al. 1985, Ishiyama et al. 1984). High-temperature susceptibility measurements confirm a Curie-Weiss-like behaviour for  $\text{YCo}_2$  and  $\text{LuCo}_2$  (Burzo and Lemaire 1992).

From band-structure calculations on  $\text{YCo}_2$  it has been concluded that most of the outstanding features observed in the family of the  $R\text{Co}_2$  compounds can at least partly be understood when considering the position of the Fermi level, which is situated near a local peak of the hybridized d-band, formed by the Co 3d electrons and the d electrons of the rare earth element (Yamada et al. 1984). The high value, together with a steep negative slope and a positive curvature of the density of d states,  $N(\varepsilon)$ , near  $\varepsilon_F$  promote the development of spin fluctuations in the hybridized d-band.

Probably one of the most interesting observations is that the magnetic transition is of the first-order type in some of the heavy  $R\text{Co}_2$  compounds ( $R = \text{Dy}, \text{Ho}, \text{Er}, \text{Tm}$ ). Figure 54 shows the temperature dependence of the resistivity of  $\text{DyCo}_2$ ,  $\text{HoCo}_2$ ,  $\text{ErCo}_2$  and  $\text{TmCo}_2$  (Gratz and Zuckermann 1982b). The inset in this figure gives the  $\rho$  versus  $T$  curve of  $\text{TmCo}_2$  in the vicinity of the Curie temperature (Gratz et al. 1993a, b). The strong saturation tendency which characterizes the  $\rho$ - $T$  curves of the  $R\text{Co}_2$  compounds is not observable in the isostructural  $R\text{Fe}_2$  and  $R\text{Ni}_2$  compounds (see the discussion of these compounds in this chapter).

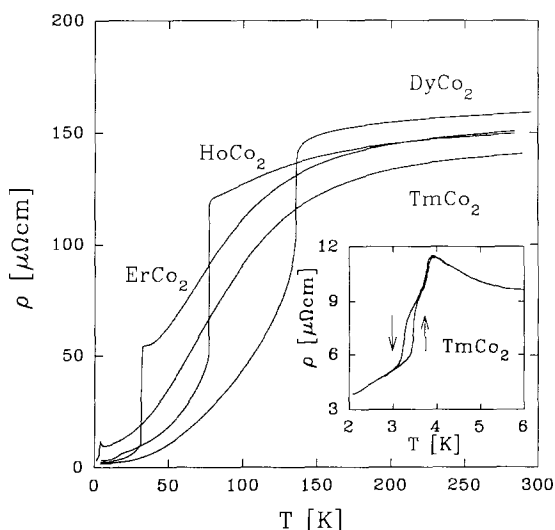


Fig. 54. The temperature dependence of the resistivity of  $R\text{Co}_2$  ( $R = \text{Dy}, \text{Ho}, \text{Er}$  and  $\text{Tm}$ ) (Gratz and Zuckermann 1982a). The inset shows the resistivity of  $\text{TmCo}_2$  around the Curie temperature (Gratz et al. 1993a, b).

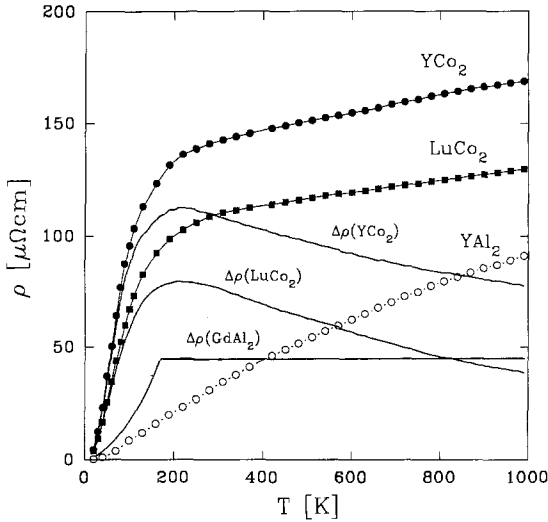


Fig. 55. The temperature dependence of the resistivity of  $\text{YCo}_2$  (Gratz et al. 1987a) and  $\text{LuCo}_2$  (Baranov et al. 1993). For the meaning of the  $\Delta\rho$ -curves see the text.

The temperature variation of the electrical resistivity of  $\text{YCo}_2$  (Gratz et al. 1987a) and  $\text{LuCo}_2$  (Baranov et al. 1993) in the range from 4.2 up to 1000 K is shown in fig. 55. For comparison the  $\rho$ - $T$  curve of  $\text{YAl}_2$  is included in the picture. The curves denoted  $\Delta\rho(\text{YCo}_2)$  and  $\Delta\rho(\text{LuCo}_2)$  represent the difference in the temperature-dependent resistivity of  $\text{YCo}_2$  ( $\text{LuCo}_2$ ) and the isostructural  $\text{YAl}_2$ , in which there are no 3d electrons in the d band. Assuming validity of the Matthiessen rule, the  $\Delta\rho$  curves can be identified as the contributions due to spin-dependent scattering processes. Accordingly,  $\Delta\rho(\text{YCo}_2)$  and  $\Delta\rho(\text{LuCo}_2)$  are caused by the spin fluctuations in the d band (in what follows  $\Delta\rho$  will be renamed as  $\rho_{\text{mag}}$ ). The  $\rho_{\text{mag}}$ -curves follow a  $T^2$ -law ( $\rho_{\text{mag}} = AT^2$ ) at low temperatures. After passing a maximum near 200 K, a decrease up to 1000 K is observable.

Figure 56 shows the  $T^2$  dependence of  $\text{YCo}_2$  under various external pressures. The inset in this figure gives the pressure dependence of the coefficient  $A$  for  $\text{YCo}_2$ . Ikeda (1977a) interpreted the  $T^2$  dependence at low temperatures in combination with the high-temperature saturation of  $\rho(T)$  for  $\text{YCo}_2$  in terms of the spin-fluctuation theory (Ueda and Moriya 1975). Because of the similarity in the behaviour of  $\text{YCo}_2$  and  $\text{LuCo}_2$ , it can be assumed that also in  $\text{LuCo}_2$  the spin-fluctuation scattering of the conduction electrons is dominating the  $\rho(T)$  behaviour.

An estimation of the spin-fluctuation temperature,  $T_{\text{sf}}$ , from the position of the maximum in  $d\rho_{\text{mag}}/dT$  gives about 45 K for  $\text{YCo}_2$  and about 55 K for  $\text{LuCo}_2$ . About the same values have been deduced from the coefficients  $A$  at zero pressure ( $A = 14 \text{ n}\Omega \text{ cm/K}^2$  for  $\text{YCo}_2$  and  $12 \text{ n}\Omega \text{ cm/K}^2$  for  $\text{LuCo}_2$ ). It is interesting to compare  $\rho_{\text{mag}}$  of  $\text{YCo}_2$  and  $\text{LuCo}_2$  with  $\rho_{\text{mag}}$  of  $\text{GdAl}_2$ . Since there is no crystal-field influence in  $\text{GdAl}_2$ , it is a prototype to demonstrate local-moment scattering of the conduction electrons. We have, therefore, included  $\Delta\rho(\text{GdAl}_2)$  in fig. 55 for comparison. Note that, although there are large 4f moments located on the Gd sites in the  $\text{MgCu}_2$  lattice,

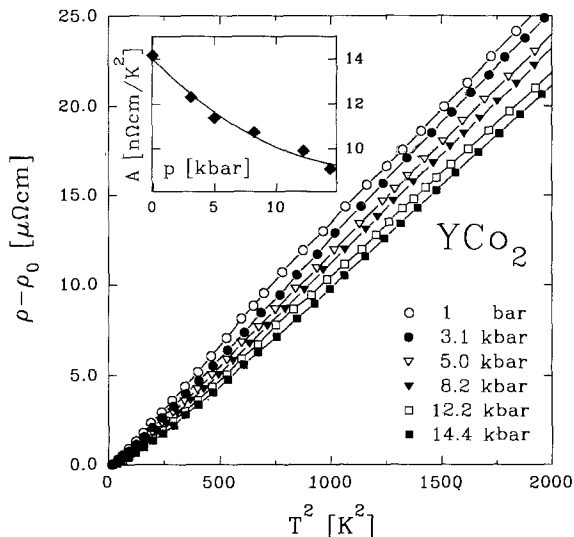


Fig. 56. The pressure influence on the  $T^2$  dependence of the resistivity for  $\text{YCo}_2$ . The inset shows the decrease of the coefficient  $A$  with increasing pressure (Gratz 1992).

$\rho_{\text{mag}}(\text{YCo}_2)$  as caused by the spin fluctuations is more than twice as large as  $\rho_{\text{mag}}(\text{GdAl}_2)$  at 200 K.

We are now coming to the discussion of the resistivity behaviour of the  $\text{RCO}_2$  compounds with first-order magnetic transitions. At high temperatures, i.e. well above  $T_C$ ,  $\rho_{\text{mag}}$  consists in general of two spin-dependent contributions. One is due to the scattering processes of the conduction electrons by the localized 4f moments and the other is due to the scattering by spin fluctuations, as in  $\text{YCo}_2$  and  $\text{LuCo}_2$ . The huge discontinuity at  $T_C$  is caused by the sudden appearance of the molecular field due to the spontaneous alignment of the R moments. The molecular field induces magnetic

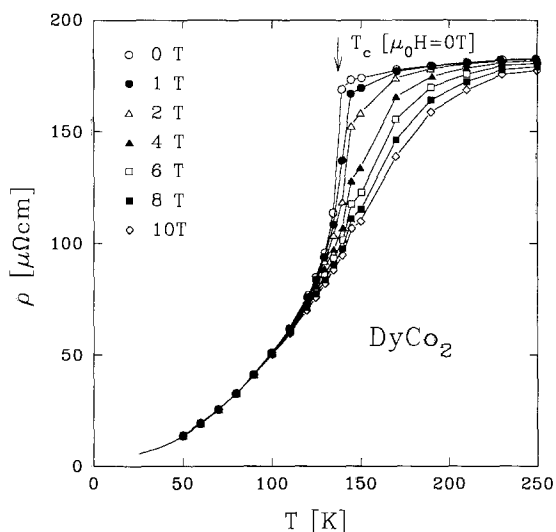


Fig. 57. The field dependence of the resistivity of  $\text{DyCo}_2$  around the Curie temperature (Gratz 1992).

moments on the Co sites and thus suppresses the spin-fluctuation scattering of the conduction electrons below  $T_c$ .

The influence of a transverse external magnetic field on the  $\rho(T)$  behaviour in  $DyCo_2$ ,  $HoCo_2$  and  $ErCo_2$  is shown in figs. 57, 58 and 59 (Gratz 1992). The longitudinal magnetoresistance of a single crystal of  $ErCo_2$  along the principal crystallographic directions ((100), (110), (111)) has been measured by Aleksandryan et al. (1988). Figure 60 shows the temperature dependence of the critical field as measured along these three directions in  $ErCo_2$ . No anisotropy of the critical field has been found for a  $HoCo_2$  single crystal (fig. 61), in contrast to  $ErCo_2$  (Baranov and Kozlov 1992).

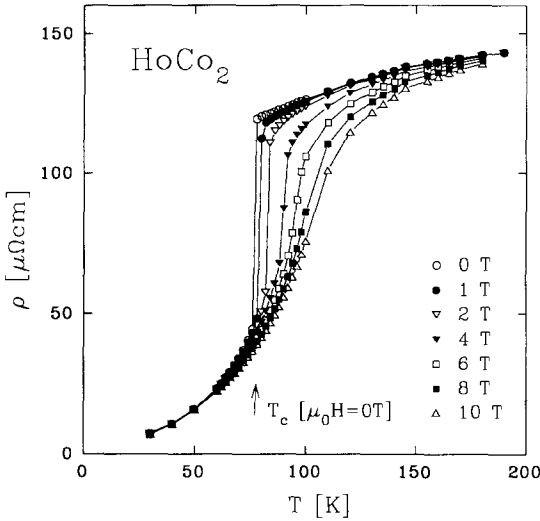


Fig. 58. The field dependence of the resistivity of  $HoCo_2$  around the Curie temperature (Gratz 1992).

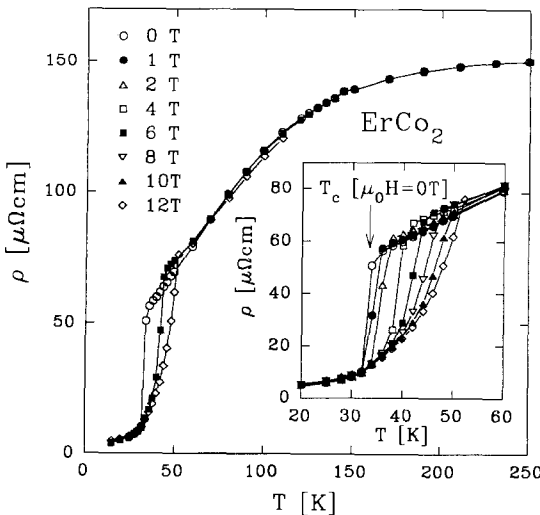


Fig. 59. The field dependence of the resistivity of  $ErCo_2$  in the temperature range 4.2 K up to room temperature. The inset shows the field dependence of  $\rho(T)$  in the vicinity of  $T_c$  (Gratz 1992).

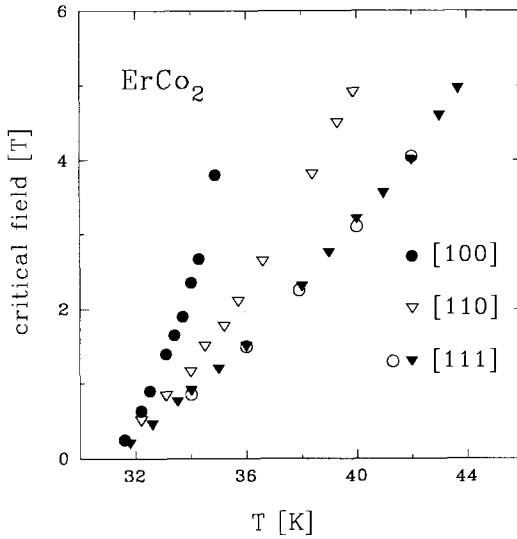


Fig. 60. The temperature dependence of the critical field measured along the three principal crystallographic directions in a ErCo<sub>2</sub> single crystal. The results obtained from resistivity measurements are given by open circles (Aleksandryan et al. 1988).

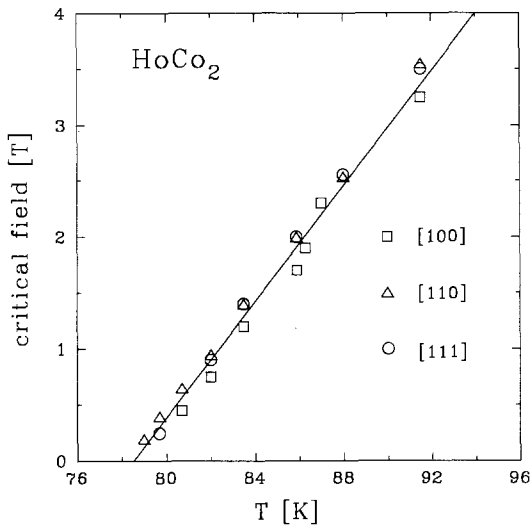


Fig. 61. The temperature dependence of the critical field measured along the three principal crystallographic directions in a HoCo<sub>2</sub> single crystal (Baranov and Kozlov 1992).

The effects of dilution of the magnetic R ions and the influence on the resistivity have been investigated for several pseudobinary compounds: (Nd, Y)Co<sub>2</sub> (Gratz and Nowotny 1982, Baranov et al. 1983), (Dy, Y)Co<sub>2</sub> and (Er, Y)Co<sub>2</sub> (Gratz et al. 1987b, Baranov et al. 1989, Duc et al. 1991a) (Ho, Y)Co<sub>2</sub> (Steiner et al. 1978) and (Tb, Y)Co<sub>2</sub> (Duc et al. 1989) (see also Duc et al. 1991b).

The transverse magnetoresistance of YCo<sub>2</sub> as a function of the magnetic field at 4.2 K is shown in fig. 62. The inset in this figure shows  $\Delta\rho/\rho$  at 10 T as a function of the temperature. The positive sign of  $\Delta\rho/\rho$  is in contrast to what the spin-fluctuation



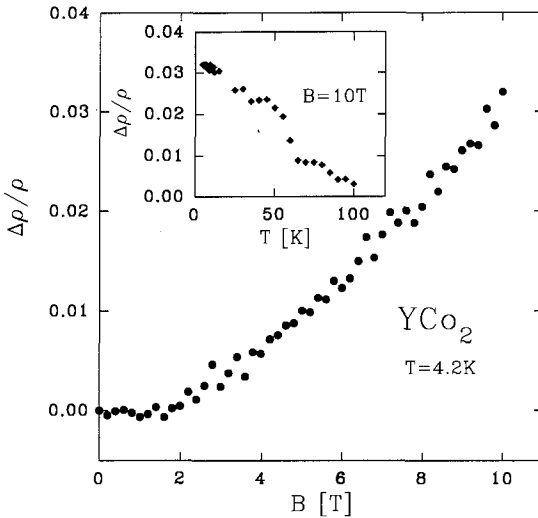


Fig. 62. The transverse magnetoresistance of  $\text{YCo}_2$  at 4.2 K in fields up to 10 T. The inset given  $\Delta\rho/\rho$  at 10 T as a function of the temperature (Gratz 1992).

theory predicts (see sect. 2.3.4). The field influence on the resistivity in  $\text{ErCo}_2$ ,  $\text{HoCo}_2$  and  $\text{DyCo}_2$  gives firstly a qualitative change of the magnetic transition (from first towards second order) and a shift of the onset of long-range magnetic order towards higher temperatures (see also figs. 60 and 61). Such a pronounced influence of an external field on the resistivity is in contrast with the comparatively small influence of a 10 T field in  $\text{YCo}_2$ . Note that a field of 12 T reduces the resistivity just above  $T_C$  by a factor of about seven in  $\text{ErCo}_2$ . The mechanism which is responsible for the strong field influence can be understood in the following way: the effect of the external field on the local moments above  $T_C$  is to line up the 4f moments, thus causing a suppression of the spin fluctuations in the d band due to the f-d exchange.

The influence of hydrostatic pressure on the resistivity of most of the  $\text{RCo}_2$  compounds has been measured (Gratz et al. 1993a, b). These experiments revealed strong negative and non-linear pressure dependences of the Curie temperatures of these compounds. If the transition is of first-order type, it is not changed by the pressure at least up to about 20 kbar. As an example we show  $\rho(T)$  of  $\text{ErCo}_2$  for various pressures in fig. 63.

Figure 64 shows the temperature dependence of the thermopower ( $S(T)$ ) for the heavy  $\text{RCo}_2$  compounds up to room temperature. As in the case of the resistivity, there is a discontinuity at  $T_C$  in  $S$  versus  $T$ , which decreases in magnitude as the ordering temperature increases.

Figure 65 shows the  $S$  versus  $T$  curve of  $\text{YCo}_2$  (Burkov et al. 1992),  $\text{LuCo}_2$  and  $\text{ScCo}_2$  (Baranov et al. 1993) in the range from 4.2 up to 600 K. The thermopower of these three spin-fluctuation systems ( $\text{ScCo}_2$  is also considered a spin-fluctuation system (Gschneidner et al. 1985)) exhibits a minimum at a temperature somewhat below  $T_{\text{sf}}$ .

Several reasons have been discussed to explain the minimum (or maximum) in the thermopower at low temperatures. As is discussed in sect. 2.3, the phonon-drag effect

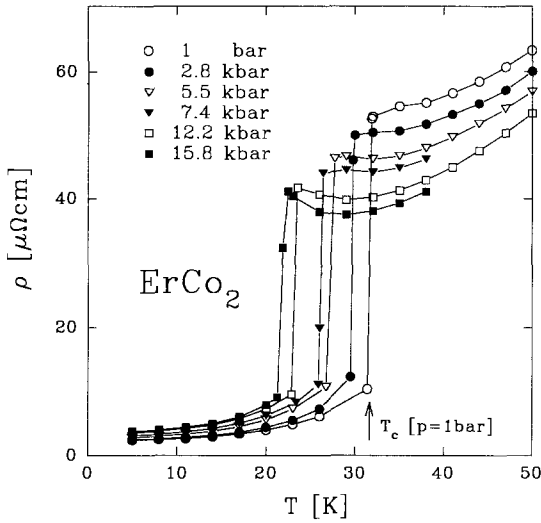


Fig. 63. The pressure dependence of the electrical resistivity of  $\text{ErCo}_2$  around  $T_C$  (Gratz et al. 1993a, b). The arrow indicates the Curie temperature at ambient pressure.

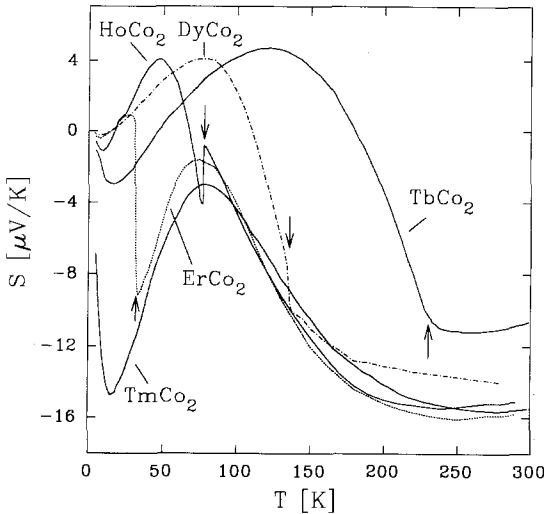


Fig. 64. The temperature dependence of the thermopower of  $\text{RCo}_2$  ( $\text{R} = \text{Tb}, \text{Dy}, \text{Ho}, \text{Er}$  and  $\text{Tm}$ ). The magnetic transition temperatures are marked by the arrows in the figure (Gratz and Zuckermann 1982b).

(Ziman 1960) or the so-called Nielson–Taylor effect (Nielson and Taylor 1974) can yield a pronounced non-linear behaviour at low temperatures. However, in spin-fluctuation systems such as  $\text{YCo}_2$ , we suggest that these minima are intimately related to the existence of the spin fluctuations. Note that a very deep minimum exists in the thermopower of  $\text{UAl}_2$ . It would be interesting to investigate whether a “paramagnon-drag” effect is the origin of the anomalous behaviour of the thermopower in these systems. However, it should be mentioned that Fischer (1974) showed that in dilute magnetic systems with localized spin fluctuations minima are expected under certain conditions, although according to Fischer’s model other mechanisms

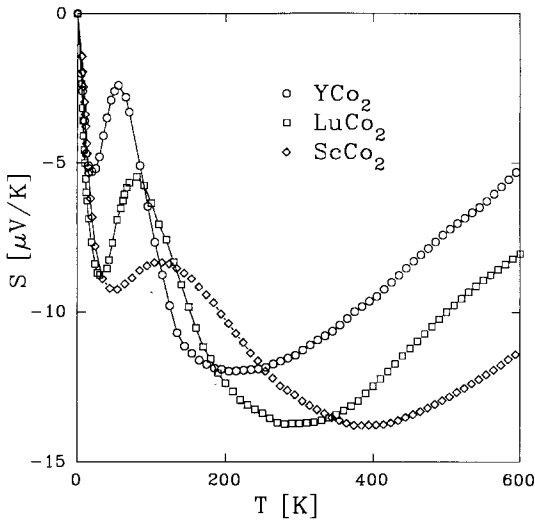


Fig. 65. The temperature dependence of the thermopower of the three spin-fluctuation systems  $\text{YCo}_2$  (Burkov et al. 1992),  $\text{LuCo}_2$  and  $\text{ScCo}_2$  (Baronov et al. 1993) in the temperature region from 4.2 up to 600 K.

than a drag effect are held responsible for this non-linear behaviour of the thermopower.

In a qualitative analysis of the high-temperature thermopower data of  $\text{YCo}_2$  Burkov et al. (1990) could show that mainly density of state features at the Fermi level determine the sign and the curvature of  $S$  versus  $T$  in the high-temperature region.

#### 3.4.6. $\text{UCo}_2$

$\text{UCo}_2$  is one of the  $\text{AnCo}_2$  cubic Laves phases which show no magnetic order at any temperature, unless An is a magnetic actinide element. The U-U spacing is 3.03 Å, which is below the Hill limit.

Investigations of the susceptibility of  $\text{UCo}_x$  compounds with variable composition reveal that in the sample with  $x = 1.987$  the susceptibility is practically temperature independent and one of the smallest in the investigated series (Hrebik and Coles 1977). Samples with this composition also show the largest value for the resistivity ratio  $\rho(295)/\rho(4.2)$ . These observations led the authors to the conclusion that in a sample with the composition  $x = 1.987$  the number of the Co atoms occupying wrong lattice sites is minimal.

Figure 66 shows the temperature dependence of the resistivity of  $\text{UCo}_2$  in the temperature range up to room temperature. Note that at 50 K an inflection point is observable. Investigation of the temperature dependence of the electrical resistivity reveals that for all the concentrations a shallow minimum appears in  $\rho$  versus  $T$  around 5 K. The position of the minimum depends slightly on the concentration (Hrebik and Coles 1977). Above the minimum in  $\rho$  versus  $T$  a  $T^2$  dependence exists. The reason for this minimum was thought to be Kondo-like scattering processes on the local Co moments which were assumed to exist on wrong lattice sites. The inset in fig. 66 shows the  $\rho(T)$  behaviour as a  $\rho$  versus  $T^2$  plot. From the enhanced  $\gamma$ -value of  $\text{UCo}_2$  (35 mJ/mol K<sup>2</sup>), the  $T^2$  behaviour, the saturation tendency in the resistivity,

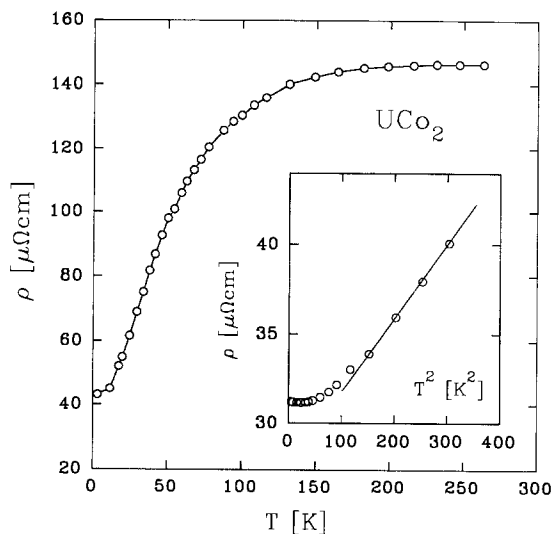


Fig. 66. The temperature dependence of the electrical resistivity of  $\text{UCo}_2$  (Hrebik 1977). The inset shows the low-temperature resistivity in a  $\rho$  versus  $T^2$  diagram. The deviation from  $T^2$  dependence has been attributed to Kondo-like scattering processes (Hrebik and Coles 1977).

as well as from the  $T^3 \ln T$  term in the specific heat (Franse et al. 1981), the existence of spin fluctuations at low temperatures follows.

Hrebik and Coles (1977) determined a spin-fluctuation temperature of 150 K. From the coefficient  $A$  ( $40 \times 10^{-3} \mu\Omega \text{ cm}/\text{K}^2$ ) in the relation  $\rho = \rho_0 + AT^2$  we estimated the spin-fluctuation temperature to be 27 K. It would be interesting to investigate whether in the temperature variation of the thermopower a minimum in the low-temperature region exists, as in spin-fluctuation systems like  $\text{UAl}_2$ ,  $\text{YCo}_2$ ,  $\text{LuCo}_2$ , etc.

### 3.4.7. $\text{RNi}_2$

The group of intermetallics of R with 3d metals which crystallize in the cubic Laves phase ends with the  $\text{RNi}_2$  series, since the  $\text{RCu}_2$  compounds show the orthorhombic  $\text{CeCu}_2$ -type structure ( $D_{2h}^{28}$ ).

Magnetic investigations reveal that the Ni atoms carry no magnetic moment (Burzo and Laforest 1972), thus the contribution to the magnetism of the Ni atoms is small compared to the Mn, Fe or Co atoms in the corresponding  $\text{RM}_2$  cubic Laves phases.

Band-structure calculations confirmed the non-magnetic state of the Ni atoms. According to the first calculation of Cyrot and Lavagna (1979), the 3d band of Ni is full, thus the density of states at the Fermi level is small. In a more recent paper Yamada et al. (1984) emphasized: "It is often considered that the d-band of the Ni is filled by electrons in  $\text{YNi}_2$  and  $\text{RNi}_2$  compounds and then the Ni atoms become non-magnetic. This is not true. The d band of Ni is mixed with the d band of Y. Up to the Fermi level, the number of d electrons of Ni is 9.4 per atom. The remaining states of Ni, with 0.6 electrons per atom, exist above the Fermi level due to the mixing of the d bands of the Ni and Y atoms. The reason why the Ni atom becomes non-magnetic is that the local density of states of Ni is very low at the Fermi level". The small  $\gamma$ -value measured for  $\text{YNi}_2$  ( $6.0 \text{ mJ/mol K}^2$ ) is obviously a further indication of

the small density of states, as deduced from all the band-structure calculations (Mori et al. 1982).

The  $RNi_2$  compounds are to some extent similar to the  $RAI_2$  compounds. The indirect coupling of the R moments is of the RKKY-type. The magnetic ordering temperatures in the  $RNi_2$  series are considerably lower than those observed in the  $RFe_2$  and  $RCo_2$  series. The highest ordering temperature, observed for  $GdNi_2$ , is even lower than that for the corresponding  $RAI_2$  compound. Above the Curie temperature the susceptibilities show a Curie-Weiss behaviour, except in  $SmNi_2$  where a large van Vleck term exists due to the low-lying Sm multiplet. This observation is well known for many other Sm compounds (De Wijn et al. 1976, Gratz et al. 1990).

Both  $YNi_2$  and  $LuNi_2$  show weak Pauli paramagnetism. The  $\gamma$ -value of  $LaNi_2$  is enhanced,  $\gamma(LaAl_2) = 12.5 \text{ mJ/mol K}^2$  (Mori et al. 1982), but it is questionable whether  $LaNi_2$  can be stabilized in the cubic Laves-phase structure (Paul-Boncour et al. 1988). For the two non-ordered compounds  $PrNi_2$  and  $TmNi_2$  Curie-Weiss behaviour is only observed at high temperatures, whereas at low temperatures van Vleck paramagnetism has been measured (Burzo and Laforest 1972). The position of  $CeNi_2$  is exceptional, since the Ce ion is in an intermediate valence state in this compound, according to Sakurai et al. (1985).

Investigations of the transport properties of the  $RNi_2$  compounds will now be discussed (Resel 1991). Figure 67 shows the temperature dependence of the electrical resistivity of  $RNi_2$  compounds which could be prepared as single-phase samples ( $PrNi_2$  and  $NdNi_2$  could not be prepared as single phase). High-temperature measurements of the resistivity revealed in some of the  $RNi_2$  compounds ( $R = Gd, Y$  and  $Sm$ ) discontinuities in  $\rho$  versus  $T$ . As can be seen in fig. 67, the "transitions" are connected with hysteresis loops, indicating a first-order type of transition. The transition temperatures are:  $630 \pm 10 \text{ K}$  for  $GdNi_2$ ,  $690 \pm 20 \text{ K}$  for  $YNi_2$  and  $920 \pm 30 \text{ K}$  for  $SmNi_2$ . X-ray diffraction measurements performed on powdered

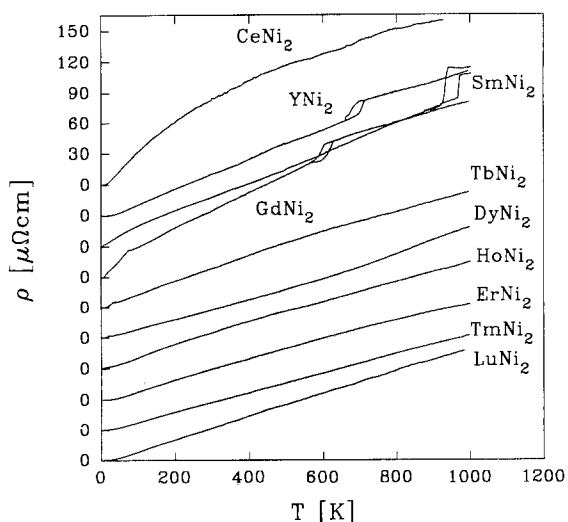


Fig. 67. The temperature dependence of the electrical resistivity of the  $RNi_2$  compounds in the temperature region from 4.2 up to 1000 K. The discontinuities in  $\rho(T)$  of  $YNi_2$ ,  $SmNi_2$  and  $GdNi_2$  are due to structural transitions (Resel 1991).

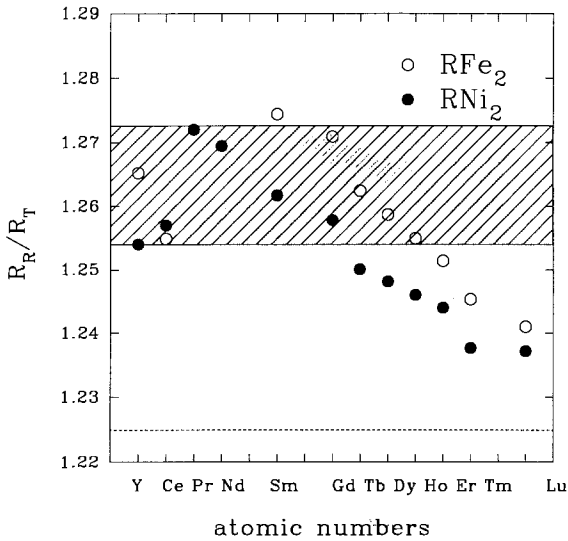


Fig. 68. The  $R_R/R_T$  ratio versus the atomic number of rare earths.  $R_R$  is half the R–R distance obtained from the lattice constant for the corresponding  $RM_2$  ( $M = \text{Ni}, \text{Fe}$ ) cubic Laves phases,  $R_T$  is the atomic radius of Ni or Fe. The ideal ratio for a cubic Laves phase is 1.225, which is marked as a dashed line.

samples below and above these transition temperatures have shown that these anomalies are connected with a change of the crystal structure (Gratz et al. 1991). A phenomenological explanation can be given considering the ratio  $R_R/R_T$  ( $R_R = 3^{1/2}/8a$  is half the R–R distance as obtained from the lattice constant  $a$ ,  $R_T$  is the atomic radius of the transition metal). In fig. 68 this ratio is plotted for the  $R\text{Ni}_2$  and the  $R\text{Fe}_2$  intermetallics versus the atomic number of the rare earth. As can be seen in that figure, the deviation of  $R_R/R_T$  from the ideal value for the cubic Laves phases (1.225) increases towards the light R compounds. Experience shows that there is obviously a critical threshold of the ratio of about 1.26. If  $R_R/R_T$  for a cubic Laves-phase compound is near to this critical value, the preparation of a single-phase sample is extremely difficult.

Concerning the question why the C15 structure becomes unstable at high temperatures for only a few of the  $R\text{Ni}_2$  compounds, note that the ratio of the three  $R\text{Ni}_2$  compounds ( $R = \text{Y}, \text{Sm}$  and  $\text{Gd}$ ) is near to, or above, this critical value. Thermal expansion will cause a further increase of  $R_R/R_T$  with increasing temperature, thus giving rise to a structural transition. Since this anomaly exists in the paramagnetic region of  $\text{SmNi}_2$  and  $\text{GdNi}_2$  as well as in the paramagnetic  $\text{YNi}_2$ , the transition cannot be of magnetic origin. Considering the  $R\text{Fe}_2$  compounds, similar transitions can be expected for  $\text{GdFe}_2$  and  $\text{SmFe}_2$  at high temperatures (see fig. 68).

To learn more about the physical origin of this change in the structure, other transport phenomena have been studied. As an example, the resistivity, thermopower and thermal conductivity of  $\text{YNi}_2$  are depicted in fig. 69 in the vicinity of the transition temperature (700 K) (Gratz et al. 1991). Since at such high temperatures the phonons are mainly responsible for the conduction-electron scattering, it has been assumed that the step-like change in  $\rho(T)$ ,  $S(T)$  and  $\lambda(T)$  is caused by a change in the phonon dynamics connected with the transition. This can be concluded because of the different gradients in  $\rho(T)$  and  $\lambda(T)$  above and below the transition (see fig. 69), although it

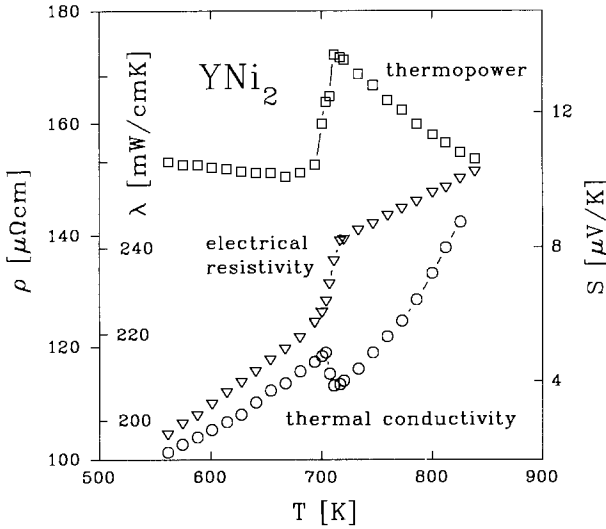


Fig. 69. The temperature dependence of the resistivity, thermopower and thermal conductivity of  $\text{YNi}_2$  in the vicinity of the transition temperature (Gratz et al. 1991).

cannot be excluded that a change in the band structure (associated with the transition) has an influence as well. The discontinuity in the thermopower is an indication for this, since the thermopower is very sensitive to a change in  $N(\epsilon_F)$ .

As for the  $\text{RAl}_2$  and  $\text{RPt}$  compounds,  $\rho_{\text{spd}}$  can be determined for the magnetic-ordered  $\text{RNi}_2$  compounds by subtracting  $\rho(\text{YNi}_2)$ . The  $\rho_{\text{spd}}$ -values thus obtained for the heavy  $\text{RNi}_2$  compounds are roughly proportional to the de Gennes factor, in agreement with eq. (50) (see fig. 25 in sect. 3.3.1).

#### 3.4.8. $\text{UNi}_2$

Within the family of the U-3d transition metal compounds  $\text{UNi}_2$  has several unique features.  $\text{UNi}_2$  is not isomorphous with  $\text{UMn}_2$ ,  $\text{UFe}_2$  and  $\text{UCo}_2$ , but forms a hexagonal C14-type Laves-phase compound. The axial ratio for  $\text{UNi}_2$ ,  $c/a = 1.662$  (Baenzinger et al. 1950), differs significantly from the ideal value (1.633). Another interesting observation is the appearance of ferromagnetism below 21 K. This is the case although the U-U interatomic distance is far below the Hill limit (Fournier 1985), which would be necessary for the formation of local moments. The question arises what mechanism can be held responsible for the long-range magnetic order.

One of the two attempts to explain the appearance of ferromagnetism was proposed by Franse et al. (1981). They concluded from the strong negative pressure dependence of  $\mu_s$  (saturation magnetization) that the ferromagnetism is due to a low concentration of Ni atoms occupying wrong lattice sites in the hexagonal C14 structure. According to this model the antistructure Ni-atoms carry magnetic moments and then cause a weak ferromagnetism. The non-ideal axial  $c/a$  ratio seems to support this idea, but Fournier (1985) observed no influence of the pressure on the value of  $T_C$ , in contrast to what Franse et al. (1981) found. Sechovsky et al. (1985) studied the influence of a variation in the 1:2 ratio between U and Ni in  $\text{UNi}_{2+x}$  (with  $0.02 \leq x \leq 0.1$ ) on  $T_C$  and the saturation moment. They could hardly observe any influence of the stoichio-

metry on the ordering temperature and the magnetization. These observations were used as an argument against the antistructure-atom model.

An alternative model to explain the appearance of the magnetism in  $\text{UNi}_2$  was given by Fournier (1980) and Sechovsky et al. (1980). They assumed that charge transfer of (5f/6d) electrons towards the energetically lower 3d states of Ni fills this d band, and then the ferromagnetism arises, according to this model, due to the narrow uranium 5f band. Polarized-neutron diffraction studies on  $\text{UNi}_2$  (Fournier et al. 1986) unambiguously show that magnetization exists only on the U sites. The small saturation moment ( $0.06\mu_B$ ) is the result of an almost cancellation between the spin and the orbital moments of the itinerant 5f electrons ( $\mu_s = -0.45\mu_B$  and  $\mu_l = +0.53\mu_B$ ), while a very small and negative contribution is due to nickel. As in the case of  $\text{UFe}_2$ , these results agree with band-structure calculations (Severin et al. 1992), showing that itinerant 5f electrons partly preserve their orbital moment in the presence of strong spin-orbit coupling. Magnetization measurements on single crystals proved that the hexagonal axis is the easy axis of magnetization (Frings et al. 1986).

Concluding the discussion concerning the origin of the magnetic order, it has been found that the high density of the 5f states at the Fermi level is finally responsible for the magnetic features of  $\text{UNi}_2$ . The comparatively high  $\gamma$ -value ( $65 \text{ mJ/mol K}^2$ ) may be a further indication for the high density of states at  $\epsilon_F$  and, as a consequence, for the appearance of spin fluctuations.

Coming now to the transport properties, the only measured transport phenomenon is the temperature dependence of the electrical resistivity, which is given in fig. 70 (Sechovsky et al. 1980). The arrow indicates the ordering temperature as obtained from the maximum in  $d\rho/dT$ , which is also given in this figure. The most interesting is the pronounced negative curvature in  $\rho$  versus  $T$ , beginning above the Curie

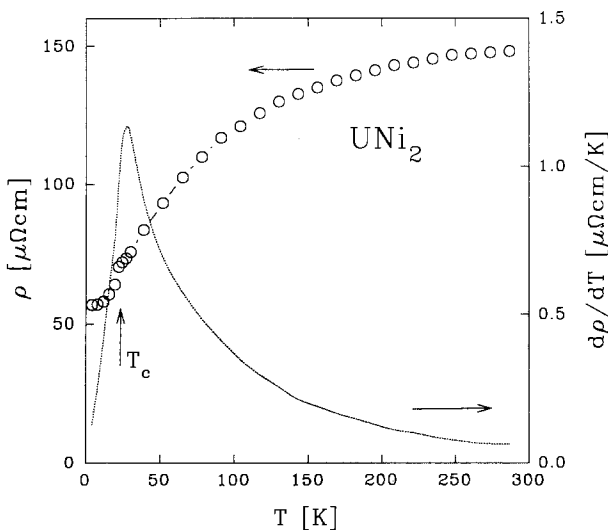


Fig. 70. The temperature dependence of the resistivity of  $\text{UNi}_2$ . The arrow indicates the Curie temperature. The dashed line gives  $d\rho/dT$  (Sechovsky et al. 1980).



temperature, which indicates the dominating contribution to the resistivity from spin fluctuations in the narrow 5f band.

Comparing the transport phenomena of the R- and An-3d-metal Laves phases, we ascertain that among R-3d series the  $RNi_2$  compounds are most easily to understand. Since the d band of Ni is almost filled, the 3d electrons are not involved in the transport processes. Magnetic scattering appears only due to the well-localized 4f moments of the R ions. An explanation of the transport properties of the  $RCo_2$  and  $RMn_2$  compounds is more difficult. This is because the magnetic state of the Co and Mn atoms depends very sensitively on whether the R ions carry magnetic moments. For example, in the  $RCo_2$  compounds induced Co moments exist in the magnetic-ordered state. The transport phenomena in these compounds are strongly influenced by spin fluctuations in the paramagnetic state. The effect of the spin fluctuations is most clearly observable in the transport phenomena of the non-magnetic  $YCo_2$  and  $LuCo_2$  compounds. The resistivity data of  $RFe_2$  show that the Fe 3d moments behave more like local moments, which clearly follows from considering the temperature variation of the resistivity and the thermopower of  $YFe_2$  and  $LuFe_2$ .

Since there are mainly electrical resistivity data of U-3d compounds available, only these data are used for the comparison. Within this family  $UNi_2$  is not isomorphous with the others, but crystallizes in the hexagonal C14 Laves phase.  $UNi_2$  and  $UFe_2$  show ferromagnetism, whereas  $UMn_2$  and  $UCo_2$  are non-magnetic. Due to the itinerant nature of the ferromagnetism in  $UNi_2$  a very weak anomaly appears in  $\rho$  versus  $T$  at  $T_C$ . This is in contrast with the sharp kink which is observed in the  $RNi_2$  compounds at  $T_C$ .

The temperature variation of the resistivity of all the  $UT_2$  compounds can be fitted by a  $T^2$  term at low temperatures. The prefactor  $A$  is enhanced, typically one order of magnitude larger than those for the  $RFe_2$  compounds. A further characteristic feature of the  $UT_2$   $\rho(T)$  curves is the curvature at elevated temperatures, irrespective whether the material is magnetically ordered or not. Both the large coefficient  $A$  and the saturation tendency at higher temperatures underline the pronounced influence of spin fluctuations on the resistivity in the  $UT_2$  group of intermetallics. Among the  $RT_2$  series the compounds with Ce behave in all cases exceptionally. Note that the resistivity dependence on the temperature of  $CeFe_2$  and  $UFe_2$  are similar in many aspects (see the inset in fig. 53). Although an investigation of the pseudobinary (U, Ce) $Fe_2$  system by Roy et al. (1989) seems to show that the hybridization of the U 5f electrons with the d band is stronger than that of the Ce 4f electrons.

### 3.5. $RM_3$ and $AnM_3$ intermetallics ( $M = In, Sn$ )

Most of the R and An intermetallics of the 1:3 stoichiometry with non-magnetic partner elements belonging to group III or IV of the periodic table crystallize in the simple cubic  $AuCu_3$ -type structure. In this section compounds with In and Sn are discussed as appropriate characteristic examples.

3.5.1.  $RIn_3$

Antiferromagnetism has been observed for  $RIn_3$  compounds with long-range magnetic order (Buschow et al. 1969a). The highest ordering temperature has been found for  $GdIn_3$  ( $T_N = 48$  K). Magnetization measurements on single crystals performed with some of the  $RIn_3$  compounds in the magnetically ordered state revealed multiple-step magnetization processes in the different crystallographic directions (Stalinsky et al. 1979).

$LaIn_3$  represents one of the non-magnetic members in the family of the  $RIn_3$  compounds. The superconduction transition temperature is 0.71 K. Measurements of the normal-state magnetic susceptibility have been interpreted in terms of the strong exchange-enhanced conduction electron spin susceptibility of the La d band (Toxen and Gambino 1968). The coefficient  $\gamma$  of the electronic specific heat of  $LaIn_3$ , as shown by Grobman (1972), is about  $2 \text{ mJ/mol K}^2$ . This value is surprisingly small when taking into account that the electron-phonon coupling (which obviously exists in this superconducting material) additionally increases the  $\gamma$ -value. The temperature dependence of the resistivity of  $LaIn_3$ , which is given in fig. 71, is typical for a normally non-magnetic intermetallic compound. The inset in this figure shows the Kohler plot ( $\Delta\rho/\rho_0$  versus  $H/\rho_0$ ) of the transverse magnetoresistance of  $LaIn_3$  for various temperatures. As can be seen, the Kohler plot is valid over a wide temperature and field region, indicating the absence of spin-dependent scattering in this material (see section 2.4). From the temperature independence of the Hall coefficient in the range from 4.2 K up to room temperature it was concluded that the density of holes and electrons at the Fermi level is hardly changed by temperature changes (Grobman 1972). The Hall coefficient is depicted in fig. 72. The applied field was 2 T. It is interesting to compare the Hall coefficient of  $LaIn_3$  with that of pure copper at room temperature:  $R_H(\text{Cu}) = -6.09 \times 10^{-11} \text{ m}^3/\text{A s}$ .

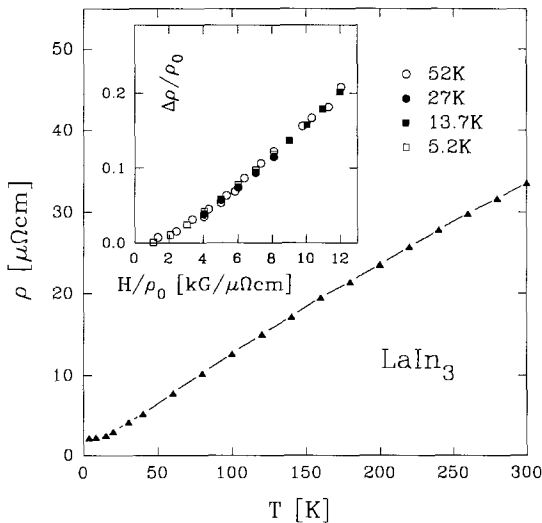


Fig. 71. The temperature dependence of the electrical resistivity of  $LaIn_3$  (Grobman 1972). The inset shows the Kohler plot of the transversal magnetoresistance.

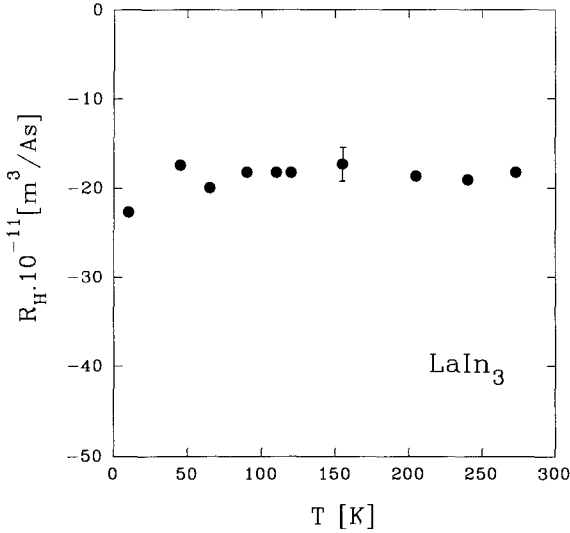


Fig. 72. The Hall coefficient of  $\text{LaIn}_3$  as a function of temperature in a field of  $2\text{ T}$  (Grobman 1972).

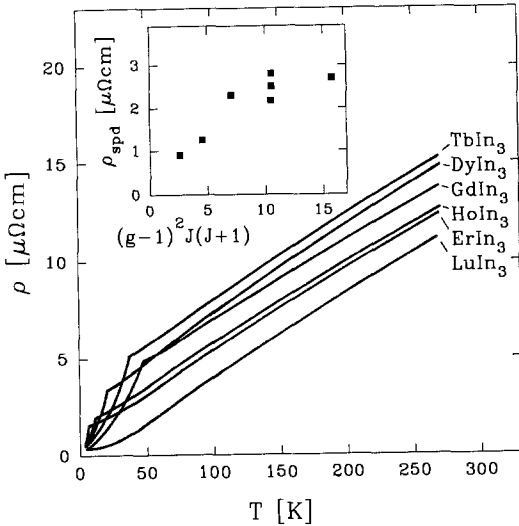


Fig. 73. The temperature dependence of the electrical resistivity of single crystalline  $\text{RIn}_3$  samples measured along the  $\langle 100 \rangle$  direction (Kletowski and Sławinski 1990, Kletowski et al. 1991, Kletowski 1992). The inset shows  $\rho_{\text{spd}}$  as a function of the de Gennes factor,  $(g-1)^2 J(J+1)$ .

Figure 73 shows the temperature dependence of the electrical resistivity of some  $\text{RIn}_3$  compounds obtained with monocrystalline samples along the  $\langle 100 \rangle$  direction (Kletowski and Sławinski 1990, Kletowski 1992, Kletowski et al. 1991). The temperature variation of  $\rho_{\text{mag}}$  has been deduced using  $\rho$  versus  $T$  of  $\text{LuIn}_3$  for the phonon part. These results are plotted in fig. 74. The pronounced curvature observable in  $\rho_{\text{mag}}$  versus  $T$  for  $\text{PrIn}_3$ ,  $\text{NdIn}_3$ ,  $\text{DyIn}_3$ , etc. is due to crystal-field influence. A fit of the  $\rho_{\text{mag}}$  data for  $\text{PrIn}_3$  using eq. (51) has been done with great success by Kletowski and Markowski (1987). The values of  $\rho_{\text{spd}} (\equiv \rho_{\text{mag}}(300\text{ K}))$  do not show proportionality

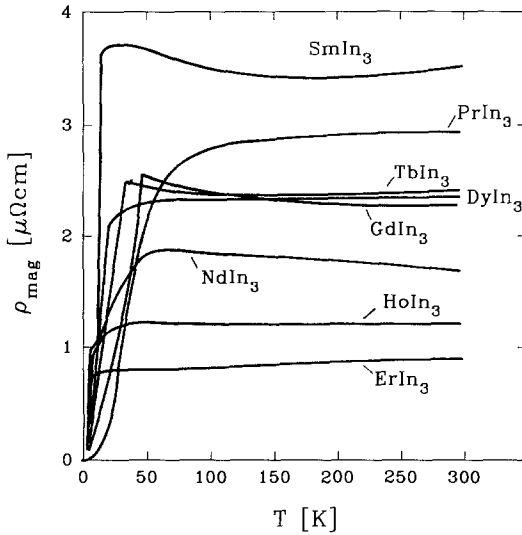


Fig. 74. The temperature variation of  $\rho_{\text{mag}}$  for  $R\text{In}_3$  compounds (Kletowski 1992).

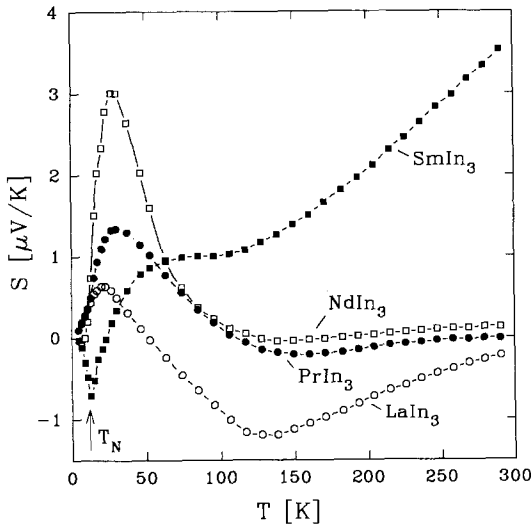


Fig. 75. The temperature dependence of the thermopower of light  $R\text{In}_3$  compounds (Kletowski 1992).

to the de Gennes factor (see the inset in fig. 73). This is understandable since in antiferromagnetic compounds superzone boundary effects influence the resistivity below  $T_N$ . Note that this influence does not exist in the paramagnetic region (Elliott and Wedgwood 1963). A proportionality of  $\rho_{\text{spd}}$  to  $(g - 1)^2 J(J + 1)$  can therefore not be expected (as in ferromagnetically ordered systems like  $\text{RAI}_2$ ).

Figures 75 and 76 show the temperature dependence of the thermopower for some light and heavy  $R\text{In}_3$  compounds, respectively. Since we have a set of thermopower data for almost all the  $R\text{In}_3$  compounds, it is of interest to discuss in more detail which mechanisms determine the sign and the temperature variation of the thermopower. As can be seen from fig. 75, the light  $R\text{In}_3$  compounds (except  $\text{SmIn}_3$ ) show

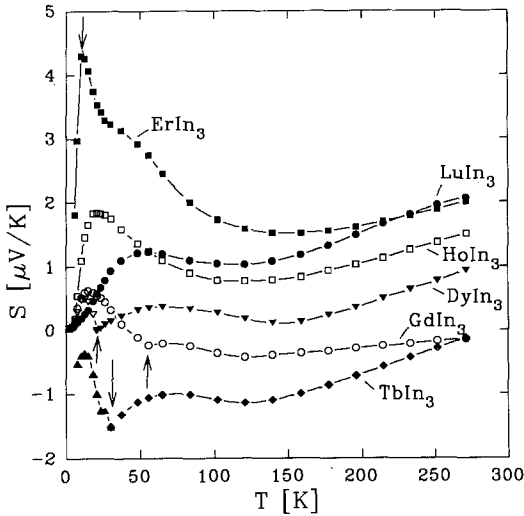


Fig. 76. The temperature dependence of the thermopower of heavy  $RIn_3$  compounds (Kletowski 1992).

small thermopower values around room temperature. There is, however, a systematic increase of the  $S$ -values towards  $LuIn_3$  observable. As has been discussed in sect. 2.3, the sign of the thermopower and its value in the high-temperature region (room temperature is already high in this sense) are mainly determined by the derivative of the density of states at the Fermi level. From the small  $S$ -values observed for the light  $RIn_3$  compounds, we may conclude that the Fermi level is situated in a flat  $N(\epsilon)$  region with a small value of  $N(\epsilon_F)$ . It appears that for the heavy  $RIn_3$  compounds  $\epsilon_F$  shifts towards a region with larger  $dN(\epsilon)/d\epsilon$ . The small  $\gamma$ -value observed for  $LaIn_3$  is evidence for the above conclusion. The exceptional behaviour of  $SmIn_3$  (also with respect to its resistivity behaviour) within this series may be connected with an instability of the  $Sm$  ion, but this has to be studied in more detail.

The onset of magnetic order causes sharp kinks in  $S$  versus  $T$  of  $SmIn_3$ ,  $GdIn_3$ ,  $TbIn_3$ ,  $DyIn_3$  and  $ErIn_3$ . However, the question remains which mechanism is responsible for the humps in the temperature variation of the thermopower below about 100 K. The hump is observed in all the  $S(T)$  curves, with slightly different positions. Since this non-linearity in  $S$  versus  $T$  is observable for all compounds, it is evident that spin-dependent scattering processes alone cannot be the reason. Note that these maxima appear for  $LaIn_3$  and  $LuIn_3$  too, where no magnetic moments exist. This fact also excludes the influence of the crystal field as the only reason for the maxima in  $S$  versus  $T$ .

According to the discussion in the paper of Gratz and Nowotny (1985), it follows that these anomalies are caused by the electron-phonon scattering contribution,  $S_{ph}$ , in eq. (35). Note that we are not speaking of the phonon-drag effect, which can also give rise to anomalies in  $S$  versus  $T$ , but at much lower temperatures (Ziman 1972). The temperature dependences of the resistivity and the thermopower of  $CeIn_3$  are given in fig. 77. The Néel temperature of  $CeIn_3$  is 10 K, obtained from specific-heat experiments (van Diepen et al. 1971, Gao et al. 1985). The  $\gamma$ -value (136 mJ/mol K<sup>2</sup>) is more than fifty times higher than that of  $LaIn_3$ . The intermediate-valence character

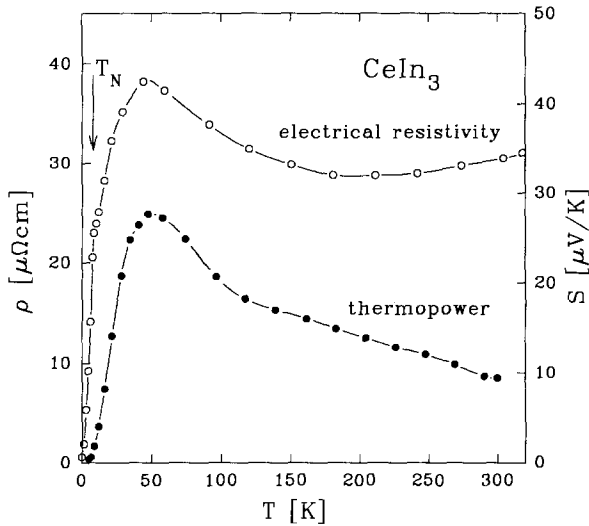


Fig. 77. The temperature dependence of the electrical resistivity (Gao et al. 1985) and thermopower (Kletowsky 1989) of  $\text{CeIn}_3$ .

of the Ce ion in this compound is confirmed by inelastic neutron scattering experiments. The ionic surroundings with cubic symmetry splits the  $J = \frac{5}{2}$  level scheme of Ce into a  $\Gamma_7$  doublet and a  $\Gamma_8$  quartet (Groß et al. 1980). From specific-heat experiments it has been concluded that the doublet is the lower-lying level, with an overall level separation to the quartet of about 150 K. Very similar results were obtained for the isostructural  $\text{CePd}_3$  system (Holland-Moritz and Wohlleben 1982).

### 3.5.2. $\text{AnIn}_3$

$\text{UIn}_3$  orders antiferromagnetically below 95 K (Buschow and van Daal 1971). In the antiferromagnetic state the magnetic moment on the U sites is  $1\mu_B$  (Fournier and Troč 1985). The electronic specific heat coefficient,  $\gamma$ , is about  $50 \text{ mJ/mol K}^2$  (van Maaren et al. 1974).

The temperature-dependent electrical resistivity of  $\text{UIn}_3$  is given in fig. 78. There is a change in the slope of  $\rho$  versus  $T$  around 95 K, but this kink is by far not as sharp as in systems with well-localized 4f moments (compare, e.g., the  $\rho$  versus  $T$  curves of the  $\text{RIn}_3$  compounds).  $\rho_{\text{spd}}(T > T_C)$  is about  $80 \mu\Omega \text{ cm}$  near 100 K, which is high considering the fact that there is a moment of only  $1\mu_B$  responsible for the magnetic scattering. Note that  $\rho_{\text{spd}}$  is only about  $2.5 \mu\Omega \text{ cm}$  for  $\text{GdIn}_3$ . The inset in fig. 78 shows  $\Delta\rho$  versus  $T$  in a bilogarithmic plot ( $\Delta\rho = \rho(T) - \rho_0$ ,  $\rho_0$  is the residual resistivity). An estimation of the coefficient  $A$  from a  $\rho = AT^2$  fit gives a value of about  $25 \text{ n}\Omega \text{ cm/K}^2$ . The comparatively large  $A$  coefficient together with the enhanced  $\gamma$ -value indicates the existence of spin fluctuations in  $\text{UIn}_3$ . The extremely large  $\rho_{\text{spd}}$ -value is understandable since in  $\text{UIn}_3$  the partly delocalized 5f moments order below 95 K.

From the measurements presented in the paper of Buschow and van Daal (1971) it is not clear whether the slope of  $\Delta\rho$  versus  $T$  in the log-log plot changes at low temperatures due to spin-wave scattering. Note that such a change in the coefficient  $A$  has been observed for  $\text{UFe}_2$  and  $\text{CeFe}_2$  in the low-temperature region.

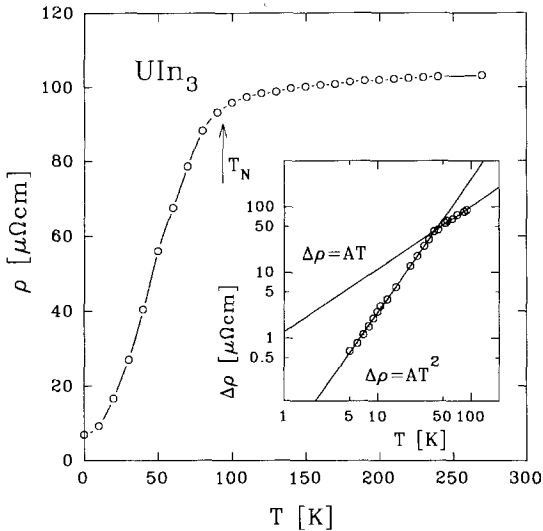


Fig. 78. The temperature dependence of the electrical resistivity of  $\text{UIn}_3$  (Buschow and van Daal 1971). The Néel temperature is marked by an arrow. The inset shows the  $T^2$  dependence of  $\Delta\rho = \rho(T) - \rho_0$  in the low-temperature region.

$\text{NpIn}_3$  orders antiferromagnetically below  $T_N = 10$  K, but the ordered Np-moment is larger than in the above-mentioned compound. Mössbauer experiments revealed an ordered moment of  $1.5\mu_B$ . From susceptibility measurements an effective moment  $\mu_{\text{eff}} = 2\mu_B$  has been obtained. The temperature dependence of the electrical resistivity of  $\text{NpIn}_3$  is shown in fig. 79. Besides a small maximum at  $T_N$  a second transition occurs near 15 K. Metamagnetism has been found between 10 and 15 K. It is interesting to note that 75% of the maximum resistivity value is already reached at 15 K, which is in contrast to the enormous increase of  $\rho$  above  $T_N$  in  $\text{NpSn}_3$ . Nevertheless, there is still a large increase of  $\Delta\rho(T)$  in the paramagnetic range, which can be attributed to crystal-field effects in a localized picture.

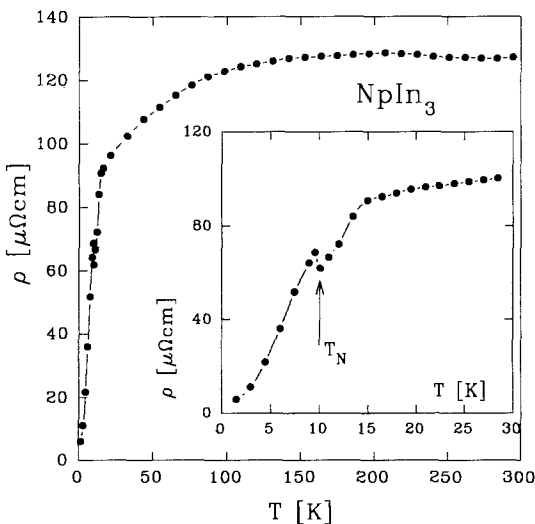


Fig. 79. The temperature dependence of the electrical resistivity of  $\text{NpIn}_3$  (Sanchez et al. 1993). The low-temperature region is enlarged in the inset (the Néel temperature is marked by an arrow).

3.5.3.  $RSn_3$

Among the  $LaM_3$  ( $M = Sn, Pb, In, \text{etc.}$ ) intermetallics  $LaSn_3$  exhibits perhaps the most unusual physical properties.  $LaSn_3$  has a relatively high superconduction transition temperature ( $T_S = 6.42 \text{ K}$ ,  $T_S(LaPb_3) = 4.05 \text{ K}$  and  $T_S(LaIn_3) = 0.7 \text{ K}$  (Toxen et al. 1967)), and its normal-state susceptibility follows the Curie–Weiss law above about 100 K, with an effective moment of about  $1\mu_B$  per formula unit (Welsh et al. 1971). Measurements of the susceptibility performed ten years later by Costa et al. (1981) did not show this Curie–Weiss behaviour, but revealed a nearly temperature-independent susceptibility above 200 K. The experimental value of  $\chi$  is given by these authors as  $165 \times 10^{-6} \text{ emu/mol}$ .

NMR measurements suggested that this large paramagnetic susceptibility is mainly due to the La d orbital contribution (Welsh et al. 1971). In addition, the coefficient  $\gamma$  of the electronic specific heat ( $3 \text{ mJ/mol K}^2$ ) was found to be enhanced by about one third compared to that of  $LaIn_3$  (Grobman 1972), suggesting a significant electron-mass enhancement due to the electron–phonon interaction in  $LaSn_3$ . To study this effect, Stassis et al. (1981) investigated the lattice dynamics of  $LaSn_3$ . A comparison of the phonon dispersion curve of  $LaSn_3$  with that of  $CeSn_3$  reveals that there are differences in the phonon frequency only in the vicinity of some, very few symmetry points. An estimation of the electron-mass enhancement factor ( $\lambda$ ) due to the electron–phonon interaction, in  $\gamma = \gamma_0(1 + \lambda)$  gives for  $LaSn_3$   $\lambda = 0.59$ , which has to be compared with  $\lambda = 0.76$  estimated from McMillan’s formula (McMillan 1968) using the superconducting transition temperature  $T_S = 6.42 \text{ K}$  and the Debye temperature  $\Theta = 230 \text{ K}$ . The calculated density of states reveals a peak just below  $\epsilon_F$ , arising from the flat doubly degenerated bands of the Sn p and La d electrons.

We come now to the transport properties of  $LaSn_3$ . The temperature variation of the electrical resistivity is given in fig. 80. The inset in fig. 80 shows that the Kohler rule (eq. (67)) is valid for  $LaSn_3$  over a wide temperature and field range. This is an

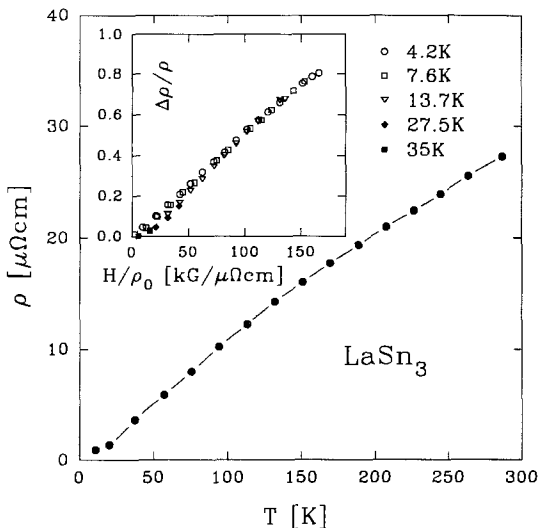


Fig. 80. The temperature dependence of the electrical resistivity of  $LaSn_3$ . The inset shows the Kohler plot of the longitudinal magnetoresistance (Grobman 1972).



indication for the absence of local moments, which has already been concluded from the susceptibility measurements of Welsh et al. (1971). A comparison of the four isostructural  $RM_3$  compounds ( $LaSn_3$ ,  $LaIn_3$ ,  $LuIn_3$  and  $LuGa_3$ ) with respect to their resistivity behaviour has been given by Kletowski (1988). From that investigation follows that the  $\rho$  versus  $T$  curves between 4.2 and 300 K show the most pronounced increase and negative curvature for  $LaSn_3$ , whereas  $LaIn_3$ ,  $LuIn_3$  and  $LuGa_3$  show hardly any curvature, although the increase of  $\rho(T)$  for  $LaIn_3$  is somewhat larger than that of the  $\rho(T)$  curves for the Lu compounds. The increase of the resistivity at low temperature does not follow the predicted  $T^5$ -law according to the Bloch–Grüneisen relation, in any of these four sample. The values of the exponents in a  $T^n$ -law range between 2.2 and 3.6. Kletowski explained the observed deviations from the  $T^5$ -law of the low-temperature resistivity behavior of the  $RM_3$  series as a consequence of the d electron contribution to the scattering processes of the conduction electrons. In our opinion the reason for the steeper increase of  $\rho$  versus  $T$  (observed in almost all of the La compounds) is the much larger electron–phonon interaction existing in most of the La compounds (see also the discussion on  $RAI_2$ ).

The temperature variation of the electrical resistivity of some of the magnetic  $RSn_3$  compounds has been investigated by Stalinsky et al. (1973, 1975). The results for  $GdSn_3$  and  $EuSn_3$ , together with those for  $LaSn_3$ , are depicted in fig. 81. The difference in the slopes of  $\rho$  versus  $T$  of  $EuSn_3$  and  $GdSn_3$  is caused by the crystal-field influence on the Eu ion. An attempt to fit  $\rho_{mag}$  for  $NdSn_3$  to the theory including the crystal-field influence (see eq. (51)), has been made by Kletowsky et al. (1980). The cubic crystal-field parameters  $W = 0.123$  meV and  $x = 0.24$ , obtained from inelastic neutron scattering measurements published by Lethuillier et al. (1975), have been used in the calculation. Good qualitative agreement between the theoretical calculations and experimental data has been obtained.

Resistivity measurements on single crystal samples along the  $\langle 001 \rangle$  direction revealed that  $\rho_{spd}$  of the  $RSn_3$  compounds is not proportional to the de Gennes

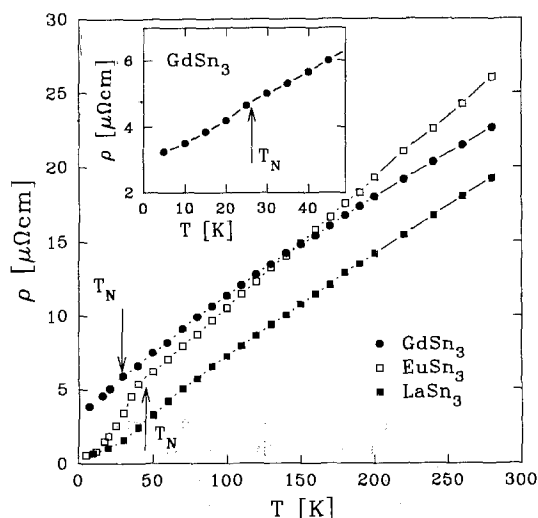


Fig. 81. The temperature dependence of the electrical resistivity of  $EuSn_3$  and  $GdSn_3$  compared with that of  $LaSn_3$  (Stalinski et al. 1975). The temperature range in the vicinity of  $T_N$  is enlarged for  $GdSn_3$  in the inset.

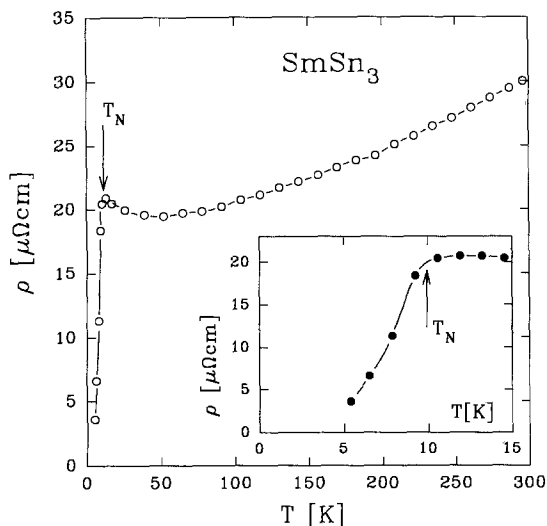


Fig. 82. The electrical resistivity of  $\text{SmSn}_3$  as a function of temperature (Kasaya et al. 1985). The low-temperature range is enlarged in the inset.

factor. Since these materials are antiferromagnets, superzone boundary effects might render an estimation of  $\rho_{\text{spd}}$  impossible (see the discussion on the resistivity of pure R metals).

Among the  $\text{RSn}_3$  compounds  $\text{SmSn}_3$  is a very interesting material. This is because Kasaya et al. (1985) discovered that  $\text{SmSn}_3$  shows Kondo-like behaviour. As is shown in fig. 82, above the Néel temperature ( $T_N = 9.6$  K) the  $\rho$  versus  $T$  curve exhibits a minimum, somewhat above 50 K. Such resistivity minima above the Néel temperature have been found in a number of Ce-based Kondo compounds, such as  $\text{CeAl}_2$ ,  $\text{CeCu}_2$ ,  $\text{CeCu}_5$ , etc.  $\text{SmSn}_3$  was one of the first examples showing the Kondo effect in the family of Sm compounds. It is interesting to see that there is no sign of a Kondo effect

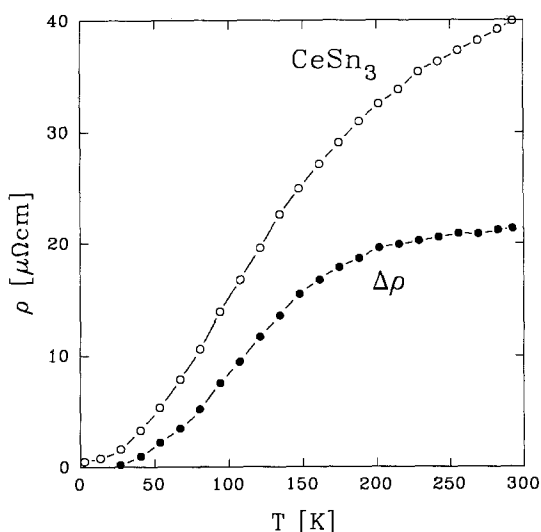


Fig. 83. The electrical resistivity of  $\text{CeSn}_3$  and the difference  $\rho(\text{CeSn}_3) - \rho(\text{LaSn}_3)$  as a function of temperature (Sereni 1980).

observable in  $\text{SmIn}_3$ . From a comparison of the temperature variations of the lattice constants of  $\text{SmSn}_3$  and  $\text{LaSn}_3$  it was concluded that Sm does not exhibit intermediate-valence effects in  $\text{SmSn}_3$ .

As in nearly all the cases discussed so far, the corresponding Ce compound in the series behaves exceptionally. A first hint for the intermediate-valence state of Ce in  $\text{CeSn}_3$  has been found from the lattice constant when it is compared to the lattice constant of  $\text{LaSn}_3$ . In fig. 83 the temperature variation of the resistivity of the  $\text{CeSn}_3$  compound is shown, together with the difference  $\Delta\rho = \rho(\text{CeSn}_3) - \rho(\text{LaSn}_3)$  (Sereni 1980). Sereni (1980) explained the increase of  $\Delta\rho$  with increasing temperature by the temperature-induced  $\text{Ce}^{4+} \rightarrow \text{Ce}^{3+}$  transition.

### 3.5.4. $\text{AnSn}_3$

For the series of the  $\text{UX}_3$  intermetallics (X means an element belonging to group IV in the periodic table, i.e. Si, Ge, Sn and Pb) various experiments revealed that the 5f electrons are to a large extent delocalized in  $\text{USi}_3$  and exhibit a more narrow band-like behaviour as X goes from Si to Pb. For example, as the lattice constant becomes larger ( $\text{USi}_3$ : 4.035 Å,  $\text{UGe}_3$ : 4.206 Å,  $\text{USn}_3$ : 4.626 Å and  $\text{UPb}_3$ : 4.792 Å), the  $\gamma$ -value in the specific heat increases from 14 mJ/mol K<sup>2</sup> for  $\text{USi}_3$  to 170 mJ/mol K<sup>2</sup> for  $\text{USn}_3$  (Sechovsky and Havela 1988).  $\text{UPb}_3$  is an antiferromagnet with a Néel temperature of 31 K (Yuen et al. 1990). For this magnetically ordered system a strongly enhanced  $\gamma$ -value (173 mJ/mol K<sup>2</sup>) has been measured. Alloying experiments with Pb indicate that  $\text{USn}_3$  is an exchange-enhanced paramagnet close to a magnetic instability (Lin et al. 1985). Moreover, alloys of  $\text{USn}_3$  with In show heavy-fermion behaviour (Zhou et al. 1985). A careful discussion of the specific-heat data by Norman and Koelling (1986) revealed that below 10 K these data can be made consistent with the existence of a  $T^3 \ln T$  term, but, as was shown in that publication, subtraction of a realistic phonon heat-capacity contribution removes this term. Note that from the

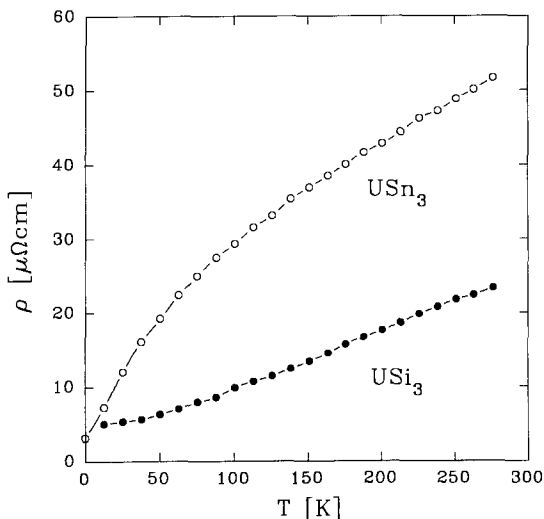


Fig. 84. The temperature dependence of the electrical resistivity of  $\text{USn}_3$  and  $\text{USi}_3$  (Buschow and van Daal 1972).

Fermi-liquid theory a  $T^3 \ln T$  contribution to the specific heat, due to spin fluctuations, is predicted. The question why there is no  $T^3 \ln T$  contribution in  $USn_3$  can possibly be understood from the fact that  $USn_3$  seems to be close to an antiferromagnetic instability. It is known that there is no  $T^3 \ln T$  term for antiferromagnetic spin fluctuations (Moriya 1970).

In fig. 84 the temperature variation of the resistivity of  $USn_3$  is depicted. For comparison the  $\rho$  versus  $T$  curve of  $USi_3$  is also given in this picture. The low-temperature variation of  $\rho(T)$  for  $USn_3$  is proportional to  $T^2$ . Plotting the coefficient  $A$  ( $300 \text{ n}\Omega \text{ cm/K}^2$ ) from the  $T^2$ -fit versus the  $\gamma$ -value reveals that  $USn_3$  fits well into the general sequence of spin-fluctuation compounds.

$NpSn_3$  is an antiferromagnet below  $T_N = 9.5 \text{ K}$ , with a strongly reduced magnetic moment of  $0.3\mu_B/Np$ , as determined from Mössbauer-effect measurements. The electronic specific heat coefficient,  $\gamma$ , is very large in the paramagnetic range ( $242 \text{ mJ/mol K}^2$ ) and decreases to  $88 \text{ mJ/mol K}^2$  in the magnetically ordered state (Aldred et al. 1976). Due to the reduced value of the ordered Np-moment,  $NpSn_3$  was considered as an itinerant magnetically ordered compound. But when the heavy fermions were discovered, the very large coefficient  $\gamma$  was attributed to an extremely narrow 5f band. Now  $NpSn_3$  is classified as a heavy-fermion system with a magnetically ordered ground state. Mössbauer-effect studies under pressure are in agreement with this point of view (Kalvius et al. 1990).

Sanchez et al. (1993) have measured the electrical resistivity of a well-characterized polycrystalline  $NpSn_3$  sample. The temperature dependence of the resistivity is reported in fig. 85. The most interesting feature of this  $\rho$  versus  $T$  curve is the huge maximum around 180 K, followed by a Kondo-like decrease towards higher temperatures. Note that the absolute value of  $\rho$  at 180 K is about ten times higher than the resistivity value at  $T_N$ . A simple explanation can be given within the scope of the Kondo model, assuming that the Kondo-screening reduces the moments. With

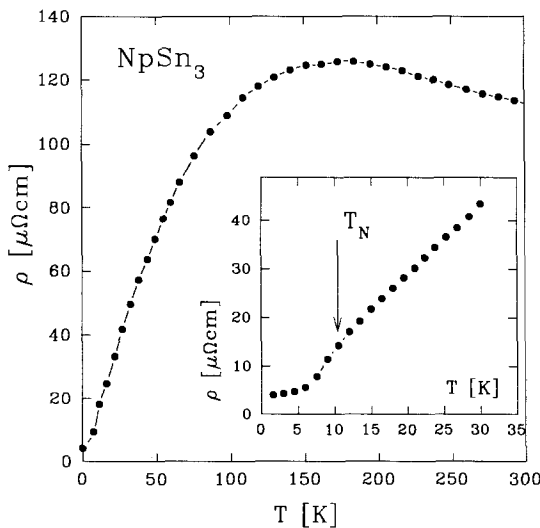


Fig. 85. The temperature dependence of the electrical resistivity of  $NpSn_3$  (Sanchez et al. 1993). The low-temperature region is enlarged in the inset (the Néel temperature is indicated by the arrow).

increasing temperature the screening progressively fades away and thus the Np moments increase. In fact, at high temperatures a Curie–Weiss behaviour is observable with an effective moment much larger than  $0.3\mu_B$  (Sanchez et al. 1993).

### 3.6. $RCu_5$ and $UCu_5$ intermetallics

#### 3.6.1. $RCu_5$

Depending on the ionic R-element radius, the  $RCu_5$  compounds crystallize either in the hexagonal  $CaCu_5$ -type structure (light  $RCu_5$ : R = La up to Sm) or in the cubic  $AuBe_5$ -type structure (heavy  $RCu_5$ : R = Er, Tm and Lu). In the intermediate ionic radius region (Gd, Tb, Dy, Ho and Y) both structures occur, depending on the sample preparation (Buschow et al. 1969). The difficulties in the sample preparation are probably the reason why only very few data concerning their transport properties are given in the literature.

Magnetic susceptibility measurement reveals antiferromagnetic ordering in  $SmCu_5$  at  $T_N = 9$  K (Svoboda et al. 1990), while  $NdCu_5$  orders ferromagnetically at  $T_C = 14.5$  K (Barthem et al. 1989). The temperature-dependent resistivity of  $NdCu_5$  is given in fig. 86. The inset in this figure clearly shows the onset of magnetic order, which is connected with the pronounced decrease of  $\rho_{mag}$  below  $T_C$  (Barthem et al. 1989).

In contrast,  $PrCu_5$  does not exhibit magnetic order, due to a singlet ground state of the  $Pr^{3+}$  ion (Andreeff et al. 1981).  $PrCu_5$  can serve as a convenient example to illustrate the influence of the crystal-field splitting on the transport properties, because of its non-magnetic ground state and the comparatively small energy separation between the ground state and the first excited state ( $\Gamma_6 - \Gamma_1 = 37.5$  K). In fig. 87 the temperature dependence of the electrical resistivity of  $PrCu_5$ , together with that of  $LaCu_5$ , is shown. Assuming that  $\rho_{ph}(PrCu_5) = \rho_{ph}(LaCu_5)$ , the temperature dependence of  $\rho_{mag}$  for  $PrCu_5$  has been obtained, and is depicted in fig. 88. Using the

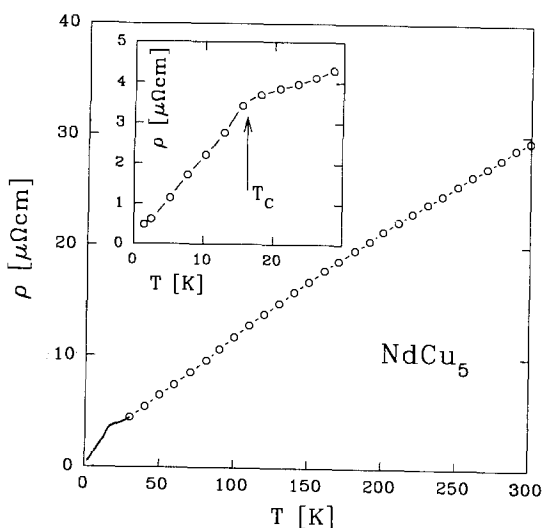


Fig. 86. The temperature dependence of the electrical resistivity of  $NdCu_5$  (Barthem et al. 1989). The low-temperature region is enlarged in the inset.

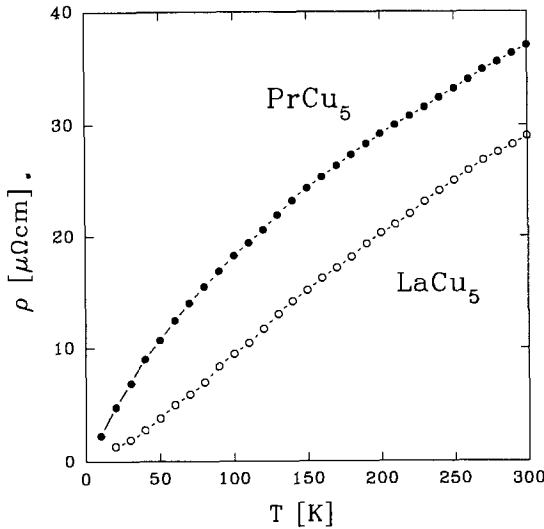


Fig. 87. The temperature dependence of the electrical resistivity of PrCu<sub>5</sub> and LaCu<sub>5</sub> (Takayanagi 1984).

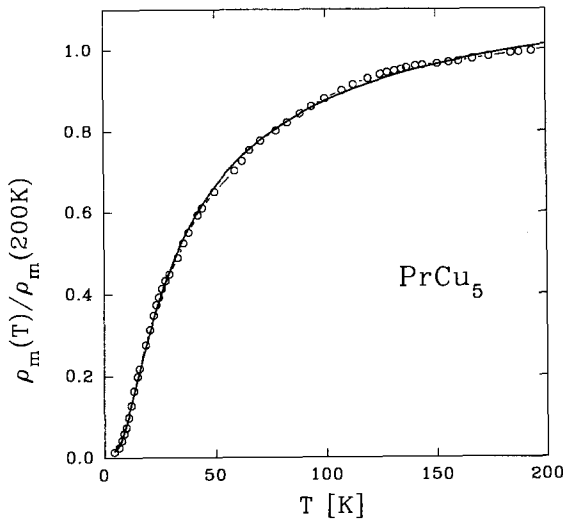


Fig. 88. The magnetic contribution to the resistivity normalized to  $\rho_{\text{mag}}(200\text{K})$  as a function of temperature for PrCu<sub>5</sub> (Takayanagi 1984). The solid curve is calculated using the crystal-field level scheme of Pr<sup>3+</sup> taken from Goremychkin et al. (1988).

crystal-field parameters from inelastic neutron scattering experiments (Goremychkin et al. 1988), the temperature dependence of  $\rho_{\text{mag}}$  has been calculated with eq. (51) by Takayanagi (1984). Comparison with the experiment shows good agreement (see fig. 88).

A fascinating variety in the transport phenomena is observable in the Ce- and Yb-based Cu<sub>5</sub> compounds. Owing to the proximity of the respective 4f<sup>1</sup> and 4f<sup>13</sup> configurations to that of an empty or a completely filled shell, the 4f-electronic configuration may become unstable.

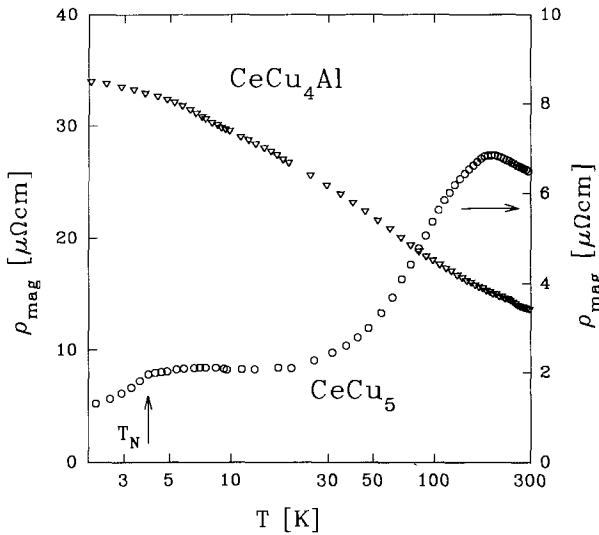


Fig. 89. The magnetic contribution to the electrical resistivity of  $\text{CeCu}_5$  and  $\text{CeCu}_4\text{Al}$  plotted as  $\rho_{\text{mag}}$  versus  $\ln T$  (Bauer et al. 1991).

As is discussed in sect. 2.3, the resulting hybridization of the 4f states with the conduction band is associated with the appearance of a Kondo-type interaction (Ce compound) and valence fluctuation (Yb compound). In fig. 89 the temperature dependence of  $\rho_{\text{mag}}$  of  $\text{CeCu}_5$  is given. At 4 K a phase transition to a magnetic-ordered state occurs, which is followed by a certain type of magnetic reorientation slightly below  $T_N$ . A shallow minimum above the ordering temperature has been attributed to the Kondo effect (Bauer 1991). A doublet ground state, well-separated from the first excited level, is proposed as the Ce-ion crystal-field level scheme (providing a large difference between the Kondo temperature and the crystal-field splitting), to explain the transport properties of  $\text{CeCu}_5$  (Bauer et al. 1987b). Investigations of the temperature dependence of the thermopower by Bauer et al. (1987b) confirm the influence of both the Kondo and the crystal-field effect on this transport coefficient.

A variety of different behaviours of the transport coefficients has been observed in CeCu-based compounds where Cu is substituted by Al or Ga. Such substitutions are possible for at least two Cu atoms without altering the  $\text{CaCu}_5$ -structure. The change of the physical properties has been attributed to a strong variation of mutual interaction mechanisms as the Kondo effect, the crystal-field splitting or the RKKY interaction (Bauer et al. 1990a, 1991, Bauer 1991).

In fig. 89  $\rho_{\text{mag}}(T)$  for  $\text{CeCu}_5$  and  $\text{CeCu}_4\text{Al}$  is compared;  $\rho_{\text{ph}}$  was taken from the corresponding isostructural La compounds. The temperature variation of  $\rho_{\text{mag}}$  of  $\text{CeCu}_5$  consists of two  $-\ln T$  regions, which are separated by a maximum at about 190 K. This maximum shifts towards lower temperatures with increasing Al content. For  $\text{CeCu}_4\text{Al}$  this maximum has vanished, while a single, rather extended  $-\ln T$  range now dominates the  $\rho_{\text{mag}}$  versus  $T$  behaviour. At the same time, the long-range magnetic order vanishes at more than 20% Al substitution.

Since the high-temperature maximum in  $\rho_{\text{mag}}$  versus  $T$  is caused by the crystal-field splitting (Cornut and Coqblin 1972), the resistivity data indicate a decrease of the

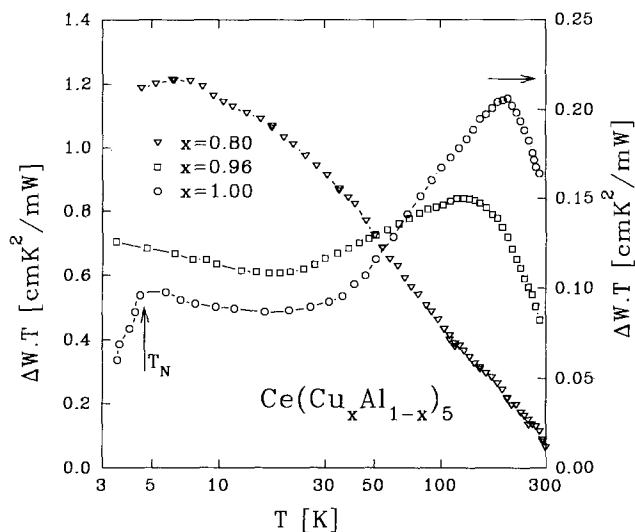


Fig. 90. The magnetic contribution to the thermal resistivity of  $\text{Ce}(\text{Cu}_x\text{Al}_{1-x})_5$  ( $x = 1.0, 0.96$  and  $0.8$ ) plotted as  $T\Delta W$  versus  $\ln T$  (Bauer et al. 1992a).

crystal-field splitting with increasing Al content. The same conclusion has been drawn from the temperature dependence in the thermal conductivity data (see fig. 90). Inelastic neutron scattering experiments finally confirmed the decrease in the energy splitting between the ground-state doublet and the first excited level, from 17 meV in  $\text{CeCu}_5$  down to 5.5 meV in  $\text{CeCu}_4\text{Al}$  (Gignoux et al. 1990).

The decrease of the crystal-field influence is an indication that the 4f states become more delocalized due to the substitution of Cu by Al. This tendency is obviously confirmed by a comparison of the transport properties in the whole concentration range. In fig. 91 the temperature dependence of the normalized electrical resistivity,

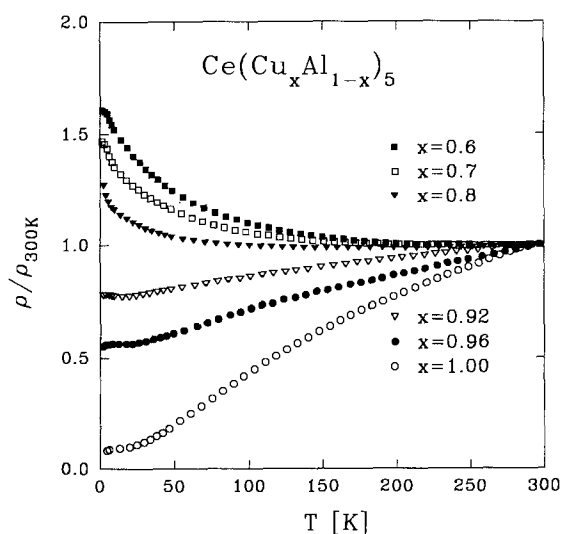


Fig. 91. The normalized resistivity  $\rho/\rho_{300}$  of different  $\text{Ce}(\text{Cu}_{1-x}\text{Al}_x)_5$  compounds as a function of temperature (Bauer 1991).



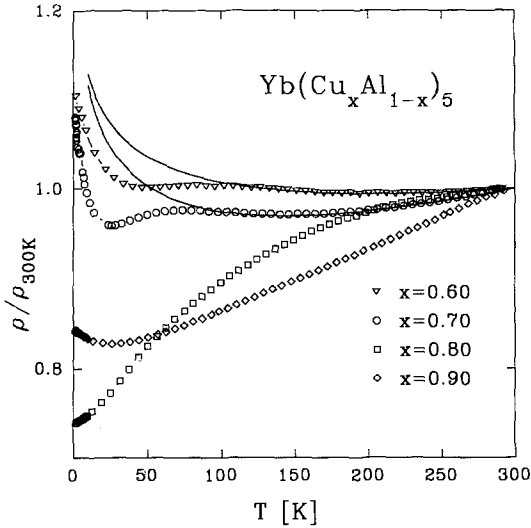


Fig. 92. The temperature dependence of the normalized electrical resistivity  $\rho/\rho_{300}$  of the different  $\text{Yb}(\text{Cu}_x\text{Al}_{1-x})_5$  compounds (Bauer et al. 1992b). The solid lines are the calculated  $\rho(T)$  dependences using the formula  $\rho(T) = \rho_0 + bT + c \ln T$  (see the text).

$\rho/\rho_{300}$  of some  $\text{Ce}(\text{Cu}_x\text{Al}_{1-x})_5$  compounds is given. A normalized representation of the data is chosen in fig. 91 to emphasize the change of  $\rho$  versus  $T$  for  $x = 1$  to 0.6. A joint analysis of the electrical resistivity, magnetic susceptibility and specific-heat data leads to the conclusion that the substitution of Al increases the strength of the Kondo interaction and that a simultaneous cross-over to a non-magnetic heavy-fermion state occurs. Especially  $\text{CeCu}_4\text{Al}$  is characterized by a huge electronic contribution to the specific heat ( $2800 \text{ mJ/mol K}^2$ ) at zero temperature (Kohlmann et al. 1988).

The  $\text{Ce}(\text{Cu}_x\text{Ga}_{1-x})_5$  systems show the same qualitative behaviour (Kohlmann et al. 1988, Bauer et al. 1990b). The long-range magnetic order vanishes at  $x = 0.82$  in this series, while a heavy-fermion state appears.  $\text{YbCu}_5$  crystallizes, like  $\text{CeCu}_5$ , in the  $\text{CaCu}_5$ -type structure. The Yb ion is divalent (or almost divalent) and, therefore, non-magnetic (Iandelli and Palenzona 1971). To study whether a substitution of Cu by Al in  $\text{YbCu}_5$  has an influence on the intermediate-valence state of Yb, investigations of the  $\text{Yb}(\text{Cu}_x\text{Al}_{1-x})_5$  series have been carried out. In fact, a cross-over from the intermediate-valence state to the  $3+$  state for the Yb ion was observed in this series (Bauer et al. 1992b). For the samples with  $x = 0.7$  and 0.6 clear evidence for a  $3+$  state of the Yb ion have been found from the Curie-Weiss behaviour of the magnetic susceptibility. In fig. 92 the  $\rho$  versus  $T$  dependence of the normalized resistivity for samples with various  $x$ -values are depicted. The solid lines in fig. 92 represent the theoretical behaviour according to  $\rho(T) = \rho_0 + \rho_{\text{ph}}(T) + \rho_{\text{mag}}(T)$  for the samples with  $x = 0.7$  and 0.6. The fact that the resistivity data could satisfactorily be fitted, assuming that Kondo-type scattering is dominating  $\rho_{\text{mag}}(T)$  in the higher-temperature region, confirms the assumption that these samples can be considered as Kondo lattices. The discrepancies between theory and experiment below about 100 K are attributed to the crystal-field influence, which splits the  $\frac{7}{2}$  ground state of  $\text{Yb}^{3+}$  into four doublets with eigenstates  $J_z = \pm \frac{1}{2}, \pm \frac{3}{2}, \pm(\alpha\frac{7}{2} + \beta\frac{5}{2})$  and  $\pm(\alpha\frac{7}{2} - \beta\frac{5}{2})$ . If in  $\text{YbCu}_5$  Cu is

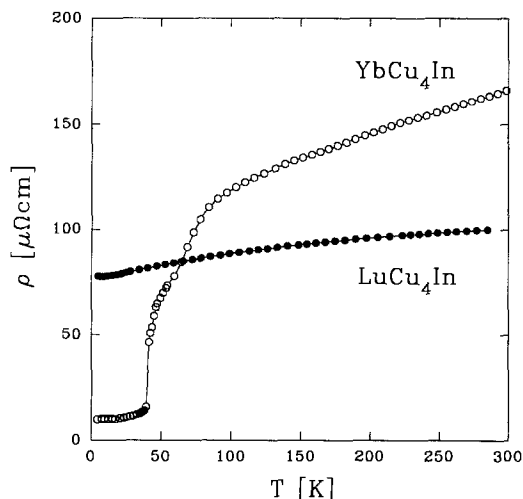


Fig. 93. The temperature dependence of the electrical resistivity of the  $\text{YbCu}_4\text{In}$  and  $\text{LuCu}_4\text{In}$  compounds (Müller et al. 1988). The discontinuity at 40 K indicates the temperature-induced valence transition.

substituted by Ag, In, Au or Pd, the samples exhibit the cubic  $\text{AuBe}_5$ -type of structure (Rossel et al. 1987, Müller et al. 1988). A Kondo-like behaviour was observed for  $\text{YbCu}_4\text{Ag}$  (Besnus et al. 1990).

However, the most interesting behaviour has been found for  $\text{YbCu}_4\text{In}$ , since in that case a temperature-induced valence transition at 40 K occurs (Felner et al. 1987, Yoshimura et al. 1988, Severing et al. 1990). The temperature dependence of the electrical resistivity of  $\text{YbCu}_4\text{In}$  is plotted in fig. 93, together with that of the stable, isostructural  $\text{LuCu}_4\text{In}$  compound (Müller et al. 1988). The sharp drop in  $\rho$  versus  $T$  at 40 K indicates a temperature-induced transition from  $\text{Yb}^{3+}$  at high temperatures to a non-magnetic intermediate-valence state.  $\text{LuCu}_4\text{In}$  exhibits a weak temperature-dependent variation in  $\rho$ , but  $\rho$  is characterized by a large residual resistivity, absent in  $\text{YbCu}_4\text{In}$ .

### 3.6.2. $\text{UCu}_5$

Like most of the U compounds with 1:5 stoichiometry,  $\text{UCu}_5$  crystallizes in the cubic  $\text{AuBe}_5$ -type structure (Misiuk et al. 1973). The magnetic and transport data are rather incomplete for this compound (Sechovsky and Havela 1988).  $\text{UCu}_5$  orders antiferromagnetically at 15 K with an U moment of about  $1.3\mu_B$  (Chakravarthy et al. 1985). Its magnetic susceptibility shows a maximum in the temperature dependence. A value  $\mu_{\text{eff}} = 3.6\mu_B/\text{f.u.}$  was deduced from the linear part of the  $1/\chi$  versus  $T$  plot, measured between 400 and 900 K (Misiuk et al. 1973). Brodsky and Bridger (1973) obtained the values  $\mu_{\text{eff}} = 2.28\mu_B/\text{f.u.}$ ,  $\Theta_p = -78$  K and  $\chi_0 = 1 \times 10^{-8} \text{ m}^3/\text{mol}$  from susceptibility measurements (see also Havela et al. 1986). The electronic specific heat coefficient,  $\gamma$ , of  $\text{UCu}_5$  is about  $200 \text{ mJ/mol K}^2$ , while that of the isostructural  $\text{UNi}_5$  compound is five times smaller,  $\gamma(\text{UNi}_5) = 40 \text{ mJ/mol K}^2$  (van Daal et al. 1975).

To ascertain the role of the 5f electrons in the magnetic and transport properties of  $\text{UCu}_5$ , van Daal et al. (1975) investigated the  $\text{UNi}_{5-x}\text{Cu}_x$  system, in which magnetic order exists only in the vicinity of  $\text{UCu}_5$ , i.e. for  $x > 4.5$ . The resistivity of some

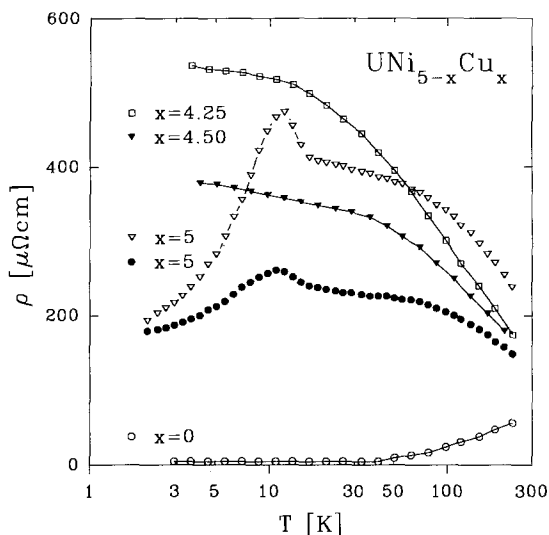


Fig. 94. The resistivity,  $\rho$ , of as-cast samples of  $\text{UNi}_{5-x}\text{Cu}_x$  ( $x > 0$ ) as a function of  $\log_{10} T$ , corrected for the term  $\rho(T) - \rho(0)$  obtained for  $\text{UNi}_5$ . For  $\text{UCu}_5$ , the results after annealing at  $850^\circ\text{C}$  for 1 week are marked with an asterisk.

$\text{UNi}_{5-x}\text{Cu}_x$  compounds is presented in fig. 94 as a  $\rho$  versus  $\log_{10} T$  plot. From these data the phonon resistivity  $\rho_{\text{ph}}$  (as deduced from  $\text{UNi}_5$ ) and  $\rho_0$  are subtracted. The  $\rho$  versus  $T$  curve of  $\text{UCu}_5$  shows a rapid decrease below 15 K, due to the onset of antiferromagnetism. In the paper of van Daal et al. (1975) evidence is given that for samples in which Cu is partly substituted by Ni ( $x \geq 4.0$ ), the U ion is in a mixed-valence state ( $\text{U}^{4+} - \text{U}^{3+}$ ). This is in agreement with an additional increase of the lattice parameter in this concentration region and also with thermopower measurements. The existence of this mixed-valence state of the U ions in the  $\text{UNi}_{5-x}\text{Cu}_x$  compounds and hence f-d hybridization between 3d and 5f electrons have later been shown by X-ray photoemission measurements (Schneider et al. 1982).

The sensitivity of  $\rho$  to deviations from stoichiometry and to the heat-treatment procedure has also been demonstrated by van Daal et al. (1975). This effect can explain some discrepancies between their data and those of Brodsky and Bridger (1973).

Ott et al. (1985) treated  $\text{UCu}_5$  as an example of a magnetically ordered heavy-fermion system. From  $\rho(T)$  measurement they found an additional phase transition in the vicinity of 1 K, which appears to be due to gaps in the excitation spectrum of the heavy quasiparticles (Ott 1987). In connection with this transition, the  $\rho(T)$  dependence of  $\text{UCu}_5$  passes through a minimum at about 1.6 K and increases below that temperature, down to 0.02 K, by a factor of seven. The high value of  $\rho$  observed at 0.02 K is unusual for a heavy-electron ground state and has to be studied in more detail.

### 3.7. An and Ce monopnictides and monochalcogenides

The actinide monopnictides  $\text{AnX}$  ( $X = \text{N, P, As, Sb, Bi}$ ) and monochalcogenides  $\text{AnY}$  ( $Y = \text{S, Se, Te}$ ) crystallize in the NaCl-type structure, with a large variety of magnetic properties (see, e.g., Freeman and Lander 1984, 1985).

From simple volume considerations one might expect essentially trivalent  $An^{3+}$  states in all these compounds, with the possible exception of the nitrides and uranium chalcogenides. Thus, with the pnictogen elements having a  $p^3$  configuration a charge transfer of three electrons fills the p band, so that insulating or semimetallic behaviour can be expected in the  $AnX$  compounds (as is observed in trivalent lanthanide monpnictides). On the other hand, since the chalcogen elements have a  $p^4$  configuration, only two electrons have to be transferred to fill its p band, and all trivalent monochalcogenides should be metallic, with about one electron per formula unit in the 6d-derived conduction band (as in the case of divalent lanthanides, e.g. Eu, for which semiconducting or semimetallic behaviour is observed). This crude description is corroborated by band-structure calculations (Brooks and Glötzel 1980).

### 3.7.1. Actinide monpnictides

While the uranium and neptunium monpnictides are antiferromagnets, plutonium compounds are mostly ferromagnetic (Fournier and Troč 1985). UN is a simple antiferromagnet of type I with  $T_N = 53$  K. The magnetic ( $H-T$ ) phase diagrams of UP and UAs are very complex (figs. 95 and 96). In UP a single- $k$  antiferromagnetic phase (type I) exists below  $T_N = 125$  K, and a transition from a single to a double- $k$  antiferromagnetic phase, type I as well, occurs at about 21 K. In UAs, the same type I single- $k$  antiferromagnetic structure exists below  $T_N = 123$  K. However, below 64 K a double- $k$  type I antiferromagnetic structure is realized. As pointed out by Rossat-Mignod et al. (1984), the difference between the low-temperature phase transitions in UP and UAs is that in the former material no change in the value of the wave vector occurs, whereas in UAs it changes from 1 to  $\frac{1}{2}$ . This modifies the related gap opening at the Fermi surface.

Three features characterize the  $\rho$  versus  $T$  diagram of the simple, antiferromagnetic UN compound, given in fig. 97: (i) a small kink at  $T_N$ , (ii) in the ordered region  $\rho$  is

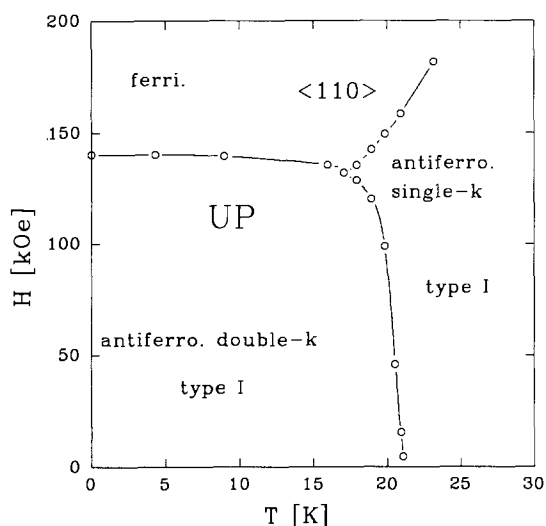


Fig. 95. The magnetic phase diagram of UP (Vogt et al. 1980).

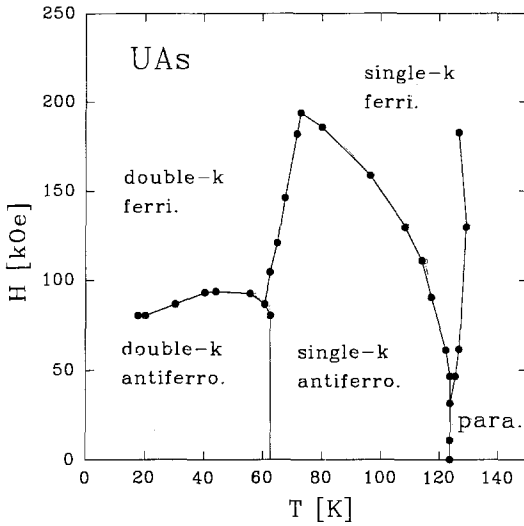


Fig. 96. The magnetic phase diagram of UAs (Rossat-Mignod et al. 1982).

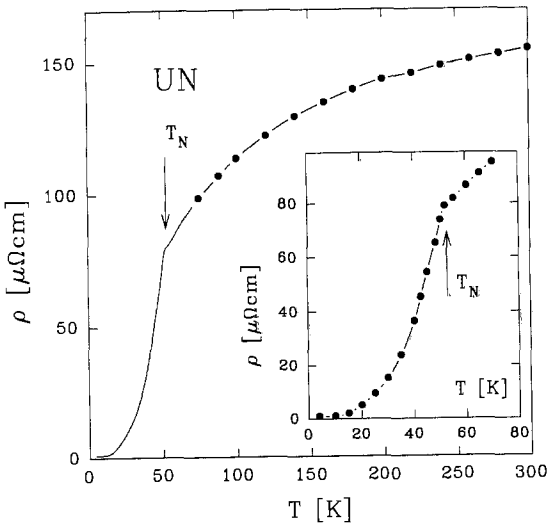


Fig. 97. The temperature dependence of the electrical resistivity of UN (van Doorn and DuPlessis 1977). The low-temperature region is enlarged in the inset.

proportional to  $1 - M_n^{-2}$  ( $M_n$  is the reduced sublattice magnetization) and (iii) a large and non-linear increase above  $T_N$ .

The temperature dependence of the electrical resistivity of UP and UAs, depicted in fig. 98, reflects their magnetic phase diagrams. The transition at 23 K in UP is connected with a discontinuity in  $\rho$  versus  $T$  of  $60 \mu\Omega \text{ cm}$ . The transition from the paramagnetic to the single- $k$  antiferromagnetic phase in UAs leads to a drop in  $\rho(T)$ , very similar to that of UP. The transition to the double- $k$  structure at 64 K is, however, marked by a small peak. Below about 50 K the resistivity of UAs is linear in  $T$ . A strong influence of the magnetic field on the resistivity behaviour has been observed

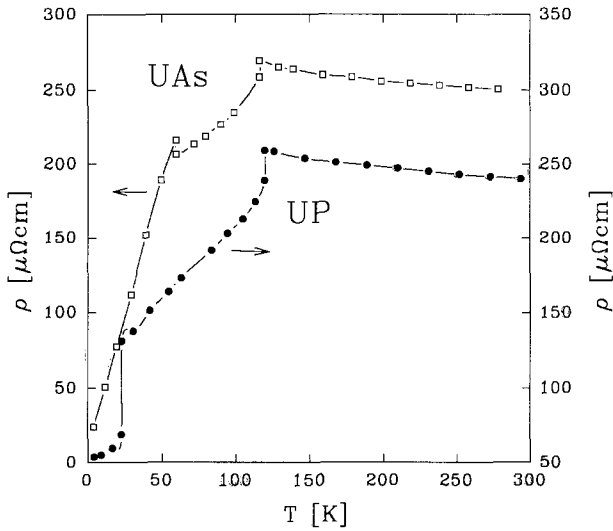


Fig. 98. The temperature dependence of the electrical resistivity of UAs and UP (Schoenes et al. 1984).

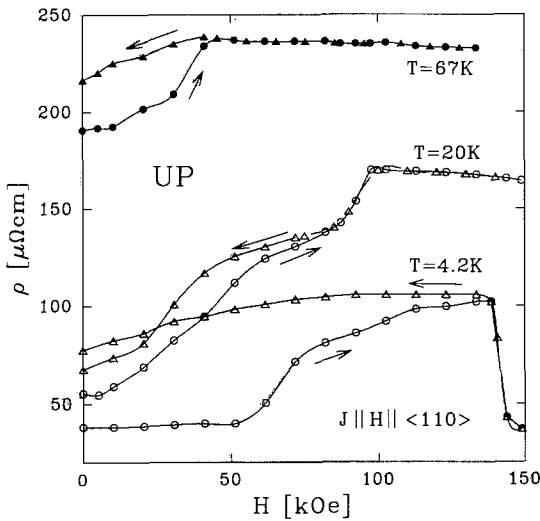


Fig. 99. The electrical resistivity of UP single crystal as a function of the magnetic field for different temperatures (Therond et al. 1987).

in UP and UAs (see figs. 99 and 100). In UP hysteresis in  $\rho$  versus  $H$  in the magnetic ordered state was found by Therond et al. (1987) (see fig. 99). This is in contrast to the almost field-independent  $\rho$  found by Schoenes et al. (1984). These hysteresis effects in  $\rho$  versus  $H$  are strongly dependent on the magnetic history of the sample and seem to be correlated with the distribution of domains in the crystal. However, it is unlikely that this is due to scattering of the conduction electrons by the domain walls, since the variation of the resistivity is too large and, additionally, opposite to what would be expected. Probably this is evidence for anisotropy of the magnetic resistivity.

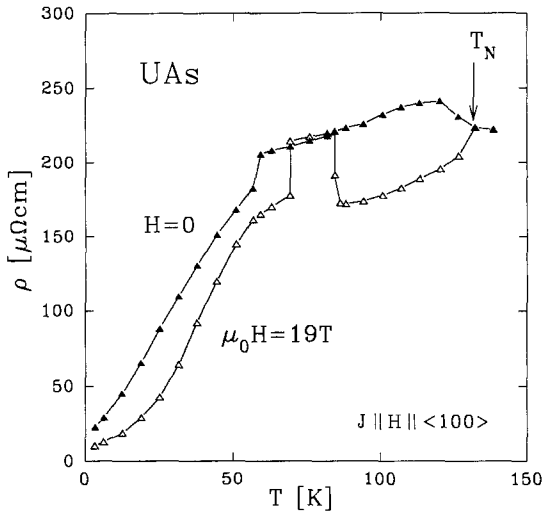


Fig. 100. The temperature dependence of the electrical resistivity of UAs for  $H=0$  and 190 kOe applied parallel to the current direction ( $\langle 100 \rangle$  axis) (Therond et al. 1987).

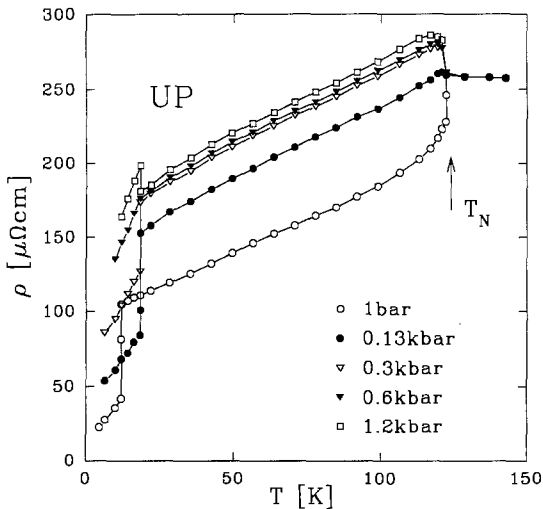


Fig. 101. The temperature variation of the electrical resistivity of a UP single crystal for different pressures applied parallel to the current direction ( $\langle 100 \rangle$  axis) (Bartholin et al. 1990).

A strong influence of uniaxial pressure has been observed by Bartholin et al. (1990) in UP and UAs (see fig. 101). The pressure measurements plotted in figs. 101 and 102 show that a very small uniaxial pressure can change the sign of the resistivity jump.

The temperature dependence of the resistivity of USb, given in fig. 103, is markedly different from that of UP and UAs. It is dominated by a very large and broad maximum centred at 140 K. The value of more than  $1000 \mu\Omega\text{cm}$  at this maximum is typical for a semimetal. As is shown in the inset in fig. 103, the Néel temperature appears as a maximum in  $d\rho/dT$  at  $T_N = 215 \text{ K}$ . The resistivity follows  $T^4$  behaviour up to 45 K; however, a fit with  $T^2 \exp(-\Delta/k_B T)$  is also possible. Both relations have

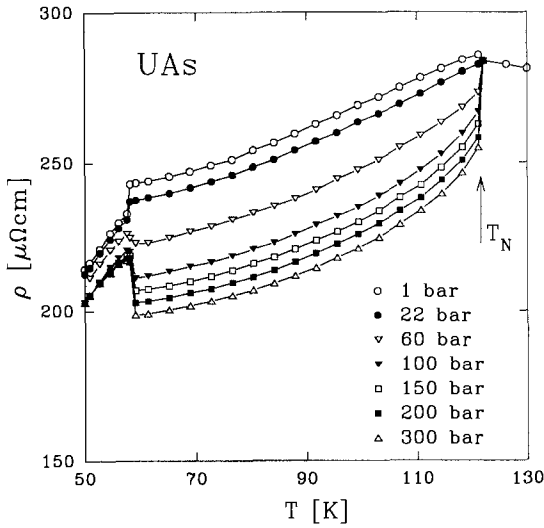


Fig. 102. The temperature variation of the electrical resistivity of a UAs single crystal for different pressures applied parallel to the current direction ( $\langle 100 \rangle$  axis) (Bartholin et al. 1990).

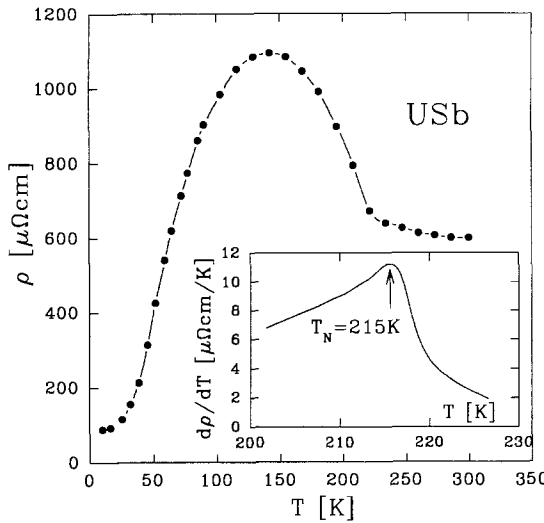


Fig. 103. The temperature dependence of the electrical resistivity of USb. The inset shows  $d\rho/dT$  near  $T_N$  (Schoenes et al. 1984).

been observed in antiferromagnetic spin wave systems. The increase of the resistivity by more than  $400 \mu\Omega\text{cm}$  and the following decrease by about  $1000 \mu\Omega\text{cm}$  when cooling down to 4 K are quite unique and can have their origin in the semimetal-like Fermi surface. We will see below that this is also the case in NpAs and NpSb, which demonstrate the extreme sensitivity of the Fermi surface to the triple- $k$  type I antiferromagnetic structure. Only minor changes are observed in  $\rho$  versus  $T$  in fields up to 10 T.

The temperature variation of the Hall coefficient,  $R_H$ , of USb is displayed in fig. 104 (Schoenes et al. 1984).  $R_H(T)$  increases with decreasing temperature down to  $T_N$ . This



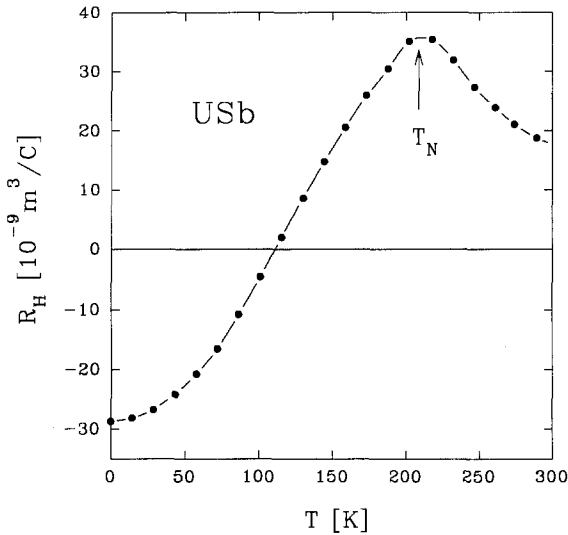


Fig. 104. The temperature dependence of the total Hall coefficient of USb (Schoenes et al. 1984).

can be attributed to  $R_s$ , but no analysis is given in this article. Below  $T_N$  (since the Hall resistivity is always linear in the field) a separation into an ordinary and an extraordinary part is not possible. The assumption  $R_H = R_0$  at 4 K ( $R_s \rightarrow 0$  as  $T \rightarrow 0$ ) gives, in a one-band model, 0.02 electrons per formula unit, confirming the semimetallic nature of USb. Resistivity measurements on NpAs, NpSb and NpBi were performed by Fournier et al. (1992a). While NpAs has a complex magnetic phase diagram with a triple- $k$  type I antiferromagnetic structure in zero field at 4 K (see fig. 105), NpSb simply becomes antiferromagnetic (triple- $k$  type I structure) below  $T_N = 200$  K (Sanchez et al. 1988). The same behaviour has been observed for NpBi below  $T_N$  (191 K) (Sanchez et al. 1993).

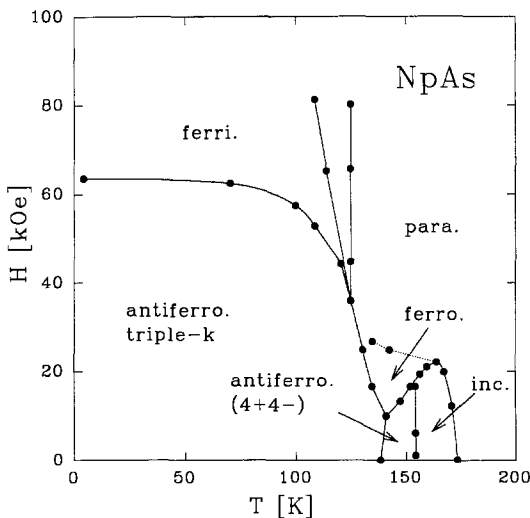


Fig. 105. The magnetic phase diagram of NpAs (Burlet et al. 1987).

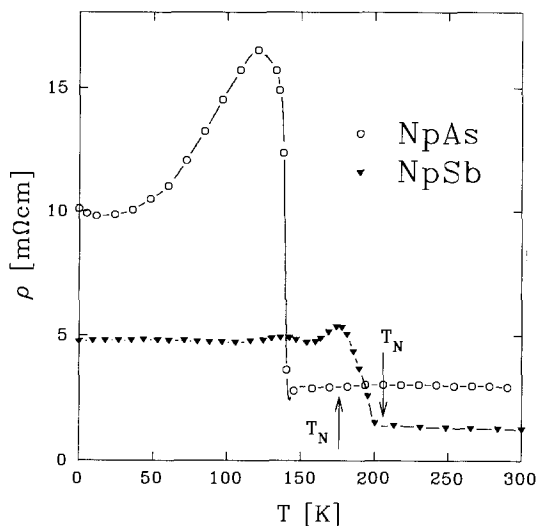


Fig. 106. The temperature dependence of the electrical resistivity of NpAs and NpSb (Fournier et al. 1992a).

The electrical resistivities of NpAs and NpSb are displayed in fig. 106. In NpAs  $\rho$  is about  $3000 \mu\Omega \text{ cm}$  at 300 K and reaches  $16400 \mu\Omega \text{ cm}$  at 123 K. The value at 1.5 K is near to  $10000 \mu\Omega \text{ cm}$ , which is about three times higher than the room-temperature value. Very small anomalies are observed at  $T_N$  (173 K) and at the incommensurate-commensurate transition at 156 K, while at 140 K (which corresponds to the onset of the triple- $k$  type I antiferromagnetic structure) a huge jump appears. This jump is obviously due to a change of the Fermi surface. Below 140 K a strong decrease of the number of carriers occurs. This has been attributed to a reduction of the electron pocket at the  $X$ -point in the Brillouin zone, which corresponds in fact to the magnetic wave vector ( $k$  being parallel  $\langle 001 \rangle$ ).

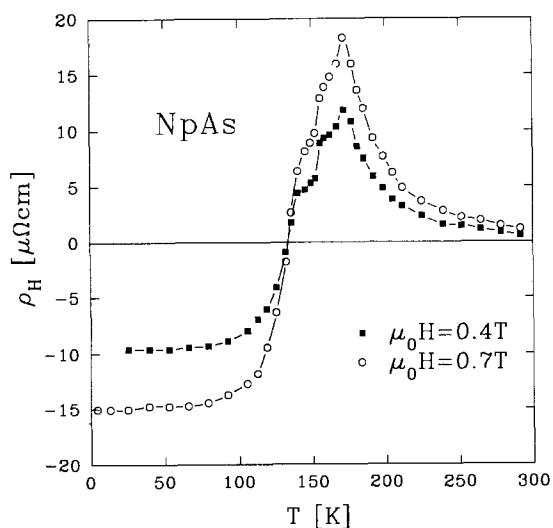


Fig. 107. The temperature dependence of the Hall resistivity of NpAs in fields of 0.4 and 0.7 T (Fournier et al. 1992a).

The temperature dependence of  $\rho_H$  of NpAs has been measured by Fournier et al. (1992a) in magnetic fields of 0.4 and 0.7 T (see fig. 107). The analysis confirms the hypothesis of a strong reduction of the number of electrons, since  $R_0$ , which is about  $0.9 \times 10^{-8} \text{ m}^3 \text{ C}^{-1}$  in the paramagnetic state, becomes about  $21.5 \times 10^{-8} \text{ m}^3 \text{ C}^{-1}$  in the triple- $k$  phase. Simultaneously,  $R_s$  decreases from about  $700 \times 10^{-8} \text{ m}^3 \text{ C}^{-1}$  in the paramagnetic range to the very low value of about  $3 \times 10^{-8} \text{ m}^3 \text{ C}^{-1}$  below 50 K.

The  $\rho$  values of NpSb are smaller than those of NpAs, but the resistivity is still very high compared to metallic systems (see fig. 106). The transition to the triple- $k$  type I antiferromagnetic structure at  $T_N = 200$  K is, as in the case of NpAs, connected with a discontinuity in  $\rho$  versus  $T$ , although it is less sharp and smaller. The resistivity of NpBi (Fournier et al. 1992a) is depicted in fig. 108. While the absolute value at room temperature is only  $800 \mu\Omega \text{ cm}$ , it increases enormously, up to  $154000 \mu\Omega \text{ cm}$  at 1.5 K, without showing a saturation tendency. Thus, while NpAs and NpSb behave as semimetals, with a decrease of the number of charge carries below the onset of the triple- $k$  type I antiferromagnetic structure, in NpBi gaps are opened at low temperatures, causing an enormous increase of  $\rho$  at the lowest temperatures.

PuSb is the only plutonium monopnictide for which detailed resistivity measurements are reported (Blaise et al. 1987, Therond 1986). Above  $T_N$  (82 K) the resistivity has a broad maximum (see fig. 109), above which  $\rho_{\text{mag}}$  shows a Kondo-like behaviour. Below about 60 K PuSb is a ferromagnet. In the ferromagnetic state, above 15 K its resistivity follows an  $AT^2$  behaviour with the coefficient  $A = 90 \text{ n}\Omega \text{ cm/K}^2$ .

Hall effect measurements have been performed on a PuSb single crystal by Therond (1986). The temperature variation of  $\rho_H$  is given in fig. 110. In the paramagnetic phase analysis yields a very low and positive  $R_0$ -value ( $\approx 10^{-2} \mu\Omega \text{ cm/T}$ ). Since the electron mobility (bottom of the 6d band) is larger than the hole mobility (top of the p band), one might assume from eq. (79) that the majority carriers are p-holes. In

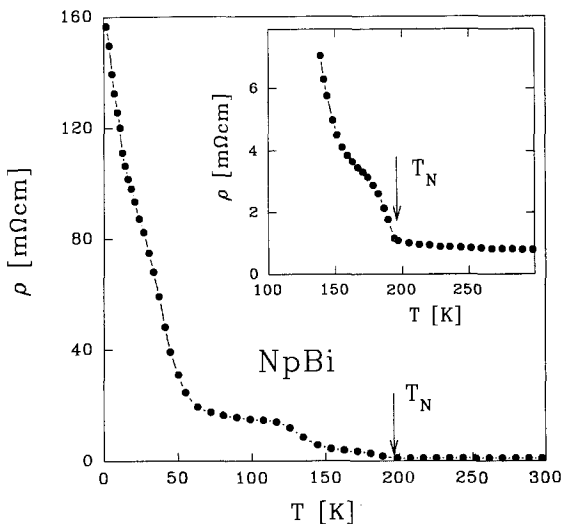


Fig. 108. The temperature dependence of the electrical resistivity of NpBi (Fournier et al. 1992a). The inset shows the temperature region around  $T_N$ .

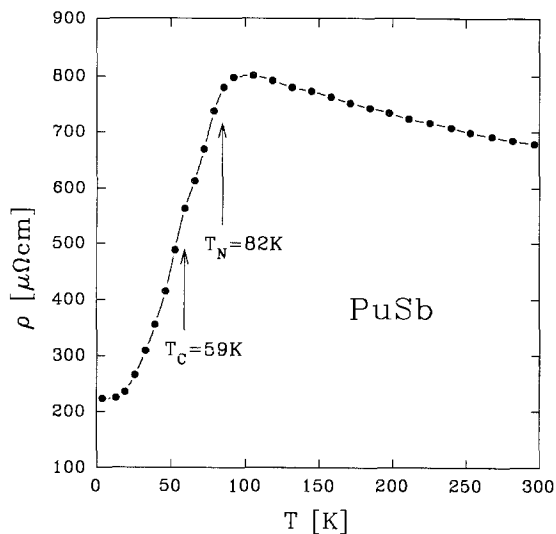


Fig. 109. The temperature dependence of the electrical resistivity of PuSb (Therond 1986).

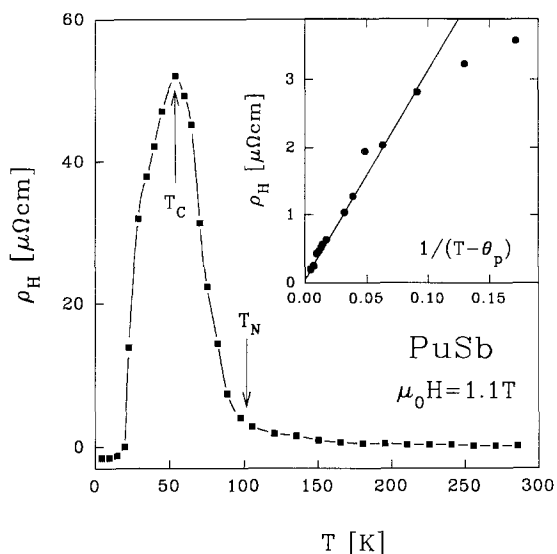


Fig. 110. The temperature dependence of the Hall resistivity of PuSb (Therond 1986). The inset shows the Hall resistivity versus  $1/(T - \theta_p)$  in the paramagnetic region.

the paramagnetic phase  $R_s \approx 200 \mu\Omega \text{ cm}/T$ , i.e.  $R_s$  is four orders of magnitude larger than  $R_0$ . In the ferromagnetic phase  $R_0$  becomes negative and much larger than in the paramagnetic phase:  $R_0 = -0.7 \mu\Omega \text{ cm}/T$ . The thermal variation of  $R_s$  in the ferromagnetic range is similar to that of the electrical resistivity.

In conclusion, actinide monopnictides are essentially semimetals (except the metallic nitrides); the lowest electrical conductivity, found so far, is observed in NpBi, which becomes semiconducting below its Néel point. Thus, the simplest band scheme based on an  $\text{An}^{3+}$  state with an almost filled p band and an almost empty 6d band, is

appropriate to explain their transport behaviour. The narrow 5f band hybridizes weakly, mainly with the p band, which results in highly anisotropic magnetic states. The gap opening due to the onset of the triple- $k$  type I antiferromagnetic structure is very efficient, probably mainly for the electron pocket around the X-point in the Brillouin zone.

### 3.7.2. Actinide monochalcogenides

Uranium monochalcogenides are ferromagnets, while neptunium compounds are antiferromagnets. Surprisingly, plutonium monochalcogenides are non-magnetic, although the  $\text{Pu}^{3+}$  ion is a Kramers ion having a  $5f^5$  configuration.

The temperature dependence of the resistivity of US, USe and UTe single crystals is given in fig. 111 (Schoenes et al. 1984). Below 100 K  $\rho(T)$  of US can satisfactorily be fitted by  $\rho(T) = \rho_0 + AT^2$  with  $A = 3.6 \text{ n}\Omega \text{ cm/K}^2$ . The small coefficient  $A$  is typical for magnon scattering. An estimation of  $\rho_{\text{mag}}(T > T_C)$  gives about  $142 \mu\Omega \text{ cm}$ . The low-temperature data for USe and UTe were fitted to the expression  $\rho(T) = \rho_0 + \rho_{\text{ph}} + c_m T^2 e^{-\Delta/T}$ , giving the values  $c_m = 10 \text{ n}\Omega \text{ cm/K}^2$  for USe and  $33 \text{ n}\Omega \text{ cm/K}$  for UTe. The values for the magnon gap ( $\Delta$ ) are 135 K for USe and 95 K for UTe. Above 140 K  $\rho(T)$  of UTe exhibits an  $\ln T$  decrease when heating up to 750 K. UTe was thus classified as an example of a Kondo lattice with a ferromagnetic ground state (Schoenes et al. 1984).

High-pressure resistance studies on UTe shed more light on this very interesting compound (Link et al. 1992). It was found (fig. 112) that the Kondo-like behaviour is rapidly suppressed;  $T_C$  increases from 104 K (at ambient pressure) to 180 K at about 60 kbar;  $\rho_0$  decreases by a factor two in the same pressure range. Earlier magnetization measurements under smaller pressure (Bartholin et al. 1987) agree well with these results. The variation of  $T_C$  with pressure is 1.43 K/kbar. It was also found that the magnetization decreases under pressure.

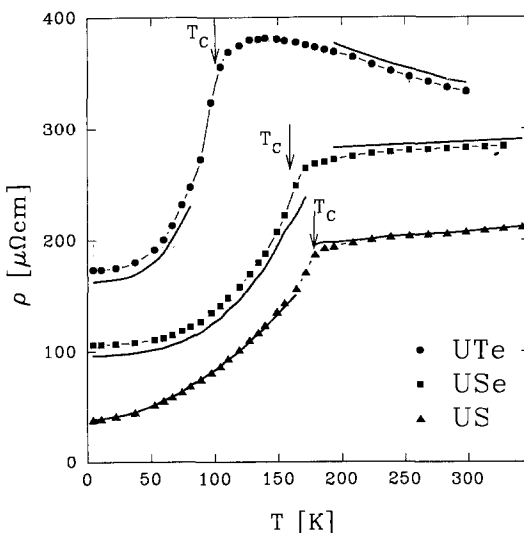


Fig. 111. The temperature dependence of the electrical resistivity of US, USe and UTe (Schoenes et al. 1984). Arrows indicate the ordering temperatures as determined from the maximum in  $d\rho/dT$ . The fits (solid lines) have been shifted by a constant,  $\Delta\rho$ , for clarity in the figure.

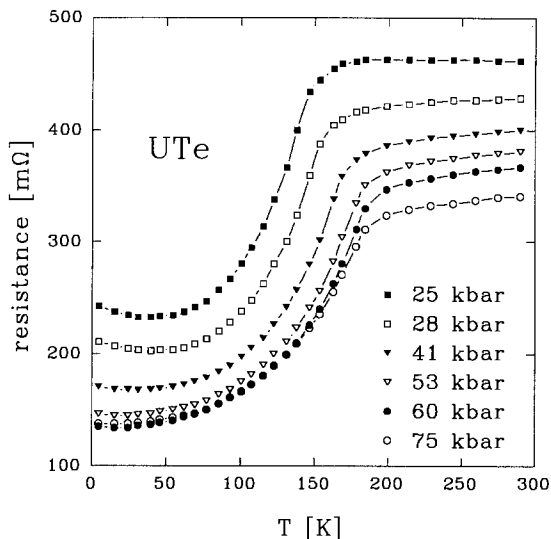


Fig. 112. The electrical resistivity of UTe at various pressures from 25 to 75 kbar (Link et al. 1992).

Resistivity data on neptunium and plutonium monochalcogenides have been obtained on single crystals below room temperature. NpS and NpSe are antiferromagnets (type II) (Blaise et al. 1992), while in NpTe only short-range order appears (Burlet et al. 1990) to be present.

The resistivity versus temperature of a NpS single crystal is depicted in fig. 113 (Fournier et al. 1992b). The relatively high value of  $\rho$  in the paramagnetic range indicates a semimetallic behaviour. Below  $T_N = 23$  K an abrupt increase of the resistivity is observed; its value at 2 K is six times higher than at 25 K. This behaviour is similar to that of NpBi (fig. 108): also here gap opening occurs when

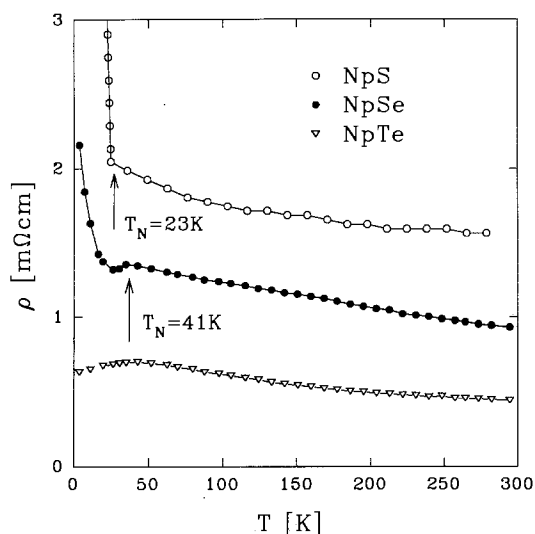


Fig. 113. The temperature dependence of the electrical resistivity of NpS, NpSe and NpTe (Fournier et al. 1992b).

antiferromagnetic order sets in. However, the starting, semimetallic behaviour in the paramagnetic range is much more puzzling, since Np is trivalent in both NpBi and NpS, and one electron is added in NpS. One possible explanation is that strong 5f–6d hybridization induces a gap in the conduction band. This hybridization may also be the origin of the anomalously low ordered moment in NpS ( $\mu_0 = 0.9\mu_B$ ).

The behaviour of NpSe (Fournier et al. 1992b) is slightly different (fig. 113). Below  $T_N = 41$  K  $\rho$  passes through a small minimum around 28 K and then increases rapidly down to 4 K. Above  $T_N$  the resistivity decreases, following Kondo-type behaviour, the room-temperature value being smaller than that of NpS.

In the case of NpTe (Pleska et al. 1988) the resistivity at high temperatures follows Kondo-type behaviour (fig. 113). However, at low temperatures the resistivity goes through a broad maximum around 40 K and then  $\rho(T)$  decreases down to 1.5 K. A comparison of all the three neptunium monochalcogenides is instructive to see the trends in the series, as in the case of the uranium monochalcogenides. Around room temperature the  $\rho$ -values are too high to classify these compounds as metals. It is proposed by Fournier et al. (1992b) that 5f–6d hybridization gives rise to a minimum in the density of 6d states at the Fermi energy (hybridization gap). This might also be the origin of the Kondo-type behaviour. In the case of NpTe this hybridization is strong enough to suppress the long-range magnetic ordering.

Plutonium monochalcogenides form a very interesting series of compounds because of the absence of magnetic order. Considering the lattice parameters, the Pu ion is essentially trivalent ( $\text{Pu}^{3+}$ ), being thus a Kramers ion with a  $5f^5$  configuration, and it should be magnetic. But the susceptibility measured on polycrystalline (Raphael and De Novion 1969, Allbutt et al. 1970, Lam et al. 1974a) and on single crystal compounds (Vogt and Mattenberger 1987) is very small, isotropic and temperature independent, except for a small increase at low temperatures ( $\chi \simeq 300 \times 10^{-6}$  emu/mol).

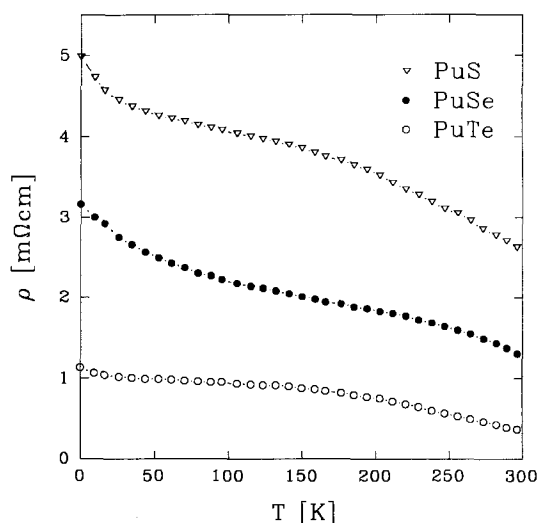


Fig. 114. The temperature dependence of the electrical resistivity of PuS, PuSe and PuTe (Fournier et al. 1990).

The resistivities of three Pu chalcogenides (PuS, PuSe and PuTe single crystals) have been measured by Therond et al. (1987) and Fournier et al. (1990) (fig. 114). The  $\rho(T)$  dependence suggests a semiconducting-like behaviour for all the three compounds. The  $\rho$  versus  $T$  curve for PuS fits around 300 K to high temperature  $\rho(T)$  measurements on a sintered PuS sample (see fig. 115) (Kruger and Moser 1967). Two changes in the slope of  $\rho$  versus  $T$ , at 30 and 200 K, are clearly visible. However, the standard analysis (exponential decay) has little significance, since it requires  $k_B T \ll E_a$ , where  $E_a$  is the activation energy. It is possible at high temperatures in

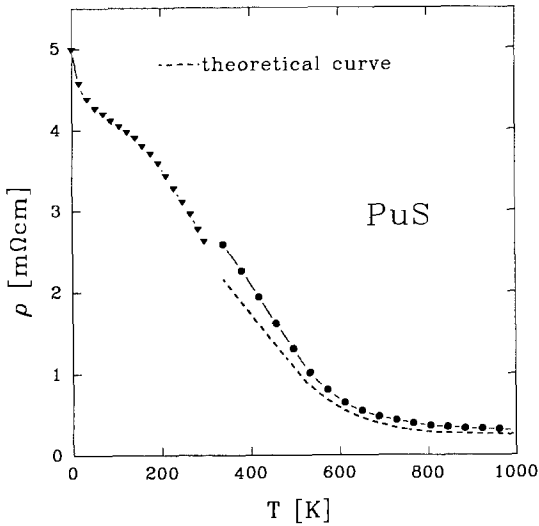


Fig. 115. The temperature dependence of the electrical resistivity of PuS between 2 and 1000 K (Fournier et al. 1990, Kruger and Moser 1967). For the theoretical curve see Kruger and Moser (1967).

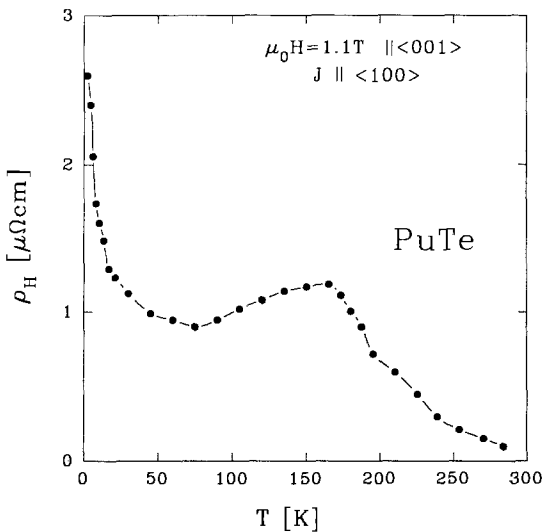


Fig. 116. The temperature dependence of the Hall resistivity of PuTe in a field of 1.1 T (Therond et al. 1987).



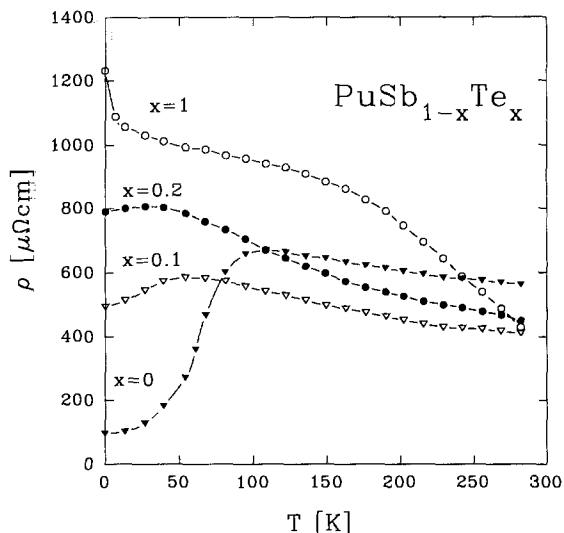


Fig. 117. The temperature dependence of the electrical resistivity of some  $\text{PuSb}_{1-x}\text{Te}_x$  compounds (Therond et al. 1987).

the case of PuS, for which an activation energy of 240 meV was measured by Kruger and Moser (1967). As in the case of the Np monochalcogenides, a gap opening in the conduction band due to 5f–6d hybridization is assumed (Fournier et al. 1990). Hall-effect measurements on PuTe, given in fig. 116 (Therond et al. 1987), support the semiconduction hypothesis.

The fundamental difference between Np and Pu results from the  $5f^5$  configuration of Pu: in such a case, as well as for the  $4f^1$  configuration of cerium, complete Kondo screening is possible, leading to a non-magnetic ground state. This Kondo-type behaviour with localized 5f states seems to be supported by photoemission measurements (Naegle et al. 1989), which show a full p band together with localized 5f states in the final-state spectrum. From susceptibility measurements a Kondo temperature of 400 K is estimated.

The temperature dependence of the resistivity of  $\text{PuSb}_{1-x}\text{Te}_x$  solid solutions is given in fig. 117. Note that a substitution of 10% Te is sufficient to suppress the magnetic order in PuSb. This has been referred as due to p-band filling (Therond et al. 1987).

### 3.7.3. Cerium monpnictides and monochalcogenides

The cerium monpnictides  $\text{CeX}$  ( $X = \text{N, P, As, Sb and Bi}$ ) are isostructural with the actinide ones (NaCl-type structure). These compounds exhibit very unusual magnetic properties (Rossat-Mignod et al. 1984). Kasuya et al. (1982) have shown that both the electronic structure and the  $4f^1$ -level position are important for their magnetic properties.

CeN is a golden material in which the 4f level is pinned at the Fermi energy, so that it is considered as an intermediate-valence compound at low temperatures (Baer and Züricher 1977). Above room temperature there is a progressive localization of the 4f shell, and CeN becomes trivalent at very high temperatures ( $T > 1200$  K). The

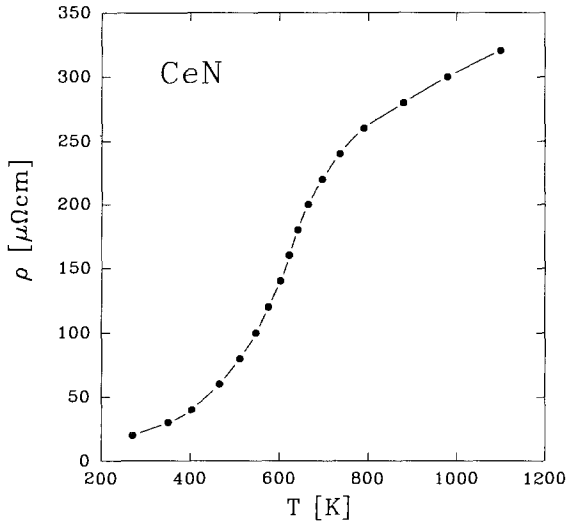


Fig. 118. The temperature dependence of the electrical resistivity of CeN above room temperature (Von Essen and Klemm 1962).

$\rho$  versus  $T$  curve above 300 K is shown in fig. 118 (Von Essen and Klemm 1962). The rapid increase of  $\rho(T)$  above 300 K corresponds to the increasing spin-disorder contribution ( $\rho_{spd}$ ) caused by the progressive localization of the disordered Ce magnetic moments.

All the other Ce mononictides are antiferromagnets with Néel temperatures below 30 K. Hulliger and Ott (1978) have shown that at low temperatures the physical properties of CeP and CeAs are very sensitive to the quality of the crystal and the chemical composition. As an example, the temperature dependence of the resistivity of two single crystals of CeAs is given in fig. 119. As can be seen, in one of these measurements the sharp peak at  $T_N$ , as well as the pronounced saturation around

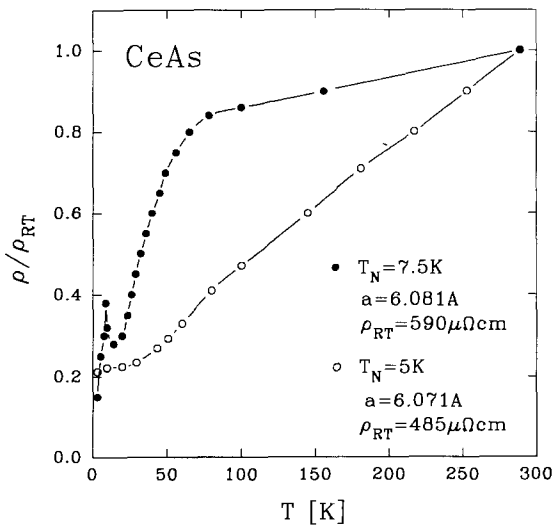


Fig. 119. The normalized temperature dependence of the electrical resistivity of two different CeAs single crystals (Hulliger and Ott 1978).

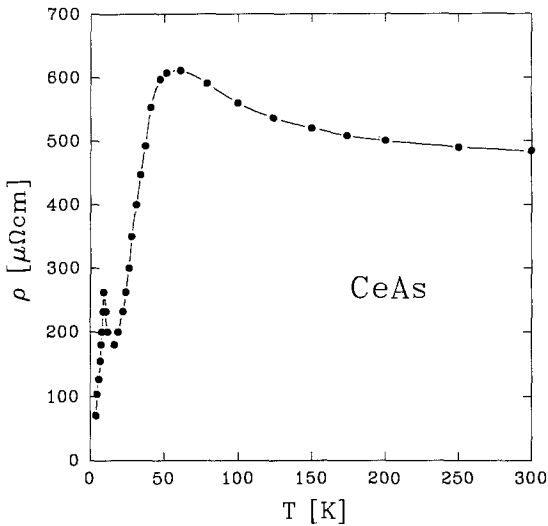


Fig. 120. The temperature dependence of the electrical resistivity of a CeAs single crystal (Suzuki et al. 1990).

70 K are completely absent. This sensitivity is probably due to the fact that CeP and CeAs are semimetals with an extremely low carrier concentration of about 0.001 electron/Ce-atom (Suzuki et al. 1990).

The temperature-dependent electrical resistivity of a good-quality CeAs single crystal, measured by Suzuki et al. (1990), is shown in fig. 120. Apart from the sharp peak at  $T_N = 7.6$  K a broad maximum appears around 60 K, with a Kondo-type behaviour in the higher-temperature region. It was concluded that the Kondo effect is due to the excited  $\Gamma_8$  crystal-field level, which becomes populated thermally. The value of the resistivity at 1.7 K ( $70 \mu\Omega\text{cm}$ ) reflects the low carrier concentration.

In the case of CeP, no sharp peak in  $\rho$  versus  $T$  was observed (Hulliger and Ott 1978). Kwon et al. (1991) grew very good single crystals using a recrystallization method with an excess of P. The temperature dependence of the electrical resistivity of CeP is shown in fig. 121 (Kwon et al. 1991). This result is very similar to that obtained for CeAs (see fig. 120), and in fact the carrier concentration determined by the de Haas–van Alphen (dHvA) effect is nearly the same as that obtained for CeAs (0.001 electron/Ce-atom).

Of great interest are specific-heat data, since the obtained  $\gamma$ -value for CeAs ( $17 \text{ mJ/mol K}^2$ ) is nearly the same as those for CeSb and CeBi (Kwon et al. 1991), although CeSb and CeBi have carrier concentrations of about 0.02 electron/Ce-atom (determined by the dHvA effect), with a mass enhancement factor of about 25. Thus, the mass enhancement for CeAs must be very large, and one can consider it as a heavy-fermion system with an extremely low carrier concentration.

Okayama et al. (1992) published interesting electrical-resistance data of CeP, CeAs, CeSb and CeBi under various external pressures. The resistance,  $R$ , of CeAs at different pressures is given in fig. 122. With increasing pressure the low-temperature peak disappears, as well as the decrease of  $R$  versus  $T$ . At 30 kbar the  $R(T)$  curve of CeAs resembles fairly well that of CeSb at ambient pressure. It is reported that CeP

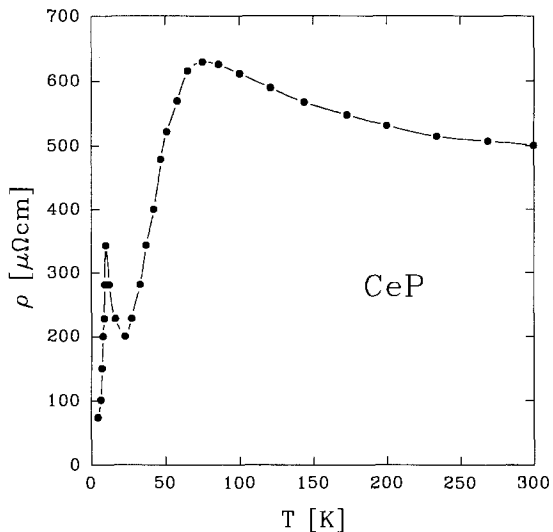


Fig. 121. The temperature dependence of the electrical resistivity of a high-quality CeP single crystal (Kwon et al. 1991).

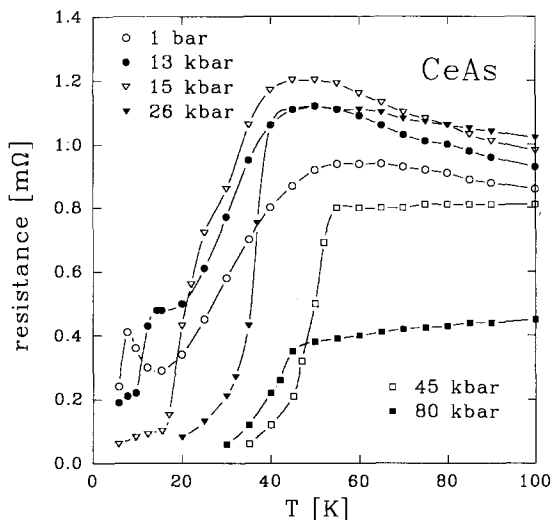


Fig. 122. The temperature dependence of the electrical resistance of CeAs at various external pressures (Okayama et al. 1992).

displays a quite similar pressure dependence; however, no results are given in the literature.

Electrical resistivity measurements on CeSb and CeBi single crystals are displayed in fig. 123 (Suzuki et al. 1981). For CeSb a sharp decrease of  $\rho$  versus  $T$  is observed at  $T_N$  (16.5 K), indicating a first-order magnetic transition. A shallow minimum follows around 80 K. Subtracting  $\rho_{\text{ph}}(T)$ , determined from the isostructural LaSb compound, reveals that  $\rho_{\text{mag}}$  is proportional to  $-\ln T$ , which is typical for a Kondo lattice (Kasuya et al. 1982). The magnetic-field dependence of the electrical resistivity of CeSb at various temperatures is given in fig. 124.

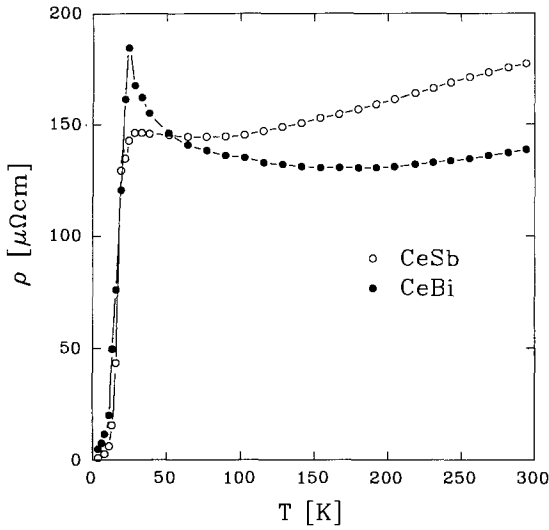


Fig. 123. The temperature dependence of the electrical resistivity of CeSb and CeBi single crystals (Suzuki et al. 1981).

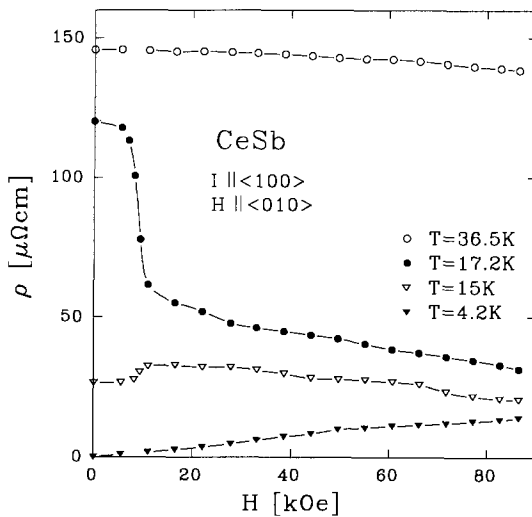


Fig. 124. The magnetic-field dependence of the electrical resistivity of CeSb at various temperatures (Suzuki et al. 1981).

Although in CeBi the magnetic phase transition is of second order, the decrease in its  $\rho(T)$  curve at  $T_N$  (25.5 K) is as sharp as for CeSb. As in the case of CeSb, the complex field dependence of the electrical resistivity of CeBi indicates the existence of different magnetic phase transitions (see fig. 125).

The temperature dependence of the electrical resistivity of CeSb and CeBi at different pressures is reported in figs. 126 and 127, respectively (Okayama et al. 1992). An enormous increase of the resistivity of CeSb is observable near 30 K under pressures above 15 kbar, where a maximum appears in  $\rho$  versus  $T$ . In the case of CeBi there is a smaller change up to 20 kbar. At higher pressure the sharp peak at  $T_N$  changes into a hump, which disappears gradually.

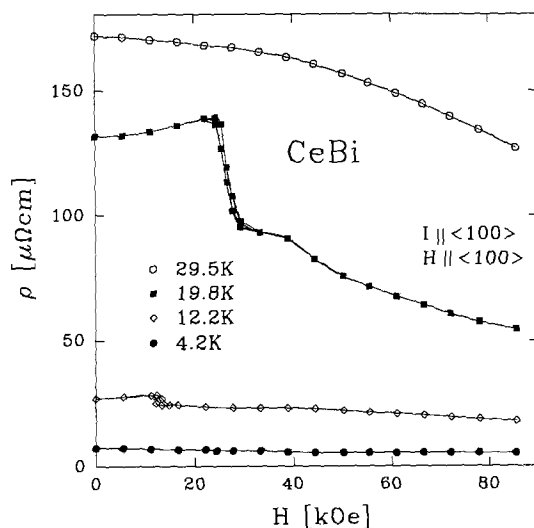


Fig. 125. The magnetic-field dependence of the electrical resistivity of CeBi at various temperatures (Suzuki et al. 1981).

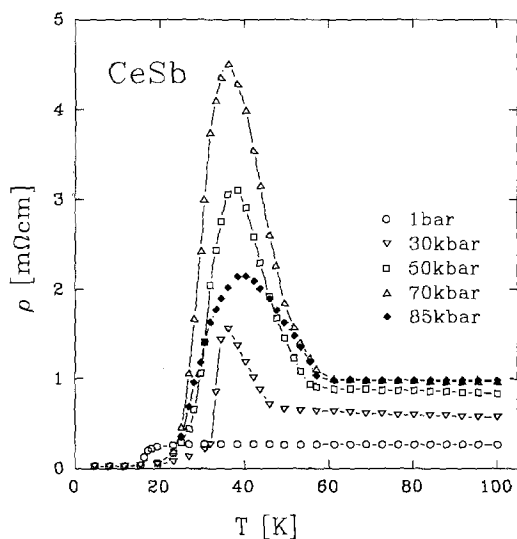


Fig. 126. The pressure dependence of  $\rho$  versus  $T$  of CeSb (Okayama et al. 1992).

No Hall-effect measurements are given for CeP and CeAs. However, Hall-effect measurements have been published for CeSb and CeBi. Since the results for CeSb and CeBi are quite comparable, we present in fig. 128  $R_H$  versus  $T$  only for CeBi, as published by Sera et al. (1985a). The pronounced maximum corresponds to  $T_N$ .  $R_H$  follows the resistivity behaviour well, but the sharp increase towards  $0.8T_N$  is not understood yet.  $R_H$  is nearly constant at high temperatures. Assuming a very small hole mobility (because of strong p-f mixing), the number of free electrons is estimated to be about 0.13 electron/Ce-atom. This is not in agreement with results from the dHvA effect leading to 0.02–0.03 electron/Ce-atom, with a mass enhancement of about

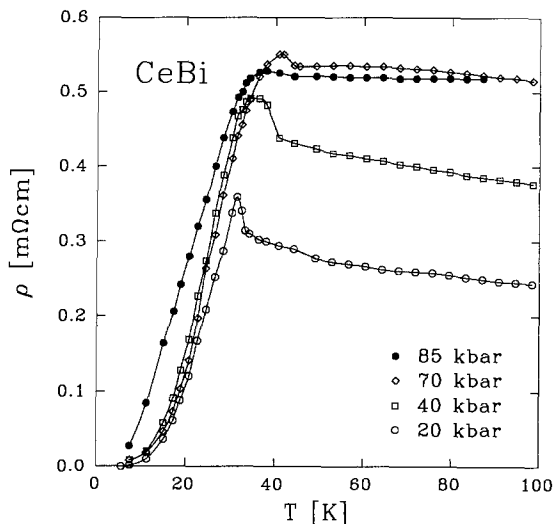


Fig. 127. The pressure dependence of  $\rho$  versus  $T$  of CeBi (Okayama et al. 1992).

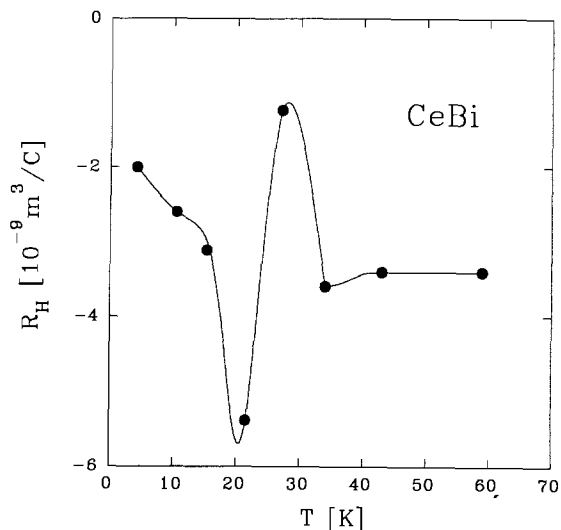


Fig. 128. The temperature dependence of the Hall coefficient of CeBi in the low-temperature region (Sera et al. 1985a).

20. This result illustrates how questionable it is to extract the carrier concentration only from Hall-effect measurements.

Much less efforts have been put in the study of the cerium monochalcogenides CeY (Y = S, Se and Te), since they were considered as rare examples of cerium compounds with normal behaviour. However, the first resistivity measurements on CeS (Schoenes and Hulliger 1985) displayed a temperature dependence similar to that found in CeAl<sub>2</sub>. This prompted a more systematic investigation of the electrical resistivity of CeS, CeSe and CeTe on single crystals in a large temperature region (2 to 1000 K).

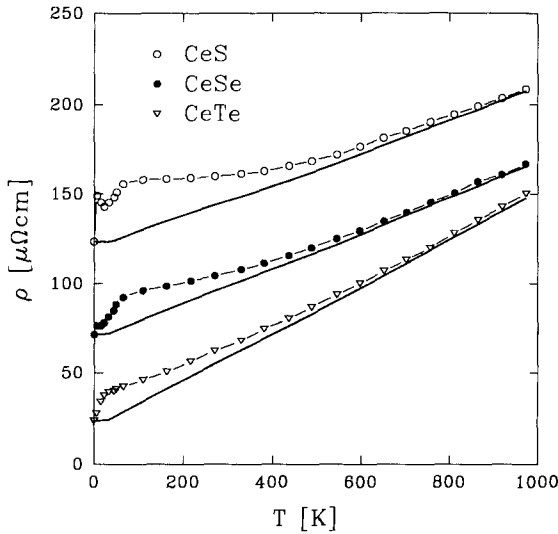


Fig. 129. The electrical resistivity of CeS, CeSe and CeTe single crystals between 2 and 1000 K. The curves for CeSe and CeTe have been shifted down by 50 and 100  $\mu\Omega\text{cm}$ , respectively. The straight lines correspond to the phonon contributions (Schoenes and Hulliger 1987).

The extension to high temperatures allows to derive directly the electron-phonon contribution (fig. 129 shows these results).

The data for CeTe between 2 and 300 K are very similar to those of Sera et al. (1985a). For all these compounds  $\rho$  versus  $T$  approaches asymptotically a straight line when heating to 1000 K, which might be identified as the electron-phonon contribution. Figure 130 shows the temperature dependence of the magnetic resistivity for these three chalcogenides in a  $\rho_{\text{mag}}$  versus  $\log T$  diagram. The temperature variation of  $\rho_{\text{mag}}$  of CeSe and CeS is very similar to that observed for typical Kondo lattices

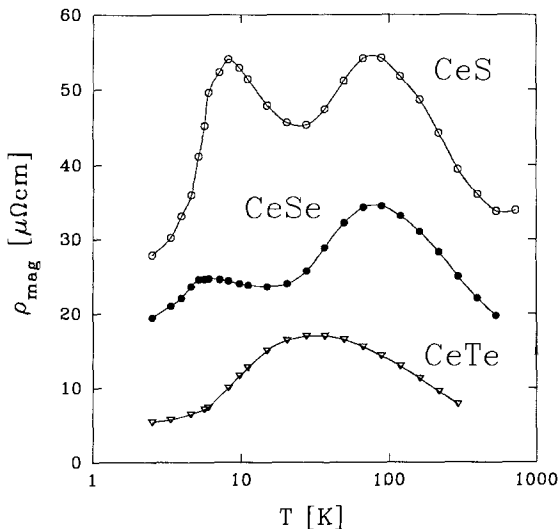


Fig. 130. The magnetic contribution,  $\rho_{\text{mag}}$ , to the electrical resistivity for CeS, CeSe and CeTe in a  $\rho$  versus  $\log T$  diagram. The curves for CeSe and CeS have been shifted up for clarity by 15 and 20  $\mu\Omega\text{cm}$ , respectively (Schoenes and Hulliger 1987).



like  $\text{CeAl}_2$  (see sect. 3.3) and was, therefore, discussed within the scope of the model of Cornut and Coqblin (1972). Thus, cerium monochalcogenides can be classified as dense Kondo systems. The overall crystal-field splitting deduced from the resistivity data is in agreement with that obtained from the susceptibility and inelastic neutron scattering.

Hall-effect measurements on CeTe (Sera et al. 1985b) show an essentially constant  $R_H(T)$ . The normal Hall constant yields one free electron per Ce atom.

A comparison of Ce and An monpnictides and monochalcogenides is very instructive. Although the superimposed p-d band structures are very similar, being issued from that of the corresponding La compounds, the detailed behaviour of the 4f and 5f electrons leads to changes of their transport properties which are really drastic.

Ce-based monpnictides show evidently how difficult it is to obtain reliable data on semimetals having a very small number of carriers. For NpAs the number of carriers (as deduced from Hall-effect measurements) is of the order of 0.001 electron/Np-atom, whereas for CeAs the resistivity behaviour at low temperatures might not be intrinsic and new measurements with samples of good quality are very desirable.

In NpAs, NpSb and USb the onset of a triple- $k$  antiferromagnetic structure gives rise to a strong increase of the resistivity; extrapolating to NpBi, which becomes semiconducting-like. The question is why such a behaviour is not observed in CeAs and CeP, although they have the same magnetic structure. Strong mass enhancement has been found in CeSb and CeBi from Hall-effect measurements. In USb the number of carriers is ten times less. Thus on the 0.001 scale the absolute value of the resistivity is comparable with that of CeP and CeAs. So, due to less mass enhancement, the carrier concentration in NpAs and NpSb might be much less than 0.001, which would be in agreement with the much larger resistivity values. It would be of much interest to have specific-heat data as well as dHvA data for NpAs.

In the case of the monochalcogenides the Kondo effect is present in all of them, but the most exciting behaviour is observed in Np and Pu chalcogenides. Thus, when going from NpBi to NpS, one conduction electron is added, but the  $\rho$  versus  $T$  curve is still the same, with semiconducting behaviour below  $T_N$ ! The reduced ordered moments observed in NpS, NpSe and CeTe are believed to be due to Kondo screening. The most intriguing case is, of course, that of the Pu chalcogenides, which are non-magnetic and semiconducting. It is assumed that complete screening leads to a singlet ground state with a hybridization gap (Fournier et al. 1990). The estimated Kondo temperatures are rather high (400 K), therefore these materials can also be classified as intermediate-valence compounds (Wachter et al. 1991). In that case the 5f states should be pinned at the Fermi level, but photoemission results seem to indicate a more local character of the 5f electrons (Naegle et al. 1989).

Summing up, one can say that the understanding of the transport properties in R and An intermetallics is far better than that of the monpnictides and monochalcogenides. Having available more experimental data would certainly help to improve the theoretical understanding of the transport phenomena in this fascinating group of materials.

#### 4. Summary

In the theoretical introduction the classical transport theory, based on the Boltzmann formalism, is outlined. The aim was to give those readers not familiar with transport phenomena insight into this field of solid-state physics. The discussion of the sum rules (Matthiessen rule, Kohler rule and Nordheim–Gorter rule) is useful since these rules are frequently used in the literature, although their application is limited. The magnetic (spin-dependent) scattering is treated in more detail since this kind of interaction modifies strongly the transport behaviour of the R and An intermetallics.

Difficulties with the selection of the experimental data arose, since the available transport data are unbalanced in favour of the R compounds, except in the case of the monpnictides and monochalcogenides, which are treated at the end of sect. 3. But there is also a striking unbalance for the various transport phenomena. A large number of resistivity measurements is available, but there are only few data on the thermal conductivity, the thermopower, the magnetoresistance and the Hall effect. In spite of these problems we have attempted to find typical isostructural R and An compounds with various f- and d-electron states. If the R (or An) and the partner element are non-magnetic, the temperature variation of their transport phenomena is dominated by electron–phonon scattering. LaPt, ThPt, YAl<sub>2</sub>, YNi<sub>2</sub>, LaIn<sub>3</sub> and LaSn<sub>3</sub> are typical examples.

If the R or An component of the compound has a well-localized magnetic moment, but the other components are non-magnetic in the above-mentioned sense, the behaviour of the resistivity is correctly described by fig. 2 (as long as the crystal-field influence is small). These compounds are usually magnetically ordered via the RKKY interaction mechanism. A sharp kink always occurs at the ordering temperature in all the transport properties. The compounds RPt, RAl<sub>2</sub>, RNi<sub>2</sub>, RIn<sub>3</sub> and RSn<sub>3</sub> are given as examples. The resistivity in the paramagnetic regime is dominated by the temperature-independent spin-disorder scattering contribution,  $\rho_{spd}$ , on which a linear contribution from electron–phonon scattering is superimposed. The influence of the crystal field (if existing) might give rise to a temperature dependence of  $\rho_{spd}$ . With the RPt and RIn<sub>3</sub> systems examples are given where a crystal-field effect on  $\rho_{spd}$  is observable.

Due to the hybridization of the 5f states with the d band, spin fluctuations appear mainly in the light An compounds. UAl<sub>2</sub> has been discussed as a typical example of a spin-fluctuation system which does not order magnetically. Further spin-fluctuation systems with a non-magnetic ground state belonging to the R group are YCo<sub>2</sub>, LuCo<sub>2</sub> and ScCo<sub>2</sub>. The appearance of spin fluctuations is closely connected with the Co 3d states at the Fermi level. The temperature variation of the electrical resistivity of spin-fluctuation systems no longer obeys the Bloch–Grüneisen law, but tends to saturation and exhibits a pronounced  $T^2$  dependence at low temperatures. In all these spin-fluctuation systems with non-magnetic ground state, minima in the low-temperature region of the thermopower appear somewhat below the spin-fluctuation temperature (UAl<sub>2</sub>, YCo<sub>2</sub>, LuCo<sub>2</sub> and ScCo<sub>2</sub> are presented).

The suppression of the spin fluctuations under pressure clearly follows from resistivity experiments on UAl<sub>2</sub> and YCo<sub>2</sub>. The positive sign of the magnetoresistance

observed for  $\text{YCo}_2$  is not in agreement with the theory, which predicts a negative sign for  $\Delta\rho/\rho$  caused by the spin fluctuations. However, this might be due to the superposition of the classical magnetoresistance in  $\text{YCo}_2$ . The temperature variation of the classical magnetoresistance (which is positive in the whole temperature range) is shown for the case of  $\text{YAl}_2$ .

The suppression of the spin fluctuations due to the onset of magnetic order in the 4f moment system is demonstrated in  $\text{RCo}_2$ . The application of an external magnetic field or external pressure reveals a dramatic change in  $\rho$  versus  $T$  of  $\text{RCo}_2$  systems.

Some insight into the role of spin fluctuations has been gained in the magnetically ordered  $\text{UM}_2$  Laves phases ( $M = \text{Fe}, \text{Mn}, \text{Ni}$ ). Within the group of  $\text{RFe}_2$  it is shown that  $\text{CeFe}_2$  is an exception. Its resistivity behaviour is comparable in many aspects to that of  $\text{UFe}_2$ . In both compounds the Fe moments are strongly reduced, but all characteristics of spin fluctuations are observable.

In the  $\text{RM}_3$  and  $\text{AnM}_3$  intermetallics, where M is Sn or In, intermediate-valence and/or heavy-fermion behaviour is realized.

As a representative example of a Kondo system we have selected the  $\text{CeCu}_5$  compound and related systems in which Cu is partly replaced by Al:  $\text{CeCu}_4\text{Al}$ ,  $\text{CeCu}_3\text{Al}_2$ . The Al-substitution leads to a non-magnetic ground state with a pronounced heavy-fermion character.

An example of a temperature-induced valence transition is given with the Yb compound  $\text{YbCu}_4\text{In}$ .

Monopnictides form a very interesting ensemble with respect to their magnetic and their transport properties. A large and complex variety of transport phenomena is reported in this category of R and An compounds. The theoretical description of the experimental results is difficult and far from complete. There are compounds with extremely low carrier concentrations. Some of them (CeP) can be considered as heavy-fermion systems with a small number of charge carriers. The study of these compounds is certainly one of the most interesting problems for the future.

### Acknowledgements

We particularly wish to thank Ashot Markosyan for many stimulating discussions, for the critical reading of the manuscript and for his help during the preparation of the chapter. We acknowledge with gratitude the help of Roland Resel in the preparation of the figures. One of us (E.G.) is very grateful to Ernst Bauer, Robert Hauser, Markus Maikis, Andreas Lindbaum and Helmut Nowotny for collaboration.

This work was supported by the Austrian "Fonds zur Förderung der wissenschaftlichen Forschung" project numbers P7994-TEC and P7608-TEC.

## References

- Aldred, A.T., 1979, *J. Magn. & Magn. Mater.* **10**, 42.
- Aldred, A.T., B.D. Dunlap, D.J. Lam and G.K. Shenoy, 1976, in: *Transplutonium 1975*, eds W. Müller and R. Lindner (North-Holland, Amsterdam) p. 191.
- Aleksandryan, V.V., N.V. Baranov, A.I. Kozlov and A.S. Markosyan, 1988, *Phys. Met. & Metallogr.* **66**, 50.
- Allbutt, M., R. Dell and A.R. Junkison, 1970, *The Chemistry of Defects in Non-metallic Solids* (North-Holland, Amsterdam) p. 124.
- Allen, P.B., 1978, *Phys. Rev. B* **17**, 3725.
- Andreoff, A., E.A. Goremychkin, H. Griesmann, L.P. Kaun, I. Lippold, W. Matz, O.D. Chistyakov, E.M. Savitskii and P.G. Ivanitskii, 1981, *Phys. Status Solidi b* **108**, 261.
- Andreev, A.V., A.V. Deryagin, R.Z. Levitin, A.S. Markosyan and M. Zeleny, 1979, *Phys. Status Solidi a* **52**, K13.
- Arko, A.J., and M.B. Brodsky, 1970, *Nucl. Metall.* **17**, 364.
- Arko, A.J., M.B. Brodsky and W.J. Nellis, 1972, *Phys. Rev. B* **5**, 4564.
- Asano, S., and S. Ishida, 1988, *J. Phys. F* **18**, 501.
- Ausloss, M., and K. Durczewski, 1985, *J. Magn. & Magn. Mater.* **53**, 243.
- Baber, W.G., 1937, *Proc. Roy. Soc.* **258**, 383.
- Baenzinger, N.C., R.E. Rundle, A.I. Snow and A.S. Wilson, 1950, *Acta Crystallogr.* **3**, 34.
- Baer, Y., and Ch. Züricher, 1977, *Phys. Rev. Lett.* **39**, 956.
- Ballou, R., J. Deportes, R. Lemaire, Y. Nakamura and B. Ouladdiaf, 1987, *J. Magn. & Magn. Mater.* **70**, 129.
- Baranov, N.V., and A.I. Kozlov, 1992, *J. Alloys & Compounds* **190**, 83.
- Baranov, N.V., E. Gratz, H. Nowotny and W. Steiner, 1983, *J. Magn. & Magn. Mater.* **37**, 206.
- Baranov, N.V., A.I. Kozlov, A.N. Pirogov and E.V. Simitsyn, 1989, *Sov. Phys. JETP* **69**, 382.
- Baranov, N.V., E. Bauer, E. Gratz, R. Hauser, A.S. Markosyan and R. Resel, 1993, *Proc. ICPTM 92 (Darmstadt)*, *Int. J. Mod. Phys. B*, in press.
- Barthem, V.M.T.S., D. Gignoux, A. Nait-Saada, D. Schmitt and A.Y. Takeuchi, 1989, *J. Magn. & Magn. Mater.* **80**, 142.
- Bartholin, H., J. Voiron, J. Schoenes and O. Vogt, 1987, *J. Magn. & Magn. Mater.* **63&64**, 175.
- Bartholin, H., C. Breandon, R. Tchapotian, E. Nigrelli, K. Mattenberger and O. Vogt, 1990, *Physica B* **163**, 707.
- Bauer, E., 1991, *Adv. Phys.* **40**, 417.
- Bauer, E., E. Gratz, W. Mikovits, H. Sassik and H. Kirchmayr, 1982, *J. Magn. & Magn. Mater.* **29**, 192.
- Bauer, E., E. Gratz, H. Kirchmayr and N. Pillmayr, 1985, *J. Less-Common Met.* **11**, 369.
- Bauer, E., E. Gratz and G. Adam, 1986, *J. Phys. F* **16**, 493.
- Bauer, E., E. Gratz and H. Kirchmayr, 1987a, *Z. Phys. B* **68**, 63.
- Bauer, E., E. Gratz and C. Schmitzer, 1987b, *J. Magn. & Magn. Mater.* **63&64**, 37.
- Bauer, E., E. Gratz, J. Kohlmann, K. Winzer, D. Gignoux and D. Schmitt, 1990a, *Z. Phys. B* **80**, 263.
- Bauer, E., J. Kohlmann, K. Winzer, D. Gignoux and D. Schmitt, 1990b, *Physica B* **163**, 686.
- Bauer, E., E. Gratz, G. Hutflesz and H. Müller, 1991, *J. Phys.: Condens. Matter* **3**, 7641.
- Bauer, E., I.S. Dubenko, E. Gratz, R. Hauser, A.S. Markosyan and K. Payer, 1992a, *Proc. ICPTM 92 (Darmstadt)*, to be published.
- Bauer, E., E. Gratz, G. Hutflesz, A.K. Bhattacharjee and B. Coqblin, 1992b, *J. Magn. & Magn. Mater.* **108**, 159.
- Bauer, E., R. Hauser, E. Gratz, D. Gignoux, D. Schmitt and J. Sereni, 1992c, *J. Phys.: Condens. Matter*, in press.
- Berger, L., and D. Bergman, 1979, in: *The Hall Effect and its Application*, eds C.L. Chien and C.R. Westgate (Plenum Press, New York) ch. 3.
- Besnus, M.J., P. Haen, N. Hamdaoui, A. Herr and A. Meyer, 1990, *Physica B* **163**, 571.
- Bhattacharjee, A.K., and B. Coqblin, 1988, *Phys. Rev. B* **38**, 338.
- Blaise, A., J.M. Collard, J.M. Fournier, J. Rebizant, J.C. Spirlet and O. Vogt, 1987, *J. Magn. & Magn. Mater.* **63&64**, 142.
- Blaise, A., M.N. Bouillet, F. Bourdarot, P. Bulet, J. Rebizant, J. Rossat-Mignod, J.P. Sanchez, J.C. Spirlet and O. Vogt, 1992, *J. Magn. & Magn. Mater.* **104-107**, 33.
- Blatt, F.J., P.A. Schroeder, C.L. Foiles and D. Greig, 1976, *Thermoelectric Power of Metals* (Plenum Press, New York).
- Blatt, F.L., 1968, *Physics of Electronic Conduction in Solids* (McGraw-Hill, New York).
- Boys, D.W., and S. Legvold, 1968, *Phys. Rev. B* **13**, 174.
- Brandt, N.B., and V.V. Moshchalkov, 1984, *Adv. Phys.* **33**, 373.

- Bristow, G.K., T.R. Finlayson and T.F. Smith, 1977, *Phys. Status Solidi b* **82**, K81.
- Brodsky, M.B., 1965, *Phys. Rev. A* **137**, 1423.
- Brodsky, M.B., 1971, in: *Rare Earths and Actinides*, *Inst. Phys. Conf. Ser.* 3, p. 75.
- Brodsky, M.B., and N.J. Bridger, 1973, in: *Magnetism and Magnetic Materials*, *AIP Conf. Proc.*, Vol. 18, eds C.D. Graham Jr and J.J. Rhyne (American Institute of Physics, New York) p. 357.
- Brodsky, M.B., and R.J. Friddle, 1973, *Phys. Rev. B* **7**, 3255.
- Brodsky, M.B., A.J. Arko, A.R. Harvey and W.J. Nellis, 1974, in: *The Actinides, Electronic Structure and Related Properties*, Vol. 2, eds A.J. Freeman and J.B. Darby Jr (Academic Press, New York) ch. 5.
- Brooks, M.S.S., and D. Glötzel, 1980, *J. Magn. & Magn. Mater.* **15-18**, 873.
- Brooks, M.S.S., O. Eriksson, B. Johansson, J.J.M. Franse and P.H. Frings, 1988, *J. Phys. F* **18**, L33.
- Brown, P.J., B. Ouladdiaf, R. Ballou, J. Deportes and A.S. Markosyan, 1992, *J. Phys.: Condens. Matter.* **4**, 1103.
- Burkov, A.T., M. Vedernikov and E. Gratz, 1992, *Physica B* **176**, 263.
- Burlet, P., D. Bonnisseau, S. Quezel, J. Rossat-Mignod, J.C. Spirlet, J. Rebizant and O. Vogt, 1987, *J. Magn. & Magn. Mater.* **63&64**, 151.
- Burlet, P., J.M. Fournier, E. Pleska, J. Rossat-Mignod, J.P. Sanchez, J. Rebizant, J.C. Spirlet and O. Vogt, 1990, 20me Journées des Actinides, Prague, unpublished.
- Burzo, E., and J. Laforest, 1972, *Int. J. Magn.* **3**, 171.
- Burzo, E., and R. Lemaire, 1992, *Solid State Commun.* **84**, 1145.
- Buschow, K.H.J., and R.C. Sherwood, 1977, *J. Appl. Phys.* **48**, 4643.
- Buschow, K.H.J., and H.J. van Daal, 1972, in: *Magnetism and Magnetic Materials - 1971*, *AIP Conf. Proc.*, Vol. 5, eds C.D. Graham Jr and J.J. Rhyne (AIP, New York) p. 1464.
- Buschow, K.H.J., H.W. de Wijn and A.M. van Diepen, 1969a, *J. Chem. Phys.* **50**, 137.
- Buschow, K.H.J., A.S. van der Goot and J. Birkan, 1969b, *J. Less-Common Met.* **19**, 433.
- Castets, A., D. Gignoux and J.C. Gómez-Sal, 1980, *J. Solid State Chem.* **31**, 197.
- Castets, A., D. Gignoux, J.C. Gómez-Sal and E. Roudaut, 1982, *Solid State Commun.* **44**, 1329.
- Chakravarty, R., S.K. Paranjpe, M.R.L.N. Murdhy, L.M. Rao and N.S. Satyamurthy, 1985, *Phys. Status Solidi a* **88**, K155.
- Coqblin, B., and J.R. Schrieffer, 1969, *Phys. Rev.* **185**, 847.
- Coqblin, B., J.R. Iglesias-Sicardi and R. Jullien, 1978, *Contemp. Phys.* **19**, 327.
- Corliss, L.M., and J.M. Hastings, 1964, *J. Appl. Phys.* **35**, 1051.
- Cornelius, C.A., and T.F. Smith, 1980, *J. Low Temp. Phys.* **40**, 391.
- Cornelius, C.A., and T.F. Smith, 1981, *Solid State Commun.* **38**, 599.
- Cornut, B., and B. Coqblin, 1972, *Phys. Rev. B* **5**, 4541.
- Costa, G.A., F. Canepa and G.L. Olcese, 1981, *Solid State Commun.* **40**, 169.
- Cyrot, M., and M. Lavagna, 1979, *J. Phys. (Paris)* **40**, 763.
- De Gennes, P.G., and J. Friedel, 1958, *J. Phys. & Chem. Solids* **4**, 71.
- De Groot, R.A., D.D. Koelling and M. Weger, 1985, *Phys. Rev. B* **32**, 2659.
- De Wijn, H.W., A.M. van Diepen and K.H.J. Buschow, 1976, *Phys. Status Solidi* **76**, 11.
- Dekker, A.J., 1965, *J. Appl. Phys.* **36**, 906.
- Deportes, J., D. Givord and K.R.A. Ziebeck, 1981, *J. Appl. Phys.* **53**, 2074.
- Deportes, J., B. Ouladdiaf and K.R.A. Ziebeck, 1987, *J. Magn. & Magn. Mater.* **70**, 14.
- Dommann, A., and F. Hulliger, 1988, *Solid State Commun.* **65**, 1093.
- Doniach, S., 1974, in: *The Actinides, Electronic Structure and Related Properties*, Vol. 2, eds A.J. Freeman and J.B. Darby Jr (Academic Press, New York) ch. 2.
- Doniach, S., and S. Engelsberg, 1966, *Phys. Rev. Lett.* **17**, 750.
- Duc, N.H., T.D. Hien, P.P. Mai, N.H.K. Ngan, N.H. Sinh, P.E. Brommer and J.J.M. Franse, 1989, *Physica B* **160**, 199.
- Duc, N.H., T.D. Hien, P.E. Brommer and J.J.M. Franse, 1991a, *J. Phys. F* **18**, 275.
- Duc, N.H., T.D. Hien, P.P. Mai and P.E. Brommer, 1991b, *Physica B* **172**, 399.
- Dwight, A.E., R.A. Conner and J.W. Donway Jr, 1965, *Acta Crystallogr.* **18**, 835.
- Elliott, R.J., and F.A. Wedgwood, 1963, *Proc. Phys. Soc.* **81**, 846.
- Eriksson, O., L. Nordström, M.S.S. Brooks and B. Johansson, 1988, *Phys. Rev. Lett.* **60**, 2523.
- Felner, I., I. Nowik, D. Vaknin, U. Potzel, J. Moser, G.M. Kalvius, G. Wortmann, G. Schmiester, G. Hilscher, E. Gratz, C. Schmitzer, N. Pillmayr,

- K.G. Prasad, H. de Waard and H. Pinto, 1987, *Phys. Rev. B* **35**, 6956.
- Fert, A., 1974, *J. Phys. (Paris)* **35**, L107.
- Fert, A., and P.M. Levy, 1987, *Phys. Rev. B* **36**, 1907.
- Fischer, K., 1974, *J. Low Temp. Phys.* **17**, B7.
- Fisk, Z., H.R. Ott, T.M. Rice and J.L. Smith, 1986, *Nature* **320**, 124.
- Fournier, J.M., 1975, Ph.D. Thesis, Univ. of Grenoble, CNRS Nr. 10568, unpublished.
- Fournier, J.M., 1979, *Solid State Commun.* **29**, 111.
- Fournier, J.M., 1980, *Solid State Commun.* **36**, 245.
- Fournier, J.M., 1985, *Physica B* **130**, 268 and references therein.
- Fournier, J.M., and M. Amanowicz, 1992, unpublished.
- Fournier, J.M., and J. Beille, 1979, *J. Phys. Colloq. (Paris)* **40**, C4-145.
- Fournier, J.M., and R. Troč, 1985, in: *Handbook on the Physics and Chemistry of the Actinides*, Vol. 2, eds A.J. Freeman and G.H. Lander (North-Holland, Amsterdam) p. 61.
- Fournier, J.M., A. Boeuf, P.H. Frings, M. Bonnet, J.X. Boucherle, A. Delapalme and A. Menovsky, 1986, *J. Less-Common Met.* **121**, 249.
- Fournier, J.M., E. Pleska, J. Chiapusio, J. Rossat-Mignod, J. Rebizant, J.C. Spirlet and O. Vogt, 1990, *Physica B* **163**, 493.
- Fournier, J.M., M. Amanowicz, E. Pleska, J. Chiapusio, J. Rossat-Mignod, J. Rebizant, J.C. Spirlet and O. Vogt, 1992a, to be published.
- Fournier, J.M., E. Pleska, J. Chiapusio, J. Rebizant and J.C. Spirlet, 1992b, to be published.
- Fransé, J.J.M., P.H. Frings, F.R. de Boer and A. Menovsky, 1981, in: *Physics of Solids under Pressure*, eds S.S. Schilling and R.N. Shelton (North-Holland, Amsterdam) p. 181.
- Freeman, A.J., and G.H. Lander, eds, 1984, *Handbook on the Physics and Chemistry of the Actinides*, Vol. 1 (North-Holland, Amsterdam).
- Freeman, A.J., and G.H. Lander, eds, 1985, *Handbook on the Physics and Chemistry of the Actinides*, Vol. 2 (North-Holland, Amsterdam).
- Frings, P.H., and J.J.M. Fransé, 1985, *J. Magn. & Magn. Mater.* **51**, 141.
- Frings, P.H., J.J.M. Fransé, F.R. de Boer and A. Menovsky, 1983, *J. Magn. & Magn. Mater.* **31-34**, 240.
- Frings, P.H., J.J.M. Fransé, A. Menovsky, S. Zemirli and B. Barbara, 1986, *J. Magn. & Magn. Mater.* **54-57**, 541.
- Fulde, P., J. Keller and G. Zwicky, 1988, *Solid State Phys.* **41**, 1.
- Gao, Q.Z., E. Kanda, H. Kitziwara, M. Sera, T. Goto, T. Fujita, T. Suzuki, T. Fujimuta and T. Kasuya, 1985, *J. Magn. & Magn. Mater.* **47&48**, 69.
- Gaydukova, I.Yu., and A.S. Markosyan, 1982, *Phys. Met. & Metallogr.* **54**, 168.
- Gaydukova, I.Yu., S.B. Kruglyashov, A.S. Markosyan, R.Z. Levitin, Yu.G. Pastushenkov and V.V. Snegirev, 1983, *Sov. Phys. JETP* **57**, 1083.
- Gaydukova, I.Yu., I.S. Dubenko and A.S. Markosyan, 1985, *Phys. Met. & Metallogr.* **59**, 79.
- Gignoux, D., D. Schmitt, E. Bauer and A.P. Murani, 1990, *J. Magn. & Magn. Mater.* **88**, 63.
- Gómez-Sal, J.C., J. Rodríguez Fernández, R.J. López Sánchez and D. Gignoux, 1986, *Solid State Commun.* **59**, 771.
- Goremychkin, E.A., E. Mühle and I. Natkaniec, 1988, *Phys. Status Solidi b* **145**, K15.
- Gratz, E., 1981, *J. Magn. & Magn. Mater.* **24**, 1.
- Gratz, E., 1992, unpublished data.
- Gratz, E., and H. Nowotny, 1983, in: *Proc. Int. Conf. on Magnetism of Rare Earth and Actinides*, eds E. Burzo and H. Rogalski (Bucharest) p. 17.
- Gratz, E., and H. Nowotny, 1985, *Physica B* **130**, 75.
- Gratz, E., and N. Nowotny, 1982, *J. Magn. & Magn. Mater.* **29**, 127.
- Gratz, E., and V. Sechovsky, 1980, *Solid State Commun.* **34**, 967.
- Gratz, E., and M.J. Zuckermann, 1982a, in: *Handbook on the Physics and Chemistry of Rare Earths*, Vol. 5, eds K.A. Gschneidner Jr and L. Eyring (North-Holland, Amsterdam) ch. 42.
- Gratz, E., and M.J. Zuckermann, 1982b, *J. Magn. & Magn. Mater.* **29**, 181.
- Gratz, E., E. Bauer and H. Nowotny, 1987a, *J. Magn. & Magn. Mater.* **70**, 118.
- Gratz, E., N. Pillmayr, E. Bauer and G. Hilscher, 1987b, *J. Magn. & Magn. Mater.* **70**, 159.
- Gratz, E., E. Bauer, S. Pöllinger, H. Nowotny, A.T. Burkov and M.V. Vedernikov, 1988, *J. Phys. (Paris)* **C8-49**, 511.
- Gratz, E., E. Bauer, H. Nowotny, A.T. Burkov and M.V. Vedernikov, 1989, *Solid State Commun.* **69**, 1007.
- Gratz, E., N. Pillmayr, E. Bauer, H. Müller, B. Barbara and M. Loewenhaupt, 1990, *J. Phys: Condens. Matter* **2**, 1485.
- Gratz, E., E. Bauer, R. Resel, S. Pöllinger, M. Mantler and H. Nowotny, 1991, *Eur. J.*

- Solid State Inorg. Chem. **28**, 511.
- Gratz, E., E. Bauer, R. Hauser, M. Maikis, P. Haen and A.S. Markosyan, 1993a, *Int. J. Mod. Phys. B*, in press.
- Gratz, E., R. Hauser, A. Lindbaum, M. Maikis, R. Resel, G. Schaudy, R.Z. Levitin, A.S. Markosyan, I.S. Dubenko and A.Yu. Sokolov, 1993b, *J. Phys.: Condens. Matter*, in press.
- Groß, W., K. Knorr, A.P. Murani and K.H.J. Buschow, 1980, *Z. Phys. B* **37**, 123.
- Grobman, W.D., 1972, *Phys. Rev.* **5**, 2924.
- Gschneidner Jr, K.A., and K. Ikeda, 1983, *J. Magn. & Magn. Mater.* **31&34**, 265.
- Gschneidner Jr, K.A., and R. Smoluchowski, 1963, *J. Less-Common Met.* **5**, 374.
- Gschneidner Jr, K.A., K. Ikeda, W.E. Tsang, O.D. McMasters, R.J. Stierman, S.S. Eucker, S.E. Lambert, M.B. Maple and C. Buchal, 1985, *Physica B* **130**, 202.
- Hall, R.O.A., and C.J. Purser, 1971, in: *Rare Earths and Actinides*, *Inst. Phys. Conf. Ser.*, Vol. 3 (Institute of Physics, London) p. 61.
- Hardman, K., J.J. Rhyne, S.K. Malik and W.E. Wallace, 1982, *J. Appl. Phys.* **53**, 1944.
- Hasegawa, A., and A. Yanase, 1980, *J. Phys. F* **10**, 847.
- Havela, L., J. Hrebik and A.V. Andreev, 1986, *Acta Phys. Slovaca* **36**, 182.
- Hill, H.H., and R.O. Elliott, 1971, *Phys. Lett. A* **35**, 75.
- Holland-Moritz, E., and D. Wohlleben, 1982, *Phys. Rev. B* **25**, 7482.
- Hrebik, J., 1977, Ph.D. thesis, Charles Univ., Prague, unpublished.
- Hrebik, J., and B.R. Coles, 1977, *Physica B* **86-88**, 169.
- Hrebik, J., and B.R. Coles, 1980, *J. Magn. & Magn. Mater.* **15-18**, 1255.
- Hubbard, J., 1963, *Proc. Roy. Soc. A* **276**, 238.
- Hulliger, F., and H.R. Ott, 1978, *Z. Phys. B* **29**, 47.
- Huntley, D.J., and R.F. Frindt, 1974, *Can. J. Phys.* **52**, 861.
- Hurd, C.M., 1972, *The Hall Effect in Metals and Alloys* (Plenum Press, New York) ch. 3.
- Iandelli, A., and A. Palenzona, 1971, *J. Less-Common Met.* **25**, 333.
- Ikeda, K., 1977a, *J. Phys. Soc. Jpn.* **42**, 1541.
- Ikeda, K., and K.A. Gschneidner Jr, 1980, *Phys. Rev. Lett.* **45**, 1341.
- Irkhin, Yu.P., A.N. Voloshinskiĭ and S.S. Abel'skii, 1967, *Phys. Status Solidi* **22**, 309.
- Ishiyama, K., A. Shinogi and K. Endo, 1984, *J. Phys. Soc. Jpn.* **53**, 2456.
- Izuyama, T., D.J. Kim and R. Kube, 1963, *J. Phys. Soc. Jpn.* **18**, 1025.
- Jones, H., 1956, *Encyclopedia of Physics*, Vol. XIX (Springer, Berlin) p. 227.
- Jullien, R., M.S. Béal-Monod and B. Coqblin, 1974, *Phys. Rev. B* **9**, 1441.
- Kadowaki, K., and S.B. Woods, 1986, *Solid State Commun.* **58**, 507.
- Kalvius, G.M., S. Zwirner, U. Potzel, J. Moser, W. Potzel, F.J. Litterst, J. Gal and J.C. Spirlet, 1990, *Physica B* **163**, 487.
- Kamimura, H., J. Sakurai, Y. Komura, H. Nakamura, M. Shiga and Y. Nakamura, 1987, *J. Magn. & Magn. Mater.* **70**, 145.
- Kasaya, M., B. Liu, M. Sera, T. Kasuya, D. Endoh, T. Goto and T. Fujimura, 1985, *J. Magn. & Magn. Mater.* **52**, 289.
- Kasuya, T., 1959, *Prog. Theor. Phys. (Kyoto)* **16**, 227.
- Kasuya, T., K. Takegahara, Y. Aoki, T. Suzuki, S. Kunii, M. Sera, N. Sato, T. Fujita, T. Goto, A. Tamaki and T. Komatsubara, 1982, in: *Valence Instabilities*, eds P. Wachter and H. Boppart (North-Holland, Amsterdam) p. 359.
- Katz, G., and A.J. Jacobs, 1962, *J. Nucl. Mater.* **5**, 338.
- Kletowski, Z., 1988, *Phys. Status Solidi a* **108**, 363.
- Kletowski, Z., 1989, *Solid State Commun.* **72**, 901.
- Kletowski, Z., 1992, *Solid State Commun.* **81**, 297.
- Kletowski, Z., and P.J. Markowski, 1987, *Solid State Commun.* **62**, 299.
- Kletowski, Z., and P. Stawinski, 1990, *Solid State Commun.* **76**, 867.
- Kletowski, Z., B. Stalinski and J. Mulak, 1980, *J. Magn. & Magn. Mater.* **15-18**, 53.
- Kletowski, Z., P. Sławinski and A. Czopnik, 1991, *Solid State Commun.* **80**, 981.
- Kohlmann, J., K. Winzer and E. Bauer, 1988, *Europhys. Lett.* **5**, 541.
- Kondo, J., 1962, *Prog. Theor. Phys.* **27**, 772.
- Koskenmaki, D.C., and K.A. Gschneidner Jr, 1978, in: *Handbook on the Physics and Chemistry of Rare Earths*, Vol. 1, eds K.A. Gschneidner Jr and L. Eyring (North-Holland, Amsterdam) ch. 4.
- Kruger, O.L., and J.B. Moser, 1967, *J. Chem. Phys.* **46**, 891.
- Kubo, R., 1959, *Lectures in Theoretical Physics*, Vol. 1 (Interscience, New York).
- Kwon, Y.S., Y. Haga, O. Nakamura, T. Suzuki and T. Kasuya, 1991, *Physica B* **171**, 324.

- Labroo, S., and N. Ali, 1990, *J. Appl. Phys.* **67**, 5292.
- Labroo, S., F. Willis and N. Ali, 1990, *J. Appl. Phys.* **67**, 5295.
- Lam, D.J., and A.T. Aldred, 1975, *AIP Conf. Proc.* **24**, 349.
- Lam, D.J., J.B. Darby and N.V. Nevitt, 1974a, in: *The Actinides: Electronic Structure and Related Properties*, Vol. 2, eds A.J. Freeman and J.B. Darby Jr (Academic Press, New York) p. 119.
- Lam, D.J., B.D. Dunlap, A.R. Harvey, M.M. Mueller, A.T. Aldred, I. Nowik and G.H. Lander, 1974b, *Proc. ICM'73* (Nauka, Moscow).
- Lapierre, F., P. Haen, R. Briggs, A. Hamzic, A. Fert and J.P. Kappler, 1987, *J. Magn. & Magn. Mater.* **63&64**, 338.
- Lawson, A.C., 1970, *Phys. Lett. A* **33**, 231.
- Lawson, A.C., A. Williams, J.G. Huber and R.B. Roof, 1986, *J. Less-Common Met.* **120**, 113.
- Lawson, A.C., A.C. Larson, R.B. von Dreele, A.T. Oritz, J.L. Smith, J. Faber, R.L. Hitterman and M.H. Mueller, 1987, *J. Less Comm. Met.* **132**, 229.
- Le Roy, J., J.M. Moreau, D. Paccard and E. Parthe, 1978, *Acta Crystallogr. B* **34**, 9.
- Lee, J.A., 1971, in: *Rare Earths and Actinides*, *Inst. Phys. Conf. Ser.*, Vol. 3 (Institute of Physics, London) p. 50.
- Lee, J.A., P.W. Sutcliffe and K. Mendelssohn, 1969, *Phys. Lett. A* **30**, 106.
- Lethuiller, P., J. Pierre, K. Knorr and W. Drexel, 1975, *J. Phys. (Paris)* **36**, 329.
- Lin, C.L., L.W. Zhou, J.E. Crow and R.P. Guertin, 1985, *J. Appl. Phys.* **57**, 3146.
- Lin, S.T., and A.R. Kaufmann, 1957, *Phys. Rev.* **108**, 1171.
- Link, P., U. Benedict, J. Wittig and H. Wühl, 1992, *J. Phys.: Condens. Matter* **4**, 5585.
- Liu, S.H., P. Burgardt, K.A. Gschneidner Jr and S. Legvold, 1976, *J. Phys. F* **6**, L55.
- Loong, C.-K., M. Loewenhaupt and M.L. Vrtis, 1986, *Physica B* **136**, 413.
- Luengo, C.A., M.B. Maple and J.G. Huber, 1976, *J. Magn. & Magn. Mater.* **3**, 305.
- Makahara, Y., Y. Andoh, Y. Hashimoto, H. Fujii, M. Hasuo and T. Okamoto, 1983, *J. Phys. Soc. Jpn.* **52**, 629.
- Malik, S.K., and W.E. Wallace, 1981, *J. Magn. & Magn. Mater.* **24**, 23.
- Marpoe Jr, G.R., and G.H. Lander, 1978, *Solid State Commun.* **26**, 599.
- McEwen, K.A., 1978, in: *Handbook on the Physics and Chemistry of Rare Earths*, Vol. 1, eds K.A. Gschneidner Jr and L. Eyring (North-Holland, Amsterdam) ch. 6.
- McMillan, W.L., 1968, *Phys. Rev.* **167**, 10.
- Méot-Raymond, S., and J.M. Fournier, 1992, *Rev. Sci. & Tech. CEA-DAM* **6**, 83.
- Meyer, C., F. Hartmann-Boutron, Y. Gros and Y. Berthier, 1981, *J. Phys. (Paris)* **42**, 605.
- Mills, D.L., and P. Lederer, 1966, *J. Phys. & Chem. Solids* **27**, 1805.
- Misiuk, A., J. Mulak and A. Czopnik, 1973, *Bull. Acad. Pol. Sci. (Ser. Sci. Chem.)* **21**, 487.
- Moon, R.M., W.C. Koehler and J. Farrell, 1965, *J. Appl. Phys.* **36**, 978.
- Mori, H., T. Satoh, H. Suzuki and T. Ohtsuka, 1982, *J. Phys. Soc. Jpn.* **51**, 1785.
- Moriya, T., 1970, *Phys. Rev. Lett.* **24**, 1433.
- Moriya, T., 1985, *Spin fluctuations in Itinerant Electron Magnetism* (Springer, Berlin).
- Mott, N.F., and H. Jones, 1936, *The Theory of the Properties of Metals and Alloys* (Oxford).
- Müller, H., E. Bauer, E. Gratz, K. Yoshimura, T. Nitta and M. Mekata, 1988, *J. Magn. & Magn. Mater.* **76&77**, 159.
- Naegele, J., F. Schiavo and J.C. Spirlet, 1989, *19emes Journees des Actinides*, Madonna di Campiglio, Italy, unpublished.
- Nakamura, Y., M. Shiga and S. Kawano, 1983, *Physica B* **120**, 212.
- Nicolas-Francillon, M., and D. Jerome, 1973, *Solid State Commun.* **12**, 523.
- Nielson, P.E., and P.L. Taylor, 1974, *Phys. Rev. B* **10**, 4061.
- Nishihara, Y., M. Tokumoto, Y. Yamaguchi and G. Kido, 1987, *J. Magn. & Magn. Mater.* **70**, 173.
- Norman, M.R., and D.D. Koelling, 1986, *Phys. Rev. B* **33**, 3803.
- Okayama, Y., H. Takahashi, N. Mori, Y.S. Kwon, Y. Haga and T. Suzuki, 1992, *J. Magn. & Magn. Mater.* **108**, 113.
- Oomi, G., T. Terada, M. Shiga and Y. Nakamura, 1987, *J. Magn. & Magn. Mater.* **70**, 137.
- Ott, H.R., 1987, *Helv. Phys. Acta* **60**, 62.
- Ott, H.R., H. Rudigier, E. Felder, Z. Fisk and B. Batlogg, 1985, *Phys. Rev. Lett.* **55**, 1595.
- Parrott, J.E., and D. Stuckes, 1975, *Thermal Conductivity of Solids* (Pion Applied Physics, London).
- Paul-Boncour, V., C. Lartigue, A. Percheron-Guégan, J. Achard and J. Pannetier, 1988, *J. Less-Common Met.* **143**, 301.
- Peterson, D.T., D.F. Page, R.B. Rumpard and



- D.K. Finnemore, 1967, *Phys. Rev.* **153**, 701.
- Pippard, A.B., 1989, *Magnetoresistance in Metals* (Cambridge University Press, UK).
- Pleska, E., J.M. Fournier, J. Chiapusio, J. Rossat-Mignod, J.C. Spirlet, J. Rebizant and O. Vogt, 1988, *J. Phys. (Paris)* **C8-49**, 493.
- Popov, Yu.F., R.Z. Levitin, M. Zeleny, A.V. Deryagin and A.V. Andreev, 1980, *Sov. Phys. JETP* **51**, 1223.
- Purwins, H.G., and A. Leson, 1990, *Adv. Phys.*, **39**, 309.
- Ramakrishnan, T., V. Coleman and P.W. Anderson, 1985, *J. Magn. & Magn. Mater.* **47&48**, 493.
- Raphael, G., and C.M. De Novion, 1969, *J. Phys. (Paris)* **30**, 261.
- Rastogi, A.K., G. Hilscher, E. Gratz and N. Pillmayr, 1988, *J. Phys. Colloq. (Paris)* **49**, C8-277.
- Ratto, C.F., B. Coqblin and E. Galleani d'Agliano, 1969, *Adv. Phys.* **18**, 489.
- Reinders, P.H., H. Springford, P.T. Coleridge, R. Boulet and D. Ravot, 1987, *J. Magn. & Magn. Mater.* **63&64**, 297.
- Resel, R., 1991, Diplomarbeit, Tech. Univ. Vienna, unpublished.
- Rhyne, J.J., 1969, *J. Appl. Phys.* **40**, 1001.
- Rosen, M., G. Erez and S. Shtrikman, 1968, *Phys. Rev. Lett.* **21**, 430.
- Rossat-Mignod, J., P. Burlet, S. Quezel, O. Vogt and H. Bartholin, 1982, in: *Crystalline Electric Field Effects in f-electron Magnetism*, Proc. 4th Int. Conf., Wroclaw, Poland, eds R.P. Guertin, W. Suski and Z. Zolnierek (Plenum Press, New York) p. 501.
- Rossat-Mignod, J., G.H. Lander and P. Burlet, 1984, in: *Handbook on the Physics and Chemistry of the Actinides*, Vol. 1, eds A.J. Freeman and G.H. Lander (North-Holland, Amsterdam) ch. 6.
- Rossel, C., K.N. Yang, M.B. Maple, Z. Fisk, E. Zirngiebl and J.D. Thompson, 1987, *Phys. Rev. B* **35**, 1914.
- Roy, S.B., G. Williams and B.R. Coles, 1989, *J. Phys. (Paris)* **50**, 2773.
- Sakurai, J., Y. Tagawara and Y. Komura, 1985, *J. Magn. & Magn. Mater.* **52**, 205.
- Sanchez, J.P., P. Burlet, S. Quezel, D. Bonnisseau, J. Rossat-Mignod, J.C. Spirlet, J. Rebizant and O. Vogt, 1988, *Solid State Commun.* **67**, 999.
- Sanchez, J.P., M.N. Bouillet, E. Colineau, A. Blaise, M. Amanowicz, P. Burlet, J.M. Fournier, T. Charvolin and J. Larroque, 1993, *Physica B*, in press.
- Sandenaw, T.A., 1961, *Plutonium 1960* (Cleaver-Hume Press, London) p. 79.
- Schenkel, R., 1977, *Solid State Commun.* **23**, 389.
- Schinkel, C.J., 1978, *J. Phys. F* **8**, L87.
- Schneider, W.-D., B. Reihl, N. Martensson and A.J. Arko, 1982, *Phys. Rev. B* **26**, 423.
- Schoenes, J., and F. Hulliger, 1985, *Helv. Phys. Acta* **58**, 784.
- Schoenes, J., and F. Hulliger, 1987, *J. Magn. & Magn. Mater.* **63&64**, 43.
- Schoenes, J., B. Frick and O. Vogt, 1984, *Phys. Rev. B* **30**, 6578.
- Schrieffer, J.R., 1968, *J. Appl. Phys.* **39**, 642.
- Sechovsky, V., and L. Havela, 1988, in: *Ferromagnetic Materials*, Vol. 4, *Intermetallic Compounds and Actinides*, eds E.P. Wohlfarth and K.H.J. Buschow (North-Holland, Amsterdam) ch. 4.
- Sechovsky, V., Z. Smetana, G. Hilscher, E. Gratz and H. Sassik, 1980, *Physica B* **102**, 227.
- Sechovsky, V., L. Havela, J. Hrebik, A. Zentko, P. Diko and J. Sternberk, 1985, *Physica B* **133**, 243.
- Sera, M., P. Haen, O. Laborde, H. Bartholin and T. Kasuya, 1985a, *J. Magn. & Magn. Mater.* **47&48**, 89.
- Sera, M., T. Kasuya, P. Haen, J.L. Tholence, H. Bartholin, J. Rossat-Mignod and G. Lapertot, 1985b, *J. Magn. & Magn. Mater.* **52**, 377.
- Sereni, J.G., 1980, *J. Phys. F* **10**, 283.
- Severin, L., L. Nordström, M.S.S. Brooks and B. Johansson, 1992, *Phys. Rev. B* **44**, 9392.
- Severing, A., E. Gratz, B.D. Rainford and K. Yoshimura, 1990, *Physica B* **163**, 409.
- Slebarski, A., and D. Wohlleben, 1985, *Z. Phys. B* **60**, 449.
- Smith, H.G., and G.H. Lander, 1984, *Phys. Rev. B* **30**, 5407.
- Smith, J.L., and H.H. Hill, 1974, *Phys. Status Solidi b* **64**, 343.
- Stalinski, B., Z. Kletowski and Z. Henkie, 1973, *Phys. Status Solidi a* **19**, K165.
- Stalinski, B., Z. Kletowski and Z. Henkie, 1975, *Bull. Acad. Polon. Sci. (Ser. Sci. Chim.)* **23**, 827.
- Stalinski, B., N. Czopnik, N. Iliw and T. Mydlarz, 1979, *J. Phys. (Paris)* **40**, 149.
- Stassis, C., J. Zarestky, C.K. Loong and O.D. McMasters, 1981, *Phys. Rev.* **5**, 2227.
- Steiner, W., E. Gratz, H. Ortbauer and H.W. Camen, 1978, *J. Phys. F* **8**, 1525.
- Stewart, G.R., 1984, *Rev. Mod. Phys.* **56**, 755.
- Stoner, E.C., 1938, *Proc. R. Soc. A* **165**, 372.
- Suzuki, T., M. Sera, H. Shida, K. Takegahara, H. Takahashi, A. Yanase and T. Kasuya, 1981, in: *Valence Fluctuations in Solids*, eds

- L.M. Falikov, W. Hanke and M.B. Maple (North-Holland, Amsterdam) p. 255.
- Suzuki, T., Y.S. Kwon, S. Ozeki, Y. Haga and T. Kasuya, 1990, *J. Magn. & Magn. Mater.* **90&91**, 493.
- Svoboda, P., M. Divis, J. Bishof, Z. Smetana, R. Cerny and J. Buriánek, 1990, *Phys. Status Solidi a* **119**, K67.
- Tagawa, Y., J. Sakurai, Y. Komura, H. Wada, M. Shiga and Y. Nakamura, 1985, *J. Phys. Soc. Jpn.* **54**, 591.
- Taillefer, L., R. Newbury, G.G. Lonzarich, Z. Fisk and J. Smith, 1987, *J. Magn. & Magn. Mater.* **63&64**, 372.
- Takayanagi, S., 1984, *J. Phys. Soc. Jpn.* **53**, 676.
- Therond, P.G., 1986, Ph.D. Thesis, Univ. Grenoble, unpublished.
- Therond, P.G., J.M. Fournier, J. Schoenes and O. Vogt, 1987, *J. Magn. & Magn. Mater.* **66**, 45.
- Toxen, A.M., and R.J. Gambino, 1968, *Phys. Lett. A* **28**, 214.
- Toxen, A.M., R.J. Gambino and N.R. Stemple, 1967, *Bull. Am. Phys. Soc.* **12**, 57.
- Trainor, R.J., M.B. Brodsky and H.V. Culbert, 1975, *Phys. Rev. Lett.* **34**, 1019.
- Trainor, R.J., M.B. Brodsky and G.S. Knapp, 1976, in: *Plutonium and other Actinides*, eds H. Blank and R. Lindner (North-Holland, Amsterdam) p. 475.
- Ueda, K., and T. Moriya, 1975, *J. Phys. Soc. Jpn.* **39**, 605.
- Van Daal, H.J., and K.H.J. Buschow, 1969, *Solid State Commun.* **7**, 217.
- van Daal, H.J., K.H.J. Buschow, P.B. van Aken and M.H. van Maaren, 1975, *Phys. Rev. Lett.* **34**, 1457.
- van Diepen, A.M., R.S. Craig and W.E. Wallace, 1971, *J. Phys. & Chem. Solids* **32**, 1867.
- van Doorn, C.F., and P. de V. DuPlessis, 1977, *J. Low Temp. Phys.* **28**, 391.
- van Maaren, M.H., H.J. van Daal and K.H.J. Buschow, 1974, *Solid State Commun.* **14**, 145.
- Varma, C.M., 1985, *Commun. Solid State Phys.* **11**, 221.
- Vogt, O., P. Wachter and H. Bartholin, 1980, *Physica B* **102**, 226.
- Vogt, O.R., and K. Mattenberger, 1987, *J. Less-Common Met.* **133**, 53.
- Von Essen, V.U., and W. Klemm, 1962, *Z. Anorg. Allg. Chem.* **317**, 26.
- Vucht, R.J.M., H. van Kempen and P. Wyder, 1985, *Rep. Prog. Phys.* **48**, 853.
- Wachter, P., F. Marabelli and B. Bucher, 1991, *Phys. Rev. B* **43**, 11136.
- Wada, H., M. Shiga and Y. Nakamura, 1989, *Physica B* **161**, 197.
- Welsh, L.B., A.M. Toxen and R.J. Gambino, 1971, *Phys. Rev.* **4**, 2921.
- Wire, M.S., J.D. Thompson and S. Fisk, 1984, *Phys. Rev. B* **30**, 5591.
- Wohlleben, D., and B. Wittershagen, 1985, *Adv. Phys.* **34**, 403.
- Wulff, M., B. Lebeck, A. Delapalme, G.H. Lander, J. Rebizant and J.C. Spirlet, 1989, *Physica B* **156-157**, 836.
- Yamada, H., and S. Takada, 1974, *Prog. Theor. Phys.* **52**, 1077.
- Yamada, H., J. Inoue, K. Terao, S. Kanda and M. Shimizu, 1984, *J. Phys. F* **14**, 1943.
- Yessik, M., 1969, *J. Appl. Phys.* **40**, 1133.
- Yoshimura, K., T. Nitta, M. Mekata, T. Shimizu, T. Sakakibara, T. Goto and G. Kido, 1988, *Phys. Rev. Lett.* **60**, 851.
- Yosida, K., 1957, *Phys. Rev.* **107**, 397.
- Yuen, T., Y. Gao, I. Perez and J.E. Crow, 1990, *J. Appl. Phys.* **67**, 4827.
- Zhou, L.W., C.L. Lin, J.E. Crow, S. Bloom, R.P. Guertin, S. Foner and G. Stewart, 1985, *Physica B* **135**, 99.
- Ziman, J.M., 1960, *Electrons and Phonons* (Oxford University Press, Oxford).

## Chapter 116

# MÖSSBAUER STUDIES ON ELECTRONIC STRUCTURE OF INTERMETALLICS COMPOUNDS\*

W. POTZEL and G.M. KALVIUS

*Physics Department, Technical University Munich, D-85747 Garching, Germany*

J. GAL

*Nuclear Research Center Negev (NRCN), Beer Sheva, Israel; Department of Nuclear Engineering, Ben-Gurion University of the Negev, Beer-Sheva, Israel*

---

### Contents

1. Introduction and overview	541	3.2.2. Spectrometer for pressures up to ~12 GPa	570
2. Mössbauer spectroscopy	544	3.2.3. Spectrometer for pressures up to ~50 GPa	572
2.1. Basics of the Mössbauer effect	544	4. Contrasts in lanthanide and actinide electron structure as seen by Mössbauer spectroscopy	574
2.2. Mössbauer spectra	547	4.1. Intermediate valence	574
2.3. Hyperfine interactions	550	4.2. Delocalization of 5f-electrons and magnetism	576
2.3.1. Isomer shifts and the contact electron density	550	5. Lanthanide and actinide electron structure under reduced volume	578
2.3.2. Magnetic hyperfine splittings and the hyperfine field	552	5.1. Rocksalt type compounds	579
2.3.3. Quadrupole splittings and the electric field gradient	557	5.1.1. Eu mono-chalcogenides	579
2.3.4. Combined interactions	559	5.1.2. Neptunium mono-pnictide NpAs	582
2.4. Comparison of resolution	560	5.2. Laves phases	583
2.5. General systematics of hyperfine interactions	562	5.2.1. EuAl <sub>2</sub>	584
3. Experimental considerations	565	5.2.2. DyAl <sub>2</sub>	588
3.1. Mössbauer transitions in lanthanides and actinides	565	5.2.3. NpAl <sub>2</sub> and NpOs <sub>2</sub>	589
3.1.1. General features	565	5.3. The AuCu <sub>3</sub> structure (NpSn <sub>3</sub> )	591
3.1.2. Mössbauer sources	565	5.4. Non-cubic compounds	593
3.2. Mössbauer spectrometers	568	5.4.1. YbCuAl	593
3.2.1. Spectrometers for the study under ambient pressure	568		

\*This work has been funded by the German Federal Minister for Research and Technology (Bundesminister für Forschung und Technologie [BMFT]) under Contract Nos. KA2TUM and GAL2BEE, and by the National Council for Research and Development, Israel.

5.4.2. NpCo <sub>2</sub> Si <sub>2</sub>	595	6.5. Compounds with the ThCr <sub>2</sub> Si <sub>2</sub> structure	610
5.5. Summary	595	6.6. Other related compounds	615
6. Systematics of electronic structure properties in intermetallic systems	596	7. Spin-glass behavior of lanthanide and actinide intermetallics	617
6.1. (An or Ln)X <sub>2</sub> compounds	596	7.1. HoFe <sub>4</sub> Al <sub>8</sub>	618
6.1.1. Cubic Laves phases NpX <sub>2</sub> and some related Ln compounds	598	7.2. AnFe <sub>4</sub> Al <sub>8</sub>	620
6.1.2. Other NpX <sub>2</sub> compounds	602	7.3. Comparison	622
6.2. Compounds with the NaCl structure	602	8. Heavy-electron properties in Np intermetallics	623
6.3. Compounds with the AuCu <sub>3</sub> structure	607	9. Conclusions	628
6.4. Np charge state in cubic intermetallics	609	References	629

## Symbols

$A$	isotopic abundance	$F_L^M(\theta)$	angular dependence of multipole radiation
$\tilde{A}$	magnetic hyperfine tensor	$f$	Lamb-Mössbauer fraction; resonant fraction; recoil-free fraction
$a_{\text{hf}}$	hyperfine coupling constant	$f_s, f_a$	$f$ for source and absorber nuclei, respectively
$a_s, a_{\text{ns}}$	hyperfine coupling constant to conduction electrons with s and non-s character	$f(\theta, \phi)$	angular distribution of $f$
$b_Q$	quadrupole coupling constant	$g_I$	gyromagnetic ratio of nuclear state with spin $I$
$B_{\text{hf}}$	magnetic hyperfine field	$\hbar$	Planck's constant $h$ divided by $2\pi$ ( $6.5822 \times 10^{-16}$ eV s)
$B_{\text{orb}}$	orbital contribution to $B_{\text{hf}}$	$\mathcal{H}_m$	magnetic hyperfine interaction Hamiltonian
$B_{\text{core}}$	core-polarization contribution to $B_{\text{hf}}$	$\mathcal{H}_Q$	quadrupole hyperfine interaction Hamiltonian
$B_{\text{thf}}$	contribution of transferred hyperfine fields to $B_{\text{hf}}$	$I$	nuclear spin vector
$B_{\text{dip}}$	contribution of dipolar field from neighboring moments to $B_{\text{hf}}$	$I_e, I_g$	excited-state and ground-state nuclear spins
$B_0$	bulk modulus	$I(\theta)$	angular distribution of $\gamma$ radiation
$B'_0$	pressure derivative of $B_0$	$J$	electronic angular-momentum vector
$c$	speed of light	$J_{4f}$	exchange integral between 4f and conduction electrons
$e$	electric charge of electron	$J_0(x)$	Bessel function of first kind and order zero
$E$	energy	$\langle J \  N \  J \rangle$	reduced matrix element for $B_{\text{hf}}$
$E_D$	Doppler shift of the emission or absorption line	$\langle J \  \alpha \  J \rangle$	reduced matrix element for $eq$
$E_e, E_g$	nuclear excited state and ground state energies	$k$	Boltzmann's constant ( $8.617 \times 10^{-5}$ eV/K)
$E_F$	Fermi energy	$k_F$	Fermi vector
$E_{\text{hf}}$	total hyperfine interaction energy	$L$	multipolarity of electromagnetic radiation
$E_0$	nuclear transition energy	$M$	nuclear mass
$E_m$	eigenvalues of $\mathcal{H}_m$	$M$	difference in magnetic quantum number of excited and ground states
$E_Q$	eigenvalues of $\mathcal{H}_Q$ ; quadrupole hyperfine interaction energy (axial symmetry)	$m_l, m_j$	nuclear and electron magnetic quantum numbers
$E_R$	nuclear recoil energy following $\gamma$ emission or absorption		
$eq$	principal component of $V_{ij}$ (electric field gradient)		
$eq_{\text{ion}}, eq_{\text{latt}}$	ionic and lattice contribution to $eq$		
FWHM	full width at half maximum		

$N(E)$	spectral distribution of $\gamma$ -ray emission	$W_0$	minimum observable FWHM for resonant spectral lines in velocity units
$N_0$	number of $\gamma$ -rays emitted per unit time	$Y_0$	resonance effect
$q$	wave vector of antiferromagnetic structure	$Y(v)$	$\gamma$ -ray count-rate at velocity $v$ between source and absorber
$Q$	nuclear quadrupole moment	$Z$	nuclear charge
$Q_{ij}$	nuclear quadrupole moment tensor components	$Z$	number of conduction electrons per atom
$\langle r^2 \rangle$	second moment of nuclear charge distribution (mean square nuclear charge radius)	$\alpha$	isomer shift calibration constant
$\Delta \langle r^2 \rangle$	difference in $\langle r^2 \rangle$ between nuclear excited and ground states	$\alpha_i$	total internal conversion coefficient
$\langle r^{-3} \rangle$	average of $1/r^3$ for open-shell electrons	$\gamma_\infty$	inner Sternheimer factor
$R_i$	position vector of spin $i$	$\gamma(\theta)$	coefficient of electronic specific heat for $T \rightarrow 0$
$R_Q$	outer Sternheimer factor	$\Gamma$	FWHM of emission or absorption line (energy units)
$S$	isomer shift in velocity units	$\eta$	electric field gradient asymmetry parameter
$S_{Eu}$	4f spin on the Eu ion	$\mu$	electronic magnetic moment
$\langle S_z \rangle_{Eu}$	z-component of expectation value of $S_{Eu}$	$\mu_B$	Bohr magneton ( $0.57884 \times 10^{-8}$ eV/kG)
$S_{SOD}$	second-order Doppler shift in velocity units	$\mu_I$	magnetic moment of nuclear state with spin $I$
$\langle s_z \rangle_s$	spin polarization of s-like and non-s-like conduction electrons	$\mu_N$	nuclear magneton ( $0.31525 \times 10^{-8}$ eV/kG)
$\langle s_z \rangle_{ns}$	spin polarization of non-s-like conduction electrons	$\nu_m$	fluctuation rate of electronic magnetic moments
$T$	absolute temperature	$\nu_Q$	fluctuation rate of ionic electric field gradient
$T_{1/2}$	half-life of radioactive nuclei	$\rho(0)$	electronic charge density at the nuclear center
$T_C$	Curie temperature	$\rho_{ce}(0)$	contribution to $\rho(0)$ by conduction electrons
$T_N$	Néel temperature	$\Delta\rho(0)$	difference of $\rho(0)$ between source and absorber
$T_{OG}$	transition temperature from aligned to random spin-glass	$\sigma_0$	maximum resonant cross-section
$T_{SG}(B)$	spin-glass transition temperature observed in magnetic field $B$	$\sigma(E)$	resonant cross-section energy distribution
$t_a$	effective absorber thickness	$\tau_e$	excited nuclear state mean life
$\langle u^2 \rangle$	mean-square displacement of nucleus from equilibrium position	$\theta$	Debye temperature
$v$	Doppler velocity used to shift $\gamma$ -ray energy	$\Theta$	angle between $B_{hf}$ and $eq$
$V$	volume of unit cell		
$V_{ij}$	electric field gradient tensor component		
$W$	effective linewidth in velocity units		

## 1. Introduction and overview

Shortly after the discovery of transuranic elements about 50 years ago (see Morss and Fuger 1992), Seaborg suggested that the heaviest elements form a 5f transition series, which came to be known as the actinides, in analogy to the well known 4f series of the lanthanides. A glance at a modern periodic system of elements shows this basic concept to be still accepted, despite the fact that pronounced differences

between 4f and 5f electronic structure soon became apparent, especially in connection with condensed-matter properties. These differences have their root in the comparatively wider spatial extent of 5f electrons and also in the more dominant influence of relativistic effects. This will be outlined in more detail in section 4.

The differences in electronic structure between lanthanides and actinides can be brought out particularly well through investigations of their magnetic properties. Whereas members of the former series usually are classical examples for localized magnetism, those of the latter series often strongly tend towards itinerant (band-like) magnetism as best known for the 3d transition elements. Inequalities between 4f and 5f electron properties are plenty, as this volume gives ample evidence. Without doubt, the actinides are a species of their own and the comparative study of lanthanide and actinide compounds remains still a rich and widely open field of research.

Mössbauer spectroscopy is a well established tool for probing aspects of electronic structure, especially those which are reflected in magnetic properties. The needed information is gained by determination of hyperfine interaction energies, i.e., the coupling between the electron shell and its nucleus. Hence it is a strictly local probe; meaning, e.g., that in compounds it senses only the properties of the constituent ion which is Mössbauer active. But these properties may well depend on long-range behavior of the sample material. Of importance in actinide research is the insensitivity to impurities as long as those do not influence the bulk behavior of the material. Unlike microwave methods, Mössbauer spectroscopy does not require the probe atoms or nuclei to be polarized and hence can be performed in zero field. Furthermore, it samples the bulk of material without giving preference to atoms on the surface or in domain walls. Of practical importance is also that Mössbauer experiments require comparatively little material ( $\sim 100$  mg) and single crystals are not needed. Special external conditions such as high pressure, high magnetic fields or ultra-low temperatures are fairly easily applied. The most unique feature of Mössbauer spectroscopy is the possibility to gain rather direct information on the charge state of the resonant atom via the so-called isomer shift. The most serious drawback of the Mössbauer method is two-fold. Firstly, the temperature range covered is often seriously limited to low temperatures and, secondly, a signal is given only by solid materials. However, they need not be crystalline, meaning that glasses, frozen solutions and amorphous solids can be studied.

For the sake of completeness and in order to help the uninitiated reader to understand the *termini technici* we start out with a short summary of the essential physical background of Mössbauer spectroscopy and of the physical nature of the parameters to be extracted from a Mössbauer spectrum (section 2). A brief overview of the basics of the technique particularly with respect to measurements on Np and high-pressure experiments as carried out by our group follows in section 3.

The upper part of fig. 1 presents an overview of the lanthanide and actinide elements usable for Mössbauer effect studies. Not all of the candidates shown are useful for electronic structure investigations. Either they are hampered by severe technical difficulties which prevent systematic studies of a large number of compounds or, more seriously, their resolution is too limited to extract critical information. Extensive studies have been carried out within the lanthanides for Eu, Gd, Dy and Yb. Within

Ce	Pr	Nd	Pm	Sm	Eu	Gd	Tb	Dy	Ho	Er	Tm	Yb	Lu
Th	Pa	U	Np	Pu	Am	Cm	Bk	Cf	Es	Fm	Md	No	Lr

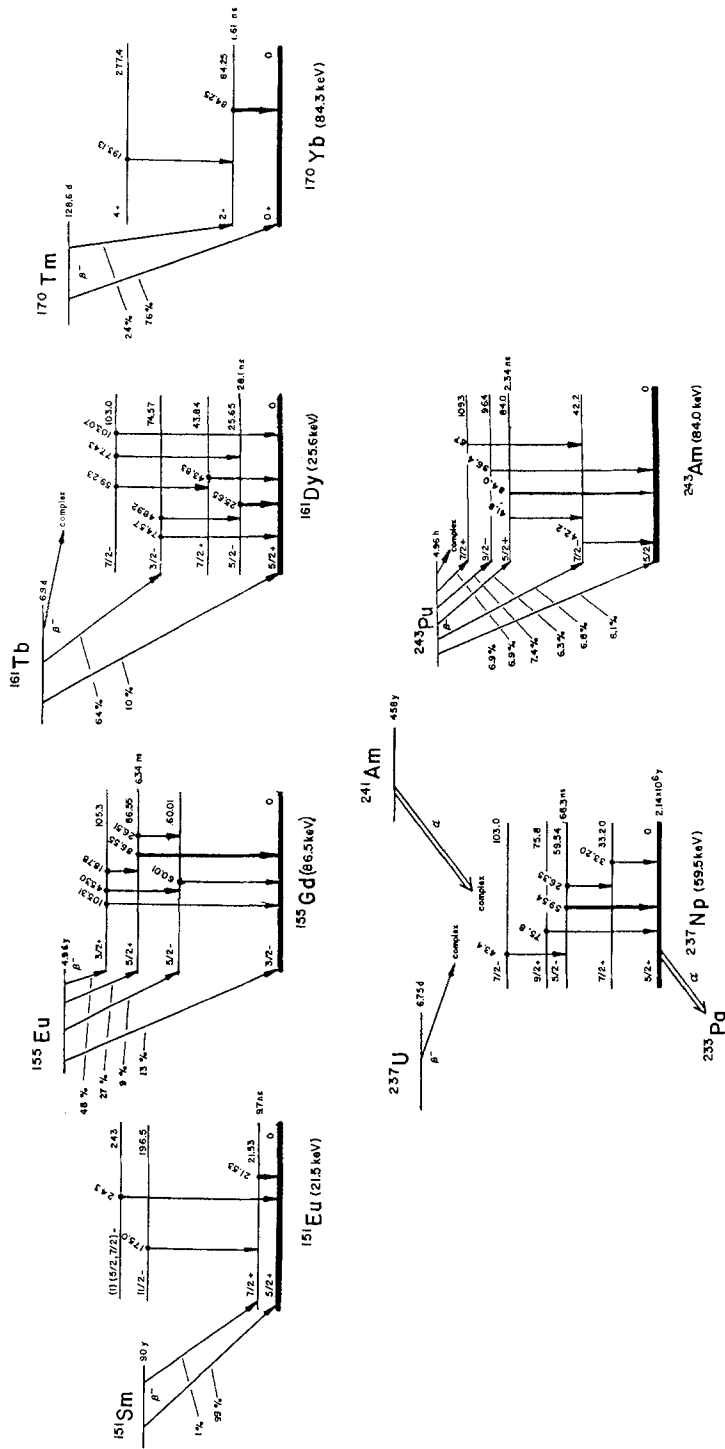


Fig. 1. Upper part: Lanthanide and actinide series. For shaded elements Mössbauer spectroscopy cannot be carried out. For underlined elements Mössbauer spectroscopy is well established and numerous systematic data exist. Lower part: Widely used Mössbauer transitions (underlined elements) in the lanthanides and actinides. [After Stevens and Stevens (1976).]

the actinides systematic data exist only for Np and to a much lesser degree for Am. The relevant  $\gamma$ -transitions of these selected cases are depicted in the lower part of fig. 1. Obviously, Mössbauer results are available mainly for the heavy lanthanides (in which the 4f electrons are particularly well localized) and the light actinides (which are prone to 5f delocalization). It is unfortunate that Mössbauer spectroscopy studies cannot be carried out for cerium compounds and that Mössbauer data on uranium materials are not very informative (and rather difficult to get). For that reason this technique has contributed little towards an understanding of the exotic electron structure properties like heavy-fermion and Kondo-lattice behavior, which is found predominantly amongst Ce and U compounds. The few existing data on Np materials will be reviewed in section 8. The situation hopefully will improve in the future when more neptunium intermetallics are prepared. Surely some "anomalous" systems will be amongst them and they could well be studied, provided the constant inflation of superfluous safety regulations does not make such experiments altogether impossible!

Reviews of Mössbauer spectroscopy applied to lanthanides (Ofer et al. 1968, Barnes 1979, Taneja and Kimball 1983) and actinides (Dunlap and Kalvius 1985) are available, but progress has of course been made in recent years. The purpose of this article, however, is not to systematically update the information now available. We wish rather to discuss selected examples where the differences between lanthanides and actinides can best be contrasted. We shall deal exclusively with intermetallic compounds.

The situation with respect to high-pressure Mössbauer experiments is discussed in section 5. General systematics within the most thoroughly studied series of intermetallics are presented in section 6. Section 7 briefly highlights the spin-glass behavior of a class of lanthanide and actinide intermetallics.

## 2. Mössbauer spectroscopy

### 2.1 Basics of the Mössbauer effect

We introduce briefly the physical principles of the Mössbauer effect. For more details we refer the reader to more extended reviews, for example, Kalvius (1987), Dunlap and Kalvius (1985), Thosar et al. (1983) or Goldanskii and Makarov (1968) as well as the literature cited therein.

The basis of the Mössbauer effect is resonance absorption of  $\gamma$ -rays (see fig. 2). It means that a  $\gamma$ -ray emitted in the de-excitation of a nuclear excited state to its ground

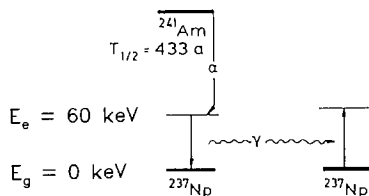


Fig. 2. Principle of  $\gamma$ -ray resonance fluorescence. The example is  $^{237}\text{Np}$ .



state can be used to re-excite another nucleus of the same kind. The  $\gamma$ -ray vanishes in this process, it is absorbed. By definition resonance absorption can only occur if the emission energy exactly matched the absorption energy. This is the essential point. This requires that we look in more detail at the energy distribution  $N(E)$  of the emitted  $\gamma$ -ray and at the absorption cross section  $\sigma(E)$  of the resonant nuclei. Both  $N(E)$  and  $\sigma(E)$  are of Lorentzian shape with a full width at half maximum  $\Gamma$  given by Heisenberg's uncertainty principle

$$\Gamma = \hbar/\tau_e, \quad (1)$$

where  $\tau_e$  is the mean life of the excited nuclear state. If the nucleus were to stay totally at rest during the emission or absorption process then  $N(E)$  and  $\sigma(E)$  would both be centered at the  $\gamma$ -transition energy  $E_0 = E_e - E_g$ ,

$$N(E) = N_0 \frac{(\Gamma/2)^2}{(E - E_0)^2 + (\Gamma/2)^2} \quad (2)$$

and

$$\sigma(E) = \sigma_0 \frac{(\Gamma/2)^2}{(E - E_0)^2 + (\Gamma/2)^2}. \quad (3)$$

Here  $\sigma_0$  is the maximum resonance cross section given by

$$\sigma_0 = \frac{2\pi c^2 \hbar^2}{E_0^2} \frac{2I_e + 1}{2I_g + 1} \frac{1}{1 + \alpha_t}, \quad (4)$$

with  $I_e$  and  $I_g$  being the spins of the nuclear excited and ground states, respectively, and  $\alpha_t$  the total electron conversion coefficient. The cross section  $\sigma_0$  can become quite large (see table 3 in section 3.1.1). The  $\gamma$ -ray carries momentum. Its conservation in the emission and absorption processes makes the nucleus recoil with energy

$$E_R = \frac{E_0^2}{2Mc^2}, \quad (5)$$

where  $M$  is the nuclear mass. Hence  $N(E)$  now centers at  $E_0 - E_R$  and  $\sigma(E)$  at  $E_0 + E_R$ . The life times  $\tau_e$  of low-lying nuclear states can be quite long (several ns) and consequently  $\Gamma$  is quite narrow ( $\sim 10^{-8}$  eV). A quick estimate shows that  $E_R \approx 10^{-2}$  eV. Consequently  $E_R \gg \Gamma$  and the resonance condition is altogether violated.

The trick, introduced by Mössbauer (1958), to circumvent this problem is to use nuclei bound in a solid as emitter and absorber. The bonding energy  $E_B$  of atoms is in the eV range and thus  $E_R \gg E_B$ , i.e., the nuclei cannot recoil freely. Their only means to exchange energy with the lattice is to create or absorb a phonon while the  $\gamma$ -ray transition (either  $E_e \rightarrow E_g$  or  $E_g \rightarrow E_e$ ) takes place. There is a certain probability  $f$  (called the recoil-free or resonant fraction) for the phonon state of the crystal to remain unaltered while the  $\gamma$ -ray is emitted or absorbed. In other words,  $f$  gives the probability for a zero-phonon  $\gamma$ -transition.  $N(E)$  and  $\sigma(E)$  attain the shape schematically shown in fig. 3. The zero-phonon lines in  $N(E)$  and  $\sigma(E)$  are centered at  $E_0$  and for them eqs. (2) and (3) apply when multiplied by their proper  $f$ -factors

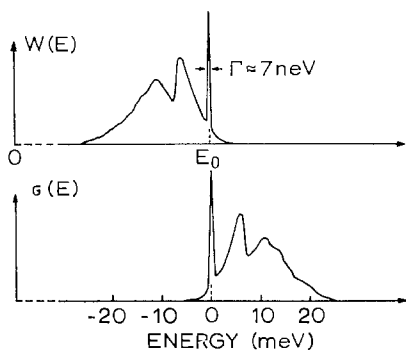


Fig. 3. Schematic representation of emission probability and absorption cross section for nuclei bound in a solid after Visscher (1960). The sharp line arises from zero-phonon processes, the broad distribution from one- and multi-phonon processes. The  $f$  factor equals the ratio of the area under the sharp line to the total area. Height and width of the zero-phonon line are not to scale. The energy scale corresponds to the case of  $^{237}\text{Np}$ . [Taken from Dunlap and Kalvius (1985).]

( $f_s$  for the emitter (source) and  $f_a$  for the absorber). The resonance condition is fulfilled in part and resonance absorption can take place but with reduced probability given by  $f_s$  and  $f_a$ .

Theoretically the situation is closely related to the question of energy transfer in Bragg scattering of X-rays or neutrons. Consequently the  $f$ -factor has a form quite analogous to the well known Debye-Waller factor,

$$f = \exp\left(-\frac{E_0^2}{\hbar^2 c^2} \langle u^2 \rangle\right), \quad (6)$$

where  $\langle u^2 \rangle$  is the mean-square displacement of the nuclei which undergo the  $\gamma$  transitions. In any real lattice,  $f = 1$  cannot be obtained even at  $T = 0$  since zero-point motion is still present. The mean-square displacement increases with temperature, decreases as the binding forces in the solid become stronger, and decreases as the mass of the nucleus increases. It should be mentioned that a regular lattice structure is not a prerequisite for obtaining a sizeable resonant fraction. Amorphous solids can easily be studied by Mössbauer spectroscopy. In liquids the Mössbauer effect is observed only if the viscosity is extremely large, e.g. in glasses. No Mössbauer effect is possible in gaseous materials.

In practice one usually evaluates the resonant fraction in terms of the Debye model for the phonon spectrum (see, e.g., Boyle and Hall 1962)

$$f(T) = \exp\left\{-\frac{6E_R}{k\theta} \left[ \frac{1}{4} + \left(\frac{T}{\theta}\right)^2 \int_0^{\theta/T} \frac{x dx}{e^x - 1} \right]\right\}. \quad (7)$$

Here  $T$  is the actual and  $\theta$  the Debye temperature. The last term is the Debye integral, which can be found in mathematical tabulations. In the limit of  $T \rightarrow 0$  one may approximate eq. (7) by

$$f = \exp(-3E_R/2k\theta). \quad (8)$$

For  $T > \theta$  a good approximation is

$$f = \exp(-6E_R T/k\theta^2). \quad (9)$$

It follows that  $-\ln f$  is proportional to  $T$ . Figure 4 depicts the situation for  $^{237}\text{Np}$ .

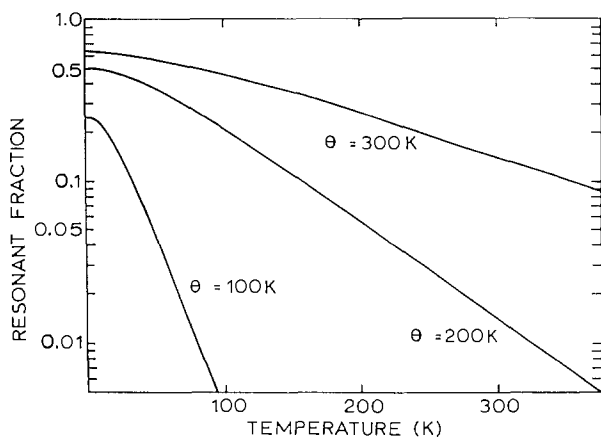


Fig. 4. Temperature dependence of the recoil-free (resonant) fraction  $f$  of the  $^{237}\text{Np}$  resonance in the Debye approximation for different Debye temperatures  $\theta$ . For intermetallics  $\theta = 200$  K is an appropriate choice. [Taken from Dunlap and Kalvius (1985).]

In summary, to render the recoil-free fraction large, i.e., to have a reasonable resonance absorption effect, one has to fulfil two conditions. Firstly,  $E_R < k\theta$  where  $\theta$  refers to the solids serving as source or absorber. This limits the  $\gamma$ -transition energy to  $\sim 100$  keV in lighter and to  $\sim 150$  keV in heavier nuclei. Secondly,  $T < \theta$  except in cases of very low transition energies ( $E_R \ll k\theta$ ). This restricts the temperature range accessible by Mössbauer spectroscopy. For example, it is difficult to carry out Mössbauer experiments with  $^{237}\text{Np}$  much above  $\sim 100$  K. We further recall that only  $\gamma$ -ray transitions which lead to the ground state of a stable or at least long-lived (minimum a few years) nucleus are suitable. Due to these restrictions the number of Mössbauer transitions available throughout the periodic system is limited. In practice some other considerations may also come into play.

The existence of a proper  $\gamma$ -ray transition is an outcome of nuclear structure. Therefore, a Mössbauer transition is coupled to a certain isotope of the atom of interest. A low isotopic abundance of the resonant isotope may be a serious restriction. Next, if the excited state is rather short lived then  $\Gamma$  becomes wide and the resolution for hyperfine spectroscopy (see section 2.3) becomes too limited. The same effect can be caused by unfortunate values of nuclear moments of the two states involved in the Mössbauer transition. Finally, difficulties to produce the source activity may hinder a wider application of measurements with that particular isotope. Difficulties in source preparation and poor resolution are, for example, present in  $^{238}\text{U}$  and have prevented Mössbauer spectroscopic studies of compounds of this most interesting actinide.

## 2.2. Mössbauer spectra

The usual experimental set-up works in transmission geometry as shown in fig. 5 (top): The strength of resonance absorption is determined by the reduction of  $\gamma$ -ray intensity reaching the detector. Not taking into account the hyperfine interactions, to be discussed later, and neglecting a small relativistic effect (the second-order Doppler shift) one has an exact energy match for the zero-phonon lines of  $N(E)$  and  $\sigma(E)$  (see fig. 3) if both source and absorber are at rest. Resonance absorption is now strongest.

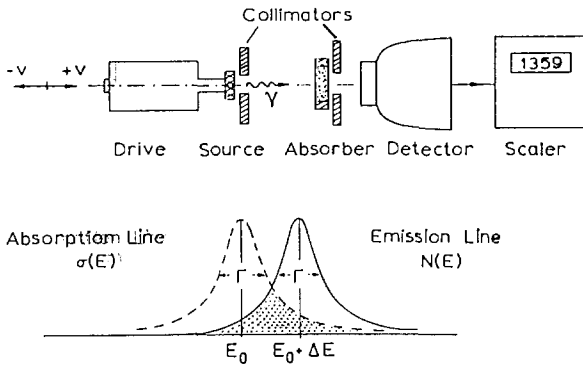


Fig. 5. Principle of Mössbauer spectroscopy. Top: Set-up for measurement in transmission geometry. Bottom: Overlap of Doppler-shifted zero-phonon emission line with the zero-phonon absorption line. The shift  $\Delta E$  is given by eq. (10). [Taken from Kalvius (1987).]

An energy shift  $\Delta E$  between  $N(E)$  and  $\sigma(E)$  can be created via the Doppler effect,

$$\Delta E = \frac{vE_0}{c}, \tag{10}$$

by moving with the drive unit the source towards (with velocity  $+v$ ) or away ( $-v$ ) from the absorber. This reduces the overlap of emission and absorption lines (fig. 5, bottom) and thus weakens resonant absorption. The count rate at the detector will rise. The Mössbauer spectrum is then a plot of transmitted count rate  $Y(v)$  versus (source) velocity as shown in fig. 6. Under the circumstances defined above,  $Y(v)$  is in first approximation (infinitely thin absorber) again a Lorentzian,

$$Y(v) = 1 - \frac{Y_0}{1 + 4v^2/W_0^2}, \tag{11}$$

with a FWHM of

$$W_0 = \frac{2\Gamma c}{E_0}. \tag{12}$$

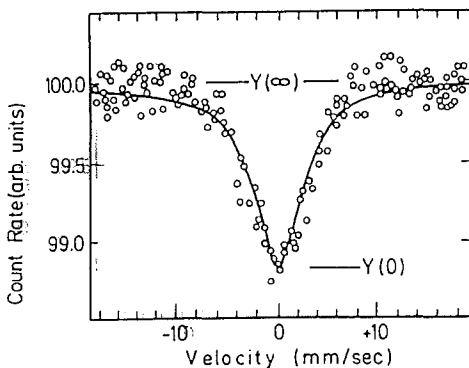


Fig. 6. Mössbauer spectrum. The circles are the measured count rate at different source velocities, the solid line is the theoretical function given by eqs. (11) to (15). The scatter of data points due to counting statistics is clearly visible. [Taken from Kalvius (1987).]

This is twice the resonance width expressed in velocity units. For not too thick absorbers eq. (11) is still a reasonable approximation but corrections have to be included in eq. (12),

$$W = W_0(1 + 0.135t_a), \quad (13)$$

where

$$t_a = n\sigma_0 f_a A \quad (14)$$

is a measure of absorber thickness. Here  $n$  is the number of atoms per unit area of the Mössbauer element and  $A$  is the isotopic abundance. The maximum absorption is given by

$$Y_0 = \frac{Y(v = \infty) - Y(v = 0)}{Y(v = \infty)} = f_s [1 - \exp(-t_a/2) J_0(it_a/2)], \quad (15)$$

where  $J_0(ix)$  is the Bessel function of first kind and order zero with imaginary argument (see Abramowitz and Stegun 1972). Clearly, a compromise in effective absorber thickness has to be found to keep line broadenings small but to guarantee a sizeable absorption strength. More details can be found in Asch and Kalvius (1981a) and references given therein. A suitable choice is  $t_a = 2$ .

In some cases, e.g. in  $^{237}\text{Np}$ , the resonance lineshape contains in addition to the Lorentzian term of eq. (11) a weak dispersion term which has to be taken into account in precise data analysis (Goldwire and Hannon 1977). The situation in  $^{237}\text{Np}$  is discussed by Asch et al. (1978). Due to the sharpness of  $\Gamma$  the velocities needed to destroy resonance absorption are quite small, usually in the range of 10 to 100 mm/s. The actual construction of Mössbauer spectrometers will be reviewed briefly in section 3.1.

We have discussed the basic procedures how to obtain a Mössbauer spectrum. However, a spectrum like fig. 6 contains only lattice dynamical information via  $Y_0$  and allows to determine  $\tau_c$  from  $W$ . Yet, our interest lies in electronic structure properties. To understand how those are reflected in a Mössbauer spectrum we have first to discuss hyperfine interactions. Before entering this topic a few final words on dealing with a Mössbauer spectrum are appropriate.

Mössbauer experiments are nuclear counting experiments and hence a certain number of counts has to be collected to make the statistical error small compared to the strength of resonance absorption. The latter is typically in the region of  $10^{-2}$ , this means that  $10^6$  counts per channel have to be stored to make the counting statistics  $10^{-3}$ . Characteristic running times for a single spectrum vary between a day and a week. After the desired collection time has passed, an appropriate theoretical spectral curve is least-squares fitted to the counts-versus-velocity histogram which represents the measured spectrum. The fit variables are experimental parameters like effective linewidth  $W$  and resonance strength  $Y_0$  as well as hyperfine parameters like isomer shift, hyperfine field, and electric field gradient (see next section). The essential point is that one has to have an a priori notion of the general nature of the hyperfine interaction before adjustment to the measured spectrum. A fit may not necessarily be unique.

### 2.3. Hyperfine interactions

The hyperfine interaction energy arises from the electromagnetic coupling of the nucleus to all surrounding charges. Primarily these are the electronic charges in the nucleus' own atomic shell. The hyperfine energies are small, around  $10^{-5}$  eV, and affect both the electronic and the nuclear states. The former effect is visible in high-resolution optical spectroscopy. It leads to line-shifts and line-splittings far beyond the fine structure caused by spin-orbit coupling. This has given those interactions their name. To see the influence of hyperfine interactions directly on nuclear radiation was only possible after the discovery of the Mössbauer effect. In favorable cases, like  $^{237}\text{Np}$ , the natural width  $\Gamma$  of the zero-phonon line is small ( $\sim 10^{-8}$  eV) compared to the hyperfine energy and the shape of  $N(E)$  or  $\sigma(E)$  will noticeably be influenced. We will discuss this further below and turn first towards a quick description of the essentials of the theory of hyperfine coupling.

To carry out the calculations it is customary to use a multipole expansion and to separate electric and magnetic couplings. A nucleus can only possess even electric moments, i.e. a monopole moment ( $l = 0$ ), namely its protonic charge and a quadrupole moment ( $l = 2$ ) if the charge distribution is not spherical. Higher moments are neglected. Magnetically only odd moments exist. It suffices to consider the dipole moment ( $l = 1$ ).

#### 2.3.1. Isomer shifts and the contact electron density

The electric monopole term has its origin in the fact that the nucleus extends over a finite volume and that shell electrons of s or  $p_{1/2}$  character can penetrate into the nuclear volume. The resulting Coulomb interaction between protonic and electronic charges inside the nucleus causes a shift in nuclear energy levels. Under the assumption that the electronic charge density is constant throughout the nuclear volume and equals its value  $\rho(0)$  at the origin, one obtains for this energy shift (Dunlap and Kalvius 1978)

$$\delta E = \frac{2\pi}{3} e^2 Z \rho(0) \langle r^2 \rangle. \quad (16)$$

The parameter  $\langle r^2 \rangle$  is a measure of the radial extent of nuclear charge. It is called the mean square nuclear charge radius. The electronic density  $\rho(0)$  is often referred to as the contact charge density. The shift  $\delta E$  will in general be different for the nuclear ground (index g) and excited (index e) states since a nuclear excitation slightly alters the nuclear configuration and hence  $\langle r^2 \rangle$ . The energy of a  $\gamma$ -ray emitted by the source nuclei (index s) will be

$$(E_e + \delta E_e)_s - (E_g + \delta E_g)_s = E_0 + \frac{2\pi}{3} e^2 Z \rho_s(0) \Delta \langle r^2 \rangle = E_0 + \Delta E_s, \quad (17)$$

where

$$\Delta \langle r^2 \rangle = \langle r^2 \rangle_e - \langle r^2 \rangle_g. \quad (18)$$

Normally, the absorber material is a different chemical compound than the source material. Hence the absorption cross section centers at  $E_0 - \Delta E_a$ , where  $\Delta E_a$  is given by eq. (17) if one replaces  $\rho_s(0)$  by  $\rho_a(0)$ .

To obtain full resonance absorption these shifts have to be compensated by an appropriate Doppler shift

$$S = \frac{c\Delta E_0}{E_0}, \quad (19)$$

with

$$\Delta E_0 = \frac{2\pi}{3} c^2 Z \Delta\rho(0) \Delta\langle r^2 \rangle \quad (20)$$

and

$$\Delta\rho(0) = \rho_s(0) - \rho_a(0). \quad (21)$$

The Mössbauer spectrum now has its absorption maximum at  $v = S$  instead of  $v = 0$ . Figure 7 gives an example.

One calls  $S$  the isomer shift. From an electron structure point of view, the parameter of interest is  $\Delta\rho(0)$  and one combines all other factors into the isomer shift calibration constant  $\alpha$ , i.e.

$$S = \alpha\Delta\rho(0). \quad (22)$$

Unfortunately, it is not possible to calculate  $\alpha$  (i.e.,  $\Delta\langle r^2 \rangle$ ) theoretically with any degree of reliability. Common practice is a semi-empirical calibration: The shift  $S$  is measured (with the same source) for two compounds to be considered rather ionic with the resonant atom in two different charge states. Pertinent examples would be  $\text{NpF}_3$  and  $\text{NpF}_4$ . Contact densities calculated with a self-consistent procedure for the free ions are used to obtain  $\Delta\rho(0)$ . The constant  $\alpha$  is then determined according to eq. (22). One certainly can raise a number of objections towards this method but it is still the most universal one. It is important, especially for the lanthanides and actinides, that relativistic charge densities  $\rho(0)$  are used. Details concerning isomer

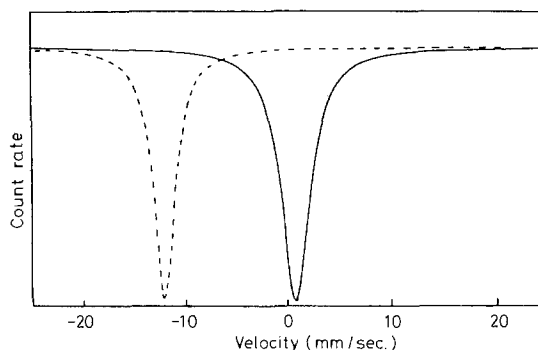


Fig. 7. Comparison of the  $^{151}\text{Eu}$  Mössbauer spectrum of  $\text{Eu}^{3+}$  in  $\text{Eu}_2\text{O}_3$  (solid line) and  $\text{Eu}^{2+}$  in  $\text{EuO}$  (broken line). The data points have been omitted for clarity. The essential point is the difference in location of maximum absorption (isomer shift). The source is  $^{151}\text{Sm}$  in  $\text{SmF}_3$ . [Taken from Kalvius (1987).]

shifts of most Mössbauer resonances are available in the book edited by Shenoy and Wagner (1978).

In addition to the monopole interaction, a shift of resonance is also caused by the second-order Doppler effect already mentioned. Its origin is the vibrational motion of emitting and absorbing nuclei. According to Josephson (1960) and Pound and Rebka (1959) time dilatation produces the shift  $S_{\text{SOD}}$  if a difference  $\Delta T$  exists between the measuring temperature at the source and absorber and/or source and absorber compounds differ in their Debye temperatures by  $\Delta\theta$ . One finds at high temperatures ( $T \gg \theta$ ),

$$S_{\text{SOD}} = -\frac{3k\Delta T}{2Mc^2}, \quad (23)$$

and at low temperatures ( $T \ll \theta$ ),

$$S_{\text{SOD}} = -\frac{9k\Delta\theta}{16Mc^2}. \quad (24)$$

Isomer and second-order Doppler shifts are nearly impossible to separate. Fortunately,  $S_{\text{SOD}}$  is large only for  $\gamma$  transitions of relatively high energy in light nuclei. For heavy nuclei like the lanthanides and actinides the second-order Doppler shift can safely be neglected.

It is important to realize that isomer shifts (in mm/s) cannot be compared for different resonances. Not only does  $\alpha$  vary widely (and can have a positive or negative sign) but the transition energy  $E_0$  also enters [e.g. in eq. (19)]. For any given isotope the isomer shifts are commonly referred to a certain compound representing the zero point of the isomer shift scale. For example, in  $^{237}\text{Np}$  the intermetallic  $\text{NpAl}_2$  serves as reference. For other Mössbauer resonances see Cohen and Kalvius (1970).

We have thus far assumed a stable ionic charge state leading to a fixed, static isomer shift. As mentioned, in some lanthanides the phenomenon of charge fluctuations may be present. Then the shift alternates between two values corresponding to the different charge states. If the fluctuations are fast (i.e.,  $h\nu_{\text{charge}} > \Delta E_0$ ) then a single resonance at the position of the mean shift will be observed. If fluctuations are slow then two resonances with the two different shifts will appear. For intermediately fast fluctuations the resonance lines broaden out and overlap. This case is usually referred to as a relaxation spectrum. Examples concerning unstable valences will be discussed in section 4.

### 2.3.2. Magnetic hyperfine splittings and the hyperfine field

Magnetic moments have their origin in spinning charges. Hence we can write the magnetic interaction Hamiltonian as the coupling between nuclear spin  $I$  and atomic angular momentum  $J$ ,

$$\mathcal{H}_m = I \cdot \tilde{\mathbf{A}} \cdot J, \quad (25)$$

where  $\tilde{\mathbf{A}}$  is the hyperfine tensor. Diagonalization of this Hamiltonian can be quite cumbersome, particularly if  $I$  and/or  $J$  are larger than  $\frac{1}{2}$ . The situation improves if



one is able to simplify  $\mathcal{H}_m$  on account of symmetry arguments. The most straightforward case is uniaxial symmetry which gives

$$\mathcal{H}_m = A_z I_z J_z. \quad (26)$$

Such an approximation is applicable if either a strongly anisotropic electronic  $g$ -factor is present or if the magnetic atoms are exposed to a strong magnetic field. This can be, for example, the exchange field in ordered magnets.

In essence, eq. (26) describes the interaction of a point dipole in a homogeneous field. Using the nuclear dipole moment

$$\boldsymbol{\mu}_I = g_I \mu_N \mathbf{I} \quad (27)$$

where  $\mu_N$  is the nuclear magneton and  $g_I$  the  $g$ -factor of the nuclear state with spin  $I$  and representing the electronic contribution by an effective magnetic field (the hyperfine field  $B_{\text{hf}}$ ) produced by the open-shell electrons leads to eigenvalues of eq. (26) of the form

$$E_m = -\frac{\mu_I}{I} \mu_N m_I B_{\text{hf}}, \quad (28)$$

with  $m_I$  being the magnetic quantum number associated with the nuclear spin  $I$ .

It follows that a nuclear state  $I$  will split into an equidistant set of  $2I + 1$  substates, characterized by  $m_I$ . The separation of two consecutive substates is given by  $(\mu/I)\mu_N B_{\text{hf}}$ . This is known as the Zeeman splitting of a nuclear level. The situation for the case of  $^{237}\text{Np}$  ( $I_g = I_e = \frac{5}{2}$ ,  $\mu_g = 2.5\mu_N$  and  $\mu_e = 0.536\mu_g$ ) is presented in fig. 8. Both the ground and excited state split into six hyperfine sublevels. The intensities of the  $\gamma$  transitions between the hyperfine states are given by

$$I(\vartheta) = CF_L^M(\vartheta) |\langle I_g m_g L M | I_e m_e \rangle|^2 \quad (29)$$

with  $M = m_e - m_g$  and  $L =$  multipolarity of the  $\gamma$ -ray transition.  $C$  is a normalization factor;  $F_L^M(\vartheta)$  describes the angular dependence of the resonant  $\gamma$  radiation with  $\vartheta$  being the angle between the direction of observation and the quantization axis which defines  $m_g$  and  $m_e$ ;  $\langle \dots | \dots \rangle$  is the Clebsch–Gordon coefficient (for details see Asch and Kalvius 1981b). The bar diagram in fig. 8 shows the energetic positions and relative intensities of the hyperfine lines under the assumption that the axis of quantization is randomly distributed throughout the sample. The  $\gamma$  transition in  $^{237}\text{Np}$  has (electric) dipole character and hence only  $M = 0, \pm 1$  is allowed. The other case encountered in Mössbauer spectroscopy is quadrupolar  $\gamma$  transitions with  $M = 0, \pm 1, \pm 2$ . In some cases one has mixed multiplicities.

To measure a hyperfine interaction one proceeds as follows. One selects a source compound where no magnetic hyperfine field is present. Then  $N(E)$  remains a single line. The absorber nuclei shall be subject to Zeeman splitting. Hence  $\sigma(E)$  consists of a multitude of lines according to the allowed hyperfine transitions between nuclear ground and excited states (for the example of  $^{237}\text{Np}$  see the bar diagram in fig. 8). Within the resonance width not all transitions need necessarily be resolved. Shifting the single source line by Doppler motion over the multiline absorption pattern then leads to the hyperfine split Mössbauer spectrum of fig. 9 which directly reflects the

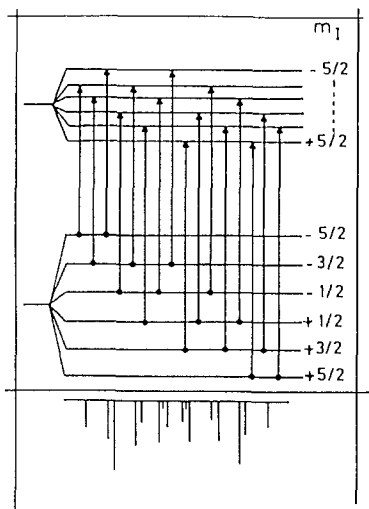


Fig. 8. Zeeman splitting of the nuclear ground and excited states of  $^{237}\text{Np}$ . Both states have the same spin ( $I = \frac{5}{2}$ ) but the ground-state magnetic moment is larger than that of the excited state. The bar diagram (lower part) shows position and intensities of the 16 allowed  $\gamma$  transitions between the hyperfine levels.

allowed  $\gamma$  transitions between the Zeeman states of the nuclear ground and excited state. Since  $I_e, I_g, \mu_g$  and the multipolarity are usually known, one can extract  $B_{\text{hf}}$ , the hyperfine field which carries information on electronic structure. It may be added that one can, of course, reverse the game, i.e., having Zeeman interaction in the source and none in the absorber. In special cases one may even work with multiple line sources and absorbers, but the spectrum is then quite complex.

When will a Zeeman splitting be observed? Clearly, we need a paramagnetic atom (ion) to begin with. In the paramagnetic regime the magnetic moments fluctuate rapidly and in the absence of an external field both the bulk and the local (at the atom in question) magnetization is zero. In other words  $\langle B_{\text{hf}} \rangle = 0$  and no splitting is seen. We can enforce  $B_{\text{hf}} \neq 0$  by applying an external field. The magnitude of  $B_{\text{hf}}$  is then given by the appropriate Brillouin function and  $B_{\text{hf}}/B_{\text{ext}}$  is a measure of the local susceptibility (see, e.g. Gal et al. 1989a).

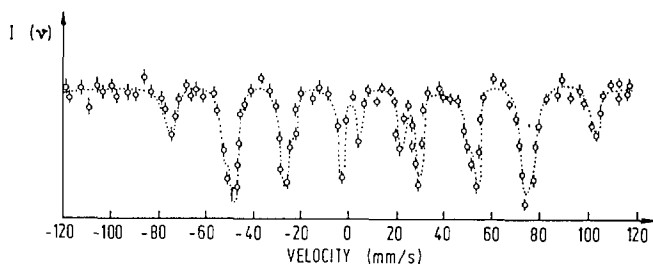


Fig. 9. Magnetic hyperfine spectrum of  $^{237}\text{Np}$  in ferromagnetic  $\text{NpAl}_2$  at 4.2 K. The source is  $^{241}\text{Am}$  metal which emits an unsplit line. The theoretical spectrum (broken line) is calculated according to the bar diagram of fig. 8. From the line positions one obtains  $B_{\text{hf}} = 330$  T.

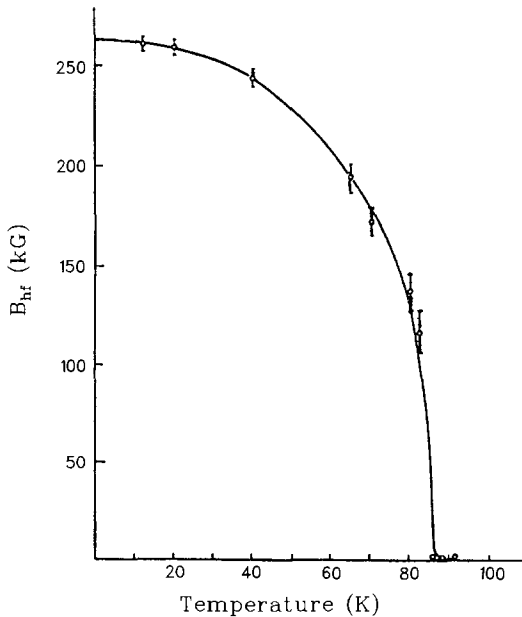


Fig. 10. Temperature dependence of the hyperfine field in Eu metal as measured with the  $^{151}\text{Eu}$  resonance. The solid line corresponds to the magnetization curve for  $S = \frac{7}{2}$ . [After Kienle (1964).]

If the material undergoes a transition into an ordered magnetic state (i.e., passing the Curie or Néel temperature) then the exchange field plays the role of the external field discussed above. We have  $B_{hf} \neq 0$  (in zero applied field). The hyperfine field will be temperature-dependent, it follows roughly the domain magnetization. An example is given in fig. 10. The measurement of the internal field at the nucleus (and the ordering temperature) of a magnetically ordered material is the most widespread application of Mössbauer spectroscopy to magnetism. One should keep in mind that Mössbauer spectroscopy is not a diffraction technique and hence long-range order is not required. Zeeman splittings can well be observed in short-range ordered materials like, for example, spin glasses or amorphous magnets. As a rule,  $B_{hf}$  is not well defined in such substances and rather “washed out” Mössbauer Zeeman spectra are found.

The underlying assumption in the foregoing discussion is that the fluctuation of magnetic moments (with frequency  $\nu_m$ ) in the solid is rapid (i.e.  $h\nu_m \geq E_m$ ). The other extreme ( $h\nu_m \leq E_m$ ) may also occur, but more rarely. Then, even in a paramagnet we have  $\langle B_{hf} \rangle \neq 0$  in zero field since averaging to zero does not take place within the time scale of magnetic hyperfine interactions (but will take place, for example, on the time scale of bulk magnetization measurements). We can then, however, not assume a priori that eq. (26) is applicable (that depends on the symmetry of the magnetic state) and one is often forced to fully diagonalize eq. (25). Even more than one electronic state (i.e. different  $J$ ) may be occupied and the lack of fast fluctuations will not average out the contributions from the different states. In short, such paramagnetic hyperfine spectra can be extremely complex. Fortunately, they are only rarely observed, especially in metallic materials. One may also have to deal with the case of intermediately fast fluctuations ( $h\nu_m \approx E_m$ ). Then a partial wash-out of the hyperfine

spectra occurs. On the fast side, the single absorption line usually observed in a paramagnet is severely broadened, on the slow side, a split spectrum will appear but with non-Lorentzian lines and additional intensities in the center. One speaks of (magnetic) relaxation spectra. Again a diagonalization of the full Hamiltonian (25) may be required. Extensive discussions of theory are given by Wickmann and Wertheim (1968), Wegener (1965), Clauser and Blume (1971), Blume and Tjon (1968) and Dattagupta (1983). Relaxation spectra can also be seen in the magnetically ordered state if the moment fluctuations are not fast enough (Nowik and Wickmann 1966). The problem is that these dynamical hyperfine spectra are difficult to distinguish from those produced in the presence of a (static) distribution of hyperfine fields (i.e. amorphous magnet). We shall come back to some of these difficulties in our discussion of  $^{237}\text{Np}$  hyperfine spectra.

The last task to deal with in this subsection is the origin of the hyperfine field.  $B_{\text{hf}}$  consists of a contribution  $B_{\text{orb}}$  produced by the orbital angular momentum of open-shell electrons plus a contribution  $B_{\text{core}}$  arising from the polarization of core electrons by outer-shell electrons producing unpaired spin density at the nucleus. In nonrelativistic theory,  $B_{\text{orb}}$  is given by

$$B_{\text{orb}} = a_{\text{hf}} \langle J \| N \| J \rangle \langle r^{-3} \rangle m_J. \quad (30)$$

Here  $\langle J \| N \| J \rangle$  is a reduced matrix element. In effect, it is simply a number depending on  $J$  which can be found in tabulations by Elliott and Stevens (1953). The factor  $\langle r^{-3} \rangle$  is the quantum mechanical average of  $1/r^3$  using the wave functions of the open-shell electrons. It is commonly given in units of  $a_0^3$  ( $a_0$  is the Bohr radius) and denoted as atomic units (au). In that case, the value of the hyperfine coupling constant is  $a_{\text{hf}} = 12.51 \text{ kT/au}$ .

The core field in nonrelativistic theory is given by

$$B_{\text{core}} = \frac{2\mu_0}{3} \mu_B \sum_n S [\rho_{ns}^\uparrow(0) - \rho_{ns}^\downarrow(0)] \quad (31)$$

where  $\rho_{ns}^\uparrow(0)$  or  $\rho_{ns}^\downarrow(0)$  are the contact density of  $s$  electrons of the  $n$ th shell having spin up or spin down and  $S$  is the net spin of the open-shell electrons. The sum in eq. (31) has to be carried out over all occupied shells, not just the open shell. Calculation of core fields are reviewed by Watson and Freeman (1967) and Desclaux et al. (1977).

Inclusion of relativity in the theory of hyperfine interactions has two major effects (Sandars and Beck 1965). The expression for  $B_{\text{orb}}$  has a more complicated form than the above. In addition, modifications occur regarding the way in which  $r^{-3}$  enters into the expression. Basic aspects of the theory are given by Dunlap and Kalvius (1974) and Dunlap (1971). Related calculations have been published by Kalish et al. (1975). The radial parameters are generally obtained from atomic self-consistent field calculations for free atoms, there being essentially no calculations in condensed materials. It is important to recognize that these calculations for the lanthanides and actinides must be done relativistically (i.e. Dirac-Fock), since the neglect of relativity causes serious errors for  $f$  electrons.

Thus far it was tacitly assumed that the magnetic moments rest on the Mössbauer atoms. For Mössbauer spectroscopy with lanthanide and actinide resonances this is

reasonable. One may, however, use a compound where one of the ligand is a non magnetic atom. Cases of interest are, e.g.,  $^{119}\text{Sn}$  spectroscopy on  $\text{NpSn}_3$ ,  $^{121}\text{Sb}$  spectroscopy on  $\text{PuSb}$ , or  $^{125}\text{Te}$  spectroscopy on  $\text{UTe}$ . The ordered moment on the actinide (or lanthanide) atom will produce a weak dipolar magnetic field at the ligand atom and a much stronger core field by polarization of the ligand's electron shell. One speaks of transferred hyperfine fields. They are in general much weaker than the direct hyperfine field of the paramagnetic ion. They can still give, however, important information on moment formation and in particular on the type of magnetic spin structure which exists in the ordered state. A pertinent example is the study by Sanchez et al. (1976) on  $\text{RSn}_3$  compounds ( $\text{R} = \text{lanthanide}$ ).

In summary, hyperfine fields are the Mössbauer electronic structure parameter most susceptible to theoretical calculations and hence most readily susceptible to theoretical interpretations.

### 2.3.3. *Quadrupole splittings and the electric field gradient*

The third term of hyperfine energy is the electric interaction between a nonspherical nuclear charge distribution (described by a nuclear quadrupole tensor with components  $Q_{ij}$ ) and a nonspherical electronic charge distribution (described by the electric field gradient tensor with components  $V_{ij}$  consisting of the second spatial derivatives  $(\partial^2 V / \partial x_i \partial x_j)_{r \rightarrow 0}$  of the electric potential  $V$  produced by extra-nuclear charges at the nuclear site). One commonly assumes that the nuclear charge distribution is at least of axial symmetry. Then only one of the components  $Q_{ij}$  is nonvanishing. It is called the nuclear quadrupole moment  $Q$ . No general assumption can be made concerning the symmetry of electronic charge distribution. It is always possible to find a principal axis coordinate system for the electric field gradient tensor. Then only the diagonal components will be present. Laplace's equation requires  $V_{xx} + V_{yy} + V_{zz} = 0$  and the electric field gradient tensor has only two independent components. One labels the axes such that

$$|V_{xx}| \leq |V_{yy}| \leq |V_{zz}| \quad (32)$$

and then defines these two components by

$$eq = V_{zz}, \quad (33)$$

called the electric field gradient, and

$$\eta = \left| \frac{V_{xx} - V_{yy}}{V_{zz}} \right|, \quad (34)$$

called the asymmetry parameter. For the latter it follows that  $0 \leq \eta \leq 1$ , the case  $\eta = 0$  referring to axial symmetry.

The Hamiltonian for quadrupolar coupling has the form (Cohen and Reif 1957)

$$\mathcal{H}_Q = \frac{e^2 q Q}{4I(2I - 1)} (3I_z^2 - I^2 + \eta(I_x^2 - I_y^2)). \quad (35)$$

A general solution in closed form is available only for axial symmetry ( $\eta = 0$ ). The

eigenvalues for this case are

$$E_Q = \frac{e^2 q Q}{4I(2I - 1)} [3m_I^2 - I(I + 1)]. \quad (36)$$

The degeneracy of a nuclear state of spin  $I$  is now only lifted in part (i.e. with respect to  $m_I^2$ ) in contrast to magnetic splitting. The relative intensities between the hyperfine lines are given by eq. (29) as in the magnetic case. For  $I = 0$  and  $I = \frac{1}{2}$  the quadrupole coupling vanishes. In case of half-integer nuclear spins  $I$  the introduction of  $\eta$  will cause changes in the magnitude of  $E_Q$  but not lift further the degeneracy (Kramers theorem). In contrast, the action of  $\eta$  on nuclear states with integer spins will lift the remaining degeneracy in  $m_I^2$ . However, the splitting will not be equidistant as in the case of Zeeman interaction. Furthermore  $m_I$  is no longer a good quantum number. The admixture of  $m_I$  states has to be taken into account when calculating transition probabilities. A tabulation of splitting energies and line position can be found in Shenoy and Dunlap (1981).

The relative intensities of quadrupolar hyperfine lines can strongly deviate from their theoretical values even for powder samples having a completely random orientation of crystallites. The origin for this is the so-called Goldanskii–Karyagin effect. Each of the hyperfine transitions has a characteristic angular dependence. The  $f$  factor in crystals of low symmetry (which consequently have a large electric field gradient) is often also anisotropic since lattice vibration may have a preferred axis. When the averaging in a powder is carried out, the anisotropic  $f$  factor will give different weights to different spatial directions and thus produce line intensities as if certain crystalline directions were preferably present in the sample. True partial orientation of crystalline axes may also occur; one then speaks of texture. The separation of texture effects from the Goldanskii–Karyagin effect is difficult. An example of a quadrupolar spectrum exhibiting the Goldanskii–Karyagin effect is given in fig. 11.

It is customary to express the electric field gradient as the sum of two terms,

$$eq = eq_{\text{lat}}(1 - \gamma_\infty) + e \langle q_{\text{ion}} \rangle_T (1 - R). \quad (37)$$

The term  $eq_{\text{lat}}$  is referred to as the “lattice” gradient. It arises from the ionic charges

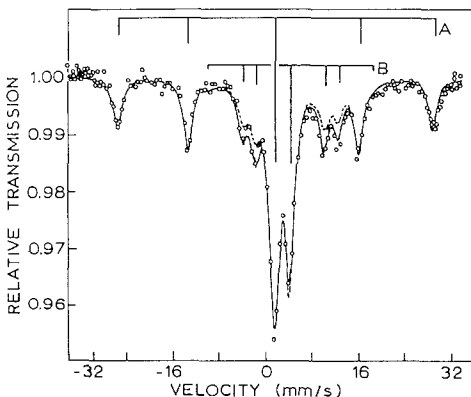


Fig. 11. Quadrupole hyperfine spectrum of  $^{237}\text{Np}$  in Np metal. The bar diagram shows the decomposition into two quadrupole patterns meaning that Np occupies two lattice sites with different local symmetries. In both cases the electric field gradient is not rotationally symmetric ( $\eta \neq 0$ ). The fit (solid line) includes the Goldanskii–Karyagin effect (see text). The dashed line shows the spectrum expected in case of full isotropy. [Taken from Dunlap et al. (1970).]

on all neighboring lattice atoms. This field gradient from sources outside the atom will induce a polarization of the own electronic shell of the nucleus. One describes the enhancement of  $eq_{\text{lat}}$  by this mechanism with the help of the so-called Sternheimer antishielding factor  $\gamma_{\infty}$ . Unfortunately it is not a very well-known quantity, although its magnitude is quite large ( $\gamma_{\infty} \approx -120$  for uranium). Theoretical estimates of  $eq_{\text{lat}}$  are difficult. Usually one employs lattice sum calculations (see, e.g., Bancroft 1981). The lattice gradient will vanish if the site symmetry at the resonant atom (not the symmetry of the crystal lattice!) has at least two  $n$ -fold rotational axes with  $n > 2$  (e.g. cubic symmetry).

The second term ( $eq_{\text{ion}}$ ) describes the "ionic" field gradient arising from nonspherical charge distribution of open-shell electrons of the resonant atom. It is in most cases dominant over  $eq_{\text{lat}}$ . For  $f$  transition elements one finds (Bleaney 1967) in the nonrelativistic approximation

$$q_{\text{ion}} = -b_Q \langle J \| \alpha \| J \rangle [3m_J^2 - J(J+1)] \langle r^{-3} \rangle, \quad (38)$$

where  $\langle J \| \alpha \| J \rangle$  are again reduced matrix elements (Elliott and Stevens 1953). The coupling constant has the value  $b_Q = 0.975 \times 10^{18} \text{ V/cm}^2$  if  $\langle r^{-3} \rangle$  is in atomic units. The relativistic treatment of Sandars and Beck (1965) shows that eq. (38) remains valid in good approximation if corrected values of  $\langle r^{-3} \rangle_Q$  are used. The index  $Q$  indicates that relativistically one has to distinguish between  $\langle r^{-3} \rangle$  for the orbital hyperfine field and the electric field gradient.

Crystalline field interactions will split the Hund's rule ground state into a set of levels characterized by different values of  $J_z$  and thus different ionic field gradients. Usually, more than one of the crystalline field states is occupied at finite temperatures  $T$ . Thermally driven fluctuations of  $q_{\text{ion}}$  are always fast in this situation (i.e.,  $h\nu_Q \gg E_Q$ ) and hence the thermal average of the ionic electric field gradient will be responsible for the quadrupolar interaction. This is taken into account in eq. (37). One must further realize that  $\langle q_{\text{ion}} \rangle_T \neq 0$  will only be possible if a local quantization axis exist. This can be provided by  $q_{\text{lat}}$ . Thus, if  $q_{\text{lat}} = 0$  (i.e. cubic symmetry) then  $\langle q_{\text{ion}} \rangle_T = 0$  as well and no quadrupole splitting is observed at all. But a local quantization axis can also be provided by  $B_{\text{hf}}$ . Then quadrupole splittings can be observed even in cubic crystalline surroundings. One speaks of magnetically induced quadrupole interactions which typically are seen in magnetically ordered compounds of lanthanides and actinides.

The gradient  $eq_{\text{ion}}$  will be shielded by core electrons. This is expressed by the inner Sternheimer shielding factor  $R$ . This shielding is much less severe than the antishielding described by  $\gamma_{\infty}$ . Values of  $R$  vary between 0.2 and 0.4. A measurement for  $^{237}\text{Np}$  ( $R = 0.35$ ) has been published by Dunlap et al. (1971).

In metallic materials there might be an additional contribution from conduction electrons in a band of non-s character. Field gradients from conduction electrons still present many open questions, one of which is the choice of an appropriate Sternheimer factor.

#### 2.3.4. Combined interactions

The fact that we have dealt with the three types of hyperfine coupling separately does not imply that they will not appear in combination in real cases. The monopole

interaction, for example, is always present. This causes no serious problem since the isomer shift does not depend on either the magnitude ( $I$ ) or the orientation ( $m_I$ ) of nuclear spin, in contrast to the other two interactions. The monopole interaction produces only shifts of nuclear states without lifting their degeneracy. In contrast, magnetic and quadrupole interactions split the nuclear states without shifting their center of gravity. Therefore one can always treat the monopole interaction independently. It is visible as a shift of the center of gravity of the whole hyperfine pattern. Yet, to extract in reality the isomer shift from a multi-line Mössbauer pattern can be a problem if the hyperfine splitting effects are not fully understood theoretically. To take the center of gravity of the recorded spectrum can lead to erroneous results if line intensities (e.g., by texture effects or the Goldanskii–Karyagin effect) or, more severely, line shapes (i.e., via relaxation phenomena) are seriously distorted. The problem is discussed in some detail by Shenoy et al. (1978).

If magnetic and quadrupole interactions are simultaneously present, the treatment of hyperfine splitting may become quite complex since the choice of quantization axis is not a priori clear. One is forced to diagonalize the full Hamiltonian containing the sum of the two interactions. Clearly,  $m_I$  is then no longer a good quantum number. The situation is characterized by the appearance of additional hyperfine transitions, which are forbidden according to the selection rules for pure  $m_I$  states.

Exceptions from this situation are present if one of the two interactions dominates and thus provides the axis of quantization in good approximation. One first solves the Hamiltonian of the major interaction and treats in a second step the weak interaction as a perturbation. Fortunately, in reality one often finds  $E_m \gg E_Q$ . The simple approach

$$E_{\text{hf}} = E_m + E_Q \quad (39)$$

is independent of the relative strength of the two interactions if  $B_{\text{hf}}$  and  $eq$  are collinear, because now only one preferred axis is present. Furthermore, eq. (39) is still an acceptable approximation if collinearity is violated but axial symmetry prevails for the quadrupolar coupling. One then has to use in eq. (36) an effective field gradient

$$q_{\text{eff}} = q(1 - 3 \cos^2 \Theta)/2, \quad (40)$$

where  $\Theta$  is the angle between  $B_{\text{hf}}$  and  $eq$ . Note that for  $\Theta = \arccos(1/\sqrt{3})$  the electric field gradient appears to vanish (magic angle). In general, a pure Zeeman pattern is always symmetric to its center of gravity (the isomer shift). Violations of this symmetry is an indicator that an additional quadrupolar coupling may be present.

#### 2.4. Comparison of resolution

We refer to the resonances summarized in fig. 1, bottom. With the exception of  $^{170}\text{Yb}$  all resonances show easy to measure isomer shifts.  $^{151}\text{Eu}$ ,  $^{237}\text{Np}$  and  $^{243}\text{Am}$  are especially powerful in this direction. Magnetic hyperfine splittings can be resolved by all resonances under consideration, the weakest candidate being  $^{155}\text{Gd}$ . In  $^{237}\text{Np}$ , for example, it is easy to determine the hyperfine splitting caused by a moment on the Np ion as small as  $0.3\mu_B$ . This is demonstrated in fig. 12 which refers to  $\text{NpSn}_3$ ,



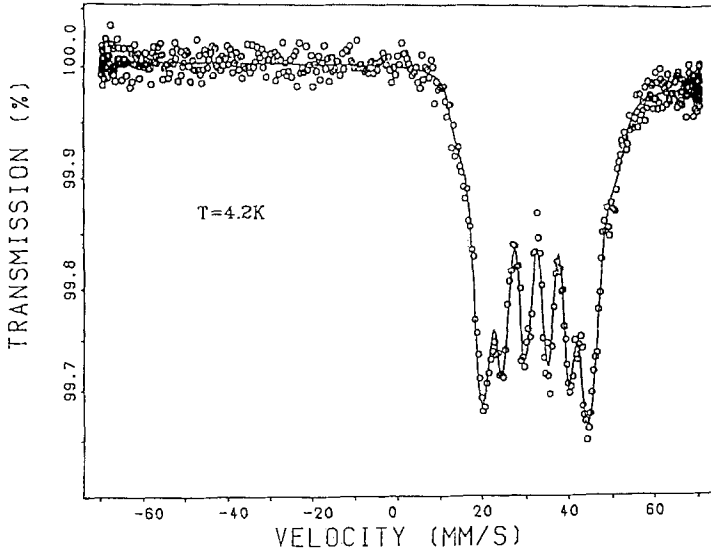


Fig. 12.  $^{237}\text{Np}$  Mössbauer hyperfine spectrum for antiferromagnetic  $\text{NpSn}_3$  at 4.2 K. The hyperfine field is only 66 T corresponding to a moment on Np of  $0.3\mu_B$ . [Taken from Kalvius et al. (1990).]

a compound we shall discuss in detail later. Small quadrupole splittings are difficult to resolve in Eu and also Dy, Np and Am are only moderately resolving. The champions are Gd and Yb and, indeed, most work on quadrupolar interactions refer to these resonances. In summary, all isotopes listed are useful for the study of electronic structure properties via the measurement of the appropriate hyperfine interaction. In table 1 the nuclear hyperfine parameters of the Mössbauer resonances of interest are summarized.

TABLE I  
Nuclear hyperfine parameters of important Mössbauer resonances in the actinides and lanthanides.

Quantity	Resonant nucleus					
	$^{151}\text{Eu}$	$^{155}\text{Gd}$	$^{161}\text{Dy}$	$^{170}\text{Yb}$	$^{237}\text{Np}$	$^{243}\text{Am}$
Transition energy $E_0$ (ke V)	21.5	86.5	25.7	84.3	59.5	83.9
Spin sequence $I_e - I_g$	$\frac{7}{2} - \frac{5}{2}$	$\frac{5}{2} - \frac{3}{2}$	$\frac{5}{2} - \frac{5}{2}$	2-0	$\frac{5}{2} - \frac{5}{2}$	$\frac{5}{2} - \frac{5}{2}$
Ground-state magn. moment $\mu_g$ ( $\mu_N$ )	3.465	-0.2584	-0.479	0	2.5	1.59
Excited-state magn. moment $\mu_e$ ( $\mu_N$ )	2.587	-0.529	0.592	0.669	1.34	?
Ground-state quadr. moment $Q_g$ ( $10^{-24} \text{ cm}^2$ )	1.14	1.59	2.35	0	4.1	4.9
Excited-state quadr. moment $Q_e$ ( $10^{-24} \text{ cm}^2$ )	1.50	0.32	2.34	-2.11	4.1	4.7
Isomer shift calibr. constant $\alpha$ ( $a_0^3 \text{ mm/s}$ )	0.353	-0.025	0.116	0.006	-0.257	-0.290

### 2.5. General systematics of hyperfine interactions

In fig. 13 the isomer shift of selected compounds are summarized for the lanthanide and actinide Mössbauer resonances under consideration. As stated, shifts (in mm/s) between different isotopes cannot be compared directly. To avoid unnecessary confusion we have inverted the velocity scale for  $^{155}\text{Gd}$  such that the contact density  $\rho(0)$  increases from bottom to top in all cases. First, one notes that going from  $f^n$  to  $f^{n-1}$  causes  $\rho(0)$  to increase although an electron is removed. Naively one would expect  $\rho(0)$  to decrease. This, however, is only true if one deals with an electron whose charge density enters the nuclear volume, that is s or  $p_{1/2}$  electrons. Removal of a  $p_{3/2}$ , d or f electron has no direct influence on  $\rho(0)$ . It just alters the potential in which the core s and  $p_{1/2}$  electrons move. This change in potential is such that the probability to find an s or  $p_{1/2}$  electron inside the nucleus is slightly increased which is reflected in the isomer shift. The variation in shift within a given ionic state for nonconducting compounds is largely due to various degrees of covalency in the bond. The halides and sulphates always have the extreme shifts. This covalency effect is particularly strong in the higher charge states of Np. One notices that the hexavalent and the pentavalent neptunyl compounds [i.e.  $(\text{NpO}_2)^{2+}$  and  $(\text{NpO}_2)^+$ ] can shift markedly away from the position of the much more ionic halides. A comparison between Eu and Np also clearly demonstrates that deviation from ionic charge states is much less pronounced in the heavy lanthanides than in the light actinides, as expected. Second, we find that conducting compounds tend to have a higher contact density than insulating compounds of the same ionic state. This means that for the conduction electrons the s-character dominates. The variation within one charge state reflects in part the effect of lattice pressure, in part various degrees of hybridization. This will be discussed in detail later.

Calculated free-ion hyperfine fields for the elements under discussion are summarized in table 2. Hund's rule configuration is assumed. This gives the maximum hyperfine field possible for each charge state since it sets  $m_J = J$ . This is appropriate in ordered materials if the free-ion configuration is present and if exchange interaction dominates all other energies. Usually this situation prevails in the heavy lanthanides. Examples will be given later on. Crystal field effects can reduce  $B_{\text{hf}}$  and this aspect will also be discussed.

As shown by Dunlap and Lander (1974) a simple linear relation

$$\frac{B_{\text{hf}}}{\mu} = 215 \left[ \frac{T}{\mu_{\text{B}}} \right] \quad (41)$$

holds between the hyperfine field  $B_{\text{hf}}$  measured by Mössbauer spectroscopy and the ordered magnetic moment  $\mu$  determined by neutron diffraction for magnets containing Np (see fig. 14). This allows to obtain values of the magnetic moment on Np from Mössbauer data.

Table 2 also lists the free-ion valence electric field gradient (for  $T \rightarrow 0$ ). The free-ion field gradient should be observed in a cubic ordered magnet if the free-ion hyperfine field is present. If  $B_{\text{hf}}$  is reduced from the free-ion value one may use the observed

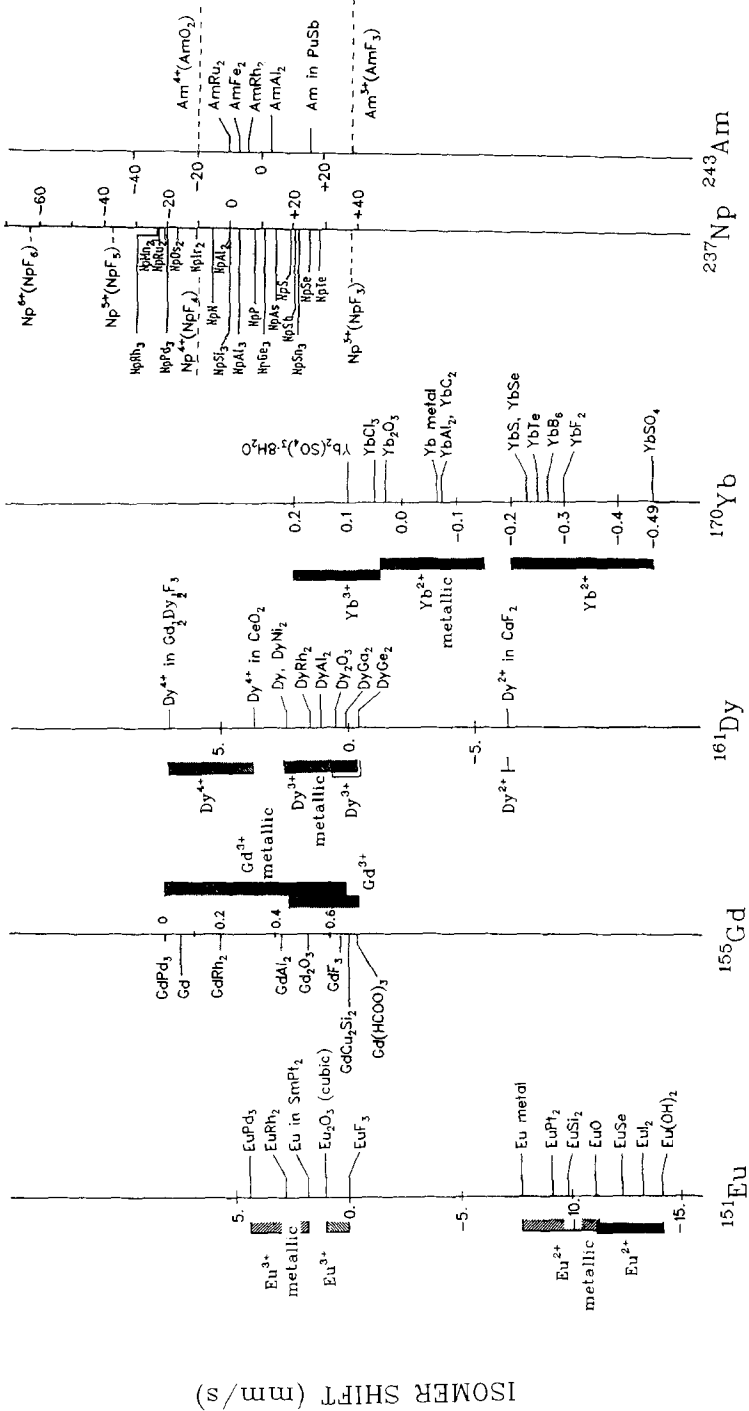


Fig. 13. Plot of isomer shifts for different compounds of the important zero Mössbauer resonances in lanthanides and actinides. The contact density  $\rho(0)$  always increases from bottom to top. The actual values of shifts cannot be compared directly for the different resonances (see text), but their general tendencies can. In the lanthanides it is possible to separate roughly conducting and nonconducting compounds. In the actinides this is more difficult and needs more detailed analysis (see section 6). In all cases, however, conduction electrons produce an increase in contact density.

TABLE 2  
 Calculated free-ion hyperfine fields and ionic electric field gradients (without Sternheimer shielding) in the lanthanides and actinides of interest.

Ion	Configuration	$B_{\text{hf}}$ (T)	$(eq_{\text{ion}})_{\text{max}}$ ( $10^{18}$ V/cm <sup>2</sup> )
Eu <sup>3+</sup>	4f <sup>6</sup> : <sup>7</sup> F <sub>0</sub>	0	0
Eu <sup>2+</sup>	4f <sup>7</sup> : <sup>8</sup> S <sub>7/2</sub>	-340	0
Gd <sup>3+</sup>	4f <sup>7</sup> : <sup>8</sup> S <sub>7/2</sub>	-340	0
Dy <sup>3+</sup>	4f <sup>9</sup> : <sup>6</sup> H <sub>15/2</sub>	620	5.9
Yb <sup>3+</sup>	4f <sup>13</sup> : <sup>2</sup> F <sub>7/2</sub>	420	-7.8
Yb <sup>2+</sup>	4f <sup>14</sup> : <sup>1</sup> S <sub>0</sub>	0	0
Np <sup>3+</sup>	5f <sup>4</sup> : <sup>5</sup> I <sub>4</sub>	530	-1.3
Np <sup>4+</sup>	5f <sup>3</sup> : <sup>4</sup> I <sub>9/2</sub>	590	1.6
Np <sup>5+</sup>	5f <sup>2</sup> : <sup>3</sup> H <sub>4</sub>	550	4.4
Np <sup>6+</sup>	5f <sup>1</sup> : <sup>2</sup> F <sub>5/2</sub>	380	4.6
Am <sup>2+</sup>	4f <sup>7</sup> : <sup>8</sup> S <sub>7/2</sub>	-220	0
Am <sup>3+</sup>	4f <sup>6</sup> : <sup>7</sup> F <sub>0</sub>	0	0

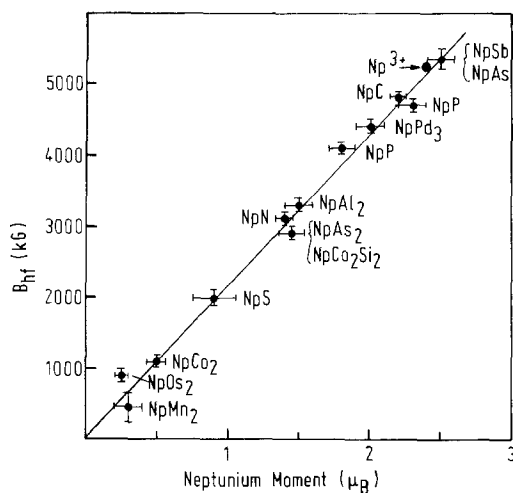


Fig. 14. Plot of hyperfine fields (as measured by <sup>237</sup>Np Mössbauer spectroscopy) versus the moment on Np (as measured by neutron diffraction) for various magnetically ordered neptunium intermetallics. A general, linear relation emerges independent of details of magnetic or crystallographic structure (Dunlap-Lander relation). [Taken from Dunlap and Lander (1974).]

value of  $B_{\text{hf}}$  to deduce an effective value of  $\langle J_z^2 \rangle \approx \langle J_z \rangle^2$  to calculate the expected electric field gradient. This appears to be quite well fulfilled in the Np monopnictides (Dunlap and Kalvius 1985).

On the whole, little systematic data is available on electric field gradients, mainly because of the problems with calculating the lattice contribution.

### 3. Experimental considerations

#### 3.1. Mössbauer transitions in lanthanides and actinides

##### 3.1.1. General features

An overview of  $f$  transition elements for which widespread systematic Mössbauer data exist are the lanthanides Eu, Gd, Dy and Yb as well as the actinides Np and Am (see fig. 1). The resonances employed are summarized in table 3 together with their important parameters and relevant data on source activities. The low-energy nuclear structures of  $^{161}\text{Dy}$  and  $^{237}\text{Np}$  are quite analogous, consequently the two Mössbauer resonances have much in common and are ideally suited for comparison. The main difference is the transition energy. Interestingly enough, both resonances are subject to severe broadening of the emission line (typically a factor of 15 for Dy and 25 for Np). The origins of this effect remain enigmatic. It reduces the effective resonant amplitude and the resolution for hyperfine studies accordingly. Fortunately these limitations are not severe in both cases and studies can continue.

It was stated in the preceding section that  $t_a \approx 2$  is a suitable choice of effective absorber thickness. Table 4 presents the needed area density of the lanthanide (in natural isotopic abundance) or the actinide for different measuring temperatures and various Debye temperatures. For intermetallic compounds  $\Theta \approx 200$  K is a good guess. A typical Mössbauer absorber covers an area of 2–4 cm<sup>2</sup>. For most cases about 0.5 g of material suffices. As said before, powder samples are fine, single crystals are not necessary.

For the high-energy transitions ( $^{155}\text{Gd}$ ,  $^{170}\text{Yb}$ ,  $^{237}\text{Np}$ ,  $^{243}\text{Am}$ ) cooling of the source to liquid He temperatures (or thereabout) is essential. Even with this condition fulfilled it is difficult to obtain good spectra for absorber temperatures much above 100 K. This is a most serious restriction. Especially for  $^{170}\text{Yb}$  the use of isotopically enriched samples can be helpful. For  $^{151}\text{Eu}$  and  $^{161}\text{Dy}$  the  $f$  factors are high. The source can conveniently be kept at room temperature and absorbers may be heated well above room temperature, quite analogous to the case of the standard Mössbauer resonance,  $^{57}\text{Fe}$ .

##### 3.1.2. Mössbauer sources

Sources for  $^{151}\text{Eu}$  are commercially available. The long half-life of  $^{151}\text{Sm}$  makes them a permanent possession. The main disadvantage is their relatively low specific activity which calls for long counting times under adverse conditions like high-pressure measurements. Sources for the other lanthanide resonances have to be prepared by neutron activation. In case of  $^{161}\text{Dy}$  the fairly short life-time of the source requires routine access to an irradiation facility at a reactor having at least medium flux. The activated source compounds often need thermal or even chemical treatment afterwards to perform as desired. Hence a laboratory for the handling of radioactive substances needs also be at hand. This limits the general applicability of the lanthanide resonances with the exception of  $^{151}\text{Eu}$  and  $^{155}\text{Gd}$ .

The conventional method of Mössbauer spectroscopy needs modifications when working with actinides. First radiation safety rules are much stricter; second, one has

TABLE 3  
Parameters of selected Mössbauer resonances in lanthanides and actinides.

Quantity	$^{151}\text{Eu}$	$^{155}\text{Gd}$	$^{161}\text{Dy}$	$^{170}\text{Yb}$	$^{237}\text{Np}$	$^{243}\text{Am}$
$E_0$ (keV)	21.53	86.54	25.66	84.25	59.54	84.0
$I_{\text{ex}}^{\text{n}} - I_{\text{gr}}^{\text{n}}$	$\frac{7+5+}{2}$	$\frac{5-3-}{2}$	$\frac{5-5+}{2}$	$2^{+} - 0^{+}$	$\frac{5-5+}{2}$	$\frac{5+5-}{2}$
Multipol.	M1	E1	E1	E2	E1	E1
$\tau_e$ (ns)	14	9.1	40.6	2.3	98.5	3.38
$\alpha_1$	28.6	0.43	2.9	6.1	1.1	0.2
$\sigma_0$ ( $10^{-20} \text{ cm}^{-2}$ )	23.8	33.9	9.5	24.2	30.6	27.6
$W$ (mm/s)	1.3	0.5	0.38 <sup>a</sup>	2.0	0.07 <sup>b</sup>	1.4
Isot. abund. (%)	47.8	14.7	18.9	3.0	(100)	(100)
Source activity	$^{151}\text{Sm}$ (90 y)	$^{155}\text{Eu}$ ( $\sim 2$ y)	$^{161}\text{Tb}$ (6.9 d)	$^{170}\text{Tm}$ (128.6 d)	(manmade in fission reactors) $^{241}\text{Am}$ (458 y)	(manmade in fission reactors) $^{243}\text{Pu}$ (5 h)
$(T_{1/2})$						
Production reaction	fission product	$^{154}\text{Sm}(\text{n}, \gamma)^{155}\text{Sm}$ $^{155}\text{Sm}(\beta, 23 \text{ min})^{155}\text{Eu}$	$^{160}\text{Gd}(\text{n}, \gamma)^{161}\text{Gd}$ $^{161}\text{Gd}(\beta, 3.7 \text{ min})^{161}\text{Tb}$	$^{169}\text{Tm}(\text{n}, \gamma)^{170}\text{Tm}$	made in fission reactors	$^{242}\text{Pu}(\text{n}, \gamma)^{243}\text{Pu}$
Typical source compd.	$\text{SmF}_3, \text{Sm}_2\text{O}_3$	$\text{SmPd}_3, \text{Eu}$ in Pd	$\text{GdF}_3$	$\text{Tm}_{0.03}\text{Si}_{0.95}\text{TmBe}_{1.2}$	$\text{Am}_{0.1}\text{Th}_{0.9}$ Am metal	$\text{PuAl}_2$ $\text{PuAl}_4$

<sup>a</sup> Effective linewidth  $\sim 3.5$  m/s.

<sup>b</sup> Effective linewidth  $\sim 2.5$  mm/s.

TABLE 4

Typical required absorber thickness (in  $\text{mg}/\text{cm}^2$  of natural isotopic admixture of the resonant atoms) for selected Mössbauer resonances in the lanthanides and actinides for different Debye temperatures  $\theta$  and measuring temperatures  $T$ .

		Resonant atom				
		$^{151}\text{Eu}$	$^{155}\text{Gd}$	$^{161}\text{Dy}$	$^{170}\text{Yb}$	$^{237}\text{Np}$
Transition Energy (keV)		21.5	86.5	25.6	84.2	59.6
$\theta = 150\text{ K}$	$T = 300\text{ K}$	22	—	260	—	—
	$T = 77\text{ K}$	7	—	55	—	500
	$T = 4.2\text{ K}$	5	260	40	1200	150
$\theta = 200\text{ K}$	$T = 300\text{ K}$	11	—	100	—	—
	$T = 77\text{ K}$	6	800	40	3000	200
	$T = 4.2\text{ K}$	5	110	40	600	100
$\theta = 250\text{ K}$	$T = 300\text{ K}$	8	—	70	—	—
	$T = 77\text{ K}$	5	200	40	1000	150
	$T = 4.2\text{ K}$	5	70	30	400	90

the additional complication that the absorber materials are also radioactive. This explains why actinide Mössbauer data are restricted and available only from a few laboratories over the world.

For  $^{237}\text{Np}$  the  $\beta^-$ , the  $\beta^+$  and the  $\alpha$  decay parents are all available. The  $\beta^+$  source activity (45 d  $^{237}\text{Pu}$ ) has never been used since it is difficult to produce. Originally (Stone and Pillinger 1964) the  $\beta^-$  decay activity (6.8 d  $^{237}\text{U}$ , which, however, is cumbersome to obtain in pure form) had been used as source since it was feared at the time that the massive recoil imparted by the  $\alpha$  decay of  $^{241}\text{Am}$  would cause severe distortions of the emission spectrum. Such behavior was known as “after effects” (Wickmann and Wertheim 1968) and typical results are multiple emission lines. This is indeed the case when nonconduction source compounds are used (Friedt et al. 1979), but in metallic materials the after effects of the  $\alpha$  decay are found to be minimal and, in particular, a reduction of the recoil-free fraction due to local heating from the  $\alpha$  recoil [“heat spike”, see Mullen (1965)] proves to be nonexistent (Asch et al. 1981). Hence  $^{241}\text{Am}$  with its convenient half-life ( $T_{1/2} = 500\text{ y}$ ) is now solely employed as source activity. One particular advantage of the  $^{241}\text{Am}$  decay is that the 60 keV  $\gamma$  radiation is emitted in high proportion and that it dominates totally the  $\gamma$ -ray spectrum. The specific activity of  $^{241}\text{Am}$  is  $\sim 3.4\text{ mCi}/\text{mg}$ . Typical sources contain between 10 and 100 mg of  $^{241}\text{Am}$ . The most straightforward source compound is Am metal. It emits a single line roughly 30 times the natural width. Since Am metal is hexagonal, one thought to improve the situation by using a cubic Am alloy such as Am in Th. If the Am concentration is kept low (5%) then a considerable narrower line (12 times the natural width) can be obtained but with the penalty of reduced  $\gamma$  intensity. For most applications, the resolution achievable with an  $^{241}\text{Am}$  metal source suffices. As stated, the origin of the line broadening remains unknown. The  $\alpha$

decay is not responsible, as a careful comparison with  $\beta$  decay sources has shown (Meeker et al. 1976).

The construction of the Am source used in our laboratory is as follows (Potzel et al. 1983): The Am metal is evaporated onto a tantalum disk. This is pressed against the bottom of the stainless steel container by a CuBe spring in order to ensure good thermal contact. The container is permanently sealed by electron-beam welding. Preferably this should be done in a He atmosphere because the He gas provides additional thermal contact at low temperatures.

Fortunately,  $^{237}\text{Np}$  is the most commonly available isotope of Np and its rather long half-life ( $T_{1/2} = 2 \times 10^6$  y) makes its specific activity low. The radioactivity of the Np sample is a problem only with respect to the health hazard, but does not interfere seriously with the Mössbauer measurement. Standard transmission geometry can be used. One should not place the absorber too close to the detector to keep down nonresonant background radiation. It is recommended to triply seal the absorber container, especially if powder samples are used. Details are given in Potzel et al. (1983).

The parent activity for  $^{243}\text{Am}$  is  $^{243}\text{Pu}$ , which beta decays with  $T_{1/2} = 5$  h. It is produced by neutron activation of  $^{242}\text{Pu}$ , a long-lived, nonfissionable isotope available in high purity. Cubic metallic matrices like  $\delta$ -Pu,  $\text{PuAl}_2$  and  $\text{PuAl}_4$  work well (Bode et al. 1976). The half-life of  $^{243}\text{Am}$  is short enough to make absorbers reasonably radioactive. Some precautions regarding energy selection in the nuclear counting channel have to be taken (see Dunlap and Kalvius 1985). Unfortunately  $^{243}\text{Am}$  is not the most common isotope of Am, although it offers the advantage of being less susceptible to radiation self-damage when compared with the more abundant  $^{241}\text{Am}$ . The difficulty in obtaining good samples, together with the somewhat more involved experimental procedures, have prevented the wide application of this otherwise excellent resonance.

In conclusion, we might mention that  $^{231}\text{Pa}$  (84 keV) is basically also a fine Mössbauer resonance in the actinide regime. Unfortunately the scarcity of Pa has prevented this resonance to come into greater use despite the fact that the original source problems could be overcome (Friedt et al. 1981). Perhaps the future will bring improvement, a strong effort would be commendable.

### 3.2. Mössbauer spectrometers

#### 3.2.1. Spectrometers for the study under ambient pressure

Mössbauer measurements in the lanthanides and actinides are carried out in transmission geometry (see fig. 5). In case the source can be kept at room temperature (e.g.  $^{151}\text{Eu}$ ,  $^{161}\text{Dy}$ ) one best mounts the absorber inside the tail of a helium cryostat and has the  $\gamma$ -ray beam passing horizontally through it. The other resonances require the source to be kept around liquid helium temperature. A vertical geometry as depicted in fig. 15 is commonly used. Both source and absorber are mounted inside the central tube of a liquid-helium cryostat. Thermal contact is provided by exchange gas. The absorber temperature can be elevated to about 150 K by controlled electric heating. The exchange gas must then be pumped out to break thermal contact between



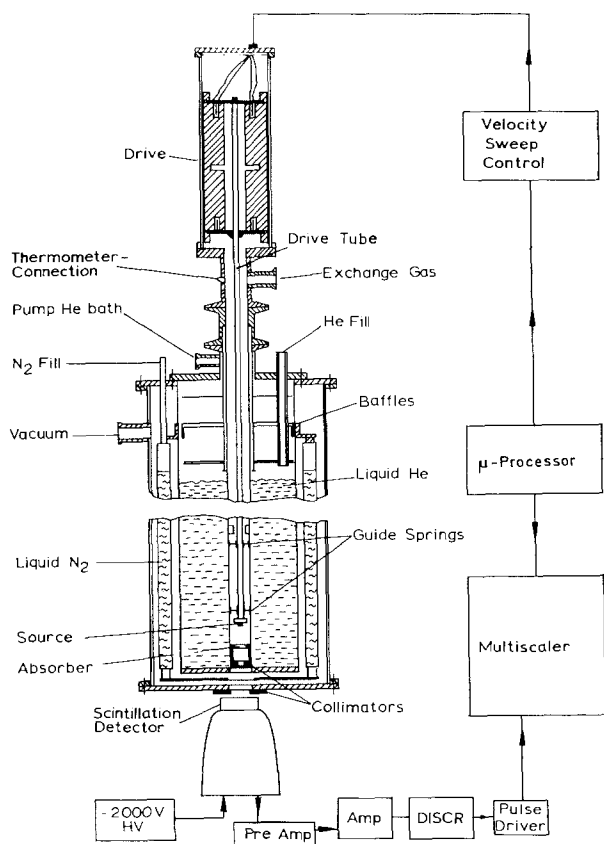


Fig. 15. Mössbauer spectrometer for source and absorber at cryogenic temperatures. [Taken from Dunlap and Kalvius (1985).]

absorber and bath. The source is kept at as low a temperature as possible by relying on the mechanical contact (guide springs) for heat transfer.

The Doppler motion is generated by an electromechanical drive unit. It consists of a loudspeaker movement which is excited by an appropriate electrical signal delivered by the drive amplifier and a second loudspeaker movement, mechanically coupled very rigidly to the drive system, which serves as an inductive velocity pick-up. The pick-up voltage is compared with the signal from a reference generator in a negative feedback loop at the velocity sweep control box. In case of any deviation from the proper motion, a correction signal is sent to the drive. Typically, the source motion deviates less than 0.2% from the ideal wave form. This, in turn, is provided by the highly stable sweep generator. The drive unit is always kept at room temperature. In case of a cooled source (fig. 15) the motion is fed into the cryogenic region by a thin stainless steel tube (drive tube). It is essential that source and absorber are precisely aligned, which is sometimes difficult for actinide samples in their bulky safety containers. Furthermore, any lateral source motion must be carefully avoided. This is achieved by appropriately shaped concentric guide springs along the drive rod.

The full velocity spectrum is automatically recorded by sweeping the source in a carefully controlled manner between its extreme values  $+v_{\max}$  and  $-v_{\max}$ . Synchronously the counts delivered by the  $\gamma$ -ray detection system are stored in a histogramming memory (multi-scaler). A velocity interval  $\Delta v$  is assigned to each memory address (channel). Commonly used are 1024 to 4096 channels. It is of course essential that the velocity sweep and the channel sweep are exactly in phase. This is achieved by deriving the velocity sweep wave form digitally and synchronizing each velocity increment with the channel advance pulses. Linear and sinusoidal velocity sweeps are in use. The latter is more easily controlled particularly if high velocities for cooled sources are needed. For example, to record a magnetic spectrum in  $^{237}\text{Np}$  may need a velocity range of  $\pm 200$  mm/s. Using such an extended velocity range requires to keep the amplitude of source motion small in order to avoid geometrical distortions. This calls for a relatively high frequency of the sweep signal. Our spectrometers operate around 70 Hz in sinusoidal mode. Good collimation is another point which needs attention.

Finally a few words regarding the nuclear counting chain. As  $\gamma$ -ray detector one uses in most cases a Ge or Si diode. For  $^{237}\text{Np}$  a simple NaI(Tl) scintillation counter suffices since the  $\gamma$ -ray spectrum is unusually clean. The single-channel analyzer (SCA) selects counting pulses (after amplification) corresponding in  $\gamma$ -ray energy to the resonant transition for storage by a multi-channel histogramming device, while rejecting counts from radiation of other energies (nonresonant background). In general, it is more important for the nuclear counting system (pre-amplifier, amplifier and single-channel analyzer) to be insensitive to pulse overload than to deliver the highest spectral resolution.

Mössbauer spectrometers for standard applications have changed little over the past decade in their basic design. More information can, for example, be found in Shenoy et al. (1978). Multi-channel analyzers for histogram storage are now replaced by special memories or by a personal computer.

### 3.2.2. Spectrometer for pressures up to $\sim 12$ GPa

As shall be discussed in sections 4 and 5, the change in electronic structure properties under the application of external pressure gives important information. It may lead to novel phenomena and in addition the volume dependence is a crucial parameter in testing theoretical models. For example, certain intermetallics may be driven from a localized to an itinerant magnetic state with reduced volume. Mössbauer spectroscopy is well suited for such studies.

We present the essential features of a spectrometer for measurements under applied high pressure as used in our laboratory particularly for the  $^{237}\text{Np}$  resonance. The samples under pressure are used as absorbers. The high-pressure cell is displayed in fig. 16. A steel cylinder (4) with teflon washers (5) seals the inner parts of the cell. The two symmetrical anvils (1) made from  $\text{B}_4\text{C}$  apply the pressure to the absorber. The inset of fig. 16 shows more clearly the location of the actinide sample (6) between the anvils. For high-pressure work we clearly cannot use our bulky standard absorber container. Yet, the sample must still be encapsulated if the high-pressure apparatus is outside a closed-atmosphere box. We use a small Al container which self-seals

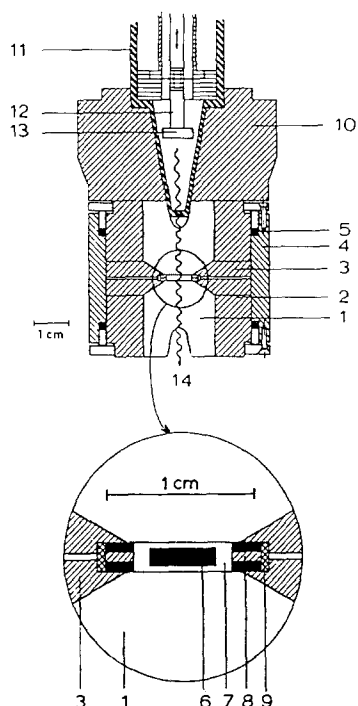


Fig. 16. High-pressure cell: (1)  $B_4C$ -anvils; (2) binding rings; (3) supporting rings; (4) steel cylinder; (5) teflon washers; (6) absorber; (7) aluminum container for absorber; (8) sandwich gasket; (9) extrusion ring; (10) backing block; (11) part of aluminum enclosure; (12) drive rod with guidance spring; (13) source; (14)  $\gamma$ -ray. [Taken from Moser et al. (1981).]

under pressure. The sample diameter is 4 mm, the container has an outer diameter of 7 mm and a height of 1.5 mm. These are rather large dimensions for high-pressure work and several improvements on the cell design were necessary to prevent a radial flow under pressure. First, a new type of gasket (8) was designed: a steel ring is sandwiched between two pyrophyllite rings. Thus, the inner friction forces in the pyrophyllite rings are increased. This is necessary to allow the pressure to decrease from its maximum value at the centre to zero at the rim of the supporting rings (3). Second, in order to further stabilize the sandwich gasket and to keep it strictly centered between the anvils, an extrusion ring (9) made of Cu-Be bronze is backed by the supporting rings (3). This construction greatly reduces the risk of a “blow-out”.

The high-pressure cell is then mounted inside the pressure clamp depicted in fig. 17. The cell is pressure loaded under a hydraulic press exerting a force up to 600 kN. The force is stored in the springs (24) below the cell by rigidly tightening the main clamp screw (15) with the cell still under the press. The loaded clamp is then removed, placed into the exchange gas container and inserted from the top into the He vessel of a metal cryostat. The pressure and the pressure gradient at the actinide sample are determined in situ by a lead manometer (Willer and Moser 1979) which makes use of the pressure dependence of the superconducting transition temperature of lead. Quasi-hydrostatic pressures up to 9 GPa with gradients less than 5% were obtained. Reducing the sample size extends the usable range to 12 GPa.



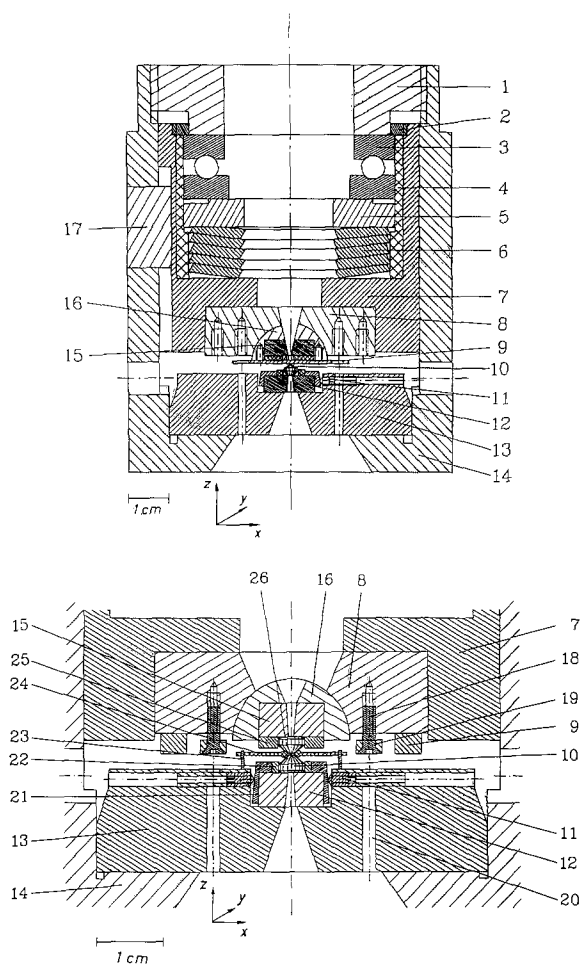


Fig. 18. High-pressure clamp and cell with diamond anvils for pressures up to 50 GPa. The upper part shows the full pressure clamp. Details of the pressure cell are indicated in the lower part. Some features are drawn only in one of the two pictures for clarity. (1) Top screw; (2) spacer; (3) ball bearing; (4) centering tube; (5) spacer for springs; (6) steel springs; (7) pressure cylinder; (8, 16) two half-cylinders (oriented perpendicular to each other) for alignment of upper anvil; (9, 19) alignment frame; (10) diamond anvils; (11, 18) set screws; (12, 15) backing rings; (13) lower supporting block; (14) clamp mantle; (17) adjustment block; (20) access hole to set screw; (21, 22, 25) centering device for anvils; (23) support for gasket; (24) gasket; (26) sample. [Taken from Gleissner (1992).]

transmits the force to the upper diamond is held in place by two adjustable half-cylinders (8, 16). One can be turned around the  $y$ -axis. It fits into the second half-cylinder turnable around the  $x$ -axis. Both half-cylinders are aligned and fixed by set screws via the adjustment frames (9, 19). The proper alignment of the opposed anvils is checked through a microscope.

Pressure is applied by turning the top screw (1) with a worm gear (not shown). A ball bearing (3) reduces frictional forces which might spoil the alignment. Together with a spacer (5) it slides within the centering tube (4) and compresses the steel springs (6). The pressure cylinder (7) moves inside the clamp (14) exerting force onto the half-cylinders (8, 16) holding the upper diamond anvil. During application of pressure the sample area is viewed through the diamonds by the microscope.

The determination of pressure and of pressure gradient is based on the pressure dependence (Mao et al. 1978) of the red fluorescence light of ruby: Several tiny ruby

crystals are placed inside the sample volume and their fluorescence doublet (at 6942 and 6928 Å under ambient pressure) is excited by laser light. It is very convenient in this context to make use of a stereo microscope where the laser beam can be brought in via one viewing port and focused onto the sample by the objective lenses. The output fluorescent light coming through both viewing ports of the microscope is transmitted via light guides to a spectrum analyzer. Its data is read out to a computer for analysis. When pressure is applied the doublet shifts to longer wavelengths and the separation between the two lines increases. In addition, at a fixed temperature the widths of the two lines give information on the pressure gradient within the sample volume. The disadvantage of low light intensity scattered from the small ruby crystals can partially be compensated by the large light gathering power of a stereo microscope. In contrast to the lead manometer, the pressure determination cannot be carried out easily with the clamp mounted inside the cryostat. Thus far, we have made pressure determinations only down to 77 K. They indeed show a noticeable pressure rise when cooling the clamp down, on account of thermal contraction. This is expected to have reached saturation at liquid-nitrogen temperatures and the very difficult measurements at lower temperatures are judged nonessential.

#### **4. Contrasts in lanthanide and actinide electron structure as seen by Mössbauer spectroscopy**

The primary challenge is to explore the conditions under which a f-transition element or compound deviates from the “standard rare earth” electron configuration, i.e., a highly localized trivalent ionic configuration  $f^{n-1}$  derived from the configuration  $f^{n-1}(f^1 \text{ or } d^1)s^2$  of the free atoms. In the lanthanides (Ln) 4f, 5d and 6s electrons are involved, in actinides (An) 5f, 6d and 7s electrons.

##### *4.1. Intermediate valence*

Next to an empty, a half-filled or a full f-shell, the neighboring charge states are also stable. In the Ln series these are  $Ce^{4+}$ ,  $Eu^{2+}$  and  $Yb^{2+}$ . But they are found not necessarily in their pure form. One observes the phenomenon of intermediate valence (IV) or valence fluctuations (Varma 1976). This is the most common type of unusual f-electron structure in lanthanide compounds. It is not altogether restricted to the elements mentioned above. IV is also found in certain compounds of Sm and Tm, for example. The occurrence of IV will affect all three hyperfine parameters (contact electron density, hyperfine field, electric field gradient) determining the shape of a Mössbauer spectrum: Unique is the measurement of mean valence via the isomer shift. Since one of the two states involved in IV is usually nonmagnetic (e.g.  $Ce^{4+}$ ,  $Eu^{3+}$ ,  $Yb^{2+}$ ) the magnetic properties of the compound will depend on its mean relative population. Similar arguments can be brought forward for the ionic electric field gradient. The relative population of the two charge states, i.e. the mean valence, can be influenced by variation of either temperature and volume. Hence measuring the combined temperature and pressure dependence of at least two of the hyperfine

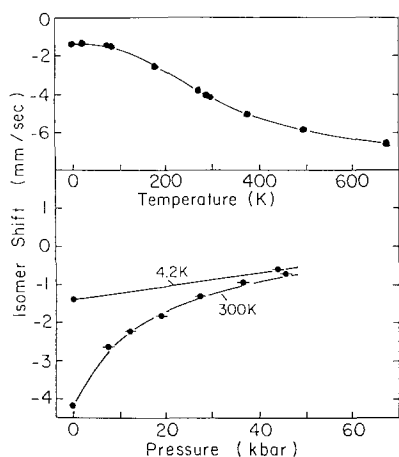


Fig. 19.  $^{151}\text{Eu}$  isomer shift in  $\text{EuCu}_2\text{Si}_2$  as a function of temperature at ambient pressure (top) and as a function of applied pressure at 300 K and at 4.2 K (bottom). For details see text. 10 kbar = 1 GPa. [After Nowik (1983).]

parameters is a reliable indicator for the occurrence of IV and allows the extraction of most relevant microscopic parameters (Nowik 1983).

The situation is briefly explained using the example of  $\text{EuCu}_2\text{Si}_2$  a rather clearcut mixed-valence system (Röhler et al. 1982). Figure 13 tells us that a characteristic isomer shift of  $\sim 14$  mm/s exists between  $\text{Eu}^{2+}$  and  $\text{Eu}^{3+}$  compounds. This is about ten times the experimental width and thus easily measured with high accuracy. Figure 19 (top) shows the isomer shift of  $\text{EuCu}_2\text{Si}_2$  to be strongly temperature dependent. At liquid-He temperatures the shift corresponds to a charge state  $\text{Eu}^{+\nu}$  with  $\nu \approx 2.8$ , whereas at high temperatures (673 K) the valence drops to  $\nu \approx 2.35$ . The change of  $S$  with applied pressure at 300 K is equally dramatic (fig. 19, bottom). The valence has increased to  $\nu \approx 2.9$  at 4.5 GPa compared to  $\nu \approx 2.6$  at ambient pressure. At 4.2 K the valence has practically reached its limit closest to the  $\text{Eu}^{3+}$  state. The now much weaker pressure dependence of the isomer shift reflects mainly the increase in contact density due to the compression of conduction electrons.

The model used to describe the temperature and pressure dependences of the Eu charge state has been discussed in detail by Nowik (1983). The basic situation is indicated in fig. 20. Rapid charge fluctuations are assumed between the  $4f^7$  ( $\text{Eu}^{2+}$ ) state and the  $4f^6$  ( $\text{Eu}^{3+}$ ) state, which is formed by giving one  $4f$  electron to the conduction band. The fluctuation rate determines the width  $\Delta = kT_f$  of the  $4f^n$  state. Usually the excitation energy  $E_{\text{ex}}$  between the Fermi energy  $E_F$  and the energy of the  $4f^n$  state is considered to be independent of temperature, whereas  $E_{\text{ex}}$  decreases and  $\Delta$  increases when pressure is applied. The ratio of population of the two charge states is given by

$$\frac{P(4f^n)}{P(4f^{n-1})} = \frac{Z(4f^n)}{Z(4f^{n-1})} \exp \left[ \frac{-E_{\text{ex}}}{\sqrt{T^2 + T_f^2}} \right], \quad (42)$$

where  $Z$  is the normal partition function. This ratio determines the valence  $\nu$ . As a consequence of the finite width  $\Delta$ ,  $P(4f^n)$  does not vanish even at very low temperatures (i.e.  $\nu = 3$  will not be reached even for  $T = 0$ ). On account of the rapid fluctuations

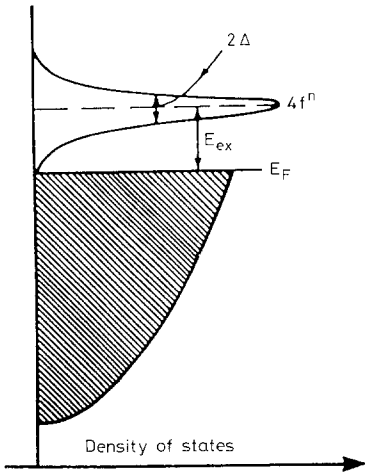


Fig. 20. Energy level and band diagram of metallic Eu systems in which valence fluctuations take place. [After Nowik (1983).]

one sees in the Mössbauer spectrum the mean isomer shift

$$S = S(4f^n) P(4f^n) + S(4f^{n-1}) P(4f^{n-1}).$$

Observation of a pronounced temperature dependence of the isomer shift is thus a very strong indication for the presence of valence fluctuations. The nature of the pressure dependence of  $S$  is much more complex and not necessarily due to changes of  $v$ . The volume compression of conduction electrons together with increasing overlap with electrons of the alloying partner can cause an increase of  $S$  which is comparable to the change originating from the increase in  $v$ . The measure of volume dependence of  $S$  alone will not suffice to establish the formation of IV behavior under applied pressure (which is, one suspects, the ultimate fate of conducting divalent europium compounds). One also needs to establish a well developed temperature dependence of  $S$  at constant but elevated pressures.

In the An series the presence of IV is not definitely established. According to the rules for Ln the likely candidates would be Pa and Am. Unfortunately, little systematic data (not only Mössbauer data but information of solid state properties in general) exist for compounds of these elements. Like in Sm one may suspect IV to exist also in analogous Pu compounds and indeed there is some indication in that direction (Wachter et al. 1991). Unfortunately once more, a good Mössbauer isotope of Pu which would allow the measurement of isomer shifts does not exist.

#### 4.2. Delocalization of 5f electrons and magnetism

The common deviation from standard f electron structure in the light An is other than IV. As substantiated, for example, by relativistic self-consistent field type calculations (Freeman and Koelling 1974, Freeman 1980, Arko et al. 1985) the radial extend of 5f electrons is large and comparable to that of 3d electrons in transition



metals. This means that the 5f electrons can participate in the bond and may form via f–f overlap or f–d, f–s and perhaps f–p hybridization more or less wide bands. Delocalization of 4f electrons is known under ambient conditions rather exclusively for Ce. Itinerant f electron behavior is believed to be the basis for perhaps the most anomalous f electron properties, namely Kondo lattice and heavy-fermion behavior (Grewe and Steglich 1991) discovered in Ce intermetallics. The most strongly delocalized actinide is U and many heavy-fermion compounds containing this element are also known. We have already pointed out in section 1 that this puts the Mössbauer effect on the sideline for information regarding these still enigmatic properties since there are no good resonances in either Ce or U. But in Np the 5f electrons can be fairly delocalized as well and indeed at least one typical heavy-fermion compound (NpBe<sub>13</sub>) is known to exist.

Magnetic properties mirror well details of f electron structure. In Ln elements and compounds the pronounced localization of 4f electrons leads to the free-ion paramagnetic moment of the Hund's rule ground state. The crystalline electric field (CEF) is well shielded from the valence electron shell and spin–orbit (SO) coupling is not affected ( $\mathcal{H}_{SO} \gg \mathcal{H}_{CEF}$ ) meaning that  $\mathcal{H}_{CEF}$  can only mix the various  $J_z$  states of the Hund ground state. This can lead to an appropriate reduction of moment according to the thermal population of CEF states. As a rule we also find the exchange (EX) to dominate ( $\mathcal{H}_{EX} \gg \mathcal{H}_{CEF}$ ) and then the pure maximum  $J_z$  state will be lowest. This is the basis for the observation that in many Ln magnets one finds the free-ion moment and with it the free-ion hyperfine field and electric field gradient (table 2).

The more itinerant character of 5f electrons makes the magnetic properties of light An approach those of 3d transition elements and compounds. Now  $\mathcal{H}_{CEF} \approx \mathcal{H}_{SO}$  making  $J$  no longer necessarily a good quantum number and the ground state of an An ion in a solid might be formed by mixing the different levels of the lowest  $J$  multiplet (Chan and Lam 1974). In contrast to the 3d series a quenching of orbital moment will not occur for itinerant 5f electrons on account of their strong relativistic nature (Johansson et al. 1991). This constant presence of an orbital moment is probably the cause for the Dunlap–Lander relation (fig. 14) and the fact that when using eq. (41) one finds full equivalence of bulk susceptibility and local susceptibility as measured by Mössbauer spectroscopy on paramagnetic Np compounds in an applied field (Gal et al. 1989a).

The formation of 5f bands will reduce the local moment on Np and with it the saturation ( $T \rightarrow 0$ ) hyperfine field. It is, however, not easy to distinguish the reduction of moment on account of f electron itineracy from that caused by CEF interaction on a localized moment. Measurements under high pressure are of great help. They allow the determination of the volume coefficients  $-\partial \ln B_{hf}/\partial \ln V = -\partial \ln \mu/\partial \ln V$  and  $-\partial \ln T_m/\partial \ln V$  where  $T_m$  is a magnetic transition point (Curie or Néel temperature) provided the pressure/volume relation (compressibility) is known. Therefore we have determined compressibilities of the compounds under study independently by X-ray diffraction (Potzel 1990). For a well localized magnetic material one expects  $-\partial \ln \mu/\partial \ln V$  to be more or less constant while the magnetic transition temperature should rise with reduced volume. In contrast, a highly itinerant magnet will show

large negative values for both coefficients  $-\partial \ln T_m / \partial \ln V$  and  $-\partial \ln \mu / \partial \ln V$  [see also Fournier et al. (1979, 1980)].

On the basis of electron structure calculations one expects that lanthanide-like localization of 5f electrons occurs at Am and beyond. Indeed Cm metal appears to be the first elemental An to undergo magnetic order (Fournier et al. 1977, Kannelakopoulos et al. 1975) since in Am the trivalent charge state is nonmagnetic ( $^7F_0$ ). In the elemental metals up to Pu the overlap of 5f orbitals of neighbouring atoms produces a broad 5f band with substantial hybridization with the 6d and 7s bands. Magnetic order does not form. In intermetallic compounds of U, Np and Pu the actinide–actinide separation can easily get larger. The 5f overlap now reduces, and the 5f bands become narrower and less hybridized. The actinide ion can then support a magnetic moment and in case of wide separation even strongly localized magnetism may exist. Hill (1970) was the first to point out that the actinide–actinide separation is a crucial parameter determining the transition from localized to delocalized magnetic behaviour. This concept is often depicted in a “Hill plot” where the magnetic ordering temperature is plotted against the An–An separation. If the latter decreases below a critical value, called the “Hill limit”, the 5f electrons become too much delocalized to support magnetic order. This rather global view of the origin of 5f delocalization works astonishingly well despite the fact that it neglects both the influence of chemical nature of the alloying partner, as well as the effect of bond symmetry on the hybridization of 5f with ligand electrons. As will be shown from systematic studies of hyperfine parameters in intermetallic compounds under ambient and applied pressure some series behave more Hill-like, while others are predominantly sensitive to the type of ligand.

In summary, the two pronounced deviations from standard f electron structure, i.e., valence fluctuations and f band formation can both be studied well by Mössbauer spectroscopy. High-pressure studies are of profound importance in this context.

## 5. Lanthanide and actinide electron structure under reduced volume

High-pressure Mössbauer experiments in compounds of Eu, Dy, Yb and Np will be reviewed. In most examples a pressure range up to  $\sim 10$  GPa is covered but in the case of Eu pressures up to  $\sim 50$  GPa have been reached. The results on Eu and Yb primarily serve to discuss intermediate valence behavior and to gain insight into related microscopic properties. Data on Dy are mainly used as reference for highly localized magnetism which is then contrasted to results on analogous compounds of Np with the aim to gain information on 5f electron delocalization. In all magnetically ordered systems the question of stability of the spin structure under reduced volume arises. We had already mentioned that simultaneously to the Mössbauer high pressure experiments the pressure–volume relation has been determined by X-ray diffraction in order to be able to convert pressure coefficients into volume coefficients. In the following we have subgrouped the discussion according to series of compounds with various crystal structures.

## 5.1. Rocksalt type compounds

### 5.1.1. *Eu mono-chalcogenides*

The compounds of the type  $\text{EuX}$  ( $X = \text{O}, \text{S}, \text{Se}, \text{Te}$ ) are considered the closest real systems to a Heisenberg magnet.  $\text{EuO}$  and  $\text{EuS}$  are ferromagnets ( $T_C = 69$  and  $16.6$  K, respectively) while  $\text{EuSe}$  is a meta-magnet ( $T_N = 4.6$  K) reaching in zero field below  $1.8$  K a simple type-I antiferromagnetic structure. The same type of antiferromagnetism is well developed in  $\text{EuTe}$  below  $T_N = 9.6$  K. Because of the instability of magnetic structure already under ambient condition the case of  $\text{EuSe}$  has not been pursued by high-pressure measurements in detail.

The magnetic behavior of  $\text{EuX}$  materials can be explained by the interplay of two effective exchange integrals:  $J_1$  between nearest and  $J_2$  between next-nearest neighbors (Zinn 1976). The Eu ion is in the divalent state and remains so at least up to  $\sim 10$  GPa. At higher pressures the valence of Eu in  $\text{EuO}$  is a matter of controversy to which we shall return further below. The  $^8\text{S}_{7/2}$  configuration of the free  $\text{Eu}^{2+}$  ion leads to pure spin magnetism. In terms of the hyperfine field at the Eu nucleus this means that  $B_{\text{orb}}$  which dominates in other lanthanide ions (except  $\text{Gd}^{3+}$  which also has  $^8\text{S}_{7/2}$ ) is absent here. We may write

$$B_{\text{hf}} = B_{\text{core}} + B_{\text{cep}} + B_{\text{thf}} + B_{\text{dip}}. \quad (43)$$

$B_{\text{core}}$  is the Fermi contact term arising from the polarisation of core electrons as discussed in section 2.3.2;  $B_{\text{cep}}$  is another contact term due to the polarisation of conduction electrons (if present) by the  $4f$  magnetic moment; the term  $B_{\text{thf}}$  (transferred hyperfine field) represents the contact field arising from the influence of moments on neighboring ions via conduction electron polarisation, overlap and covalency; finally,  $B_{\text{dip}}$  is the direct dipolar field contribution from the neighboring moments, and can be neglected in most cases. In insulating compounds we have  $B_{\text{hf}} = B_{\text{core}} \approx -34$  T. In conducting compounds one finds roughly  $B_{\text{thf}} \approx 0$  to  $-11$  T and  $B_{\text{cep}} \approx +5$  to  $+20$  T (Nowik et al. 1973). The resulting  $B_{\text{hf}}$  is smaller than the free-ion value but clearly its exact number depends on the near cancellation of  $B_{\text{thf}}$  and  $B_{\text{cep}}$ . All three terms in eq. (43) beyond  $B_{\text{core}}$  had been omitted in our earlier discussion (section 2.3.2) since they are usually (i.e. in non-S ions) overwhelmed by  $B_{\text{orb}}$  and then  $B_{\text{core}}$  plays only the role of a correction (Dunlap and Kalvius 1972).

In fig. 21 the pressure-induced variation of magnetic transition temperatures and hyperfine field are shown for ferromagnetic  $\text{EuO}$ ,  $\text{EuS}$  and antiferromagnetic  $\text{EuTe}$  (Klein et al. 1976, 1977). It is safe to assume that  $B_{\text{core}}$  in eq. (43) is pressure-independent and also  $B_{\text{cep}}$  is considered to vary at best only weakly with volume (Devine 1982, Abd-Elmeguid et al. 1981, 1982). The whole volume dependence of  $B_{\text{hf}}$  rests with changes in  $B_{\text{thf}}$ . We may split this in a transferred field from nearest neighbors ( $J_1$ ) and a supertransferred field from next-nearest neighbors ( $J_2$ ). In  $\text{EuO}$  and  $\text{EuS}$  the move towards a more negative hyperfine field is mainly caused by the rapidly increasing  $J_1$  overlap. The supertransferred fields are much less affected by volume reduction and remain in first approximation constant. In antiferromagnetic  $\text{EuTe}$  all contributions from nearest neighbors nearly cancel each other resulting in the very weak volume dependence of  $B_{\text{hf}}$ . In summary, the pressure dependence of magnetic

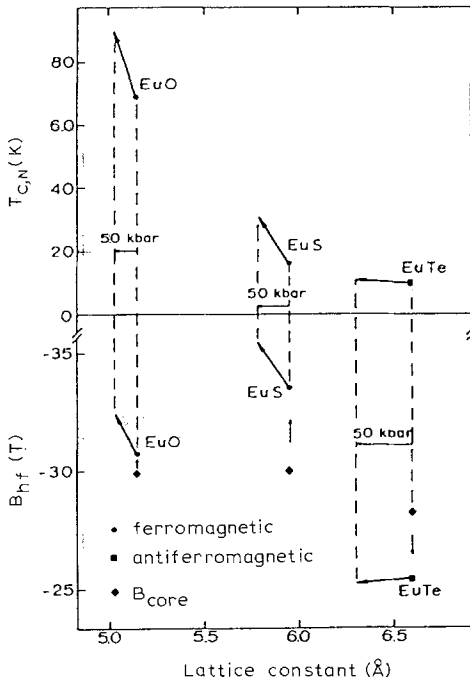


Fig. 21. Magnetic ordering temperatures ( $T_c$  or  $T_N$ ) and saturation ( $T \rightarrow 0$ ) hyperfine fields in EuX compounds as function of lattice constant from pressure experiments. The value of  $B_{core}$  is also indicated. [Taken from Klein et al. (1977).]

parameters in EuX compounds can be explained consistently by assuming two exchange integrals  $J_1$  and  $J_2$  with a dependence on lattice constant as shown in fig. 22.

Let us now turn to the question of valence stability in *EuO* at higher pressures.  $L_{III}$  edge measurements (Röhler et al. 1985) suggested a nonlinear increase of valence between 5 and 12 GPa. Mössbauer data disproved this claim since the isomer shift neither showed irregularities nor particular temperature dependences between 4.2 and 300 K.

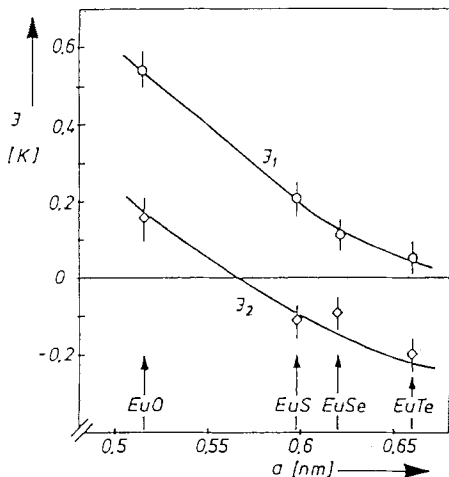


Fig. 22. Dependence of the effective exchange integrals  $J_1$  and  $J_2$  on lattice constant in EuX compounds. [Taken from Zinn (1976).]

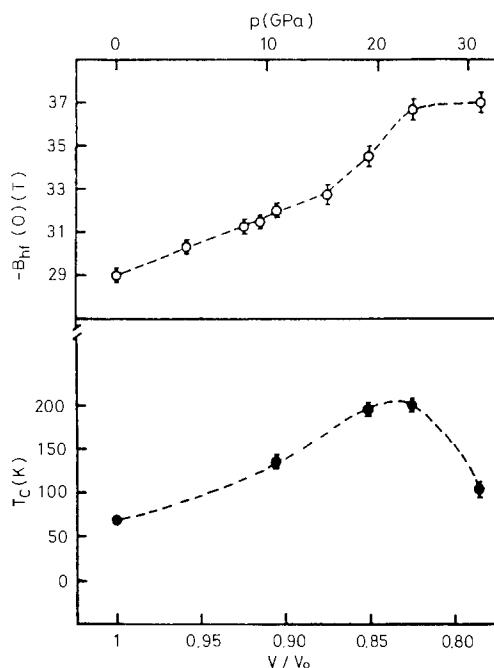


Fig. 23. Volume dependence of saturation ( $T \rightarrow 0$ ) hyperfine field and Curie temperature of EuO. The dashed lines are only guides for the eye. [Taken from Abd-Elmeguid and Taylor (1990).]

for pressures up to  $\sim 15$  GPa (Moser et al. 1988). Reflection spectra at high pressures indicated a metal–insulator transition at  $\sim 15$  GPa and the simultaneously determined pressure–volume relation suggested a continuous valence change starting there and continuing up to 40 GPa where EuO transforms into the CsCl structure (Zimmer et al. 1984). More recent Mössbauer measurements up to 31 GPa (Abd-Elmeguid and Taylor 1990) showed that the  $s$ -electron density  $\rho(0)$  at the  $^{151}\text{Eu}$  nucleus increases more steeply above 15 GPa. However,  $\rho(0)$  remains practically unaffected when at a fixed pressure the temperature is changed between 4.2 and 300 K. The metal–insulator transition therefore is not accompanied by more than a minute valence change at best.

The Curie temperature  $T_C$  and the magnetic hyperfine field  $B_{\text{hf}}$  are quite markedly affected by volume (fig. 23).  $T_C$  increases from  $\sim 65$  K at ambient pressure to  $\sim 210$  K at 22 GPa, which corresponds to a volume reduction of  $\sim 17\%$ . At the same time  $B_{\text{hf}}$  changes from  $-29$  to  $-37$  T. At still higher pressures (31 GPa), however, the magnetic behaviour is different again:  $T_C$  decreases to  $\sim 100$  K and  $B_{\text{hf}}$  remains virtually constant. These are strong indications that the magnetic  $4f$  moment ( $\mu_{4f}$ ) is starting to collapse. Still, at 31 GPa the valence change  $\Delta v$  as determined from the temperature dependence of the isomer shift is negligible ( $\Delta v \lesssim 0.05$ ). An IV situation is clearly not present. The conclusion put forward is that hybridization with conduction electrons broadens the  $4f$  level which leads to a decrease of  $\mu_{4f}$  accompanied by further increase of the  $s$  electron density at the  $^{151}\text{Eu}$  nucleus because the shielding of  $s$  electrons by the  $4f$  electrons now is reduced.

### 5.1.2. Neptunium mono-pnictide NpAs

For the Np mono-chalcogenides NpS, NpSe and NpTe (NpO does not exist) only Mössbauer data at ambient pressure are available. Within the mono-pnictide series NpN, NpP, NpAs and NpBi a high-pressure study has been carried out for NpAs (Potzel et al. 1989, Kalvius 1989). The question of valence instability is not at issue; the study was undertaken to gain information on the degree of 5f localization and on changes in magnetic structure. The Np–Np spacing in NpAs is  $\sim 4.1 \text{ \AA}$ , far above the Hill limit ( $\sim 3.25 \text{ \AA}$ ). Therefore, a lanthanide-like 5f electron structure is expected. Indeed, in Mössbauer experiments at ambient pressure (Aldred et al. 1974a) a saturation magnetic hyperfine field of 542 T was observed. This large value of  $B_{\text{hf}}$  and of the induced quadrupole interaction ( $eq_{\text{ion}} = -1.7 \times 10^{18} \text{ V/cm}^2$ ) as well as the isomer shift of  $\sim 16 \text{ mm/s}$  are in full accordance with a trivalent ionic  $5f^4$  configuration.

The magnetic phase diagram of NpAs is complex, even at ambient pressure (Aldred et al. 1974a, Burlet et al. 1986). Below  $T_{\text{N}} = 173 \text{ K}$  a sinusoidally modulated incommensurate antiferromagnetic spin structure is formed. The phase transition is of first order, the NaCl lattice distorts tetragonally and the volume of the unit cell is suddenly reduced. At  $T_{\text{IC}} \approx 153 \text{ K}$  the sinusoidal modulation squares up and locks into a  $4\uparrow 4\downarrow$  sequence. At  $T_{\text{O}} \approx 138 \text{ K}$  the lattice returns to the NaCl structure, however, with a lattice constant (and hence a unit cell volume) considerably larger than at  $T_{\text{N}}$ . Simultaneously the magnetic structure changes into a type-I ( $\uparrow\downarrow$ ), but noncollinear (3k) sequence. For details regarding the multiple- $k$  magnetic structure in the NpX compounds we refer the reader to Lander (1993) or Rossat-Mignod et al. (1984). This transition from a collinear  $4\uparrow 4\downarrow$  into the noncollinear  $\uparrow\downarrow$  structure is signaled in the Mössbauer spectrum by a sudden increase in  $B_{\text{hf}}$  of  $\sim 10\%$  (see also fig. 42).

The pressure dependences of  $B_{\text{hf}}$ ,  $T_{\text{N}}$  and  $S$  are summarized in fig. 24. The changes of isomer shift and especially of hyperfine field are unexpectedly large. Essential is that both  $B_{\text{hf}}$  and  $T_{\text{N}}$  are decreasing when pressure is applied ( $-\partial \ln B_{\text{hf}}/\partial \ln V = -0.8$  and  $-\partial \ln T_{\text{N}}/\partial \ln V = -1.3$ ). As stated, such a behavior indicates 5f itineracy. Thus, despite its location on the Hill plot and its large hyperfine field, NpAs cannot be considered as a fully localized system. It appears that the 5f electrons of Np hybridize with s and p electrons of As when the volume is reduced.

Remarkably, above  $\sim 2.5 \text{ GPa}$ , two separate hyperfine spectra with slightly different hyperfine fields (magnetic moments at Np) are found. The origin of the second hyperfine field is not fully understood at present. The following, still tentative explanation might be put forward. At ambient pressure the unit-cell volume in the range of existence of the noncollinear  $\uparrow\downarrow$  structure ( $T \ll 138 \text{ K}$ ) is larger than that in the range of the collinear  $4\uparrow 4\downarrow$  structure. The reduction in volume caused by the application of external pressure at low temperatures (4.2 K) then might favor the development of a collinear spin structure. Indeed, the second hyperfine field appearing at  $P \geq 2.5 \text{ GPa}$  is 10% smaller, just like the hyperfine field of the collinear  $4\uparrow 4\downarrow$  structure appearing at ambient pressure above 138 K. A comparison with the Ce and U mono-pnictides indicates that the formation of a particular spin structure is the result of a subtle interplay of three interactions (Coqblin and Schrieffer 1969, Cooper 1982): a short-range anisotropic exchange interaction causing superexchange via covalent bonds with the As ligands; the long-range RKKY interaction and the crystal

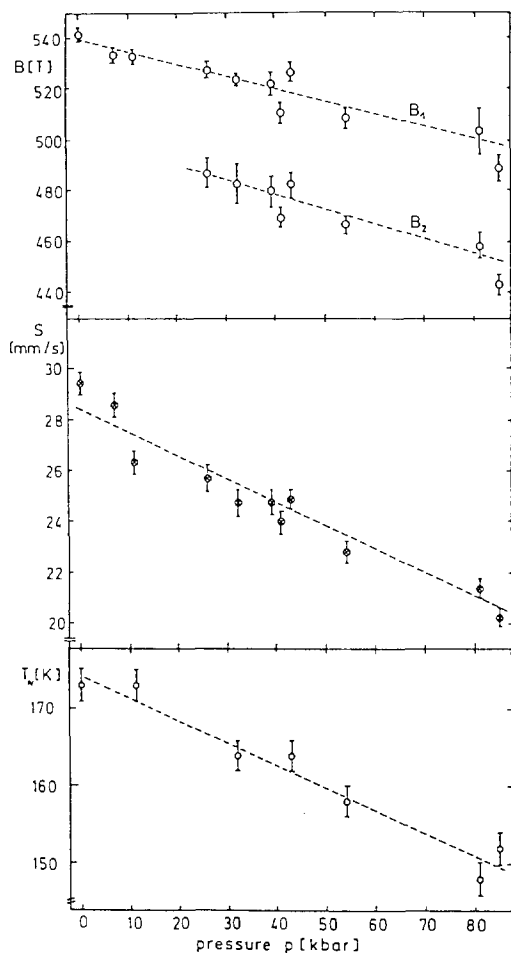


Fig. 24. Hyperfine field, isomer shift and Néel temperature of NpAs as function of pressure. At  $\sim 2.5$  GPa (25 kbar) a second hyperfine field appears as discussed in text. The shifts are given relative to the Am source. 13.9 mm/s have to be subtracted to get the shift relative to  $\text{NpAl}_2$ . At 8 GPa (80 kbar) the volume is reduced by  $\sim 2.4\%$ . [Taken from Potzel et al. (1989).]

field interaction. The relative strengths of these interactions change with the volume of the unit cell and magnetic phase transitions may consequently be induced. As fig. 25 demonstrates, we do not observe a sudden change of magnetic structure with pressure but rather the coexistence of two structures over a wide pressure range. Our pressure data lead us to the preliminary phase diagram depicted in fig. 26. Broken lines are tentative.

## 5.2. Laves phases

The compounds to be discussed are of the type  $\text{LnX}_2$  or  $\text{AnX}_2$  which form the cubic (C15) Laves phase ( $\text{MgCu}_2$  structure). X can either be a nonmagnetic ligand like Al, Ru, Os, ..., or a 3d magnetic transition element like Fe, Co, Ni. No high-pressure Mössbauer data exist for the latter type of ligand. From the former we shall

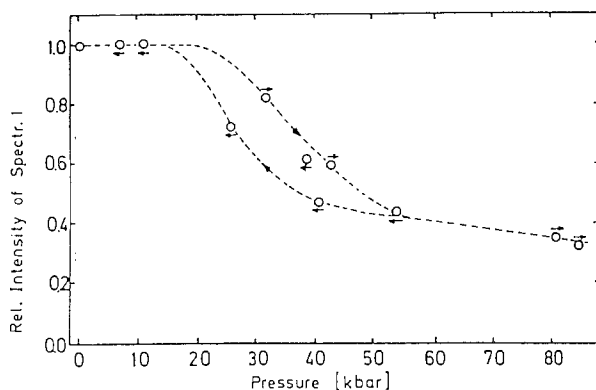


Fig. 25. Pressure variation of the relative intensity of the Zeeman pattern in NpAs with the larger value of  $B_{hf}$ . Arrows to the right mean increasing, to the left decreasing pressure. Data were taken at 4.2 K. 10 kbar = 1 GPa. [Taken from Kalvius (1990).]

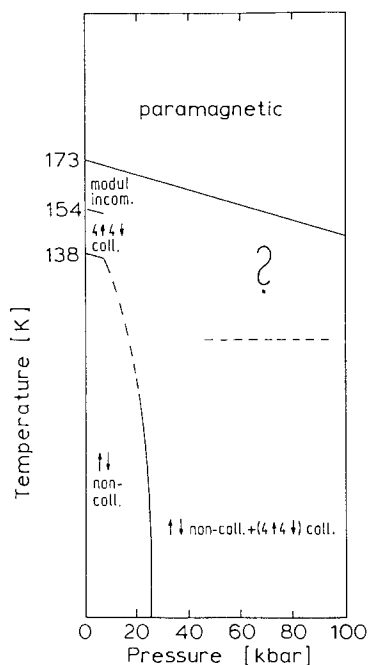


Fig. 26. Magnetic phase diagram of NpAs. The behavior at ambient pressure is well established but the volume dependence must be considered to be tentative. 10 kbar = 1 GPa. [Taken from Kalvius (1989).]

discuss  $\text{EuAl}_2$  in the context of mixed valence.  $\text{DyAl}_2$ ,  $\text{NpAl}_2$  and  $\text{NpOs}_2$  will be looked at with respect to the interplay of localized to itinerant  $f$  electron structure.

### 5.2.1. $\text{EuAl}_2$

The bulk moduli for  $\text{EuAl}_2$  at room temperature were found to be  $B_0 = 53.8 \pm 1.8$  and  $B'_0 = 4.2 \pm 0.4$  GPa (Gleissner 1992) which – as shown in fig. 27 – is lower than  $B_0$  of typically trivalent rare earth Laves phase systems like  $\text{ErAl}_2$  and  $\text{DyAl}_2$  but still larger than  $B_0$  of the IV compound  $\text{YbAl}_2$ . From this point of view



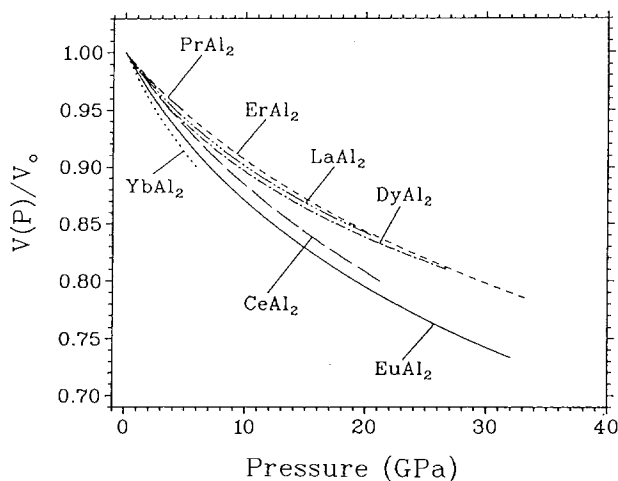


Fig. 27. Volume–pressure relation for different  $\text{LnAl}_2$  Laves phase compounds. [Taken from Gleissner (1992).]

$\text{EuAl}_2$  might be expected to exhibit IV behaviour when high external pressure is applied. As we shall see, this is not the case. The valence of Eu in  $\text{EuAl}_2$  remains close to  $2+$  up to very high pressures. Thus  $\text{EuAl}_2$  gives us information on the behavior of a stable divalent lanthanide compound when volume is reduced by as much as 30%. These findings on  $\text{EuAl}_2$  give further support that in  $\text{EuO}$  the valence is stable as well.

Figure 28 shows the volume dependence of the magnetic hyperfine field, the Néel temperature and the isomer shift. All three parameters change continuously by large amounts with reduced volume. Only at the highest pressure ( $\sim 49$  GPa)  $B_{\text{hf}}$  seems to increase rather little ( $T_{\text{N}}$ , unfortunately, could not be determined for technical reasons.)

The isomer shift  $S = -2.7$  mm/s found at 41 GPa is already fairly close to that of a trivalent material (see fig. 13). Yet,  $\text{EuAl}_2$  continues to exhibit a strong magnetic interaction which makes a substantial admixture of the trivalent configuration unlikely. Furthermore, the enormous increase of  $T_{\text{N}}$  with reduction of the unit cell volume strongly suggests that  $\text{EuAl}_2$  is a system with very well localized 4f spins. The large increase of  $B_{\text{hf}}$ , however, appears to be contradictory to the statement made earlier that for a localized 4f system the hyperfine field (i.e. the local magnetic moment) should remain constant when volume is reduced. The solution lies in the fact that changes in  $B_{\text{hf}}$  are caused here by the transferred hyperfine field  $B_{\text{thf}}$  which dominates because  $B_{\text{orb}} = 0$ . At ambient pressure we have  $B_{\text{core}} = -34$  T,  $B_{\text{cep}} = +10$  T (Nowik et al. 1973). With  $B_{\text{hf}} = -26.8$  T (as measured) one gets  $B_{\text{thf}} = -2.8$  T.

For a localized spin system  $B_{\text{thf}}$  and  $T_{\text{N}}$  can be treated within the RKKY formalism. According to Kropp et al. (1979) one finds

$$B_{\text{thf}} = -2a_{\text{s}} \langle s_z \rangle_{\text{s}} - 2a_{\text{ns}} \langle s_z \rangle_{\text{ns}}, \quad (44)$$

and

$$T_{\text{N}} = \frac{S_{\text{Eu}}(S_{\text{Eu}} + 1)}{3k \langle S_z \rangle_{\text{Eu}}} (J_{4\text{f-s}} \langle s_z \rangle_{\text{s}} + J_{4\text{f-ns}} \langle s_z \rangle_{\text{ns}}), \quad (45)$$

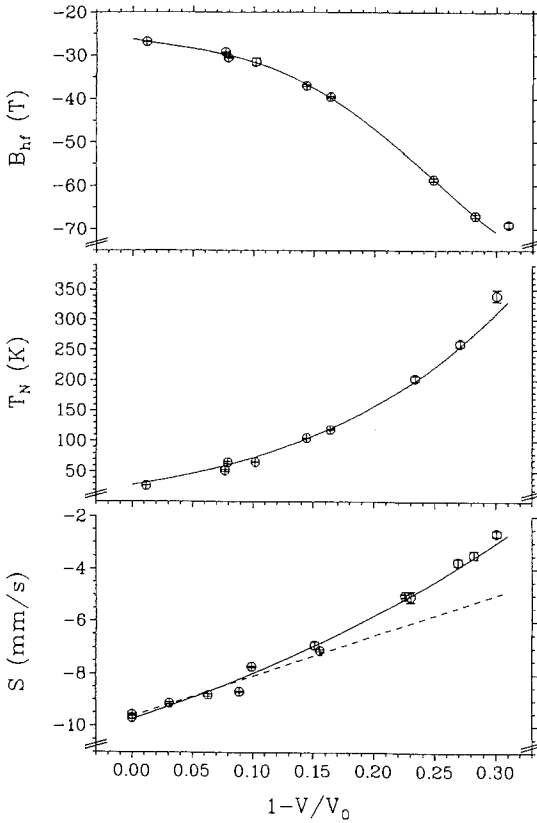


Fig. 28. Volume dependencies of hyperfine field ( $T \rightarrow 0$ ), Néel temperature and isomer shift ( $T = 300$  K) of  $\text{EuAl}_2$ . Isomer shift: The dashed line gives the initial slope of  $dS/d \ln V$ . The solid line is the hyperbolic fit discussed in text. Hyperfine field and Néel temperature: The solid line is a power expansion fit. The value of  $B_{\text{hf}}$  at highest pressure was not included in the fit, to emphasize its weak increase. [Taken from Gleissner (1992).]

where  $a$  are hyperfine coupling constants and  $J$  exchange integrals. The index  $s$  refers to conduction electrons with  $s$  and  $ns$  to those with non- $s$  character. One usually has  $a_{ns} \approx 0.1a_s$  and  $J_{4f-s} \approx J_{4f-ns} = J_{4f}$ .  $S_{\text{Eu}}$  is the  $4f$  spin on the Eu ion. The spin polarization of  $s$ -like and non- $s$ -like conduction electrons can be expressed as

$$\langle s_z \rangle_s + \langle s_z \rangle_{ns} = -\frac{9\pi Z^2}{4E_F} J_{4f} \langle S_z \rangle_{\text{Eu}} \sum_i F(2\mathbf{k}_F \cdot \mathbf{R}_i) \cos(\mathbf{q} \cdot \mathbf{R}_i), \quad (46)$$

where  $E_F$  is the Fermi energy,  $\mathbf{k}_F$  the Fermi vector,  $Z$  the number of conduction electrons per atom,  $\mathbf{q}$  the wave vector of the antiferromagnetic structure,  $\mathbf{R}_i$  the position vector of spin  $i$  and  $F(x) = (x \cos x - \sin x)/x^4$ . Using (Kropp et al. 1979)  $a_s = 375 \text{ T/spin } \frac{1}{2}$  and  $J_{4f} = 0.16 \text{ eV}$  together with the values of  $B_{\text{hf}}$  and  $T_N$  for  $\text{EuAl}_2$  at ambient pressure we find

$$\langle s_z \rangle_{ns} = -0.0143, \quad \text{and} \quad \langle s_z \rangle_s = +0.00457,$$

i.e. ferromagnetic polarization of non- $s$  electrons and antiferromagnetic polarization of  $s$  electrons. The polarization of non- $s$  electrons is important. Combining eqs. (44)

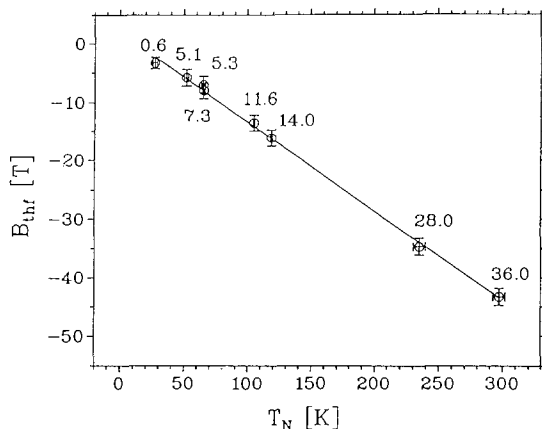


Fig. 29. Relation between transferred hyperfine field (deduced from the measured  $B_{hf}$  as described in text) and Néel temperature of  $\text{EuAl}_2$  for various pressures (number given at each data point in GPa). [Taken from Gleissner (1992).]

and (45) gives (Gleissner et al. 1993)

$$\frac{B_{thf}}{T_N} = 6k \frac{\langle S_z \rangle_{\text{Eu}}}{S_{\text{Eu}}(S_{\text{Eu}} + 1) J_{4f}} \frac{a_s \langle s_z \rangle_s - 0.1 \langle s_z \rangle_{ns}}{\langle s_z \rangle_s + \langle s_z \rangle_{ns}}. \quad (47)$$

In eq. (46) the sum is independent of pressure. Since  $E_F$  should only be weakly sensitive to pressure one concludes that  $J_{4f}$  has the same volume dependence as the conduction electron polarization.

Remembering that changes in  $B_{hf}$  are caused by  $B_{thf}$ , leads to the interesting experimental finding (fig. 29) that the ratio  $B_{thf}/T_N$  is independent of volume. With the reasonable assumption that the pressure dependence of polarization of s and non-s conduction electrons is roughly equivalent it follows from eq. (47) that  $a_s$  must have the same volume dependence as  $J_{4f}$ . This disagrees with Abd-Elmeguid et al. (1981) where a pressure-independent  $a_s$  was assumed. It should be noted that the  $\text{EuAl}_2$  data cover a much larger volume change ( $\sim 30\%$ ) than previous data.

The RKKY formalism allows also to relate the changes in Néel temperature with those of the contact electron density as measured by isomer shift. The combination of eqs. (45) and (46) leads to

$$T_N = \frac{S_{\text{Eu}}(S_{\text{Eu}} + 1) 4E_F}{3k \langle S_z \rangle_{\text{Eu}}^2} \frac{(\langle s_z \rangle_s + \langle s_z \rangle_{ns})^2}{9\pi Z^2 \sum_i F(2\mathbf{k}_F \cdot \mathbf{R}_i) \cos(\mathbf{q} \cdot \mathbf{R}_i)}. \quad (48)$$

A volume change of conduction electron polarization [the squared term in eq. (48)] should be reflected in the change of their density at the Eu nucleus, i.e., in the pressure variation of isomer shift. This then demands that

$$\Delta \sqrt{T_N} \propto \Delta \rho_{ce}(0) \propto \Delta S. \quad (49)$$

This is experimentally fulfilled with high precision (fig. 30). Because of the linear relation depicted in fig. 29, the same correlation exists for the changes in  $B_{hf}$ .

The result of fig. 30 not only justifies the assumptions made above, but in particular it shows that the RKKY formalism is applicable here and that we deal with a localized

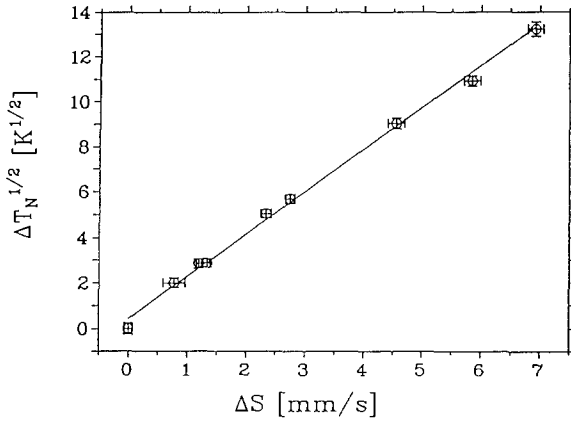


Fig. 30. Proof of linear relation between changes in  $T_N$  and isomer shift as predicted for localized spin systems (see text). The data points are from measurements at increasing pressure from left to right. [Taken from Gleissner (1992).]

4f system. The correlation (49) had previously been derived from the expression for  $T_N$  in the Ruderman–Kittel–Arrott model for localized spins by Potzel et al. (1981) in discussing the case of  $\text{NpCo}_2\text{Si}_2$  (see section 5.4.2). In essence both treatments are the same.

Finally let us return to the volume dependence of isomer shift. In fig. 28 (bottom) a strong deviation from the linear extrapolation of initial slope  $dS/d \ln V = 15 \text{ mm/s}$  is apparent. The change in contact density by the compression of conduction electrons can be described by (Kalvius et al. 1974)

$$\frac{d\rho(0)}{d \ln V} = \gamma\rho(0). \quad (50)$$

With  $\gamma \approx -1$  one finds

$$\frac{d\rho(0)}{\rho(0)} = -\frac{dV}{V}, \quad \text{or } \rho(0)V = \text{const.} \quad (51)$$

The volume dependence of  $\rho(0)$  is expected to be hyperbolic and indeed such a fit connects very well the experimental points (solid line in fig. 28, bottom). Volume reduction simply compresses the conduction electron gas. This result questions somewhat the suggested break around 15 GPa in the  $S(V)$  dependence of EuO (see Abd-Elmeguid and Taylor 1990) which had been derived from linear fits. In one sense this point is academic since a valence change was excluded from the lack of temperature variation. But one may ask why the occurrence of an insulator–metal transition is not reflected in the isomer shift.

### 5.2.2. $\text{DyAl}_2$

This lanthanide Laves phase becomes ferromagnetic at  $T_C = 61 \text{ K}$  under ambient conditions. The saturation hyperfine field and magnetically induced quadrupolar coupling correspond within the experimental errors to the free-ion values (see also fig. 37). Similarly, the isomer shift lies well inside the typical range of metallic trivalent

compounds (Nowik et al. 1966). Hence  $DyAl_2$  is a compound with the fully localized  $4f^9: {}^6H_{15/2}$  configuration. It contrasts to the just discussed case of  $EuAl_2$  in the sense that  $B_{hf}$  is highly dominated by  $B_{orb}$ .

High-pressure experiments up to 8.3 GPa at 4.2 K were carried out by Kratzer et al. (1986). The observed rise in Curie temperature  $dT_C/dP = 3.5 \pm 0.3 \text{ K GPa}^{-1}$  is well within the range predicted by a calculation using a modified RKKY exchange (Jaakkola and Hänninen 1980). The pressure coefficient of  $B_{hf}$  is extremely small  $dB_{hf}/dP = -0.4 \pm 0.1 \text{ T GPa}^{-1}$ . Similarly, the ionic electric field gradient decreases by  $\sim 5\%$  between ambient pressure and 8.3 GPa. Isomer shifts exhibit the linear pressure dependence expected from a compression of mainly s-like conduction electrons.

In summary, the high-pressure data on  $DyAl_2$  confirm well the behavior expected for localized f electron magnetism with dominating orbital contribution: The hyperfine field (magnetic moment on  $Dy^{3+}$ ) is only very weakly dependent on volume while the magnetic ordering temperature rises markedly under reduced volume.

### 5.2.3. $NpAl_2$ and $NpOs_2$

Both Laves-phase compounds have Np–Np spacings  $d_{Np}$  close to the Hill limit. They are ferromagnets with  $T_C = 58 \text{ K}$  ( $NpAl_2$ ) and  $T_C = 9 \text{ K}$  ( $NpOs_2$ ). The response of  $T_C$ ,  $B_{hf}$  and  $S$  to a reduction in  $d_{Np}$  for the pressure range up to  $\sim 3 \text{ GPa}$  are summarized in fig. 31. All three parameters decrease drastically with pressure. For the 60 keV  ${}^{237}\text{Np}$  resonance a decrease of isomer shift means an increase in  $\rho(0)$ . From X-ray data the bulk moduli of  $B_0 = 120 \pm 29 \text{ GPa}$  ( $NpAl_2$ ) and  $B_0 = 910 \pm 50 \text{ GPa}$  ( $NpOs_2$ ) were obtained (Zänkert et al. 1984, Potzel 1990). The extremely

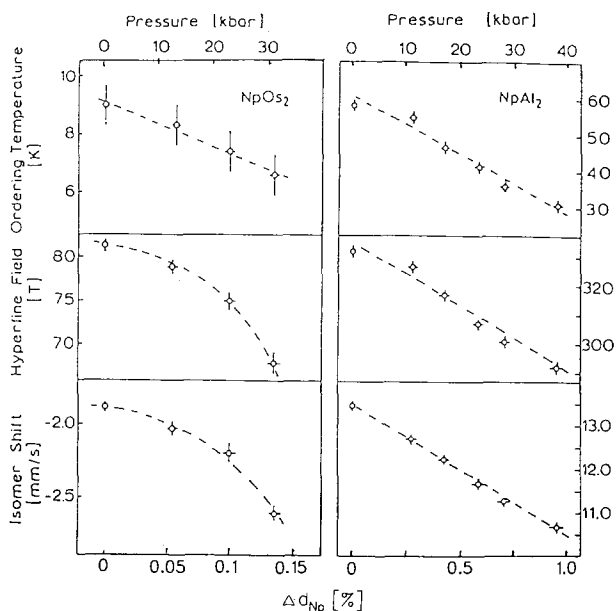


Fig. 31. Dependencies of Curie temperature, hyperfine field ( $T \rightarrow 0$ ) and isomer shift ( $T = 4.2 \text{ K}$ ) on the relative change of Np–Np separation ( $\Delta d_{Np}$ ) as induced by application of pressure for the cubic Laves phases  $NpOs_2$  and  $NpAl_2$ . Note the extremely small compressibility of  $NpOs_2$ . 10 kbar = 1 GPa.

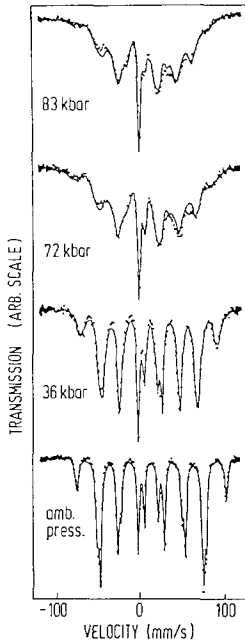


Fig. 32.  $^{237}\text{Np}$  Mössbauer hyperfine spectra of  $\text{NpAl}_2$  at 4.2 K and various pressures. 10 kbar = 1 GPa. [Taken from Litterst et al. (1986).]

small compressibility of  $\text{NpOs}_2$  should be noted. It is the typical signature of an itinerant electron metal. The pressure dependences of  $B_{\text{hf}}$  and  $S$  are markedly nonlinear in  $\text{NpOs}_2$ . However, plotting  $B_{\text{hf}}$  versus the contact density (isomer shift), a precise linear correlation is observed (Kalvius et al. 1985). The changes in  $B_{\text{hf}}$  and  $\rho(0)$  must have the same origin.

The volume coefficients  $-\partial \ln T_C / \partial \ln V = -16$  and  $-\partial \ln B_{\text{hf}} / \partial \ln V = -3.6$  for  $\text{NpAl}_2$  as well as  $-\partial \ln T_C / \partial \ln V = -80$  and  $-\partial \ln B_{\text{hf}} / \partial \ln V = -46$  for  $\text{NpOs}_2$  fulfil the criterion of strong 5f delocalization with reduced atomic volume. The volume coefficient of isomer shift in  $\text{NpOs}_2$  is more than twice that of more localized Np intermetallics like  $\text{NpCo}_2\text{Si}_2$  and  $\text{NpAs}$ . The strong delocalization of 5f electrons diminishes the shielding of inner s electron density and thus increases  $\rho(0)$  much more than the simple effect of compression of s-type conduction electrons. For this reason both  $S(V)$  and  $B_{\text{hf}}(V)$  exhibit the same nonlinearity (fig. 31). The 5f delocalization process is much more pronounced in  $\text{NpOs}_2$  than in  $\text{NpAl}_2$ . This is in accordance with Hill behavior because  $\text{NpOs}_2$  is much closer to the Hill limit than  $\text{NpAl}_2$ . In fact,  $\text{NpAl}_2$  was originally considered a fairly localized system, the slight reduction in  $B_{\text{hf}}$  explained by crystal field effects. The high-pressure data prove otherwise.

From the Mössbauer hyperfine spectra of  $\text{NpAl}_2$  under pressures up to 8.3 GPa (Litterst et al. 1986) another interesting feature has been observed: the 5f delocalization induced by reduction of atomic volume is linked to dynamical processes. It is evident from fig. 32 that the spectra at higher pressures cannot be derived simply by a reduction of hyperfine field. This would, for example, not explain the growth of the

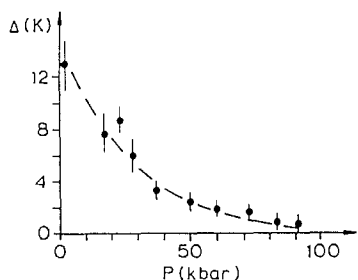


Fig. 33. Pressure dependence of the separation  $\Delta$  between the strong and the weak magnetic state in  $\text{NpAl}_2$ . The solid line is a guide for the eye only. For details see text. 10 kbar = 1 GPa. [Taken from Litterst et al. (1986).]

strong resonance line close to zero velocity. The fits – shown as solid line in fig. 32 – were obtained with the following model: Fluctuations occur between a strong magnetic ground state with  $\mu \approx 1.5\mu_B$  (i.e., with a more localized 5f electron structure) and a second less magnetic state with  $\mu \approx 1\mu_B$  (i.e., with a more itinerant 5f electron structure). The two states are separated by  $\Delta$  and possess different isomer shifts. This feature, however, appears only to be essential at low pressures (Kalvius et al. 1985). At high pressures, the important fact is that both states suffer from Zeeman splitting by exchange interaction. To obtain the fit shown in fig. 32 additional fluctuations [ferromagnetic relaxation, see Nowik and Wickmann (1966)] between the Zeeman levels of each state (intra-state) and between the levels of the two states (inter-state) had to be assumed. Relaxation rates are mainly temperature dependent and in the range of 1–10 GHz, the upper value referring to temperatures close to  $T_C$ . Pressure primarily influences  $\Delta$ , its values resulting from the fits to the measured spectra are plotted in fig. 33. It is interesting to note that the strong reduction of  $\Delta$  up to 5 GPa goes along with a marked reduction in  $T_C$  from 56 to 25 K. But increasing pressure up to 9 GPa reduces  $T_C$  only down to 15 K and similarly  $\Delta$  does not change significantly. Compressibility data show a break in the pressure–volume relation near 5 GPa (Zänkert et al. 1984). Although this model may have its faults (fitting the data does not prove it right) it indicates that the 5f delocalization process can be treated in a frame closely related to the model discussed earlier for valence fluctuations (Nowik 1983), but only involves states of the same charge state, although with different magnetic properties.

The question arises if such relaxation processes also play a role in  $\text{NpOs}_2$ . Unfortunately, the hyperfine field in  $\text{NpOs}_2$  is considerably reduced which also diminishes the sensitivity for observation of dynamical phenomena.

### 5.3. The $\text{AuCu}_3$ structure ( $\text{NpSn}_3$ )

Compounds of type  $\text{AnX}_3$  ( $X = \text{Al, Ge, Rh, Pd}$  and  $\text{Sn}$ ) crystallizing in the (cubic)  $\text{AuCu}_3$  structure represent, together with the Laves phases, the largest series of intermetallics studied so far. The interactinide distance  $d_{\text{An}}$  is large and far from the Hill limit, hence one would expect highly localized magnetism in all members of the series. This, however, is by no means the case, only about half of the compounds investigated to date are magnetic at all (Fournier and Troc 1985). This explicitly

indicates the importance of 5f electron hybridization with ligand electrons. That point is discussed in more detail in section 6.3. High-pressure Mössbauer measurements have been carried out only for  $NpSn_3$ . Analogous Ln compounds exist. Mössbauer data on  $RSn_3$  under ambient pressure are available (e.g., Sanchez et al. 1976), but no high-pressure measurements are reported to our knowledge. Thus,  $NpSn_3$  is a lonely candidate in this group. The findings of the high-pressure study, however, run quite contrary to expectations and warrant some discussion.

On the basis of specific-heat data and Mössbauer spectroscopy at low temperatures,  $NpSn_3$  ( $T_N = 9.5$  K) has been assigned as a model itinerant-electron antiferromagnet (Brodsky and Trainor 1977). The paramagnetic electronic specific-heat coefficient was determined to be  $\gamma = 242$  mJ/(mol K<sup>2</sup>) if data for  $T > T_N$  are considered. The low-temperature extrapolation gives only  $\gamma = 83$  mJ/(mol K<sup>2</sup>). Mössbauer experiments below  $T_N$  gave  $B_{hf} \approx 66$  T which corresponds to  $\mu_{Np} \approx 0.3\mu_B$ . The spectrum has already been shown in fig. 12. Additional measurements using the <sup>119</sup>Sn (24 keV) resonance showed that roughly half of the Sn nuclei see a transferred hyperfine field, the other half does not (Trainor et al. 1976). This is expected for a simple type-I ( $\uparrow\downarrow$ ) magnetic structure (Sanchez et al. 1976, Shenoy et al. 1970b). We wish to mention that the least-squares fit to the <sup>237</sup>Np hyperfine spectrum shown in fig. 12 assumes a small distribution in hyperfine field. Possibly,  $NpSn_3$  possesses some modulation (most likely with a long wavelength) in the basic  $\uparrow\downarrow$  spin structure. Neutron scattering data do not yet exist. Susceptibility data are in agreement with antiferromagnet ordering. The specific-heat data (Trainor et al. 1976) are quite like those of  $NpOs_2$ , which also has a low moment ( $\sim 0.4\mu_B$ ) and is surely rather itinerant (see section 5.2.3) but a ferromagnet. In addition, the magnetic entropy of  $NpSn_3$  is rather small ( $\sim -0.01R \ln 2$ ). All these findings have led to the assignment of  $NpSn_3$  as an itinerant-electron antiferromagnet. This view is at least in part supported by band structure calculations which indicate the formation of an (albeit narrow) 5f band (Norman and Koelling 1986). Consequently, the behavior under high pressure was expected to be similar to that of  $NpOs_2$ . This is not the case.

TABLE 5

Volume coefficients of the magnetic transition temperature ( $T_{ord}$ ), the ordered magnetic moment  $\mu$  at Np (or Dy), and the electronic charge density at the Np (or Dy) nucleus [ $\rho(0)$ ]. The Np–Np separation  $d_{Np}$  is also given.

Compound	$-\frac{d \ln T_{ord}}{d \ln V}$	$-\frac{d \ln \mu}{d \ln V}$	$-\frac{d \ln \rho(0)}{d \ln V}$	$d_{Np}(\text{\AA})$
DyAl <sub>2</sub>	+5.3	+0.1	$+5.6 \times 10^{-5}$	...
NpCo <sub>2</sub> Si <sub>2</sub>	+3.3	+0.1	$+2.4 \times 10^{-5}$	3.90
NpAs	-1.3	-0.8	$+4.2 \times 10^{-5}$	4.07
NpAl <sub>2</sub>	-16.0	-4.0	$+5.0 \times 10^{-5}$	3.37
NpOs <sub>2</sub>	-80.0	-46.0	$+12.5 \times 10^{-5}$	3.28
NpSn <sub>3</sub>	+8.0	$\leq +1.0$	+2.0	4.62



Mössbauer spectroscopy and X-ray diffraction in the pressure range up to 6.2 GPa between 1.5 and 100 K were carried out by Kalvius et al. (1990). The measured volume coefficients of the  $^{237}\text{Np}$  hyperfine parameters are summarized in table 5 and compared to similar data found in other Np intermetallics. The hyperfine field in  $\text{NpSn}_3$  is hardly affected by volume change, while  $T_N$  rises quickly, a behavior also found in  $\text{DyAl}_2$  and  $\text{NpCo}_2\text{Si}_2$ . This is the signature of a localized f electron structure. Clearly, the pressure coefficients are quite different from those of itinerant  $\text{NpOs}_2$ . This localized-electron behavior of  $\text{NpSn}_3$  is further corroborated when plotting the increase of  $T_N$  versus the change in  $S$ . In terms of the rigid-spin model of Ruderman, Kittel and Arrot again the linear relation  $\Delta(\sqrt{T_N}) \propto \Delta S$  is fulfilled (see section 5.2.1) as in the case of highly localized f systems (e.g. rare earths). In summary, we are forced to conclude that  $\text{NpSn}_3$  under pressure does not behave like an itinerant-electron magnet. The already mentioned band-structure calculations unfortunately do not track the properties of a 5f electron structure with volume.

The problem is to reconcile the rather low magnetic moment and the small entropy change with the localized response under high pressure. The Mössbauer isomer shift of  $\text{NpSn}_3$  is +20 mm/s relative to  $\text{NpAl}_2$  suggesting a  $\text{Np}^{3+}(5f^4)$  non-Kramers ion with the  $^5I_4$  Hund's rule ground state. In a cubic crystalline electric field the  $^5I_4$  state splits into a singlet  $\Gamma_1$ , a non-Kramers doublet  $\Gamma_3$ , and two triplets  $\Gamma_4$  and  $\Gamma_5$  with  $\Gamma_5$  as ground state (Lea et al. 1962). Thus, the ordered moment calculated by conventional crystalline electric field interactions is much too large when compared to  $0.3 \mu_B$  (Cooper and Vogt 1971).

The experimental results can satisfactorily be explained by invoking the Kondo effect with a critical temperature of  $T^* \sim 30$  K. This implies that the moment originating from the  $\Gamma_5$  levels is partially quenched by the conduction electrons. A similar explanation has been proposed by Barbara et al. (1977) for the well established concentrated Kondo system  $\text{CeAl}_2$  at ambient pressure to explain the reduction of ordered moment.

For concentrated Kondo systems orbitally driven anisotropic hybridization of the f electrons with conduction electrons is crucial (Cooper et al. 1988, Levy and Zhang 1989). The anisotropic part of the mixing interaction causes a substructure within the rather narrow f band, which leads to crystal-field effects even in highly itinerant-electron systems. On account of this crystal-field dressing a localized 5f electron in  $\text{NpSn}_3$  might develop.

## 5.4. *Noncubic compounds*

### 5.4.1. *YbCuAl*

This intermetallic crystallizes in hexagonal  $\text{Fe}_2\text{P}$  structure and is an established intermediate valence compound ( $v \approx 2.8$ ) at ambient pressure which was suspected to move towards the full  $\text{Yb}^{3+}$  configuration under volume reduction. We have said before that the use of the  $^{170}\text{Yb}$  resonance does not allow the precise enough measurement of isomer shift. Thus a possible valence change can only be traced via

magnetic properties and the electric field gradient. Again combined pressure and temperature sweeps are essential.

Divalent ytterbium has the  $4f^{14}$  configuration with the Hund's rule ground state  $^1S_0$ . It shows no magnetism and no ionic electric field gradient. In contrast, the Hund's rule ground state of trivalent ytterbium with the  $4f^{13}$  configuration is  $^2F_{7/2}$ . Since  $L \neq 0$  an ionic electric field gradient and a large orbital contribution to the magnetic hyperfine field will be present (see table 2).

*YbCuAl* has been studied up to 13 GPa between 1.6 and 77 K by Schöppner et al. (1986). Only a small electric field gradient on account of the noncubic crystal structure is seen at ambient pressure. It rises strongly when 13 GPa are applied and shows a marked temperature dependence at elevated pressure (fig. 34). Both effects are expected when  $Yb^{3+}$  has been formed. The temperature dependence in particular is typical for crystalline-field interactions on the  $Yb^{3+}$  ion. No magnetic hyperfine splitting was observed down to 1.6 K although the transition from  $Yb^{2+}$  to  $Yb^{3+}$  is believed to be complete at 13 GPa. At the lowest temperature, however, some line-broadening was observed which could well be fitted assuming paramagnetic relaxation as discussed by Wickmann and Wertheim (1968). Such behavior is not possible for  $Yb^{2+}$ .

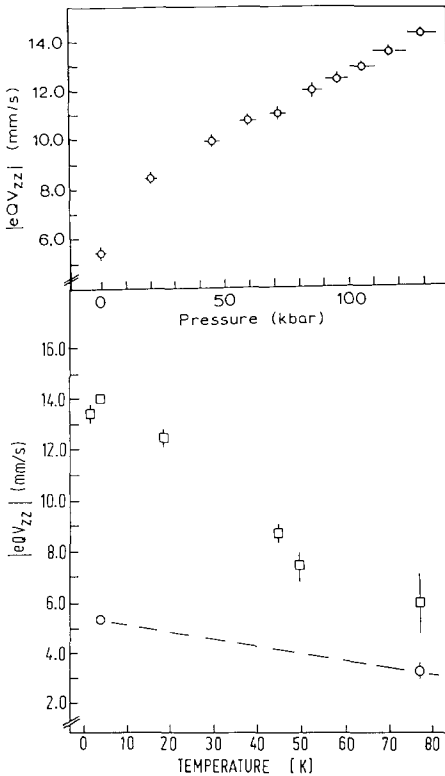


Fig. 34. Variation of quadrupole coupling with pressure (top) at 4.2 K and with temperature (bottom) at ambient pressure (broken line) and at 13 GPa or 130 kbar (squares) for *YbCuAl*. [Taken from Schöppner et al. (1986).]

#### 5.4.2. $NpCo_2Si_2$

This compound crystallizes in the tetragonal (I4/mmm) structure. At ambient pressure it is an antiferromagnet with  $T_N = 46$  K. From neutron diffraction data (de Novion et al. 1980), it is known that a moment of  $1.5\mu_B$  is localized at the Np ion, while the Co carries no moment. The position of  $NpCo_2Si_2$  in the Hill plot is well above the Hill limit and a highly localized 5f structure is possible. But, as the cases of Np mono-chalcogenides and mono-pnictides as well as the  $AuCu_3$  intermetallics show, the location in the Hill plot is an indicator but no proof of 5f localization.  $^{237}Np$  Mössbauer spectroscopy at pressures up to 3.5 GPa for temperatures between 1.4 and 77 K have been performed by Potzel et al. (1981). The isomer shift decreases and the Néel temperature increases with pressure whereas the hyperfine field stays essentially constant. The volume coefficient of these three parameters can be found in table 5 (section 5.3). They characterize a lanthanide-like localized f electron structure. This is further corroborated by the fulfillment of the relation  $\Delta\sqrt{T} \propto \Delta\rho(0)$ , which has previously been discussed for the cases of  $EuAl_2$  and  $NpSn_3$ . Historically,  $NpCo_2Si_2$  was the first case where this important relation could be established [using the Rudermann–Kittel–Arrott formalism for localized spins – see Arrott (1966)].

The isostructural compound  $EuCo_2Si_2$  has also been studied by Mössbauer spectroscopy, although only at ambient pressures (Nowik and Felner 1977). It was found to contain both  $Eu^{2+}$  and  $Eu^{3+}$  as stable ions. This appearance of two different species of Eu seems to be a problem in this structure, but is probably connected to the preparation and not intrinsic. In contrast to the stable valence in  $EuCo_2Si_2$ , it was shown that  $EuCu_2Si_2$  exhibits well developed intermediate valence properties. This compound has been discussed as a reference IV material in section 4. Clearly, it is difficult to make a priori statements concerning the stability of f electron structure in this intermetallic series.

#### 5.5. Summary

High-pressure Mössbauer experiments are the most reliable means to establish deviations in f electron structure from that of the corresponding free ion (i.e. a highly localized configuration) in f transition metals and compounds. For the case of the lanthanides we have discussed how the appearance of intermediate valence is mirrored in the combined temperature and pressure dependence of hyperfine parameters. It was shown in particular that  $EuAl_2$  and  $EuO$  are stable divalent materials (at least up to 30–50 GPa), contrary to expectation. In the light actinides the transition to an itinerant 5f electron structure is of prime interest. Its development can be traced by the combination of the volume coefficients of magnetic transition temperature and hyperfine field (or Np magnetic moment). This is once more demonstrated in the plot of fig. 35. One finds  $NpCo_2Si_2$  and  $NpSn_3$  to be localized in the sense of standard lanthanide f electron structure. For  $NpSn_3$  this was certainly a surprise and is not easily reconciled with its magnetic properties under ambient pressure. NpAs is a narrow band case, in contrast to its location on the Hill plot. It is characterized by overlap with ligand electrons. The width of the 5f band increases strongly when moving

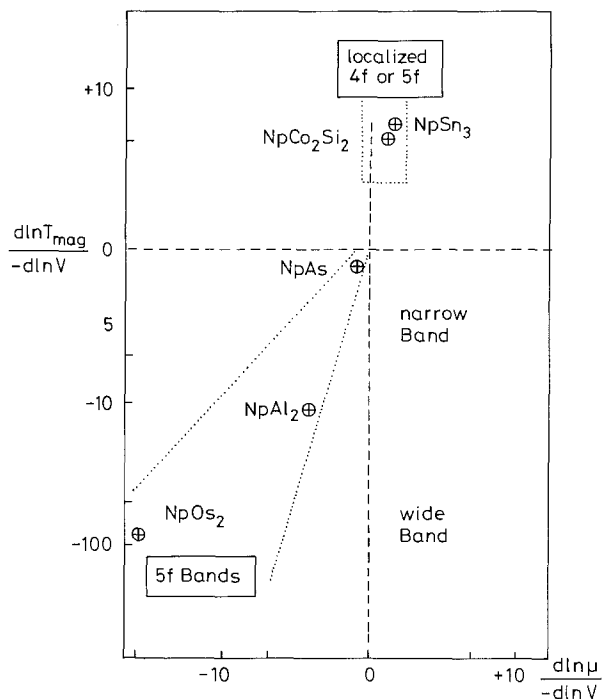


Fig. 35. Plot of the volume coefficient of magnetic ordering temperature against the volume coefficient of magnetic moment (hyperfine field) for Np intermetallics. The areas for localized and band-like f electron configurations are indicated. The logarithmic scales are for convenience and have no physical relevance.

from  $\text{NpAl}_2$  to  $\text{NpOs}_2$ . This is in full accordance with the model by Hill and therefore f-f overlap is the decisive parameter.

## 6. Systematics of electronic structure properties in intermetallic systems

In the preceding section the influence of volume change induced by applied pressure on the electronic structure of some Ln- and An-intermetallics has been reviewed. Atomic volume is altered as well when the ligand is changed within a given series of intermetallics. Here, however, the chemical influence of the ligands on electronic structure is often equally important or even dominating. This interplay between the effects of varying atomic volume and chemical nature of ligand on the properties of Ln and An ions will be under review in this chapter for series of intermetallic compounds where systematic Mössbauer spectroscopic data at ambient pressure are available.

### 6.1. (An or Ln) $X_2$ compounds

Our prime interest lies with Np compounds. Their main properties of interest here are summarized in table 6 together with references to the original literature. We shall discuss predominantly those intermetallics which crystallize in the cubic Laves phase ( $\text{MgCu}_2$ , Fd3m) structure. This series has been studied in detail by a wide variety of

TABLE 6

Magnetic and electronic properties of  $\text{NpX}_2$  intermetallic systems (F = ferromagnet, AF = antiferromagnet, P = paramagnet, SF = spin fluctuator; a) moment derived from neutron scattering or Mössbauer spectroscopy, b) Saturation moment from magnetization.)

Compound	Crystal structure	Lattice parameter (Å)	Magn. struc.	$T_N$ or $T_c$ (K)	$\mu_{\text{ord}}$ ( $\mu_B$ )	$\mu_{\text{eff}}$ ( $\mu_B$ )	S (mm/s)	$B_{\text{hf}}$ (T)	$eq$ ( $10^{18}\text{V}/\text{cm}^2$ )	Ref.
<b><math>\text{NpX}_2</math> with X a 3p element partner</b>										
$\text{NpAl}_2$	Fd3m	7.785	F	56	a) 1.5 b) 1.38	2.3	0.0	330(5)	$\sim 0$	[1-4]
$\text{NpAs}_2$	P4/nmm	$a=3.96$ $c=8.76$	AF/F	52/18	a) 1.5 b) 1.32	1.88	3.0	288(5)	+1.1	[5]
$\text{NpSi}_2$	ThSi <sub>2</sub>	$a=3.968$ $c=13.71$	F	48	a) 1.1 b) 0.8	2.15	7.9	244(5)	$\sim 0$	[1]
$\text{NpGa}_2$	AlBi <sub>2</sub>	$a=4.259$ $b=4.077$	F	55	a) 2.39 b) 2.4	2.60	15.2	525(5)	$\sim 0$	[1]
$\text{NpSb}_2$	LaSb <sub>2</sub>	$a=6.17$ $b=6.04$ $c=17.50$	F	45	a) 1.9 b) 1.3	2.87	18.0	390(5)	$\sim 0$	[6]
$\text{NpTe}_2$	P4/nmm	$a=4.424$ $c=9.004$	P			2.88	28.0		$\sim 0.57$	[6]
<b><math>\text{NpX}_2</math> with X a 3d element partner</b>										
$\text{NpMn}_2$	Fd3m	7.230	F	18	a) 0.3 b) 0.4	2.44	-20.0	45	$\sim 0$	[7]
$\text{NpFe}_2$	Fd3m	7.144	F	492	a) 1.1/Np 1.1/Fe 2.6/fu	4.09	-24.0	184	$\sim 0$	[7, 4]
$\text{NpCo}_2$	Fd3m	7.043	AF	12	a) 0.5/Np	2.5	-22	110	$\sim 0$	[4, 7-9]
$\text{NpNi}_2$	Fd3m	7.098	F	32	a) 1.0/Np <0.3/Ni	1.95	-18	227	$\sim 0$	[7] [4]
<b><math>\text{NpX}_2</math> Laves phase with other elements</b>										
$\text{NpRu}_2$	Fd3m	7.446	P			2.8	-19		$\sim 0.1$	[10-12]
$\text{NpOs}_2$	Fd3m	7.528	F	7.5	a) 0.4 b) 0.34	2.37	-15	90	$\sim 0$	[2, 3]
$\text{NpIr}_2$	Fd3m	7.509	AF	9	a) 0.6	2.1	-11	130	$\sim 0$	[4, 10, 13]
<b>Other <math>\text{NpX}_x</math> compounds</b>										
$\text{NpH}_2$	CaF <sub>2</sub>	5.39	SF					18	$\sim 0$	[14]
$\text{NpH}_{2+x}$	CaF <sub>2</sub>	5.33	P					18	Variable	[15]
$\text{NpRe}_2$	MgZn <sub>2</sub>	$a=5.396$ $b=8.77$	F	47	a) 0.84 b) 0.9	2.1	-19	186	0.2	[14]

\*References: [1] Yaar et al. (1992); [2] Moser et al. (1981); [3] Aldred et al. (1976); [4] Gal et al. (1973b); [5] Bogé et al. (1982); [6] Bogé et al. (1981); [7] Aldred et al. (1975b); [8] Kalvius et al. (1985); [9] Sanchez et al. (1992); [10] Gal et al. (1989a); [11] Aldred et al. (1974b); [12] Aldred et al. (1975a); [13] Aldred et al. (1974c); [14] Gal, unpublished; [15] Mintz et al. (1981).

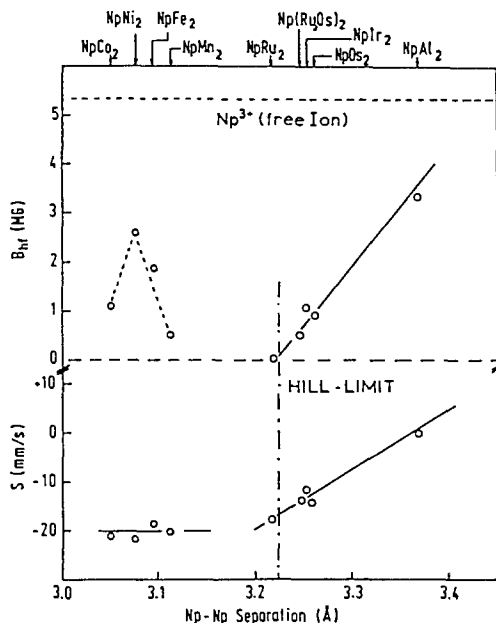


Fig. 36. Hyperfine fields and isomer shifts for cubic Laves phases  $NpX_2$  against the separation of neptunium ions. (1 MG = 100 T). The lattice constant is  $a = 2.31d_{Np}$ . [Taken from Kalvius et al. (1992).]

methods (see Fournier and Troč 1985). The information available on  $NpX_2$  materials crystallizing in other structures will only briefly be summarized subsequently.

#### 6.1.1. Cubic Laves phases $NpX_2$ and some related Ln compounds.

In fig. 36 the hyperfine field and the isomer shift are plotted for  $NpX_2$  cubic Laves phases as function of the neptunium-neptunium separation ( $d_{Np}$ ). Let us first consider materials where X is a nonmagnetic ligand (right-hand side of fig. 36). The behavior of  $B_{hf}$  shows clearly that these compounds are good examples for Hill behavior.  $NpRu_2$  lies below the Hill limit and, as expected, does not order magnetically.  $NpOs_2$  and  $NpIr_2$  are situated just above it and thus exhibit very low hyperfine fields (or ordered magnetic moments). The region exactly around the Hill limit has successfully been traced by the pseudo-binaries  $NpOs_{2-x}Ru_x$  (Aldred et al. 1975a). This means that the width of the bands containing the 5f electrons broadens continuously and at the Hill limit magnetic order simply vanishes on account of the Stoner criterion which, however, has to be somewhat redefined due to the strongly relativistic behavior of 5f electrons (Eriksson et al. 1989).

$NpAl_2$  with its fairly large Np-Np separation exhibits a substantial hyperfine field, but the free-ion limit is not reached. This somewhat surprising result has recently quantitatively been explained by a theoretical band structure calculation (Eriksson et al. 1990) taking into account a relativistic treatment of spin-orbit coupling and orbital polarization. All these basic findings are well corroborated by high-pressure measurements as discussed in section 5. The extreme itinerant 5f electron behavior of  $NpOs_2$  has been stressed. It is interesting to note that  $NpOs_2$  is so far the only

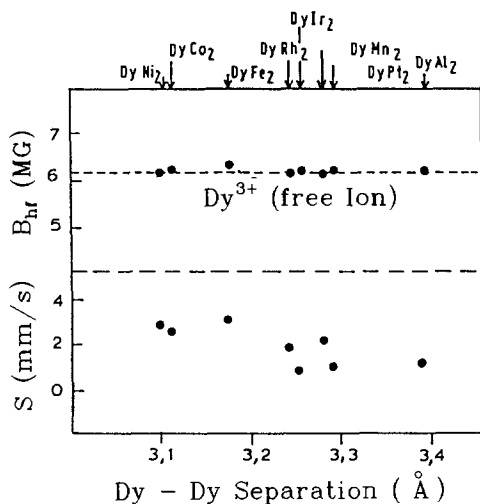


Fig. 37. Similar plot as fig. 36 for  $DyX_2$  cubic Laves-phase compounds. [Taken from Kalvius et al. (1992).]

magnetic Np intermetallic which falls slightly off the Dunlap–Lander relation (fig. 14). A possible mechanism has been discussed by Dunlap and Kalvius (1985).

As stated earlier, Hill behavior means that 5f–5f overlap is the decisive feature. Hence, one would not expect to find a similarly strong volume dependence of hyperfine parameters in a corresponding lanthanide series. This is evident in fig. 37, which shows a plot similar to that of fig. 36 for the  $DyX_2$  series. Here,  $B_{hr}$  is independent of the lattice constant and always equal to the free-ion value as is typical for localized behavior.

We turn now to the isomer shift. Its variation for  $NpX_2$  intermetallics ( $X = \text{non-magnetic}$ ) indicates a continuous change of electronic structure with lattice constant (or  $d_{Np}$ ). The slope  $\Delta S/\Delta d_{Np}$  on the right-hand side of fig. 36 is practically the same as the one found as a function of applied pressure in  $NpAl_2$ . In essence, the systematics of isomer shift supports the continuous change of f electron structure outlined just above. As expected, the Hill limit is not noticeable in the isomer shift. It does not constitute a break in electron structure.

The isomer shift within the  $DyX_2$  (fig. 37) series shows little variation, and one concludes that the electronic configuration of  $Dy^{3+}$  is not affected by volume changes. In summary, these data are the most illustrative example of the fundamental differences between heavy lanthanide (mostly localized) and light actinide (often itinerant) electronic properties.

The straightforward Hill behavior in  $NpX_2$  Laves phases is lost, however, when 3d electrons of the ligands are involved. As the left-hand side of fig. 36 demonstrates, the compounds  $NpMn_2$ ,  $NpFe_2$ ,  $NpNi_2$  and  $NpCo_2$  do not follow the same trend as the materials discussed above. The isomer shift now shows little variation and gives evidence that the strong coupling of electronic structure to atomic volume is lost. The compounds order magnetically, although their Np–Np separation is well below the Hill limit. Hyperfine fields vary substantially but no correlation to the lattice parameter is evident. There might still be a small underlying volume effect: Mössbauer

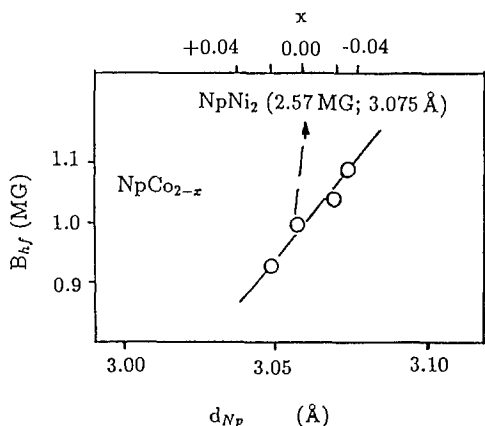


Fig. 38. Hyperfine field against Np separation for  $NpCo_{2-x}$  compounds. [Taken from Kalvius et al. (1992).]

studies on  $NpCo_{2-x}$  where the variation in stoichiometry is coupled to changes in lattice constant (Kalvius et al. 1985) showed a systematic variation of  $B_{hf}$  (fig. 38) with Np–Np separation. Yet, its slope is considerably less than that of the connecting line between  $B_{hf}(NpCo_2)$  and  $B_{hf}(NpNi_2)$  in fig. 36 and also about a factor of four smaller than that between  $NpOs_2$  and  $NpAl_2$ . Hence the dominating influence on electronic structure properties does not arise from volume effects here. Most probably, hybridization of 5f with 3d electrons is essential.

At first sight, one is tempted to argue that the magnetism of the 3d ligand pulls the neptunium into magnetic order. This view has problems. Although there is a sizeable moment on Fe ( $\sim 1.1\mu_B$ ) in  $NpFe_2$ , the moment on Ni in  $NpNi_2$  is very small ( $\leq 0.3\mu_B$ ), yet this compound exhibits the largest hyperfine field. In  $NpCo_2$ , the moment on Co is minute ( $0.06\mu_B$ ). Obviously, no correlation between the Np hyperfine field and the magnetism of the 3d ligand can be established. However, the proper trend exists for the magnetic transition temperatures ( $NpFe_2$ :  $T_C = 492$  K;  $NpNi_2$ :  $T_C = 32$  K;  $NpCo_2$ :  $T_N = 15$  K).

The Mössbauer spectra of the ferro- or antiferromagnetic  $NpX_2$  Laves phase compounds show hyperfine spectra which can be fitted with a single hyperfine field, i.e. all Np ions carry the same moment. Some line broadening, especially just below the magnetic ordering temperature is evident in nearly all samples. The reasons are most likely relaxation phenomena as discussed in section 2.3.2. The observed spectra (Gal et al. 1973b) could well be fitted with the model of ferromagnetic relaxation by Wegener (1965).

The trouble child is  $NpCo_2$ . Mössbauer data point rather strongly towards a magnetic ordering transition around 13 K. Resonance lines are wide and stay significantly above the typical effective width even at temperatures as low as 1.5 K (Sanchez et al. 1992). Neutron diffraction on a single-crystalline sample (Sanchez et al. 1992) could not detect Bragg peaks in zero field for  $T < 13$  K. One might suspect short-range (spin-glass type) order, but Mössbauer spectra taken in external field as well as magnetization measurements argue against it. As far as one can tell, the line broadenings are dynamic in origin, rather than due to a static distribution of hyperfine



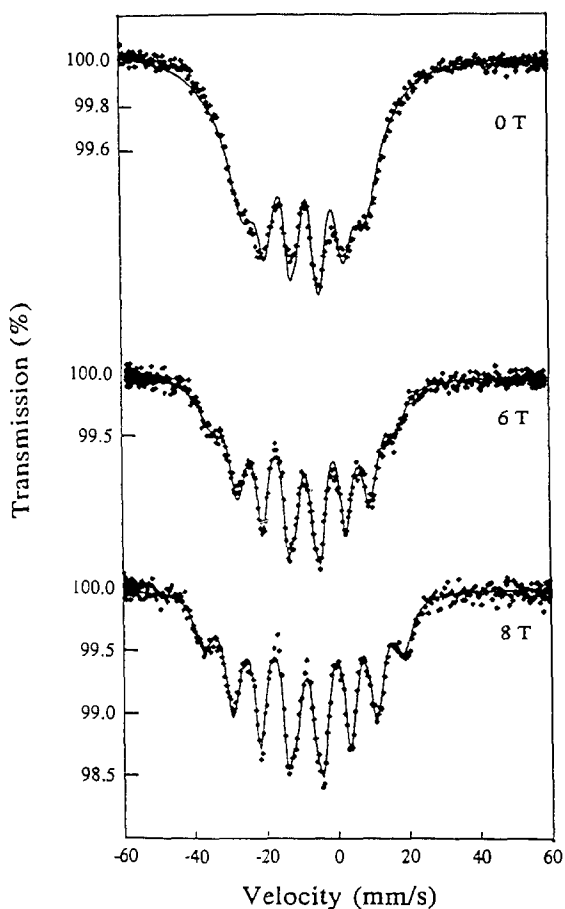


Fig. 39. Mössbauer spectra of  $\text{NpCo}_2$  at 4.2 K as a function of external field applied parallel to the  $\gamma$ -ray direction. The fits were carried out using the magnetic relaxation model of Wegener. [Taken from Sanchez et al. (1992).]

fields on account of a fairly randomized spin order. A fit evoking the relaxation formalism of Wegener (1965) gives consistent results over all temperatures. Spectra taken in applied field (see fig. 39) show a reduction in line broadening. This is consistent also with the assumption of magnetic moment fluctuations as the source of non-Lorentzian and broadened resonance lines. It is quite possible that the nonvanishing magnetic fluctuations at lowest temperatures are an intrinsic property of highly hybridized magnetic materials (Gal et al. 1973a, b). From the hyperfine field data an ordered magnetic moment on Np of  $0.47\mu_B$  is deduced. For  $B > 5$  T the field-induced ferromagnetic state is reached, but saturation could not be achieved even at 8 T. The contrast between Mössbauer and neutron diffraction data remains unsolved at this point and no definite conclusion as to the ground state of  $\text{NpCo}_2$  is possible. Before ending this subsection we briefly mention that  $^{57}\text{Fe}$  Mössbauer spectroscopy has been carried out on  $\text{AnFe}_2$  intermetallics ( $\text{An} = \text{U}, \text{Np}, \text{Pu}, \text{Am}$ ) by Gal et al. (1970) and Lander et al. (1977). A steady increase of  $B_{\text{hf}}$  at the Fe nucleus is observed as

one moves across the actinide series. This is likely due to a decrease in hybridization between 5f and 3d electrons as actinide contraction occurs.

Ruby et al. (1969) have studied  $UFe_2$  with the  $^{238}\text{U}$  resonance. No magnetic hyperfine splitting could be resolved, in agreement with the very small moment of  $0.06\mu_B$  on the U atom obtained by neutron diffraction (Wulff et al. 1989). Data on  $^{243}\text{Am}$  in  $AmFe_2$  by Lander et al. (1977) showed some increase in linewidth below the magnetic transition temperature. This result is consistent with the moment of  $0.4\mu_B$  on Am detected by neutrons. For a fully localized  $Am^{3+}(5f^6:7F_0)$  configuration the magnetic moment vanishes. Strong hybridization must be present. In this case one expects  $\mu_L/\mu_s < 1$  and the moment should be antiparallel to the iron moment (Lander et al. 1991). This was confirmed by neutron scattering. The  $AmX_2$  compounds formed with nonmagnetic ligands do not show the presence of a magnetic hyperfine field in their Mössbauer spectra, indicating a nearly pure  $Am^{3+}$  configuration. Their isomer shifts exhibit the same basic trend as the  $NpX_2$  series. These results emphasize once more the special situation when 3d electrons of ligands have to be considered.

### 6.1.2. Other $NpX_2$ compounds

$NpSi_2$  and  $NpGe_2$  have noncubic structures. They order ferromagnetically.  $NpSi_2$  shows a rather small hyperfine field (corresponding to a moment of  $\sim 1.1\mu_B$ ). In contrast  $NpGa_2$  exhibits the free-ion hyperfine field of  $Np^{3+}$ , the charge state which the isomer shift would suggest. This points strongly towards 5f localization. But one should then expect that also the magnetically induced free-ion field gradient to be present, which curiously is not the case. Tetragonal  $NpAs_2$  undergoes a transition at 52 K into an incommensurate antiferromagnetic state, followed by a first-order transition at 18 K into ferromagnetism. The isomer shift allows a tetravalent configuration. The substantial reduction in  $B_{hf}$  from the free-ion hyperfine field is probably due to crystalline field interactions. Little systematics can be extracted from the  $NpX_2$  ( $X = As, Sb, Te$ ) compounds. Both  $NpSb_2$  and  $NpTe_2$  appear to possess the  $Np^{3+}$  ion on account of their isomer shift. While  $NpSb_2$  is ferromagnetic with a substantial moment remains  $NpTe_2$  paramagnetic down to 4.2 K. More detailed studies are needed.

### 6.2. Compounds with the NaCl structure

In more detail we shall look at the mono-chalcogenides and mono-pnictides of Np. Their hyperfine parameters are summarized in table 7. The materials are conducting and most of them order magnetically, often in rather complex antiferromagnetic structures (Burlet et al. 1986, Lander 1993). The Mössbauer hyperfine spectra reflect such complexities, but in themselves cannot definitely give an answer as to which spatial spin arrangement is present. We will return to this latter point briefly further below.

Although  $d_{Np}$  in the  $NpX$  series is well above the Hill limit, the expected simple localized lanthanide-like f electron structure is not observed as was already pointed out on occasion of the high-pressure data for  $NpAs$ . If lanthanide-like behavior were present no correlation between hyperfine parameters and lattice constant and/or

TABLE 7

Magnetic and electronic properties of NpX intermetallic systems [F = ferromagnet, AF = antiferromagnet, CAF = complex antiferromagnet (e.g. modulated structure); SRO = short-range order; a) ordered moment derived from a Mössbauer or neutron measurements; b) Saturation moment from magnetization.

Compound	Crystal structure	Lattice parameter (Å)	Type of magnetic order	$T_N, T_C$ (K)	$\mu_{ord}$ ( $\mu_B$ )	$\mu_{eff}$ ( $\mu_B$ )	$S^b$ (mm/s)	$B_{hyp}$ (T)	$eq$ ( $10^{18}V/cm^2$ )	Ref. <sup>a</sup>
NpN	NaCl	4.898	F	82	a) 1.4 b) 0.9	2.01	-6.0	306	0.22	[1]
NpP	NaCl	5.615	CAF	130 24	a) 1.8/2.3 b) 2.3	2.8	7.0	471 413	-0.70 -0.60	[1, 2]
NpAs	NaCl	5.838	CAF	173	a) 2.5 b) 2.3	3.0	16.0	538	-1.71	[1, 3]
NpSb	NaCl	6.254	AF	207	a) 2.25	2.3	20.0	534	-1.46	[1]
NpBi	NaCl	6.4	AF	192	a) 2.6	-	25.1	565	-1.54	[4]
NpS	NaCl	5.527	AF	23	a) 0.9	1.49	18.0	197	-1.4	[5, 6]
NpSe	NaCl	5.8	CAF	38	a) ~ 1.4	1.95	24.5	~ 300	-0.3	[7]
NpTe	NaCl	6.1	SRO	-30	a) ~ 2	2.3	28.5	~ 440	0.65	[8]
								(broad distribution)		
NpC	NaCl	5.005	AF/F	~ 310/ ~ 225	b) 0.9 a) 2.25 b) 1.4	3.2	-18.0	490	~ 0	[9-11]

<sup>a</sup>References: [1] Aldred et al. (1974a); [2] Lander et al. (1973); [3] Potzel et al. (1989); [4] Sanchez et al. (1991); [5] Lam et al. (1974); [6] Burlet et al. (1992); [7] Bogé et al. (1988); [8] Burlet et al. (1990) [9] Lam et al. (1971); [10] Dunlap and Kalvius (1985); [11] Stone and Pillings (1967).

<sup>b</sup>Relative to NpAl<sub>2</sub>.

chemical nature of ligands should exist, as was the case for DyX<sub>2</sub> Laves phase compounds (fig. 37). As fig. 40 clearly shows the opposite situation prevails. The chemical influence shows up in the clear separation of trends in isomer shift and hyperfine field between the pnictides and the chalcogenides. But each series taken by itself follows a straight volume dependence. In the pnictide series, the hyperfine field reaches at NpAs the free-ion limit. Consequently, it does not significantly change when going to the even wider spaced NpSb and NpBi. In accordance with the high-pressure study on NpAs it is concluded that in this compound, and also in NpP, a noticeable, but not large, deviation from purely localized behavior is present on account of hybridization with ligand p electrons, which leads to fairly narrow 5f bands.

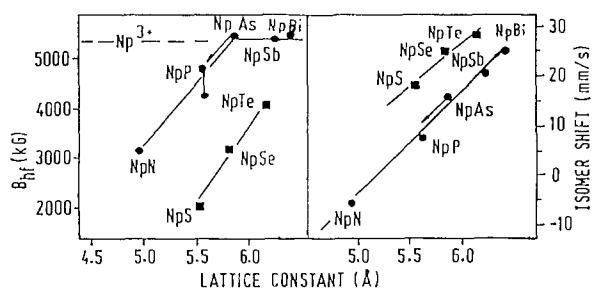


Fig. 40. Dependence of hyperfine field (left) and isomer shift (right) on lattice constant for Np mono-pnictides (circles) and mono-chalcogenides (squares).  $d_{Np} = 0.707a$ . The dashed line is the Np<sup>3+</sup> free-ion field. The arrow shows the change in hyperfine parameters of NpAs under 8.3 GPa applied pressure. [Taken from Kalvius et al. (1992).]

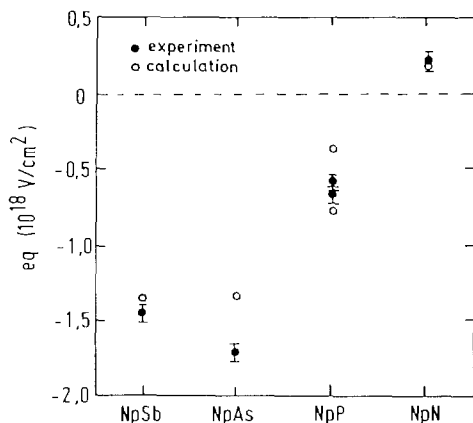


Fig. 41. Comparison of measured ionic electric field gradient on Np monopnictides with calculated values. [Taken from Dunlap and Kalvius (1985).]

The chalcogenides show systematically lower hyperfine fields and one notices that NpTe with an Np–Np spacing about that of NpSb has not reached the free-ion field by a substantial margin. Hybridization in the chalcogenides must be much stronger, causing a larger width of the bands containing 5f electrons.

Looking at the behavior of the isomer shift, the same general trends are manifested but no break in the linear correlation of shift with volume is observed between NpAs and NpSb. In contrast to the behavior of the hyperfine field, the isomer shift in none of the materials reach the theoretical free-ion  $\text{Np}^{3+}$  value, stressing the lingering influence of ligand electrons within the whole series. The systematic difference in isomer shift between the pnictides and the chalcogenides corresponds to a higher covalency of the latter in accordance with the behavior of the hyperfine field.

In the NpX series the magnetically induced quadrupole interaction is clearly present in all cases, quite in contrast to the  $\text{NpX}_2$  compounds, especially the Laves phases. This underlines once more the fairly ionic (narrow band) 5f electron structure in the pnictides and chalcogenides. The free-ion field gradient is only seen for NpBi and nearly so for NpSb. The variation in electric field gradient in the mono-pnictides could be well explained by extracting an effective  $J$  from the hyperfine field and using this to calculate  $q_{\text{ion}}$  (Dunlap and Kalvius 1985) as discussed in section 2.5. The good agreement between experiment and theory is demonstrated in fig. 41.

Mössbauer data on the analogous DyX data are available for the pnictides DyP, DyAs and DySb (Gorobchenko et al. 1971). Isomer shifts are not given. A small variation in  $B_{\text{hf}}$  is seen. DySb has the free-ion field, in DyAs the field is 4% and in DyP about 5% lower. The authors discuss the variations of  $B_{\text{hf}}$  in terms of crystalline field interaction. While the trend of  $B_{\text{hf}}$  in the Dy mono-pnictides is similar to that in the Np mono-pnictides (i.e., the phosphide being lower) the change in  $B_{\text{hf}}$  between NpSb and NpP is much larger ( $\sim 15\%$ ). A small influence of crystalline electric field cannot be excluded for the NpX compounds, but hybridization with ligand electrons dominates.

We turn now to the magnetic structure. NpN is a ferromagnet, neutron and Mössbauer data are in agreement. NpP exhibits an incommensurate modulated

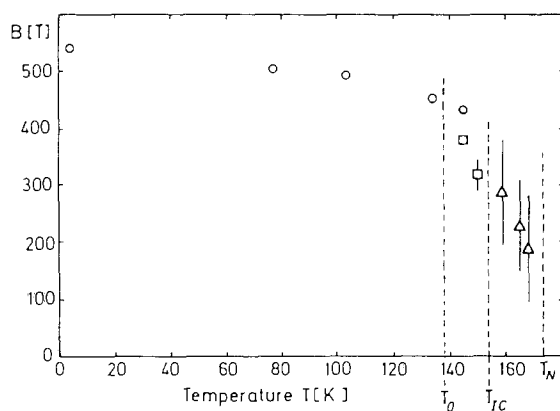


Fig. 42. Temperature dependence of the hyperfine field in NpAs. The various magnetic transitions are explained in text. [Taken from Kalvius (1989).]

structure beginning at 130 K which then turns into a commensurate, nearly squared up, modulated structure. The Mössbauer spectrum shows two distinct hyperfine fields. Their relative intensities together with neutron powder diffraction data made possible to establish the spin structure just mentioned (Lander et al. 1973).

The rather complex magnetic phase diagram of *NpAs* has already been introduced [see fig. 26 and also Jones et al. (1991)]. In fig. 42 the temperature variation of the hyperfine field is shown (Potzel et al. 1989, Kalvius 1989). The sudden drop in  $B_{\text{hf}}$  by 10% when going from the noncollinear  $\uparrow\downarrow$  to the collinear  $4\uparrow 4\downarrow$  structure around 138 K has been pointed out earlier. Neutron diffraction sees the corresponding discontinuity in the ordered Np moment (Burlet et al. 1986). In the regime of the incommensurately modulated structure between 153 K and  $T_N$ , the Mössbauer hyperfine spectra show broad lines resulting from a distribution of hyperfine fields. Figure 42 displays the maximum field, but the uncertainty is substantial. Nevertheless a typical magnetization curve seems to be followed.

*NpSb* possesses the type-I ( $3k$ ) antiferromagnetic order and shows a clean magnetic hyperfine spectrum (Sanchez et al. 1988a). The same is true for *NpBi* (Burlet et al. 1992, Sanchez et al. 1991). Sanchez et al. (1990) also studied solid solutions  $NpSb_{1-x}Te_x$  for  $x$  up to 0.25 combining Mössbauer measurements with the  $^{237}\text{Np}$ ,  $^{121}\text{Sb}$  and  $^{125}\text{Te}$  resonances. The data (especially with respect to the transferred hyperfine fields on Te and Sb at 4.2 K) suggest that the magnetic structure changes from type-I to type-IA or ferrimagnetic ( $\uparrow\uparrow\downarrow$ ) at  $x = 0.05$ . Neutron experiments performed shortly after showed ferromagnetic order below  $T_C = 143$  K and a non-collinear ferrimagnetic structure below  $T_0 = 90$  K. This transition was also detected in the transferred field at the Te site (Bouillet et al. 1992). Increasing the Te content from  $x = 0.05$  to  $x = 0.25$  reduces the ordered moment on Np smoothly from 570 to 530 T.

The mono-chalcogenide NpS undergoes an antiferromagnetic transition near 23 K. Mössbauer spectra in the range from 23 to 20 K (Bogé et al. 1988) consist of a superposition of a magnetically split and a single-line pattern, indicating a first-order transition. This was also seen by neutron diffraction. Even at lower temperatures a single-site magnetic pattern gave only a poor fit to the data. A distribution of hyperfine

field is clearly present. The average hyperfine field leads to an ordered moment around  $0.9\mu_B$ . Neutron diffraction could not yet fully unravel the spin structure but a type-II double- $k$  sequence seems the most probable (Blaise et al. 1992).

The Mössbauer spectra of  $NpSe$  below  $T_N \approx 38$  K exhibit a fairly broad distribution of hyperfine fields pointing towards an incommensurate spin structure. The field distribution clearly changes shape with temperature meaning that details of the spin modulation are also temperature dependent. The spectral shape near  $T_N$  indicates a first-order phase transition. A positive determination of spin structure by neutron diffraction is still outstanding (Blaise et al. 1992). At low temperatures type-II multi- $k$  order seems to be indicated, but this does not explain the distribution in hyperfine fields which still prevails at 4.2 K in the Mössbauer spectrum.

The situation in  $NpTe$  is equally unsatisfactory. A maximum in susceptibility at  $T = 30$  K was interpreted as the Néel point, but no resolved magnetic hyperfine pattern could be observed in this temperature range. At 4.2 K hyperfine splitting is seen but with a very broad distribution of hyperfine fields. Neutron diffraction on a single crystal failed to detect any magnetic Bragg reflection even at lowest temperatures. It was concluded (Burlet et al. 1990) that no long-range order develops but only strong enough short-range correlations to bring spin relaxation times sufficiently far down to allow the observation of hyperfine splitting in a Mössbauer experiment. Recently, P. Burlet (private communication) found type-II order at  $\sim 30$  K in a newly prepared crystal of  $NpTe$ . The ordered moment derived is  $1.3\mu_B$  while the average Mössbauer hyperfine field corresponds to  $\mu_{Np} \approx 2\mu_B$ . A straightforward type-II structure is incompatible with the above-mentioned broad distribution of hyperfine fields. Furthermore, Sanchez et al. found in Mössbauer measurements with the  $^{125}Te$  resonance a transferred hyperfine field of roughly 4 T at the Te nuclei. For symmetry reasons the transferred field should vanish in a type-II spin arrangement. At present, neutron and Mössbauer data are incompatible for  $NpTe$ . Nonstoichiometry may play an important role. The situation also highlights the importance to perform *all* types of measurements on the *same* sample, especially when actinides are concerned.

In conclusion, the magnetic behavior of Np mono-chalcogenides and -pnictides is far from understood. Even the corresponding U compounds which have been explored and characterized rather thoroughly are not understood in all details.

The magnetic hyperfine spectra of Dy mono-pnictides are also curious. For example,  $DyAs$  and  $DyP$  are considered ferrimagnets with a HoP-type structure and moments considerably below the free-ion value. In contrast, the Mössbauer spectra exhibit a single hyperfine pattern only with a saturation field rather close to the free-ion value. This point also urgently needs clarification in the future.

We briefly mention the studies on U mono-pnictides using the  $^{238}U$  resonance by Shenoy et al. (1970a, 1972). The plot of hyperfine field against uranium magnetic moment is shown in fig. 43. Independent of the assignment of U charge state ( $U^{3+}$  or  $U^{4+}$  – isomer shifts can not be resolved by the  $^{238}U$  resonance!), the perfect proportionality (Dunlap–Lander plot) between field and moment present in Np compounds (see fig. 14) is not observed. Possible causes for this difference have been discussed by Dunlap and Kalvius (1985).

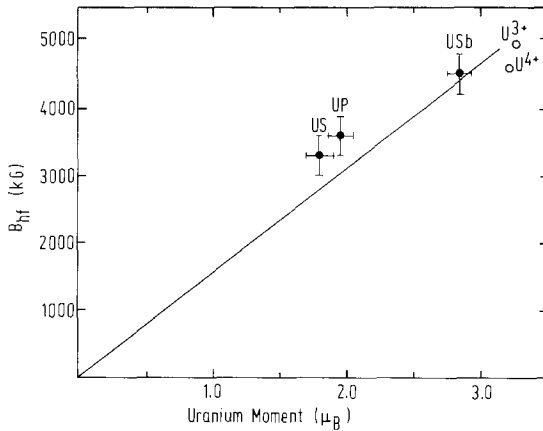


Fig. 43. Uranium hyperfine fields against uranium ordered moment.  $U^{3+}$  and  $U^{4+}$  represent the free-ion fields. The line corresponds to the Dunlap–Lander relation (see fig. 14 for the case of Np). [Taken from Dunlap and Kalvius (1985).]

Finally, a measurement using  $^{243}\text{PuSb}$  as the source for the  $^{243}\text{Am}$  resonance has been reported (Sanchez et al. 1986). A hyperfine field of 37 T on the Am was found. It was interpreted as a transferred field under the assumption that the Am is in the pure nonmagnetic trivalent state. This is supported by the fact, that the field is not largely different from the transferred field (22 T) at the Sb ion (Sanchez et al. 1985).

### 6.3. Compounds with the $\text{AuCu}_3$ structure

Only Np containing materials will be discussed. Table 8 summarizes the parameters of interest for  $\text{NpX}_3$  compounds including some which do not have the  $\text{AuCu}_3$

TABLE 8

Magnetic and electronic properties of  $\text{NpX}_3$  intermetallic systems (explanation of symbols see table 7).

Compound	Crystal structure	Lattice parameter (Å)	Type	$T_N$ $T_C$ (K)	$\mu_{\text{ord}}$ ( $\mu_B$ )	$\mu_{\text{eff}}$ ( $\mu_B$ )	$S^b$ (mm/s)	$B_{\text{hyp}}$ (T)	$eg$ ( $10^{18}$ V/cm $^2$ )	Ref. <sup>a</sup>
$\text{NpSi}_3$	$\text{AuCu}_3$	4.003	P				0	~0	~0	[1]
$\text{NpAl}_3$	$\text{AuCu}_3$	4.266	F	62	a) 1.2	2.5	2	294	~0	[1, 2]
$\text{NpGa}_3$	$\text{AuCu}_3$	4.243	(F)		a) 1.5	2.0	6	340	~0	[1]
$\text{NpGe}_3$	$\text{AuCu}_3$	4.212	P				7.6		~0	[1]
$\text{NpSn}_3$	$\text{AuCu}_3$	4.627	AF	9.5	a) 0.28 b) 0.5?	1.6	18	60	~0	[3–5]
$\text{NpIn}_3$	$\text{AuCu}_3$	4.619	CAF Modulated	16.5	a) 1.5 b) 0.8	2.1	19.5	287	~0	[1]
$\text{NpPd}_3$	$\text{AuCu}_3$	4.095	AF	55	a) 1.9	2.7	–22	421	~0	[6, 7]
$\text{NpPd}_3$	$\text{HexTiNi}_3$	$a = 5.767$ $c = 9.544$	SRO			2.8	–22			[7]
$\text{NpPt}_3$	$\text{MgCd}_3$	$a = 5.764$ $c = 4.990$	AF	22	a) 1.99	2.9	–21	440	~0	[8]
$\text{NpRh}_3$	$\text{AuCu}_3$	4.007	P			3.6	–31		~0	[6]

<sup>a</sup>References: [1] Gal et al. (1992); [2] Aldred et al. (1974b); [3] Kalvius et al. (1990); [4] Trainor et al. (1976); [5] Gal et al. (1973a); [6] Gal et al. (1976); [7] Nellis et al. (1974); [8] Gal, unpublished.

<sup>b</sup>Relative to  $\text{NpAl}_2$ .

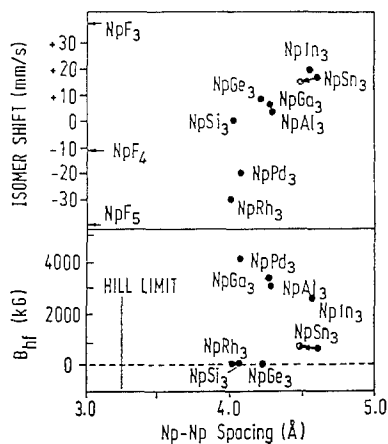


Fig. 44. Hyperfine fields (bottom) and isomer shift (top) for Np intermetallics with the  $\text{AuCu}_3$  structures against Np separation (equal to lattice constant). The arrows indicate the change of parameters for  $\text{NpSn}_3$  under 6 GPa applied pressure. [Taken from Kalvius et al. (1992).]

structure. Figure 44 shows that no clear dependence of isomer shift on Np–Np separation exists for the  $\text{AuCu}_3$  series. The range of shifts, however, is very large: It extends from the value for ionic  $\text{Np}^{5+}$  compounds to that of  $\text{Np}^{3+}$  compounds. Thus, the electron configurations must vary substantially. One can discern a certain clustering for d electron ligands ( $\text{NpRh}_3$ ,  $\text{NpPd}_3$ ) at more negative shifts and p electron ligands ( $\text{NpSi}_3$  to  $\text{NpSn}_3$ ) at more positive shifts. Also within the p ligands, the higher the principal quantum number (2p, 3p, 4p), the more positive the shift.

For the hyperfine field, it is even more difficult to extract any systematic behavior. However, a certain influence of chemical properties of the ligand can again be extracted. The group-IV ligands (Si, Ge, Sn) produce nonmagnetic or weakly magnetic compounds. Group-III ligands (Al, Ga, In) cause comparatively strong magnetism. The group-VIII ligands (Pd, Rh) show no clear-cut behavior, but it must be remembered that especially in  $\text{NpPd}_3$  the  $\text{AuCu}_3$  structure is unstable. This material crystallizes also in the hexagonal  $\text{TiNi}_3$  structure and then exhibits a quite different magnetic behavior. The cubic form is an antiferromagnet with  $T_N = 55$  K and a fairly substantial ordered moment on Np. For the hexagonal form neutrons could not detect long-range order. Its Mössbauer spectrum is diffuse and compatible with only short-range order. The surprising feature is that in both crystallographic forms, the first two nearest-neighbor configurations are very similar. Significant changes occur only in the third nearest-neighbor shell. It is not understood why this causes such a marked difference in magnetic properties. The isomer shift of both structures is the same, indicating that a marked change in electronic structure does not occur.

Another compound with surprising magnetic properties is  $\text{NpSn}_3$  as has been discussed in the preceding section. At ambient pressure the most prominent feature is the rather small ordered moment on Np ( $\sim 0.3\mu_B$ ).  $\text{NpIn}_3$  which differs by only one 5p electron behaves quite differently. As expected, the additional p electron will not affect  $\rho(0)$  significantly and the isomer shifts of  $\text{NpSn}_3$  and  $\text{NpIn}_3$  are quite alike. But  $\text{NpIn}_3$  has a higher magnetic ordering temperature (17 K). The magnetic hyperfine spectrum is an overlay of several subspectra with different hyperfine fields.



This indicates a modulated spin structure. The maximum  $B_{\text{hf}}$  is around 300 T corresponding to a moment of  $1.5 \mu_{\text{B}}$  quite in contrast to the low moment of  $\text{NpSn}_3$ . From high-pressure data it was concluded that  $\text{NpSn}_3$  is a Kondo lattice system. Kondo behavior may also be present in  $\text{NpIn}_3$  as suggested by recent resistivity data (Gal et al. 1992).

In summary, the magnetic properties range from temperature-independent paramagnetism to antiferromagnetism with modulated spin structure. Although the ordered magnetic moments for  $\text{NpAl}_3$ ,  $\text{NpGa}_3$  and  $\text{NpIn}_3$  are close to the value ( $\sim 1.5 \mu_{\text{B}}$ ) calculated within a localized crystalline electric field (CEF) model for a  $^5I_4$  ( $5f^4$ ) ground state of  $\text{Np}^{3+}$ , the situation is far more complex. The often nearly full suppression of magnetic moment cannot be explained by CEF interaction alone. It rather has to be considered as being mainly the result of anisotropic hybridization of  $5f$  electrons with  $s$  and  $p$  band electrons, as already discussed for the case of  $\text{NpSn}_3$ . The induced electric field gradient is small, if present at all (see table 8). This is also in agreement with a localized CEF model suggesting a  $\Gamma_5$  ground state.

#### 6.4. *Np charge state in cubic intermetallics*

The assignment of a charge state to Np in intermetallic compounds from magnetic data alone is unreliable since the two most likely states  $\text{Np}^{3+}$  and  $\text{Np}^{4+}$  have rather similar free-ion fields (or moments) as demonstrated in table 2. Similarly, the magnetic form factor which can be derived by neutron scattering is not significantly different. Mössbauer spectroscopy offers additional information via the isomer shift. But, isomer shift data alone are also of limited use since the contribution of conduction electrons to  $\rho(0)$  is difficult to estimate. But as has been shown in fig. 13 the presence of conduction electrons will always increase  $\rho(0)$ . For Np this means that the shift of a metallic compound will always be more negative when compared to a nonconducting material containing Np in the same ionic form. The most reliable clue comes from a plot of hyperfine field versus isomer shift as given in fig. 45 for the cubic intermetallics

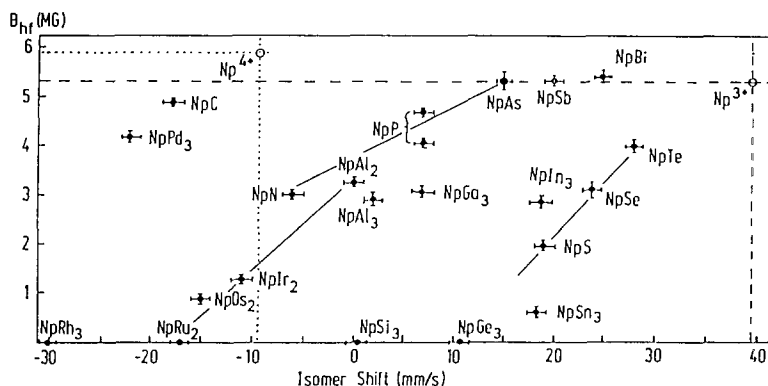


Fig. 45. Correlation between hyperfine field and isomer shift for cubic Np intermetallics. The dashed line corresponds to the  $\text{Np}^{3+}$ , the dotted line to the  $\text{Np}^{4+}$  free-ion values. [Taken from Kalvius et al. (1992).]

of Np. The region to the right of  $-9$  mm/s (the isomer shift of fully ionic  $\text{Np}^{4+}$ ) can only be occupied by compounds containing trivalent neptunium. The mono-chalcogenides and mono-pnictides fall into this region and hence are trivalent, including NpN which comes close to the border line. In contrast, NpC, which also has a rocksalt structure, should be tetravalent. A similar conclusion was reached from various magnetic data.

The  $\text{NpX}_2$  series starts out with  $\text{NpAl}_2$  in the trivalent region and then crosses over into the tetravalent region. We, however, consider all  $\text{NpX}_2$  ( $X =$  nonmagnetic) compounds trivalent since there is no break in the smooth dependence of  $B_{\text{hf}}$  versus isomer shift between  $\text{NpAl}_2$  on the one side and  $\text{NpIr}_2$ ,  $\text{NpOs}_2$  and  $\text{NpRu}_2$  on the other. The situation is less clear for the compounds with 3d ligands. They could be tetravalent since the systematic behavior invoked above is not given and – as discussed earlier – the electronic structure must be different in comparison with the other  $\text{NpX}_2$  members. One other hint for a tetravalent charge state is the occurrence of strong ferromagnetic relaxation in  $\text{NpCo}_2$ . Such effects are predominant in a Kramers ion with high angular momentum like  $\text{Np}^{4+}:^4\text{I}_{9/2}$ .

Also in  $\text{AuCu}_3$  materials, it might well be possible that the p ligands lead to a trivalent and the d ligands to a tetravalent configuration. Perhaps this is the reason for the instability of the  $\text{AuCu}_3$  structure in the latter compounds. In any case, one should be aware that the notion of a definable charge state is somewhat dubious in strongly hybridized systems.

### 6.5. Compounds with the $\text{ThCr}_2\text{Si}_2$ structure

These are materials of the type  $\text{NpM}_2\text{Si}_2$  and  $\text{NpM}_2\text{Ge}_2$ , where M is a d transition element. The crystal structure is tetragonal (space group 4I/mmm). The actinide/lanthanide ions occupy a single crystallographic site. Hyperfine parameters of the Np intermetallics are listed in table 9. Attempts to correlate either  $B_{\text{hf}}$  or the isomer shift to typical lattice quantities such as  $a$ ,  $c$ , or  $c/a$  failed. Neither can a systematic difference between Si and Ge compounds be extracted. The most informative clue as to their electronic structure can be drawn from a plot of hyperfine field versus isomer shift (fig. 46). In accordance with the discussion of the foregoing subsection one concludes that all  $\text{NpM}_2\text{Si}_2$  and  $\text{NpM}_2\text{Ge}_2$  compounds contain the trivalent Np ion. It is further likely that they all have a fairly localized 5f electron structure. This was unambiguously shown for one member of the series ( $\text{NpCo}_2\text{Si}_2$ ) by high-pressure Mössbauer spectroscopy (see section 5.4.2). Roughly, the hyperfine fields of most of the compounds lie in the vicinity of 350 T. One of the possible crystalline field levels of the  $^5\text{I}_4$  Hund's rule ground state of  $\text{Np}^{3+}$  in tetragonal symmetry is the magnetic doublet  $\Gamma_5^t$ . It mainly contains the  $|\pm 3\rangle$  wave function and thus produces a hyperfine field around 380 T. We believe that it is the crystalline field interaction on a fairly localized  $\text{Np}^{3+}$  ion which is responsible in first order for the hyperfine fields in the majority of the  $\text{ThCr}_2\text{Si}_2$ -type compounds.

The corresponding lanthanide compounds have thoroughly been investigated by various methods. The most detailed Mössbauer studies exist for the  $\text{GdM}_2\text{Si}_2$  series with M being a 3d, 4d or 5d transition element (Czjzek et al. 1989, Dirken et al. 1989).

TABLE 9

Lattice parameters, magnetic ordering temperatures and  $^{237}\text{Np}$  hyperfine parameters of Np intermetallics with the  $\text{ThCr}_2\text{Si}_2$  (I4/mmm) structure.

Compound	$a$ (Å)	$c$ (Å)	$T_N$ (K)	$B_{\text{hf}}^a$ (kG)	$e^2qQ^b$ (MHz)	$S^c$ (mm/s)	Ref <sup>d</sup>
$\text{NpCo}_2\text{Ge}_2$	3.800	9.556	36	3220	15/0	+7.7	[1] <sup>e</sup>
$\text{NpCr}_2\text{Si}_2$	3.863	9.367	73	2950	-370/1240	+1.8	[2] <sup>e</sup>
$\text{NpFe}_2\text{Si}_2$	3.869	9.962	87	3300	-1650/1650	-2.3	[2]
$\text{NpCo}_2\text{Si}_2$	3.877	9.732	42	2800	+400/0	-1.2	[2, 3]
$\text{NpCu}_2\text{Ge}_2$	3.888	9.418	34	3050	?/1150	+20.0	[1] <sup>e</sup>
$\text{NpMn}_2\text{Si}_2$	3.895	9.538	> 300( $T_C$ )	2410	-360/?	-1.4	[2] <sup>e</sup>
$\text{NpNi}_2\text{Ge}_2$	3.903	9.556	27	3410	+1330/1060	+8.6	[1] <sup>e</sup>
$\text{NpCr}_2\text{Ge}_2$	3.909	9.470	62	3900	-460/1250	+7.8	[1] <sup>e</sup>
$\text{NpFe}_2\text{Ge}_2$	3.918	9.403	28	2360	-1340/1440	+7.1	[1] <sup>e</sup>
$\text{NpCu}_2\text{Si}_2$	3.922	9.411	34	4460	-1000/1200	+14.7	[2] <sup>e</sup>
$\text{NpNi}_2\text{Si}_2$	3.935	9.466	33	2610	0/0	+1.4	[2] <sup>e</sup>
$\text{NpRh}_2\text{Si}_2$	4.010	10.022	73	~3000 <sup>d</sup>	+580/1050	+5.0	[4]
$\text{NpMn}_2\text{Ge}_2$	4.011	10.815	> 300( $T_C$ )	3100	-900/?	+10.0	[5, 6]
$\text{NpPd}_2\text{Si}_2$	4.113	10.045	59	3960 <sup>e</sup>	-600/~250	+11.0	[6]
				3660	-370/~250	+9.2	
$\text{NpRh}_2\text{Ge}_2$	4.127	10.103	?	5050 <sup>e</sup>	-125/?	+16.2	[6]
				4700	-90/?	+16.2	
$\text{NpRu}_2\text{Si}_2$	4.129	9.586	28	~3000 <sup>d</sup>	+3000/?	+0.5	[7]

<sup>a</sup> Typical error:  $\pm 50$  kG.

<sup>b</sup> The first number refers to  $T < T_N$ , the second to  $T > T_N$ . Typical error:  $\pm 10$  MHz. Sign can only be determined for  $T < T_N$ .

<sup>c</sup> Typical error:  $\pm 0.5$  mm/s.  $S$  is given relative to  $\text{NpAl}_2$ .

<sup>d</sup> Multiple magnetic sites (incommensurate modulated antiferromagnet).

<sup>e</sup> Two magnetic sites.

<sup>f</sup> References: [1] Gal et al. (1976); [2] Gal et al. (1977); [3] Potzel et al. (1981); [4] Sanchez et al. (1988b); [5] Schäfer et al. (1987); [6] Wastin (1991); [7] Bogé et al. (1989).

\*Rechecked by Gal, unpublished.

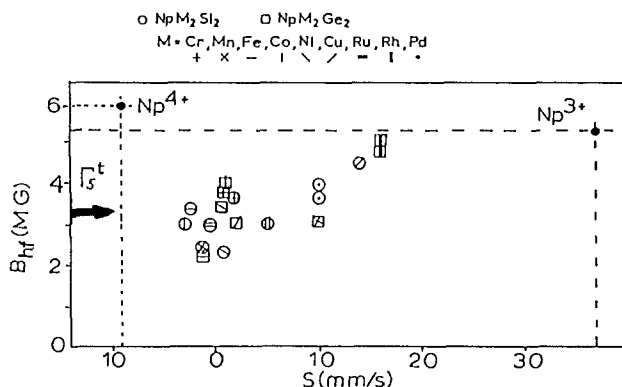


Fig. 46. Hyperfine fields against isomer shift for Np intermetallics with the  $\text{ThCr}_2\text{Si}_2$  structure.  $\text{Np}^{4+}$  and  $\text{Np}^{3+}$  free-ion values are indicated. The arrow marked  $\Gamma_5^t$  refers to the hyperfine field of this crystalline field state. [Taken from Kalvius et al. (1992).]

TABLE 10

Comparison of hyperfine parameters and magnetic transition temperature for tetragonal  $RM_2Si_2$  intermetallics where M is a 3d or 4d transition element, respectively, and R is either Gd or Np. The Gd data are average values of those listed by Czjzek et al. (1989) and Dirken et al. (1989). The original literature for Np is given in table 9.

Compound	$e^2qQ$ (MHz) <sup>a</sup>		$S$ (mm/s) <sup>b</sup>		$B_{hf}/B_{hf}^{3+}$ <sup>c</sup>		$T_N$ (K)	
	Gd	Np	Gd	Np	Gd	Np	Gd	Np
RCr <sub>2</sub> Si <sub>2</sub>	-230	-370	-0.8	-12.9	0.72	0.56		73
RMn <sub>2</sub> Si <sub>2</sub>	-210	-355	-0.9	-16.1	0.76	0.45	65	>300(T <sub>C</sub> )
RFe <sub>2</sub> Si <sub>2</sub>	-290	-1650	-1.8	-17.0	0.85	0.62	8	87
RCo <sub>2</sub> Si <sub>2</sub>	-150	+400	-1.2	-15.9	0.89	0.53	45	42
RNi <sub>2</sub> Si <sub>2</sub>	-40	0	-0.8	-13.3	0.84	0.49	15	33
RCu <sub>2</sub> Si <sub>2</sub>	+90	-1000	0	0	0.77	0.84	12	34
RRu <sub>2</sub> Si <sub>2</sub>	-570	+3000	-1.6	-14.2	0.83	~0.6	44	28
RRh <sub>2</sub> Si <sub>2</sub>	-230	+580	-0.9	-9.7	0.94	~0.6	106	73
RPd <sub>2</sub> Si <sub>2</sub>	-20	-600/-370	-0.3	-3.7	0.78	~0.7	16	59

<sup>a</sup>The ratio of the ground-state nuclear quadrupole moments is  $Q^{Np}/Q^{Gd} \approx 2.6$  (table 1).

<sup>b</sup>Relative to the isomer shift of Gd<sub>2</sub>Cu<sub>2</sub>Si<sub>2</sub> (+0.6 mm/s versus the <sup>155</sup>Eu: Pd source) or NpCu<sub>2</sub>Si<sub>2</sub> (+14.7 mm/s versus NpAl<sub>2</sub>), respectively. The ratio of isomer shift calibration constants is  $\alpha^{Np}/\alpha^{Gd} \approx 10$  (table 1).

<sup>c</sup> $B_{hf}^{3+}$  is the field of the free trivalent ion (see table 2).

Sanchez (private communication) pointed out that an astonishing similarity exists in the general trend of the magnitude of quadrupolar interactions in GdM<sub>2</sub>Si<sub>2</sub> and NpM<sub>2</sub>Si<sub>2</sub> for both 3d and 4d ligands [Np compounds with 5d ligands crystallize in a different structure; see Wastin (1991)]. The situation is summarized in table 10. The similarity exists even more pronounced for the isomer shifts. In both series, the compound with the most positive shift (i.e. closest to the Np<sup>3+</sup> free-ion value) is the copper silicide. To render the comparison more easy the isomer shifts in table 10 are given relative to GdCu<sub>2</sub>Si<sub>2</sub> or NpCu<sub>2</sub>Si<sub>2</sub>, respectively. It is interesting to note that NpCu<sub>2</sub>Ge<sub>2</sub> has by no means as extreme a shift as NpCu<sub>2</sub>Si<sub>2</sub> and hence a similar relation cannot be established for the Ge compounds.

Czjzek et al. (1989) correlate the systematic variations in quadrupole coupling and isomer shift when moving from Fe to Cu or Ru to Pd, that is with the filling of the transition metal d band, to a progressive occupation of 5d states in Gd. The same must then be true for Np. For both elements (Gd and Np) a more negative isomer shift means a higher contact density. The effect of d electrons is a shielding of s electron density and consequently a reduction in contact density. Thus the observed variation in isomer shift is quite compatible to a higher occupation of d states at Gd or Np. Similarly one would understand that the presence of d electrons will enhance the electric field gradient.

At a more elementary level, the lanthanide compounds surely possess a fairly ionic trivalent f electron configuration, and the similarities just outlined can be considered

as further support to the notion put forward earlier that the  $\text{NpM}_2\text{X}_2$  series contain a rather localized trivalent Np ion.

The hyperfine field is reduced compared to the free-ion value in both the Gd and Np silicides. But in this case the cause is different for the two series and hence a strong correlation between the trends in  $B_{\text{hf}}$  does not exist.  $\text{Gd}^{3+}$  is an S-state ion like  $\text{Eu}^{2+}$ . The various contributions to  $B_{\text{hf}}$  are then given by eq. (43).  $B_{\text{core}}$  is the free-ion field ( $-34$  T) and a reduction in field magnitude is due to the influence of  $B_{\text{cep}}$  and (here probably to a minor degree) of  $B_{\text{thf}}$  as discussed for  $\text{Eu}^{2+}$  compounds in section 5.1.1. In contrast, for  $\text{Np}^{3+}$  the orbital field dominates and all other contributions are of little importance. The average value of  $B_{\text{hf}}$  in the silicides is  $\sim 0.6B_{\text{hf}}^{3+}$ . This is quite close to what one expects if crystalline electric field interactions put the  $\Gamma_5^+$  level lowest. As shall be seen further below this crystalline field situation is strongly evidenced in the magnetic behavior of  $\text{NpCr}_2\text{Si}_2$ .

Czjzek et al. (1989) also correlate the magnetic transition temperatures with band filling in the 3d ligands. They notice that  $T_{\text{N}}$  is highest always for the second element (i.e., Co, Rh, Ir) in the transition series. This behavior is not apparent for the Np compounds (table 10). On the average, the transition temperatures are higher for the Np silicides.

Magnetic structures can be complex in the lanthanide as well as the actinide series. For the latter a complete data set is missing, in particular with respect to neutron diffraction data. All Np compounds listed in table 9 order magnetically. They are anti-ferromagnets with the exception of  $\text{M} = \text{Mn}$  which stabilizes ferromagnetically and a high ordering temperature. Also, only in the Mn-containing compounds (lanthanide and actinide series alike) a moment is present on the transition element. The presence of complex antiferromagnetic order is reflected in the Mössbauer hyperfine spectra of several compounds (see table 9), in which more than one field value or even a broad distribution of  $B_{\text{hf}}$  is observed. A typical example is  $\text{NpRu}_2\text{Si}_2$  (Bonnisseau et al. 1988, Bogé et al. 1989). The Néel point is 28 K. The Mössbauer spectrum at 22 K (fig. 47, top) has been fitted with an overlay of four hyperfine spectra. Even at 1.6 K a simple magnetic pattern is not seen (fig. 47, bottom) and an overlay of three spectra is still needed to produce an acceptable fit. Neutron diffraction showed the presence of an incommensurate sine wave modulation with longitudinal polarization. The modulation squares up but the incommensurability remains even at very low temperatures as also evidenced in the Mössbauer spectra. The maximum hyperfine field corresponds to an ordered moment  $\mu_{\text{Np}} = 1.5\mu_{\text{B}}$ .

The temperature dependence of  $B_{\text{hf}}$  in  $\text{NpCu}_2\text{Si}_2$  (fig. 48) was originally interpreted as an indicator of a first-order magnetic transition while all other materials of this structure show second-order behavior. However, bulk magnetic measurements as well as neutron diffraction (de Novion et al. 1980) did not support the first-order character. A re-examination of the situation (Kalvius et al. 1985) showed that the sudden appearance of a magnetic hyperfine spectrum in addition to the paramagnetic single-line spectrum over a temperature range of several K around  $T_{\text{N}}$  (see fig. 48) is caused rather by peculiarities of the crystal field interactions shown schematically in fig. 49. The Hund's rule state of  $\text{Np}^{3+}$  is  $^5\text{I}_4$ . The crystal field interactions in cubic symmetry split this state into a nonmagnetic singlet ( $\Gamma_1$ ), a nonmagnetic doublet

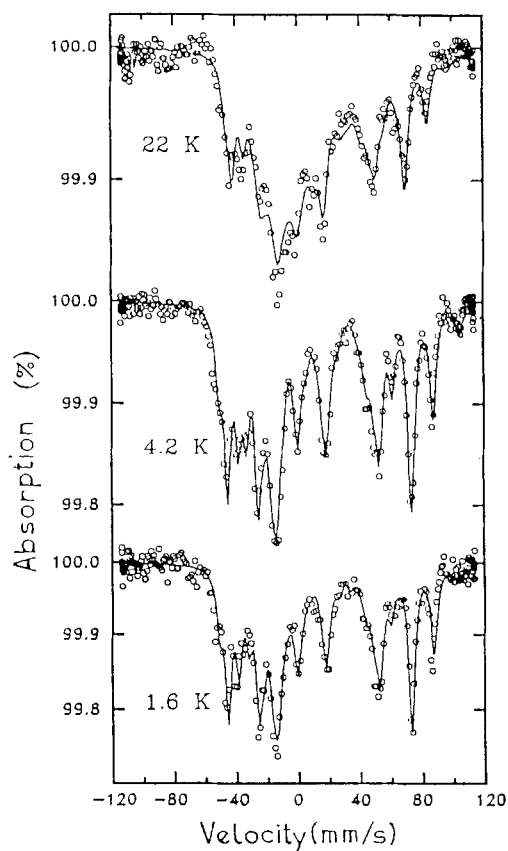


Fig. 47. Hyperfine spectra of antiferromagnetically ordered  $\text{NpRu}_2\text{Si}_2$ . For details see text. [Taken from Bogé et al. (1989).]

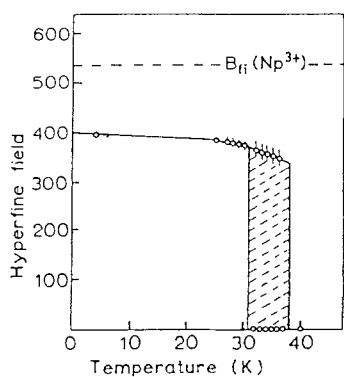


Fig. 48. Temperature dependence of the magnetic hyperfine field (in T) for  $\text{NpCu}_2\text{Si}_2$ . In the shaded region both a single line and a split pattern appear. The relative intensity of the single-line pattern diminishes with lower temperature and vanishes around 31 K. The dashed line gives the  $\text{Np}^{3+}$  free-ion field. [Taken from Kalvius et al. (1985).]

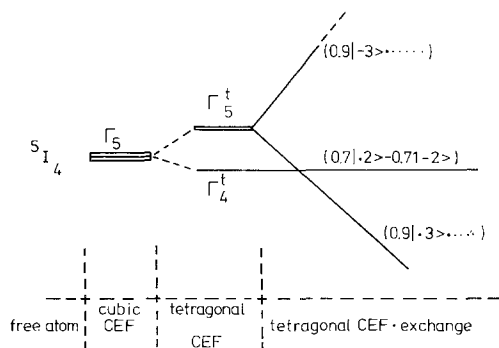


Fig. 49. Schematic representation of the splitting of the  $^5I_4$  Hund's rule ground state of  $Np^{3+}$  in a tetragonal (elongated) crystalline electric field (CEF). Exchange splitting of the  $\Gamma_5$  begins at  $T_N$  and increases with lowering the temperature. The major wave function components of the CEF states are indicated. [Taken from Kalvius et al. (1985).]

( $\Gamma_3$ ) and two magnetic triplets ( $\Gamma_4$  and  $\Gamma_5$ ). In tetragonal symmetry these triplets will split into a singlet ( $\Gamma_4^t$ ) and a doublet ( $\Gamma_5^t$ ) each. The measured hyperfine field of 380 T indicates that we deal with the states derived from the  $\Gamma_5$  triplet. The elongated tetragonal distortion puts the  $\Gamma_4^t$  (nonmagnetic) below the  $\Gamma_5^t$  (magnetic). Exchange interaction commencing below  $T_N$  lifts the degeneracy of the  $\Gamma_5^t$ . One of its components will rapidly move below the  $\Gamma_4^t$  which is unaffected by the exchange field as the temperature is lowered. Slightly below  $T_N$  the separation between the  $\Gamma_4^t$  and the  $\Gamma_5^t$  components is small. Both states are occupied and the combination of a single-line spectrum (nonmagnetic  $\Gamma_4^t$ ) and a magnetically split spectrum (magnetic  $\Gamma_5^t$  component) can be seen. At lower temperatures only the  $\Gamma_5^t$  component will have occupancy and a pure Zeeman pattern emerges.

In summary, we believe that in these tetragonal systems the crystalline electric field interaction plays the essential role and that it can be treated within the picture of a fairly localized trivalent Np ion.

### 6.6. Other related compounds

The compounds  $LnM_4Al_8$  and  $AnM_4Al_8$  with M a transition metal (Cr, Fe, Cu) also crystallize in a tetragonal structure within the  $I4/mmm$  space group and hence are closely related to the  $ThCr_2Si_2$  materials. In the latter  $c/a \approx 2.3$ , in the former  $c/a \approx 0.6$ . They have recently become of considerable interest mainly due to their magnetic properties. Here we shall discuss  $NpCr_4Al_8$  and  $NpCu_4Al_8$ . The intermetallics containing Fe will be dealt with in the next section on account of their spin glass behavior. In general, the hyperfine parameters of the  $NpM_4Al_8$  series fits well the systematics of the  $ThCr_2Si_2$  type compounds. This means, we have here as well the  $Np^{3+}$  ion with a fairly localized f electron configuration and crystalline electric field effects are important. One of the fundamental differences to the  $ThCr_2Si_2$  systems is that here the actinide or the lanthanide as well as the transition element carry a magnetic moment in the ordered state.

Magnetic hyperfine splitting is observed in the Mössbauer spectra of  $NpCr_4Al_8$  below  $\sim 50$  K (Gal et al. 1987b). The temperature variation of  $B_{hf}$  is consistent with a second-order transition into antiferromagnetism around this temperature.

Susceptibility data indicate that the ordering temperatures of both the Np and the Cr sublattices are very close. The hyperfine spectra, particularly when coming close to  $T_N$  show severe line broadenings. At this point it is not clear whether this is due to relaxation effects or to some deviation in stoichiometry (loss of Al in the preparation) for which these compounds are notorious.

A peculiar case is  $NpCu_4Al_8$  (Gal et al. 1985). Although at temperatures below 40 K the onset of magnetic hyperfine splitting is seen (see fig. 50, bottom), albeit with broad lines, neutron diffraction measurements failed to detect magnetic order down to 2 K. Again, crystalline electric field effects have to be evoked. The situation is basically similar to the case of  $NpCu_2Si_2$  discussed just above, i.e., we have as ground states the closely spaced  $\Gamma_4^t$  singlet and the  $\Gamma_5^t$  doublet. The important difference is that the tetragonal distortion is of opposite sign, positioning the  $\Gamma_5^t$  below the  $\Gamma_4^t$  and that due to the absence of magnetic order exchange splitting of the  $\Gamma_5^t$  does not occur (see fig. 50, top). The hyperfine spectra seen below 40 K arise from slow paramagnetic relaxation. Within the two states of the  $\Gamma_5^t$  which mainly contain the  $J_z = |\pm 3\rangle$  wave function spin relaxation is severely hindered. It is possible, however via the  $\Gamma_4^t$  states containing  $J_z = |2\rangle$  and  $J_z = |-2\rangle$  wave functions. But, if  $T \ll \Delta$ , the separation of the two crystalline field states (fig. 50, top), then the  $\Gamma_4^t$  is no longer populated and relaxation rates slow down quickly. At 4.2 K only the  $\Gamma_5^t$  is occupied and we

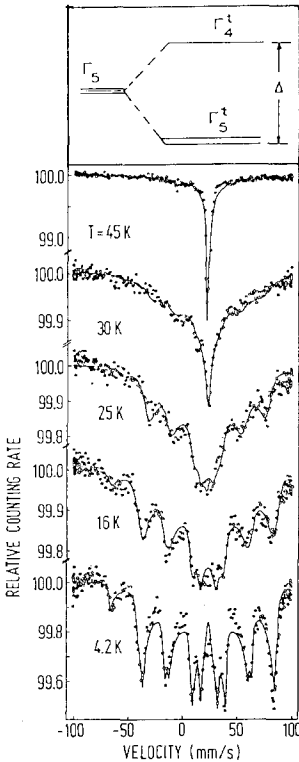


Fig. 50.  $NpCu_4Al_8$ ; top: lowest crystalline electric field states; bottom: Mössbauer hyperfine spectra at various temperatures. The relaxation rates are 330 GHz at 45 K, 30 GHz at 30 K and 12 GHz at 4.2 K as obtained from the fits.



should expect a normal Zeeman pattern. As seen from fig. 50, the line shape is still asymmetric. This is not due to relaxation but rather caused by a small splitting of the  $\Gamma_5^1$  of the order of 0.1 K. This is possible since the  $\Gamma_5^1$  is not a Kramers doublet. It originates from random distortions of symmetry lower than tetragonal which may have their source either in stoichiometry problems or in a partial site exchange between Al and Cu. Together with a weak magnetic field of dipolar origin the small, random splitting of the doublet causes an asymmetric distribution in  $\langle |J_z| \rangle$ . Within this model just discussed the spectra of  $\text{NpCu}_4\text{Al}_8$  could well be fitted at all temperatures as demonstrated in fig. 50, bottom, leading to  $\Delta = 25$  K and the relaxation rates indicated. The hyperfine field of 330 T agrees well with the field calculated for a  $\Gamma_5^1$  ground state.

The fact that the Mössbauer data on the tetragonal compounds, especially of  $\text{NpCu}_2\text{Si}_2$  and  $\text{NpCu}_4\text{Al}_8$ , can be well understood in terms of a straightforward crystalline field model is of course no definite proof of its validity. It is known that the use of crystalline field interactions in uranium compounds have mostly not survived. But Np is more localized than U and for  $\text{NpCo}_2\text{Si}_2$  a lanthanide-like behavior has been proven by high-pressure Mössbauer data as discussed. Thus the chances of survival are better here. Important tests would come from bulk magnetic measurements. To our knowledge they do not exist for  $\text{NpCu}_4\text{Al}_8$ . Definite proof could be obtained by deriving the crystalline field level scheme by inelastic neutron scattering, a task for the future. Magnetization data are truly meaningful only for a single-crystalline specimen, since large anisotropies are to be expected. Sample purity is another crucial factor here. Inelastic neutron scattering can be performed on powders, but requires fairly large amounts of material (10–20 g). This stresses once more the advantage of Mössbauer spectroscopy which needs only small amounts ( $\sim 0.5$  g) of polycrystalline material and is not disturbed by impurities.

The uranium analogue  $\text{UCu}_{4+x}\text{Al}_{8-x}$  has quite similar structural parameters and exists in the range  $0.1 \leq x \leq 1.25$ . It is antiferromagnetic for  $x \leq 1.25$  and moves into a Fermi liquid state for  $x \geq 1.5$ . This transition is reflected in a rapid increase of the coefficient for electronic specific heat from 100 to 800 mJ/(K<sup>2</sup>mol). Even at  $x \approx 1.25$ , the Néel temperature is 10 K. The ordered moment however has sunk from 1.6 (at small values of  $x$ ) to less than  $0.25\mu_B$  (Krimmel et al. 1992a). The Np sample used in the measurements discussed above has shown to be close to stoichiometry by neutron diffraction. It does not order magnetically, yet exhibits a slightly larger moment than the stoichiometric uranium compound (as deduced from the slow-relaxing paramagnetic hyperfine spectrum shown in fig. 50). Investigations of non stoichiometric  $\text{NpCu}_4\text{Al}_8$  compounds have (to our knowledge) not been carried out. Also specific-heat data are not available.

## 7. Spin-glass behavior of lanthanide and actinide intermetallics

Irreversible magnetic phenomena such as the dependence of magnetic parameters on previous history and nonlinearities in the magnetic response of the substance below a characteristic temperature have been reported for the body-centered

tetragonal (space group  $I4/mmm$ )  $\text{LnFe}_{4+x}\text{Al}_{8-x}$  (Felner and Nowik 1988) and  $\text{AnFe}_{4+x}\text{Al}_{8-x}$  systems (Baran and Suski 1985, Gal et al. 1990). The 4f or 5f transition element nominally occupies the 2a site, iron the 8f site and Al the 8i and 8j sites. These compounds tend to be off stoichiometry since in the melt process some Al is likely to evaporate. The samples to be discussed below have been checked by neutron scattering to be close to stoichiometry. Another problem, however, is that a small amount of iron occupies also the 8j site. This observation will be addressed further below. The argument has been put forward that some of these intermetallics might be regarded concentrated spin-glass systems (Gal et al. 1989b, Felner and Nowik 1988). In a typical spin-glass a rapid decrease in spin relaxation times occurs, leading to a more or less random frozen local spin order when passing a characteristic temperature, the spin-glass temperature  $T_{\text{SG}}$ . For details we refer the reader to Staufer and Binder (1978), Chowdhury (1986) and Yeung et al. (1988). Random frozen spin order is reflected in the Mössbauer spectra by the appearance of a magnetic pattern with a broad distribution of hyperfine fields. But it must be understood that the assignment of a magnet as a concentrated spin-glass cannot be done on such an observation alone. For example, a broad distribution of hyperfine fields may well be connected with long-range magnetic order if the spin structure is incommensurately modulated. We have discussed such examples. However, a dependence on magnetic history should then be absent and in neutron scattering the intensities of the appropriate Bragg peaks must not show time-dependent irreversibilities.

In the rare earth materials a spin-glass state has definitely been established for  $\text{TbFe}_4\text{Al}_8$  (Felner and Nowik 1988) and  $\text{HoFe}_4\text{Al}_8$  (Gal et al. 1989b), but  $\text{YFe}_4\text{Al}_8$  appears to be a straightforward antiferromagnet. Spin-glass properties are found only for strongly aluminum-deficient samples (Felner and Nowik 1986). In contrast, spin-glass type behavior is not only seen in  $\text{UFe}_4\text{Al}_8$  and  $\text{NpFe}_4\text{Al}_8$ , but also in  $\text{ThFe}_4\text{Al}_8$ . Clearly, there are significant differences between the U and Np systems when compared to the Th compound due to the absence of a magnetic actinide lattice. As the lanthanide example we shall discuss  $\text{HoFe}_4\text{Al}_8$  since more detailed data are available for this compound. Its features are then to be contrasted with the behavior of the actinide materials mentioned. It must be stressed that spin-glass like order is not restricted to the iron magnetic sublattice in both series.

### 7.1. $\text{HoFe}_4\text{Al}_8$

Neutron diffraction below  $\sim 180$  K shows irreversible changes of intensities induced by application of an external field for satellites to the (200) and (220) nuclear reflections. Also time-dependent effects were noticed below  $\sim 150$  K (Gal et al. 1989b). Only below 20 K none of the just mentioned effects remain in the diffractogram. Its features below 20 K have been interpreted as antiferromagnetic order with a conical spiral component in the Fe sublattice (Schäfer and Will 1983) and ferromagnetic ordering in the Ho sublattice (Schäfer et al. 1988).

Ho is not a practical Mössbauer isotope, thus Mössbauer spectroscopy is restricted to  $^{57}\text{Fe}$ . Some spectra are shown in fig. 51. At high temperatures one observes a pure quadrupole pattern (two lines); below  $\sim 175$  K an additional magnetic pattern

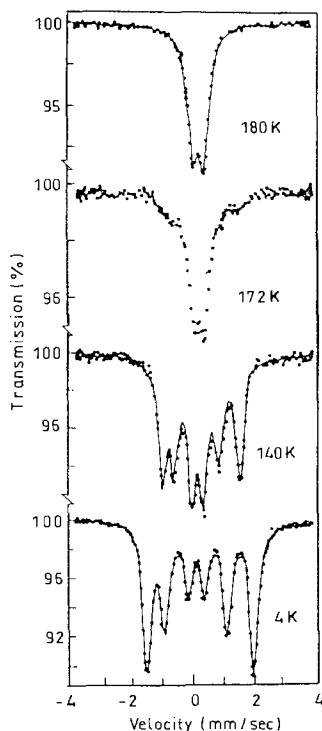


Fig. 51.  $^{57}\text{Fe}$  Mössbauer spectra of  $\text{HoFe}_4\text{Al}_8$  at various temperatures. [Taken from Gal et al. (1989b).]

(six lines) begins to emerge while the quadrupole pattern gradually vanishes. The appearance of a magnetic spectrum is considered to arise from spin freezing and the broad width of its resonance lines proves the existence of randomness in the spin lattice. Furthermore, below  $\sim 175$  K the relative intensities of the second and fifth resonance lines showed temperature-dependent irreversibilities under the influence of an external field of 6 T. These line intensities are sensitive to the direction of sample magnetization (with respect to the  $\gamma$ -ray beam axis). Effects of this type are well known to occur in established spin-glasses. Below 20 K the hyperfine pattern is constant and long-range magnetic order as suggested by the neutron diffraction data is fully supported.

In susceptibility measurements (see fig. 52 for an example) the dependence on magnetic history of the sample is once more apparent. A broad maximum occurs around 150 K and at this temperature also the irreversible components of magnetization vanish. We take this to be the spin-glass transition temperature  $T_{\text{SG}}$ . This is also roughly the temperature where the magnetic Mössbauer pattern is fully established. A sharp upturn in magnetization is seen around 50 K. This temperature is labeled  $T_{\text{OG}}$ . It indicates alignment of Ho spins, a feature which becomes more pronounced in an applied field.  $T_{\text{OG}}$  which varies between 40 and 70 K depending on the strength of the applied field is a second characteristic temperature of this system, namely the transition from an aligned to a random spin-glass (Gal et al. 1989b). One typical spin-glass feature, however, is absent: No cusp in the AC

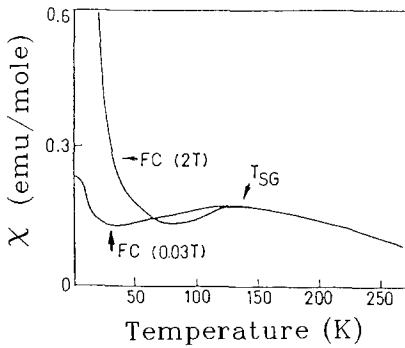


Fig. 52. DC susceptibility of  $\text{HoFe}_4\text{Al}_8$  field cooled in 2T and 0.03 T. The data were taken in a field of 0.03 T. The broad maximum defines  $T_{\text{SG}}$ , the sharp upturn  $T_{\text{OG}}$ . [Taken from Gal et al. (1989b).]

susceptibility could be found. If present at all it must be broadened so severely that it escapes detection. However, this behavior is in agreement with Monte Carlo calculations of Stauer and Binder (1978) for dilute spin-glass systems, where a smooth, broad maximum but no cusp is predicted for the temperature behavior of the AC susceptibility at  $T_{\text{SG}}$ .

## 7.2. $\text{AnFe}_4\text{Al}_8$

Combined AC and DC susceptibility, neutron diffraction and Mössbauer spectroscopy in  $\text{AnFe}_4\text{Al}_8$  with  $\text{An} = \text{U}, \text{Np}$  argue for the establishment of a spin-glass state below  $\sim 110 \text{ K}$  (Gal et al. 1990, Schäfer et al. 1989, 1992).  $T_{\text{SG}}$ , which is now coupled to a peak in AC susceptibility, decreases with rising strength of applied field. Figure 53 depicts DC magnetization curves. Clearly they are remarkably different from those of the Ho compound (see, e.g., fig. 52). The essential point is that the upturn which defines  $T_{\text{OG}}$  lies now above (i.e., near 150 K) the broad peak occurring at  $T_{\text{SG}}$  which is, as mentioned, strongly field dependent. According to neutron diffraction  $T_{\text{OG}}$  signals the freezing of the An moments aligned in a strong applied magnetic field as in the lanthanide case.

$^{57}\text{Fe}$  Mössbauer spectroscopy on  $\text{UFe}_4\text{Al}_8$  and  $\text{NpFe}_4\text{Al}_8$  shows the onset of broad magnetic hyperfine spectra at temperatures in good agreement with  $T_{\text{SG}}(0)$ . The spectra of the two compounds as well as their temperature dependencies are quite alike. Np Mössbauer spectra are depicted in fig. 54. Above 130 K pure quadrupole patterns are seen (paramagnetic regime). The magnetic pattern observed at low temperatures exhibits a very pronounced distribution demonstrating that spin disorder is present in the actinide sublattice as well.

The neutron diffraction patterns again signal antiferromagnetic couplings in the Fe(8f) sublattice, and ferromagnetic coupling for the actinides at the 2a site. The application of external magnetic fields from 2 to 7 T perpendicular to the neutron scattering vector enhances the ferromagnetic alignment of the An moments parallel to the magnetic field direction. It is associated with strong preferred orientation effects of the grains in the powder even at room temperature. When switching off the applied field the aligned moments remain frozen in the direction of the field for at least 48 h at

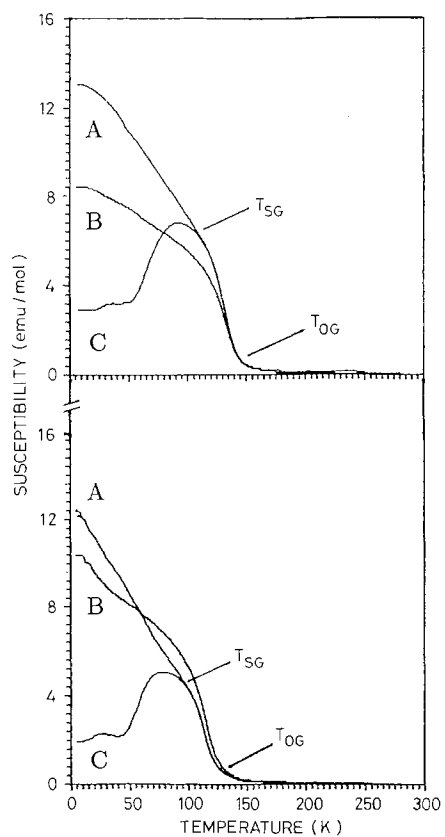


Fig. 53. DC magnetization of  $UFe_4Al_8$  (top) and  $NpFe_4Al_8$  (bottom). A: field cooled in 2 T; B: field cooled in 0.03 T and then exposed to 2 T for 5 min; C: field cooled in 0.03 T. All measurements were carried out in 0.1 T. [Taken from Gal et al. (1990).]

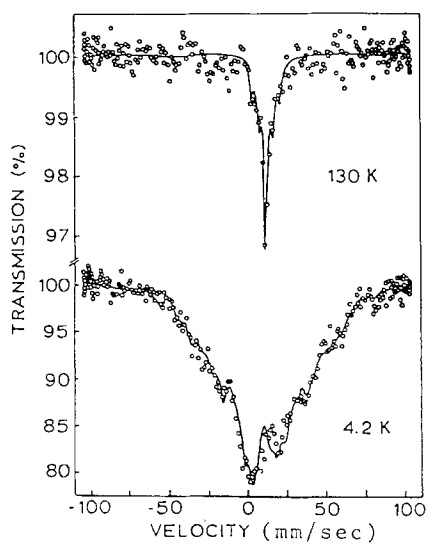


Fig. 54.  $^{237}Np$  Mössbauer spectra of  $NpFe_4Al_8$ . [Taken from Gal et al. (1990).]

5 K. These features allow to define a transition temperature of  $\sim 145$  K which coincides with  $T_{OG}$  defined earlier.

The AC susceptibility in  $\text{ThFe}_4\text{Al}_8$  shows a strong step-like increase at 110 K but no sharp cusp. Neutron diffraction establishes antiferromagnetic coupling of the iron moments as well. Spin-glass features are clearly observable, predominantly in thermoremanent magnetization (Gal et al. 1990).

### 7.3. Comparison

Due to the fact that spin-glass properties could not be detected in  $\text{YFe}_4\text{Al}_8$  it has been proposed by Felner and Nowik (1988) that a small amount of iron atoms residing on Al sites produces enough randomness of exchange interactions to lead to a spin-glass state. Indeed their sample ( $\text{TbFe}_4\text{Al}_8$ ) had about 12% iron on aluminum sites as deduced from  $^{57}\text{Fe}$  Mössbauer spectra. The samples discussed here, especially the actinide materials had a much lower site exchange (of the order of 4%). Furthermore the picture of site exchange as the sole cause for spin disorder does not explain the contrasting behavior of  $\text{ThFe}_4\text{Al}_8$  and  $\text{YFe}_4\text{Al}_8$ . Another possible mechanism has been forwarded by Schäfer et al. (1988): A reduction in the quadrupole interaction by a factor of  $\sim 2$  between the paramagnetic and the magnetic states in the  $^{57}\text{Fe}$  spectra shows that the direction of the Fe moments and the main axis of the electric field gradient are at right angles meaning that the Fe spins are randomly frozen within the basal plane perpendicular to the tetragonal  $c$  direction. Frustration in the 8f sublattice comes from the competition between the ferro- and anti-ferromagnetic components leading to asymmetric (odd) basal plane configurations in the  $I4/mmm$  tetragonal structure ( $G$  type). Such a frustration is described in essence by the Anderson model for a two-dimensional spin-glass system (Anderson 1978).

Spin freezing conditions exist for the 2a site (if occupied by magnetic lanthanide or actinide ions) as well. It is believed (Gal et al. 1990) that this behavior of the lanthanide or actinide sublattice is an outcome of conflicting RKKY interactions between the antiferromagnetically coupled (Fe) moments on the 8f site and the ferromagnetic (An) moments on the 2a sites.

The transition temperature of aligned frozen 2a spins was defined as  $T_{OG}$ . In the An compounds where  $T_{OG}$  is largely field independent (see fig. 53) we have  $T_{OG} \geq T_{SG}$ . In addition:

$$T_{SG}(B=0) \rightarrow T_{OG} \quad \text{and} \quad T_{SG}(B \rightarrow \infty) \rightarrow 0.$$

Hence  $T_{OG}$  is the upper limit of the freezing temperature of both the 2a and 8f sites. In contrast, for the lanthanide compound holds  $T_{OG} \leq T_{SG}$ . Also (as apparent from fig. 52) one finds here a field dependence of  $T_{OG}$  which leads to

$$T_{OG}(B \rightarrow \infty) \rightarrow T_{SG}(0), \quad \text{and} \quad T_{OG}(B \rightarrow 0) \rightarrow 0.$$

It is argued by Gal et al. (1990) that these differences have their roots in the itinerant character of the 5f electrons due to the large spatial distribution of their wave functions leading to a more long-range character of the interactions in the spin-glass state. f-p

and f-d electron hybridization mediated by the Al 3p electrons leads to nearly the same freezing temperatures of the An(2a) and Fe(8f) sites. In contrast the localized character of the 4f electrons is the reason for the opposing behavior of  $T_{OG}$  in  $\text{HoFe}_4\text{Al}_8$ . It should also be remembered that the Ho compound finally achieves magnetic order while the Np compound (e.g., fig. 54) does not. The character of the hyperfine field at the Ho nucleus, however, is not known at present. NMR studies of the Ho failed, as no resonance was observed (C. Carboni, Manchester, UK; private communication).

## 8. Heavy-electron properties in Np intermetallics

There is still no overall consistent theoretical picture to explain the unusual transport and magnetic properties (Grewe and Steglich 1991) of compounds with heavy-electron behavior, briefly called heavy-fermion systems (HFS). With one known exception ( $\text{CeCu}_6$ ), superconductivity or antiferromagnetism is present at very low temperatures. In some cases superconductivity coexists with antiferromagnetism. The question of the true ground state of a HFS remains open at this point. The term "heavy-fermion system" arises from the fact that the most characteristic feature of those compounds is an extremely large coefficient  $\gamma$  (Sommerfeld constant) of the electronic specific heat (Stewart 1984). While normal metals have values  $\gamma \lesssim 10 \text{ mJ}/(\text{K}^2 \text{ mol})$ , the HFS can reach values more than 100 times bigger. The large  $\gamma$  can be related to a large effective mass  $m^*$  of conduction electrons, i.e., they are "heavy". The strongly enhanced value of  $m^*$  is reflected in the magnetic susceptibility and in the electrical resistivity or other transport properties at low temperatures. We have already stated in the introduction that the situation concerning the investigation of local (particularly magnetic) properties of HFS by Mössbauer spectroscopy is not favorable, because known HFS are intermetallic compounds of either Ce or U. The former has no Mössbauer isotope at all, the latter is difficult to handle experimentally and gives only rudimentary information on account of severe limitations in sensitivity. Few HFS containing Np are known. The best established example is  $\text{NpBe}_{13}$  (Stewart et al. 1984). It is magnetic. Also the highly itinerant Laves-phase compounds  $\text{NpOs}_2$  and  $\text{NpIr}_2$  have enhanced values of  $\gamma$  and are sometimes viewed as "medium-heavy-fermion" systems, although in  $\text{NpOs}_2$  this view is questionable on account of its ferromagnetic ground state. In addition,  $\text{NpRu}_2$  which suffers a tetragonal distortion at low temperatures may be included, but it does not order magnetically.

To date, superconductivity in HFS of Np has not been reported. In turn, some of the Np compounds mentioned can be stabilized either in a magnetically ordered state or in a paramagnetic state, depending on the specific stoichiometry of the sample and on its annealing history (Gal et al. 1987a). Examples for such instability are shown in figs. 55 and 56 for  $\text{NpIr}_2$  and  $\text{NpBe}_{13}$ , respectively. These findings recall the instability of the superconducting state in some HFS of either U or Ce. The magnetic instability might be attributable to the sensitivity of spatial distribution of the 5f electron wave functions to hybridization with nearest ligand orbitals. Stewart et al. (1984) clearly saw from specific-heat data that in their sample of  $\text{NpBe}_{13}$  magnetic

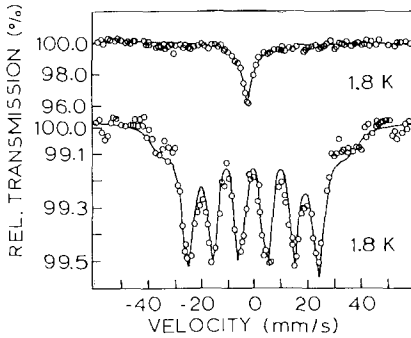


Fig. 55. Mössbauer spectra of stoichiometric  $\text{NpIr}_2$ . Top: recorded after first cooldown. Bottom: recorded after repeated cooling and warming cycles between 300 and 4.2 K. [Taken from Gal et al. (1987a).]

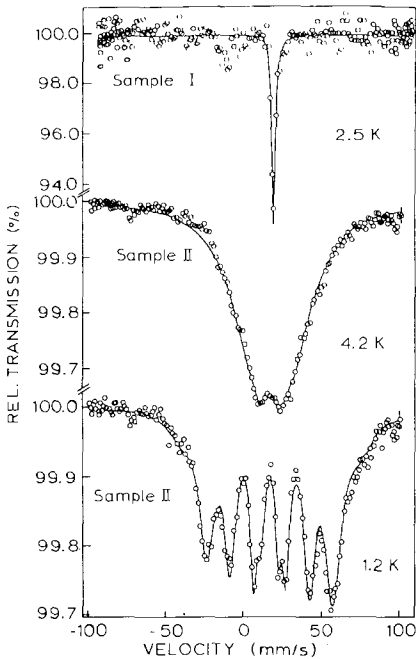


Fig. 56. Mössbauer spectra of two samples of  $\text{NpBe}_{13}$ . Sample I has slight Be excess and is nonmagnetic down to 2 K. Sample II is deficient in Be and orders magnetically around 4.9 K. This corresponds to the behavior reported in the literature [see Stewart (1984). [Taken from Gal et al. (1987a).]

order is present at 3.4 K. The type of order could not be established. The Mössbauer data of fig. 56 show a fairly well resolved, clean Zeeman pattern for sample II. This rules out a modulated structure, but no statement concerning the antiferromagnetic spin sequence can be made. For the compounds  $\text{NpRu}_2$ ,  $\text{NpOs}_2$ ,  $\text{NpIr}_2$  and  $\text{NpBe}_{13}$  it was noted that a linear correlation between isomer shift  $S$  and Sommerfeld constant  $\gamma(0)$  for  $T \rightarrow 0$  can be established (Gal et al. 1989a), i.e., between the electron contact density  $\rho(0)$  and the electron density of states at the Fermi surface  $D(E_F)$ . With increasing  $\gamma(0)$  the isomer shift becomes more negative, the contact density rises. As discussed in section 6.1, the 5f-5f hybridization increases from  $\text{NpIr}_2 \rightarrow \text{NpRu}_2$  due to the reduction in lattice constant. This broadens  $D(E_F)$  compared to  $\text{NpBe}_{13}$  and



hence reduces  $\gamma(0)$ . At the same time the shielding due to 5f electrons is reduced and  $\rho(0)$  rises. For the same set of compounds it had been shown that the local susceptibility  $\chi_L$  as measured by Mössbauer spectroscopy of paramagnets in an external field is proportional to the bulk susceptibility  $\chi_B$  if the Dunlap–Lander relation of eq. (41) is applied (Gal et al. 1989a). The existence of a strong correlation has emerged (Jones 1985) between  $\gamma$  and  $\chi_B(0)$  for a wide variety of HFS and mixed-valence compounds if the two quantities are plotted on a per f-atom basis in double logarithmic scale (see also Lee et al. 1986, Liu 1993). The Jones plot specifically includes  $\text{NpOs}_2$ ,  $\text{NpIr}_2$  and  $\text{NpBe}_{13}$ . Particularly the heaviest materials (in terms of  $m^*$ ) seem to cluster around the straight line given by setting the Wilson ratio

$$R_w = (\chi_B/g_J^2 J(J+1)\mu_B^2/(\gamma/\pi^2 k^2)) = 1.$$

$R_w$  measures the relative enhancement of susceptibility over the coefficient of specific heat and unity holds for noninteracting fermions. Exchange interaction in particular would put the data points to the right of the  $R_w = 1$  line which, in part, is observed. Using  $\chi_L = \chi_B$  from Gal et al. (1989a) with the assumption that  $\chi_L$  measured at liquid He temperature is close enough to  $\chi(0)$  and  $\gamma \propto S$  from Gal et al. (1987) the validity of (or the deviations from) the Jones plot could be checked by Mössbauer measurements on Np systems. Not only would this be an independent method with respect to bulk measurements, it also is a technique which is more easily accessible to radioactive Np and can use powder samples. This, however, is for the future when hopefully more HFS of Np become available.

$\text{NpSn}_3$  also has an enhanced value of  $\gamma \approx 240 \text{ mJ}/(\text{K}^2 \text{ mol})$  in the paramagnetic regime. Mössbauer spectroscopic results on this material, particularly under high pressure, have been discussed in section 5.3. Localized behavior was found under volume reduction and the results had been discussed in analogy to  $\text{CeAl}_2$ , which classifies  $\text{NpSn}_3$  as a concentrated Kondo system.

Data for three intermetallics of Np which are isostructural to uranium compounds with heavy-fermion properties are available. The first case is  $\text{NpRu}_2\text{Si}_2$  which has been discussed in section 6.5. The second is  $\text{NpCu}_4\text{Al}_8$ . It has been dealt with in section 6.6. Finally, we have  $\text{NpPd}_2\text{Al}_3$  which recently has been synthesized and for which first Mössbauer data have become available (Zwirner et al. 1992).

Both  $\text{NpPd}_2\text{Al}_3$  and  $\text{UPd}_2\text{Al}_3$  crystallize in the hexagonal  $\text{PrNi}_2\text{Al}_3$  structure (space group P6/mmm). The hexagonal cell is strongly compressed, the  $c/a$  ratio being 0.78. The intensive research which was directed towards  $\text{UPd}_2\text{Al}_3$  since its discovery as a HFS (Geibel et al. 1991) stems from the fact that superconductivity ( $T_c = 2 \text{ K}$ ) coexists with antiferromagnetic order ( $T_N = 14 \text{ K}$ ) with U carrying a substantial ordered moment (0.85) (Krimmel et al. 1992b). This is about a factor of 50 larger than in the previously established cases  $\text{URu}_2\text{Si}_2$  and  $\text{UPt}_3$ . Another material with similar behavior is  $\text{UNi}_2\text{Pd}_3$  but the ordered moment is considerably smaller ( $0.1 \mu_B$ ). The  $\gamma$  coefficient of  $\text{UPd}_2\text{Al}_3$  is  $210 \text{ mJ}/(\text{K}^2 \text{ mol})$  in the paramagnetic state. It drops to  $150 \text{ mJ}/(\text{K}^2 \text{ mol})$  in the antiferromagnetic phase. Neutron diffraction established antiferromagnetic order with a propagation vector  $\mathbf{k} = [0, 0, \frac{1}{2}]$  in  $\text{UPd}_2\text{Al}_3$  below 15 K. Between 15 and 20 K an incommensurate structure ( $\mathbf{k} = [0, 0, 0.52]$ ) was detected.

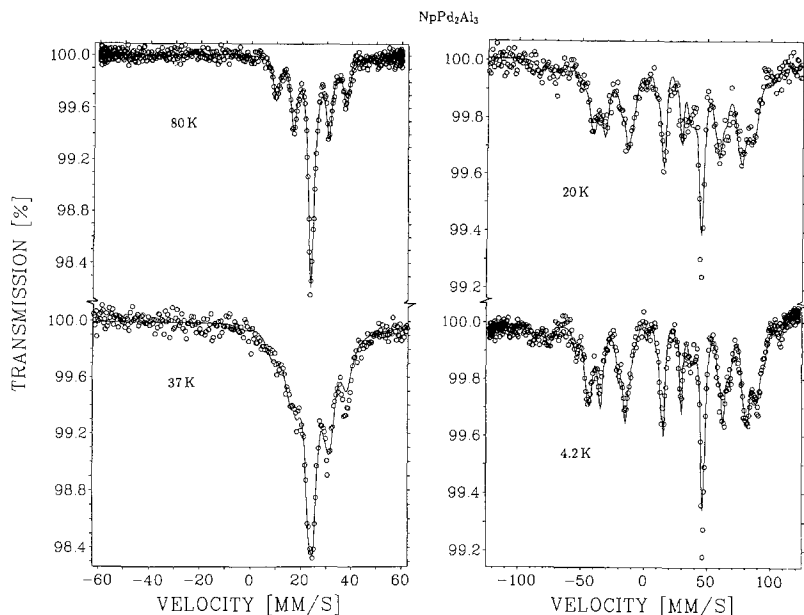


Fig. 57. Mössbauer spectra of  $\text{NpPd}_2\text{Al}_3$  at various temperatures. Note the difference in velocity scales left and right. [Taken from Zwirner et al. (1992).]

To our knowledge no transport or specific heat data exist yet for  $\text{NpPd}_2\text{Al}_3$  and hence we cannot say whether it is also a HFS and whether superconductivity exists. The Mössbauer spectra, however, clearly establish the presence of magnetic ordering (fig. 57). A phase transition of second order was found at 38(1) K. The paramagnetic spectrum consists of a pure quadrupole pattern. It clearly shows that all Np ions see the same local surroundings. Full rotational symmetry ( $\eta = 0$ ) is maintained. The magnetic spectra had to be fitted with an overlay of three magnetic patterns including quadrupole interaction. The hyperfine parameters resulting for these fits are summarized in table 11. All three magnetic sites were constrained to experience the same electric field gradient  $eq$ , but its value was a free parameter. The fit to the 37 K

TABLE 11  
Hyperfine parameters and linewidth of  $\text{NpPd}_2\text{Al}_3$ .

$T$ (K)	$B_{\text{hf}}[1]$ (T)	$\text{Int}[1]$ (%)	$B_{\text{hf}}[2]$ (T)	$\text{Int}[2]$ (%)	$B_{\text{hf}}[3]$ (T)	$\text{Int}[3]$ (%)	$eq$ ( $10^8 \text{ V/cm}^2$ )	$S^a$ mm/s	FWHM mm/s
80	—	—	—	—	—	—	+2.27(4)	+10.0(1)	2.8(1)
20	342(2)	32(3)	296(2)	56(3)	118(3)	12(2)	+2.29(4)	+9.5(3)	2.6(1)
4.2	360(1)	37(3)	316(1)	55(3)	121(3)	8(2)	+2.30(3)	+10.4(2)	2.1(1)

<sup>a</sup>Isomer shift is given relative to  $\text{NpAl}_2$ .

spectrum shown in fig. 57 was heavily constrained and thus its parameters do not enter in table 11. The presence of three magnetic sites with different occupations points towards a modulated structure. The relatively small number of sites, and the absence of very small fields suggest the modulation to be fairly squared and commensurate at low temperatures. Spectra beyond 30 K require more intensity of the small field and the linewidth (FWHM) increases. The latter, however, might be due to relaxation effects. The maximum saturation hyperfine field corresponds to an ordered moment on Np of  $1.67\mu_B$ . This is about twice the moment on U in antiferromagnetic  $UPd_2Al_3$ . The same value of quadrupolar coupling was found above and below  $T_N$ . This means that the spins point in the same direction as the electric field gradient, probably the  $c$  axis. The isomer shift relative to  $NpAl_2$  is  $+10$  mm/s. Using the systematics displayed in fig. 45 this means that the  $Np^{3+}$  ion with the Hund's rule ground state  $^5I_4$  is present. From susceptibility data at elevated temperatures a  $U^{4+}$  charge state was deduced in  $UPd_2Al_3$  (Grauel et al. 1992). The surprising fact is that the Hund's rule state of  $U^{4+}$  is also a  $J = 4$  multiplet ( $^3H_4$ ). The isoelectronic ( $f^2$ ) state is  $Np^{5+}$  which can definitely be excluded. One might be tempted to assume that the crystal symmetry enforces a  $J = 4$  ground multiplet. The easier way for Np to reach this is the trivalent charge state. The additional  $f$  electron (strictly speaking two additional  $f$  electrons, but one just compensates the increase in nuclear charge) may be necessary since Np tends to be less hybridized than U, and can perhaps not attract as much  $d$  electron density from the ligand. A recent band structure calculation of electronic and magnetic structure of  $UPd_2Al_3$  by Sticht and Kübler (1992) discusses the chemical bond in some detail and emphasizes Pd  $d$ -U  $f$  hybridization. In addition  $pd$  states are shared between Al and Pd. The relatively small ordered moment is explained by a near compensation of spin and orbital contributions.

The saturation hyperfine field in  $NpPd_2Al_3$  (table 11) is only about  $\frac{2}{3}$  of the  $Np^{3+}$  free-ion field (table 2). It is thought that the main cause for the reduction comes from crystalline electric field interactions. The magnitude of the electric field gradient ( $eq$ ) is about twice that of the  $Np^{3+}$  free ion value (table 2) and of opposite sign. Any crystalline field interaction will diminish the magnitude of the ionic gradient. This means that the other sources to  $eq$  are essential. This is for one the lattice gradient, but despite its large Sternheimer antishielding factor ( $\gamma_\infty \approx -130$ ) for Np it is unlikely that it can by itself account for the large gradient observed. It is most probable that conduction electron bands with strong  $d$  character produce an additional large contribution.

In summary it appears that the Np analogues of U compounds with heavy-fermion properties tend to have more pronounced magnetic character. It is unlikely that  $NpRu_2Si_2$ ,  $NpCu_4Al_8$  and  $NpPd_2Al_3$  can be regarded as true HFS. The stronger magnetic properties of Np are particularly apparent in the comparison between  $USn_3$  and  $NpSn_3$ . The former is a typical spin fluctuator showing no magnetic order within easily accessible temperatures. In contrast, the latter is a Kondo lattice system which undergoes antiferromagnetic order around 10 K. It would be most interesting to trace this tendency toward a well established magnetic groundstate by measuring mixed U-Np intermetallics. Technically this is quite feasible and the project is a challenge for the future. Superconductivity has not yet been discovered in Np intermetallics.

One problem is that temperatures below  $\sim 0.5$  K cannot easily be reached because of radioactive self-heating.

## 9. Conclusions

Mössbauer spectroscopy is a powerful tool to gain essential information on the difference in electron structure between intermetallic compounds of 4f and 5f elements. In the latter series the work concentrates on Np materials. For this actinide bulk magnetic and transport data are still scarce and even neutron diffraction results are not plentiful. Mössbauer spectroscopy is thus in some sense a forerunner. It has been shown that measurements under high pressures are pivotal for a deeper insight of electronic properties, in particular with the question of 3d-like itinerant versus 4f-like localized electron behavior of the 5f electrons in Np. It becomes more and more apparent that U and Np behave often quite differently mainly because of the somewhat more pronounced tendency of the latter towards f localization. Nevertheless, the formation of 5f bands via hybridization plays a central role also in Np metallic compounds.

We have reviewed several series of intermetallics with different structures, concentrating on cubic compounds. Their properties range from typical Hill behavior, i.e., a strong dependence on the separation of neighboring actinide ions, via pronounced dependencies on the chemical nature of ligands, to a more lanthanide-like independence of either the two influences. But the fully developed lanthanide behavior, in which for example, the magnetic properties are close to that of the free ion, is rare in Np materials.

One of the special problems with actinides is that they can easily form different charge states. The question which charge state exists in some uranium compounds is often a matter of heated debate. Here, Mössbauer spectroscopy on Np has a definite edge due to the unique information available from the isomer shift. Still, isomer shift data have to be interpreted with care, but we hope to have shown that important information towards the nature of the charge state can be deduced. Mössbauer spectroscopy cannot solve magnetic structures but it can give initial information on whether a simple spin structure or a more complex one like the modulated or even incommensurate structures exists. One of the big advantages of Mössbauer spectroscopy is that it needs basically only powder samples and not very large amounts at that. The samples can be safely encapsulated and measurements with Np do not need a closed-atmosphere box (but of course the sample preparation and packing does). Finally, we should mention that Mössbauer spectroscopy is a very powerful method for checking phase purity of a sample. Impurities are detected predominantly by their different isomer shift. The sensitivity often exceeds that of X-ray analysis. The two methods, however, detect the impurities via different properties (electronic configuration versus crystallographic structure) and hence should be regarded as complementary.

Clearly, there is still much to do with Np. But the new frontiers are Am and Pa. For both elements Mössbauer spectroscopy is well suited, albeit not quite as simple

experimentally as Np. The wider use has been hindered by the difficulty of obtaining compounds containing  $^{243}\text{Am}$  or  $^{231}\text{Pa}$ . The situation in U (whatever isotope one takes) and Pu is not favorable, and Mössbauer spectroscopy can contribute little towards the understanding of these actinides. The last decade of Np Mössbauer spectroscopy has brought a rich harvest. Let us look forward that this will continue in the years ahead.

## References

- Abd-Elmeguid, M.M., and R.D. Taylor, 1990, *Phys. Rev. B* **42**, 1048.
- Abd-Elmeguid, M.M., H. Micklitz and G. Kaindl, 1981, *Phys. Rev. B* **23**, 75.
- Abd-Elmeguid, M.M., H. Micklitz, G. Kaindl and D. Wagner, 1982, *Phys. Rev. B* **25**, 7055.
- Abramowitz, M., and I.A. Stegun, 1972, *Handbook of Mathematical Functions* (Dover, New York).
- Aldred, A.T., B.D. Dunlap, A.R. Harvey, D.J. Lam, G.H. Lander and M.H. Mueller, 1974a, *Phys. Rev. B* **9**, 3766.
- Aldred, A.T., B.D. Dunlap and D.J. Lam, 1974b, *AIP Conf. Proc.* **18**, 366.
- Aldred, A.T., B.D. Dunlap, D.J. Lam and I. Nowik, 1974c, *Phys. Rev. B* **10**, 1011.
- Aldred, A.T., D.J. Lam, A.R. Harvey and B.D. Dunlap, 1975a, *Phys. Rev. B* **11**, 1169.
- Aldred, A.T., B.D. Dunlap, D.J. Lam, G.H. Lander, M.H. Mueller and I. Nowik, 1975b, *Phys. Rev. B* **11**, 530.
- Aldred, A.T., B.D. Dunlap and G.H. Lander, 1976, *Phys. Rev. B* **14**, 1276.
- Anderson, P.W., 1978, *J. Less-Comm. Met.* **62**, 291.
- Arko, A.J., D.D. Koelling and J.E. Schirber, 1985, in: *Handbook on the Physics and Chemistry of the Actinides*, Vol. 2, eds A.J. Freeman and G.H. Lander (North-Holland, Amsterdam) p. 175.
- Arrott, A.T., 1966, in: *Magnetism*, Vol IIB, eds G. Rado and H. Suhl (Academic Press, New York) p. 296.
- Asch, L., and G.M. Kalvius, 1981a, in: *Handbook of Spectroscopy*, Vol. 3, ed. I.W. Robinson (CRC Press, Boca Raton, FL) p. 404.
- Asch, L., and G.M. Kalvius, 1981b, in: *Handbook of Spectroscopy*, Vol. 3, ed. I.W. Robinson (CRC Press, Boca Raton, FL) p. 432.
- Asch, L., W. Potzel, G.M. Kalvius, J.C. Spirlet and W. Müller, 1978, *Hyperfine Interactions* **5**, 457.
- Asch, L., W. Potzel, O. Beck, J.C. Spirlet, W. Müller and G.M. Kalvius, 1981, *Hyperfine Interactions* **10**, 663.
- Bancroft, G.M., 1981, in: *Handbook of Spectroscopy*, Vol. 3, ed. I.W. Robinson (CRC Press, Boca Raton, FL) p. 480.
- Baran, A., and W. Suski, 1985, *Physica B* **130**, 219.
- Barbara, B., J.X. Boucherle, J.L. Buevoz, M.F. Rossignol and J. Schweizer, 1977, *Solid State Commun.* **24**, 481.
- Barnes, R.G., 1979, in: *Handbook on the Physics and Chemistry of Rare Earths*, Vol. 2, eds K.A. Gschneidner Jr and L. Eyring (North-Holland, Amsterdam) p. 387.
- Bassett, W.A., T. Takahasi and P.W. Stook, 1967, *Rev. Sci. Instrum.* **38**, 37.
- Blaise, A., M.N. Bouilliet, F. Bourdarot, P. Burlet, J. Rebizant, J. Rossat-Mignod, J.P. Sanchez, J.C. Spirlet and O. Vogt, 1992, *J. Magn. & Magn. Mater.* **104-107**, 33.
- Bleaney, B., 1967, in: *Hyperfine Interactions*, eds A.J. Freeman and R.B. Frankel (Academic Press, New York) p. 1.
- Blume, M., and J. Tjon, 1968, *Phys. Rev.* **165**, 446.
- Bodé, D.D., J.F. Wild and E.K. Hulet, 1976, *J. Inorg. Nucl. Chem.* **38**, 1291.
- Bogé, M., J. Chappert, L. Asch, G.M. Kalvius, A. Blaise, J.M. Fournier, D. Damien and A. Wojakowski, 1981, in: *Actinides 1981*, Report LBL-12441 (Lawrence Berkeley Laboratory) p. 165.
- Bogé, M., J. Chappert, L. Asch, G.M. Kalvius, A. Blaise, J.M. Fournier, D. Damien and A. Wojakowski, 1982, *J. Magn. & Magn. Mater.* **30**, 127.
- Bogé, M., D. Bonnisseau, L. Asch, G.M. Kalvius, J.C. Spirlet and J. Rebizant, 1988, *Hyperfine Interactions* **40**, 377.
- Bogé, M., D. Bonnisseau, P. Burlet, J.M. Fournier, E. Pleska, S. Quezel, J. Rebizant, J. Rossat-Mignod, J.C. Spirlet and M. Wulff, 1989, *J.*

- Nucl. Mater. **166**, 77.
- Bonnisseau, D., P. Burlet, M. Bogé, S. Quézel, J. Rossat-Mignod, J.C. Spirlet and J. Rebizant, 1988, *J. Phys. Colloq. (Paris)* **49**, C8-491.
- Bouillet, M.N., J.P. Sanchez, K. Tomala, P. Burlet, J. Rebizant, J.C. Spirlet and O. Vogt, 1992, 22emes Journées des Actinides, Meribel, France, unpublished.
- Boyle, A.J.F., and H.E. Hall, 1962, *Rep. Prog. Phys.* **25**, 441.
- Brodsky, M.B., and R.J. Trainor, 1977, *Physica B* **91**, 271.
- Burlet, P., S. Quézel, M. Kusnietz, D. Bonnisseau, J. Rossat-Mignod, J.C. Spirlet, J. Rebizant and O. Vogt, 1986, *J. Less-Common. Met.* **121**, 325.
- Burlet, P., J.M. Fournier, E. Pleska, J. Rossat-Mignod, J.P. Sanchez, J. Rebizant, J.C. Spirlet and O. Vogt, 1990, in: *Proc. 20emes Journées des Actinides*, Prague, CSFR, unpublished.
- Burlet, P., F. Bourdarot, J. Rossat-Mignod, J.P. Sanchez, J.C. Spirlet, J. Rebizant and O. Vogt, 1992, *Physica B* **180-181**, 131.
- Chan, S.K., and D.J. Lam, 1974, in: *The Actinides: Electronic Structure and Related Properties*, eds A.J. Freeman and J.B. Darby Jr (Academic Press, New York) p. 1.
- Chowdhury, D., 1986, in: *Spin Glass and Other Frustrated Systems* (World Scientific, Singapore) pp. 1, 31.
- Clauser, M.J., and M. Blume, 1971, *Phys. Rev. B* **3**, 583.
- Cohen, M.H., and F. Reif, 1957, in: *Solid State Physics*, Vol. 5, eds F. Seitz and D. Turnbull (Academic Press, New York) p. 322.
- Cohen, R.L., and G.M. Kalvius, 1970, *Nucl. Instrum. & Methods* **86**, 209.
- Cooper, B.R., 1982, *J. Magn. & Magn. Mater.* **29**, 230.
- Cooper, B.R., and O. Vogt, 1971, *J. Phys. Colloq. (Paris)* **32**, C1-958.
- Cooper, B.R., J.M. Wills, N. Kioussis and Q.G. Sheng, 1988, *J. Phys. Colloq. (Paris)* **49**, C8-463.
- Coqblin, B., and J.R. Schrieffer, 1969, *Phys. Rev.* **185**, 847.
- Czjzek, G., V. Oestreich, H. Schmidt, K. Latka and K. Tomala, 1989, *J. Magn. & Magn. Mater.* **79**, 42.
- Dattagupta, S., 1983, in: *Advances in Mössbauer Spectroscopy*, eds B.V. Thosar, P.K. Iyengar, J.K. Shrivasta and S.G. Bhargava (Elsevier, Amsterdam) p. 586.
- de Novion, C.H., J. Gal and J.L. Buevoz, 1980, *J. Magn. & Magn. Mater.* **21**, 85.
- Desclaux, J.P., A.J. Freeman and J.V. Mallow, 1977, *J. Magn. & Magn. Mater.* **5**, 265.
- Devine, R.A.B., 1982, *Phys. Rev. B* **25**, 7052.
- Dirken, M.W., R.C. Thiel and K.H.J. Buschow, 1989, *J. Less-Common Met.* **147**, 97.
- Dunlap, B.D., 1971, in: *Mössbauer Effect Methodology*, Vol. 7, ed. I. Gruverman (Plenum Press, New York) p. 123.
- Dunlap, B.D., and G.M. Kalvius, 1972, *Int. J. Magn.* **2**, 231.
- Dunlap, B.D., and G.M. Kalvius, 1974, in: *The Actinides: Electronic Structure and Related Properties*, Vol. 1, eds A.J. Freeman and J.B. Darby Jr (Academic Press, New York) p. 237.
- Dunlap, B.D., and G.M. Kalvius, 1978, in: *Mössbauer Isomer Shifts*, eds G.K. Shenoy and F.E. Wagner (North-Holland, Amsterdam) p. 15.
- Dunlap, B.D., and G.M. Kalvius, 1985, in: *Handbook on the Physics and Chemistry of the Actinides*, Vol. 2, eds A.J. Freeman and G.H. Lander (North-Holland, Amsterdam) p. 329.
- Dunlap, B.D., and G.H. Lander, 1974, *Phys. Rev. Lett.* **33**, 1046.
- Dunlap, B.D., M.B. Brodsky, G.K. Shenoy and G.M. Kalvius, 1970, *Phys. Rev. B* **1**, 44.
- Dunlap, B.D., G.M. Kalvius and G.K. Shenoy, 1971, *Phys. Rev. Lett.* **26**, 1085.
- Elliott, R.J., and K.W.H. Stevens, 1953, *Proc. R. Soc. A* **218**, 553.
- Eriksson, O., M.S.S. Brooks and B. Johansson, 1989, *Phys. Rev. B* **39**, 13115.
- Eriksson, O., B. Johansson and M.S.S. Brooks, 1990, *J. Phys.: Condens. Matter* **2**, 1529.
- Felner, I., and I. Nowik, 1986, *J. Magn. & Magn. Mater.* **58**, 169.
- Felner, I., and I. Nowik, 1988, *J. Magn. & Magn. Mater.* **74**, 31.
- Fournier, J.M., and R. Troč, 1985, in: *Handbook on the Physics and Chemistry of the Actinides*, Vol. 2, eds A.J. Freeman and G.H. Lander (North-Holland, Amsterdam) p. 29.
- Fournier, J.M., A. Blaise, W. Müller and J.C. Spirlet, 1977, *Physica B* **86-88**, 30.
- Fournier, J.M., J. Beille and C.H. de Novion, 1979, *J. Phys. Colloq. (Paris)* **40**, C4-32.
- Fournier, J.M., J. Beille, A. Boef, C. Vettier and A. Wedgwood, 1980, *Physica B* **102**, 282.
- Freeman, A.J., 1980, *Physica B* **102**, 3.
- Freeman, A.J., and D.D. Koelling, 1974, in: *The Actinides: Electronic Structure and Related Properties*, Vol. 1, eds A.J. Freeman and

- J.B. Darby Jr (Academic Press, New York) p. 51.
- Friedt, J.M., R. Poinso, J. Rebizant and W. Müller, 1979, *J. Phys. & Chem. Solids* **40**, 279.
- Friedt, J.M., R. Poinso, J. Rebizant and J.C. Spirlet, 1981, in: *Actinides 1981*, Report LBL-124441 (Lawrence Berkeley Laboratory) p. 168.
- Gal, J., Z. Hadari, E.R. Bauminger, I. Nowik, S. Ofer and M. Perkal, 1970, *Phys. Lett. A* **31**, 511.
- Gal, J., Z. Hadari, E.R. Bauminger, I. Nowik and S. Ofer, 1973a, *Solid State Commun.* **13**, 647.
- Gal, J., Z. Hadari, U. Atzmony, E.R. Bauminger, I. Nowik and S. Ofer, 1973b, *Phys. Rev. B* **8**, 1901.
- Gal, J., M. Kroup, Z. Hadari and I. Nowik, 1976, *Solid State Commun.* **20**, 515.
- Gal, J., M. Kroup, Z. Hadari and I. Nowik, 1977, *Phys. Rev. B* **16**, 3913.
- Gal, J., H. Pinto, S. Fredo, M. Melamud, H. Shaked, R. Caciuffo, F.J. Litterst, L. Asch, W. Potzel and G.M. Kalvius, 1985, *J. Magn. & Magn. Mater.* **50**, L123.
- Gal, J., F.J. Litterst, W. Potzel, J. Moser, U. Potzel, G.M. Kalvius, S. Fredo and S. Tapuchi, 1987a, *Phys. Rev. B* **36**, 2457.
- Gal, J., H. Pinto, S. Fredo, H. Shaked, W. Schäfer, G. Will, F.J. Litterst, W. Potzel, L. Asch and G.M. Kalvius, 1987b, *Hyperfine Interactions* **33**, 173.
- Gal, J., F.J. Litterst, W. Potzel, J. Moser, U. Potzel, S. Fredo, S. Tapuchi, G. Shani, J. Jove, A. Cousson, M. Pagès and G.M. Kalvius, 1989a, *Phys. Rev. Lett.* **63**, 2413.
- Gal, J., I. Yaar, E. Arbaboff, H. Etedgi, F.J. Litterst, K. Aggarwal, J.A. Pareda, G.M. Kalvius, G. Will and W. Schäfer, 1989b, *Phys. Rev. B* **40**, 745.
- Gal, J., I. Yaar, D. Regev, S. Fredo, G. Shani, E. Arbaboff, W. Potzel, K. Aggarwal, J.A. Pareda, G.M. Kalvius, F.J. Litterst, W. Schäfer and G. Will, 1990, *Phys. Rev. B* **42**, 8507.
- Gal, J., I. Yaar, S. Fredo, I. Halevy, W. Potzel, S. Zwirner and G.M. Kalvius, 1992, *Phys. Rev. B* **46**, 5351.
- Geibel, C., C. Schank, S. Thies, H. Kitazawa, C.D. Bredl, A. Böhm, M. Rau, A. Grauel, R. Caspary, R. Helfrich, U. Ahlheim, G. Weber and F. Steglich, 1991, *Z. Phys. B* **84**, 1.
- Gleissner, A., 1992, Ph.D. Thesis, Technical University Munich, unpublished.
- Gleissner, A., W. Potzel, J. Moser and G.M. Kalvius, 1993, *Phys. Rev. Lett.* **70**, 2032.
- Goldanskii, V.I., and E.F. Makarov, 1968, in: *Chemical Applications of Mössbauer Spectroscopy*, eds V.I. Goldanskii and R.H. Herber (Academic Press, New York) p. 102.
- Goldwire, H.C., and J.P. Hannon, 1977, *Phys. Rev. B* **16**, 1875.
- Gorobchenko, V.D., I.I. Lukashevich, V.G. Stankevich, N.I. Filippov, V.I. Chukalin and E.I. Yarembash, 1971, *Sov. Phys.-Solid State* **13**, 901.
- Grauel, A., A. Böhm, H. Fischer, C. Geibel, R. Köhler, R. Modler, C. Schank, F. Steglich, G. Weber, T. Komatsubara and N. Sato, 1992, *Phys. Rev. B* **46**, 5818.
- Grewe, N., and F. Steglich, 1991, in: *Handbook on the Physics and Chemistry of Rare Earths*, Vol. 14, eds K.A. Gschneidner Jr and L. Eyring (North-Holland, Amsterdam) p. 343.
- Hill, H.H., 1970, in: *Plutonium 1970 and Other Actinides*, ed. W. Miner (Metall. Soc. of Amer. Inst. Mining, Metall. and Pet. Engrs, New York) p. 2.
- Huber, G., K. Syassen and W.B. Holzapfel, 1977, *Phys. Rev. B* **15**, 5123.
- Jaakkola, S.M., and M.K. Hänninen, 1980, *Solid State Commun.* **36**, 275.
- Johansson, B., O. Eriksson, L. Nordström, L. Severin and M.S.S. Brooks, 1991, *Physica B* **172**, 101.
- Jones, B.A., 1985, cited as private communication by Lee et al. (1986).
- Jones, D.L., W.G. Stirling, G.H. Lander, J. Rebizant, J.C. Spirlet, M. Alba and O. Vogt, 1991, *J. Phys.: Condens. Matter* **3**, 3551.
- Josephson, B.D., 1960, *Phys. Rev. Lett.* **4**, 341.
- Kalish, R., U. Shreter and J. Grunzweig-Genossar, 1975, *Hyperfine Interactions* **1**, 65.
- Kalvius, G.M., 1987, in: *Encyclopedia of Physical Science and Technology*, Vol. 8 (Academic Press, New York) p. 565.
- Kalvius, G.M., 1989, *J. Nucl. Mater.* **166**, 5.
- Kalvius, G.M., 1990, *High-Pressure Research* **2**, 315.
- Kalvius, G.M., U.F. Klein and G. Wortmann, 1974, *J. Phys. Colloq. (Paris)* **35**, C6-139.
- Kalvius, G.M., W. Potzel, J. Moser, F.J. Litterst, L. Asch, J. Zänkert, U. Potzel, A. Kratzer, M. Wunsch, J. Gal, S. Fredo, D. Dayan, M.P. Dariel, M. Bogé, J. Chappert, J.C. Spirlet, U. Benedict and B.D. Dunlap, 1985, *Physica B* **130**, 393.
- Kalvius, G.M., S. Zwirner, U. Potzel, J. Moser, W. Potzel, F.J. Litterst, J. Gal, S. Fredo, I. Yaar and J.C. Spirlet, 1990, *Phys. Rev. Lett.* **65**, 2290.

- Kalvius, G.M., J. Gal, L. Asch and W. Potzel, 1992, *Hyperfine Interactions* **72**, 77.
- Kannelakopoulos, B., A. Blaise, J.M. Fournier and W. Müller, 1975, *Solid State Commun.* **17**, 713.
- Kienle, P., 1964, *Rev. Mod. Phys.* **36**, 372.
- Klein, U.F., G. Wortmann and G.M. Kalvius, 1976, *J. Magn. & Magn. Mater.* **3**, 50.
- Klein, U.F., J. Moser, G. Wortmann and G.M. Kalvius, 1977, *Physica B* **86-88**, 118.
- Kratzer, A., U. Potzel, J. Moser, F.J. Litterst, W. Potzel and G.M. Kalvius, 1986, *J. Magn. & Magn. Mater.* **54-57**, 489.
- Krimmel, A., A. Loidl, C. Geibel, F. Steglich and G.J. McIntyre, 1992a, *J. Magn. & Magn. Mater.* **104-107**, 25.
- Krimmel, A., P. Fischer, B. Roesli, H. Maletta, C. Geibel, C. Schank, A. Grauel, A. Loidl and F. Steglich, 1992b, *Z. Phys. B* **86**, 161.
- Kropp, H., W. Zipf, E. Dormann and K.H.J. Buschow, 1979, *J. Magn. & Magn. Mater.* **13**, 224.
- Lam, D.J., M.H. Mueller, A.P. Paulikas and G.H. Lander, 1971, *J. Phys. Colloq. (Paris)* **40**, C1-917.
- Lam, D.J., B.D. Dunlap, A.R. Harvey, M.H. Mueller, A.T. Aldred, I. Nowik and G.H. Lander, 1974, in: *Proc. Int. Conf. on Magnetism, ICM-73 (Nauka, Moscow)* p. 74.
- Lander, G.H., 1993, ch. 117, this volume.
- Lander, G.H., B.D. Dunlap, M.H. Mueller, I. Nowik and J.F. Reddy, 1973, *Int. J. Magn.* **4**, 99.
- Lander, G.H., A.T. Aldred, B.D. Dunlap and G.K. Shenoy, 1977, *Physica B* **86-88**, 1977.
- Lander, G.H., M.S.S. Brooks and B. Johansson, 1991, *Phys. Rev. B* **43**, 13672.
- Lea, K.R., M.J.M. Leask and W.P. Wolf, 1962, *J. Phys. & Chem. Solids* **23**, 1381.
- Lee, P.A., T.M. Rice, J.W. Serene, L.J. Sham and J.W. Wilkins, 1986, *Comm. Condens. Matter Phys.* **XII**, 99.
- Levy, P.M., and S. Zhang, 1989, *Phys. Rev. Lett.* **62**, 78.
- Litterst, F.J., J. Moser, W. Potzel, U. Potzel, G.M. Kalvius, L. Asch, J. Gal and J.C. Spirlet, 1986, *Physica B* **144**, 41.
- Liu, S.H., 1993, ch. 111, this volume.
- Mao, H.K., P.M. Bell, J.W. Shauer and D.J. Steinberg, 1978, *J. Appl. Phys.* **49**, 3276.
- Meeker, R.D., B.D. Dunlap and D. Cohen, 1976, *J. Phys. & Chem. Solids* **37**, 551.
- Mintz, M.H., U. Atzmony, Z. Hadari, S. Fredo and J. Gal, 1981, in: *Actinides 1981*, Report LBL-12441 (Lawrence Berkeley Laboratory) p. 158.
- Morss, L.R., and J. Fuger, eds, 1992, *Transuranium Elements, A Half Century* (American Chemical Society, Washington DC).
- Moser, J., W. Potzel, B.D. Dunlap, G.M. Kalvius, J. Gal, G. Wortmann, D.J. Lam, J.C. Spirlet and I. Nowik, 1981, in: *Physics of Solids Under High Pressures*, eds J.S. Schilling and R.N. Shelton (North-Holland, New York) p. 271.
- Moser, J., G.M. Kalvius and W. Zinn, 1988, *Hyperfine Interactions* **41**, 499.
- Mössbauer, R.L., 1958, *Z. Phys.* **151**, 124.
- Mullen, J.G., 1965, *Phys. Lett.* **15**, 15.
- Nellis, W.J., A.R. Harvey, G.H. Lander, B.D. Dunlap, M.B. Brodsky, M.H. Mueller, J.F. Reddy and G.R. Davidson, 1974, *Phys. Rev.* **9**, 1041.
- Norman, M.R., and D.D. Koelling, 1986, *Phys. Rev. B* **33**, 3803.
- Nowik, I., 1983, *Hyperfine Interactions* **13**, 89.
- Nowik, I., and I. Felner, 1977, *J. Phys. & Chem. Solids* **38**, 1031.
- Nowik, I., and H.H. Wickmann, 1966, *Phys. Rev. Lett.* **17**, 949.
- Nowik, I., S. Ofer and J.H. Wernick, 1966, *Phys. Lett.* **20**, 232.
- Nowik, I., B.D. Dunlap and J.H. Wernick, 1973, *Phys. Rev. B* **8**, 238.
- Ofer, S., I. Nowik and S.G. Cohen, 1968, in: *Chemical Applications of Mössbauer Spectroscopy*, eds V.I. Goldanskii and R.H. Herber (Academic Press, New York) p. 426.
- Potzel, U., J. Moser, W. Potzel, S. Zwirner, W. Schiessl, F.J. Litterst, G.M. Kalvius, J. Gal, S. Fredo, S. Tapuchi and J.C. Spirlet, 1989, *Hyperfine Interactions* **47**, 399.
- Potzel, W., 1990, *High-Pressure Research* **2**, 367.
- Potzel, W., J. Moser, G.M. Kalvius, C.H. de Novion, J.C. Spirlet and J. Gal, 1981, *Phys. Rev. B* **24**, 6762.
- Potzel, W., J. Moser, L. Asch and G.M. Kalvius, 1983, *Hyperfine Interactions* **13**, 175.
- Pound, R.V., and G.A. Rebka, 1959, *Phys. Rev. Lett.* **3**, 439.
- Röhler, J., D. Wohlleben, G. Kaindl and H. Balster, 1982, *Phys. Rev. Lett.* **49**, 65.
- Röhler, J., E. Dartyge, A. Fontaine, A. Jucha, K. Keulerz and D. Sayers, 1985, in: *EXAFS and Near Edge Structure III* (Springer, Berlin) p. 385.
- Rossat-Mignod, J., G.H. Lander and P. Burllet, 1984, in: *Handbook on the Physics and Chemistry of the Actinides*, Vol. 1, eds A.J. Freeman and G.H. Lander (North-Holland, Amsterdam) p. 452.



- Ruby, S.L., G.M. Kalvius, B.D. Dunlap, G.K. Shenoy, D. Cohen, M.B. Brodsky and D.J. Lam, 1969, *Phys. Rev.* **184**, 374.
- Sanchez, J.P., J.M. Friedt, G.K. Shenoy, A. Percheron and J.C. Achard, 1976, *J. Phys. C* **9**, 2207.
- Sanchez, J.P., J.M. Friedt, J. Rebizant, J.C. Spirlet and O. Vogt, 1985, *Proc. 15emes Journees des Actinides*, Liège, Belgium, unpublished.
- Sanchez, J.P., R. Poinsot, J. Rebizant, J.C. Spirlet and G.H. Lander, 1986, *Phys. Lett. A* **115**, 71.
- Sanchez, J.P., P. Burllet, S. Quézel, D. Bonnisseau, J. Rossat-Mignod, J.C. Spirlet, J. Rebizant and O. Vogt, 1988a, *Solid State Commun.* **67**, 999.
- Sanchez, J.P., J. Rebizant and J.C. Spirlet, 1988b, *Phys. Lett. A* **128**, 297.
- Sanchez, J.P., K. Tomala, J. Rebizant, J.C. Spirlet and O. Vogt, 1990, *Hyperfine Interactions* **54**, 701.
- Sanchez, J.P., A. Blaise, M.N. Bouillet, F. Bourdarot, P. Burllet, J. Rossat-Mignod, J. Rebizant, J.C. Spirlet and O. Vogt, 1991, in: *Proc. 21emes Journees des Actinides*, Montechoro, Portugal, unpublished.
- Sanchez, J.P., B. Lebech, M. Wulff, G.H. Lander, K. Tomala, K. Mattenberger, O. Vogt, A. Blaise, J. Rebizant, J.C. Spirlet and P.J. Brown, 1992, *J. Phys.: Condens. Matter* **4**, 9423.
- Sanders, P.G.H., and J. Beck, 1965, *Proc. R. Soc. A* **89**, 97.
- Schäfer, W., and G. Will, 1983, *J. Less-Common Met.* **94**, 205.
- Schäfer, W., G. Will, F.J. Litterst, W. Potzel, G.M. Kalvius, S. Fredo and J. Gal, 1987, *Inorg. Chim. Acta* **140**, 83.
- Schäfer, W., M. Gronefeld, G. Will and J. Gal, 1988, in: *Proc. Neutron Scattering Symp.* Sydney, Australia, *Mater. Sci. Forum* **27–28**, 243.
- Schäfer, W., G. Will, J. Gal and W. Suski, 1989, *J. Less-Common Met.* **149**, 237.
- Schäfer, W., G. Will, W. Potzel, G.M. Kalvius, I. Yaar, E. Arbaboff and J. Gal, 1992, *Physica B* **180–181**, 73.
- Schöppner, M., J. Moser, A. Kratzer, U. Potzel, J.M. Mignot and G.M. Kalvius, 1986, *Z. Phys. B* **63**, 25.
- Shenoy, G.K., and B.D. Dunlap, 1981, in: *Handbook of Spectroscopy*, Vol. 3, ed. I.W. Robinson (CRC Press, Boca Raton, FL) p. 476.
- Shenoy, G.K., and F.E. Wagner, eds, 1978, *Mössbauer Isomer Shifts* (North-Holland, Amsterdam).
- Shenoy, G.K., G.M. Kalvius, S.L. Ruby, B.D. Dunlap, M. Kuznietz and F.P. Campos, 1970a, *Int. J. Magn.* **1**, 23.
- Shenoy, G.K., B.D. Dunlap, G.M. Kalvius, A.M. Toxen and R.J. Gambino, 1970b, *J. Appl. Phys.* **41**, 1317.
- Shenoy, G.K., M. Kuznietz, B.D. Dunlap and G.M. Kalvius, 1972, *Phys. Lett. A* **42**, 61.
- Shenoy, G.K., F.E. Wagner and G.M. Kalvius, 1978, in: *Mössbauer Isomer Shifts*, eds G.K. Shenoy and F.E. Wagner (North-Holland, Amsterdam) p. 49.
- Staufer, D., and K. Binder, 1978, *Z. Phys. B* **30**, 313.
- Stevens, J.G., and V.E. Stevens, 1976, *Mössbauer Effect Data Index 1976* (Adam Hilger, London).
- Stewart, G.R., 1984, *Rev. Mod. Phys.* **56**, 755.
- Stewart, G.R., Z. Fisk, J.L. Smith, J.O. Willis and M.S. Wire, 1984, *Phys. Rev. B* **30**, 1249.
- Sticht, J., and J. Kübler, 1992, *Z. Phys. B* **87**, 299.
- Stone, J.A., and W.L. Pillinger, 1964, *Phys. Rev. Lett.* **13**, 200.
- Stone, J.A., and W.L. Pillinger, 1967, *Symp. Farad. Soc.* **1**, 77.
- Taneja, S.P., and C.W. Kimball, 1983, in: *Advances in Mössbauer Spectroscopy*, eds B.V. Thosar, P.K. Iyengar, J.K. Shrivasta and S.G. Bhargava (Elsevier, Amsterdam) ch. 15, p. 814.
- Thosar, B.V., P.K. Iyengar, J.K. Shrivasta and S.G. Bhargava, eds, 1983, *Advances in Mössbauer Spectroscopy* (Elsevier, Amsterdam).
- Trainor, R.J., M.B. Brodsky, B.D. Dunlap and G.K. Shenoy, 1976, *Phys. Rev. Lett.* **37**, 1511.
- Varma, C.M., 1976, *Rev. Mod. Phys.* **48**, 219.
- Visscher, W.M., 1960, *Ann. Phys. (NY)* **9**, 194.
- Wachter, P., F. Marabelli and B. Bucher, 1991, *Phys. Rev. B* **43**, 11136.
- Wastin, F., 1991, Ph.D. Thesis, University of Liège, Lab. Chim. Anal. et Radioch., unpublished.
- Watson, R.E., and A.J. Freeman, 1967, in: *Hyperfine Interactions*, eds A.J. Freeman and R.B. Frankel (Academic Press, New York) p. 53.
- Wegener, H., 1965, *Z. Phys.* **186**, 498.
- Wickmann, H.H., and G.K. Wertheim, 1968, in: *Chemical Applications of Mössbauer Spectroscopy*, eds V.I. Goldanskii and R.H. Herber (Academic Press, New York) p. 428.
- Willer, J., and J. Moser, 1979, *J. Phys. E* **12**, 886.
- Wulff, M., G.H. Lander, B. Lebech and A. Delapalme, 1989, *Phys. Rev. B* **39**, 4719.
- Yaar, I., S. Fredo, J. Gal, W. Potzel, G.M. Kalvius and F.J. Litterst, 1992, *Phys. Rev. B* **45**, 9765.
- Yeung, I., W. Ruan and R.M. Roshko, 1988, *J. Magn. & Magn. Mater.* **74**, 59.

Zänkert, J., U. Potzel, J. Moser, W. Potzel, Th. Obenhuber, M. Wunsch, G.M. Kalvius, J. Gal and U. Benedict, 1984, *High Temperatures-High Pressures* **16**, 533.  
Zimmer, H.G., K. Takemura and K. Syassen, 1984, *Phys. Rev. B* **29**, 2350.

Zinn, W., 1976, *J. Magn. & Magn. Mater.* **3**, 23.  
Zwirner, S., J.C. Spirlet, J. Rebizant, W. Potzel, G.M. Kalvius, C. Geibel and F. Steglich, 1992, in: *Proc. Int. Conf. on Strongly Correlated Electron Systems*, Sendai, Japan, *Physica B*, to be published.

## Chapter 117

# NEUTRON ELASTIC SCATTERING FROM ACTINIDES AND ANOMALOUS LANTHANIDES

**G. H. LANDER**

*Commission of the European Communities, Joint Research Centre, Institute for  
Transuranium Elements, Postfach 2340, D-76125 Karlsruhe, Federal Republic of  
Germany*

---

### Contents

Symbols	636	4.3.6.2. UAs–USe solid solutions	678
1. Introduction	636	4.3.6.3. USb–ThSb solid solutions	679
1.1. Nuclear scattering	639	4.3.7. Solid solutions containing transuranium cations	680
1.2. Magnetic scattering	640	4.3.7.1. NpAs–NpSe solid solutions	680
1.3. Separation of nuclear and magnetic scattering	641	4.3.7.2. NpSb–NpTe solid solutions	681
2. Structural effects	642	4.3.7.3. PuSb–PuTe solid solutions	681
2.1. The actinide metals	642	4.3.8. Concluding remarks – NaCl systems	681
2.2. Questions of stoichiometry	646	4.4. Trends in actinide magnetic structures	682
3. Magnetic form factors	647	4.4.1. Cubic intermetallics	682
3.1. Theoretical aspects	647	4.4.2. UTX compounds	684
3.2. Determination of ground-state wavefunctions	650	4.4.3. UT <sub>2</sub> X <sub>2</sub> compounds	686
3.3. Delocalized densities	652	4.4.4. Nature of the long-range order in heavy-fermion compounds	689
3.4. Spin and orbital contributions	656	4.5. Insulating actinide compounds	690
3.5. Application to mixed-valent states	659	4.6. Studies of spin glasses	691
3.6. Quenching of the orbital moment by hybridization	660	4.7. Measurements of magnetic anisotropy with neutrons	692
4. Magnetic structures	665	5. Magnetic critical scattering	694
4.1. Magnetic structure and neutron diffraction	665	5.1. Anisotropy of critical fluctuations	695
4.2. Multi- <i>k</i> structures	666	5.2. Comparison of critical exponents with theory	698
4.3. Magnetic structures of NaCl-type compounds	667	5.3. Dynamical aspects of critical scattering	698
4.3.1. General remarks	667	6. Summary	699
4.3.2. General comparisons between Ce and actinides	669	References	703
4.3.3. Actinide mononictides	670		
4.3.4. Actinide monochalcogenides	675		
4.3.5. Solid solutions – overview	676		
4.3.6. Uranium solid solutions	678		
4.3.6.1. UP–US solid solutions	678		

---

---

 Symbols

$b$	bound scattering length (eq. (3))	$\mu$	magnetic moment in Bohr magnetons ( $\mu_B$ )
$b_c$	coherent scattering length	$\mu_{cep}$	conduction-electron polarisation
$C_2$	coefficient of $\langle j_2 \rangle$ in form factor (eqs. (17) and (18))	$\mu_L$	orbital component of magnetic moment (eq. (20))
CDW	charge density wave	$\mu_S$	spin component of magnetic moment (eq. (20))
$f(Q)$	magnetic form factor (eq. (15))	$\sigma_a$	absorption cross section (eqs. (1), (6))
ILL	Institute Laue-Langevin, Grenoble, France	$\sigma_c$	coherent cross section (eq. (7))
$k$	wavevector of magnetic structure	$\sigma_{cap}$	absorption capture cross section (eq. (1))
$k_f$	final neutron wavevector	$\sigma_{fission}$	fission cross section (eq. (1))
$k_i$	initial neutron wavevector	$\sigma_i$	incoherent cross section (eq. (8))
$Q$	momentum transfer		
rlu	reciprocal lattice units		

---

## 1. Introduction

The merits of neutron radiation for condensed matter science are well known and enumerated in many textbooks on the subject (e.g. Marshall and Lovesey 1971, Bacon 1975, Squires 1978, Lovesey 1984, Price and Sköld 1986, and Balcar and Lovesey 1989). In brief, these are:

- (a) the wavelength of thermal neutrons is comparable to the separation between nuclei in crystals,
- (b) the neutron is a neutral particle and thus very penetrating,
- (c) the neutron–nuclei interactions depend in an irregular way on the atomic number of the nucleus, and are also isotope dependent,
- (d) the neutron has a magnetic moment that interacts with unpaired electrons in the solid,
- (e) the change in the energy of thermal neutrons due to inelastic scattering processes is frequently of the same order of magnitude as their initial energy.

The first property allows, using diffraction experiments, to probe the arrangement of the nuclei and, in conjunction with property (d), information to be obtained on the configuration of the unpaired electrons in the solid. Property (b) is particularly useful in allowing neutrons to examine materials under extreme conditions of temperature, pressure, etc. Furthermore, in the case of the actinides beyond uranium, the samples must be completely encapsulated, often more than once. The penetrating power of neutron beams has made it possible to examine materials up to Cm; in contrast, with surface-sensitive techniques, such as photoemission, one has barely started examining even Np compounds.

The irregular nature of the neutron–nuclei interactions (property (c)) means, for example, that the interactions with oxygen and uranium are similar for neutrons, but they are different for X-rays. In crystallographic studies with X-rays, actinide ions completely dominate so that the positions of light atoms are often a matter of guesswork. It will not be our objective in this chapter to cover the area of actinide

crystallography, but, especially with powder techniques, it is an active one. We will mention (sect. 2) a few studies of phase transitions and diffuse scattering, in particular those probing the movement of lighter atoms in an actinide structure.

The neutron–electron spin interaction is the most important as far as this chapter is concerned. It gives us information on the spatial extent of the unpaired electrons that contribute to the spin and orbital moments (sect. 3), the arrangements of magnetic moments in solids (magnetic structure, sect. 4) and the interesting correlation effects between magnetic moments that occur when materials are close to their ordering temperature (critical scattering, sect. 5).

A discussion of neutron inelastic scattering (property (e)) can be found in the chapters by Holland-Moritz and Lander and Aepli and Broholm in volume 19 in this series. Work up to about 1984 was reviewed by Buyers and Holden (1985).

Although the advantages of neutrons in understanding the microscopic properties of condensed matter are formidable, so are their disadvantages. First, their rarity – one needs either a high-flux reactor or a spallation source. Neither is routinely available on most university campuses. Second, their low intensity. Even today, with the developed technology, e.g., at the Institute Laue–Langevin in Grenoble, France, the most intense monochromatic beam incident on a sample rarely reaches  $10^8 \text{ n s}^{-1} \text{ cm}^{-2}$ . An equivalent flux of photons is readily available from an ordinary sealed X-ray tube. Synchrotron sources of X-rays can be more intense by as much as eight orders of magnitude. Moreover, neutron interactions are themselves much weaker than those between photons and electrons, so that vis-à-vis those encountered at synchrotrons the scattered neutron intensities are much smaller. However, their unique properties remain, so that the two techniques are truly complementary, despite the disparity in incident flux on the sample.

One way of making up for the intensity disadvantages (the weak interaction is not really a disadvantage – neutrons well obey the second Born approximation – since we can interpret the intensities without making complex multiple-scattering corrections) is by using larger samples, often by two orders of magnitude, for neutrons compared to those used in X-ray studies. For studies of polycrystalline cerium or uranium compounds this is not a serious problem, but it does become so for inelastic scattering, in which the quantities needed often exceed about 20 g, and poses particular problems for experiments on transuranium materials. Although safety and security concerns become important when gram samples of Np, Pu, and Am are present, such quantities simply do not exist for heavier elements. In some cases novel ways have been found to work with smaller samples – a good example being the work done on  $\sim 50 \text{ mg}$  samples of  $^{248}\text{Cm}$  oxides at Argonne National Laboratory. However, inelastic-scattering experiments on Am and heavier elements remain beyond our capability. The situation with respect to studies on single crystals is more positive, begging the question, of course, of how such crystals are to be prepared. For example, we report in this chapter complete studies on single crystals of  $\text{NpRu}_2\text{Si}_2$  of 2 mg.

A particularly serious disadvantage when performing neutron experiments on Eu, Sm, Gd, Np, and Pu compounds is the high *absorption* of the most abundant isotopes for thermal neutron scattering. The capture cross section,  $\sigma_{\text{cap}}$ , arises when neutrons are captured by the nucleus, which subsequently emits  $\gamma$ -rays. Because of resonance

TABLE 1

Properties of actinide isotopes useful in neutron studies.  $c$  is the abundance or for a radioactive element the half-life (in years) in parenthesis.  $b_c$  is the coherent scattering length (in fm,  $10^{-13}$  cm).  $\sigma_c$ ,  $\sigma_i$ ,  $\sigma_{cap}$ ,  $\sigma_{fission}$  (all in b =  $10^{-24}$  cm<sup>2</sup>) are the coherent, incoherent, capture, and fission cross sections, respectively. All refer to an energy of 25.3 meV, neutron velocity 2200 m/s, wavelength = 1.8 Å. (Adapted from Sears (1986).)

Element	Isotope	$c$	$b_c$	$\alpha_c$	$\sigma_i$	$\sigma_{cap}$	$\sigma_{fission}$
Th	232	100	10.0(10)	13.36(8)	0	7.4	0.04
Pa	231	( $3.3 \times 10^4$ )	9.1(3)	10.4(7)	0.1(3.3)	201	0
U			8.417(5)	8.90(1)	0.005(16)	3.6	4
	233	( $1.6 \times 10^5$ )	10.1(2)	12.8(5)	0.1(6)	37	538
	234	0.005	12.4(3)	19.3(9)	0	100	0.5
	235	0.720	10.47(4)	13.8(1)	0.2(2)	99	582
	238	99.275	8.402(5)	8.87(1)	0	2.7	0
Np	237	( $2.1 \times 10^6$ )	10.55(10)	14.0(3)	0.5(5)	162	0.02
Pu							
	238	(87.7)	14.1(5)	25(2)	0	547	16.5
	239	( $2.4 \times 10^4$ )	7.7(1)	7.5(2)	0.2(6)	269	743
	240	( $6.6 \times 10^3$ )	3.5(1)	1.5(1)	0	290	0.03
	242	( $3.8 \times 10^5$ )	8.1(1)	8.2(2)	0	18.5	<0.2
Am	243	( $7.4 \times 10^3$ )	8.3(2)	8.7(4)	0.3(2.6)	79	<0.1
Cm							
	244	(18.1)	9.5(3)	11.3(7)	0	14	1.2
	246	( $4.7 \times 10^3$ )	9.3(2)	10.9(5)	0	1.3	0.2
	248	( $3.5 \times 10^5$ )	7.7(2)	7.5(4)	0	4	0.34

effects, all the large capture cross sections in both the actinide and the rare earth nuclei are strongly energy dependent. Some useful numbers with respect to neutron-nuclei interactions are given in table 1. Of course, in the case of  $^{239}\text{Pu}$  (and  $^{235}\text{U}$ ) most of the total absorption  $\sigma_a$  (at a thermal neutron energy of 25.3 meV),

$$\sigma_a = \sigma_{cap} + \sigma_{fission}, \quad (1)$$

arises from the fission cross section, which is strongly dependent on energy. These problems of a high absorption may be avoided by selecting special isotopes, e.g.  $^{242}\text{Pu}$ , but this is expensive and difficult to obtain.

A remark on the fission cross section of uranium is in order here. U compounds are available to many workers and a large number of them has been examined at both reactor and spallation sources. Natural uranium has a fission cross section of  $\sim 4$  b, and even depleted U contains a measurable quantity of  $^{235}\text{U}$ . What this means, of course, is that when a beam of slow or thermal neutrons is incident on the sample, the fission process gives rise to *fast* neutrons. These are difficult to stop, thermalize in a variety of ways, and contribute to the background not only on the instrument being used, but, more embarrassing, often on neighboring instruments as well! The experimentalist should be aware of this problem, which becomes worse the lower the energy of the incident neutrons. In our experience care in the form of extra

shielding for fast neutrons should be taken with any sample containing  $> 1$  g of natural uranium. Time-of-flight spectrometers (such as at a spallation source) have an advantage, since the fission neutrons reach the detectors essentially instantaneously, and thus are separated from the scattered neutrons by the time of their arrival.

### 1.1. Nuclear scattering

The scattering of a neutron ( $\lambda \sim 10^{-8}$  cm) by a nucleus (radius  $10^{-13}$  to  $10^{-12}$  cm) may be regarded as an S-wave process, so that there is *no* angular dependence, and the interaction may be described by the so-called Fermi pseudopotential. In general, the scattering of a neutron by a single bound nucleus is described within the Born approximation by the Fermi pseudopotential,

$$V(r) = \left( \frac{2\pi\hbar^2}{m} \right) b \delta(r), \quad (2)$$

in which  $r$  is the position of the nucleus,  $m$  the neutron mass, and  $b$  the bound scattering length, which is in general complex

$$b = b' - ib''. \quad (3)$$

The effective scattering length must also take into account the interaction between the spin,  $s$ , of the neutron and that of the nucleus,  $I$ , so that

$$b = b_c + \frac{2b_i}{\sqrt{I(I+1)}} s \cdot I, \quad (4)$$

in which  $b_c$  and  $b_i$  are called the bound coherent and incoherent scattering length. The total scattering cross section is given by

$$\sigma_s = 4\pi \langle |b|^2 \rangle, \quad (5)$$

in which  $\langle \dots \rangle$  denotes a statistical average over the neutron and nuclear spins. The absorption cross section is given by

$$\sigma_a = \frac{4\pi}{k} \langle b'' \rangle, \quad (6)$$

where  $k$  is the length of the incident-neutron wavevector. Normally the nucleus is in an unpolarized state, so that the incoherent cross section does not enter into the absorption. If we restrict our discussions to non-polarized nuclei (in practice a finite nuclear polarization can be obtained only at very low temperatures,  $< 1$  K, and high fields), then the coherent scattering cross section is given by

$$\sigma_c = 4\pi |b_c|^2 = 4\pi \sum_j c_j |b_{c_j}|^2, \quad (7)$$

where  $c_j$  is the mole fraction of isotope  $j$  each with coherent scattering length  $b_{c_j}$ , and the incoherent scattering length is

$$\sigma_i = 4\pi \sum_{j \neq j'} c_j c_{j'} |b_{c_j} - b_{c_{j'}}|^2. \quad (8)$$

The coherent scattering arises from the so-called average nucleus and contains strong interference between waves scattered by each nucleus. For incoherent scattering there is no interference but only the sum of the contribution from each atom, arising from a random distribution of the deviations of the scattering lengths from their mean value. As can be seen from table 1, the incoherent scattering cross sections of actinide (and rare earth) nuclei are small. In both this chapter and that concerned with inelastic scattering (in vol. 19), we will not use the incoherent scattering, for us it represents an unwanted background, but the reader should be aware of the interest in this scattering, especially from hydrogenous materials.

The total coherent scattering cross section from one set of nuclei can now be expressed in terms of the coherent scattering length (see table 1), the position of the nuclei,  $\mathbf{R}_n$ , in the unit cell, and the scattering vector,  $\mathbf{Q}$ ,

$$(d\sigma/d\Omega)_{\text{coh}} = b_c^2 \left| \sum_n \exp(i\mathbf{Q} \cdot \mathbf{R}_n) \right|^2, \quad (9)$$

where  $\mathbf{Q} = \mathbf{k}_i - \mathbf{k}_f$ , and  $\mathbf{k}_i$  and  $\mathbf{k}_f$  are the initial and final neutron wavevectors, respectively. It is convenient to denote this quantity as the *nuclear structure factor*, where the sum is over all atoms in the unit cell

$$\begin{aligned} (d\sigma/d\Omega)_N &= \left| \sum_j b_j \exp(i\mathbf{Q} \cdot \mathbf{R}_j) e^{-w_j} \right|^2 \\ &= |F_N(\mathbf{Q})|^2, \end{aligned} \quad (10)$$

where  $e^{-w_j}$  is the Debye–Waller factor.

It is this intensity that will be measured in the nuclear Bragg peaks. As we remarked earlier, it does not decrease with  $|\mathbf{Q}|$ , apart from the Debye–Waller factor, and is insensitive to the polarization of the incident neutrons.

## 1.2. Magnetic scattering

This interaction is more complex than the nuclear scattering discussed above, and involves the neutron magnetic moment,  $\boldsymbol{\mu}_n$ , which has a magnitude given by the nuclear magneton times the gyromagnetic ratio of the neutron, and the magnetic field due to the combined spin and orbital current of the unpaired electrons around the nucleus. If the position of such an unpaired electron, with spin  $s_j$  and momentum  $\mathbf{p}_j$ , is given by  $\mathbf{r}_j$ , then we define the magnetic scattering amplitude as

$$a_M(\mathbf{Q}) = -\gamma_0 \boldsymbol{\sigma} \sum_j \left[ \hat{\mathbf{Q}} \times 2s_j \times \hat{\mathbf{Q}} + \frac{i}{hQ} (\mathbf{p}_j \times \hat{\mathbf{Q}}) \right] \exp(i\mathbf{Q} \cdot \mathbf{r}_j), \quad (11)$$

where  $\gamma_0 = 0.2696 \times 10^{-12}$  cm (or 2.696 fm),  $\boldsymbol{\sigma}$  is the Pauli spin matrix, and  $\hat{\mathbf{Q}}$  is the unit scattering vector. Note that the prefactor of 2.7 fm has the same order of magnitude as the nuclear scattering lengths (table 1), so that magnetic scattering is quite easy to observe with neutrons – unlike the case of X-rays (Balcar and Lovesey 1989).



The full evaluation of eq. (11) is a complex task; see, e.g., Marshall and Lovesey (1971) or Squires (1978). Instead of repeating this, we will simply adopt the so-called *dipole approximation*, which is valid for small  $Q$ -values. In principle, this works for all magnetic-structure determinations (sect. 4) and for critical scattering (sect. 5). For an examination of the form factors (sect. 3) it must be reconsidered.

Within the dipole approximation we find that the factor in brackets simplifies to

$$[\ ] \sim [\hat{Q} \times (2s_j + l_j) \times \hat{Q}], \quad (12)$$

where  $l_j$  is the orbital angular momentum of electron  $j$ . This is a clean result, which does not depend on the dipole approximation, and shows that the scattering in the forward direction ( $Q \rightarrow 0$ ) is directly proportional to the square of the total moment,

$$-\boldsymbol{\mu}_j = 2s_j + l_j.$$

The  $Q$ -dependence of the magnetic scattering depends on the Fourier transform of the magnetization density, in a similar way as the scattering factor in X-ray crystallography and its dependence on the charge density.

The vector product in eq. (12) gives important information in neutron scattering. We define a function

$$\boldsymbol{\mu}_\perp = \hat{Q} \times \boldsymbol{\mu} \times \hat{Q} = \boldsymbol{\mu} - (Q \cdot \boldsymbol{\mu})\hat{Q}, \quad (13)$$

where  $\boldsymbol{\mu}_\perp$  is the component of the total magnetic moment that is perpendicular to the scattering vector  $Q$ .

The magnetic scattering amplitude, eq. (11), thus becomes

$$a_M(Q) = \gamma_0 f(Q) \boldsymbol{\mu}_\perp,$$

and for a collection of atoms, in analogy with eq. (10) for nuclear scattering, we have

$$\begin{aligned} (d\sigma/d\Omega)_M &= \gamma_0^2 \left| \sum_j (\boldsymbol{\mu}_\perp)_j f_j(Q) \exp(iQ \cdot \mathbf{r}) e^{-w_j} \right|^2 \\ &= |F_M(Q)|^2. \end{aligned} \quad (14)$$

### 1.3. Separation of nuclear and magnetic scattering

Our discussion in the two previous sections has made it clear that both nuclear and magnetic interactions are present in neutron scattering. It may seem at first sight that it is difficult to separate the two, but, at least for elastic scattering (the subject of this chapter), it is relatively straightforward. The first point to make is that nuclear scattering occurs at all temperatures (up to the melting point) and is essentially independent of  $Q$ . Magnetic scattering, on the other hand, decreases sharply as  $Q$  increases, and appears only below the ordering temperature ( $T_N$  or  $T_C$ ) of the material. In the case of an antiferromagnet the repeating unit cell is usually (but not necessarily) different from the atomic cell; as a result new peaks appear in the scattering diagram. For a ferromagnet this is not the case, the nuclear and magnetic peaks overlap. By subtracting the low ( $T < T_C$ ) from the high ( $T > T_C$ ) temperature data an estimate of the magnetic scattering can be made. A more sophisticated method uses eq. (11),

which tells us that the magnetic-scattering amplitude depends on the spin of the neutron; thus by using polarized incident neutrons and changing their spin we can reverse the sign of  $F_M(\mathbf{Q})$ , and thus can separate it from  $F_N(\mathbf{Q})$ , which is independent of the neutron spin.

In special cases, e.g., when weak nuclear peaks may arise from magnetoelastic distortions, the separation of magnetic and nuclear Bragg peaks may be difficult, but in the vast majority of cases it does not constitute a problem. This is different from the case of inelastic scattering; in that case, as we will see, the separation is often difficult.

## 2. Structural effects

The two areas of solid-state physics in which neutrons have played an overwhelming role are studies of magnetism and of structural phase transitions. This chapter is replete with examples of magnetism, but the number of purely structural effects that we will discuss is relatively small. An example of the latter is the phase transition to an incommensurate state in  $\text{ThBr}_4$  found by Bernard et al. (1983). More recently, examples of phasons and amplitudons have been measured in this material (Currat 1989). Interesting effects are found at high temperatures in single crystal studies of the actinide oxides (Clausen et al. 1984, 1985), and, recently, a series of unusual phase transitions have been found in the actinide organometallic compound  $\text{U}(\text{C}_5\text{H}_5)_3\text{Cl}$  below room temperature (Raison et al. 1992). In this latter case the fragile packing of the large molecules suggests that many such phase transitions will be found in related compounds when the kinetic energy of the proton motion is reduced at low temperature. However, in none of these examples is it yet clear what, if any, role is played by electronic forces, so we shall not discuss these transitions any further.

### 2.1. *The actinide metals*

One of the themes developed in this chapter, and many others, is the importance of bonding or hybridization effects in actinide systems. We encounter these “bonding” phenomena immediately in the discussion of the early actinide metals U, Np, and Pu. For a more complete theoretical discussion of this aspect see Brooks et al. (1984, and references therein) and for effects of pressure on the metals see Benedict (1987) and chapter 113 in this volume. The unusual structure of  $\alpha$ -U (fig. 1) occurs in other actinide metals (and cerium) when they are put under pressure, and it is commonly assumed that it represents a structure in which the 5f electrons are participating in the bonding. For complete crystallographic details see Donohue (1974). Some details are also given in Rossat-Mignod et al. (1984), p. 429 et seq. It is for this reason that the *low-temperature phase transitions* found in  $\alpha$ -U are so interesting. The kinds of experiments described below can only be performed on single crystals, and for other actinides (or Ce under pressure) such samples do not exist. Thus, it is possible, but not proven, that a charge density wave (CDW) such as found at low temperature in  $\alpha$ -U will exist also in the other materials.

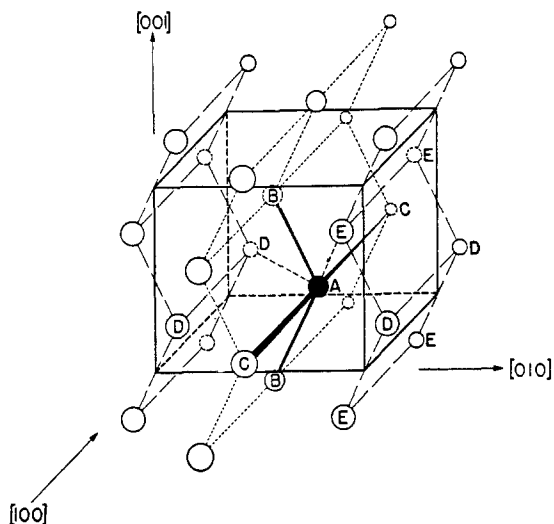


Fig. 1. Structure of  $\alpha$ -U (orthorhombic A20, Cmcm). The distances are  $d_1(AB) = 2.75 \text{ \AA}$ ,  $d_2(AC) = 2.85 \text{ \AA}$ ,  $d_3(AD) = 3.26 \text{ \AA}$ ,  $d_4(AE) = 3.34 \text{ \AA}$ . The CDW has its main motion along  $[100]$  of  $\epsilon = 0.03 \text{ \AA}$ . (Figure taken from Fisher and Dever (1968).)

The history of  $\alpha$ -U is a long and complicated saga that merits a special review (Fisher, Lander, and Bader, to be published). Reviews on the elastic-constant anomalies (Fisher 1974), superconductivity (Smith and Fisher 1973), and structural effects discovered up to 1984 (Smith and Lander 1984) are already available. Briefly, all physical-property measurements show an anomaly at  $\sim 43 \text{ K}$ , and many show subsequent anomalies at 37 and 22 K. The phase diagram under pressure of  $\alpha$ -U is given in fig. 2. At low temperature, i.e. below the solid line,  $\alpha$ -U is a superconductor. Assigning the phases  $\alpha_1, \alpha_2, \alpha_3$  as we have done in the caption in fig. 2, may not be correct since, strictly speaking, the phase boundaries have been determined at zero pressure

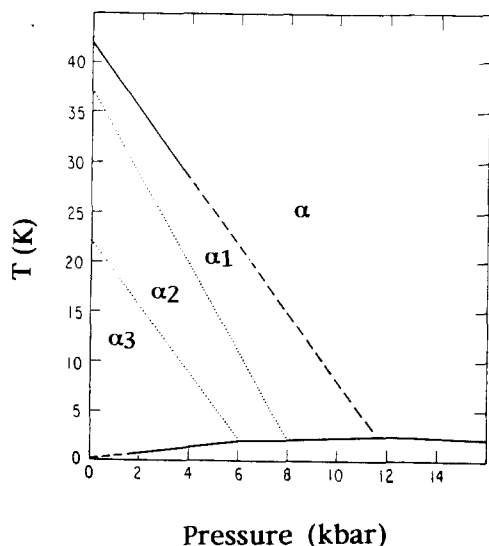


Fig. 2. Phase diagram of uranium at low temperatures (taken from Smith and Fisher 1973). The  $\alpha$  state is the normal orthorhombic structure. In the  $\alpha_1$  state all components  $q_x, q_y,$  and  $a_z$  of the CDW are incommensurate. In the  $\alpha_2$  state  $q_x = \frac{1}{2}$ . In the  $\alpha_3$  state  $q_x = \frac{1}{2}$  and  $q_y = \frac{1}{6}$ . At the lowest temperatures, i.e. below the solid line,  $\alpha$ -U is a superconductor.

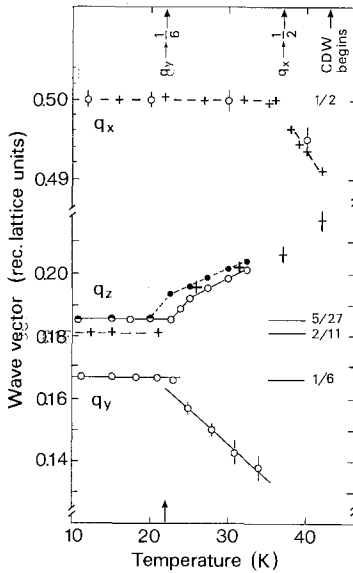


Fig. 3. Evolution of  $q_x$ ,  $q_y$ , and  $q_z$  as a function of temperature as measured using neutrons (solid and open points, Marmeggi et al. (1990)) and X-rays (crosses, Grübel et al. (1991)). Some of the hysteresis effects above 22 K are indicated by the solid (cooling) and open (heating) points. The commensurate values of the wavevector are indicated by the fractions on the right-hand side.

only. The variation of these components of the CDW are shown in fig. 3. It is worth noting that the values of  $q_z$  determined using X-rays and neutrons are slightly different. We shall come across this phenomenon again in connection with determining the wavevectors in magnetic materials. Although there is no proven explanation, the fact that X-rays have such a high absorption in actinides naturally leads to the suggestion that they are more sensitive to surface effects, and that the bulk properties are better measured with neutrons. In the case of uranium it would be interesting to increase the X-ray energy (and thus increase the penetration) and see whether the neutron value of  $q_z$  is obtained.

In addition to the unusual behavior of the  $q_z$ -component of the CDW wavevector, higher harmonics have also been found in the diffraction pattern of  $\alpha$ -U. We show in fig. 4 harmonics up to the ninth order as observed by Marmeggi et al. (1990) with neutrons at the D-10 instrument at ILL. The difference between the very weak ninth peak and the strong nuclear peaks is six orders of magnitude. It is quite amazing that coherent elastic effects can exist over such a dynamic range. The presence of higher harmonics suggests the occurrence of squaring of the initially sinusoidal atomic displacement. However, Marmeggi et al. (1990) have shown that the intensities of the higher harmonics are insufficient to result in a perfect square wave; moreover, the widths of the higher harmonics also suggest that they have a limited coherence length, which itself depends on the order of the harmonic. We shall see later that some of these diffraction effects are found also in complex magnetic structures.

The different values of  $q_z$  found for neutrons ( $\frac{5}{27}$ ) compared to X-rays ( $\frac{2}{11}$ ), but both being rational fractions, led Grübel et al. (1991) to consider a slightly different model for the CDW modulation, in which “phase-slips” lead to faults in the regular CDW displacement. The higher harmonics can then be thought of as peaks arising from these fault regions in the structure. This is a conceptually rather different model

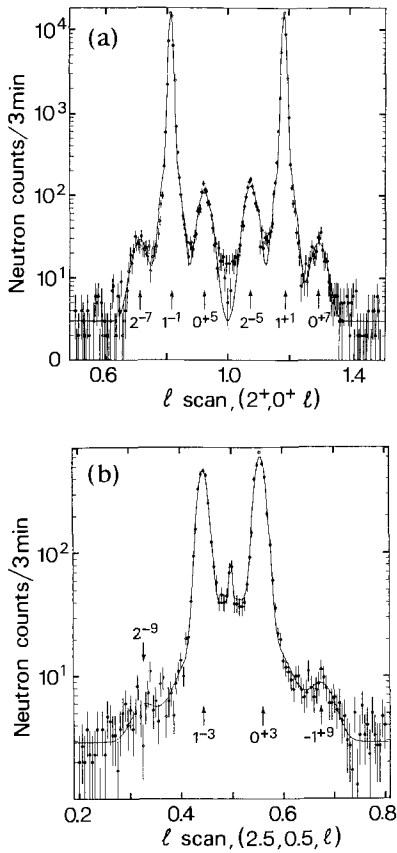


Fig. 4. Scans along the  $l$  direction in  $\alpha$ -U as reported by Marmeggi et al. (1990). (a) Scan showing first-, fifth- and seventh-order harmonics of the CDW modulation at 15 K. (b) Scan showing the third- and ninth-order harmonics. The small sharp peak in the center of this last scan is from the  $\frac{1}{2}\lambda$  component of the incident neutrons. Note the logarithmic scale of the intensity.

from that introduced by Marmeggi et al. (1990). In fact it is clear that neither model fully describes the diffraction patterns seen in  $\alpha$ -U, but both are good approximations for starting the discussion.

The CDW distortion corresponds to a new unit cell which is larger by a factor  $2a \times 6b \times (\sim 6c)$ . The “coherence” distances for these displacements are clearly very long, indicating that important forces are present. Indeed, one of the unfortunate aspects of the  $\alpha$ -U story is that, whereas we understand the diffraction pattern in considerable detail, we still do not understand “why” the CDW is formed. Our conventional picture of a CDW is that electronic forces arising from the spatial arrangement of the conduction-electron wavefunctions require a slightly different configuration to minimize their energy than the configuration arising from purely electrostatic forces between the atoms and the core-electron cloud. At high temperatures the thermal energy is sufficient so that this “confrontation of requirements” can be avoided, but as the atomic vibrations reduce in amplitude a CDW is the most acceptable compromise. The intermediaries for this compromise between electronic and electrostatic (and elastic) forces are the phonons. The dispersion curves (Crummett et al. 1979) clearly show the presence of an instability along the  $[100]$  direction, and

it is this mode that condenses at low temperature to give the doubling of the unit cell in the [100] direction, which is the principal motion ( $\sim 0.03 \text{ \AA}$ ) of the atoms in the CDW. The interatomic distances in  $\alpha$ -U are quite short (well below the Hill limit for example) and it might be tempting to invoke some bond-charge model for the CDW state. In fact, as can be seen in fig. 1, the CDW motion along [100] changes more drastically the second nearest-neighbor distance, and it leaves the first unaltered. To make further progress in our understanding we clearly need band-structure calculations and de Haas-van Alphen experiments. A good start has been made on both (Arko et al. 1985), but a full picture is not available.

Although there are a number of details about the CDW that are not yet understood (see original papers of Grübel et al. (1991) and Marmeggi et al. (1990) for details), probably the most interesting question left to answer concerns the nature of the superconductivity in  $\alpha$ -U. As shown in fig. 2,  $T_c$  increases with pressure with an initial derivative  $dT_c/dP \sim 0.2 \text{ K/kbar}$ , which was greater than any material until the discovery of high- $T_c$  superconductors. Another unusual feature of  $\alpha$ -U is that the isotope effect is positive, i.e.  $T_c \propto M^2$  (Fowler et al. 1967), whereas the conventional BCS superconductor has  $T_c \propto M^{-1/2}$ . A detailed discussion of these effects and their possible electronic origin was given by Bader et al. (1975). At that time the CDW was not yet discovered in  $\alpha$ -U (this happened in 1980), so that the authors spend considerable effort to demolish the "magnetic" model, which was then in vogue to explain the low-temperature phase transitions in  $\alpha$ -U. It does appear from their arguments that a combination of unusual phonon and electronic properties might explain the anomalies, but detailed arguments have not yet been given. One statement that fig. 2 implies is that the superconductivity and the CDW state exist simultaneously. We have no proof of that.

We have dealt at length with the  $\alpha$ -U story because it illustrates aptly the complexity of actinide research when the 5f electrons participate in the bonding. Suitable samples for this level of sophisticated research do not yet exist for Np or Pu (or Ce under pressure), but it is safe to predict that a similar complex story will emerge when they do become available. A start has been recently made by looking at Pu metal at low temperature with neutrons (Lawson et al. 1991), but, although the use of polycrystalline samples was sufficient to solve the structure of  $\beta$ -U (stable between 935 and 1045 K) by Lawson et al. (1988), this is unlikely to be the case for Pu at low temperature. Our experience with  $\alpha$ -U has shown the necessity of using single crystals to probe the subtleties of the interactions between the electronic and lattice effects at low temperature.

## 2.2. Questions of stoichiometry

The sensitivity of neutrons to light atoms in the presence of heavier ones has made this technique of special interest in the study of actinide defect structures. This subject is somewhat tangential to the scientific area covered in this review, so we will just mention the large body of work on  $\text{UO}_2$  and  $\text{ThO}_2$  (Clausen et al. 1984, 1989) and on defect  $\text{UO}_{2.13}$ . Most of the measurements have been done at high temperature, up to  $\sim 2700 \text{ K}$  in the case of  $\text{UO}_2$ , and give information on the elastic constants

and the Frenkel anion disorder which is thermally induced for  $T > 2000$  K. In the case of  $\text{UO}_{2.13}$  the diffuse scattering measured on a single crystal is consistent with the earlier model proposed by Willis (1978) from diffraction data. Much of this work forms part of an extensive effort on fluorite materials, discussed at length by Hutchings et al. (1984) and Hutchings (1987).

A long standing problem in the science of actinide oxides has been the susceptibility and properties of  $\text{CmO}_2$ . Assuming Cm is tetravalent  $\text{Cm}^{4+}$ , then it should be in a  $5f^6$ , i.e.  $J = 0$ , ground state. The susceptibility at low temperature should be flat, since the gap to the first excited,  $J = 1$ , state is  $\sim 2500 \text{ cm}^{-1}$  ( $\sim 3600$  K). Instead, many different studies of  $\text{CmO}_2$  in the past have found a sloping susceptibility, corresponding to  $\mu_{\text{eff}} \sim 3\mu_{\text{B}}$ . Since  $\text{Cm}^{3+}$  has a  $5f^7$  ground state with  $J = \frac{7}{2}$  and a magnetic moment of  $7\mu_{\text{B}}$ , it has always been assumed that the  $\mu_{\text{eff}}$  measured in  $\text{CmO}_2$  arises from a certain amount ( $\sim 20\%$  in the case of  $\mu_{\text{eff}} \sim 3\mu_{\text{B}}$ ) of  $\text{Cm}^{3+}$  impurity. However, the sample should then be substoichiometric,  $\text{CmO}_{1.9}$ , and possibly show some superstructure in the oxygen sublattice. Although one earlier neutron experiment with Cm had been performed (Lander and Mueller 1971), it used the highly radioactive isotope  $^{244}\text{Cm}$ . For studies of the stoichiometry the much longer living isotope  $^{248}\text{Cm}$  ( $^{244}\text{Cm}$   $t_{1/2} = 18$  y,  $^{248}\text{Cm}$   $t_{1/2} = 4.4 \times 10^5$  y) was available and a neutron experiment (Morss et al. 1989) was performed at the spallation source at Argonne National Laboratory. The mass of the polycrystalline sample was 55 mg, so that the precision of the experiments was not extremely high. Adding to the difficulties was the spontaneous emission of neutrons (mainly from trace impurities of  $^{252}\text{Cf}$ ), which added substantially ( $\sim 30\%$  extra) to the background scattering. Nevertheless, Morss et al. (1989) did see scattering from the sample and they were able to use the Rietveld method to analyze the results. They found no evidence of any additional peaks in the pattern, nor any significant deviation from stoichiometry. The mystery of why such a large  $\mu_{\text{eff}}$  is found in  $\text{CmO}_2$  thus remains.

### 3. Magnetic form factors

As we discussed in the introduction, the fact that neutrons are scattered magnetically from the spin and orbital components, which have a finite spatial distribution, means that, unlike in the case of nuclear scattering, there is an angular dependence of the magnetic scattering. We call this angular dependence the magnetic form factor, and it is the exact analogue of the scattering factor for X-rays. Since it is related to the spatial extent of the unpaired electrons, studies of it have been particularly useful in elucidating the ground-state wavefunctions in both d and f electron systems.

#### 3.1. Theoretical aspects

A detailed discussion of this subject already exists in textbooks (Marshall and Lovesey 1971, Balcar and Lovesey 1989) as well as in the chapter by Rossat-Mignod et al. (1984). We recapitulate here to make a few points necessary for our discussion.

The scattering-amplitude operator is given by eq. (11)

$$a_{\mathbf{M}}(\mathbf{Q}) = -\gamma_0 \boldsymbol{\sigma} \sum_j \left[ \hat{\mathbf{Q}} \times 2s_j \times \hat{\mathbf{Q}} + \frac{i}{\hbar Q} (\mathbf{p}_j \times \hat{\mathbf{Q}}) \right] \exp(i\mathbf{Q} \cdot \mathbf{r}_j),$$

where  $\gamma_0 = \gamma e^2 / (2mc^2) = 0.2696 \times 10^{-12}$  cm,  $\gamma$  is the gyromagnetic ratio of the neutron,  $\boldsymbol{\sigma}$  is the Pauli spin matrix,  $\hat{\mathbf{Q}}$  is the unit scattering vector, and  $s$  and  $p$  are the spin and momentum of electron  $j$ , which is at position  $\mathbf{r}_j$ . To evaluate this completely requires an excursion into tensor algebra which we shall avoid here, simply referring to Balcar et al. (1970), Lander and Brun (1970), Marshall and Lovesey (1971), Stassis and Deckman (1975, 1976), and Balcar and Lovesey (1989). Instead, we will immediately proceed to the dipole approximation, which is valid in most practical cases. An explanatory comment is required here. To calculate the full cross section we need to be able to write down the electron wavefunction  $|\psi_e\rangle$  in terms of the  $L$  and  $S$  component wavefunctions. This is possible (so far) *only* with strictly localized systems, e.g. the heavy lanthanides. We shall give some examples of this approach. Difficulties arise when hybridization of the wavefunctions occurs and no description of  $|\psi_e\rangle$  in the  $|\alpha SLM\rangle$  basis can be readily constructed. For these cases, which are invariably the most interesting, we have to resort to the dipole approximation. The dipole approximation, as its name implies, is characterized by the symmetry and selection rules for a tensor of rank one. This limits the expansion in terms of spherical harmonics  $Y_{lm}(\mathbf{Q})$  to terms with  $l = 0$ . It is valid exactly for  $Q = 0$  but not for high  $Q$ . Nevertheless it is a useful place to start. Within the dipole approximation the operator in brackets becomes, see eq. (12),

$$a_{\mathbf{M}}(\mathbf{Q}) \approx -\gamma_0 \boldsymbol{\sigma} \sum_j [\hat{\mathbf{Q}} \times (2s_j + l_j) \times \hat{\mathbf{Q}}] \exp(i\mathbf{Q} \cdot \mathbf{r}_j),$$

where we recover the well-known fact that the scattering of neutrons is proportional to the total moment, the spin plus orbital components,

$$d\sigma/d\Omega \propto (\mu)^2,$$

where values of  $\mu$  are expressed in Bohr magnetons and where  $\mu = \mu_S + \mu_L$ . In Russell–Saunders coupling  $\mu = gJ$ , where  $g$  is the Landé splitting factor. This total moment is an integration over the spatial extent of the magnetization,  $M(\mathbf{r})$ , so that

$$\boldsymbol{\mu} = \int M(\mathbf{r}) d\mathbf{r}.$$

We should remember here that magnetization densities are, in principle, vector quantities,  $M(\mathbf{r})$ , since their direction as well as magnitude may change. Calculations within the  $|\alpha SLJ\rangle$  basis, i.e. for localized systems, show that these vectorial aspects are small, i.e., that the direction of the moment may be factored out of the magnetization density. For more complicated cases no theoretical estimates exist, so we neglect the possible complication in interpreting the experimental results. No doubt interesting effects along this line will be found in future investigations.

The form factor is then defined as

$$f(\mathbf{Q}) = \int M(\mathbf{r}) e^{i\mathbf{Q} \cdot \mathbf{r}} d\mathbf{r}, \quad (15)$$



where we recognize that  $M(\mathbf{r})$  has two components, the spin and the orbital contribution,  $M_S(\mathbf{r})$  and  $M_L(\mathbf{r})$ , respectively.

In certain cases, especially calculations starting from the density-functional approach, the magnetization density may be calculated directly and can then be compared with experiment. However, with the  $|\alpha SLJM\rangle$  basis representation it is possible to use standard tensor algebra to calculate the full cross section, including its angular dependence. This technique, first developed by Johnston (1966), is particularly useful for f electrons, for which the first approximation can usually be with Russell–Saunders coupling. The results may be expressed as coefficients of terms  $Y_{lm}(\Theta, \Phi) \langle j_i(Q) \rangle$ . The spherical harmonics  $Y_{lm}(\Theta, \Phi)$  are functions of the angle  $\Theta$  between the moment direction,  $\boldsymbol{\mu}$ , and the scattering vector,  $\mathbf{Q}$ , and the angle  $\Phi$  defines a direction in the plane perpendicular to  $\boldsymbol{\mu}$  (the azimuthal angle). The  $\langle j_i(Q) \rangle$  are given by

$$\langle j_i(Q) \rangle = \int_0^\infty U^2(r) j_i(Qr) dr, \quad (16)$$

where  $U^2(r)$  is the probability distribution of the radial part of the 5f single-electron wavefunction, such that

$$\int_0^\infty U^2(r) dr = 1,$$

and  $j_i(Qr)$  is the usual spherical Bessel function. The radial  $\langle j_i \rangle$  integrals obtained with Dirac–Fock solutions for  $U^{4+}$  are shown in fig. 5. A complete set of these integrals

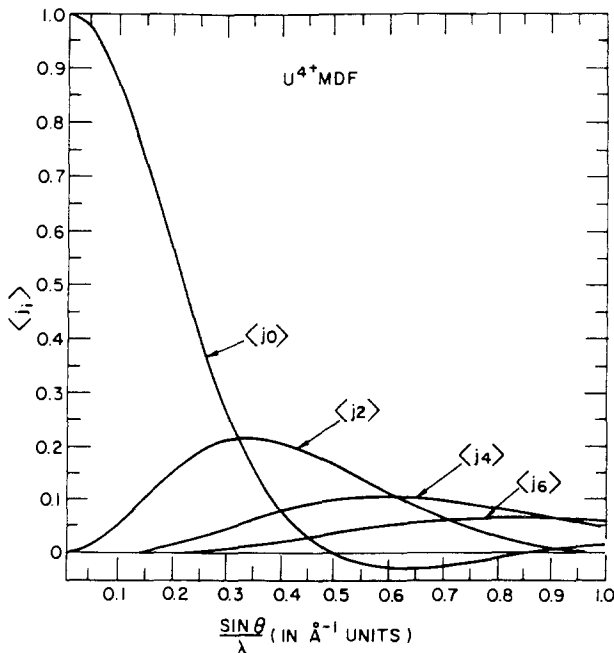


Fig. 5. Radial integrals  $\langle j_i \rangle$  obtained for  $U^{4+}$ . (Taken from Desclaux and Freeman (1984).)

is given in Desclaux and Freeman (1984). These integrals do not vary greatly for the f elements, although  $\langle j_0 \rangle$  falls faster with  $Q$  for the 5f than for the 4f electrons, and the maximum in  $\langle j_2 \rangle$  is at a slightly smaller  $Q$  for the 5f electrons.

The result of this approach is that we may write

$$f(\mathbf{Q}) = \langle j_0 \rangle + C_2 \langle j_2 \rangle + C_4 \langle j_4 \rangle + C_6 \langle j_6 \rangle, \quad (17)$$

where the coefficients  $C_i$  are functions of  $(\Theta, \Phi)$  but *not* of  $Q$ .

In the dipole approximation

$$C_2 = \frac{J(J+1) + L(l+1) - S(S+1)}{3J(J+1) + S(S+1) - L(L+1)}, \quad (18)$$

where we assume, again, that an *SLJ* basis for  $|\psi_e\rangle$  can be used. This has a close connection to the Landé  $g$ -factor. In fact,  $C_2 = (2 - g)/g$ , so that if  $g = 2$  (spin-only magnetism),  $C_2 = 0$ , so that the spin form factor

$$f_S(Q) \approx \langle j_0 \rangle.$$

For  $g = 1$  (orbit-only magnetism),  $C_2 = 1$ , so that the orbital form factor is given by

$$f_L(Q) \approx \langle j_0 \rangle + \langle j_2 \rangle.$$

### 3.2. Determination of ground-state wavefunctions

The full form factor, eq. (17) above, contains terms in  $\langle j_2 \rangle$  and  $\langle j_4 \rangle$  that give a measurable anisotropy when measurements are done with sufficient precision. By "measurable anisotropy" we mean that  $f(\mathbf{Q}_1) \neq f(\mathbf{Q}_2)$  even though  $|Q_1| = |Q_2|$ . This is well-illustrated in fig. 6, which is taken from the work of Boucherle and Schweizer (1985). It gives a theoretical example of the form factors calculated for the two different ground states of a  $\text{Ce}^{3+}$  ion in a cubic environment. The anisotropy of the form factor is clearly much greater when the  $\Gamma_7$  ground state is present. An experimental example is provided by the data (fig. 7) on the system  $\text{CeAl}_2$ . Here the  $\text{Ce}^{3+}$  state is split into a  $\Gamma_8$  quartet and a  $\Gamma_7$  doublet by the crystal field. Neutron inelastic scattering can provide information on the energy difference between the levels, but, if only two levels are present, it cannot be used to determine the ground state. The form factor data shown unambiguously that  $\Gamma_7$  is the ground state.

Similar examples occur for the actinides. For example, in the case of USb (Lander et al. 1976) the ground state was found to be a  $\Gamma_8$  quartet, but with a major component  $|M = \frac{7}{2}\rangle$ . Such a wavefunction has an oblate shape (like the magnetization density shown in the top inset of fig. 6 and favours a  $\langle 111 \rangle$  easy magnetization axis. At the time this measurement was not understood, since it was thought that the easy axis was  $\langle 100 \rangle$ . Subsequently, Rossat-Mignod et al. (1984) showed that USb has the  $3k$  magnetic structure (see sect. 4), in which the moments do, in fact, point along alternating  $\langle 111 \rangle$  axes. It is also now believed (Hu et al. 1988) that hybridization effects in USb (and other actinide and cerium systems) result in the ground-state wavefunction being oblate in shape.

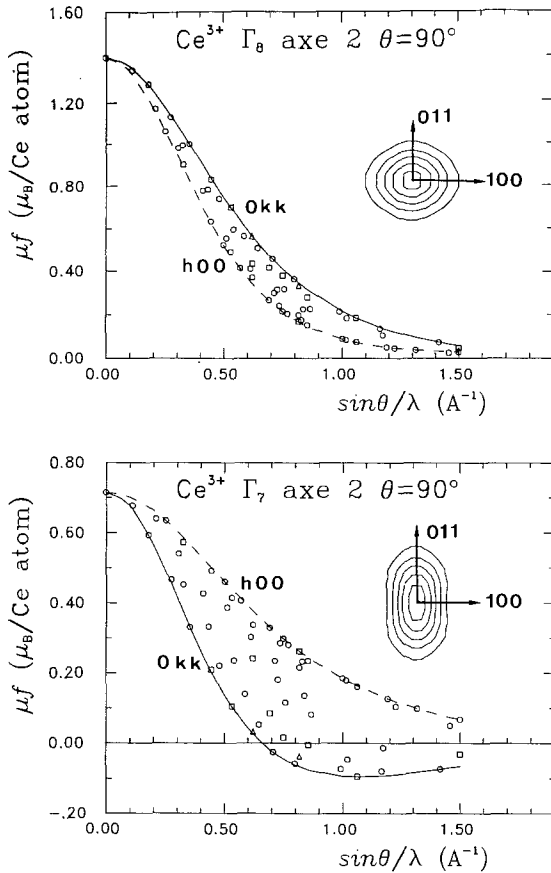


Fig. 6. Calculation of the magnetic form factors and (inset) magnetization density for a [011] projection for the two states  $\Gamma_8$  (above) and  $\Gamma_7$  (below) for  $\text{Ce}^{3+}$ . The full lines correspond to (0kk) reflections and the dashed to (h00) ones. (Taken from Boucherle and Schweizer (1985).)

Another good example is the measurements on PuSb (Lander et al. 1984, 1985), which are shown in fig. 8. These measurements unambiguously showed that the ground state is  $\Gamma_8$ , with again an oblate-shaped magnetization density, whereas the compound SmSb has a  $\Gamma_7$  ground state, which is prolate. In both PuSb and SmSb the cations are trivalent with five f electrons. Hybridization effects in PuSb (Hu et al. 1988) have also been used to explain the large anisotropy found in PuSb (Cooper et al. 1983).

Unfortunately, in many compounds of interest the form factor exhibits considerably less anisotropy than the examples shown in figs. 6–8. The difficulty then is to be certain that the ground-state wavefunction can properly be represented in the  $|SLJ\rangle$  basis. An early example is US, measured by Wedgwood (1972). No doubt to his disappointment, he measured a form factor that showed an almost steadily smooth decrease as a function of  $Q$ . A similar situation was found by Busch et al. (1979) in studies of the ferromagnets UTe and  $\text{USb}_{0.8}\text{Te}_{0.2}$ , and is also evident in the measurements on CeSb (Boucherle and Schweizer 1985) and CeTe (Boucherle et al. 1982a). In all these materials, particularly the uranium compounds, there is remarkably

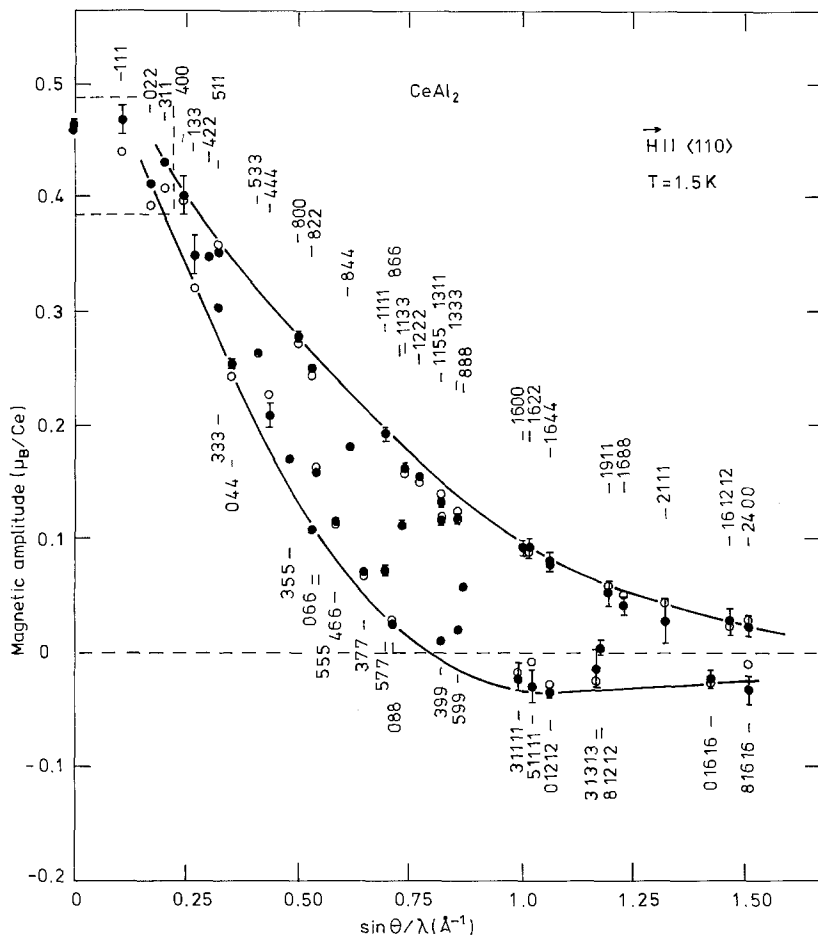


Fig. 7. Form factor of  $\text{CeAl}_2$  ( $T = 1.5$  K,  $H = 4.65$  T  $\parallel$  [011]). Solid points are observations, open points are calculations with the  $\Gamma_7$  ground state. (Taken from Boucherle and Schweizer (1985).)

little anisotropy in the form factor, and it is not possible to uniquely define the ground state. Models can be set up to describe the data, and sometimes they fit very well, but we have to ask the question of whether  $|\psi_c\rangle$  is more complex than considered and, in particular, whether any  $|\alpha SLJ\rangle$  description is appropriate.

### 3.3. Delocalized densities

We saw in eq. (15) that the form factor is sensitive to the total magnetization density in the unit cell. The most accurate method employed for measurements involves using a beam of polarized neutrons to measure the interference between nuclear and magnetic scattering at Bragg peaks (Nathans et al. 1959, Brown et al. 1980). The smallest  $Q$ -value,  $Q_{\min}$ , is therefore given by the longest d-plane spacing in the solid.

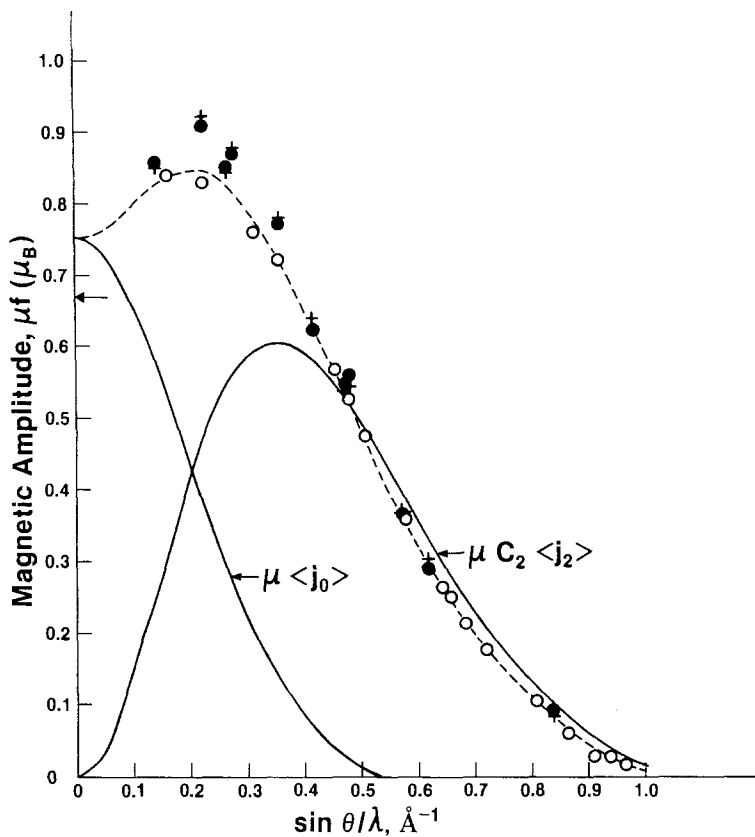


Fig. 8. The magnetic amplitude as a function of  $\sin \theta/\lambda$  ( $= Q/4\pi$ ) for ferromagnetic PuSb at 10 K. The individual values of  $\mu \langle j_0 \rangle$  and  $\mu C_2 \langle j_2 \rangle$  are shown as well. The value of  $C_2$  is 3.8. The open points are fit with the broken line. The solid points correspond to reflections that exhibit anisotropy and have an additional contribution in  $\langle j_2 \rangle$ . They are fit with the crosses, showing unambiguously that  $\Gamma_8$  is the ground state. The arrow on the ordinate axis shows the total moment derived from the magnetization. (From Lander et al. (1984).)

However, if we consider a plane-wave state with a spatially very extended wavefunction, then its form factor may well drop to a small value at  $Q_{\min}$ . Such a situation is the case for 6d states, as illustrated in fig. 9. It is clear, therefore, that if an appreciable amount of the magnetization density is 6d-like, then it will not be seen in form-factor measurements that are dependent on Bragg scattering. Such a density will, of course, be picked up by bulk magnetization techniques since then an integration over the whole unit cell is performed.

Similar effects have been found in the transition metals (Mook 1966) and in the heavy lanthanides (see, e.g., measurements on gadolinium by Moon et al. 1972). In actinide systems (so far) the spatial extent of the delocalized electrons, presumably with 7s and/or 6d nature, is sufficiently great that they have not been seen directly in form-factor measurements. The case of PuSb, shown in fig. 8, is typical, the

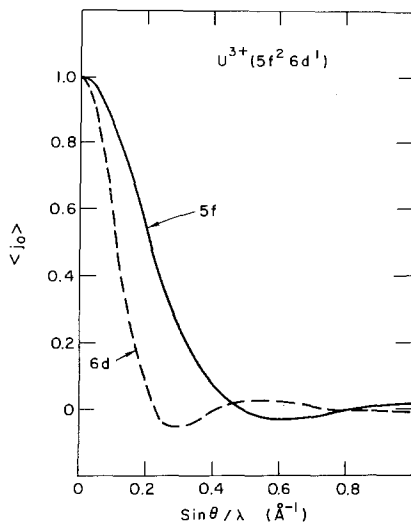


Fig. 9. Comparison of  $\langle j_0 \rangle$  for the 5f and 6d electrons in the configuration  $U^{3+}(5f^2, 6d^1)$  (From Freeman et al. (1976).)

magnetization value,  $\mu_{\text{mag}}$ , being lower than  $\mu_{\text{N}}$ , the neutron-determined moment. The difference ( $\sim -0.1\mu_{\text{B}}$  in the case of PuSb) is usually called the conduction-electron polarization,  $\mu_{\text{cep}}$ , and is seen to be antiparallel to the resultant 5f moment.

Experimentally,  $\mu_{\text{cep}}$  is found to be *parallel* to the spin of the dominant localized electrons in the unit cell. This is true for all actinides studied and the quantities vary between  $-0.05$  and  $-0.2\mu_{\text{B}}$ . We would expect  $\mu_{\text{cep}}$  to become positive at Cm and beyond, but no measurements exist. However, whereas these statements are found to be true in all the lanthanides beyond cerium, compounds of the latter exhibit a number of interesting effects which we will cover briefly.

The antiparallel coupling between the conduction- and localized-electron states in cerium compounds is unique, and not found in uranium compounds. A relatively straightforward explanation may be found in terms of the Anderson model, in which such antiparallel coupling leads to the Kondo effect. However, such an explanation may be too simple since we should then expect only those compounds that are anomalous (e.g.  $\text{CeSn}_3$ ,  $\text{CeAl}_2$ ) to exhibit such effects, whereas more localized systems (e.g.  $\text{CeSb}$ ) would not. What is missing from these models is the large orbital moment. In fact,  $\text{Ce}^{3+}$  with its high ratio  $-\mu_{\text{L}}/\mu_{\text{S}}$  (see below for more on this), is a case in which the orbital contribution may play a key role in the coupling to the conduction-electron states. This ratio  $-\mu_{\text{L}}/\mu_{\text{S}}$  is already reduced in uranium, with  $5f^3$  electrons. Thus, the  $S = \frac{1}{2}$  state in  $\text{Ce}^{3+}$  may be the key factor; unfortunately the analogous compounds with  $5f^1$ ,  $\text{Pa}^{4+}$ , have not been studied. Moreover, it is unlikely that such a  $5f^1$  configuration can be stabilized, because of the large bandwidth of the 5f electrons in the early actinides and their tendency to completely delocalize. Cerium form factors also are known to be temperature dependent. The first reported unusual behavior of a Ce form factor was by Stassis et al. (1979) on  $\text{CeSn}_3$ . In more recent years Boucherle et al. (1986, 1990) have shown that samples of  $\text{CeSn}_3$  are susceptible to the development of fault regions of  $\text{Ce}_2\text{Sn}_5$ ; however, the original

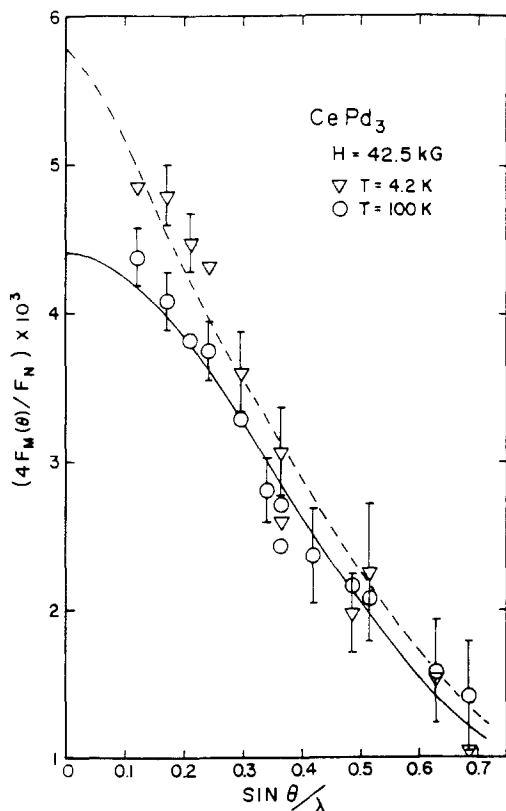


Fig. 10. Paramagnetic form factors of CePd<sub>3</sub> at 100 and 4.2 K plotted versus  $\sin \theta/\lambda$ . The solid line has been obtained by fitting the 100 K data to the 4f form factor of Ce<sup>3+</sup>. The dashed line was obtained by assuming an 83% 4f and 17% 5d contribution (Stassis et al. 1982).

measurements by Stassis et al. were verified in a stoichiometric sample. To avoid these problems we show the form factor of CePd<sub>3</sub> (Stassis et al. 1982) in fig. 10. An increase in susceptibility is found at low temperatures in both CeSn<sub>3</sub> and CePd<sub>3</sub>, and the change of wavefunction and increasing polarization of the 5d electrons can account, at least in part, for the increase in the bulk susceptibility. Interestingly, these compounds are one of the few cases in which the form factors actually change as a function of temperature. Since both CeSn<sub>3</sub> and CePd<sub>3</sub> have other unusual properties (they have been called both intermediate-valent and Kondo systems), it is gratifying that in neutrons experiments evidence is found of mixing between the 4f and conduction-electron (5d) states at low temperature, and a theory along these lines has been proposed by Liu et al. (1980). In this case the arguments advanced in the preceding paragraph concerning the antiparallel, rather than parallel, coupling between the local and conduction-electron spins would seem applicable.

The discovery of these "delocalized" states at low-temperature led naturally to the hope that similar effects would be found in the form factors of heavy-fermion materials, in which it is known that some type of "coherent" state develops at low temperature. This hope has not been realized. Studies of UPt<sub>3</sub>, UBe<sub>13</sub>, CeCu<sub>2</sub>Si<sub>2</sub> (Stassis et al. 1986) and CeCu<sub>6</sub> (Vrtis et al. 1987) have found no variation as a function of temperature.

This is especially puzzling for the superconducting materials, in which we would expect the spin susceptibility to disappear because of the formation of Cooper pairs. (A classic example of this is the paper on  $V_3Si$  by Shull and Wedgwood (1966).) These results suggest that the susceptibility is well-described by localized  $U^{3+}$  or  $Ce^{3+}$   $f$  electrons. Two remarks are in order here. First, unlike the case of  $CeSn_3$  and  $CePd_3$ , the bulk susceptibilities of the heavy-fermion materials show no anomalous increase at low temperature. Second, it must be remembered that the form factor is an elastic neutron measurement (i.e. long-time average). Differences between localized and itinerant states may depend on certain aspects of the temporal behavior of the electrons (Liu 1989); these are not addressed here, but under favorable conditions may be probed by neutron inelastic studies.

### 3.4. Spin and orbital contributions

We have seen earlier, sect. 3.1, that the spin and orbital contributions to the magnetization density give rise to slightly different contributions to the form factor, thus

$$\begin{aligned}\mu &= \mu_S + \mu_L, \\ \mu f(Q) &= \mu_S \langle j_0 \rangle + \mu_L (\langle j_0 \rangle + \langle j_2 \rangle) = \mu \langle j_0 \rangle + \mu_L \langle j_2 \rangle = \mu (\langle j_0 \rangle + C_2 \langle j_2 \rangle),\end{aligned}\quad (19)$$

where  $C_2 = \mu_L/\mu$ . Recall that this formulation is valid only within the dipole approximation.

The first question to ask is: how important are the orbital moments in actinide systems? The answer is very important. We illustrate this in fig. 11, taken from Maglic et al. (1978), with *uranium metal*. This indicates unambiguously that in uranium metal the  $5f$  electrons form a wide band and the orbital moment is quenched, i.e.  $g \sim 2$ ,  $C_2 \sim 0$ . In contrast, all other actinide compounds exhibit form factors that have an appreciable  $\langle j_2 \rangle$  contribution; the curves in general fall in the hatched region of fig. 11.

TABLE 2  
Ionic states,  $g$  (Landé factor) and  $C_2$  (dipole approximation) for  $f^n$  states in Russell–Saunders and intermediate coupling.

$f^n$	Ionic states 4f		Ionic states 5f		RS coupling		Intermediate coupling	
	$g$	$C_2$	$g$	$C_2$	$g$	$C_2$	$g$	$C_2$
1	$Ce^{3+}$	$Pr^{4+}$			0.857	1.33	0.857	1.33
2	$Pr^{3+}$		$U^{4+}$		0.800	1.50	0.821	1.43
3	$Nd^{3+}$		$U^{3+}$	$Np^{4+}$	0.727	1.75	0.759	1.64
4	$Pm^{3+}$		$Np^{3+}$	$Pu^{4+}$	0.600	2.33	0.643	2.11
5	$Sm^{3+}$		$Pu^{3+}$	$Am^{4+}$	0.286	6.00	0.414	3.83
6	$Sm^{2+}$	$Eu^{3+}$	$Am^{3+}$	$Cm^{4+}$	—	—	—	—
7	$Eu^{2+}$	$Gd^{3+}$	$Cm^{3+}$	$Bk^{4+}$	2.000	0	1.931	0.04



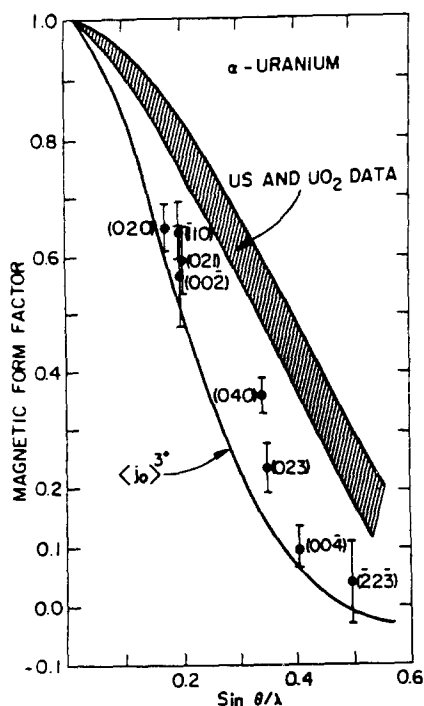


Fig. 11. Induced form factor of uranium metal at low temperature. Note how close the points are to a  $\langle j_0 \rangle$  curve, indicating the almost total quenching of the orbital moment (Maglic et al. 1978).

It is worth contrasting the behavior of U metal with that of  $\gamma$ -cerium (Stassis et al. 1978). In the case of  $\gamma$ -Ce an excellent fit to the  $\text{Ce}^{3+}$  form factor, which includes a large orbital moment, was found. Thus in  $\gamma$ -Ce (unfortunately measurements have not been done on the interesting collapsed  $\alpha$ -phase) the bands are sufficiently narrow in energy that we recover the free-ion  $\text{Ce}^{3+}$  form factor.

Following our earlier discussion, eq. (17), it is clear that if we follow Russell-Saunders (RS) coupling, then we may readily calculate  $g$  and hence  $C_2$ . These numbers are given in table 2. A well-known difference between the 4f and 5f series is that the spin-orbit coupling parameter (Carnall and Wybourne 1964, Wybourne 1965, and all textbooks on spectroscopy) is approximately twice as large in the actinides as in the lanthanides. This has two spectroscopic consequences. The first is that the energy separation between  $J$ -states is greater (again by a factor of  $\sim 2$ ) in the actinides. The second is that within a given  $J$ -manifold the mixing of  $SL$ -states (we call this intermediate coupling) will be more important for the actinides than for lanthanides. Thus the values of  $g$  for the actinides have to reflect this intermediate coupling and are different from the corresponding values in the lanthanides; this is reflected, of course, also in  $C_2$ .

The increase in  $C_2$  as the number of electrons increases reflects the increased cancellation of  $\mu_S$  and  $\mu_L$ , where

$$\begin{aligned} \mu_S &= 2(g-1)J, \\ \mu_L &= (2-g)J, \end{aligned} \tag{20}$$

and is particularly interesting since it gives rise to unusual form factors that have maxima at  $Q > 0$  (because of the large  $C_2$  contribution). We have already seen one of these form factors in the case of PuSb (fig. 8). This fits well to a  $5f^5$  configuration with  $C_2 = 3.80$ . (In this section we will neglect the crystal-field interaction, which

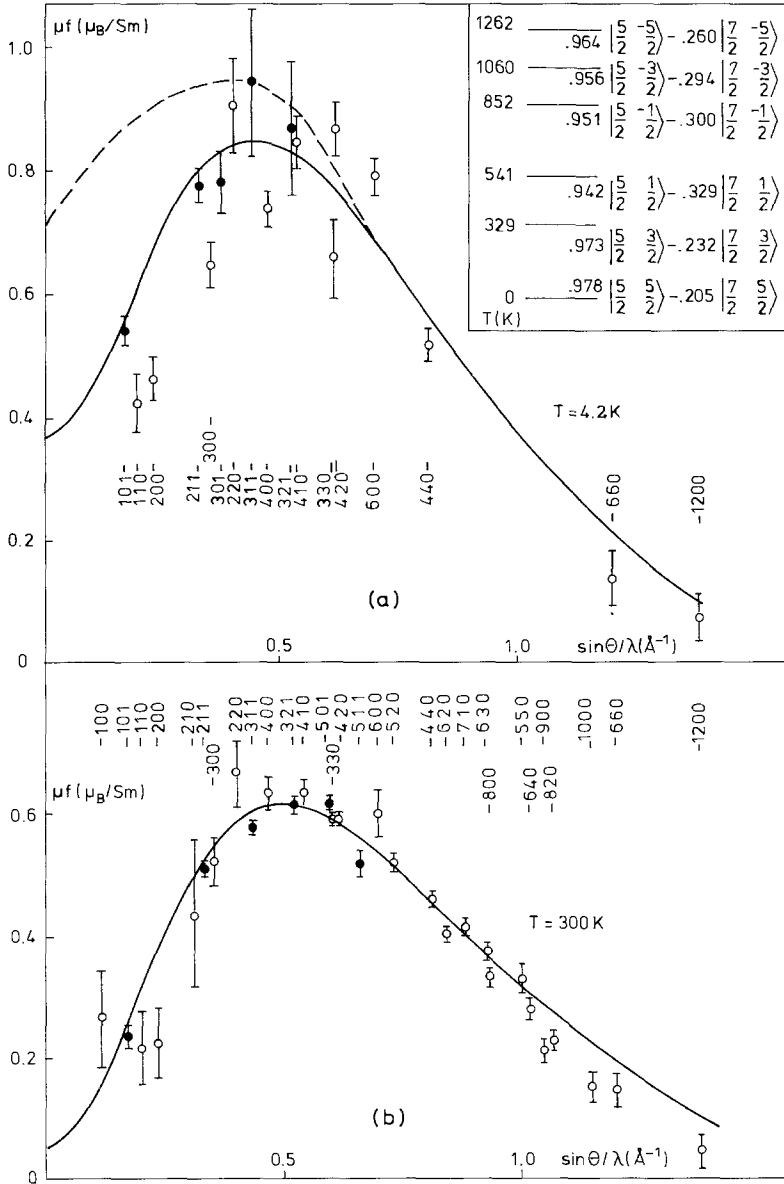


Fig. 12. Samarium magnetic amplitudes at 4.2 and 300 K in  $\text{SmCo}_5$ . The dashed line corresponds to the saturated state  $\left| \frac{5}{2}, \frac{5}{2} \right\rangle$  and the full line to the level scheme proposed (Boucherle et al. 1982a, b).

changes  $C_2$  slightly, but, more importantly, requires one to go further than the dipole approximation, as we saw in sect. 3.2.) An even more dramatic situation is found for Sm compounds, which also have a  $f^5$  configuration. We show the case of  $\text{SmCo}_5$  (Givord et al. 1979) in fig. 12. A full review of work on Sm compounds is given by Boucherle et al. (1982a,b). Figure 12 illustrates two important points. First, the cancellation of the spin and orbital contributions gives rise to a remarkable form factor, which was seen first in Sm metal itself (Koehler and Moon 1972). Second, when the temperature is raised, the mixing of the  $J = \frac{7}{2}$  excited state (at  $\sim 120$  meV or 1400 K from the ground state) into the ground-state wavefunction leads to a modification of the form factor. We should emphasize, however, that both these effects are well understood in terms of localized 4f electrons.

### 3.5. Application to mixed-valent states

The so-called mixed- or intermediate-valent compounds have been of considerable interest since their discovery in the early 1970s (see Varma (1976) for a review). SmS is a classic example (Jayaraman et al. 1970), which transforms under pressure from divalent ( $\text{Sm}^{2+}$ ) to a valence of  $\sim 2.8$ . In the divalent state the susceptibility, which is small, arises from van Vleck contributions mixing neighboring  $J$ -levels. Moon et al. (1978) have calculated an effective  $C_2 \sim -1$  for these contributions. Reference to table 2 shows that the  $\text{Sm}^{3+}$  state has  $C_2 = 6.0$ , so that the form factor would seem to be an excellent method by which to test the concept of mixed valence.

No doubt to their surprise, Moon et al. (1978) found in SmS, and in a later experiment on  $\text{Sm}_{0.76}\text{Y}_{0.24}\text{S}$  (Moon et al. 1983), that the form factor in all cases followed closely that of  $\text{Sm}^{2+}$ . They deduced the amount of  $4f^5$  configuration as  $\sim 0.1$ , whereas lattice-parameter measurements suggest a population between 0.3 and 0.5 over the temperature range studied. Since both the lattice parameter and the neutron form factor are long-time "average" values, this discrepancy is not understood.

A rather similar attempt to use the form factor to understand the electronic ground-state of PuTe was performed by Lander et al. (1987). The Pu chalcogenides are very interesting in that they have  $T$ -independent susceptibilities down to 50 K, a small rise in  $\chi$  at low temperature, which may be due to defects since it is slightly sample dependent, and no sign of magnetic order. The question is then whether there is a mixed-valent state, involving a fractional occupation of the  $\text{Pu}^{3+}$  ( $5f^5$ ) state. Since the latter has a characteristic form factor (fig. 8), a neutron experiment was undertaken, but this gave  $C_2 = 1.0 \pm 0.5$ . In the Pu case such a form factor could come from a wide band (as in the case of uranium), but many other measurements, particularly those on transport properties (Therond et al. 1987), contradict such an interpretation. Wachter et al. (1991) have proposed an interesting model for the Pu chalcogenides in which the  $f$ - $d$  hybridization causes a double-peak structure of  $f$ -like quasiparticles superimposed on a more or less classical  $d$ -band density of states. The model is closely related to the one the authors use to understand the mixed-valent nature of the Sm chalcogenides (see the chapter by Wachter in this series for more details), and can explain many of the properties of both the collapsed-phase Sm and Pu chalcogenides. The neutron scattering from such a model has not been calculated

quantitatively, but it seems reasonable to assume that the orbital contribution is much reduced, in agreement with the observations in both SmS and PuTe.

### 3.6. Quenching of the orbital moment by hybridization

We now come to what has certainly been the most interesting development in form-factor studies in the last decade. Historically, as always in research, the understanding evolved tortuously and by no means in a straight line. In an attempt at clarity we will start at the end and assume the workers understood the total picture from the beginning, which is certainly not true!

We start with the question of what happens to the large orbital moment of f electrons when they are hybridized with other states in solids. This question, of course, is central to understanding the unusual properties of actinide (and cerium) compounds. Form-factor measurements had shown the importance of hybridization effects in compounds such as UGe<sub>3</sub> (Lander et al. 1980), but at that time no theory had been developed to handle these effects; in particular the orbital contribution was known to be incorrectly treated in band-structure calculations (Brooks et al. 1984, Brooks 1985). Brooks, Johansson, and their collaborators corrected this deficiency by adding an orbital polarization term in the density-functional approximation (see the chapter by Brooks and Johansson (ch. 112) in this volume). When they made calculations on a series of intermetallic compounds, particularly those with a transition metal in the compact fcc Laves phase, they found that the value of  $\mu_L$  was *reduced* compared to the free-ion values. Loosely speaking, we can associate such a partial quenching of the  $\mu_L$ -value with the fact that the 5f electrons have become partially itinerant, and we know that fully itinerant electrons (in the 3d metals, for example) have  $\mu_L \sim 0$ .

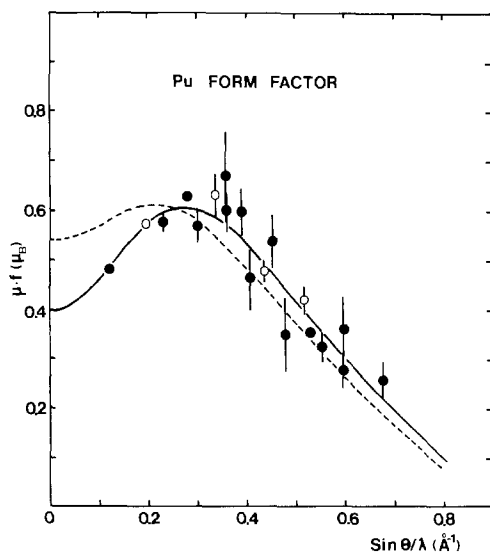


Fig. 13. The experimental points for the Pu form factor of PuFe<sub>2</sub>. The open circles are those from reflections with contributions from Pu atoms only. The solid circles contain contributions from the Fe site, for which we have used the conventional form factor. The solid line is a best fit with  $C_2 = 6.0$  and the dashed line is a best fit using the value of  $C_2 = 3.8$  found in PuSb (Wulff et al. 1988).

But the quenching of the  $\mu_L$ -value has the consequence that it changes the ratio  $\mu_L/\mu_S$ , and hence  $C_2$  in the form factor, as shown in eq. (19).

These ideas were given considerable encouragement by the measurement by Wulff et al. (1988) of the magnetic form factor of  $\text{PuFe}_2$ , which is shown in fig. 13. Although the form factor is still not as "humped" as that of  $\text{Sm}$  in fig. 12, the larger spin-orbit parameter and much larger separation of the  $J = \frac{7}{2}$  excited state in  $\text{Pu}$  as compared to  $\text{Sm}$  means that the free-ion theory cannot give  $C_2 > 4.5$ . Thus, finding  $C_2 = 6.0 \pm 0.2$  was unexpected. In fact, some years prior to this, Fournier et al. (1986) had measured  $\text{UNi}_2$  and found  $C_2 \sim 7$ ; but there were no theoretical predictions at that time. Furthermore,  $\text{UNi}_2$  has a more complicated hexagonal structure than the cubic Laves phases discussed here. Severin et al. (1991) have recently treated  $\text{UNi}_2$  theoretically, and obtained good agreement with the measured form factor.

In calculations on  $\text{UFe}_2$  the theory actually predicted (Brooks et al. 1988) a quenching of  $\mu_L$  so that its magnitude would correspond to that of the (oppositely directed) spin moment,  $\mu_S$ . This gives a total moment  $\mu \sim 0$  and under these circumstances the form factor should look simply like a  $\langle j_2 \rangle$  function. This was found experimentally by Wulff et al. (1989) and Lebech et al. (1989), and the U form factor is shown in fig. 14a. The  $C_2$ -value found was  $23 \pm 1$ , corresponding to an almost complete cancellation of  $\mu_L$  and  $\mu_S$ . Neutron experiments give not only the ratio  $\mu_L/\mu_S$ , which we will return to below, but also the individual values. These, together with some other quantities of interest, are gathered in table 3, which has been reproduced from Lebech et al. (1991). Experimental and theoretical values for  $\text{NpCo}_2$  (Wulff et al. 1990a) are also included. Although the values of  $C_2$ , which is proportional to the ratio  $\mu_L/\mu_S$ , as measured and predicted are in good agreement (to compare with the free-ion values in table 2 note that these compounds are all almost trivalent), the individual value of  $\mu_L$  and  $\mu_S$  are very different. The measured values are much smaller than those predicted, often by a factor of 2 to 3. This may represent shortcomings of the local-density approximation; for further comments the reader should refer to the chapter by Brooks and Johansson (ch. 112).

TABLE 3

Comparison between the results of polarized neutron scattering experiments (Exp.) and self-consistent electronic band structure calculations including all Hund's rules (Calc.). All units except  $C_2$  and  $\mu_L/\mu_S$  are in  $\mu_B$ . The experimental values for  $\text{NpCo}_2$  marked by an asterisk, have been scaled (see original work, Wulff et al. (1990a)).

	$\text{UFe}_2$		$\text{NpCo}_2$		$\text{PuFe}_2$	
	Exp.	Calc.	Exp.	Calc.	Exp.	Calc.
$\mu_{3d}$	0.60(1)	0.77	0.18(3)*		1.73(1)	1.25
$\mu_{5f}$	0.01(1)	0.05	0.63(3)*	0.87	0.39(2)	0.33
$C_2$	23(1)	18	3.7(3)	4	6.0(2)	11
$\mu_L$	0.23(1)	0.88	2.4(3)*	3.54	2.3(1)	3.52
$\mu_S$	-0.22(1)	-0.83	-1.8(3)*	-2.67	-2.0(1)	-3.19
$\mu_L/\mu_S$	-1.04(1)	-1.06	-1.37(5)	-1.32	-1.20(1)	-1.10
$\mu_{spd}$	-0.23(2)	-0.13				

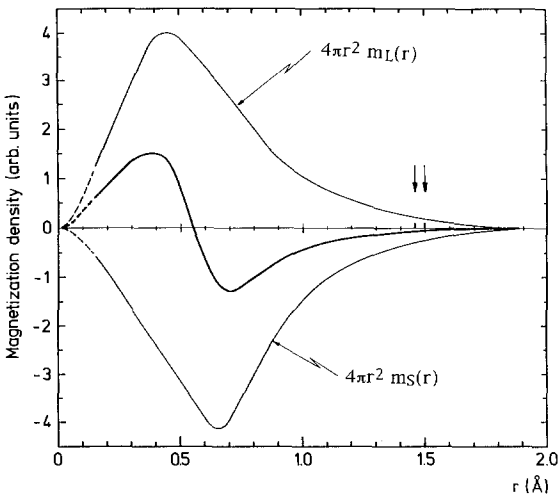
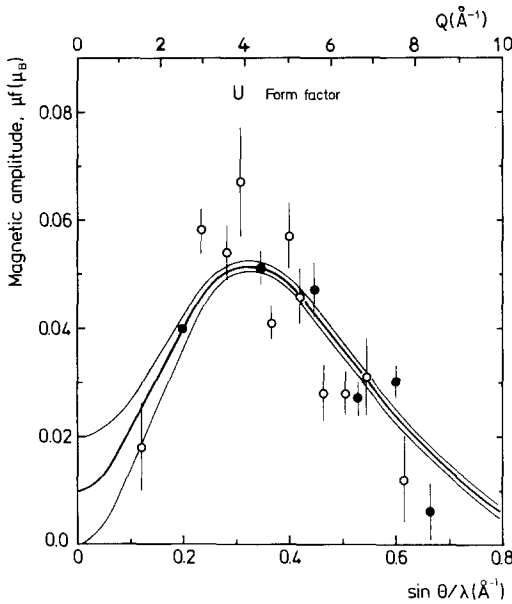


Fig. 14. (a) The magnitude of the magnetic scattering on the uranium sublattice in  $\text{UFe}_2$  as a function of the scattering angle. The extrapolation to  $\sin \theta / \lambda = 0$  gives the total moment, in this case almost zero. Note the maximum in the scattering cross section for  $\sin \theta / \lambda = 0.3 \text{\AA}^{-1}$ . The various solid lines indicate the limits of the extrapolated moment on uranium  $0 \leq \mu \leq 0.02 \mu_B$ . (b) Schematic representation of the orbital ( $4\pi r^2 M_L$ ) and spin ( $4\pi r^2 M_S$ ) components of the uranium magnetization density in  $\text{UFe}_2$  as a function of the distance,  $r$ , from the nucleus (oscillations at small  $r$  have been omitted for clarity). The difference (bold line) gives the total magnetization density, which clearly has two peaks, one positive and one negative. The integrated area of the two is the same, so that in this case the total moment is zero. The form factor is the Fourier transform of the bold line; this has maximum at  $Q > 0$  because of the reversal of sign of the bold line (Wulff et al. 1989).

Returning to the concept of a varying  $\mu_L / \mu_S$  ratio, we note that

$$\frac{\mu_L}{\mu_S} = \frac{C_2}{1 - C_2} = \frac{1 - \frac{1}{2}g}{g - 1}, \tag{21}$$

which allows us to construct a graph of this ratio versus the f-electron count, as shown in fig. 15. Whereas in some cases, e.g.  $\text{Pu}_2\text{O}_3$ , the f count is known, in many cases it is not. Fortunately, most of the intermetallic compounds have a 5f occupancy

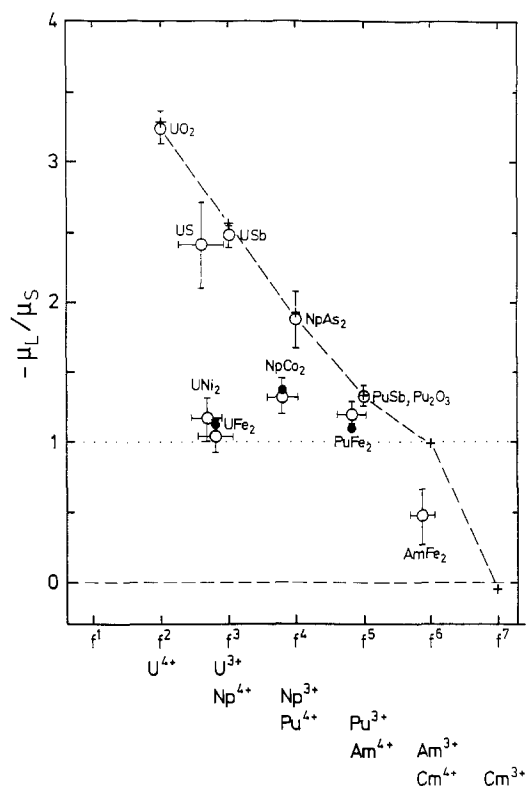


Fig. 15. Dependence of the ratio of the orbital,  $\mu_L$ , and the spin,  $\mu_S$ , moment on the  $f$  count in actinide materials. The crosses are derived from spectroscopic  $g$ -values, which include intermediate coupling, and assume localized  $f$  electrons. Experimental values derived from neutron experiments are shown as open circles. The values derived from the theory are shown as solid circles (Lander et al. 1991a).

that is close to that of a trivalent ion, so that the abscissa is not in dispute. The first point to note is that many, if not most, actinide compounds fall on the dashed line that corresponds to single-ion theory. In this respect materials like USb, NpAs<sub>2</sub>, and PuSb are like their lanthanide analogues, and of course the oxides behave also in a manner compatible with  $5f$  localized states. However, the observed values for  $-\mu_L/\mu_S$  for the intermetallic compounds all deviate substantially from the free-ion curve.

This decrease of  $-\mu_L/\mu_S$  is a consequence of a partial quenching of  $\mu_L$ , and this occurs as a direct consequence of hybridization with the  $3d$  electrons on the transition metal partner. If the quenching was complete then  $\langle \mu_L \rangle = 0$ , but this is not the case. A new type of coupling scheme is thus required for the actinides (Eriksson et al. 1991).

More recently, measurements have started on compounds with the 1:1:1 structure, such as URhAl (Paixão et al. 1992). Here again we expect considerable hybridization between the Rh  $4d$  and the U  $5f$  electrons, and a reduction in the  $\mu_L/\mu_S$  ratio is also found. Equally interesting is the discovery of a sizeable moment ( $\sim 0.3\mu_B$ ) on the Rh atom which lies close to the U atom in the (001) plane of the hexagonal structure. A second set of Rh atoms, approximately the same distance from the U atoms but in a different direction, has a negligible moment. These results show that the hybridization is anisotropic, which is not altogether surprising when we consider the

spatial form of the 5f electron orbitals and the anisotropic effects described in sect. 5 below.

We may ask at this stage whether any similar effects are found in the lanthanides. The answer is yes, but only in Ce. In fact, very interesting effects have been predicted for CeFe<sub>2</sub> (Eriksson et al. 1988), in which  $-\mu_L/\mu_S$  is changed from the RS free-ion value of 2.7 to  $\sim 6.2$ , i.e., an almost complete quenching of  $\mu_L$ . Unfortunately, no measurements have been reported yet.

Before concluding we will just touch on the case of AmFe<sub>2</sub>. The experiments, many years ago at Argonne National Laboratory on polycrystalline material, provided a major surprise in that they showed that the net moment on the Am site was directed antiparallel to the dominant Fe moment (Lander et al. 1977). This was unexpected since the net moment in all light f-system (f count < 7) is found parallel to the transition-metal spin (Brooks et al. 1989). If the 5f electrons in Am are localized, the f<sup>6</sup> configuration implies that the Russell–Saunders values of  $\mu$ ,  $\mu_L$ , and  $\mu_S$  are all zero. However, for a strongly hybridizing system,  $\mu_S$  approaches saturation and the  $\mu_L$  induced by spin–orbit coupling is large, but less than  $\mu_S$ . Hence,  $\mu_L/\mu_S < 1$ , and the Am moment,  $\mu$ , is antiparallel to the Fe moment. This interpretation is consistent with the experimental data, but predicts an  $f(Q)$  that changes sign at  $\sin \theta/\lambda \sim 0.35 \text{ \AA}^{-1}$ , and this would be most interesting to measure if a single crystal could be obtained.

In conclusion, we have demonstrated the importance of considering the actinide intermetallic compounds as itinerant-electron systems. Fully spin-polarized calculations that include an orbital polarization term predict a reduction of the orbital moment as compared to the 4f-like picture (alternatively, the orbital moment is large as compared to a conventional d-transition-metal system). The reduction of the orbital contribution has been observed directly in neutron experiments. There are a number of interesting consequences of this orbital-band magnetism. The first is that we can envisage “magnetic” materials with zero ordered moment. This can arise when  $\mu_L$  and  $\mu_S$  exactly cancel, so that the net moment is zero. Since the Wigner–Eckart theorem for the lowest  $J$ -multiplet is not used in the energy-band calculations as it is for localized systems, the relationship between the local  $\mu_L$  and  $\mu_S$  components is a function of the position in  $k$ -space. The total integrated moment may be zero, but because the band splitting depends only on the spin density, it is the net spin which is the order parameter. A magnetic transition to this net zero-moment state would therefore not be seen by magnetization techniques, but would be observable in specific-heat or neutron experiments at  $Q$ -values corresponding to the maximum in fig. 14a of  $\mu f(Q)$ . A second implication that also follows from the fact that we cannot apply the Wigner–Eckart theorem, affects the neutron inelastic response function  $S(Q, \omega)$ . It is not at all clear that sharp spin excitations should be seen in the case that none of  $S$ ,  $L$ , and  $J$  are good quantum numbers, and it is interesting that broad featureless response functions have been found for materials such as UN and US, in which the U–U distances are short and hybridization effects are proposed (Buyers and Holden 1985). A third consequence is that we anticipate a breakdown in the relationship between the total moment,  $\mu$ , and the Mössbauer hyperfine field,  $H_{\text{hf}}$ , which has been shown to exist for Np compounds over a wide range of  $\mu$  values (Dunlap and



Lander 1974). This relationship depends on the dominance of the orbital moment, and our present theory indicates that this should become invalid. More precise experiments on systems such as  $\text{NpOs}_2$  would clearly be worthwhile.

## 4. Magnetic structures

### 4.1. Magnetic structure and neutron diffraction

Since the early measurements on such materials as  $\text{MnO}$  and  $\text{MnF}_2$ , neutron diffraction has been the primary method in determining the arrangement of the magnetic moments in solids. As described in sect. 1, as well as in the recommended textbooks on neutron scattering, the power of the neutron technique is that the interaction of the neutron magnetic moment with the magnetic moments in the solid is a strong one and is vectorial in nature. To determine a complete magnetic structure we need *four* essential facts:

(1) The temperature at which the moments develop some type of long-range order, for antiferromagnets this is the Néel temperature ( $T_N$ ), whereas for ferromagnets it is the Curie temperature ( $T_C$ ). Another type of long-range correlation appears in so-called spin glasses, here  $T_{\text{SG}}$  is defined as that temperature at which the spin glass freezes. Frequently  $T_{\text{SG}}$  is a function of the magnetic field and possibly also the frequency of the probe with which the experiments are performed. Usually  $T_N$  and  $T_C$  are relatively insensitive to applied magnetic fields or pressures.

(2) The wavevector of the magnetic modulation. To distinguish this from modulations of the nuclei and general reciprocal lattice wavevectors we will denote the wavevectors describing magnetic structures with  $\mathbf{k}$ . This is consistent with the texts of Rossat-Mignod et al. (1984) and Rossat-Mignod (1987), but the notation  $\mathbf{q}$  is also used frequently. If  $|\mathbf{k}|$  is equal to a reciprocal lattice vector or a simple fraction thereof, we call the structure commensurate, other values are called incommensurate. In the latter case the magnetic moments on crystallographically equivalent atoms are different; this situation is unstable at low temperatures, when entropy requirements call for a uniform moment throughout. Thus we frequently find a transition from an incommensurate to commensurate state, which is often called a “lock-in” transition.

(3) The direction of the magnetic moments. Normally this is done by inspection in magnetic structure investigations. We recall that when the scattering vector,  $\mathbf{Q}$ , is parallel to the magnetic moment, the magnetic intensity is zero. Thus, once the crystallographic symmetry of the magnetic structure is found, it is usually a simple matter to find the series of  $(hkl)$  reflections that are absent because they arise from scattering vectors parallel to  $\boldsymbol{\mu}$ . An important exception to this rule are the so-called  $2\mathbf{k}$  and  $3\mathbf{k}$  structures, which we will discuss in some detail below.

(4) The magnitude of the magnetic moments on the different sites. To obtain these we need to assume a certain form factor,  $f(\mathbf{Q})$ . A standard  $f(\mathbf{Q})$  is usually assumed; it is only in exceptional circumstances that  $f(\mathbf{Q})$ 's like those of fig. 14 will be found, but, of course, one should be aware of the possibility of such a form factor.

#### 4.2. Multi- $k$ structures

Before proceeding to a discussion of specific magnetic structures we will say a few words about the multi- $k$  phenomenon. Such systems were in fact first proposed for transition-metal compounds many years ago (Kouvel and Kasper 1963). As an example we will take the simple fcc unit cell and assume that the magnetic moments are parallel to the  $\langle 100 \rangle$  direction. It is straightforward to see that there must be three equivalent components:  $m_x \parallel [100]$ ,  $m_y \parallel [010]$ , and  $m_z \parallel [001]$ . One normally thinks of these existing in three separate domains. Because of translational symmetry, at the (110) reflection only  $m_z$  domains contribute, and one would expect to see an intensity proportional to  $(m_z)^2 V_z$ , where  $V_z$  is the volume of the  $m_z$ -type domains. Examination of the (101) reflections involves  $m_y$ , and, similarly, (011) involves  $m_x$  domains. If the domain size is small and no external forces, such as a magnetic field or stress, are present, then  $V_x \sim V_y \sim V_z \sim \frac{1}{3}V$ , so that the reflections will have equal intensities ( $= \frac{1}{3}m^2V$ ). This is the single- $k$  structure, and is illustrated in fig. 16 (left-hand side). It is clear from this description that when  $V_x$ ,  $V_y$ , or  $V_z$  is varied, usually by cooling the crystal through  $T_N$  in a magnetic field or applying uniaxial stress, then the presence of a single- $k$  structure may be proven unambiguously.

The triple- $k$  structure may be simply described as one in which each component is present in the total volume. However, the intensity seen for the (110) reflection, for example, corresponds to that component that has the translational symmetry  $\frac{1}{2}a + \frac{1}{2}b$  and is just  $(m/\sqrt{3})^2V$ , which is exactly the same as for a single- $k$  structure. An illustration of the  $3k$  structure is found in fig. 16 on the right-hand side. The double- $k$  structure is a simple extension of the ideas already presented.

There are important differences between the single- and multi- $k$  structures, as fig. 16 makes clear. The most important is that the resultant moment directions are different, corresponding, respectively, to  $\langle 100 \rangle$ ,  $\langle 110 \rangle$ , and  $\langle 111 \rangle$  for the  $1k$ ,  $2k$ , and  $3k$  structure. Therefore, neutron diffraction experiments cannot, in this case, give the

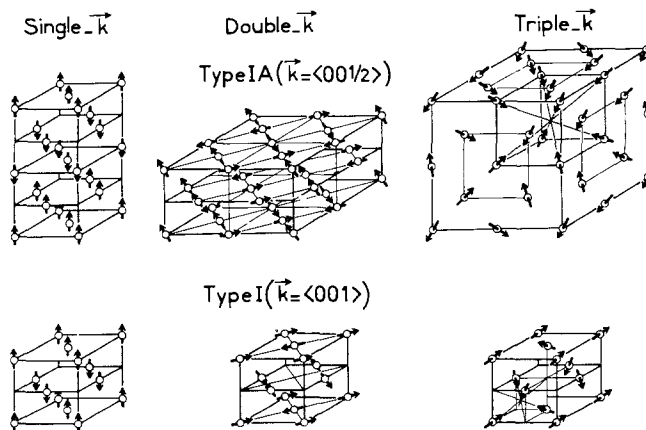


Fig. 16. Multi- $k$  structures associated with an ordering of type I ( $k = (001)$ ) and type IA ( $k = (00\frac{1}{2})$ ) for a face centered lattice and  $m_k$  parallel to  $k$ .

direction of the resultant moment, only the directions of the individual components. The *exact* direction of the resultant moment clearly requires knowledge of the phase relationships between the individual components, if more than one is involved. Diffraction experiments give *no* information on this aspect, so the exact  $\langle 111 \rangle$  direction chosen at a given atom for the  $3\mathbf{k}$  structure illustrated in fig. 16 remains unknown. Further, the symmetries of the  $1\mathbf{k}$ ,  $2\mathbf{k}$ , and  $3\mathbf{k}$  structures, as shown in fig. 16, are tetragonal, tetragonal, and cubic, respectively. In particular, the *cubic* symmetry of the  $3\mathbf{k}$  structure is interesting in that magnetic ordering can occur without any accompanying magnetoelastic distortion, which would be expected in the case of  $1\mathbf{k}$  or  $2\mathbf{k}$  structures. In summary, the presence of multi- $\mathbf{k}$  structures can be best examined by performing experiments in applied fields or with uniaxial stress. It remains for us to try to understand why these multi- $\mathbf{k}$  structures are formed.

### 4.3. Magnetic structures of NaCl-type compounds

#### 4.3.1. General remarks

The largest group of actinide materials that have been examined is those with the NaCl crystal structure. Compounds crystallizing in this structure are the actinides (and lanthanides) with elements of group VA (monopnictides) and VIA (monochalcogenides) and carbides. In addition to these compounds forming an isostructural set, they are also available, for the most part, as single crystals. The development of the technology used to grow these crystals, including those of the transuranium materials, is described by Spirlet and Vogt (1984). Since many of the properties, e.g. the magnetization (see the chapter by Vogt and Mattenberger (ch. 114) in this volume) and the critical scattering (see sect. 5), are highly anisotropic, the microscopic behavior can be determined only if single crystals are used.

The details of the magnetic structures are given in table 4. We have omitted the carbides (group IV) since no work has been done on them since the review by Rossat-Mignod et al. (1984). Included also in the table are the details of cerium compounds. The  $f$  count for these materials is Ce- $f^1$ , U- $f^3$ , Np- $f^4$ , and Pu- $f^5$ , thus they are trivalent, or nearly so. If we assume the RS coupling to be applicable to the lanthanides, then we would expect the ordering temperature and the ordered moment, both of which are proportional to the exchange, to peak in the region  $f^2$  to  $f^3$ , and this is indeed the case. Furthermore, the moments approach  $3\mu_B$ , which is the free-ion value for an  $f^3$  configuration, and for the  $f^5$  configuration (Pu) they are near to  $1\mu_B$ . Thus, in a global view, many of the properties seem to justify our approaching these systems in the same manner as the localized 4f analogues. It is only when we take the next level of detail that serious problems arise. In the analogues 4f systems the next level of interaction is the crystal-field (CF) potential. Often it dominates the magnetic behavior, e.g. for a non-Kramers ion like  $\text{Pr}^{3+}$  ( $4f^2$ ) a singlet ground state is found, in which there is no spontaneous magnetic order, as exemplified by the Pr monopnictides. In the AnX compounds  $5f^2$  configurations do not exist, so this analogy cannot be made, but we might anticipate some singlet ground states in  $\text{Np}^{3+}$  ( $5f^4$ ), whereas none are found. More specifically we would expect to be able to *measure* the crystal-field energy levels for the actinides in the same manner as is possible for

TABLE 4

Magnetic properties of Ce, U, Np, and Pu monopnictides and monochalcogenides. For Ce pnictides see Hulliger (1974, 1978), Rossat-Mignod et al. (1977), Fischer et al. (1978), and Rossat-Mignod et al. (1985). For the Ce chalcogenides see Schobinger-Papamantellos et al. (1974), Hulliger et al. (1978), Ott et al. (1979), and Ott (1980). Information on the actinides is taken principally from Rossat-Mignod et al. (1984) and Burlet et al. (1986, 1988a, b, 1992), but other references will be found in the text. Comm. and incomm. refer to commensurate and incommensurate structures, respectively. TIP indicates temperature-independent paramagnetism.

	$a$ (Å) (300 K)	$T_N$ (K)	$T_C$ (K)	$k$	Ordering	Easy axis	$\mu_B$ ( $T=0$ )
CeP	5.932	8		(001)	1 <i>k</i> type I	<001>	0.83
CeAs	6.078	8		(001)	1 <i>k</i> type I	<001>	0.7
CeSb	6.412	16		incomm.	complex	<001>	
		<8		(00 $\frac{1}{2}$ )	1 <i>k</i> type IA	<001>	2.0
CeBi	6.487	25.4		(001)	1 <i>k</i> type I	<001>	
		12.5		(00 $\frac{1}{2}$ )	1 <i>k</i> type IA	<001>	2.14
UN	4.890	53		(001)	1 <i>k</i> type I	<001>	0.75
UP	5.589	122		(001)	1 <i>k</i> type I	<001>	1.7
		22		(001)	2 <i>k</i> type I	<110>	1.9
UAs	5.779	124		(001)	1 <i>k</i> type I	<001>	1.9
		62		(00 $\frac{1}{2}$ )	2 <i>k</i> type IA	<110>	2.25
USb	6.191	213		(001)	3 <i>k</i> type I	<111>	2.85
UBi	6.364	285		(001)	type I	?	3.0
NpN	4.897		87	0	ferro	<111>	1.4
NpP	5.615	130		(0, 0, 0.36)	incomm	<001>	
		74		(00 $\frac{1}{3}$ )	3+, 3-	<001>	2.2
NpAs	5.838	173		(0, 0, $\frac{1}{4} - \epsilon$ )	1 <i>k</i> incomm.	<001>	
		154		(00 $\frac{1}{4}$ )	1 <i>k</i> 4, 4-	<001>	
		138		(001)	3 <i>k</i> type I	<111>	2.5
NpSb	6.254	202		(001)	3 <i>k</i> type I	<111>	2.5
NpBi	6.438	193		(001)	3 <i>k</i> type I	<111>	2.48
PuN	4.905	13?					
PuP	5.550		126	0	ferro	<100>	0.75
PuAs	5.780		125	0	ferro	<100>	0.67
PuSb	6.240	85		(0, 0, 0.13)	1 <i>k</i> , incomm.	<100>	
			70	0	ferro	<100>	0.74
PuBi	6.350	58		(0, 0, 0.23)	1 <i>k</i> comm	<100>	0.50
CeS	5.779	7.0		( $\frac{111}{222}$ )	type II	?	0.6
CeSe	5.992	5.4		( $\frac{111}{222}$ )	4 <i>k</i> ? type II	?	0.6
CeTe	6.361	2.2		( $\frac{111}{222}$ )	4 <i>k</i> type II	?	0.2
US	5.489		170	0	ferro	<111>	1.70
USe	5.750		160	0	ferro	<111>	2.0
UTe	6.155		104	0	ferro	<111>	2.25
NpS	5.527	23		( $\frac{111}{222}$ )	type II	?	0.7
NpSe	5.804	38		( $\frac{111}{222}$ )	type II	?	1.0
NpTe	6.198	30?		( $\frac{111}{222}$ )	type II	?	1.2
PuS	5.536	TIP?					
PuSe	5.775	SIP					
PuTe	6.151	TIP					

the lanthanides (see, e.g., Fulde and Loewenhaupt 1986, Stirling and McEwen 1987), but this has not been possible, as is discussed in more detail in the chapter by Holland-Moritz and Lander (in vol. 19) in this series. Thus, the importance of the crystal field remains obscure; we know it is present, but because of other, often anisotropic, interactions it does not lead to a well-defined set of energy levels.

Another example of the problems in understanding these materials can be illustrated by the Pu chalcogenides, PuS, PuSe, and PuTe. If we follow the lanthanide example, then we would expect these materials to be divalent, which explains their non-magnetic ground state, since  $\text{Pu}^{2+}$  has a  $5f^6$  configuration with  $L = 3 = -S$  and hence  $J = 0$ . However, the volume of the divalent ion should be  $\sim 25\%$  greater than the corresponding trivalent state, as is found in comparing SmS with SmP, for example. This is not the case for the Pu compounds; as shown in table 4 the lattice parameters of the monochalcogenides are actually a little smaller (by  $\sim 1.5\%$ ) than those of the corresponding monpnictides. Once again we find that the simple ideas that work so well for the localized  $4f$  materials fail in the actinides. It is this aspect, of course, which has made these structures so interesting.

#### 4.3.2. General comparisons between Ce and actinides

We have included the Ce compounds in table 4 because they are also anomalous (Cooper et al. 1985). They form a natural bridge between the "normal", i.e. localized  $4f$ , lanthanides, and the abnormal actinides. For example, the crystal-field potential has been known for many years to be unusually small in the CeX compounds compared to the other LnX systems (Turberfield et al. 1970, 1971). On the other hand, well-defined crystal-field levels *are* observed in the CeX compounds, which is not the case in AnX compounds.

To illustrate the complexity of the CeX compounds, especially with the application of an applied field, we show in fig. 17 the magnetic phase diagram of CeSb as a function of  $H$  and  $T$ . Although at first sight there are some similarities between this phase diagram and those of AnX compounds shown below, there are also important differences. An important similarity, and one which we will find in all the monpnictides in table 4, is that the structure may be described as the stacking of ordered (001) ferromagnetic planes, with the moment direction perpendicular, i.e.  $\mu \parallel [001]$ , to the planes. This is a *longitudinally modulated structure*. By this we mean that the components  $m_k$  are parallel to the propagation direction,  $k$ . As we will see below (sect. 5), anisotropic interactions are responsible for the strong intra-planar exchange, with only weak exchange between the planes in the  $[001]$  direction.

However, there are two important differences between the Ce and An systems. First, the Ce systems exhibit commensurate structures only. By this we mean that the individual moment values in the planes are either  $\mu$  or zero and do not take a range of values. Second, planes containing atoms with zero moment exist, which is unusual. The presence of these "paramagnetic" planes has been verified by inelastic magnetic scattering (Rossat-Mignod et al. 1985). No evidence of such paramagnetic planes has been found in AnX compounds. Third, the structures in the CeX systems are single- $k$  magnetic structures; this is in contrast to the AnX systems, in which multi- $k$  structures are frequently found.

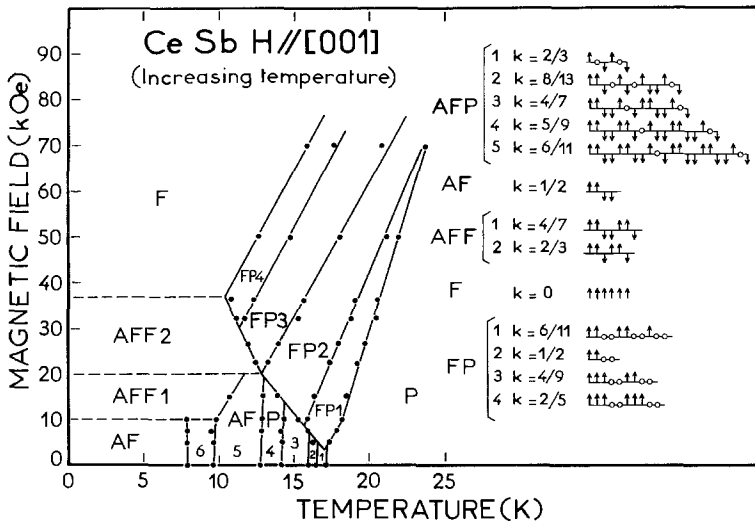


Fig. 17. Magnetic phase diagram of CeSb as a function of temperature and magnetic field (taken from Rossat-Mignod et al. 1985). It should be remembered that the structures are all longitudinal, the transverse structures shown in the figures at the right are drawn in this way to save space.

A further similarity, as can be seen from table 4, is that the chalcogenides exhibit more bizarre behavior than the pnictides. More details of the theory invoked to explain these effects may be found in Rossat-Mignod (1987), Takahashi and Kasuya (1985), and Cooper et al. (1985, 1992).

#### 4.3.3. Actinide mononpnictides

To illustrate the extreme complexity of the phase diagrams of these materials, we show in fig. 18 the magnetic phase diagram of UAs as a function of  $H$  and  $T$ . This shows an interplay between single- and double- $k$  structures. There is no evidence for incommensurate modulations in UAs below  $T_N$ . The model that has been introduced for UAs at high field and low temperature is one in which there is a change in the stacking of the ferromagnetic planes. The material remains a  $2k$  structure even when a ferromagnetic component is induced. In the  $2k$  structure there are components  $K_{xy}$ ,  $K_{yz}$  and  $K_{zx}$ , but with a field applied parallel to  $[001]$  only the last two, having a  $z$ -component, will be affected. Thus the problem is to define the arrangement of spins along the  $z$ -axis, recalling that the moment component along this direction must be reduced by  $\sqrt{2}$ , since the real components lie along the  $[101]$  and  $[011]$  direction in the  $2k$  structure, see fig. 16. Considering just the  $z$ -component, we imagine blocks of planes, the antiferromagnetic components being of the form A ( $++--$ ), and one containing a ferromagnetic component of the form F ( $++-$ ). These are then stacked; e.g., AFAFF is written  $(AF)^2F$  and has a wavevector  $k = \frac{10}{17} = 0.5882$ . (To obtain this value note that the waveform makes five  $2\pi$  cycles in 17 layers or 8.5 unit cells, i.e.  $k = 5/17/2 = 10/17$ .) This model for the spin arrangements predicts a certain net ferromagnetic component; in the above case there are 10  $+$  planes to 7  $-$  planes,

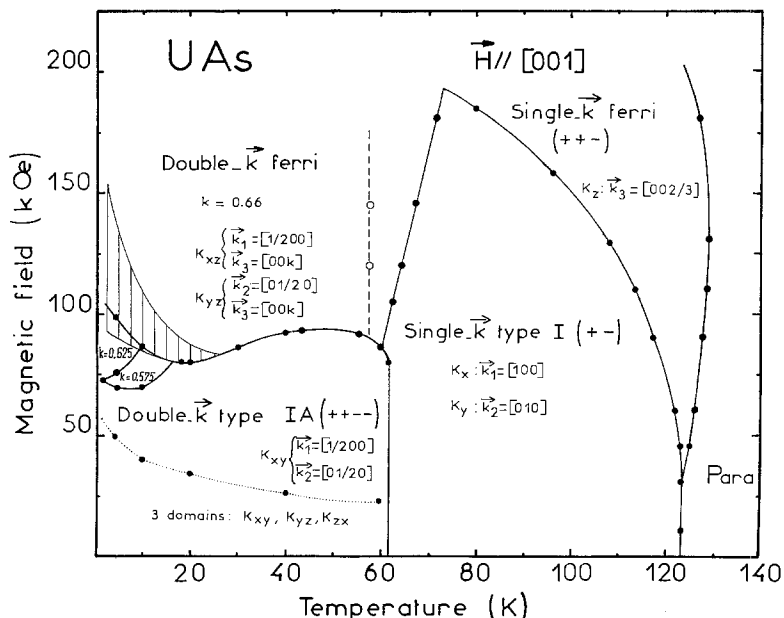


Fig. 18. Magnetic phase diagram of UAs as a function of temperature and magnetic field applied along the [001] axis, derived from magnetization ( $H \leq 200$  kOe) and neutron diffraction ( $H \leq 100$  kOe) measurements. (Taken from Rossat-Mignod et al. 1984.)

so that the net moment is  $\frac{3}{17}$  of the U moment, i.e.  $\frac{3}{17} \times 2.25/\sqrt{2}\mu_B = 0.281\mu_B$ , and this is in good agreement with the magnetization result of  $0.27\mu_B$  obtained on UAs at high fields. These complex structures also give rise to higher harmonics in the diffraction pattern, and these have been detected in measurements on UAs by Rossat-Mignod et al. (1982).

These experiments have given an interesting first view of the complex plane stacking that can appear when a field is applied. The experiments are particularly difficult because the components that are of interest are those along the field direction. The large fields required, the low intensities of the higher-order harmonics, and the relatively poor  $k$ -space resolution of the neutron instruments used, all mean that more information will probably emerge when new experiments can be performed under better experimental conditions. The model outlined above raises at least two interesting questions. First, does the stacking modulation always remain commensurate? Second, why does such a complex arrangement not show additional "faults" in the stacking? To answer both questions we require higher  $k$ -space resolution in order to measure accurately the positions of (to answer the first question) and the widths of (to answer the second one) the higher-order satellites. We will discuss this aspect in more detail in connection with our studies of NpAs below.

Since the review of 1984 a considerable amount of work has been done on single crystals of transuranium compounds (Burllet et al. 1988b, and references therein), and we will discuss a few of these results. The magnetic phase diagram of NpAs is

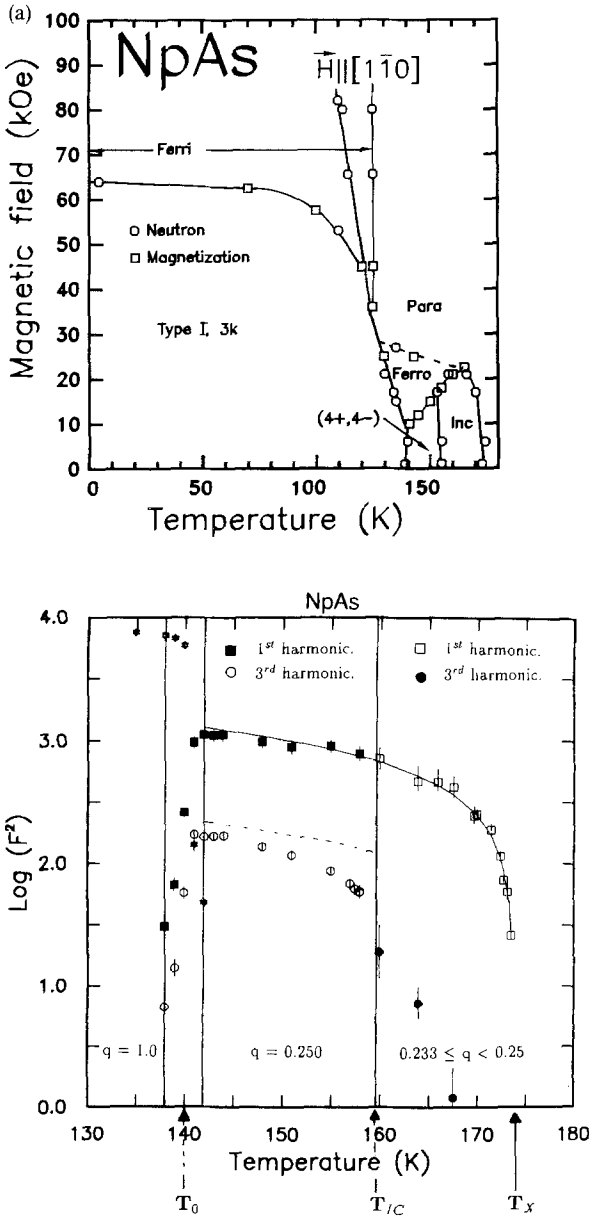


Fig. 19. Magnetic phase diagram of NpAs (a) as a function of magnetic field applied in the  $[110]$  direction, taken from Burlet et al. (1987b) and (b) details of the high-temperature part, showing the growth of the third harmonic to make the 4+, 4- square-wave structure. Taken from Jones et al. (1991).

shown in fig. 19. There are a number of features worth noting. First, at high temperature, the structure is incommensurate with a wavevector somewhat less than  $q = \frac{1}{4}$ , with therefore a repeat cell ( $1/q$ ) of slightly more than four unit cells. This phase can be easily destroyed by a magnetic field (fig. 19a) and converted into a paramagnetic state. At lower temperature,  $T_0 < T < T_{IC}$  the material locks into a commensurate structure, in this case  $q = 1/4$ , corresponding to almost a square wave with a modula-



tion  $4+$ ,  $4-$ ,  $4+$ ,  $4-$ , etc. Application of a magnetic field to this structure results first in a ferromagnetic state, and then, at the relatively low field of  $\sim 30$  kOe, a paramagnetic state is induced.

At  $T_0 \sim 140$  K a dramatic transition occurs in NpAs, which is a first-order transition to a type I,  $+-+ -$  stacking of planes with  $q = 1$ , magnetic structure. The structure is of the  $3\mathbf{k}$ -type, in which the resultant moment is actually along  $\langle 111 \rangle$ , but the diffraction experiments pick out a particular component  $m_x$ ,  $m_y$ , or  $m_z$ . The magnetic structure now has cubic symmetry, so that the lattice symmetry also returns to cubic (Aldred et al. 1974). The  $3\mathbf{k}$  structure is a common feature of many of the actinide NaCl compounds, particularly with the heavier anions Sb and Bi, and is extremely stable against an applied magnetic field. In fig. 19a we see that fields of over 60 kOe are required before even a single ferromagnetic component is induced.

The transition to the type I structure in NpAs is almost certainly an electronic one. On cooling into this phase the resistivity increases (Aldred et al. 1974) by a factor of almost 100. Further work is needed to determine whether it are the 5f electrons that are partially localizing at  $T_0$ , and thus causing a reduction in the resistivity. Certainly the materials with the  $3\mathbf{k}$  structure exhibit properties resembling localized systems. One of the normal criteria for a localized–delocalized transition is a volume change; however, magnetoelastic effects often prevent a clear identification of a purely electronic transition.

Before leaving NpAs, we will return briefly to the high-temperature phase and mention some of the new diffraction experiments to examine the modulation with higher precision. These experiments indicate that a higher level of complexity may exist in these structures than presently supposed. In the incommensurate state ( $T > T_{IC}$ ) it is possible to measure the position, intensity, and width of not only the 1st and 3rd harmonics, but also of possible higher orders. These latter satellites overlap with the first and third in the commensurate state. An experiment of this type has been reported by Jones et al. (1992) on NpAs. In fig. 20 we show the intensities of the third and fifth harmonics plotted as a function of that of the first harmonic. According to Landau theory (Pynn et al. 1976), which is also the basis for the McMillan (1976) approach to the incommensurate–commensurate (lock-in) phase transition, the amplitude of the  $n$ th harmonic should be proportional to  $M^n$ . Figure 20 shows that this relationship is obeyed for the 3rd- and 5th-order harmonics, but neither extrapolates to the origin of the plot. This implies that they appear progressively, and that near  $T_N$  the modulation is completely sinusoidal. By examining the widths of the diffraction peaks in the incommensurate phase Jones et al. (1992) were also able to show that they are not constant. The results are shown in fig. 21. The instrumental resolution is  $\sim 0.008$  rlu, and the widths plotted in fig. 21 are the extra widths above the instrumental resolution. Below  $T_{IC}$  the widths are resolution limited. As yet, we have no quantitative understanding of why the widths increase so much near  $T_{IC}$  and why this increase seems to depend on the order of the harmonic. One possible model involves the introduction of pseudo-random “faults” in the arrangement of the ferromagnetic planes that will make up the modulation along the cubic axis. Clearly, these arguments have a bearing on the previous discussion of the diffraction effects in UAs in high fields.

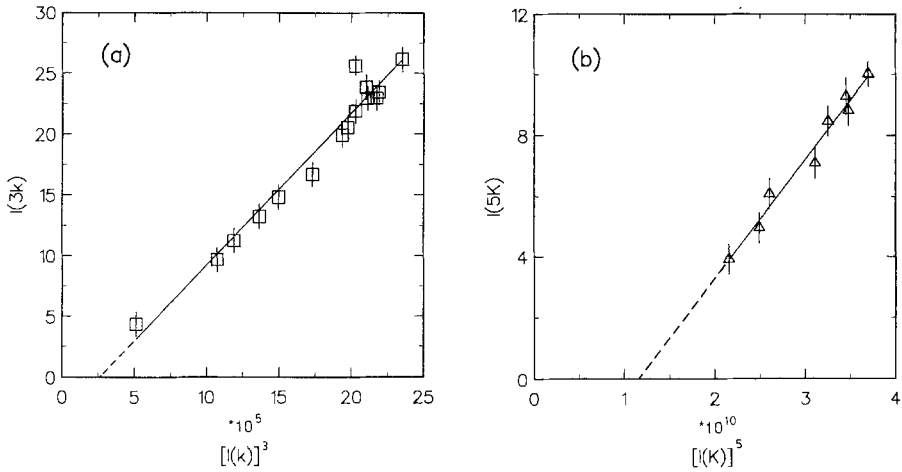


Fig. 20. (a) The integrated intensity of the third harmonic as a function of the cube of the fundamental (first) satellite intensity. (b) Same for the fifth satellite with the fifth power of the first satellite intensity. (From Jones et al. (1992)).

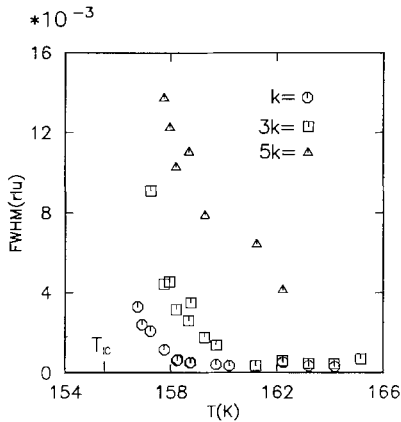


Fig. 21. Temperature dependence of the widths of the first, third, and fifth-order satellites in the incommensurate phase,  $T > T_{IC}$ , in NpAs. (From Jones et al. (1992).)

It may be worth speculating here that the “first-generation” structural investigations of these materials are now coming to an end. In a “second-generation” round of experiments, using better instrumental resolution, we can anticipate the discovery of new effects. The situation may well parallel that of the lanthanide metals, for which the higher resolution available with synchrotron X-ray machines allowed the introduction of the spin-slip model (Bohr et al. 1989).

For the plutonium monopnictides a fairly complete study has been performed on PuAs and PuSb (Burlet et al. 1984), but the production of single crystals using the non-absorbing isotope  $^{242}\text{Pu}$  led to repeating some of the measurements on PuSb (Burlet et al. 1987a). PuAs is ferromagnetic, but PuSb initially orders ( $T_N = 85$  K) with an incommensurate wavevector, with a value of  $q$  not far from  $\frac{1}{8} = 0.125$ , and

as  $T$  decreases, so does  $k$ , the wavevector. At  $T_{IC} = 67$  K, PuSb transforms to a true ferromagnet with  $k = 0$ . Burlet et al. (1984) also remark that close to  $T_{IC}$  the superlattice peaks have a larger width than the nuclear peaks, and we may presume that the behavior shown in fig. 21 is quite general for systems that exhibit a lock-in transition. However, unlike the case of NpAs, in PuSb only the first-order satellites have been found so far, the third-order satellites being less than  $10^{-3}$  of the first-order ones. Further work would seem necessary on PuSb, since the modulation in PuBi (Burlet et al. 1987b) appears to be a good square wave with a modulation (4+, 4-, 5+, 4-, 4+, 5-) giving  $k = \frac{3}{13}$ . A third-order harmonic was seen in this material and it would seem an excellent candidate for higher-resolution studies of the type already performed in NpAs.

The Am mononictides are non-magnetic with a temperature independent susceptibility. Such behavior indicates a  $5f^6$  single ground state with  $J = 0$ , so that the valence is  $\text{Am}^{3+}$ .

#### 4.3.4. Actinide monochalcogenides

The actinide monochalcogenides have been of considerable interest since their properties were first studied over 20 years ago, see Fournier and Troč (1985). The cerium chalcogenides are equally interesting, see Ott (1980) for a review. They all order with the type II antiferromagnetic structure, but with small moments, as opposed to the mononictides, which have large moments and complex magnetic structures, as discussed in the previous section. The type II structure is quite common in lanthanide compounds with the NaCl structure, but it is not yet clear whether the cerium materials have single- $k$  or  $4k$  structures. A similar question still applies to the Np chalcogenides.

As is well known, the U chalcogenides are all ferromagnets; we will discuss them more extensively in connection with inelastic neutron experiments, see the chapter by Holland-Moritz and Lander in vol. 19. For Np the situation is clear only for NpS and NpSe. NpS was studied many years ago in polycrystalline form (Lam et al. 1974), and recent single crystal work (Blaise et al. 1992) has confirmed that the structure is of type II with  $k = (\frac{1}{2}, \frac{1}{2}, \frac{1}{2})$  and the Fourier components,  $m_k$ , directed along either  $\langle 100 \rangle$  or  $\langle 22-1 \rangle$ . Cooling in a magnetic field has no influence on the intensities of the reflections, so the authors conclude that it has a multi- $k$  structure. Possible structures include  $2k$ ,  $3k$ , or  $4k$  arrangements and, depending on the phasing of the individual components, there can be different moments on similar Np atoms. This would agree with Mössbauer results that suggest a distribution of the magnetic moments in the ordered state. The ordering at  $T_N$  appears to be of first order. NpSe appears somewhat similar to NpS, albeit with a slightly larger moment.

The case of NpTe is intriguing and not yet solved. Mössbauer experiments (Sanchez et al., unpublished) show quite clearly a large hyperfine field corresponding to local moments of  $\sim 2\mu_B$  per Np atom and an ordering temperature of  $\sim 30$  K. The resistivity (Pleska et al. 1988) shows a clear maximum also at  $\sim 40$  K, and the susceptibility shows a clear maximum at  $\sim 30$  K (Mattenberger et al. 1990). From these measurements we might conclude that the material orders antiferromagnetically at  $\sim 30$  K. However, in the early neutron experiments on both powders and single crystals of

NpTe no magnetic scattering was observed at low temperatures. More recently (Burllet, unpublished), long-range order has been observed with neutron diffraction, and the magnetic moment is  $1.2\mu_B$ . It seems likely that the properties of NpTe may be sensitive to the stoichiometry, much in the same way as they are for TmSe. The ordering observed in the new sample has the type II form with  $\mathbf{k} = (\frac{1}{2}, \frac{1}{2}, \frac{1}{2})$  and  $T_N = 40.5$  K.

Specific-heat experiments by Stewart et al. (1991) have been analyzed and give an electronic specific heat of  $130 \pm 10 \text{ mJ mol}^{-1} \text{ K}^{-2}$  and no clear evidence for the 30 K transition was found. This is the highest value of  $\gamma$  yet found for a NaCl-type compound and speculation that it may be a "medium-weight" fermion system cannot as yet be excluded.

The Pu chalcogenides are even more puzzling than those of neptunium, but since none of them order magnetically the only contribution made so far by neutrons has been a form-factor experiment on PuTe (Lander et al. 1987), which showed that the conventional  $\text{Pu}^{3+}$  form factor would not fit the data. These Pu systems have been the subject of a considerable amount of work, especially concerning magnetization (Mattenberger et al. 1986) and resistivity (Fournier et al. 1990). Recently, Wachter et al. (1991) have discussed the problem of the Pu chalcogenides in terms of the concept of intermediate valence. In particular, they claim that the Pu chalcogenides represent the high-pressure intermediate form of the isoelectronic Sm chalcogenides. This paper contains an impressive synthesis of all the available experimental evidence and makes a number of important predictions. We might make two remarks with respect to neutrons. First, the theory developed definitively shows that the upturn in  $\chi$  (the magnetic susceptibility) at low temperature is intrinsic and not due to impurities; neutron experiments (Lander et al. 1987) point to this interpretation. Second, making crystals of  $^{242}\text{PuTe}$  and attempting inelastic neutron scattering would seem a worthwhile endeavor.

#### 4.3.5. *Solid solutions – overview*

Studies of solid solutions have been particularly rich in detail when considering the actinide rock salt compounds. Some seven pages in the work by Rossat-Mignod et al. (1984) are devoted to these studies and references go back to the 1960s. The principal reasons for the popularity of these studies are as follows:

(a) All systems with adjoining pnictogens or chalcogens form complete solid solutions. These extend to Th also.

(b) Since the valence of the pnictogen is  $X^{3-}$  and that of the chalcogen  $Z^{2-}$ , it was initially thought that a change of cation valence would be exhibited as a function of concentration in the solid solution.

(c) With the development of the mineralization technique (Spirlet and Vogt 1984) single crystals of almost any composition of the solid solutions can be made.

Reason (b), which was the driving scientific reason for studying these systems, is now recognized to be much more complex. Divalent uranium or other actinide species are almost impossible to stabilize, and so are not expected. Numerous studies, see the reviews by Schoenes (1984), Brooks et al. (1984), and Baer (1984), have shown that all the monopnictides and monochalcogenides (and thus all the solid solutions as well) are essentially semimetals. It is generally accepted that the monopnictides are

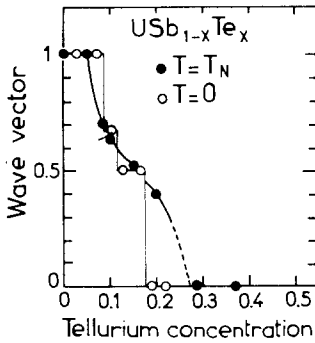


Fig. 22. Value of the wavevector as a function of tellurium concentration at  $T = T_N$  and  $T = 0$  for the solid solution  $USb_{1-x}Te_x$ . (From Rossat-Mignod et al. (1984).)

the more localized. By this we mean that the 5f density of states (DOS) is further removed from the Fermi level,  $E_F$ , than is found in the monochalcogenides. The 5f density of states is narrower (i.e. there is less hybridization) for a heavier anion. Adding Te to the solid solution  $USb_{1-x}Te_x$ , for example, is equivalent to increasing the conduction-electron density, and has the effect of driving the peak in the 5f DOS nearer to  $E_F$ . An *exactly* analogous effect is found when substituting tetravalent  $Th^{4+}$  for trivalent  $U^{3+}$  in  $U_{1-x}Th_xSb$ . Spectroscopically, such effects have been seen directly by Reihl et al. (1981a, b) using resonant photoemission techniques. Band-structure calculations (Brooks et al. 1984, 1986) have also suggested that there are about three 5f electrons for all these compounds.

What is much more complex to establish is the degree and effect of hybridization between the 5f and the band electrons. It is this aspect on which Cooper and his colleagues have worked so diligently, and aspects of the magnetic-structure behavior are addressed in Cooper et al. (1985), and more details are given in Cooper et al. (1992) and references therein. The chalcogenides have a stronger hybridization than the pnictides because the added p electron pushes the Fermi energy into a region with a high d-band density of states. The correlations caused by this hybridization favor ferromagnetic alignment of the ordered moment, i.e.  $k = 0$ . As a result we find that in the solid solutions  $k$ , the ordering wavevector, is a decreasing function of  $x$ , where  $x$  is the chalcogenide concentration. An example is given in fig. 22. A similar phase diagram exists for  $U_{1-x}Th_xSb$  (Rossat-Mignod 1987); in particular, both systems become ferromagnetic at  $x \sim 0.2$ . Once a ferromagnetic component appears, the material distorts to rhombohedral because there is a direct coupling between the  $k = 0$  component and the lattice.

Predicting these magnetic structures is extremely difficult since in each case there is a fine balance between different interactions. Probably the considerations discussed earlier will be necessary, together with some features of the anisotropic next-nearest-neighbor interaction model (ANNNI), as expounded by Bak and van Boehm (1980), Villain and Gordon (1980), and Fisher and Selke (1980).

Solid solutions can be found also for the cerium compounds, and Rossat-Mignod et al. (1985) have discussed the system  $CeSb_{1-x}Te_x$ . A small amount of Te doping has a pronounced effect on the magnetism of CeSb. By 4% doping the complex ordering found in CeSb gives way to simple type I order and at higher concentra-

tion the compositions exhibit a strong Kondo-type behavior. There are two major differences between actinide and cerium systems that are worth emphasizing. First, in the cerium systems we find magnetic structures which contain *paramagnetic* planes of moments. This is particularly true when a magnetic field is applied. So far *no* structures containing paramagnetic planes have been reported in the actinides. (Some comments on this appear in the discussion of USb–ThSb solid solutions below). Second, the cerium systems are all single-*k* structures, multiaxial multi-*k* structures seem to be confined (at least within the NaCl family) to the actinides. Some of the differences may be explained by the fact that the crystal field is more important for the cerium compounds and the hybridization effects less important. In addition to the work of Cooper et al. (1992) already referred to, the reader should also be aware of the p–f mixing model proposed for the Ce compounds by Takahashi and Kasuya (1985).

#### 4.3.6. Uranium solid solutions

Many of these are discussed by Rossat-Mignod et al. (1984), and a review concentrating on magnetization studies is given by Vogt and Mattenberger (1987). We shall concentrate here on a few of the detailed studies that have been made since 1984 on single crystals.

4.3.6.1. *UP–US solid solutions.* These were some of the first studied, but as more details have been examined the phase diagram has become progressively more complex. The latest version from Kuznietz et al. (1987a) is shown in fig. 23. There are two points worth noting in this diagram, besides its considerable complexity. Around a sulphur concentration of 20%, i.e.  $x = 0.2$ , which is close to the preferred ferromagnetic state, the magnetic wavevector is initially incommensurate ( $k \sim 0.38$  rlu), then locks in to  $k = \frac{1}{3}$  rlu (the 3+, 3– structure), and then abruptly increases to  $\frac{1}{2}$ , with a first-order phase transition at 42 K (Kuznietz et al. 1987b). The *increase* in  $k$  at lower  $T$  is unusual (see, e.g., fig. 22), but is similar to that found in NpAs (fig. 19). It probably indicates an electronic transition; in the case of NpAs this is accompanied by a substantial increase in the resistivity at lower temperature. The second point of interest concerns the coupling of the magnetism to the lattice. The low-temperature phase at  $x = 0$  is a  $2k$  configuration. These structures have  $\langle 110 \rangle$  as the easy axis and exist as ferromagnets for  $0.3 < x < 0.5$ . Then, the strong anisotropy requiring a  $\langle 111 \rangle$  easy axis becomes the most important, and the moment rotates to  $\langle 111 \rangle$  and induces a rhombohedral distortion. Although the magnetization data are clear on this matter, no low-temperature structural data have yet been published. In principle, the ferromagnetic phase for  $0.3 < x < 0.5$  should have monoclinic symmetry, arising from a system with a  $\langle 110 \rangle$  easy axis. The evolution of this cubic (or more probably monoclinic) structure to a rhombohedral one would seem a point worth further study.

4.3.6.2. *UAs–USE solid solutions.* These have also been the subject of extensive investigations with single crystals and an applied magnetic field (Kuznietz et al. 1986a,

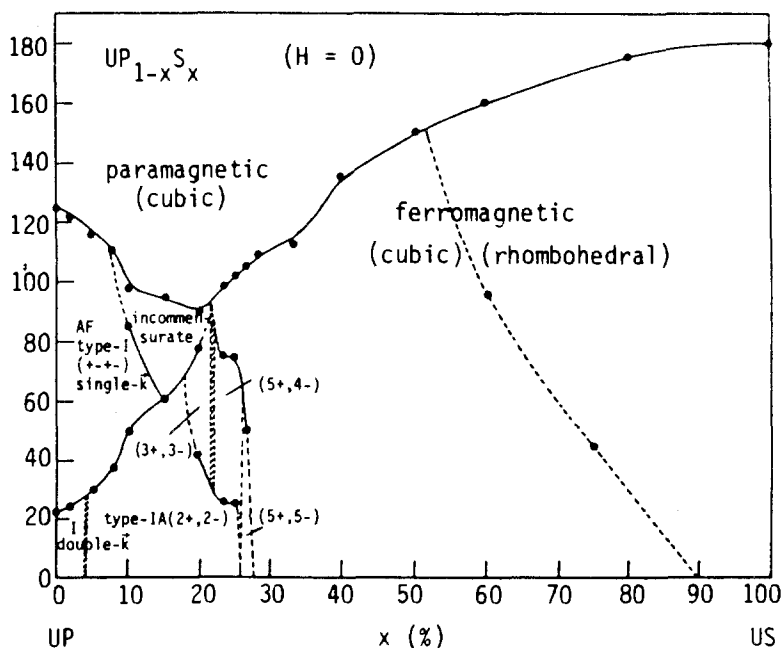


Fig. 23. The magnetic phase diagram of the UP-US solid solutions, from Kuznietz et al. (1987a).

b, 1987c). In this system, as a function of  $x$  (Se concentration), we find single- $k$ , double- $k$ , and triple- $k$  structures. It is interesting to note that in both the  $x = 0.25$  and  $0.30$  composition the *width* of the incommensurate peak varies strongly just before the lock-in phase transition, in both cases to  $k = 0.5$  rlu. This is a phenomenon we have already encountered in discussing NpAs (Jones et al. 1992) and may merit further modelling.

4.3.6.3. *USb-ThSb solid solutions.* Although the USb-ThSb phase diagram was reported by Rossat-Mignod et al. (1984), one sample near the critical composition for the appearance of ferromagnetism (Th concentration  $\sim 15\%$ ,  $x \sim 0.15$ ) has been recently reexamined, not only by the conventional techniques of magnetization and with neutrons, but also by resonant X-ray magnetic scattering at a synchrotron source. This combination of techniques has given some new insights in the magnetic structure (Paixão et al. 1993). In particular, we show in fig. 24 the magnetic modulations in the bulk proposed from the neutrons experiments, fig. 24b, and the near-surface behaviour as seen by X-rays, fig. 24c. The presence of a  $k = \frac{1}{2}$  component, in addition to the ferromagnetic  $k = 0$  and the components  $k = \frac{1}{4}$  and  $\frac{3}{4}$ , makes it impossible to simulate a square-wave modulation at low temperature. Furthermore, the near-surface behavior is different from that in the bulk. In both cases it seems quite probable that paramagnetic planes, as proposed for CeSb, for example (Rossat-Mignod 1987), exist in this material, and possibly in other systems as well.

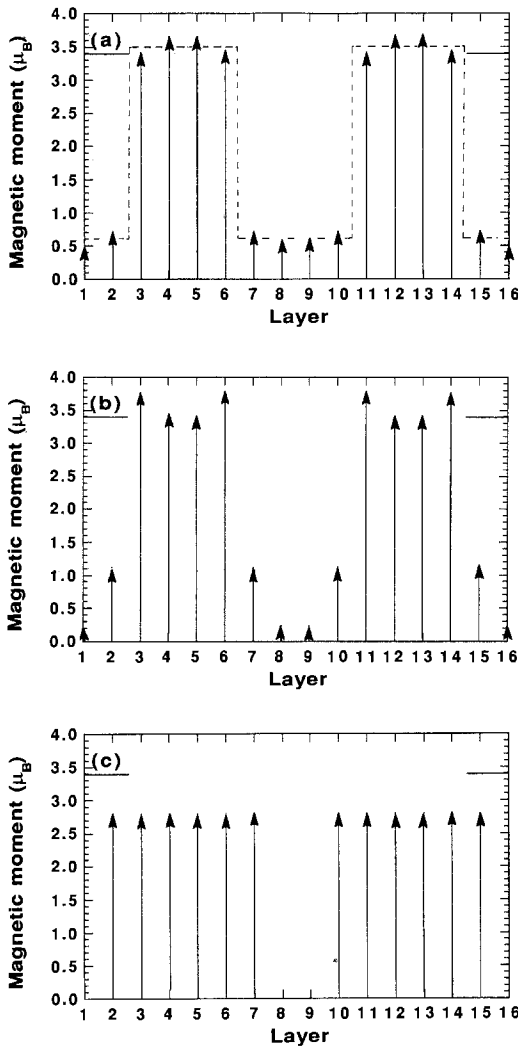


Fig. 24. Models of the magnetic configuration at low temperature in  $U_{0.85}Th_{0.15}Sb$ . The horizontal line at  $3.4\mu_B$  is the maximum possible moment,  $gJ$ , for a  $U f^3$  state. In each case two complete magnetic repeat units are shown. Recall that the modulation is longitudinal, but is shown as transverse for simplicity. (a) Result of combining the observed neutron  $F_0$ ,  $F_{1/4}$ , and  $F_{3/4}$  components and minimizing the entropy. The square-wave modulation (with the theoretical ratio between  $F_{1/4}$  and  $F_{3/4}$  is shown as a dashed line). (b) Result of adding the observed  $F_{1/2}$  component, which results in a strong distortion of the wave. (c) In the X-ray case the observed  $F_{1/2}$  is even larger and the wave is more distorted. Another possible model for the X-ray (near-surface) structure involves two paramagnetic planes, as shown in the lower frame.

#### 4.3.7. Solid solutions containing transuranium cations

Since about 1985 single crystals of transuranium NaCl-compositions have been produced in the European Institute for Transuranium Elements, Karlsruhe. We have already discussed the great differences between the pnictides and the chalcogenides, so that, given their complete solubility, it is natural to consider making solid solutions.

4.3.7.1. *NpAs–NpSe solid solutions.* These have only recently been made, and the first studies are reported by Mattenberger et al. (1992). Already some new effects are seen. At small doping,  $x = 0.05$ , of Se in NpAs the structure changes drastically from that of pure NpAs, and two components are seen at low temperature, as indicated in fig. 25. The large ferromagnetic component along  $\langle 111 \rangle$  together with  $k = 1$  components



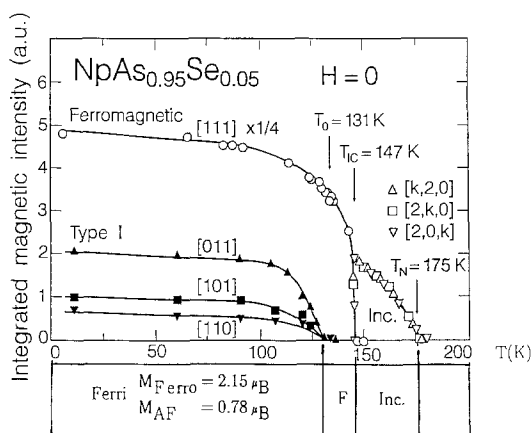


Fig. 25. Neutron diffraction phase diagram of  $\text{NpAs}_{0.95}\text{Se}_{0.05}$ , from Mattenberger et al. (1992).

along the  $\langle 100 \rangle$  directions give rise to a non-collinear structure. It should be emphasized that neither  $\text{NpAs}$  nor  $\text{NpSe}$  are ferromagnetic, so the finding of a large ferromagnetic component up to  $x = 0.15$  (Se concentration) is unusual.

**4.3.7.2.  $\text{NpSb}$ – $\text{NpTe}$  solid solutions.** These have been studied by magnetization, neutron (Mattenberger et al. 1990) and Mössbauer (Sanchez et al. 1988, 1990) techniques. As with the  $\text{NpAs}$ – $\text{NpSe}$  solid solutions, a ferromagnetic state is found with  $x = 0.10$  (Te concentration) and  $x = 0.15$  and two components are found in the  $x = 0.05$  sample. These experiments with low values of  $x$  have not, as yet, thrown any light on the magnetic ground state of  $\text{NpTe}$ .

**4.3.7.3.  $\text{PuSb}$ – $\text{PuTe}$  solid solutions.** In the plutonium systems a series of interesting experiments have been performed on the  $\text{PuSb}$ – $\text{PuTe}$  solid solutions (Sanchez et al. 1987). The resistivity (Therond et al. 1987) and magnetization have shown that for small Te doping (expressed as  $x$ ) the ferromagnetic state at low temperature in  $\text{PuSb}$  is changed to antiferromagnetic order. The decrease in the ordering temperature as a function of  $x$  suggests that samples with  $x > 0.3$  will not order magnetically. Because of the large absorption cross section of  $^{239}\text{Pu}$  for slow neutrons, such experiments are rather difficult, and none have yet been reported.

#### 4.3.8. Concluding remarks – $\text{NaCl}$ systems

Despite intensive efforts the electronic structure of the actinide monpnictides and monochalcogenides remains elusive. We have developed theories to explain many of the experimental results, but in most cases they have little predictive capability, especially with respect to something so basic as the magnetic structure. We will return to these theories when discussing the critical effects near the ordering temperature (sect. 5). Interestingly, in these discussions of properties more complicated than the magnetic structure we will find a closer accord between theory and experiment, together with more predictive capability on the part of the theory. This may seem strange at first glance, but it must be realized that the complex magnetic behavior

we have discussed is the result of many competing interactions and it is an almost impossible job to calculate these with enough accuracy to predict the magnetic structure.

The major mystery that remains is the ground state of the Np and Pu chalcogenides – here we note the important work of Wachter et al. (1991). Many aspects of the phase transitions are still unsolved, e.g., in NpTe, and also unknown is how the lattice energy accommodates the rotation of the magnetic moment from the face diagonal to the cube diagonal in the UP–US solid solutions. The nature of the lock-in magnetic phase transitions is also unusual and worthy of further study. There is also the need to consider compounds of Am, with nominally a  $J = 0$  singlet ground state, and Cm compounds. Hopefully, these problems will be addressed in the future.

#### 4.4. Trends in actinide magnetic structures

In the previous section we have already illustrated the complex magnetic structures that often exist in cubic NaCl-type actinide compounds. Not surprisingly, when we consider more complex actinide crystal structures the magnetic structures can become even more complicated. So many uranium compounds are now being synthesized and examined that it is impossible to cover all these studies in one review.

The major impetus to examine in detail more complicated actinide compounds has come from the discovery of heavy-fermion behavior, initially by Steglich et al. (1979) in  $\text{CeCu}_2\text{Si}_2$ , and then shortly thereafter in  $\text{UPt}_3$ ,  $\text{UBe}_{13}$ , and  $\text{URu}_2\text{Si}_2$  (Stewart 1984). Heavy-fermion behavior is discussed in more detail in a number of chapters in this volume. A full description of the neutron experiments on single crystals of heavy fermions is given by Aeppli and Broholm in a later volume. The interest in heavy fermions has, of course, been a considerable stimulation for all the actinide research and has been responsible for the concentration on *intermetallic* compounds. Our review reflects this change of emphasis. For a more complete review of the magnetic properties of actinide intermetallic compounds the reader should consult Fournier and Troč (1985), Sechovsky and Havela (1988), and various chapters in this volume.

##### 4.4.1. Cubic intermetallics

Prominent in this category are the actinide Laves phases  $\text{AB}_2$  and the compounds with the  $\text{AuCu}_3$  structure. We have already discussed the Laves phases in sect. 3, in connection with the determination of the orbital and spin moments. The magnetic structure of the Laves-phase compound  $\text{CeAl}_2$ , with  $T_N = 3.8 \text{ K}$ , continues to be of interest. Early experiments by Barbara et al. (1977, 1979) established a long-period sinusoidal modulation with a propagation vector  $\mathbf{k} = (0.5 + \delta, 0.5 - \delta, 0.5)$ , where  $\delta \sim 0.11 \text{ rlu}$ , so that the modulation repeats itself after about nine atomic unit cells. The most recent results are from Forgan et al. (1990), in which a single-domain crystal was produced by applying a magnetic field. They propose a  $2\mathbf{k}$ -spiral structure in which the moments in the different sublattices rotate in opposite directions. This is a so-called non-chiral spiral. Furthermore, the resultant moments are always greater than zero, which is not the case for single- $\mathbf{k}$  modulation, and lie between  $0.53$  and  $0.75\mu_B$ .

The majority of the actinide Laves phases is ferromagnetic; one exception is  $\text{NpCo}_2$ . Early publications (Gal et al. 1973, Aldred et al. 1975) claimed that the material was a simple antiferromagnet with  $T_N \sim 15$  K. As a result of the interest stemming from polarized-neutron experiments (Wulff et al. 1990a) and the reduction of the  $\mu_L/\mu_S$  ratio (see sect. 3), this material has been studied in more detail with both single crystal and polycrystalline samples. In spite of a considerable effort with neutrons, no direct evidence for AF order was found. Moreover, aspects of both the magnetization and Mössbauer experiments are also inconsistent with simple AF order. A review of these experiments is given by Sanchez et al. (1993), although no definite conclusion is drawn as to the nature of the low-temperature magnetic ground state.

Turning to the cubic  $\text{AuCu}_3$  structure we consider  $\text{CePb}_3$ . This has a reasonably high  $\gamma$ -value of  $225 \text{ mJ mol}^{-1} \text{ K}^{-2}$ , but orders antiferromagnetically at  $1.16(5)$  K, according to neutron experiments by Vettier et al. (1986). The magnetic ordering is complex, being incommensurate in two components, thus  $\mathbf{k} = (q_x, q_y, \frac{1}{2})$ , with  $q_x = 0.135(1)$  and  $q_y = 0.058(1)$  at 30 mK. Of these  $q_x$  appears independent of temperature (perhaps because it is commensurate with  $\frac{2}{15} = 0.1333?$ ), whereas  $q_y$  changes rapidly. The moments are  $0.55(10)\mu_B$  at the lowest temperature and are parallel to the  $[001]$  direction. No evidence for a higher-order modulation, which would indicate partial squaring, was found. This is a particularly unusual magnetic structure and the authors claim that it represents one possible ground state of a Kondo system. In this an interplay exists between the localized 4f electrons and the conduction electrons, resulting in different moments on different sites. A similar situation has been advanced for  $\text{CeAl}_2$ .

Of the actinide compounds with this crystal structure, there continues to be much interest in materials like  $\text{NpSn}_3$ , but there are, as yet, no reports of any neutron experiments. This is a small-moment, so-called itinerant, system and it would be interesting to confirm these results by neutron experiments. Attempts have been made to predict the magnetic structure from the Mössbauer spectra (Kalvius et al. 1990, Norman and Koelling 1986). Another system that warrants further study is  $\text{NpPd}_3$ , which exists in both the cubic  $\text{AuCu}_3$  structure and a hexagonal modification ( $\text{TiNi}_3 \text{ DO}_{24}$  structure). The cubic system orders magnetically, whereas hexagonal  $\text{NpPd}_3$  exhibits some type of complex short-range order (Nellis et al. 1974). This material thus joins  $\text{NpTe}$  and  $\text{NpCo}_2$  in having some kind of unusual magnetic correlations at low temperature. Experiments on single crystals would surely be interesting.

Another compound which crystallizes in two different atomic structures is  $\text{UH}_3$  or  $\text{UD}_3$ .  $\beta\text{-UH}_3$  was the first actinide ferromagnetic to be discovered with  $T_C \sim 165$  K (Ward 1985). Both allotropes, the  $\alpha$  and  $\beta$  form, crystallize in the same space group, the cubic  $\text{Pm}\bar{3}n$ .  $\alpha\text{-UH}_3$  has only two U atoms of the same type ( $a_0 = 4.161 \text{ \AA}$ ), whereas  $\beta\text{-UH}_3$  has a bigger unit cell ( $a_0 = 6.644 \text{ \AA}$ ) and eight U atoms per cell. It is almost impossible to make pure  $\alpha\text{-UH}_3$ , so that reports of its  $T_C$  being close to that of  $\beta\text{-UH}_3$  were always subject to doubt. In a recent experiment using spallation-source neutrons Lawson et al. (1991) have shown that the  $\alpha$  form (in this case using the deuteride) does not order at all, or at least with  $\mu_U < 0.5\mu_B$ . Since the moment in  $\beta\text{-UD}_3$  is  $\sim 1.4\mu_B$  this is an unexpected result. The density of the  $\alpha$  form is slightly higher ( $11.3 \text{ g/cm}^3$ ) compared to the  $\beta$  form ( $10.9 \text{ g/cm}^3$ ), but there must, in addition, be stronger bonding

in  $\alpha$ -UH<sub>3</sub> to drive the system into a wide-band metal with a 5f bandwidth too great to sustain an ordered magnetic moment.

#### 4.4.2. UTX compounds

A large family of compounds exist in this group, and they have been reviewed in detail by Sechovsky and Havela (1988). Five different crystal structures are involved, of which the most common is the ZrNiAl (or ordered Fe<sub>2</sub>P structure), which is hexagonal. In these materials, which include a transition metal T, a number of complex interactions and strong hybridization between the 5f and d wavefunctions can be anticipated. So far no really heavy fermions, as judged by the electronic specific heat parameter  $\gamma$ , have been found (UPdIn has a  $\gamma$  of  $\sim 280 \text{ mJ mol}^{-1} \text{ K}^{-2}$ , which is the highest so far in this group), but many other properties are interesting. No studies of the physical properties of transuranium materials with this structure type have been reported, although efforts in this direction are in progress. One of the properties of considerable interest is the huge magnetic anisotropy present in these materials, and the fact that it is present also in the paramagnetic state. Fortunately, it has proved fairly easy to grow single crystals of the U compounds, so that these anisotropy questions can be studied in some detail.

UCoAl and URhAl have been studied with polarized neutrons to obtain the magnetization densities. Both have the hexagonal ZrNiAl structure, in which there is one U site but two transition metal sites, T<sub>1</sub> and T<sub>2</sub>. The structure is shown in fig. 26. UCoAl does not order magnetically, but has a large susceptibility, so that in a field of 5 T Wulff et al. (1990b) were able to induce a moment of  $\sim 0.35 \mu_B$  per mol. Since this structure is non-centrosymmetric, the neutron results have an ambiguity in the phase, unless one confines the study to a centrosymmetric projection. This method was used by Wulff et al. (1990b) in their preliminary report, but it limits the amount of information that can be extracted. They found a small ( $\sim 15\%$  of the total) moment on the Co atoms, but did not distinguish between the Co<sub>I</sub> and Co<sub>II</sub> sites. Somewhat surprising, the form factor looked like that of a conventional U material with  $-\mu_I/\mu_S = 2.7(6)$ , whereas the free-ion value is 2.6. This suggests that the U-Co hybridization is small in UCoAl, and yet it shows a large anisotropy in the high-temperature magnetization.

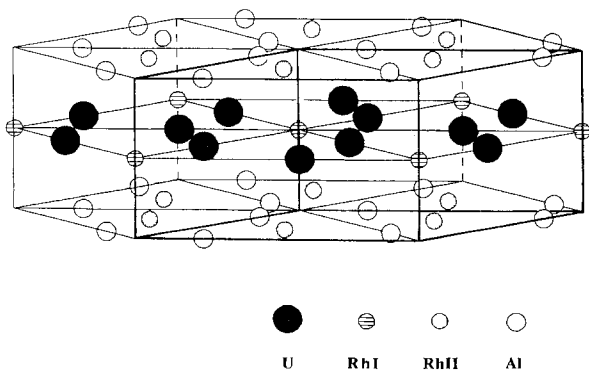


Fig. 26. Schematic representation of the UCoAl and URhAl hexagonal (ZrNiAl) structure. The volume shown contains three unit cells and nine U atoms. The bold edges highlight one unit cell. (From Paixão et al. (1992).)

The study (Paixão et al. 1992) of URhAl is more extensive than that reported so far for UCoAl. Here, fig. 27 shows unambiguously the presence of a moment on both the U and Rh<sub>I</sub> site. This material is a ferromagnet ( $T_C = 27$  K) and the moment on the U site is  $0.91(9)\mu_B$ , consisting of an orbital part of  $2.10(3)\mu_B$  and a spin part of  $-1.16(3)\mu_B$ , so  $-\mu_L/\mu_S = 1.8(1)$ , and a moment of  $0.28(3)\mu_B$  at the Rh<sub>I</sub> site. At the Rh<sub>II</sub> site the moment is  $0.03(3)\mu_B$ , i.e. not significantly different from zero. The  $\mu_L/\mu_S$  ratio is significantly below the  $f^3$  free-ion value of 2.6, so that the authors argue that the strong anisotropy is a consequence of 5f-4d hybridization lining up the moments parallel to the unique hexagonal axis. A reduction of  $-\mu_L/\mu_S$  is not, of course, an absolute requirement for hybridization, but the strong polarization of the U-T<sub>1</sub> plane may well turn out to be a significant feature of the magnetic ground state of these compounds; however, these studies require single crystals. Neutron studies are now under way on UNiAl and URuAl, and more are likely to be reported in the future.

Of the compounds with the ZrNiAl crystal structure one of the more complicated magnetic phase diagrams is exhibited by UNiAl, and even with single crystals this is proving difficult to solve. UNiGa, on the other hand, has been found to have a relatively simple  $+ - +$  antiferromagnetic structure (Maletta et al. 1992) with a moment of  $1.4(2)\mu_B$  per U atom. These experiments on polycrystalline samples will be insensitive to small moments at the Ni site.

Another structural type of the UTX compounds is the CeCu<sub>2</sub>-type structure (space group orthorhombic Imma). The observation of a first-order antiferromagnetic phase transition at 43.3 K has been reported for UNiGe by Murasik et al. (1991). The magnetic unit cell is doubled along both the [100] and [001] directions, corresponding to a propagation vector  $\mathbf{k} = (\frac{1}{2}, 0, \frac{1}{2})$ . The ordered moment at low temperature on the U atom was found to be  $1.37(7)\mu_B$ . The use of a polycrystalline sample prevented any study of the (presumably small) moment that might be present on the Ni. Experiments on UPtGe have been reported by both Robinson et al. (1993a) and Kawamata et al. (1992). This material has the CeCu<sub>2</sub> orthorhombic (or possibly the ordered NiSiTi)

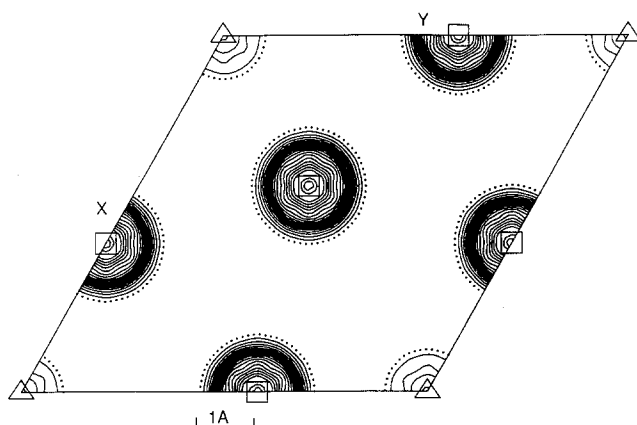


Fig. 27. Magnetization density at the  $z = \frac{1}{2}$  level in URhAl, showing the presence of magnetic moments localized at both the U and Rh<sub>I</sub> sites in the structure. (From Paixão et al. (1992).)

structure.  $T_N = 51$  K and the ordering wavevector is  $\mathbf{k} = (0, 0.554, 0)$  with a moment of  $1\mu_B$ . The moments are confined to the  $b$ - $c$ -plane, but rotate by a constant angle between each layer of uranium atoms. The most reasonable model for the structure gives that all the moments have the same value. In few systems we find actinide moments varying in direction between planes in the magnetic structure, so this is unusual. As yet, so little is known about either the crystal fields or the anisotropy in these systems, that a further analyses is impossible.

Yet another structure is the cubic MgAgAs type. Neutrons have shown that UNiSn (Yethiraj et al. 1989) is antiferromagnetic ( $T_N = 47$  K), with a moment of  $1.42(3)\mu_B$  per atom. Note that in earlier work it was concluded that this material is paramagnetic even at low temperature (Sechovsky and Havela 1988), so this emphasizes the importance of performing neutron diffraction, even on polycrystalline samples, as used here. In the case of UNiSn the situation is complicated by differences that appear to depend on the sample preparation. A theoretical effort, in part undertaken to explain some of these unusual anomalies, led to the suggestion that the material is a strong "half-metallic ferromagnet" (Albers et al. 1987) with a giant magneto-optical Kerr effect (Daalderop et al. 1988). While these ideas are of interest in the context of the UTX compounds, they apparently do not apply to UNiSn.

Neutron experiments have also been reported on polycrystalline samples of UPdSn (Robinson et al. 1991, 1992). This material was thought to have the hexagonal  $\text{CaIn}_2$  (space group  $\text{P6}_3/\text{mmc}$ ) structure, but the authors find a better fit of the structural data with space group  $\text{P6}_3\text{mc}$ , in which the Pd and Sn atoms are ordered. The magnetic structure is a complicated one ( $T_N = 43$  K) with non-collinear components and uranium moments of  $2.05(4)\mu_B$ . The resultant moments are canted away from the hexagonal axis by  $\sim 55\%$  and rotate about the cone axis. This is an unusual situation since normally in actinide compounds the anisotropy is large and the moment direction does not vary as a function of temperature. Recently, Robinson et al. (1993b) have examined the lattice distortions in this complex magnetic structure. These experiments are a good example of the power of high-resolution neutron powder diffraction experiments. Robinson et al. (1993c) also report work on UAuSn, which has the hexagonal  $\text{CaIn}_2$  structure. This material orders at 36 K with a relatively simple antiferromagnetic structure and a moment of  $1.10(5)\mu_B$  at the uranium site.

#### 4.4.3. $UT_2X_2$ compounds

The great interest in this type of material stems from the heavy-fermion compounds  $\text{CeCu}_2\text{Si}_2$  and  $\text{URu}_2\text{Si}_2$  (Stewart 1984, Ott and Fisk 1987, Aeppli and Broholm in vol. 19 of this series). Both of these, and also  $\text{CeRu}_2\text{Si}_2$ , have the body-centered tetragonal structure (space group  $\text{I4}/\text{mmm}$ ). Another variant is the orthorhombic ( $\text{P4}/\text{mmm}$ )  $\text{CaBe}_2\text{Ge}_2$  type. In these structures  $X = \text{Si}$  or  $\text{Ge}$ . Although we concentrate on the experiments performed since about 1984, we include all the compositions in table 5 that have been studied by neutrons. For a complete survey of the magnetic properties of these materials the reader should consult Sechovsky and Havela (1988).

One of the most complete experiments has been performed on  $\text{UNi}_2\text{Si}_2$ , of which single crystals have been produced. The various magnetic structures are shown in fig. 28. The high-temperature phase has  $\mathbf{k} = (0, 0, 0.75 - \delta)$ , where  $\delta \sim 0.01$  at  $T_N$ , decreases,

TABLE 5

Details of the U and Np compounds with the  $\text{ThCr}_2\text{Si}_2$  tetragonal structure. AF and F stand for antiferromagnetism and ferromagnetism. The moment is that determined using neutrons at low temperature.

Compound	$a$ (Å)	$c$ (Å)	Order	$T_C, T_N$ (K)	$\mu$ ( $\mu_B$ )	Easy axis	Ref. <sup>b</sup>
$\text{UNi}_2\text{Si}_2$	3.97	9.52	AF	124	2.2	[001]	[1]
$\text{UCu}_2\text{Si}_2$	3.99	9.95	F	103	2.0	[001]	[2]
$\text{U}(\text{Cu}_{0.75}\text{MnO}_{0.25})\text{Si}_2$	—	—	F	—	1.7	[001]	[2]
$\text{URu}_2\text{Si}_2$	4.13	9.57	AF	17.5	—	—	[3]
$\text{U}(\text{Ru}_{1.2}\text{Re}_{0.8})\text{Si}_2$	—	—	F?	30	0.5	—	[4]
$\text{URh}_2\text{Si}_2$	4.01	10.02	AF	137	2.0	[001]	[5]
$\text{UPd}_2\text{Si}_2$	4.23	9.87	AF	150	2.0	[001]	[5]
$\text{UPt}_2\text{Si}_2^a$	4.19	9.68	AF	34	1.6	[001]	[6]
$\text{UCo}_2\text{Ge}_2$	4.02	9.87	AF	175	1.5	[001]	[7]
$\text{UNi}_2\text{Ge}_2$	4.09	9.47	AF	74	—	—	[8]
$\text{UCu}_2\text{Ge}_2$	4.06	10.21	F/AF	105	—	—	[8, 9]
$\text{UPd}_2\text{Ge}_2$	4.20	10.23	AF	139	2.0	[001]	[5]
$\text{NpCo}_2\text{Si}_2$	3.88	9.73	AF	46	1.5	$\sim [\frac{1}{2}01]$	[10]
$\text{NpCu}_2\text{Si}_2$	3.92	9.41	F	41	2.0	[001]	[10]
$\text{NpRu}_2\text{Si}_2$	4.14	9.54	AF	28	1.6	[001]	[11]
$\text{NpCo}_2\text{Ge}_2$	3.80	9.56	AF	36	1.6	[001]	[12]
$\text{NpCu}_2\text{Ge}_2$	3.89	9.42	AF	34?	1.2?	—	[12]

<sup>a</sup>This material has the  $\text{CaBe}_2\text{Ge}_2$  structure.

<sup>b</sup>References: [1] Lin et al. (1991). [2] Giorgi et al. (1988). [3] Broholm et al. (1991). [4] Torikachvili et al. (1990). [5] Ptasiewicz et al. (1981); Shemirani et al. (1993). [6] Steeman et al. (1988). [7] Kuznietz et al. (1989). [8] Chelmicki et al. (1985). [9] Kuznietz et al. (1990). [10] De Novion et al. (1980). [11] Bogé et al. (1989). [12] Gal et al. (1989b).

and then (surprisingly) increases to 0.02 before the transition to a  $\mathbf{k} = (0, 0, 1)$  state at  $\sim 103$  K. A ferromagnetic moment appears below 53 K and it seems reasonable to propose a square-wave modulation. No moment was reported on the Ni site. It is worth remarking here that the lanthanide  $\text{LnNi}_2\text{Si}_2$  compounds order at much lower temperatures ( $< 20$  K) and that  $\text{CeNi}_2\text{Si}_2$  is a Pauli paramagnet (Leciejewicz and Szytula 1987, Szytula and Leciejewicz 1989, Pinto et al. 1985).

Giorgi et al. (1988) reported experiments on polycrystalline  $\text{UCu}_2\text{Si}_2$  and  $\text{U}(\text{Cu}_{0.75}\text{Mn}_{0.25})\text{Si}_2$ , both of which are ferromagnetic. Interestingly, they did report the need to place a small moment of  $0.16(5)\mu_B$  on the (Cu, Mn) site in the latter compound. These materials are of interest because they have high coercive fields; unfortunately  $T_C$  is too low for any practical use.

A large number of experiments have been reported on  $\text{URu}_2\text{Si}_2$ . The latest, by Broholm et al. (1991), covers the magnetic structure in detail, as does the chapter by Aeppli and Broholm in vol. 19 of this series. Substituting Re for Ru increases the ordering temperature and the ordered moment (Torikachvili et al. 1990, 1992), although the exact form of the ordering in this mixed compound is not firmly established. The Np compounds have been studied in some detail, particularly with the Mössbauer technique, but also in a few cases with neutrons. In view of the interest in  $\text{CeRu}_2\text{Si}_2$

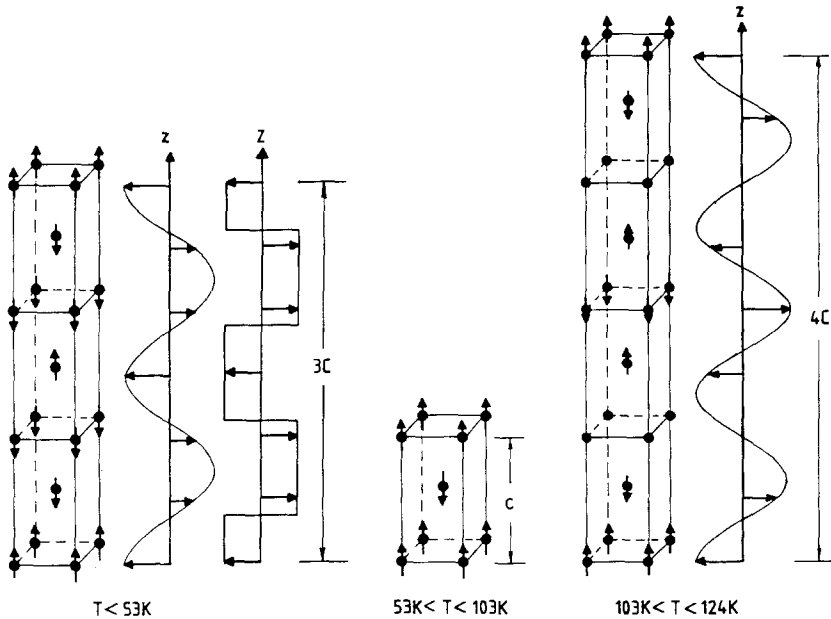


Fig. 28. Magnetic structure for the three phases of  $\text{UNi}_2\text{Si}_2$ . Two possible structures are shown on the left for the low-temperature phase; the longitudinal spin-density wave. The high-temperature phase (on the right) is almost commensurate,  $\mathbf{k} = (0,0,0.75)$ , but differs slightly from this. (From Lin et al. (1991).)

and  $\text{URu}_2\text{Si}_2$ , it is interesting to study  $\text{NpRu}_2\text{Si}_2$ , and a detailed report using many different techniques has been presented by Bogé et al. (1989). A small (2 mg,  $1.7 \times 1 \times 0.2 \text{ mm}^3$ ) crystal was available and this was used successfully in a neutron experiment. The material orders (at 28 K) with a longitudinal wave type structure identical to that shown on the right-hand side of fig. 28. The  $\mathbf{k}$ -vector is written as  $(0,0,k)$ , where  $k = 0.760(5)\text{r.l.u.}$  at  $T_N$  and increases to  $0.865(5)\text{r.l.u.}$  at 1.3 K. There is no sign of any lock-in transition. At low-temperature a third-order harmonic is observed, but it is too small for the wave form to be squared. At the lowest temperature, therefore, there are different Np moments present, a fact also consistent with the Mössbauer spectra. The model proposed from a combination of neutron and Mössbauer experiments is that there are primarily two types of Np sites, one with  $1.5\mu_B$  and a population of  $\frac{1}{3}$  and one with  $1.2\mu_B$  and a population of  $\frac{2}{3}$ . This model is very similar to that proposed for NpP by Aldred et al. (1974).

Finally, it is worth mentioning that in neutron experiments on  $\text{NpCu}_2\text{Ge}_2$ , which from other measurements was claimed to be antiferromagnetic with  $T_N = 34 \text{ K}$  and  $\sim 1.2\mu_B/\text{Np}$ , one failed to find any evidence of long-range magnetic order.

Comparisons with the lanthanide compounds are difficult due to the complexity found in the different systems. Most of the lanthanide compounds order at much lower temperature ( $< 20 \text{ K}$ ) than the U compounds. A good example is the recent work of Loidl et al. (1992) on the compounds  $\text{CeM}_2\text{Ge}_2$ , where  $M = \text{Cu, Ru, Ag, and Au}$ . All except  $M = \text{Ru}$  are antiferromagnets, and the  $M = \text{Ag}$  compound has a



particularly complex magnetic structure with  $\mathbf{k} = (0.285, 0, 0.90)$ , with a magnetic moment of  $1.85\mu_B$  (almost the free-ion value), and the moments along the  $a$ -axis of the tetragonal structure. The ordering temperatures are all below 20 K. For cerium compounds the ordering temperatures are always low, except when the alloying atom is Mn, then the compounds order at high temperature ( $> 300$  K) because of the ordering of the Mn sublattice. For the heavy lanthanides the magnetic ordering is complex, but at low temperature, as expected, the moments have their full free-ion values. That is not the case with either U or Np compounds, where the moments are considerably below the free-ion values of  $\sim 3\mu_B$ . Crystal-field effects may play a role, but more likely are hybridization effects between the 5f and d electrons. Similarly, the easy direction of magnetization may be related in the first instance to the dominant term  $B_0^2$  in the crystal-field Hamiltonian, but if  $U^{3+}$  ( $5f^3$ ) implies a negative  $B_0^2$  with  $\mathbf{m} \parallel \mathbf{c}$ , then  $Np^{3+}$  ( $5f^4$ ) should have a positive  $B_0^2$  and thus the moments should lie in the basal plane. Unlike the lanthanide case, the actinides behave inconsistently. This is a frequent occurrence in actinide compounds; it does not mean that the crystal-field interactions are unimportant, only that other interactions dominate.

We have discussed these types of structures at some length, because it is likely that future work will concentrate on intermetallic compounds. For example, Steglich et al. (1991) have reported the discovery of the heavy-fermion compounds  $UNi_2Al_3$  and  $UPd_2Al_3$ , and both exhibit some type of magnetic order as well as superconductivity at temperatures of  $\sim 2$  K. Much remains to be done in having these results of macroscopic experiments followed by systematic neutron investigations on the microscopic properties.

#### 4.4.4. Nature of the long-range order in heavy-fermion compounds

A number of heavy-fermion compounds is found to exhibit magnetic ordering, e.g.  $CePb_3$  (Vettier et al. 1986) and  $U_2Zn_{17}$  (Cox et al. 1986), and it was thought initially that the ground state of these materials would be either magnetic or superconducting. Such a division is too simple. Indeed, those heavy-fermion compounds that become superconducting almost always show some kind of antiferromagnetic correlations as well, even in the superconducting state (see Lander and Aeppli (1991) for references). The largest body of work has been done on  $UPt_3$  and  $URu_2Si_2$ ; in both cases excellent single crystals are available. In both these systems the magnetic moments in the so-called antiferromagnetically "ordered state" are extremely small,  $\sim 0.02\mu_B$  for  $UPt_3$  (Aeppli et al. 1988) and  $0.04\mu_B$  in the case of  $URu_2Si_2$  (Broholm et al. 1991). The antiferromagnetic structures are relatively simple, but the presence of such small moments raises a number of interesting questions. How are they stabilized, and is the structure truly long range? The first is a theoretical question, but the second is open to verification by diffraction techniques. Truly long-range order implies that the Bragg diffraction peak has an infinitely narrow width in reciprocal space, but since the instrumental resolution is always finite, the real question is how close is the magnetic peak to the instrumental resolution. Better resolution can be obtained with synchrotron X-rays than is possible with neutrons (primarily because of the intrinsically narrow divergence of the photons emerging from a synchrotron), and using resonant X-ray magnetic scattering Isaacs et al. (1990) examined  $URu_2Si_2$  in the superconducting

state. They found that the “ordered” magnetism consists of correlations up to  $\sim 500 \text{ \AA}$  in length. So far, few of these kind of experiments have been done, so we cannot be sure of the nature of this ordering in the ground state of these interesting materials; no doubt more high-resolution studies will be performed in the future.

#### 4.5. *Insulating actinide compounds*

As mentioned in sect. 4.4, there has been strong emphasis in the last ten years on intermetallic actinide compounds, although the oxides still have a special fascination; we shall discuss them in connection with inelastic scattering in a later chapter in vol. 19.

A series of both elastic and inelastic experiments on uranium trihalides has been undertaken by Murasik and collaborators.  $\text{UF}_3$  crystallizes in the  $\text{LaF}_3$  hexagonal structure and shows no evidence of cooperative magnetism down to 1.9 K.  $\text{UCl}_3$  and  $\text{UBr}_3$  both crystallize in the hexagonal  $\text{UCl}_3$  structure (space group  $\text{P6}_3/\text{m}$ ) and show complex magnetic order (Murasik et al. 1985, Schmid et al. 1990). Below the respective  $T_N$ 's of 6.5 and 5.4 K the magnetic structure consists of an unusual configuration, in which two sublattices are coupled antiferromagnetically, but the third is disordered. This occurs because of frustration effects. The uranium moments form antiferromagnetic chains along the  $c$ -axis, indicating a dominant antiferromagnetic exchange in this direction. At  $\sim 4 \text{ K}$  magnetic moments of  $1.8(1)\mu_B$  and  $2.1(1)\mu_B$  are present in  $\text{UCl}_3$  and  $\text{UBr}_3$ , respectively, and these are oriented along the  $c$ -axis. At 3.8 K in  $\text{UCl}_3$  and 3.0 K in  $\text{UBr}_3$  complete magnetic ordering occurs, but with a lowering of the ordered moments to  $\sim 0.8\mu_B$  and a reorientation of the moments along the  $b$ -axis. In  $\text{UI}_3$ , which has an orthorhombic structure,  $T_N = 3.4 \text{ K}$  and only one magnetic transition occurs, to a three-dimensional ordered state.

These systems would be particularly interesting to study if single crystals were available, since lower-dimensional materials are rare in 5f systems. All the experiments so far, have been performed on polycrystalline samples. Reorientations of the moments are relatively rare in actinide magnetic structures. This is because the anisotropy is usually enormous (see sect. 4.7 below), especially in intermetallics, and in all cases determines the easy-moment direction. In ionic systems, in which the hybridization between  $f$  and plane-wave (conduction-electron) state is absent, the moment directions are determined by an interplay between the exchange and crystal-field interactions, as is found in lanthanide systems. Clearly this is the case in the above trihalides.

A change in the wavevector, rather than a reorientation of the moment, is found also in  $\beta\text{-Pu}_2\text{O}_3$  at low temperature. Early work on this material (McCart et al. 1981) failed to establish the magnetic structure, but a recent experiment using the high resolution and high intensity of the powder diffractometer at the Institut Laue-Langevin, Grenoble, solved the structure (Wulff and Lander 1988), which involves a doubling of the cell in all three directions for  $4 < T < T_N = 19 \text{ K}$ . The ordered moment is  $0.60(2)\mu_B$  and the Pu ion, as expected, is in a  $5f^5$  state. At 4 K the wavevector becomes commensurate with the chemical unit cell, although this has not yet been conclusively proven by neutron diffraction.

Experiments have also been reported on the Np oxychalcogenides  $\text{NpOZ}$  ( $Z = \text{S}, \text{Se}$ ) by Amoretti et al. (1989). The structure is quite simple in the case of  $\text{NpOSe}$  with

$\mu = 1.64\mu_B$ , but no magnetic lines were seen in the case of NpOS, even though  $\mu \sim 0.7\mu_B$  is predicted from the Mössbauer hyperfine field; this may be just a question of sensitivity. The results of this work have been successfully interpreted with a crystal-field model.

With the discovery of high- $T_c$  superconducting oxides, there is now much interest in materials with the perovskite-like ( $K_2NiF_4$ ) structure and its modifications. The classic high- $T_c$  material is, of course,  $La_2CuO_4$ , with  $Sr^{2+}$  or  $Ba^{2+}$  doping. Soderholm et al. (1991) have had the interesting idea of preparing  $Cm_2CuO_4$  and substituting the  $Cm^{3+}$  by  $Th^{4+}$ . This is an analogue of the "electron" superconductor  $R_{1.85}Ce_{0.15}CuO_4$  with the so-called  $T'$  structure (Takagi et al. 1989), and the Cm compounds crystallize in this structure also.  $Cm_2CuO_4$  is antiferromagnetic at  $T_N \sim 25$  K and Soderholm et al. (1992) have recently determined the magnetic structure with neutrons, the first time a *magnetic* structure has been determined in a Cm compound. The doped compound  $Cm_{1.83}Th_{0.17}CuO_4$  is neither antiferromagnetic nor superconducting. Goodman and Soderholm (1990) have explained these (and those involving the  $Pr^{3+}$  ion in  $PrBa_2Cu_3O_7$ ) results as a consequence of mixing between the f states and the CuO states. This mixing involves no significant net charge transfer.

#### 4.6. Studies of spin glasses

The phenomenon of "spin-glass behavior" has been confined to date almost exclusively to d-electron systems. The presence of large anisotropy associated with the orbital moment in f-electron systems tends to select a discrete direction for the magnetic moment, and this is even more common in 5f than in 4f systems. If the lattice itself has no long-range order, e.g. is amorphous, spin-glass effects are found in lanthanide (4f) systems (Spano and Rhyne 1985), but they are rare in actinide systems. We have speculated above (sect. 4) that systems like  $NpCo_2$  may have certain characteristics of a spin glass, but it is more likely that they exhibit some type of short-range order, perhaps with a temporal fluctuation of the moments, rather than true spin-glass behavior.

On the other hand, Gal et al. (1990) have shown that the actinide-containing compounds  $AnFe_4Al_8$  ( $An = Th, U, Np$ ) are all spin glasses. The so-called spin-glass temperatures,  $T_{SG}$ , where hysteretic and irreversible effects in the magnetization occur, are all about 120 K for these materials. Neutron diffraction (and Mössbauer also, in the case of the Np compound) experiments show that a moment exists on the U and Np sites, but it is not clear from these studies on polycrystalline samples whether the moment directions are random or uniaxial. The dominant *spin-glass* behavior is, of course, provided by the Fe sublattice. This is not only shown by the various measurements, but also by the fact that  $T_{SG}$  is much the same for the Th compound (no 5f moments exist on the Th) as for the other actinide compounds.

Similar experiments have been reported by this group (Gal et al. 1989b) on the isostructural 4f compound  $HoFe_4Al_8$ . In this case the Ho moment can be aligned ferromagnetically at low temperature to give  $\sim 8\mu_B$ , but if the field is then switched off the Ho moments relax into a more complex arrangement, consistent with exchange

coupling to the (spin-glass) Fe sublattice.  $T_{SG}$  is  $\sim 180$  K. Such a process might also be occurring in the actinide compounds, but is more difficult to prove directly because of the small moments. Once again, this is a system in which single crystals would be worth obtaining.

#### 4.7. Measurements of magnetic anisotropy with neutrons

We have discussed at length in the section on magnetic structures, sect. 4.4, the concept of anisotropy of the magnetization, and this anisotropy will occur again in our discussion of the critical (sect. 5) scattering. There exists a quantitative measure of the anisotropy in terms of the energy required to rotate the moments from their easy direction into the direction of the applied field,  $\mathbf{H}$ . If we restrict our consideration to *cubic* systems, then a single so-called anisotropy constant  $K_1$  normally dominates the anisotropy. The magnetic energy (Clark 1980) is given by

$$E = K_1(\alpha_1^2\alpha_2^2 + \alpha_2^2\alpha_3^2 + \alpha_3^2\alpha_1^2) - \boldsymbol{\mu} \cdot \mathbf{H},$$

where  $\alpha_i$  are the direction cosines of the moment  $\boldsymbol{\mu}$  with the three cube axes of the crystal. The units of  $K_1$  are  $\text{erg/cm}^3$  ( $10^7 \text{ erg/cm}^3 = 1 \text{ MJ/m}^3$ ), and, to give an idea, Fe has a  $K_1 = 5 \times 10^5 \text{ erg/cm}^3$  at low temperature and it is relatively easy with a field of  $\sim 0.1$  T to rotate the moment into the field direction. On the other hand, the cubic Laves phases of the lanthanides, such as  $\text{TbFe}_2$  ( $T_C = 700$  K), have  $|K_1| = 5 \times 10^8 \text{ erg/cm}^3$  at 0 K. In this material fields greater than 10 T are required to turn the moment away from the easy direction. ( $K_1 > 0$  corresponds to a  $\langle 100 \rangle$  easy axis, whereas  $K_1 < 0$  corresponds to an  $\langle 111 \rangle$  easy axis.)

We certainly anticipate actinide materials to have  $|K_1| > 10^8 \text{ erg/cm}^3$ , but the question is how much greater. This question was first addressed using magnetization experiments by Gardner and Smith (1968) with single crystals of US. Their estimates gave  $K_1 < 10^8 \text{ erg/cm}^3$ , but the difficulty is that systematic errors, such as small misalignments, can seriously affect the results. Using magnetic torque measurements Tillwick and DuPlessis (1976) estimated  $9 \times 10^8 \text{ erg/cm}^3$  at 0 K. Recently Lander et al. (1990, 1991b) have demonstrated that the anisotropy constant can also be measured with polarized neutrons. The method is based on the vectorial interaction between the neutron's spin and the microscopic magnetic moments in the solid. This allows a simultaneous measurement of the magnitude of the induced moment as well as the direction of that moment in real space relative to the applied magnetic field. These two quantities are shown for a single crystal of US in fig. 29. The easy axis of magnetization is  $\langle 111 \rangle$  in US, so that at low temperature the moments are along this direction and are not rotated any measurable amount by the field of 4.6 T. At intermediate temperatures, however, the moment rotates from  $\langle 111 \rangle$  to the direction of  $\mathbf{H}$ . With knowledge of the geometry one may solve the energy equation above, obtaining the value of  $K_1$ . From symmetry considerations (Callen and Callen 1966) it is known that the temperature dependence of  $K_1$  may be expressed in terms of the reduced magnetization ( $\mu/\mu_0$ ) in the form

$$K_1(T)/K_1(0) = I_{9/2}[\mathcal{L}^{-1}(\mu/\mu_0)],$$

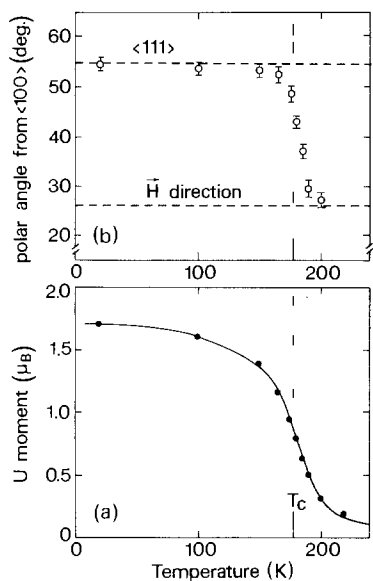


Fig. 29. (a) Magnetic moment on the uranium atom as a function of temperature in an applied field of 4.6 T. The solid line is the result of a magnetization experiment on a small single crystal with  $H \parallel \langle 111 \rangle$ . (b) Polar angle,  $\Theta$ , from a certain  $\langle 100 \rangle$  direction and the magnetic moment as determined using polarized neutrons. (Taken from Lander et al. (1990).)

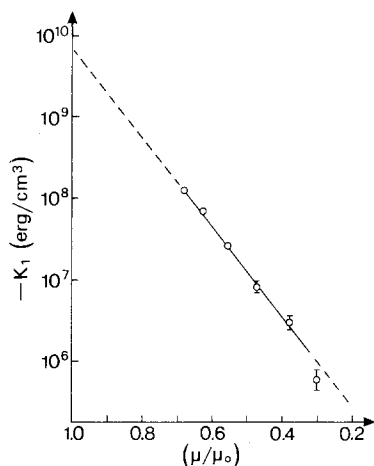


Fig. 30. Variation of  $K_1$  with the reduced moment, where temperature is an implicit parameter. The negative sign of  $K_1$  indicates that the easy axis is  $\langle 111 \rangle$ . (Taken from Lander et al. (1990).)

where the expression on the right-hand side is the hyperbolic Bessel function. For  $\sim 0.4 < \mu/\mu_0 < 1$ , this function is approximately a straight line on a semilog plot, which is shown in fig. 30. The fact that US obeys this relationship over almost three orders of magnitude gives confidence in the extrapolation to 0 K and the value of  $\sim 10^{10}$  erg/cm<sup>3</sup>. This is  $\sim 20$  times larger than the highest known value for a cubic lanthanide-containing material, viz. TbFe<sub>2</sub> (Clark 1980).

These experiments show clearly the enhanced anisotropy as compared with lanthanide compounds and provide a quantitative measure for the statements made about anisotropy in this, and other, chapters. They also raise the question of whether

uranium compounds could be useful for device applications, since anisotropy is one of the important parameters in many devices. The difficulty here, as with the possible use of uranium in magneto-optical devices, is that  $T_C$  is normally too low. In US  $T_C = 178$  K, so that it is unsuitable for device applications. By combining uranium with transition metals (much as is done in  $\text{TbFe}_2$  and  $\text{SmCo}_5$ ) the Curie temperature may be increased above room temperature. A good example is the alloy system (Baran et al. 1985, Ptasiewicz-Bak et al. 1988)  $\text{U}(\text{Al}_{1-x}\text{Fe}_x)_{12}$ , for which  $T_C = 355$  K at  $x = 0.5$ . If  $T_C$  could be increased to  $\sim 600$  K then these materials might well become technologically important.

## 5. Magnetic critical scattering

The previous section on magnetic structures addressed the *static* arrangement of magnetic moments that exists below the ordering temperature of magnetic materials. The experiments are constrained to observing the intensity and position of magnetically diffracted *peaks* in the ordered phase. The order is assumed infinite in extent, so that the peaks are delta functions in reciprocal space. If the infinite three-dimensional aspect of the magnetic correlation begins to break down, then the sharp delta functions in reciprocal space also change their form. Thus the loss of long-range magnetic order as the material is heated towards its ordering temperature is reflected in the change of form of the scattering. In this way magnetic critical scattering has given unique information on both the varying static and dynamic arrangements of magnetic moments near their ordering temperatures.

If we confine ourselves initially to the spatial correlations of the magnetic moments (some remarks on dynamical behavior are made at the end of this section), then we may relate the scattering at a wavevector  $\mathbf{Q}$  to the wavelength-dependent susceptibility,  $\chi^{\alpha\beta}(\mathbf{Q})$ , by

$$\left(\frac{d\sigma}{d\Omega}\right)_{\text{diffuse}} = N\gamma_0 f^2(\mathbf{Q}) \frac{k_i}{k_f} \sum_{\alpha\beta} (\delta_{\alpha\beta} - Q_\alpha Q_\beta) \left(\frac{k_B T}{g^2 \mu_B^2}\right) \chi^{\alpha\beta}(\mathbf{Q}), \quad (22)$$

where  $f(\mathbf{Q})$  is the form factor,  $\alpha$  and  $\beta$  refer to Cartesian coordinates of the lattice,  $Q_\alpha$  and  $Q_\beta$  are the components of the scattering vector in the directions  $\alpha$  and  $\beta$ , respectively,  $k_B$  is Boltzmann's constant. The  $\delta$ -function in the parentheses ensures that the scattering is sensitive only to those components of the fluctuation perpendicular to the scattering vector  $\mathbf{Q}$ .

The *vector* interaction between the neutron and the magnetic moments is again a crucial factor here, as it is of course throughout magnetic scattering. The first use of this aspect was by Schulhof et al. (1970) on  $\text{MnF}_2$  and by Birgeneau et al. (1970, 1971) on  $\text{K}_2\text{NiF}_4$ . Since these experiments require single crystals (and, if the moments are small, even relatively large crystals) it took some time for the first experiments on actinides or lanthanides to be reported. However, the first experiments (Lander et al. 1978) on  $\text{USb}$  gave immediately important information on the microscopic interactions in these materials. Much of this has been discussed at length in

Rossat-Mignod et al. (1984) and we will not repeat the full details as presented there. Instead, our objective is to bring that account up to date over the last decade, record the theoretical involvement, and make comparisons with Ce compounds. We shall end with a few remarks on the dynamical aspects (i.e. temporal rather than spatial aspect of the magnetic fluctuations). For a complete description of magnetic critical scattering the reader should consult the monograph of Collins (1989). Not only does this give a description of the fundamentals of the subject, but it places the results on materials such as USb and UAs in a broader context.

### 5.1. Anisotropy of critical fluctuations

The vectorial nature of eq. (22) lends itself immediately to investigating directional effects. As we have seen in sect. 4, one feature that occurs repeatedly in the actinide NaCl-structure compounds is the ferromagnetic sheets coupled in some complicated way along the propagation vector,  $\mathbf{k}$ , of the magnetic structure. Thus, figs. 17–19 give complex phase diagrams of materials in which the only simplifying features are that there are (001) planes of magnetic moments, with the moment component  $\mu_{\mathbf{k}}$  parallel to the propagation direction  $\mathbf{m}_{\mathbf{k}}$  and perpendicular to the (001) plane. The ferromagnetically coupled planes may then be stacked in a vast assortment of ways. The underlying simplicity of the (001) ferromagnetic planes suggests, but does not prove, that the intra-layer coupling within such planes is much stronger than the inter-layer coupling between planes. Recall that these materials are cubic, so that there is no inherent anisotropy because of unequal atomic separations, as is the case, e.g., in  $\text{K}_2\text{NiF}_4$  (Birgeneau et al. 1970, 1971).

Our interest, therefore, is in probing the wavevector susceptibility  $\chi^{a\beta}(\mathbf{Q})$  just above the ordering temperature, where the spatial correlations between magnetic moments are only short-range. We want to measure the strength of this interaction, recalling that the “correlation” length  $\xi$  is the important parameter (Stanley 1971). This is related to the half width at half maximum (HWHM) of the critical scattering profile, assuming it has a Lorentzian form, by  $\text{HWHM} = \xi^{-1}$ . Of course, this assumes that the intrinsic instrumental resolution is infinitely small, which is never the case, so that a deconvolution of experimental data with the instrumental resolution function is almost always required. That is what makes these experiments difficult. Nor are they possible in such a simple form for a ferromagnet, because all the domains contribute their scattering at the same  $q = 0$  reduced wavevector. This is also where nuclear scattering occurs. Thus, the studies of anisotropic spatial correlations are confined in practice to antiferromagnets.

To illustrate these effects, we show in fig. 31 a schematic representation of the diffuse scattering around the (110) point in UAs at  $T_N + 1.2$  K (Sinha et al. 1981) Along the [001] direction  $\mathbf{q}$  is parallel to the propagation direction and the moment component  $\mathbf{m}_{\mathbf{k}}$  in the ordered state, so that this probes  $\chi_{\parallel}(\mathbf{Q})$ . We see that the scattering width is wide, so  $\xi_{\parallel}$  is correspondingly small. Conversely, in the  $[\xi\xi 0]$  direction we probe  $\chi_{\perp}(\mathbf{Q})$ , the inter-layer susceptibility, as discussed earlier, and the widths are quite sharp, leading to a large value of  $\xi_{\perp}$ . These values of  $\xi$  can be measured as a function of temperature (we shall discuss this below), but their *ratio* is found to be

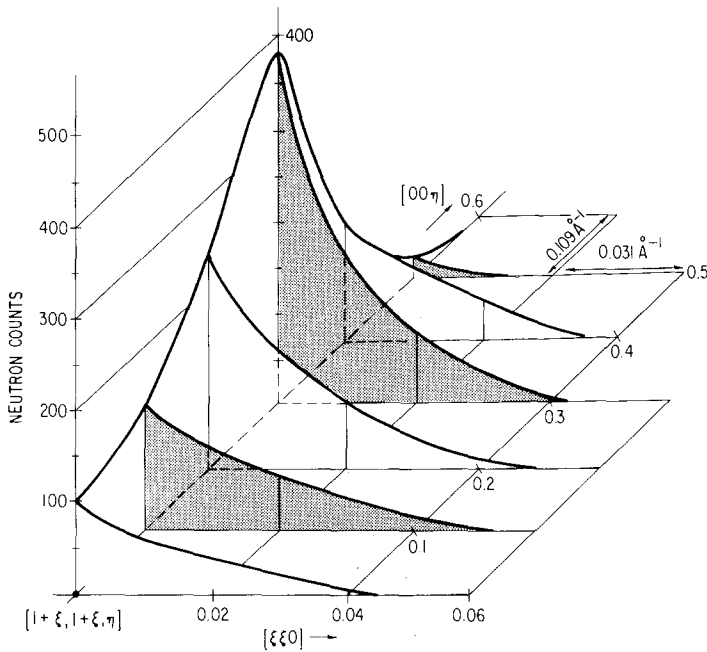


Fig. 31. Schematic representation of the diffuse scattering around the (110) lattice point at  $T_N + 1.2$  K in UAs. The reciprocal lattice projection is  $[1\bar{1}0]$ . Note the difference in scale in the  $[\xi\xi 0]$  and  $[00\eta]$  direction. The instrumental resolution functions have a HWHM of  $\Delta\xi = 0.006$  and  $\Delta\eta = 0.003$  in appropriate reciprocal-lattice units. (From Sinha et al. (1981))

independent of temperature. This ratio,  $R = \xi_{\perp}/\xi_{\parallel}$ , is called the anisotropy ratio, and is tabulated for various materials in table 6. This ratio is often given in the literature in terms of the *inverse* correlation range parameters,  $\kappa_{\parallel}$  and  $\kappa_{\perp}$ , which are directly proportional to the observed widths in reciprocal space. Then  $R = \kappa_{\parallel}/\kappa_{\perp}$ . Notice that some Ce compounds have been measured, but because of the generally complex magnetic structures (Hulliger 1978) of other LnX materials, no measurements have been reported on other lanthanide compounds. In general, the structures of the other lanthanide NaCl-type compounds cannot be described as a simple stacking of (001) planes, as is the case for Ce and actinide materials.

Hälg and Furrer (1984) also made the point that the value of  $R$  is correlated with the order parameter. We reproduce their figure, plotting  $R$  versus  $T_N$  on a log scale, in fig. 32. This figure shows that the stronger the total exchange process (giving a measure of  $T_N$ ), the larger we expect the observed anisotropy to be. Interestingly, the Ce and U compounds fit on a good straight line, but PuSb is far from this line.

The anisotropy ratio,  $R$ , has been considered for Ce and Pu systems by Kioussis and Cooper (1986), Hu et al. (1987), and Cooper et al. (1987). The observed  $R$ -values for these systems do not exceed three, and these workers obtain reasonable agreement with experiment. We should emphasize that the introduction of anisotropic interactions is central to the theories of Cooper et al. (1985), so the first-principles



TABLE 6

Summary of critical parameters in Ce, U, Np, and Pu monopnictides.  $R$  is the anisotropy ratio. Numbers in parentheses refer to standard deviations of the least significant digit.

	Lattice parameter (Å)	$T_N$ (K)	$\beta$	$\nu$	$R$	Ref. <sup>a</sup>
CeAs	6.078	8			0.6(1)	[1]
CeSb	6.412	16	First-order transition		1.8(2)	[2]
CeBi	6.487	25.4	0.317(5)	0.63(6)	2.5(2)	[3]
UN	4.890	~54	0.31(3)	0.84(5)	2.8(3)	[4]
UAs	5.779	124	First-order transition		3.8(5)	[5]
USb	6.191	212.2	0.32(2)	0.68(4)	5.0(5)	[6]
NpAs	5.838	173.6	0.38(1)	0.73(2)	2.9(5)	[7]
NpSb	6.254	199.0	0.257(5)	—	4.5(10)	[7]
NpBi	6.438	192.5	0.31(2)			[8]
PuSb	6.225	85.3	0.31(2)	0.58(5)	1.8(3)	[9]
Classical mean field			0.5	0.5		
3D Heisenberg			0.345	~0.7		
3D Ising			0.3125	0.64		
2D Ising			0.125	1.0		

<sup>a</sup>References: [1] Hälgl and Furrer (1986). [2] Hälgl et al. (1981). [3] Hälgl et al. (1982). [4] Holden et al. (1982). [5] Sinha et al. (1980). [6] Lander et al. (1978), Hagen et al. (1988). [7] Jones et al. (1991). [8] Bourdarot and Burlet (1990). [9] Burlet et al. (1987b).

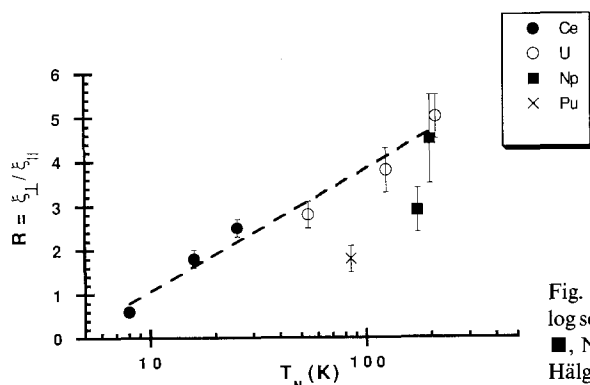


Fig. 32. Anisotropy ratio  $R$  versus  $T_N$  (on a log scale). ●, Ce compounds; ○, U compounds; ■, Np compounds; ×, PuSb. (Adapted from Hälgl and Furrer (1984).)

calculation of these  $R$ -values represents an important test for these calculations. As noted by Burlet et al. (1987a), the  $R$ -values are largest for USb and NpSb, both of which have a triple- $k$  structure. This suggests that these strong interactions, which give rise to a high ordering temperature, are also important in stabilizing the triple- $k$  structure, and have been discussed (Sinha et al. 1981, Burlet et al. 1987a) in terms of direct mixing between the  $5f$  electrons and the anion  $p$ -band. Evidence for such mixing can be found in Mössbauer experiments at the Sb site in USb and NpSb (Sanchez et al. 1988, 1990).

### 5.2. Comparison of critical exponents with theory

As discussed, e.g., by Stanley (1971) and Ma (1976) one of the great successes of modern condensed matter theory has been the development of the so-called renormalization technique. Among other things, these advances have led to an accurate evaluation of the critical exponents (relating to the temperature dependence of various quantities) for different classes of systems. The theoretical values of  $\beta$  (related to the magnetization as  $M/M_0 \propto t^\beta$ , where  $t$  is the reduced temperature parameter) and  $\nu$  (related to the  $T$ -dependence of the inverse correlation range as  $\kappa \propto |t|^{-\nu}$ ) are given in table 6. Except for NpSb and NpAs, the values of  $\beta$  are in good agreement with the 3D Ising model ( $\beta = 0.3125$ ). However, the values of  $\nu$  appear to be more scattered. Some caution is necessary here. Although the theoretical values of the critical exponents depend, in principle, only on the dimensionality of the system, there are exceptions. In particular the presence of so-called Lifschitz points (Sinha et al. 1980) can cause problems.

It is not our intention here to discuss in great detail the complex phase transitions that occur near  $T_N$  in systems such as UAs, CeAs, and CeSb. Suffice it to say that in all three, in UAs by Sinha et al. (1980, 1981), in CeAs by Halg et al. (1981), and in CeSb by Halg et al. (1986, 1987), unusual effects are found. It is, therefore, not totally surprising that the values of the critical exponents are not in agreement with theory. Ott et al. (1979) have also pointed out that theory predicts a first-order transition in the case of the Ce chalcogenides with the type II structure, but that a second-order phase transition is found, with  $\beta$  values of 0.36(4). An exact calculation of these parameters is only possible within the framework of a model such as employed by Kaski and Selke (1985).

Some efforts have also been made to determine the critical exponents of the uranium ferromagnets (Aldred et al. 1980), but neutrons can play only a small role because of the overlap of the magnetic and nuclear scattering. The values of the critical exponents are not greatly different, as might be expected.

### 5.3. Dynamical aspects of critical scattering

The use of a three-axis spectrometer, which we will discuss in more detail in the chapter by Holland-Moritz and Lander in vol. 19 of this series, allows not only the measurements of the width of the scattering in the reciprocal lattice (as shown in fig. 31), but also the frequency width,  $\Gamma(\mathbf{q})$ . Assuming that the temporal fluctuations of the moment follow a Lorentzian form (Marshall and Lovesey 1971, Collins 1989), we anticipate

$$\Gamma(\mathbf{q}) = \Gamma_0 [1 + (q_{\parallel}/K_{\parallel})^2 + (q_{\perp}/K_{\perp})^2]. \quad (23)$$

In this equation  $\mathbf{q}$  is the offset from the ordering wavevector, where the frequency half width is  $\Gamma_0$ , and  $q_{\parallel}$  and  $q_{\perp}$  are its parallel and perpendicular components in the spirit of the previous discussion. What this equation implies is a direct relationship between the temporal and spatial fluctuations – we call this a scaling relationship. The measured frequency half-width depends solely on the offset in reciprocal space,  $\mathbf{q}$ , and its directional components. Furthermore, according to critical theory,  $\Gamma_0(T) \propto |t|^\Delta$  where  $\Delta \sim 1.5$  for the 3D Heisenberg model.

We alluded earlier to the fact that the determination of the spatial correlation functions is difficult, due primarily to the need to worry about the instrumental resolution. This problem is worse when experiments are attempted in the frequency domain. So far, the qualitative measurements that have been reported are those by Holden et al. (1982) on UN and a more complete report on USb by Hagen et al. (1988). The measurements on UN, which are also discussed by Buyers and Holden (1985), were hampered by the rather poor quality of the UN crystals. Some of the difficulties in these experiments may be seen in the values of  $\Gamma_0$  for USb (Hagen et al. 1988), which range from  $\sim 500$  to  $4\mu\text{eV}$  as  $t$ , the reduced temperature, varies from  $5 \times 10^{-2}$  to  $\sim 1$ . Since the instrumental HWHM is about  $18\mu\text{eV}$ , it is clear that the lower end of the  $\Gamma_0$ -range requires considerable confidence in the experimental analysis. Nevertheless, the scaling behavior was found (with the caveats discussed above) for both UN and USb.

## 6. Summary

The discovery of heavy fermions (HF) in uranium compounds, notably  $\text{UPt}_3$  and  $\text{UBe}_{13}$  (see Stewart (1984) or Ott and Fisk (1987) for reviews), has led to an explosion of work on uranium systems in the last decade. The great interest in how and why the heavy-fermion materials become superconductors in the presence of "magnetic" electrons (indeed, with the possible exception of  $\text{UBe}_{13}$ , all HF materials exhibit some kind of magnetic correlation in the superconducting state) is still a compelling theme in condensed-matter research. Interestingly, the discovery of high- $T_c$  materials has also emphasized our lack of understanding of the interactions between the spin-pairing (superconductivity) and spin-alignment (magnetism) mechanisms. Much more can be found on HF systems, notably the chapters by Liu (ch. 111) and Aeppli and Broholm in vol. 19 of this series. Since all HF materials are metallic in nature, the main emphasis in actinide research has shifted to intermetallic compounds. To gain an understanding of the bonding in such intermetallic systems has, for example, been the motivation behind the large amount of work on  $\text{UTX}$ , and  $\text{UT}_2\text{X}_2$  compounds, discussed in this and other chapters.

With respect to structural studies, the successful experiments to elucidate the geometric arrangement of the atomic displacements in the charge density wave (CDW) in uranium with both neutrons and X-rays have been one of the highlights of the last decade (sect. 2). The relatively low-symmetry structure of  $\alpha$ -uranium has been ascribed for many years to the presence of f-bonding orbitals, but a more quantitative picture requires more detailed de Haas-van Alphen work, and a theoretical effort using the correct structure. The role of true electronic effects in the CDW mode remains obscure, although we have made major progress in understanding this state itself. An equally compelling question is the low-temperature state of both Np and Pu; in both cases transport measurements (Fournier and Troć 1985) indicate the presence of "anomalies". The direct confirmation of a CDW state in these elements at low temperature requires the use of single crystals, but, because of their complex phase diagrams as a function of temperature, these are very difficult to produce. Hopefully an effort can be made in this direction. If a CDW were found, this would

provide strong circumstantial evidence that electronic effects in U, Np, and Pu are similar.

The magnetic form factors representing the spatial extent of the magnetization densities are discussed in sect. 3. Although there are some obvious similarities in these measurements, such as the determination of the ground-state wavefunctions in CeSb, CeAl<sub>2</sub>, SmCo<sub>5</sub>, USb, and PuSb, there are also important differences. For the Ce compounds CeSn<sub>3</sub> and CePd<sub>3</sub> the delocalized (or conduction-electron polarization) density has been observed to change as a function of temperature. No similar effects have been found in either mixed-valent lanthanide compounds, heavy fermion compounds, or actinides. Of course, the thermal energies are small on the scale of the band density of states ( $kT \sim 25$  meV for room temperature, whereas band widths are measured in eV), so that CePd<sub>3</sub> may represent the special case of a narrow band that intersects the Fermi level,  $E_F$ ; the latter being intrinsically  $T$  dependent.

A different situation pertains to the Sm mixed-valent compounds and PuTe. In both cases the orbital moment is much reduced as compared to that of a  $5f^5$  free ion (the nominal trivalent state for both Sm and Pu). Such a reduced value of  $\mu_L$  may be achieved by either quenching  $\mu_L$  by broadening the  $f$  bands considerably or strong hybridization between the  $5f$  and  $d$  electrons. Hybridization at one site, e.g.  $5f-6d$  (*intra-site*) mixing, can, under special conditions, give rise to an unusual structure in the density of states (Wachter et al. 1991). This may be case in Sm and Pu chalcogenides, although a complete calculation of  $f(Q)$  has not been reported.

*Inter-site* mixing between the actinide  $5f$  and transition-metal  $3d$  electrons is another way to reduce the orbital  $\mu_L$  contribution to the form factor, and this is the subject of sect. 3.6. In this case, the theoretical predictions of Brooks, Johansson and collaborators (see the chapter by Brooks and Johansson (ch. 112) in this series) has been of major importance, not only in understanding the experimental results, but also in suggesting new compounds for study. This combination of experiment and theory (see fig. 15, for example) has provided a *quantitative* understanding of hybridization, and thus represents a major advance in the last seven years. Predictions also exist for CeFe<sub>2</sub>, but no experiments have been reported.

Section 4, on magnetic structures, represents the largest single section of this chapter. The magnetic structures of many of the materials are so complex (e.g. UPdSn) that we can do no more than simply describe them and tabulate some of the parameters. Some themes emerge, especially if we confine our initial discussion to the NaCl systems, on which by far the greatest amount of work has been reported, and most of it on single crystals.

(1) Multi- $k$  structures exist in many compounds and solid solutions. They do not, apparently, exist in isostructural Ce monopnictides, but they may exist in the cerium monochalcogenides (Ott et al. 1979).

(2) The common feature of these structures is strongly coupled (001) ferromagnetic planes, which are then coupled in a complex way along the propagation direction. The structures are all *longitudinal*, in that  $\mu$  is parallel to  $k$ . All these features are common to actinide and cerium monopnictides. The essential physics underlying this common theme is addressed in the section on critical magnetic scattering (sect. 5), in

which we discuss the anisotropy of the intra- and inter-plane interactions. This question has been considered theoretically by Cooper and his colleagues.

(3) The magnetic modulations usually are a square-wave modulation at low temperature. In special cases it appears that a more complicated modulation may exist, this was already found in NpP about 20 years ago, and (in other crystal structures) CeAl<sub>2</sub>, CeCu<sub>2</sub> (Nunez et al. 1992), NpAs<sub>2</sub>, and NpRu<sub>2</sub>Si<sub>2</sub> (Rossat-Mignod et al. 1984) have all been found to have modulated structures at low temperature. There has been speculation that the varying magnetic moment at low temperatures is due to a "Kondo"-type cancellation of the moments of the localized *f* and itinerant *s-d* states, but the systematics is sufficiently sparse that no clear trends emerge. However, up to this point the U structures, as least in the NaCl-type compounds and solid solutions, have all been described as square-wave modulations. More recent work on the USB-ThSb phase diagrams (including X-ray synchrotron studies) suggests a modulated structure at low temperature. It is quite likely that so-called "paramagnetic planes" also exist in U solid solutions. The advent of "resonant magnetic X-ray scattering" with synchrotron sources tuned to the actinide M<sub>IV</sub> edge at 3.73 keV has brought an important new technique for the examination of actinide magnetic structures, and we are likely to see more of this in the years ahead (McWhan et al. 1990, Isaacs et al. 1990, Tang et al. 1992, Paixão et al. 1993).

In the case of the actinide monochalcogenides the situation is quite different. The Ce compounds are antiferromagnetic with a type II structure, although we do not yet know whether they are multi-*k*. The moments found in these materials are low, and they are clearly on the verge of being non-magnetic. The U compounds are ferromagnetic. NpS and NpSe are antiferromagnets, whereas NpTe remains something of a puzzle,  $\langle 111 \rangle$  is the easy axis in all these materials. Presumably, the changing electron concentration between AnX (X = N, P, As, etc.) and AnZ (Z = S, Se, Te) leads to a rotation of the easy axis. The synthesis of single crystals of Np and Pu chalcogenides has allowed their properties to be examined in considerable detail. Viewing the systematics of the Ce, U, Np, and Pu monochalcogenides suggests that even the simple ferromagnetic ordering of the UZ compounds may mask more complex physics.

The role of the crystal-field interaction remain obscure in *all* these systems, both for actinides and cerium. Whereas in the other lanthanide NaCl-type compounds, LnX and LnZ, the easy directions are given by straightforward crystal-field considerations and the value of the crystal-field potential varies in a systematic way across the lanthanide series, this is not the case in the materials discussed here. The crystal-field energy levels can be measured in the cerium compounds with neutron inelastic scattering, but have not been observed in the uranium (or higher) actinides. It is assumed that this inability to observe directly the crystal-field levels is because they are strongly broadened by the interaction between the 5*f* and conduction electrons. This has been the subject of much work by Cooper and his collaborators.

Moving away from the NaCl-type compounds it becomes difficult to perceive common themes. We have already noted the complexities in structures such as those found in UNiSn and UPdSn. The latter is unusual in that the moments rotate as a function of temperature, something that has not been observed previously in actinide

systems. In the  $\text{AnT}_2\text{X}_2$  compounds (table 5) the easy axis is always along the unique [001] tetragonal axis. Although the crystal-field interaction may account for such an easy axis, it seems likely that hybridization effects (such as already found in URhAl) also play a role. In the insulating compounds we want to highlight the neutron experiments performed on  $\text{CmCu}_2\text{O}_4$ . This is the first time a magnetic structure of a Cm compound has been determined using neutrons. The sample weight was  $\sim 50$  mg.

The determination of  $K_1$  as a function of  $T$  in US using polarized neutrons (sect. 4.7) represents a new type of study, with special application to the actinides, although the technique as presently described requires single crystals.

The magnetic critical scattering (sect. 5) continues to attract much theoretical interest. Since the earlier work (Rossat-Mignod et al. 1984) the experiments (and theory) have been extended to transuranium compounds. The early systematics (fig. 32) of Ce and U compounds with respect to the anisotropy ratio,  $R$ , do not appear to be followed by the Np and Pu compounds, particularly PuSb. Another point to make is the important challenge for theory to arrive at  $R$ -values as great as five, and to consider whether the fact that USb and NpSb have  $3k$  structures has any connection with the large  $R$ -values.

In conclusion, efforts to produce single crystals of intermetallics and transuranium NaCl-type compounds have clearly provided considerable dividend in the last decade. For the intermetallics, the form-factor work (sect. 3) and the evidence for a changing  $\mu_L/\mu_S$  ratio is of importance for increasing our understanding of the mechanism of hybridization of 5f and (in this case) 3d electron states on neighboring atoms (Lebech et al. 1991). The magnetic structures of many intermetallics are proving complicated and often require single crystals for their solution. Magnetic structures in general will benefit in the future from the newly developed technique of magnetic resonant X-ray scattering (McWhan et al. 1990, Isaacs et al. 1990, Tang et al. 1992, Paixão et al. 1993). This technique will also allow examination of compounds containing heavier actinides, since the samples required need only be a few micrograms. The neutron limit is probably  $\sim 1$  mg for single crystals and  $> 10$  mg for polycrystalline samples. The production of transuranium single crystals with NaCl structure has allowed a number of detailed experiments, in addition to neutron experiments, to be performed on these compounds; perhaps the most surprising results concern the Np and Pu chalcogenides. This is a good example in which the knowledge of the isostructural U compounds gives no preview of the surprises in store when the higher actinides are produced. In all cases the aim of these studies with elastic scattering should be to prepare the way towards experiments involving inelastic scattering that can probe the complex nature of the  $S(\mathbf{Q}, \omega)$  response.

### Acknowledgement

I am grateful to many people for collaboration and discussions over a number of years. On the experimental side, particularly mentioned should be Jane Brown, Paul Burlet, Debbie Jones, Bente Lebech, Jean-Claude Marmeggi, José Antonio Paixão, Jean Rossat-Mignod, Jean Rebizant, Bill Stirling, and Michael Wulff. The crystal-

growing capabilities of Oscar Vogt, Kurt Mattenberger, and the team at EITU in Karlsruhe remain central to much of the work described in this chapter. I have benefitted from discussions of theoretical matters with Mike Brooks, Barry Cooper, Olle Erickson, and Borje Johansson. Last, but not least, I thank my wife for typing this manuscript.

## References

- Aeppli, G., E. Bucher, C.L. Broholm, J.K. Kjems, J. Baumann and J. Hufnagl, 1988, *Phys. Rev. Lett.* **60**, 615.
- Albers, R.C., A.M. Boring, G.H.O. Daalderop and F.M. Mueller, 1987, *Phys. Rev. B* **36**, 3661.
- Aldred, A.T., B.D. Dunlap, A.R. Harvey, D.J. Lam, G.H. Lander and M.H. Mueller, 1974, *Phys. Rev. B* **9**, 3766.
- Aldred, A.T., B.D. Dunlap, D.J. Lam, G.H. Lander, M.H. Mueller and I. Nowik, 1975, *Phys. Rev. B* **11**, 530.
- Aldred, A.T., P. de V. DuPlessis and G.H. Lander, 1980, *J. Magn. & Magn. Mater.* **20**, 236.
- Amoretti, G., A. Blaise, M. Bogé, D. Bonnisseau, P. Burlet, J.M. Collard, J.M. Fournier, S. Quezel, J. Rossat-Mignod and J. Larroque, 1989, *J. Magn. & Magn. Mater.* **79**, 207.
- Arko, A.J., D.D. Koelling and J.E. Schirber, 1985, in: *Handbook on the Physics and Chemistry of the Actinides*, Vol. 2, eds A.J. Freeman and G.H. Lander (North-Holland, Amsterdam) pp. 224–228.
- Bacon, G.E., 1975, *Neutron Diffraction*, 3rd Ed. (Clarendon Press, Oxford).
- Bader, S.D., N.E. Phillips and E.S. Fisher, 1975, *Phys. Rev. B* **12**, 4929.
- Baer, Y., 1984, in: *Handbook on the Physics and Chemistry of the Actinides*, Vol. 1, eds A.J. Freeman and G.H. Lander (North-Holland, Amsterdam) p. 271.
- Bak, P., and J. van Boehm, 1980, *Phys. Rev. B* **21**, 5291.
- Balcar, E., and S.W. Lovesey, 1989, *Theory of Magnetic Neutron and Photon Scattering* (Clarendon Press, Oxford).
- Balcar, E., S.W. Lovesey and F.A. Wedgwood, 1970, *J. Phys. C* **3**, 1292.
- Baran, A., W. Suski and T. Mydlarz, 1985, *Physica B* **130**, 219.
- Barbara, B., J.X. Boucherle, J.L. Bouevoz, M.F. Rossignol and J. Schweizer, 1977, *Solid State Commun.* **24**, 481.
- Barbara, B., M.F. Rossignol, J.X. Boucherle, J. Schweizer and J.L. Bouevoz, 1979, *J. Appl. Phys.* **50**, 2300.
- Benedict, U., 1987, in: *Handbook on the Physics and Chemistry of the Actinides*, Vol. 5, eds A.J. Freeman and G.H. Lander (North-Holland, Amsterdam) pp. 227–269.
- Bernard, L., R. Currat, P. Delamoye, C.M.E. Zeyen, S. Hubert and D. de Kouchkovsky, 1983, *J. Phys. C* **16**, 433–456.
- Birgeneau, R.J., J. Skalyo and G. Shirane, 1970, *J. Appl. Phys.* **41**, 1303.
- Birgeneau, R.J., J. Skalyo and G. Shirane, 1971, *Phys. Rev. B* **3**, 1736.
- Blaise, A., M.N. Bouillet, F. Bourdarot, P. Burlet, J. Rebizant, J. Rossat-Mignod, J.P. Sanchez, J.C. Spirlet and O. Vogt, 1992, *J. Magn. & Magn. Mater.* **104–107**, 33.
- Bogé, M., D. Bonnisseau, P. Burlet, J.M. Fournier, E. Pleska, S. Quezel, J. Rebizant, J. Rossat-Mignod, J.C. Spirlet and O. Vogt, 1989, *J. Nucl. Mater.* **166**, 77.
- Bohr, J., D. Gibbs, J.D. Axe, D.E. Moncton, K.L. D'Amico, C.F. Majkrzak, J. Kwo, G. Hong, C.L. Chien and J. Jensen, 1989, *Physica B* **159**,\* 93.
- Boucherle, J.X., and J. Schweizer, 1985, *Physica B* **130**, 337.
- Boucherle, J.X., D. Givord and J. Schweizer, 1982a, *J. Phys. (Paris)* **43**, C7-199.
- Boucherle, J.X., D. Ravot and J. Schweizer, 1982b, *J. Phys. (Paris)* **43**, C7-263.
- Boucherle, J.X., G. Fillon, J. Flouquet, F. Givord, P. Lejay and J. Schweizer, 1986, *J. Magn. & Magn. Mater.* **54–57**, 421; **62**, 277.
- Boucherle, J.X., G. Fillon, J. Flouquet, F. Givord, P. Lejay and J. Schweizer, 1990, *Physica B* **163**, 635.
- Bourdarot, F., and P. Burlet, 1990, private communication.
- Broholm, C., H. Lin, P.T. Matthews, T.E. Mason, W.J.L. Buyers, M.F. Collins, A.A. Menovsky, J.A. Mydosh and J.K. Kjems, 1991, *Phys. Rev. B* **43**, 12809.
- Brooks, M.S.S., 1985, *Physica B* **130**, 6.
- Brooks, M.S.S., B. Johansson and H.L. Skriver, 1984, in: *Handbook on the Physics and Chemistry of the Actinides*, Vol. 1, eds

- A.J. Freeman and G.H. Lander (North-Holland, Amsterdam) pp. 153–270.
- Brooks, M.S.S., B. Johansson, O. Eriksson and H.L. Skriver, 1986, *Physica B* **144**, 1.
- Brooks, M.S.S., O. Eriksson, B. Johansson, J.J.M. Franse and P.H. Frings, 1988, *J. Phys. F* **18**, L33.
- Brooks, M.S.S., O. Eriksson and B. Johansson, 1989, *J. Phys.: Condens. Matter* **1**, 5861.
- Brown, P.J., J.B. Forsyth and R. Mason, 1980, *Philos. Trans. R. Soc. (London) Ser. B* **290**, 481.
- Burlet, P., S. Quezel, J. Rossat-Mignod, J.C. Spirlet, J. Rebizant, W. Mueller and O. Vogt, 1984, *Phys. Rev. B* **30**, 6660.
- Burlet, P., J. Rossat-Mignod, S. Quezel, O. Vogt, J.C. Spirlet and J. Rebizant, 1986, *J. Less-Common Met.* **121**, 121.
- Burlet, P., J. Rossat-Mignod, G.H. Lander, J.C. Spirlet, J. Rebizant and O. Vogt, 1987a, *Phys. Rev. B* **36**, 5306.
- Burlet, P., S. Quezel, J. Rossat-Mignod, J.C. Spirlet, J. Rebizant and O. Vogt, 1987b, *J. Magn. & Magn. Mater.* **63–64**, 145.
- Burlet, P., S. Quezel, D. Bonnissieu, J. Rossat-Mignod, J.C. Spirlet and J. Rebizant, 1988a, *Solid State Commun.* **67**, 999.
- Burlet, P., J.M. Fournier, E. Pleska, S. Quezel, J. Rossat-Mignod, J.C. Spirlet, J. Rebizant and O. Vogt, 1988b, *J. Phys. Colloq. (Paris)* **49**, C8-469.
- Burlet, P., F. Bourdarot, J. Rossat-Mignod, J.P. Sanchez, J.C. Spirlet, J. Rebizant and O. Vogt, 1992, *Physica B* **180–181**, 131.
- Busch, G., O. Vogt, A. Delapalme and G.H. Lander, 1979, *J. Phys. C* **12**, 1391.
- Buyers, W.J.L., and T.M. Holden, 1985, in: *Handbook on the Physics and Chemistry of the Actinides*, Vol. 2, eds A.J. Freeman and G.H. Lander (North-Holland, Amsterdam) pp. 239–328.
- Callen, E., and H.B. Callen, 1966, *J. Phys. & Chem. Solids* **27**, 1271.
- Carnall, W.T., and B.G. Wybourne, 1964, *J. Chem. Phys.* **40**, 3428.
- Chelmicki, L., J. Leciejewicz and A. Zygmunt, 1985, *J. Phys. & Chem. Solids* **46**, 529.
- Clark, A.E., 1980, in: *Ferromagnetic Materials*, Vol. 1, ed. E.P. Wohlfarth (North-Holland, Amsterdam) p. 540.
- Clausen, K., W. Hayes, J.E. MacDonald, R. Osborn and M.T. Hutchings, 1984, *Phys. Rev. Lett.* **52**, 1238.
- Clausen, K., W. Hayes, M.T. Hutchings, J.K. Kjems, J.E. MacDonald and R. Osborn, 1985, *High Temp. Sci.* **19**, 189.
- Clausen, K., M.A. Hackett, W. Hayes, S. Hull, M.T. Hutchings, J.E. MacDonald, K.A. McEwen, R. Osborn and U. Steigenberger, 1989, *Physica B* **156–157**, 103.
- Collins, M.F., 1989, *Magnetic Critical Scattering* (Oxford University Press, London).
- Cooper, B.R., P. Thayamballi, J.C. Spirlet, W. Müller and O. Vogt, 1983, *Phys. Rev. Lett.* **51**, 2418.
- Cooper, B.R., R. Siemann, D. Yang, P. Thayamballi and A. Banerjee, 1985, in: *Handbook on the Physics and Chemistry of the Actinides*, Vol. 2, eds A.J. Freeman and G.H. Lander (North-Holland, Amsterdam) pp. 435–498.
- Cooper, B.R., G.J. Hu, N. Kioussis and J.M. Wills, 1987, *J. Magn. & Magn. Mater.* **63–64**, 121.
- Cooper, B.R., Q.G. Sheng, S.P. Lim, C. Sanchez-Castro, N. Kioussis and J.M. Wills, 1992, *J. Magn. & Magn. Mater.* **108**, 10.
- Cox, D.E., G. Shirane, S.K. Shapiro, G. Aeppli, Z. Fisk, J.L. Smith, J.M. Kjems and H.R. Ott, 1986, *Phys. Rev. B* **33**, 3614.
- Crummett, W.P., H.G. Smith, R.M. Nicklow and N. Wakabashi, 1979, *Phys. Rev. B* **19**, 6028.
- Currat, R., 1989, *Physica B* **156–157**, 1.
- Daalderop, G.H.O., F.M. Mueller, R.C. Albers and A.M. Boring, 1988, *Appl. Phys. Lett.* **52**, 1636.
- de Novion, C.H., J. Gal and J.L. Buevoz, 1980, *J. Magn. & Magn. Mater.* **21**, 85.
- Desclaux, J.P., and A.J. Freeman, 1984, in: *Handbook on the Physics and Chemistry of the Actinides*, Vol. 1, eds A.J. Freeman and G.H. Lander (North-Holland, Amsterdam) p. 1.
- Donohue, J., 1974, *The Structures of the Elements* (Wiley, New York).
- Dunlap, B.D., and G.H. Lander, 1974, *Phys. Rev. Lett.* **33**, 1046.
- Eriksson, O., L. Nordström, M.S.S. Brooks and B. Johansson, 1988, *Phys. Rev. Lett.* **60**, 2523.
- Eriksson, O., M.S.S. Brooks, B. Johansson, R.C. Albers and M. Boring, 1991, *J. Appl. Phys.* **69**, 5897.
- Fischer, P., B. Lebeck, G. Meier, B.D. Rainford and O. Vogt, 1978, *J. Phys. C* **11**, 345.
- Fisher, E.S., 1974, in: *The Actinides: Electronic Structure and Related Properties*, Vol. II, eds A.J. Freeman and J.B. Darby Jr (Academic Press, New York) pp. 289–343.
- Fisher, E.S., and D. Dever, 1968, *Phys. Rev.* **170**, 607.
- Fisher, E.S., G.H. Lander and S.D. Bader, 1993, to be published. For a popular press account see:



- G.H. Lander, 1990, *Endeavour* **14**, 179–184.
- Fisher, M.E., and W. Selke, 1980, *Phys. Rev. Lett.* **44**, 1502.
- Forgan, E.M., B.D. Rainford, S.L. Lee, J.S. Abell and Y. Bi, 1990, *J. Phys.: Condens. Matter* **2**, 10211.
- Fournier, J.M., and R. Troč, 1985, in: *Handbook on the Physics and Chemistry of the Actinides*, Vol. 2, eds A.J. Freeman and G.H. Lander (North-Holland, Amsterdam) p. 29.
- Fournier, J.M., A. Boeuf, P.H. Frings, M. Bonnet, J.X. Boucherle, A.A. Delapalme and A.A. Menovsky, 1986, *J. Less-Common Met.* **121**, 249.
- Fournier, J.M., E. Pleska, J. Chiapusio, J. Rossat-Mignod, J. Rebizant, J.C. Spirlet and O. Vogt, 1990, *Physica B* **163**, 493.
- Fowler, R.D., J.D.G. Lindsay, R.W. White, H.H. Hill and B.T. Matthias, 1967, *Phys. Rev. Lett.* **19**, 892.
- Freeman, A.J., J.P. Desclaux, G.H. Lander and J. Faber, 1976, *Phys. Rev. B* **13**, 1168.
- Fulde, P., and M. Loewenhaupt, 1986, *Adv. Phys.* **34**, 589.
- Gal, J., Z. Hadari, U. Atzmony, E.R. Bauminger, I. Nowik and S. Ofer, 1973, *Phys. Rev. B* **8**, 1901.
- Gal, J., W. Schäfer, G. Will, F.J. Litterst and G.M. Kalvius, 1989a, *J. Less-Common Met.* **149**, 243.
- Gal, J., I. Yaar, E. Arbaboff, H. Etedgi, F.J. Litterst, K. Aggarwal, J.A. Pereda, G.M. Kalvius, G. Will and W. Schäfer, 1989b, *Phys. Rev. B* **40**, 745.
- Gal, J., I. Yaar, D. Regev, S. Fredo, G. Shani, E. Arbaboff, W. Potzel, K. Aggarwal, J.A. Pereda, G.M. Kalvius, F.J. Litterst, W. Schäfer and G. Will, 1990, *Phys. Rev. B* **42**, 8507.
- Gardner, W.E., and T.F. Smith, 1968, in: *Proc. 11th Int. Conf. on Low Temperature Physics*, Vol. 2, eds J.F. Allen, D.M. Finlayon and D.M. McCall (St. Andrews University, St. Andrews, Scotland) p. 1377.
- Giorgi, A.L., A.C. Lawson, J.A. Goldstone, K.J. Volin and J.D. Jorgensen, 1988, *J. Appl. Phys.* **63**, 3604.
- Givord, D., J. Laforest, J. Schweizer and F. Tasset, 1979, *J. Appl. Phys.* **50**, 2008.
- Goodman, G., and L. Soderholm, 1990, *Physica C* **171**, 528.
- Grübel, G., J.D. Axe, D. Gibbs, G.H. Lander, J.C. Marmeggi and T. Brückel, 1991, *Phys. B* **43**, 8803.
- Hagen, M., W.G. Stirling and G.H. Lander, 1988, *Phys. Rev. B* **37**, 1984.
- Hälg, B., and A. Furrer, 1984, *J. Appl. Phys.* **55**, 1860.
- Hälg, B., and A. Furrer, 1986, *Phys. Rev.* **34**, 6258.
- Hälg, B., A. Furrer, W. Hälg and O. Vogt, 1981, *J. Phys. C* **14**, L961.
- Hälg, B., A. Furrer, W. Hälg and O. Vogt, 1982, *J. Magn. & Magn. Mater.* **29**, 151.
- Hälg, B., A. Furrer and O. Vogt, 1986, *Phys. Rev. Lett.* **57**, 2745.
- Hälg, B., A. Furrer and J.K. Kjems, 1987, *Phys. Rev. Lett.* **59**, 1034.
- Holden, T.M., W.J.L. Buyers, E.C. Svensson and G.H. Lander, 1982, *Phys. Rev. B* **26**, 6227.
- Holden, T.M., W.J.L. Buyers, E.C. Svensson and G.H. Lander, 1984, *Phys. Rev. B* **30**, 114.
- Hu, G.J., N. Kioussis, B.R. Cooper and A. Banerjea, 1987, *J. Appl. Phys.* **61**, 3385.
- Hu, G.J., N. Kioussis, A. Banerjea and B.R. Cooper, 1988, *Phys. Rev. B* **38**, 2639.
- Hulliger, F., 1974, in: *Handbook on the Physics and Chemistry of Rare Earths*, Vol. 4, eds K.A. Gschneidner Jr and L. Eyring (North-Holland, Amsterdam) pp. 190ff.
- Hulliger, F., 1978, *J. Magn. & Magn. Mater.* **8**, 183.
- Hulliger, F., B. Natterer and H.R. Ott, 1978, *J. Magn. & Magn. Mater.* **8**, 87.
- Hutchings, M.T., 1987, *J. Chem. Soc. Farad. Trans.* **83**, 1083.
- Hutchings, M.T., K. Clausen, M.H. Dickens, W. Hayes, J.K. Kjems, P.G. Schnabel and C. Smith, 1984, *J. Phys. C* **17**, 3903.
- Isaacs, E.D., D.B. McWhan, R.N. Kleinman, D.J. Bishop, G.E. Ice, P. Zschak, B.D. Gaulin, T.E. Mason, J.D. Garrett and W.J.L. Buyers, 1990, *Phys. Rev. Lett.* **65**, 3185.
- Jayaraman, A., V. Narayanamurti, E. Bucher and R.G. Maines, 1970, *Phys. Rev. Lett.* **25**, 1430.
- Johnston, D.F., 1966, *Proc. Phys. Soc.* **88**, 37.
- Jones, D.L., W.G. Stirling, G.H. Lander, J. Rebizant, J.C. Spirlet, M. Alba and O. Vogt, 1991, *J. Phys.: Condens. Matter* **3**, 3551.
- Jones, D.L., S. Langridge, W.G. Stirling, G.H. Lander, J. Rebizant, J.C. Spirlet, M. Alba and O. Vogt, 1992, *Physica B* **180–181**, 88.
- Kalvius, G.M., S. Zwirner, U. Potzel, J. Moser, W. Potzel, F.J. Litterst, J. Gal, S. Fredo, I. Yaar and J.C. Spirlet, 1990, *Phys. Rev. Lett.* **65**, 2290.
- Kaski, K., and W. Selke, 1985, *Phys. Rev. B* **31**, 3128.
- Kawamata, S., K. Ishimoto, Y. Yamaguchi and

- T. Komatsubara, 1992, *J. Magn. & Magn. Mater.* **104-107**, 51.
- Kioussis, N., and B.R. Cooper, 1986, *Phys. Rev. B* **34**, 3261.
- Koehler, W.C., and R.M. Moon, 1972, *Phys. Rev. Lett.* **29**, 1468.
- Kouvel, J.S., and J.S. Kasper, 1963, *J. Phys. & Chem. Solids* **24**, 529.
- Kuznietz, M., P. Burllet, J. Rossat-Mignod and O. Vogt, 1986a, *J. Magn. & Magn. Mater.* **61**, 246.
- Kuznietz, M., P. Burllet, J. Rossat-Mignod and O. Vogt, 1986b, *J. Less-Common Met.* **121**, 217.
- Kuznietz, M., P. Burllet, J. Rossat-Mignod and O. Vogt, 1987a, *J. Magn. & Magn. Mater.* **63-64**, 165.
- Kuznietz, M., P. Burllet, J. Rossat-Mignod, O. Vogt and K. Mattenberger, 1987b, *Phys. Rev. B* **35**, 7142.
- Kuznietz, M., P. Burllet, J. Rossat-Mignod and O. Vogt, 1987c, *J. Magn. & Magn. Mater.* **69**, 12.
- Kuznietz, M., H. Pinto, H. Ehedgui and M. Melamud, 1989, *Phys. Rev. B* **40**, 7328.
- Kuznietz, M., H. Pinto and M. Melamud, 1990, *J. Magn. & Magn. Mater.* **83**, 321.
- Lam, D.J., B.D. Dunlap, A.R. Harvey, M.H. Mueller, A.T. Aldred and G.H. Lander, 1974, in: *Proc. Int. Conf. Magnetism*, 1973, Vol. IV (Nauka, Moscow).
- Lander, G.H., and G. Aeppli, 1991, *J. Magn. & Magn. Mater* **100**, 151.
- Lander, G.H., and T.O. Brun, 1970, *J. Chem. Phys.* **53**, 1387.
- Lander, G.H., and M.H. Mueller, 1971, *Acta Crystallogr. B* **27**, 2284.
- Lander, G.H., M.H. Mueller, D.M. Sparlin and O. Vogt, 1976, *Phys. Rev. B* **14**, 5035.
- Lander, G.H., A.T. Aldred, B.D. Dunlap and G.K. Shenoy, 1977, *Physica B* **86-88**, 152.
- Lander, G.H., S.K. Sinha, D.M. Sparlin and O. Vogt, 1978, *Phys. Rev. Lett.* **40**, 523.
- Lander, G.H., J.F. Reddy, A. Delapalme and P.J. Brown, 1980, *Phys. Rev. Lett.* **44**, 403.
- Lander, G.H., A. Delapalme, P.J. Brown, J.C. Spirlet, J. Rebizant and O. Vogt, 1984, *Phys. Rev. Lett.* **53**, 2262.
- Lander, G.H., A. Delapalme, P.J. Brown, J.C. Spirlet, J. Rebizant and O. Vogt, 1985, *J. Appl. Phys.* **57**, 3748.
- Lander, G.H., J. Rebizant, J.C. Spirlet, A. Delapalme, P.J. Brown, O. Vogt and K. Mattenberger, 1987, *Physica B* **146**, 341.
- Lander, G.H., M.S.S. Brooks, B. Lebech, P.J. Brown, O. Vogt and K. Mattenberger, 1990, *Appl. Phys. Lett.* **57**, 989.
- Lander, G.H., M.S.S. Brooks and B. Johansson, 1991a, *Phys. Rev. B* **43**, 13, 672.
- Lander, G.H., M.S.S. Brooks, B. Lebech, P.J. Brown, O. Vogt and K. Mattenberger, 1991b, *J. Appl. Phys.* **69**, 4803.
- Lawson, A.C., C.E. Olsen, J.W. Richardson, M.H. Mueller and G.H. Lander, 1988, *Acta Crystallogr. B* **44**, 89.
- Lawson, A.C., J.A. Goldstone, J.G. Huber, A.L. Giorgi, J.W. Conant, A. Severing, B. Cort and R.A. Robinson, 1991, *J. Appl. Phys.* **69**, 5112.
- Lebech, B., M. Wulff, G.H. Lander, J. Rebizant, J.C. Spirlet and A. Delapalme, 1989, *J. Phys.: Condens. Matter* **1**, 10, 229.
- Lebech, B., M. Wulff and G.H. Lander, 1991, *J. Appl. Phys.* **69**, 5891.
- Leciejewicz, J., and A. Szytuła, 1987, *Magnetic Ordering in Ternary Intermetallic MT<sub>2</sub>X<sub>2</sub> Systems* (Jagellonian University, Warsaw and Krakow).
- Lin, H., L. Rebersky, M.F. Collins, J.D. Garrett and W.J.L. Buyers, 1991, *Phys. Rev. B* **43**, 13, 232.
- Liu, S.H., 1989, *Phys. Rev. B* **39**, 7381.
- Liu, S.H., B.N. Harmon, C. Stassis and S. Symeonides, 1980, *J. Magn. & Magn. Mater.* **15-18**, 942.
- Loidl, A., K. Knorr, G. Knopp, A. Krimmel, R. Caspary, A. Böhm, G. Sparr, C. Geibel, F. Steglich and A.P. Murani, 1992, *Phys. Rev. B* **46**, 9341.
- Lovesey, S., 1984, *Theory of Neutron Scattering from Condensed Matter* (Oxford University Press, Oxford).
- Ma, S.-K., 1976, *Modern Theory of Critical Phenomena*, *Frontiers in Physics*, Vol. 46 (Benjamin, New York).
- Maglic, R.C., G.H. Lander, M.H. Mueller and R. Kleb, 1978, *Phys. Rev. B* **17**, 308.
- Maletta, H., R.A. Robinson, A.C. Lawson, V. Sechovsky, L. Havela, L. Jirman, M. Divis, E. Brück, F.R. de Boer, A.V. Andreev, K.H.J. Buschow and P. Burllet, 1992, *J. Magn. & Magn. Mater.* **104-107**, 21.
- Marmeggi, J.C., G.H. Lander, S. van Smaalen, T. Brückel and C.M.E. Zeyen, 1990, *Phys. Rev. B* **42**, 9365.
- Marshall, W., and S.W. Lovesey, 1971, *Theory of Thermal Neutron Scattering* (Oxford University Press, Oxford).

- Mattenberger, K., O. Vogt, J.C. Spirlet and J. Rebizant, 1986, *J. Less-Common Met.* **121**, 285.
- Mattenberger, K., O. Vogt, J. Rebizant, J.C. Spirlet, P. Burllet, E. Pleska and J. Rossat-Mignod, 1990, *Physica B* **163**, 488.
- Mattenberger, K., O. Vogt, J. Rebizant, J.C. Spirlet, F. Bourdarot, P. Burllet, J. Rossat-Mignod, M.N. Bouillet, A. Blaise and J.P. Sanchez, 1992, *J. Magn. & Magn. Mater.* **104-107**, 43.
- McCart, B., G.H. Lander and A.T. Aldred, 1981, *J. Chem. Phys.* **74**, 5263.
- McMillan, W.L., 1976, *Phys. Rev. B* **14**, 1496.
- McWhan, D.B., C. Vettier, E.D. Isaacs, G.E. Ice, D.P. Siddons, J.B. Hastings, C. Peters and O. Vogt, 1990, *Phys. Rev. B* **42**, 6007.
- Mook, H.A., 1966, *Phys. Rev.* **148**, 495.
- Moon, R.M., W.C. Koehler, J.W. Cable and H.R. Child, 1972, *Phys. Rev. B* **5**, 997.
- Moon, R.M., W.C. Koehler, D.B. McWhan and F. Holtzberg, 1978, *J. Appl. Phys.* **49**, 2107.
- Moon, R.M., S.H. Liu and K. Werner, 1983, *J. Magn. & Magn. Mater.* **31-34**, 387.
- Morss, L.R., J.W. Richardson, C.W. Williams, G.H. Lander, A.C. Lawson, N.M. Edelstein and G.V. Shalimoff, 1989, *J. Less-Common Met.* **156**, 273.
- Murasik, A., P. Fischer, A. Furrer and W. Szczepaniak, 1985, *J. Phys. C* **18**, 2909.
- Murasik, A., P. Fischer, R. Troč and V.H. Tran, 1991, *J. Phys.: Condens. Matter* **3**, 1841.
- Nathans, R., C.G. Shull, G. Shirane and A. Andresen, 1959, *J. Phys. & Chem. Solids* **10**, 13.
- Nellis, W.J., A.R. Harvey, G.H. Lander, B.D. Dunlap, M.B. Brodsky, M.H. Mueller, J.F. Reddy and G.R. Davidson, 1974, *Phys. Rev. B* **9**, 1041.
- Norman, M.R., and D.D. Koelling, 1986, *Phys. Rev. B* **33**, 3803.
- Nunez, V., R. Trump, P.J. Brown, T. Chattopadhyay, M. Loewenhaupt and F. Tasset, 1992, *J. Phys.: Condens. Matter* **4**, 1115.
- Ott, H.R., 1980, in: *Crystalline Electric Fields and Structural Effects in f-Electron Systems*, eds J.E. Crow, R.P. Guertin and T.W. Mihalisin (Plenum Press, New York) pp. 9-21.
- Ott, H.R., and Z. Fisk, 1987, in: *Handbook on the Physics and Chemistry of the Actinides*, Vol. 5, eds A.J. Freeman and G.H. Lander (North-Holland, Amsterdam) pp. 85-225.
- Ott, H.R., J.K. Kjems and F. Hulliger, 1979, *Phys. Rev. Lett.* **42**, 1378.
- Paixão, J.A., G.H. Lander, P.J. Brown, H. Nakotte, F.R. de Boer and E. Brück, 1992, *J. Phys.: Condens. Matter* **4**, 829.
- Paixão, J.A., G.H. Lander, C.C. Tang, W.G. Stirling, A. Blaise, P. Burllet, P.J. Brown and O. Vogt, 1993, *Phys. Rev. B* **47**, 8634.
- Pinto, H., M. Melamud, M. Kuznietz and H. Shaked, 1985, *Phys. Rev. B* **31**, 508.
- Pleska, E., J.M. Fournier, J. Chiapusio, J. Rossat-Mignod, J.C. Spirlet, J. Rebizant and O. Vogt, 1988, *J. Phys. (Paris)* **49**, C8-493.
- Price, D.L., and K. Sköld, eds, 1986, *Methods of Experimental Physics*, Vol. 23, Paris A-C (Academic Press, New York).
- Ptasiewicz, H., J. Leciejewicz and A. Zygmunt, 1981, *J. Phys. F* **11**, 1225.
- Ptasiewicz-Bak, B., A. Baran, W. Suski and J. Leciejewicz, 1988, *J. Magn. & Magn. Mater.* **76-77**, 439.
- Pynn, R., W. Press, S.M. Shapiro and S.A. Werner, 1976, *Phys. Rev. B* **13**, 295.
- Raison, P., A. Delapalme, G.H. Lander, R. Kahn, C. Carlile, J. Williams, B. Kanellakopoulos, C. Apostolidis and J. Rebizant, 1992, *Physica B* **180-181**, 720.
- Reihl, B., N. Martensson, D.E. Eastman and O. Vogt, 1981a, *Phys. Rev. B* **24**, 406.
- Reihl, B., N. Martensson, P. Heimann, D.E. Eastman and O. Vogt, 1981b, *Phys. Rev. Lett.* **46**, 1480.
- Robinson, R.A., A.C. Lawson, K.H.J. Buschow, F.R. de Boer, V. Sechovsky and R.B. von Dreele, 1991, *J. Magn. & Magn. Mater.* **98**, 147.
- Robinson, R.A., A.C. Lawson, J.W. Lynn and K.H.J. Buschow, 1992a, *Phys. Rev. B* **45**, 2939.
- Robinson, R.A., A.C. Lawson, J.W. Lynn and K.H.J. Buschow, 1993a, *Phys. Rev. B* **47**, 6138.
- Robinson, R.A., A.C. Lawson, J.A. Goldstone and K.H.J. Buschow, 1993b, *J. Magn. & Magn. Mater.*, in press.
- Robinson, R.A., J.W. Lynn, V. Nunez, K.H.J. Buschow, H. Nakotte and A.C. Lawson, 1993c, *Phys. Rev. B* **47**, 5090.
- Rossat-Mignod, J., 1987, in: *Methods of Experimental Physics*, Vol. 23C, eds K. Sköld and D.L. Price (Academic Press, New York) pp. 69-158.
- Rossat-Mignod, J., P. Burllet, J. Villain, H. Bartholin, W. Tchong-Si, D. Florence and O. Vogt, 1977, *Phys. Rev. B* **16**, 440.
- Rossat-Mignod, J., P. Burllet, S. Quezel, O. Vogt and H. Bartholin, 1982, in: *Crystalline Electric Field Effects in f-Electron Magnetism*, eds R.P. Guertin, W. Suski and Z. Zolnierek (Plenum Press, New York) p. 501.

- Rossat-Mignod, J., G.H. Lander and P. Burlet, 1984, in: *Handbook on the Physics and Chemistry of the Actinides*, Vol. 1, eds A.J. Freeman and G.H. Lander (North-Holland, Amsterdam) pp. 415-515.
- Rossat-Mignod, J., J.M. Effantin, P. Burlet, T. Chattopadhyay, L.P. Regnault, H. Bartholin, C. Vettier, O. Vogt, D. Ravot and J.C. Achard, 1985, *J. Magn. & Magn. Mater.* **52**, 111.
- Sanchez, J.P., J.C. Spirlet, J. Rebizant and O. Vogt, 1987, *J. Magn. & Magn. Mater.* **63-64**, 139.
- Sanchez, J.P., P. Burlet, S. Quezel, D. Bonnissseau, J. Rossat-Mignod, J.C. Spirlet, J. Rebizant and O. Vogt, 1988, *Solid State Commun.* **67**, 999.
- Sanchez, J.P., K. Tomala, J. Rebizant, J.C. Spirlet and O. Vogt, 1990, *Hyperfine Interactions* **54**, 701.
- Sanchez, J.P., B. Lebech, M. Wulff, G.H. Lander, K. Tomala, K. Mattenberger, O. Vogt, A. Blaise, J. Rebizant, J.C. Spirlet and P.J. Brown, 1992, *J. Phys.: Condens. Matter* **4**, 9423.
- Schmid, B., A. Murasik, P. Fischer, A. Furrer and B. Kanellakopoulos, 1990, *J. Phys.: Condens. Matter* **2**, 3369.
- Schobinger-Papamantellos, P., P. Fischer, A. Niggli, E. Kaldis and V. Hildebrand, 1974, *J. Phys. C* **7**, 2023.
- Schoenes, J., 1984, in: *Handbook on the Physics and Chemistry of the Actinides*, Vol. 1, eds A.J. Freeman and G.H. Lander (North-Holland, Amsterdam) p. 341.
- Schulhof, M.P., P. Heller, R. Nathans and A. Linz, 1970, *Phys. Rev. B* **1**, 2304.
- Sears, V.F., 1986, in: *Methods of Experimental Physics*, Vol. 23A, eds D. Price and K. Sköld (Academic Press, New York).
- Sechovsky, V., and L. Havela, 1988, in: *Ferromagnetic Materials*, Vol. 4, eds E.P. Wohlfarth and K.H.J. Buschow, (North-Holland, Amsterdam) p. 309.
- Severin, L., L. Nordström, M.S.S. Brooks and B. Johansson, 1991, *Phys. Rev. B* **44**, 9392.
- Shemirani, B., H. Lin, M.F. Collins, C.V. Stager, J.D. Garrett and W.J.L. Buyers, 1993, *Phys. Rev. B* **47**, 8672.
- Shull, C.G., and A. Wedgwood, 1966, *Phys. Rev. Lett.* **16**, 513.
- Sinha, S.K., G.H. Lander, S.M. Shapiro and O. Vogt, 1980, *Phys. Rev. Lett.* **45**, 1028.
- Sinha, S.K., G.H. Lander, S.M. Shapiro and O. Vogt, 1981, *Phys. Rev. B* **23**, 4556.
- Smith, H.G., and G.H. Lander, 1984, *Phys. Rev. B* **30**, 5407.
- Smith, T.F., and E.S. Fisher, 1973, *J. Low Temp. Phys.* **12**, 631-641.
- Soderholm, L., C.W. Williams and U. Welp, 1991, *Physica C* **179**, 440.
- Soderholm, L., et al., 1992, unpublished.
- Spano, M.L., and J.J. Rhyne, 1985, *J. Appl. Phys.* **57**, 3303 and references therein.
- Spirlet, J.C., and O. Vogt, 1984, in: *Handbook on the Physics and Chemistry of the Actinides*, Vol. 1, eds A.J. Freeman and G.H. Lander (North-Holland, Amsterdam) pp. 79-151.
- Squires, G.L., 1978, *Thermal Neutron Scattering* (Cambridge University Press, London).
- Stanley, H.E., 1971, *Introduction to Phase Transitions and Critical Phenomena* (Clarendon Press, Oxford).
- Stassis, C., and H.W. Deckman, 1975, *Phys. Rev. B* **12**, 1885.
- Stassis, C., and H.W. Deckman, 1976, *J. Phys. C* **9**, 2241.
- Stassis, C., C.K. Loong and G.R. Kline, 1978, *J. Appl. Phys.* **49**, 2113.
- Stassis, C., C.K. Loong, O.D. McMasters and R.M. Moon, 1979, *J. Appl. Phys.* **50**, 2091, 7567.
- Stassis, C., C.K. Loong, J. Zarestky, O.D. McMasters, R.M. Moon and J.R. Thompson, 1982, *J. Appl. Phys.* **53**, 7890.
- Stassis, C., J. Arthur, C.F. Majkrzak, J.D. Axe, B. Batlogg, J. Remeika, Z. Fisk, J.L. Smith and A.S. Edelstein, 1986, *Phys. Rev. B* **34**, 4382.
- Steman, R.A., E. Frikkee, C. van Dijk, G.J. Nieuwenhuys and A.A. Menovsky, 1988, *J. Magn. & Magn. Mater.* **76-77**, 435.
- Steglich, F., J. Aarts, C.D. Bredl, W. Lieke, D. Meschede, W. Franz and W. Schaffer, 1979, *Phys. Rev. Lett.* **43**, 1892.
- Steglich, F., U. Alheim, A. Böhm, C.D. Bredl, R. Caspary, C. Geibel, A. Grauel, R. Helfrich, R. Köhler, M. Lang, A. Mehner, R. Modler, C. Schank, C. Wassilew, G. Weber, W. Assmus, N. Sato and T. Komatsubara, 1991, *Physica C* **185-189**, 379.
- Stewart, G.R., 1984, *Rev. Mod. Phys.* **56**, 755.
- Stewart, G.R., R.G. Haire, J.C. Spirlet and J. Rebizant, 1991, *J. Alloys & Compounds* **177**, 167.
- Stirling, W.G., and K.A. McEwen, 1987, in: *Methods of Experimental Physics*, Vol. 23C, eds K. Sköld and D.L. Price (Academic Press, New York) pp. 159-240.
- Szytula, A., and J. Leciejewicz, 1989, in: *Handbook on the Physics and Chemistry of Rare Earths*, Vol. 12, eds K.A. Gschneidner Jr and L. Eyring (North-Holland, Amsterdam) p. 133.

- Takagi, H., S. Uchida and Y. Tokura, 1989, *Phys. Rev. Lett.* **62**, 1197.
- Takahashi, H., and T. Kasuya, 1985, *J. Phys. C* **18**, 2697.
- Tang, C.C., W.G. Stirling, G.H. Lander, D. Gibbs, W. Herzog, P. Carra, B.T. Thole, K. Mattenberger and O. Vogt, 1992, *Phys. Rev. B* **46**, 5287.
- Therond, P.G., A. Blaise, J.M. Fournier, J. Rossat-Mignod, J.C. Spirlet, J. Rebizant and O. Vogt, 1987, *J. Magn. & Magn. Mater.* **63-64**, 142.
- Tillwick, D.L., and P. de V. DuPlessis, 1976, *J. Magn. & Magn. Mater.* **3**, 329.
- Torikachvili, M.S., L. Rebersky, K. Motoya, S.M. Shapiro, Y. Dalichaouch and M.B. Maple, 1990, *Physica B* **163**, 117.
- Torikachvili, M.S., L. Rebersky, K. Motoya, S.M. Shapiro, Y. Dalichaouch and M.B. Maple, 1992, *Phys. Rev. B* **45**, 2262.
- Turberfield, K.C., L. Passell, R.J. Birgeneau and E. Bucher, 1970, *Phys. Rev. Lett.* **25**, 752.
- Turberfield, K.C., L. Passell, R.J. Birgeneau and E. Bucher, 1971, *J. Appl. Phys.* **42**, 1746.
- Varma, C.M., 1976, *Rev. Mod. Phys.* **48**, 219.
- Vettier, C., P. Morin and J. Flouquet, 1986, *Phys. Rev. Lett.* **56**, 1980.
- Villain, J., and M.B. Gordon, 1980, *J. Phys. C* **13**, 3117.
- Vogt, O., and K. Mattenberger, 1987, *J. Less-Common Met.* **133**, 53.
- Vogt, O., and K. Mattenberger, 1993, ch. 114, this volume.
- Vrtis, M.L., C.K. Loong, D.G. Hinks, C. Stassis and J. Arthur, 1987, *J. Appl. Phys.* **61**, 3174.
- Wachter, P., F. Marabelli and B. Bucher, 1991, *Phys. Rev. B* **43**, 11, 136.
- Ward, J.W., 1985, in: *Handbook on the Physics and Chemistry of the Actinides*, Vol. 3, eds A.J. Freeman and C. Keller (North-Holland, Amsterdam) p. 1.
- Wedgwood, F.A., 1972, *J. Phys. C* **5**, 2427.
- Willis, B.T.M., 1978, *Acta Crystallogr. A* **34**, 88.
- Wulff, M., and G.H. Lander, 1988, *J. Chem. Phys.* **89**, 3295.
- Wulff, M., G.H. Lander, J. Rebizant, J.C. Spirlet, B. Lebech and P.J. Brown, 1988, *Phys. Rev. B* **39**, 5577.
- Wulff, M., G.H. Lander, B. Lebech and A. Delapalme, 1989, *Phys. Rev. B* **39**, 4719.
- Wulff, M., O. Eriksson, B. Johansson, B. Lebech, M.S.S. Brooks, G.H. Lander, J. Rebizant, J.C. Spirlet and P.J. Brown, 1990a, *Europhys. Lett.* **11**, 269.
- Wulff, M., J.M. Fournier, A. Delapalme, B. Gillon, V. Sechovsky, L. Havela and A.V. Andreev, 1990b, *Physica B* **163**, 331.
- Wybourne, B.G., 1965, *Spectroscopic Properties of Rare Earths* (Interscience, New York).
- Yethiraj, M., R.A. Robinson, J.J. Rhyne, J.A. Gotaas and K.H.J. Buschow, 1989, *J. Magn. & Magn. Mater.* **79**, 355.

## SUBJECT INDEX

- absorber 547, 549, 551
- absorber container 568
- absorber thickness 549
- absorber thickness, effective 549, 565
- absorbing nuclei 552
- absorption cross section 545, 546, 551
- absorption energy 545
- absorption line 548
- absorption maximum 551
- absorption strength 549
- AC susceptibility 620, 622
  - cusp in 619, 620
  - initial 377
  - lack of sharp cusp 622
- actinide atom 557
- actinide compounds
  - 1:1 compounds 302
  - actinide carbides 277, 281
  - actinide dioxides and CeO<sub>2</sub> 290
  - actinide intermetallics 544
  - actinide monocarbides 248
  - actinide monochalcogenides 516
  - actinide mononictides 507
  - AnAl<sub>2</sub> 449, 459
  - AnCo<sub>2</sub> 482
  - AnFe<sub>2</sub> 473, 601
  - AnFe<sub>2</sub> (An = U, Np, Pu, Am) 601
  - AnFe<sub>4+x</sub>Al<sub>8-x</sub> systems 618
  - AnIn<sub>3</sub> 493
  - AnM<sub>2</sub> Laves phases 465
  - AnM<sub>3</sub> intermetallics (M = In, Sn) 488
  - AnM<sub>4</sub>Al<sub>8</sub> 615
  - AnO<sub>2</sub> 288
  - AnPt 448
  - AnPt intermetallics 446
  - AnSn<sub>3</sub> 498
  - AnX 245, 506
  - AnX<sub>2</sub> 583, 596
  - AnX<sub>3</sub> (X = Al, Ge, Rh, Pd and Sn) 591
  - MX compounds 272
  - MXY compounds 245
  - MX<sub>2</sub> compounds 245, 288
  - MX<sub>3</sub> compounds 245, 292
  - MX<sub>4</sub> compounds 245, 294
  - MX<sub>6</sub> compounds 245, 294
  - MX<sub>12</sub> compounds 245, 294
  - M<sub>2</sub>X<sub>3</sub> compounds 245, 285
  - M<sub>3</sub>X<sub>4</sub> compounds 245
  - mixed Ln–An phosphides and sulfides 377
  - substitutional alloy 233
- actinide metals
  - stability of trigonal phase 268
- actinide Mössbauer resonances 557, 562
- actinide series 543
- actinide sublattice 620
- actinide surfaces 208
- actinide–actinide separation 578
- actinides 541, 551, 552, 556, 565, 566
  - light 544, 562, 595
- adiabatic theory 316
- after effects 567
- allowed  $\gamma$ -transitions
  - intensities 52
  - positions 555
- alloy systems 268
- alloys 245
- $\alpha$  decay 567
- $\alpha$  decay of <sup>241</sup>Am 567
- $\alpha$  decay parents 567
- aluminum-deficient samples 618
- Am–Cm 268
- ambient pressure 568
- americium 443, 544, 561, 565
  - Am in Th 567
  - <sup>241</sup>Am 567
  - $\alpha$ -decay of 567
  - <sup>241</sup>Am metal 554
  - <sup>241</sup>Am metal source 567
  - <sup>243</sup>Am 560, 565, 568, 602
  - <sup>243</sup>Am resonance 607
- americium compounds
  - AmAs 305
  - AmBi 305
  - AmFe<sub>2</sub> 473, 602, 664
  - AmN 305
  - AmTe 305
  - AmX<sub>2</sub> 602
- amorphous magnet 555, 556
- amorphous solids 546
- amplifier 570

- An moments, freezing of 620  
 Anderson model 622  
 Anderson type of superexchange 311  
 angular dependence 553, 558  
 anisotropic electronic  $g$  factor 553  
 anisotropic exchange 303, 304, 323  
 anisotropic  $f$  factor 558  
 anisotropic hybridization of 5f electrons with s and p band electrons 609  
 anisotropy gap 366  
 anisotropy ratio 696, 697  
 annealing history 623  
 ANNNI (anisotropic next-nearest-neighbor interaction) model 360  
 anomalous systems 544  
 anti-Fe<sub>3</sub>As structure 290  
 anti-Th<sub>3</sub>P<sub>4</sub> structure 285  
 antiferrimagnetic spin structure  
 – sinusoidally modulated incommensurate 582  
 antiferromagnet 595, 608, 618, 641, 691, 701  
 antiferromagnetic correlations 689  
 antiferromagnetic coupling 620, 622  
 antiferromagnetic exchange 690  
 antiferromagnetic order 592, 618, 625, 627  
 antiferromagnetic polarization of s electrons 586  
 antiferromagnetic spin sequence 624  
 antiferromagnetic structure 675  
 antiferromagnetic transition 605  
 antiferromagnetism 609, 615, 623  
 asymmetry parameter 557  
 atomic angular momentum  $J$  552  
 atomic self-consistent field calculations 556  
 atomic shell 550  
 atomic units (au) 556  
 AuCu<sub>3</sub>  
 – materials 608, 610  
 – structure 591, 607  
 – – instability of 610  
 axial symmetry 557  
 axial symmetry ( $\eta = 0$ ) 557  
  
 B1–B2 phase transition 279, 280  
 B1-type compounds, *see also* NaCl-type structure 247, 283  
 B2 compounds  
 – metastable 279  
 B2-type compounds, *see also* CsCl-type structure 278, 279  
 band centre, unhybridized 167  
 band diagram 576  
 band mass 167  
 band mass parameters 170  
 band structure calculations 104, 113, 131, 592, 598, 627  
  
 band theory 8  
 bandwidth parameter 169  
 bar diagram 553, 554  
 Bessel function 549  
 $\beta^-$  decay activity, 6.8d <sup>237</sup>U 567  
 $\beta^+$  source activity, 45d <sup>237</sup>Pu 567  
 binding forces 546  
 biquadratic contribution 323  
 biquadratic exchange 342  
 Birch equation 257  
 Bk–Cf 268  
 blow-out 571  
 Bohr radius 556  
 Boltzmann equation 414, 415, 419, 453, 459  
 Boltzmann formalism 412, 414  
 bonding 642  
 – electrons 367  
 – energy 545  
 – pressure 187  
 Born–Oppenheimer approximation 164  
 Born approximation 639  
 Bragg peaks 600, 618  
 Bragg scattering 546  
 Brillouin function 349, 554  
 broadening of emission 565  
 bulk modulus 192, 245, 269, 279, 288, 584, 589  
 – isothermal 270, 275, 279, 281, 286, 289, 291  
 bulk susceptibility 577, 625  
  
 C15-type compounds, *see* Laves phase compounds  
 CaF<sub>2</sub>-type (fluorite) structure 288  
 calibration constant  $\alpha$  551  
 californium compounds  
 – CfAs 341  
 – CfN 341  
 – CfSb 341  
 cation/anion ratio 284  
 center of gravity 560  
 centrifugal potential 168  
 cerium 204, 442, 446, 544, 577  
 –  $\alpha$ -Ce 207, 442, 443, 446  
 –  $\beta$ -Ce 443  
 – Ce<sup>4+</sup> 574  
 –  $\gamma$ -Ce 205, 442, 443, 446  
 –  $\gamma$ - $\alpha$  transition 204  
 cerium alloys 412, 577  
 – CeBi–CeTe 395  
 – CeSb–CeTe 395  
 – CeSn<sub>3</sub>–CeIn<sub>3</sub>–CePb<sub>3</sub> 18  
 cerium compounds  
 – CeAl<sub>2</sub> 50, 51, 269, 450–452, 457, 497, 526, 528, 625, 682, 683, 700, 701  
 – CeAl<sub>3</sub> 464  
 – CeAs 390, 521–523, 525, 528

- cerium compounds (*cont'd*)
- CeB<sub>6</sub> 55–57
  - CeBi 42, 393, 395, 522–526, 528
  - – effect of pressure 333, 334
  - CeCu<sub>2</sub> 483, 497
  - CeCu<sub>5</sub> 497, 502–504, 530
  - CeCu<sub>6</sub> 58–60, 623
  - CeCu<sub>3</sub>Al<sub>2</sub> 530
  - CeCu<sub>4</sub>Al 502, 503, 530
  - CeCu<sub>2</sub>Si<sub>2</sub> 62, 67–69, 269
  - CeFe<sub>2</sub> 470–474, 488, 493, 530, 664, 700
  - CeIn<sub>1-x</sub> 27
  - CeIn<sub>3</sub> 10, 11, 18, 26, 27, 492
  - Ce<sub>0.1</sub>La<sub>0.9</sub>Sb 392
  - CeN 389, 520, 521
  - CeNi 47, 48
  - CeNi<sub>2</sub> 484
  - CeO<sub>2</sub> 290
  - CeP 389, 521–523, 525, 528
  - CePb<sub>3</sub> 10, 11, 18, 19, 683, 689
  - CePd 12
  - CePd<sub>3</sub> 11, 14–16, 493, 655
  - CeRh 12, 14, 16
  - CeRh<sub>3</sub> 13, 15, 17
  - CeRh<sub>3</sub>B<sub>2</sub> 62
  - CeRu<sub>2</sub> 49
  - CeRu<sub>2</sub>Ge<sub>2</sub> 65
  - CeRu<sub>2</sub>Si<sub>2</sub> 63–65, 464
  - CeS 395, 526, 527
  - CeSb 41–43, 45, 391, 395, 522–525, 528, 669, 677, 698, 700
  - CeSe 395, 526, 527
  - CeSn 10
  - CeSn<sub>3</sub> 15, 18, 19, 22–24, 497, 498
  - CeTe 395, 526–528
  - Ce<sub>0.1</sub>Y<sub>0.9</sub>Sb 392
  - monopnictides and monochalcogenides 520
  - chalcogenides 277, 281, 303, 338, 604
  - stability ranges 278, 279
  - charge density wave (CDW) 444, 642, 644–646, 699
  - charge distribution 550
  - charge fluctuations 68, 552, 575
  - charge state 542, 551, 627
  - chemical environment 303
  - Clebsch–Gordon coefficient 553
  - cohesive energy 153, 177, 198
  - collapsed phases 261, 262
  - collection time 549
  - collective excitations 363
  - collinear 4↑4↓ structure 582, 605
  - collinear spin structure 582
  - collinearity 560
  - combined interactions 559
  - commensurate 605, 665, 671, 672, 683, 690
  - nearly squared up, modulated structure 605
  - comparison of resolution 560
  - compressibility 245, 269
  - conduction electron 562
  - bands 627
  - field gradient from 559
  - gas 588
  - polarisation 579
  - spin moment 220
  - volume dependence 587
  - conduction electron, compression of 575, 576, 588
  - conical spiral component 618
  - contact charge density 550
  - contact density 551, 556, 563
  - contact electron density 587
  - core electrons 556
  - polarization of 579
  - core field 556, 557
  - Coulomb interaction 550
  - coupling constant 559
  - covalency 222, 562, 579, 604
  - Cr sublattices 616
  - critical exponents 698
  - critical field 478
  - critical magnetic scattering 700
  - critical nearest-neighbor distance 267
  - critical radius ratios 252
  - critical scattering 335
  - critical temperature 593
  - cross section measurements 362
  - crystal field 304, 447, 449, 450, 476, 490, 492, 494, 496, 500–504, 522, 528, 529, 577, 604, 667, 669, 689, 690, 701, 702
  - cubic 593
  - effects 562, 593, 616
  - eigenstates 363
  - interaction 559, 582, 583, 594, 602, 604, 613, 615, 627
  - localized 609
  - lowest states 616
  - splitting 306
  - states 559
  - theory 316
  - thermal population 577
  - crystal matrix 303
  - crystalline electric field, *see* crystal field 604
  - CsCl-type structure, *see also* B2-type compounds 278, 581
  - cubic intermetallics 609
  - Curie–Weiss behaviour 304, 460, 469, 475, 484, 495, 500, 504
  - Curie–Weiss law, modified 344



- Curie temperature 211, 314, 446, 452, 472, 475,  
480, 484, 487, 488, 555, 581
- curium 441
- curium compounds
- CmAs 311
  - CmCu<sub>2</sub>O<sub>4</sub> 702
  - Cm<sub>2</sub>CuO<sub>4</sub> 691
  - CmN 311
  - CmO<sub>2</sub> 647
  - CmP 311
  - CmSb 311
- d band occupation 265
- d electron density 627
- d electron number, effective 265
- 3d–5f hybridization 236, 600, 602
- 3d-like itinerant electron behavior 628
- 3d transition elements 542
- 5d states in Gd, occupation of 612
- DC magnetization 620, 621
- DC susceptibility 620
- de-excitation 544
- de Gennes factor 339, 422, 424, 438, 447, 450,  
459, 470, 486, 491, 496, 497
- de Haas–van Alphen effect 103, 126
- de Haas–van Alphen measurements 9, 10, 20, 22,  
23, 28, 30–36, 42–45, 47, 48, 50, 55, 57–62, 64,  
128
- Debye–Waller factor 546
- Debye approximation 547
- Debye integral 546
- Debye model 546
- Debye temperature 451, 546, 547, 552, 565
- defect structures 646
- degeneracy 558
- degrees of hybridization 562
- delocalization 295, 351
- delocalized density 652, 654, 700
- density functional theory 3, 8, 9, 44, 150,  
165
- density of states 462, 468, 472
- diagonal disorder 233
- diagonalization 552, 556
- diamond anvil 572, 573
- dilatation 335
- Dingle temperature 136
- dipolar magnetic field 557
- dipole approximation 641, 648, 650
- dipole character 553
- dipole moment 553
- Dirac–Fock calculation 556
- Dirac equation 175
- direct dipolar field contribution 579
- distorted structures 207
- domain effects 310, 366
- domain magnetization 555
- domain switching 342
- Doppler effect 548
- Doppler motion 553, 569
- Doppler shift 548, 551
- Dunlap–Lander relation 562, 564, 577, 599, 607,  
625
- dynamical exchange 342
- dynamical hyperfine spectra 556
- dynamical processes 590
- dysprosium 542, 561, 565, 578
- <sup>161</sup>Dy 565
- dysprosium compounds
- chalcogenides 338
  - DyAl<sub>2</sub> 450, 452, 453, 455, 584, 588, 589, 592
  - DyAs 331, 604, 606
  - DyBi 331
  - DyCo<sub>2</sub> 475, 477, 478, 480, 481
  - DyFe<sub>2</sub> 470–472
  - DyIn<sub>3</sub> 490–492
  - DyN 331
  - DyNi<sub>2</sub> 484
  - DyP 331, 604, 606
  - DySb 331, 604
  - DyX 604
  - DyX<sub>2</sub> 599
  - Dy<sub>0.2</sub>Y<sub>0.8</sub>Sb 335
  - monopnictides 606
  - – trend of hyperfine field 604
- EOS, *see* equation of state
- effective field 217
- gradient 560
- effective internal magnetic field 322
- effective magnetic field 553
- effective mass 428, 623
- effective moments 308
- eigenvalues 553, 558
- elastic constants 203
- electric couplings 550
- electric field gradient 549, 557–559, 564, 577,  
627
- in monopnictides 604
  - tensor 557
  - thermal average 559
- electric moments 550
- electrical resistivity 413, 414, 429, 455, 456,  
461–465, 476, 482, 484, 487, 488, 490, 493–495,  
499, 500, 503, 504, 508, 513, 515, 522–524,  
526, 623
- electromagnetic coupling 550
- electromechanical drive unit 569

- electron, *see also* conduction electron
  - behavior 628
  - concentration 311
  - conversion coefficient 545
  - shell 542
  - structure 551, 628
  - – under reduced volume 578
- electron density 550
- electron-phonon 495
  - contribution 527
  - coupling 452, 489
  - interaction 454, 496
  - scattering 492, 529
- electronic charge density 550
  - volume dependence 588
- electronic charge distribution 557
- electronic charges 550
- electronic contribution 553
- electronic environment 303
- electronic polaron model 127
- electronic pressure 171, 217
  - formula 151
- electronic properties 628
- electronic shell 559
- electronic specific heat 185, 443, 448, 623
  - coefficient 428, 448, 467, 469, 484, 487, 492, 495, 498, 499, 592, 617, 623, 625
  - – correlation with isomer shift 624
- electronic state 555
- electronic structure 1, 150, 542, 549, 554, 610
  - parameter 557
  - properties 561, 596
- electronic transition 276, 282, 295
- emission energy 545
- emission line 548
- emission or absorption proces 545
- emission probability 546
- emitting nuclei 552
- energy band, unhybridized 169
- enhanced Pauli paramagnetism 305, 389
- equation of state 190, 250, 252, 254–262, 265, 267
- erbium compounds
  - chalcogenides 338
  - ErAl<sub>2</sub> 455
  - ErAs 336
  - ErBi 336
  - ErCo<sub>2</sub> 475, 478–481
  - ErFe<sub>2</sub> 470–472
  - ErIn<sub>3</sub> 490–492
  - ErMn<sub>2</sub> 466
  - ErN 336
  - ErNi<sub>2</sub> 484
  - ErP 336
  - ErSb 336
  - sample dependence: 336
- error ellipsoids 257, 259
- europium 542, 561, 562, 565, 578
  - Eu<sup>2+</sup> 551, 574, 575
  - – free 579
  - Eu<sup>3+</sup> 574, 575
  - – Mössbauer spectrum 551
  - <sup>151</sup>Eu 551, 560, 565, 572
  - – resonance 555
  - metal 555
  - – energy level 576
- europium compounds
  - divalent 576
  - EuAl<sub>2</sub> 584, 585, 587, 595
  - – valence of Eu in 585
  - EuAs 304
  - EuCo<sub>2</sub>Si<sub>2</sub> 595
  - EuCu<sub>2</sub>Si<sub>2</sub> 575, 595
  - EuN 304
  - EuO 311, 551, 579, 581, 595
  - – valence of Eu at high pressure 579, 580
  - Eu<sub>2</sub>O<sub>3</sub> 551
  - EuP 304, 305
  - – impurities, effects of 305
  - EuS 311, 579
  - EuSb 304
  - EuSe 311, 579
  - EuSe–CaS 311
  - EuSe–YSe 311
  - EuSn<sub>3</sub> 496
  - Eu<sub>x</sub>Sr<sub>1-x</sub> 312
  - Eu<sub>x</sub>Sr<sub>1-x</sub>S 311
  - EuTe 311, 579
  - EuX (X = O, S, Se, Te) 579, 580
  - metallic systems
  - monochalcogenides 579
- exchange
  - field 553, 555
  - integrals 580, 586
  - interaction 177, 562, 577, 615
  - splitting 615
- exchange integrals, effective 579, 580
- exchange interactions
  - randomness of 622
- excitation energy  $E_{ex}$  575
  
- f band formation 578
- f electron configuration, localized 615
- f electron magnetism, localized 589
- f electron structure, deviations from standard 578
- f hole screening 129
- f-parameter 194

- f-shells
  - reshaped 341
- f systems
  - localized 593
- f–f overlap 577, 596
- 4f and 5f moments, localized 266
- 4f electrons, delocalization of 577, 700
- 4f electrons, localized 544
- 4f-like localized electron behavior 628
- 4f spins, well localized 585
- 4f system, localized 587, 588
- 5f band 578
  - formation 628
  - narrow 603
- 5f bandwidth 184
- 5f delocalization 544, 590
- 5f electron delocalization 578
- 5f electron structure
  - localized 304, 610
  - narrow band
    - – chalcogenides 604
    - – pnictides 604
- 5f electrons, delocalization of 246, 576
- 5f electrons, localized 246, 261
- 5f electrons, radial extent of 542, 576, 622
- 5f hybridization 257, 266
  - 5f–3d 236, 600, 602
  - f–d 230, 577, 623, 627
  - 5f–5f 624
  - f–p 373, 577, 622, 623
  - f–s 577
  - ligand electrons 591
- 5f localization 578, 582, 602
- 5f structure
  - localized 595
- 5f–5f overlap 599
- fast fluctuations 555
- Fe<sub>2</sub>As-type structure 290, 291
- Fe<sub>2</sub>P-type structure 593
- Fe sublattice 618
- Fermi contact term 579
- Fermi energy 461, 463, 575, 586
- Fermi gas pressure 253
- Fermi level 451, 454, 461, 475
- Fermi liquid models 105
- Fermi liquid state 617
- Fermi pseudopotential 639
- Fermi surface 1, 439, 459
- Fermi vector 586
- fermions
  - noninteracting 625
- ferrimagnet 324, 606
- ferromagnet 459, 579, 604, 641, 675, 695
- ferromagnetic 673, 681, 683, 687, 695, 700, 701
  - ferromagnetic coupling 620
  - ferromagnetic ordering 605, 618
  - ferromagnetic polarization of non-s-electrons 586
  - ferromagnetic relaxation 591, 600, 610
  - field gradient 559
  - filling of the transition metal d band 612
  - fine structure 550
  - first-order transition 602, 605, 606
  - fluctuation 552, 555
    - intermediately fast 552, 555
  - fluorescence doublet 574
  - fluorescence light 573
  - force theorem 151
  - form factor 352
  - Fourier components 304
  - free atoms 556
  - free-ion
    - configuration 562
    - field gradient 562
    - – magnetically induced 602
    - free ion 551
    - hyperfine field 562, 564, 577
    - moment 577
    - paramagnetic moment 577
    - valence electric field gradient 562
    - value 310, 599
  - frozen-core approximation 199
  - frustration 622
- g factor 553
- gadolinium 38–40, 542, 561, 565
  - <sup>155</sup>Gd 560, 565
- gadolinium compounds
  - GdAl<sub>2</sub> 450, 452, 453, 455, 457, 459–461, 476
  - GdAs 308
  - GdBi 308
  - GdCu<sub>2</sub>Si<sub>2</sub> 612
  - GdFe<sub>2</sub> 470, 471, 474, 485
  - GdIn<sub>3</sub> 490–493
  - GdM<sub>2</sub>Si<sub>2</sub> series 610
  - GdN 308
    - – stoichiometric 309
  - GdN<sub>1–x</sub>O<sub>x</sub> 312
  - GdNi<sub>2</sub> 484, 485
  - GdP 308
  - GdP–GdS 312
  - GdP<sub>1–x</sub>Se<sub>x</sub> 312
  - GdPt 446, 447
  - GdS<sub>1–x</sub> 312
  - GdS 310
  - GdSb 308
  - GdSb<sub>1–x</sub>Te<sub>x</sub> 312
  - GdSe 310
  - Gd silicides 613

- gadolinium compounds (*cont'd*)  
 – GdSn<sub>3</sub> 496  
 – GdTe 310  
 $\gamma$ -radiation, resonant 553  
 $\gamma$ -ray 544, 545  
 – energy distribution 539  
 $\Gamma_5$  level 613  
 $\gamma$ -ray intensity 547  
 $\gamma$ -ray transition 544–547, 552, 553  
 $\gamma$ -value, *see also* electronic specific heat coefficient  
 generalized phase diagram 249, 256, 268  
 geometrical distortions 570  
 Goldanskii–Karyagin effect 558, 560  
 ground state 544, 545, 547  
 group-III ligands (Al, Ga, In) 608  
 group-IV ligands (Si, Ge, Sn) 608
- half-integer nuclear spins 558  
 halides 562  
 – dihalides 245, 291  
 Hall coefficient  
 – anomalous 435  
 – normal 434, 528  
 Hall effect 412, 434, 440, 444–446, 464, 514, 520, 525, 526, 528, 529  
 – anomalous 435  
 – normal 434  
 Hamiltonian 552, 556, 557, 560  
 harmonics 644  
 health hazard of Np 568  
 heat of sublimation 157  
 heavy fermion 87–146, 381, 385, 412, 429, 463, 465, 498, 499, 506, 530, 544, 682, 684, 689, 699  
 – behavior 577, 623  
 – compounds 269, 577  
 – properties 269, 627  
 – regime 428  
 – superconductivity 623, 683, 699  
 – – charge fluctuations 68  
 – – phonons 67  
 – – spin fluctuations 69  
 – system 522, 530, 623  
 – – medium mass 623  
 heavy lanthanides 544, 562  
 heavy nuclei 552  
 Heisenberg magnet 579  
 Heisenberg-type exchange 312  
 Heisenberg's uncertainty principle 545  
 Hellmann–Feynman theorem 170  
 high-energy transitions 552, 565  
 high-field susceptibility 311  
 high magnetic fields 542  
 high pressure 542, 628  
 high-pressure, high-temperature synthesis 245, 271, 292  
 high-pressure apparatus 570–574  
 high-pressure experiments 396, 542  
 – Mössbauer 544, 578  
 – on NpAs 603  
 high-pressure Mössbauer data 282, 617  
 high-pressure phases 278, 288  
 high-pressure structure 283  
 high-pressure X-ray diffraction 270, 275, 282  
 Hill limit 267, 303, 578, 582, 589–591, 599  
 Hill plot 578, 590, 598, 599, 628  
 Hill transition zone 280  
 HoP-type structure 328, 606  
 Ho spins alignment 619  
 holmium compounds  
 – chalcogenides 338  
 – HoAl<sub>2</sub> 455  
 – HoAs 324  
 – HoBi 324  
 – – tetragonal distortion 329  
 – HoCo<sub>2</sub> 475, 478–481  
 – HoFe<sub>2</sub> 470–472  
 – HoFe<sub>4</sub>Al<sub>8</sub> 618–620, 623  
 – HoIn<sub>3</sub> 490–492  
 – HoMn<sub>2</sub> 465  
 – HoN 324  
 – HoNi<sub>2</sub> 484  
 – HoP 324  
 – HoSb 324  
 – – diluted 329  
 – – tilted moments 328  
 – Ho<sub>x</sub>Y<sub>1-x</sub>Sb 330  
 – Ho<sub>0.2</sub>Y<sub>0.8</sub>Sb 330  
 homogeneous field 553  
 Hund's rule configuration 562  
 Hund's rule ground state 559, 577, 594, 613  
 – splitting of the <sup>5</sup>I<sub>4</sub> 615  
 Hund's rule ground state, <sup>5</sup>I<sub>4</sub> 610  
 hybridization, *see also* 5f hybridization 227, 303, 350, 578, 604, 628, 642, 648, 651, 660, 663, 664, 677, 678, 684, 685, 689, 690, 700, 702  
 hybridization  
 – weak 341  
 hybridization, *see also* 5f hybridization  
 – with conduction electrons 581  
 – with ligand electrons 603, 604  
 hybridized magnetic materials 601  
 hyperfine coupling 550, 559  
 – constant 556, 586  
 hyperfine energy 550, 557  
 hyperfine field, *see also* magnetic hyperfine field 549, 553–557, 561, 562, 581, 585, 611, 614, 623  
 – and isomer shift, correlation between 609

- hyperfine field (*cont'd*)  
 – broad distribution of 606  
 – dependence of 603  
 – direct 557  
 – distribution of<sup>+</sup> 592, 605, 606, 618  
 – pressure dependence 582, 590  
 – reduction in, from the free ion field 602  
 – saturation 582, 588, 627  
 – saturation ( $T \rightarrow 0$ ) 577, 580  
 – static distribution 556, 600, 601  
 – temperature dependence 555, 605  
 – transferred 557, 579, 585, 592, 606, 607  
 – – on Te and Sb 605  
 – trend in Dy monopnictides 604  
 – uranium 607  
 – variations of 604  
 hyperfine interaction 542, 547, 549, 550, 553, 556, 561  
 hyperfine levels 553, 554  
 hyperfine lines 553, 558  
 – energetic positions 553  
 – relative intensities 553, 558  
 hyperfine parameters 549, 602, 626  
 – and lattice constant, correlation between 328  
 – temperature and pressure dependence 595  
 hyperfine pattern, center of gravity of the whole 560  
 hyperfine spectra 555; 556  
 hyperfine sublevels 553  
 hyperfine tensor 552  
 hyperfine transitions 553, 558, 560  
 hysteresis loop 363  
 hysteresis to re-transformation 279  
 hysteresis zone 279, 280  
 – equilibrium transition pressure 279  
  
 incommensurate 665, 672–674, 678, 679, 683  
 – antiferromagnetics state 602  
 – modulated structure 604, 605  
 – sine wave modulation 613  
 – spin structure 606  
 – structure 625  
 induced moment 338  
 inelastic neutron scattering 110, 140  
 insulating compounds 579  
 integer spins 558  
 interlanthanide and interactinide alloys 268  
 intermediate valence, *see also* mixed valence 381, 388, 450, 463, 484, 492, 505, 574, 595  
 – behavior 578  
 – compound 520, 593  
 – compounds 659  
 – effects 498  
 – indicator for 575  
 – properties 595  
 – regime 428  
 – state 498, 504  
 intermetallic compounds 245, 269, 272, 544  
 – of 4f and 5f elements 628  
 intermetallic systems 596  
 internal distortions 366  
 internal field 555  
 ionic charge states, deviation from 562  
 ionic electric field gradient 559, 564, 574; 604<sup>+</sup>  
 ionic state 562  
 irreversible changes of intensities 618  
 irreversible magnetic phenomena 617  
 isomer shift 542, 549, 551, 552, 560, 562, 576, 585, 595, 599, 603, 604, 611, 628  
 – and hyperfine field, correlation between 609  
 – and the contact electron density 550  
 – correlation with electronic specific heat coefficient 624  
 – mean valence from 574  
 – of NpSn<sub>3</sub> and NpIn<sub>3</sub> 608  
 – pressure dependence 582, 587  
 – temperature dependence 576  
 – – EuCu<sub>2</sub>Si<sub>2</sub> 575  
 – volume dependence 588  
 isomorphism 272  
 isostructural phase transition 268  
 isostructural volume collapses 273, 276, 281, 282  
 isotropic bilinear exchange 323  
 isotropic exchange 303, 304  
 itinerant 246, 295, 411  
 itinerant electron antiferromagnet 592  
 itinerant electron systems 593  
 itinerant f electron behavior 577  
 itinerant 5f electron structure 591, 595  
 itinerant 5f electrons 577, 622  
 itinerant magnet 577  
 itinerant magnetic state 570  
 itinerant magnetism 542  
  
 $J = 4$  ground multiplet 627  
 $J$ -mixing 349  
 Jahn–Teller–Peierls distortions 197  
 Jones plot 625  
  
 Knight shift 450  
 Kohler rule 418, 419, 495; 529  
 Kondo behavior 499, 505, 516, 518, 520, 522, 609  
 Kondo cancellation 701  
 Kondo effect 450, 498, 502, 528, 593  
 Kondo hybridization 386  
 Kondo interaction 504  
 Kondo lattice 114, 428, 504, 516, 523, 527, 544, 577, 609, 627

- Kondo scattering 427
- Kondo screening 528
- Kondo system 391, 464, 530, 683
  - concentrated 528, 593, 625
  - – CeAl<sub>2</sub> 593
- Kondo temperature 463, 502, 520, 528
- Kondo volume collapse 205
- Kramers ion 610
- Kramers theorem 558
  
- L<sub>III</sub> edge measurements 580
- lanthanide atom 557
- lanthanide compounds
  - 1:1 compounds 302
  - lanthanide intermetallics 544
  - lanthanide monochalcogenides 273
  - LnAl<sub>2</sub> Laves phase compounds 585
  - LnFe<sub>4+x</sub>Al<sub>8-x</sub> 618
  - LnM<sub>4</sub>Al<sub>8</sub> 615
  - Ln monopnictides 276
  - LnO<sub>2</sub> 288
  - LnOF and LnSF compounds 245
  - Ln pnictides and chalcogenides 275
  - LnX compounds 245, 583
  - LnX<sub>2</sub> compounds 596
  - MX compounds 272
  - MX<sub>2</sub> compounds 245, 288
  - MX<sub>3</sub> compounds 245, 292
  - MX<sub>4</sub> compounds 245, 294
  - MX<sub>6</sub> compounds 245, 294
  - MX<sub>12</sub> compounds 245, 294
  - M<sub>2</sub>X<sub>3</sub> compounds 245, 286
  - M<sub>3</sub>X<sub>4</sub> compounds 245
  - MXY compounds 245
  - mixed Ln–An phosphides and sulfides 377
  - RAl<sub>2</sub> 449–452, 454, 456, 457, 470, 471, 484, 486, 496, 529
  - RAl<sub>3</sub> 451
  - RCo<sub>2</sub> 475, 480, 484, 488, 530
  - RCo<sub>2</sub>Si<sub>2</sub> 612
  - RCr<sub>2</sub>Si<sub>2</sub> 612
  - RCu<sub>2</sub> 483
  - RCu<sub>5</sub> 500
  - RCu<sub>2</sub>Si<sub>2</sub> 612
  - RFe<sub>2</sub> 470–473, 475, 484, 485, 488, 530
  - R<sub>2</sub>Fe<sub>14</sub>B 211
  - RFe<sub>2</sub>Si<sub>2</sub> 612
  - RIn<sub>3</sub> 489–493, 529
  - RM<sub>3</sub> intermetallics (M = In, Sn) 488
  - RM<sub>2</sub> Laves phases 465
  - RMn<sub>2</sub> 465, 467, 468, 488
  - RMn<sub>2</sub>Si<sub>2</sub> 612
  - RNi<sub>2</sub> 450, 451, 470, 475, 483–486, 488, 529
  - RNi<sub>2</sub>Si<sub>2</sub> 612
  - RPd<sub>2</sub>Si<sub>2</sub> 612
  - RPt 446, 450, 470, 471, 486, 529
  - RPt intermetallics 446
  - RRh<sub>2</sub>Si<sub>2</sub> 612
  - RRu<sub>2</sub>Si<sub>2</sub> 612
  - RSn<sub>3</sub> 495–497, 529, 592
  - sesquioxides 286
- lanthanide f electron structure, standard 574, 595
- lanthanide-like 5f electron structure 582
- lanthanide Mössbauer resonances 557, 562
- lanthanide series 543
- lanthanides 541, 542, 551, 552, 556, 565, 566
  - structure sequence 160, 194
- lanthanum 443
- lanthanum compounds
  - LaAl<sub>2</sub> 50, 51, 451, 452, 454–456, 462, 484
  - LaAl<sub>3</sub> 452
  - LaB<sub>6</sub> 56, 57
  - LaCu<sub>5</sub> 500, 501
  - LaCu<sub>6</sub> 60
  - LaIn<sub>3</sub> 489–492, 495, 496, 529
  - LaM<sub>3</sub> 495
  - LaNi<sub>2</sub> 484
  - LaPb<sub>3</sub> 495
  - LaPt 446, 529
  - LaSb 523
  - LaSn 496, 498
  - LaSn<sub>3</sub> 495, 496, 498, 529
- Laplace's equation 557
- lattice 545
- lattice constant 580, 599
  - for Np monopnictides 603
  - hyperfine parameters, variation of 328
  - variations and stoichiometry 600
- lattice contribution 564
- lattice dynamical information 549
- lattice gradient 558, 627
  - enhancement 559
- lattice parameter, *see* lattice constant
- lattice pressure 562
- lattice sum calculations 559
- lattice vibration 558
- Laves phase compounds 218, 245, 269, 272, 583, 589, 623
  - cubic 583, 596
  - NpX<sub>2</sub> 598
- life times 545
- Lifshitz point 360
- ligand atom 557
- ligand effect 233
- ligand's electron shell 557
- light nuclei 552
- LMTO method, *see* linearized muffin-tin orbital method 166

- line broadening 549, 567, 600
- line shapes 560
- line shifts 550
- line splittings 550
- linearized muffin-tin orbital method 166
- local density approximation (LDA) 3–5, 7, 8, 13, 22, 24, 29, 30, 34, 35, 42–47, 51, 53, 56, 59, 60, 62, 65, 74, 76, 104, 113, 126, 128, 131, 133, 150
- local exchange interactions 210
- local probe 542
- local spin density approximation 3, 5–7, 30, 42, 54, 75
- local spin order
  - random frozen 618
- local susceptibility 554, 577, 625
- local symmetries 558
- localization 411
- localized and delocalized f states
  - dualism between 295
- localized behavior 599, 625
- localized configuration, fully 589
- localized magnetism 542, 570, 577, 578, 591
- localized to delocalized magnetic behaviour 578
- long-range magnetic order 618, 619
- longitudinal polarization 613
- Lorentzian 545, 548, 549
- low-symmetry structures 247
- LSDA, *see* local spin density approximation
- lutetium 443
- lutetium compounds
  - LuAl<sub>2</sub> 450–452, 455, 456
  - LuCo<sub>2</sub> 461, 464, 467, 469, 475, 476, 480, 483, 488, 529
  - LuCu<sub>4</sub> 505
  - LuCu<sub>4</sub>In 505
  - LuFe<sub>2</sub> 470–472, 488
  - LuGa<sub>3</sub> 496
  - LuIn<sub>3</sub> 490, 492, 496
  - LuNi<sub>2</sub> 484
- Madelung contribution 225
- Madelung energy 197
- magic angle 560
- magnetic anisotropy 684, 686, 689, 692, 693, 702
- magnetic atoms 553
- magnetic behavior of NpCr<sub>2</sub>Si<sub>2</sub> 613
- magnetic compounds
  - weakly 608
- magnetic couplings 550
- magnetic critical scattering 694, 702
- magnetic entropy of NpSn<sub>3</sub> 592
- magnetic excitation 352
- magnetic field 553
- magnetic form factor 647, 650, 700
- magnetic history 618, 619
- magnetic hyperfine field, *see also* hyperfine field 553, 585, 614
  - contribution of
    - core polarization 556, 579
    - orbitals 556
    - transferred hyperfine field 579
  - volume dependence 585
- magnetic hyperfine interactions 555
- magnetic hyperfine spectrum 554
- magnetic hyperfine splittings 560
- magnetic instability 623
- magnetic interaction Hamiltonian 552
- magnetic ions
  - reshaping of 304
- magnetic moment 328, 552, 554–556
  - fluctuations 601
  - temperature dependent 307
- magnetic ordering 556, 559, 578, 616, 623, 626
  - temperature 579, 580, 596, 600
- magnetic phase diagram 328, 368
- magnetic relaxation model of Wegener 601
- magnetic relaxation spectra 556
- magnetic response
  - nonlinearities 617
- magnetic spin structure 557
- magnetic splitting 558
- magnetic state 555, 570
  - in NpAl<sub>2</sub> 591
- magnetic structure 628, 665, 673, 682, 683, 686, 688, 690, 700–702
  - changes in 582
  - multi-*k* 666, 670, 678, 679, 682, 697, 700, 702
  - solid solutions 676
  - type-I (↑↓) 579, 592
  - type-IA or ferrimagnetic (↑↑↓) 605
  - type-II double-*k* sequence 606
  - type-II multi-*k* order 606
  - type-II order 606
  - type-I (3*k*) antiferromagnetic order 605
  - wavevector 665
- magnetic susceptibility, *see also* susceptibility 93, 107, 116, 135, 623
  - pressure dependence 317
- magnetic transitions, *see also* magnetic ordering
  - temperature 583, 605
- magnetically split and single-line pattern, superposition 605
- magnetization 460, 461, 489, 508, 554, 555
  - bulk 554, 555
- magnetization density 317, 351, 641, 648, 649, 651–653, 700
- magneto-volume effect 174
- magnetochemistry 302

- magnetoresistance 95, 118, 137, 412, 430, 459, 460, 465, 479, 529, 530
  - Mahan–Nozières–de Dominicis singularity 130, 136
  - Matthiessen rule 412, 418, 456, 476, 529
  - metal–insulator transition 581
  - metamagnetic Nd pnictides 342
  - metamagnetic state 214
  - MgCu<sub>2</sub>-type structure, *see* Laves phase compounds
  - mixed valence, *see also* intermediate valence 94, 95, 99, 102, 104, 128, 381
    - hybridization 383
    - state 266, 506
    - system 575
  - modulated spin structure 609, 627
  - molecular-field approximation 312
  - moment fluctuations 556
  - moment formation 557
  - moment jump 359, 360
  - moment wash-out 345
  - monochalcogenides 248, 276, 283, 602, 603, 605, 610, 667, 668, 676, 677, 681, 701, 702
  - monopnictides 248, 283, 582, 602, 610, 667, 668, 670, 675, 676, 681, 696, 700, 702
  - monopole interaction 552
  - monopole moment 550
  - monopole term 550
  - Monte Carlo calculations 620
  - Mössbauer
    - atoms 556
    - effect 539–629
      - basics of 544
      - excited states 547, 550
      - experiment 542, 549
      - resolution 542, 547
    - high-pressure experiments 578
      - pressure coefficients 578
    - isomer shifts of NpSn<sub>3</sub> 593
    - measurements 352
    - resonance 545, 552, 556, 561, 566
      - <sup>57</sup>Fe 565
      - selected parameters 566
      - standard 565
    - resonance absorption 544, 546–549, 551
    - resonance absorption effect 547
    - resonance condition 545, 546
    - resonance fluorescence 544
    - resonance lineshape 549
    - resonance strength 549
    - resonance width 549, 553
    - resonant atom 551
    - resonant fraction 545, 546, 558
    - resonant isotope 547
    - shift 550, 551
      - chemical influence on 603
      - in a metallic compound 609
    - sources 547, 551, 554, 565
      - activity 547, 565, 566
      - <sup>241</sup>Am 567
      - <sup>241</sup>Am metal 554, 567
      - <sup>243</sup>Am 560, 565, 568, 602
      - <sup>243</sup>Am resonance 607
      - compounds 553
        - <sup>161</sup>Dy 565
        - <sup>151</sup>Eu 551, 560, 565, 572
        - <sup>57</sup>Fe 572
        - <sup>155</sup>Gd 560, 565
        - <sup>127</sup>I 572
        - <sup>237</sup>Np 547, 549, 550, 552–554, 556, 558, 560, 565, 567, 568, 605
          - nuclei 550
          - <sup>232</sup>Pa (84 keV) 568
          - preparation 547
          - <sup>243</sup>Pu 568
          - radiation self-damage 568
          - <sup>121</sup>Sb 605
          - <sup>121</sup>Sb spectroscopy on PuSb 557
          - <sup>151</sup>Sm 551, 565
          - <sup>119</sup>Sn (24 keV) resonance 592
          - <sup>119</sup>Sn spectroscopy 557
          - <sup>125</sup>Te resonances 605
          - <sup>125</sup>Te spectroscopy on UTe 557
          - <sup>238</sup>U 547
          - <sup>238</sup>U resonance 602
          - velocities 548
          - <sup>170</sup>Yb 560, 565
      - spectra 547, 626
        - theoretical 554
      - spectrometer 549, 568
      - spectroscopy 542, 547, 548, 553, 555, 556, 628
        - application to magnetism 555
      - spectrum 548, 549
      - texture effects 558, 560
      - transition 547, 565
      - Zeeman spectra 555
- Mott transition 220
- muffin-tin orbital method 166
- multi-*k* magnetic structure 303, 582
- 
- n*-fold rotational axes 559
- NMR studies 355, 623
- NaCl-type structure, *see also* B2-type compounds 302, 602
- NaI(Tl) scintillation counter 570
- Néel temperature 448, 466, 467, 492, 497, 521, 555, 585, 587, 595, 617
- negative elastic constant 366
- negative feedback loop 569



- neodymium compounds
- NdAl<sub>2</sub> 452, 453, 457
  - NdAs 341
  - NdB<sub>6</sub> 57
  - NdBi 341
  - NdCu<sub>5</sub> 500
  - NdCu<sub>6</sub> 60
  - NdIn<sub>3</sub> 490, 491
  - NdN 341
  - NdNi<sub>2</sub> 484
  - NdP 341<sup>†</sup>
  - NdS 379
  - NdSb 341
  - NdSe 379
  - NdTe 379
  - NdTeNd<sub>x</sub>(La<sub>0.46</sub>Y<sub>0.34</sub>)<sub>1-x</sub>As 343
  - pnictides
    - - metamagnetic 342
- neptunium 441, 518, 544, 558, 561, 562, 565, 578
- α-Np 443:
  - charge state 609, 627
  - health hazard of 568
  - moment on 561
  - Np<sup>3+</sup> 610
    - - free-ion hyperfine field 602
    - - <sup>5</sup>I<sub>4</sub> (5f<sup>4</sup>) ground state of 609, 613, 614
  - <sup>237</sup>Np 547, 549, 550, 552-554, 556, 558, 560, 565, 567, 568, 605
  - Np-Np separation 598, 599
  - Np-Np spacing 582
  - Np ion, localized trivalent 613
  - Np sublattice 616
- neptunium alloys
- NpOs<sub>2-x</sub>Ru<sub>x</sub> 598
- neptunium compounds
- monopnictides 603, 604
  - neptunyl compounds 562
    - - hexavalent 562
    - - pentavalent 562
  - NpAl<sub>2</sub> 51, 461, 465, 552, 584, 589, 590, 592, 596, 598, 610
    - - ferromagnetic 554
  - NpAl<sub>3</sub> 607, 609
  - NpAs 344, 511-514, 528, 582, 592, 595, 602-604, 671-673, 680
    - - hyperfine field 605
    - - magnetic phase diagram 582, 584, 605
    - - pressure dependence
      - - - hyperfine field 582, 583
      - - - isomer shift 582, 583
      - - - Néel temperature 582, 583
  - NpAs<sub>2</sub> 602
  - NpAs<sub>x</sub>Se<sub>1-x</sub> 348
    - NpBe<sub>13</sub> 577, 623-625
    - NpBi 344, 512, 514, 515, 517, 518, 528, 582, 603-605
    - NpC 603, 610
    - NpCo<sub>2-x</sub> 600
    - NpCo<sub>2</sub> 599-601, 610, 661, 683, 691
    - NpCo<sub>2</sub>Ge<sub>2</sub> 611
    - NpCo<sub>2</sub>Si<sub>2</sub> 588, 592, 595, 610, 611, 617
    - NpCr<sub>4</sub>Al<sub>8</sub> 615
    - NpCr<sub>2</sub>Ge<sub>2</sub> 611
    - NpCr<sub>2</sub>Si<sub>2</sub> 611
    - NpCu<sub>4</sub>Al<sub>8</sub> 615-617, 625, 627
      - - tetragonal distortion 616
    - NpCu<sub>2</sub>Ge<sub>2</sub> 611
    - NpCu<sub>2</sub>Si<sub>2</sub> 611-614, 616, 617
    - NpF<sub>3</sub> 551
    - NpF<sub>4</sub> 551
    - NpFe 600
      - NpFe<sub>2</sub> 473, 599, 600
      - NpFe<sub>4</sub>Al<sub>8</sub> 618, 620, 621
      - NpFe<sub>2</sub>Ge<sub>2</sub> 611
      - NpFe<sub>2</sub>Si<sub>2</sub> 611
    - NpGa<sub>2</sub> 602
    - NpGa<sub>3</sub> 607, 609
    - NpGe<sub>2</sub> 602
    - NpGe<sub>3</sub> 607
    - NpIn<sub>3</sub> 494, 607-609
    - Np intermetallics 609
      - - with the ThCr<sub>2</sub>Si<sub>2</sub> structure 611
    - NpIr<sub>2</sub> 598, 610, 623-625
    - NpM<sub>4</sub>Al<sub>8</sub> 615
    - NpM<sub>2</sub>Ge<sub>2</sub> compounds 610
    - NpM<sub>2</sub>Si<sub>2</sub> 610
    - NpM<sub>2</sub>X<sub>2</sub> series 613
    - NpMn<sub>2</sub> 599
      - NpMn<sub>2</sub>Ge<sub>2</sub> 611
      - NpMn<sub>2</sub>Si<sub>2</sub> 611
    - NpN 344, 582, 603, 604, 610
    - NpNi<sub>2</sub> 599, 600
    - NpNi<sub>2</sub>Ge<sub>2</sub> 611
    - NpNi<sub>2</sub>Si<sub>2</sub> 611
    - NpOs<sub>2</sub> 584, 589-592, 596, 598, 610, 623-625
    - NpP 344, 582, 603, 604
    - NpPd<sub>3</sub> 607, 608
    - NpPd<sub>2</sub>Al<sub>3</sub> 625-627
    - NpPd<sub>2</sub>Si<sub>2</sub> 611
    - NpPt 448, 449
    - NpPt<sub>3</sub> 607
    - NpRh<sub>3</sub> 607, 608
    - NpRh<sub>2</sub>Ge<sub>2</sub> 611
    - NpRh<sub>2</sub>Si<sub>2</sub> 611
    - NpRu<sub>2</sub> 598, 610, 623, 624
    - NpRu<sub>2</sub>Si<sub>2</sub> 611, 613, 625, 627, 688, 701

- neptunium compounds (*cont'd*)
- NpS 377, 517, 518, 528, 582, 603, 605, 675, 701
  - NpSb 344, 511-514, 528, 603-605
  - NpSb<sub>2</sub> 602
  - NpSb-NpTe 379
  - NpSb<sub>x</sub>Te<sub>1-x</sub> 348
  - NpSb<sub>1-x</sub>Te<sub>x</sub> 605
  - NpSe 377, 517, 518, 528, 582, 603, 606, 675, 680, 701
  - NpSi<sub>2</sub> 602
  - NpSi<sub>3</sub> 607, 608
  - Np silicides 613
  - NpSn<sub>3</sub> 22, 24-26, 494, 499, 557, 560, 591, 592, 595, 607-609, 625, 627
  - - antiferromagnetic 561
  - - localized electron behavior 593
  - NpTe 377, 517, 518, 582, 603, 606, 675, 676, 681, 682, 701
  - NpTe<sub>2</sub> 602
  - NpX 582, 604
  - NpX<sub>2</sub> 610
  - - Laves phase compounds 598-600
  - - (X = As, Sb, Te) 602
  - NpX<sub>3</sub> 607
- neutron absorption 681
- neutron activation 565
- of <sup>242</sup>Pu 568
- neutron diffraction 595, 600, 605, 613, 616, 618, 620, 622, 625
- neutron paramagnetic form factor 99
- neutron scattering 592, 602
- line shape 112, 126, 140
- neutron-nuclei interactions 636
- neutrons
- absorption 637, 639
  - coherent cross section 640
  - comparisons with X-rays 637
  - cross sections 638
  - fissions 638
  - incoherent cross section 640
  - interaction with nuclei 636, 639
  - magnetic interaction 637, 640, 692, 694
- non-Lorentzian lines 556
- noncollinear structure 304, 582, 605
- Nordheim-Gorter rule 412, 418, 419, 453, 454, 529
- normalized stress 260
- nuclear charge 550
- mean squared radius of 550
- occupation numbers
- partial 188
- open shell electrons 553, 556, 559
- optical measurements 363
- orbital angular momentum 556
- orbital hyperfine field 559
- orbital moment 577, 647, 650, 656, ~~660~~, ~~661~~, 663, 664, 685, 700, 702
- orbitally driven 342
- anisotropic hybridization 593
- ordered magnetic moment 557, 562, 609, 617
- ordered magnetic state 555
- ordered magnets 553
- outer-shell electrons 556
- p-d mixing 311
- paramagnetic hyperfine spectra 555
- paramagnetic moments 314
- paramagnetic relaxation 594
- paramagnetism
- temperature independent 305, 609
- paramagnon drag 463, 464, 481
- partition function 575
- PbCl<sub>2</sub>-type structure 290, 291
- phase purity 628
- phase transition 245, 270, 582, 642
- of second order 626
- phonon
- LA 141, 143
- phonon drag 464, 480, 492
- phonon processes
- multi 546
  - one 546
  - zero 546
- phonon softening 141
- phonon spectrum 546
- photoemission 389
- photoemission experiments 232
- plutonium 441, 444
- α-Pu 441, 443, 445
  - β-Pu 445, 446
  - δ-Pu 442, 443, 568
  - <sup>243</sup>Pu 568
  - saturation magnetization 448
- plutonium alloys
- Pu-Am 268
- plutonium compounds
- PuAl<sub>2</sub> 461, 465, 568
  - PuAl<sub>4</sub> 568
  - PuAs 348, 674
  - PuBi 348
  - PuFe<sub>2</sub> 473, 661
  - PuN 348
  - PuP 348
  - PuPt 448
  - PuS 387, 518-520

- plutonium compounds (*cont'd*)  
 – PuSb 348, 514, 515, 520, 651, 653, 674, 675,  
   681, 696, 700, 702  
 – –  $^{243}\text{PuSb}$  607  
 –  $\text{PuSb}_x\text{Te}_{1-x}$  352  
 – PuSe 387, 518, 519  
 –  $\text{PuSn}_3$  22, 25  
 – PuTe 352, 387, 518–520, 659, 676, 681, 682,  
   700  
 pnictides 277, 281, 303  
 – stability ranges 278, 279  
 pnictogen–chalcogen systems 373  
 polarized neutron 642, 652, 683  
 powder, averaging in 558  
 $\text{PrNi}_2\text{Al}_3$ -type structure 625  
 praseodymium 28, 37  
 praseodymium compounds  
 –  $\text{PrAl}_2$  452, 453, 457  
 – PrAs 317  
 –  $\text{PrB}_6$  57  
 – PrBi 317  
 –  $\text{PrCu}_5$  500, 501  
 –  $\text{PrCu}_6$  60  
 –  $\text{PrIn}_3$  490, 491  
 – PrN 317  
 –  $\text{PrNi}_2$  484  
 – PrP 317  
 – PrS 319  
 – PrSb 317  
 – PrSe 319  
 – PrTe 319  
 preferred orientation effects 620  
 pressure derivative 270, 275, 281, 286, 289, 291  
 pressure-induced structural transitions 274, 277,  
   282, 289  
 pressure–temperature-induced transition 287, 288,  
   291  
 promethium alloys  
 –  $\text{Pm}_{0.7}\text{Sm}_{0.3}$  268  
 promotion energy 203  
 promotion of electrons 295  
 pseudobinary alloys 232, 234, 303  
 –  $\text{NpOs}_2-x\text{Ru}_x$  598  
 –  $\text{Tb}_2\text{Y}_{1-x}\text{Sb}$  321  
  
 quadrupole contribution 342  
 quadrupole coupling 557  
 – magnetically induced 588  
 quadrupole  $\gamma$ -transitions 553  
 quadrupole hyperfine spectrum 558  
 quadrupole interaction 559, 622  
 – induced 582  
 – magnetically induced 559, 604  
 quadrupole moment 550  
  
 quadrupole pattern 558, 626  
 quadrupole splittings 561  
 – in cubic crystalline surroundings 559  
  
 radiation damage 305  
 reactivity 302  
 recoil-free fraction 545–547  
 – temperature dependence 547  
 reduced matrix element 556, 559  
 reflection spectra 581  
 relativistic charge densities  $\rho(\mathbf{r})$  551  
 relativistic (Dirac–Fock) calculations 556  
 relativistic effect 542, 547  
 relativistic nature 577  
 relativistic theory 556  
 relativistic volume effect 175  
 relaxation formalism 601  
 relaxation phenomena 600  
 relaxation processes 591  
 relaxation rates 591, 616  
 relaxation spectrum 552, 556  
 renormalized band 3  
 – theories 8, 9  
 residual resistivity 452–454  
 residual resistivity ratio 437, 482  
 resistivity 95, 117, 453, 460–462, 464–470,  
   473–476, 479, 480, 482, 484, 485, 488, 489,  
   491, 492, 494, 496–500, 504, 505, 508, 509,  
   511, 512, 514, 517, 520, 524, 528, 529, 609  
 – rare earth and actinide metals 437–446  
 rhombohedral distortion 339  
 RKKY exchange 386  
 RKKY formalism 585, 587  
 RKKY interaction 428, 622  
 – long range 582  
 Rudermann–Kittel–Arrott formalism 595  
 – model for localized spins 588  
 – rigid-spin model 593  
 Russell–Saunders (RS) coupling 657  
  
 s-character 562  
 s electrons, shielding 581  
 S-state compounds 311  
 S-state ions 307  
 samarium 574  
 –  $^{151}\text{Sm}$  551, 565  
 samarium compounds 659  
 –  $\text{SmAl}_2$  450, 452, 453, 457  
 – SmAs 305  
 – SmBi 305  
 –  $\text{SmCu}_5$  500  
 –  $\text{SmF}_3$  551  
 –  $\text{SmFe}_2$  485  
 –  $\text{SmIn}_3$  491, 492

- samarium compounds (*cont'd*)
- SmMn<sub>2</sub> 465
  - SmN 305
  - SmNi<sub>2</sub> 484, 485
  - SmP 305
  - SmS 46, 47, 381
  - SmSb 305
  - SmSe 381
  - SmSn 498
  - SmSn<sub>3</sub> 497
  - SmTe 381
- satellites 618
- scaling rules 245, 265
- scandium compounds
- ScAl<sub>2</sub> 451, 452
  - ScCo<sub>2</sub> 464, 475, 480, 529
- scattering length 639
- screening factor 379
- second-order Doppler shift 547, 552
- self-irradiation 438
- semiconductor→metal transition 276
- semimetal 510, 511, 515, 522
- shifted homology 268, 282, 283
- short-range anisotropic exchange interaction 582
- short-range correlations 606
- short-range order 608
- spin-glass type 600
- short-range ordered materials 555
- singlet ground state 304, 314
- sinusoidal modulation 582
- site exchange 622
- between Al and Cu 617
- skew scattering 464, 465
- slave-boson 3, 9, 68
- slow paramagnetic relaxation 616
- slow-relaxing paramagnetic hyperfine spectrum 617
- Sommerfeld constant, *see* electronic specific heat coefficient
- specific heat 91, 109, 116, 123, 133
- data 592, 623
  - measurements 306, 335
- spin correlations 363
- spin density
- unpaired 556
- spin disorder 450, 620, 622
- scattering 422
- spin dynamic 383
- spin fluctuation 20, 31–33, 69, 70, 72–74, 424, 426, 441, 445, 460–465, 467–469, 474–481, 483, 488, 493, 499, 529, 530, 627
- compound 236
  - model 424
  - resonance 119
  - temperature 476, 483
- spin glass 312, 555, 619, 620, 622, 691
- aligned 619
  - behavior 544, 615, 617
  - temperature 618, 619
  - two-dimensional 622
- spin-glass systems, concentrated 618
- spin-glass systems, dilute 620
- spin lattice
- randomness in 619
- spin moment 647, 650, 656, 660, 661, 663, 664, 685, 702
- spin order
- randomized 601
- spin polarization 177
- of s-like and non s-like conduction electrons 586
- spin relaxation times 618
- spin-reorientation 310
- spin wave scattering 440
- spin-orbit coupling 550, 577
- spin-orbit coupling and orbital polarization
- relativistic treatment of 598
- spin-orbit splitting 176
- square wave 644
- square-well pseudopotential 186
- Sternheimer antishielding factor 559, 627
- Sternheimer shielding factor *R*, inner 559
- Stoner criterion 598
- Stoner factor 424
- strong correlation 625
- strong hybridization 354
- strong magnetism 608
- structural systematics 293
- structure constants 167
- sum rules 417, 418, 529
- superconducting state, instability of 623
- supertransferred field 579
- surrounding charges 550
- susceptibility, *see also* magnetic susceptibility
- 123, 308, 450, 459, 460, 463, 465, 469, 475, 482, 484, 489, 494–496, 500, 504, 505, 518, 528
  - enhancement of 625
  - measurements 619
- symmetry
- random distortions of 617
- synchrotron X-rays 674, 679, 689, 702
- terbium compounds
- chalcogenides 338
  - TbAl<sub>2</sub> 450, 452, 453, 455, 457
  - TbAs 320
  - TbBi 320
  - TbCo<sub>2</sub> 481

- terbium compounds (*cont'd*)
- TbFe<sub>2</sub> 470–472
  - TbFe<sub>4</sub>Al<sub>8</sub> 618, 622
  - TbIn<sub>3</sub> 491, 492
  - TbN 320
  - TbNi<sub>2</sub> 484
  - TbP 320
  - TbSb 320
  - Tb<sub>2</sub>Y<sub>1-z</sub>Sb 321
- ternary and quaternary compounds 245, 294
- tetragonal high-pressure structures 280
- Th<sub>3</sub>P<sub>4</sub>-type structure 285
- thermal conductivity 413, 414, 421, 429, 455, 456, 485, 503, 529
- thermal resistivity, *see also* thermal conductivity 456
- thermopower 137, 413, 414, 421, 429, 452–455, 463, 464, 468, 469, 471–473, 480–482, 485, 486, 488, 491, 492, 502, 506, 529
- thermoremanent magnetization 622
- thorium 441, 444
- thorium compounds
- ThBe<sub>13</sub> 269
  - ThC 45, 46
  - ThCr<sub>2</sub>Si<sub>2</sub> 610, 615
  - ThFe<sub>4</sub>Al<sub>8</sub> 618, 622
  - ThPt 448, 529
- thulium 574
- thulium compounds
- TmAl<sub>2</sub> 455
  - TmAs 314
  - TmCo<sub>2</sub> 475, 481
  - TmFe<sub>2</sub> 470–472
  - TmIn<sub>3</sub> 490
  - TmMn<sub>2</sub> 466
  - TmN 314
  - TmNi<sub>2</sub> 484
  - TmP 314
  - TmS 382
  - TmSb 314
  - TmSe 46, 47, 382
  - TmTe 46, 47, 382
  - Tm<sub>0.53</sub>Y<sub>0.47</sub>Sb 315
- TiNi<sub>3</sub>-type structure 608
- total energy 198
- transition energy 547, 552, 565
- transition pressures 250, 279, 284, 288
- forward 264
- uranium 444, 544, 577
- α-U 443, 642–646
  - – superconducting 689
  - <sup>238</sup>U 547
  - <sup>238</sup>U resonance 602
- uranium alloys, *see also* uranium compounds 412
- U–Np 268
- uranium compounds
- intermetallics 412
  - mononpnictides 606
  - UAl<sub>2</sub> 51, 460–465, 467, 529
  - UAl<sub>3</sub> 483
  - UAs 354, 507–511, 670, 671, 678, 695, 698
  - UAs–ThAs 368
  - UAs–ThSe 369
  - UAs–US 374
  - UAs–USe 375
  - UAs–YAs 369
  - UB<sub>12</sub> 61
  - UB<sub>13</sub> 69
  - UBe<sub>13</sub> 61, 67, 68
  - UBi 354
  - UC 45, 46
  - UCo<sub>x</sub> 482
  - UCo<sub>2</sub> 482, 486, 488
  - UCoAl 684
  - UCu<sub>2</sub> 53
  - UCu<sub>5</sub> 52, 54, 500, 505, 506
  - UCu<sub>4+x</sub>Al<sub>5-x</sub> 617
  - UFe<sub>2</sub> 473, 474, 486, 488, 493, 530, 602, 661
  - UFe<sub>4</sub>Al<sub>8</sub> 618, 620, 621
  - UGe<sub>3</sub> 10, 15, 18–21, 498
  - UIn<sub>3</sub> 10, 11, 26, 493, 494
  - UIn<sub>1-x</sub>Sn<sub>x</sub> 27
  - UIr<sub>3</sub> 10, 12, 14, 15
  - UMn<sub>2</sub> 466, 469, 486, 488
  - UN 354, 507, 508
  - UNi<sub>2</sub> 486–488, 661
  - UNi<sub>5</sub> 506
  - UNi<sub>2</sub>Pd<sub>3</sub> 625
  - UNi<sub>2</sub>Si<sub>2</sub> 686
  - UP 354, 507–510
  - UP–ThP 368
  - UP–UAs 373
  - UP–US 373
  - UP–USe 373
  - UPb<sub>3</sub> 10, 11, 18, 19, 498
  - UPd<sub>3</sub> 11, 28, 34–37
  - UPd<sub>2</sub>Al<sub>3</sub> 625, 627
  - UPdSn 686, 700
  - UPt 448, 449
  - UPt<sub>3</sub> 28, 29, 31–37, 67–71, 269, 464, 625, 689, 699
  - U<sub>2</sub>PtC<sub>2</sub> 67, 68
  - URh 10, 12
  - URh<sub>3</sub> 14, 15, 17
  - URhAl 663, 684
  - URu 12
  - URu<sub>3</sub> 10, 14

- uranium compounds (*cont'd*)
- URu<sub>2</sub>Si<sub>2</sub> 63, 66–69, 269, 625, 687, 689
  - US 363, 516, 692–694
  - US–ThS 367
  - US–YS 367
  - USb 354, 510–512, 528, 650, 679, 694, 695, 697, 699, 700, 702
  - USb–ThSb 370
  - USb–UTe 375
  - USb–YSb 371
  - USb<sub>0.9</sub>Te<sub>0.1</sub> 354
  - USe 363, 516
  - USe–ThSe 367
  - USi<sub>3</sub> 18–20, 498, 499
  - USn<sub>3</sub> 10, 18–20, 22, 24, 498, 499, 627
  - UTe 363, 516
  - UTe–LaTe 367
  - UTe–YTe 367
- valence
- bond energies 202
  - change 396
  - - continuous 581
  - electron shell 577
  - fluctuation 381, 502, 574, 576, 578, 591
  - mean value from isomer shift 574
  - of Eu in EuAl<sub>2</sub> 585
  - of Eu in EuO 579
  - stable 304, 580
  - - divalent 595
  - transition 505
  - unstable 304, 381, 574–576, 582
- valencies, assignment of 152
- van der Waals interaction 173
- van Vleck formula 319
- Vegard's law 217
- virtual crystal approximation 234
- volume change 217, 587
- decrease 288
  - of conduction electron polarization 587
- volume coefficient 577, 578, 590, 592, 595, 596
- of magnetic moment (hyperfine field) 596
- volume collapse, *see also* isostructural volume collapse 206, 251
- volume–pressure relation 585
- wavevector 665
- Weiss molecular field 308
- Wiedemann–Franz law 419, 423, 426, 456, 459
- Wigner–Seitz radius 251
- Wilson ratio 625
- ytterbium 542, 561, 565, 578
- divalent 594
  - Yb<sup>2+</sup> 574
  - Yb<sup>3+</sup> ion 594
  - <sup>170</sup>Yb 560, 565
- ytterbium compounds
- YbAl<sub>2</sub> 450
  - YbAs 384
  - YbCu<sub>4</sub> 505, 530
  - YbCu<sub>5</sub> 504
  - YbCu<sub>4</sub>Ag 505
  - YbCuAl 593, 594
  - YbCu<sub>4</sub>In 505
  - YbN 384
  - YbP 384
  - YbSb 384
- yttrium 443
- yttrium compounds
- YAl<sub>2</sub> 451–456, 458, 459, 476, 529, 530
  - YCo<sub>2</sub> 461, 464, 467, 469, 474–477, 479–481, 483, 488, 529, 530
  - YFe<sub>2</sub> 470–473, 488
  - YFe<sub>4</sub>Al<sub>8</sub> 618, 622
  - YMn<sub>2</sub> 466–468
  - YNi<sub>2</sub> 483–486, 529
  - YSb 321
- Zeeman interaction 554, 558
- Zeeman pattern 615, 624
- Zeeman splitting 553–555, 591
- zero-phonon line 545–548, 550
- zero-phonon transition 545
- zero point 552
- zero-point motion 546